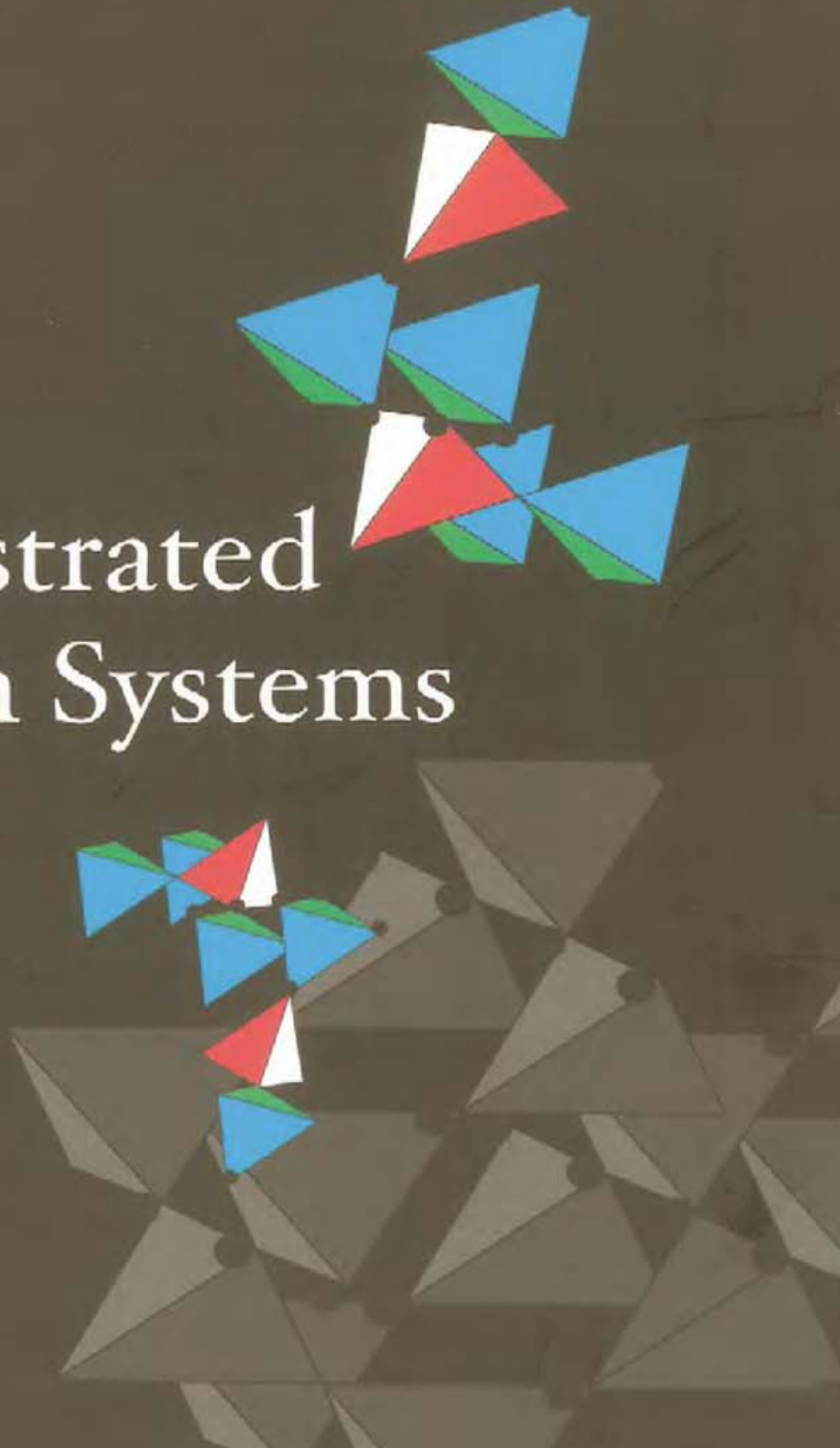
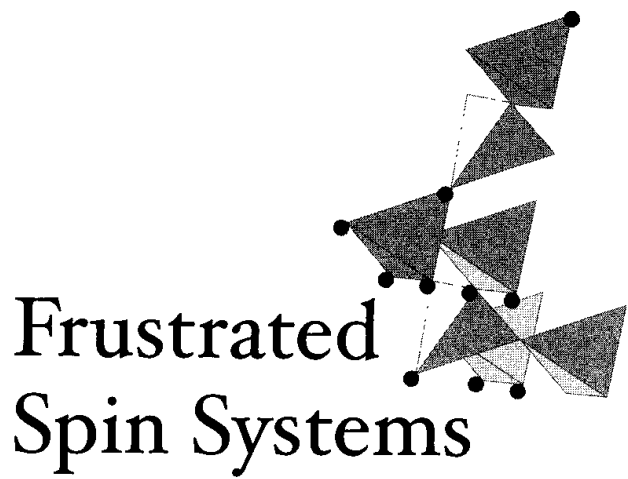


H. T. Diep *editor*

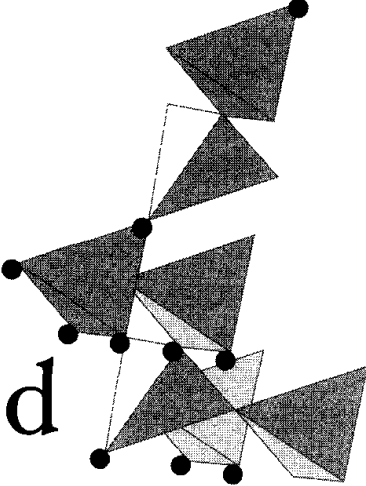
# Frustrated Spin Systems





Frustrated  
Spin Systems





# Frustrated Spin Systems

*editor*

**H. T. Diep**

*University of Cergy-Pontoise, France*



NEW JERSEY • LONDON • SINGAPORE • BEIJING • SHANGHAI • HONG KONG • TAIPEI • CHENNAI

*Published by*

World Scientific Publishing Co. Pte. Ltd.

5 Toh Tuck Link, Singapore 596224

*USA office:* 27 Warren Street, Suite 401-402, Hackensack, NJ 07601

*UK office:* 57 Shelton Street, Covent Garden, London WC2H 9HE

**British Library Cataloguing-in-Publication Data**

A catalogue record for this book is available from the British Library.

**FRUSTRATED SPIN SYSTEMS**

Copyright © 2004 by World Scientific Publishing Co. Pte. Ltd.

*All rights reserved. This book, or parts thereof, may not be reproduced in any form or by any means, electronic or mechanical, including photocopying, recording or any information storage and retrieval system now known or to be invented, without written permission from the Publisher.*

For photocopying of material in this volume, please pay a copying fee through the Copyright Clearance Center, Inc., 222 Rosewood Drive, Danvers, MA 01923, USA. In this case permission to photocopy is not required from the publisher.

ISBN 981-256-091-2

## PREFACE

This book covers recent theoretical, numerical and experimental developments in the field of frustrated spin systems. The first edition of the book appeared in 1994 under the title " Magnetic Systems with Competing Interactions" (World Scientific) where most of works until that year have been reviewed.

The present book contains nine chapters, seven of them are new. Two chapters of the first edition have been revised with new references and comments added: these are chapter 1, Frustration - Exactly Solved Frustrated Models, and chapter 2, Properties and Phase Transition in Frustrated Spin Systems.

Frustrated spin systems have been first investigated five decades ago. Well-known examples include the Ising model on the antiferromagnetic triangular lattice studied by G. H. Wannier in 1950 and the Heisenberg helical structure discovered independently by A. Yoshimori, J. Villain and T. A. Kaplan in 1959. However, extensive investigations on frustrated spin systems have really started with the concept of frustration introduced at the same time by G. Toulouse and J. Villain in 1977 in the context of spin glasses. The frustration is generated by the competition of different kinds of interaction and/or by the lattice geometry. As a result, in the ground state all bonds are not fully satisfied. In frustrated Ising spin systems, a number of spins behave as free spins. In frustrated vector spin systems, the ground-state configuration is usually non-collinear. The ground-state of frustrated spin systems is therefore highly degenerate and new induced symmetries give rise to spectacular and often unexpected behaviors at finite temperatures.

Many properties of frustrated systems are still not well understood at present. Recent studies shown in this book reveal that established theories, numerical simulations as well as experimental techniques have encountered many difficulties in dealing with frustrated systems. In some sense, frus-

trated systems provide an excellent testing ground for approximations and theories.

The chapters of this book are written by researchers who have actively contributed to the field. Many results are from recent works of the authors.

The book is intended for post-graduate students as well as researchers in statistical physics, magnetism, materials science and various domains where real systems can be described with the spin language. Explicit demonstrations of formulae and full arguments leading to important results are given where it is possible to do so.

The book is organized as follows. The first two chapters deal with properties and phase transition in frustrated Ising spin systems. The two following chapters deal with the nature of the phase transition in frustrated vector spin systems. Chapters 5 and 6 treat low-dimensional frustrated quantum spin models. Chapter 7 studies the spin ice and chapter 8 shows recent experimental results on pyrochlores which are real frustrated materials. Chapter 9 deals with the classical and quantum spin glasses where both disorder and frustration act simultaneously.

I summarize in the following the contents of each chapter.

Chapter 1 shows the frustration effects in exactly solved two-dimensional Ising models. The systems considered in this chapter are periodically defined (without bond disorder). The frustration due to competing interactions will itself induce disorder in the spin orientations. After a detailed presentation of 16- and 32-vertex models, applications are made to some selected systems which possess most of the spectacular features due to the frustration such as high ground-state degeneracy, reentrance, successive phase transitions and disorder solutions. In some simple models, up to five transitions separated by two reentrant paramagnetic phases are found. A conjecture is made on the origin of the paramagnetic reentrant phase. The nature of ordering as well as the relation between the considered systems and the random-field Ising model are discussed. The relevance of disorder solutions for the reentrance phenomena is also pointed out. Evidence of the existence of partial disorder and of reentrance in complicated, non exactly solved systems is shown and discussed.

Chapter 2 deals mainly with the Ising model on the antiferromagnetic triangular and stacked triangular lattices. Ground-state properties and the nature of the phase transition are studied by various methods, as functions of the spin magnitude  $S$  and nearest- and next-nearest-neighbor interactions. It is shown in this chapter that the symmetry of spin ordering strongly depends on  $S$ . Furthermore, due to the frustration, there exist "free" spins

or "free" linear-chains, on which internal fields are cancelled out. These free spins and free linear-chains play an important role as for spin orderings. Another characteristic feature of frustrated Ising spin systems is the existence of various metastable states which is closely related to the degeneracy of ground state and also to the excited states. These metastable states may give rise to a first order phase transition as found in some models. The effects of the far-neighbor interactions on the antiferromagnetic triangular and stacked triangular lattices are clarified.

Chapter 3 is devoted to the recent advances in the renormalization group (RG) approaches to the physics of frustrated classical vector spin systems in three dimensions. The main features of the field theoretical approach to these systems including considerations on symmetries, symmetry breaking schemes, continuum limits, topological contents, ... are recalled here. An overview is provided on the phenomenological situation with emphasis put on the most striking aspect of the physics of frustrated magnets: the existence of *non universal scaling* behaviors. A review is then given on the various perturbative and non-perturbative RG approaches that have been used to investigate frustrated magnets. Finally, a large part of this chapter is devoted to a recent non-perturbative approach that has clarified the intricate physical situation of frustrated magnets.

Chapter 4 is devoted to a review on recent numerical studies dealing with frustrated vector spin systems between two and four dimensions. It is shown that various breakdowns of symmetry can occur, contrary to the case of ferromagnetic systems. The author shows that in three dimensions the transition is always of first order in the thermodynamic limit. However for "small" sizes in numerical simulations or for temperatures not "too close" to the transition temperatures in experiments, the system could display an "almost universality class" for an  $O(N)/O(N-2)$  breakdown of symmetry. Many compounds studied experimentally are in this class. In two dimensions the situation is much less clear. Indeed the topological defects can play a fundamental role and their couplings with a discrete symmetry (Ising or Potts models) is not well known. In contrast to the two-dimensional case, our understanding of the three-dimensional case has increased considerably in the last decade.

Chapter 5 is devoted to a review on some theoretical advances in the field of quantum magnetism in two-dimensional systems. It is known that the spin- $\frac{1}{2}$  nearest-neighbor 2-dimensional Heisenberg models on Bravais lattices (square, triangular) are Néel ordered at  $T = 0$ . Frustration, small coordination number, competition between interactions can lead to specific

quantum phases without magnetic long-ranged order. This long-standing subject is revived by the discovery of high- $T_c$  superconductivity in the doped cuprates and fuelled by numerous experimental studies of 2D antiferromagnetic insulators. The authors of this chapter show results on several models. They show also general properties of valence-bond crystals (VBC) and related states, as well as large- $N$  generalizations of the Heisenberg model. Some results of quantum dimer models (QDM) are presented. They provide useful insights onto the phenomenology of VBC and other systems. The authors also review some results concerning models with multiple-spin exchange and the Heisenberg model on the Kagomé lattice (and related models). Despite of an important activity on this subject, the understanding of the low-energy physics of the spin- $\frac{1}{2}$  Kagomé antiferromagnet remains a challenging problem.

Chapter 6 is devoted to an overview of some of the zero-temperature quantum spin liquid phases with unbroken SU(2) spin symmetry that have been found in one dimension. The main characteristics of these phases are discussed by means of the bosonization approach. A special emphasis is put on the interplay between frustration and quantum fluctuations in one dimension. The author presents the different spin liquid phases that occur in spin chains and spin ladders. The main effects of frustration in one-dimensional spin liquids are described. In particular, it is observed that frustration plays its trick by allowing deconfined spinons (carrying fractional  $S = 1/2$  quantum number) as elementary excitations and it provides a non-trivial source of incommensurability.

Chapter 7 is devoted to the theoretical and experimental study of so-called “spin ice”, the magnetic equivalent of Pauling’s model of hydrogen disorder in water ice. This represents the prototypical frustrated system, with a macroscopically degenerate ground state and extensive zero point entropy. Pauling’s concept was extended by Wannier, Anderson and others to include magnetic systems and was later developed to include statistical “vertex models”, some of which are exactly soluble (see Chapter 1). Spin Ice is a sixteen vertex model of “ferromagnetic frustration” that, remarkably, is found to apply to certain rare earth oxide materials. The search for a detailed microscopic understanding of these spin ice materials has cast light on many aspects of magnetic frustration and uncovered several new features of magnetic interactions (particularly the dipole interaction). For these reasons, spin ice represents an ideal laboratory in which to develop our understanding of frustrated spin systems. This chapter is a comprehensive review of the physics of spin ice including both theoretical and experimental

aspects. The authors start with the concept of spin ice and its relation to the historic problem of water ice and to other frustrated systems. The following sections review the current understanding of the zero field spin ice state, the numerous field-induced states and the magnetic dynamics of the spin ice materials. Some materials related to spin ice are briefly described.

Chapter 8 describes experimental results on geometrically-frustrated magnetic systems. Much recent experimental progress has been made in the study of magnetic materials made up of antiferromagnetically-coupled magnetic moments residing on networks of corner-sharing tetrahedra. They are found in nature in a variety of cubic pyrochlore, spinel and Laves phase materials, with the magnetic moments arising from either rare earth or transition metal electrons. This review focusses on experimental progress in this area from the last ten years primarily due to neutron scattering studies. Even within this subset of three frustrated materials, quite different exotic ground states are found: the enigmatic cooperative paramagnetic ground state of  $Tb_2Ti_2O_7$ ; the spin glass ground state of  $Y_2Mo_2O_7$ ; and the composite spin degrees of freedom and distorted pyrochlore lattice in  $ZnCr_2O_4$ . It is very rewarding to appreciate the richness of the complex ground states which geometrical frustration has enabled in these real materials. There seems little doubt that this richness will continue as a theme in the elucidation of the physical properties of geometrically frustrated magnets in the near future.

Chapter 9 is devoted to a review on recent progress in spin glasses. Both the equilibrium properties and the dynamic properties are covered. The authors focus on progress in theoretical, in particular numerical, studies, while its relationship to real magnetic materials is also mentioned. A brief overview of two well-known paradigms on spin glasses is given and a summary of the predictions derived from them is presented. Then, equilibrium properties of Ising spin glass models are shown and discussed. In particular, a recent active debate, as to which paradigm is appropriate for realistic short-range spin glass models in three dimensions, is presented. Then, the dynamical properties are examined using these paradigms on a different ground, with an emphasis on aging phenomena. Some other non-equilibrium properties are also discussed. Models with continuous degrees of freedom as well as the Potts spin glass models are mentioned. The effects of weak disorder are discussed and compared to those of strong disorder. Several exact relations can be found and play an important role in shedding light on the issue under debate. Finally, results from the interplay between quantum fluctuations and randomness in spin glasses are also reviewed.

Since several problems treated in this book are currently investigated, I alert the reader that the authors of each chapter have taken the liberty to express their viewpoint on each unsettled issue.

H. T. Diep  
University of Cergy-Pontoise  
Cergy-Pontoise, France

## CONTENTS

<i>Preface</i>	v
----------------	---

<b>1 FRUSTRATION - EXACTLY SOLVED</b>	
<b>FRUSTRATED MODELS</b>	<b>1</b>
<i>H. T. Diep and H. Giacomini</i>	
1.1 Frustration: an introduction . . . . .	1
1.1.1 Definition . . . . .	2
1.1.2 Non collinear spin configurations . . . . .	5
1.2 Frustrated Ising spin systems . . . . .	8
1.3 Mapping between Ising models and vertex models . . . . .	10
1.3.1 The 16-vertex model . . . . .	10
1.3.2 The 32-vertex model . . . . .	12
1.3.3 Disorder solutions for two-dimensional Ising models	23
1.4 Reentrance in exactly solved frustrated Ising spin systems .	26
1.4.1 Centered square lattice . . . . .	27
1.4.1.1 Phase diagram . . . . .	28
1.4.1.2 Nature of ordering and disorder solutions .	28
1.4.2 Kagomé lattice . . . . .	31
1.4.2.1 Model with nn and nnn interactions . . . . .	31
1.4.2.2 Generalized Kagomé lattice . . . . .	31
1.4.3 Centered honeycomb lattice . . . . .	37
1.4.4 Periodically dilute centered square lattices . . . . .	40
1.4.4.1 Model with three centers . . . . .	44
1.4.4.2 Model with two adjacent centers . . . . .	46
1.4.4.3 Model with one center . . . . .	47
1.4.5 Random-field aspects of the models . . . . .	48

1.5 Evidence of partial disorder and reentrance in other frustrated systems . . . . .	50
1.6 Conclusion . . . . .	54
Acknowledgements . . . . .	57
References . . . . .	57
<b>2 PROPERTIES AND PHASE TRANSITIONS IN FRUSTRATED ISING SYSTEMS</b>	<b>59</b>
<i>Ojiro Nagai, Tsuyoshi Horiguchi and Seiji Miyashita</i>	
2.1 Introduction . . . . .	59
2.2 Ising model on two-dimensional frustrated lattice and on stacked frustrated lattice . . . . .	62
2.3 Ising model on antiferromagnetic triangular lattice . . . . .	65
2.4 Ising model on stacked antiferromagnetic triangular lattice . . . . .	71
2.5 Ising model with large $S$ on antiferromagnetic triangular lattice . . . . .	76
2.6 Ising model with infinite-spin on antiferromagnetic triangular lattice . . . . .	80
2.7 Ising-like Heisenberg model on antiferromagnetic triangular lattice . . . . .	82
2.8 Ising model with infinite-spin on stacked antiferromagnetic triangular lattice . . . . .	82
2.9 Phase diagram in spin-magnitude versus temperature for Ising models with spin $S$ on stacked antiferromagnetic triangular lattice . . . . .	87
2.10 Effect of antiferromagnetic interaction between next-nearest-neighbor spins in $xy$ -plane . . . . .	90
2.11 Three-dimensional Ising paramagnet . . . . .	96
2.12 Concluding remarks . . . . .	102
Acknowledgements . . . . .	103
References . . . . .	103
<b>3 RENORMALIZATION GROUP APPROACHES TO FRUSTRATED MAGNETS IN D=3</b>	<b>107</b>
<i>B. Delamotte, D. Mouhanna and M. Tissier</i>	
3.1 Introduction . . . . .	107

3.2	The STA model and generalization . . . . .	109
3.2.1	The lattice model, its continuum limit and symmetries . . . . .	109
3.2.2	The Heisenberg case . . . . .	112
3.2.3	The XY case . . . . .	115
3.2.4	Generalization . . . . .	116
3.3	Experimental and numerical situations . . . . .	116
3.3.1	The XY systems . . . . .	116
3.3.1.1	The experimental situation . . . . .	117
3.3.1.2	The numerical situation . . . . .	119
3.3.1.3	Summary . . . . .	121
3.3.2	The Heisenberg systems . . . . .	122
3.3.2.1	The experimental situation . . . . .	122
3.3.2.2	The numerical situation . . . . .	124
3.3.2.3	Summary . . . . .	126
3.3.3	The $N = 6$ STA . . . . .	126
3.3.4	Conclusion . . . . .	127
3.4	A brief chronological survey of the theoretical approaches .	127
3.5	The perturbative situation . . . . .	131
3.5.1	The Nonlinear Sigma ( $\text{NL}\sigma$ ) model approach . . . . .	131
3.5.2	The Ginzburg-Landau-Wilson (GLW) model approach . . . . .	136
3.5.2.1	The RG flow . . . . .	136
3.5.2.2	The three and five-loop results in $d = 4 - \epsilon$ .	137
3.5.2.3	The improved three and five-loop results .	137
3.5.2.4	The three-loop results in $d = 3$ . . . . .	138
3.5.2.5	The large- $N$ results . . . . .	138
3.5.2.6	The six-loop results in $d = 3$ . . . . .	139
3.5.3	The six-loop results in $d = 3$ re-examined . . . . .	141
3.5.3.1	Conclusion . . . . .	143
3.6	The effective average action method . . . . .	143
3.6.1	The effective average action equation . . . . .	143
3.6.2	Properties . . . . .	148
3.6.3	Truncations . . . . .	149
3.6.4	Principle of the calculation . . . . .	150
3.6.5	The $O(N) \times O(2)$ model . . . . .	151
3.6.5.1	The flow equations . . . . .	153

3.6.6	Tests of the method and first results . . . . .	154
3.6.7	The physics in $d = 3$ according to the NPRG approach . . . . .	158
3.6.7.1	The physics in $d = 3$ just below $N_c(d)$ : Scaling with a pseudo-fixed point and minimum of the flow . . . . .	159
3.6.7.2	Scaling with or without pseudo-fixed point: The Heisenberg and XY cases . . . . .	161
3.6.7.3	The integration of the RG flow . . . . .	164
3.6.7.4	The Heisenberg case . . . . .	165
3.6.7.5	The XY case . . . . .	167
3.6.8	Conclusion . . . . .	169
3.7	Conclusion and prospects . . . . .	169
	Acknowledgements . . . . .	171
	References . . . . .	171
<b>4</b>	<b>PHASE TRANSITIONS IN FRUSTRATED VECTOR SPIN SYSTEMS: NUMERICAL STUDIES</b>	<b>177</b>
	<i>D. Loison</i>	
	Abbreviations . . . . .	177
4.1	Introduction . . . . .	177
4.2	Breakdown of symmetry . . . . .	178
4.2.1	Symmetry in the high-temperature region . . . . .	179
4.2.2	Breakdown of symmetry for ferromagnetic systems .	179
4.2.3	Breakdown of symmetry for frustrated systems . .	181
4.2.3.1	Stacked triangular antiferromagnetic lattices	181
4.2.3.2	bct helimagnets . . . . .	184
4.2.3.3	Stacked $J_1-J_2$ square lattices . . . . .	185
4.2.3.4	The simple cubic $J_1-J_2$ lattice . . . . .	185
4.2.3.5	$J_1-J_2-J_3$ lattice . . . . .	186
4.2.3.6	Villain lattice and fully frustrated simple cubic lattice . . . . .	186
4.2.3.7	Face-centered cubic lattice (fcc) . . . . .	187
4.2.3.8	Hexagonal–close–packed lattice (hcp) . . . .	187
4.2.3.9	Pyrochlores . . . . .	188
4.2.3.10	Other lattices . . . . .	188
4.2.3.11	STAR lattices . . . . .	188

4.2.3.12 Dihedral lattices $V_{N,2}$ . . . . .	189
4.2.3.13 Right-handed trihedral lattices $V_{3,3}$ . . . . .	189
4.2.3.14 P-hedral lattices $V_{N,P}$ . . . . .	190
4.2.3.15 Ising and Potts- $V_{N,1}$ model . . . . .	190
4.2.3.16 Ising and Potts- $V_{N,2}$ model . . . . .	191
4.2.3.17 Landau-Ginzburg model . . . . .	191
4.2.3.18 Cubic term in Hamiltonian . . . . .	191
4.2.3.19 Summary . . . . .	192
4.3 Phase transitions between two and four dimensions: $2 < d \leq 4$ . . . . .	192
4.3.1 $O(N)/O(N - 2)$ breakdown of symmetry . . . . .	193
4.3.1.1 Fixed points . . . . .	193
4.3.1.2 MCRG and first-order transition . . . . .	195
4.3.1.3 Complex fixed point or minimum in the flow	196
4.3.1.4 Experiment . . . . .	200
4.3.1.5 Value of $N_c$ . . . . .	201
4.3.1.6 Phase diagram $(N, d)$ . . . . .	202
4.3.1.7 Renormalization-group expansions . . . . .	202
4.3.1.8 Short historical review . . . . .	204
4.3.1.9 Relations with the Potts model . . . . .	205
4.3.2 $O(N)/O(N - P)$ breakdown of symmetry for $d = 3$ .	206
4.3.3 $Z_2 \otimes SO(N)/SO(N - 1)$ breakdown of symmetry for $d = 3$ . . . . .	207
4.3.4 $Z_3 \otimes SO(N)/SO(N - 1)$ breakdown of symmetry for $d = 3$ . . . . .	208
4.3.5 $Z_q \otimes O(N)/O(N - 2)$ and other breakdown of symmetry in $d = 3$ . . . . .	208
4.4 Conclusion . . . . .	209
4.5 $O(N)$ frustrated vector spins in $d = 2$ . . . . .	210
4.5.1 Introduction . . . . .	210
4.5.2 Non frustrated $XY$ spin systems . . . . .	210
4.5.3 Frustrated $XY$ spin systems: $Z_2 \otimes SO(2)$ . . . . .	210
4.5.4 Frustrated $XY$ spin systems: $Z_3 \otimes SO(2)$ . . . . .	213
4.5.5 Frustrated $XY$ spin systems: $Z_2 \otimes Z_2 \otimes SO(2)$ and $Z_3 \otimes Z_2 \otimes SO(2)$ . . . . .	214
4.5.6 Frustrated Heisenberg spin systems: $SO(3)$ . . . . .	214

4.5.7 Frustrated Heisenberg spin systems: $Z_2 \otimes SO(3)$ , $Z_3 \otimes SO(3)$ . . . . .	215
4.5.8 Topological defects for $N \geq 4$ . . . . .	216
4.6 General conclusions . . . . .	216
Acknowledgements . . . . .	216
Appendix A: Monte Carlo simulation . . . . .	216
Appendix B: Renormalization group . . . . .	220
References . . . . .	223
<b>5 TWO-DIMENSIONAL QUANTUM ANTIFERROMAGNETS</b>	<b>229</b>
<i>Grégoire Misguich and Claire Lhuillier</i>	
5.1 Introduction . . . . .	229
5.2 $J_1-J_2$ model on the square lattice . . . . .	231
5.2.1 Classical ground-state and spin-wave analysis . . . . .	231
5.2.2 Order by disorder ( $J_2 > J_1/2$ ) . . . . .	232
5.2.3 Non-magnetic region ( $J_2 \simeq J_1/2$ ) . . . . .	233
5.2.3.1 Series expansions . . . . .	234
5.2.3.2 Exact diagonalizations . . . . .	236
5.2.3.3 Quantum Monte Carlo . . . . .	236
5.3 Valence-bond crystals . . . . .	238
5.3.1 Definitions . . . . .	238
5.3.2 One-dimensional and quasi one-dimensional examples (spin- $\frac{1}{2}$ systems) . . . . .	239
5.3.3 Valence bond solids . . . . .	240
5.3.4 Two-dimensional examples of VBC . . . . .	241
5.3.4.1 Without spontaneous lattice symmetry breaking . . . . .	241
5.3.4.2 With spontaneous lattice symmetry breaking . . . . .	243
5.3.5 Methods . . . . .	245
5.3.6 Summary of the properties of VBC phases . . . . .	246
5.4 Large- $N$ methods . . . . .	247
5.4.1 Bond variables . . . . .	248
5.4.2 $SU(N)$ . . . . .	249
5.4.3 $Sp(N)$ . . . . .	249
5.4.3.1 Gauge invariance . . . . .	251

5.4.3.2	Mean-field ( $N = \infty$ limit) . . . . .	251
5.4.3.3	Fluctuations about the mean-field solution .	252
5.4.3.4	Topological effects - Instantons and spontaneous dimerization . . . . .	254
5.4.3.5	Deconfined phases . . . . .	255
5.5	Quantum dimer models . . . . .	256
5.5.1	Hamiltonian . . . . .	256
5.5.2	Relation with spin- $\frac{1}{2}$ models . . . . .	257
5.5.3	Square lattice . . . . .	259
5.5.3.1	Transition graphs and topological sectors .	259
5.5.3.2	Staggered VBC for $V/J > 1$ . . . . .	260
5.5.3.3	Columnar crystal for $V < 0$ . . . . .	260
5.5.3.4	Plaquette phase . . . . .	261
5.5.3.5	Rokhsar-Kivelson point . . . . .	261
5.5.4	Hexagonal lattice . . . . .	262
5.5.5	Triangular lattice . . . . .	263
5.5.5.1	RVB liquid at the RK point . . . . .	264
5.5.5.2	Topological order . . . . .	265
5.5.6	Solvable QDM on the Kagomé lattice . . . . .	266
5.5.6.1	Hamiltonian . . . . .	266
5.5.6.2	RK ground-state . . . . .	266
5.5.6.3	Ising pseudo-spin variables . . . . .	268
5.5.6.4	Dimer-dimer correlations . . . . .	269
5.5.6.5	Visons excitations . . . . .	269
5.5.6.6	Spinons deconfinement . . . . .	271
5.5.6.7	$\mathbb{Z}_2$ gauge theory . . . . .	272
5.5.7	A QDM with an extensive ground-state entropy .	273
5.6	Multiple-spin exchange models . . . . .	274
5.6.1	Physical realizations of multiple-spin interactions .	274
5.6.1.1	Nuclear magnetism of solid ${}^3\text{He}$ . . . . .	274
5.6.1.2	Wigner crystal . . . . .	276
5.6.1.3	Cuprates . . . . .	276
5.6.2	Two-leg ladders . . . . .	276
5.6.3	MSE model on the square lattice . . . . .	278
5.6.4	RVB phase of the triangular $J_2$ - $J_4$ MSE . . . . .	278
5.6.4.1	Non-planar classical ground-states . . . . .	279
5.6.4.2	Absence of Néel LRO . . . . .	279

5.6.4.3	Local singlet-singlet correlations - Absence of lattice symmetry breaking . . . . .	280
5.6.4.4	Topological degeneracy and Lieb-Schultz- Mattis theorem . . . . .	281
5.6.4.5	Deconfined spinons . . . . .	282
5.6.5	Other models with MSE interactions . . . . .	283
5.7	Antiferromagnets on the Kagomé (and related) lattices . .	284
5.7.1	Miscellaneous models on the kagome lattice . . . . .	284
5.7.2	Spin- $\frac{1}{2}$ Heisenberg model on the Kagomé lattice: An extreme play-ground for “quantum fluctuations” . . . . .	285
5.7.2.1	Ground-state energy per spin . . . . .	285
5.7.2.2	Correlations . . . . .	286
5.7.2.3	Spin-gap . . . . .	286
5.7.2.4	An exceptional density of low lying excitations in the singlet sector . . . . .	287
5.7.2.5	Absence of gap in the singlet sector . . . . .	290
5.7.2.6	Anomalous density of states in other spin sectors . . . . .	291
5.7.3	Nearest-neighbor RVB description of the spin- $\frac{1}{2}$ Kagomé antiferromagnet . . . . .	292
5.7.4	Experiments in compounds with Kagomé-like lattices	293
5.7.5	“Haldane’s conjecture” . . . . .	293
5.8	Conclusions . . . . .	294
	Acknowledgements . . . . .	296
	References . . . . .	296
<b>6</b>	<b>ONE-DIMENSIONAL SPIN LIQUIDS</b>	<b>307</b>
	<i>P. Lecheminant</i>	
6.1	Introduction . . . . .	307
6.2	Unfrustrated spin chains . . . . .	310
6.2.1	Spin- $\frac{1}{2}$ Heisenberg chain . . . . .	310
6.2.2	Haldane’s conjecture . . . . .	313
6.2.3	Haldane spin liquid: Spin-1 Heisenberg chain . . . . .	315
6.2.4	General spin- $S$ case . . . . .	319
6.2.5	Two-leg spin ladder . . . . .	321
6.2.6	Non-Haldane spin liquid . . . . .	327
6.3	Frustration effects . . . . .	331

6.3.1	Semiclassical analysis . . . . .	331
6.3.2	Spin liquid phase with massive deconfined spinons .	334
6.3.3	Field theory of spin liquid with incommensurate correlations . . . . .	341
6.3.4	Extended criticality stabilized by frustration . . . .	345
6.3.4.1	Critical phases with SU(N) quantum criticality . . . . .	346
6.3.4.2	Chirally stabilized critical spin liquid . . . .	350
6.4	Concluding remarks . . . . .	353
	Acknowledgements . . . . .	356
	References . . . . .	356
<b>7</b>	<b>SPIN ICE</b>	<b>367</b>
<i>Steven T. Bramwell, Michel J. P. Gingras and Peter C. W. Holdsworth</i>		
7.1	Introduction . . . . .	368
7.2	From water ice to spin ice . . . . .	371
7.2.1	Pauling's model . . . . .	371
7.2.2	Why is the zero point entropy not zero? . . . .	373
7.2.3	Generalizations of Pauling's model . . . . .	374
7.2.3.1	Wannier's model . . . . .	374
7.2.3.2	Anderson's model . . . . .	375
7.2.3.3	Vertex models . . . . .	376
7.2.3.4	Possibility of realizing magnetic vertex models . . . . .	376
7.2.4	Spin ice . . . . .	378
7.2.4.1	Definition of the spin ice model and its application to $\text{Ho}_2\text{Ti}_2\text{O}_7$ . . . . .	378
7.2.4.2	Identification of spin ice materials . . . .	380
7.2.4.3	Basic properties of the spin ice materials .	380
7.2.5	Spin ice as a frustrated magnet . . . . .	383
7.2.5.1	Frustration and underconstraining . . . .	383
7.2.5.2	$\langle 111 \rangle$ pyrochlore models . . . . .	384
7.3	Properties of the zero field spin ice state . . . . .	385
7.3.1	Experimental properties . . . . .	385
7.3.1.1	Heat capacity: Zero point entropy . . . .	385

7.3.1.2	Low field magnetic susceptibility: Spin freezing . . . . .	389
7.3.1.3	Spin arrangement observed by neutron scattering . . . . .	390
7.3.2	Microscopic theories and experimental tests . . . . .	391
7.3.2.1	Near-neighbour spin ice model: Successes and failures . . . . .	391
7.3.2.2	The problem of treating the dipolar interaction . . . . .	393
7.3.2.3	The Ewald Monte Carlo . . . . .	397
7.3.2.4	Mean-field theory . . . . .	401
7.3.2.5	The loop Monte Carlo . . . . .	404
7.3.2.6	Application of the dipolar model to neutron scattering results . . . . .	413
7.3.2.7	How realistic is the dipolar model? . . . . .	413
7.4	Field-induced phases . . . . .	414
7.4.1	Theory . . . . .	415
7.4.1.1	Near neighbour model . . . . .	415
7.4.1.2	Dipolar model . . . . .	418
7.4.2	Magnetization measurements above $T = 1$ K . . . . .	418
7.4.3	Bulk measurements at low temperature . . . . .	419
7.4.3.1	[111] direction . . . . .	419
7.4.3.2	[110] direction . . . . .	423
7.4.3.3	[100] direction . . . . .	423
7.4.3.4	[211] direction . . . . .	424
7.4.3.5	Powder measurements . . . . .	425
7.4.4	Neutron scattering results . . . . .	426
7.4.4.1	[110] direction . . . . .	426
7.4.4.2	[100], [111] and [211] directions . . . . .	428
7.4.5	Kagomé ice . . . . .	428
7.4.5.1	Basic Kagomé ice model and mappings . . . . .	429
7.4.5.2	Experimental results: Specific heat . . . . .	431
7.4.5.3	Theory of the Kagomé ice state: Kastelyn transition . . . . .	432
7.5	Spin dynamics of the spin ice materials . . . . .	433
7.5.1	Experimental quantities of interest . . . . .	433

7.5.1.1	Correlation functions and neutron scattering . . . . .	433
7.5.1.2	Fluctuation-dissipation theorem and AC-susceptibility . . . . .	434
7.5.1.3	Spectral shape function . . . . .	434
7.5.1.4	Exponential relaxation . . . . .	435
7.5.2	Differences between $\text{Ho}_2\text{Ti}_2\text{O}_7$ and $\text{Dy}_2\text{Ti}_2\text{O}_7$ . . . . .	436
7.5.3	Relaxation at high temperature, $T \sim 15$ K and above . . . . .	436
7.5.3.1	AC-susceptibility (AC- $\chi$ ) . . . . .	436
7.5.3.2	Neutron Spin Echo (NSE) . . . . .	436
7.5.3.3	Origin of the 15 K AC-susceptibility peak .	439
7.5.4	Relaxation in the range $1 \text{ K} \leq T \leq 15 \text{ K}$ . . . . .	441
7.5.4.1	AC-susceptibility: Phenomenological model	441
7.5.4.2	AC-susceptibility: Towards a microscopic model . . . . .	441
7.5.5	Spin dynamics in the spin ice regime below 1 K . . . . .	443
7.5.5.1	Slow relaxation . . . . .	443
7.5.5.2	Evidence for residual dynamics in the frozen state . . . . .	444
7.5.6	Doped spin ice . . . . .	445
7.5.7	Spin ice under pressure . . . . .	446
7.6	Spin ice related materials . . . . .	446
7.6.1	Rare earth titanates . . . . .	447
7.6.2	Other pyrochlores related to spin ice . . . . .	448
7.7	Conclusions . . . . .	449
	Acknowledgements . . . . .	450
	References . . . . .	451
<b>8</b>	<b>EXPERIMENTAL STUDIES OF FRUSTRATED PYROCHLORE ANTIFERROMAGNETS</b>	<b>457</b>
	<i>Bruce D. Gaulin and Jason S. Gardner</i>	
8.1	Introduction . . . . .	458
8.2	Pyrochlore lattices . . . . .	459
8.3	Neutron scattering techniques . . . . .	461
8.4	Cooperative paramagnetism in $\text{Tb}_2\text{Ti}_2\text{O}_7$ . . . . .	463
8.5	The spin glass ground state in $\text{Y}_2\text{Mo}_2\text{O}_7$ . . . . .	474

8.6	Composite spin degrees of freedom and spin-Peierls-like ground state in the frustrated spinel $ZnCr_2O_4$ . . . . .	483
8.7	Conclusions and outlook . . . . .	486
	Acknowledgements . . . . .	486
	References . . . . .	487
<b>9</b>	<b>RECENT PROGRESS IN SPIN GLASSES</b>	<b>491</b>
	<i>N. Kawashima and H. Rieger</i>	
9.1	Two pictures . . . . .	492
	9.1.1 Mean-field picture . . . . .	493
	9.1.2 Droplet picture . . . . .	496
9.2	Equilibrium properties of two-dimensional Ising spin glasses . . . . .	498
	9.2.1 Zero-temperature transition? . . . . .	498
	9.2.2 Droplet argument for Gaussian-coupling models . . . . .	500
	9.2.3 Droplets in Gaussian-coupling models: Numerics . . . . .	500
	9.2.4 Finite-temperature transition? . . . . .	503
9.3	Equilibrium properties of three-dimensional models . . . . .	503
	9.3.1 Finite temperature transition? . . . . .	504
	9.3.2 Universality class . . . . .	505
	9.3.3 Low-temperature phase of the $\pm J$ model . . . . .	507
	9.3.4 Low-temperature phase of the Gaussian-coupling model . . . . .	511
	9.3.5 Effect of magnetic fields . . . . .	517
	9.3.6 Sponge-like excitations . . . . .	518
	9.3.7 TNT picture — Introduction of a new scaling length . . . . .	519
	9.3.8 Arguments supporting the droplet picture . . . . .	520
9.4	Models in four or higher dimensions . . . . .	521
9.5	Aging . . . . .	523
	9.5.1 A growing length scale during aging? . . . . .	523
	9.5.2 Two time quantities: Isothermal aging . . . . .	528
	9.5.3 More complicated temperature protocols . . . . .	533
	9.5.4 Violation of the fluctuation-dissipation theorem . . . . .	538
	9.5.5 Hysteresis in spin glasses . . . . .	541
9.6	Equilibrium properties of classical $XY$ and Heisenberg spin glasses . . . . .	544

9.6.1	Continuous spin models in three dimensions . . . . .	544
9.6.2	Continuous spin models in higher dimensions . . . . .	549
9.6.3	Potts spin glasses . . . . .	550
9.7	Weak disorder . . . . .	551
9.7.1	Phase diagram of the discrete spin models . . . . .	552
9.7.2	Dynamical properties . . . . .	554
9.7.3	The renormalization group approach for the discrete models . . . . .	555
9.7.4	The location of the multi-critical point . . . . .	558
9.7.5	Phase diagram of the random $XY$ model in two dimensions . . . . .	560
9.8	Quantum spin glasses . . . . .	562
9.8.1	Random transverse Ising models . . . . .	563
9.8.2	Mean-field theory . . . . .	571
9.8.3	Mean-field theory — Dissipative effects . . . . .	575
9.8.4	Mean-field theory — Dynamics . . . . .	579
9.8.5	Heisenberg quantum spin glasses . . . . .	581
9.8.5.1	Finite dimensions . . . . .	582
9.8.5.2	Mean-field model . . . . .	582
9.9	Summary and remaining problems . . . . .	584
	Acknowledgements . . . . .	586
	References . . . . .	587
	<i>Index</i>	597



## CHAPTER 1

### FRUSTRATION - EXACTLY SOLVED FRUSTRATED MODELS

H. T. Diep

*Laboratoire de Physique Théorique et Modélisation*

*CNRS-Université de Cergy-Pontoise, UMR 8089*

*5, mail Gay-Lussac, Neuville sur Oise, 95031 Cergy-Pontoise Cedex - France*

*E-mail: diep@ptm.u-cergy.fr*

and

H. Giacomini

*Laboratoire de Mathématiques et Physique Théorique , CNRS-Université de Tours, UMR 6083*

*Parc de Grandmont, 37200 Tours, France*

*E-mail:giacomini@univ-tours.fr*

After a short introduction on frustrated spin systems, we study in this chapter several two-dimensional frustrated Ising spin systems which can be exactly solved by using vertex models. We show that these systems contain most of the spectacular effects due to the frustration: high ground-state degeneracy, existence of several phases in the ground-state phase diagram, multiple phase transitions with increasing temperature, reentrance, disorder lines, partial disorder at equilibrium. Evidences of such effects in non solvable models are also shown and discussed.

#### 1.1. Frustration: an introduction

The study of order-disorder phenomena is a fundamental task of equilibrium statistical mechanics. Great efforts have been made to understand the basic mechanisms responsible for spontaneous ordering as well as the nature of the phase transition in many kinds of systems. In particular, during

the last 25 years, much attention has been paid to frustrated models.<sup>1</sup> The word "frustration" has been introduced<sup>2,3</sup> to describe the situation where a spin (or a number of spins) in the system cannot find an orientation to *fully* satisfy all the interactions with its neighboring spins (see below). This definition can be applied to Ising spins, Potts models and vector spins. In general, the frustration is caused either by competing interactions (such as the Villain model<sup>3</sup>) or by lattice structure as in the triangular, face-centered cubic (fcc) and hexagonal-close-packed (hcp) lattices, with antiferromagnetic nearest-neighbor (nn) interaction. The effects of frustration are rich and often unexpected. Many of them are not understood yet at present (see the other chapters of this book).

In addition to the fact that real magnetic materials are often frustrated due to several kinds of interactions (see the chapter by Gaulin and Gardner, this book), frustrated spin systems have their own interest in statistical mechanics. Recent studies show that many established statistical methods and theories have encountered many difficulties in dealing with frustrated systems. In some sense, frustrated systems are excellent candidates to test approximations and improve theories. Since the mechanisms of many phenomena are not understood in real systems (disordered systems, systems with long-range interaction, three-dimensional systems, etc), it is worth to search for the origins of those phenomena in exactly solved systems. These exact results will help to understand qualitatively the behavior of real systems which are in general much more complicated.

### 1.1.1. Definition

Let us give here some basic definitions to help readers unfamiliar with these subjects to read the remaining chapters of this book.

Consider two spins  $\mathbf{S}_i$  and  $\mathbf{S}_j$  with an interaction  $J$ . The interaction energy is  $E = -J(\mathbf{S}_i \cdot \mathbf{S}_j)$ . If  $J$  is positive (ferromagnetic interaction) then the minimum of  $E$  is  $-J$  corresponding to the configuration in which  $\mathbf{S}_i$  is parallel to  $\mathbf{S}_j$ . If  $J$  is negative (antiferromagnetic interaction), the minimum of  $E$  corresponds to the configuration where  $\mathbf{S}_i$  is antiparallel to  $\mathbf{S}_j$ . It is easy to see that in a spin system with nn ferromagnetic interaction, the ground state (GS) of the system corresponds to the spin configuration where all spins are parallel: the interaction of every pair of spins is fully satisfied. This is true for any lattice structure. If  $J$  is antiferromagnetic, the spin configuration of the GS depends on the lattice structure: i) for lattices containing no elementary triangles, i.e. bipartite lattices (such as square

lattice, simple cubic lattices, ...) the GS is the configuration in which each spin is antiparallel to its neighbors, i.e. every bond is fully satisfied. ii) for lattices containing elementary triangles such as the triangular lattice, the fcc lattice and the hcp lattice, one cannot construct a GS where all bonds are fully satisfied (see Fig. 1.1). The GS does not correspond to the minimum of the interaction of every spin pair. In this case, one says that the system is frustrated.

We consider another situation where the spin system can be frustrated: this is the case with different kinds of conflicting interactions and the GS does not correspond to the minimum of each kind of interaction. For example, consider a chain of spins where the nn interaction  $J_1$  is ferromagnetic while the next nn (nnn) interaction  $J_2$  is antiferromagnetic. As long as  $|J_2| \ll J_1$ , the GS is ferromagnetic: every nn bond is then satisfied but the nnn ones are not. Of course, when  $|J_2|$  exceeds a critical value, the ferromagnetic GS is no longer valid (see an example below): both the nn and nnn bonds are not fully satisfied.

In a general manner, we can say that a spin system is frustrated when one cannot find a configuration of spins to fully satisfy the interaction (bond) between every pair of spins. In other words, the minimum of the total energy does not correspond to the minimum of each bond. This situation arises when there is a competition between different kinds of interactions acting on a spin by its neighbors or when the lattice geometry does not allow to satisfy all the bonds simultaneously. With this definition, the chain with nn ferromagnetic and nnn antiferromagnetic interactions discussed above is frustrated even in the case where the ferromagnetic spin configuration is its GS ( $|J_2| \ll J_1$ ).

The first frustrated system which was studied in 1950 is the triangular lattice with Ising spins interacting with each other via a nn antiferromagnetic interaction<sup>4</sup>. For vector spins, non collinear spin configurations due to competing interactions were first discovered in 1959 independently by Yoshimori<sup>5</sup>, Villain<sup>6</sup> and Kaplan<sup>7</sup>.

Consider an elementary cell of the lattice. This cell is a polygon formed by faces hereafter called "plaquettes". For example, the elementary cell of the simple cubic lattice is a cube with six square plaquettes, the elementary cell of the fcc lattice is a tetrahedron formed by four triangular plaquettes. Let  $J_{i,j}$  be the interaction between two nn spins of the plaquette. According to the definition of Toulouse,<sup>2</sup> the plaquette is frustrated if the parameter

$P$  defined below is negative

$$P = \prod_{\langle i,j \rangle} \text{sign}(J_{i,j}), \quad (1)$$

where the product is performed over all  $J_{i,j}$  around the plaquette. Two examples of frustrated plaquettes are shown in Fig. 1.1: a triangle with three antiferromagnetic bonds and a square with three ferromagnetic bonds and one antiferromagnetic bond.  $P$  is negative in both cases. One sees that if one tries to put Ising spins on those plaquettes, at least one of the bonds around the plaquette will not be satisfied. For vector spins, we show below that in the lowest energy state, each bond is only partially satisfied.

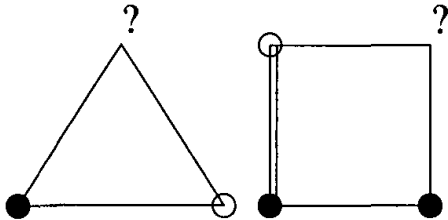


Fig. 1.1. Examples of frustrated plaquettes: ferro- and antiferromagnetic interactions,  $J$  and  $-J$ , are shown by single and double lines,  $\uparrow$  and  $\downarrow$  Ising spins by black and void circles, respectively. Choosing any orientation for the spin marked by the question mark will leave one of its bonds unsatisfied (frustrated bond).

One sees that for the triangular plaquette, the degeneracy is three, and for the square plaquette it is four, in addition to the degeneracy associated with returning all spins. Therefore, the degeneracy of an infinite lattice composed of such plaquettes is infinite, in contrast to the unfrustrated case.

At this stage, we note that although in the above discussion we have taken the interaction between two spins to be of the form  $E = -J(\mathbf{S}_i \cdot \mathbf{S}_j)$ , the concept of frustration can be applied to other types of interactions such as the Dzyaloshinski-Moriya interaction  $E = -J|(\mathbf{S}_i \wedge \mathbf{S}_j)|$ : a spin system is frustrated whenever the minimum of the system energy does not correspond to the minimum of all local interactions, whatever the form of interaction. We note however that this definition of frustration is more general than the one using Eq. (1).

The determination of the GS of various frustrated Ising spin systems as well as discussions on their properties will be shown. In the following section, we analyze the GS of XY and Heisenberg spins.

### 1.1.2. Non collinear spin configurations

Let us return to the plaquettes shown in Fig. 1.1. In the case of  $XY$  spins, one can calculate the GS configuration by minimizing the energy of the plaquette  $E$  while keeping the spin modulus constant. In the case of the triangular plaquette, suppose that spin  $\mathbf{S}_i$  ( $i = 1, 2, 3$ ) of amplitude  $S$  makes an angle  $\theta_i$  with the  $\mathbf{Ox}$  axis. Writing  $E$  and minimizing it with respect to the angles  $\theta_i$ , one has

$$\begin{aligned} E &= J(\mathbf{S}_1 \cdot \mathbf{S}_2 + \mathbf{S}_2 \cdot \mathbf{S}_3 + \mathbf{S}_3 \cdot \mathbf{S}_1) \\ &= JS^2 [\cos(\theta_1 - \theta_2) + \cos(\theta_2 - \theta_3) + \cos(\theta_3 - \theta_1)], \\ \frac{\partial E}{\partial \theta_1} &= -JS^2 [\sin(\theta_1 - \theta_2) - \sin(\theta_3 - \theta_1)] = 0, \\ \frac{\partial E}{\partial \theta_2} &= -JS^2 [\sin(\theta_2 - \theta_3) - \sin(\theta_1 - \theta_2)] = 0, \\ \frac{\partial E}{\partial \theta_3} &= -JS^2 [\sin(\theta_3 - \theta_1) - \sin(\theta_2 - \theta_3)] = 0. \end{aligned}$$

A solution of the last three equations is  $\theta_1 - \theta_2 = \theta_2 - \theta_3 = \theta_3 - \theta_1 = 2\pi/3$ . One can also write

$$E = J(\mathbf{S}_1 \cdot \mathbf{S}_2 + \mathbf{S}_2 \cdot \mathbf{S}_3 + \mathbf{S}_3 \cdot \mathbf{S}_1) = -\frac{3}{2}JS^2 + \frac{J}{2}(\mathbf{S}_1 + \mathbf{S}_2 + \mathbf{S}_3)^2.$$

The minimum here evidently corresponds to  $\mathbf{S}_1 + \mathbf{S}_2 + \mathbf{S}_3 = 0$  which yields the  $120^\circ$  structure. This is true also for Heisenberg spins.

We can do the same calculation for the case of the frustrated square plaquette. Suppose that the antiferromagnetic bond connects the spins  $\mathbf{S}_1$  and  $\mathbf{S}_2$ . We find

$$\theta_2 - \theta_1 = \theta_3 - \theta_2 = \theta_4 - \theta_3 = \frac{\pi}{4} \text{ and } \theta_1 - \theta_4 = \frac{3\pi}{4} \quad (2)$$

If the antiferromagnetic bond is equal to  $-\eta J$ , the solution for the angles is<sup>8</sup>

$$\cos \theta_{32} = \cos \theta_{43} = \cos \theta_{14} \equiv \theta = \frac{1}{2} \left[ \frac{\eta + 1}{\eta} \right]^{1/2} \quad (3)$$

and  $|\theta_{21}| = 3|\theta|$ , where  $\cos \theta_{ij} \equiv \cos \theta_i - \cos \theta_j$ .

This solution exists if  $|\cos \theta| \leq 1$ , namely  $\eta > \eta_c = 1/3$ . One can check that when  $\eta = 1$ , one has  $\theta = \pi/4$ ,  $\theta_{21} = 3\pi/4$ .

We show the frustrated triangular and square lattices in Fig. 1.2 with  $XY$  spins ( $N = 2$ ).

One observes that there is a two-fold degeneracy resulting from the symmetry by mirror reflecting with respect to an axis, for example the  $y$

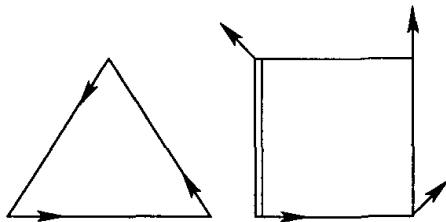


Fig. 1.2. Non collinear spin configuration of frustrated triangular and square plaquettes with  $XY$  spins: ferro- and antiferromagnetic interactions  $J$  and  $-J$  are indicated by thin and double lines, respectively.

axis in Fig. 1.2. Therefore the symmetry of these plaquettes is of Ising type  $O(1)$ , in addition to the symmetry  $SO(2)$  due to the invariance by global rotation of the spins in the plane. The lattices formed by these plaquettes will be called in the following "antiferromagnetic triangular lattice" and "Villain lattice", respectively.

It is expected from the GS symmetry of these systems that the transitions due to the respective breaking of  $O(1)$  and  $SO(2)$  symmetries, if they occur at different temperatures, belongs respectively to the 2D Ising universality class and to the Kosterlitz-Thouless universality class. The question of whether the two phase transitions would occur at the same temperature and the nature of their universality remains at present an open question. See more discussion in the chapter by Loison, this book.

The reader can find in Refs. [9] and [10] the derivation of the non-trivial classical ground-state configuration of the fully frustrated simple cubic lattice formed by stacking the two-dimensional Villain lattices, in the case of Heisenberg and  $XY$  spins.

Another example is the case of a chain of Heisenberg spins with ferromagnetic interaction  $J_1(> 0)$  between nn and antiferromagnetic interaction  $J_2(< 0)$  between nnn. When  $\varepsilon = |J_2|/J_1$  is larger than a critical value  $\varepsilon_c$ , the spin configuration of the GS becomes non collinear. One shows that the helical configuration displayed in Fig. 1.3 is obtained by minimizing the

interaction energy:

$$\begin{aligned}
 E &= -J_1 \sum_i \mathbf{S}_i \cdot \mathbf{S}_{i+1} + |J_2| \sum_i \mathbf{S}_i \cdot \mathbf{S}_{i+2} \\
 &= S^2 [-J_1 \cos \theta + |J_2| \cos(2\theta)] \sum_i 1 \\
 \frac{\partial E}{\partial \theta} &= S^2 [J_1 \sin \theta - 2|J_2| \sin(2\theta)] \sum_i 1 = 0 \\
 &= S^2 [J_1 \sin \theta - 4|J_2| \sin \theta \cos \theta] \sum_i 1 = 0,
 \end{aligned} \tag{4}$$

where one has supposed that the angle between nn spins is  $\theta$ .

The two solutions are

$$\sin \theta = 0 \longrightarrow \theta = 0 \text{ (ferromagnetic solution)}$$

and

$$\cos \theta = \frac{J_1}{4|J_2|} \longrightarrow \theta = \pm \arccos \left( \frac{J_1}{4|J_2|} \right). \tag{5}$$

The last solution is possible if  $-1 \leq \cos \theta \leq 1$ , i.e.  $J_1/(4|J_2|) \leq 1$  or  $|J_2|/J_1 \geq 1/4 \equiv \varepsilon_c$ .

Again in this example, there are two degenerate configurations: clockwise and counter-clockwise.

One defines in the following a chiral order parameter for each plaquette. For example, in the case of a triangular plaquette, the chiral parameter is given by

$$\kappa = \frac{2}{3\sqrt{3}} [\mathbf{S}_1 \wedge \mathbf{S}_2 + \mathbf{S}_2 \wedge \mathbf{S}_3 + \mathbf{S}_3 \wedge \mathbf{S}_1], \tag{6}$$

where coefficient  $2/(3\sqrt{3})$  was introduced so that the  $\pm 2\pi/3$  degeneracy corresponds to  $\kappa_i = \pm 1$ .

We can form a triangular lattice using plaquettes as shown in Fig. 1.4. The GS corresponds to the state where all plaquettes of the same orientation have the same chirality: plaquettes  $\triangle$  have positive chirality ( $\kappa = 1$ ) and plaquettes  $\nabla$  have negative chirality ( $\kappa = -1$ ). In terms of Ising spins, we have a perfect antiferromagnetic order. This order is broken at a phase transition temperature where  $\kappa$  vanishes.

Let us enumerate two frequently encountered frustrated spin systems where the nn interaction is antiferromagnetic: the fcc lattice and the hcp lattice. These two lattices are formed by stacking tetrahedra with four triangular faces. The frustration due to the lattice structure such as in these cases is called "geometry frustration".

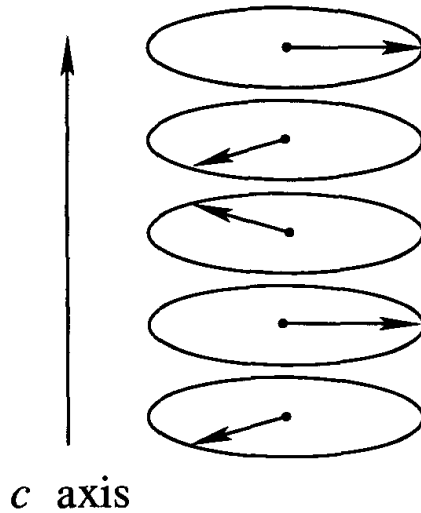


Fig. 1.3. Helical configuration when  $\varepsilon = |J_2|/J_1 > \varepsilon_c = 1/4$  ( $J_1 > 0, J_2 < 0$ ).

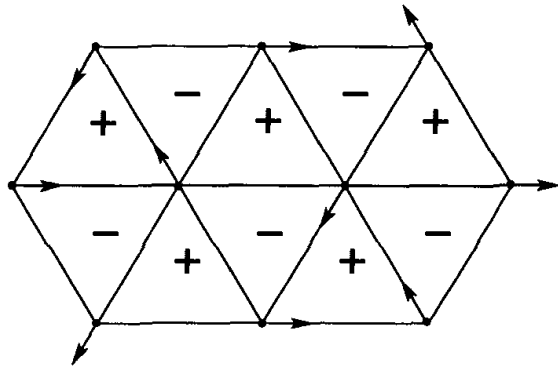


Fig. 1.4. Antiferromagnetic triangular lattice with  $XY$  spins. The positive and negative chiralities are indicated by + and -.

## 1.2. Frustrated Ising spin systems

We are interested here in frustrated Ising spin systems without disorder. A review of early works (up to about 1985) on frustrated Ising systems with periodic interactions, i.e. no bond disorder, has been given by Liebmann.<sup>1</sup> These systems have their own interest in statistical mechanics because they are periodically defined and thus subject to exact treatment. To date, very few systems are exactly solvable. They are limited to one and two dimensions (2D).<sup>11</sup> A few well-known systems showing remarkable properties include the centered square lattice<sup>12</sup> and its generalized versions,<sup>13,14</sup> the

Kagomé lattice,<sup>15,16,17</sup> an anisotropic centered honeycomb lattice,<sup>18</sup> and several periodically dilute centered square lattices.<sup>19</sup> Complicated cluster models,<sup>20</sup> and a particular three-dimensional case have also been solved.<sup>21</sup> The phase diagrams in frustrated models show a rich behavior. Let us mention a few remarkable consequences of the frustration which are in connection with what will be shown in this chapter. The degeneracy of the ground state is very high, often infinite. At finite temperatures, in some systems the degeneracy is reduced by thermal fluctuations which select a number of states with largest entropy. This has been called "Order by Disorder",<sup>22</sup> in the Ising case. Quantum fluctuations and/or thermal fluctuations can also select particular spin configurations in the case of vector spins.<sup>23,24</sup> Another striking phenomenon is the coexistence of Order and Disorder at equilibrium: a number of spins in the system are disordered at all temperatures even in an ordered phase.<sup>16</sup> The frustration is also at the origin of the reentrance phenomenon. A reentrant phase can be defined as a phase with no long-range order, or no order at all, occurring in a region below an ordered phase on the temperature scale. In addition, the frustration can also give rise to disorder lines in the phase diagram of many systems as will be shown below.

In this chapter, we confine ourselves to exactly solved Ising spin systems that show remarkable features in the phase diagram such as the reentrance, successive transitions, disorder lines and partial disorder. Other Ising systems are treated in the chapter by Nagai et al. Also, the reentrance in disordered systems such as spin glasses is discussed in the chapter by Kawashima and Rieger.

The systems we consider in this chapter are periodically defined (without bond disorder). The frustration due to competing interactions will itself induce disorder in the spin orientations. The results obtained can be applied to physical systems that can be mapped into a spin language. The chapter is organized as follows. In the next section, we outline the method which allows to calculate the partition function and the critical varieties of 2D Ising models without crossing interactions. In particular, we show in detail the mapping of these models onto the 16- and 32-vertex models. We also explain a decimation method for finding disorder solutions. The purpose of this section is to give the reader enough mathematical details so that, if he wishes, he can apply these techniques to 2D Ising models with non-crossing interactions. In section 4, we shall apply the results of section 3 in some systems which present remarkable physical properties. The systems studied in section 4 contain most of interesting features of the frustration:

high ground state degeneracy, reentrance, partial disorder, disorder lines, successive phase transitions, and some aspects of the random-field Ising model. In section 4 we show some evidences of reentrance and partial disorder found in three-dimensional systems and in systems with spins other than the Ising model (Potts model, classical vector spins, quantum spins). A discussion on the origin of the reentrance phenomenon and concluding remarks are given in section 5.

### 1.3. Mapping between Ising models and vertex models

The 2D Ising model with non-crossing interactions is exactly soluble. The problem of finding the partition function can be transformed in a free-fermion model. If the lattice is a complicated one, the mathematical problem to solve is very cumbersome.

For numerous two-dimensional Ising models with non-crossing interactions, there exists another method, by far easier, to find the exact partition function. This method consists in mapping the model on a 16-vertex model or a 32-vertex model. If the Ising model does not have crossing interactions, the resulting vertex model will be exactly soluble. We will apply this method for finding the exact solution of several Ising models in two-dimensional lattices with non-crossing interactions.

Let us at first introduce the 16-vertex model and the 32- vertex model, and the cases for which these models satisfy the free-fermion condition.

#### 1.3.1. The 16-vertex model

The 16-vertex model which we will consider is a square lattice of  $N$  points, connected by edges between neighboring sites. These edges can assume two states, symbolized by right- and left- or up-and down-pointing arrows, respectively. The allowed configurations of the system are characterized by specifying the arrangement of arrows around each lattice point. In characterizing these so-called vertex configurations, we follow the enumeration of Baxter<sup>11</sup>( see Fig.1.5).

To each vertex we assign an energy  $\epsilon_k$  ( $k = 1, 2, \dots, 16$ ) and a corresponding vertex weight ( Boltzmann factor)  $\omega_k = e^{\beta\epsilon_k}$  , where  $\beta = (1)/(k_B T)$  ,  $T$  being the temperature and  $k_B$  the Boltzmann constant. Then the partition function is

$$Z = \sum_C e^{-\beta(n_1\epsilon_1 + \dots + n_{16}\epsilon_{16})} \quad (7)$$

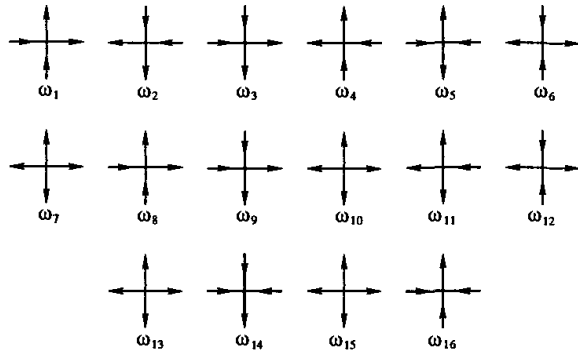


Fig. 1.5. Arrow configurations and vertex weights of the 16-vertex model.

where the sum is over all allowed configurations C of arrows on the lattice,  $n_j$  is the number of vertex arrangements of type j in configuration C. It is clear from Eq.(7) that Z is a function of the eight Boltzmann weights  $\omega_k (k = 1, 2, \dots, 16)$  :

$$Z = Z(\omega_1, \dots, \omega_{16}) \quad (8)$$

So far, exact results have only been obtained for three subclasses of the general 16-vertex model, i.e. the 6-vertex ( or ferroelectric ) model, the symmetric eight-vertex model and the free-fermion model.<sup>11,25</sup> Here we will consider only the case where the free-fermion condition is satisfied, because in these cases the 16-vertex model can be related to 2D Ising models without crossing interactions. Generally, a vertex model is soluble if the vertex weights satisfy certain conditions so that the partition function is reducible to the S matrix of a many-fermion system.<sup>25</sup> In the present problem these constraints are the following :

$$\begin{aligned} \omega_1 &= \omega_2, \omega_3 = \omega_4 \\ \omega_5 &= \omega_6, \omega_7 = \omega_8 \\ \omega_9 &= \omega_{10} = \omega_{11} = \omega_{12} \\ \omega_{13} &= \omega_{14} = \omega_{15} = \omega_{16} \\ \omega_1\omega_3 + \omega_5\omega_7 - \omega_9\omega_{11} - \omega_{13}\omega_{15} &= 0 \end{aligned} \quad (9)$$

If these conditions are satisfied, the free energy of the model can be expressed, in the thermodynamical limit, as follows :

$$f = -\frac{1}{4\pi\beta} \int_0^{2\pi} d\phi \log\{A(\phi) + [Q(\phi)]^{1/2}\} \quad (10)$$

where

$$\begin{aligned}
 A(\phi) &= a + c \cos(\phi) \\
 Q(\phi) &= y^2 + z^2 - x^2 - 2yz \cos(\phi) + x^2 \cos^2(\phi) \\
 a &= \frac{1}{2}(\omega_1^2 + \omega_3^2 + 2\omega_1\omega_3 + \omega_5^2 + \omega_7^2 + 2\omega_5\omega_7) + 2(\omega_9^2 + \omega_{13}^2) \\
 c &= 2[\omega_9(\omega_1 + \omega_3) - \omega_{13}(\omega_5 + \omega_7)] \\
 y &= 2[\omega_9(\omega_1 + \omega_3) + \omega_{13}(\omega_5 + \omega_7)] \\
 z &= \frac{1}{2}[(\omega_1 + \omega_3)^2 - (\omega_5 + \omega_7)^2] + 2(\omega_9^2 - \omega_{13}^2) \\
 x^2 &= z^2 - \frac{1}{4}[(\omega_1 - \omega_3)^2 - (\omega_5 - \omega_7)^2]
 \end{aligned} \tag{11}$$

Phase transitions occur when one or more pairs of zeros of the expression  $Q(\phi)$  close in on the real  $\phi$  axis and "pinch" the path of integration in the expression on the right-hand side of Eq. (10). This happens when  $y^2 = z^2$ , i.e. when

$$\omega_1 + \omega_3 + \omega_5 + \omega_7 + 2\omega_9 + 2\omega_{13} = 2\max\{\omega_1 + \omega_3, \omega_5 + \omega_7, 2\omega_9, 2\omega_{13}\} \tag{12}$$

The type of singularity in the specific heat depends on whether

$$(\omega_1 - \omega_3)^2 - (\omega_5 - \omega_7)^2 \neq 0 \quad (\text{logarithmic singularity})$$

or

$$(\omega_1 - \omega_3)^2 - (\omega_5 - \omega_7)^2 = 0 \quad (\text{inverse square-root singularity}) \tag{13}$$

### 1.3.2. The 32-vertex model

The 32-vertex model is defined by a triangular lattice of  $N$  points, connected by edges between neighboring sites. These edges can assume two states, symbolized by an arrow pointing in or pointing out of a site. In the general case, there are 64 allowed vertex configurations. If only an odd number of arrows pointing into a site are allowed, we have 32 possible vertex configurations. This is the constraint that characterizes the 32-vertex model. To each allowed vertex configuration we assign an energy  $\epsilon_k$  ( $k = 1, 2, \dots, 32$ ) and a corresponding vertex weight, defined as it is shown in Fig. 1.6, where  $\omega = e^{-\beta\epsilon_1}$ ,  $\bar{\omega} = e^{-\beta\epsilon_2}$ ,  $\omega_{56} = e^{-\beta\epsilon_3}$ ,  $\bar{\omega}_{56} = e^{-\beta\epsilon_4}$ , etc.

This notation for the Boltzmann vertex weights has been introduced by Sacco and Wu,<sup>26</sup> and is used also by Baxter.<sup>11</sup> This model is not exactly soluble in the general case, but there are several particular cases that are

soluble.<sup>26</sup> Here we will consider one of such cases, when the model satisfy the free-fermion condition :

$$\begin{aligned}\omega\bar{\omega} &= \omega_{12}\bar{\omega}_{12} - \omega_{13}\bar{\omega}_{13} + \omega_{14}\bar{\omega}_{14} - \omega_{15}\bar{\omega}_{15} + \omega_{16}\bar{\omega}_{16} \\ \omega\omega_{mn} &= \omega_{ij}\omega_{kl} - \omega_{ik}\omega_{jl} + \omega_{il}\omega_{jk}\end{aligned}\quad (14)$$

for all permutations i, j, k, l, m, n of 1, 2, ..., 6 such that  $m < n$  and  $i < j < k < l$ . There are 15 such permutations ( corresponding to the 15 choices of m and n ), and hence a total of 16 conditions.

The rather complicated notation for the Boltzmann weights is justified by the condensed form of the free-fermion conditions Eq. (14).

When these conditions are satisfied, the free energy in the thermodynamical limit can be expressed as

$$f = -\frac{1}{8\pi^2\beta} \int_0^{2\pi} d\theta \int_0^{2\pi} d\phi \log[\omega^2 D(\theta, \phi)] \quad (15)$$

where

$$\begin{aligned}\omega^2 D(\theta, \phi) &= \Omega_1^2 + \Omega_2^2 + \Omega_3^2 + \Omega_4^2 - 2(\Omega_1\Omega_3 - \Omega_2\Omega_4)\cos(\theta) \\ &\quad - 2(\Omega_1\Omega_4 - \Omega_2\Omega_3)\cos(\phi) + 2(\Omega_3\Omega_4 - \Omega_5\Omega_6)\cos(\theta + \phi) \\ &\quad + 2(\Omega_5\Omega_6 - \Omega_1\Omega_2)\cos(\theta - \phi) - 4a\sin(\phi)\sin(\theta + \phi) \\ &\quad - 4b\sin(\theta)\sin(\theta + \phi) - 2c\sin^2(\theta + \phi) - 2d\sin^2(\theta) - 2e\sin^2(\phi)\end{aligned}\quad (16)$$

with

$$\begin{aligned}\Omega_1 &= \omega + \bar{\omega}, & \Omega_2 &= \omega_{25} + \bar{\omega}_{25} \\ \Omega_3 &= \omega_{14} + \bar{\omega}_{14}, & \Omega_4 &= \omega_{36} + \bar{\omega}_{36} \\ \Omega_5\Omega_6 &= \omega_{15}\omega_{24} + \bar{\omega}_{15}\bar{\omega}_{24} + \omega_{14}\bar{\omega}_{25} + \omega_{25}\bar{\omega}_{14} \\ a &= \omega_{12}\omega_{45} + \bar{\omega}_{12}\bar{\omega}_{45} - \omega\bar{\omega}_{36} - \bar{\omega}\omega_{36} \\ b &= \omega_{23}\omega_{56} + \bar{\omega}_{23}\bar{\omega}_{56} - \omega\bar{\omega}_{14} - \bar{\omega}\omega_{14} \\ c &= \omega\bar{\omega} + \omega_{13}\bar{\omega}_{13} - \omega_{12}\bar{\omega}_{12} - \omega_{23}\bar{\omega}_{23} \\ d &= \omega\bar{\omega} + \omega_{26}\bar{\omega}_{26} - \omega_{16}\bar{\omega}_{16} - \omega_{12}\bar{\omega}_{12} \\ e &= \omega\bar{\omega} + \omega_{15}\bar{\omega}_{15} - \omega_{56}\bar{\omega}_{56} - \omega_{16}\bar{\omega}_{16}\end{aligned}\quad (17)$$

The critical temperature is determined from the equation

$$\Omega_1 + \Omega_2 + \Omega_3 + \Omega_4 = 2\max(\Omega_1, \Omega_2, \Omega_3, \Omega_4) \quad (18)$$

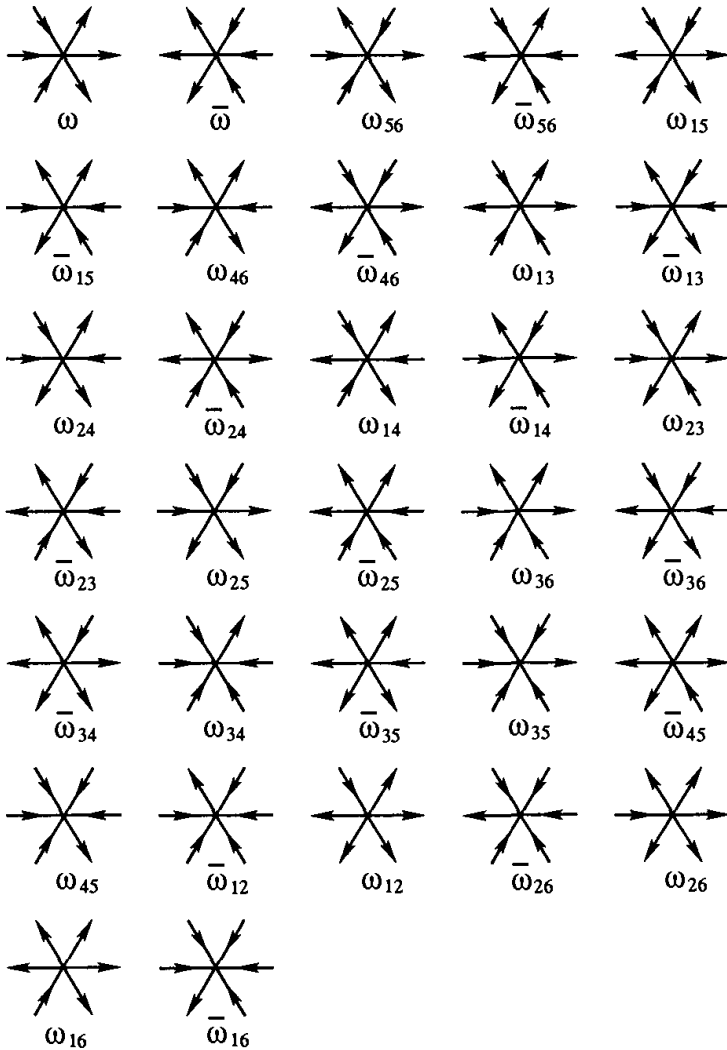


Fig. 1.6. Arrow configurations and vertex weights of the 32-vertex model.

We will show now how different 2D Ising models without crossing interactions can be mapped onto the 16-vertex model or the 32-vertex model, with the free-fermion condition automatically satisfied in such cases.

Let us consider at first an Ising model defined on a Kagomé lattice, with two-spin interactions between nearest neighbors (nn) and between next-nearest neighbors (nnn),  $J_1$  and  $J_2$ , respectively, as shown in Fig. 1.7.

The Hamiltonian is written as

$$H = -J_1 \sum_{(ij)} \sigma_i \sigma_j - J_2 \sum_{(ij)} \sigma_i \sigma_j \quad (19)$$

where and the first and second sums run over the spin pairs connected by

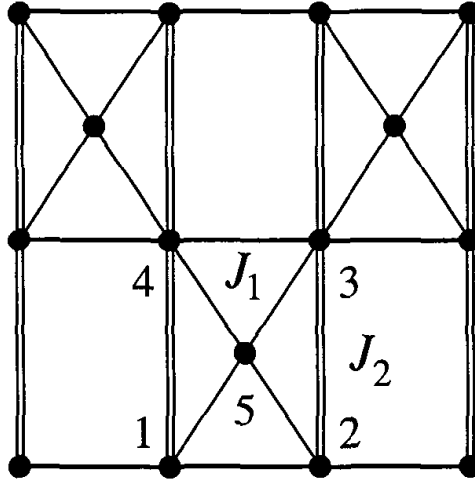


Fig. 1.7. Kagomé lattice. Interactions between nearest neighbors and between next-nearest neighbors,  $J_1$  and  $J_2$ , are shown by single and double bonds, respectively. The lattice sites in a cell are numbered for decimation demonstration.

single and double bonds, respectively.

The partition function is written as

$$Z = \sum_{\sigma} \prod_c \exp[K_1(\sigma_1\sigma_5 + \sigma_2\sigma_5 + \sigma_3\sigma_5 + \sigma_4\sigma_5 + \sigma_1\sigma_2 + \sigma_3\sigma_4) + K_2(\sigma_1\sigma_4 + \sigma_3\sigma_2)] \quad (20)$$

where  $K_{1,2} = J_{1,2}/k_B T$  and where the sum is performed over all spin configurations and the product is taken over all elementary cells of the lattice.

Since there are no crossing bond interactions, the system can be transformed into an exactly solvable free-fermion model. We decimate the central spin of each elementary cell of the lattice. In doing so, we obtain a checkerboard Ising model with multispin interactions (see Fig. 1.8).

The Boltzmann weight associated to each shaded square is given by

$$W(\sigma_1, \sigma_2, \sigma_3, \sigma_4) = 2 \cosh(K_1(\sigma_1 + \sigma_2 + \sigma_3 + \sigma_4)) \exp[K_2(\sigma_1\sigma_4 + \sigma_2\sigma_3) + K_1(\sigma_1\sigma_2 + \sigma_3\sigma_4)] \quad (21)$$

The partition function of this checkerboard Ising model is given by

$$Z = \sum_{\sigma} \prod W(\sigma_1, \sigma_2, \sigma_3, \sigma_4) \quad (22)$$

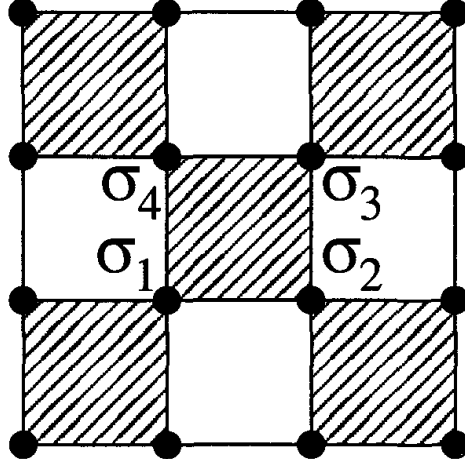


Fig. 1.8. The checkerboard lattice. At each shaded square is associated the Boltzmann weight  $W(\sigma_1, \sigma_2, \sigma_3, \sigma_4)$ , given in the text.

where the sum is performed over all spin configurations and the product is taken over all the shaded squares of the lattice.

In order to map this model onto the 16-vertex model, let us introduce another square lattice where each site is placed at the center of each shaded square of the checkerboard lattice, as shown in Fig. 1.9.

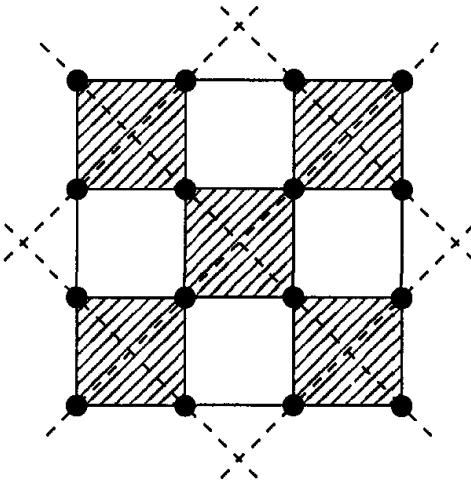


Fig. 1.9. The checkerboard lattice and the associated square lattice with their bonds indicated by dashed lines.

At each bond of this lattice we associate an arrow pointing out of the site if the Ising spin that is traversed by this bond is equal to +1, and pointing into the site if the Ising spin is equal to -1, as it is shown in Fig. 1.10.

In this way, we have a 16-vertex model on the associated square lattice. The Boltzmann weights of this vertex model are expressed in terms of the Boltzmann weights of the checkerboard Ising model, as follows

$$\begin{aligned}
 \omega_1 &= W(-, -, +, +) & \omega_5 &= W(-, +, -, +) \\
 \omega_2 &= W(+, +, -, -) & \omega_6 &= W(+, -, +, -) \\
 \omega_3 &= W(-, +, +, -) & \omega_7 &= W(+, +, +, +) \\
 \omega_4 &= W(+, -, -, +) & \omega_8 &= W(-, -, -, -) \\
 \omega_9 &= W(-, +, +, +) & \omega_{13} &= W(+, -, +, +) \\
 \omega_{10} &= W(+, -, -, -) & \omega_{14} &= W(-, +, -, -) \\
 \omega_{11} &= W(+, +, -, +) & \omega_{15} &= W(+, +, +, -) \\
 \omega_{12} &= W(-, -, +, -) & \omega_{16} &= W(-, -, -, +)
 \end{aligned} \tag{23}$$

Taking Eq. (21) into account, we obtain

$$\begin{aligned}
 \omega_1 = \omega_2 &= 2e^{-2K_2+2K_1} \\
 \omega_3 = \omega_4 &= 2e^{2K_2-2K_1} \\
 \omega_5 = \omega_6 &= 2e^{-2K_2-2K_1} \\
 \omega_7 = \omega_8 &= 2e^{2K_2+2K_1} \cosh(4K_1) \\
 \omega_9 = \omega_{10} = \omega_{11} = \omega_{12} &= \omega_{13} = \omega_{14} = \omega_{15} = \omega_{16} = 2 \cosh(2K_1)
 \end{aligned} \tag{24}$$

As can be easily verified, the free-fermion conditions Eq. (9) are identically satisfied by the Boltzmann weights Eq. (24), for arbitrary values of  $K_1$  and  $K_2$ . If we replace Eq. (24) in Eq. (10) and Eq. (11), we can obtain the explicit expression of the free energy of the model. Moreover, by replacing Eq. (24) in Eq. (12) we obtain the critical condition for this system :

$$\begin{aligned}
 &\frac{1}{2} [\exp(2K_1 + 2K_2) \cosh(4K_1) + \exp(-2K_1 - 2K_2)] + \\
 &\cosh(2K_1 - 2K_2) + 2 \cosh(2K_1) = 2 \max\left\{\frac{1}{2} [\exp(2K_1 + 2K_2) \cosh(4K_1) + \right. \\
 &\left. \exp(-2K_1 - 2K_2)] ; \cosh(2K_2 - 2K_1) ; \cosh(2K_1)\right\}
 \end{aligned} \tag{25}$$

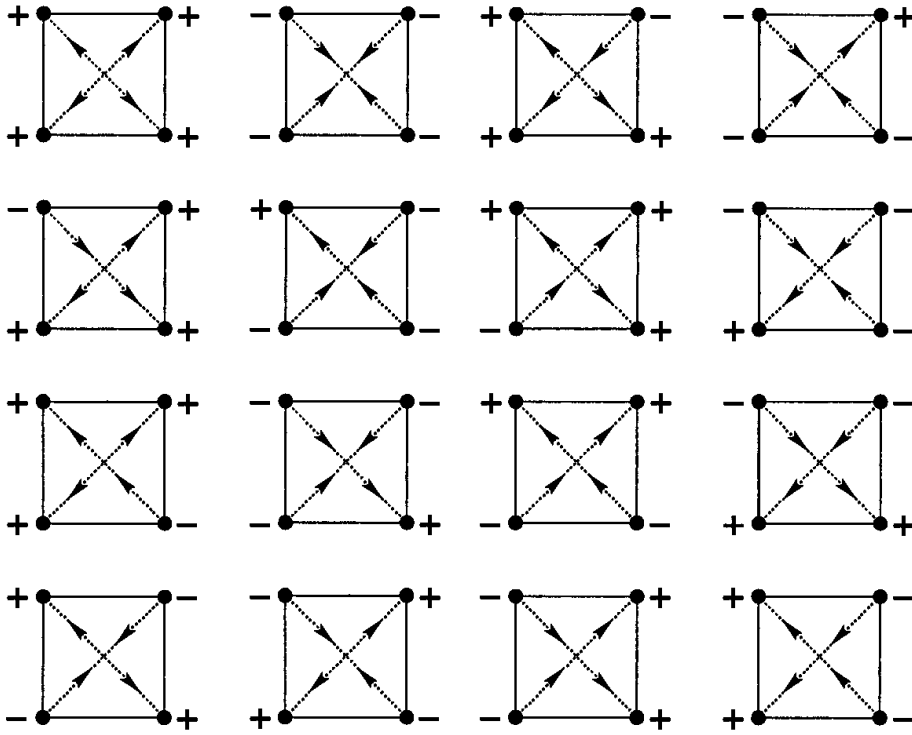


Fig. 1.10. The relation between spin configurations and arrow configurations of the associated vertex model.

which is decomposed into four critical lines depending on the values of  $J_1$  and  $J_2$ .

The singularity of the free energy is everywhere logarithmic.

Now, we will consider another 2D Ising model with two-spin interactions and without crossing bonds. This model is defined on a centered honeycomb lattice, as shown in Fig. 1.11.

The Hamiltonian of this model is as follows :

$$H = -J_1 \sum_{(ij)} \sigma_i \sigma_j - J_2 \sum_{(ij)} \sigma_i \sigma_j - J_3 \sum_{(ij)} \sigma_i \sigma_j \quad (26)$$

where  $\sigma_i = \pm 1$  is an Ising spin occupying the lattice site  $i$ , and the first, second, and third sums run over the spin pairs connected by heavy, light, and doubly light bonds, respectively ( see Fig. 1.11). When  $J_2 = J_3 = 0$ , one recovers the honeycomb lattice, and when  $J_1 = 0 = J_2 = J_3$ , one has the triangular lattice.

Let us denote the central spin in a lattice cell, shown in Fig. 1.11, by  $\sigma$ , and number the other spins from  $\sigma_1$  to  $\sigma_6$ . The Boltzmann weight associated

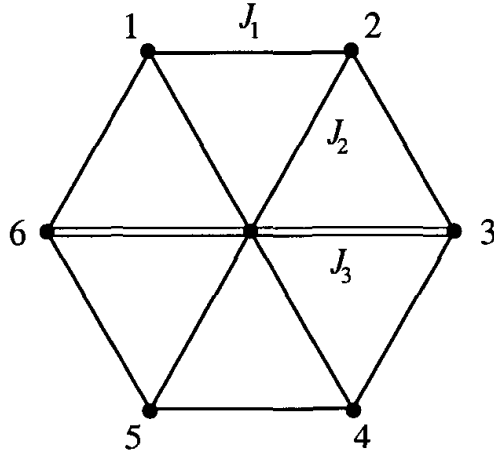


Fig. 1.11. Unit cell of the centered honeycomb lattice: heavy, light, and double-light bonds denote the interactions  $J_1$ ,  $J_2$ , and  $J_3$ , respectively. The sites on the honeycomb are numbered from 1 to 6 for decimation demonstration (see text).

to the elementary cell is given by

$$W = \exp[K_1(\sigma_1\sigma_2 + \sigma_2\sigma_3 + \sigma_3\sigma_4 + \sigma_4\sigma_5 + \sigma_5\sigma_6 + \sigma_6\sigma_1) + K_2\sigma(\sigma_1 + \sigma_2 + \sigma_4 + \sigma_5) + K_3\sigma(\sigma_3 + \sigma_6)] \quad (27)$$

The partition function of the model is written as

$$Z = \sum_{\sigma} \prod_c W \quad (28)$$

where the sum is performed over all spin configurations and the product is taken over all elementary cells of the lattice. Periodic boundary conditions are imposed. Since there is no crossing-bond interaction, the model is exactly soluble. To obtain the exact solution, we decimate the central spin of each elementary cell of the lattice. In doing so, we obtain a honeycomb Ising model with multispin interactions.

After decimation of each central spin, the Boltzmann factor associated to an elementary cell is given by

$$W' = 2 \exp[K_1(\sigma_1\sigma_2 + \sigma_2\sigma_3 + \sigma_3\sigma_4 + \sigma_4\sigma_5 + \sigma_5\sigma_6 + \sigma_6\sigma_1)] \times \cosh[K_2(\sigma_1 + \sigma_2 + \sigma_4 + \sigma_5) + K_3(\sigma_3 + \sigma_6)] \quad (29)$$

We will show in the following that this model is equivalent to a special case of the 32-vertex model on the triangular lattice that satisfies the free-fermion condition.

Let us consider the dual lattice of the honeycomb lattice, i.e. the triangular lattice.<sup>11</sup> The sites of the dual lattice are placed at the center of each elementary cell and their bonds are perpendicular to bonds of the honeycomb lattice, as it is shown in Fig. 1.12.

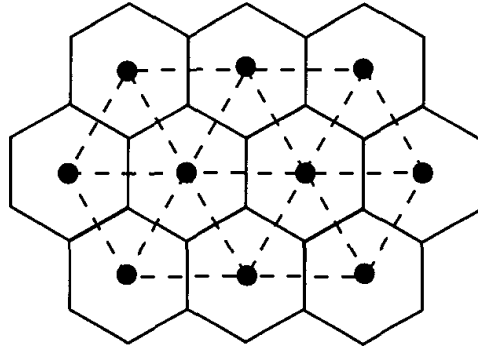


Fig. 1.12. The honeycomb lattice and the dual triangular lattice, with their bonds indicated by dashed lines.

Each site of the triangular lattice is surrounded by 6 sites of the honeycomb lattice. At each bond of the triangular lattice we associate an arrow. We take the arrow configuration shown in Fig. 1.13 as the standard one. We can establish a two-to-one correspondence between spin configurations of the honeycomb lattice and arrow configurations in the triangular lattice. This can be done in the following way : if the spins on either side of a bond of the triangular lattice are equal ( different ), place an arrow on the bond pointing in the same ( opposite ) way as the standard. If we do this for all bonds, then at each site of the triangular lattice there must be an even number of non-standard arrows on the six incident bonds, and hence an odd number of incoming ( and outgoing ) arrows. This is the property that characterize the 32 vertex model on the triangular lattice.

In Fig. 1.14 we show two cases of the relation between arrow configurations on the triangular lattice and spin configurations on the honeycomb lattice.

In consequence, the Boltzmann weights of the 32-vertex model will be a function of the Boltzmann weights  $W'(\sigma_1, \sigma_2, \sigma_3, \sigma_4, \sigma_5, \sigma_6)$ , associated to

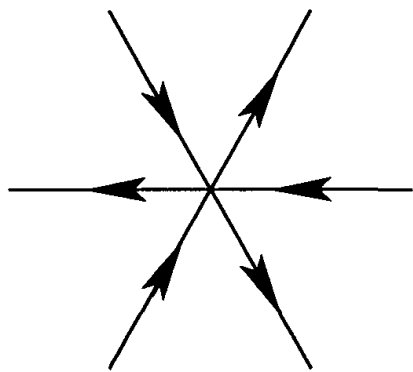


Fig. 1.13. The standard arrow configuration for the triangular lattice.

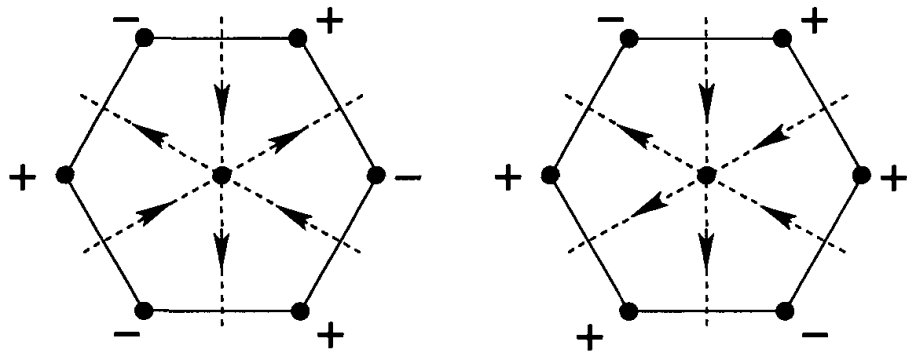


Fig. 1.14. Two cases of the correspondence between arrow configurations and spin configurations.

a face of the honeycomb lattice. By using the relation between vertex and spin configurations described above and expression Eq. (29), we find

$$\begin{aligned}
\omega &= W'(+, -, -, -, +, +) = 2e^{2K_1} \\
\bar{\omega} &= W'(+, +, -, +, +, -) = 2e^{-2K_1} \cosh(4K_2 - 2K_3) \\
\omega_{56} &= W'(+, -, +, -, +, +) = 2e^{-2K_1} \cosh(2K_3) \\
\bar{\omega}_{56} &= W'(+, +, +, +, +, -) = 2e^{2K_1} \cosh(4K_2) \\
\omega_{15} &= W'(+, +, +, -, +, +) = 2e^{2K_1} \cosh(2K_2 + 2K_3) \\
\bar{\omega}_{15} &= W'(+, -, +, +, +, -) = 2e^{-2K_1} \cosh(2K_2) \\
\omega_{46} &= W'(+, -, +, +, +, +) = 2e^{2K_1} \cosh(2K_2 + 2K_3) \\
\bar{\omega}_{46} &= W'(+, +, +, -, +, -) = 2e^{-2K_1} \cosh(2K_2) \\
\omega_{13} &= W'(+, +, +, +, -, +) = 2e^{2K_1} \cosh(2K_2 + 2K_3) \\
\bar{\omega}_{13} &= W'(+, -, +, -, -, -) = 2e^{-2K_1} \cosh(2K_2) \\
\omega_{24} &= W'(+, -, -, -, -, -) = 2e^{2K_1} \cosh(2K_2 + 2K_3) \\
\bar{\omega}_{24} &= W'(+, +, -, +, -, +) = 2e^{-2K_1} \cosh(2K_2) \\
\omega_{14} &= W'(+, +, +, +, +, +) = 2e^{6K_1} \cosh(4K_2 + 2K_3) \\
\bar{\omega}_{14} &= W'(+, -, +, -, +, -) = 2e^{-6K_1} \\
\omega_{23} &= W'(+, -, -, -, +, -) = 2e^{-2K_1} \cosh(2K_3) \\
\bar{\omega}_{23} &= W'(+, +, -, +, +, +) = 2e^{2K_1} \cosh(4K_2) \\
\omega_{25} &= W'(+, -, -, +, -, -) = 2e^{-2K_1} \cosh(2K_3) \\
\bar{\omega}_{25} &= W'(+, +, -, -, -, +) = 2e^{2K_1} \\
\omega_{36} &= W'(+, -, +, +, -, +) = 2e^{-2K_1} \cosh(2K_3) \\
\bar{\omega}_{36} &= W'(+, +, +, -, -, -) = 2e^{2K_1} \\
\bar{\omega}_{34} &= W'(+, +, -, +, -, -) = 2e^{-2K_1} \cosh(2K_2 - 2K_3) \\
\omega_{34} &= W'(+, -, -, -, -, +) = 2e^{2K_1} \cosh(2K_2) \\
\bar{\omega}_{35} &= W'(+, +, -, -, -, -) = 2e^{2K_1} \cosh(2K_3) \\
\omega_{35} &= W'(+, -, -, +, -, +) = 2e^{-2K_1} \\
\bar{\omega}_{45} &= W'(+, +, -, -, +, -) = 2e^{-2K_1} \cosh(2K_2 - 2K_3) \\
\omega_{45} &= W'(+, -, -, +, +, +) = 2e^{2K_1} \cosh(2K_2) \\
\bar{\omega}_{12} &= W'(+, -, +, -, -, +) = 2e^{-2K_1} \cosh(-2K_2 + 2K_3) \\
\omega_{12} &= W'(+, +, +, +, -, -) = 2e^{2K_1} \cosh(2K_2) \\
\bar{\omega}_{26} &= W'(+, +, +, -, -, +) = 2e^{2K_1} \cosh(2K_3) \\
\omega_{26} &= W'(+, -, +, +, -, -) = 2e^{-2K_1} \\
\omega_{16} &= W'(+, +, -, -, +, +) = 2e^{2K_1} \cosh(2K_2) \\
\bar{\omega}_{16} &= W'(+, -, -, +, +, -) = 2e^{-2K_1} \cosh(2K_2 - 2K_3)
\end{aligned} \tag{30}$$

Using the above expressions in Eqs. (15), (16) and (17) we can obtain the expression of the free energy of the centered honeycomb lattice Ising model.

Taking into account Eqs. (30), (17) and (18), the critical temperature of the model is determined from the equation :

$$\begin{aligned} e^{2K_1} + e^{-2K_1} \cosh(4K_2 - 2K_3) + 2e^{-2K_1} \cosh(2K_3) + 2e^{2K_1} + \\ e^{6K_1} \cosh(4K_2 + 2K_3) + e^{-6K_1} = 2\max\{e^{2K_1} + e^{-2K_1} \cosh(4K_2 - 2K_3); \\ e^{2K_1} + e^{-2K_1} \cosh(2K_3); e^{6K_1} \cosh(4K_1 + 2K_3) + e^{-6K_1}\} \quad (31) \end{aligned}$$

The solutions of this equation are analyzed in the next section.

We think that with the two cases studied above, the reader will be able to apply this procedure to other 2D Ising models without crossing bonds as, for instance, the Ising model on the centered square lattice. After decimation of the central spin in each square, this model can be mapped into a special case of the 16-vertex model, by following the same procedure that we have employed for the honeycomb lattice model.

### 1.3.3. *Disorder solutions for two-dimensional Ising models*

Disorder solutions are very useful for clarifying the phase diagrams of anisotropic models and also imply constraints on the analytical behavior of the partition function of these models.

A great variety of anisotropic models (with different coupling constants in the different directions of the lattice) are known to posses remarkable submanifolds in the space of parameters, where the partition function is computable and takes a very simple form. These are the disorder solutions.

All the methods applied for obtaining these solutions rely on the same mechanism : a certain local decoupling of the degrees of freedom of the model, which results in an effective reduction of dimensionality for the lattice system. Such a property is provided by a simple local condition imposed on the Boltzmann weights of the elementary cell generating the lattice.<sup>27</sup>

Some completely integrable models present disorder solutions, e.g. the triangular Ising model and the symmetric 8-vertex model. But very important models that are not integrable, also present this type of solutions, e.g. the triangular Ising model with a field, the triangular q-state Potts model, and the general 8-vertex model. Here we will consider only two dimensional Ising models.

In order to introduce the method, we will analyze, at the first place, the simplest case, i.e. the anisotropic Ising model on the triangular lattice ( see Fig. 1.15).

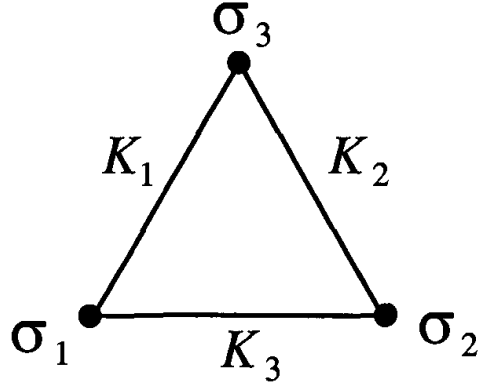


Fig. 1.15. The elementary cell of the triangular lattice, with three interactions  $K_1$ ,  $K_2$ , and  $K_3$ .

The Boltzmann weight of the elementary cell is

$$W(\sigma_1, \sigma_2, \sigma_3) = \exp\left[\frac{1}{2}(K_1\sigma_1\sigma_3 + K_2\sigma_2\sigma_3 + K_3\sigma_1\sigma_2)\right] \quad (32)$$

In every case, the local criterion will be defined by the following condition : after summation over some of its spins ( to be defined in each case ), the Boltzmann weight associated with the elementary cell of the model must not depend on the remaining spins any longer. For instance, for the triangular lattice, we will require

$$\sum_{\sigma_3} W(\sigma_1, \sigma_2, \sigma_3) = \lambda(K_1, K_2, K_3) \quad (33)$$

where  $\lambda$  is a function only of  $K_1$ ,  $K_2$  and  $K_3$  ( it is independent of  $\sigma_1$  and  $\sigma_2$  ). By using Eq. (32) we find

$$\sum_{\sigma_3} W(\sigma_1, \sigma_2, \sigma_3) = \exp\left(\frac{1}{2}K_3\sigma_1\sigma_2\right) \cosh\left[\frac{1}{2}(K_1\sigma_1 + K_2\sigma_2)\right] \quad (34)$$

But, as it is well known, we can write

$$\cosh\left[\frac{1}{2}(K_1\sigma_1 + K_2\sigma_2)\right] = A \exp(K\sigma_1\sigma_2) \quad (35)$$

with

$$A = \left[\cosh\left(\frac{K_1 + K_2}{2}\right) \cosh\left(\frac{K_1 - K_2}{2}\right)\right]^{\frac{1}{2}} \quad (36)$$

$$K = \frac{1}{2} \log \left[ \frac{\cosh(\frac{K_1+K_2}{2})}{\cosh(\frac{K_1-K_2}{2})} \right] \quad (37)$$

In order that  $\sum_{\sigma_3} W(\sigma_1, \sigma_2, \sigma_3)$  be independent of  $\sigma_1$  and  $\sigma_2$  we must impose the condition  $K = -\frac{1}{2}K_3$ . From this condition we find

$$e^{K_3} \cosh\left(\frac{K_1 + K_2}{2}\right) = \cosh\left(\frac{K_1 - K_2}{2}\right) \quad (38)$$

from which we can determine the expression of  $\lambda$ :

$$\lambda(K_1, K_2, K_3) = [\cosh\left(\frac{K_1 + K_2}{2}\right) \cosh\left(\frac{K_1 - K_2}{2}\right)]^{\frac{1}{2}} \quad (39)$$

It is easy to verify that Eq.(38) can be written as

$$\tanh(K_1) \tanh(K_2) + \tanh(K_3) = 0 \quad (40)$$

This 2D subvariety in the space of parameters is called the disorder variety of the model.

Let us now impose particular boundary conditions for the lattice ( see Fig. 1.16) : on the upper layer, all interactions are missing, so that the spins of the upper layer only interact with those of the lower one. It immediately follows that if one sums over all the spins of the upper layer and if one requires the disorder condition Eq. (40) , the same boundary conditions reappear for the next layer.

Iterating the procedure leads one to an exact expression for the partition function, when restricted to subvariety Eq. (40):

$$Z = \lambda(K_1, K_2, K_3)^N \quad (41)$$

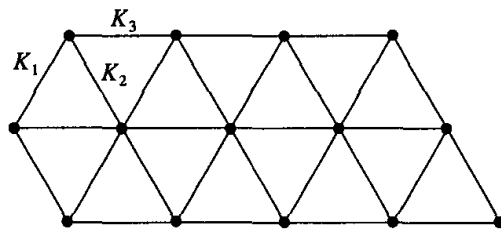


Fig. 1.16. Two layers of the triangular lattice.

where  $N$  is the number of sites of the lattice. The free energy in the thermodynamic limit is given by

$$f = -\frac{1}{2\beta} \log[\cosh(\frac{K_1 + K_2}{2}) \cosh(\frac{K_1 - K_2}{2})] \quad (42)$$

The partition function Eq. (41) corresponds to lattices with unusual boundary conditions. In the physical domain, where the coupling constants are real, these do not affect the partition function per site (or the free energy per site) in the thermodynamic limit, and the expression Eq. (42) also corresponds to the free energy per site with standard periodic boundary conditions. On the contrary, in the non-physical domain (complex coupling constants), the boundary conditions are known to play an important role, even after taking the thermodynamic limit.

Let us consider now the Kagomé lattice Ising model with two-spin interactions between nn and nnn, studied in the next section. If we apply the same procedure that for the triangular lattice Ising model, we obtain for the disorder variety:

$$e^{4K_2} = \frac{2(e^{4K_1} + 1)}{e^{8K_1} + 3} \quad (43)$$

This disorder variety does not have intersection with the critical variety of the model.

Following the method that we have exposed for the Ising model on the triangular lattice, the reader will be able to find the disorder varieties for other 2D Ising models with anisotropic interactions.

#### 1.4. Reentrance in exactly solved frustrated Ising spin systems

In this section, we show and discuss the phase diagrams of several selected 2D frustrated Ising systems that have been recently solved. For general exact methods, the reader is referred to the book by Baxter,<sup>11</sup> and to the preceding section. In the following, we consider only frustrated systems that exhibit the **reentrance phenomenon**. A reentrant phase can be defined as a phase with no long-range order, or no order at all, occurring in a region below an ordered phase on the temperature ( $T$ ) scale. A well-known example is the reentrant phase in spin-glasses (see the review by Binder and Young<sup>28</sup>). The origin of the reentrance in spin-glasses is not well understood. It is believed that it is due to a combination of frustration and bond disorder. In order to see the role of the frustration alone, we show here

the exact results on a number of periodically frustrated Ising systems. The idea behind the works shown in this section is to search for the ingredients responsible for the occurrence of the reentrant phase. Let us review in the following a few models showing a reentrant phase. Discussion on the origin of the reentrance will be given in the conclusion.

#### 1.4.1. Centered square lattice

Even before the concept of frustration was introduced,<sup>2</sup> systems with competing interactions were found to possess rich critical behavior and non-trivial ordered states. Among these models, the centered square lattice Ising model (see Fig. 1.17), introduced by Vaks et al,<sup>12</sup> with nn and nnn interactions,  $J_1$  and  $J_2$ , respectively, is to our knowledge the first exactly soluble model which exhibits successive phase transitions with a reentrant paramagnetic phase at low  $T$ . Exact expression for the free energy, some correlation functions, and the magnetization of one sublattice were given in the original work of Vaks et al.

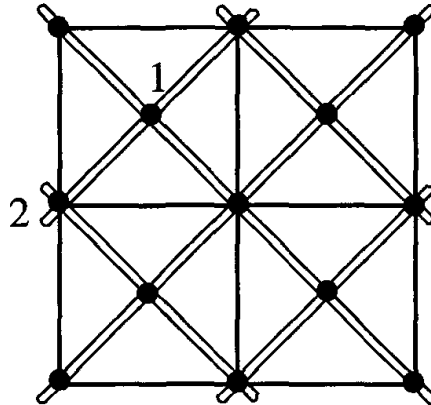


Fig. 1.17. Centered square lattice. Interactions between nn and nnn,  $J_1$  and  $J_2$ , are denoted by white and black bonds, respectively. The two sublattices are numbered 1 and 2.

We distinguish two sublattices 1 and 2. Sublattice 1 contains the spins at the square centers, and sublattice 2 generates a square lattice with interaction  $J_2$  in both horizontal and vertical directions. Spins of sublattice 1 interact only with spins of sublattice 2 via diagonal interactions  $J_1$ . The ground state properties of this model are as follows : for  $a = J_2 / |J_1| > -1$ , spins of sublattice 2 orders ferromagnetically and the spins of sublattice 1

are parallel (antiparallel) to the spins of sublattice 2 if  $J_1 > 0$  ( $< 0$ ); for  $a < -1$ , spins of sublattice 2 orders antiferromagnetically, leaving the centered spins free to flip.

#### 1.4.1.1. Phase diagram

The phase diagram of this model is given by Vaks et al.<sup>12</sup> Except for  $a = -1$ , there is always a finite critical temperature.

When  $J_2$  is antiferromagnetic ( $> 0$ ) and  $J_2/J_1$  is in a small region near 1, the system is successively in the paramagnetic state, an ordered state, the reentrant paramagnetic state, and another ordered state, with decreasing temperature (see Fig. 1.18).

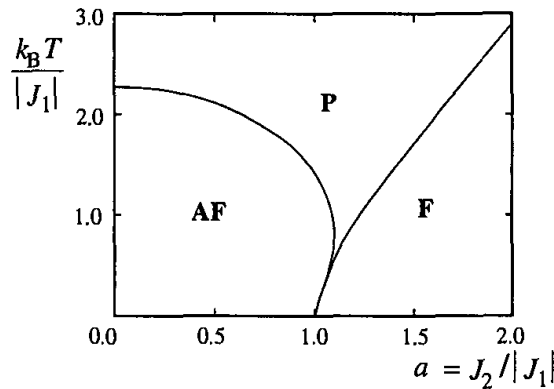


Fig. 1.18. Phase diagram of centered square lattice.<sup>12</sup>

The centered square Ising lattice has been generalized to include several kinds of interaction.<sup>13,14</sup> For example, when the vertical interaction  $J_2$  is different from the horizontal one, say  $J_3$ , the phase diagram becomes more complicated.

#### 1.4.1.2. Nature of ordering and disorder solutions

For the sake of simplicity, let us consider hereafter the case of nn and nnn interactions only, namely  $J_1$  and  $J_2$  ( $J_3 = J_2$ ). Note that though an exact critical line was obtained,<sup>12</sup> the order parameter was not calculated, though the magnetization of one sublattice were given in the original work of Vaks et al.<sup>12</sup> Later, Choy and Baxter<sup>29</sup> have obtained the total magnetization for this model in the ferromagnetic region. However, the ordering in

the antiferromagnetic (frustrated) region has not been exactly calculated, despite the fact that it may provide an interesting ground for understanding the reentrance phenomenon. We have studied this aspect by means of Monte Carlo (MC) simulations.<sup>30</sup> The question which naturally arises is whether or not the disorder of sublattice 1 at  $T = 0$  remains at finite  $T$ . If the spins of sublattice 1 remains disordered at finite  $T$  in the antiferromagnetic region we have a remarkable kind of ordered state: namely the coexistence between order and disorder. This behavior has been observed in three-dimensional Ising spin models<sup>31,32</sup> and in an exactly soluble model (the Kagomé lattice).<sup>16</sup> In the latter system, which is similar to the present model (discussed in the next subsection), it was shown that the coexistence of order and disorder at finite  $T$  shed some light on the reentrance phenomena. To verify the coexistence between order and disorder in the centered square lattice, we have performed Monte Carlo (MC) simulations. The results for the Edwards-Anderson sublattice order parameters  $q_i$  and the staggered susceptibility of sublattice 2, as functions of  $T$ , are shown in Fig. 1.19 in the case  $a = -2$ .

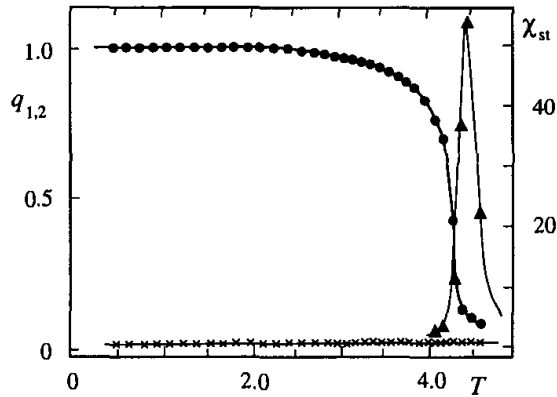


Fig. 1.19. Temperature dependence of sublattice Edwards-Anderson order parameters,  $q_1$  and  $q_2$  (crosses and black circles, respectively) in the case  $a = J_2 / |J_1| = -2$ , by Monte Carlo simulation. Susceptibility calculated by fluctuations of magnetization of sublattice 2 is also shown. The lattice used contains  $N = 2 \times 60 \times 60$  spins with periodic boundary conditions.<sup>30</sup>

As is seen, sublattice 2 is ordered up to the transition at  $T_c$  while sublattice 1 stays disordered at all  $T$ . This result shows a new example where order and disorder coexists in an equilibrium state. This result supports the conjecture formulated by Azaria et al,<sup>16</sup> namely the coexistence of

order and disorder is a necessary condition for the reentrant behavior to occur. The partial disorder just compensates the loss of entropy due to the partial ordering of the high- $T$  phase. In a previous paper,<sup>16</sup> the importance of the disorder line in understanding the reentrance phenomenon has been emphasized. There has been suggested that this type of line may be necessary for the change of ordering from the high- $T$  ordered phase to the low- $T$  one. In the narrow reentrant paramagnetic region, preordering fluctuations with different symmetries exist near each critical line. Therefore the correlation functions change their behavior as the temperature is varied in the reentrant paramagnetic region. As a consequence of the change of symmetries there exist spins for which the two-point correlation function (between nn spins) has different signs, near the two critical lines , in the reentrant paramagnetic region. Hence it is reasonable to expect that it has to vanish at a disorder temperature  $T_D$  . This point can be considered as a non-critical transition point which separates two different paramagnetic phases. The two-point correlation function defined above may be thought of as a non-local 'disorder parameter'. This particular point is just the one which has been called a disorder point by Stephenson<sup>33</sup> in analyzing the behavior of correlation functions for systems with competing interactions. For the centered square lattice Ising model considered here, the Stephenson disorder line is<sup>30</sup>

$$\cosh(4J_1/k_B T_D) = \exp(-4J_2/k_B T_D) \quad (44)$$

The two-point correlation function at  $T_D$  between spins of sublattice 2 separated by a distance  $r$  is zero for odd  $r$  and decay like  $r^{-1/2}[\tanh(J_2/k_B T_D)]^r$  for  $r$  even.<sup>33</sup> However, there is *no dimensional reduction* on the Stephenson line given above. Usually, one defines the disorder point as the temperature where there is an effective reduction of dimensionality in such a way that physical quantities become simplified spectacularly.<sup>27</sup> In general, these two types of disorder line are equivalent, as for example , in the case of the Kagomé lattice Ising model (see below). This is not the case here. In order to calculate this disorder line for the centered square lattice, we recall that this model is equivalent to an 8-vertex model that verifies the free-fermion condition.<sup>34</sup> The disorder line corresponding to dimensional reduction, was given for the general 8-vertex model by Giacomini.<sup>35</sup> When this result is applied to the centered square lattice, one finds that the disorder variety is given by

$$\exp(4J_2/k_B T) = (1 - i \sinh(4J_1/k_B T))^{-1} \quad (45)$$

where  $i^2 = -1$ . This disorder line lies on the unphysical (complex) region of the parameter space of this system. When calculated on the line Eq. (45), the magnetization of this model, evaluated recently by Choy and Baxter<sup>29</sup> in the ferromagnetic region, becomes singular, as it is usually the case for the disorder solutions with dimensional reduction.<sup>36</sup> Since in the centered square lattice, the two kinds of disorder line are not equivalent, we conclude, according to the arguments presented above, that the Stephenson disorder line Eq. (44) is the relevant one for the reentrance phenomenon.

Disorder solutions have recently found interesting applications, as for example in the problem of cellular automata (for a review see Rujan<sup>37</sup>). Moreover, they also serve to built a new kind of series expansion for lattice spin systems.<sup>27</sup>

### 1.4.2. *Kagomé lattice*

#### 1.4.2.1. *Model with nn and nnn interactions*

Another model of interest is the Kagomé lattice shown in Fig. 1.7. The Kagomé Ising lattice with nn interaction  $J_1$  has been solved a long time ago<sup>15</sup> showing no phase transition at finite  $T$  when  $J_1$  is antiferromagnetic. Taking into account the nnn interaction  $J_2$  [see Fig. 1.7 and Eq. (19)], we have solved<sup>16</sup> this model by transforming it into a 16-vertex model which satisfies the free-fermion condition.

The critical condition is given by Eq. (25). For the whole phase diagram, the reader is referred to the paper by Azaria et al.<sup>16</sup> We show in Fig. 1.20 only the small region of  $J_2/J_1$  in the phase diagram which has the reentrant paramagnetic phase and a disorder line.

The phase X indicates a partially ordered phase where the central spins are free (the nature of ordering was determined by MC simulations).<sup>16</sup> Here again, the reentrant phase takes place between a low- $T$  ordered phase and a partially disordered phase. This suggests that a partial disorder at the high- $T$  phase is necessary to ensure that the entropy is larger than that of the reentrant phase.

#### 1.4.2.2. *Generalized Kagomé lattice*

When all the interactions are different in the model shown in Fig. 1.7, i.e. the horizontal bonds  $J_3$ , the vertical bonds  $J_2$  and the diagonal ones are not equal (see Fig. 1.21), the phase diagram becomes complicated with new features:<sup>17</sup> in particular, we show that the reentrance can occur in an

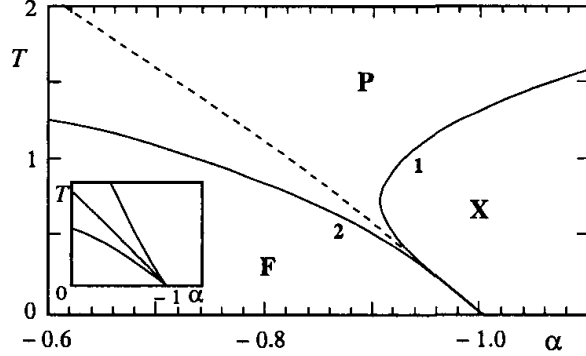


Fig. 1.20. Phase diagram of the Kagomé lattice with nnn interaction in the region  $J_1 > 0$  of the space ( $\alpha = J_2/J_1, T$ ).  $T$  is measured in the unit of  $J_1/k_B$ . Solid lines are critical lines, dashed line is the disorder line. P, F and X stand for paramagnetic, ferromagnetic and partially disordered phases, respectively. The inset shows schematically enlarged region of the endpoint.

*infinite region* of phase space. In addition, there may be *several reentrant phases* occurring for a given set of interactions when  $T$  varies.

The Hamiltonian is written as

$$H = -J_1 \sum_{(ij)} \sigma_i \sigma_j - J_2 \sum_{(ij)} \sigma_i \sigma_j - J_3 \sum_{(ij)} \sigma_i \sigma_j \quad (46)$$

where  $\sigma_i = \pm 1$  is an Ising spin occupying the lattice site  $i$ , and the first, second, and third sums run over the spin pairs connected by diagonal, vertical and horizontal bonds, respectively. When  $J_2 = 0$  and  $J_1 = J_3$ , one recovers the original nn Kagomé lattice.<sup>15</sup> The effect of  $J_2$  in the case  $J_1 = J_3$  has been shown above.

The phase diagram at temperature  $T = 0$  is shown in Fig. 1.21 in the space ( $\alpha = J_2/J_1, \beta = J_3/J_1$ ) for positive  $J_1$ . The ground-state spin configurations are also displayed. The hatched regions indicate the three partially disordered phases (I, II, and III) where the central spins are free. Note that the phase diagram is mirror-symmetric with respect to the change of the sign of  $J_1$ . With negative  $J_1$ , it suffices to reverse the central spin in the spin configuration shown in Fig. 1.21. Furthermore, the interchange of  $J_2$  and  $J_3$  leaves the system invariant, since it is equivalent to a  $\pi/2$  rotation of the lattice. Let us consider the effect of the temperature on the phase diagram shown in Fig. 1.21. Partial disorder in the ground state often gives rise to the reentrance phenomenon as in systems shown above. Therefore, similar effects are to be expected in the present system. As it will

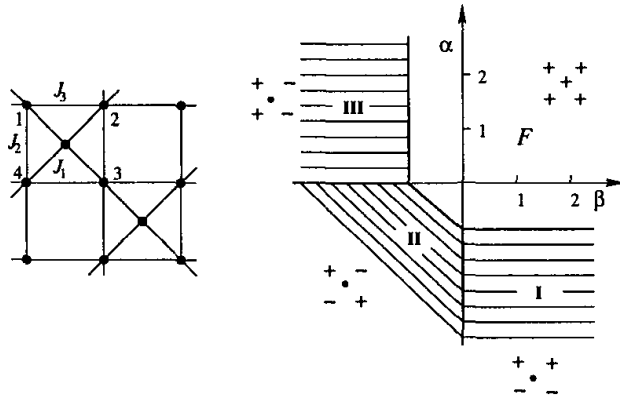


Fig. 1.21. Left: Generalized Kagomé lattice: diagonal, vertical and horizontal bonds denote the interactions  $J_1$ ,  $J_2$  and  $J_3$ , respectively. Right: Phase diagram of the ground state shown in the plane ( $\alpha = J_2/J_1$ ,  $\beta = J_3/J_1$ ). Heavy lines separate different phases and spin configuration of each phase is indicated (up, down and free spins are denoted by +, - and o, respectively). The three kinds of partially disordered phases and the ferromagnetic phase are denoted by I, II, III and F, respectively.

be shown below, we find a new and richer behavior of the phase diagram: in particular, the reentrance region is found to be extended to infinity, unlike systems previously studied, and for some given set of interactions, there exist *two disorder lines* which divide the paramagnetic phase into regions of different kinds of fluctuations with a reentrant behavior.

Following the method exposed in section 3, one obtains a checkerboard Ising model with multispin interactions. This resulting model is equivalent to a symmetric 16-vertex model which satisfies the free-fermion condition.<sup>25,38,39</sup> The critical temperature of the model is given by

$$\begin{aligned} & \cosh(4K_1) \exp(2K_2 + 2K_3) + \exp(-2K_2 - 2K_3) \\ &= 2 \cosh(2K_3 - 2K_2) \pm 4 \cosh(2K_1) \end{aligned} \quad (47)$$

Note that Eq. (47) is invariant when changing  $K_1 \rightarrow -K_1$  and interchanging  $K_2$  and  $K_3$  as stated earlier. The phase diagram in the three-dimensional space  $(K_1, K_2, K_3)$  is rather complicated to show. Instead, we show in the following the phase diagram in the plane ( $\beta = J_3/J_1, T$ ) for typical values of  $\alpha = J_2/J_1$ . To describe each case and to follow the evolution of the phase diagram, let us go in the direction of decreasing  $\alpha$ :

#### A. $\alpha > 0$

This case is shown in Fig. 1.22. Two critical lines are found with a paramagnetic reentrance having a usual shape (Fig. 1.22a) between the partially disordered (PD) phase of type III (see Fig. 1.21) and the ferromagnetic (F)

phase with an endpoint at  $\beta = -1$ . The width of the reentrance region  $[-1, \beta_1]$  decreases with decreasing  $\alpha$ , from  $\beta_1 = 0$  for  $\alpha$  at infinity to  $\beta_1 = -1$  for  $\alpha = 0$  (zero width). Note that as  $\alpha$  decreases, the PD phase III is depressed and disappears at  $\alpha = 0$ , leaving only the F phase (one critical line, see Fig. 1.22b). The absence of order at zero  $\alpha$  for  $\beta$  smaller than -1 results from the fact that in the ground state, this region of parameters corresponds to a superdegenerate line separating the two PD phases II and III (see Fig. 1.21). So, along this line, the disorder contaminates the system for all  $T$ . As for disorder solutions, for positive  $\alpha$  we find in the reentrant paramagnetic region a disorder line with dimension reduction<sup>33</sup> given by

$$\exp(4K_3) = 2 \cosh(2K_2)/[\cosh(4K_1) \exp(2K_2) + \exp(-2K_2)] \quad (48)$$

This is shown by the dotted lines in Fig. 1.22.

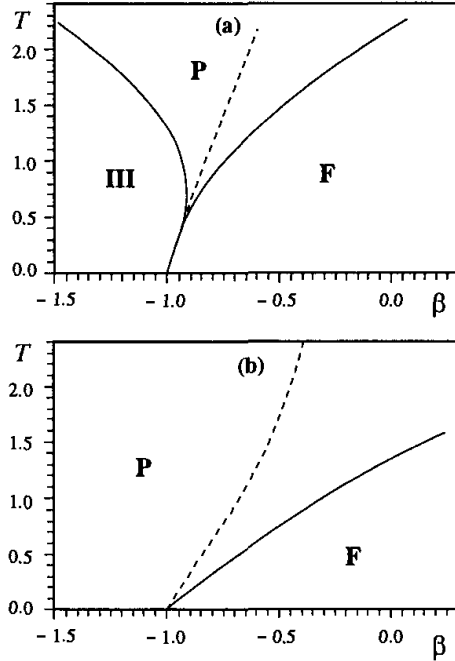


Fig. 1.22. Phase diagram in the plane ( $\beta = J_3/J_1, T$ ) for positive values of  $\alpha = J_2/J_1$ : (a)  $\alpha = 1$ , (b)  $\alpha = 0$ . Solid lines are critical lines which separate different phases: paramagnetic (P), ferromagnetic (F), partially disordered phase of type III (III). Dotted line shows the disorder line.

### B. $0 > \alpha > -1$

In this range of  $\alpha$ , there are three critical lines. The critical line separating the F and P phases and the one separating the PD phase I from

the P phase have a common horizontal asymptote as  $\beta$  tends to infinity. They form a reentrant paramagnetic phase between the F phase and the PD phase I for positive  $b$  between a value  $\beta_2$  and infinite  $\beta$  (Fig. 23). Infinite region of reentrance like this has never been found before this model. As  $\alpha$  decreases,  $\beta_2$  tends to zero and the F phase is contracted. For  $\alpha < -1$ , the F phase disappears together with the reentrance.

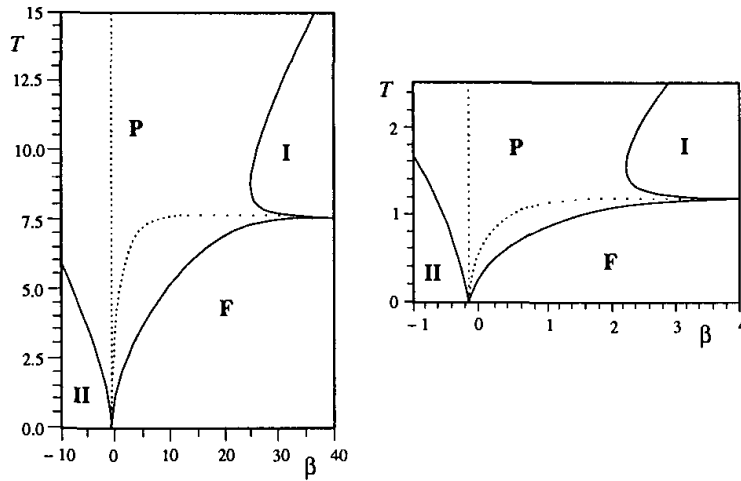


Fig. 1.23. Phase diagram in the plane ( $\beta = J_3/J_1, T$ ) for negative values of  $\alpha = J_2/J_1$ . Left:  $\alpha = -0.25$ , Right:  $\alpha = -0.8$ . Solid lines are critical lines which separate different phases: paramagnetic (P), ferromagnetic (F), partially disordered phases of type I and III. Dotted lines show the disorder lines.

In the interval  $0 > \alpha > -1$ , the phase diagram possesses two disorder lines, the first being given by Eq. (48), and the second by

$$\exp(4K_3) = 2 \sinh(2K_2)/[-\cosh(4K_1)\exp(2K_2) + \exp(-2K_2)] \quad (49)$$

These two disorder lines are issued from a point near  $\beta = -1$  for small negative  $\alpha$ ; this point tends to zero as  $\alpha$  tends to -1. The disorder line given by Eq. (49) enters the reentrant region which separates the F phase and the PD phase I (Fig. 1.23, left), and the one given by Eq. (48) tends to infinity with the asymptote  $\beta = 0$  as  $T \rightarrow \infty$ . The most striking feature is the behavior of these two disorder lines at low  $T$ : they cross each other in the P phase for  $0 > \alpha > -0.5$ , forming regions of fluctuations of different nature (Fig. 1.24a). For  $-0.5 > \alpha > -1$ , the two disorder lines do no longer cross each other (see Fig. 1.24b). The one given by Eq. (48) has a reentrant aspect: in a small region of negative values of  $\beta$ , one crosses three times this line in the P phase with decreasing  $T$ .

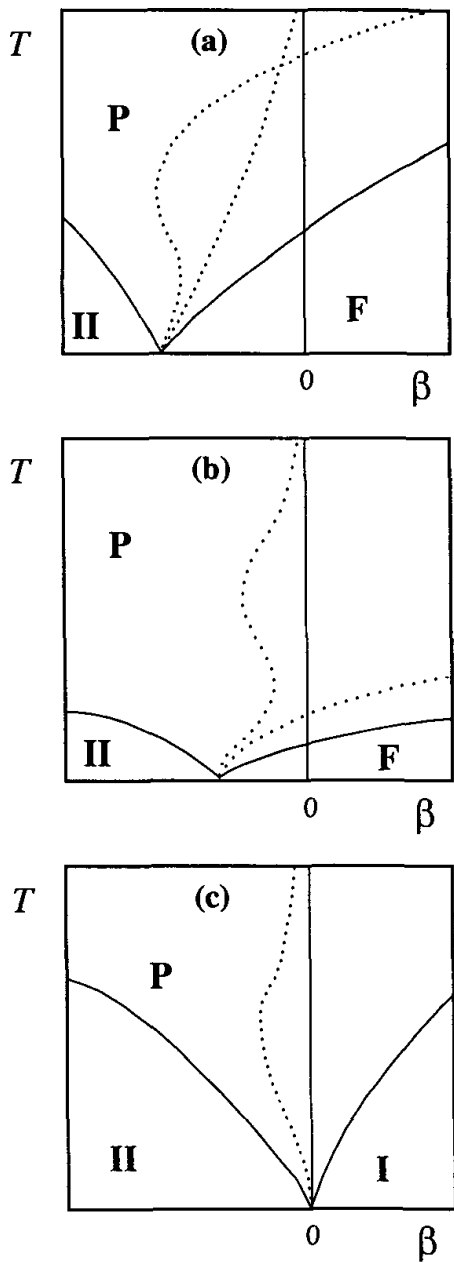


Fig. 1.24. The behavior of the disorder lines (dotted) is schematically enlarged in the case (a)  $\alpha = -0.25$ , (b)  $\alpha = -0.8$ , (c)  $\alpha = -1.5$ .

### C. $\alpha \leq -1$

For  $\alpha$  smaller than -1, there are two critical lines and no reentrance (Fig. 1.25). Only the disorder line given by Eq. (48) survives with a reentrant aspect: in a small region of negative values of  $\beta$ , one crosses twice this line in

the P phase with decreasing  $T$ . This behavior, being undistinguishable in the scale of Fig. 1.25, is schematically enlarged in Fig. 1.24c. The multicritical point where the P, I and II phases meet is found at  $\beta = 0$  and  $T = 0$ .

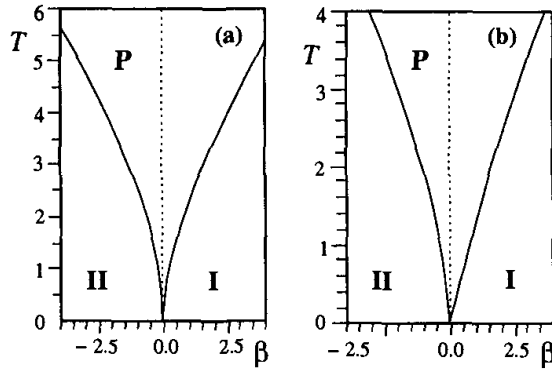


Fig. 1.25. The same caption as that of Fig. 1.23 with (a)  $\alpha = -1$ , (b)  $\alpha = -1.5$ .

At this stage, it is interesting to note that while reentrance and disorder lines occur along the horizontal axis  $\alpha = -1$  and along the vertical axis  $\beta = -1$  of Fig. 1.21 when the temperature is switched on, the most frustrated region ( $\alpha < 0$  and  $\beta < 0$ ) of the ground state does not show successive phase transitions (see Fig. 1.25, for example). Therefore, the existence of a reentrance may require a sufficient frustration, but not overfrustration. Otherwise, the system may have either a PD phase (Fig. 1.25) or no order at all (Fig. 1.22b).

The origin of the reentrance phenomenon will be discussed again in the conclusion.

#### 1.4.3. Centered honeycomb lattice

In order to find common aspects of the reentrance phenomenon, we have constructed a few other models which possess a partially disordered phase next to an ordered phase in the ground state. Let us mention here the anisotropic centered honeycomb lattice shown in Fig. 1.11.<sup>18</sup> The Hamiltonian is given by Eq. (25), with three kinds of interactions  $J_1$ ,  $J_2$ , and  $J_3$  denoting the interactions between the spin pairs connected by heavy, light, and double-light bonds, respectively. We recall that when  $J_2 = J_3 = 0$ , one recovers the honeycomb lattice, and when  $J_1 = J_2 = J_3$  one has the triangular lattice.

Fig. 1.26 shows the phase diagram at temperature  $T = 0$  for three cases ( $J_1 \neq J_2 = J_3$ ), ( $J_1 \neq J_3, J_2 = 0$ ) and ( $J_1 \neq J_2, J_3 = 0$ ). The ground-state spin configurations are also indicated.

The phase diagram is symmetric with respect to the horizontal axis: the transformation  $(J_2, \sigma) \rightarrow (-J_2, -\sigma)$ , or  $(J_3, \sigma) \rightarrow (-J_3, -\sigma)$ , leaves the system invariant. In each case, there is a phase where the central spins are free to flip ("partially disordered phase"). In view of this common feature with other models studied so far, one expects a reentrant phase occurring between the partially disordered phase and its neighboring phase at finite  $T$ . As it will be shown below, though a partial disorder exists in the ground state, it does not in all cases studied here yield a reentrant phase at finite  $T$ . Only the case ( $J_1 \neq J_2, J_3 = 0$ ) does show a reentrance.

To obtain the exact solution of our model, we decimate the central spin of each elementary cell of the lattice as outlined in the section 3. The resulting model is equivalent to a special case of the 32-vertex model<sup>26</sup> on a triangular lattice that satisfies the free-fermion condition. The explicit expression of the free energy as a function of interaction parameters  $K_1$ ,  $K_2$ , and  $K_3$  is very complicated, as seen by replacing Eq. (29) in Eqs. (15), (16) and (17). The critical temperature is given by Eq. (30).

We have analyzed, in particular, the three cases ( $K_1 \neq K_2 = K_3$ ), ( $K_1 \neq K_3, K_2 = 0$ ) and ( $K_1 \neq K_2, K_3 = 0$ ).

When  $K_2 = K_3$ , the critical line obtained from Eq.(30) is

$$\exp(3K_1) \cosh(6K_2) + \exp(-3K_1) = 3[\exp(K_1) + \exp(-K_1) \cosh(2K_2)] \quad (50)$$

In the case  $K_2 = 0$ , the critical line is given by

$$\exp(3K_1) \cosh(2K_3) + \exp(-3K_1) = 3[\exp(K_1) + \exp(-K_1) \cosh(2K_3)] \quad (51)$$

Note that these equations are invariant with respect to the transformation  $K_2 \rightarrow -K_2$  (see Eq.(50)) and  $K_3 \rightarrow -K_3$  (see Eq.(51)).

The phase diagrams obtained from Eqs. (44) and (45) are shown in Fig. 1.27a and Fig. 1.27b, respectively.

These two cases do not present the reentrance phenomenon though a partially disordered phase exists next to an ordered phase in the ground state (this is seen by plotting a line from the origin, i.e. from infinite  $T$ : this line never crosses twice a critical line whatever its slope, i.e. the ratio  $K_{2,3}/K_1$ , is). In the ordered phase II, the partial disorder, which exists in the ground state, remains so up to the phase transition. This has been verified by examining the Edwards-Anderson order parameter associated

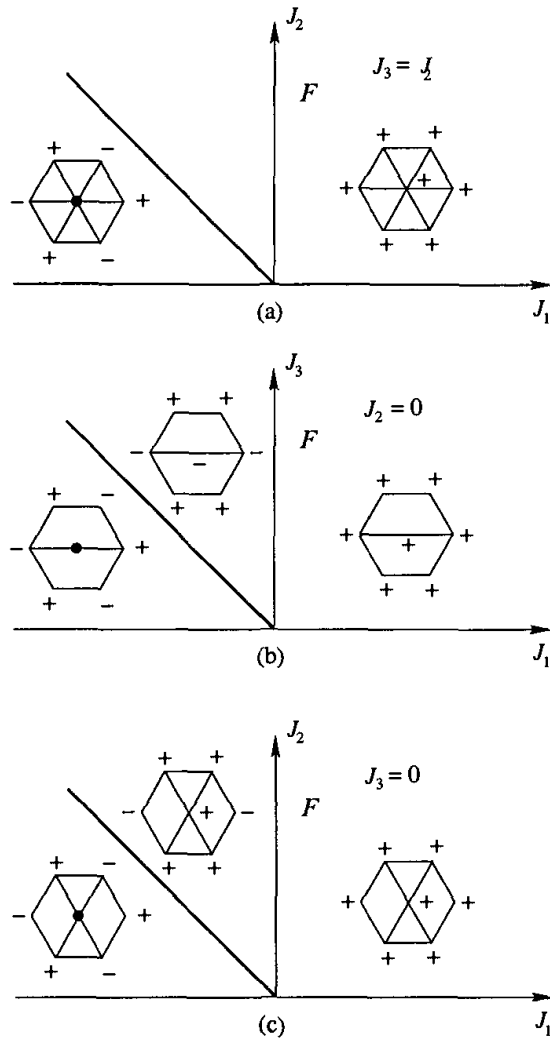


Fig. 1.26. Phase diagram of the ground state shown in the space: (a)  $(J_1, J_2 = J_3)$ ; (b)  $(J_1, J_3)$  with  $J_2 = 0$ ; (c)  $(J_1, J_2)$  with  $J_3 = 0$ . Heavy lines separate different phases and spin configuration of each phase is indicated (up, down and free spins are denoted by +, - and o, respectively).

with the central spins in MC simulations.<sup>18</sup> Note that when  $K_2 = K_3 = 0$ , one recovers the transition at finite temperature found for the honeycomb lattice,<sup>40</sup> and when  $K_2 = K_3 = K_1 = -1$  one recovers the antiferromagnetic triangular lattice which has no phase transition at finite temperature.<sup>4</sup> The case  $K_2 = 0$  (Fig. 1.27b) does not have a phase transition at finite  $T$  in the range  $-\infty < K_3/K_1 < -1$ , and phase II has a partial disorder as that in Fig. 1.22a.

The case  $K_3 = 0$  shows on the other hand a reentrant phase. The critical

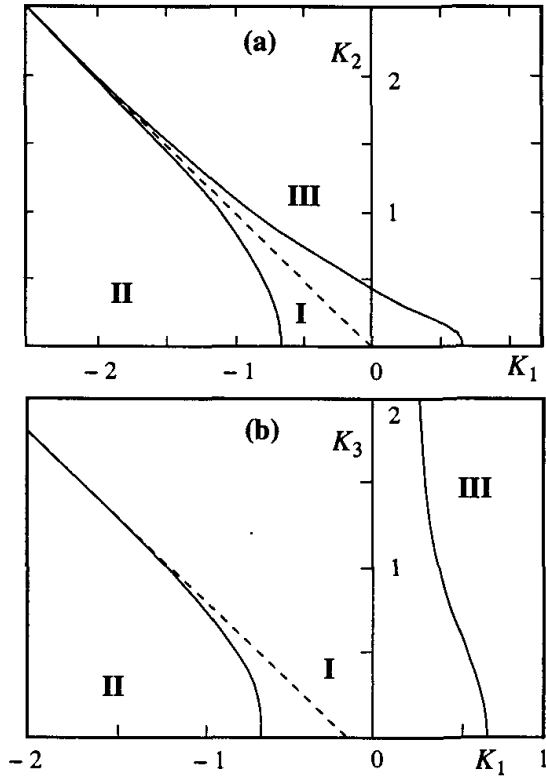


Fig. 1.27. Phase diagram shown in the space (a) ( $K_1, K_2 = K_3$ ) ; (b) ( $K_1, K_3, K_2 = 0$ ). Solid lines are critical lines which separate paramagnetic (I) , partially disordered (II) and ordered (III) phases. Discontinued lines of slope -1 are the asymptotes.

lines are determined from the equations

$$\cosh(4K_2) = \frac{\exp(4K_1) + 2\exp(2K_1) + 1}{[1 - \exp(4K_1)]\exp(2K_1)} \quad (52)$$

$$\cosh(4K_2) = \frac{3\exp(4K_1) + 2\exp(2K_1) - 1}{[\exp(4K_1) - 1]\exp(2K_1)} \quad (53)$$

Fig. 1.28 shows the phase diagram obtained from Eqs. (52) and (53) . The reentrant paramagnetic phase goes down to zero temperature with an end point at  $\alpha = -0.5$  (see Fig. 1.28 right).

Note that the honeycomb model that we have studied here does not present a disorder solution with a dimensional reduction.

#### 1.4.4. Periodically dilute centered square lattices

In this subsection, we show the exact results on several periodically dilute centered square Ising lattices by transforming them into 8-vertex models

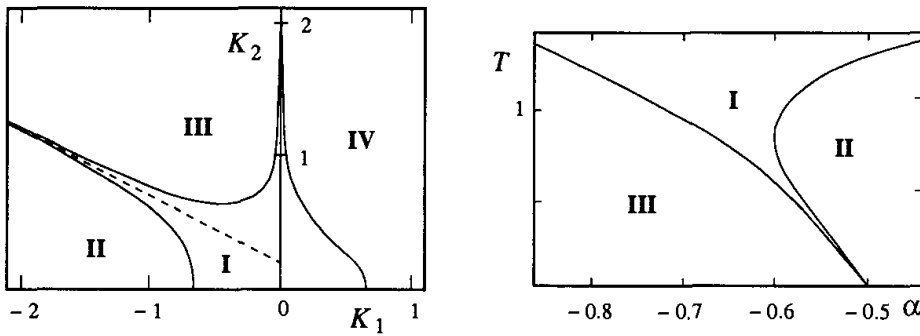


Fig. 1.28. Phase diagram of the centered honeycomb lattice with reentrance in the space  $(K_1, K_2)$  (left) and in the space  $(T, \alpha = K_2/K_1)$  (right). I, II, III phases are paramagnetic, partially disordered and ordered phases, respectively. Discontinued line is the asymptote.

of different vertex statistical weights that satisfy the free-fermion condition. The dilution is introduced by taking away a number of centered spins in a periodic manner. For a given set of interactions , there may be five transitions with decreasing temperature with two reentrant paramagnetic phases. These two phases extend to infinity in the space of interaction parameters. Moreover, two additional reentrant phases are found, each in a limited region of phase space.<sup>19</sup>

Let us consider several periodically dilute centered square lattices defined from the centered square lattice shown in Fig. 1.29.

The Hamiltonian of these models is given by

$$H = -J_1 \sum_{(ij)} \sigma_i \sigma_j - J_2 \sum_{(ij)} \sigma_i \sigma_j - J_3 \sum_{(ij)} \sigma_i \sigma_j \quad (54)$$

where  $\sigma_i = \pm 1$  is an Ising spin occupying the lattice site  $i$ , and the first, second and third sums run over the spin pairs connected by diagonal, vertical and horizontal bonds, respectively. All these models have at least one partially disordered phase in the ground state, caused by the competing interactions.

The model shown in Fig. 1.29c is in fact the generalized Kagomé lattice<sup>17</sup> which is shown above. The other models are less symmetric, require different vertex weights as seen below.

Let us show in Fig. 1.30 the phase diagrams, at  $T = 0$ , of the models shown in Figs. 25a, 25b and 25d, in the space  $(a, b)$  where  $a = J_2/J_1$  and  $b = J_3/J_1$ . The spin configurations in different phases are also displayed. The three-center case (Fig. 1.30a), has six phases (numbered from I to VI), five of which (I, II, IV, V and VI) are partially disordered (with, at least,

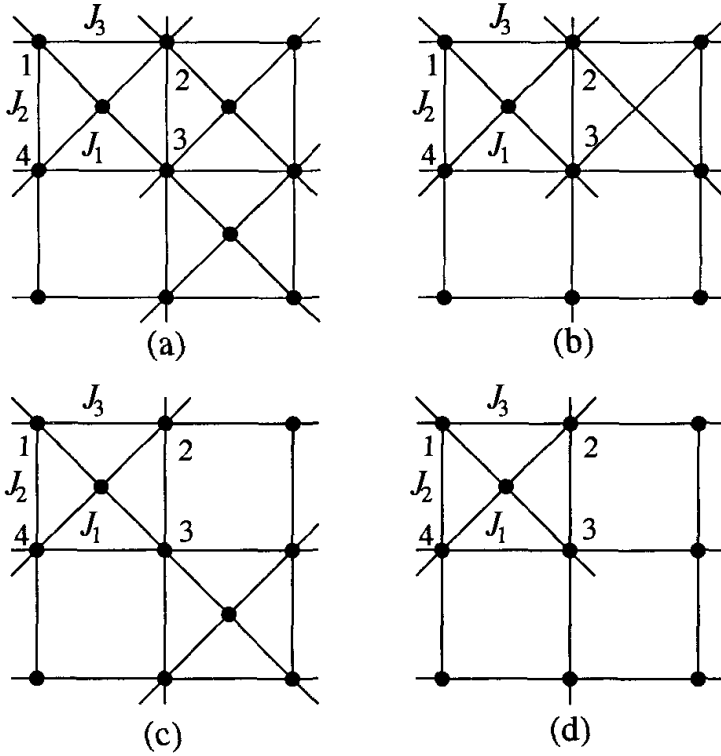


Fig. 1.29. Elementary cells of periodically dilute centered square lattice: (a) three-center case, (b) two-adjacent-center case, (c) two-diagonal-center case, (d) one-center case. Interactions along diagonal, vertical and horizontal bonds are  $J_1$ ,  $J_2$ , and  $J_3$ , respectively.

one centered spin being free), while the two-center case (Fig. 1.30b) has five phases, three of which (I, IV, and V) are partially disordered. Finally, the one-center case has seven phases with three partially disordered ones (I, VI and VII).

As will be shown later, in each model, the reentrance occurs along most of the critical lines when the temperature is switched on. This is a very special feature of the models shown in Fig. 1.29 which has not been found in other models.

The partition function is written as

$$Z = \prod_j \sum_{\sigma} W_j \quad (55)$$

where the sum is performed over all spin configurations and the product over all elementary squares.  $W_j$  is the statistical weight of the  $j$ -th square. Let us denote the centered spin (when it exists) by  $\sigma$  and the spins at the

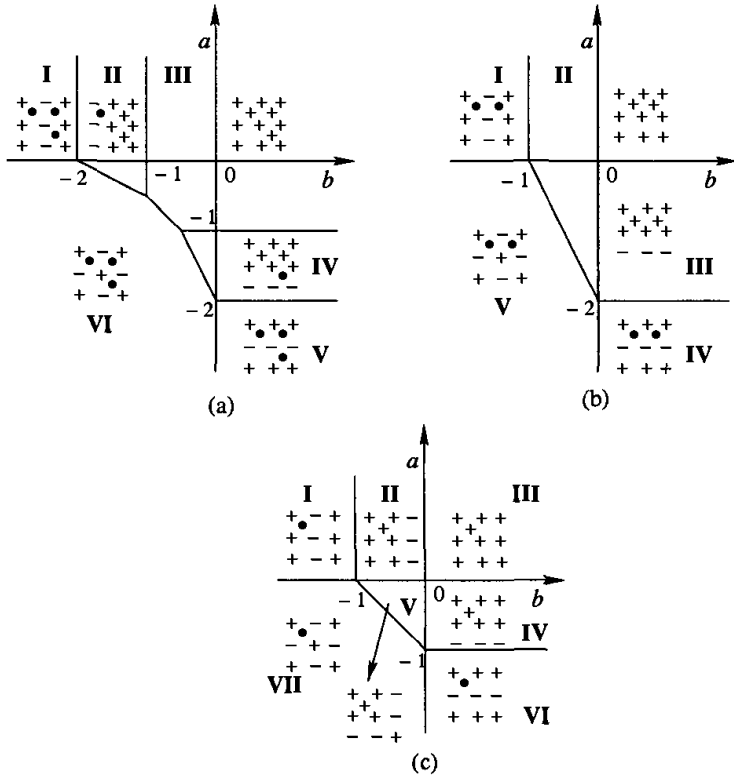


Fig. 1.30. Phase diagrams in the plane ( $a = J_2/J_1$ ,  $b = J_3/J_1$ ) at  $T = 0$  are shown for the three-center case (a), two-adjacent center case (b), and one-center case (c). Critical lines are drawn by heavy lines. Each phase is numbered and the spin configuration is indicated (+, -, and o are up, down, and free spins, respectively). Degenerate configurations are obtained by reversing all spins.

square corners by  $\sigma_1$ ,  $\sigma_2$ ,  $\sigma_3$  and  $\sigma_4$ . If the centered site exists, the statistical weight  $W_j$  of the square is

$$W_j = \exp[K_1(\sigma_1\sigma_2 + \sigma_3\sigma_4) + K_2(\sigma_1\sigma_4 + \sigma_2\sigma_3) + K_3\sigma(\sigma_1 + \sigma_2 + \sigma_3 + \sigma_4)] \quad (56)$$

Otherwise, it is given by

$$W_j = \exp[K_1(\sigma_1\sigma_2 + \sigma_3\sigma_4) + K_2(\sigma_1\sigma_4 + \sigma_2\sigma_3)] \quad (57)$$

where  $K_i = J_i/k_B T$  ( $i = 1, 2, 3$ ).

In order to obtain the exact solution of these models, we decimate the central spins of the centered squares. The resulting system is equivalent to an eight-vertex model on a square lattice, but with *different vertex weights*. For example, when one center is missing (Fig. 1.29d), three squares over four have the same weight  $W_i$ , and the fourth has a weight  $W'_i \neq W_i$ . So, we have to define four different sublattices with different statistical

weights. The problem has been studied by Hsue, Lin and Wu for two different sublattices<sup>41</sup> and Lin and Wang<sup>42</sup> for four sublattices. They showed that exact solution can be obtained provided that all different statistical weights satisfy the free-fermion condition.<sup>11,25,41,42</sup> This is indeed our case and we get the exact partition function in terms of interaction parameters. The critical surfaces of our models are obtained by

$$\Omega_1 + \Omega_2 + \Omega_3 + \Omega_4 = 2\max(\Omega_1, \Omega_2, \Omega_3, \Omega_4) \quad (58)$$

where  $W_i$  are functions of  $K_1$ ,  $K_2$  and  $K_3$ . We explicit this equation and we obtain a second order equation for  $X$  which is a function of  $K_2$  only :

$$A(K_1, K_3)X^2 + B(K_1, K_3)X + C(K_1, K_3) = 0 \quad (59)$$

with a priori four possible values of  $A$ ,  $B$  and  $C$  for each model.

For given values of  $K_1$  and  $K_3$ , the critical surface is determined by the value of  $K_2$  which satisfies Eq.(59) through  $X$ .  $X$  must be real positive. We show in the following the expressions of  $A$ ,  $B$  and  $C$  for which this condition is fulfilled for each model. Eq. (58) may have as much as five solutions for the critical temperature,<sup>42</sup> and the system may, for some given values of interaction parameters, exhibit up to five phase transitions. This happens for the model with three centers, when one of the interaction is large positive and the other slightly negative, the diagonal one being taken as unit. In general, we obtain one or three solutions for  $T_c$ .

#### 1.4.4.1. Model with three centers

(Fig. 1.29a)

The quantities which satisfy Eq. (59) are given by

$$\begin{aligned} X &= \exp(4K_2) \\ A &= \exp(4K_1) \cosh^3(4K_3) + \exp(-4K_1) - \cosh^2(4K_3) - \cosh(4K_3) \\ B &= \pm \{1 + 3 \cosh(4K_3) + 8 \cosh^3(2K_3) + [\cosh(4K_3) + \cosh^2(4K_3)] \exp(4K_1) \\ &\quad + 2 \exp(-4K_1)\} \\ C &= [\exp(2K_1) - \exp(-2K_1)]^2 \\ A &= \exp(4K_1) \cosh^3(4K_3) + \exp(-4K_1) + \cosh^2(4K_3) + \cosh(4K_3) \\ B &= [1 + 3 \cosh(4K_3) + 8 \cosh^3(2K_3) - (\cosh(4K_3) + \cosh^2(4K_3)) \exp(4K_1) \\ &\quad - 2 \exp(-4K_1)] \\ C &= [\exp(2K_1) + \exp(-2K_1)]^2 \end{aligned} \quad (60)$$

Let us describe now in detail the phase diagram of the three-center model (Fig. 1.29a).

For clarity, we show in Fig. 1.31 the phase diagram in the space ( $a = J_2/J_1, T$ ) for typical values of  $b = J_3/J_1$ .

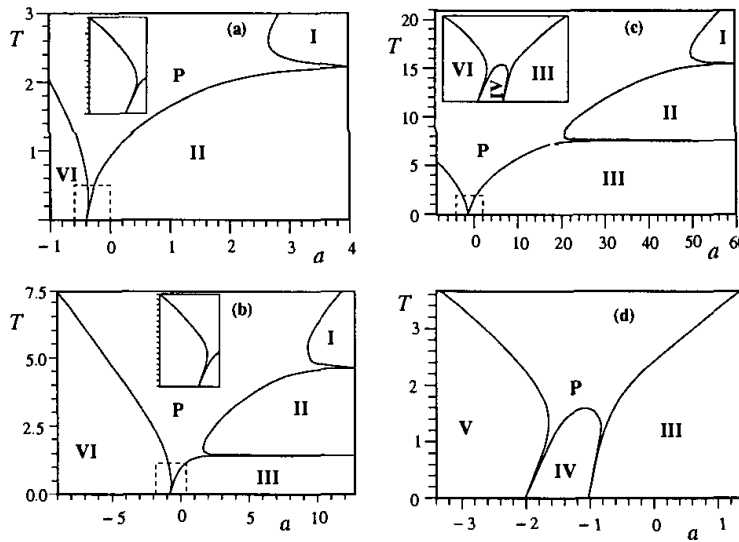


Fig. 1.31. Phase diagrams in the plane ( $T, a = J_2/J_1$ ) for several values of  $b = J_3/J_1$ : (a)  $b = -1.25$ , (b)  $b = -0.75$ , (c)  $b = -0.25$ , (d)  $b = 0.75$ . Reentrant regions on negative sides of  $a$  (limited by discontinued lines) are schematically enlarged in the insets. The nature of ordering in each phase is indicated by a number which is referred to the corresponding spin configuration in Fig. 1.30. P is paramagnetic phase.

For  $b < -1$ , there are two reentrances. Fig. 1.31a shows the case of  $b = -1.25$  where the nature of the ordering in each phase is indicated using the same numbers of corresponding ground state configurations (see Fig. 1.30). Note that all phases (I, II and VI) are partially disordered: the centered spins which are disordered at  $T = 0$  (Fig. 1.30a) remain so at all  $T$ . As seen, one paramagnetic reentrance is found in a small region of negative  $a$  (schematically enlarged in the inset of Fig. 1.31a), and the other on the positive  $a$  extending to infinity. The two critical lines in this region have a common horizontal asymptote.

For  $-1 < b < -0.5$ , there are three reentrant paramagnetic regions as shown in Fig. 1.31b: the reentrant region on the negative  $a$  is very narrow (inset), and the two on the positive  $a$  become so narrower while  $a$  goes to infinity that they cannot be seen on the scale of Fig. 1.31. Note that the critical lines in these regions have horizontal asymptotes. For a large

value of  $a$ , one has five transitions with decreasing  $T$ : paramagnetic state - partially disordered phase I - reentrant paramagnetic phase - partially disordered phase II - reentrant paramagnetic phase- ferromagnetic phase (see Fig. 1.31b). So far, this is the first model that exhibits such successive phase transitions with two reentrances.

For  $-0.5 < b < 0$ , there is an additional reentrance for  $a < -1$ : this is shown in the inset of Fig. 1.31c. As  $b$  increases from negative values, the ferromagnetic region (III) in the phase diagram "pushes" the two partially disordered phases (I and II) toward higher  $T$ . At  $b = 0$ , these two phases disappear at infinite  $T$ , leaving only the ferromagnetic phase. For positive  $b$ , there are thus only two reentrances remaining on a negative region of  $a$ , with endpoints at  $a = -2$  and  $a = -1$ , at  $T = 0$  (see Fig. 1.31d).

#### 1.4.4.2. Model with two adjacent centers

(Fig. 1.29b)

The quantities which satisfy Eq. (59) are given by

$$\begin{aligned}
 X &= \exp(2K_2) \\
 A &= \exp(2K_1) \cosh(4K_3) + \exp(-2K_1) \\
 B &= 2[\exp(2K_1) \cosh^2(2K_3) - \exp(-2K_1)] \\
 C &= \exp(2K_1) + \exp(-2K_1) \\
 A &= \exp(2K_1) \cosh(4K_3) - \exp(-2K_1) \\
 B &= \pm 2[\exp(2K_1) \cosh^2(2K_3) + \exp(-2K_1)] \\
 C &= \exp(2K_1) - \exp(-2K_1)
 \end{aligned} \tag{61}$$

The phase diagram is shown in Fig. 1.32.

For  $b < -1$ , this model shows only one transition at a finite  $T$  for a given value of  $a$ , except when  $a = 0$  where the paramagnetic state goes down to  $T = 0$  ( see Fig. 1.32a).

However, for  $-1 < b < 0$ , two reentrances appear, the first one separating phases I and II goes to infinity with increasing  $a$ , and the second one exists in a small region of negative  $a$  with an endpoint at  $(a = -2 - 2b, T = 0)$ . The slope of the critical lines at  $a = 0$  is vertical (see inset of Fig. 1.32b).

As  $b$  becomes positive, the reentrance on the positive side of  $a$  disappears (Fig. 1.32c), leaving only phase III (ferromagnetic).

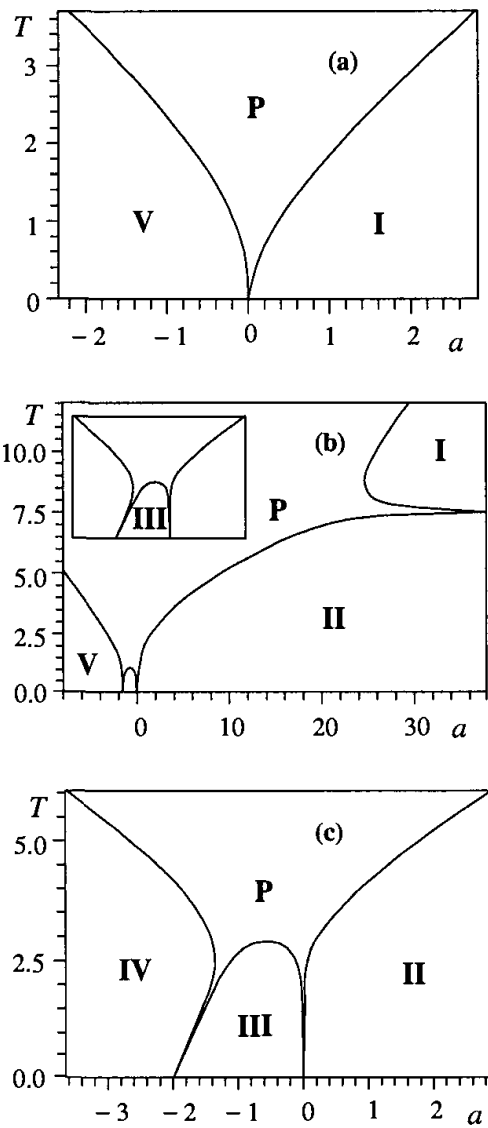


Fig. 1.32. Two-center model: the same caption as that of Fig. 1.31 with (a)  $b = -1.25$ , (b)  $b = -0.25$ , (c)  $b = 2$ .

#### 1.4.4.3. Model with one center

(Fig. 1.29d)

For this case, the quantities which satisfy Eq. (59) are given by

$$\begin{aligned}
X &= \exp(4K_2) \\
A &= \exp(4K_1) \cosh(4K_3) + \exp(-4K_1) - 2 \cosh^2(2K_3) \\
B &= \pm 2\{[\cosh(2K_3) + 1]^2 + [\exp(2K_1) \cosh(2K_3) + \exp(-2K_1)]^2\} \\
C &= [\exp(2K_1) - \exp(-2K_1)]^2 \\
A &= \exp(4K_1) \cosh(4K_3) + \exp(-4K_1) + 2 \cosh^2(2K_3) \\
B &= \pm 2\{[\cosh(2K_3) + 1]^2 - [\exp(2K_1) \cosh(2K_3) - \exp(-2K_1)]^2\} \\
C &= [\exp(2K_1) + \exp(-2K_1)]^2
\end{aligned} \tag{62}$$

The phase diagrams of this model shown in Fig. 1.33 for  $b < -1$ ,  $-1 < b < 0$  and  $b > 0$  are very similar to those of the two-center model shown in Fig. 1.32. This is not unexpected if one examines the ground state phase diagrams of the two cases (Figs. 25b and 25c): their common point is the existence of a partially disordered phase next to an ordered phase. The difference between the one- and two-center cases and the three-center case shown above is that the latter has, in addition, two boundaries, each of which separates two partially disordered phases (see Fig. 1.30a). It is along these boundaries that the two additional reentrances take place at finite  $T$  in the three-center case.

In conclusion of this subsection, we summarize that in simple models such as those shown in Fig. 1.29, we have found two reentrant phases occurring on the temperature scale at a given set of interaction parameters. A striking feature is the existence of a reentrant phase between *two partially disordered phases* which has not been found so far in any other model (we recall that in other models, a reentrant phase is found between an ordered phase and a partially disordered phase).

#### 1.4.5. Random-field aspects of the models

Let us touch upon the random-field aspect of the model. A connection between the Ising models presented above and the random-field problem can be established. Consider for instance the centered square lattice (Fig. 1.17). In the region of antiferromagnetic ordering of sublattice 2 ( $a = J_2 / |J_1| < -1$ ), the spins on sublattice 1 (centered spins) are free to flip. They act on their neighboring spins (sublattice 2) as an annealed random field  $h$ . The probability distribution of this random field at a site of sublattice 2 is given by

$$P(h) = \frac{1}{16}[6\delta(h) + 4\delta(h+2J_1) + 4\delta(h-2J_1) + \delta(h+4J_1) + \delta(h-4J_1)] \tag{63}$$

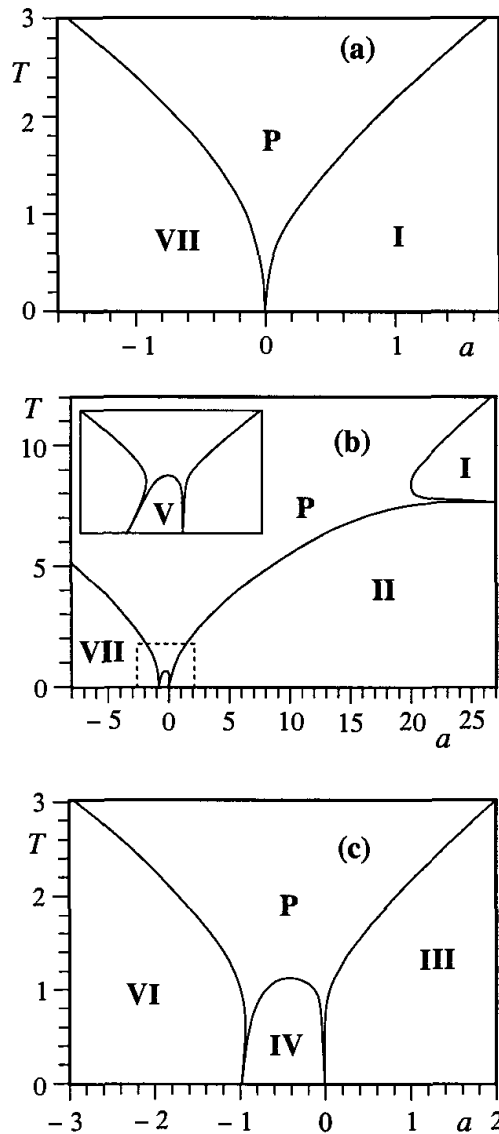


Fig. 1.33. One-center case: the same caption as that of Fig. 1.31 with (a)  $b = -1.25$ , (b)  $b = -0.25$ , (c)  $b = 0.5$ .

The random field at a number of spins is thus zero (diluted). Moreover, this field distribution is somewhat correlated because each spin of sublattice 1 acts on four spins of sublattice 2. Since the spins on sublattice 1 are completely disordered at all  $T$ , it is reasonable to consider this effective random-field distribution as quenched. In addition to possible local annealed effects, the phase transition at a finite  $T$  of this model may be a consequence of the above mentioned dilution and correlations of the field distribution, because

it is known that in 2D random-field Ising model (without dilution) there is no such a transition.<sup>43</sup>

The same argument is applied to other models studied above.

### **1.5. Evidence of partial disorder and reentrance in other frustrated systems**

The partial disorder and the reentrance which occur in exactly solved Ising systems shown above are expected to occur also in models other than the Ising one as well as in some three-dimensional systems. Unfortunately, these systems cannot be exactly solved. One has to use approximations or numerical simulations to study them. This renders difficult the interpretation of the results. Nevertheless, in the light of what has been found in exactly solved systems, we can introduce the necessary ingredients into the model under study if we expect the same phenomenon to occur.

As seen above, the most important ingredient for a partial disorder and a reentrance to occur at low  $T$  in the Ising model is the existence of a number of free spins in the ground state.

In three dimensions, apart from a particular exactly solved case<sup>21</sup> showing a reentrance, a few Ising systems such as the fully frustrated simple cubic lattice,<sup>31,32</sup> a stacked triangular Ising antiferromagnet<sup>44,45</sup> and a body-centered cubic (bcc) crystal<sup>46</sup> exhibit a partially disordered phase in the ground state. We believe that reentrance should also exist in the phase space of such systems though evidence is found numerically only for the bcc case.<sup>46</sup>

In two dimensions, a few non-Ising models show also evidence of a reentrance. For the  $q$ -state Potts model, evidence of a reentrance is found in a recent study of the two-dimensional frustrated Villain lattice (the so-called piled-up domino model) by a numerical transfer matrix calculation<sup>47,48</sup>. It is noted that the reentrance occurs near the fully frustrated situation, i.e.  $\alpha_c = J_{AF}/J_F = -1$  (equal antiferromagnetic and ferromagnetic bond strengths), for  $q$  between  $\simeq 1.0$  and  $\simeq 4$ . Note that there is no reentrance in the case  $q = 2$ . Below (above) this  $q$  value, the reentrance occurs above (below) the fully frustrated point  $\alpha_c$  as shown in Figs. 30 and 31. For  $q$  larger than  $\simeq 4$ , the reentrance disappears.<sup>48</sup>

A frustrated checkerboard lattice with XY spins shows also evidence of a paramagnetic reentrance.<sup>49</sup>

In vector spin models such as the Heisenberg and XY models, the frustration is shared by all bonds so that no free spins exist in the ground state.

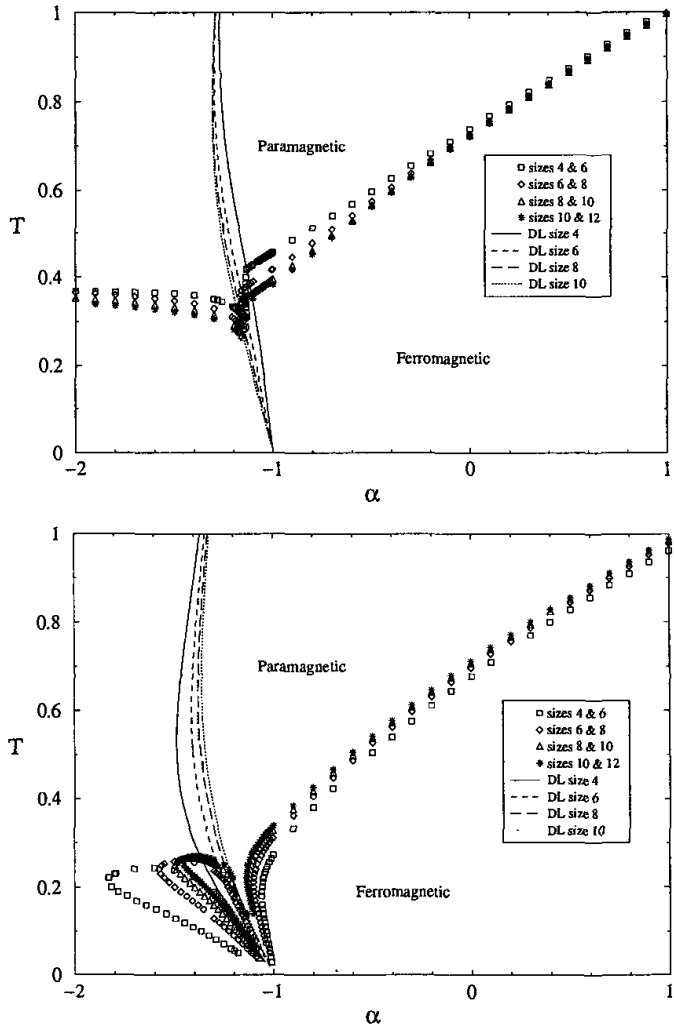


Fig. 1.34. Phase diagram for the Potts piled-up-domino model with  $q = 3$ : periodic boundary conditions (top) and free boundary conditions (bottom). The disorder lines are shown as lines, and the phase boundaries as symbols. The numerical uncertainty is smaller than the size of the symbols.<sup>47</sup>

However, one can argue that if there are several kinds of local field in the ground state due to several kinds of interaction, then there is a possibility that a subsystem with weak local field is disordered at low  $T$  while those of stronger local field stay ordered up to higher temperatures. This conjecture has been verified in a number of recent works on classical<sup>50</sup> and quantum spins<sup>51,52</sup>. Consider for example Heisenberg spins  $\mathbf{S}_i$  on a bcc lattice with a unit cell shown in Fig. 1.36.<sup>50</sup>

For convenience, let us call sublattice 1 the sublattice containing the

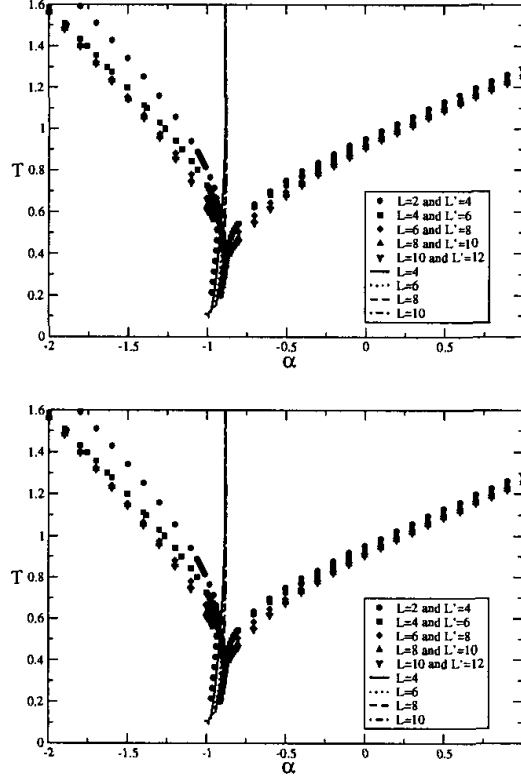


Fig. 1.35. The phase diagram for  $q = 1.5$  found using transfer matrices and the phenomenological renormalization group with periodic (top) and free boundary conditions (bottom). The points correspond to finite-size estimates for  $T_c$ , whilst the lines correspond to the estimates for the disorder line, ( $\alpha = J_2/J_1$ ).<sup>48</sup>

sites at the cube centers and sublattice 2 the other sublattice. The Hamiltonian reads

$$H = -\frac{1}{2} \sum_{\langle i,j \rangle_1} \mathbf{S}_i \cdot \mathbf{S}_j - \frac{1}{2} \sum_{\langle i,j \rangle_2} \mathbf{S}_i \cdot \mathbf{S}_j$$

where  $\sum_{\langle i,j \rangle_1}$  indicates the sum over the nn spin pairs with exchange coupling  $J_1$ , while  $\sum_{\langle i,j \rangle_2}$  is limited to the nnn spin pairs belonging to sublattice 2 with exchange coupling  $J_2$ . It is easy to see that when  $J_2$  is antiferromagnetic the spin configuration is non collinear for  $J_2/|J_1| < -2/3$ . In the non collinear case, one can verify that the local field acting a center spin (sublattice 1) is weaker in magnitude than that acting on a corner spin (sublattice 2). The partial disorder is observed in Fig. 1.37: the sublattice of black spins (sublattice 1) is disordered at a low  $T$ .

The same argument is applied for quantum spins.<sup>52</sup> Consider the bcc crystal as shown in Fig. 1.36, but the sublattices are supposed now to have different spin magnitudes, for example  $S_A = 1/2$  (sublattice 1) and

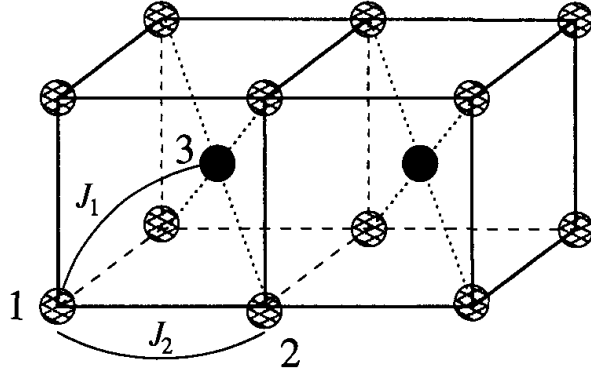


Fig. 1.36. bcc lattice. Spins are shown by gray and black circles. Interaction between nn (spins numbered 1 and 3) is denoted by  $J_1$  and that between nnn (spins 1 and 2) by  $J_2$ . Note that there is no interaction between black spins.

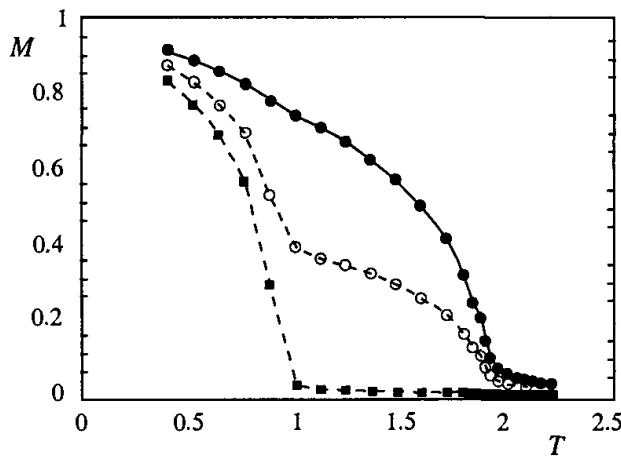


Fig. 1.37. Monte Carlo results for sublattice magnetizations vs  $T$  in the case  $J_1 = -1$ ,  $J_2 = -1.4$ : black squares and black circles are for sublattices 1 and 2, respectively. Void circles indicate the total magnetization.

$S_B = 1$  (sublattice 2). In addition, one can include nnn interactions in both sublattices, namely  $J_{2A}$  and  $J_{2B}$ . The Green function technique is then applied for this quantum system.<sup>52</sup> We show in Fig. 1.38 the partial disorder observed in two cases: sublattice 1 is disordered (Fig. 1.38a) or sublattice 2 is disordered (Fig. 1.38b). In each case, one can verify, using the corresponding parameters, that in the ground state the spin of the disordered sublattice has an energy lower than a spin in the other sublattice.

We show in Fig. 1.39 the specific heat versus  $T$  for the parameters used

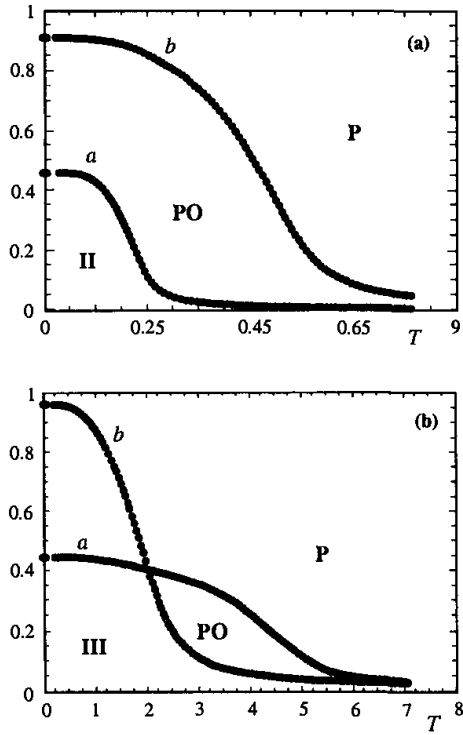


Fig. 1.38. Sublattice magnetizations vs  $T$  in the case  $S_A = 1/2$ ,  $S_B = 1$ : (a) curve  $a$  (b) is the sublattice-1(2) magnetization in the case  $J_{2A}/|J_1| = 0.2$  and  $J_{2B}/|J_1| = 0.9$  (b) curve  $a$  (b) is the sublattice-1(2) magnetization in the case  $J_{2A}/|J_1| = 2.2$  and  $J_{2B}/|J_1| = 0.1$ . P is the paramagnetic phase, PO the partial order phase (only one sublattice is ordered), II and III are non collinear spin configuration phases. See text for comments.

in Fig. 1.38. One observes the two peaks corresponding to the two phase transitions associated with the loss of sublattice magnetizations.

The necessary condition for the occurrence of a partial disorder at finite  $T$  is thus the existence of several kinds of site with different energies in the ground state. This has been so far verified in a number of systems as shown above.

## 1.6. Conclusion

In this chapter, we have discussed some properties of periodically frustrated Ising systems. We have limited the discussion to exactly solved models which possess at least a reentrant phase. Other Ising systems which involved approximations are discussed in the chapter by Nagai et al (this book) and in the book by Liebmann.<sup>1</sup>.

Let us emphasize that simple models having no bond disorder like those

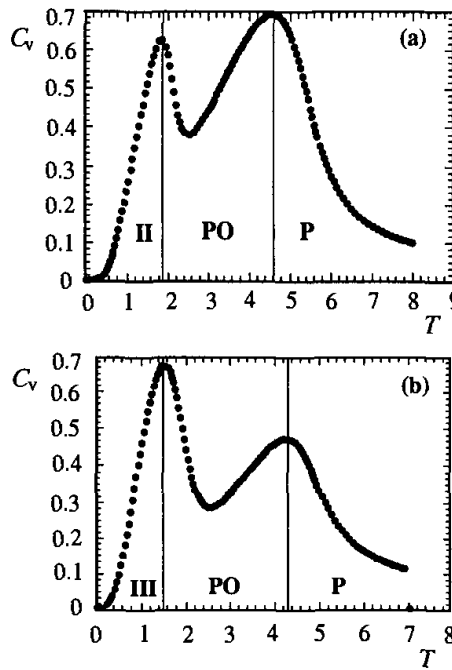


Fig. 1.39. Specific heat versus  $T$  of the parameters used in Fig. 1.38,  $S_A = 1/2$ ,  $S_B = 1$ : (a)  $J_{2A}/|J_1| = 0.2$  and  $J_{2B}/|J_1| = 0.9$  (b)  $J_{2A}/|J_1| = 2.2$  and  $J_{2B}/|J_1| = 0.1$ . See the caption of Fig. 1.38 for the meaning of P, PO, II and III. See text for comments.

presented in this chapter can possess complicated phase diagrams due to the frustration generated by competing interactions. Many interesting physical phenomena such as successive phase transitions, disorder lines, and reentrance are found. In particular, a reentrant phase can occur in an infinite region of parameters. For a given set of interaction parameters in this region, successive phase transitions take place on the temperature scale, with one or two paramagnetic reentrant phases.

The relevance of disorder solutions for the reentrance phenomena has also been pointed out. An interesting finding is the occurrence of two disorder lines which divide the paramagnetic phase into regions of different kinds of fluctuations (section 4.2). Therefore, care should be taken in analyzing experimental data such as correlation functions, susceptibility, etc. in the paramagnetic phase of frustrated systems.

Although the reentrance is found in the models shown above by exact calculations, there is no theoretical explanation why such a phase can occur. In other words, what is the necessary and sufficient condition for the occurrence of a reentrance? We have conjectured<sup>16,19</sup> that the necessary condition for a reentrance to take place is the existence of at least a

partially disordered phase next to an ordered phase or another partially disordered phase in the ground state. The partial disorder is due to the competition between different interactions.

The existence of a partial disorder yields the occurrence of a reentrance in most of known cases,<sup>12,13,14,16,17,19</sup> except in some particular regions of interaction parameters in the centered honeycomb lattice (section 4.3.): the partial disorder alone is not sufficient to make a reentrance as shown in Fig. 1.27a and Fig. 1.27b, the finite zero-point entropy due to the partial disorder of the ground state is the same for three cases considered in Fig. 1.26, i.e.  $S_0 = \log(2)/3$  per spin, but only one case yields a reentrance. Therefore, the existence of a partial disorder is a necessary, but not sufficient, condition for the occurrence of a reentrance.

The anisotropic character of the interactions can also favor the occurrence of the reentrance. For example, the reentrant region is enlarged by anisotropic interactions as in the centered square lattice,<sup>14</sup> and becomes infinite in the generalized Kagomé model (section 4.2.). But again, this alone cannot cause a reentrance as seen by comparing the anisotropic cases shown in Fig. 1.26b and Fig. 1.26c: only in the latter case a reentrance does occur. The presence of a reentrance may also require a coordination number at a disordered site large enough to influence the neighboring ordered sites. When it is too small such as in the case shown in Fig. 1.26b (equal to two), it cannot induce a reentrance. However, it may have an upper limit to avoid the disorder contamination of the whole system such as in the case shown in Fig. 1.27a where the coordination number is equal to six. So far, the 'right' number is four in known reentrant systems shown above. Systematic investigations of all possible ingredients are therefore desirable to obtain a sufficient condition for the existence of a reentrance.

Finally, let us emphasize that when a phase transition occurs between states of different symmetries which have no special group-subgroup relation, it is generally accepted that the transition is of first order. However, the reentrance phenomenon is a symmetry breaking alternative which allows one ordered phase to change into another incompatible ordered phase by going through an intermediate reentrant phase. A question which naturally arises is under which circumstances does a system prefer an intermediate reentrant phase to a first-order transition. In order to analyze this aspect we have generalized the centered square lattice Ising model into three dimensions.<sup>46</sup> This is a special bcc lattice. We have found that at low  $T$  the reentrant region observed in the centered square lattice shrinks into a first order transition line which is ended at a multicritical point from which two

second order lines emerge forming a narrow reentrant region.<sup>46</sup>

As a final remark, let us mention that although the exactly solved systems shown in this chapter are models in statistical physics, we believe that the results obtained in this work have qualitative bearing on real frustrated magnetic systems. In view of the simplicity of these models, we believe that the results found here will have several applications in various areas of physics.

### Acknowledgments

The authors wish to thank Patrick Azaria and Marianne Debauche for their close collaborations in the works presented in this chapter. They are grateful to Ngo Van Thanh, Sylvain Reynal and Karim Drouiche for technical helps.

### References

1. R. Liebmann, *Statistical Mechanics of Periodic Frustrated Ising Systems*, Lecture Notes in Physics, vol. 251 (Springer-Verlag, Berlin, 1986).
2. G. Toulouse, *Commun. Phys.* **2**, 115 (1977).
3. J. Villain, *J. Phys. C***10**, 1717 (1977).
4. G. H. Wannier, *Phys. Rev.* **79**, 357 (1950); *Phys. Rev. B* **7**, 5017 (E) (1973).
5. A. Yoshimori, *J. Phys. Soc. Jpn.* **14**, 807 (1959).
6. J. Villain, *Phys. Chem. Solids* **11**, 303 (1959).
7. T. A. Kaplan, *Phys. Rev.* **116**, 888 (1959).
8. B. Berge, H. T. Diep, A. Ghazali, and P. Lallemand, *Phys. Rev. B* **34**, 3177 (1986).
9. P. Lallemand, H.T. Diep, A. Ghazali, and G. Toulouse, *Physique Lett.* **46**, L-1087 (1985).
10. H. T. Diep, A. Ghazali and P. Lallemand, *J. Phys. C***18**, 5881 (1985).
11. R. J. Baxter, *Exactly solved Models in Statistical Mechanics* (Academic, New York, 1982).
12. V. Vaks , A. Larkin and Y. Ovchinnikov, *Sov. Phys. JEPT* **22**, 820 (1966).
13. T. Morita, *J. Phys. A* **19**, 1701 (1987).
14. T. Chikyu and M. Suzuki, *Prog. Theor. Phys.* **78**, 1242(1987).
15. K. Kano and S. Naya, *Prog. Theor. Phys.* **10**, 158 (1953).
16. P. Azaria, H. T. Diep and H. Giacomini, *Phys. Rev. Lett.* **59**, 1629 (1987).
17. M. Debauche, H.T. Diep, P. Azaria, and H. Giacomini, *Phys. Rev. B* **44**, 2369 (1991).
18. H.T. Diep, M. Debauche and H. Giacomini, *Phys. Rev. B* **43**, 8759 (1991).
19. M. Debauche and H. T. Diep, *Phys. Rev. B* **46**, 8214 (1992); H. T. Diep, M. Debauche and H. Giacomini, *J. of Mag. and Mag. Mater.* **104**, 184 (1992).
20. H. Kitatani, S. Miyashita and M. Suzuki, *J. Phys. Soc. Jpn.* **55** (1986) 865; *Phys. Lett. A* **158**, 45 (1985).
21. T. Horiguchi, *Physica A* **146**, 613 (1987).

22. J. Villain, R. Bidaux, J.P. Carton, and R. Conte, *J. Physique* **41**, 1263 (1980).
23. T. Oguchi, H. Nishimori, and Y. Taguchi, *J. Phys. Jpn.* **54**, 4494 (1985).
24. C. Henley, *Phys. Rev. Lett.* **62**, 2056 (1989).
25. A. Gaff and J. Hijmann, *Physica A* **80**, 149 (1975).
26. J. E. Sacco and F. Y. Wu, *J. Phys. A* **8**, 1780 (1975).
27. J. Maillard , *Second conference on Statistical Mechanics*, California Davies (1986), unpublished.
28. K. Binder and A. P. Young, *Rev. Mod. Phys.* **58**, 801 (1986).
29. T. Choy and R. Baxter, *Phys. Lett. A* **125**, 365 (1987).
30. P. Azaria, H. T. Diep and H. Giacomini, *Phys. Rev. B* **39**, 740 (1989).
31. D. Blankschtein, M. Ma and A. Berker, *Phys. Rev. B* **30**, 1362 (1984).
32. H. T. Diep, P. Lallemand and O. Nagai, *J. Phys. C* **18**, 1067 (1985).
33. J. Stephenson, *J. Math. Phys.* **11**, 420 (1970); *Can. J. Phys.* **48**, 2118 (1970); *Phys. Rev. B* **1**, 4405 (1970) .
34. F. Y. Wu and K.Y. Lin , *J. Phys. A* **20**, 5737 (1987).
35. H. Giacomini , *J. Phys. A* **19**, L335 (1986) .
36. R. Baxter , *Proc. R. Soc. A* **404**, 1 (1986).
37. P. Rujan , *J. Stat. Phys.* **49**, 139 (1987) .
38. M. Suzuki and M. Fisher, *J. Math. Phys.* **12**, 235 (1971).
39. F. Y. Wu, *Solid Stat. Comm.* **10**, 115 (1972) .
40. L. Onsager, *Phys. Rev.* **65**, 117 (1944).
41. C. S. Hsue, K. Y. Lin, and F.Y. Wu, *Phys. Rev. B* **12**, 429 (1975).
42. K. Y. Lin and I. P. Wang, *J. Phys. A* **10**, 813 (1977).
43. J. Imbrie, *Phys. Rev. Lett.* **53**, 1747 (1984).
44. D. Blankschtein, M. Ma , A. Nihat Berker, G. S. Grest, and C. M. Soukoulis, *Phys. Rev. B* **29**, 5250 (1984).
45. See the chapter by O. Nagai, T. Horiguchi and S. Miyashita, this book.
46. P. Azaria, H. T. Diep and H. Giacomini, *Europhys. Lett.* **9**, 755 (1989).
47. D.P. Foster, C. Gérard and I. Puha, *J. Phys. A: Math. Gen.* **34**, 5183 (2001).
48. D.P. Foster and C. Gérard, *Phys. Rev. B* to appear (2004).
49. E. H. Boubcheur, R. Quartu, H. T. Diep and O. Nagai, *Phys. Rev. B* **58**, 400 (1998).
50. C. Santamaria and H. T. Diep, *J. Appl. Phys.* **81**, 5276 (1997).
51. C. Santamaria, R. Quartu and H. T. Diep, *J. Appl. Phys.* **84**, 1953 (1998).
52. R. Quartu and H. T. Diep, *Phys. Rev. B* **55**, 2975 (1997).

## CHAPTER 2

### PROPERTIES AND PHASE TRANSITIONS IN FRUSTRATED ISING SYSTEMS

Ojiro Nagai

*Department of Physics, Faculty of Science, Kobe University, Kobe 657-0013,  
Japan*

Tsuyoshi Horiguchi

*Department of Computer and Mathematical Sciences, GSIS, Tohoku University,  
Sendai 980-0845, Japan*

and

Seiji Miyashita

*Department of Applied Physics, Graduate School of Engineering, The University  
of Tokyo, Tokyo 113-8656, Japan*

#### 2.1. Introduction

Frustration is one of the most interesting concepts in condensed matter physics. Historically, a striking affair concerning frustration was a discovery of helical spin structure in 1959.<sup>1,2,3</sup> Until that year, nobody has reached at the finding of this structure, in spite of the fact that there are many substances noticed later as helical magnets and also in spite of the fact that the mathematical procedure to derive the helical spin structure is quite easily understood. The concept of frustration has a very important role on spin systems, including Ising spin systems, classical vector spin systems such as  $XY$  model, classical Heisenberg model and so on, and also quantum spin systems. The spin glasses are one of the most interesting problems in the spin systems, in which the frustration plays an important role. Experimentally in the Ising spin systems, there exist various Ising magnets with

hexagonal symmetry and also the ordered problem of adsorbates on a crystal plane. Note that the binary alloy problem is equivalent to Ising models. According to recent findings, the neuron systems are deeply related to the Ising spin systems with frustration.<sup>4</sup>

The word "frustration" was first introduced by Toulouse<sup>5,6</sup> in 1977 for a plaquette shown in Fig.2.1. Here the plaquette is composed of three ferromagnetic bonds and one antiferromagnetic bond. An Ising spin,  $\sigma_j = \pm 1$ , is located at the  $j$ th vertex (or site). The Hamiltonian of this four-spin system is written as

$$H = -J_{12}\sigma_1\sigma_2 - J_{23}\sigma_2\sigma_3 - J_{34}\sigma_3\sigma_4 - J_{41}\sigma_4\sigma_1. \quad (1)$$

The absolute value of  $J_{ij}$  is assumed to be equal to  $J$ . Then the degeneracy of ground state for this system with Hamiltonian  $H$  is eight. A frustration parameter  $G$  defined by the sign of the product of interaction constants  $\{J_{ij}\}$ , namely  $G = \text{sign}(J_{12}J_{23}J_{34}J_{41})$ , is negative for the plaquette shown in Fig.2.1. If  $G$  is negative (or positive), the plaquette is frustrated (or non-

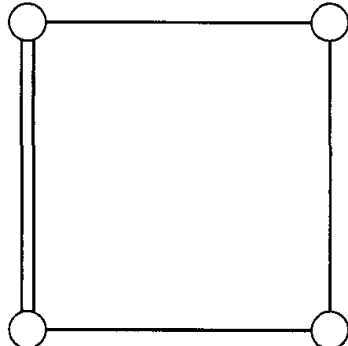


Fig. 2.1. A frustrated plaquette. A single bond and double bonds denote a ferromagnetic interaction and an antiferromagnetic interaction, respectively.

frustrated). When all the plaquettes of the square lattice are frustrated, the Ising model on the square lattice is called the odd model or Villain lattice (Fig.2.2).<sup>7,8</sup> A spin model on a frustrated lattice is also called a frustrated spin model (or a spin model with frustration) on a lattice in this chapter. The simplest fully frustrated lattice is the antiferromagnetic triangular lattice. The frustrated plaquettes are formed on all the triangles with antiferromagnetic interactions, and the frustration parameter  $G$  is negative for all plaquettes. The Ising model on the antiferromagnetic triangular lattice was exactly solved by Wannier,<sup>9</sup> Houtappel,<sup>10</sup> Husimi and Syoji,<sup>11,12</sup> Stephenson<sup>13,14</sup> and so on.<sup>15</sup> Zero-point entropy of this system is of the or-

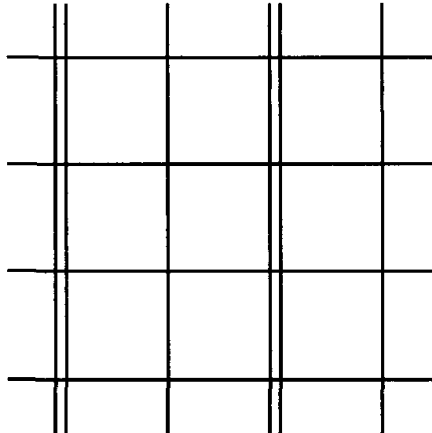


Fig. 2.2. The odd model or Villain lattice. The lattice is fully frustrated.

der of  $N$ , where  $N$  denotes the total number of the lattice sites or spins, and no long range order exists at any finite temperatures. Peculiar effects of the frustration on the ordering in real materials have been pointed out on the stacked triangular lattice by Mekata.<sup>16</sup> He found that the frustration causes so-called partially ordered (PD) phase in which two of the three sublattices are ordered antiferromagnetically, but the last one remains disorder.

The partition function of the Ising model on the Villain lattice has been also exactly calculated.<sup>7,8</sup> Zero-point entropy is of the order of  $N$  and no long range order of spins exists in this system at any finite temperatures as well as for the triangular lattice.

To discuss the properties of frustrated lattice, one may use the concept of local gauge invariant. When we change the way of expression of the variable at a site  $i$ , in order to keep the Hamiltonian (or Lagrangian) to be the same, one has to change the expression of the interactions including the site  $i$ . If both changes are done consistently, then the Hamiltonian is kept invariant.

For the Ising model, the local gauge transformation means that we replace a spin  $\sigma_i$  by  $-\sigma_i$ , and simultaneously replace the coupling constant  $J_{ij}$  by  $-J_{ij}$  for all  $j$ . It is local gauge invariant whether a lattice is frustrated or not, because a local gauge transformation changes two of the coupling constants in a plaquette at once.

Using the local gauge transformation, we can change the distribution of ferro- and antiferro-magnetic bonds, but can not change the distribution of the frustrated plaquettes. Therefore, the important characteristic of the

lattice is the distribution of the frustrated plaquettes but not that of ferro- and antiferro-magnetic bonds.<sup>17</sup>

In this chapter, we are concerned with Ising and Ising-like (uniaxial anisotropy) models on the lattices with frustration. We mainly consider the antiferromagnetic triangular (AFT) lattice and on the stacked AFT lattice. We explicitly demonstrate important formulae and develop full arguments leading to important results for these systems. A comprehensive review of frustrated Ising spin systems has been presented by Liebmann.<sup>18</sup> The articles and monographs until 1984 may be found in that textbook.

Frustrated Ising spin systems are characterized by large degeneracy of the ground state. Since the number of degeneracy is strongly related to the spin ordering, the internal degree of freedom of spin, or the magnitude  $S$  of spin (i.e.  $M = -S, -S + 1, \dots, S$ ), is an important physical parameter in the frustrated Ising spin systems. We show in this chapter that the spin ordering is strongly dependent on the magnitude  $S$  of spin. There exist "free" spins or "free" linear-chains, on which internal fields are cancelled out, in some frustrated Ising spin systems. These free spins and free linear-chains play an important role as for spin orderings.

Another characteristic feature of frustrated Ising spin systems is that various metastable states exist in these systems. Existence of metastable states is closely related to the degeneracy of ground state and also to the excited states. Furthermore, the metastable states may give rise to a first order phase transition. Actually, some models introduced in this chapter show a first order phase transition. From this viewpoint, we try to understand the physics of frustrated Ising spin systems in this chapter.

## **2.2. Ising model on two-dimensional frustrated lattice and on stacked frustrated lattice**

The critical temperature of the Ising model on the Villain lattice is zero.<sup>7</sup> However, the critical temperature of the Ising model on the stacked Villain lattice is not zero.<sup>19</sup> We start with a brief explanation for this fact. The lattice structure of the stacked Villain lattice is shown in Fig.2.3. In this lattice, each  $xy$ -plane is frustrated but none of  $yz$ - nor  $zx$ -planes are frustrated. Each ferromagnetic  $yz$ -plane is connected by the ferro- and antiferro-magnetic bonds with its nearest  $yz$ -planes. Since the number of the ferromagnetic bonds and that of the antiferromagnetic bonds are the same between two successive  $yz$ -planes, it is easily supposed that the critical temperature of this system is non-zero and close to that of the Ising model

on the square lattice. Actually, according to the Monte Carlo (MC) simulations, the critical temperature  $T_c$  of the Ising model on the stacked Villain lattice is given by  $kT_c/J \cong 2.9$ .<sup>19</sup> Here we notice that the critical temperature of the Ising model on the square lattice is given by  $kT_c/J \cong 2.27$ .<sup>20</sup> These two values are in fact close.

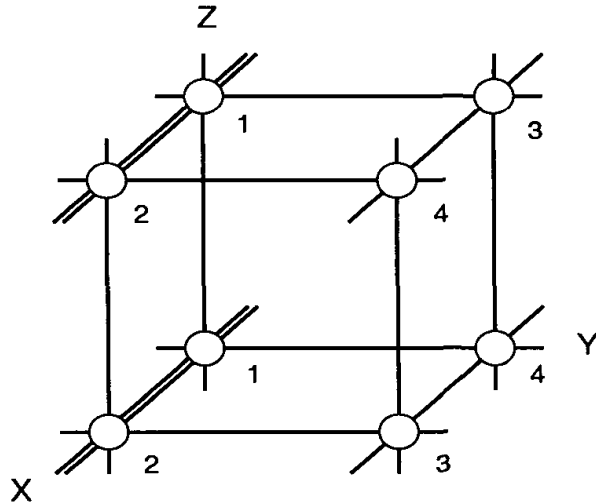


Fig. 2.3. The Stacked Villain lattice.

The lattice structure of the stacked AFT lattice is shown in Fig.2.4. We assume that the nearest-neighbor interaction between spins on each  $xy$ -plane is  $-J$  ( $J > 0$ ) and that between a spin on an  $xy$ -plane and one on its nearest  $xy$ -plane is  $J_z > 0$ . In this system, none of planes including the  $z$  axis are frustrated. The square lattices in the  $zx$ -plane or  $yz$ -plane are composed of the antiferromagnetic bond  $J$  and the ferromagnetic bond  $J_z$ . However, the effect of the  $J$  bonds cancels out each other on the ordering problem of those  $xy$ -planes. Therefore, the critical temperature of the Ising model on the stacked AFT lattice is supposed to be close to that of the Ising model on the square lattice composed of  $J$  and  $J_z$ . In order to see this, we calculate  $kT_c/J_z$  as a function of  $J/J_z$ . The critical temperature for the Ising model on the square lattice with  $J$  and  $J_z$  is calculated from the following equation:<sup>20</sup>

$$\sinh(2K_c) \sinh(2K_c^z) = 1, \quad (2)$$

where  $K_c = J/kT_c$  and  $K_c^z = J_z/kT_c$ . The critical temperature of the Ising model on the stacked AFT lattice is computed by the MC simulations.<sup>19</sup>

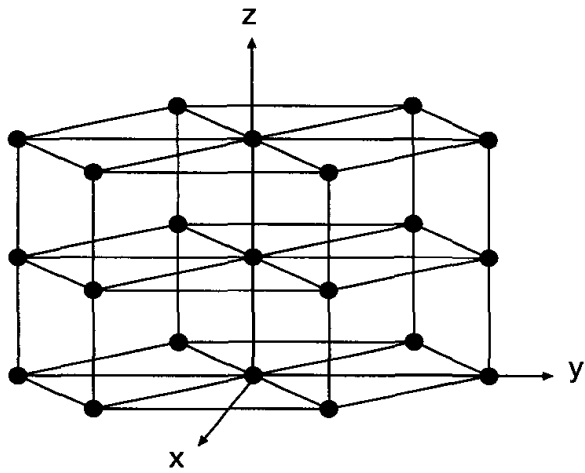


Fig. 2.4. The stacked AFT lattice.

These two critical temperatures are compared in Fig. 2.5. We see that  $J/J_z$  dependencies of  $kT_c/J_z$  for these two systems show a similar behavior. This behavior supports our physical interpretation.

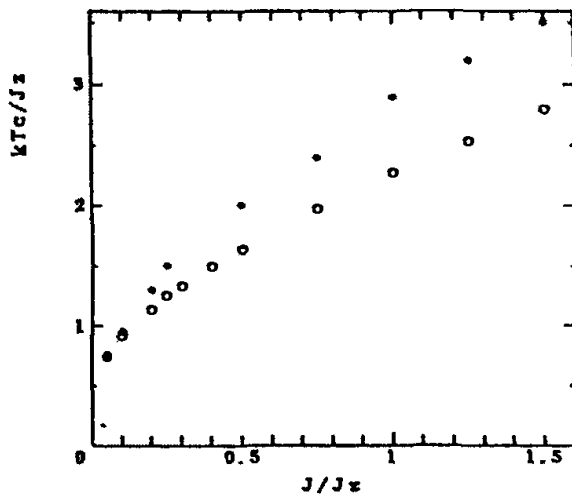


Fig. 2.5.  $J/J_z$  dependence of  $kT_c/J_z$ . The open circles denote the critical temperature for the Ising model on the square lattice and the solid circles for the Ising model on the stacked AFT lattice.

In the Ising model on two-dimensional fully-frustrated lattices such as the Villain lattice and the AFT lattice, there appear many free spins.<sup>21</sup> Corresponding to the free spins, there appear many free linear-chains in the Ising model on the stacked frustrated lattices.<sup>22</sup> The role of free linear-chains will be explicitly discussed in later sections.

### 2.3. Ising model on antiferromagnetic triangular lattice

The Ising model is considered on the AFT lattice shown in Fig.2.6; the lattice is divided into *A*-, *B*- and *C*-sublattice. We call spins on the *A*-

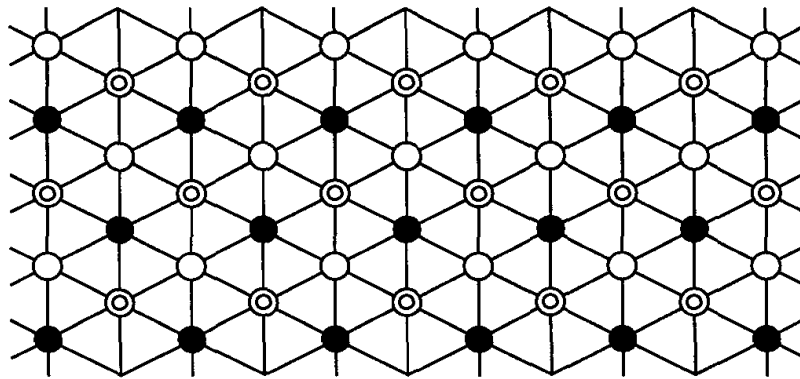


Fig. 2.6. The AFT lattice. The solid circles, the open circles and the double circles denote the lattice sites belonging to *A*-, *B*-, and *C*-sublattice, respectively.

sublattice *A* spins, those on the *B*-sublattice *B* spins and those on the *C*-sublattice *C* spins hereafter. We consider the nearest-neighbor (nn) interaction, and the Hamiltonian is written as

$$H_0 = J \sum_{(ij)} \sigma_i \sigma_j, \quad (3)$$

where the summation with respect to  $(ij)$  means that the sum is taken over all the nn pairs of lattice sites. The Ising AFT model has been solved exactly.<sup>9,10,11,12</sup> There are many degenerate states in the ground-state, and the number of degeneracy is  $\exp(0.323N)$ . Because of this macroscopic degeneracy, if a very small perturbational energy is added to Eq.(3), an ordered spin-state may be chosen due to the perturbation. The critical indices

are investigated by Horiguchi et al.<sup>15</sup> Although no long-range order exists in this system even at zero temperature, the correlation function does not show an exponential decay but a power law decay at  $T = 0$ <sup>13,14</sup>

$$\langle \sigma_i \sigma_j \rangle \propto r_{ij}^{-\eta}, \quad (4)$$

where  $\eta = 1/2$ , and  $r_{ij}$  denotes the distance between the sites  $i$  and  $j$ .

This suggests that the sublattice order tends to develop. As such perturbations, we may consider a next nearest neighbor (nnn) interaction  $J_2$  which connects the spins in the same sublattices. If we add the nnn interaction on the Villain lattice, a phase transition appears and the critical exponents depend on the strength of  $J_2$ .<sup>23</sup> On the triangular lattice, the nnn interaction also causes phase transitions,<sup>24,25,26,27,28</sup> which will be discussed in the following.

Now, we study the effect of ferromagnetic next-nearest-neighbor interaction. First, we show spin-states chosen by adding a small ferromagnetic interaction,  $J_2$ , between next-nearest-neighbor (nnn) pairs. We see in Fig.2.6 that an nnn pair corresponds to an nn pair within a sublattice. The Hamiltonian  $H_3$  for the system is written as

$$H_3 = H_0 - J_2 \left( \sum_{(i,i')}^A \sigma_i \sigma_{i'} + \sum_{(j,j')}^B \sigma_j \sigma_{j'} + \sum_{(k,k')}^C \sigma_k \sigma_{k'} \right), \quad (5)$$

where  $\sum^A$  ( $\sum^B$  and  $\sum^C$ ) denotes the sum over nn pairs within  $A$  sublattice ( $B$  and  $C$  sublattices). We use this kind of notations throughout this chapter. We call this system with the nnn interaction in all the three sublattices S3. The nnn interaction enhances a spin ordering within the sublattice.<sup>24,25,26,27,28</sup>

In order to study properties of the spin ordering, we investigate the set of sublattice magnetizations,  $\mathbf{M}$ :

$$\mathbf{M} = \frac{3}{N} \left( \sum_{i \in A} \sigma_i, \sum_{j \in B} \sigma_j, \sum_{k \in C} \sigma_k \right). \quad (6)$$

The spin-state for this system at low temperatures is of the so-called ferromagnetic (FR) structure. The FR structure, which is shown in Fig.2.7, is one of spin-states in the ground state occurring in the system with  $J_2 = 0$ . The MC results of the specific heat,  $c = C/Nk$ , versus temperature,  $kT/J$ , are shown in Fig.2.8 for the case  $J_2 = 0.1$ . Two peaks are observed in the specific heat. The temperature dependence of sublattice magnetizations is shown in Fig.2.9. The higher transition temperature is estimated to be  $kT_1/J \cong 1.5$  and the lower transition temperature to be  $kT_2/J \cong 0.4$ .

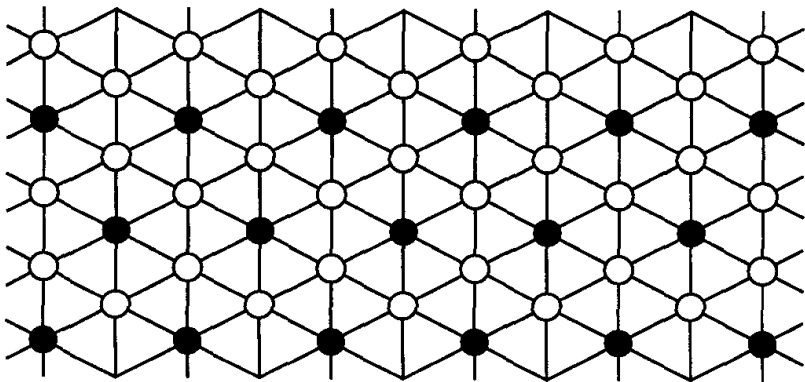


Fig. 2.7. The ferrimagnetic (FR) structure,  $(1, -1, -1)$ . The solid and open circles show up- and down-spins, respectively.

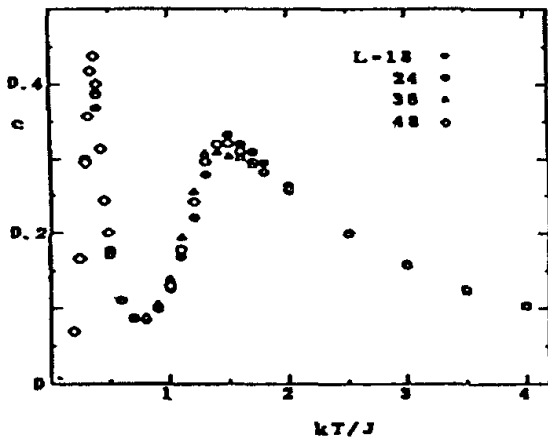


Fig. 2.8. Specific heat for S3 with  $J_2 = 0.1J$ .

The ordering mechanism of the model S3 has been studied in the relation with the six-state clock model.<sup>25</sup> As the ground state spin configuration on a triangle there are six possible combinations which are energetically degenerate, i.e.,  $(1, -1, -1)$ ,  $(1, -1, 1)$ ,  $(-1, -1, 1)$ ,  $(-1, 1, 1)$ ,  $(-1, 1, -1)$ , and  $(1, 1, -1)$ . We can map these six states to those for the six-state clock model as depicted in Fig. 2.10. It is well known that the six-state clock model has two Kosterlitz-Thouless transitions.<sup>29,30</sup> The two peaks in the Fig. 2.8 correspond to the two Kosterlitz-Thouless transitions.

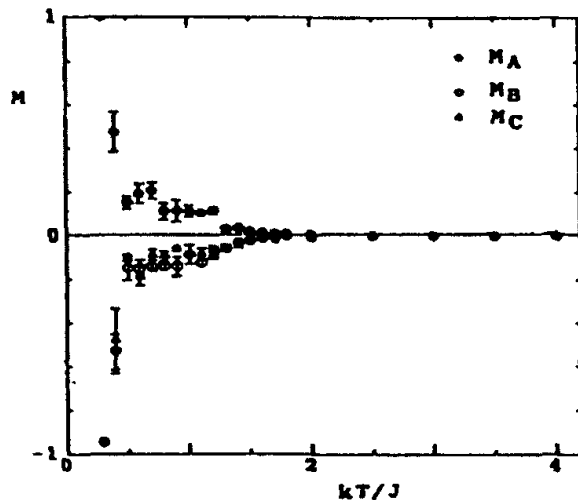


Fig. 2.9. Sublattice magnetizations for S3 with  $J_2 = 0.1J$ .

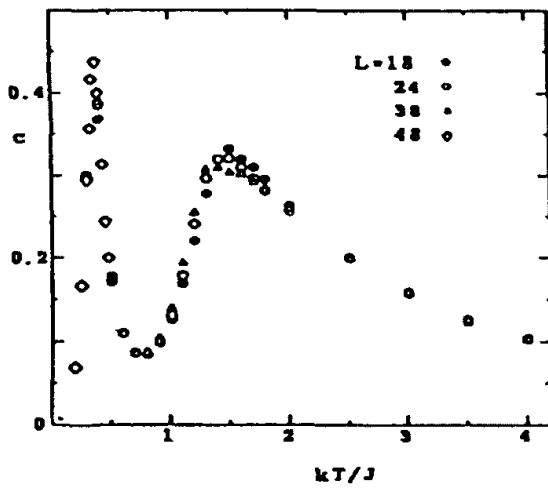


Fig. 2.10. Relation between the six-clock state model and the AFT model(left). The interaction energy of the generalized six-state clock model(right).

Next, we consider the system in which the ferromagnetic interaction,  $J_2$ , exists between nn pairs within  $A$ -sublattice and also between those within  $B$ -sublattice. We call this system S2. At low temperatures, we assume that all the  $A$  spins take +1 and all the  $B$  spins take -1. Then the internal field to each of  $C$  spins vanishes. This spin-state corresponds to the partial disorder (PD) structure  $(1, -1, 0)$ . We show an example of the PD structure

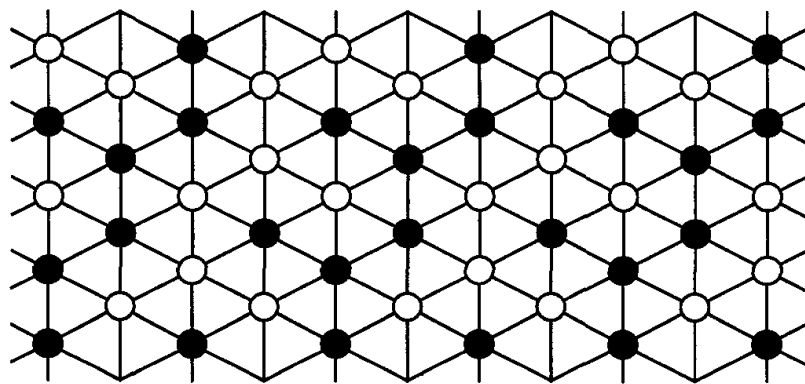
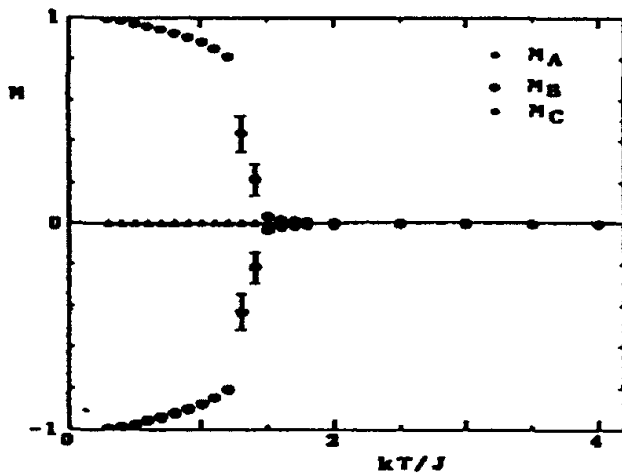
Fig. 2.11. One of the PD structures,  $(1, -1, 0)$ .

Fig. 2.12. MC data of sublattice magnetizations for S2.

in Fig.2.11. In other words, all the  $C$  spins are free. Thus the number of degeneracy of this PD structure is  $2^{N/3}$ . The MC data on the sublattice magnetizations for the case of  $J_2 = 0.1J$  are shown in Fig.2.12. The temperature dependence of specific heat is shown in Fig.2.13. Here we have only one phase transition.

Finally, let us consider the system where the ferromagnetic interaction,

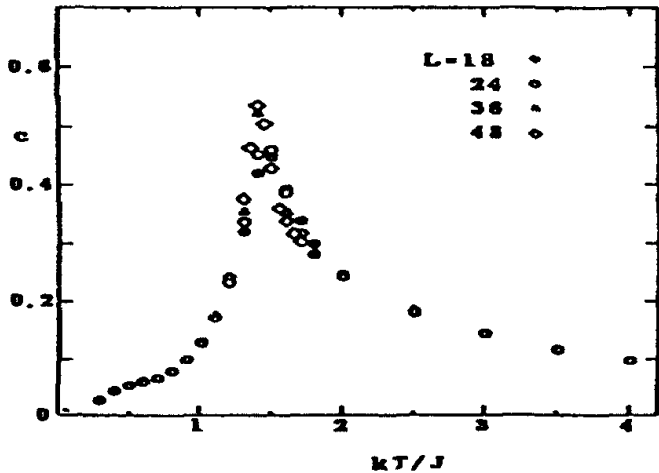


Fig. 2.13. MC data of specific heat for S2.

$J_2$ , exists only between nn pairs within the  $A$ -sublattice. We call this system S1. The spin-state in the ground state for this system is represented by  $(1, -1/2, -1/2)$ . This spin-state was proposed by Blankschtein et al.<sup>31</sup> as a low temperature phase for the Ising model on the stacked AFT lattice (see Fig.2.4). We call this spin-state the BL structure. The reason why the system takes the BL structure at low temperatures will be explained as follows. Let us assume all the  $A$  spins take +1. The  $B$  spins or the  $C$  spins may be free. If one of  $B$  spins is reversed, then the directions of three  $C$  spins surrounding the  $B$  spin are fixed. The MC results for the sublattice magnetizations for the case  $J_2 = 0.1J$  are shown in Fig.2.14. The specific heat shows a temperature dependence similar to that in Fig.2.13. The spin-state of the BL structure is included in the Wannier state for the system with  $J_2 = 0$ . This BL structure is realized as the ground state, when a uniform magnetic field is applied to the spins in one of sublattices, as can be easily supposed.

We have seen that the FR, PD, and BL structures, respectively, appear for the S3, S2, and S1 at  $T = 0$ . If a perturbational interaction between far-neighbor spins is assumed, there may appear a multi-sublattice spin-structure as the ground state.

Interaction among the transverse components (i.e. the  $xy$  interaction) also causes to resolve the macroscopic degeneracy. We will study the effect of the  $xy$  component in the classical spin systems which corresponds  $S = \infty$

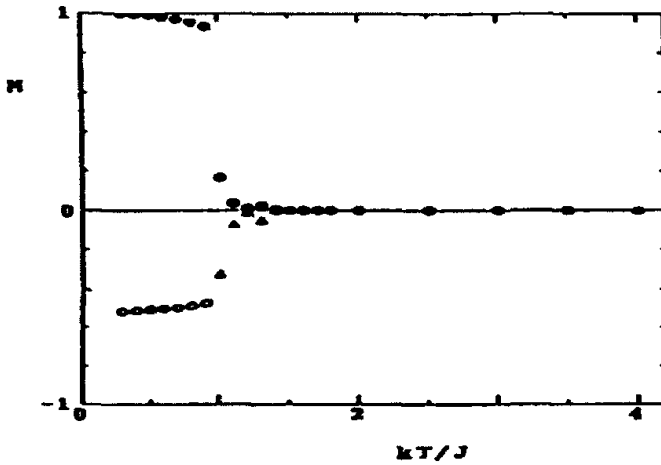


Fig. 2.14. MC data of sublattice magnetizations for S1.

model in the later section.<sup>32,33,34</sup> In  $S = 1/2$  system the interaction of the  $xy$  components causes the quantum effect, which would bring a new quantum state, so-called resonating valence-bond (RVB).<sup>35,36</sup> Furthermore, the effect of the transverse field has been studied, where the ground state degeneracy is resolved and the system has an extra peak of the specific heat at a low temperature.<sup>37</sup>

#### 2.4. Ising model on stacked antiferromagnetic triangular lattice

The Hamiltonian of the Ising model on the stacked AFT lattice is written as

$$H = J \sum_{(i,j)}^{xy} \sigma_i \sigma_j - J_z \sum_{(i,j)}^z \sigma_i \sigma_j, \quad (7)$$

where  $J$  denotes the nearest-neighbor (nn) interaction constant in the  $xy$ -plane and  $J_z$  the nn interaction constant along the  $z$  axis (see Fig. 2.4). Here  $J$  and  $J_z$  are both positive. The sum runs over the nn pairs either in the  $xy$ -plane or along the  $z$  direction. It is noticed that a long-range order appears at a temperature  $kT/J \cong 2.9$  when  $J/J_z = 1$ . Below the critical temperature, the spin-state is the PD structure,  $(M, 0, -M)$ .<sup>38,39</sup> At  $T = 0$ , since the spins along the  $z$  axis are parallel to each other, the spin-state in the  $xy$ -plane should be the same as that of the AFT lattice.

That is, no long range order exists in the  $xy$ -plane at  $T = 0$ . Hence, there occurs some crossover from the PD structure to the Wannier state at a low temperature. In the MC simulations, two peaks are observed for the specific heat at  $T \cong 2.9J/k (= T_1)$  and at  $T \cong 0.9J/k (= T_2)$ . The peak at  $T_1$  is due to the phase transition. The reason that the second peak at  $T_2$  appears is as follows. We know that there exist many free spins in the AFT lattice at  $T = 0$ . Corresponding to these free spins, there exist many free linear-chains in the stacked AFT lattice. The free linear-chains in the system are parallel to the  $z$  axis. It is known that the specific heat of Ising model on the linear chain shows a Schottky-type peak at  $kT/J \cong 0.9$ . By using the MC simulations, we calculate the specific heat,  $c$ , for the Ising model on the stacked AFT lattice for various values of  $J/J_z$ ; we use  $c$  given by

$$c = \frac{1}{N} \left( \frac{J_z}{kT} \right)^2 \left[ \langle \left( \frac{H}{J_z} \right)^2 \rangle - \langle \frac{H}{J_z} \rangle^2 \right]. \quad (8)$$

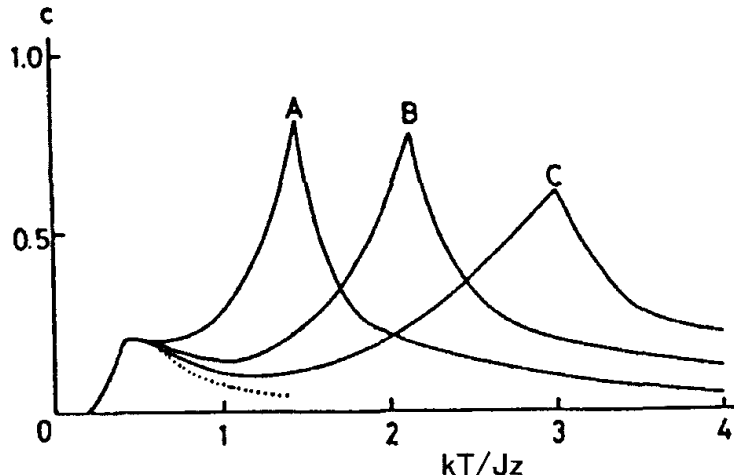


Fig. 2.15. MC data of the specific heat for various values of  $J/J_z$ :  $J/J_z = 1$  (A), 2.0 (B), and 3.0 (C). The dotted line is explained in the text. Here  $J_0$  is used in place of  $J_z$ .

In Fig. 2.15, the MC data of the specific heat are shown as a function of  $kT/J_z$ . There is a small peak or bump in the specific heat. The position, the height, and the shape of the bump on the low temperature side are not affected by the value of the  $J/J_z$ . Hence, it is conjectured that this bump is due to the linear-chain-like excitations in the system, where the interaction

constant of the "linear chain" is given by  $J_z$ .<sup>22</sup> Another interesting point is that the conventional single-spin-flip Monte Carlo simulation method may fail for this system at low temperatures. Let us consider the MC simulations for the Ising model on the linear chain. As is well-known, the internal energy,  $U$ , of the Ising model on the linear chain is given by

$$U = -LJ_z \tanh \frac{J_z}{kT} = -LJ_z [1 - 2 \exp(-\frac{2J_z}{kT}) + \dots], \quad (9)$$

where  $L$  denotes the total number of spins in the linear chain. This expression indicates that the first excited energy is equal to  $2J_z$  and also that the first excited state includes only one kink. Thus, it is needed to adopt the

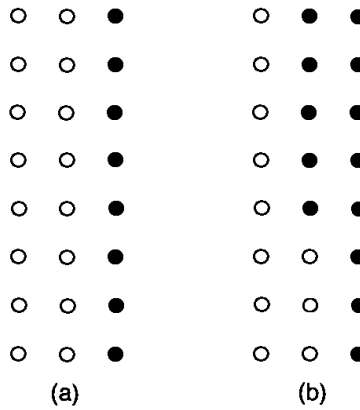


Fig. 2.16. (a) The ground state of a free linear-chain in the system. The solid and open circles denote the up- and down-spins, respectively. (b) The first excited state. The excitation energy is  $2J_z$ .

cluster-flip Monte Carlo method, where the cluster in the system is a free linear-chain. We schematically show the ground state and the first excited state in the system in Fig. 2.16(a) and (b). We take up the temperature dependence of long-range order-parameters in the whole temperature range. Let us define the order parameter  $X$  and the sublattice order-parameter  $Y$  by the following equations:

$$X = \frac{1}{N^2} \langle (\sum_i \sigma_i)^2 \rangle, \quad (10)$$

$$Y = \left(\frac{3}{N}\right)^2 \langle (\sum_{i \in A} \sigma_i)^2 + (\sum_j \sigma_{j \in B})^2 + (\sum_k \sigma_{k \in C})^2 \rangle. \quad (11)$$

It is easily seen that  $X = 0$  and  $Y = 2$  for the PD structure,  $(1, -1, 0)$ , and  $X = 1$  and  $Y = 3$  for the FR structure,  $(1, -1, -1)$ . The temperature dependencies of  $X$  and  $Y$  in the MC simulations are shown in Fig.2.17. We see that  $X = 0$  in the whole temperature range and the values of  $Y$

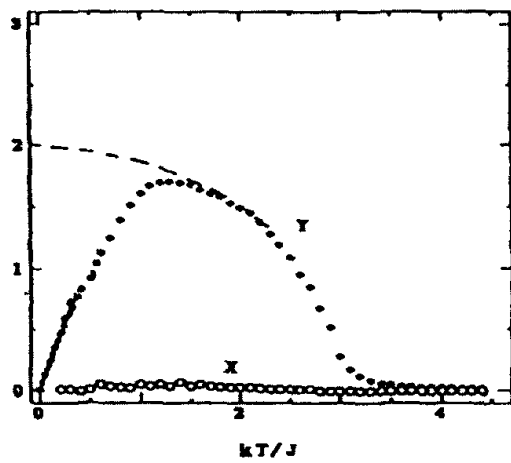


Fig. 2.17. MC data of  $X$  and  $Y$  for the Ising model on the stacked AFT lattice.

agree with those for the PD structure (dashed line) above  $kT/J \cong 1.2$ . Here these spin pairs are belonging to the  $A$ -sublattice or  $B$ -sublattice. Remember system S2 in the section 3. The dashed line in Fig.2.17 shows an extrapolation to the state with the PD structure. We may assume that a temperature region between  $kT/J = 0$  and 2.0 is the crossover region between a three-dimensional ordered state and the Wannier state. The number of free linear-chains, which is denoted by  $\gamma N^{2/3}$  at low temperatures, may be estimated from the MC data of the specific heat. The dotted line for the specific heat in Fig.2.15 is obtained by assuming  $\gamma = 0.376$ .<sup>40</sup>

The phase transitions of this model with the nnn interaction in the three dimensions was studied by Mekata.<sup>16</sup> He obtained three phases: PD phase and the three-sublattice-ferrimagnetic phase (FR3) where all the three sublattices have different magnetizations, and the two sublattice ferrimagnetic phase (FR) which corresponds to  $(1, -1, -1)$  phase. Thus the nature of the phases are very different from that in the two dimensions. We may also map the three dimensional model to the six-state clock model.<sup>41,42,43</sup> It has been found that the six-state clock model in the three dimensions has only one

phase transition below which the discreteness of the six state is relevant. In two dimensions, there are two phase transitions, and the discreteness is irrelevant in the intermediate phase. In three dimensions, there is no intermediate phase corresponding to that in the two dimensions, although the macroscopic quantities such as the specific heat and the magnetization show rather-well defined crossover phenomena.<sup>44,42</sup> From this point of view, one may consider that there is only one phase below the temperature where the sublattice order develops, and the quantitative changes below this temperature is just due to the crossover. However, in the so-called generalized six-state clock model where the interaction energy between the six states is generalized as shown in Fig.2.10,<sup>45</sup> it has been found that the system has an intermediate phase and a low temperature phase. This intermediate phase corresponds to the PD phase, and the low temperature phase to the FR type. The PD phase changes directly to FR phase, although the FR3 phase exists between them in the mean-field analysis. The phase transition is of the first order. It is mystery that the specific heat has very small (or no) latent heat, mechanism of which is under investigation.<sup>46,47</sup>

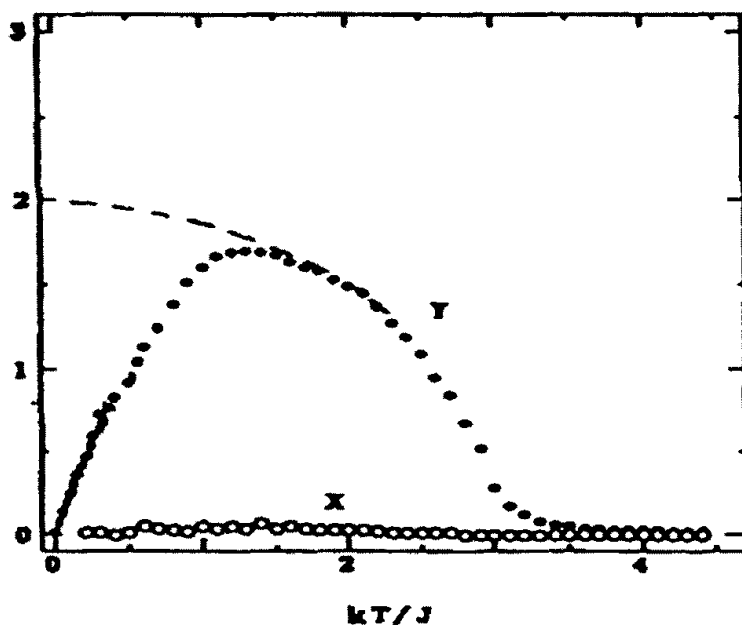


Fig. 2.18. The specific heat of the stacked AFT Ising model with  $J_2 = 0.1$ .

## 2.5. Ising model with large $S$ on antiferromagnetic triangular lattice

We know that there is no long-range order in the ground state of the Ising model with spin 1/2 on the AFT lattice. This property may change if the magnitude  $S$  of spin changes. For the Ising model with infinite-spin, there exists a long range order, as will be shown in this section, and hence there is an evidence of a phase transition at a finite temperature. The frustrated systems such as the Ising model with spin 1/2 on the AFT lattice are characterized by a large degeneracy of the ground state. The effect of magnitude  $S$  of spin on the ordering properties of frustrated Ising spin systems is an interesting problem.<sup>48,49</sup> It is interesting to show in this section that the nature of the spin ordering for the Ising model with large  $S$  is quite different from that with spin 1/2 on the AFT lattice.<sup>50,51,52,53,54</sup>

The Hamiltonian of the Ising model with spin  $S$  on the AFT lattice is given by

$$H = J \sum_{(i,j)} \sigma_i \sigma_j, \quad (12)$$

where  $\sigma_i = S_i/S$ .  $S_i$  denotes the Ising spin of magnitude  $S$  on the  $i$ th lattice site and takes one of the  $2S + 1$  values,  $S, S - 1, \dots, -S$ . The spin with the limit of  $S$  infinity is also called the continuous Ising-spin since

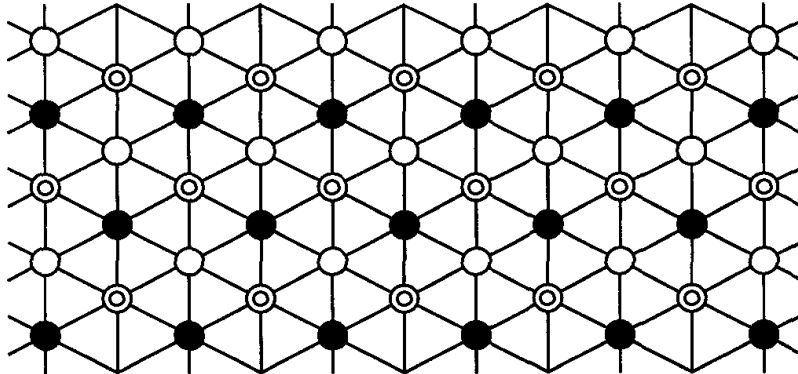


Fig. 2.19. The partially disordered structure of the Ising model with spin  $S$  on the AFT lattice. The solid and open circles denote  $+S$  spin and  $-S$  spin, respectively. The free spin is represented by the double circles.

$\sigma_i$  takes on  $[-1, 1]$ ; we assume that the limit of  $S$  infinity is taken before the thermodynamic limit. The set of sublattice magnetizations at  $T = 0$  is given by Eq.(6). At free spins the internal fields are canceled out. For the present model, each free spin can take a value out of  $2S + 1$  values. Therefore,  $n$  free spins causes  $(2S + 1)^n$ -fold degeneracy of the ground state. The spin structure with maximum number of the free spins is the PD structure (Fig.2.19) where say the  $A$ -sublattice take  $+S$ , and all the spins in the  $B$ -sublattice take  $-S$ , and all the spins in the  $C$ -sublattice are free. In this case, the set of the sublattice magnetizations,  $\mathbf{M}$ , is  $(1, -1, 0)$  and the degeneracy of the spin-states is equal to  $(2S + 1)^{N/3}$ .

We consider a spin on the  $A$ -sublattice ( $A$  spin) in the partially disordered structure of  $(1, -1, 0)$  type. In order to make the spin free, the neighboring three  $C$  spins must be fixed to be  $+S$ . Thus, the number of free spins is reduced by 2 as depicted in Fig.2.20. We call the cluster of

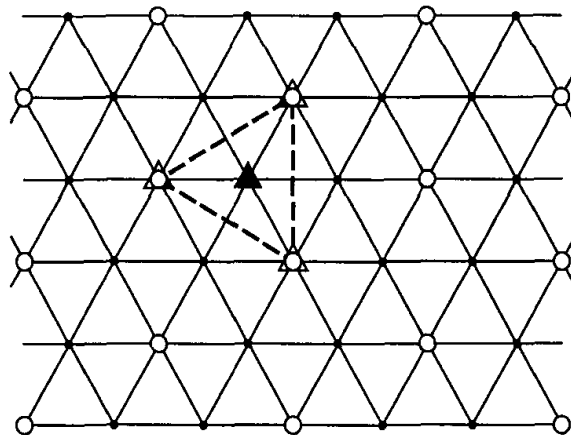


Fig. 2.20. A misfit cluster in the PD structure of  $(1, -1, 0)$ . The triangles represent the spins in the misfit cluster. The circles denote the free spins. The boundary of the misfit cluster is shown by the dashed lines.

those four spins ‘a misfit cluster’ of  $(0, -1, 1)$  type. The boundary of the misfit cluster is drawn by the closed dashed lines in Fig.2.20. We may also consider a misfit cluster in a  $B$  spin free. In order to study the stability of the PD structure, we study the degeneracy due to the misfit clusters. When

$n$  independent misfit clusters exist, the ground state degeneracy,  $W_n$ , is

$$W_n \cong (2S + 1)^{\frac{N}{3} - 2n} \binom{\frac{2N}{3}}{n}. \quad (13)$$

The condition for the maximum degeneracy is

$$\frac{\partial}{\partial n} \ln W_n = 0, \quad (14)$$

which yields

$$n = \frac{2N}{3} \frac{1}{(2S + 1)^2}. \quad (15)$$

This relation indicates that  $n = 0$  for  $S = \infty$ . If the density of misfits,  $n/N$ , is low enough, the orderings in  $A$  and  $B$  sublattice would remain. This problem is similar to the percolation problem and we expect that there exists a critical value of the magnitude of spin,  $S_c$  for the sublattice long-range order.

Following the Peierls' argument<sup>55,56</sup> for the spin ordering of the Ising model with spin 1/2 on the square lattice, we discuss a condition for the existence of long range order in the Ising model with spin  $S$  on the AFT lattice.<sup>53</sup> We consider spin configurations with a boundary condition which induces the order of  $(1, -1, 0)$  type. There are various kinds of misfit clusters of larger size; an example is given in Fig. 2.21. As depicted in Figs. 2.20 and

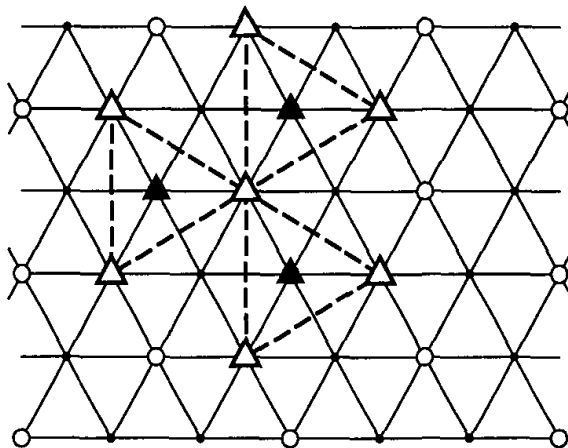


Fig. 2.21. A misfit cluster of large size.

2.21. we define the length of boundary,  $f$ , measuring in unit of  $\sqrt{3} \times$  bond length. E.g.,  $f = 3$  in Fig.2.20 and  $f = 9$  in Fig.2.21. Let  $d$  denote the reduction in the number of free spins due to the appearance of misfit cluster, e.g.,  $d = 2$  in the case of Fig.2.20 and  $d = 4$  in the case of Fig.2.21. Generally, the relation

$$f \leq 3d \quad (16)$$

is satisfied. Consider a spin on the  $A$ -sublattice. Let  $p_+$  be the probability that the spin is found in the cluster of  $(1, -1, 0)$  type or  $(1, 0, -1)$  type. Similarly, let  $p_-$  be the probability that the spin is found in the cluster of  $(-1, 1, 0)$  type or  $(-1, 0, 1)$  type and let  $p_0$  be the probability that the spin is found in the cluster of  $(0, 1, -1)$  type or  $(0, -1, 1)$  type. Since  $p_+ + p_- + p_0 = 1$ , we have

$$\langle \sigma_A \rangle = \frac{3}{NS} \left\langle \sum_{i \in A} S_i \right\rangle = p_+ - p_- = 1 - p_0 - 2p_-, \quad (17)$$

where  $\langle \dots \rangle$  denotes the average over all the spin-states in the ground state instead of the canonical weight in the case of Peierls' argument. As in the usual Peierls' argument, we compare the number of degeneracies of the cases with and without the boundary of  $p_0$  and we have the inequality

$$p_0 < \sum_f \sum_k m_k (2S+1)^{-d}, \quad (18)$$

where  $k = k(f)$  denotes the  $k$ th cluster and  $d = d(k, f)$  the reduction in the number of free spins due to the appearance of the cluster.  $m_k$  is the number of sites of the  $A$ -sublattice in the  $k$ th cluster. The number of clusters  $C_f$  with the boundary satisfies the relation

$$C_f \leq 2(z-1)^f, \quad (19)$$

where  $z (= 6)$  is the number of nearest-neighbor sites. The factor 2 is due to the fact that there are two kinds of misfit clusters with free  $A$  spins, namely the clusters of  $(0, 1, -1)$  type and those of  $(0, -1, 1)$  type. Using Eq.(19) and the relation,  $m_k < f^2$ , we have

$$\sum_k m_k (2S+1)^{-d} < 2f^2 \left( \frac{5^3}{2S+1} \right)^{f/3}. \quad (20)$$

Therefore, the series Eq.(18) converges if  $2S+1 > 5^3$ .  $p_-$  is estimated in the same way. Thus the long range sublattice order persists finite for large values of  $S$ .

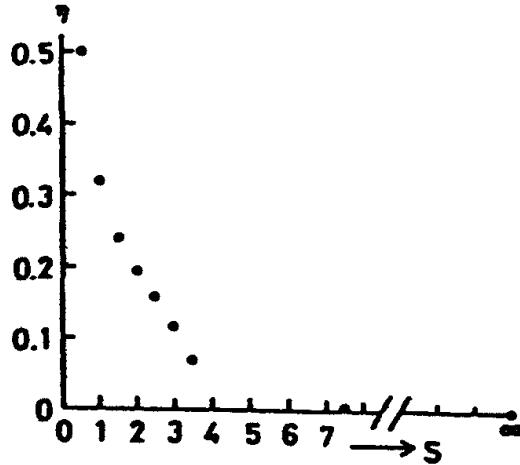


Fig. 2.22.  $S$  dependence of  $\eta$ ;  $\eta$  is the exponent for the correlation function.

The sublattice spin-pair correlation-function decays by a power law

$$\langle \sigma_i \sigma_{i+r} \rangle \sim r^{-\eta}, \quad \eta = 1/2 \quad (21)$$

for  $S = 1/2$ . For the sublattice long-range order,  $\eta$  is zero. It is an interesting problem to figure out how  $\eta$  reduces as  $S$  increases. In order to study  $\eta$ , we calculate the quantity  $A$ , which is defined by

$$A = \frac{1}{N} \left\langle \left( \sum_{i \in A} \sigma_i \right)^2 + \left( \sum_{i \in B} \sigma_i \right)^2 + \left( \sum_{i \in C} \sigma_i \right)^2 \right\rangle \quad (22)$$

by the Monte Carlo simulations. The values of  $\eta$  are obtained from the size dependence of  $A$ :

$$A \sim L^{2-\eta} \quad (23)$$

The  $S$  dependence of  $\eta$  is shown in Fig. 2.22. The threshold  $S_c$  has been estimated to be 3.<sup>57,58,59,60</sup>

## 2.6. Ising model with infinite-spin on antiferromagnetic triangular lattice

It is interesting to study the magnetic properties of the Ising model with infinite-spin on the AFT lattice. We show the MC data of the specific heat for various values of  $S$  in Fig. 2.23. The shape around the peak of specific heat,  $c$ , for the Ising model with infinite-spin is rather sharper than that

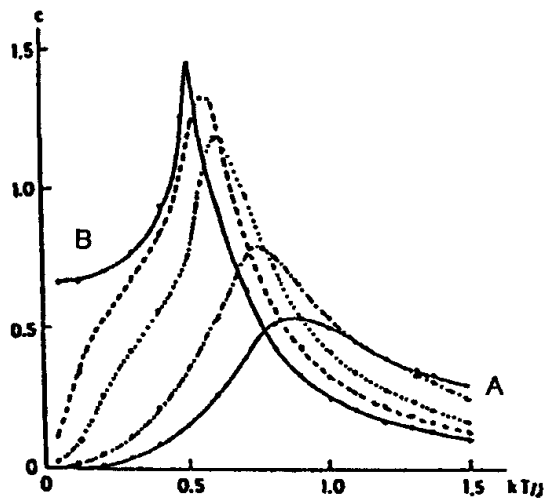


Fig. 2.23. MC data of specific heat for the Ising model with spin  $S$  on the AFT lattice for various values of  $S$ . The solid line (A) is for  $S = 1/2$ , the dash-dot line for  $S = 3/2$ , the dotted line for  $S = 7/2$ , the dashed line for  $S = 15/2$ , and the solid line (B) for  $S = \infty$ .

for the Ising model with finite  $S$ , as can be seen in Fig. 2.23. However, any size dependence was not observed in the peak of  $c$  for the Ising model with infinite-spin. The sublattice magnetizations of PD structure,  $(M, 0, -M)$ ,

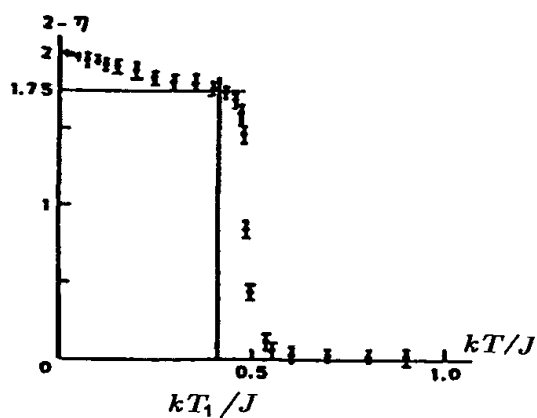


Fig. 2.24. MC data of  $2 - \eta$  as a function of the temperature for the Ising model with infinite-spin. The KT value, 1.75, is found at  $T = 0.41J/k$ .

were apparently observed up to the temperature  $T = 0.1J/k$  for a fairly large lattice size ( $L = 240$ ) and a long MC average time ( $t_{\text{MC}} = 10^6$  MC steps per spin).<sup>52</sup> However, the temperature dependence of  $2 - \eta$  decreases with respect to  $T$  and reaches at 1.75 at  $T \sim 0.41J/k (= T_1)$  and suddenly decreases to zero as shown in Fig.2.24. Here  $\eta$  denotes the exponent for correlation function and the value of  $\eta$  is 0.25 at the Kosterlitz-Thouless phase transition temperature. Since  $\eta$  should be zero in the spin-ordered region, no long range order exists at any finite temperatures except at very low temperatures for the Ising model of infinite-spin on the AFT lattice. It is desired to be investigated in detail the behavior of  $\eta$  near  $T = 0$  whether the long-range order exists or not at very low temperatures. On the other hand,  $\eta$  should be equal to 2 in the paramagnetic region. Thus, the MC data of  $\eta$  seem to indicate that the Kosterlitz-Thouless-type (KT-type) phase transition occurs at  $T_1$ .

## 2.7. Ising-like Heisenberg model on antiferromagnetic triangular lattice

It has been pointed out that the transverse interaction, i.e., interaction of the  $xy$  components, causes successive phase transitions at  $T_1$  and  $T_2$ . Below the higher critical temperature  $T_1$  the  $z$  component of the spin is ordered in the FR type configuration, while the  $xy$  components is still disordered. Below the lower critical temperature, the  $xy$  components are also ordered to form a non-collinear structure.<sup>32,33,34</sup> It has been pointed out that the ground state of this model has a non-trivial continuous degeneracy which can not resolved even if we take the entropy effect into account. Because of many nearly degenerate structures, this model has a rich structure of phases in the magnetic field.<sup>61</sup> The phase diagram in the  $(T, H)$  plane is depicted in Fig.2.25, which has been found in  $\text{GdPd}_2\text{AL}_3$ .<sup>62</sup> Quantum effect on the magnetization process has been also studied.<sup>63</sup>

## 2.8. Ising model with infinite-spin on stacked antiferromagnetic triangular lattice

In the ground state, the Ising model with spin 1/2 on the AFT lattice does not show any long range order. While, the Ising model with infinite-spin on the AFT lattice shows a partial-disordered (PD) structure which is expressed as  $(1, 0, -1)$ , for example. Similarly, the spin structure for the Ising model with infinite-spin on the stacked AFT lattice is quite different from that for the Ising model with spin 1/2. The Ising model with infinite-

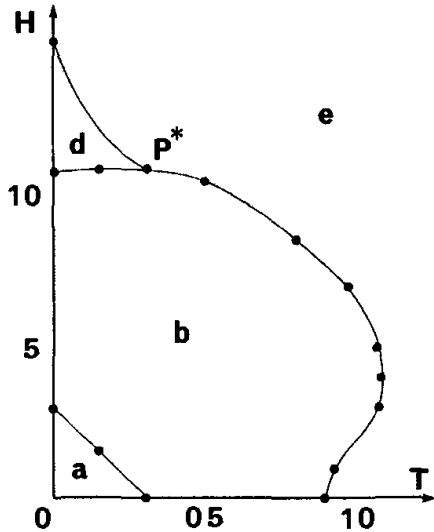


Fig. 2.25. The phase diagram in the  $(T, H)$  plane of the Ising-like Heisenberg model on antiferromagnetic triangular lattice.

spin shows a phase transition at a finite temperature. The spin structure in an intermediate temperature region is the PD structure but it is the ferrimagnetic (FR) structure,  $(M, -m', -m')$ , in a low temperature region. This FR structure is quite stable up to  $T = 0$ . This can be seen by the use of low-temperature-series-expansion (LTSE).<sup>64,65,50,51</sup>

The Hamiltonian of the present model is given by

$$H = J \sum_{(i,j)}^{xy} x_i x_j - J_z \sum_{(i,j)}^z x_i x_j, \quad (24)$$

where  $x_i$  takes on  $[-1, 1]$ . We assume  $J = J_z$  in the present section. The MC data for the sublattice magnetizations are shown in Fig. 2.26. As can be seen in Fig. 2.26, the system takes the PD structure in a temperature region,  $T_1 < T < T_c$ , where  $T_1 \cong 0.8J/k$  and  $T_c \cong 1.20J/k$ . The FR structure is observed in a temperature region,  $0 < T < T_1$ . A sharp peak in the specific heat is observed at the temperature  $T_c$ . Although we think that the phase transition at  $T = T_1$  is of the first order, the singularity of the specific heat is very weak.

Let us study theoretically the stability of the FR structure at low temperatures observed by the MC simulations. The partition function  $Z$  is written as

$$Z = \int_{-1}^1 dx_1 \cdots \int_{-1}^1 dx_N \exp(-\beta H). \quad (25)$$

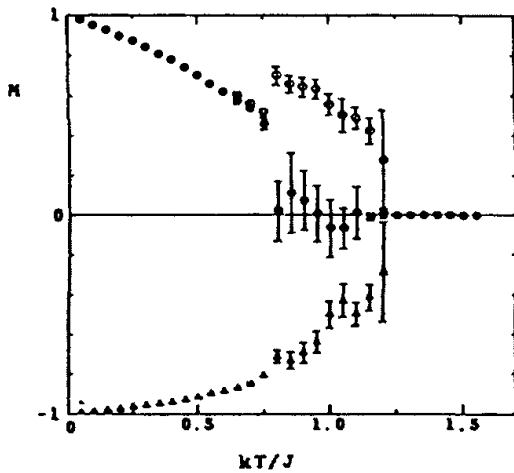


Fig. 2.26. MC data of sublattice magnetizations. The spin structure is the FR structure for  $T < T_1$  and it is the PD structure for  $T_1 < T < T_c$ .

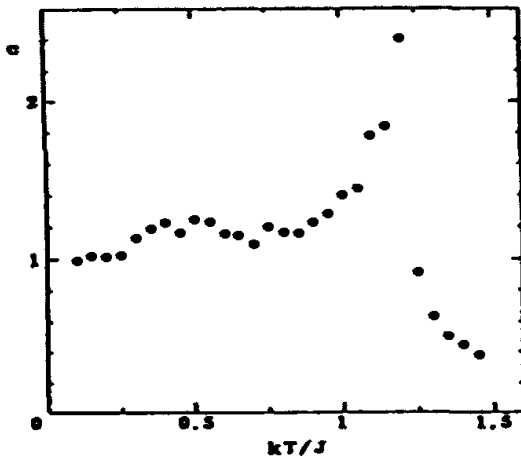


Fig. 2.27. MC data of specific heat.

We introduce new variables  $u$  and  $v$  for up- and down-spins, respectively:  $x_i = 1 - u_i$  and  $x_j = -1 + v_j$ . Then  $Z$  is written as

$$Z = \int_0^2 du_1 \cdots \int_0^2 du_{N/3} \int_0^2 dv_1 \cdots \int_0^2 dv_{2N/3} \exp(-\beta H), \quad (26)$$

where

$$H = -N(J + J_z) + (6J + 2J_z) \sum_i^A u_i + 2J_z (\sum_j^B v_j + \sum_k^C v_k) + H'. \quad (27)$$

Here  $H'$  contains quadratic terms of  $u$  or  $v$ . A precise expression of  $H'$  will be omitted in this text. At low temperatures, we use the following replacement for the integrations

$$\int_0^2 du \rightarrow \int_0^\infty du \quad \text{and} \quad \int_0^2 dv \rightarrow \int_0^\infty dv. \quad (28)$$

Then, the free energy is obtained by the LTSE as

$$F = -N(J + J_z) - \frac{NkT}{3} \ln \left[ \frac{kT}{6J + 2J_z} \right] - \frac{2NkT}{3} \ln \frac{kT}{2J} - \frac{N}{4} \left( \frac{kT}{J_z} \right)^2 Q + \dots, \quad (29)$$

where

$$Q = J(a^3 + 5a^2 + 6a - 9)/(a + 3)^2, \quad (30)$$

and  $a = J_z/J$ . The internal energy  $U$  is given by

$$U = -N(J + J_z) + NkT + \frac{N}{4} \left( \frac{kT}{J_z} \right)^2 Q + \dots. \quad (31)$$

The above expansions are not correct when  $J_z < kT$ , since free spins appear in the system and the above LTSE becomes invalid. When  $J_z = J$ , Eq.(31) agrees well with the MC data of  $U$  for  $kT/J < 0.75$ . Let us consider a FR structure with a single misfit which is defined in Fig.2.28. This structure is constructed from the FR structure in Fig.2.7 by replacing an open circle with a solid circle. Therefore there exist  $L(2L^2/3 - 1)$  down-spins and  $L(L^2/3 + 1)$  up-spins in the spin-state shown in Fig.2.28. Let us consider the difference between the free energy of FR structure and that of ferrimagnetic-with-misfit (FRm) structure. The difference is given as

$$\begin{aligned} \Delta F &= F(\text{FR}) - F(\text{FRm}) \\ &= 3NkT \left\{ \ln \left[ \frac{2}{kT} (2J + J_z) \right] + \ln \left[ \frac{2}{kT} (J + J_z) \right] - \ln \left[ \frac{2}{kT} (3J + J_z) \right] - \ln \frac{2J_z}{kT} + \dots \right\}. \end{aligned} \quad (32)$$

The above equation is rewritten as

$$\Delta F = -3NkT \ln \left[ \frac{(a+1)(a+2)}{a(a+3)} \right] + \dots. \quad (33)$$

$\Delta F$  is negative for any positive value of  $a$ . Hence, the FR structure is more stable than the FRm structure. Furthermore, we notice that there are many

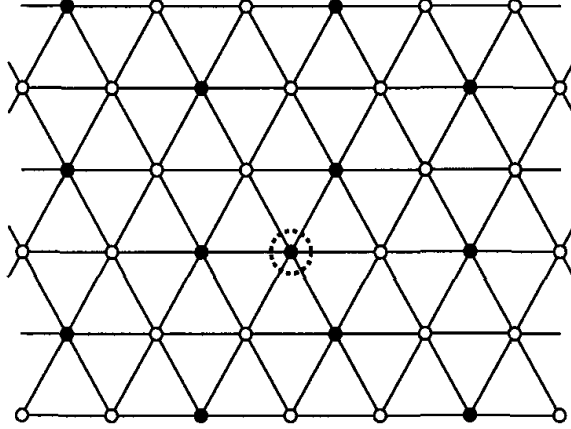


Fig. 2.28. The FR structure with a single misfit. The misfit is marked by a dashed circle.

metastable states. One of the possible metastable states will be the so-called  $(2 \times 1)$  structure, which is shown in Fig. 2.29. The free energy of this state is calculated by LTSE as

$$F(2 \times 1) = -N(J + J_z) + NkT \ln\left[\frac{2}{kT}(J + J_z)\right] + \dots \quad (34)$$

The difference between  $F(\text{FR})$  and  $F(2 \times 1)$  is as follow:

$$F(\text{FR}) - F(2 \times 1) = -\frac{NkT}{3} \ln \frac{(a+1)^3}{a^2(a+3)} + \dots \quad (35)$$

We see from Eq.(35) that  $F(\text{FR}) - F(2 \times 1)$  is negative for any positive value of  $a$ . Thus, the FR structure is more stable than the  $2 \times 1$  structure at low temperatures. In this way, it turns out that the FRm structure and the  $(2 \times 1)$  structure are both metastable.<sup>66</sup> In a similar way, it turns out that the PD structure is also metastable. Furthermore, the spin-states in a "stacked" Wannier state are all metastable. Here a "stacked" Wannier state is defined by a set of spin-states each of which belongs to one of the Wannier states for the ground state of the Ising model on the AFT lattice in any  $xy$ -plane and is stacked in such way that all the spins on a column along the  $z$  axis have the same direction. Hence the number of metastable states in the system is of the order of  $N^{2/3}$ .

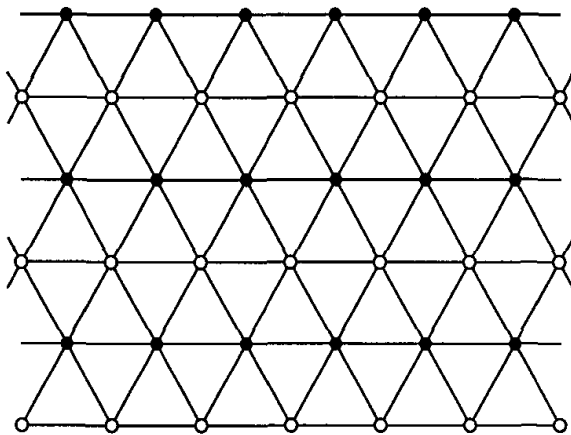


Fig. 2.29. A  $2 \times 1$  structure.

### 2.9. Phase diagram in spin-magnitude versus temperature for Ising models with spin $S$ on stacked antiferromagnetic triangular lattice

The magnetic property of the Ising model with infinite-spin on the stacked AFT lattice is well understood. That is, the system takes the PD structure in an intermediate temperature region and the FR structure in a low temperature region. Although the Wannier state is realized in the ground state, the FR structure is achieved in the limit of  $T = 0$ . On the other hand, the Ising model with spin  $1/2$  on the stacked AFT lattice takes the PD structure in an intermediate temperature region but the system falls into the Wannier state in the limit of  $T = 0$ . Because, the spins on a column along the  $z$  axis are each parallel to others at low temperatures and then the column may be regarded as a single Ising spin. Therefore, there is a crossover region in the temperature axis from the state of the three-dimensional PD structure to the two-dimensional Wannier state. Then, it is interesting to study the phase transition for the Ising model with general spin  $S$ .

We restrict our interest to the systems with  $J = J_z$  in this section. The energy for the first excited state in the Ising model with spin  $S$  is of the order of  $J/S$ . Hence, if the temperature is lower than  $J/kS$ , the spins on a column along the  $z$  axis are each parallel to others and then the system will show the behavior of the Ising model on the AFT lattice. Hence the boundary of the temperature for the crossover region will depend on the

value of  $J/S$ .<sup>67</sup>

In order to see the phase transitions in the systems, we calculate the sublattice magnetizations,  $X$  and  $Y$  defined by Eqs.(10) and (11), respectively, and also the specific heat. We show the MC data for the Ising model

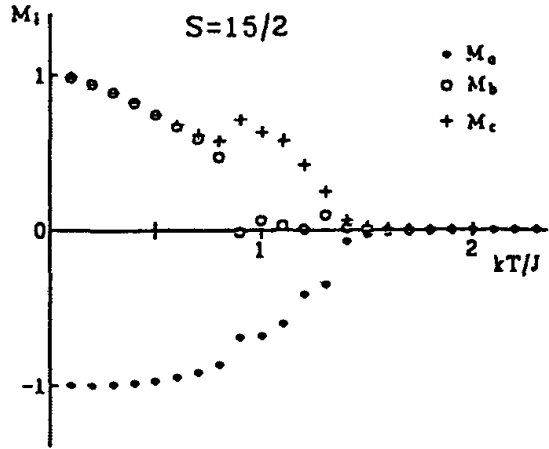


Fig. 2.30. MC data of the sublattice magnetizations for the Ising model with spin 15/2. The magnetic structure is the PD structure in the intermediate temperature region and the FR structure in the low temperature region.

with spin 15/2. We have  $X = 0$  and  $Y = 2$  for the PD structure,  $(1, 0, -1)$ ,  $X = 1$  and  $Y = 3$  for the FR structure,  $(1, -1, -1)$ , and  $Y = 0$  and  $X = 0$  for the Wannier state. The sublattice magnetizations are shown as functions of the temperature in Fig.2.30. The temperature dependencies of  $Y$  and  $X$  are shown in Fig.2.31. The specific heat is shown in Fig.2.32.  $T_1$  denotes the critical temperature at which the sublattice magnetizations appear,  $Y$  becomes non-zero, and the peak of the specific heat is observed.  $T_2$  denotes a transition temperature at which the uniform magnetization  $X$  becomes non-zero and the curvature of  $Y$  changes. Note that any appreciable anomaly is not observed in the specific heat at  $T_2$ . There is no crossover region from the three-dimensional ordered-state to the two-dimensional Wannier-state for  $kT/J > 0.1$  in this case.

Next we show the MC data for the Ising model with spin 5/2. Since the statistical errors in the MC data of the sublattice magnetizations are very large, we show only the data of  $X$  and  $Y$ . The temperature dependencies of  $Y$  and  $X$  are shown in Fig.2.33. In this figure,  $T_1$  denotes the critical

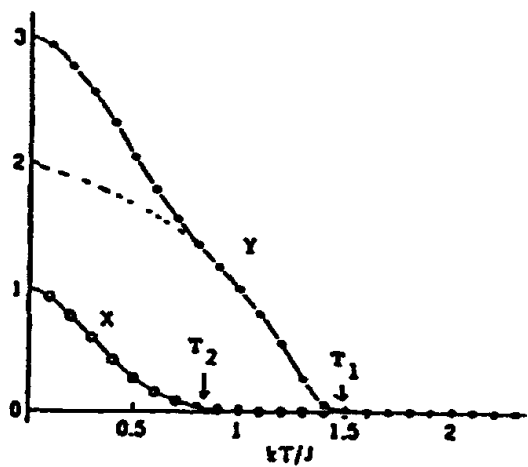


Fig. 2.31. MC data of  $Y$  and  $X$ . The dashed line denotes the extrapolation to the zero temperature. The arrows indicate the transition points.

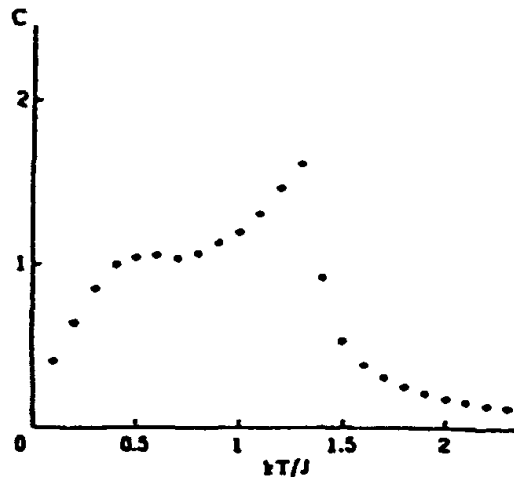


Fig. 2.32. MC data of specific heat for the Ising model with spin  $15/2$ .

temperature of the phase transition from the paramagnetic state to the state with the PD structure.  $T_2$  is a transition temperature of the first order from the state with the PD structure to that with the FR structure.  $T_3$  denotes a turning point where the FR structure becomes unstable. The curve of  $Y$  between  $T_1$  and  $T_2$  tends toward the value 2 at  $T = 0$  but the curve between  $T_2$  and  $T_3$  tends towards the value 3 at  $T = 0$ . However, the

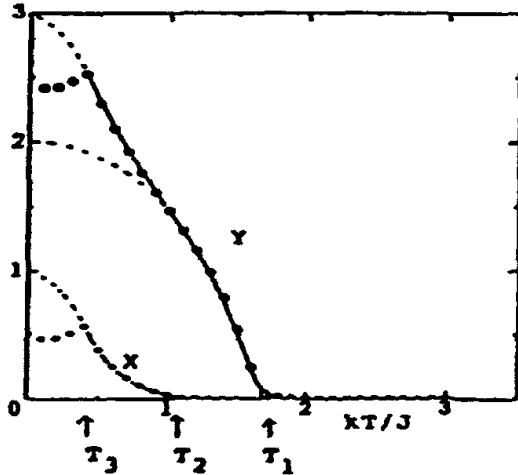


Fig. 2.33. MC data of  $Y$  and  $X$  for the Ising model with spin  $5/2$ . See the text for the explanation of  $T_1$ ,  $T_2$  and  $T_3$ .

data of  $Y$  suddenly becomes small at  $T_3$  and seem to tend towards zero at  $T = 0$ . Similarly the MC data of  $X$  between  $T_2$  and  $T_3$  tend towards the value 1 at  $T = 0$  but suddenly becomes small at  $T_3$  and tend towards zero at  $T = 0$ . We think that the temperature region between  $T_3$  and zero is a crossover region for the system from the state with the FR structure to the Wannier state as the temperature decreases.

Thus, in this spin system there are two transition temperatures  $T_1$  and  $T_2$ , and one turning point  $T_3$  below which the system is in the crossover region. Similar analyses are made for the Ising models with various spin  $S$  on the stacked AFT lattice and an obtained  $S - T$  phase diagram is shown in Fig.2.34. In Fig.2.34, the dashed line denotes the  $S$  dependence of  $T_3$ , which is an upper bound of the crossover region obtained by the MC simulations. As stated above, the dashed line behaves as a linear function of  $J/S$ . The phase transition at  $T_2$  seems to be of first order as we see from the discontinuous change in Fig.2.30, which is resemble to that of stacked  $S = 1/2$  Ising AFT with nnn interaction.<sup>47</sup>

## 2.10. Effect of antiferromagnetic interaction between next-nearest-neighbor spins in $xy$ -plane

In this section, we discuss the effect of antiferromagnetic interaction  $J_2$  in the Ising models with spin  $S$  and with infinite-spin on the AFT lattice and on the stacked AFT lattice. The Hamiltonian for both systems is given as

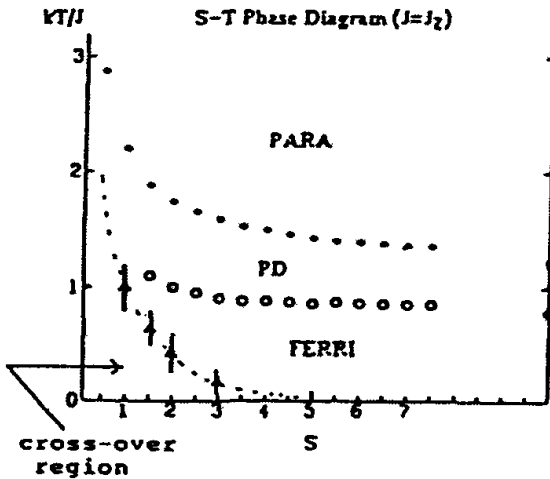


Fig. 2.34.  $S - T$  phase diagram for the Ising model with spin  $S$  on the stacked AFT lattice. The dashed line shows an upper bound of the crossover region obtained by the MC simulations.

follows:

$$H = J \sum_{(i,j)}^{xy} \sigma_i \sigma_j - J_z \sum_{(i,j)}^z \sigma_i \sigma_j + J_2 \sum_{(i,j)}' \sigma_i \sigma_j. \quad (36)$$

Here  $\sum'$  denotes the sum over the nnn pairs in the  $xy$ -plane. The effect of  $J_2$  on the Ising model with spin 1/2 on the AFT lattice was previously studied by Saito.<sup>68</sup> However, it has not been noticed that there exist long range orders in the Ising models with spin  $S$ , including the Ising model with infinite-spin, on the stacked AFT lattice.

The ground state shows the  $2 \times 1$  structure given in Fig.2.29 if the antiferromagnetic interactions  $J_2$  exist between the nnn pairs in the  $xy$ -plane. However, this  $2 \times 1$  structure is metastable when  $J_2 = 0$ . In order to see this, we make the MC simulations for the case of  $J_2 = 0$  by assuming the  $2 \times 1$  structure as an initial spin configuration. We define the order parameter,  $Y_4$ , assuming a four-sublattice structure for a lattice in the  $xy$ -plane as follows:

$$Y_4 = \left( \frac{4}{N} \right)^2 \left\langle \left( \sum_i^A \sigma_i \right)^2 + \left( \sum_j^B \sigma_j \right)^2 + \left( \sum_k^C \sigma_k \right)^2 + \left( \sum_l^D \sigma_l \right)^2 \right\rangle. \quad (37)$$

We show the temperature dependence of  $Y_4$  for the Ising model with spin 1/2 on the stacked AFT lattice in Fig.2.35. The  $2 \times 1$  structure is stable

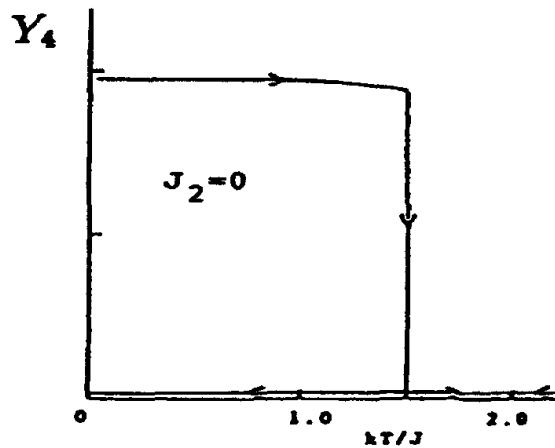


Fig. 2.35. MC data of  $Y_4$  for the Ising model with spin 1/2 on the stacked AFT lattice with  $J_z = J$  and  $J_2 = 0$ .

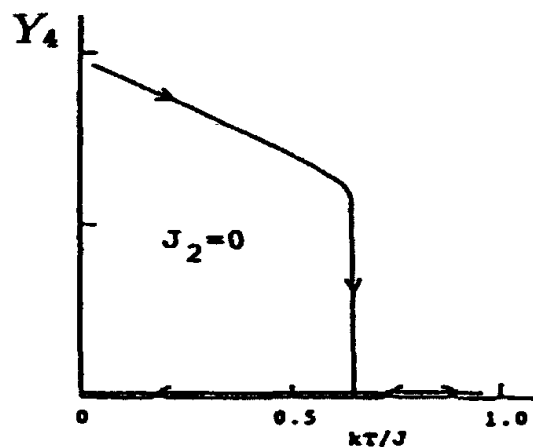


Fig. 2.36. MC data of  $Y_4$  for the Ising model with infinite-spin on the stacked AFT lattice with  $J_z = J$  and  $J_2 = 0$ .

up to  $T \cong 1.5J/k$ , as can be seen in Fig. 2.35. The temperature dependence of  $Y_4$  for the Ising model with infinite-spin on the stacked AFT lattice is shown in Fig. 2.36 when  $J_2 = 0$ . We see the  $2 \times 1$  structure is stable up to  $T \cong 0.65J/k$ . The existence of "stable" metastable states suggests the

appearance of a first order phase transition in the systems. Actually we find a first order phase transition in the systems.<sup>66</sup>

The energy for the  $2 \times 1$  structure is given by

$$E_0 = -N(J + J_z + J_2). \quad (38)$$

When the ground state is the  $2 \times 1$  structure in the AFT lattice, the  $2 \times 1$  structure also appears in each sublattice which is one of three sublattices in section 2.3. Hence, we may suppose that the phase diagram of  $T$  versus  $J$  is similar to that of  $T$  versus  $J_2$ . We found this similarity by the MC simulations as seen below. Hence we discuss only the case of  $0 \leq J_2 \leq J$ .

In Fig.2.37, we show the phase diagram obtained by the MC simulations for the Ising model with spin 1/2 on the AFT lattice. In this system,

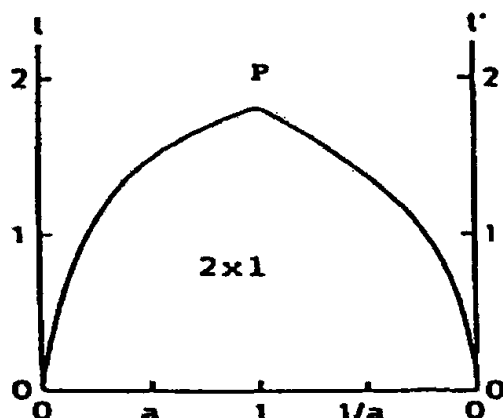


Fig. 2.37. Phase diagram for the Ising model with spin 1/2 on the AFT lattice.  $a$ ,  $t$  and  $t'$  denote  $J_2/J$ ,  $kT/J$  and  $kT/J_2$ , respectively.

there appear the paramagnetic state and the ordered state with the  $2 \times 1$  structure. The paramagnetic state is denoted by  $P$  and the state with the  $2 \times 1$  structure by  $2 \times 1$  in Fig.2.37 and also in the following figures.

In Fig.2.38, we show the phase diagram obtained by the MC simulations for the Ising model with spin 1/2 on the stacked AFT lattice. In the system, the spin structure is not clarified yet in an intermediate temperature region for small  $J_2$  and even in the case of  $J_2 = 0$  at low temperatures. In fact, the spin state observed in the MC simulations shows some complex structure in this region and very sensitive to the values of parameters,  $J_z$ ,  $J_2$  and  $T$ .

Hence we use the symbol  $C$  in Fig. 2.38 to denote this complex spin-state. However, the phase boundaries are easily obtained by the MC simulations through  $Y_4$  and other quantities. The spin structure at low temperatures is the  $2 \times 1$  structure. We calculate the free energies in the LTSE for various spin-states. Since there is no free linear-chains in the system for the case of  $J_2 \neq 0$ , it is sufficient to take single-spin-flip-type excitations into account. The free energy for the  $2 \times 1$  structure,  $F(2 \times 1)$ , is given as

$$F(2 \times 1) = -N(J + J_z + J_2) - NkT \exp\left[-\frac{4}{kT}(J + J_z + J_2)\right] + \dots \quad (39)$$

The free energies for the FR structure and the PD structure are given as follows:

$$F(\text{FR}) = -N(J + J_z - 3J_2) - \frac{2NkT}{3} \exp\left[-\frac{4}{kT}(J_z - 3J_2)\right] + \dots \quad (40)$$

$$F(\text{PD}) = -N(J + J_z - \frac{5}{3}J_2) - \frac{NkT}{3} \exp\left[-\frac{4}{kT}(J_z + J_2)\right] + \dots \quad (41)$$

According to these equations, we have at  $T = 0$

$$F(2 \times 1) < F(\text{PD}) < F(\text{FR}), \quad (42)$$

while the PD or FR structure becomes stable at  $T \neq 0$ .

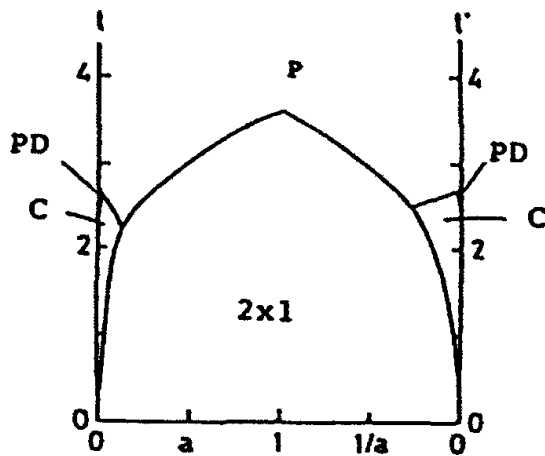


Fig. 2.38. Phase diagram for the Ising model with spin 1/2 on the stacked AFT lattice with  $J = J_z$ .  $a, t$  and  $t'$  denote  $J_2/J, kT/J$  and  $kT/J_2$ , respectively.

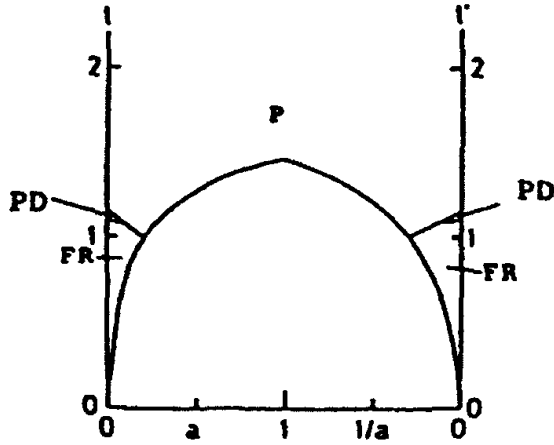


Fig. 2.39. Phase diagram for the Ising model with infinite-spin on the stacked AFT lattice with  $J = J_z$ .  $a$ ,  $t$  and  $t'$  denote  $J_2/J$ ,  $kT/J$  and  $kT/J_2$ , respectively.

In Fig.2.39, we show the phase diagram obtained by the MC simulations for the Ising model with infinite-spin on the stacked AFT lattice.

The spin structures of the ordered states in this system are well-defined. For a very small value of  $J_2$ , we find that the spin structure is the  $2 \times 1$  structure in a low temperature region, the FR structure in an intermediate low-temperature region and PD structure in an intermediate high-temperature region, as seen in Fig.2.39. In the LTSE, the free energy for the  $2 \times 1$  structure is given as

$$F(2 \times 1) = -N(J + J_z + J_2) + NkT \ln\left[\frac{2}{kT}(J + J_z + J_2)\right] + \dots \quad (43)$$

The free energy for the FR structure is given as

$$F(\text{FR}) = -N(J + J_z - 3J_2) + \frac{NkT}{3} \ln\left[\left(\frac{1}{kT}\right)^3 (6J + 2J_z - 6J_2)(2J_z - J_2)^2\right] + \dots \quad (44)$$

The free energies for the  $2 \times 1$  and the FR structure for the system with  $J_z = 0.3J$  and  $J_2 = 0.05J$  are shown in Fig.2.40. In Fig.2.41, we show the results by the LTSE for the internal energy  $u = U/NJ$  together with the results by the MC simulations for the system with  $J_z = 0.3J$  and  $J_2 = 0.05J$ . A first order phase transition occurs at  $T = 0.165J/k$ . A small hysteresis,  $\Delta(kT/J) = 0.01$ , is observed in this case, as shown in Fig.2.41.

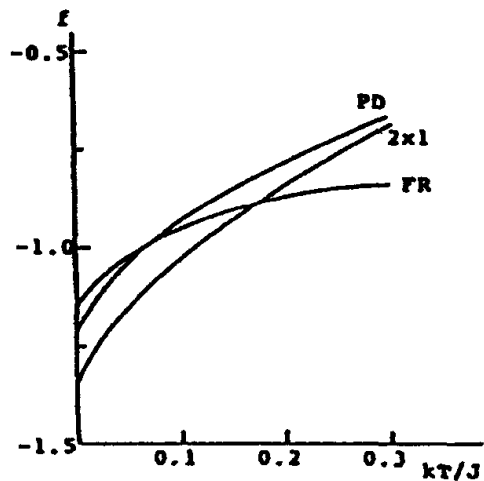


Fig. 2.40. The free energy by the low temperature expansion.

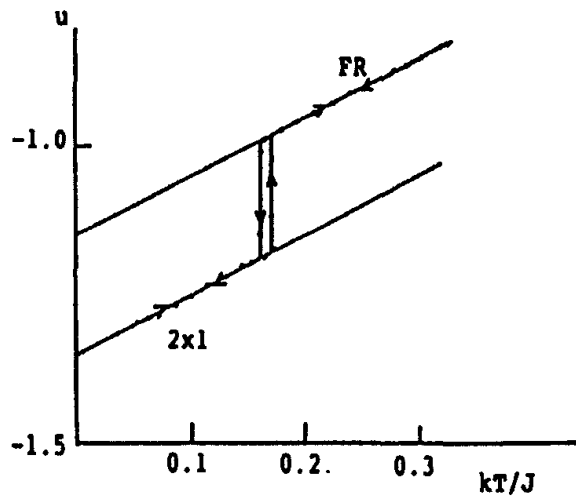


Fig. 2.41. The internal energy. The dots show the MC results and the solid lines the theoretical results. A first order phase transition is observed.

## 2.11. Three-dimensional Ising paramagnet

Various frustrated Ising spin systems have been designed and studied to understand the effect of frustration in connection with the spin-glass problem.<sup>69,70,71</sup> It is well known that the frustration in general disturbs formation of long range order in spin systems. In spin systems on three

dimensional lattices, however, some long range orders driven by thermal fluctuations can be found easily even in fully-frustrated Ising models. No long range order appears in the Ising model on the AFT lattice as a typical example, but the Ising model on the antiferromagnetic face-centered cubic lattice shows the phase transition from the paramagnetic state to a periodic long range order at a finite temperature.<sup>18</sup> The Ising model on the stacked Villain lattice, being different from the Ising model on the Villain lattice, also comes under this category. Then we have a following question. "Is there a 3d-Ising spin system which shows the paramagnetic behavior at all finite temperatures ?" We take up this problem in this section. It is possible in principle because we may construct such a 3d-Ising model from the Ising model on the AFT lattice or the Villain lattice by using a glue-Hamiltonian.<sup>72</sup> But we propose a realistic candidate for the 3d-Ising paramagnet and demonstrate some magnetic properties of the candidate by the MC simulations in order to understand the paramagnetic nature of the system.<sup>73,74</sup>

An Ising model proposed for the 3d-paramagnet is composed in the following way. Consider a cube with lattice-spacing  $a$  where an Ising spin of spin 1/2 is located at each corner of the cube and the neighboring spins are coupled by a ferromagnetic interaction  $J$  (see Figs. 2.42 and 2.43 in the next page). This cube is named a  $J$ -cube. Imagine a simple cubic (sc) lattice with lattice-spacing  $2a$ . Place the center of a  $J$ -cube on each lattice site of the sc lattice and let each of edges of  $J$ -cube parallel to that of the sc lattice. Let an Ising spin on a corner of  $J$ -cube interact with its nearest Ising spins on the other  $J$ -cubes through  $+J_1$  or  $-J_1$  interaction constant as shown in Fig.2.42. When  $J = J_1$ , the  $xy$ -,  $yz$ - or  $zx$ -plane in the resultant lattice corresponds to the so-called chessboard (CB) plane where the frustrated and non-frustrated plaquettes are alternately arranged, as shown in Fig.2.43. We call this resultant lattice the CB3 lattice since all the three planes are of the CB type.

The CB3 lattice contains another kind of cubes which are made up by  $+J_1$  and  $-J_1$  bonds. Each of these cubes is named a  $J_1$ -cube. Note that the  $J_1$ -cube is not frustrated. For the Ising model on the CB3 lattice with  $N$  sites, called the CB3 system hereafter, the number of both  $J$ -cubes and  $J_1$ -cubes amounts to  $N/8$ . The Hamiltonian of the CB3 system is written as

$$H = - \sum_{(i,j)} J_{ij} \sigma_i \sigma_j, \quad (45)$$

where  $J_{ij}$  stands for the interaction constant between  $\sigma_i$  and  $\sigma_j$  and  $\sum_{(ij)}$  indicates the sum over all the nn spin-pairs. It is easy to see that the ground state energy of CB3 system is  $E_0 = -(1/2)NJ$  and the zero-point entropy is  $S_0 = (N/8)\ln 2$  if  $J = J_1$ . Similarly, if  $J < J_1$ , we have  $E_0 = -(1/2)NJ_1$  and  $S_0 = (N/8)\ln 2$ . For the case of  $J = J_1$ , the ferromagnetic state (F-state) is one of the spin states in the ground state, since  $E_0 = -(1/2)NJ$ . Because there are at least  $N/4$  free spins in this F-state, we have  $S_0 \geq (N/4)\ln 2$  for the CB3 system when  $J = J_1$ . Let us make a thought experiment for the CB3 system according to the concept of the MC simulations. When  $J_1 = 0$ , the CB3 system is obviously paramagnetic at any finite temperatures.

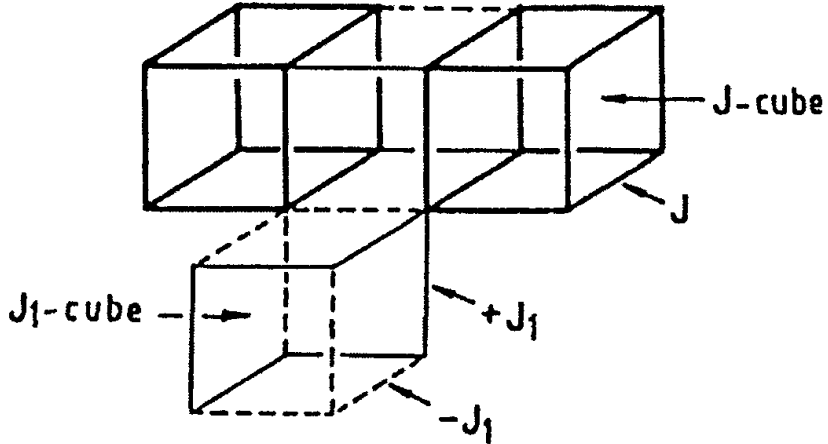


Fig. 2.42. A local structure of the CB3 system.

However, if the conventional single-spin-flip (SSF) MC method is applied to the CB3 system, we are confronted with a crucial contradiction that a spin-glass order parameter tends to unity in the limit of temperature  $T = 0$ ; the spin-glass order parameter,  $q$ , is defined by

$$q = \frac{1}{N} \sum_i |\langle \sigma_i \rangle|, \quad (46)$$

where the brackets denote the MC average. This discrepancy can be removed if we use the multi-spin-flip (MSF) MC method which updates all the spin configurations in a spin cluster at the same time.

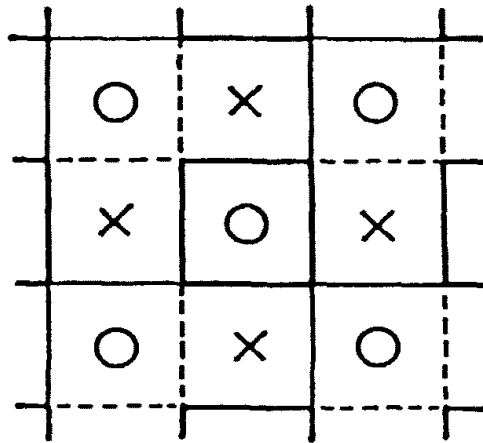


Fig. 2.43. A chessboard plane of alternating frustrated (marked by crosses) and non-frustrated (marked by circles) plaquettes.

We now take a  $J$ -cube as a spin cluster in the MC calculation for the CB3 system.  $2^8$  states of a spin-cluster are chosen as the achieved state of the cluster at each MC trial, according to the heat-bath importance sampling. We take advantage of the MSF as well as SSF methods for the present system. We calculate the specific heat, the susceptibility and the spin-glass order parameter. It is found that the spin-glass order parameter,  $q$ , vanishes at all temperatures for any  $J_1$  value. In Fig. 2.44, the MC results of the specific heat,  $c = C/Nk$ , is shown for  $J_1 = J$  (solid circles) and  $J_1 = J/2$  (open circles). The exact result for  $J_1 = 0$  is also plotted by the solid curve. No size dependence is observed in the specific heat data. Also the peak position at  $T \cong 1.9J/k$  is nearly fixed for different values of  $J_1$ . In the case of  $J_1 = 0$ , the peak of specific heat is undoubtedly caused by the energy fluctuation of the paramagnetic  $J$ -cubes. We suppose that the peak, even for the case of  $J = J_1$ , is due to nothing more than the energy fluctuations of  $J$ -cubes or  $J_1$ -cubes. Since the  $J$ -cubes (or  $J_1$ -cubes) are connected by  $\pm J_1$  bonds (or  $J$  bonds), the above fluctuation is now suppressed with no shift of the peak position in the case of  $J_1 \neq J$ . The MC results in Fig. 2.44 are consistent with this tendency as the strength of  $J_1$  increases.

In the limit of  $J$  infinity, the  $J$ -cube is regarded as a large "block spins" whose value is +8 or -8. Since these  $N/8$  block-spins interact with each

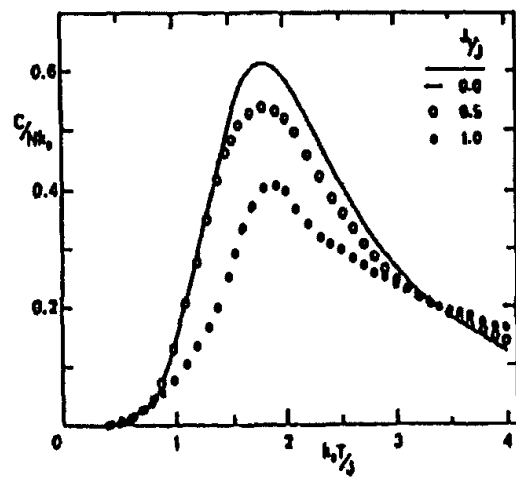


Fig. 2.44. MC data of the specific heat for the CB3 system.

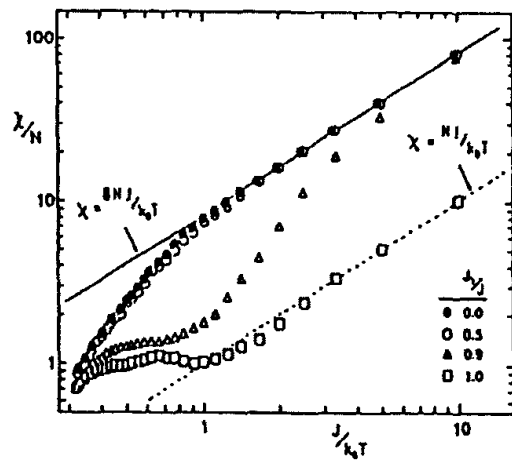


Fig. 2.45. MC data of the susceptibility for the CB3 system.

other via  $\pm J_1$  in the CB3 system, the critical temperature should be zero in this limit.

A similar conjecture holds for the case of  $J > J_1$  at very low temperatures, because of the strong correlation between spins on the  $J$ -cube. Then,

the susceptibility of the system must be written as

$$\chi = \frac{8NJ}{kT}. \quad (47)$$

Actually, the MC results of susceptibility show this paramagnetic behavior at low temperatures as seen in Fig.2.45. On the other hand, the low temperature behavior of  $\chi$  in the MC results behaves as the Curie law of  $\chi = NJ/kT$  for the case of  $J = J_1$ . This does not indicate that there exist  $N$  free spins in the system, but should be read as a suggestion that the system may include a large number of not only free block spins but also free spins, induced by the frustration effect. The MC data of  $\chi$  at low temperatures give another reason for us to support why we have to use the MSF MC method for this system: the excitations within the  $J$ -cube are more dominant in the system.

It is interesting that the correlation functions of the Ising model on the two dimensional chessboard lattice<sup>75</sup> decay exponentially at all temperatures, in contrast to those on the two dimensional purely frustrated lattice where a power-law decaying correlation appears in the ground state. In view of its paramagnetic behaviors, the CB3 system is expected to have the correlation functions of the exponential decay at all temperatures.

The spin ordering in so-called corner-sharing tetrahedron lattices, such as ferrite, pyrochlore and the Laves phase, attracts interest.<sup>76,77,78,79,80</sup> They are extensions of the Kagomé lattice in two dimensions. The effect of frustration is very strong and interesting ordering process reflecting spin configuration on a tetrahedron has been reported. In some cases, such as  $Dy_2Ti_2O_7$ , a strong uniaxial single spin anisotropy exists and the spins can take only two states, i.e. inward or outward to the tetrahedron. Therefore, this system has another interesting ordering process. In these systems, the residual entropy plays an important role and they are called a ‘spin-ice’ system.<sup>78,79,80,81</sup>

As to the Kagomé lattice antiferromagnet, it has been known that any of Ising ( $S = 1/2$ ), XY and Heisenberg model does not have phase transition at all temperature including  $T = 0$ .<sup>82,83</sup> Therefore, even the continuous Ising model does not have phase transition. However, it has been pointed out that the interaction of the transverse components causes a phase transition at a finite temperature.<sup>84</sup> The low temperature phase has a uniform magnetization, and the phase transition belongs to the universality class of the ferromagnetic Ising model. This phase transition is attributed to the existence of uncompensated magnetic magnetization of the three spins on a triangle due to the non-collinear spin structure. The phase transition dis-

appears in the Heisenberg limit where no uniaxial anisotropy exists and also in the limit of the continuous Ising model where the anisotropy is infinite. Thus this phase transition occurs only in finitely uniaxial anisotropic systems. As well as the case in the triangular lattice,<sup>35,36</sup> the quantum effect on the kagomé lattice also provides various peculiar properties such as the double peak in the specific heat and existence of many low lying singlets states.<sup>85,86,87</sup> This is another of examples how the ordering process is sensitive to types of perturbations.

## **2.12. Concluding remarks**

We discussed in this chapter several interesting features of the Ising spin systems with frustration. For the Ising model on the two-dimensional frustrated lattices such as the antiferromagnetic triangular (AFT) lattice and the Villain lattice, exact solutions were known. Based on those results, we focused our attention mainly to the following problems: spin orderings, effects of interactions between next-nearest-neighbor spin-pairs and effects of magnitude  $S$  of spin in Ising spin systems on the AFT lattice and on the stacked AFT lattice.

One of characteristic features of the Ising spin systems on frustrated lattices is the existence of "free" spins. There also appear "free" spin-clusters such as "free" linear-chains and "free" cubes. In those frustrated systems, cluster flip-type excitations exist in the low-lying energy states. Consequently, a cluster flip-type Monte Carlo method is needed in the MC simulations for the those frustrated systems.

The effects of the far-neighbor interactions in the Ising model on the AFT lattice and the stacked AFT lattice were clarified in this chapter. The ground state of the Ising model with only nearest-neighbor interactions on the AFT lattice is infinitely degenerate and is called the Wannier state. The Wannier state includes many states. Then if a perturbational interaction exists between spins on far-neighbor sites, the large degeneracy of the ground state is lifted and there appears a multi-sublattice spin structure corresponding to the symmetry of the far-neighbor interaction. It is intriguing to find the phase diagrams for those systems, and the Ising models with the perturbational interaction between spins on the next-nearest-neighbor sites were studied. As an alternate perturbation, effects of the interaction between the  $xy$  component were also briefly discussed in both classical and quantum cases.

Recently, it has been noticed that the magnitude  $S$  of spin can be an

important physical parameter in both of classical spin systems and quantum spin systems. In the quantum spin systems, the Haldane problem is one of controversial problems. In frustrated Ising spin systems, the universality class may depend strongly on the magnitude  $S$  of spin, although no such  $S$  dependence is found in the Ising models on the non-frustrated lattices. We discussed  $S$ -dependencies of spin ordering for the Ising spin systems on the frustrated lattices in sections 4, 5 and 6. We hope that more active investigations will be done in order to clarify  $S$ -dependent properties of the Ising spin systems on the frustrated lattices.

### Acknowledgements

We thank M. Kang, Y. Yamada, M. Tanaka and N. Todoroki for their help in numerical computations and in preparing this chapter.

### References

1. J. Villain, *Phys. Chem. Solids* **11**, 303 (1959).
2. A. Yoshimori, *J. Phys. Soc. Jpn.* **14**, 807 (1959).
3. T. A. Kaplan, *Phys. Rev.* **116**, 888 (1959).
4. D. J. Amit, *Modeling Brain Function: the world of attractor neural networks*, Cambridge University Press, Cambridge (1989).
5. G. Toulouse, *Commun. Phys.* **2**, 115 (1977).
6. J. Vannimenus and G. Toulouse, *J. Phys.* **C10**, L537 (1977).
7. J. Villain, *J. Phys.* **C10**, 1717 (1977).
8. G. Forgacs, *Phys. Rev.* **B22**, 4478 (1980).
9. G. H. Wannier, *Phys. Rev.* **79**, 357 (1950).
10. M. Houtappel, *Physica* **16**, 425 (1950).
11. K. Husimi and I. Syoji, *Prog. Theor. Phys.* **5**, 177 (1950).
12. I. Syoji, *Prog. Theor. Phys.* **5**, 341 (1950).
13. J. Stephenson, *Can. J. Phys.* **47**, 2621 (1969).
14. J. Stephenson, *J. Math. Phys.* **11**, 413 (1970).
15. T. Horiguchi, K. Tanaka, and T. Morita, *J. Phys. Soc. Jpn.* **61**, 64 (1992).
16. M. Mekata, *J. Phys. Soc. Jpn.* **42**, 76 (1977).
17. D. C. Mattis, *The Theory of Magnetism II*, Springer-Verlag, Berlin (1985).
18. R. Liebmann, *Statistical Mechanics of Periodic Frustrated Ising Systems*, Springer-Verlag, Berlin (1986).
19. O. Nagai, Y. Yamada, and H. T. Diep, *Phys. Rev.* **B32**, 480 (1985).
20. L. Onsager, *Phys. Rev.* **65**, 117 (1944).
21. O. Nagai, K. Nishino, J. J. Kim, and Y. Yamada, *Phys. Rev.* **B37**, 5448 (1988).
22. J. J. Kim, Y. Yamada, O. and Nagai, *Phys. Rev.* **B41**, 4760 (1990).
23. S. Miyashita, *J. Phys. Soc. Jpn.* **52**, 780 (1983).

24. H. Takayama, K. Matsumoto, H. Kawahara, and K. Wada, *J. Phys. Soc. Jpn.* **52**, 2888 (1983).
25. S. Fujiki, K. Shutoh, Y. Abe, and S. Katsura, *J. Phys. Soc. Jpn.* **52**, 1531 (1983).
26. L. P. Landau, *Phys. Rev.* **B27**, 5604 (1983).
27. O. Nagai, M. Kang, and S. Miyashita, *Phys. Lett.* **A196**, 101 (1994).
28. S. Miyashita, H. Kitatani, and Y. Kanada, *J. Phys. Soc. Jpn.* **60**, 523 (1991).
29. S. Elitzur, P. B. Pearson, and J. Shigemitsu, *Phys. Rev.* **D19**, 3698 (1979).
30. J. L. Cardy, *J. Phys.* **A26**, 6201 (1982).
31. D. Blankschtein, M. Ma, A. N. Berker, G. S. Grest, and C. M. Soukoulis, *Phys. Rev.* **B29**, 5250 (1984).
32. S. Miyashita, and H. Kawamura, *J. Phys. Soc. Jpn.* **54**, 3385 (1985).
33. S. Watarai, and S. Miyashita, *J. Phys. Soc. Jpn.* **63**, 1916 (1994).
34. S. Watarai, and S. Miyashita, *J. Phys. Soc. Jpn.* **67**, 816 (1998).
35. P. W. Anderson, *Mater. Res. Bull.* **8**, 153 (1973).
36. P. Fazekas, and P. W. Anderson, *Philos. Mag.* **30**, 423 (1974).
37. M. V. Mostovoy, D. I. Khomskii, J. Knoester, and N. V. Prokof'ev, *Phys. Rev. Lett.* **90**, 14723 (2003).
38. A. N. Berker, G. S. Grest, C. M. Soukoulis, D. Blankschtein, and M. Ma, *J. Appl. Phys.* **55**, 2416 (1984).
39. F. Matsubara and S. Inawashiro, *J. Phys. Soc. Jpn.* **56**, 2666 (1987).
40. S. N. Coppersmith, *Phys. Rev.* **B32**, 1584 (1985).
41. J. R. Banavar, G. G. Grestand, and D. Jasnow, *Phys. Rev.* **B25**, 4639 (1982).
42. S. Miyashita, *J. Phys. Soc. Jpn.* **66**, 3411 (1997).
43. M. Oshikawa, *Phys. Rev.* **B61**, 3430 (2000).
44. F. Matsubara and S. Inawashiro, *J. Phys. Soc. Jpn.* **53**, 4347 (1984).
45. N. Todoroki, Y. Ueno, and S. Miyashita, *Phys. Rev.* **B66**, 214405 (2002).
46. O. Koseki and F. Matsubara, *J. Phys. Soc. Jpn.* **69**, 1202 (2000).
47. N. Todoroki and S. Miyashita, unpublished (2003).
48. D. C. Mattis, *Phys. Rev. Lett.* **42**, 1503 (1979).
49. S. Miyashita, *Prog. Theor. Phys. Suppl.* **87** pp. 112-126 (1986).
50. T. Horiguchi, O. Nagai, and S. Miyashita, *J. Phys. Soc. Jpn.* **60**, 1513 (1991).
51. T. Horiguchi, O. Nagai, and S. Miyashita, *J. Phys. Soc. Jpn.* **61**, 308 (1992).
52. T. Horiguchi, O. Nagai, S. Miyashita, Y. Miyatake, and Y. Seo, *J. Phys. Soc. Jpn.* **61**, 3114 (1992).
53. O. Nagai, S. Miyashita, and T. Horiguchi, *Phys. Rev.* **B47**, 202 (1993).
54. O. Nagai, T. Horiguchi, and S. Miyashita, *Phys. Lett.* **A186**, 186 (1994).
55. R. Peierls, *Proc. Cambridge Phil. Soc.* **32**, 477 (1936).
56. R. B. Griffiths, in *Phase Transitions and Critical Phenomena*, ed. C. Domb and M. S. Green, Academic Press, London, 1 p.1 (1972).
57. A. Lipowski, T. Horiguchi, and D. Lipowska, *Phys. Rev. Lett.* **74**, 3888 (1995).
58. A. Lipowski and T. Horiguchi, *J. Phys. A: Math. Gen.* **28**, 3371 (1995).
59. Y. Honda, A. Lipowski, and T. Horiguchi, *Phys. Rev.* **B52**, 13429 (1995).
60. A. Lipowski, Y. Honda, T. Horiguchi, and Y. Hondai, *Physica* **A237**, 297 (1997).
61. S. Miyashita, *J. Phys. Soc. Jpn.* **55**, 3605 (1986).

62. H. Kitazawa, H. Suzuki, H. Abe, J. Tang, and G. Kido, *Physica B* **259-261**, 890 (1999).
63. H. Nishimori, and S. Miyashita, *J. Phys. Soc. Jpn.*, **55**, 4448 (1986).
64. C. Domb, in *Phase Transitions and Critical Phenomena*, ed. C. Domb and M. S. Green, Academic Press, London, **3** p.1 (1974).
65. T. Horiguchi, *J. Phys. Soc. Jpn.* **59**, 3142 (1990).
66. O. Nagai, M. Kang, T. Horiguchi, and H. T. Diep, *Phys. Lett.* **A186**, 186 (1994).
67. O. Nagai, M. Kang, Y. Yamada, and T. Horiguchi, *Phys. Lett.* **A195**, 195 (1994).
68. Y. Saito, *Phys. Rev.* **B24**, 6652 (1981).
69. K. Binder, and A. P. Young, *Rev. Mod. Phys.* **58**, 801 (1986).
70. S. Kirkpatrick, in *Disordered Systems and Localization*, ed. C. Castellani, C. Di Castro and L. Peliti, Springer-Verlag, Berlin, p.280 (1981).
71. A. P. Young, *Spin Glasses and Random Fields*, ed. by A. P. Young, World Scientific, Singapore (1998)
72. T. Horiguchi, *Physica* **146A**, 613 (1987).
73. H. T. Diep, P. Lallemand, and O. Nagai, *J. Phys. C* **18**, 1067 (1985).
74. J. J. Kim, K. Nishino, Y. Yamada, and O. Nagai, in *Proceeding of Fourth Asia Pacific Physics Conference*, ed. S. H. Ahn, S. H. Choh, H. T. Cheon and C. Lee, World Scientific, Singapore (1990).
75. G. André, R. Bidaux, J.-P. Carton, R. Conte, and L. de Seze, *J. Physique* **40**, 479 (1979).
76. P. W. Anderson, *Phys. Rev.* **102**, 1008 (1996).
77. Y. Kobayashi, T. Takagi, and M. Mekata, *J. Phys. Soc. Jpn.* **67**, 3906 (1998).
78. M. J. Harris et al. *Phys. Rev. Lett.* **79**, 2554 (1997).
79. R. Siddharthan et al. *Phys. Rev. Lett.* **83**, 1854 (1999).
80. M. Udagawa, M. Ogata, and Z. Hiroi, *J. Phys. Soc. Jpn.* **71**, 2365 (2002).
81. T. Sakakibara, T. Tayama, Z. Hiroi, K. Matsuhira, and S. Takagi, *Phys. Rev. Lett.* **90**, 207205-1-4 (2003).
82. H. Barry, H. Khatun, and T. Tanaka, *Phys. Rev.* **B37**, 5193 (1998).
83. D. A. Huseand, and A. D. Rutenberg, *Phys. Rev.* **B45**, 7536 (1992).
84. A. Kuroda, and S. Miyashita, *J. Phys. Soc. Jpn.* **64**, 4509 (1995).
85. V. Elser, *Phys. Rev. Lett.* **62**, 2405 (1989).
86. T. Nakamura, and S. Miyashita, *Phys. Rev.* **B52**, 9174 (1995).
87. F. Mila, *Phys. Rev. Lett.* **81**, 2356 (1998).



## CHAPTER 3

### RENORMALIZATION GROUP APPROACHES TO FRUSTRATED MAGNETS IN D=3

B. Delamotte and D. Mouhanna

*Laboratoire de Physique Théorique et Hautes Energies, CNRS UMR 7589  
Universités Paris VI-Pierre et Marie Curie - Paris VII-Denis Diderot  
2 Place Jussieu, 75251 Paris Cedex 05, France  
E-mail: delamotte@lpthe.jussieu.fr, mouhanna@lpthe.jussieu.fr*

M. Tissier

*Laboratoire de Physique Théorique des Liquides, CNRS UMR 7600  
Université Paris VI-Pierre et Marie Curie  
4 Place Jussieu, 75252 Paris Cedex 05, France  
E-mail: tissier@lptl.jussieu.fr*

This chapter is devoted to the recent advances in the renormalization group (RG) approaches to the physics of classical frustrated magnets in three dimensions. We first recall the main features of the field theoretical approach to these systems including considerations on symmetries, symmetry breaking schemes, continuum limits, topological contents, etc. We then provide an overview of the phenomenological situation, stressing on the most striking aspect of the physics of frustrated magnets: the existence of *nonuniversal scaling* behaviors. We then review the various perturbative and nonperturbative RG approaches that have been used to investigate frustrated magnets. Finally, a large part of this chapter is devoted to a recent nonperturbative approach that has clarified the intricate physical situation of frustrated magnets.

#### 3.1. Introduction

Magnetic systems with competing interactions — or *frustrated magnets* — like helimagnets or geometrically frustrated magnets represent one of the most celebrated class of systems whose critical physics, although studied for more than twenty five years, is still strongly debated. The specificity of

frustrated magnets is that the competition between the interactions generates nontrivial ground states together with original symmetry breaking schemes. For continuous spins for instance, the ground state is no longer made of aligned or anti-aligned spins. This is well-known from the case of the Stacked Triangular Antiferromagnets (STA) whose ground state gives rise to the famous  $120^\circ$  structure. Also, in the case of Heisenberg spins, the  $SO(3)$  rotational symmetry group is *fully* broken at low-temperature. This contrasts with the ferromagnetic case for which the corresponding symmetry breaking scheme is given by  $SO(3) \rightarrow SO(2)$ . These nontrivial ground state and symmetry breaking schemes imply that both the spin-wave physics and the topological content differ from those of nonfrustrated systems. As a consequence of these features, the situation appears to be much more intricate for frustrated magnets than for nonfrustrated ones, as we now describe.

Firstly, experimentally and numerically, there is no clear, unambiguous, picture of the three dimensional physics for both XY and Heisenberg systems. On the contrary, the phenomenology of frustrated magnets displays quite unconventional features: almost all experiments exhibit scaling laws around the transition temperature but with *nonuniversal* critical exponents, *i.e.* with critical exponents that vary from one compound to the other. Moreover, other strange behaviors are encountered: scaling laws are violated, the anomalous dimension is negative at the transition, etc. This strongly contrasts with the situation for nonfrustrated systems and makes very doubtful the proposition that frustrated magnets would belong to a new universality class, the so-called “chiral universality class”<sup>1,2,3,4,5,6</sup>.

Secondly, the theoretical situation in these systems is also far from being clear: *i*) independently of the phenomenological context, the results obtained within the usual perturbative approaches — in dimensions  $d = 2 + \epsilon$ , in  $d = 4 - \epsilon$  or directly in  $d = 3$  — conflict. Indeed, the Nonlinear Sigma ( $NL\sigma$ ) model approach performed around two dimensions predicts a second order phase transition of the standard  $O(4)/O(3)$  universality class<sup>7,8</sup>. On the other hand, the weak coupling expansion performed on the suitable Ginzburg-Landau-Wilson (GLW) model in the vicinity of  $d = 4$  leads to a first order phase transition due to the lack of a stable fixed point<sup>1,9,2</sup>. Finally, high-order perturbative approaches performed directly in  $d = 3$  predict a second order phase transition different from the  $O(4)/O(3)$  universality class. *ii*) Neither the low-temperature expansion around  $d = 2$  nor high-order weak-coupling calculations performed around  $d = 4$  or directly in  $d = 3$  — at least, when interpreted in a conventional way — succeed in

reproducing the whole phenomenology of frustrated magnets.

During the last years, there have been considerable progress in the understanding of both the theoretical and the phenomenological features of the physics of frustrated magnets. These progress have been the consequence of several facts. First, the acknowledgment of the nonuniversal character of the phase transitions in these systems: it is now more and more accepted that frustrated magnets do not constitute a new universality class. Second, and greatly motivated by the first point, the recognition of the inadequacy of the conventional theoretical approaches. This has led to the use of new or improved methods — high-order perturbative approaches<sup>10,11,12,13</sup>, nonperturbative renormalization group (NPRG) methods<sup>14,15,16,17,18,19</sup> — and concepts — pseudo-fixed point<sup>14,15,17,19</sup>, continuously varying exponents<sup>18,19,11,12</sup> — suitable for the description of new kinds of critical behaviors.

It is the aim of this chapter to review these major advances in the RG analysis of frustrated systems that have led to an almost complete understanding of the physics of these systems in three dimensions, with a particular emphasis on the NPRG approach.

### 3.2. The STA model and generalization

#### 3.2.1. *The lattice model, its continuum limit and symmetries*

We now describe the archetype of frustrated spin systems, the Stacked Triangular Antiferromagnets (STA). This system is composed of two-dimensional triangular lattices which are piled-up in the third direction. At each lattice site, there is a magnetic ion whose spin is described by a classical vector. The interaction between the spins is given by the usual lattice hamiltonian:

$$H = \sum_{\langle ij \rangle} J_{ij} \vec{S}_i \cdot \vec{S}_j \quad (1)$$

where, depending on the anisotropies, the  $\vec{S}_i$  are two or three-component vectors and the sum runs over all pairs of nearest neighbor spins. The coupling constants  $J_{ij}$  equals  $J_{||}$  for a pair of sites inside a plane and  $J_{\perp}$  between planes. The interactions between nearest neighbor spins within a plane is antiferromagnetic, *i.e.*  $J_{||} > 0$ . This induces frustration in the system and, in the ground state, gives rise to the famous 120° structure of the spins, see Fig. 3.1a.

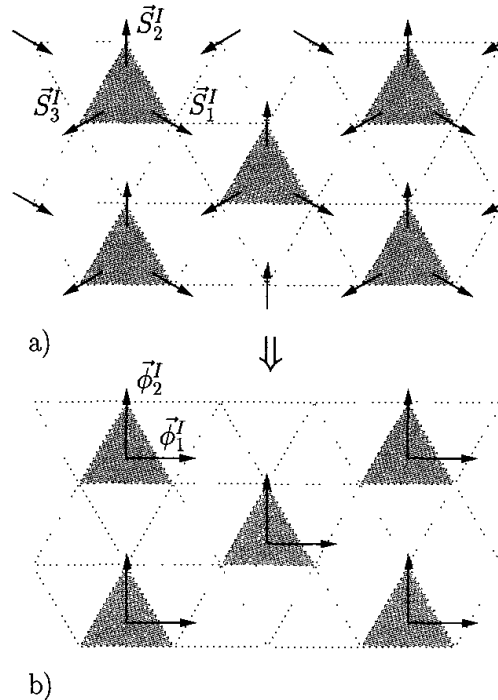


Fig. 3.1. The ground state configurations a) of the spins on the triangular lattice and b) of the order parameter made of two orthonormal vectors. The plaquettes, which constitute the magnetic cell, are indexed by  $I$  and are shaded.

This nontrivial magnetic structure is invariant under translations of length  $\sqrt{3}$  times the initial lattice spacing. The magnetic cell, indexed by  $I$ , which is replicated all over the system, is a plaquette of three spins  $\vec{S}_1^I$ ,  $\vec{S}_2^I$  and  $\vec{S}_3^I$ , see Fig. 3.1a. Note that the nearest-neighbor out-of-plane interaction  $J_\perp$  is, depending on the compounds, ferro- or antiferro-magnetic, but the two cases can be treated simultaneously since no extra frustration appears through this interaction. Finally, interactions between more distant spins (next-to-nearest neighbors, etc) also exist but are neglected in the following since they are supposed to be irrelevant.

There have been numerous derivations of the long distance effective field theory supposed to describe the critical physics of this system<sup>1,2,20,6</sup>. We now sketch the derivation which is most appropriate for our purpose.

The Hamiltonian (1) has the usual rotational symmetry acting on the spin components:  $O(2)$  or  $O(3)$  for XY or Heisenberg spins, respectively. To identify the order parameter, it is also necessary to consider the symmetry of the magnetic cell. For the triangular lattice, this is the  $C_{3v}$  group that interchanges the spins inside a plaquette.

The identification of the order parameter is close in spirit to what is done in the nonfrustrated case, *e.g.* for the antiferromagnets on a square lattice. At zero temperature, the sum of the three spins for a given plaquette  $I$ :

$$\vec{\Sigma}^I = \vec{S}_1^I + \vec{S}_2^I + \vec{S}_3^I \quad (2)$$

is vanishing <sup>a</sup>. In average, this is also the case at any finite temperature so that the thermal average of:

$$\vec{\Sigma} = \sum_I \vec{\Sigma}^I, \quad (3)$$

where the sum runs on all plaquettes, cannot be an order parameter: the associated modes are never critical. We therefore replace  $\vec{\Sigma}^I$  by its average value:

$$\vec{\Sigma}^I \rightarrow \langle \vec{\Sigma}^I \rangle = \vec{0} \quad (4)$$

which is equivalent to freezing the fluctuations of the spins inside each plaquette. The constraint  $\vec{\Sigma}^I = \vec{0}$  is called the “local rigidity constraint”. Having eliminated  $\vec{\Sigma}$ , we keep only two vectors per plaquette  $(\vec{\phi}_1^I, \vec{\phi}_2^I)$  which represent the local order parameter. For  $\vec{\phi}_2^I$ , we choose one of the spins of the plaquette, see Figs. 3.1a and b. For the other,  $\vec{\phi}_1^I$ , we choose the linear combination of the spins which is orthogonal to  $\vec{\phi}_2^I$  and of unit norm, see Fig. 3.1b. The local order parameter thus obeys on each plaquette:

$$\vec{\phi}_i^I \cdot \vec{\phi}_j^I = \delta_{ij} \quad \text{with} \quad i, j \in \{1, 2\}. \quad (5)$$

The dihedral  $(\vec{\phi}_1^I, \vec{\phi}_2^I)$  plays a role analogous to the staggered magnetization in the nonfrustrated case.

As usual, once the model is reformulated in terms of its order parameter, the effective interaction — from plaquette to plaquette — becomes ferromagnetic, see Fig. 3.1b. By taking the dihedral  $(\vec{\phi}_1^I, \vec{\phi}_2^I)$  on the center of the plaquette  $I$ , we indeed find that it interacts ferromagnetically with the dihedral  $(\vec{\phi}_1^J, \vec{\phi}_2^J)$  defined on the center of the plaquette  $J$  — the plaquettes  $I$  and  $J$  being nearest neighbours — such that  $\vec{\phi}_1^I$  interacts only with  $\vec{\phi}_1^J$  and  $\vec{\phi}_2^I$  only with  $\vec{\phi}_2^J$ . A more detailed analysis shows that the two vectors  $\vec{\phi}_1^I$  and  $\vec{\phi}_2^I$  play symmetric roles <sup>2</sup>. As a consequence, the effective Hamiltonian reads:

$$H = -J \sum_{\langle I, J \rangle} \left( \vec{\phi}_1^I \cdot \vec{\phi}_1^J + \vec{\phi}_2^I \cdot \vec{\phi}_2^J \right) \quad (6)$$

---

<sup>a</sup> $\vec{\Sigma}^I$  is analogous to the local magnetization of nonfrustrated antiferromagnets —  $\vec{\Sigma}^I = \vec{S}_1^I + \vec{S}_2^I$  in this last case — that also vanishes in the ground state.

with the same coupling constant  $J > 0$  for the  $\vec{\phi}_1^I$ 's and for the  $\vec{\phi}_2^I$ 's. Moreover, since the anisotropies resulting from the stacked structure of the lattice are supposed to be irrelevant, we take the same coupling constant for the interactions inside a plane and between the planes. The continuum limit is now trivial and proceeds as in the usual ferromagnetic case. The effective Hamiltonian in the continuum thus writes, up to constants:

$$H = - \int d^d \mathbf{x} \left( (\partial \vec{\phi}_1(\mathbf{x}))^2 + (\partial \vec{\phi}_2(\mathbf{x}))^2 \right) \quad (7)$$

with the constraint that  $\vec{\phi}_1$  and  $\vec{\phi}_2$  are orthonormal. This model is called the Stiefel  $V_{N,2}$  model with  $N = 2$  in the XY case and  $N = 3$  in the Heisenberg case. In  $V_{N,2}$ , the index 2 means that we are considering *two* orthonormal vectors  $\vec{\phi}_1$  and  $\vec{\phi}_2$ .

It is convenient to gather the vectors  $\vec{\phi}_1$  and  $\vec{\phi}_2$  into a rectangular matrix:

$$\Phi = (\vec{\phi}_1, \vec{\phi}_2) \quad (8)$$

and to rewrite  $H$  as:

$$H = - \int d^d \mathbf{x} \text{Tr} (\partial {}^t \Phi(\mathbf{x}) \cdot \partial \Phi(\mathbf{x})) \quad (9)$$

where  $({}^t \Phi)_{ij} = \Phi_{ji}$ .

In the following two sections, we consider successively the case of Heisenberg and XY spins.

### 3.2.2. The Heisenberg case

In this case,  $H$  is invariant under the usual left  $O(3)$  rotation and inversion group acting on the spins:

$$\Phi' = R\Phi, \quad R \in O(3). \quad (10)$$

It is also invariant under a right  $O(2)$ :

$$\Phi' = \Phi U, \quad U \in O(2). \quad (11)$$

This last symmetry encodes the fact that  $\vec{\phi}_1$  and  $\vec{\phi}_2$  play the same role which, itself, is reminiscent of the  $C_{3v}$  symmetry of the triangular plaquette. The system is thus symmetric under  $G = O(3) \times O(2)$ . In the low-temperature phase, a typical ground state configuration is given by (see

Fig. 3.1b):

$$\Phi_0 \propto \begin{pmatrix} 1 & 0 \\ 0 & 1 \\ 0 & 0 \end{pmatrix}. \quad (12)$$

It is symmetric under the diagonal group —  $O(2)_{\text{diag}}$  — built from the right  $O(2)$  and from a particular left  $O(2)$  in  $O(3)$ :

$$\Phi_0 = \begin{pmatrix} \epsilon \cos \theta & -\sin \theta & 0 \\ \epsilon \sin \theta & \cos \theta & 0 \\ 0 & 0 & 1 \end{pmatrix} \Phi_0 \begin{pmatrix} \epsilon \cos \theta & \epsilon \sin \theta \\ -\sin \theta & \cos \theta \end{pmatrix} \quad (13)$$

where  $\epsilon = \pm 1$  encodes the  $\mathbb{Z}_2$  part of  $O(2)_{\text{diag}}$ . Apart from the previous  $\mathbb{Z}_2$  contained in the  $O(2)_{\text{diag}}$ , another  $\mathbb{Z}_2$  is also left unbroken. It is the combination of a  $\mathbb{Z}_2$  included into the right  $O(2)$  of  $G$ , Eq. (11), and of a rotation of  $\pi$  around the  $x$ -axis contained in the rotation group  $SO(3)$  of  $G$ . Thus,  $G$  is spontaneously broken down to  $H = \mathbb{Z}_2 \times O(2)_{\text{diag}}$ . As a consequence, the symmetry breaking scheme reads:

$$G = O(3) \times O(2) \rightarrow H = \mathbb{Z}_2 \times O(2)_{\text{diag}} \quad (14)$$

which is often referred to as the  $SO(3) \times SO(2)/SO(2)$  model, when all the discrete  $\mathbb{Z}_2$  groups have been cancelled.

Here appears the main feature of frustrated magnets: the  $SO(3)$  group is *fully* broken in the low-temperature phase whereas it is only broken down to  $SO(2)$  in nonfrustrated magnets. This has two important consequences that are at the very origin of the nontrivial critical behavior encountered in frustrated magnets.

First, there are three Goldstone modes in the broken phase instead of two in the nonfrustrated case. This implies a spin-wave physics different from that of  $O(3)/O(2)$  model. Second, the order parameter space  $SO(3)$  having a nontrivial first homotopy group <sup>21</sup>:

$$\pi_1(SO(3)) = \mathbb{Z}_2 \quad (15)$$

there exist stable nontrivial topological configurations called vortices. Because of the  $\mathbb{Z}_2$  homotopy group, only one kind of vortex exists, contrarily to the well-known case of XY ferromagnets where there are infinitely many different kinds of vortices, each one being indexed by an integer, the winding number.

It has been established first by Kawamura and Miyashita <sup>22</sup> that the existence of vortices is important in two dimensions. This has been largely confirmed by subsequent works studying the temperature dependence of ther-

modynamical quantities such as the correlation length, the spin-stiffness, etc<sup>23,24,25,26,27,28</sup>. Actually, although this has not been directly established, they certainly also play an important role for the critical physics of the STA in three dimensions. A simple argument allows to argue to that end: let us go back on the lattice and introduce, on each plaquette  $I$ , together with  $\vec{\phi}_1^I$  and  $\vec{\phi}_2^I$ , a third vector  $\vec{\phi}_3^I$  defined by:

$$\vec{\phi}_3^I = \vec{\phi}_1^I \wedge \vec{\phi}_2^I . \quad (16)$$

Let us then gather them into a  $3 \times 3$  matrix:

$$\Phi^I = (\vec{\phi}_1^I, \vec{\phi}_2^I, \vec{\phi}_3^I) . \quad (17)$$

Since  $(\vec{\phi}_1^I, \vec{\phi}_2^I, \vec{\phi}_3^I)$  are three orthonormal vectors, one has  ${}^t\Phi^I \cdot \Phi^I = \mathbb{1}$  and, therefore,  $\Phi^I$  is a  $SO(3)$  matrix. This allows to rewrite the Hamiltonian (6) on the lattice as:

$$H = - \sum_{\langle I, J \rangle} \text{Tr} (\mathcal{P} {}^t\Phi^I \cdot \Phi^J) \quad (18)$$

where  $\mathcal{P}$  is a diagonal matrix of coupling constants that characterizes the interaction between the  $\vec{\phi}_1^I$ 's, between the  $\vec{\phi}_2^I$ 's and between the  $\vec{\phi}_3^I$ 's. One has, from the microscopic derivation,  $\mathcal{P} = \text{diag}(J, J, 0)$ , *i.e.* the interaction is the same between the  $\vec{\phi}_1^I$ 's and between the  $\vec{\phi}_2^I$ 's and there is no interaction between the  $\vec{\phi}_3^I$ 's. However, for the present purpose, we consider, without loss of generality, the case where the interaction is nonvanishing and identical between all vectors. One thus has  $\mathcal{P} = J\mathbb{1}$ . Now, we use the decomposition of a rotation matrix  $\Phi^I$  of  $SO(3)$  in terms of a four-component unit vector  $\widetilde{S}^I = (S_0^I, S_1^I, S_2^I, S_3^I)$ :

$$\Phi_{kl}^I = 2 \left( S_k^I S_l^I - \frac{1}{4} \delta_{kl} \right) + 2\epsilon_{klm} S_0^I S_m^I + 2 \left( S_0^{I2} - \frac{1}{4} \right) \delta_{kl} . \quad (19)$$

In terms of the vector  $\widetilde{S}^I$ , the Hamiltonian (18) writes:

$$H = -4J \sum_{\langle I, J \rangle} \left( \widetilde{S}^I \cdot \widetilde{S}^J \right)^2 \quad (20)$$

which is the Hamiltonian for *four*-component nonfrustrated spins with the peculiarity that each vector  $\widetilde{S}^I$  appears quadratically. Therefore, the Hamiltonian (20) is invariant under a global  $O(4)$  group and under a *local — gauge —*  $\mathbb{Z}_2$  group that changes  $\widetilde{S}^I$  to  $-\widetilde{S}^I$ . It corresponds to

the  $RP^3 = SO(4)/(SO(3) \times \mathbb{Z}_2)$  model<sup>b</sup>. For three-component spins, an analogous Hamiltonian, the  $RP^2$  model, had been introduced by Maier and Saupe<sup>29</sup> and by Lebwohl and Lasher<sup>30</sup> to investigate the isotropic-nematic transition in liquid crystals. An extensive study of the  $RP^2$  model, as well as a detailed investigation of the role of vortices in this transition, has been performed by Lammert *et al.*<sup>31,32</sup>. These authors have shown, in particular, that these nontrivial topological configurations favor the first order character of the transition. In the case of four-component spins no such detailed analysis has been performed. However, the  $RP^N = SO(N)/(SO(N - 1) \times \mathbb{Z}_2)$  models that generalizes Hamiltonian (20) to  $N$ -component spins with  $2 \leq N \leq 4$  have been numerically studied by Kohring and Shrock<sup>33</sup>. These systems have been shown to undergo a first order phase transition. Since the only difference between the  $RP^N$  and the  $SO(N)/SO(N - 1)$  models lies in their topological properties, one is naturally led to attribute the origin of the first order character of the phase transition in the  $RP^N$  models to the  $\mathbb{Z}_2$  vortices. Finally, since the Hamiltonian (18), relevant to STA, can be mapped onto the Hamiltonian (20) — up to the  $O(4)$ -breaking terms — one can expect that the topological configurations also favor first order phase transitions in frustrated magnets in three dimensions.

### 3.2.3. The XY case

In the XY case, the Hamiltonian (9) is still invariant under the right  $O(2)$  group, see Eq. (11), while the left symmetry group becomes  $O(2)$ . In the low-temperature phase, the rotational symmetry is broken and, since the spins are constrained to be in a plane, the permutation symmetry between  $\vec{\phi}_1$  and  $\vec{\phi}_2$  is also broken. As a consequence, the symmetry breaking scheme is:

$$G = O(2) \times O(2) \rightarrow H = O(2)_{\text{diag}}. \quad (21)$$

This symmetry-breaking scheme is usually referred to as  $SO(2) \times \mathbb{Z}_2 \rightarrow \mathbb{1}$ . The  $\mathbb{Z}_2$  degrees of freedom are known as chirality variables<sup>34,22,35,6</sup>.

In this case there also exist topological defects since:

$$\pi_1(SO(2)) = \mathbb{Z}. \quad (22)$$

---

<sup>b</sup>Note that, had we kept the microscopical content, with  $\mathcal{P} = \text{diag}(J, J, 0)$ , the Hamiltonian (20) would be supplemented by terms breaking the  $SO(4)$  global symmetry, leaving untouched the  $\mathbb{Z}_2$  local symmetry which is the important point for our purpose.

These defects are identical to those of the ferromagnetic XY model that drive the famous Berezinskii-Kosterlitz-Thouless transition in two dimensions<sup>36,37</sup>. However, in the frustrated case, they very likely interact non trivially with the chirality degrees of freedom which are critical in  $d = 3$  at the same temperature as the spin-wave degrees of freedom. This is apparent from the fact that one observes a unique phase transition and not two distinct Ising-like and XY-like transitions<sup>38</sup>. As a consequence one can expect, in the frustrated case, a physics different and probably more complicated than in the nonfrustrated  $O(2)$  model that undergoes a standard second order phase transition in three dimensions.

### **3.2.4. Generalization**

For reasons that will become clear in the following, we consider the generalization of Hamiltonian (1) to  $N$ -component spins. It is straightforward to extend the previous considerations to this case. One finds the following symmetry breaking scheme:

$$G = O(N) \times O(2) \rightarrow H = O(N - 2) \times O(2)_{\text{diag}}. \quad (23)$$

In the following, we shall drop the “diag” index for simplicity. Note that the previous Heisenberg and XY cases are recovered trivially provided that we identify  $O(0)$  with the trivial group  $\mathbb{1}$  and  $O(1)$  with  $\mathbb{Z}_2$ .

We now give an overview of the experimental and numerical situations in XY and Heisenberg cases.

## **3.3. Experimental and numerical situations**

As said in the Introduction, due to their specific symmetry breaking scheme, frustrated spin systems have been proposed to belong to a new universality class<sup>1,2,3,4,5,6</sup>. However, in view of the experimental and numerical results relevant to the physics of frustrated magnets, the situation is far from being so simple. In effect, as emphasized by the present authors<sup>18,19</sup>, the phenomenology of frustrated magnets shows that these systems display scaling *without* universality, a behavior not compatible with a usual second order phase transition. Moreover, there also exist clear indications of weak first order phase transitions.

### **3.3.1. The XY systems**

Let us first discuss the XY case since the experimental situation is richer than in the Heisenberg case. Also, the symptoms of the existence of a problem in the interpretation of the results are clearer than in the latter case.

### 3.3.1.1. The experimental situation

Two classes of materials are supposed to be described by Hamiltonian (9). The first one is made of  $\text{ABX}_3$  hexagonal perovskites — where A is an alkali metal, B a transition metal and X a halogen atom — which are physical realizations of XY STA. The most studied ones are  $\text{CsMnBr}_3$ ,  $\text{CsCuCl}_3$ ,  $\text{CsNiCl}_3$  and  $\text{CsMnI}_3$  (see Collins and Petrenko<sup>39</sup> for a review and Weber *et al.*<sup>40</sup> for  $\text{RbMnBr}_3$ ). We have excluded this material since the measurement of its specific heat presents a shoulderlike anomaly near  $T_c$  which renders the determination of  $\alpha$  and  $\beta$  doubtful). The second one is made of rare earth helimagnets: Ho, Dy, Tb. For most materials, the transitions are found continuous but *not* with the same critical exponents. For  $\text{CsCuCl}_3$ , the transition is found to be weakly of first order, *i.e.* with small discontinuities. The results are summarized in Table 3.1.

Table 3.1. The critical exponents of XY frustrated materials. For  $\text{CsCuCl}_3$ , the transition has been found of first order and the exponents mentioned here hold only for a reduced temperature larger than  $5.10^{-3}$  (see Weber *et al.*<sup>40</sup>).

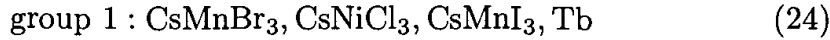
Materials	Critical exponents
$\text{CsMnBr}_3$	$\alpha=0.39(9)$ <sup>41</sup> , $0.40(5)$ <sup>42</sup> , $0.44(5)$ <sup>42</sup> ; $\beta=0.21(1)$ <sup>38</sup> , $0.21(2)$ <sup>43</sup> , $0.22(2)$ <sup>44</sup> , $0.24(2)$ <sup>45</sup> , $0.25(1)$ <sup>46</sup> ; $\gamma=1.01(8)$ <sup>43</sup> , $1.10(5)$ <sup>47</sup> ; $\nu=0.54(3)$ <sup>43</sup> , $0.57(3)$ <sup>47</sup>
$\text{CsNiCl}_3$	$\alpha=0.342(5)$ <sup>48</sup> , $0.37(6)$ <sup>49</sup> , $0.37(8)$ <sup>49</sup> ; $\beta=0.243(5)$ <sup>50</sup>
$\text{CsMnI}_3$	$\alpha=0.34(6)$ <sup>49</sup>
$\text{CsCuCl}_3$	$\alpha=0.35(5)$ <sup>40</sup> ; $\beta=0.23(2)$ <sup>51</sup> , $0.24(2)$ <sup>51</sup> , $0.25(2)$ <sup>51</sup> ; 1 <sup>st</sup> order <sup>40</sup>
Tb	$\alpha=0.20(3)$ <sup>52</sup> ; $\beta=0.21(2)$ <sup>53</sup> , $0.23(4)$ <sup>54</sup> ; $\nu=0.53$ <sup>55</sup>
Ho	$\alpha=0.27(2)$ <sup>56</sup> , $0.1-0.22$ <sup>41</sup> ; $\beta=0.30(10)$ <sup>57</sup> , $0.37(10)$ <sup>57</sup> , $0.38(1)$ <sup>58</sup> , $0.39(3)$ <sup>59</sup> , $0.39(2)$ <sup>60</sup> , $0.39(4)$ <sup>61</sup> , $0.39(4)$ <sup>62</sup> , $0.41(4)$ <sup>62</sup> ; $\gamma=1.14(10)$ <sup>63</sup> , $1.24(15)$ <sup>57</sup> ; $\nu=0.54(4)$ <sup>57</sup> , $0.57(4)$ <sup>63</sup> ; 1 <sup>st</sup> order <sup>64</sup>
Dy	$\alpha=0.24(2)$ <sup>65</sup> ; $\beta=0.335(10)$ <sup>66</sup> , $0.38(2)$ <sup>60</sup> , $0.39(1)$ <sup>59</sup> , $0.39^{+0.04}_{-0.02}$ <sup>67</sup> ; $\gamma=1.05(7)$ <sup>63</sup> ; $\nu=0.57(5)$ <sup>63</sup>

We highlight four striking characteristics<sup>18,19</sup> of these data<sup>c</sup>. Their consequences for the physics of frustrated magnets will be then discussed.

<sup>c</sup>The details concerning the computations of the average values of the critical exponents as well as their error bars have been given by the present authors<sup>18,19</sup>.

*i) There are two groups of incompatible exponents.* In the present discussion, we mainly use the exponent  $\beta$  to analyze the results since it is by far the most precisely measured exponent. Clearly, there are two groups of materials, each of which being characterized by a set of exponents,  $\beta$  in particular.

In the first one — that we call group 1 — made up of:



one has:

$$\beta \sim 0.237(4) \quad (25)$$

while in the second — group 2 — made up of:



one has:

$$\beta \sim 0.389(7) . \quad (27)$$

Note that, as far as we know, there is no determination of the exponent  $\beta$  for  $\text{CsMnI}_3$  that, being given its composition, has been included in the group 1 of materials. Anyway, our conclusions are not affected by this fact.

The two values of  $\beta$  given by (25) and (27) are completely incompatible. Actually, we find for the average exponents for the materials of group 1 (except Tb for which the results are not fully under control):

$$\beta = 0.237(4), \quad \nu = 0.555(21), \quad \alpha = 0.344(5), \quad \gamma = 1.075(42) . \quad (28)$$

For materials of group 2 (Ho and Dy) we find:

$$\beta = 0.389(7), \quad \nu = 0.558(25), \quad \gamma = 1.10(5) . \quad (29)$$

We do not give a value for  $\alpha$  which is poorly determined.

Let us also indicate that the exponents vary much from compound to compound in group 1. Although less accurately determined than  $\beta$ ,  $\alpha$  is only marginally compatible between  $\text{CsNiCl}_3$  and  $\text{CsMnBr}_3$ . Note moreover that, even for the same material, the data are not fully compatible among themselves:  $\beta$  in  $\text{CsMnBr}_3$  shows a large dispersion.

*ii) The anomalous dimension  $\eta$  is negative for group 1 while it cannot be so for a second order phase transition*<sup>d</sup>.

---

<sup>d</sup> $\eta$  is always positive if the underlying field theory is a Ginzburg-Landau-Wilson  $\varphi^4$ -like theory<sup>138</sup>, as it is the case here<sup>2</sup>.

If one assumes that the transition is of second order for group 1, one can use the scaling relations to compute  $\eta$ . In particular, the precise determination of  $\beta$  allows to use  $\eta = 2\beta/\nu - 1$  to determine rather accurately  $\eta$ . The exponent  $\nu$  itself can be obtained directly from the experiments or deduced using the scaling relation:

$$\nu = (2 - \alpha)/3 . \quad (30)$$

The large number of experiments devoted to the determination of  $\alpha$  allows a precise determination of  $\nu$ . By using the scaling relation Eq. (30), we find  $\nu = 0.528(11)$  if we consider the experimental results for  $\text{CsMnBr}_3$  alone and  $\nu = 0.552(2)$  if we consider  $\text{CsMnBr}_3$ ,  $\text{CsNiCl}_3$  and  $\text{CsMnI}_3$ . By using the relation  $\eta = 2\beta/\nu - 1$  together with Eq. (30) or the relation  $\eta = 6\beta/(2 - \alpha) - 1$  and by considering the data of  $\text{CsMnBr}_3$  alone or the data of the materials of group 1 (except Tb for which it is not sure that the data are reliable) we can obtain four determinations of  $\eta$ . In the four cases, we find  $\eta$  negative by at least 4.1 standard deviations and the probability to find it positive always less than  $10^{-5}$ . In fact, the most precise determination is obtained by combining all the data of group 1, Eq. (28), and by using the relation  $\eta = 6\beta/(2 - \alpha) - 1$ . In this case, we obtain  $\eta = -0.141(14)$  and thus a (almost) vanishing probability to find it positive. Note also that, although  $\beta$  and  $\nu$  are less accurately known in Tb — for which experiments are anyway delicate —,  $\eta$  is also found negative.

*iii) For group 2, the scaling relation  $\gamma + 2\beta - 3\nu = 0$  is violated.* From Eq. (29) it is possible to check the scaling relations. We find  $\gamma + 2\beta - 3\nu = 0.202(92)$  and thus a violation by 2.2 standard deviations.

*iv)  $\text{CsCuCl}_3$  undergoes a weak first order phase transition.* Until recently,  $\text{CsCuCl}_3$  was believed to undergo a second order phase transition with exponents compatible with those of group 1, see Table 3.1. It has been finally found to display a weak first order phase transition <sup>40</sup>.

### 3.3.1.2. The numerical situation

Monte Carlo simulations have been performed on five different kinds of XY systems. The first one is the STA itself <sup>68,69,5,4,70,71,72</sup>. The second model is the STAR (where R stands for rigidity) which consists in a STA for which the local rigidity constraint — Eq. (4) — has been imposed on each plaquette at all temperatures <sup>73</sup>. The third model is the Stiefel  $V_{2,2}$  model whose Hamiltonian is given by Eq. (6) <sup>74,73</sup>. This is a hard spin, discretized version of the  $\text{NL}\sigma$  model relevant to frustrated magnets. Also a soft spin,

discretized version of the GLW model has recently been studied by Itakura<sup>72</sup> who also re-studied the STA model for large sizes. Finally, a helimagnetic system defined on a body-centered-tetragonal (BCT) lattice — the “BCT model” — has been investigated<sup>75</sup>.

Here, we emphasize that the local rigidity constraint — Eq. (4) — as well as the manipulations that lead to the STAR, Stiefel  $V_{2,2}$ , GLW and BCT models only affect the *massive* — noncritical — modes. Thus, all the STA, STAR, Stiefel  $V_{2,2}$ , GLW and BCT models have the same *critical* modes, the same symmetries and the same order parameter. Therefore, one could expect a common critical behavior for all these systems.

Let us comment the results of the simulations given in Table 3.2. Note that, due to the its novel character, we shall comment the recent work of Itakura<sup>72</sup> separately.

Table 3.2. The critical exponents of the XY frustrated systems.

Systems	Critical exponents
STA	$\alpha = 0.34(6)^{4,68}, 0.46(10)^{70}, 0.43(10)^{71};$ $\beta = 0.24(2)^{70}, 0.253(10)^{4,68};$ $\gamma = 1.03(4)^{70}, 1.13(5)^{4,68};$ $\nu = 0.48(2)^{71}, 0.50(1)^{70}, 0.54(2)^{4,68};$ $\eta = -0.09(8)^{4,68}, -0.06(4)^{70};$ 1 <sup>st</sup> order <sup>72</sup>
STAR, $V_{2,2}$ , BCT, GLW	1 <sup>st</sup> order <sup>75,73,72</sup>

i) For STA, scaling laws are found with exponents compatible with those of group 1. Let us however notice that, similarly to what happens for the materials of group 1 there exists, in the numerical simulations of STA, a rather large dispersion of the results. For instance, the two extreme values of  $\nu$  differ by 2.1 standard deviations.

Let us make two other remarks. First, the good agreement between the numerical results for STA and the experimental ones for materials of group 1 has been repeatedly interpreted in the literature as a proof of the existence of a second order transition and even as an evidence of the existence of the chiral fixed point of the GLW model<sup>6</sup>. We emphasize here that the fact that a Monte Carlo simulation reproduces the experimental results only means that the Hamiltonian of the simulated system is a good approximation of the microscopic Hamiltonian describing the physics of real materials. However, this neither explains nor proves anything else — and *certainly not* the existence of a second order phase transition — since Monte Carlo simulations suffer from problems analogous to those encountered in

experiments: a weakly first order phase transition is very difficult to identify and to distinguish from a second order one.

Let us now come to our second remark. In a beautiful experiment, Plakhty *et al.*<sup>38</sup> have measured the so-called chiral critical exponents  $\beta_c$  and  $\gamma_c$  in CsMnBr<sub>3</sub>. They have found values compatible with those found numerically in STA<sup>68</sup>. Let us emphasize, again, that this agreement simply means that the parameters characterizing the numerical simulations are not too far from those associated to the experiments. By no means it implies — or gives a new indication of the existence of — a second order transition. Let us notice that  $\beta_c$  has also been measured in Ho<sup>58</sup>. The value found completely disagrees with the result found in STA and in CsMnBr<sub>3</sub>.

*ii) The anomalous dimension  $\eta$  is negative for STA.* As shown by Loison and Schotte<sup>73</sup>,  $\eta$  is found negative using the two scaling relations  $\eta = 2\beta/\nu - 1$  and  $\eta = 2 - \gamma/\nu$  for the two simulations where these calculations can be performed.

*iii) The simulations performed on STAR, V<sub>2,2</sub> and BCT models give first order transitions.* Therefore, the modifications in the microscopic details which change STA into STAR, V<sub>2,2</sub> and BCT affect drastically the scaling behavior.

*iv) In a remarkable work, Itakura has recently performed Monte Carlo and Monte Carlo RG approaches of the STA and its GLW model version that has led to a clear first order behavior<sup>72</sup>.* Itakura has performed standard Monte Carlo simulations of the STA involving sizes up to  $126 \times 144 \times 126$  leading to clear first order transitions. In particular, for these lattice sizes, the double-peak of the probability distribution of the energy at the transition is clearly identified. Itakura has also used an improved Monte Carlo RG simulation of the STA and its GLW model version. One advantage of this approach compared with previous RG Monte Carlo studies is that it allows to reach the asymptotic critical behavior using systems of moderately large lattice sizes. Within this approach, Itakura has found several evidences for a first order behavior with, notably, a runaway behavior of the RG flow and the absence of any nontrivial fixed point.

### 3.3.1.3. Summary

Let us now summarize the XY case. The experimental and numerical data reveal some striking features:

1) Scaling laws are found in STA and helimagnetic materials on a rather wide range of temperature. This is also the case within all — but an im-

portant one<sup>72</sup> — numerical simulations of the STA.

2) There are two groups of systems that differ by their exponents. The first one includes the group 1 of materials and the numerical STA model. The second one corresponds to the group 2 of materials. One also observes variations of critical exponents inside a given group of exponents.

3) The anomalous dimension  $\eta$  is negative for the materials of group 1 and for the numerical STA model. This is very significant from the experimental results, less from the numerical ones.

4) For group 2, the scaling relations are violated by 2.2 standard deviations.

5)  $\text{CsCuCl}_3$  is found to undergo a weak first order transition.

6) STAR,  $V_{2,2}$  and BCT models undergo strong first order transitions.

7) Recent Monte Carlo and Monte Carlo RG approaches of STA and the soft spin discretized version of the GLW model give clear indications of first order behaviors.

We now review the experimental and numerical results obtained for the Heisenberg systems.

### **3.3.2. The Heisenberg systems**

#### *3.3.2.1. The experimental situation*

Contrarily to the XY case, there is no Heisenberg helimagnets (see however Garel and Pfeuty<sup>1</sup>). Therefore there remain, *a priori*, only the Heisenberg STA materials. In fact, the A/B phase transition of  $\text{He}_3$  can be described by the same GLW Hamiltonian as the Heisenberg STA<sup>76,9</sup>. It is thus a candidate. Unfortunately, the narrowness of the critical region of this transition does not allow a reliable study of the critical behavior of this system and there are no available data concerning the transition.

Three classes of Heisenberg STA materials have been studied. The first class is made up of systems like  $\text{VCl}_2$ ,  $\text{VBr}_2$ ,  $\text{Cu}(\text{HCOO})_2\text{CO}(\text{ND}_2)_2\text{D}_2\text{O}$  and  $\text{Fe}[\text{S}_2\text{CN}(\text{C}_2\text{H}_5)_2]_2\text{Cl}$  which are generically quasi-XY except in a particular range of temperature where their anisotropies are irrelevant. The second class is made up of systems which become isotropic thanks to a magnetic field that exactly counterbalances the anisotropies. This is the case of  $\text{CsNiCl}_3$  and  $\text{CsMnI}_3$  at their multicritical point. Finally, the third class is made up of systems which become isotropic because they have been prepared in a fine-tuned stoichiometry such that the Ising-like and XY-like anisotropies cancel each other to form an isotropic material. This is the case of  $\text{CsMn}(\text{Br}_{0.19}\text{I}_{0.81})_3$ .

Let us comment the experimental results summarized in Table 3.3.

Table 3.3. The critical exponents of the Heisenberg frustrated materials. The abbreviations A, B and C stand for  $\text{Cu}(\text{HCOO})_2\text{CO}(\text{ND}_2)_2\text{D}_2\text{O}$ ,  $\text{Fe}[\text{S}_2\text{CN}(\text{C}_2\text{H}_5)_2]_2\text{Cl}$  and  $\text{CsMn}(\text{Br}_{0.19}\text{I}_{0.81})_3$  respectively. The data in brackets are suspected to be incorrect. They are given for completeness.

Materials	Critical exponents
$\text{VCl}_2$	$\beta=0.20(2)$ <sup>77</sup> ; $\gamma=1.05(3)$ <sup>77</sup> ; $\nu=0.62(5)$ <sup>77</sup>
$\text{VBr}_2$	$\alpha=0.30(5)$ <sup>78</sup>
A	$\beta=0.22(2)$ <sup>79</sup>
B	$\alpha=0.244(5)$ <sup>80</sup> ; $\beta=0.24(1)$ <sup>81,82,83</sup> ; $\gamma=1.16(3)$ <sup>81,82,83</sup>
$\text{CsNiCl}_3$	$\alpha=0.25(8)$ <sup>49,84</sup> , $0.23(4)$ <sup>48</sup> ; $\beta=0.28(3)$ <sup>50</sup>
$\text{CsMnI}_3$	$\alpha=0.28(6)$ <sup>49</sup>
C	$\alpha=0.23(7)$ <sup>85</sup> ; $\beta=0.29(1)$ <sup>86</sup> ; $0.28(2)$ <sup>87</sup> ; $[\gamma=0.75(4)]$ <sup>86</sup> , $[\nu=0.42(3)]$ <sup>86</sup>

i) As in the XY case, the Heisenberg materials fall into two groups. The group 1, made up of:

$$\begin{aligned} \text{group 1 : } & \text{ Cu}(\text{HCOO})_2\text{CO}(\text{ND}_2)_2\text{D}_2\text{O}, \\ & \text{Fe}[\text{S}_2\text{CN}(\text{C}_2\text{H}_5)_2]_2\text{Cl}, \\ & \text{VCl}_2, \text{VBr}_2 \end{aligned} \quad (31)$$

is characterized by:

$$\beta = 0.230(8) \quad (32)$$

while for group 2, made up of:

$$\text{CsNiCl}_3, \text{CsMnI}_3, \text{CsMn}(\text{Br}_{0.19}, \text{I}_{0.81})_3 \quad (33)$$

one finds:

$$\beta = 0.287(8) . \quad (34)$$

Note that, strictly speaking, the values of  $\beta$  for  $\text{VBr}_2$  and for  $\text{CsMnI}_3$  are not known and, thus, our classification is somewhat improper. It seems however logical to suppose that  $\text{VBr}_2$  is close to  $\text{VCl}_2$  and  $\text{CsMnI}_3$  close to  $\text{CsNiCl}_3$ . Anyway, it will be clear in the following that our analysis is almost insensitive to this point.

For group 1, the average values of the critical exponents are given by:

$$\beta = 0.230(8), \quad \alpha = 0.272(35), \quad \nu = 0.62(5), \quad \gamma = 1.105(21) . \quad (35)$$

A very severe difficulty in the study of the materials of group 1 is their two-dimensional character and Ising-like anisotropies. The temperature range where the systems behave effectively as three-dimensional Heisenberg systems is narrow. This is the case of  $\text{VCl}_2$  where this range is less than two decades and where, closer to the critical temperature, the system becomes Ising-like. For this group of materials the exponent  $\beta$  is very small and it has been noticed that such small values have also been found in materials where dimensional cross-over is suspected <sup>77</sup>. Thus, it is not clear whether the whole set of results really corresponds to a three-dimensional Heisenberg STA.

For group 2, the experimental situation seems to be better under control. The average values of the critical exponents are given by:

$$\beta = 0.287(9), \quad \alpha = 0.243(3), \quad \nu = 0.585(9), \quad \gamma = 1.181(33) \quad (36)$$

where the scaling relations have been used to compute  $\nu$  and  $\gamma$ . Note that the values of  $\nu$  and  $\gamma$  thus obtained differ significantly from those of  $\text{CsMn}(\text{Br}_{0.19}\text{I}_{0.81})_3$  whose critical behavior has been claimed to be perturbed by disorder.

*ii) For group 1, the anomalous dimension  $\eta$  is significantly negative.* Using the two exponents that have been measured at least twice in group 1 —  $\beta$  and  $\gamma$  — we can compute the anomalous dimension from  $\eta = (4\beta - \gamma)/(2\beta + \gamma)$ . We find  $\eta = -0.118(25)$  which is thus negative by 4.8 standard deviations.

*iii) For group 2, the anomalous dimension  $\eta$  is marginally negative.* Using the critical exponents given in Eq. (36), one obtains, for the anomalous dimension:  $\eta = -0.018(33)$ . Thus  $\eta$  is found negative but not significantly, contrarily to what happens in group 1.

*iv) For group 1, the scaling relations  $\gamma + 2\beta - 2 + \alpha = 0 = 2\beta + \gamma - 3\nu$  are violated.* Indeed,  $\gamma + 2\beta - 2 + \alpha = -0.135(56)$  and  $2\beta + \gamma - 3\nu = -0.29(15)$ . Of course, none of these violations is completely significant in itself because of the lack of experimental data. However, since they are both independently violated it remains only a very small probability that the scaling relations are actually valid.

### 3.3.2.2. The numerical situation

In the Heisenberg case, as in the XY case, five different kinds of systems: STA, STAR, Stiefel ( $V_{3,2}$  in this case), BCT and GLW models have been studied. The results of the simulations are given in Table 3.4.

Table 3.4. The critical exponents of the Heisenberg frustrated systems.  $\eta$  is computed by  $\gamma/\nu = 2 - \eta$  and, apart in the work of Kawamura<sup>68</sup> and Kunz and Zumbach<sup>74</sup>,  $\alpha$  is computed by  $3\nu = 2 - \alpha$ .

Systems	Critical exponents
STA	$\alpha=0.240(80)$ <sup>3,68</sup> , $0.242(24)$ <sup>88</sup> , $0.245(27)$ <sup>89</sup> , $0.230(30)$ <sup>90</sup> ; $\beta=0.300(20)$ <sup>3,68</sup> , $0.285(11)$ <sup>88</sup> , $0.289(15)$ <sup>89</sup> , $0.280(15)$ <sup>90</sup> ; $\gamma=1.170(70)$ <sup>3,68</sup> , $1.185(3)$ <sup>88</sup> , $1.176(26)$ <sup>89</sup> ; $\nu=0.590(20)$ <sup>3,68</sup> , $0.586(8)$ <sup>88</sup> , $0.585(9)$ <sup>89</sup> , $0.590(10)$ <sup>90</sup> , $0.589(7)$ <sup>91</sup> ; $\eta=0.020(180)$ <sup>3,68</sup> , $-0.033(19)$ <sup>88</sup> , $-0.011(14)$ <sup>89</sup> , $0.000(40)$ <sup>90</sup> ; 1st order <sup>72</sup>
STAR	$\alpha=0.488(30)$ <sup>92</sup> ; $\beta=0.221(9)$ <sup>92</sup> ; $\gamma=1.074(29)$ <sup>92</sup> ; $\nu=0.504(10)$ <sup>92</sup> ; $\eta=-0.131(13)$ <sup>92</sup>
$V_{3,2}$	$\alpha=0.479(24)$ <sup>92</sup> , $0.460(30)$ <sup>74</sup> ; $\beta=0.193(4)$ <sup>92</sup> ; $\gamma=1.136(23)$ <sup>92</sup> , $1.100(100)$ <sup>74</sup> ; $\nu=0.507(8)$ <sup>92</sup> , $0.515(10)$ <sup>74</sup> ; $\eta=-0.240(10)$ <sup>92</sup> , $-0.100(50)$ <sup>74</sup> ; 1st order <sup>72</sup>
BCT	$\alpha=0.287(30)$ <sup>93</sup> ; $\beta=0.247(10)$ <sup>93</sup> ; $\gamma=1.217(32)$ <sup>93</sup> ; $\nu=0.571(10)$ <sup>93</sup> ; $\eta=-0.131(18)$ <sup>93</sup>
GLW	1st order <sup>72</sup>

Let us comment them. Again, we put aside the work of Itakura<sup>72</sup>.

i) For the STA, scaling laws are found with an exponent  $\beta$  close to that of group 2. The average values for the exponents of STA are:

$$\beta = 0.288(6), \quad \gamma = 1.185(3), \quad \nu = 0.587(5). \quad (37)$$

$\beta$  is thus extremely close to the experimental value of group 2 and  $\nu$  and  $\gamma$  are extremely close to the experimental values deduced from the scaling relations, Eq. (36). The scaling relation  $\gamma + 2\beta - 3\nu = 0$  is very well verified since  $\gamma + 2\beta - 3\nu = 10^{-4} \pm 6.10^{-2}$ .

ii) For the STA,  $\eta$  is negative. Using the values of  $\beta/\nu$  and  $\gamma/\nu$  obtained directly in the simulations, one can compute the average value of  $\eta$ :  $-0.0182(89)$ . The probability of it being positive is 0.02 and is thus small although not vanishing.

iii) For the STAR,  $V_{3,2}$  and BCT models, the values of  $\beta$  are all incompatible with that of STA (three standard deviations at least) and are all incompatible among each others. This has been interpreted as an indication of very weak first order phase transitions<sup>92</sup>. This is to be compared with the XY case, where the transitions for STAR and the  $V_{2,2}$  model are strongly of first order.

iv) For the BCT, STAR and  $V_{3,2}$  models,  $\eta$  is always found significantly negative. See Table 3.4 where  $\eta$  has been calculated from  $\gamma/\nu$ .

v) The Monte Carlo and Monte Carlo RG approaches of the STA,  $V_{3,2}$

and GLW model performed by Itakura has led to clear first order behaviors<sup>72</sup>. For Heisenberg STA, contrarily to the XY case, even for the largest lattice sizes —  $84 \times 96 \times 84$  — the double-peak of the probability distribution of the energy is not observed. However, the  $V_{3,2}$  model displays a clear double-peak. Moreover, for the STA and the  $V_{3,2}$  model, the RG flow clearly does not exhibit any fixed point. Instead, a runaway of the RG flow toward the region of instability is found which indicates first order transitions. The transitions are thus — weakly — of first order. The transition is also weaker of first order for Heisenberg than for XY spins.

### 3.3.2.3. Summary

We now summarize the experimental and numerical situations in the Heisenberg case. In this case, the experimental situation is much poorer than in the XY case and is still unclear on many aspects. On the contrary, the numerical results are numerous and more precise than in the XY case.

- 1) Scaling laws are found in STA materials on a rather wide range of temperatures as well as in all Monte Carlo simulations apart the one based on Monte Carlo RG.
- 2) There are two groups of materials that do not have the same exponents. The exponent  $\beta$  of the numerical STA model agrees very well with that of group 2.
- 3) The anomalous dimension is manifestly negative for group 1 and very marginally for group 2. For the numerical STA model,  $\eta$  is found negative although not completely significantly. For STAR,  $V_{3,2}$  and BCT,  $\eta$  is found significantly negative.
- 4) For group 1, the scaling relations are violated.
- 5) STAR,  $V_{3,2}$  and BCT exhibit scaling behaviors without universality. Also, the results are incompatible with those of the numerical STA model.
- 6) A Monte Carlo RG approach of the STA,  $V_{3,2}$  and GLW models has led to clear first order behaviors.

### 3.3.3. The $N = 6$ STA

Before concluding, let us quote a simulation of the STA with six-component spins that has been performed by Loison *et al.*<sup>94</sup>. The results are given in Table 3.5. Six-component spins were chosen since it was expected that the transition was of second order. Loison *et al.* have clearly identified scaling laws at the transition with a positive anomalous dimension. Let us emphasize that, even if the transition is actually of first order, as suggested

by the recent results of Calabrese *et al.*<sup>12</sup>, it should be extremely weakly of first order — see the following. Thus, scaling laws should hold for all temperatures but those very close to  $T_c$ . In this respect, the exponents for  $N = 6$  are therefore very trustable so that reproducing them is a challenge for the theoretical approaches.

Table 3.5. Monte Carlo critical exponents for six-component spins in the STA system<sup>94</sup>.

System	$\alpha$	$\beta$	$\gamma$	$\nu$	$\eta$
$N = 6$ STA	-0.100(33)	0.359(14)	1.383(36)	0.700(11)	0.025(20)

### 3.3.4. Conclusion

Let us now draw some conclusions about the experimental and numerical situations. In the XY and in the Heisenberg cases, one observes the following phenomena: the different materials split into two groups, the anomalous dimension is found negative in many materials and in most numerical simulations, the scaling relations are violated in some materials and there is no universality in the exponents found in the simulations since changes of microscopic details induce changes of scaling behaviors. Therefore, it appears that an explanation of the critical physics of frustrated systems based on the existence of a standard and *unique* universality class is excluded. The theoretical challenge is to explain this situation and to reproduce the whole set of experimental and numerical data.

## 3.4. A brief chronological survey of the theoretical approaches

Let us briefly review the most important theoretical developments concerning this subject.

The first microscopic derivation and RG study — at one- and two-loop order in  $d = 4 - \epsilon$  — of the effective GLW model relevant for STA — see below — was performed for  $\text{He}_3$  by Jones *et al.*<sup>76</sup> in 1976 and by Bailin *et al.*<sup>9</sup> in 1977. The model was re-derived and re-studied in the context of helimagnets (for general  $N$ ) by several groups including Bak *et al.*<sup>95</sup> (1976), Garel and Pfeuty<sup>1</sup> (1976) and Barak and Walker<sup>96</sup> (1982). It was established at that time that, around  $d = 4$ , the transitions for Heisenberg spin systems had to be of first order. More precisely, these authors found

that there exists a critical value  $N_c(d)$  of the number  $N$  of spin components, above which the transition is of second order and below which it is of first order. They found<sup>76,9</sup> :

$$\begin{aligned} N_c(d = 4 - \epsilon) &= 4(3 + \sqrt{6}) - 4 \left( 3 + \frac{7}{\sqrt{6}} \right) \epsilon + O(\epsilon^2) \\ &\sim 21.8 - 23.4 \epsilon + O(\epsilon^2) \end{aligned} \quad (38)$$

with  $\epsilon = 4 - d$ . A first large- $N$  expansion was also studied, in particular for  $d = 3$ , by Bailin *et al.*<sup>9</sup> in 1977.

A group theoretical derivation of the GLW model relevant to the XY STA was performed by Yosefin and Domany<sup>2</sup> in 1985. They found the same Hamiltonian as for helimagnets. Between 1985 and 1988 Kawamura<sup>3,4,5,6</sup> have performed this analysis for  $N$ -component STA. He has shown that the Hamiltonian is the same as for  $\text{He}_3$  or helimagnets, the RG analysis giving obviously the same results. This author has also extrapolated the two-loop result for  $N_c(d)$  of Eq. (38) in  $d = 3$  and found  $N_c(d = 3) < 2$ . This led him to conjecture the existence of a new universality class for frustrated magnets. However, as well-known, this direct extrapolation cannot be reliable since it is notorious that the perturbative series must be resummed.

In 1988, Dombre and Read<sup>20</sup> derived, in the quantum case, the Non-linear Sigma ( $\text{NL}\sigma$ ) model relevant to frustrated magnets. In 1990, Azaria *et al.*<sup>7</sup> studied the classical version of the  $\text{NL}\sigma$  model around  $d = 2$ . They found a fixed point of the RG flow in a two-loop calculation for any  $N \geq 3$ . For  $N = 3$ , they found the phenomenon of enlarged symmetry: at the fixed point the symmetry becomes  $SO(3) \times SO(3) \sim SO(4)$  instead of  $SO(3) \times SO(2)$ . Thus, their conclusion was that, if the transition is of second order, it is characterized by  $O(4)/O(3)$  critical exponents — at least for  $\nu$ . Another possibility proposed by these authors was that the transition could be also mean-field tricritical or of first order. However, *none* of the experimental or numerical results are compatible with the  $O(4)/O(3)$  or mean-field tricritical exponents. Note finally that these authors supposed that, if tricritical, the behavior at the transition should be mean-field tricritical in  $d = 3$ , something which is mandatory only for  $O(N)/O(N - 1)$  models, but not for more complex models.

The first nonperturbative renormalization group (NPRG) approach to frustrated magnets was performed by Zumbach<sup>14,74,15</sup> in 1993. He wrote down the NPRG equations for the GLW models suited to the description of frustrated systems. He studied them within the Local Potential Approximation (LPA) of the Wilson-Polchinski equation — analogous to the Wegner-

Houghton approximation<sup>97</sup> — and found  $N_c(d = 3) \sim 4.7$ . Since he found no fixed point for  $N = 2$  and  $N = 3$  he claimed that the transition is of first order in these cases. In the case  $N = 3$ , he has shown that there is a minimum in the RG flow, a pseudo-fixed point, that fakes a true fixed point (see below for details). The transition was thus conjectured to be *weakly* of first order with pseudo-scaling characterized by pseudo-critical exponents. Note that, within the LPA, all derivative terms in the Hamiltonian are neglected so that the anomalous dimension is zero. This has two important consequences. First, the pseudo-critical exponents found by Zumbach were not very reliable and thus difficult to compare with the experimental and numerical results. Second, this approach neglects terms — the so-called current-term (see below) — that are fundamental within the perturbative approach of the NL $\sigma$  model performed around two dimensions. Thus, within Zumbach's approach, it was *not* possible to match with these results. Finally note that, in the  $N = 2$  case, *no* minimum in the RG flow was found and, thus, no pseudo-critical exponents were obtained, in contradiction with the scaling behaviors observed in the experimental and numerical contexts.

Then, three-loop calculations have been performed by Antonenko *et al.*<sup>98,99</sup> in 1994 and 1995 on the GLW model. In  $d = 3$  this has led, after Padé-Borel resummation, to  $N_c(d = 3) = 3.91$ <sup>98</sup>. In  $d = 4 - \epsilon$ , they have determined the three-loop contribution —  $7.1 \epsilon^2$  — to  $N_c(d = 4 - \epsilon)$ , see Eq. (38). This has led to  $N_c(d = 3) = 3.39$ <sup>99</sup>. The authors have mentioned that, contrarily to the  $O(N)$  models, their three-loop results were not well converged.

In 1996, Jolicœur and David<sup>100</sup> have studied a generalization of the Stiefel model that involves  $N$  vectors with  $N$  components. They have shown within a mean field approximation and a one-loop calculation performed in  $d = 2 + \epsilon$  that a first order line should appear in a nontrivial dimension above two. It should isolate the chiral fixed point in the metastability region in such a way that this point should no longer play any role. Above this dimension the transition should therefore be of first order.

In 2000-2002, using the technique of the effective average action, including derivative terms, the present authors performed a nonperturbative study of frustrated magnets for any dimension between two and four<sup>16,17,18,19</sup>. They recovered *all* known perturbative results at one loop in two and four dimensions as well as for  $N \rightarrow \infty$ . They determined  $N_c(d)$  for all  $d$  and found  $N_c(d = 3) = 5.1$ . Accordingly, for  $N = 6$ , they found a second order phase transition. Their exponents were in very good agree-

ment with those found numerically. For  $N = 3$ , they recovered<sup>17</sup> Zumbach's result — presence of a minimum in the RG flow — and improved his approach: they found pseudo-critical exponents in good agreement with *some* experimental realizations of frustrated magnets. However, regarding the spreading of the experimental and numerical data, the recourse to a minimum, leading to a *unique* set of pseudo-critical exponents, was clearly not the end of the story. During the study of the  $N = 2$  case<sup>18</sup>, the present authors realized that the property of pseudo-scaling and even more, generic pseudo-scaling, does not rely on the existence of a minimum of the flow. Pseudo-scaling appears as a consequence of the existence of a *whole region* in the flow diagram in which the flow is slow. This allowed them to account for the *nonuniversal scaling* that occurs in XY as well as in Heisenberg frustrated magnets.

In 2001, Pelissetto *et al.*<sup>10</sup> derived the six-loop series for the GLW model. They used sophisticated resummation methods in order to find the fixed points and to determine the critical exponents of the model. For  $N \gtrsim 7$ , they found a fixed point of the same nature as that obtained at large- $N$  and in the  $4-\epsilon$  expansion. Thus, a second order phase transition is expected in this case. For  $5 \lesssim N \lesssim 7$ , they considered that their resummed series were not well converged, the number of fixed points depending strongly of the number of loops considered. This led them to interpret this result as an indication that  $N_c(d=3) \sim 6$ . Finally and surprisingly, for  $N \lesssim 5$  and, in particular, for the physically relevant cases  $N = 2$  and  $N = 3$ , they found stable fixed points. Thus, a second order phase transition was also predicted in these cases. However, the critical exponents found were far from all experimental and numerical data (see the following). Moreover, regarding again the spreading of these data, an interpretation in terms of a unique set of exponents was clearly insufficient.

In another work<sup>101</sup>, assuming that  $N_c(d=2) = 2$ , Pelissetto *et al.* have reformulated the three-loop version of the series of Eq. (38) — see below — to make it compatible with this last guess. The series seemed to have better convergence properties — see however below — and allowed Pelissetto *et al.* to compute  $N_c(d)$ . They found  $N_c(d=3) = 5.3$ , in good agreement with the value —  $N_c(d=3) = 5.1$  — obtained from the NPRG approach<sup>17,19</sup>.

Recent re-investigations of the five and six-loop perturbative series<sup>11,12</sup> have led Calabrese *et al.* to conjecture that the fixed point found by Pelissetto *et al.* — that correspond to a *focus* fixed point — could explain the existence of the spreading of critical exponents encountered in frustrated magnets. Indeed, they observed that, due to the specific structure of the

fixed point, the critical exponents display strong variations along the RG trajectories that could explain the lack of universality observed experimentally and numerically. They have also given estimates of the critical number of spin components for which there is a change of the order of the phase transition. They have found that there is a first order phase transition in the whole domain  $5.7(3) < N < 6.4(4)$  and a second order phase transition for the other values of  $N$  and, in particular, for  $N = 2$  and  $N = 3$ .

Finally, a very recent computation of the five-loop  $\beta$  function of the GLW model in a  $4 - \epsilon$  expansion has lead to a novel estimation of  $N_c(d)$ . Calabrese and Parruccini<sup>102</sup> have found the value  $N_c(d = 3) = 6.1(6)$  which is compatible with the value  $N_c(d = 3) = 6.4(4)$  found within the six-loop computation performed in three dimensions<sup>11,12</sup>.

Since several aspects of the recent perturbative and nonperturbative approaches differ, in particular in their interpretations of the origin of the nonuniversal scaling found in frustrated magnets, we postpone the detailed discussion of these last developments of both methods to the following sections.

### 3.5. The perturbative situation

There are essentially two different methods to analyze the critical behavior of the system described by the Hamiltonian (9). They correspond to two different methods to deal with the constraints obeyed by the microscopic degrees of freedom, Eq. (5). They lead to the NL $\sigma$  and GLW models that have been both perturbatively analyzed around their respective critical dimension, as well as directly in  $d = 3$  for the latter model. Let us review the results of these approaches.

#### 3.5.1. The Nonlinear Sigma (NL $\sigma$ ) model approach

The idea underlying the construction of this model is to consider the system in its low-temperature — symmetry broken — phase and to take into account small fluctuations of the fields around the direction of the order parameter. The corresponding treatment is thus, by construction, a low-temperature expansion. Its actual validity is in fact less stringent than that: it is enough that the system is *locally* ordered and that the temperature is small. This explains why this approach is valid even in two dimensions for systems obeying the Mermin-Wagner theorem. Note that this approach applies — *a priori* (see Section 3.2.2 and the discussion at the end of this section) — only for  $N \geq 3$ . Indeed, in the  $N = 2$  case, the low-temperature

expansion of the NL $\sigma$  model leads to a trivial result, *i.e.* the theory is perturbatively free. This result is however not reliable since there exist topological as well as Ising-like degrees of freedom in the XY frustrated case (see Section 3.2). These degrees of freedom, that are completely missed within the low-temperature perturbative approach, drastically affect the physics at finite temperature as in the famous Berezinskii-Kosterlitz-Thouless phase transition<sup>36,37</sup>.

Within the NL $\sigma$  model approach, the partition function of the  $SO(3) \times SO(2)$ -symmetric model follows from the Hamiltonian Eq. (7) together with the constraints of Eq. (5)<sup>20</sup>:

$$\mathcal{Z} = \int \mathcal{D}\vec{\phi}_1 \mathcal{D}\vec{\phi}_2 \prod_{i \leq j} \delta(\vec{\phi}_i \cdot \vec{\phi}_j - \delta_{ij}) \exp\left(-\frac{1}{2T} \int d^d \mathbf{x} \left((\partial\tilde{\phi}_1)^2 + (\partial\tilde{\phi}_2)^2\right)\right). \quad (39)$$

The delta-functionals allow the integration of the three massive modes among the six degrees of freedom of  $\vec{\phi}_1$  and  $\vec{\phi}_2$ . Therefore, only the three — Goldstone — modes  $\vec{\pi}$  remain, in terms of which the partition function writes<sup>103,7,8</sup>:

$$Z = \int_{|\vec{\pi}| \leq 1} D\vec{\pi} \exp\left(-\frac{1}{2T} \int d^d \mathbf{x} g_{ij}(\pi) \partial\pi^i \partial\pi^j\right). \quad (40)$$

The Eq. (40), where  $g_{ij}(\pi)$  embodies the interaction, is the suitable expression for a low-temperature expansion of the  $SO(3) \times SO(2)/SO(2)$  NL $\sigma$  model.

The low-temperature expansion of such NL $\sigma$  models has been studied in general but rather abstract terms by Friedan<sup>103</sup>. The specific study of the  $SO(3) \times SO(2)/SO(2)$  model and its generalization to  $N$ -component spins — the  $O(N) \times O(2)/(O(N-2) \times O(2))$  model — has been performed by Azaria *et al.*<sup>7,8</sup> (see also Pelissetto *et al.*<sup>101</sup>). The RG analysis requires to consider the most general Hamiltonian invariant under  $O(N) \times O(2)$  and renormalizable around  $d = 2$ . This Hamiltonian involves not only the usual kinetic terms for  $\vec{\phi}_1$  and  $\vec{\phi}_2$ , Eq. (39), but also a nontrivial derivative term, called the “current-term”, which reads:

$$\int d^d \mathbf{x} \left(\tilde{\phi}_1 \cdot \partial\tilde{\phi}_2 - \tilde{\phi}_2 \cdot \partial\tilde{\phi}_1\right)^2. \quad (41)$$

This term must be included in the model since it has the right symmetry, is power-counting renormalizable around  $d = 2$  and is thus generated during the RG flow. The correct NL $\sigma$  model — in the sense of stability under RG

transformations — is given by (for any  $N \geq 3$ ) <sup>7</sup>:

$$H = \int d^d \mathbf{x} \left( \frac{\eta_1}{2} \left( \left( \partial \vec{\phi}_1 \right)^2 + \left( \partial \vec{\phi}_2 \right)^2 \right) + \left( \frac{\eta_2}{8} - \frac{\eta_1}{4} \right) \left( \vec{\phi}_1 \cdot \partial \vec{\phi}_2 - \vec{\phi}_2 \cdot \partial \vec{\phi}_1 \right)^2 \right) \quad (42)$$

where we have chosen to reparametrize the coupling constants in a way convenient for what follows. Now, the Hamiltonian of the naïve continuum limit Eq. (39) is just the initial condition of the RG flow corresponding to  $\eta_1 = \eta_2/2 = 1/T$ <sup>e</sup>.

For the special case  $N = 3$ , it is convenient to rewrite the model differently. We define, as in Eq. (16), a third vector  $\vec{\phi}_3$  by:

$$\vec{\phi}_3 = \vec{\phi}_1 \wedge \vec{\phi}_2 . \quad (43)$$

With this expression, it is easy to verify that the current-term, Eq. (41), is nothing but a linear combination of the kinetic terms of  $\vec{\phi}_1$ ,  $\vec{\phi}_2$  and  $\vec{\phi}_3$ :

$$\int d^d \mathbf{x} \left( \vec{\phi}_1 \cdot \partial \vec{\phi}_2 - \vec{\phi}_2 \cdot \partial \vec{\phi}_1 \right)^2 = 2 \int d^d \mathbf{x} \left( \left( \partial \vec{\phi}_1 \right)^2 + \left( \partial \vec{\phi}_2 \right)^2 - \left( \partial \vec{\phi}_3 \right)^2 \right). \quad (44)$$

One can then gather the three vectors  $\vec{\phi}_1$ ,  $\vec{\phi}_2$  and  $\vec{\phi}_3$  into a  $3 \times 3$  matrix:

$$\Phi = \left( \vec{\phi}_1, \vec{\phi}_2, \vec{\phi}_3 \right) . \quad (45)$$

Since  $(\vec{\phi}_1, \vec{\phi}_2, \vec{\phi}_3)$  are three orthonormal vectors, one has  ${}^t \Phi \Phi = \mathbb{1}$  and  $\Phi$  is therefore a  $SO(3)$  matrix.

The partition function thus reads:

$$\mathcal{Z} = \int \mathcal{D}\Phi \delta({}^t \Phi \Phi - \mathbb{1}) e^{- \int d^d \mathbf{x} \text{Tr} (\mathcal{P} \partial {}^t \Phi \partial \Phi)} \quad (46)$$

where  $\mathcal{P}$  is a diagonal matrix of coupling constants:  $\mathcal{P} = \text{diag}(p_1 = p_2 = \eta_2/4, p_3 = \eta_1/2 - \eta_2/4)$ .

It is easy to check on Eq. (46) that the model is invariant under the right transformation:

$$\Phi \rightarrow \Phi \cdot V \quad (47)$$

with  $V$  being the subset of  $SO(3)$  matrices that commute with  $\mathcal{P}$ . When  $p_3 \neq p_1$ , i.e.  $\eta_1 \neq \eta_2$ ,  $V$  is isomorphic to  $SO(2)$ . When  $\mathcal{P}$  is proportional to

---

<sup>e</sup>We have included the temperature in the coupling constants.

the identity,  $V$  is isomorphic to the whole  $SO(3)$  group. In this last case, the high-temperature symmetry group is  $G = SO(3) \times SO(3) \sim SO(4)$ . Note that this identity has to be understood at the level of the Lie algebras since  $SO(3) \times SO(3)$  and  $SO(4)$  are locally isomorphic but differ globally and have different topological properties.

The RG equations for the  $O(N) \times O(2)/(O(N-2) \times O(2))$  model have been computed at two-loop order in  $d = 2 + \epsilon$ <sup>7,8</sup>. We recall here the one-loop result:

$$\begin{cases} \beta_{\eta_1} = -(d-2)\eta_1 + N - 2 - \frac{\eta_2}{2\eta_1} \\ \beta_{\eta_2} = -(d-2)\eta_2 + \frac{N-2}{2} \left(\frac{\eta_2}{\eta_1}\right)^2 \end{cases} \quad (48)$$

A fixed point is found for any  $N \geq 3$ . For  $N = 3$ , it corresponds to  $p_1^* = p_3^*$ , *i.e.*  $\eta_1^* = \eta_2^*$ , and thus to an enlarged symmetry:  $SO(3) \times SO(3)/SO(3) \sim SO(4)/SO(3)$ . This fixed point has only one direction of instability — the direction of the temperature — and thus corresponds to a second order phase transition. Surprisingly, the critical behavior is thus predicted to be governed by the usual ferromagnetic Wilson-Fisher fixed point with the subtlety that it corresponds to *four-component* spins. This situation corresponds precisely to the particular case considered in Section 3.2.2 (see in particular the discussion following Eq.(20)). Another subtlety is that since, here, the order parameter is a matrix instead of a vector — it is a  $SO(4)$  tensor — the anomalous dimension is different from the usual anomalous dimension of the four-component vector model. Only the exponent  $\nu$  is independent of the nature of the order parameter and is thus identical to the usual value of  $\nu$  of the Wilson-Fisher  $N = 4$  universality class<sup>7,8</sup>.

In fact, it is easy to convince oneself that this fixed point exists at all order of perturbation theory. Actually, the crucial fact is that, in  $d = 2 + \epsilon$ , the *perturbative*  $\beta$  functions of a NL $\sigma$  model associated with the symmetry breaking scheme  $G \rightarrow H$  only depend on the *local geometrical* structure of the manifold  $G/H$  which is itself determined by the Lie algebras of  $G$  and  $H$ <sup>7,8</sup>. Since the Lie algebras of  $SO(3) \times SO(3)$  and of  $SO(4)$  are identical, the perturbative  $\beta$  function for the — remaining — coupling constant of the model with  $p_1 = p_3$  is identical at all orders to the perturbative  $\beta$  function of the usual  $SO(4)/SO(3)$  NL $\sigma$  model. The existence of a fixed point for the  $SO(3) \times SO(3)/SO(3)$  NL $\sigma$  model at all order of perturbation theory follows from the fact that its existence makes no doubt for the  $SO(4)/SO(3)$  NL $\sigma$  model. At the time of the first investigation of the  $O(N) \times O(2)/(O(N-2) \times O(2))$  model, the most natural position was to extend this equivalence

beyond perturbation theory and to assume that the  $SO(3) \times SO(3)/SO(3)$  fixed point exists everywhere between two and four dimensions, as it is the case for the  $SO(4)/SO(3)$  fixed point. This was, in particular, the position advocated by Azaria *et al.*<sup>7,8</sup>.

The outstanding fact is that although the  $SO(4)$  behavior has indeed been seen numerically in  $d = 2$ <sup>24,28</sup>, it actually does *not exist* far from two dimensions. This is clear since *no* such fixed point is found in  $d = 4 - \epsilon$  and since, as already emphasized, the  $SO(4)$  behavior is not seen in any numerical or experimental data in  $d = 3$ . It is thus extremely probable that either the NL $\sigma$  model fixed point disappears in a nontrivial dimension smaller than 3 or it survives in  $d = 3$  while being no longer the usual  $N = 4$  fixed point. Note that, in the first case, its  $SO(4)$  nature can also change before it disappears. Anyway, this fixed point must disappear below  $d = 4$ . The situation is thus more involved than in the “usual”  $SO(4)/SO(3)$  model. There must exist nonperturbative reasons explaining the disappearance of the fixed point and/or the loss of its  $SO(4)$  character.

Actually, it is clear that the perturbative low-temperature expansion performed on the NL $\sigma$  model misses several nonanalytic terms in  $T$  — typically terms that behave as  $\exp(-1/T)$  — that could be responsible for the disappearance of the fixed point and/or its change of nature. There are, at least, two origins for such terms.

1) The first one consists in the nontrivial topological configurations — see the discussion in Section (3.2.2) following Eq. (15) — that are neglected in the low-temperature expansion of the NL $\sigma$  models. Indeed this expansion relies, by construction, on the local geometrical properties of the manifold  $G/H$  and is insensitive to its global — topological — structure. Thus it ignores vortex-like configurations that likely play an important role in three dimensions.

2) The second origin of nonanalytic corrections to the low-temperature  $\beta$  function is more technical. The low-temperature expansion is performed in terms of the Goldstone — or pseudo-Goldstone in  $d = 2$  — modes that are represented by fields constrained to have a modulus less than one, see Eq. (40). This inequality cannot be taken into account in the perturbative treatment<sup>104</sup> and is thus relaxed, leading to neglect terms of order  $\exp(-1/T)$ . All these terms are negligible for the critical behavior when the critical temperature is very small, which is the case near  $d = 2$ . However, they become important when  $T_c \sim 1$  which is typically the case in  $d = 3$ .

### 3.5.2. The Ginzburg-Landau-Wilson (GLW) model approach

The GLW model for the  $O(N) \times O(2)/(O(N-2) \times O(2))$  model can be deduced from a generalization of Eq. (39) to  $N$ -component vectors, by replacing the functional delta-constraint by the most general potential that favors the field configurations obeying the initial constraint. For convenience, we choose to parametrize it by:

$$\prod_{i \leq j} \delta(\vec{\phi}_i \cdot \vec{\phi}_j - \delta_{ij}) \rightarrow e^{-U} \quad (49)$$

with:

$$U = \int d^d \mathbf{x} \left( \frac{r}{2} (\vec{\phi}_1^2 + \vec{\phi}_2^2) + \frac{\lambda + \mu}{16} (\vec{\phi}_1^2 + \vec{\phi}_2^2)^2 - \frac{\mu}{4} (\vec{\phi}_1^2 \vec{\phi}_2^2 - (\vec{\phi}_1 \cdot \vec{\phi}_2)^2) \right) \quad (50)$$

where, as usual,  $r$  is proportional to the reduced temperature while  $\lambda$  and  $\mu$  are  $\phi^4$ -like coupling constants.

All field-dependent terms in Eq. (50) can be rewritten in terms of the rectangular matrix  $\Phi$  defined in Eq. (8). The corresponding Hamiltonian then reads:

$$H = \int d^d \mathbf{x} \left( \frac{1}{2} \text{Tr} (\partial^t \Phi \partial \Phi) + \frac{r}{2} \rho + \frac{\lambda}{16} \rho^2 + \frac{\mu}{4} \tau \right) \quad (51)$$

with  $\rho = \text{Tr}(\Phi^t \Phi)$  and  $\tau = \frac{1}{2} \text{Tr} (\Phi^t \Phi - \mathbb{1} \rho/2)^2$  being the only  $O(N) \times O(2)$  independent invariants that can be built out the fields. Note that minimizing the term in front of  $\mu$  corresponds to imposing  $\Phi^t \Phi \propto \mathbb{1}$ , *i.e.* to imposing that  $\vec{\phi}_1$  and  $\vec{\phi}_2$  are orthogonal and of same norm, in agreement with the characteristics of the ground state of frustrated magnets — see Fig. 3.1b.

#### 3.5.2.1. The RG flow

The RG equations for the coupling constants entering in Hamiltonian (51) have been computed in the  $\epsilon = 4 - d$ -expansion up to five-loop order<sup>102</sup> and in a weak-coupling expansion in  $d = 3$  up to six-loop order<sup>10</sup>. We recall here only the one-loop result of the  $\epsilon$ -expansion to discuss qualitatively the flow diagram:

$$\begin{cases} \beta_\lambda = -\epsilon \lambda + \frac{1}{16\pi^2} (4\lambda\mu + 4\mu^2 + \lambda^2(N+4)) \\ \beta_\mu = -\epsilon \mu + \frac{1}{16\pi^2} (6\lambda\mu + N\mu^2) . \end{cases} \quad (52)$$

As well-known, for any  $N > N_c(d = 4 - \epsilon) = 21.8 + O(\epsilon)$  there exist four fixed points: the Gaussian —  $G$  — the vector  $O(2N)$  —  $V$  — and two others called the chiral —  $C_+$  — and anti-chiral —  $C_-$  — fixed points. Among these fixed points one,  $C_+$ , is stable and governs the critical properties of the system and the others are unstable (see Fig. 3.2a). When, at a given dimension  $d$  close to four,  $N$  is decreased,  $C_+$  and  $C_-$  move closer together, coalesce at  $N_c(d)$  and then disappear (see Fig. 3.2b). More precisely, for  $N < N_c(d)$ , the roots of the  $\beta$  functions acquire an imaginary part. Since no stable fixed point exists below  $N_c(d)$  and since the flow drives the system in a region of instability, it is believed that the transition is of first order. Note that for  $N < N'_c(d = 4 - \epsilon) = 2.2 + O(\epsilon)$ ,  $C_+$  and  $C_-$  reappear but not in the physically relevant region to frustrated magnets.

For completeness we give the exponent  $\nu$  at one-loop:

$$\nu = \frac{1}{2} + \frac{(N-3)(N+4)\sqrt{48-24N+N^2} + N(48+N+N^2)}{8(144-24N+4N^2+N^3)} \epsilon \quad (53)$$

and recall that the anomalous dimension vanishes at this order. Note that the square root becomes complex for  $2.2 < N < 21.8$ , which is reminiscent of the critical values  $N_c(d)$  and  $N'_c(d)$  of the number of spin components, see above.

### 3.5.2.2. The three and five-loop results in $d = 4 - \epsilon$

In  $4-\epsilon$  dimensions, the critical value  $N_c(d)$  has been computed at three-loop order <sup>99</sup> and, very recently, at five-loop order <sup>102</sup>:

$$N_c(d = 4 - \epsilon) = 21.80 - 23.43\epsilon + 7.09\epsilon^2 - 0.03\epsilon^3 + 4.26\epsilon^4 + O(\epsilon^5). \quad (54)$$

In fact, as it is often the case within this kind of expansion, the series are not well behaved and it is difficult to obtain reliable results even after resummation <sup>99,94,102</sup>. We however indicate the value found at three-loop order <sup>99</sup>:  $N_c(d = 3) = 3.39$  and at five-loop order <sup>102</sup>:  $N_c(d = 3) = 5.45$ .

### 3.5.2.3. The improved three and five-loop results

It has been conjectured by Pelissetto *et al.* <sup>101</sup> that  $N_c(d = 2) = 2$ , a result which is however somewhat controversial <sup>102</sup>. It is possible to use this nonperturbative information to reformulate the series obtained within the  $4-\epsilon$  expansion. Imposing the constraint  $N_c(d = 2) = 2$  to the three-loop series, Pelissetto *et al.* have obtained <sup>101</sup>:

$$N_c(d = 4 - \epsilon) = 2 + (2 - \epsilon)(9.90 - 6.77\epsilon + 0.16\epsilon^2) + O(\epsilon^3). \quad (55)$$

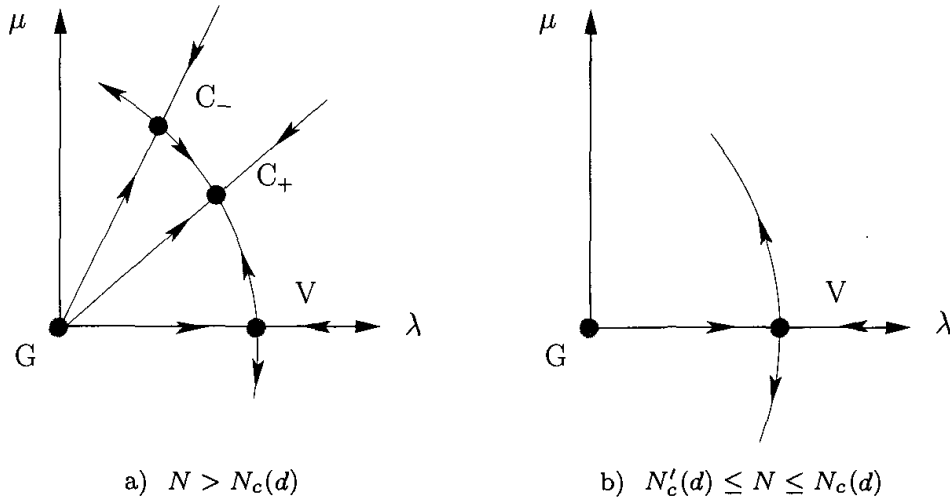


Fig. 3.2. Flow diagram for a)  $N$  above  $N_c(d)$  and b)  $N$  below  $N_c(d)$ . The fixed points  $C_+$  and  $C_-$  that exist above  $N_c(d)$  coalesce at  $N_c(d)$  and then disappear.  $G$  and  $V$  are the Gaussian and vector  $O(2N)$  fixed points.

Reformulated in this way, the coefficients of the series decrease rapidly. It is thus reasonable to use this expression to estimate  $N_c(d = 3)$ . Pelissetto *et al.* have thus obtained <sup>101</sup>:  $N_c(d = 3) = 5.3(2)$  where the error bar indicates how  $N_c(d = 3)$  varies from two to three loops. However, Calabrese and Parruccini have shown that, extended to five loops, the same series behaves badly <sup>102</sup>:

$$N_c(d = 4 - \epsilon) = 2 + (2 - \epsilon)(9.90 - 6.77\epsilon + 0.16\epsilon^2 + 0.06\epsilon^3 + 2.16\epsilon^4) + O(\epsilon^5). \quad (56)$$

Using different kinds of tricks, notably the inverse of the series, they have obtained, from the five-loop series, the value  $N_c(d = 3) = 6.1(6)$ .

### 3.5.2.4. The three-loop results in $d = 3$

A weak-coupling analysis has been performed by Antonenko and Sokolov <sup>98</sup> directly in  $d = 3$  at three-loop order. This leads to  $N_c(d = 3) = 3.91$ . However, as already emphasized, this result is not well converged.

### 3.5.2.5. The large- $N$ results

The large- $N$  expansion was first performed by Bailin *et al.* <sup>9</sup>. It was then re-examined by Kawamura <sup>6</sup> and Pelissetto *et al.* <sup>101</sup>. A fixed point is found within this expansion in all dimensions between 2 and 4. The exponents  $\nu$

and  $\eta$  have been computed up to order  $1/N^2$  in  $d = 3$ <sup>101</sup>:

$$\begin{cases} \nu = 1 - \frac{16}{\pi^2} \frac{1}{N} - \left( \frac{56}{\pi^2} - \frac{640}{3\pi^4} \right) \frac{1}{N^2} + O(1/N^3) \\ \eta = \frac{4}{\pi^2} \frac{1}{N} - \frac{64}{3\pi^4} \frac{1}{N^2} + O(1/N^3) . \end{cases} \quad (57)$$

Around  $d = 4$  and  $d = 2$  the perturbative results of, respectively, the GLW and NL $\sigma$  models are recovered once the limit  $N \rightarrow \infty$  has been performed. This suggests that, at least for sufficiently large  $N$ , the two models belong indeed to the same universality class in all dimensions. However, within this approach, no  $N_c(d)$  line is found (see however Pelissetto *et al.*<sup>101</sup>). It is thus impossible to extrapolate to finite  $N$  the results obtained within this approach.

### 3.5.2.6. The six-loop results in $d = 3$

In three dimensions, a six-loop computation has been performed by Pelissetto *et al.*<sup>10</sup> and re-examined by Calabrese *et al.*<sup>11,12</sup>, see below. The results are the following:

- 1) For  $N$  sufficiently large —  $N > 6.4(4)$  — there exist four fixed points, one stable and three unstable, in agreement with the usual picture given above, see Fig. 3.2. The transition is thus of second order.
- 2) For  $5.7(3) < N < 6.4(4)$ , there is no nontrivial fixed point and the transition is expected to be of first order.
- 3) For  $N < 5.7(3)$  and, in particular, for  $N = 2$  and  $N = 3$  a *stable fixed point* is found and a second order phase transition is expected.

According to Pelissetto *et al.*<sup>10,101</sup>, the fixed points found for  $N = 2$  and  $N = 3$  should be non analytically connected with those found in the  $1/N$  and  $4 - \epsilon$  approaches. Therefore, it should be impossible to obtain them by following smoothly those obtained at large- $N$  or close to  $d = 4$ .

The critical exponents obtained by Pelissetto *et al.* are given in Table 3.6. Let us discuss them.

*The XY case.* First, one should indicate that the exponents  $\gamma$  and  $\nu$

Table 3.6. The six-loop perturbative results in  $d = 3$  by Pelissetto *et al.*<sup>10</sup>

System	$\alpha$	$\beta$	$\gamma$	$\nu$
XY	0.29(9)	0.31(2)	1.10(4)	0.57(3)
Heisenberg	0.35(9)	0.30(2)	1.06(5)	0.55(3)

computed from the six-loop approach compare reasonably well with the data of group 1. However, as already mentioned, the value of  $\eta$  found by the scaling relations must be positive when there exists a fixed point. One finds, with the data of Table 3.6,  $\eta \sim 0.08$  which is significantly positive. Let us recall that this is *not* the case for the experiments performed on the materials of group 1 and for the numerical simulations performed on STA. Note, moreover, that the value of  $\beta$  found within the six-loop calculation is very far — around four theoretical error bars — from the average experimental ones which are  $\beta = 0.228(6)$  for  $\text{CsMnBr}_3$  alone, and  $\beta = 0.237(4)$  for the whole group 1. It is also far from the numerical values obtained for STA:  $\beta = 0.24 - 0.25$ . Thus, contrarily to what is asserted by Pelissetto *et al.*<sup>10</sup>, it seems extremely improbable that the exponents found at six-loop order could fit with those of group 1 and with those of the numerical STA model. Actually, this is also the case for the materials of group 2 for which the average  $\beta$  is  $\beta = 0.389(7)$ .

*The Heisenberg case.* First, one notes that the agreement between the  $\gamma$  and  $\nu$  exponents obtained from the six-loop approach and from the experimental or numerical data is not as good as it is in the XY case. Concerning  $\eta$ , one finds, with the data of Table 3.6,  $\eta \sim 0.08$ . This has to be compared with the value of  $\eta$  obtained *i*) for the materials of group 1, which is significantly negative —  $\eta = -0.118(25)$  — *ii*) for materials of group 2, which is marginally negative —  $\eta = -0.018(33)$  — and *iii*) in the simulations of the STA which is also negative although not completely significantly:  $\eta = -0.0182(89)$ . The negativity of  $\eta$  is a first indication of a mismatch between the six-loop result and the data for the Heisenberg systems even if it cannot be used as a definitive argument against a second order phase transition. The exponent  $\gamma$  obtained from the numerical simulations of the Heisenberg STA model provides a further information. Its average value —  $\gamma = 1.185(3)$  — is rather far — 2.5 theoretical error bars — from the six-loop result<sup>f</sup>.

From the previous analysis one can conclude that, as such, the fixed point obtained within the six-loop approach turns out to be *not* directly relevant to the phenomenology of XY and Heisenberg materials or simulated systems.

---

<sup>f</sup>This result would be almost unchanged if the numerical error bar — and especially the one quoted in Mailhot *et al.*<sup>88</sup> — was largely underestimated since it would surely be much less than the theoretical one.

### 3.5.3. The six-loop results in $d = 3$ re-examined

In order to cope with the discrepancy between the six-loop results obtained by Pelissetto *et al.* and the experimental and numerical data, Calabrese *et al.* have reconsidered the resummed six-loop series<sup>11,12,13</sup>. They claim that they can account for the unusual properties of the critical exponents for XY and Heisenberg frustrated systems in  $d = 3$  — negative anomalous dimension and weak universality — by the fact that the RG trajectories around the stable — focus — fixed point found at six-loop by Pelissetto *et al.* are spiral-like, see Fig. 3.3.

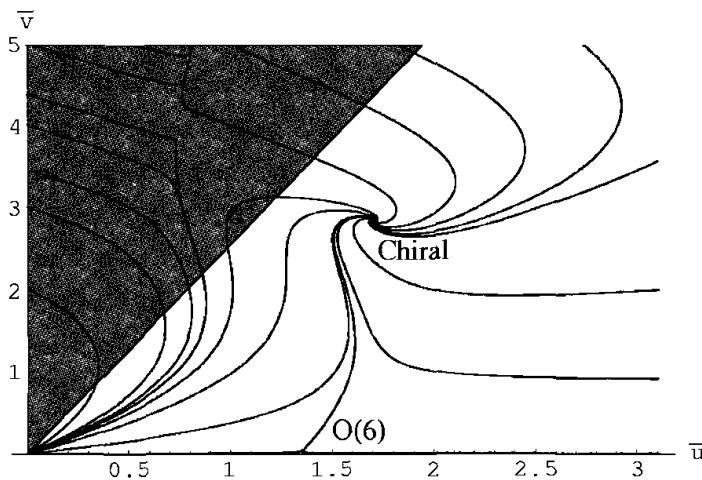


Fig. 3.3. RG flow for  $N = 3$ . (From Calabrese *et al.*<sup>11</sup>.)

In practice, Calabrese *et al.* have integrated the resummed  $\beta$  functions for the two coupling constants  $(\bar{u}, \bar{v})$  of the GLW model and computed the effective exponents  $\eta(\bar{u}, \bar{v})$  and  $\nu(\bar{u}, \bar{v})$  along the RG trajectories. They have found that these exponents display large variations in a transient regime, see Fig. 3.4. These authors then argue that the scaling properties of the system are governed over several decades of temperature by the preasymptotic regime so that the effective exponents observed experimentally can differ significantly from their asymptotic values, *i.e.* those defined at the fixed point.

Let us underline here several drawbacks concerning this scenario.

First, it is based on the existence of stable fixed points that are not related to any already known fixed point. In particular, the fixed points found for  $N = 2$  and  $N = 3$  within this computation in  $d = 3$  are, according

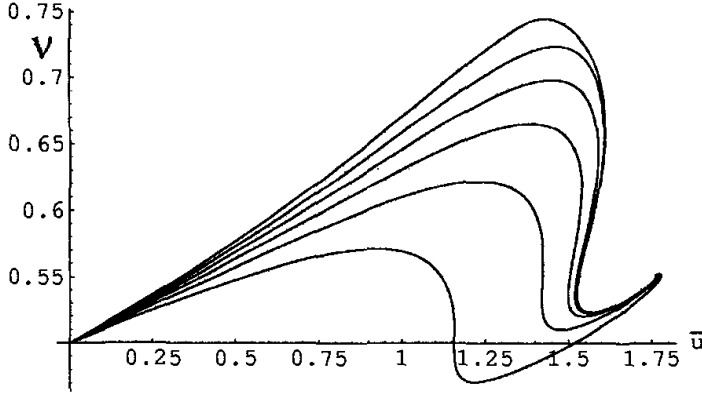


Fig. 3.4. Effective exponent  $\nu$  for  $N = 3$  along RG trajectories as function of the effective coupling constant  $\tilde{u}$  for different initial conditions. (From Calabrese *et al.*<sup>11</sup>.)

to Pelissetto *et al.* and Calabrese *et al.*, *non analytically* related to those found in the large- $N$  as well as in the  $4 - \epsilon$  expansions. This means that there is no way to check their existence using these perturbative methods. This is specifically problematic in the context of frustrated magnets where the properties of the fixed points appear to be very unusual: *i*) the existence of the stable fixed points strongly depends on the order of perturbation — they are not present at three-loop order and only show up, as far as we know, at five-loop order *ii*) the location of the fixed points, as  $N$  and  $d$  are varied, seems to have, in the  $(N, d)$  plane, a very particular structure since, in three dimensions, they only exist when  $N$  is below *another* critical value of  $N$  — which is found to be equal to 5.7(3).

Second, it is very difficult, in the computation of Calabrese *et al.*, to relate the initial conditions of the RG flow to the microscopic characteristics of real systems. This would require to handle the infinity of coupling constants entering into the microscopic Hamiltonian obtained from the Hubbard-Stratonovitch transformation. This is impossible, at least within the usual perturbation theory.

Third, it is very difficult to account, in this framework, for the first order behavior deduced from the numerical simulations of Itakura<sup>72</sup>. We have also already noticed that XY-systems have a stronger tendency to undergo first order transitions than Heisenberg systems. However, there is no natural explanation for this phenomenon in the scenario of Calabrese *et al.*.

Fourth, in this scenario, it is also very difficult to explain why there

is no physical system characterized by the asymptotic critical exponents, *i.e.* those corresponding the fixed point found by Pelissetto *et al.*. This seems to require very unnatural experimental circumstances such that the initial conditions of the flow corresponding to the physical realizations of frustrated magnets are very close to the Gaussian fixed point in such a way that their long distance properties are *never* controlled by the nontrivial fixed point.

Finally, there is no possible explanation of the breakdown of the NL $\sigma$  model predictions.

### 3.5.3.1. Conclusion

XY and Heisenberg frustrated magnets represent systems for which the perturbative results obtained within a low-temperature expansion around two dimensions, within a weak-coupling expansion around four dimensions or within a large- $N$  expansion fail to describe their critical physics in three dimensions. Moreover, these different perturbative predictions are in contradiction with each other. Contrarily to the  $O(N)$  nonfrustrated case, there is no possible smooth interpolation of these results between two and four dimensions and, at fixed dimension, between  $N = \infty$  and  $N = 2, 3$ . More surprisingly, and again in contradiction with what happens in the  $O(N)$  nonfrustrated case, high-order calculations performed directly in  $d = 3$  also fail to reproduce the phenomenology when they are interpreted in the usual way. This situation reveals the difficulties of the conventional approaches to tackle with the physics of frustrated magnets. Only new interpretations or methods can allow to shed light on the problems encountered here. We have presented the solution proposed by Calabrese *et al.* on the basis of a high-order perturbative calculation and underlined its difficulties. We now present the nonperturbative method which has been used by the present authors to explain the unusual behavior of frustrated magnets.

## 3.6. The effective average action method

### 3.6.1. The effective average action equation

Recently the present authors, following the pioneering work of Zumbach<sup>14,74,15</sup>, have used a nonperturbative method to investigate the physics of frustrated magnets. They have used the effective average action method that has allowed them to smoothly interpolate between the  $d = 2$  and  $d = 4$  results and, therefore, to understand the mismatch between the NL $\sigma$  and

the GLW model approaches. This method has also allowed them to improve the determination of pseudo-critical exponents found by Zumbach in three dimensions for Heisenberg system. But the main feature of this approach is that it has allowed to show that the property of pseudo-scaling encountered in frustrated magnets does not, in general, rely on the concept of minimum of the flow or pseudo-fixed point introduced by Zumbach. In fact, pseudo-scaling appears as a consequence of the existence of a *whole region* in the flow diagram in which the flow is slow. This has allowed the present authors to account for and to reproduce the *nonuniversal scaling* that occurs in XY as well as in Heisenberg frustrated magnets.

The effective average action method <sup>105,106,107,108,109</sup>, as well as many other NPRG techniques, is based on the well-known concept of “block spin” <sup>110,111,112</sup>: when dealing with any strongly correlated system, it is fruitful to integrate out the fluctuations step by step and, more precisely, scale by scale. In practice, one first gathers the initial — microscopic — degrees of freedom into small “blocks”. It is then possible, at least formally, to integrate out, in the partition function of the system, the internal fluctuations of the blocks. This “decimation” is followed by a rescaling of length-scales, coupling constants and fields. In this way, starting from a “bare” GLW Hamiltonian, one gets an effective Hamiltonian for the block degrees of freedom, *i.e.* for the low-energy modes. By iterating this procedure, one generates a sequence of — scale-dependent — effective hamiltonians, parametrized by a running scale  $k$ , that all share the same long-distance physics. This sequence defines a Wilsonian RG flow <sup>112</sup>. At a fixed point of this flow, the system displays scale invariance. This allows to obtain the critical quantities through an analysis of the neighborhood of the fixed point in the flow of effective Hamiltonians <sup>112</sup>.

Although it has been originally formulated in terms of Hamiltonians, the most recent and successful implementation of the block spin idea in the continuum involves the effective (average) action <sup>108,113,114</sup>. In the same way as in the original Wilson’s approach, one builds a *running* Gibbs free energy  $\Gamma_k$ , also called effective average action <sup>108</sup>, that only includes high-energy fluctuations with momenta  $q^2 > k^2$ . This implies that, on the one hand, at the underlying microscopic scale  $k = \Lambda$ ,  $\Gamma_k$  coincides with the classical Hamiltonian  $H$  since no fluctuation has yet been taken into account. On the other hand, when the running scale is lowered to  $k = 0$ , *i.e.* when *all* fluctuations have been integrated out, the standard Gibbs free energy  $\Gamma$  is recovered. To summarize,  $\Gamma_k$  continuously interpolates between the

microscopic Hamiltonian  $H$  and the free energy  $\Gamma$ :

$$\begin{cases} \Gamma_{k=\Lambda} = H \\ \Gamma_{k=0} = \Gamma . \end{cases} \quad (58)$$

Let us consider, for simplicity, the case of a system described, *at a typical microscopic scale*  $\Lambda$ , by a scalar field  $\zeta(\mathbf{x})$ . The construction of the effective average action proceeds in two steps. First, one should decouple the low-energy modes — with momenta  $\mathbf{q}^2 > \mathbf{k}^2$  — in the partition function in order to get a theory involving only the high-energy ones that will be summed over. Second, in this modified theory, one builds the Gibbs free energy by a Legendre transform. This gives  $\Gamma_k$ . Let us now study how this is implemented in practice.

The first step is conveniently implemented by changing the partition function  $\mathcal{Z}$  into  $\mathcal{Z}_k$  for which a  $k$ -dependent term, quadratic in the fields and thus analogous to a mass-term is added to the microscopic Hamiltonian<sup>108,109</sup>. With this “mass-term”, the partition function in presence of a source  $J$  writes:

$$\mathcal{Z}_k[J] = \int \mathcal{D}\zeta \exp \left( -H[\zeta] - \Delta H_k[\zeta] + J \cdot \zeta \right) \quad (59)$$

with  $J \cdot \zeta = \int d^d\mathbf{q} \mathbf{J}(\mathbf{q})\zeta(-\mathbf{q})$  and

$$\Delta H_k[\zeta] = \frac{1}{2} \int \frac{d^d\mathbf{q} d^d\mathbf{q}'}{(2\pi)^{2d}} \mathcal{R}_k(\mathbf{q}, \mathbf{q}') \zeta(\mathbf{q}) \zeta(\mathbf{q}') \quad (60)$$

$$= \frac{1}{2} \int \frac{d^d\mathbf{q}}{(2\pi)^d} R_k(\mathbf{q}^2) \zeta(\mathbf{q}) \zeta(-\mathbf{q}) \quad (61)$$

with  $\mathcal{R}_k(\mathbf{q}, \mathbf{q}') = (2\pi)^d \delta(\mathbf{q} + \mathbf{q}') \mathbf{R}_k(\mathbf{q}^2)$ . In Eq.(61),  $R_k(\mathbf{q}^2)$  is the cut-off function that controls the separation between the low- and high-energy modes. To decouple the low-energy modes, it must act as a large-mass term for small  $\mathbf{q}$  whereas it must vanish for large  $\mathbf{q}$  to keep unchanged the high-energy sector of the theory. Thus:

$$R_k(\mathbf{q}^2) \sim k^2 \quad \text{for} \quad \mathbf{q}^2 \ll k^2 \quad (62)$$

and

$$R_k(\mathbf{q}^2) \rightarrow 0 \quad \text{when} \quad \mathbf{q}^2 \gg k^2 . \quad (63)$$

The first constraint means that, for momenta lower than  $k$ ,  $R_k(\mathbf{q}^2)$  essentially acts as a mass — *i.e.* an IR cut-off — which prevents the propagation of the low-energy modes. The second ensures that the high-energy modes

are fully taken into account in  $\mathcal{Z}_k[J]$  and thus in the effective average action. Moreover, since we want to recover the original theory when  $k \rightarrow 0$ , *i.e.* when all fluctuations have been integrated out,  $R_k(\mathbf{q}^2)$  must vanish in this limit. Thus one requires:

$$R_k(\mathbf{q}^2) \rightarrow 0 \text{ identically when } \mathbf{k} \rightarrow \mathbf{0} \quad (64)$$

which ensures that  $\mathcal{Z}_{k=0}[J] = \mathcal{Z}[J]$ . On the other hand, when  $k \rightarrow \Lambda$ , *i.e.* when no fluctuation has been integrated out,  $\Gamma_k$  should coincide with the microscopic Hamiltonian. This is achieved by requiring (see below for the proof):

$$R_k(\mathbf{q}^2) \rightarrow \infty \text{ identically when } \mathbf{k} \rightarrow \mathbf{\Lambda}. \quad (65)$$

Note that, since we shall not be interested in the precise relation between the microscopic characteristics — defined at scale  $\Lambda$  — of a given system and its critical or pseudo-critical properties, we set  $\Lambda = \infty$  in the following.

A widely used cut-off function is provided by <sup>115</sup>:

$$R_k(\mathbf{q}^2) = \frac{Z\mathbf{q}^2}{e^{\mathbf{q}^2/k^2} - 1} \quad (66)$$

where  $Z$  is the field renormalization. Including it in  $R_k$  allows to suppress the explicit  $Z$  dependence in the final RG equations. The cut-off function  $R_k(\mathbf{q}^2)$  corresponding to Eq. (66) is plotted on Fig. 3.5. Another useful

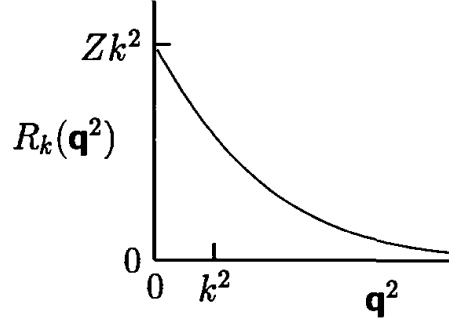


Fig. 3.5. A typical realization of the separation of high- and low-momentum modes provided by the cut-off function  $R_k(\mathbf{q}^2)$ . At low momentum,  $R_k(\mathbf{q}^2)$  acts as an effective mass of order  $Zk^2$  while the high-momentum behavior is not modified.

cut-off function has been proposed by Litim <sup>116</sup>. It writes:

$$R_k(\mathbf{q}^2) = Z(k^2 - \mathbf{q}^2) \Theta(k^2 - \mathbf{q}^2) \quad (67)$$

where  $\Theta$  is the usual step function.

The second step consists in defining the effective average action. The free energy at scale  $k$  is given — up to a factor  $-k_B T$  — by:

$$W_k[J] = \ln \mathcal{Z}_k[J] . \quad (68)$$

From (68), one defines the order parameter  $\phi_k(\mathbf{q})$  at scale  $k$  as the average value of the microscopic field  $\zeta(\mathbf{q})$  in the modified theory:

$$\phi_k(\mathbf{q}) = \langle \zeta(\mathbf{q}) \rangle = \frac{\delta \mathbf{W}_k[\mathbf{J}]}{\delta \mathbf{J}(-\mathbf{q})} . \quad (69)$$

Thanks to the properties of  $R_k(\mathbf{q}^2)$ , the contribution to the average value in Eq. (69) coming from modes with momenta  $\mathbf{q}^2 \ll \mathbf{k}^2$  is strongly suppressed. Also,  $\phi_k(\mathbf{q})$  identifies with the true order parameter in the limit  $k \rightarrow 0$ . Note that, for simplicity, we omit, in the following, the index  $k$  to  $\phi_k$ .

The effective average action is defined by <sup>108</sup>:

$$\Gamma_k[\phi] = -W_k[J] + J.\phi - \Delta H_k[\phi] \quad (70)$$

where  $J = J[\phi]$ , see Eq. (69). Thus  $\Gamma_k[\phi]$  essentially corresponds to a Legendre transform of  $W_k[J]$  for the macroscopic field  $\phi$  — up to the mass-like term  $\Delta H_k$ . The relation (70) implies several unconventional relations. First, taking its derivative with respect to  $\phi(\mathbf{q})$  provides the relation between the source and  $\Gamma_k[\phi]$ :

$$J(-\mathbf{q}) = \frac{\delta \Gamma_k}{\delta \phi(\mathbf{q})} + \int \frac{d^d q'}{(2\pi)^{2d}} \mathcal{R}_k(\mathbf{q}, \mathbf{q}') \phi(\mathbf{q}') . \quad (71)$$

Taking the derivative of this relation with respect to  $\phi(\mathbf{q}')$  implies a second important relation:

$$\Gamma_k^{(2)}(\mathbf{q}, \mathbf{q}') + \frac{\mathcal{R}_k(\mathbf{q}, \mathbf{q}')}{(2\pi)^{2d}} = \frac{\delta J(-\mathbf{q})}{\delta \phi(\mathbf{q}')} = (2\pi)^{-2d} \left( \frac{\delta^2 W_k}{\delta J(\mathbf{q}) \delta \mathbf{J}(\mathbf{q}')} \right)^{-1} \quad (72)$$

where  $\Gamma_k^{(2)}(\mathbf{q}, \mathbf{q}') = \delta^2 \Gamma_k / \delta \phi(\mathbf{q}) \delta \phi(\mathbf{q}')$ .

Let us now show that the definition of  $\Gamma_k$ , Eq. (70), ensures that it indeed interpolates between the microscopic Hamiltonian  $H$  for  $k = \infty$  and the (true) effective action  $\Gamma$  for  $k \rightarrow 0$ , see Eq.(58). This last property follows directly from Eq.(70) and the fact that for  $k = 0$  the IR cut-off  $R_k(\mathbf{q}^2)$  identically vanishes. The fact that  $\Gamma_k$  identifies with  $H$  when  $k \rightarrow \infty$  can be shown in the following way. One has from Eqs. (59), (68), (70) and (71) the functional identity:

$$e^{-\Gamma_k[\phi]} = \int \mathcal{D}\zeta \exp \left( -H[\zeta] + \frac{\delta \Gamma_k[\phi]}{\delta \phi} \cdot (\zeta - \phi) - \Delta H_k[\zeta - \phi] \right) . \quad (73)$$

In the limit  $k \rightarrow \infty$ ,  $R_k(\mathbf{q}^2)$  goes to infinity. In this limit, the mass-term  $\exp(-\Delta H_k[\zeta - \phi])$  acts as a hard constraint on the functional integration —  $\exp(-\Delta H_k[\zeta - \phi]) \simeq \delta[\zeta - \phi]$  — so that  $\Gamma_{k=\infty}[\phi] = H[\phi]$ . With these properties,  $\Gamma_k[\phi]$  has the meaning of a coarse-grained Gibbs free energy at scale  $k^{-1}$ : lowering  $k$  corresponds to including more and more fluctuations.

The effective average action  $\Gamma_k$  follows an exact equation which controls its evolution when the running scale  $k$  is lowered, *i.e.* when more and more (low-energy) fluctuations are integrated out<sup>108,117,109,114</sup>:

$$\partial_t \Gamma_k[\phi] = \frac{1}{2} \int \frac{d^d \mathbf{q}}{(2\pi)^d} \dot{R}_k(\mathbf{q}^2) \text{Tr} \left( (2\pi)^{2d} \Gamma_k^{(2)}[\phi] + \mathcal{R}_k \right)^{-1} (\mathbf{q}, -\mathbf{q}) \quad (74)$$

with  $t = \ln k/\Lambda$  and  $\dot{R}_k = \partial_t R_k$ . In Eq. (74), Tr must be understood as a trace on internal indices — vectorial or tensorial — if  $\zeta$  spans a nontrivial representation of a group.

The equation (74) defines a RG flow for the effective action  $\Gamma_k$  analogous to the RG flow of effective Hamiltonians provided by the Wilson-Kadanoff block spin procedure.

### 3.6.2. Properties

We now give some important properties of Eq. (74). The reader interested in more details can consult the review of Berges *et al.*<sup>115</sup>.

1) Eq. (74) is *exact*. It thus contains all perturbative<sup>118,119</sup> and non-perturbative features of the underlying theory: weak- or strong-coupling behaviors, tunneling between different minima<sup>120</sup>, bound states<sup>121,122</sup>, topological excitations<sup>123</sup>, etc.

2) While it is written here in the case of a one-component scalar field theory, Eq. (74) obviously holds for any number of components and, more generally, for any kind of order parameter. The extension to fermions is also trivial (see the review of Berges *et al.*<sup>115</sup>, for instance).

3) With a cut-off function  $R_k(\mathbf{q}^2)$  which meets the condition (62) or, more generally, with a finite limit when  $\mathbf{q}^2 \rightarrow 0$ , the integral in Eq. (74) is infrared (IR) *finite* for any  $k > 0$ . This IR finiteness is ensured by the presence of the mass-term  $R_k$  which makes the quantity  $\Gamma_k^{(2)}[\phi] + R_k$  positive for  $k > 0$  even *at* the critical temperature. This allows to explore the low-temperature phase even in presence of massless — Goldstone — modes. From the UV side, the finiteness of the integral in Eq. (74) is ensured by a requirement of fast decaying behavior of  $\dot{R}_k(\mathbf{q}^2)$ .

4) One can give a graphical representation of Eq. (74), see Fig. 3.6. It displays a *one-loop* structure. Obviously, this one-loop structure must not

be mistaken for that of a weak-coupling expansion. Actually, the loop involves here the *full* — *i.e.* field-dependent — inverse propagator  $\Gamma_k^{(2)}[\phi]$  so that the graphical representation of Fig. 3.6 implicitly contains *all* powers of the coupling constants entering in the model. Note also that this one-loop structure automatically ensures that all integrals over internal momenta involved in this formalism have a one-loop structure and are thus one-dimensional. Thus they can be easily evaluated numerically and, when some particular cut-off are used, analytically. This radically differs from a weak-coupling expansion which leads to multiple loop diagrams and thus, multiple integrals. Another important feature of Eq. (74) is that very simple *ansätze* on  $\Gamma_k$  allow to recover in a unique framework the one-loop perturbative results obtained by standard perturbative calculations around two and four dimensions as well as in a large- $N$  expansion.

$$\partial_t \Gamma_k = \frac{1}{2} \quad \text{Diagram: a circle with a cross inside}$$

Fig. 3.6. A graphical representation of Eq. (74). The cross represents the function  $\dot{R}_k$  and the line the propagator  $(\Gamma_k^{(2)}(\phi) + R_k)^{-1}$ .

### 3.6.3. Truncations

Unfortunately Eq. (74) is too complicated to be solved exactly. As a consequence, the functional  $\Gamma_k$  has to be truncated. Different kinds of truncations have been considered <sup>109</sup>:

1) Field expansion where  $\Gamma_k$  is expanded in powers of the order parameter  $\phi$ . For a scalar field theory, one has:

$$\Gamma_k[\phi] = \sum_{n=0}^{\infty} \frac{1}{n!} \int \prod_{i=0}^n d^d \mathbf{x}_i \phi(\mathbf{x}_1) \dots \phi(\mathbf{x}_n) \Gamma_k^{(n)}(\mathbf{x}_1, \dots, \mathbf{x}_n) \quad (75)$$

where  $\Gamma_k^{(n)}(\mathbf{x}_1, \dots, \mathbf{x}_n)$  denotes the  $n$ -th functional derivative of  $\Gamma_k$ .

2) Derivative expansion where  $\Gamma_k$  is expanded in powers of the derivatives of the order parameter. Still for a scalar field theory, one has:

$$\Gamma_k[\phi] = \int d^d \mathbf{x} \left( U_k(\phi) + \frac{1}{2} Z_k(\phi) (\partial \phi)^2 + O(\partial^4) \right) \quad (76)$$

$U_k(\phi)$  being the potential — *i.e.* derivative-independent — part of  $\Gamma_k$  while  $Z_k(\phi)$  corresponds to the kinetic term. The physical motivation for such an

expansion in which one neglects high-order derivative terms is that since the anomalous dimension  $\eta$  is small, these terms should not drastically affect the physics.

3) Combined derivative and field expansions where one further expands, in Eq.(76), the functions  $U_k(\phi)$  and  $Z_k(\phi)$  in powers of  $\phi$  around a given field configuration  $\phi_0$ . Technically, this kind of approximation allows to transform the functional equation (74) into a set of ordinary coupled differential equations for the coefficients of the expansion. In practice, it is interesting to consider an expansion around (one of) the field configuration  $\phi_0$  that minimizes the potential  $U_k$ . For the simplest — Ising — model, this expansion writes:

$$\Gamma_k[\phi] = \int d^d x \left( \frac{1}{2} U''_k(\tilde{\rho}_0)(\rho - \tilde{\rho}_0)^2 + \frac{1}{3!} U'''_k(\tilde{\rho}_0)(\rho - \tilde{\rho}_0)^3 + \dots \right. \\ \left. + \frac{1}{2} Z'_k(\tilde{\rho}_0)(\partial\phi)^2 + \frac{1}{2} Z''_k(\tilde{\rho}_0)(\rho - \tilde{\rho}_0)(\partial\phi)^2 + \dots \right) \quad (77)$$

where  $\tilde{\rho} = \frac{1}{2}\phi^2$  and  $\tilde{\rho}_0 = \frac{1}{2}\phi_0^2$ . In Eq.(77), the quantity  $\phi_0$  has the meaning of a magnetization at scale  $k$ . The rational behind the choice (77) is that the minimum of  $U_k$  is physically the location that one wants to describe the best since thermodynamical quantities at vanishing external field are determined from the minimum of  $U_k$  at  $k = 0$ . The relevance of such a parametrization is confirmed by many works showing that the convergence of the critical quantities, when more and more powers of the field  $\phi$  are added in the truncation, is improved when compared with the same calculation performed with an expansion of  $U_k(\rho)$  and  $Z_k(\rho)$  around the  $\phi = 0$  configuration<sup>124,125</sup>.

The choice of a good truncation is a complex problem. One has to choose a manageable truncation that however encodes the relevant physics. In practice, it appears that, surprisingly, even at low-orders in powers of derivatives and fields, Eq. (74) provides correct qualitative features of the RG flow. However, the precise determination of the critical quantities requires to push the expansion to rather large orders in the field and involves a heavy algebra<sup>126,116,17,127,128</sup>.

### **3.6.4. Principle of the calculation**

We do not enter in the details of the computation of the RG flow that have been given in several articles<sup>105,106,109,115</sup> and thus only indicate the four steps of the procedure.

*i)* First, one defines the running coupling constants entering in  $\Gamma_k$  from functional derivatives of the *ansatz* of  $\Gamma_k$ . The coupling constants are defined as (combinations of) functional derivatives of  $\Gamma_k$  — the “vertex functions” — taken in a specific field-configuration of the model, for instance the minimum of the potential  $\phi_0$ .

*ii)* One then applies the operator  $\partial_t$  on these definitions. This is implemented by the use of the evolution equation (74). The flow equations for the coupling constants are then expressed as traces of products of vertex functions that are evaluated from the *ansatz* for  $\Gamma_k$ , which is given, in the case of a scalar theory, by Eq. (77).

*iii)* The flow equations involve integrals over the internal momentum. It is convenient to express these integrals as dimensionless functions, known as threshold functions<sup>109</sup> that embody the nonperturbative content of the model.

*iv)* Also, as usual, one introduces dimensionless renormalized quantities to study the scale invariant solutions of the RG equations.

### 3.6.5. The $O(N) \times O(2)$ model

We now consider frustrated magnets in this framework. As already said, since the NPRG equation (74) cannot be solved exactly, a truncation for  $\Gamma_k$  is needed. The present authors<sup>18,19</sup> have used truncations involving terms having at most two derivatives. At this order, the most general form of the  $O(N) \times O(2)$  effective average action writes<sup>19</sup>:

$$\begin{aligned} \Gamma_k[\vec{\phi}_1, \vec{\phi}_2] = & \int d^d \mathbf{x} \left( \mathbf{U}_{\mathbf{k}}(\rho, \tau) + \frac{1}{2} \mathbf{Z}_{\mathbf{k}}(\rho, \tau) \left( (\partial \vec{\phi}_1)^2 + (\partial \vec{\phi}_2)^2 \right) \right. \\ & + \frac{1}{4} Y_k^{(1)}(\rho, \tau) \left( \vec{\phi}_1 \cdot \partial \vec{\phi}_2 - \vec{\phi}_2 \cdot \partial \vec{\phi}_1 \right)^2 + \frac{1}{4} Y_k^{(2)}(\rho, \tau) \left( \vec{\phi}_1 \cdot \partial \vec{\phi}_1 + \vec{\phi}_2 \cdot \partial \vec{\phi}_2 \right)^2 \\ & \left. + \frac{1}{4} Y_k^{(3)}(\rho, \tau) \left( \left( \vec{\phi}_1 \cdot \partial \vec{\phi}_1 - \vec{\phi}_2 \cdot \partial \vec{\phi}_2 \right)^2 + \left( \vec{\phi}_1 \cdot \partial \vec{\phi}_2 + \vec{\phi}_2 \cdot \partial \vec{\phi}_1 \right)^2 \right) \right). \end{aligned} \quad (78)$$

We recall that  $\vec{\phi}_1$  and  $\vec{\phi}_2$  are the two  $N$ -component vectors that constitute the order parameter  $\Phi = (\vec{\phi}_1, \vec{\phi}_2)$  while  $\rho = \text{Tr}({}^t \Phi \cdot \Phi)$  and  $\tau = \frac{1}{2} \text{Tr}({}^t \Phi \cdot \Phi - \mathbb{1} \rho/2)^2$  are the two independent  $O(N) \times O(2)$  invariants. Here  $U_k(\rho, \tau)$  is the potential part of the effective average action while  $Z_k(\rho, \tau)$  and  $Y_k^{(i)}(\rho, \tau)$  are kinetic functions. The *ansatz* (78) can be simplified by expanding all the functions in powers of the fields around a non-vanishing field configuration which minimizes  $U_k$ . This last constraint is

satisfied when  $\vec{\phi}_1$  and  $\vec{\phi}_2$  are orthogonal, with the same norm. One can choose a particular configuration:

$$\Phi^{\text{Min}}(\mathbf{x}) = \sqrt{\tilde{\kappa}} \begin{pmatrix} 1 & 0 \\ 0 & 1 \\ 0 & 0 \\ \vdots & \vdots \\ 0 & 0 \end{pmatrix} \quad (79)$$

the physical results being, of course, independent of this particular choice. The quantity  $\sqrt{\tilde{\kappa}}$  entering in (79) is analogous to the amplitude of the magnetization  $\phi_0$  in the Ising case — see Eq.(77). While studying the critical properties of frustrated systems, the present authors have considered various truncations combining derivative and field expansions and differing by the number of monomials in  $\rho$  and  $\tau$  included in the field expansion. In order to keep our presentation concise here, we present only the simple truncation<sup>17,19</sup>:

$$\begin{aligned} \Gamma_k[\vec{\phi}_1, \vec{\phi}_2] = & \int d^d \mathbf{x} \left( \frac{\mathbf{Z}}{2} \left( (\partial \vec{\phi}_1)^2 + (\partial \vec{\phi}_2)^2 \right) + \frac{\tilde{\omega}}{4} (\vec{\phi}_1 \cdot \partial \vec{\phi}_2 - \vec{\phi}_2 \cdot \partial \vec{\phi}_1)^2 \right. \\ & \left. + \frac{\tilde{\lambda}}{4} \left( \frac{\rho}{2} - \tilde{\kappa} \right)^2 + \frac{\tilde{\mu}}{4} \tau \right) . \end{aligned} \quad (80)$$

The set  $\{\tilde{\kappa}, \tilde{\lambda}, \tilde{\mu}, Z, \tilde{\omega}\}$  denotes the scale-dependent coupling constants that parametrize the model at this order of the truncation. The first quantity in Eq.(80) corresponds to the standard kinetic term while the third and fourth correspond to the potential part. Actually, apart from the second term — called the current term —,  $\Gamma_k$  in Eq.(80) looks very much like the usual GLW Hamiltonian used to study perturbatively the critical physics of the  $O(N) \times O(2)$  model, up to trivial reparametrizations, see Eq.(51). There is however a fundamental difference since, here,  $\Gamma_k$  is *not* studied within a weak-coupling perturbative approach. This allows the presence of the current term which corresponds to a nonstandard kinetic term. This term is irrelevant by power counting around four dimensions since it is quartic in the fields and quadratic in derivatives. However, its presence is *necessary* around two dimensions to recover the results of the low-temperature approach of the NL $\sigma$  model since it contributes to the field renormalization of the Goldstone modes. Being not constrained by the usual power counting one includes this term in the ansatz.

### 3.6.5.1. The flow equations

To write the flow equations, one has to introduce the dimensionless renormalized quantities defined as:

$$\begin{cases} \kappa = Z k^{2-d} \tilde{\kappa} \\ \lambda = Z^{-2} k^{d-4} \tilde{\lambda} \\ \mu = Z^{-2} k^{d-4} \tilde{\mu} \\ \omega = Z^{-2} k^{d-2} \tilde{\omega} . \end{cases} \quad (81)$$

We do not provide the details of the computation. The general technique is given in several publications and its implementation on the specific  $O(N) \times O(2)$  model has been given by the present authors<sup>19</sup>. The  $\beta$  functions for the different coupling constants entering in (80) are given by<sup>17,19</sup>:

$$\begin{aligned} \beta_\kappa &= -(d-2+\eta)\kappa + 4v_d \left[ \frac{1}{2} l_{01}^d(0,0,\kappa\omega) + (N-2)l_{10}^d(0,0,0) + \frac{3}{2} l_{10}^d(\kappa\lambda,0,0) \right. \\ &\quad \left. + (1+2\frac{\mu}{\lambda}) l_{10}^d(\kappa\mu,0,0) + \frac{\omega}{\lambda} l_{01}^{2+d}(0,0,\kappa\omega) \right] \\ \beta_\lambda &= (d-4+2\eta)\lambda + v_d \left[ 2\lambda^2 (N-2)l_{20}^d(0,0,0) + \lambda^2 l_{02}^d(0,0,\kappa\omega) + 9\lambda^2 l_{20}^d(\kappa\lambda,0,0) \right. \\ &\quad \left. + 2(\lambda+2\mu)^2 l_{20}^d(\kappa\mu,0,0) + 4\lambda\omega l_{02}^{2+d}(0,0,\kappa\omega) + 4\omega^2 l_{02}^{4+d}(0,0,\kappa\omega) \right] \\ \beta_\mu &= (d-4+2\eta)\mu - 2v_d\mu \left[ -\frac{2}{\kappa} l_{01}^d(0,0,\kappa\omega) + \frac{3(2\lambda+\mu)}{\kappa(\mu-\lambda)} l_{10}^d(\kappa\lambda,0,0) + \frac{8\lambda+\mu}{\kappa(\lambda-\mu)} l_{10}^d(\kappa\mu,0,0) \right. \\ &\quad \left. + \mu l_{11}^d(\kappa\mu,0,\kappa\omega) + \mu(N-2)l_{20}^d(0,0,0) \right] \\ \eta &= -\frac{d \ln Z}{dt} = 2 \frac{v_d}{d\kappa} \left[ (4-d)\kappa\omega l_{01}^d(0,0,\kappa\omega) + 2\kappa^2\omega^2 l_{02}^{2+d}(0,0,\kappa\omega) + 2m_{02}^d(0,0,\kappa\omega) \right. \\ &\quad \left. - 4m_{11}^d(0,0,\kappa\omega) + 2(-2+d)\kappa\omega l_{10}^d(0,0,0) + 2m_{20}^d(0,0,\kappa\omega) \right. \\ &\quad \left. + 2\kappa^2\lambda^2 m_{2,2}^d(\kappa\lambda,0,0) + 4\kappa^2\mu^2 m_{2,2}^d(\kappa\mu,0,0) \right. \\ &\quad \left. + 4\kappa\omega n_{02}^d(0,0,\kappa\omega) - 8\kappa\omega n_{11}^d(0,0,\kappa\omega) + 4\kappa\omega n_{20}^d(0,0,\kappa\omega) \right] \quad (82) \\ \beta_\omega &= (d-2+2\eta)\omega + \frac{4v_d}{d\kappa^2} \left[ \kappa\omega \left\{ \frac{(4-d)}{2} l_{01}^d(0,0,\kappa\omega) + \frac{(d-16)}{2} l_{01}^d(\kappa\lambda,0,\kappa\omega) + \right. \right. \\ &\quad \left. \left. \kappa\omega l_{02}^{2+d}(0,0,\kappa\omega) - 3\kappa\omega l_{02}^{2+d}(\kappa\lambda,0,\kappa\omega) + (d-2)l_{10}^d(0,0,0) - \right. \right. \\ &\quad \left. \left. (d-8)l_{10}^d(\kappa\lambda,0,0) + 8\kappa\lambda l_{11}^d(\kappa\lambda,0,\kappa\omega) + 2\kappa\omega l_{20}^{2+d}(\kappa\mu,0,0) + \right. \right. \\ &\quad \left. \left. 2\kappa\omega(N-2)l_{20}^{2+d}(0,0,0) \right\} + m_{02}^d(0,0,\kappa\omega) - m_{02}^d(\kappa\lambda,0,\kappa\omega) - \right. \\ &\quad \left. 2m_{11}^d(0,0,\kappa\omega) + 2m_{11}^d(\kappa\lambda,0,\kappa\omega) + m_{20}^d(0,0,\kappa\omega) - m_{20}^d(\kappa\lambda,0,\kappa\omega) + \right. \\ &\quad \left. \kappa^2\lambda^2 m_{22}^d(\kappa\lambda,0,0) + 2\kappa^2\mu^2 m_{22}^d(\kappa\mu,0,0) + 2\kappa\omega n_{02}^d(0,0,\kappa\omega) - \right. \\ &\quad \left. 4\kappa\omega n_{02}^d(\kappa\lambda,0,\kappa\omega) - 4\kappa\omega n_{11}^d(0,0,\kappa\omega) + 8\kappa\omega n_{11}^d(\kappa\lambda,0,\kappa\omega) + \right. \\ &\quad \left. 2\kappa\omega n_{20}^d(0,0,\kappa\omega) - 4\kappa\omega n_{20}^d(\kappa\lambda,0,\kappa\omega) \right] \end{aligned}$$

In the previous set of equations appear the dimensionless functions  $l_{n1,n2}^d(w_1, w_2, a)$ ,  $m_{n1,n2}^d(w_1, w_2, a)$ ,  $n_{n1,n2}^d(w_1, w_2, a)$ , called threshold functions. They encode the nonperturbative content of the flow equations (82).

They are complicated integrals over momenta and are given by <sup>17,19</sup>:

$$\begin{aligned} l_{n_1, n_2}^d(w_1, w_2, a) &= -\frac{1}{2} \int_0^\infty dy y^{d/2} \frac{\eta r + 2yr'}{(P_1 + w_1)^{n_1} (P_2 + w_2)^{n_2}} \left( \frac{n_1}{P_1 + w_1} + \frac{n_2}{P_2 + w_2} \right) \\ n_{n_1, n_2}^d(w_1, w_2, a) &= -\frac{1}{2} \int_0^\infty dy y^{d/2} \frac{1}{(P_1 + w_1)^{n_1} (P_2 + w_2)^{n_2}} \left( y(1+a+r+yr')(\eta r + 2yr') \right. \\ &\quad \left. \cdot \left( \frac{n_1}{P_1 + w_1} + \frac{n_2}{P_2 + w_2} \right) - \eta(r+yr') - 2y(2r'+yr'') \right) \quad (83) \\ m_{n_1, n_2}^d(w_1, w_2, a) &= -\frac{1}{2} \int_0^\infty dy y^{d/2} \frac{1+a+r+yr'}{(P_1 + w_1)^{n_1} (P_2 + w_2)^{n_2}} \left( y(1+a+r+yr')(\eta r + 2yr') \right. \\ &\quad \left. \cdot \left( \frac{n_1}{P_1 + w_1} + \frac{n_2}{P_2 + w_2} \right) - 2\eta(r+yr') - 4y(2r'+yr'') \right) \end{aligned}$$

where one has introduced:

$$P_1 = P_1(y, a) = y(1 + r(y) + a) \quad (84)$$

$$P_2 = P_2(y, a) = y(1 + r(y)) \quad (85)$$

$$r(y) = \frac{R_k(yk^2)}{Zk^2y} \quad (86)$$

### 3.6.6. Tests of the method and first results

This section is devoted to all possible tests of the NPRG method as well as new results obtained with it <sup>17,19</sup>.

1) Around  $d = 4$ , one easily checks that, in the limit of small coupling constant  $\lambda$  and  $\mu$ , the set of equations (82) degenerates in that obtained from the weak-coupling expansion at one-loop:

$$\begin{cases} \beta_\lambda = -\epsilon\lambda + \frac{1}{16\pi^2} (4\lambda\mu + 4\mu^2 + \lambda^2(N+4)) \\ \beta_\mu = -\epsilon\mu + \frac{1}{16\pi^2} (6\lambda\mu + N\mu^2) \\ \beta_\kappa = -(2-\epsilon)\kappa + \frac{l_1^4(0)}{8\pi^2} \left( N + 1 + \frac{2\mu}{\lambda} \right) - \frac{3\kappa\lambda}{16\pi^2} - \frac{\kappa\mu}{8\pi^2} \left( 1 + \frac{2\mu}{\lambda} \right) \end{cases} \quad (87)$$

from which one can deduce, for instance, the expression of  $\nu$  at order  $\epsilon = 4 - d$ . It, of course, coincides with the one-loop result of Eq. (53).

2) Also, around  $d = 2$ , performing a low-temperature expansion of the equations (82):

$$\begin{cases} \beta_\kappa = -(d-2+\eta)\kappa + \frac{N-2}{2\pi} + \frac{1}{4\pi(1+\kappa\omega)} \\ \beta_\omega = (-2+d+2\eta)\omega + \frac{1+\kappa\omega+(N-1)\kappa^2\omega^2+(N-2)\kappa^3\omega^3}{2\pi\kappa^2(1+\kappa\omega)} \\ \eta = \frac{3+4\kappa\omega+2\kappa^2\omega^2}{4\pi\kappa(1+\kappa\omega)} \end{cases} \quad (88)$$

and making the change of variables:

$$\begin{cases} \eta_1 = 2\pi\kappa \\ \eta_2 = 4\pi\kappa(1 + \kappa\omega) \end{cases} \quad (89)$$

one recovers the NL $\sigma$  model  $\beta$  functions at one-loop order, Eq.(48).

3) The nonperturbative equations (82) allow to recover the critical exponents at leading order in  $1/N$ . The present authors have computed  $\eta$  and  $\nu$  for a large range of values of  $N$  and have compared their results with those calculated perturbatively at order  $1/N^2$ , Eq. (57). They have found an excellent agreement — better than 1% — for  $\nu$ , *for all*  $N > 10$ , see Fig. 3.7, a domain of values of  $N$  where one expects the  $1/N^2$  results to be very close to the exact values. We also quote, in Table 3.7, the NPRG

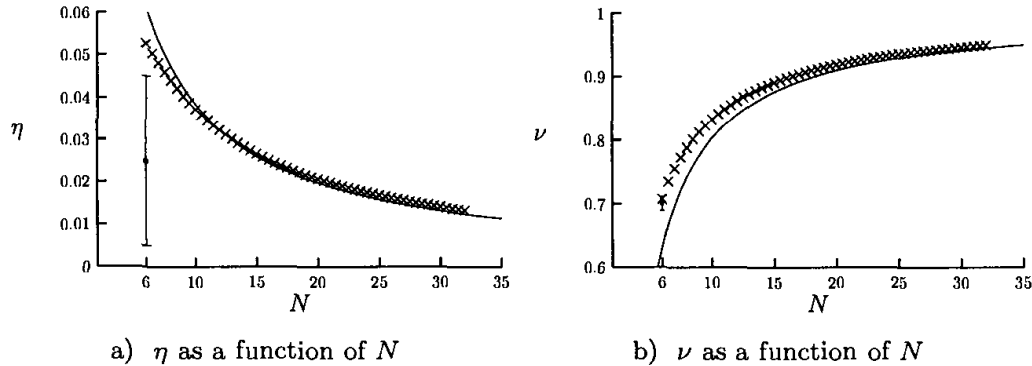


Fig. 3.7. The exponents  $\eta$  and  $\nu$  as functions of  $N$  in  $d = 3$ . The crosses represent the NPRG results and the full line the values obtained from the  $1/N$  expansion, Eqs.(57). The circles and error bars are the Monte Carlo results obtained for  $N = 6$ <sup>94</sup>.

results and those obtained by the six-loop calculation for the cases  $N = 16$  and  $N = 32$ .

4) Let us now discuss the curve  $N_c(d)$  that separates the regions of

Table 3.7. Exponents  $\nu$  and  $\eta$  computed from the  $1/N$  expansion, by the NPRG method and from the six-loop calculation.

$N$	Method	$\nu$	$\eta$
16	$1/N^{101}$	0.885	0.0245
	NPRG <sup>19</sup>	0.898	0.0252
	six-loop	0.858(4) <sup>10</sup> , 0.863(4) <sup>12</sup>	0.0246(2) <sup>12</sup>
32	$1/N^{101}$	0.946	0.0125
	NPRG <sup>19</sup>	0.950	0.0134
	six-loop	0.936(2) <sup>10</sup> , 0.936(1) <sup>12</sup>	0.01357(1) <sup>12</sup>

first and second order. The present authors have computed  $N_c(d)$  with their best truncation — involving ten powers of the fields — and with the cut-off function (67). In Fig. 3.8, we give the result obtained from the NPRG<sup>19</sup> together with the improved three-loop result given by Eq.(56) for comparison<sup>g</sup>. The two curves agree quite well. Note that it is probably a coincidence that the curves cross very close to  $d = 3$ . In this dimension, the NPRG method leads to  $N_c(d = 3) \simeq 5.1$  and the improved three loop result:  $N_c(d = 3) \simeq 5.3(2)$ . Let us emphasize that, within the NPRG method, the quantity  $N_c(d)$  is very sensitive to the order of the truncation<sup>129</sup>, much more than the exponents. This means that one probably should not consider the previous results as very reliable. In this respect, we recall the result obtained by means of the six-loop calculation of Calabrese *et al.*<sup>12</sup>:  $N_c(d = 3) = 6.4(4)$  and by means of the  $4 - \epsilon$  expansion at five-loop order<sup>102</sup>:  $N_c(d = 3) \simeq 6.1(6)$ .

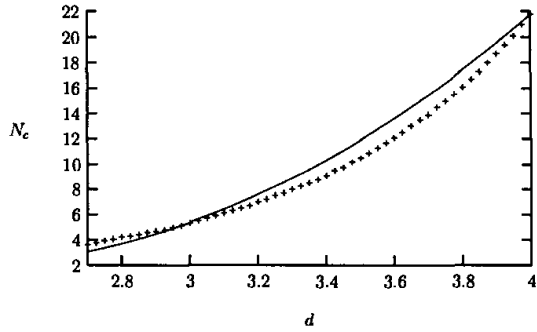


Fig. 3.8. The full line represents the curve  $N_c(d)$  obtained by the three-loop result improved by the constraint  $N_c(d = 2) = 2$ , Eq. (56). The crosses represent the NPRG calculation<sup>19</sup>.

5) Let us now consider the consequences of the NPRG approach for the NL $\sigma$  model predictions. The very probable existence of a line  $N_c(d)$  going from  $d = 2$  to  $d = 4$  confirms what has been already anticipated in Section 3.5: the predictions based on this approach are incorrect as for the physics in  $d = 3$ . Indeed, the shape of this line implies that the  $O(4)$  fixed point found in the NL $\sigma$  model approach disappears very probably between two and three dimensions. Actually, following this fixed point, called  $C_+$  for an obvious reason, from  $d = 2$  to  $d = 4$  with the simplest  $\phi^4$ -like truncation, the

<sup>g</sup>Note that, due to artefact of the field expansion performed at order  $\phi^{10}$ , is not possible to follow the chiral fixed point  $C_+$  in dimensions typically between  $d = 2.5$  and  $d = 2.1$  and thus to determine reliably the curve  $N_c(d)$  in these dimensions. This artefact could be overcome by keeping the full field dependence of the effective potential  $U(\rho, \tau)$ .

present authors have found several interesting features. First, infinitesimally close to  $d = 2$ , one finds that  $C_+$  is characterized by an exponent  $\nu$  of the  $O(4)$  universality class. Second, as  $d$  is increased, the exponent  $\nu$  associated with  $C_+$  becomes more and more different from that characterizing an  $O(4)$  transition. Third, one finds that an unstable fixed point, called  $C_-$ , shows up in a dimension  $d > 2$ . As the dimension is further increased, the fixed points  $C_+$  and  $C_-$  get closer together and eventually coalesce in a dimension less than three. This phenomenon is illustrated in Fig (3.9) in the case of the  $O(3) \times O(3)$  model at the lowest order in the field expansion <sup>16</sup>.

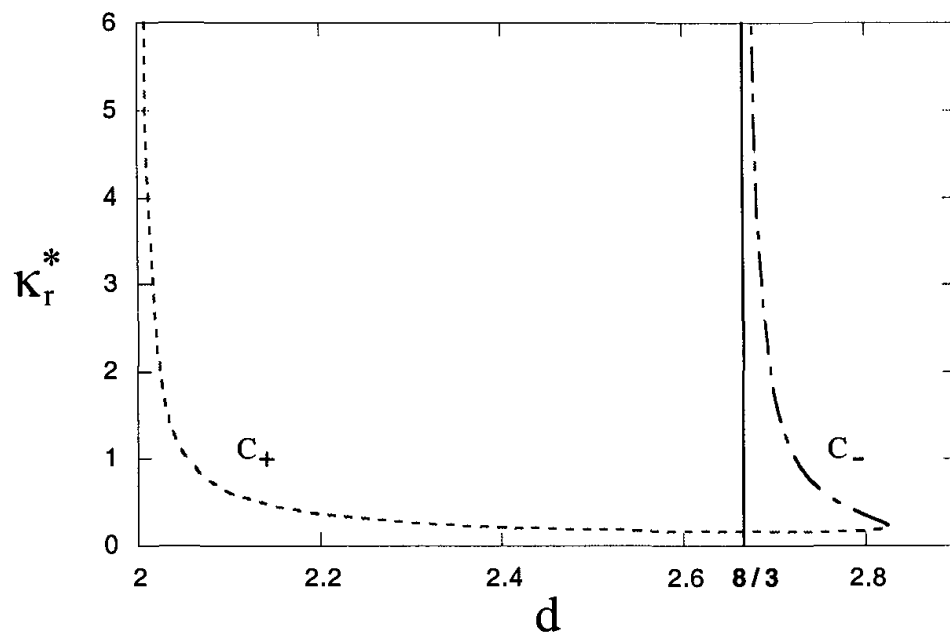


Fig. 3.9. The stable —  $C_+$  — and unstable —  $C_-$  — fixed points as functions of the dimension  $d$ . The fixed points are parametrized by the quantity  $\kappa_r^*$  which is proportional to the inverse temperature of the NL $\sigma$  model. The fixed point  $C_-$  appears in a dimension  $8/3$  in the simplest truncation and collapses with the stable fixed point  $C_+$  in  $d \simeq 2.83$ .

The collapse of the fixed points for different values of  $N$  generates the curve  $N_c(d)$ . This curve is well known from the perturbative expansion performed around four dimensions. Within the NPRG approach, this curve can be followed when the dimension is lowered down to  $d = 2$ . There, for a given — low — value of  $N$ , the curve  $N_c(d)$  provides the value of  $d_c(N)$  for which the stable fixed point obtained within the NL $\sigma$  model approach collapses with another — unstable — fixed point. Since this unstable fixed point is *not* found in the low-temperature perturbative expansion one there-

fore obtains a nonperturbative solution to the breakdown of the  $\text{NL}\sigma$  model approach. For  $N = 3$ , one gets  $d_c \simeq 2.8$  which fits well with the results of Pelissetto *et al.*<sup>101</sup>, see Fig. 3.8.

6) As already said, for  $N = 6$ <sup>94</sup>, the transition is either of second order or of extremely weakly of first order. In both cases, scaling should exist on a large domain of temperature. For the best truncation used by the present authors, the data are given in Table 3.8. Note that  $\nu$  and  $\eta$  are computed directly while  $\gamma$ ,  $\beta$  and  $\alpha$  are computed using the scaling relations. The

Table 3.8. The exponents for  $N = 6$  obtained from the NPRG — first line — and from the Monte Carlo (MC) simulation — second line.

Method	$\alpha$	$\beta$	$\gamma$	$\nu$	$\eta$
NPRG <sup>18,19</sup>	-0.121	0.372	1.377	0.707	0.053
MC <sup>94</sup>	-0.100(33)	0.359(14)	1.383(36)	0.700(11)	0.025(20)

NPRG results agree very well with the numerical ones. In particular, the error on  $\nu$ , which is as usual the best determined exponent, is only 1%. This constitutes a success of the NPRG approach from the methodological point of view.

7) Finally, let us discuss the search, within the NPRG method, of fixed points in  $d = 3$  and for  $N < N_c(d = 3) \simeq 5.1$ . We recall that, for this critical value of  $N$ , the two fixed points  $C_+$  and  $C_-$  — see Fig. 3.2 — coalesce. This means that these fixed points — that can be followed smoothly in the  $(d, N)$  plane from the gaussian in  $d = 4$  — cease to be real below this value of  $N$ . However, this does not imply the absence of other real fixed points. One has to test the existence of fixed points non trivially connected with  $C_+$  and  $C_-$ , as advocated by Pelisstto *et al.*<sup>10</sup>. The present authors have thus looked for such fixed points both by directly looking for zeroes of the  $\beta$ -functions and by integrating numerically the RG flow — see below. After an intensive search, they have found *no* such fixed point. This result will be discussed in the following.

We are now in a position to discuss the physics of frustrated magnets in three dimensions.

### 3.6.7. *The physics in $d = 3$ according to the NPRG approach*

We now discuss the physics in three dimensions. Let us start by studying the physics corresponding to values of  $N$  just below  $N_c(d)$ .

### 3.6.7.1. The physics in $d = 3$ just below $N_c(d)$ : scaling with a pseudo-fixed point and minimum of the flow

In a fixed dimension  $d$ , the disappearance of the nontrivial fixed points  $C_+$  and  $C_-$ , when  $N$  crosses  $N_c(d)$ , could seem to be an abrupt process: the two fixed points collapse and disappear. Actually, when extended to the space of complex coupling constants, this process is continuous since the only change is that, when going from  $N > N_c(d)$  to  $N < N_c(d)$ , the fixed points acquire a small complex part<sup>14</sup>. This continuous character manifests itself as smooth changes of the RG flow that can be explained thanks to continuity arguments.

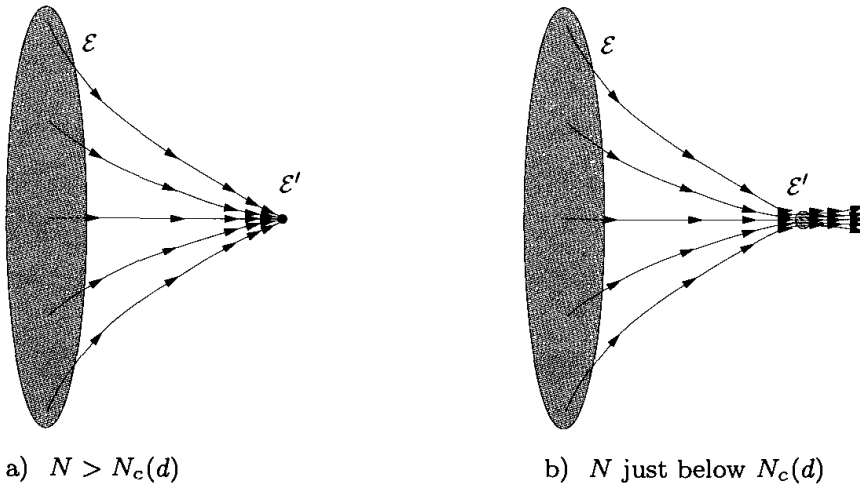


Fig. 3.10. Schematic representation of the flow for  $N$  above and just below  $N_c(d)$ . For the sake of clarity, we have represented  $\mathcal{E}'$  outside  $\mathcal{E}$  while it can be included in it.

To understand the evolution of the RG flow as  $N$  is decreased, one needs to consider the space of *all* coupling constants, *i.e.* the space such that to each point corresponds a microscopic Hamiltonian of a frustrated system. In this space, we focus on the subspace  $\mathcal{E}$  containing the representative points, at  $T = T_c$ , of STA, STAR, V<sub>N,2</sub>, BCT, of all real materials studied experimentally and, more generally, of all systems of physical interest. Let us now describe qualitatively the change of the RG trajectories as  $N$  crosses  $N_c(d)$ .

*i)* When  $N$  is larger than  $N_c(d)$ , there exists a true stable fixed point of the RG flow so that all trajectories emerging from  $\mathcal{E}$  eventually end on this fixed point, see Fig. 3.10a. All systems exhibit scaling around the critical temperature and universality holds.

*ii)* As already stated, when  $N$  is decreased slightly below  $N_c(d)$ , the fixed point  $C_+$  gets complex coordinates, and loses its direct physical meaning. In particular, the flow no longer stops at a point, see Fig. 3.10b. Consequently, the correlation lengths of systems in  $\mathcal{E}$  do not diverge at  $T_c$ . Strictly speaking, all systems undergo first order phase transitions. However two facts must be noted. *Firstly*, all the trajectories emerging from  $\mathcal{E}$  are attracted toward a small region in coupling constant space, denoted by  $\mathcal{E}'$  in Fig. 3.10b. *Secondly*, the flow in  $\mathcal{E}'$  is very slow.

From the second observation, one deduces that for all systems in  $\mathcal{E}$  the correlation lengths at the transition are very large — although finite — since they typically behave as the exponential of the RG time spent in  $\mathcal{E}'$ , time which is large. Therefore, the transitions are all extremely weakly of first order for systems in  $\mathcal{E}$ . One thus expects scaling behaviors with pseudo-critical exponents for all physical quantities, with the subtlety that this scaling aborts very close to  $T_c$  where the true first order nature of the transitions shows up.

As for the first observation — *i.e.* all trajectories are attracted toward a small region  $\mathcal{E}'$  —, it allows to conclude that all phase transitions are governed by a small region in coupling constant space and that, therefore, universality almost holds. In particular, the pseudo-critical exponents should be roughly the same for all systems whose microscopic Hamiltonian corresponds to a point in  $\mathcal{E}$ .

Let us study in greater detail the case where  $N$  is just below  $N_c(d = 3)$ . For such values of  $N$ , it is reasonable to approximate  $\mathcal{E}'$  by a point. The best approximation is clearly to choose the point in  $\mathcal{E}'$  that mimics best a fixed point, *i.e.* the point where the flow is the slowest: the minimum of the flow<sup>14,15</sup>. To determine this so-called “pseudo-fixed point”, Zumbach<sup>14,15</sup> has proposed to introduce a norm for the flow and to determine the point where the norm is minimum. He has performed this approach in the context of a NPRG equation (LPA of the Polchinski equation) where he has built the needed mathematical structures. He has shown that, when a minimum exists, pseudo-critical exponents characterizing pseudo-scaling can be associated with the pseudo-fixed point, in the same way that true exponents are associated with a true fixed point.

A natural assumption to explain the pseudo-scaling behaviors observed in real systems is that the minimum of the RG flow mimics a true fixed point even for values of  $N$  not very close to  $N_c(d = 3)$ . For the Heisenberg systems, this position has been advocated by Zumbach<sup>15</sup> and by the present authors<sup>17</sup>.

Within the NPRG approach the present authors have confirmed the existence of a minimum of the flow, for values of  $N$  just below  $N_c(d = 3)$ , leading to pseudo-scaling and pseudo-universality<sup>17</sup>. By following this minimum they have confirmed that it persists down to  $N = 3$  and have computed the associated pseudo-critical exponents, see Table 3.9. We also give in this table the exponents found by Zumbach within the LPA of the Polchinski equation for the same model<sup>15</sup> and recall those found within the six-loop approach of Pelissetto *et al.*<sup>10</sup>.

Table 3.9. The critical exponents and pseudo-critical exponents for  $N = 3$ .  $\alpha, \beta$  and  $\gamma$  have been computed assuming that the scaling relations hold. The first line corresponds to the NPRG approach of the present authors, the second to Zumbach's work. In the third line, we have recalled the six-loop results of Pelissetto *et al.* for comparison.

Method	$\alpha$	$\beta$	$\gamma$	$\nu$	$\eta$
NPRG <sup>17</sup>	0.38	0.29	1.04	0.54	0.072
LPA <sup>15</sup>	0.11	0.31	1.26	0.63	0.0
6-loop <sup>10</sup>	0.35(9)	0.30(2)	1.06(5)	0.55(3)	0.08

The values of the critical exponents obtained within the NPRG are not too far from — some of — those found experimentally for group 2 of materials, see (36), as well as those found numerically for the STA, see Table 3.4. As usual, the truncation used overestimates  $\eta$  and thus, at fixed  $\beta$ , underestimates  $\nu$ . It is remarkable that the values of the pseudo-critical exponents found at the minimum are in good agreement with those obtained within the six-loop approach. This strongly suggests that there is a common origin to these two sets of critical exponents. We shall come back on this point in the conclusion.

### 3.6.7.2. Scaling with or without pseudo-fixed point: the Heisenberg and XY cases

Let us now argue that the preceding analysis, based solely on the notion of minimum, is too naive to give an explanation of the pseudo-critical behaviors in the physically interesting cases. Let us also give a qualitative picture that supplements the concept of minimum.

The present authors have found that, when  $N$  is lowered below  $N = 3$ , the minimum of the flow is less and less pronounced and that, for some value of  $N$  between 2 and 3, it completely disappears. Since several XY

systems exhibit pseudo-scaling in experiments or in numerical simulations, this means that the concept of minimum of the flow does not constitute the definitive explanation of scaling in absence of a fixed point. One encounters here the limit of the concept of minimum of the flow. First, it darkens the important fact that the notion relevant to scaling is not the existence of a minimum of the flow but that of a whole region in coupling constant space in which the flow is slow, *i.e.* the  $\beta$  functions are small. Put it differently, the existence of a minimum does not guarantee that the flow is sufficiently slow to produce large correlation lengths. Reciprocally, one can encounter situations where the RG flow is slow, the correlation length being large so that scaling occurs even in absence of a minimum. The existence of a minimum is thus neither necessary nor sufficient to explain pseudo-scaling. Second, even when the minimum exists, reducing the region  $\mathcal{E}'$  to a point rules out the possibility of testing the violation of universality. For instance, one knows that for  $N = 3$  universality is violated, see Table 3.4, while a minimum of the RG flow is found. This feature cannot be reproduced by the unique set of exponents computed at the minimum. The opposite assumption, done first by Zumbach<sup>15</sup> and by the present authors<sup>17</sup>, was thus unjustified.

Thus, even for very weak first order transitions, the beautiful simplicity of second order transitions is lost and the finite extend of the attractive region  $\mathcal{E}'$  has to be taken into account. To be precise, one needs to define two subsets of  $\mathcal{E}$  and  $\mathcal{E}'$ :  $\mathcal{D}$  which is the region in  $\mathcal{E}$  leading to pseudo-scaling and  $\mathcal{R}$ , the subset of  $\mathcal{E}'$  which is the image of  $\mathcal{D}$  in the RG flow, see Figs. 3.11a and 3.11b. Let us now consider the characteristics of the flow when  $N$  is varied.

Since for  $N > N_c(d = 3)$  all the systems in  $\mathcal{E}$  undergo a second order phase transition, one expects — thanks to continuity arguments — that for  $N$  slightly below  $N_c(d = 3)$ , all systems in  $\mathcal{E}$  exhibit pseudo-scaling and thus that  $\mathcal{D} = \mathcal{E}$ . At the same time,  $\mathcal{E}'$ , the image of  $\mathcal{E}$  is almost point-like — see Fig. 3.10b — and universality holds.

As  $N$  is decreased below  $N_c(d)$ , two phenomena occur.

*i)* While  $\mathcal{D}$  remains equal to  $\mathcal{E}$ , the domain  $\mathcal{E}'$ , which is initially point-like, grows, see Fig. 3.11a. This means that while pseudo-scaling should be generically observed, universality starts to be significantly violated: a whole spectrum of exponents should be observed, the size of  $\mathcal{E}'$  providing a measure of this violation of universality.

*ii)* For low values of  $N$ , the region  $\mathcal{D}$  leading to pseudo-scaling can become smaller than  $\mathcal{E}$ , see Fig. 3.11b. For systems defined by initial conditions

in  $\mathcal{D}$ , the correlation lengths are still relatively large but the pseudo-critical exponents can vary from system to system according to the size of  $\mathcal{R}$ . For systems defined by initial conditions in  $\mathcal{E}$  but not in  $\mathcal{D}$ , the RG flow is always fast, producing small correlation lengths at  $T_c$ . The corresponding systems undergo strong first order phase transitions. Moreover, as  $N$  decreases, the flow in  $\mathcal{E}'$  should become more and more rapid so that, for systems in  $\mathcal{E}$ , the correlation lengths at the phase transitions should decrease. The transitions are thus expected to become more strongly of first order for lower  $N$ .

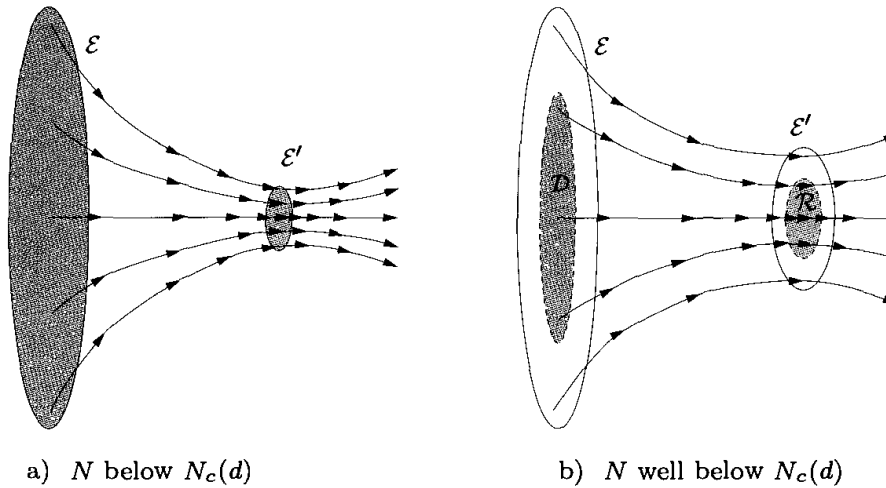


Fig. 3.11. Schematic representation of the flow, a) for  $N \simeq 3$  and b) for  $N \simeq 2$ . For the sake of clarity, we have represented  $\mathcal{E}'$  outside  $\mathcal{E}$  while it can be included in it.  $\mathcal{D}$  and  $\mathcal{R}$  are represented in grey. In a),  $\mathcal{D} = \mathcal{E}$  and  $\mathcal{R} = \mathcal{E}'$ .

The precise values of  $N$  for which these changes of behaviors occur as well as the shapes and extents of  $\mathcal{D}$ ,  $\mathcal{R}$  and  $\mathcal{E}'$  can only be obtained from a detailed analysis of both the microscopic Hamiltonian and of the RG flow. However, independently of the details of the model under study, of the precise value of  $N_c(d)$ , etc, one expects the following behavior: as  $N$  is decreased, a system that undergoes at large  $N$  a second order transition undergoes, for  $N$  just smaller than  $N_c(d)$ , a very weak first order transition governed by the minimum. Then, it should undergo a weak first order transition where the notion of minimum is irrelevant and for which universality does not hold anymore. Finally, it should undergo a strong first order phase transition. In the spectrum of models studied numerically, it is easy to see that the STAR,  $V_{N,2}$  and BCT models with XY and Heisenberg spins nicely obey this prediction. For  $N = 3$ , they all show scaling and the phase transitions should be very weakly of first order. However,

their exponents are clearly incompatible with those of STA and with those associated with the minimum, see Tables 3.4 and 3.9. The RG trajectories associated with these systems are thus expected to pass through  $\mathcal{R}$ , but far from the minimum. One thus naturally expects that, when  $N$  is decreased down to  $N = 2$ , no scaling behavior is observed for these systems. This is indeed what is found in numerical simulations, see Table 3.2. This strongly suggests that  $\mathcal{D}$  has shrunk between  $N = 3$  and  $N = 2$  and that  $N = 3$  corresponds to Fig. 3.11a and  $N = 2$  to Fig. 3.11b.

### 3.6.7.3. *The integration of the RG flow*

In the previous section it has been shown that the notion of minimum — or pseudo-fixed point — in the RG flow is neither sufficient nor necessary to explain the existence of scaling without a fixed point. For this reason, one has to resort to another method to study the physics of XY and Heisenberg frustrated magnets. In practice, one integrates numerically the RG flow around the transition temperature  $T_c$  and determines the behavior of the physical quantities such as the correlation length, the susceptibility and the “magnetization” — defined as  $\sqrt{\bar{\kappa}}$ , see Eq. (79) — as functions of the reduced temperature  $t_r = (T - T_c)/T_c$ . In principle, in the absence of universality, one should study each system independently of the others. Thus, to correctly specify the initial conditions of the RG flow, one should also keep all the microscopic information relevant to the description of a given material. This program remains, in the most general case, a theoretical challenge since this would consist in keeping track of the lattice structure as well as of the infinite number of coupling constants involved in the microscopic Hamiltonian. However it is, in principle, possible. Actually, this has been done — with much success — for certain classes of magnetic systems and fluids described by  $O(N)$  models<sup>130</sup> and this, mostly within the LPA<sup>131,132</sup>. The truncations used by the present authors — even the best one — are too restricted approximations to reach this goal since this would at least require to keep the *full* field dependence of the potential  $U_k(\rho, \tau)$ . They have thus used their flow equations to explain the generic occurrence of pseudo-scaling in frustrated systems without trying to describe the behavior of a specific system. In practice, they have computed the correlation length, magnetization and susceptibility using a simplified version of their truncation keeping only the potential part expanded up to order eight in the fields, a field-independent field renormalization and discarding all the current-terms involving four fields and two derivatives. They have checked

that this *ansatz* leads to stable results with respect to the addition of higher powers of the fields and inclusion of current terms.

A related difficulty encountered in the integration of the flow is that, in the absence of universality, the temperature dependence of the physical quantities relies on the precise temperature dependence of the microscopic coupling constants. The present authors have used several *ansätze* for the temperature dependence of the coupling constants and have observed that, although it could be important for the details of the results, it does not affect much the general conclusions. Thus, we illustrate the results with the simplest *ansatz* consisting in fixing all the couplings to temperature-independent values and by taking a linear temperature dependence for  $\kappa$  at the lattice scale:

$$\kappa_{k=\Lambda} = a + bT . \quad (90)$$

For each temperature, the present authors have integrated the flow equations and have deduced the  $t_r$ -dependence of the physical quantities, such as the “magnetization”, the correlation length, etc, around  $T_c$ . The different coupling constants parametrizing the initial condition of the flow have been varied to test the robustness of their conclusions. This has allowed the present authors<sup>19</sup> to establish the following facts.

### 3.6.7.4. The Heisenberg case

In the Heisenberg case, the following results have been obtained:

- For  $N = 3$ , there exist initial conditions of the flow such that for a wide range of reduced temperatures — up to four decades — the physical quantities behave as power laws. From an experimental viewpoint, this is all what is needed since scaling has been found on temperature ranges that are even smaller. The kind of pseudo-critical behaviors found is illustrated in Fig. 3.12.
- Varying the initial conditions of the flow, one observes that this phenomenon happens in a wide domain of the coupling constant space. This corresponds to the domain  $\mathcal{D}$  previously defined, see Fig. 3.11a.
- Within  $\mathcal{D}$ , the pseudo-critical exponents vary smoothly:  $\beta$  varies typically between 0.27 and 0.42 and  $\nu$  between 0.56 and 0.71. These are only typical values since it has been impossible to explore the whole space of coupling constants. Since for  $\beta \simeq 0.27$ , one can find  $\nu \simeq 0.56$ , the exponents of group 2 are satisfactorily reproduced, see Tables 3.3 and 3.4. This shows in particular that there exists, in  $\mathcal{D}$ , a set of “microscopic” coupling constants that lead to the behavior observed in group 2.

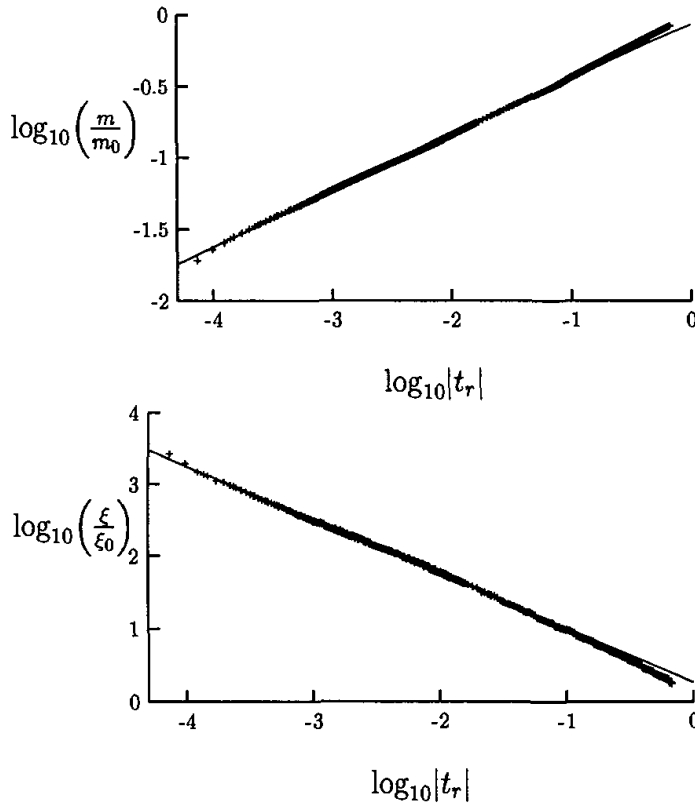


Fig. 3.12. Log-log plot of the magnetization  $m$  and of the correlation length  $\xi$  for  $N = 3$  as functions of the reduced temperature  $t_r$ . The straight lines correspond to the best power law fit of the data.

- It is easy to find initial conditions leading to pseudo-critical exponents in good agreement with those obtained in the six-loop calculation, see Table 3.6. Actually, a whole set of initial conditions lead to exactly the same (pseudo-) exponents as those found at six-loop:  $\beta = 0.30(2)$ ,  $\nu = 0.55(3)$ . This corresponds to the region of the minimum of the flow, see Table 3.9.

- In contrast, the present authors have not found initial conditions of the RG flow reproducing correctly the critical exponents of group 1, of STAR,  $V_{3,2}$  and BCT as well as negative values for  $\eta$ . This can originate *i*) in the overestimation of  $\eta$  produced by the truncation of  $\Gamma_k$  in powers of the derivatives at order  $\partial^2$ , Eq. (78), *ii*) in the impossibility to sample the whole coupling constant space, *iii*) in the too simple temperature dependence of  $\kappa_\Lambda$  that have been considered, see Eq. (90).

- For a given value of one exponent, it is possible to find several values for the other exponents. Thus one expects to find systems sharing for instance almost the same  $\beta$  but having quite different values for  $\nu$  and  $\gamma$ .

- At the border of  $\mathcal{D}$ , the temperature ranges over which power laws

hold become smaller and smaller. In a log-log plot, the  $t_r$ -dependence becomes less and less linear and the pseudo-critical exponents more and more sensitive to the choice of  $T_c$  made for the fit. Finally, outside  $\mathcal{D}$ , no more power-law behavior is observed.

- When going from  $N = 3$  to  $N = 4$ , one observes, as expected, that  $\mathcal{D}$  becomes far wider and that the power laws hold generically on larger temperature ranges. This is consistent with the discussion of Section 3.6.7.2. Reciprocally, and as also expected, when going from  $N = 3$  to  $N = 2$ ,  $\mathcal{D}$  becomes much smaller and the power laws hold generically on smaller temperature ranges. Let us discuss this point in greater detail now.

### 3.6.7.5. The XY case

In the XY case, one finds the following results.

- For  $N = 2$ , one observes qualitatively the same type of behaviors as for  $N = 3$ . However, as predicted above,  $\mathcal{D}$  is smaller and the power laws hold at best only on two decades of reduced temperature, which is consistent with what is observed experimentally. This is illustrated in Fig. 3.13 where we have represented log-log plots of the magnetization and correlation length as functions of the reduced temperature.
- Within  $\mathcal{D}$  the exponents vary on the intervals:  $0.25 < \beta < 0.38$  and  $0.47 < \nu < 0.58$ .
- One finds initial conditions leading to exponents close to those of group 2 (for Ho and Dy, see Table 3.1):  $\beta = 0.38$ ,  $\nu = 0.58$ ,  $\gamma = 1.13$ . These results are quite stable with respect to changes of microscopic parameters. This is in agreement with the stability of  $\beta$  in group 2. Interestingly, these initial conditions correspond to small  $\tilde{\mu}$  in the truncation Eq. (80), *i.e.* to initial conditions close to the  $O(4)$ -invariant line:  $\tilde{\mu} = 0$ , see Fig. 3.2 where the  $O(4)$  fixed point is denoted by  $V^h$ . Thus, during a large part of the flow, the trajectory remains close to the  $O(4)$  fixed point before bifurcating away from this point. This is perhaps the reason why the value of  $\beta$  of materials of group 2 is close to that associated with an  $O(4)$  behavior —  $\beta_{O(4)} = 0.382$  — a fact that has been repeatedly noticed by experimentalists. Note however that the other exponents are not close to the  $O(4)$  values:  $\nu_{O(4)} = 0.738$ ,  $\gamma_{O(4)} = 1.449$ .
- One also easily finds initial conditions leading to  $\beta = 0.25$ , corre-

---

<sup>h</sup>Let us emphasize that this  $O(4)$  fixed point has nothing to do with that of the frustrated Heisenberg system found around  $d = 2$  in the NL $\sigma$  model approach, see Section 3.5.1.

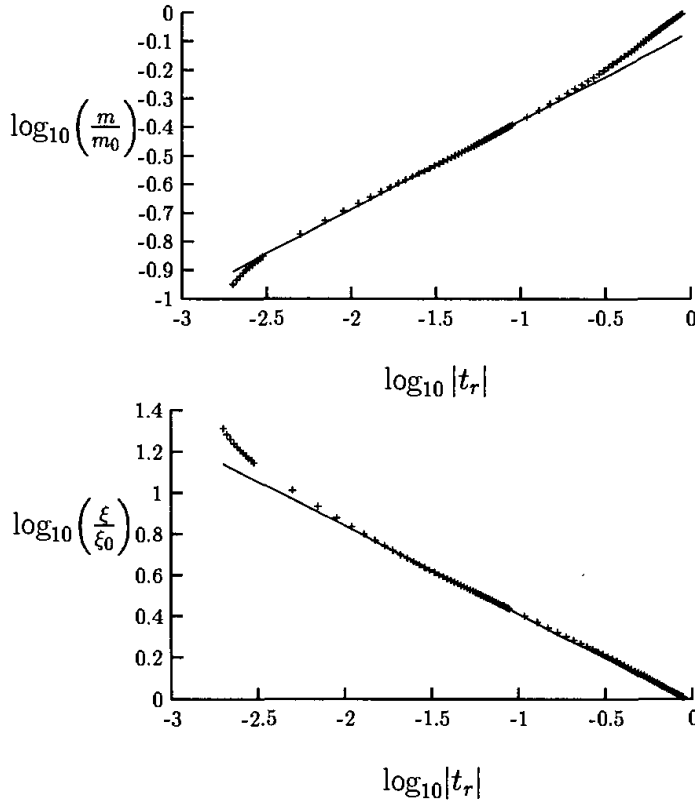


Fig. 3.13. Log-log plot of the of the magnetization  $m$  and of the correlation length  $\xi$  for  $N = 2$  as functions of the reduced temperature  $t_r$ . The straight lines correspond to the best power law fit of the data. The power-law behavior observed far from the critical temperature breaks down for small  $t_r$ . The behavior of the correlation length at small  $t_r$  is an artefact of the truncation.

sponding to group 1, essentially composed of STA systems. The power laws then hold on smaller ranges of temperatures and the critical exponent  $\beta$  is more sensitive to the determination of  $T_c$  and to the initial conditions. For such values of  $\beta$ , one finds that  $\nu$  varies between 0.47 and 0.49, which is somewhat below the value found for  $\text{CsMnBr}_3$ , see Table 3.1.

- The two previous points suggest that both helimagnets — such as Ho or Dy — and STA — such as  $\text{CsMnBr}_3$  — can be described by the same field theory but with exponents at the two ends of the spectrum. It is actually also possible that helimagnets display a different kind of physics because of the presence of long range interactions or because of the presence of surface effects <sup>133</sup>.

- As in the  $N = 3$  case, one can easily find initial conditions leading to pseudo-critical exponents close to those found in the six-loop calculation, Table 3.6. For instance, for initial conditions leading to  $\beta = 0.33$ , one finds

typically:  $\nu = 0.56$  and  $\gamma = 1.07$ .

- As in the Heisenberg case, it has not been possible to find initial conditions of the RG flow leading to negative values of  $\eta$ .

### 3.6.8. Conclusion

The main feature of the physics of Heisenberg and XY frustrated magnets — scaling behaviors *without* universality — is reproduced, at least qualitatively and, to some extent, quantitatively. This behavior finds a *natural* explanation: there exists a whole domain  $\mathcal{D}$  in the space of coupling constants such that the RG trajectories starting in  $\mathcal{D}$  are “attracted” toward a region  $\mathcal{R}$  where the RG flow is slow so that there is pseudo-scaling. Since  $\mathcal{R}$  is *not* reduced to a point, there exists a whole spectrum of exponents and not a *unique* set. The occurrence of strong first order phase transitions, that are observed in some materials and simulated systems, is explained by the RG trajectories starting out of  $\mathcal{D}$ .

Let us now stress that since universality is lost, the determination of the precise pseudo-critical exponents associated with a given material or system is obviously more difficult than the determination of the usual — universal — critical exponents characterizing a second order phase transition. As already said, computing them would indeed require to know precisely the microscopic structure of the materials or system studied — providing the initial conditions of the RG flow — and to take into account the full field-dependence of the potential  $U_k(\rho, \tau)$ .

## 3.7. Conclusion and prospects

On the basis of their specific symmetry breaking scheme, it has been proposed <sup>1,2,3,4,5,6</sup> that the critical physics of XY and Heisenberg frustrated systems in three dimensions could be characterized by critical exponents associated with a *new* universality class. From this point of view, the study of frustrated magnets has been rather disappointing, the experimental and numerical contexts excluding such an hypothesis. At the same time, the phenomenology of frustrated magnets has displayed a novel kind of critical behavior — the existence of *generic* scaling *without* universality <sup>18,19</sup> — requiring the use of new theoretical approaches.

Within the framework of a NPRG approach, this generic and nonuniversal scaling find a natural explanation in terms of slowness and “geometry” of the flow. This method has also explained the mismatch between the different perturbative approaches by means of a mechanism of annihilation of

fixed points in a dimension between two and three that invalidates the low-temperature perturbative approach performed from the  $\text{NL}\sigma$  model for low values of  $N$ . In this respect, it would be satisfying to understand the very origin of this failure. The influence of nontrivial topological configurations on the phase transition in three dimensions has been invoked (see Sections 3.2.2 and 3.5.1). It remains however to confirm that these configurations indeed play such a crucial role and to understand if they are really responsible for the first order character of the transitions in three dimensions. This is a delicate question. Indeed, the perturbative and nonperturbative RG approaches performed on the GLW model are very likely sensitive to such nontrivial topological configurations<sup>i</sup>. However, within these approaches, disentangling vortices and spin-waves remains a theoretical challenge.

High-order perturbative calculations in  $d = 3$ <sup>10,11,12</sup> provide another explanation of the lack of universality in frustrated magnets: the focus character of the fixed point found within this approach induces spiral-like RG trajectories from which, according to Calabrese *et al.*<sup>12</sup>, follows varying effective critical exponents<sup>11,12</sup>.

Even if it could appear as a rather formal question, it would be also satisfying to clarify the discrepancy between the NPRG and the six-loop perturbative approaches. In the Heisenberg case, the matching between the set of exponents found within the NPRG approach at the minimum and that found by Pelissetto *et al.*, suggests a common origin to these two set of exponents. One can formulate some hypothesis to reconcile the two approaches.

First, one can invoke the specificities of the perturbative series in the case of frustrated magnets: the series display bad convergence properties<sup>10,11,12,13</sup> and the critical properties strongly depend on the order of the series. As already said, there is no nontrivial fixed point for  $N = 2$  and  $N = 3$  up to three loops; the fixed points only appear at five-loop order. Due to these specific features one can suspect that the real fixed point found by Pelissetto *et al.* is, actually, a complex one.

Second, reciprocally, one can suspect that, within the NPRG method, the lack of fixed point in the XY and Heisenberg cases is due to artefacts of the truncation in fields and/or derivatives. Only the recourse to other kinds of expansions of the effective action  $\Gamma_k$  — involving either the *full* function  $U_k(\rho, \tau)$  or the *full* momentum dependence — could lead to unambiguous

---

<sup>i</sup>Both approaches correctly reproduce the physics of three dimensional XY nonfrustrated spin systems which is probably driven by vortices at the transition<sup>139,140</sup>.

statements.

Finally, the major characteristics of XY and Heisenberg frustrated magnets, *i.e.* the existence of scaling laws with continuously varying exponents, are probably encountered in other physical contexts, generically systems with a critical value  $N_c(d)$  of the number of components of the order parameter, separating a true second order behavior and a naïvely first order one: Abelian Higgs model<sup>134,135,136</sup>,  $O(p)$  gauge theory coupled to  $N$  scalar fields<sup>137</sup>, etc.

## Acknowledgements

We thank D. Loison for useful remarks and J. Vidal for a careful reading of the manuscript and helpful remarks.

## References

1. T. Garel and P. Pfeuty, J. Phys. C: Solid St. Phys. **9**, L245 (1976).
2. M. Yosefin and E. Domany, Phys. Rev. B **32**, 1778 (1985).
3. H. Kawamura, J. Phys. Soc. Japan **54**, 3220 (1985).
4. H. Kawamura, J. Phys. Soc. Japan **55**, 2095 (1986).
5. H. Kawamura, J. Phys. Soc. Japan **56**, 474 (1987).
6. H. Kawamura, Phys. Rev. B **38**, 4916 (1988).
7. P. Azaria, B. Delamotte, and T. Jolicœur, Phys. Rev. Lett. **64**, 3175 (1990).
8. P. Azaria, B. Delamotte, F. Delduc, and T. Jolicœur, Nucl. Phys. B [FS] **408**, 485 (1993).
9. D. Bailin, A. Love, and M. A. Moore, J. Phys. C: Solid State Phys. **10**, 1159 (1977).
10. A. Pelissetto, P. Rossi, and E. Vicari, Phys. Rev. B **63**, 140414 (2001).
11. P. Calabrese, P. Parruccini, and A. I. Sokolov, Phys. Rev. B **66**, 180403 (2002).
12. P. Calabrese, P. Parruccini, and A. I. Sokolov, cond-mat/0304154.
13. P. Parruccini, cond-mat/0305287.
14. G. Zumbach, Phys. Rev. Lett. **71**, 2421 (1993).
15. G. Zumbach, Nucl. Phys. B **413**, 771 (1994).
16. M. Tissier, D. Mouhanna, and B. Delamotte, Phys. Rev. B **61**, 15327 (2000).
17. M. Tissier, B. Delamotte, and D. Mouhanna, Phys. Rev. Lett. **84**, 5208 (2000).
18. M. Tissier, B. Delamotte, and D. Mouhanna, Phys. Rev. B **67**, 134422 (2003).
19. B. Delamotte, D. Mouhanna, and M. Tissier, cond-mat/0309101.
20. T. Dombre and N. Read, Phys. Rev. B **38**, 7181 (1988).
21. N. D. Mermin, Rev. Mod. Phys. **51**, 591 (1979).
22. H. Kawamura and S. Miyashita, J. Phys. Soc. Japan **53**, 4138 (1984).
23. W. Apel, M. Wintel, and H. Everts, Z. Phys. B **86**, 139 (1992).

24. B. W. Southern and A. P. Young, Phys. Rev. B **48**, 13170 (1993).
25. M. Wintel, H. U. Everts, and W. Apel, Europhys. Lett. **25**, 711 (1994).
26. B. W. Southern and H.-J. Xu, Phys. Rev. B **52**, 3836 (1995).
27. W. Stephan and B. W. Southern, Phys. Rev. B **61**, 11514 (2000).
28. M. Caffarel, P. Azaria, B. Delamotte, and D. Mouhanna, Phys. Rev. B **64**, 014412 (2001).
29. W. Maier and A. Saupe, Z. Naturforsch. A **14**, 882 (1959).
30. P. A. Lebwohl and G. Lasher, Phys. Rev. A **6**, 426 (1972).
31. P. E. Lammert, D. S. Rokhsar, and J. Toner, Phys. Rev. Lett. **70**, 1650 (1993).
32. P. E. Lammert, D. S. Rokhsar, and J. Toner, Phys. Rev. E **52**, 1778 (1995).
33. G. Kohring and R. E. Shrock, Nucl. Phys. B **285**, 504 (1987).
34. J. Villain, J. Phys. C: Solid St. Phys. **10**, 4793 (1977).
35. S. Miyashita and H. Shiba, J. Phys. Soc. Japan **53**, 1145 (1985).
36. V. L. Berezinskii, Sov. Phys. JETP **32**, 493 (1970).
37. J. M. Kosterlitz and D. J. Thouless, J. Phys. C **6**, 1181 (1973).
38. V. P. Plakhty, J. Kulda, D. Visser, E. V. Moskvin, and J. Wosnitza, Phys. Rev. Lett. **85**, 3942 (2000).
39. M. F. Collins and O. A. Petrenko, Can. J. Phys. **75**, 605 (1997).
40. H. B. Weber, T. Werner, J. Wosnitza, H. v. Löhneysen, and U. Schotte, Phys. Rev. B **54**, 15924 (1996).
41. J. Wang, D. P. Belanger, and B. D. Gaulin, Phys. Rev. Lett. **66**, 3195 (1991).
42. R. Deutschmann, H. von Löhneysen, J. Wosnitza, R. K. Kremer, and D. Visser, Europhys. Lett. **17**, 637 (1992).
43. T. E. Mason, B. D. Gaulin, and M. F. Collins, Phys. Rev. B **39**, 586 (1989).
44. T. E. Mason, M. F. Collins, and B. D. Gaulin, J. Phys. C: Solid St. Phys. **20**, L945 (1987).
45. B. D. Gaulin, T. E. Mason, M. F. Collins, and J. Z. Larese, Phys. Rev. Lett. **62**, 1380 (1989).
46. Y. Ajiro, T. Nakashima, Y. Unno, H. Kadowaki, M. Mekata, and N. Achiwa, J. Phys. Soc. Japan **57**, 2648 (1988).
47. H. Kadowaki, S. M. Shapiro, T. Inami, and Y. Ajiro, J. Phys. Soc. Japan **57**, 2640 (1988).
48. M. Enderle, G. Fortuna, and M. Steiner, J. Phys.: Condens. Matter **6**, L385 (1994).
49. H. Weber, D. Beckmann, J. Wosnitza, H. von Löhneysen, and D. Visser, Int. J. Mod. Phys. B **9**, 1387 (1995).
50. M. Enderle, R. Schneider, Y. Matsuoka, and K. Kakurai, Physica B **234-236**, 554 (1997).
51. U. Schotte, N. Stusser, K. D. Schotte, H. Weinfurter, H. M. Mayer, and M. Winkelmann, J. Phys.: Condens. Matter **6**, 10105 (1994).
52. K. D. Jayasuriya, A. M. Stewart, S. J. Campbell, and E. S. R. Gopal, J. Phys. F **14**, 1725 (1984).
53. C. C. Tang, W. G. Stirling, D. L. Jones, C. C. Wilson, P. W. Haycock, A. J. Rollason, A. H. Thomas, and D. Fort, J. Magn. Magn. Mater. **103**, 86 (1992).

54. C. C. Tang, P. W. Haycock, W. G. Stirling, C. C. Wilson, D. Keen, and D. Fort, *Physica B* **205**, 105 (1995).
55. K. Hirota, Y. Nakazawa, and M. Ishikawa, *J. Phys.: Condens. Matter* **3**, 4721 (1991).
56. K. D. Jayasuriya, S. J. Campbell, and A. M. Stewart, *J. Phys. F: Met. Phys.* **15**, 225 (1985).
57. T. R. Thurston, G. Helgesen, J. P. Hill, D. Gibbs, B. D. Gaulin, and P. J. Simpson, *Phys. Rev. B* **49**, 15730 (1994).
58. V. P. Plakhty, W. Schweika, T. Brückel, J. Kulda, S. V. Gavrilov, L.-P. Regnault, and D. Visser, *Phys. Rev. B* **64**, 100402 (2001).
59. G. H. F. Brits and P. de V. du Plessis, *J. Phys. F* **18**, 2659 (1988).
60. P. de V. Du Plessis, A. M. Venter, and G. H. F. Brits, *J. Phys.: Condens. Matter* **7**, 9863 (1995).
61. J. Eckert and G. Shirane, *Solid State Commun.* **19**, 911 (1976).
62. G. Helgesen, J. P. Hill, T. R. Thurston, D. Gibbs, J. Kwo, and M. Hong, *Phys. Rev. B* **50**, 2990 (1994).
63. B. D. Gaulin, M. Hagen, and H. R. Child, *J. Phys. (Paris) Colloq.* **49**, C8 (1988).
64. D. A. Tindall, M. O. Steinitz, and M. L. Plumer, *J. Phys. F* **7** (1977).
65. K. D. Jayasuriya, S. J. Campbell, and A. M. Stewart, *Phys. Rev. B* **31**, 6032 (1985).
66. E. Loh, C. L. Chien, and J. C. Walker, *Phys. Lett. A* **49**, 357 (1974).
67. P. de V. Du Plessis, C. F. van Doorn, and D. C. van Delden, *J. Magn. Magn. Mater.* **40**, 91 (1983).
68. H. Kawamura, *J. Phys. Soc. Japan* **61**, 1299 (1992).
69. H. Kawamura, *J. Phys. Soc. Japan* **58**, 584 (1989).
70. M. L. Plumer and A. Mailhot, *Phys. Rev. B* **50**, 16113 (1994).
71. E. H. Boubcheur, D. Loison, and H. T. Diep, *Phys. Rev. B* **54**, 4165 (1996).
72. M. Itakura, *J. Phys. Soc. Jap.* **72**, 74 (2003).
73. D. Loison and K. D. Schotte, *Euro. Phys. J. B* **5**, 735 (1998).
74. H. Kunz and G. Zumbach, *J. Phys. A: Math. Gen.* **26**, 3121 (1993).
75. H. Diep, *Phys. Rev. B* **39**, 397 (1989).
76. D. R. T. Jones, A. Love, and M. A. Moore, *J. Phys. C: Solid St. Phys.* **9**, 743 (1976).
77. H. Kadokami, K. Ubukoshi, K. Hirakawa, J. L. Martinez, and G. Shirane, *J. Phys. Soc. Japan* **56**, 4027 (1987).
78. J. Wosnitza, R. Deutschmann, H. von Löhneysen, and R. K. Kremer, *J. Phys.: Condens. Matter* **6**, 8045 (1994).
79. K. Koyama and M. Matsuura, *J. Phys. Soc. Japan* **54**, 4085 (1985).
80. G. C. DeFotis, M. L. Laccheo, and H. A. Katori, *Phys. Rev. B* **65**, 94403 (2002).
81. G. C. DeFotis, S. A. Palacio, and R. L. Carlin, *Physica B+C* **95**, 380 (1978).
82. G. C. DeFotis and S. A. Pugh, *Phys. Rev. B* **24**, 6497 (1981).
83. G. C. DeFotis and J. R. Laughlin, *J. Magn. Magn. Matter.* **54-57**, 713 (1986).
84. D. Beckmann, J. Wosnitza, H. v. Löhneysen, and D. Visser, *Phys. Rev. Lett.*

- 71**, 2829 (1993).
85. R. Bügel, J. Wosnitza, H. v. Löhneysen, T. Ono, and H. Tanaka, Phys. Rev. B **64**, 094406 (2001).
  86. T. Ono, H. Tanaka, T. Kato, K. Iio, K. Nakajima, and K. Kakurai, J. Magn. Magn. Mater. **177-181**, 735 (1998).
  87. T. Ono, H. Tanaka, T. Kato, K. Nakajima, and K. Kakurai, J. Phys.: Condens. Matter **11**, 4427 (1999).
  88. A. Mailhot, M. L. Plumer, and A. Caillé, Phys. Rev. B **50**, 6854 (1994).
  89. T. Bhattacharya, A. Billoire, R. Lacaze, and T. Jolicœur, J.Phys. I (Paris) **4**, 181 (1994).
  90. D. Loison and H. T. Diep, Phys. Rev. B **50**, 16453 (1994).
  91. A. Peles and B. W. Southern, Phys. Rev. B **67**, 184407 (2003).
  92. D. Loison and K. D. Schotte, Euro. Phys. J. B **14**, 125 (2000).
  93. D. Loison, Physica A **275**, 207 (1999).
  94. D. Loison, A. I. Sokolov, B. Delamotte, S. A. Antonenko, K. D. Schotte, and H. T. Diep, JETP Lett. **72**, 337 (2000).
  95. P. Bak, S. Krinsky, and D. Mukamel, Phys. Rev. Lett. **36**, 52 (1976).
  96. Z. Barak and M. B. Walker, Phys. Rev. B **25**, 1969 (1982).
  97. F. J. Wegner and A. Houghton, Phys. Rev. A **8**, 401 (1973).
  98. S. A. Antonenko and A. I. Sokolov, Phys. Rev. B **49**, 15901 (1994).
  99. S. A. Antonenko, A. I. Sokolov, and V. B. Varnashev, Phys. Lett. A **208**, 161 (1995).
  100. T. Jolicœur and F. David, Phys. Rev. Lett. **76**, 3148 (1996).
  101. A. Pelissetto, P. Rossi, and E. Vicari, Nucl. Phys. B [FS] **607**, 605 (2001).
  102. P. Calabrese and P. Parruccini, cond-mat/0308037 .
  103. D. H. Friedan, Ann. Phys. (N.Y.) **163**, 318 (1985).
  104. J. Zinn-Justin, *Quantum Field Theory and Critical Phenomena* (Oxford University Press, New York, 1989), 3rd ed.
  105. C. Wetterich, Nucl. Phys. B **352**, 529 (1991).
  106. C. Wetterich, Z. Phys. C **57**, 451 (1993).
  107. C. Wetterich, Z. Phys. C **60**, 461 (1993).
  108. C. Wetterich, Phys. Lett. B **301**, 90 (1993).
  109. N. Tetradis and C. Wetterich, Nucl. Phys. B [FS] **422**, 541 (1994).
  110. L. P. Kadanoff, Physics **2**, 263 (1966).
  111. L. P. Kadanoff, W. Götze, D. Hamblen, R. Hecht, E. A. S. Lewis, V. V. Palcianuskas, M. Rayl, J. Swift, D. Aspnes, and J. Kane, Rev. Mod. Phys. **39**, 395 (1967).
  112. K. G. Wilson and J. Kogut, Phys. Rep. C **12**, 75 (1974).
  113. U. Ellwanger, Z. Phys. C **62**, 503 (1994).
  114. T. R. Morris, Int. J. Mod. Phys. A **9**, 2411 (1994).
  115. J. Berges, N. Tetradis, and C. Wetterich, Phys. Rep. **363**, 223 (2002).
  116. D. F. Litim, Nucl. Phys. B **631**, 128 (2002).
  117. U. Ellwanger, Z. Phys. C **58**, 619 (1993).
  118. M. Bonini, M. D'Attanasio, and G. Marchesini, Nucl. Phys. B **409**, 441 (1993).
  119. T. R. Morris and J. F. Tighe, JHEP **08**, 007 (1999).

120. K. I. Aoki, A. Horikoshi, M. Taniguchi, and H. Terao, Prog. Theor. Phys. **108**, 571 (2002).
121. U. Ellwanger, M. Hirsch, and A. Weber, Eur. Phys. J. p. 563 (1998).
122. H. Gies and C. Wetterich, Phys. Rev. D **65**, 065001 (2002).
123. G. v. Gersdorff and C. Wetterich, Phys. Rev. B **64**, 054513 (2001).
124. T. R. Morris, Phys. Lett. B **334**, 355 (1994).
125. K. I. Aoki, K. Morikawa, W. Souma, J. I. Sumi, and H. Terao, Prog. Theor. Phys. **95**, 409 (1996).
126. K. I. Aoki, K. Morikawa, W. Souma, J. I. Sumi, and H. Terao, Prog. Theor. Phys. **99**, 451 (1998).
127. L. Canet, B. Delamotte, D. Mouhanna, and J. Vidal, Phys. Rev. D **67**, 065004 (2003).
128. L. Canet, B. Delamotte, D. Mouhanna, and J. Vidal, Phys. Rev. B **68**, 064421 (2003).
129. M. Tissier, D. Mouhanna, J. Vidal, and B. Delamotte, Phys. Rev. B **65**, 140402 (2002).
130. S. Seide and C. Wetterich, Nucl. Phys. B **562**, 524 (1999).
131. A. Parola and L. Reatto, Phys. Rev. A **31**, 3309 (1985).
132. A. Parola and L. Reatto, Adv. Phys. **44**, 211 (1995).
133. T. R. Thurston, G. Helgesen, D. Gibbs, J. P. Hill, B. D. Gaulin, and G. Shirane, Phys. Rev. Lett. **70**, 3151 (1993).
134. T. C. Lubensky, B. I. Halperin, and S. K. Ma, Phys. Rev. Lett. **32**, 292 (1974).
135. I. D. Lawrie, Nucl. Phys. B [FS] **200**, 1 (1982).
136. P. Arnold and L. G. Yaffe, Phys. Rev. D **49**, 3003 (1994), err. ibid **55** 1114 (1997).
137. P. Ginsparg, Nucl. Phys. B [FS] **170**, 388 (1980).
138. J. Zinn-Justin, *Quantum Field Theory and Critical Phenomena* (Oxford University Press, New York, 1989), pp. 151, 578, 3rd ed.
139. B. I. Halperin, *Physics of defects* (Les Houches XXXV NATO ASI, Eds. Balian, Kleman and Poirier, North Holland, 1981).
140. N. D. Antunes, L. M. A. Bettencourt, and A. Yates, Phys. Rev. D **64**, 065020 (2001).



## CHAPTER 4

### PHASE TRANSITIONS IN FRUSTRATED VECTOR SPIN SYSTEMS: NUMERICAL STUDIES

Damien Loison

*Institut für Theoretische Physik, Freie Universität Berlin, Arnimallee 14, 14195  
Berlin, Germany  
Damien.Loison@physik.fu-berlin.de*

#### Abbreviations

Some abbreviations are used in this chapter (by alphabetic order):

bct=body-centered-tetragonal,

BS=Breakdown of Symmetry,  $d$ =dimension, fcc=face-centered cubic lattice, FSS=Finite Size Scaling, GS=Ground State, hcp=hexagonal-close-packed lattice, KT=Kosterlitz-Thouless,  $L$ =system size, MC=Monte Carlo, MCRG=Monte Carlo Renormalization Group,  $N$ = number of components of the spin  $\mathbf{S}$ , NN=Nearest Neighbors, NNN=Next Nearest Neighbors, RG=Renormalization Group, STA=Stacked Triangular Antiferromagnetic lattices, STAR=Stacked Triangular Antiferromagnetic lattices with Rigidity,  $T$ =Temperature,  $T_c$ =critical Temperature,  $V_{N,P}$ =Stiefel model.

#### 4.1. Introduction

We present in this chapter a review on recent numerical studies dealing with frustrated vector spin systems in two and three dimensions. A system of spins is frustrated when all interactions between spin pairs cannot have simultaneously their optimal values. In other words a system is frustrated when the global order is incompatible with the local one, a definition applicable in a broader sense and not restricted to spins. For spin systems frustration has the consequence that the ordered state is different from the collinear order found for common unfrustrated antiferromagnets or ferromagnets. To study and to classify the phase transitions between the ordered

and less ordered states the symmetries these states play an important role. The critical behavior of second order transitions is principally governed by the change of symmetries. Therefore even very different systems like superfluid helium and XY spin systems can have the same critical properties. This fact is called universality and our objective is to analyze the corresponding universality classes for frustrated spin systems. We will mainly review magnetic models since they are the easiest to analyze numerically and theoretically. Nevertheless the results should be valid for any system belonging to the same universality class.

During the last decade important progress has been made in the understanding of the physics of frustrated spin systems. For example there is now convincing evidence on the genuine first order nature of the phase transition for  $XY$  and Heisenberg spins for the three dimensional Stacked Triangular Antiferromagnet (STA). This still contradicts the latest renormalization group expansion based on resummation. We think that studying phase transitions of vector spins theoretically, numerically and experimentally should have implications beyond this special field, that is for the understanding and the theory of phase transition in general.

We will concentrate our attention to the phase transition of the physical  $XY$  and Heisenberg spin systems in two and three dimensions. However, to understand these systems we have to analyze also the phase transitions of frustrated spins of  $N$  components, where  $N$  takes all integer values from 1 to  $\infty$  and not only 2 and 3 for  $XY$  and Heisenberg spins. We will also present studies for dimension  $d$  varying between two and four. Then we will review the particular case of strictly two dimensions where topological defects have a dominant role.

Frustrated Ising models are reviewed also in this book by Diep and Giacomini (chapter 1) and by Nagai, Horiguchi and Miyashita (chapter 2).

Since most of numerical simulations presented here use the Monte Carlo method, a short appendix (4.6) at the end is devoted to this technique. In addition, since the renormalization group is fundamental to the understanding of phase transitions, a small appendix (4.6) is added to discuss the methods used here for frustrated spin systems.

## **4.2. Breakdown of symmetry**

We first briefly review the fundamental concept of the reduction or the Breakdown of Symmetry (BS) in the transition from the high- to the low-temperature phases. The classification of phase transitions in universality classes is based on this concept.

#### 4.2.1. Symmetry in the high-temperature region

We will consider the Hamiltonian:

$$H = -J_1 \sum_{(ij)} \mathbf{S}_i \cdot \mathbf{S}_j \quad (1)$$

where  $\mathbf{S}_i$  are  $N$  component classical vectors of unit length and the sum is usually restricted to the nearest neighbors or at least to short range interactions. The symmetry of this Hamiltonian is  $O(N)$  or equivalently  $Z_2 \otimes SO(N)$  where  $O(N)$  is the orthogonal transformation group of  $N$ -dimensional Euclidean space. For  $SO(N)$  the determinant is unity, and the Ising symmetry  $Z_2$  corresponds to the mirror operation. If we add other terms, like dipolar interactions or anisotropies, the symmetry group will be reduced. Some other changes, like a cubic term  $(\mathbf{S}_i \cdot \mathbf{S}_j)^3$ , will not reduce the symmetry. In many experiments anisotropies will reduce Heisenberg ( $N = 3$ ) symmetry to  $XY$  ( $N = 2$ ) or Ising ( $N = 1$ ) symmetry. Long-range interactions could also be present and the interpretation of experimental results could be problematic (see the crossover section in 4.6).

We will also encounter the Potts symmetry  $Z_q$ . The Potts model has the Hamiltonian:

$$H = -J_1 \sum_{(ij)} \delta_{q_i q_j} \quad (2)$$

$\delta_{q_i q_j}$  refers to the  $q$  states Potts spin with  $\delta_{q_i q_j} = 0$  when  $q_i \neq q_j$  and  $\delta_{q_i q_j} = 1$  when  $q_i = q_j$ .

In addition we have to consider the symmetry of the lattice which is the sum of all symmetry elements which let the lattice invariant. For example, the triangular lattice has  $C_{3v}$  symmetry and the square lattice  $C_4$  symmetry.<sup>1</sup> Therefore we have to take into account the total BS composed of the  $O(N)$  spin rotations and the symmetries of the lattice.

#### 4.2.2. Breakdown of symmetry for ferromagnetic systems

If  $J_1$  in (1) is taken positive the Ground State (GS), for any lattice, is ferromagnetic with collinear spins pointing in the same direction. If  $J_1$  is negative (antiferromagnetic) but there is no frustration like for the square lattice, the GS is collinear with alternating direction. Then the BS will be identical to the ferromagnetic case. The symmetry at low temperature is

$O(N - 1)$  for the spins and the lattice symmetries are preserved. Therefore the BS is  $O(N) \rightarrow O(N - 1)$  where  $O(N)$  is the symmetry of the phase at high temperatures and  $O(N - 1)$  the symmetry at low temperatures. We will denote this BS  $O(N)/O(N - 1)$ . Keeping in mind that  $O(0) \equiv 1$ ,  $O(1) \equiv Z_2$ ,  $SO(1) \equiv 1$  and  $O(N) \equiv Z_2 \otimes SO(N)$  for  $N \geq 2$ , the BS  $O(N)/O(N - 1)$  can be written as  $Z_2$  for  $N = 1$ ,  $SO(2)$  for  $N = 2$ , and  $SO(N)/SO(N - 1)$  for  $N > 2$ .

All the ferromagnetic systems (cubic, stacked triangular, ...) with a Hamiltonian of type (1) have an identical BS and consequently belong to the same universality class. The only relevant variables are the dimension of the spin space, i.e. the number of components of the spin  $N$ , and the dimension of the real space  $d$ .

For Potts ferromagnetic system with a Hamiltonian of the type (2) and  $J_1 > 0$ , the Potts symmetry is broken in the low temperatures phase and the BS is simply  $Z_q$ . Again this does not depend on details of the system. This model has a second order phase transition for  $q \leq q_c$  and a first order phase transition for  $q > q_c$ . We know that  $q_c = 4$  in two dimensions and  $q_c < 3$  in three dimensions. Therefore, in three dimensions, for any  $q \geq 3$  the transition will be of first order.

In Table 4.1 we give the value of the critical exponents calculated by the Renormalization Group<sup>2</sup> (RG) depending on  $N$  and  $q$  in three dimensions ( $d = 3$ ). Even if  $N > 3$  does not correspond to physical systems, we will get very useful information for frustrated systems.

Table 4.1. Critical exponents for the ferromagnetic systems in three dimensions calculated by RG. <sup>(a)</sup>We cannot define exponents in a first-order transition, however in the case of a weak first-order transition the exponents found with MC and in experiments must tend to these values. <sup>(b)</sup>calculated by  $\gamma/\nu = 2 - \eta$ .

BS	$\alpha$	$\beta$	$\gamma$	$\nu$	$\eta$
$O(1)/O(0) \equiv Z_2$	0.107	0.327	1.239	0.631	0.038
$O(2)/O(1) \equiv SO(2)$	-0.010	0.348	1.315	0.670	0.039
$O(3)/O(2) \equiv SO(3)/SO(2)$	-0.117	0.366	1.386	0.706	0.038
$O(4)/O(3) \equiv SO(4)/SO(3)$	-0.213	0.382	1.449	0.738	0.036
$O(6)/O(5) \equiv SO(6)/SO(5)$	-0.370	0.407	1.556	0.790	0.031
1st order <sup>(a)</sup> ( $Z_q$ if $q > 3$ )	1	0	1	1/3	-1 <sup>(b)</sup>

### 4.2.3. Breakdown of symmetry for frustrated systems

The BS in frustrated systems is more complicated. We will present examples where the  $O(N)$  symmetry is reduced to  $O(N - 1)$ ,  $O(N - 2)$ ,  $\dots$ ,  $O(O)$  (completely broken in the last case). In addition it is possible that the lattice symmetry is also reduced, usually giving an additional  $Z_q$  (mostly  $q = 2$  and  $q = 3$ ) broken symmetry. Therefore the possible BS are  $S_{lattice} \otimes O(N)/O(N - P)$  with  $S_{lattice} = 1$ ,  $Z_2$  or  $Z_3$  and  $P$  varies from 1 to  $N$ .

#### 4.2.3.1. Stacked triangular antiferromagnetic lattices

We consider here the stacked triangular antiferromagnetic lattice (STA) with nearest-neighbor (NN) and next-nearest-neighbor (NNN)  $J_2$  antiferromagnetic interactions,  $J_1$  and  $J_2$ , respectively. There is no frustration along the  $z$  axis (the direction of stacking) and therefore the interaction can be ferromagnetic or antiferromagnetic along  $z$ . We will explain this case in detail since it shows many phenomena appearing in frustrated systems.

- **$\mathbf{J}_2 = 0$ :** Consider the case without second neighbor interaction ( $J_2 = 0$ ). It is not possible for all three spins at the corners of a triangle to have the optimal antiparallel orientation which would minimize the energy of individual pair interactions. The resulting compromise in the case of vector spins is the so-called  $120^\circ$  structure, as shown in Fig. 4.1 (see chapter 1). In frustrated systems, local minimization of the energy is not compatible with the global energy minimum (or minima). A formal definition proposed by Toulouse<sup>3</sup> (and also Villain<sup>4</sup>) in the study of spin glasses states that a geometry is frustrated if the sign of the product of exchange interactions  $J_i$  around a plaquette  $C$

$$\Phi_C = \text{sign} \left[ \prod_{i \in C} J_i \right] \quad (3)$$

is negative (where  $J_i < 0$  implies antiferromagnetic interactions). An antiferromagnetic triangular plaquette is thus frustrated as it involves a product of three  $J_i < 0$ . The triangular lattice is *fully frustrated* since all plaquettes satisfy this rule. The principal effect of the frustration here is that it gives rise to a non-collinear magnetic order. This spin-order GS (I) is planar and stable as long as next nearest neighbor interaction is small, that is  $0 \leq J_2/J_1 \leq 0.125$ .

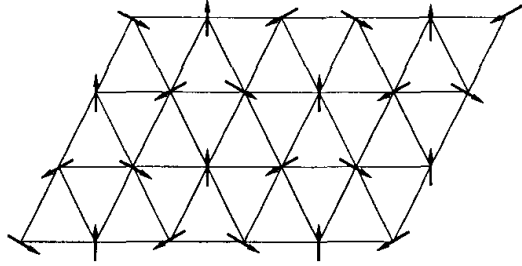


Fig. 4.1. Ground State I of the antiferromagnetic triangular lattice (first neighbors only). The GS has a  $120^\circ$  spin structure.

The BS between the disordered phase at high temperatures and the phase at low temperatures is  $O(N)/O(N - 2)$  which is equivalent to  $Z_2 \otimes SO(2)$  for  $N = 2$  and  $SO(N)/SO(N - 2)$  for  $N > 2$ . We notice that the exact value of the angle between the spin directions plays no role for the phase transition.

This system has been extensively studied in three dimensions for  $XY$  spins<sup>5,6,7,8,9</sup> for Heisenberg spin,<sup>5,8,10,11,12</sup> and for the unphysical systems  $N = 6$  in Ref. [13] and  $N = 8$  in Ref. [8]. The two dimensional systems have also been the subject of several studies for  $XY$  spins<sup>107,108,109,110,111</sup> and also for Heisenberg spins.<sup>146</sup>

- **$0.125 \leq J_2/J_1 \leq 1$ :** Consider the presence of an antiferromagnetic second neighbor interactions ( $J_2$ ) in the  $xy$  plane. The GS can be determined by minimizing the energy after a Fourier transform.<sup>14</sup> For  $0 \leq J_2/J_1 \leq 0.125$ , the GS is still the  $120^\circ$  structure. For  $0.125 \leq J_2/J_1 \leq 1$  the GS is degenerate with  $\theta$  taking any value between 0 and  $2\pi$  (see Fig. 4.2). However the degeneracy will be lifted by thermal fluctuations (spin waves) and only a collinear GS (II) will be chosen.<sup>15</sup> This phenomenon, called "order by disorder" following Villain,<sup>16</sup> is general in frustrated systems and we will see other examples (fcc, hcp) later. There are three ways to choose the parallel spins and the BS of the lattice symmetry  $C_{3v}$  is a three-state Potts symmetry  $Z_3$ . The total BS is  $Z_3 \otimes O(N)/O(N - 1)$ . For  $XY$  spins ( $N = 2$ ) it is equivalent to  $Z_3 \otimes SO(2)$ , and to  $Z_3 \otimes SO(N)/SO(N - 1)$  for  $N > 2$ . Numerical studies have been done for the three-dimensional case by Loison, Diep and Boubcheur.<sup>7,11</sup>
- $J_2/J_1 > 1$ : Now consider that  $J_2/J_1 > 1$ . The ground state is also degenerate, but this degeneracy is lifted by thermal fluctuations.

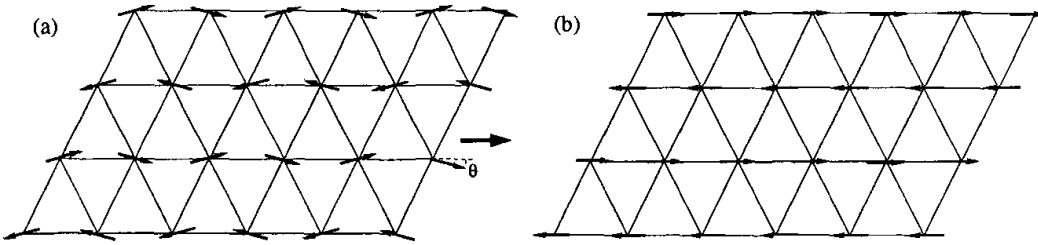


Fig. 4.2. Ground State (II) of the antiferromagnetic triangular lattice with first ( $J_1$ ) and second ( $J_2$ )-neighbor antiferromagnetic interactions.  $0.125 \leq J_2/J_1 \leq 1$ . (a)  $\theta$  can take any value between 0 and  $2\pi$ . (b) at  $T > 0$  only the “most collinear” GS is chosen.

The GS (III) is no more collinear, but still planar (see Fig. 4.3) and there is still three ways to choose the parallel spins.  $\alpha$  is determined by  $\cos(\alpha) = -0.5 \cdot (1 + J_1/J_2)$  and can be incommensurable, i.e. does not correspond to a rational value. Furthermore  $\alpha$  varies slowly as a function of the temperature. The BS is  $Z_3 \otimes O(N)/O(N-2)$  which is equivalent to  $Z_3 \otimes Z_2 \otimes SO(2)$  for  $N = 2$  ( $XY$  spins), to  $Z_3 \otimes SO(3)$  for  $N = 3$  (Heisenberg spins), and to  $Z_3 \otimes SO(N)/SO(N-2)$  if  $N \geq 4$ . Numerically the incommensurable angle is problematic. Indeed we have to impose periodic boundary conditions and since  $\alpha$  varies with the temperature, the size chosen compatible with  $\alpha(T = 0)$  is no more compatible with  $\alpha(T > 0) < \alpha(T = 0)$  for higher temperatures. Therefore the use of Finite Size Scaling technique (FSS, see 4.6) to calculate the critical exponents will be problematic.<sup>17</sup> In addition the GS III may not be stable under the new boundary constraint. Then the Potts symmetry could not be broken and the BS could be just  $O(N)/O(N-2)$ , and does not belong to the same universality class as previously. We will have an akin problem for helimagnets (see later) and for triangular lattices with two distinct nearest-neighbor interactions.<sup>17,18</sup>

This model has been studied in three dimensions by Loison, Diep and Boubcheur.<sup>7,11</sup>

- **Other BS:** We have seen the three BS which appear between the disordered phase and the GS. In addition two other transitions appear for a small range of  $J_2/J_1$  near 0.125 and 1: between the GS I and II for  $0.120 < J_2/J_1 \leq 0.125$ , and between the GS II and III for  $1 \leq J_2/J_1 < 1.05$ .<sup>7,11</sup> This is a general scheme: due to thermal fluctuation the most collinear state is favored when the temperature increases. Looking at the symmetries we can get the

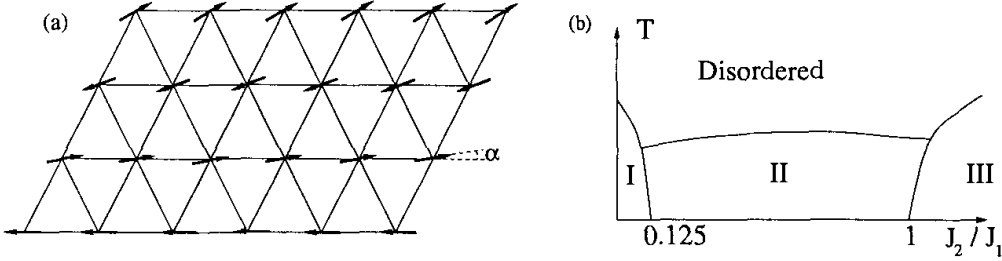


Fig. 4.3. (a) Ground State III of the antiferromagnetic triangular lattice with first ( $J_1$ ) and second ( $J_2$ ) -neighbor antiferromagnetic interactions.  $1 < J_2/J_1$ . (b) Phase diagram in the  $(J_2/J_1, T)$  space.

order and even the universality class of these transitions.

The GS III and II are compatible in the sense that at the transition  $\alpha$  will go smoothly to zero and the transition could be of second order. The BS between III and II is  $O(N - 1)/O(N - 2)$  and consequently the transition should be  $N - 1$  ferromagnetic type.

The GS I and II are incompatible because there is no way to go smoothly from one to the other and the transition should be of first order.

#### 4.2.3.2. *bct helimagnets*

We consider the body-centered-tetragonal (bct) helimagnets. The competition between the  $J_1$  and  $J_2$  interactions gives rise to a helical ordering along the  $z$  axis (see Fig. 4.4). This GS is characterized by the turn angle  $\alpha$  between spins belonging to two adjacent planes perpendicular to the  $z$  axis.  $\alpha$  is given by the formula  $\cos(\alpha) = -J_2/J_1$  and  $\alpha$  decreases slowly as function of the temperature. There is no breakdown of the symmetry of the lattice, the GS is non collinear but planar and the BS is  $O(N)/O(N - 2)$ , i.e. identical as the STA with first nearest neighbor interaction only.

Numerically we have a similar problem as for the STA with large NNN interaction:  $\alpha(T)$  varies as a function of the temperature, but with periodic boundary conditions a constraint is present.

Nevertheless effect of this constraint should not be too strong. Indeed a small constraint will not break a symmetry of the lattice and for the  $XY$ , it will not change the BS of the spin rotation because all the symmetries of the rotation group are already broken. For Heisenberg spins the GS could become non coplanar, but this is unlikely. Therefore we should find the same universality as that of the STA. The only difference will be a new

correction to the scaling laws for a second order phase transition. But for a first order one the boundary conditions would not matter.

This model has been studied by Diep and Loison<sup>19,20</sup>. A quantum version has also been considered by Quartu and Diep<sup>21</sup>.

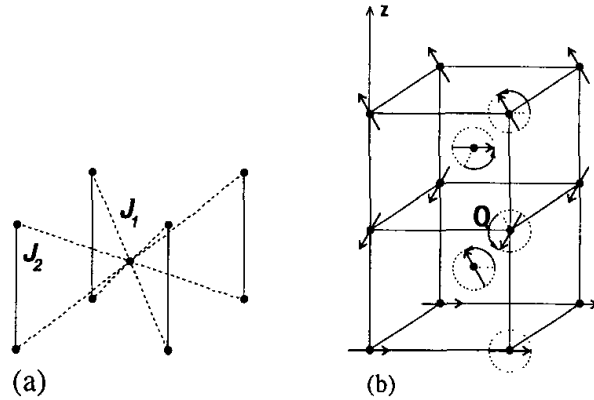


Fig. 4.4. a. Interactions for the bct. b. Ground State for the bct for  $J_2/J_1 = 0.5$ .

#### 4.2.3.3. Stacked $J_1-J_2$ square lattices

The  $J_1-J_2$  simple cubic lattice is made by stacking along the  $z$  axis the square lattices with antiferromagnetic (or ferromagnetic) first nearest neighbor interaction ( $J_1$ ) and antiferromagnetic second nearest neighbor interaction ( $J_2$ ) in the  $xy$  plane. For  $J_2/J_1 > 0.5$  the GS is degenerate but by “order by disorder” only collinear configurations appear (see Fig. 4.5). There are two ways to place the parallel spins (following the  $x$  or  $y$  axis) and a  $Z_2$  Ising symmetry of the lattice symmetry is broken. The BS will be  $Z_2 * O(N)/O(N - 1)$  or equivalently  $Z_2 \otimes SO(2)$  for  $N = 2$  and  $Z_2 \otimes SO(N)/SO(N - 1)$  for  $N > 2$ . For  $XY$  spins, there exists an identical BS as for the STA with first nearest neighbor interaction only. Therefore the two systems for  $N = 2$  should belong to the same universality class.

No numerical studies have been done on this model for the three-dimensional case. The two-dimensional case has been studied by Loison and Simon.<sup>22</sup>

#### 4.2.3.4. The simple cubic $J_1-J_2$ lattice

The simple cubic  $J_1-J_2$  lattice is similar to the stacked  $J_1-J_2$  square lattices shown above, but the second neighbor interactions are also present in the

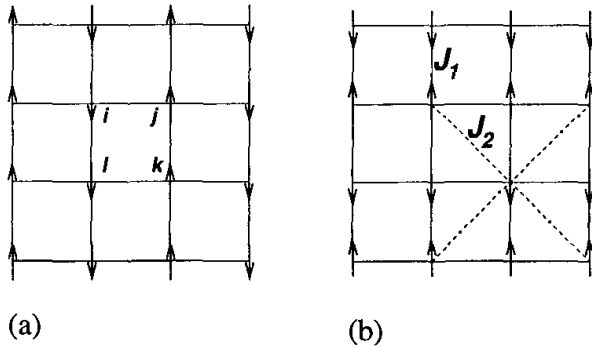


Fig. 4.5. Ground State of the stacked  $J_1$ - $J_2$  lattice with first ( $J_1$ ) and second ( $J_2$ )-neighbor antiferromagnetic interactions.  $J_2/J_1 > 0.5$ . (a) and (b) show the two possible configurations at non zero temperature.

$xz$  and  $yz$  planes. Similarly, by “order by disorder” the spin configuration is collinear, but now there are three ways to choose the direction of parallel spins (the  $z$  axis in addition to the  $x$  and  $y$  axes). Therefore the BS is  $Z_3 \otimes O(N)/O(N - 1) \equiv Z_3 \otimes SO(N)/SO(N - 1)$ . It is equivalent to the BS of the STA with intermediate NNN interaction.

This model has been studied for Heisenberg spin by Alonso et al,<sup>25</sup> and Pinettes and Diep<sup>26</sup>.

#### 4.2.3.5. $J_1$ - $J_2$ - $J_3$ lattice

The addition of a third-neighbor antiferromagnetic interaction to the previous model leads to new GS and therefore to a new BS. For some value of the interactions a non planar GS state appears.<sup>27</sup> In addition a  $Z_2$  symmetry is broken from the lattice group and the BS is hence  $Z_2 \otimes O(N)/O(N - 2)$  between the ordered phase and the disordered phase. For  $XY$  spins the BS is equivalently  $Z_2 \otimes Z_2 \otimes SO(2)$ , and for Heisenberg spins  $Z_2 \otimes SO(3)$ . There exist also various transitions between various phases, but following the discussion at the end of section 4.2.3.1 concerning STA with NNN interaction, it is not difficult to find that the transition will be of first order or of the ferromagnetic type  $SO(N - 1)/SO(N - 2)$ .

No numerical studies have been done so far on this model.

#### 4.2.3.6. Villain lattice and fully frustrated simple cubic lattice

The fully frustrated square lattice, called Villain lattice, is shown in Fig. 4.6a. This two-dimensional lattice has been extensively studied<sup>4,107,112,113,114,115,116,117,118,119,123</sup>.

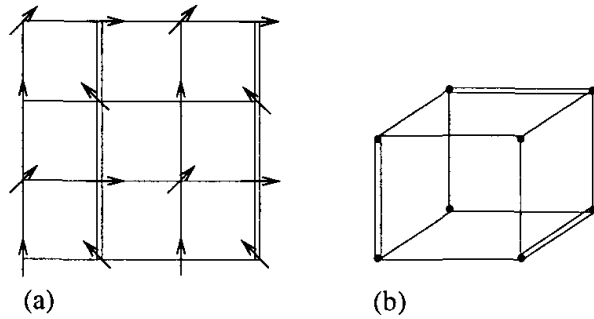


Fig. 4.6. a. Ground state of the stacked Villain lattice. The double lines are antiferromagnetic interactions. b. The fully frustrated cubic lattice.

The fully frustrated simple cubic lattice is made from the Villain lattice in three dimensions (see Fig. 4.6b). The lattice has three ferromagnetic interactions and one antiferromagnetic one for each plaquette. In this case the GS has an infinite degeneracy for Heisenberg spins and is twelve-fold degenerate for  $XY$  spins. Diep et al<sup>23,24</sup> and Alonso et al<sup>25</sup> have studied this model.

#### 4.2.3.7. Face-centered cubic lattice (*fcc*)

The face-centered cubic lattice (*fcc*) has a degenerate GS. But like the STA with NNN interaction, the “most collinear phase” is selected by thermal fluctuations. If we consider the smaller unit tetrahedral cell (see Fig. 4.7), the GS consists of two parallel and two antiparallel spin pairs. There are three ways to construct. This is equivalent to a Potts  $Z_3$  symmetry. Therefore, since the GS is collinear, the BS will be  $Z_3 \otimes O(N)/O(N - 1)$  or, equivalently,  $Z_3 \otimes SO(N)/SO(N - 1)$ . This BS is identical to the STA with intermediate NNN interaction.

This model has been studied by Diep and Kawamura<sup>28</sup> and Alonso et al.<sup>25</sup>

#### 4.2.3.8. Hexagonal-close-packed lattice (*hcp*)

The hexagonal-close-packed lattice (*hcp*) has many common features with the *fcc*. It is constructed by stacking tetrahedra (see Fig. 4.7) and an “order by disorder” mechanism lifts one part of the degeneracy of the GS resulting in a collinear GS composed with two parallel and two antiparallel spins. Equivalently to the *fcc* case, the BS will be  $Z_3 \otimes O(N)/O(N - 1)$  or equivalently  $Z_3 \otimes SO(N)/SO(N - 1)$ . This BS is identical to the STA with

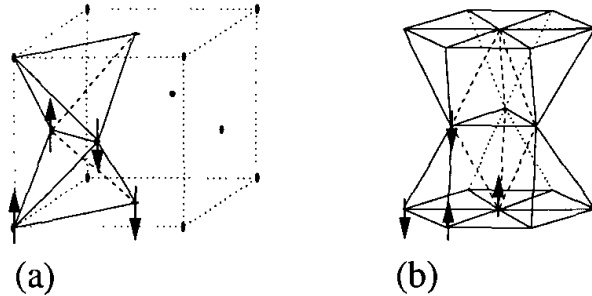


Fig. 4.7. a. Ground State of the fcc lattice. b. Ground State of the hcp lattice.

intermediate NNN interaction.

This model has been studied by Diep<sup>29</sup>

#### 4.2.3.9. Pyrochlores

The pyrochlore lattice can be made by stacking Kagomé lattices along (111) direction and is composed of an arrangement of corner-sharing tetrahedra (see the chapters by Bramwell et al, and by Gaulin and Gardner, this book). In presence of the first and third nearest neighbor interactions Reimers<sup>30</sup> has proved that the GS is collinear. Similar to the fcc and hcp cases, there are three ways to place the spins on each tetrahedron. The BS should therefore be  $Z_3 \otimes O(N)/O(N-1)$  or equivalently  $Z_3 \otimes SO(N)/SO(N-1)$ . This BS is identical to the STA with intermediate NNN interaction.

Reimers et al.<sup>30</sup> have studied this model.

#### 4.2.3.10. Other lattices

We could stack a Zig-Zag model<sup>31</sup> and various phases and phase transitions should appear. With an equivalent analysis described at the end of the section 4.2.3.1 concerning STA with NNN interaction, it is not difficult to find the nature of the transitions. Still, other lattices can be considered, however as shown later, they will have equivalent BS.

#### 4.2.3.11. STAR lattices

In addition one can construct spin systems having an identical breakdown of symmetry even if they do not correspond to a real system.

The first example is derived from the STA. Following the chapter of Delamotte et al. in this book<sup>32</sup> certain modes are irrelevant near the critical

point. In particular we can construct cells of three spins which are always in the ground state  $120^\circ$  configuration. One gets a system of cells in interaction but with a rigidity imposed inside the cells (see Fig. 4.8). We call this system STAR (Stacked Triangular Antiferromagnetic with Rigidity). The BS is then  $O(N)/O(N-2)$ , identical to STA with NN interaction.

This model has been studied in three dimensions by Dobry and Diep<sup>33</sup> and by Loison and Schotte.<sup>34,35,36</sup>

#### 4.2.3.12. Dihedral lattices $V_{N,2}$

The second example is derived from the STAR. It is composed of two vector spins  $\mathbf{e}_1$  and  $\mathbf{e}_2$  constrained to be orthogonal to each other at each lattice site. The interactions are set to be ferromagnetic and the spin  $\mathbf{e}_1$  ( $\mathbf{e}_2$ ) interacts only with the other spins  $\mathbf{e}_1$  ( $\mathbf{e}_2$ ) at other sites (see the Fig. 4.8). This model is referred to as the dihedral model  $V_{N,2}$ . We note that for  $XY$  spins  $N = 2$  the model can be right-handed or left-handed.

The Hamiltonian is defined by

$$H = J \sum_{\langle ij \rangle} \sum_{k=1}^P \left[ \mathbf{e}_k(i) \cdot \mathbf{e}_k(j) \right] \quad (4)$$

where  $P = 2$ .

At high temperatures the symmetry is  $O(N)$  for the first vector and  $O(N-1)$  for the second one, since the two vectors must be orthogonal. At low temperatures the symmetry is  $O(N-1)$  for the first vector and  $O(N-2)$  for the second one for the same reason. Therefore the BS is  $O(N)/O(N-2)$ , identical to the STA with NN interaction.

This model has been studied in three dimensions by Kunz and Zumbach<sup>37</sup> and by Loison and Schotte<sup>34,35</sup>, and in two dimensions for  $XY$  spins by Nightingale, Granato, Lee, and Kosterlitz.<sup>121,122</sup>

#### 4.2.3.13. Right-handed trihedral lattices $V_{3,3}$

For Heisenberg spins one can construct another model from the dihedral  $V_{3,2}$  with an identical BS. By adding a third vector  $\mathbf{e}_3 = \mathbf{e}_1 \times \mathbf{e}_2$  to the dihedral model no degree of freedom is added. Therefore the BS is unchanged and identical to the dihedral  $V_{3,2}$  and to the STA with NN interaction,  $O(3)/O(1) \equiv SO(3)$ .

This model has been studied in three dimensions by Loison and Diep.<sup>38</sup>

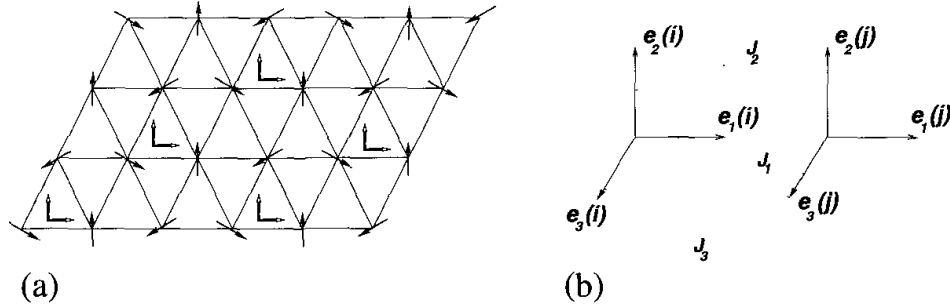


Fig. 4.8. a. STAR model and dihedral model. b. Trihedral model and  $V_{3,P}$  model.  $P = 1$  for  $J_2 = J_3 = 0$ ,  $P = 2$  for  $J_3 = 0$  and  $J_1 = J_2 = 1$ , and  $P = 3$  for  $J_1 = J_2 = J_3 = 1$ .

#### 4.2.3.14. $P$ -hedral lattices $V_{N,P}$

We can generalize the dihedral  $V_{N,2}$  model to  $V_{N,P}$  with  $P$  orthogonal vectors at each site. For  $P = N$  the  $N$  vectors can be right- or left-handed. The BS of symmetry is then  $O(N)/O(N - P)$  with  $P \leq N$ .

For  $P = 1$  we have the ferromagnetic case, i.e. a collinear GS. For  $P = 2$  we have a coplanar GS but no more collinear like in the STA with NN interaction. For  $P = 3$  the GS is no more coplanar but restricted to a space in three dimensions, and so on. The case  $N = P = 3$  could correspond to some experimental systems and spin glasses should also have this kind of breakdown of symmetry but in presence of disorder. For  $P = N$  the BS is  $O(N)/O(0) \equiv Z_2 \otimes SO(N)$ .

This model has been studied by Loison.<sup>39</sup>

#### 4.2.3.15. Ising and Potts– $V_{N,1}$ model

We define the following Hamiltonian

$$H = -J_1 \sum_{(ij)} \mathbf{S}_i \cdot \mathbf{S}_j \cdot \delta_{q_i q_j} \quad (5)$$

where  $\mathbf{S}_i$  are  $N$ -component classical vectors of unit length,  $\delta_{q_i q_j}$  are the  $q$ -state Potts spin ( $q = 2$  for Ising spin) with  $\delta_{q_i q_j} = 0$  when  $q_i \neq q_j$ , and the interaction constant  $J_1$  is taken positive (ferromagnetic interaction). The sum runs over all nearest neighbors. For  $N = 2$  this model is exactly equivalent to the dihedral  $V_{2,2}$  model introduced previously.

Obviously the BS is  $Z_q \otimes O(N)/O(N - 1)$  or equivalently  $Z_q \otimes SO(N)/SO(N - 1)$  which is identical to the stacked  $J_1$ – $J_2$  model if  $q = 2$ , and to the STA with NNN interaction, fcc, hcp if  $q = 3$ .

This model has been studied in three dimensions by Loison.<sup>40</sup> and in two dimensions for  $XY$  spins by Nightingale et al.<sup>121,122</sup>

#### 4.2.3.16. Ising and Potts– $V_{N,2}$ model

We can also define a dihedral model with the Hamiltonian (4) coupled with a Potts model in the same way as in (5). In this case the BS is  $Z_q \otimes O(N)/O(N-2)$  which is identical to the BS for the stacked  $J_1-J_2-J_3$  model if  $q = 2$  and to the STA with a large NNN for  $q = 3$ .

This model has been studied by Loison.<sup>40</sup>

#### 4.2.3.17. Landau–Ginzburg model

The Landau–Ginzburg Hamiltonian is constructed from the dihedral  $V_{N,2}$  model (see chapter of Delamotte et al.<sup>32</sup>). We release the constraints on the orthogonality of the spins and on the norm unity, replacing them by a potential we arrive at the following Hamiltonian

$$H = K \sum_{\langle ij \rangle} (\vec{\phi}(i) - \vec{\phi}(j))^2 + r \sum_i \vec{\phi}(i)^2 + u \sum_i \left( \vec{\phi}(i)^2 \right)^2 + v \sum_i \left[ (\vec{\phi}_a(i) \cdot \vec{\phi}_b(i))^2 - \vec{\phi}_a(i)^2 \vec{\phi}_b(i)^2 \right] \quad (6)$$

where  $\vec{\phi}(i) = (\vec{\phi}_a(i), \vec{\phi}_b(i))$  is an  $N + N$ -component vector defined on the lattice site  $i$ , and the summation  $\sum_{\langle ij \rangle}$  runs over all nearest neighbor pairs of the lattice. The first term represents the interactions between the sites and the last term the constraint that the spins  $\phi_a(i)$  and  $\phi_b(i)$  are orthogonal. If  $v = 0$ , the Hamiltonian is reduced to a standard  $O(2N)$  ferromagnetic problem. This is our third model that we call the chiral  $\phi^4$  model. For  $v > 0$  the BS is  $O(N)/O(N-2)$ , identical to STA with NN interaction.

This model has been studied numerically by Itakura.<sup>8</sup>

#### 4.2.3.18. Cubic term in Hamiltonian

One can introduce a model where the frustration is not geometrical but included on each link resulting in a non collinear GS. Consider the Hamiltonian for two spins:

$$H = J_1 \mathbf{S}_i \cdot \mathbf{S}_j + J_3 (\mathbf{S}_i \cdot \mathbf{S}_j)^3 \quad (7)$$

where  $\mathbf{S}_i$  is a  $N$  component classical vector of unit length,  $J_1$  is a ferromagnetic coupling constants  $J_1 < 0$  and  $J_3$  an antiferromagnetic one  $J_3 > 0$ . This cubic term has the same symmetries as the linear term and for a ferromagnetic system ( $J_3 < 0$ ) the universality class will be identical.<sup>41</sup> For  $1/3 \leq -J_3/J_1 \leq 4/3$  the minimum of  $H$  occurs when the two spins are canted with an angle  $\cos(\alpha) = \frac{1}{\sqrt{3J_3/J_1}}$ . On a cubic lattice the GS is planar, on a triangular lattice it is in three dimensions (if  $N \geq 3$ ), on a fcc lattice it is in four dimensions (if  $N \geq 4$ ), ... This phase has, at finite temperature, a transition to a ferromagnetic collinear phase. Therefore the BS will be  $O(N-1)/O(N-P)$  with  $P=2$  for the cubic lattice (planar GS),  $P=3$  for the stacked triangular,  $P=4$  for the fcc lattice ... The case  $P=2$  has been tested for Heisenberg spins and it gives indeed an  $O(2)/O(1) \equiv SO(2)$  transition, i.e. a ferromagnetic  $XY$  transition.<sup>41</sup> The case  $P=3$  has an identical BS as the STA but it has not been tested.

This model has been studied numerically by Loison.<sup>41</sup>

#### 4.2.3.19. Summary

The number of models that can be constructed by adding interactions is unlimited. However, the number of BS can only be finite. As has been shown in the previous sections, the symmetry breaking is limited to  $Z_q \otimes O(N)/O(N-P)$ . For the physically relevant cases it is restricted to  $q=1$  (Identity),  $q=2$  (Ising), or  $q=3$  (Potts),  $N=2$  ( $XY$  spins),  $N=3$  (Heisenberg spins), and  $P=1, 2$  or  $3$ . In total for Heisenberg spins there will exist 8 cases (two are identical:  $(q=1, P=3) \equiv (q=2, P=2)$ ) and 5 for  $XY$  spins.

The tables below summarize the probable BS for physical frustrated systems with  $XY$  or Heisenberg spins.

### 4.3. Phase transitions between two and four dimensions:

$$2 < d \leq 4$$

In this section we will concentrate on the nature of the various transitions mentioned in the previous section. Especially the transition for the  $O(N)/O(N-2)$  BS is considered in detail since it appears in numerous systems and was extensively debated. Then we will discuss the other BS which are less problematic.

Table 4.2. Most probable BS for frustrated  $XY$  spin systems with corresponding lattices or models

BS	lattice-model
$SO(2)$	ferromagnetic, small frustration
$Z_2 \otimes SO(2)$	STA, STAR, $V_{2,2} \equiv$ Ising- $V_{2,1}$ , bct, Stacked $J_1-J_2$ , Stacked Villain, Fully Frustrated cubic, Stacked Zig-Zag, chiral $\phi^4$ model, $(S_i \cdot S_j)^3$ term
$Z_3 \otimes SO(2)$	STA+NNN, cubic $J_1-J_2$ , fcc, hcp, pyrochlore, Potts- $V_{2,1}$
$Z_2 \otimes Z_2 \otimes SO(2)$	stacked $J_1-J_2-J_3$ , Ising- $V_{2,2}$
$Z_3 \otimes Z_2 \otimes SO(2)$	STA+NNN, Potts- $V_{2,2}$

Table 4.3. Most probable BS for frustrated Heisenberg spin systems with corresponding lattices or models

BS	lattice-model
$SO(3)/SO(2)$	ferromagnetic, small frustration
$SO(3)$	STA, STAR, $V_{3,2}$ , right-handed trihedral, bct, Stacked Villain, Stacked Zig-Zag, Fully Frustrated cubic(?), chiral $\phi^4$ model, $(S_i \cdot S_j)^3$ term
$Z_2 \otimes SO(3)/SO(2)$	Stacked $J_1-J_2$ , Ising- $V_{3,1}$
$Z_2 \otimes SO(3)$	Stacked $J_1-J_2-J_3$ , $V_{3,3} \equiv$ Ising- $V_{3,2}$ , $(S_i \cdot S_j)^3$ term, Fully Frustrated cubic(?)
$Z_2 \otimes Z_2 \otimes SO(3)$	Ising- $V_{3,3}$
$Z_3 \otimes SO(3)/SO(2)$	STA+NNN, cubic $J_1-J_2$ , fcc, hcp, pyrochlore, Potts- $V_{3,1}$
$Z_3 \otimes SO(3)$	STA+NNN, Potts- $V_{3,2}$
$Z_3 \otimes Z_2 \otimes SO(3)$	Potts- $V_{3,3}$

#### 4.3.1. $O(N)/O(N - 2)$ breakdown of symmetry

##### 4.3.1.1. Fixed points

Since many models (STA, STAR, dihedral, chiral  $\phi^4$  model,  $\dots$ , see Tables 4.2-4.3) have an identical BS, they should have equivalent critical behavior, i.e. they belong to the same universality class. However, the situation is more complicated and even with an identical BS two systems could show different behavior. To understand this fact we have plotted in Fig. 4.9 the fixed points in the critical plan for this model. Since there are two fields (eq. 6) to allow coplanar non collinear GS we will have four possible

fixed points. There are two more than the ferromagnetic case which has a collinear GS and consequently only one field.

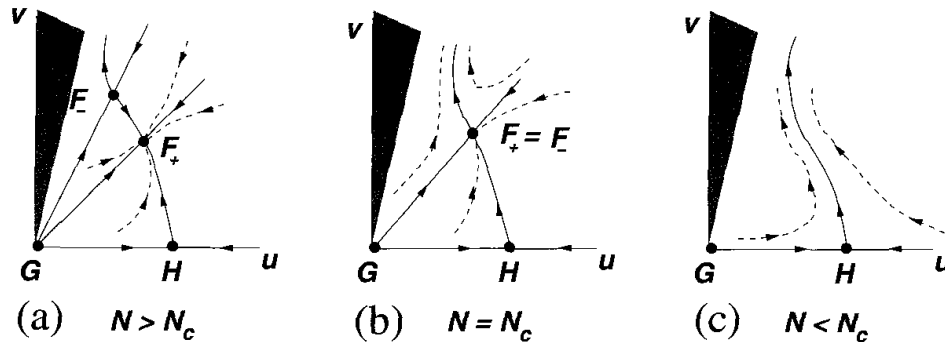


Fig. 4.9. (a), (b), (c) Hamiltonian flow induced by renormalization group transformations. The arrows indicate the direction of flow under iterations.

The fixed points are:

1. The Gaussian fixed G point at  $u^* = v^* = 0$  with mean-field critical exponents.
2. The  $O(2N)$  fixed point H at  $v^* = 0$  and  $u^* = u_H \neq 0$  with  $O(2N)$  exponents (see Table 4.1).
3. Two fixed points  $F_+$  and  $F_-$  at location  $(u_{F_+}, v_{F_+})$  and  $(u_{F_-}, v_{F_-})$  different from zero. These are the fixed points associated with a new universality class.

The existence and stability of the fixed points depend on the number of components  $N$ :

- a.  $N > N_c$ : four fixed points are present but three are unstable ( $G$ ,  $H$ ,  $F_-$ ) and a stable one  $F_+$ . Therefore the transition belongs to a new universality class different from the standard  $SO(N)/SO(N - 1)$  class. If the initial point for the RG flow is to the left of the line  $(G, F_-)$ , see Fig. 4.9a, the flow is unstable and the transition will be of first order. Therefore two systems with the same Hamiltonian and the same breakdown of symmetry could have different critical behaviors.
- b.  $N = N_c$ : the fixed points  $F_-$  and  $F_+$  coalesce to a marginally stable fixed point. One would think that the transition is “tricritical” but the exponents are different and not given by the tricritical mean-field values contrary to common belief. The reason is that there are

two non zero quartic coupling constants, see Fig. 4.9b, in contrast to the “standard” tricritical point where the quartic term disappears and a sextic term takes over.

- c.  $N < N_c$ :  $F_-$  and  $F_+$  move into the complex parameter space, see Fig. 4.9c. The absence of stable fixed points is interpreted as a signature of a first-order transition.

There are at least three questions: the value of  $N_c$ , the location of the initial point in the RG flow, and the nature of the transition.

#### 4.3.1.2. MCRG and first-order transition

The most reliable answers to these questions can be found in the article of Itakura.<sup>8</sup> He studied the STA model, dihedral model, and the chiral  $\phi^4$  model with the Hamiltonian (6), using Monte Carlo Renormalization Group (MCRG). This method is very powerful to give the flow diagram but not the critical exponents with a great precision.

He showed that the STA and dihedral models have an initial point in the RG flow under the line  $GF_-$  in the Fig. 4.9. Therefore they should belong to the same universality class provided the fixed point  $F_+$  exists, i.e.  $N > N_c$ . He found that  $N_c$  is between 3 and 8 in three dimensions which means that the real physical systems  $XY$  ( $N = 2$ ) and Heisenberg spins ( $N = 3$ ) have a first-order transition.

In addition he did a standard canonical Monte Carlo (MC) simulation for  $XY$  spins on the STA lattice for very large sizes of  $96^3$  and  $126^3$ . He found a first-order transition in agreement with MCRG study, contrary to smaller size systems which seem to have a second-order transition.<sup>5,6,7</sup> For Heisenberg spins he could not find a first-order transition but using the results of the MCRG he concludes that the first-order transition could only be seen for a size larger than  $800^3$  which is not accessible for actual computer resources. For the dihedral model with a canonical MC he found a clear first-order transition for large sizes for Heisenberg spins. For  $XY$  spins Loison and Schotte have already shown that the transition is of first order. Diep<sup>19</sup> in 1989 was the first to find a first-order transition in helimagnetics bct lattice with  $XY$  spins. This result was considered not conclusive because of problems of periodic boundary conditions in numerical simulation. However, as noted above, this is not relevant for  $XY$  spins (contrary to Heisenberg spins) and whence this conclusion is indeed correct for this BS.

We have now to address the problem why phase transitions appear continuous for small sizes but show the true first-order nature only for larger

sizes. This phenomenon is not restricted to frustrated spin systems such as STA but appears also in the weakly first-order transition of the two-dimensional Potts model with  $q = 5$  components.<sup>42,43,44</sup> More generally it appears when two fixed points collapse and disappears following one variable (like  $F_-$  and  $F_+$  in Fig. 4.9). See later for a comparison with the Potts model.

#### 4.3.1.3. Complex fixed point or minimum in the flow

The change from continuous to discontinuous transition can be understood using the concept of “complex fixed point” or “minimum in the flow” first introduced by Zumbach<sup>45</sup> and then developed by Loison and Schotte.<sup>34,35</sup> In Fig. 4.9c for  $N < N_c$  the fixed points  $F_-$  and  $F_+$  have collapsed and no solution exists in real parameter space. Instead there exists an imaginary solution plotted in Fig. 4.10a. These solutions should have an influence on the flow in the real plane as shown in Fig. 4.10b. Zumbach showed that there exists a basin of attraction due to the complex fixed points where the RG flow is very slow.

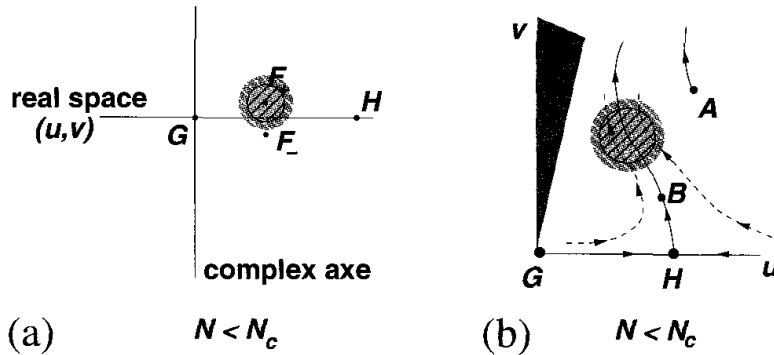


Fig. 4.10. a) For  $N < N_c$  the fixed points  $F_+$  and  $F_-$  become complex. b) Hypothesis on the Hamiltonian flow induced by renormalization-group transformations for  $N < N_c$  (see Fig. 4.9c). The arrows give the direction of flow. The two circles correspond to a low velocity region. The inner one corresponds to a minimum and hence an “almost” second-order transition. The outer circle corresponds to a slow crossover where the critical exponents will vary as a function of the system size.

If the RG flow of a system goes through this region, the number of RG iterations  $L \rightarrow L/b$  to get outside will be large. Therefore the size  $L$  of the numerical system considered, should be made large enough (see 4.6). If the size is “too small”, the flow is trapped inside of this low velocity region and the transition seems to be continuous. We immediately see that

the size  $L$  for which the true first-order transition is visible, that is when the flow is outside of the basin of attraction, will depend on the starting point. If it is located outside of the domain of low velocity and if the flow does not approach this region (point  $A$  in Fig. 4.10), then the first-order nature of transition can be seen already for small sizes. In the other case, if the initial position is such that the flow has to go through the entire region of low velocity (point  $B$  in Fig. 4.10), then the necessary size to reach the true first-order region will be very large. This explains why STA, STAR, dihedral and right-handed trihedral (for  $N = 3$ ) models having an identical breakdown of symmetry behave differently. Similarly a single system can show different behaviors for different sizes. For the Heisenberg case, for example, the right-handed trihedral model shows a strong first-order behavior even for small sizes. The dihedral model with the same BS for  $N = 3$  has a weaker first-order behavior visible only for sizes bigger than  $80^3$  spins while the STA or bct helimagnets show a second-order transition for similar sizes.

Furthermore the size of this region of low velocity will vary as a function of the distance between the complex fixed point  $F_+$  and the real plane shown in Fig. 4.10a. It has been shown that  $N_c$ , where the two fixed points  $F_-$  and  $F_+$  collapse and become complex, is bigger than 3 and the distance of  $F_+$  to the real plane will be larger for  $N = 2$  than for  $N = 3$ . Therefore the size of the domain of low velocity will be bigger for  $N = 3$  than for  $N = 2$ , and the true first-order behavior will be seen for smaller sizes in the  $XY$  case ( $N = 2$ ) than in the Heisenberg case ( $N = 3$ ). Indeed the first-order transition in the dihedral, STAR and STA can be seen from the size 12, 18 and 96, respectively, for  $XY$  spin systems (see Table 4.4). For Heisenberg spins this has been seen for the dihedral model with a size  $L = 80$  (see Table 4.6) while the estimate size for the STA should be larger than 800.<sup>8</sup> We note that a first-order transition has been found in quasi-one-dimensional STA<sup>9</sup>: the initial point in the flow diagram is outside the domain of low velocity.

For the  $XY$  case Delamotte et al.<sup>48</sup> using a non perturbative RG approach, found that there is no minimum in the flow but always a low velocity region (outer circle of Fig. 4.10b). Following the initial point in the RG flow the systems will show different sets of exponents, i.e. the system is in a crossover region. Numerical simulations tend to support this interpretation. Indeed for  $XY$  spins the STAR and the STA for small sizes ( $L < 40$ ) display a second-order transition with different critical exponents (see Tables 4.4-4.5) and for large sizes the STA shows a first-order transition as

discussed above.<sup>8</sup>

In conclusion the transition for Heisenberg spins is of first order but an "almost second-order transition" could exist for a range of "finite" sizes. This "almost second-order transition" will have a set of exponents different from the ferromagnetic ones because the breakdown of symmetry is different:  $O(N)/O(N - 2)$  in comparison to  $O(N)/O(N - 1)$  for ferromagnetic systems. This "new" universality class has been called chiral class.<sup>5</sup> For the XY case there is a crossover region with a slow velocity and exponents will vary between those of the chiral class and of weak first-order transitions ( $\nu = 1/3 \dots$  see Table 4.1). The critical exponents of this chiral class are given in Tables 4.4-4.8 for  $N$  varying from 2 to 6 for the STA, STAR, and dihedral models. With numerical simulations, exponents  $\gamma/\nu$ ,  $\beta/\nu$  and  $\nu$  are usually calculated using finite size scaling while other exponents are calculated using the scaling relation  $d\nu = 2 - \alpha$  and  $\gamma/\nu = 2 - \eta$  (see 4.6).

There is another indication given by Loison and Schotte<sup>34</sup> which suggests that the phase transition is indeed due of a "complex fixed point". Using the scaling formula  $\gamma/\nu = 2 - \eta$ , one gets a negative  $\eta$  for  $N = 2$  and  $N = 3$  for the STA, STAR or dihedral model (see Tables 4.4-4.8) which contradicts the theorem that  $\eta$  must be always positive.<sup>46,47</sup> Negative  $\eta$  can also be calculated using experimental results.<sup>48</sup> Therefore the fixed point cannot be real. Using this indication we can conclude that the continuous transition found in fully frustrated XY lattice<sup>23</sup> is indeed of first order.

Table 4.4. Critical exponents associated to the  $SO(2)$  symmetry by Monte Carlo for XY spins ( $N = 2$ ) and a BS  $Z_2 \otimes SO(2)$ . <sup>(a)</sup>Calculated by  $\gamma/\nu = 2 - \eta$ . The first result<sup>5</sup> comes from a study at high and low temperatures and uses the FSS. The second<sup>6</sup> uses the Binder parameter to find  $T_c$  and uses the FSS, the third<sup>7</sup> uses the maxima in FSS region.

system	Ref	$L_{max}$	$\alpha$	$\beta$	$\gamma$	$\nu$	$\eta$
STA	<sup>5</sup>	60	0.34(6)	0.253(10)	1.13(5)	0.54(2)	-0.09(8) <sup>(a)</sup>
STA	<sup>6</sup>	33	0.46(10)	0.24(2)	1.03(4)	0.50(1)	-0.06(4) <sup>(a)</sup>
STA	<sup>7</sup>	36	0.43(10)			0.48(2)	
STA	<sup>8</sup>	126			first order		
STA	<sup>9</sup>	35			first order		
bct	<sup>19</sup>	24			first order		
STAR	<sup>34</sup>	36			first order		
$V_{2,2}$	<sup>34</sup>	36			first order		

Table 4.5. Critical exponents associated to the  $Z_2$  symmetry (chirality  $\kappa$ ) by Monte Carlo for  $XY$  spins ( $N = 2$ ) and a BS  $Z_2 \otimes SO(2)$ . <sup>(a)</sup>Calculated by  $\gamma/\nu = 2 - \eta$ . The first result <sup>5</sup> comes from a study at high and low temperature and uses of FSS. The second <sup>6</sup> uses the Binder parameter to find  $T_c$  and uses the FSS.

system	Ref.	$L_{max}$	$\alpha$	$\beta_\kappa$	$\gamma_\kappa$	$\nu_\kappa$	$\eta_\kappa$
STA	<sup>5</sup>	60	0.34(6)	0.55(4)	0.72(8)	0.60(3)	0.80(19) <sup>(a)</sup>
STA	<sup>6</sup>	33	0.46(10)	0.38(1)	0.90(2)	0.55(1)	0.28(3) <sup>(a)</sup>
STA	<sup>8</sup>	126			first order		
STA	<sup>9</sup>	35			first order		
bct	<sup>19</sup>	24			first order		
STAR	<sup>34</sup>	36			first order		
$V_{2,2}$	<sup>34</sup>	36			first order		

Table 4.6. Critical exponents by Monte Carlo for Heisenberg spins ( $N = 3$ ) and a BS  $SO(3)$ . Calculated by <sup>(a)</sup>  $\gamma/\nu = 2 - \eta$ , <sup>(b)</sup>  $d\nu = 2 - \alpha$ , <sup>(c)</sup>  $2\beta/\nu = d - 2 + \eta$ .

system	Ref.	$L_{max}$	$\alpha$	$\beta$	$\gamma$	$\nu$	$\eta$
STA	<sup>5</sup>	60	0.240(80)	0.300(20)	1.170(70)	0.590(20)	+0.020(180) <sup>(a)</sup>
STA	<sup>10</sup>	36	0.242(24) <sup>(b)</sup>	0.285(11)	1.185(3)	0.586(8)	-0.033(19) <sup>(a)</sup>
STA	<sup>12</sup>	48	0.245(27) <sup>(b)</sup>	0.289(15)	1.176(26)	0.585(9)	-0.011(14) <sup>(a)</sup>
STA	<sup>11</sup>	36	0.230(30) <sup>(b)</sup>	0.280(15)		0.590(10)	0.000(40) <sup>(c)</sup>
bct	<sup>20</sup>	42	0.287(30) <sup>(b)</sup>	0.247(10)	1.217(32)	0.571(10)	-0.131(18) <sup>(a)</sup>
STAR	<sup>35</sup>	42	0.488(30) <sup>(b)</sup>	0.221(9)	1.074(29)	0.504(10)	-0.131(13) <sup>(a)</sup>
$V_{3,2}$	<sup>35</sup>	40	0.479(24) <sup>(b)</sup>	0.193(4)	1.136(23)	0.507(8)	-0.240(10) <sup>(a)</sup>
$V_{3,2}$	<sup>8</sup>	80			first order		

Table 4.7. Critical exponents by Monte Carlo for spins with four components ( $N = 4$ ) and a BS  $O(4)/O(2) \equiv SO(4)/SO(2)$ . Calculated by <sup>(a)</sup>  $\gamma/\nu = 2 - \eta$ , <sup>(b)</sup>  $d\nu = 2 - \alpha$ .

system	Ref.	$L_{max}$	$\alpha$	$\beta$	$\gamma$	$\nu$	$\eta$
STAR	<sup>36</sup>	42	0.287(27) <sup>(b)</sup>	0.291(11)	1.133(28)	0.571(9)	+0.015(18) <sup>(a)</sup>
$V_{4,2}$	<sup>36</sup>	40	0.278(30) <sup>(b)</sup>	0.290(12)	1.142(34)	0.574(10)	+0.011(25) <sup>(a)</sup>

Table 4.8. Critical exponents by Monte Carlo for spins with six components ( $N = 6$ ) and a BS  $O(6)/O(4) \equiv SO(6)/SO(4)$ . Calculated by <sup>(a)</sup>  $\gamma/\nu = 2 - \eta$ , <sup>(b)</sup>  $d\nu = 2 - \alpha$ .

system	Ref.	$L_{max}$	$\alpha$	$\beta$	$\gamma$	$\nu$	$\eta$
STA	<sup>13</sup>	36	-0.100(33) <sup>(b)</sup>	0.359(14)	1.383(36)	0.700(11)	+0.025(20) <sup>(a)</sup>

#### 4.3.1.4. Experiment

A resembling situation occurs in the analysis of experiments. There the correlation length  $\xi$  plays the role of the system size in numerical simulations. For a second-order transition one has  $\xi \sim (T - T_c)^{-\nu}$ . Therefore we should observe a crossover between the region of low velocity (“almost second-order transition” in Zumbach’s words) to the true first-order behavior for temperatures “closer” to the critical temperature. Unfortunately the situation is even more complicated in experimental systems with the omnipresence of planar or axial anisotropies and the one- or two-dimensional characters of the compounds. Then a succession of crossovers (see 4.6 for more details about crossovers) from 2d to 3d and from Heisenberg to Ising or  $XY$  behavior could lead to difficulties in the interpretation. Furthermore other (small) interactions could also dominate the behavior near the critical temperature and change the universality class.

**Experiments for  $XY$  spins:** All experimental results can be found in Ref. [34]. Several  $AXB_3$  compounds have the STA structure. The experiments on  $CsMnBr_3$ <sup>49,50,51,52,53,54,55,56,57,58,59</sup>  $RbMnBr_3$ <sup>60,61</sup> and  $CsVBr_3$ <sup>62</sup> give critical exponents compatible with those of MC simulation on STA and a second-order transition. We can interpret this result by the fact that the systems are under the influence of a complex fixed point, and  $t \propto T - T_c$  is too small to observe a first-order transition.

The case  $CsCuCl_3$ <sup>63</sup> is different since the authors observe a crossover from a second-order region with exponents compatible with MC results on STA for  $10^{-3} < t < 5 \cdot 10^{-2}$  to a region of first-order transition for  $5 \cdot 10^{-5} < t < 5 \cdot 10^{-3}$ . For  $t < t_0 \approx 10^{-3}$  one seems to observe the true first-order region which corroborates the scenario introduced previously.

Three kinds of helimagnetic structure have been studied: Holmium, Dysprosium and Terbium. Essentially three types of results exist: those compatible with MC ones of the STA, those with a large  $\beta$  incompatible with STA and those showing a weak first-order transition.

The results compatible with those of MC on STA for  $Ho$ <sup>65,67,66</sup>

$\text{Dy}^{66,73,74}$  and  $\text{Tb}^{78,79,80,81,82}$  can be interpreted as before: the systems are under the influence of  $F_+$ . The first-order transition for  $\text{Ho}^{64}$  and  $\text{Dy}^{71,72}$  is due to the fact that the measurements were done in the first-order region near the transition temperature. The values of the exponent  $\beta \sim 0.39$  in the case of  $\text{Ho}^{67,68,69,70}$  and  $\text{Dy}^{68,75,76,77}$  are not compatible with those found by MC ( $\beta \sim 0.25$ ). This fact can be explained by the presence of a second length scale in the critical fluctuations near  $T_c$  related to random strain fields which are localized at or near the sample surface.<sup>67</sup> Thus the critical exponent  $\beta$  measured depends on this second length.

**Experiments for Heisenberg spins:** All experimental results can be found in Ref. [34]. As explained previously, before the first-order region is reached, the crossover from Heisenberg to Ising or  $XY$  behavior prevents a first-order transition of Heisenberg type. Nevertheless the second-order transition can be studied for  $\text{VCl}_2$ ,<sup>83</sup>  $\text{VBr}_2$ ,<sup>84</sup>  $\text{Cu}(\text{HCOO})_2\text{CO}(\text{ND}_2)_2\text{D}_2\text{O}$ <sup>85</sup> and  $\text{Fe}[\text{S}_2\text{CN}(\text{C}_2\text{H}_5)_2]_2\text{Cl}$ .<sup>86</sup> For the last two examples the observed exponents might be influenced by the crossover from 2d to 3d Ising behavior. The experimental results agree quite well with the MC simulations.

#### 4.3.1.5. Value of $N_c$

Tables 4.4-4.8 allow us to get an idea of the value of  $N_c$ . The MCRG gives an estimate  $3 < N_c < 8$  but the values of  $\eta$  can give a better estimate following Ref. [34]. As can be seen for the  $XY$  and Heisenberg systems, negative values of  $\eta$  appear for the STA, STAR or dihedral model. But  $\eta$  must always be positive.<sup>46,47</sup> This is due to the use of the scaling relation  $\gamma/\nu = 2 - \eta$ . Indeed Zumbach<sup>45</sup> has shown that for an “almost second-order transition”, i.e. when the solution becomes complex, this relation has to be modified to  $\gamma/\nu = 2 - \eta + c$ ,  $c$  being a constant different from zero. We can use this relation as a criterion for real or complex fixed points. In three dimensions  $\eta$  is usually small and is almost independent of  $N$  for the ferromagnetic case, that is  $\sim 0.03$  (see Table 4.1). Our hypothesis is that it is also true for the frustrated case. Indeed for  $N = 6$  we found  $\eta \sim 0.03$  (see Table 4.8). Accepting this value  $c$  becomes zero around  $N_c \sim 4.5$ . Obviously if a bigger value of  $\eta$  is chosen,  $N_c$  will increase.

#### 4.3.1.6. Phase diagram ( $N, d$ )

In Fig. 4.11 we have plotted a phase diagram where the abscissa is the spin dimension  $N$  and the ordinate the space dimension  $d$ .

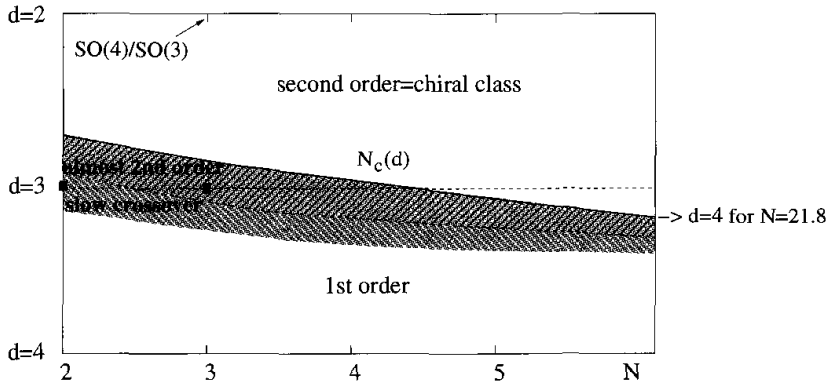


Fig. 4.11. The critical curve  $N_c(d)$  separating the first-order region for small  $N$  and large  $d$  from the second-order region for large  $N$  and low  $d$ . The squares represent the physical systems of interest ( $N = 2, 3$  in three dimensions).

There is a line which divides a region of first-order transition from a region of second-order transition. At, and near,  $d = 4$  we can use the RG  $d = 4 - \epsilon$  expansion to find  $N_c = 21.8 - 23.4\epsilon$ , and for  $d = 3$  we have seen that  $N_c \sim 4.5$ . Furthermore there is a region near this line where the transition is “almost second order”, i.e. under the influence of the complex fixed point for “small” sizes. The system will display a second-order transition with stable critical exponents. Besides, there is a slow crossover region where critical exponents vary with the system size. The sizes of these regions depend on the initial point in the flow diagram and therefore on the model.

Near two dimensions and for Heisenberg spins the transition is of the type  $SO(4)/SO(3)$ , i.e. ferromagnetic for spins with four components (see the following section and the chapter of Delamotte et al.<sup>32</sup> for more details).

#### 4.3.1.7. Renormalization-group expansions

We present here a review of the RG expansions (“non perturbative”,  $d = 4 - \epsilon$ , in fixed dimension  $d = 3$ , and  $d = 2 + \epsilon$ ). For more details see 4.6 and the chapter of this book of Delamotte et al.<sup>32</sup>

We discuss now the  $4 - \epsilon$  expansion. Using a continuous limit of the Landau Ginzburg Hamiltonian (6), it involves a perturbative extension  $(u, v)$  around the Gaussian solution with the dimension  $d$  and the number of spin

components  $N$  as parameters. To get the result for  $d = 3$  one puts  $\epsilon = 1$ . Of course the series are at best asymptotic and must be resummed, even for the ferromagnetic case.<sup>87</sup> The extension until  $\epsilon^2$  in Ref. [88] has been “resummed” (only three terms) and the value of  $N_c(d = 3) \sim 3.39$  is compatible with the numerical result  $N_c^{numerical}(d = 3) \sim 4.5$ . The calculations have been extended to  $\epsilon^4$  in Ref. [89] but unfortunately no resummation has been done on this series yet.

The expansion for fixed dimension  $d = 3$  is very similar to the  $d = 4 - \epsilon$  one. The series and the resummation will differ slightly. At three loops the result is  $N_c \sim 3.91^{90}$  which is again not far from  $N_c^{numerical}(d = 3) \sim 4.5$ . A very interesting picture emerges from the six-loop calculations.<sup>91,92</sup> First, for  $N \sim 5$ , the resummation does not converge. Second, for  $N = 3$ , the resummation gives rise to a very large variation of the critical exponents following the flow chosen to arrive at a single critical exponent at the critical point (see Fig. 5 of the reference<sup>92</sup>) which is a really “new” phenomenon. Third, for  $N = 2$  a second-order transition is predicted in contradiction to Itakura’s results<sup>8</sup> and the numerical simulations (see Tables 4.4-4.5). Manifestly we could conclude that the resummation chosen does not work for this series. To understand this we have to stress that the series has many more terms because of the double expansions in  $u$  and  $v$  compared to a single one for the ferromagnetic case. Whence it is much more difficult to find a “good” resummation scheme.

On the other hand Delamotte et al.<sup>93</sup> found that the transition must be of  $SO(4)/SO(3)$  type, i.e. equivalent to a ferromagnetic  $O(4)$  transition, near two dimension for Heisenberg spins. This study was done using the  $d = 2 + \epsilon$  expansion or equivalently the non linear  $\sigma$  model and the result is valid only near two dimensions. This prediction was checked by Southern and Young<sup>94</sup> by MC in two dimensions. But we can give arguments<sup>35</sup> using  $1/N$ -expansion and the value of the critical exponents to rule out this kind of transition in three dimensions. These arguments hold as long as the relevant operators are identical in  $1/N$  expansion and in the non linear  $\sigma$  model. Indeed for the  $1/N$  expansion, and equivalently for the  $4 - \epsilon$  expansion and in fixed dimension, we keep in the Hamiltonian only the terms which are renormalizable near  $d = 4$  or infinite  $N$ , and discard the others. Nevertheless it seems that some non renormalizable terms (see 4.6) become relevant and important for low  $N$  and  $d$  and, whatever the number of loops we cannot find the correct behavior using these expansions.

Because of the problems encountered by the standard expansions, a “non perturbative” approach could be very useful. This was introduced in

this model by Tissier et al.<sup>48</sup> We quote “non perturbative” because it is not an expansion resembling the other methods where the extension parameters ( $u, v, \epsilon$ ) are usually not small. In this non perturbative method even if we introduce only a few terms in the action, results will be very good and no resummation is necessary. We notice that the simplest action was studied by Zumbach<sup>45</sup> which allows him to introduce the “almost second-order” transition. Adding more terms, Tissier et al. found that they are able to retrieve all the previous expansions with additional information. Their value of  $N_c \sim 5.1$  is comparable to  $N_c^{numerical} \sim 4.5$ . In three dimensions they found critical exponents very close to those calculated by MC for  $N = 6$  (see Table 4.8), a minimum in the flow for  $N = 3$ , and a slow crossover for  $N = 2$  as explained in the previous section. They found also that the critical behavior is indeed that of a ferromagnetic  $O(4)$  transition near two dimensions for Heisenberg spins. Some non-renormalizable operators excluded in the  $4 - \epsilon$  and  $1/N$  expansions are included in this “non perturbative” method. These operators are always relevant between two and four dimensions whatever  $N$  is, but have an influence on the values of the critical exponents only for small  $N$  and near two dimensions. This explains the discrepancy between the  $d = 2 + \epsilon$  and  $d = 4 - \epsilon$  expansions.

#### 4.3.1.8. Short historical review

In this section we give a short historical review of studies on frustrated systems. Indeed the history was not straight if we look back at the last 25 years. The development began by a RG  $4 - \epsilon$  expansion by Jones, Love and Moore<sup>95</sup> in 1978. It is only in 1984 and in the following years that Kawamura<sup>5</sup> started with the first numerical simulations and, in combination with the results of several experiments, proposed a “new” universality class.

Then Azaria, Delamotte et al<sup>93</sup> found that the transition near two dimensions for Heisenberg spins should belong to the  $O(4)$  ferromagnetic class. Several groups (see Tables 4.4-4.8) have done numerical simulations and experiments which favored either the new universality class, a first-order transition, an  $O(4)$  transition and even a mean-field tricritical transition. During those years Sokolov et al.<sup>88,90</sup> have extended the RG expansion to three loops and found a first-order behavior for  $XY$  and Heisenberg spins.

Surely one of the most important articles to find the key to understand the physics was written by Zumbach,<sup>45</sup> using a non perturbative approach. He predicts an “almost second-order transition” for  $XY$  and

Heisenberg spins. Loison and Schotte,<sup>34,35</sup> using this concept, were able to get a clear picture for both the numerical and experimental studies. Then Tissier, Delamotte and Mouhanna,<sup>48</sup>, by extending the work of Zumbach, were able to understand the whole phase diagram for the dimension between two and four. To terminate Itakura,<sup>8</sup> confirmed the picture given by Zumbach&Loison&Schotte, which we think is the definitive answer from a numerical point of view.

#### 4.3.1.9. Relations with the Potts model

We would like now to stress the similarities between the Potts model and the frustrated case just studied.<sup>44</sup> In Fig. 4.12 we have plotted the RG flow diagram<sup>96</sup> as a function of the first- and second-neighbor ferromagnetic interactions ( $J_1$  and  $J_2$ ) and the chemical potential  $\Delta$  (corresponding to the site vacancy).

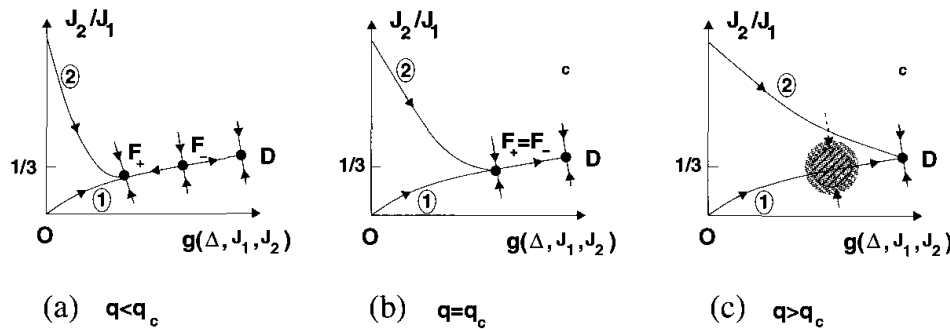


Fig. 4.12. Hypothesis of the renormalization flow in presence of second-neighbor interaction. For  $q \leq q_c$  the initial point of the flow is irrelevant to the critical behavior. For  $q > q_c$  the behavior for accessible lattice size will be different for the curve 1 (going through the basin of attraction of the fixed points  $F_+$ ) and the curve 2 (going directly to the first-order fixed point  $D$ ).

$F_+$  is the standard stable ferromagnetic fixed point and  $F_-$  is an unstable fixed point.  $D$  is a first-order fixed point.  $O$  is the initial point of the system. This figure resembles the one of the frustrated case (Fig. 4.9). For  $q < q_c$  the flow goes to the fixed point  $F_+$  and has a second-order transition. At  $q = q_c = 4$  (in two dimensions) the two points  $F_+$  and  $F_-$  collapse and a second-order phase transition with logarithm correction results. For  $q > q_c$  there is no longer a solution and the flow goes directly to the fixed point  $D$ , i.e. the system has a first-order transition. Our hypothesis is that even if the solution of  $F_+$  is complex, it has an influence on the real space and there is

a region of low velocity in the flow diagram. It can be a true minimum for  $q \gtrsim q_c$  with an “almost” second-order transition. For  $q$  bigger, no minimum should exist but, following the sizes studied, a variation of the critical exponents could occur. Indeed for  $q = 5$  a set of critical exponents was found,<sup>43</sup> corresponding to our hypothesis of “almost second-order” transition. The cases  $q = 6$  and  $q = 7$  have not been studied, but possibly one could observe a variation of critical exponents corresponding to a slow crossover to the first-order point.

We remark that depending of  $q$  we can observe clearly if the transition is of first order or second order. In Fig. 4.12 we have plotted the flow (2) in presence of the second-neighbor interaction. We observe that this flow is less influenced by the low velocity region than the flow (1) if  $q > q_c$  and it reaches  $F_+$  if  $q \leq q_c$ . Adding the third-nearest-neighbor interaction, we are able to find numerically that  $q_c = 4$  for the crossover from the first-order to second-order transitions. Contrary to the frustrated case we know roughly the coordinate of the fixed point  $F_+$  ( $J_2/J_1 \sim 0.3$ )<sup>97</sup> and  $\Delta \neq 0$ .<sup>96</sup> By consequence we know which kind of interaction must be added.

#### 4.3.2. $O(N)/O(N - P)$ breakdown of symmetry for $d = 3$

In mean-field theory, for  $N > P$  the model shows a usual second-order type, but for  $N = P$  the transition is a special one.<sup>45</sup> The BS in this case is  $Z_2 \otimes SO(N)$  and the coupling between the two symmetries leads to a special behavior which, for  $N = P = 2$  in two dimensions, has been extensively debated (see later in this chapter).

These generalized chiral models have been studied by applying the RG technique ( $d = 4 - \epsilon$  expansion).<sup>45,98,99</sup> The picture is very similar for all  $N \geq P \geq 2$ . At the lowest order in  $\epsilon$ , there are up to four fixed points, depending on the values of  $N$  and  $P$ . Amongst them are the trivial Gaussian fixed point and the standard isotropic  $O(NP)$  Heisenberg fixed point. These two fixed points are unstable. In addition, a pair of new fixed points, one stable and the other unstable, appear when  $N \geq N_c(d)$  with

$$\begin{aligned} N_c(d) = & 5P + 2 + 2\sqrt{6(P+2)(P-1)} \\ & - \left[ 5P + 2 + \frac{25P^2 + 22P - 32}{2\sqrt{6(P+2)(P-1)}} \right] \epsilon. \end{aligned} \quad (8)$$

For  $P = 2$  we find the standard result  $N_c = 21.8 - 23.4\epsilon$ . On the other hand, for  $P = 3$  we obtain  $N_c = 32.5 - 33.7\epsilon$  and for  $P = 4$  we obtain  $N_c = 42.8 - 43.9\epsilon$ . A “tricritical” line exists which separates a second-order

region for low  $d$  and large  $N$  from a first-order region for large  $d$  and small  $N$ . Applying  $\epsilon = 1$  ( $d = 3$ ), we obtained that  $N_c(d = 3) < 0$  for all  $P$ . For  $P = 2$  we know that this result does not hold and equivalently it does not apply for  $P \geq 3$ . Loison<sup>39</sup> has done some simulations for  $N = 3$  and  $N = 4$  with  $P = N$  and  $P = N - 1$  for the Stiefel  $V_{N,P}$  model. He showed that the transition is clearly of first order using numerical simulations. He generalized this result for all  $N$ . We remark that the fully frustrated cubic lattice (generalized Villain lattice) which could have an identical BS has also a first-order transition for Heisenberg spins.<sup>25</sup> In conclusion the transition in systems with a  $O(N)/O(N - P)$  the breakdown of symmetry is of first order for  $P = N$  and  $P = N - 1$  and in particular for the physical case  $N = P = 3$ , i.e. a non planar GS for Heisenberg spins.

#### 4.3.3. $Z_2 \otimes SO(N)/SO(N - 1)$ breakdown of symmetry for $d = 3$

For  $N > 2$ , this BS corresponds to a collinear ground state associated to a BS of the lattice (see Table 4.2-4.3). For example the stacked Villain lattices with first-neighbor ferromagnetic interaction  $J_1$  and a second-neighbor antiferromagnetic interaction  $J_2$  can have this BS. For  $J_2/J_1 < -0.5$  the competition between the two interactions leads to two possible ground states.<sup>22</sup> For  $N = 2$  ( $XY$  spins) the stacked Villain lattices and the stacked  $J_1-J_2$  model have the same BS as the STA and should display an analogous behavior (“almost second order” for small sizes following by a first-order transition for larger sizes).

We have simulated by MC technique the stacked Villain lattices and the stacked  $J_1-J_2$  lattice which have this kind of BS. We found that the transition seems continuous<sup>40</sup> for small lattices for  $XY$  and Heisenberg spins. For  $XY$  spins this is in agreement with the numerical simulation of STA which has an identical BS. We have also studied the Ising– $V_{N,1}$  model which has the same BS. For  $N = 2$  this model is the equivalent to the  $V_{2,2}$  model which has a strong first-order behavior as explained previously. For  $N = 3$  and  $N = 4$  we found also strong first-order transitions. Therefore it seems that the transition  $Z_2 \otimes SO(N)/SO(N - 1)$  is of first order for any  $N$  even if it could exist an “almost second-order transition” for small sizes.

#### ***$Z_3 \otimes SO(N)/SO(N - 1)$ breakdown of symmetry for $d = 3$***

This BS appears with a collinear ground state associated to a three-state Potts symmetry due to breakdown of lattice symmetries. This corresponds to various lattices where the unit cell is composed of four spins (two parallel spins and two antiparallel spins) like the STA with intermediate NNN interaction ( $0.125 < J_2/J_1 < 1$ ), the fcc, the hcp, the cubic  $J_1-J_2$  model or the pyrochlore (see Table 4.2-4.3).

As seen previously, even the coupling of an Ising symmetry ( $Z_2$ ) with  $SO(N)/SO(N - 1)$  can give a first-order transition. Whence it is expected that the transition with a three-state Potts symmetry ( $Z_3$ ) gives also a first-order transition which is even stronger if we consider that the Potts symmetry alone has a first-order transition in  $d = 3$  for  $q = 3$ . Indeed a strong first-order transition was seen in the fcc,<sup>25,28</sup> hcp,<sup>29</sup> cubic  $J_1-J_2$  model<sup>25,26</sup> pyrochlore<sup>30</sup> and STA with NNN interaction<sup>7,11</sup> for  $XY$  and Heisenberg spins.

We have done some simulations for the Potts– $V_{N,1}$  model with the Hamiltonian (5) with  $q \geq 3$ , i.e. the  $q$ -state Potts model coupled to an  $N$ -component vector. We found a strong first-order transition for any  $N$  and  $q$ .

In conclusion the transition for the  $Z_q \otimes SO(N)/SO(N - 1)$  BS in  $d = 3$  is of first order for any  $N \geq 2$  and  $q \geq 2$ .

#### ***$Z_q \otimes O(N)/O(N - 2)$ and other breakdown of symmetry in $d = 3$***

This BS appears with a planar ground state associated to a three-state Potts symmetry. One example is the STA with NNN interaction  $J_2/J_1 > 1$  (see Table 4.2-4.3).

To simulate this BS we have used a Potts– $V_{N,2}$  model for any  $q$ . We found the behavior of a strong first-order transition whatever  $N$  and  $q$  are. It is not surprising if we consider that the “less frustrated” model Potts– $V_{N,1}$  is already of first order.

We have also simulated the  $Z_q \otimes O(N)/O(N - 3)$  for  $N = 3$  which corresponds to the BS  $Z_q \otimes Z_2 \otimes SO(N)$  using a Potts– $V_{N,P}$  model. We found again a strong first-order transition. Similar results are obtained for Ising–Potts– $V_{N,1}$  and Ising–Potts– $V_{N,2}$  models.

To summarize, it seems that the coupling between a Potts or Ising symmetry and a continuous symmetry of vector spins give always rise to a first-order transition.

#### 4.4. Conclusion

We have studied breakdowns of symmetry of three-dimensional lattices for  $XY$  ( $N = 2$ ) and Heisenberg ( $N = 3$ ) spins. The general form of the breakdown of symmetry is  $S_{lattice} \otimes O(N)/O(N - P)$ .  $S_{lattice}$  is usually a Potts symmetry  $Z_q$  ( $Z_1$  corresponds to the identity,  $Z_2$  to an Ising symmetry,  $Z_3$  to a three-state Potts symmetry, ...).  $P$  runs from 1 to 3.

If the frustration is small the GS can be collinear ( $P = 1$ ) without breaking any symmetry of the lattice  $S_{lattice} = 1$ , the BS will be  $SO(N)/SO(N - 1)$  and the transition will be of second order like in ferromagnetic systems.

If the frustration is strong enough, we can have a non collinear GS with the usual planar configuration ( $P = 2$ ) like in the STA or helimagnets and  $S_{lattice} = 1$ . Depending on the model and for not “too big” sizes, the transition could appear continuous belonging to a new universality class. For an infinite size the system will have a first-order transition.

Some more complicated systems could also have a non planar GS, and for Heisenberg spins it corresponds to  $P = 3$  with usually  $S_{lattice} = 1$ . The transition will be of first order with a possible “almost second-order” behavior for small system sizes similar to the  $P = 2$  case.

Some even more complicated systems could have a non collinear GS ( $P = 2$  or  $P = 3$ ) with  $S_{lattice} = Z_q$  and  $q = 3$ . For example the STA with large NNN interaction has a strong first-order transition.

On the other hand some frustrated systems have degenerate GS but by “order by disorder” a collinear GS ( $P = 1$ ) is selected. The lattice symmetry could be broken giving an additional BS.  $S_{lattice} = Z_2$  (Ising) for the stacked Villain model, or  $S_{lattice} = Z_3$  in fcc, hcp, STA with intermediate NNN interaction, and pyrochlore. For the  $Z_3$  symmetry the transition is strongly of first order even for small sizes. For the  $Z_2$  symmetry the transition is also of first order for large sizes but looks continuous for small sizes. Therefore we cannot exclude an “almost second-order” behavior belonging to a new universality class.

In conclusion frustrated systems have a first-order transition for  $XY$  and Heisenberg spins in three dimensions even if for “small” sizes the systems would show a second-order transition. “Small” could mean sizes of thousands of lattice constants and the first-order transition will then not be observable with the actual computer resources.

## 4.5. $O(N)$ frustrated vector spins in $d = 2$

### 4.5.1. Introduction

The situations in two-dimensional systems are different from the three dimensions. The Mermin–Wagner theorem<sup>100</sup> asserts that no magnetization appears at non-zero temperature. However, a transition due to the topological defects<sup>101,102</sup> can appear. The binding–unbinding transition of vortex–antivortex pairs for  $XY$  spin systems is a classical example. We note that their exact role for three-dimensional phase transitions is not clear.<sup>103,104,105</sup> For non collinear GS, the topological properties of the system differ from those of collinear GS and new types of transition could appear. In the following we will briefly review the ferromagnetic case, then the frustrated  $XY$  case, applicable to Josephson–junction arrays in magnetic fields, and finally the frustrated Heisenberg cases.

### 4.5.2. Non frustrated $XY$ spin systems

For a non frustrated  $XY$  spin system the order parameter is  $SO(2)$ . The topological defects of this group is only the point defect classified by the homotopy group  $\Pi_1(SO(2)) = Z$ ,  $Z$  being the topological quantum number of the defect.<sup>101,102</sup> A Kosterlitz–Thouless (KT) transition<sup>106</sup> exists at the critical temperature  $T_c \sim 0.9$ , driven by the unbinding of vortex–antivortex pairs.

This transition has some special features: for  $T < T_c$  the correlation length ( $\xi$ ) is infinite, while for  $T > T_c$  it has an exponential decreasing contrary to the power-law behavior in the standard transition.

Several numerical methods exist to calculate the critical temperature and the critical exponents (see 4.6).

### 4.5.3. Frustrated $XY$ spin systems: $Z_2 \otimes SO(2)$

A frustrated  $XY$  spin system can have many order parameters as previously seen (see Table 4.2). The most studied case is  $Z_2 \otimes SO(2)$  which corresponds to a non collinear GS: triangular lattice,<sup>107,108,109,110,111</sup> Villain lattice or two-dimensional fully frustrated lattice<sup>107,4,112,113,114,115,116,117,118,119</sup> and related Zig–Zag models.<sup>31,120</sup> In combination to the topological defect point  $Z$ , there is a line of  $Z_2$  corresponding to an Ising transition. Therefore they will have similar properties as the  $J_1$ – $J_2$  model, the  $V_{2,2}$  model or any model where the  $Z_2$  symmetry comes from the lattice. We note that different models can have an identical group and there-

fore the same topological defects. The following models should have analogous properties: the Villain model on the Villain lattice,<sup>123</sup> The Ising– $V_{2,1} \equiv V_{2,2}$  model,<sup>121,122</sup> the 19-vertex model,<sup>124</sup> the 1D quantum spins,<sup>125</sup> the Coulomb gas representation,<sup>126,127,128,129</sup> the  $XY - XY$  model,<sup>130,131</sup> or the RSOS model.<sup>132</sup>

This kind of models was widely studied because it is believed to correspond to experimental systems such as Josephson–Junction arrays of weakly coupled superconducting islands<sup>133,134</sup> or films of Helium  $^3\text{He}$ .<sup>135,136,137,138</sup>

The question is to understand the coupling between the vortex–antivortex and the Ising symmetry. Contrary to the three-dimensional case discussed previously there are no clear accepted answers to these questions. We will therefore only present the different results in the high temperature region and in the FSS, giving some clues to understand the physics of these systems.

What are the possible scenarios?

1.  $T_c^{KT} < T_c^{Ising}$

The KT transition associated to the topological defects appears at a temperature lower than the one associated to the Ising transition even if they can be very close. The two transitions should have standard behaviors ( $\nu^{KT} = 0.5$ ,  $\nu^{Ising} = 1, \dots$ ).

Furthermore Olsson has proposed that the Ising behavior could be observed only when  $L \gg \xi^{KT}$ . Since  $\xi^{KT}$  is infinite for  $T \leq T_c^{KT}$  and decreases exponentially for  $T > T_c$ , it will correspond to a high temperature region with  $T \gg T_c^{KT}$ , but also  $T \gg T_c^{Ising}$  when the two transitions appear in close neighborhood. In particular the FSS region will have a non standard Ising behavior for the sizes accessible with actual computer resources. Only for a very large lattice the standard Ising behavior will be visible. We observe the similarity of this hypothesis with the one described previously in three dimensions and we could call the transition in the FSS an “almost new Ising–KT behavior”.

2.  $T_c^{KT} \sim T_c^{Ising}$

The two transitions appear at the same temperature and display different behaviors compared to the standard one. We remark that for high temperatures  $T \gg T_c$ , i.e. in the high-temperature region, we cannot assume that the coupling between the  $Z_2$  symmetry and the topological defects would be identical as for  $T \sim T_c$ . Indeed with a lot of small  $Z_2$  walls dividing the system it is not certain

that the vortex and the antivortex should play an important role and we could get a standard Ising transition.

### 3. $T_c^{KT} > T_c^{Ising}$

This hypothesis was advanced by Garel et Doniach in 1980 for the  $J_1-J_2$  model,<sup>139</sup> but numerical MC simulations have shown that it is not the case<sup>22</sup> for this system.

To choose the most probable hypothesis we will look now at the numerical results:

Some information can be provided by numerical MC simulations in the high-temperature region. Fitting the results it is possible to get the critical temperature and the critical exponents. Because of the presence of corrections and by consequence of many free parameters, the extraction of the results is difficult.

For the Ising symmetry Olsson<sup>123</sup> has found a standard ferromagnetic one with  $\nu^{Ising} \sim 1$ ) while Jose and Ramirez<sup>115</sup> found  $\nu^{Ising} \sim 0.87$ . New simulations should be done to resolve this discrepancy. If  $\nu^{Ising} \neq 1$ , it will a counter-proof to Olsson's claim (first possibility). On the other hand, if  $\nu^{Ising} = 1$ , we cannot rule out the second possibility.

The exponent of the KT transition have been only calculated by Jose and Ramirez.<sup>115</sup> They found non standard  $\nu^{KT} \sim 0.3$  to be compared to 0.5 in the ferromagnetic case. If this result is in favor of the second hypothesis, it cannot rule out the first one. Indeed we can reverse the argument given at the end of the second hypothesis. If at high temperatures the system is composed of many domains separated by walls of  $Z_2$ , the correlation between the topological defects could not be the one of the standard one. Therefore there is no definitive conclusion from the high-temperature simulations.

Now we can look at the results in the FSS.

For the Ising transition the critical exponents have been precisely determined by Loison and Simon,<sup>22,111</sup> for the  $J_1-J_2$  model using both the FSS and the dynamical properties including the first correction<sup>111</sup> due to the lattice size  $L$ . They obtained non standard critical exponents  $\nu^{Ising} = 0.815(20)$ . The "large" error is due to the inclusion of the corrections. See Ref. [111] for a review of all the numerical works. For the triangular lattice the critical temperature is known with high precision  $T_c^{Ising} = 0.5122(1)$ .

The KT transition is more problematic. First we can use the helicity<sup>106</sup>  $\Upsilon$  to find the critical temperature. If we admit the same universal jump at the critical temperature as the ferromagnetic one, we get  $T_c^{KT} = 0.5010(10)$

a temperature much smaller than  $T_c^{Ising} = 0.5122(1)$ . But we cannot be sure that  $\Upsilon_{jump}^{frustrated} = \Upsilon_{jump}^{ferromagnetic}$  and this result must be taken with care.

As explained in the previous section we can use the Binder parameter or the dynamical properties of the model to calculate  $T_c^{KT}$  and the critical exponents. Using this method we found very interesting results. First the Binder parameter shows a power-law transition and not an exponential one. In addition the critical exponents and temperatures calculated by the two methods are in good agreement with  $T_c^{KT} = 0.5102(2)$  just below  $T_c^{Ising} = 0.5122(1)$  for the triangular lattice. The critical exponent  $\eta^{KT} = 0.36(1)$  is very different from the standard one 0.25. These results are in accord with those on the  $J_1-J_2$  model. What is disturbing is that for the triangular lattice, accepting  $T_c^{KT} = 0.5102(2)$ , the helicity jump is smaller than the  $\Upsilon_{jump}^{ferromagnetic}$  although it is believed that it should be greater.

The situation is puzzling with no definitive conclusions.

#### 4.5.4. Frustrated XY spin systems: $Z_3 \otimes SO(2)$

Two-dimensional systems with an order parameter like  $Z_3 \otimes SO(2)$  are less numerous than three-dimensional systems. Following Table 4.2 we know at least two systems: the triangular lattice with intermediate NNN interaction and the Potts– $V_{2,1}$  model.

No numerical studies have been done for the former system, but we have studied<sup>141</sup> the latter one. It gives a first-order transition.

Following the reasoning of the previous section two principal hypotheses appear:

1. Olsson hypothesis: KT transition at lower temperature following the transition associated to the Potts symmetry  $Z_3$  at higher temperature. Non standard critical exponents should appear in the FSS region due to a screening length ( $\xi^{KT}$ ). The “true” standard second-order behavior will appear only for very large lattices ( $L \gg \xi^{KT}$ ) or in the high-temperature region.
2. A new behavior for the KT and Potts transitions at the same critical temperature.

The results are in favor of the second hypothesis. The Potts symmetry has a first-order transition. It means that its correlation length  $\xi_{Z_3}$  is finite at the critical temperature and less than  $\xi_{KT}$ . There will be no change even if the system size  $L$  is much larger and the system will never show

a standard three-state Potts second-order transition. Obviously we cannot apply directly this result to the Ising-KT transition since the two models are not equivalent although it is nevertheless an argument against the Olsson's hypothesis.

#### 4.5.5. *Frustrated XY spin systems: $Z_2 \otimes Z_2 \otimes SO(2)$ and $Z_3 \otimes Z_2 \otimes SO(2)$*

Following Table 4.2 the order parameter  $Z_2 \otimes Z_2 \otimes SO(2)$  can appear with a  $J_1-J_2-J_3$  lattice or an Ising- $V_{2,2}$  model. In addition  $Z_3 \otimes Z_2 \otimes SO(2)$  exists in the triangular antiferromagnetic with NNN interaction and in the Potts- $V_{2,2}$  model. No numerical studies have been done on these models.

#### 4.5.6. *Frustrated Heisenberg spin systems: $SO(3)$*

For a non frustrated Heisenberg spin system the order parameter will be  $SO(3)/SO(2)$  and no topological defects exist in two dimensions, no phase transition will appear.

For a frustrated system many order parameters can exist (see Table 4.3), but only the planar GS have received attention. In this case the order parameter is  $SO(3)$  and there exist point defects that is  $Z_2$ -vortex-antivortex<sup>101,102</sup>. These topological defects are different from the  $Z$ -vortex present in  $XY$  systems. The existence of a critical transition driven by the unbounding of vortex-antivortex was first conjectured by Kawamura and Miyashita.<sup>142</sup>

At low temperatures the spin waves will dominate the behavior of the system and forbid an infinite correlation length below  $T_c$  contrary to  $XY$  spins. The behavior should be equivalent to the one present in the four-dimensional ferromagnetic system.<sup>93</sup> This conjecture based on the non linear  $\sigma$  model ( $d = 2 + \epsilon$  expansion) and on symmetry arguments was checked by Southern and Young<sup>94</sup> and Caffarel et al.<sup>143</sup>

At higher temperatures the topological defects will clearly have a role.<sup>143,144,145,146</sup>

Caffarel et al.<sup>143</sup> have studied numerically two models having identical spin waves but not the same topological defects. One has the topological  $Z_2$  defects, the other not. They showed that the two models are equivalent at low temperatures, but show differences at higher temperatures due to the topological defects.

Southern and Xu<sup>143</sup> studying by MC simulations the vorticity associated to the vortex-antivortex proposed that the vorticity has a jump at the

critical temperature similar to that of the KT transition.

Kawamura and Kikuchi<sup>145</sup> using different boundary conditions in MC simulations also observed various phenomena associated to the vorticity which, according to them, are a proof of a phase transition.

Last, Wintel et al.<sup>146</sup> have studied theoretically and numerically the region above the suspected critical temperature for the triangular antiferromagnetic lattice ( $T_c \sim 0.29$ ). They claimed that the correlation length and susceptibility must follow a KT law.

There are numerical evidences of the importance of topological defects at finite temperatures and it seems that these systems undergo a kind a topological phase transition. Nevertheless we have no certainties that the phenomena present at finite sizes would hold for the infinite size.

#### 4.5.7. *Frustrated Heisenberg spin systems: $Z_2 \otimes SO(3)$ , $Z_3 \otimes SO(3) \dots$*

By inspecting Table 4.3 it is not difficult to see that other order parameters exist in frustrated systems. One of the most interesting should be  $Z_2 \otimes SO(3)$ . It corresponds to a non planar GS which could exist in experimental systems. Numerically the simplest system would be the Stiefel  $V_{3,3}$  model or equivalently the Ising– $V_{2,2}$  model. The comparison with the  $XY$  case would be very interesting. In particular the Ising transition could appear near the  $SO(3)$  transition (see previous section) and the coupling between the  $Z_2$  walls and the vortex could be very instructive. If we follow the second hypothesis of Olsson for the  $XY$  case (see section 4.5.3), the transition should display an “almost second-order transition”.

Symmetrically the coupling of the  $SO(3)$  vortex with a  $Z_3$  Potts model which appear in the Potts– $V_{3,2}$  model could also disclose interesting properties. Does it show first-order properties as for  $SO(2)$  vortex?

Some other breakdowns of symmetry could also appear like  $Z_3 \otimes Z_2 \otimes SO(3)$  in the antiferromagnetic triangular lattice with large NNN interaction. Similar questions appear. We note that the  $SO(3)/SO(2)$  order parameter does not have a topological transition. The transition of the type  $Z_2 \otimes SO(3)/SO(2)$  for the  $J_1-J_2$  model or  $Z_3 \otimes SO(3)/SO(2)$  for the triangular lattice with intermediate NNN interaction should have a standard transition (Ising or three-state Potts model).

#### 4.5.8. Topological defects for $N \geq 4$

Some other topological defects should exist for an order parameter of the type  $SO(N)$ , with a GS in  $N - 1$  dimensions,  $Z_2 \otimes SO(N)$ , with a GS in  $N$  dimensions, and  $Z_q \otimes SO(N)$  with a coupling of a GS in  $N - 1$  dimensions and a lattice symmetry ... All questions raised for Heisenberg spins still hold in these cases.

### 4.6. General conclusions

In this chapter we have studied the phase transition in frustrated systems between two and four dimensions. We have found various breakdowns of symmetry, contrary to the unique one for ferromagnetic systems.

In three dimensions the transition is always of first order in the thermodynamic limit. However for “small” sizes in numerical simulations or for temperatures not “too close” to the transition temperatures in experiments, the system could display an “almost universality class” for an  $O(N)/O(N - 2)$  breakdown of symmetry. Many compounds studied experimentally are in this class.

In two dimensions the situation is much less clear. Indeed the topological defects can play a fundamental role and their couplings with a discrete symmetry (Ising or Potts) is unknown. We hope that in the near future the two-dimensional case will be clarified as the three-dimensional one on which our understanding has increased considerably in the last decade.

### Acknowledgments

I am grateful to Prof. K. D. Schotte and Sonoe Sato for their support, discussions, and for critical reading of the manuscript. This work was supported by the DFG SCHO 158/10-1.

### Appendix A: Monte Carlo simulation

The purpose of this section is just to show the fastest algorithm to run Monte Carlo simulations, the best method to distinguish a first-order transition from a second-order one and to extract the critical exponents with a reliable estimate of errors.

**Markov chains and algorithms:** Since we cannot enumerate all the spin configurations, we are forced to use numerical simulations to calculate the physical quantities. The method of choice is the Monte Carlo method

generating a set of phase-space configurations from a Markov chain defined by the transition probability  $W[s, s']$  between states  $\{s\}$  and  $\{s'\}$ , where the new configuration depends only on the preceding one. There are many ways to get the transition probability  $W[s, s']$ .<sup>147</sup> The Metropolis algorithm is the simplest but not very efficient one. A new heat-bath algorithm, called Fast Linear Algorithm,<sup>140</sup> for vector spins is more efficient. For example it is three times faster than the Metropolis algorithm for a two-dimensional triangular antiferromagnetic lattice at the critical temperature. Furthermore the use of the over-relaxation<sup>147</sup> can reduce strongly the autocorrelation time.<sup>111</sup> The cluster algorithm cannot be used for frustrated spin systems. Indeed there are two problems. The first is to take into account the competition of different interactions in a plaquette. It means that many spins should be considered in one step when constructing the cluster. Second, even if we were able to construct a cluster, the BS is no more  $O(N)/O(N - 1)$ , but  $O(N)/O(N - 2)$ , for example. Consequently a symmetry to a  $N - 1$  plane used in the Wolff's algorithm<sup>148</sup> should be changed.

Thermodynamic averages are taken simply by

$$\bar{A} = (1/N_{MC}) \sum_{t=1}^{N_{MC}} A[t] \quad (9)$$

where  $N_{MC}$  is the number of new configurations generated (Monte Carlo Steps) and  $A[t]$  the value of the quantity at step  $t$ . The great advantage of this method is that the partition function  $Z = \sum_{\{s\}} e^{-\beta E[s]}$  needs not be calculated.

**To estimate the errors** of the averaged quantities we have to take into account that each new configuration is correlated with the previous one. We define the autocorrelation time  $\tau$  by the number of MC steps required to obtain two uncorrelated spin configurations. It is calculated using the autocorrelation function<sup>149</sup>  $C(t) = (1/\chi)[\langle A(t)A(0) \rangle - \langle A \rangle^2]$  where time is measured in MC steps (see comments in the appendix of Ref. [22]). If  $N \gg \tau$ , then a useful approximation for the error in  $\bar{A}$  is given by

$$(\delta \bar{A})^2 = \frac{\chi}{N_{MC}/(1 + 2\tau)} \quad (10)$$

$$\chi = \langle A^2 \rangle - \langle A \rangle^2. \quad (11)$$

This expression is identical to the standard deviation but with an effective number of independent measurements given by

$$\frac{N_{MC}}{1 + 2\tau}. \quad (12)$$

Problems arise when quantities are a combination of different averages, for example the susceptibility (11). We could try to treat  $\langle A^2 \rangle$  and  $\langle A \rangle^2$  as independent quantities and estimate the error by the sum of the errors of the two quantities. But the result will be overestimated due to the correlation between the two elements of the sum. To solve this problem we can use, for example, the Jackknife procedure.<sup>150</sup> An application of this method can be found in the appendix of Ref. [22].

**The histogram method:** The great advantage of the histogram method in the analysis of MC data is that a run at a single temperature  $T_1$  can be used to extract results for a continuous range of nearby temperatures.<sup>151</sup> In practice the range of temperature over which  $\langle A \rangle$  may be estimated from a single MC run at  $T_1$  is limited by the range over which reliable statistics can be expected for  $H(E)$ , the histogram of the energy. A rough guide is  $T_a < T < T_b$ , where  $T_a$  and  $T_b$  correspond to the energies  $\langle E_a \rangle$  and  $\langle E_b \rangle$  at which  $H(E) \simeq \frac{1}{2}H_{max}$ . Since  $H(E)$  becomes more sharply peaked with system size, the valid temperature range becomes smaller as  $L$  increases. Multiple histograms made at a number of nearby temperatures may be combined to increase accuracy.

**Nature of the transition:** Differentiating a weak first-order from a second-order transition could be difficult. The finite size scaling (FSS) for a first-order transition has been extensively studied<sup>152,153,154</sup>. A first-order transition should be identified by the following properties:

- a) The histogram of the energy,  $P_T(E)$ , has a double peak.
- b) The minimum of the fourth order energy cumulant  $W$  varies as:  $W = W^* + b L^{-d}$  where  $W^*$  is different from  $2/3$ .
- c) The temperatures  $T(L)$  at which the specific heat  $C$  or the susceptibility  $\chi$  has a maximum should vary as  $T(L) = T_c + a L^{-d}$ .
- d) The maximum of  $C$  and  $\chi$  are proportional to the volume  $L^d$ .

Obviously a double peak of  $P_T(E)$  which becomes more pronounced when the size increases is preferable (way a). If the two peaks are too close, the three other possibilities (b, c and d) can check if the probability is gaussian (second-order transition) or not (first-order transition) in the limit of infinite size.

**Second-order phase transition:** For a second-order phase transition the interesting parameters are the critical temperature and the critical ex-

ponents. There are at least three main ways to calculate them:

- a) Consider the high and low temperature regions where the correlation length  $\xi \ll L$ . There, we can fit  $\xi = a_\xi(T - T_c)^{-\nu} + \text{corrections}$ . The corrections become less important near  $T_c$ , but then  $\xi$  is very large, and a very big system size is necessary. Furthermore the autocorrelation time  $\tau \sim (T - T_c)^{-z}$  becomes also very large and the error  $\delta\xi$  becomes very big even if we can use some tricks to diminish it.<sup>155</sup>
- b) The Finite Size Scaling (FSS) region is the most powerful method. It is the region with  $\xi(\text{theoretical}) \gg L$ . The best method is to calculate the Binder cumulant<sup>156</sup>  $U_L(T) = 1 - \frac{\langle M^4 \rangle}{3\langle M^2 \rangle^2}$  for different size  $L$ .
  1. We can calculate the critical exponents directly by plotting  $\chi L^{-\gamma/\nu}$  as a function of  $U_L(T)$  and all the curves must collapse for the correct exponent  $-\gamma/\nu = \eta - 2$ .<sup>157</sup> Indeed we can write  $\chi L^{\eta-2} = h(U_L)$  with  $h$  an unknown function. The other exponents  $\beta/\nu$  and  $\nu$  can be obtained similarly using the magnetization and  $V_1 = \frac{\langle ME \rangle}{\langle M \rangle} - \langle E \rangle$ . It is the fastest way to get the critical exponents. This method works well even for the Kosterlitz-Thouless transition.<sup>158</sup>
  2. We can also use  $U_L(T)$  to calculate the critical temperature  $T_c$  using the crossing of  $U_L$  for different sizes. Very good statistics is needed because the evaluation of the first correction is necessary to get a correct value of  $T_c$ .
  3. Having determined  $T_c$  we can calculate the critical exponents using, for example,  $\chi \propto L^{+\gamma/\nu}, \dots$
  4. The last properties are also valid for the maximum (or minimum) of  $\chi$  and  $V_1$ , but we need many simulations at various temperatures to find the maxima because their locations vary as a function of the size  $L$  and are different for each quantity.
- c) The dynamical properties<sup>159,160,161,162,163</sup> are not very often used even if it is surely the fastest method available. One has to prepare a state in the GS (i.e.  $T = 0$ ) or randomly (i.e.  $T = \infty$ ), and to observe the dynamical properties of the system at the critical temperature  $T = T_c$  for a finite number of Monte Carlo steps before the equilibrium is reached. For an example see Ref. [111].

**Kosterlitz–Thouless (KT) transition:** A KT transition<sup>106</sup> exists

for two-dimensional lattices with  $XY$  spins. The unbounding of vortex–antivortex pairs appear at the critical temperature,  $T_c \sim 0.9$  for square lattice.

This transition has some special features: for  $T < T_c$  the correlation length ( $\xi$ ) is infinite, while for  $T > T_c$  it has an exponential decreasing contrary to the power law behavior in the standard transition.

To find  $T_c$  and the critical exponents we have several ways:

- a) we can fit  $\xi$  in the high temperature region, which is problematic because of the many free parameters and of the exponential form.
- b) we can use a method using the behavior of various quantities in the finite size scaling region (FSS) where  $\xi \gg L$ .
  - 1. The first one is to use the universal jump of the helicity  $\Upsilon$  at the critical temperature (in the finite size scaling region where  $\xi \gg L$ ), but this method requires the jump of  $\Upsilon(L)$  which is known for the non frustrated case, but not for the frustrated case.
  - 2. It is therefore interesting to find another method to get the critical exponent, even without calculating  $T_c$ . The method (b.1.) introduced previously for a second-order phase transition using the Binder parameter works well for the KT transition.<sup>158</sup> The Binder parameter, contrary to the common belief, crossed around  $T_c$ . Plotting  $\chi L^{\eta-2}$  as a function of  $U_L$  for various sizes, the curves collapse at the correct value of  $\eta = 0.25$ . This method can be applied whatever the form of  $\xi$  is. Therefore it should be applicable to all phase transitions.
- c) The dynamical behavior of this system can also be used.<sup>162</sup>

For the two-dimensional ferromagnetic  $XY$  spin system, all methods mentioned above are in agreement.

## Appendix B: Renormalization group: Landau-Ginzburg theory, expansions in fixed dimension $d = 3$ and for $d = 4 - \epsilon$ and its implications for experiments

In this short section we would like to give the necessary knowledge to help to understand the concepts of fixed points, flow diagrams and crossovers.

First consider a system of Heisenberg spins with a Hamiltonian:

$$H = -J_1 \sum_{(ij)} \mathbf{S}_i \cdot \mathbf{S}_j, \quad (13)$$

and the spin is restricted to be of norm  $S = 1$ . Replacing this constraint by

an exponential potential  $S = 1 \Leftrightarrow \int_0^\infty e^{u(\mathbf{S}^2 - 1)^2} \cdot dS$  the Hamiltonian can be written in the form

$$H = K \sum_{\langle ij \rangle} (\mathbf{S}(i) - \mathbf{S}(j))^2 + r \sum_i \mathbf{S}(i)^2 + u_0 \sum_i (\mathbf{S}(i)^2)^2. \quad (14)$$

Two remarks:

1. Other terms could be added in the Hamiltonian. These additional terms could be unimportant that means they become irrelevant near the fixed point (see later). Or we cannot treat them, that means they are not renormalizable in technical terms. If these neglected terms are important the method cannot describe the physics of the phase transition. This unfortunate case occurs for frustrated system for low dimensions of space and spins.<sup>32</sup>
2. In addition, since the transformation is not exact, the starting value  $u_0$  cannot be known even if it is possible to make a rough guess.<sup>32</sup>

We have plotted in the Fig. 4.13 the RG flow for this model.

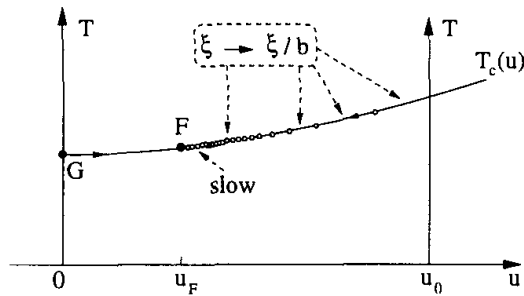


Fig. 4.13. RG flow for (14).  $F$  is the stable fixed point,  $G$  is the Gaussian one. Near  $F$  the flow is very slow.

The system will physically keep its value  $u_0$ . But its RG flow will not. Following a series of steps the value of  $u$  will change in approaching the fixed point  $F$ . At each step the correlation length of the system will be divided by a factor  $b > 1$ . In addition the flow becomes slower near the fixed point  $F$ . Consequently, to reach the neighborhood of  $F$ , where the system have a second-order transition, the initial  $\xi$  must be large “enough”. We know that  $\xi(T) \sim (T - T_c)^{-\nu}$  for a second-order phase transition. Hence, to obtain numerically or experimentally  $\xi$  which follows a power law (without too many corrections), the temperature must be close “enough” to the critical temperature  $T_c$ . Numerically, in the Finite Size Scaling (FSS) regions where  $\xi$  (theoretical) is much bigger than the size of the system  $L$ , the FSS law (see

4.6) will be valid only for  $L$  large “enough”. We observe that in the Fig. 4.9 only the plane  $T_c(u, v)$  is plotted.

Consider now a model with a  $XY$  anisotropy, for example we add to the Hamiltonian (13) a term  $D \sum_i (S_i^z)^2$  with  $0 < D \ll 1$ . We have now two parameters in our Landau-Ginzburg model:  $u$  for the length of the spin and  $v$  associated to  $D$ . The critical plane  $(u, v)$  of the flow diagram of this model is plotted in Fig. 4.14. From the initial point  $(u_0, v_0 \ll 1)$  the flow will go close to the Heisenberg fixed point  $F_H$  and then has a crossover to the  $F_{XY}$  fixed point. Near  $F_H$  the flow is very slow and needs a lot of steps to escape from the influence of  $F_H$  and reaches finally the neighborhood of  $F_{XY}$ . Therefore, to observe the “true”  $XY$  behavior, the correlation length must be very large. That means that the temperature must be very close of  $T_c$  or, if we are in the FSS region, the system size must be very large.

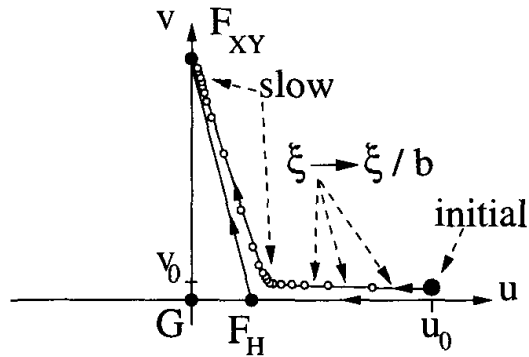


Fig. 4.14. Schematic RG flow ( $T_c(u, v)$  plane) for (14 with  $D \sum_i (S_i^z)^2$ ).  $F_H$  is the Heisenberg fixed point,  $F_{XY}$  is the  $XY$  fixed point,  $G$  is the Gaussian one. Near  $F_H$  and  $F_{XY}$  the flow is very slow.

We must know the stability of the fixed point when anisotropies are present. The “quasi” general rule is that the system goes to the fixed point with the lowest spin symmetry and the biggest space dimensions. For example consider the quasi one-dimensional system  $\text{CsMnBr}_3$ . This compound will display a one-dimensional behavior before reaching the three-dimensional behavior. Another example is  $\text{Cu}(\text{HCOO})_2\text{CO}(\text{ND}_2)_2\text{D}_2\text{O}$  which has a small Ising anisotropy. In this case the system will show a Heisenberg behavior before showing the Ising behavior. In real compounds small “anisotropies” are almost always present. Therefore many crossovers will appear when the temperature approaches the critical temperature. Consequently interpretations of experiments could be difficult.

To get the critical exponent and the flow diagram, the expansion in

fixed dimension  $d$  or in  $d = 4 - \epsilon$  consists of expanding the exponential  $e^{H\text{amiltonian}(u)}$  around the Gaussian fixed point  $u = 0$ . Results are in the form of a power series of  $u$ . Unfortunately this series is not convergent, but in the ferromagnetic case it has been shown to be resummable with Pade-Borel techniques. However, there are many ways to resum and one must be chosen following some criteria.<sup>87</sup> This resummation has been proved efficient for ferromagnetic systems, however it is not certain that it will work for frustrated systems. Indeed the presence of two vectors ( $O(N)/O(N-2)$  BS in this case (compared to the  $O(N)/O(N-1)$  BS in the ferromagnetic case) gives rise to a series of power of  $u$  and  $v$  ( $u, v, uv, u^2, \dots$ ) and this double expansion is difficult to resum.

## References

1. T. Inui, Y. Tanabe, Y. Onodera, *Group Theory and its Applications in Physics*, Springer Series in Solid-State Sciences 78, Berlin 1990
2. S.A. Antonenko, A.I. Sokolov, Phys. Rev. E **51**, 1894 (1995)
3. G. Toulouse, Commun. Phys. **2**, 115 (1977)
4. J. Villain, J. Phys. C **10**, 1717 (1977)
5. H. Kawamura, J. Phys. Soc. Jpn. **61**, 1299 (1992), **58**, 584 (1989), **56**, 474 (1987), **55**, 2095 (1986)
6. M.L. Plumer and A. Mailhot, Phys. Rev. B **50**, 16113 (1994)
7. E. H. Boubcheur, D. Loison, and H.T. Diep, Phys. Rev. B **54**, 4165 (1996)
8. M. Itakura, J. Phys. Soc. Jpn **72**, 74 (2003)
9. M.L. Plumer and A. Mailhot, J. Phys: Condens. Matter. **9**, L165 (1997)
10. M.L. Plumer and A. Mailhot, Phys. Rev. B **50**, 6854 (1994)
11. D. Loison and H.T. Diep, Phys. Rev. B **50**, 16453 (1994)
12. T. Bhattacharya, A. Billoire, R. Lacaze and Th. Jolicoeur, J. Phys. I (Paris) **4**, 181 (1994)
13. D. Loison, A.I. Sokolov, B. Delamotte, S.A. Antonenko, K.D. Schotte and H.T. Diep, JETP Letters **76**, 337 (2000)
14. Th. Jolicoeur, E. Dagotto, E. Gagliano, and S. Bacci, Phys. Rev. B **42**, 4800 (1990)
15. C.L. Henley, J. Appl. Phys. **61**, 3962 (1987). Also see: M.T. Heinilä and A.S. Oja, Phys. Rev. B **48**, 7227 (1993)
16. J. Villain, R. Bidaux, J.-P. Carton, and R. Conte, J. Phys. (Paris) **41**, 1263 (1980)
17. W. M. Saslow, M. Gabay, and W.M. Zhang, Phys. Rev. L **68**, 3627 (1992)
18. H. Kawamura, Prog. Theo. Phys. Suppl. **101**, 545 (1990), W.-M. Zhang, W.M. Saslow, M. Gabay, Phys. Rev. B **44**, 5129 (1991), 0204 (1993)
19. H.T. Diep, Europhys. Lett. **7**, 725 (1988), Phys. Rev. B **39**, 397 (1989)
20. D. Loison, Physica A **275**, 207 (1999)
21. R. Quartu and H.T. Diep, J. Magn. and Magn. Mater. **182**, 38 (1998)
22. D. Loison and P. Simon, Phys. Rev. B **61**, 6114 (2000)

23. H.T. Diep, A. Ghazali, and P. Lallemand, J. Phys. C **18**, 5881 (1985)
24. P. Lallemand, H.T. Diep, A. Ghazali, and G. Toulouse, J. Physique-Lettres **468**, 1087 (1985)
25. J.L. Alonso et al., Phys. Rev. B **53**, 2537 (1996)
26. C. Pinettes and H.T. Diep, Journal of Applied Physics, **83**, 6317 (1998)
27. A. Moreo, E. Dagotto, T. Jolicoeur, and J. Riera, Phys. Rev. B **42**, 6283 (1990), J. Ferrer, Phys. Rev. B **47**, 8769 (1993)
28. H.T. Diep and H. Kawamura, Phys. Rev. B **40**, 7019 (1989)
29. H.T. Diep, Phys. Rev. B **45**, 2863 (1992)
30. J.N. Reimers, Phys. Rev. B **45**, 7295 (1992), A. Mailhot and M. L. Plumer, Phys. Rev. B **48**, 9881 (1993), S.T. Bramwell, M.J.P. Gingras, and J.N. Reimers, J. Appl. Phys. **75**, 5523 (1994)
31. E.H. Boubcheur, R. Quartu, H.T. Diep, and O. Nagai, Phys. Rev. B **58**, 400 (1998)
32. See the chapter of B. Delamotte, D. Mouhanna, and M. Tissier in this book
33. A. Dobry and H.T. Diep, Phys. Rev. B **51**, 6731 (1995)
34. D. Loison and K.D. Schotte, Eur. Phys. J. B **5**, 735 (1998)
35. D. Loison and K.D. Schotte, Eur. Phys. J. B **14**, 125 (2000)
36. D. Loison and K.D. Schotte, Submitted to Eur. Phys. J. B
37. H. Kunz and G. Zumbach, J. Phys. A **26**, 3121 (1993)
38. H.T. Diep and D. Loison, J. Appl. Phys. **76**, 6350 (1994)
39. D. Loison, Eur. Phys. J. B **15**, 517 (2000)
40. D. Loison, not published.
41. D. Loison, Phys. Lett. A **257**, 83 (1999), Phys. Lett. A **264**, 208 (1999)
42. R.J. Baxter, J. Phys. C **6**, L445 (1973); *Exactly solved models in statistical mechanics* (Academic Press, London, 1982)
43. P. Peczak and D.P. Landau, Phys. Rev. B **39**, 11932 (1989)
44. D. Loison, submitted to Euro. J. Phys. B.
45. G. Zumbach, Nucl. Phys. B **413**, 771 (1994), Phys. Lett. A **190**, 225 (1994), Phys. Rev. Lett. **71**, 2421 (1993)
46. A.Z. Patashinskii and V.I. Pokrovskii, *Fluctuation Theory of Phase Transitions*, (Pergamon press 1979), §VII, **6**, *The S-matrix method and unitary relations*
47. J. Zinn-Justin, *Quantum Field Theory and Critical Phenomena*, (Oxford University Press, Oxford, 1996), §7.4 *Real-time quantum field theory and S-matrix*, §11.8 *Dimensional regularization, minimal subtraction: calculation of RG functions*
48. M. Tissier, D. Mouhanna, and B. Delamotte, Phys. Rev. B **61**, 15327 (2000), ibid **67**, 134422 (2003)
49. T.E. Mason, Y.S. Yang, M.F. Collins, B.D. Gaulin, K.N. Clausen and A. Harrison, J. Magn. and Magn. Mater **104-107**, 197 (1992)
50. T.E. Mason, M.F. Collins and B.D. Gaulin, J. Phys. C **20**, L945 (1987)
51. Y. Ajiro, T. Nakashima, Y. Unno, H. Kadowaki, M. Mekata and N. Achiwa, J. Phys. Soc. Japan **57**, 2648 (1988)
52. B.D. Gaulin, T.E. Mason, M.F. Collins and J.F. Larese, Phys. Rev. Lett. **62**, 1380 (1989)

53. T.E. Mason, B.D. Gaulin and M.F. Collins, Phys. Rev. B **39**, 586 (1989)
54. H. Kadowaki, S.M. Shapiro, T. Inami and Y. Ajiro, J. Phys. Soc. Japan **57**, 2640 (1988)
55. J. Wang, D.P. Belanger and B.D. Gaulin, Phys. Rev. Lett. **66**, 3195 (1991)
56. H. Weber, D. Beckmann, J. Wosnitza, H.v. Löhneysen and D. Visser, Inter. J. Modern Phys. B **9**, 1387 (1995)
57. T. Goto, T. Inami and Y. Ajiro, J. Phys. Soc. Japan **59**, 2328 (1990)
58. R. Deutschmann, H.v. Löhneysen, J. Wosnitza, R.K. Kremer and D. Visser, Euro. Phys. Lett, **17**, 637 (1992)
59. M.F. Collins, O.A. Petrenko, Can. J. Phys. **75**, 605 (1997)
60. T. Kato, T. Asano, Y. Ajiro, S. Kawano, T. Ihii and K. Iio Physica B **213-214**, 182 (1995)
61. T. Kato, K. Iio, T. Hoshimo, T. Mitsui and H. Tanaka, J. Phys. Soc. Japan **61**, 275 (1992)
62. H. Tanaka, H. Nakamo and S. Matsumo, J. Phys. Soc. Japan **63**, 3169 (1994)
63. H. B. Weber, T. Werner, J. Wosnitza H.v. Löhneysen and U. Schotte, Phys. Rev. B **54**, 15924 (1996)
64. D.A. Tindall, M.O. Steinitz and M.L. Plumer, J. Phys. F **7**, L263 (1977)
65. K.D. Jayasuriya, S.J. Campbell and A.M. Stewart, J. Phys. F **15**, 225 (1985)
66. B.D. Gaulin, M. Hagen and H.R. Child, J. Physique Coll. **49** C8, 327 (1988)
67. T.R. Thurston, G. Helgesen, D. Gibbs, J.P. Hill, B.D. Gaulin and G. Shirane, Phys. Rev. Lett. **70**, 3151 (1993), T.R. Thurston, G. Helgesen, J.P. Hill, D. Gibbs, B.D. Gaulin and P.J. Simpson, Phys. Rev. B **49**, 15730 (1994)
68. P. Du Plessis, A.M. Venter and G.H.F. Brits J. Phys. (Cond. Mat.) **7**, 9863 (1995)
69. J. Ecker and G. Shirane, Solid State Commun. **19**, 911 (1976)
70. G. Helgesen, J.P. Hill, T.R. Thurston, D. Gibbs, J. Kwo and M. Hong, Phys. Rev. B **50**, 2990 (1994)
71. S.W. Zochowski, D.A. Tindall, M. Kahrizi, J. Genosser and M.O. Steinitz, J. Magn. Magn. Mater. **54-57**, 707 (1986)
72. H.U. Åström and G. Benediktson, J. Phys. F **18**, 2113 (1988)
73. F.L. Lederman and M.B. Salomon, Solid State Commun. **15**, 1373 (1974)
74. K.D. Jayasuriya, S.J. Campbell and A.M. Stewart, Phys. Rev B **31**, 6032 (1985)
75. P. Du Plessis, C.F. Van Doorn and D.C. Van Delden, J. Magn. Magn. Mater. **40**, 91 (1983)
76. G.H.F. Brits and P. Du Plessis, J. Phys. F **18**, 2659 (1988)
77. E. Loh, C.L. Chien and J.C. Walker, Phys. Lett. **49A**, 357 (1974)
78. K.D. Jayasuriya, A.M. Stewart, S.J. Campbell and E.S.R. Gopal, J. Phys. F **14**, 1725 (1984)
79. O.W. Dietrich and J. Als-Nielsen, Phys. Rev. **162**, 315 (1967)
80. C.C. Tang, P.W. Haycock, W.G. Stirling, C.C. Wilson, D. Keen, and D. Fort, Physica B **205**, 105 (1995)
81. K.H. Hirota, G. Shirane, P.M. Gehring and C.F. Majkrzak, Phys. Rev B **49**, 11 967 (1994), P.M. Gehring, K.H. Hirota, C.F. Majkrzak and G. Shirane,

- Phys. Rev L **71**, 1087 (1993)
82. C.C. Tang, W.G. Stirling, D.L. Jones, A.J. Rollosen, A.H. Thomas and D. Fort, J. Magn. Magn. Mater. **103**, 86 (1992)
  83. H. Kadowaki, K. Ubukoshi, K. Hirakawa, J.L. Martinez and G. Shirane, J. Phys. Soc. Japan **56**, 4027 (1987)
  84. J. Wosnitza, R. Deutschmann, H.v Löhneysen and R.K. Kremer, J. Phys.: Condens. Matter **6**, 8045 (1994)
  85. K. Koyama and M. Matsuura, J. Phys. Soc. Japan **54**, 4085 (1985)
  86. G.C. DeFotis, F. Palacio and R.L. Carlin, Physica B **95**, 380 (1978), G.C. DeFotis and S.A. Pugh, Phys. Rev. B **24**, 6497 (1981), G.C. DeFotis and J.R. Laughlin, J. Magn. Magn. Mater. **54-57**, 713 (1986)
  87. J.C. Le Guillou and J. Zinn-Justin, J. Phys. (Paris) Lett. **46**, L137 (1985)
  88. S.A. Antonenko, A.I. Sokolov and V.B. Varnashev, Phys. Lett. A **208**, 161 (1995)
  89. B. Kastening, Phys. Rev. D **57**, 3567 (1998)
  90. S.A. Antonenko and A.I. Sokolov, Phys. Rev. B **49**, 15901 (1994)
  91. A. Pelissetto, P. Rossi, and E. Vicari, Phys. Rev. B **63**, 140414(R)(2001)
  92. P. Calabrese, P. Parruccini, and A.I. Sokolov, Phys. Rev. B **66**, 180403(R) (2002)
  93. P. Azaria, B. Delamotte, F. Delduc and T. Jolicoeur, Nucl. Phys. B **408**, 485 (1993), P. Azaria, B. Delamotte and T. Jolicoeur, Phys. Rev. Lett. **64**, 3175 (1990), J. App. Phys. **69**, 6170 (1991)
  94. B.W. Southern and A.P. Young, Phys. Rev. B **48**, 13170 (1993)
  95. D.R.T. Jones, A. Love, and M.A. Moore, J. Phys. C **9**, 743 (1976)
  96. B. Nienhuis, A.N. Berker, E.K. Riedel, and M. Schick, Phys. Rev. Lett. **43**, 737 (1979)
  97. M. Nauenberg and B. Nienhuis, Phys. Rev. Lett. **33**, 944 (1974)
  98. L. Saul, Phys. Rev. B **46**, 13847 (1992)
  99. H. Kawamura, J. Phys. Soc. Jpn **59**, 2305 (1990)
  100. N.D. Mermin and H. Wagner, Phys. Rev. Lett. **17**, 1133 (1966)
  101. N.D. Mermin, Rev. Mod. Phys. **51**, 591 (1979)
  102. G. Toulouse and M. Kleman, J. Physique Lett. **37**, 149 (1976)
  103. G. Kohring, R. E. Shrock, and P. Wills, Phys. Rev. Lett. **57**, 1358 (1986)
  104. G. A. Williams, Phys. Rev. Lett. **59**, 1926 (1987)
  105. S. R. Shenoy and B. Chattopadhyay, Phys. Rev. B **51**, 9129 (1995), Phys. Rev. Lett. **72**, 400 (1994), B. Chattopadhyay, M. C. Mahato, and S. R. Shenoy, Phys. Rev. B **47**, 15159 (1993), S. R. Shenoy, Phys. Rev. B **42**, 8595 (1990), Phys. Rev. B **40**, 5056 (1989)
  106. V.L. Berezinskii, Soviet Physics JETP **32**, 493 (1971), J.M. Kosterlitz and D.J. Thouless, J. Phys. C **6**, 1181 (1973), J.M. Kosterlitz, J. Phys. C **7**, 1046 (1974)
  107. J. Lee, J.M. Kosterlitz, and E. Granato, Phys. Rev. B **43**, 11531 (1991)
  108. S. Miyashita and H. Shiba, J. Phys. Soc. Jpn **53**, 1145 (1984)
  109. S. Lee and K.C. Lee, Phys. Rev. B **57**, 8472 (1998)
  110. L. Capriotti, R. Vaia, A. Cuccoli, and V. Togneti, Phys. Rev. B **58**, 273 (1998)

111. D. Loison, cond-mat/0001122, unpublished
112. S. Teitel and C. Jayaprakash, Phys. Rev. Lett. **51**, 1999 (1983); Phys. Rev. B **27**, 598 (1983)
113. B. Berge, H.T. Diep, A. Ghazali, and P. Lallemand, Phys. Rev. B **34**, 3177 (1986)
114. D.B. Nicolaides, J. Phys. A **24**, L231 (1991)
115. J.V. Jose and G. Ramirez-Santiago, Phys. Rev. Lett. **77**, 4849 (1996); **68**, 1224 (1992); Phys. Rev. B **49**, 9567 (1994)
116. J.M. Thijssen and H.J.F. Knops, Phys. Rev. B **42**, 2438 (1990)
117. E. Granato, M.P. Nightingale, Phys. Rev. B **48**, 7438 (1993)
118. S. Lee and K.C. Lee, Phys. Rev. B **49**, 15184 (1994)
119. H.J. Luo, L. Schülke, and B. Zheng, Phys. Rev. Lett. **81**, 180 (1998)
120. M. Benakly and E. Granato, Phys. Rev. B **55**, 8361 (1997)
121. M.P. Nightingale, E. Granato, and J.M. Kosterlitz, Phys. Rev. B **52**, 7402 (1995).
122. J. Lee, E. Granato, and J.M. Kosterlitz, Phys. Rev. Lett. **66**, 2090 (1991); Phys. Rev. B **44**, 4819 (1991).
123. P. Olsson, Phys. Rev. Lett. **75**, 2758 (1995); **77**, 4850 (1996); Phys. Rev. B **55**, 3585 (1997)
124. Y.M.M. Knops, B. Nienhuis, H.J.F. Knops, and J.W. Blöte, Phys. Rev. B **50**, 1061 (1994)
125. E. Granato, Phys. Rev. B **45**, 2557 (1992)
126. M. Yosefin and E. Domany, Phys. Rev. B **32**, 1778 (1985)
127. P. Minnhagen, Phys. Rev. Lett **54**, 2351 (1985); Phys. Rev. B **32**, 3088 (1985)
128. G.S. Grest, Phys. Rev. B **39**, 9267 (1989)
129. J.R. Lee, Phys. Rev. B **49**, 3317 (1994)
130. M.Y. Choi and D. Stoud, Phys. Rev. B **32**, 5773 (1985)
131. G.S. Jeon, S.Y. Park, and M.Y. Choi, Phys. Rev. B **55**, 14088 (1997)
132. S. Lee, K.C. Lee, and J.M. Kosterlitz cond-mat/9612242 (unpublished)
133. C.J. Lobb, Physica B **152**, 1 (1988)
134. X.S. Ling, H.J. Lezec, J.S. Tsai, J. Fujita, H. Numata, Y. Nakamura, Y. Ochiai, Chao Tang, P.M. Chaikin, and S. Bhattacharya, Phys. Rev. Lett. **76**, 2989 (1996)
135. T.C. Halsey, J. Phys. C **18**, 2437 (1985)
136. S.E. Korshunov, J. Stat. Phys. **43**, 17 (1986)
137. V. Kotsubo, K.D. Hahn, and J.P. Parpia, Phys. Rev. Lett. **58**, 804 (1987)
138. J. Xu and C. Crooker, Phys. Rev. Lett. **65**, 3005 (1990)
139. T. Garel and S. Doniach, J. Phys. C **13**, L887 (1980)
140. The Fast Linear Algorithm developped by D. Loison is three times faster than the Metropolis algorithm at the critical temperature for frustrated two dimensional systems. Submitted to Euro. J. Phys. B. Accessible at the home page <http://www.physik.fu-berlin.de/~loison/>
141. D. Loison, submitted to Euro. J. Phys. B.
142. H. Kawamura and S. Miyashita, J. Phys. Soc. Jpn **53**, 1145 (1985)
143. M. Caffarel, P. Azaria, B. Delamotte, and D. Mouhanna, Phys. Rev. B **64**,

- 014412 (2001)
144. B.W. Southern and H.J. Xu, Phys. Rev. B **52**, R3836 (1995)
  145. H. Kawamura and M. Kikuchi, Phys. Rev. B **47**, 1134 (1993)
  146. M. Wintel, H.U. Everts and W. Apel, Europhys. Lett. **25**, 711 (1994), Phys. Rev. B **52**, 13480 (1995)
  147. M. Creutz, Phys. rev. B **36**, 515 (1987)
  148. U. Wolff, Phys. Rev. Lett. **62**, 361 (1989), Nucl. Phys. B **322**, 759 (1989)
  149. H. Müller-Krumbhaar and K. Binder, J. Stat. Phys. **8**, 1 (1973)
  150. B. Efron, *The Jackknife, The Bootstrap and other Resampling Plans* (SIAM, Philadelphia, PA, 1982)
  151. A.M. Ferrenberg and R.H. Swendsen, Phys. Rev. Lett. **61**, (1988) 2635; *ibid* **63**, (1989) 1195; Computers in Physics, Sept/Oct (1989) 101
  152. V. Privman and M.E. Fisher, J. Stat. Phys. **33**, 385 (1983)
  153. K. Binder, Rep. Prog. Phys. **50**, 783 (1987)
  154. A. Billoire, R. Lacaze and A. Morel, Nucl. Phys. B **370**, 773 (1992)
  155. G. Prussner, D. Loison and K.D. Schotte, Physica A **299**, 557 (2001)
  156. K. Binder, Z. Phys. B **43**, 119 (1981)
  157. D. Loison, Physica A **271**, 157 (1991)
  158. D. Loison, J. Phys.: Condens. Matter, **11**, L401 (1999)
  159. Z. Phys. B **73**, 539 (1989)
  160. D.A. Huse, Phys. Rev. B **40**, 304 (1989)
  161. K. Humayun and A.J. Bray, J. Phys. A **24**, 1915 (1991)
  162. B. Zhang, Int. J. Mod. Phys. **12**, 1419 (1998)
  163. H.J. Luo and B. Zheng, Mod. Phys. Lett. B **11**, 615 (1997)

## CHAPTER 5

### TWO-DIMENSIONAL QUANTUM ANTIFERROMAGNETS

Grégoire Misguich

*Service de Physique Théorique, CEA/DSM/SPhT*

*Unité de recherche associée au CNRS*

*CEA/Saclay 91191 Gif-sur-Yvette Cédex, France*

*E-mail: gmisguich@cea.fr*

Claire Lhuillier

*Laboratoire de Physique Théorique des Liquides*

*Université P. et M. Curie and UMR 7600 of CNRS*

*Case 121, 4 Place Jussieu, 75252 Paris Cédex, France*

*E-mail: claire.lhuillier@lptl.jussieu.fr*

#### 5.1. Introduction

In this review we present some theoretical advances in the field of quantum magnetism in two-dimensional (2D) systems. The spin- $\frac{1}{2}$  nearest-neighbor 2-dimensional Heisenberg models on Bravais lattices (square<sup>1</sup>, triangular<sup>2</sup>) are Néel ordered<sup>a</sup> at  $T = 0$ . Frustration, small coordination number, competition between interactions can lead to specific quantum phases without magnetic long-ranged order. Since a decade this subject is a highly debated issue in the field of quantum magnetism. It was revived by the discovery of high- $T_c$  superconductivity in the doped cuprates and fuelled by numerous experimental studies of 2D antiferromagnetic insulators.<sup>3</sup>

---

<sup>a</sup>This generic kind of order, with a macroscopic sublattice magnetization is called in the following *magnetic* long-ranged order (LRO), in contrast to other ordered phases where the long-ranged ordered correlations concern  $S = 0$  scalar observables (on dimers, quadrupoles...)

Section 5.2 is devoted to the spin- $\frac{1}{2}$  Heisenberg model on the square lattice with first- and second-neighbor interactions ( $J_1-J_2$  model). This model is one of the most studied in the field of and this section is a short guide to the literature, with a special emphasis on the various methods used for this problem.

Section 5.3 deals with general properties of valence-bond crystals (VBC) and related states, the simplest phase which is commonly realized in frustrated spin systems without magnetic LRO.

In section 5.4 we present large- $N$  generalizations of the Heisenberg model. This approach was extensively developed by Read and Sachdev from the early 90's and has been the first to give an insight into the alternative between VBC and related phases, which have long ranged order in local singlet patterns (whence the name of crystals), and resonating valence-bond (RVB) spin-liquids (SL) which are translationally invariant phases where the quantum coherence is a central issue.

Section 5.5 presents some results of quantum dimer models (QDM). These models are effective approaches to the quantum phases of antiferromagnets which are dominated by short-range valence-bonds (or singlets). They have received recently some special attention and provide useful insights onto the phenomenology of VBC and RVB SL.

In Section 5.6 we review some results concerning models with multiple-spin exchange (MSE) (also called ring exchange) interactions. These interactions are now recognized to be present in several physical systems and appear to play an important role in the stabilization of RVB liquid groundstates.

The last section is devoted to the Heisenberg model on the kagome lattice (and related models). Despite of an important activity on this subject, the understanding of the low-energy physics of the spin- $\frac{1}{2}$  kagome antiferromagnet remains a challenging problem and we discuss some of the important results and questions.

We should warn the readers that this review is quite "inhomogeneous" and cannot, of course, replace textbooks.<sup>4,5,6,7</sup> While some parts deal with some rather recent works (QDM or MSE for instance), some others are devoted to older results which we think are still of importance for current research (beginning of the section  $J_1-J_2$ , large- $N$ ). The final part devoted to kagome reflects our own views and some unpublished material on still unsettled issues. Some parts are intended to be more pedagogical and concrete (QDM and beginning of large- $N$  section) while some others contain more qualitative discussions of the physical issues (end of the section  $J_1-J_2$ , VBC, kagome).

## 5.2. $J_1-J_2$ model on the square lattice

We consider the following Heisenberg model on the square lattice:

$$\mathcal{H} = 2J_1 \sum_{\langle ij \rangle} \vec{S}_i \cdot \vec{S}_j + 2J_2 \sum_{\langle\langle ij \rangle\rangle} \vec{S}_i \cdot \vec{S}_j \quad (1)$$

where  $\langle ij \rangle$  and  $\langle\langle ij \rangle\rangle$  denote pairs of nearest and next-nearest-neighbors respectively. Although quite simple in appearance, this spin model realizes several interesting phenomena which are relevant to a large class of 2D frustrated quantum magnets: classical degeneracy, order by disorder, destruction of some long-ranged order by quantum fluctuations, break down of the spin-wave expansion, opening of a spin gap and (possibly ?) spontaneous translation symmetry breaking, etc. For this reason we start with a general overview of some important results concerning this system. We will focus on the properties related to *frustration*. A review on the non-frustrated model ( $J_2 = 0$ ) can be found in Ref.<sup>1</sup>

### 5.2.1. Classical ground-state and spin-wave analysis

It is easy to find *some* classical ground-state of a translation invariant Heisenberg model on a Bravais lattice because the energy can always be minimized by a planar helix

$$\vec{S}_r = \vec{e}_1 \cos(\mathbf{q} \cdot \mathbf{r}) + \vec{e}_2 \sin(\mathbf{q} \cdot \mathbf{r}) \quad (2)$$

provided that the pitch  $\mathbf{q}$  minimizes the Fourier transform  $J(\mathbf{q})$  of the coupling.<sup>8</sup> In the case of the  $J_1-J_2$  model one has

$$J(\mathbf{q}) = 2J_1 (\cos(q_x) + \cos(q_y)) + 2J_2 (\cos(q_x + q_y) + \cos(q_x - q_y)) \quad (3)$$

- $J_2 < 0.5J_1$ :  $J(\mathbf{q})$  has a single minimum at  $(\pi, \pi)$ . It corresponds to the “usual” Néel state.
- $J_2 > 0.5J_1$ :  $J(\mathbf{q})$  has two isolated minima at  $(0, \pi)$  and  $(\pi, 0)$ . They correspond to ferromagnetic lines (resp. columns) arranged in an antiferromagnetic way. These states are sometimes called *collinear* (in *real* space). From these planar helix states one can build many other ground-states by rotating globally all the spins of one sublattice with respect to the other. Although this costs no energy for classical spins at zero temperature, it is known (order by disorder, see below) that configurations where both sublattices have

their staggered magnetization *collinear in spin space* are selected by thermal or quantum fluctuations.

- $J_2 = 0.5J_1$ :  $J(\mathbf{q})$  has lines of minima around the edges of the Brillouin zone. At this point the classical ground-state is highly degenerate : We can write  $\mathcal{H} = \text{cst} + J_2 \sum (S_1 + S_2 + S_3 + S_4)^2$  where the sum runs over all square plaquettes and any state where each plaquette has a vanishing total spin minimizes the classical energy.

Even at the lowest order in  $1/S$ , zero-temperature quantum corrections to the sublattice magnetization (order parameter) diverge around  $J_2 = 0.5J_1$  (Chandra and Douçot<sup>9</sup>). Such large- $S$  approximation usually tends to overestimate the stability of magnetic phases, therefore this breakdown around  $J_2 \sim 0.5J_1$  is a strong evidence for the existence of quantum disordered phase(s) in this region of parameter space.

### 5.2.2. Order by disorder ( $J_2 > J_1/2$ )

The concept of “order by disorder” was introduced in 1980 by Villain and co-workers<sup>10</sup> in the study of a frustrated Ising model on the square lattice. In this model the next neighbor couplings along the rows are ferromagnetic as well as those on the odd columns (named *A* in the following). The couplings on the even columns (named *B*) are antiferromagnetic. At  $T = 0$  the ground-state has no average magnetization and is disordered. This changes when thermal fluctuations are introduced: a *B*-chain sandwiched between two *A* chains with parallel spins has *lower excitations* than a *B* chain between two *A*-chains with anti-parallel spins. This gives a larger Boltzmann weight to ferrimagnetically ordered states. Villain *et al.* have exactly shown that the system is indeed ferrimagnetic at low temperature. They were also able to show that site dilution (non-magnetic sites) selects the same ordered pattern, whence the name of “order by disorder”.

A somewhat less drastic phenomenon has been observed in quantum systems. It is the selection of particular long-ranged ordered quantum states among a larger family of ordered solutions which are classically degenerate at  $T = 0$ .<sup>b</sup> Consider a spin system in which the molecular field created by the spins of one sublattice on the other cancels, which is the case when

---

<sup>b</sup>In Villain’s model the system is truly disordered at  $T = 0$  and an ordered solution is entropically selected at finite temperature. In the quantum  $J_1-J_2$  model above, the classical solutions can adopt various ordered patterns: quantum fluctuations select among these patterns the most ordered one, that is the situation with the highest symmetry

$J_2 > 0.5J_1$ . Shender<sup>11</sup> showed that if fluctuations are included, the system will select states in which all spins are collinear to each other. This follows from the fact that (moderate) fluctuations at one site are orthogonal to the mean value of the magnetization at that site and the system can gain some magnetic exchange energy by making such fluctuations coplanar on neighboring sites, that is to making the spins collinear. Such a selection of order by quantum fluctuations (and dilution) was discussed by Henley<sup>12</sup> and appears also quite straightly in a spin-wave expansion.<sup>13</sup>

This selection of the  $(\pi, 0)$  or  $(0, \pi)$  order spontaneously breaks a four-fold lattice symmetry. An Ising order parameter is thus generated. It takes two values depending whether the ferromagnetic correlations are locally arranged horizontally or vertically. Chandra and co-workers<sup>14</sup> have studied this mechanism and predicted the existence of a finite temperature Ising phase transition independent of the subsequent development of a sublattice magnetization. This result has been questioned recently<sup>15</sup> and the transition has not been observed so far in the spin- $\frac{1}{2}$  model.<sup>16,15</sup> It has however been confirmed by some recent Monte Carlo simulations of the *classical* Heisenberg model.<sup>17</sup> Very similar phenomena are present in the  $J_1$ - $J_2$  quantum Heisenberg model on the *triangular* lattice.<sup>18,19,20,21</sup>

Melzi *et al.*<sup>22,23</sup> have studied a quasi 2D spin- $\frac{1}{2}$  system which is believed to be a  $J_1$ - $J_2$  square lattice Heisenberg antiferromagnet. They found some evidence (splitting of NMR lines) for a collinear  $((\pi, 0)$  or  $(0, \pi)$ ) magnetic ordering. Several estimates<sup>23,24,25,16</sup> indeed point to  $J_2 > J_1$  in this compound.

### 5.2.3. Non-magnetic region ( $J_2 \simeq J_1/2$ )

Consider the two classical “Ising states” corresponding to the wave vectors  $(\pi, \pi)$  and  $(\pi, 0)$ . They can be taken as (crude) variational states for the Hamiltonian Eq. 1. Their energies (per site) are  $E_{\pi,\pi} = -J_1 + J_2$  and  $E_{\pi,0} = -J_2$ . As discussed above, these states cross at  $J_2 = \frac{1}{2}J_1$ . However, one can also consider any first-neighbor singlet (or valence-bond) covering of the lattice as another variational state. In such a completely dimerized state the expectation value of the energy per site is  $E_{dimer} = -\frac{3}{4}J_1$ , which is below the two Ising states around  $J_2 \simeq J_1/2$ . Of course this very simple argument does not prove anything since “dressing” these classical states

---

and the smallest degeneracy. The ultimate effect of these quantum fluctuations can be the destruction of the Néel order in favor of a fully quantum ground-state with  $\mathcal{O}(1)$  degeneracy.

with quantum fluctuations (spin flips in the Néel-like states or valence-bond motions in the dimerized wave-functions) will lower the energies of all these trial states and it is absolutely not clear which one may eventually win. Nevertheless, this shows in a simple way why non-magnetic states (*i.e.* rotationally invariant or spin singlet) such as dimerized states can be a route to minimize the energy in a frustrated magnet.<sup>c</sup>

### 5.2.3.1. Series expansions

High-order series expansions can be a powerful technique to investigate frustrated quantum magnets. The general method to generate zero-temperature perturbation expansions in quantum many-body systems was described by Singh *et al.*<sup>28</sup> and Gelfand *et al.*<sup>29</sup> For instance, one can consider the following anisotropic model:

$$\begin{aligned} \mathcal{H}(\lambda) = & 2J_1 \sum_{\langle ij \rangle} [S_i^z S_j^z + \lambda (S_i^x S_j^x + S_i^y S_j^y)] \\ & + 2J_2 \sum_{\langle\langle ij \rangle\rangle} [S_i^z S_j^z + \lambda (S_i^x S_j^x + S_i^y S_j^y)] \end{aligned} \quad (4)$$

$\mathcal{H}(\lambda = 0)$  is a classical Ising model which ground-state is known. The series expansion about the Ising limit amounts to compute expectation values in the ground-state  $|\lambda\rangle$  of  $\mathcal{H}(\lambda)$  in powers of  $\lambda$ :

$$\frac{\langle \lambda | \hat{O} | \lambda \rangle}{\langle \lambda | \lambda \rangle} = \sum_n a_n \lambda^n, \quad (5)$$

(energy gaps, dispersion relations and susceptibilities can also be computed in the same approach). The calculation of  $a_n$  requires the enumeration and evaluation of the *connected clusters* of size  $\sim n$ , whose number grows exponentially with  $n$ . Depending on the quantity  $\hat{O}$  and on the model, orders from 7 to 20 can typically be obtained on present computers. The series is then extrapolated to  $\lambda = 1$  by standard Padé, Dlog Padé or integrated differential approximations. Such a series expansion about the Ising limit was done by Weihong *et al.*<sup>30</sup> for the first neighbor square-lattice antiferromagnet. Oitmaa and Weihong<sup>31</sup> extended the series to the  $J_1-J_2$  model, where each  $a_n$  is now a polynomial in  $J_1$  and  $J_2$ . The disappearance of Néel

---

<sup>c</sup>Klein<sup>26</sup> introduced a general procedure to generate local and  $SU(2)$  symmetric Hamiltonians for which any first-neighbor dimerized state is an exact ground-state. These Hamiltonians are simply defined as sums of projectors which annihilate all dimer coverings. The Majumdar-Gosh<sup>27</sup> chain is the simplest example of a “Klein model”.

order in the Heisenberg model manifests itself by a vanishing sublattice magnetization as well as some singular behavior of the series for  $\lambda_c < 1$ . The results indicate the absence of Néel long-ranged order in the strongly frustrated region  $0.4 \leq J_2/J_1 \leq 0.6$ . Such an expansion can locate with a reasonable accuracy the phase boundary of the Néel ordered regions but provides no direct information on the nature of the non-magnetic phase.

To study the model around  $J_2 \simeq J_1/2$ , several other expansions have been carried out. A dimer expansion about an exactly dimerized model was done by Gelfand *et al.*,<sup>32</sup> Gelfand,<sup>33</sup> Singh *et al.*<sup>34</sup> and Kotov *et al.*<sup>35</sup> In this approach  $J_1$  and  $J_2$  are set to zero everywhere except on isolated bonds arranged in a columnar way and all the other couplings are treated perturbatively. At zeroth order the ground-state is simply a product of singlets. In these calculations the dimerized phase remains stable in the intermediate region. Singh *et al.*<sup>34</sup> also performed a different kind of zero-temperature series expansion. They started from a model of isolated 4-spin plaquettes in order to check a prediction made by Zhitomirsky and Ueda<sup>36</sup> that such plaquettes could spontaneously form around  $J_2 \simeq J_1/2$  to produce a state which is invariant under  $\pi/4$  lattice rotations. Although the ground-state energy they obtained is very close to the one obtained from the dimerized limit (within error bars of the extrapolation procedure) they observed an instability in the plaquette scenario (the triplet gap vanishes before reaching the isotropic square-lattice model) which suggests that plaquette order is not the issue (the analysis of the exact numerical spectra for 36 sites confirmed this result<sup>37</sup>).

Sushkov *et al.*<sup>38</sup> (improved numerical results compared to Ref.<sup>39</sup>) computed the susceptibility  $\chi_D$  associated with the appearance of columnar dimer order in the  $(\pi, \pi)$  Néel phase by a series expansion about the Ising limit. Such a susceptibility seems to diverge at  $J_2/J_1 = g_{c1} \simeq 0.405 \pm 0.04$ . On the other hand the disappearance of the magnetic LRO is observed (through the Néel order parameter or through the anisotropy in spin space of the spin-spin correlations) at  $J_2/J_1 = g_{c2} \simeq 0.39 \pm 0.02$ . This point could a priori be *different* from  $g_{c1}$ . In such a case the system would first break the  $\pi/4$  lattice rotation symmetry at  $g_{c1}$ , while magnetic LRO remains (gapless spin waves). Only at  $g_{c2} > g_{c1}$  the  $SU(2)$  rotation symmetry is restored and the magnetic excitations acquire a gap. From field theoretical arguments based on effective actions valid close to the critical points, Sushkov *et al.*<sup>38</sup> argue that the proximity (or possible equality) of  $g_{c1}$  and  $g_{c2}$  is a general feature in frustrated magnets which originate from the coupling of triplet and singlet excitations.

Sushkov *et al.*<sup>39</sup> computed susceptibility  $\chi_P$  associated to plaquette order by an expansion around the dimerized limit, assuming that the system has columnar dimer LRO. The result shows a divergence of  $\chi_P$  when  $J_2/J_1 \rightarrow g_{c3} = 0.5 \pm 0.02$ . From these results Sushkov *et al.* suggested that the translation symmetry along the columns is broken down at  $g_{c3}$  (giving rise to an eight-fold degenerate ground-state in the thermodynamic limit) before the  $(\pi, 0) - (0, \pi)$  magnetically ordered phase appears at  $g_{c4} \simeq 0.6$ . This picture is qualitatively consistent with the spin-spin correlations computed in a  $10 \times 10$  system with a density matrix renormalization group (DMRG) algorithm.<sup>40</sup>

Due to the relatively short series (typically of order 7) involved and the uncertainties in the extrapolation procedures, such results should be confirmed by other methods but this succession of quantum phase transitions represents a very interesting scenario. We note that if the model has a fully symmetric liquid ground-state in some parameter range, it should be difficult to capture from series expansions about limits where some lattice symmetries are explicitly broken.

### 5.2.3.2. Exact diagonalizations

Exact diagonalizations have a priori no bias, and were used very early in this field.<sup>41,42,43</sup> Large-size computations and sophisticated finite size scaling analysis are nevertheless needed to extract significant information. Schulz *et al.*<sup>44</sup> performed extensive exact diagonalizations of the  $J_1-J_2$  model for system sizes up to 36 sites. They analyzed the behavior of several quantities such as structure factors (Néel order parameter), ground-state energy, spin-wave velocities (obtained from the finite size corrections to the ground-state energy), spin stiffness and uniform susceptibility. Their analysis, including quantitative comparisons with non-linear sigma model predictions,<sup>45</sup> concluded to the absence of Néel long-ranged order in the strongly frustrated region  $0.4 \leq J_2/J_1 \leq 0.6$ . There, they show enhanced columnar dimer-dimer correlations as well as chiral ones but the size effects were not clear enough to discriminate between short or long-ranged order for these order parameters.

### 5.2.3.3. Quantum Monte Carlo

Quantum Monte Carlo (QMC) methods have been extensively applied to the  $J_1-J_2$  model in the low frustration regime giving an highly accurate description of the Néel phase (Sandvik<sup>46</sup> and Refs. therein). In the non-

magnetic and highly frustrated regime a simple QMC approach is ineffective due to the so-called sign problem. The fixed node approach is the first answer to this problem: the exact imaginary time propagator  $e^{-\tau \mathcal{H}}$  used to filter out the ground-state from a variational guess  $|\psi_g\rangle$  is replaced by an approximate propagator, which has the same nodes as  $|\psi_g\rangle$ . The quality of the result depends on the quality of the nodal regions of  $|\psi_g\rangle$ . Various schemes have been used to try to go beyond this limitation: stochastic reconfiguration (Sorella<sup>47</sup>), eventually associated to a few Lanczos iterations.<sup>48,37</sup> An alternative method has been devised by du Croo de Jongh *et al.*,<sup>40</sup> where the guiding function is replaced by the result of a DMRG calculation.<sup>49,50</sup> Both methods have their own bias. Using the first of them, Capriotti and Sorella<sup>37</sup> concluded that for  $J_2/J_1 \sim 0.45$  a Gutzwiller-projected BCS wave-function  $|p BCS\rangle$  was an excellent guiding wave-function:

$$|p BCS\rangle = \hat{\Pi} |BCS\rangle \quad (6)$$

$$|BCS\rangle = \exp \left( \sum_{i,j} f_{i,j} c_{i\uparrow}^\dagger c_{j\downarrow}^\dagger \right) |0\rangle \quad (7)$$

where  $|0\rangle$  is the fermion vacuum,  $c_{i\uparrow}^\dagger c_{j\downarrow}^\dagger$  creates a valence-bond on sites  $(i, j)$  and  $\hat{\Pi}$  projects out states with double occupancy. The pairing amplitude  $f_{i,j}$  (often called gap function  $\Delta_k$ )<sup>d</sup> is optimized with a Monte Carlo algorithm in order to minimize the energy. Capriotti and Sorella gave convincing indications that their wave-function is quite accurate. The best variational energies are obtained in the frustrated region with a pairing amplitude which mixes  $d_{x^2-y^2}$  and  $d_{xy}$  symmetries. In particular it reproduces the correct nodal structure of the ground-state in the frustrated region at least for moderate system sizes where the variational result can be checked against the exact result. This is a subtle and non-trivial information for systems which do not obey the Marshall's sign rule as this frustrated model. They concluded from these results that the system probably had no long-ranged order neither in dimer-dimer correlations nor in four-spin plaquette correlations. On the other hand, du Croo de Jongh *et al.* argued in favor of columnar dimerized phase which also break the translation symmetry along the columns (plaquette-like correlations similar to those found by series expansions<sup>39</sup>).

The comparison of the results of these different approaches shows that this problem remains a very challenging one. The model in the frustrated

---

<sup>d</sup>After the Gutzwiller projection  $\Delta_k$  is no longer the observable gap.<sup>51</sup>

regime is probably never very far from a quantum critical point and in these conditions none of the available methods seems able to discriminate between a VBC with tiny gaps both in the singlet and triplet sectors, a critical phase with a quasi order in dimers and gapless singlet excitations, or a true SL with gaps in any sector of spin but no long ranged order in any observable. As we will explain in the following sections some other frustrated models are happily deeper in the non-magnetic phases and exhibit quantum phases which are easier to characterize.

### 5.3. Valence-bond crystals

#### 5.3.1. Definitions

Among the different quantum solutions to overcome frustration the VBC is the simplest scenario. In this phase, neighboring spins arrange themselves in a regular pattern of singlets: dimers,<sup>a</sup> quadruplets or  $2n$ -mers  $S = 0$  plaquettes. The stability of this phase comes from the extreme stability of small  $S = 0$  clusters (recall that the energy of a singlet of two spins  $\frac{1}{2}$  is  $-3/4$  to be compared to the energy of two classical (or Ising) spins which is only  $-1/4$ ), and eventually from the fact that frustrated bonds between two different singlets do not contribute to the total energy.

In a VBC phase there is no  $SU(2)$  symmetry breaking, no long-ranged order in spin-spin correlations, but long-ranged order in dimer-dimer or larger singlet units. Except at a quantum critical point, all excitations of a VBC are gapped. Depending on the lattice geometry, such a wave function can spontaneously break some lattice symmetry (*spontaneous VBC*) or can remain fully symmetric (*explicit VBC*). In a strict sense, the name VBC should be reserved for systems with a spontaneous lattice symmetry breaking. However, since these two kinds of systems share many similarities we will discuss both in this section.

When the Hamiltonian has some inequivalent bonds and an integer spin in the unit cell (even number of spin- $\frac{1}{2}$  for instance) the system can take full advantage of the strong bonds and minimize the effects of the frustrating ones. In that case the *explicit* VBC is the “natural” strong coupling solution. One can build a simple Hamiltonian in which the bonds which are not occupied by the singlet objects are turned off. The resulting model is a set of small decoupled clusters (dimers or larger plaquettes) and the ground-state is a trivial product of singlets. Importantly, this strong coupling limit

---

<sup>a</sup>whence the name Spin Peierls phase sometimes given to the VBC phase.

has the same lattice symmetry as the original one. Going back to the original Hamiltonian *no quantum phase transition is encountered when going from the trivial singlet product up to real interacting ground-state*. Models with an half-odd-integer spin in the unit cell cannot realize a VBC unless they spontaneously enlarge their unit cell. In these situations there is no unique elected position for the  $2n$ -mers and a symmetry breaking must take place in order to form a VBC. Examples of these two kinds of VBC will be given below.

### 5.3.2. One-dimensional and quasi one-dimensional examples (spin- $\frac{1}{2}$ systems)

One of the simplest example of (spontaneous) VBC is observed in the  $J_1-J_2$  model on the chain for  $J_2/J_1 > (J_2/J_1)_c \sim 0.24$ .<sup>27,52,53,54,55</sup> For  $J_2/J_1 = 0.5$  the doubly degenerate ground-states are exact products of dimers:<sup>27,5</sup>

$$|MG_{\pm}\rangle = \prod_{n=1}^{N/2} |(2n, 2n \pm 1)\rangle. \quad (8)$$

Here and in the following we call “dimer” a pair of spins in a singlet state, and note it:

$$|(i, j)\rangle = \frac{1}{\sqrt{2}} [ |i, +\rangle |j, -\rangle - |i, -\rangle |j, +\rangle ]. \quad (9)$$

For all  $J_2/J_1 > (J_2/J_1)_c$ , the ground-states are products of dimers, dressed by fluctuations of valence bonds, dimer long-ranged order persists in all the range of parameters. This model has gapful excitations which can be described as pairs of scattering spin- $\frac{1}{2}$  solitons separating the two exact ground-states<sup>52</sup> (these fractionalized excitations are specific of the 1D chain).

The Heisenberg chain with alternating strong and weak bonds (Spin Peierls instability), has indeed a unique ground-state where the dimers are mainly located on the strong bonds. In that case, the spin- $\frac{1}{2}$  excitations are confined by the underlying potential and the true excitations are gapful integer magnons (<sup>56,57</sup> and refs. therein). It is an explicit VBC.

A two-leg ladder with AF rung exchange has also a unique VBC ground-state and gapped magnons as excitations.<sup>58</sup> On the other hand Nersesyan and Tsvelik<sup>59,60</sup> have proposed an example of frustrated ladder, with a spontaneously dimerized ground-state, and gapful excitations. Excitations of this last model are identified as pairs of singlet and triplet domain walls connecting the two ground-states, they form a continuum.

As can be seen from this rapid and non exhaustive enumeration, VBC ground-states are relatively frequent in frustrated one-dimensional spin- $\frac{1}{2}$  models. All these systems are gapful but the excitations could be of different nature emerging as modes (associated to integer spin excitations) or continuum of pairs of excitations that could be fractionalized (it is then specific of one-dimensional systems) or not.

### 5.3.3. Valence bond solids

The VBS wave-function was introduced by Affleck, Kennedy, Lieb and Tasaki (AKLT).<sup>61,62</sup> It can be constructed whenever the spin  $S$  on a site is a multiple of one half the coordination number  $z$ :  $2S = 0 \bmod z$ . Let us consider the simplest case  $2S = z$ . In that case the local spin  $S$  can be seen as the symmetric combination of  $2S$  (fictitious) spin- $\frac{1}{2}$ . Now on each bond of the lattice one can make a singlet between two fictitious spins- $\frac{1}{2}$ . Such a product of singlets does not belong to the physical Hilbert space of the original spin- $S$  model but to a much larger space. The VBS wave-function is defined as the projection of the singlet-product state onto the physical space. This projection amounts to symmetrize (for all lattice sites) the wave-function with respect to the fictitious spins to force them into a physical spin- $S$  state. A VBS can be viewed as an *explicit VBC of the fictitious spins*. Simple Hamiltonians with short ranged and  $SU(2)$ -symmetric interactions for which the VBS is an exact ground-state can be constructed (sum of projectors<sup>61,62</sup>). By construction the VBS wave-function is a spin singlet and *breaks no lattice symmetry*. By extension we may say that a system is in a VBS *phase* if its ground-state can be adiabatically transformed into the VBS wave-function without crossing a phase transition. As the VBC, models in the VBS phase have a gap to all excitations<sup>b</sup> but their wave-functions are slightly more complex and their order parameter is non-local. The order of VBS is associated to long-ranged singlet-singlet correlations in the *fictitious spins*. Expressing such observable in terms of the physical spins leads to a non-local quantity called *string order parameter*.<sup>63,64</sup> Contrary to explicit VBC, VBS have fractionalized degrees of freedom at the edges of the system with open boundary conditions. These are simply associated to the unpaired fictitious spins. To our knowledge these properties have not been explored in quantum 2D systems.

---

<sup>b</sup>This may however not always be true when the coordination number of the lattice is large.<sup>61</sup> In such cases the VBS wave-function is still a spin singlet but has long-ranged spin-spin correlations. We do not consider such cases here.

The spin-1 Heisenberg chain is the prototype of VBS in 1D.<sup>c</sup> Such a state has a unique ground-state, a gap in the excitations and exponentially decreasing spin-spin and dimer-dimer<sup>65</sup> correlations. See the chapter by P. Lecheminant in this volume for more details about the VBS phase of the spin-1 chain.

A spin- $\frac{3}{2}$  specific  $SU(2)$ -invariant model on the honeycomb lattice<sup>61,62</sup> is another example of 2D VBS. The spin-1 Heisenberg model on the kagome lattice was proposed to realize a VBS-like ground-state<sup>66</sup> in which singlets form on every hexagon without any spontaneous symmetry breaking (hexagonal singlet solid).<sup>d</sup> A similar approach was carried out for the spin-1 pyrochlore Heisenberg model.<sup>67</sup> In that case a lattice distortion was invoked to lift the degeneracy between the two singlet states of each tetrahedron.

### 5.3.4. Two-dimensional examples of VBC

#### 5.3.4.1. Without spontaneous lattice symmetry breaking

Two spin- $\frac{1}{2}$  experimental examples of 2D (explicit) VBC have recently attracted attention:  $\text{CaV}_4\text{O}_9$ <sup>68,69,70,71,72,73,74</sup> and  $\text{SrCu}_2(\text{BO}_3)_2$ .<sup>75,76,77,78,79,80,81,82,83,84</sup> In  $\text{CaV}_4\text{O}_9$  the  $\text{V}^{4+}$  ions are on a 1/5 depleted square lattice and in  $\text{SrCu}_2(\text{BO}_3)_2$  the exchange couplings between  $\text{Cn}^{2+}$  ions realize the Shastry Sutherland model.<sup>85</sup> A lattice embedding the main couplings of these two physical problems is drawn in Fig. 5.1. Interactions are of the Heisenberg type.<sup>e</sup>

VBC are obvious ground-states in the strong coupling limits of each problem.

The exact ground-state of the Shastry Sutherland model is built from singlets on the  $J'$  bonds.<sup>85,77</sup> For  $J'/J \gtrsim 1.55 \pm 0.05$  the model has a gap in the spectrum of excitations and is in a dimerized VBC phase.<sup>f</sup> For  $J'/J \lesssim 1.15 \pm 0.05$  the system is in the  $(\pi, \pi)$  Néel state of the square lattice (results

<sup>c</sup>In 1D, some authors call “Haldane systems” all the spin-gapped phases, whatever their true nature: VBC or VBS.

<sup>d</sup>Each kagome site belongs to two hexagons. Each physical spin-1 can be split into two spin- $\frac{1}{2}$ , each of them being involved in the formation of a singlet on one neighboring hexagon.

<sup>e</sup>Small Dzyaloshinsky-Moriya interactions have been identified in  $\text{SrCu}_2(\text{BO}_3)_2$ .<sup>86</sup>

<sup>f</sup>Consider a decomposition of the Shastry-Sutherland lattice as edge- and corner-sharing triangles. For  $J' = 2J$  the Hamiltonian is accordingly written as a sum of  $J(\vec{S}_1 + \vec{S}_2 + \vec{S}_3)^2$  terms for each triangle ( $J'$ -bonds are shared by two triangles) and each such term is minimized by the dimerized state. This shows rigorously that the dimerized state is the ground-state as soon as  $J'/J \gtrsim 2$ .

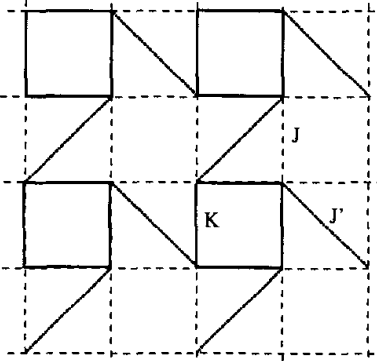


Fig. 5.1. The  $\frac{1}{5}$ -depleted lattice and the Shastry Sutherland lattice. The strong bonds of the Shastry Sutherland model are the bonds  $J'$  (dotted dashed lines): they can accommodate orthogonal dimers ( $J = K$  can be considered as a “perturbation” in the real  $\text{SrCu}_2(\text{BO}_3)_2$ ). The lattice formed by the strongest exchanges in  $\text{CaV}_4\text{O}_9$  is obtained with  $J = 0$ . The phase diagram of this model<sup>82</sup> contains (at least) collinear Néel phases, dimer and 4-spin plaquette VBC.

of zero-temperature series expansion<sup>87</sup>). The possibility of an intermediate phase, possibly with helical short-ranged correlations, has been actively discussed in the literature.<sup>88,79,89</sup> S. Miyahara and K. Ueda have recently written a review of the theory of the orthogonal dimer Heisenberg spin model for  $\text{SrCu}_2(\text{BO}_3)_2$ .<sup>84</sup>

The  $\frac{1}{5}$ -depleted Heisenberg square lattice model ( $J = 0$ ) has been studied as a function of the ratio of the two different couplings: bonds within a plaquette ( $K$ ) and dimer bonds ( $J'$ ) between plaquettes. At isotropic coupling ( $J' = K$ ) collinear long-ranged Néel order survives the depletion (the order parameter is about 35%<sup>71</sup> of the maximum classical value). A small unbalance in couplings drives the system either in a 4-spin plaquette VBC ( $K > J'$ ) or in a dimer VBC ( $K < J'$ ). Both (explicit) VBC phases have a spin gap. A recent generalization of these models by Läuchli *et al* encompasses both the  $\frac{1}{5}$ -depleted Heisenberg square lattice model and the Shastry Sutherland model<sup>82</sup> (see Fig. 5.1). Its phase diagram exhibits collinear Néel phases ( $(\pi, \pi)$  or  $(0, \pi)$ ) separated from the VBC phases by second order phase transitions. Transition between the two VBC phases which have different symmetries occurs via a first order phase transition.<sup>g</sup>

Excitations in these models come from the promotion of local singlets to

<sup>g</sup>A recent  $Sp(N)$  study of the Shastry Sutherland model<sup>89</sup> suggests that a spin liquid phase with deconfined spinons might appear in such a model. No evidence of such a phase has emerged from the  $SU(2)$  studies so far.

triplet excitations. In 2D the ordered dimer background provides a confining force for the spin- $\frac{1}{2}$  excitations. Indeed, separating two unpaired spins (that is two *spinons*) creates disruption in the ordered pattern all the way from the first to the second. The energy cost is thus proportional to the length of the string of defaults and both spin- $\frac{1}{2}$  excitations remains in fact confined. Only integer spin excitations are expected. On the other hand in these strongly coupled models single-triplet hoppings can be difficult and correlated motions might be important, leading to a large zoology of excited modes (see Ref.<sup>81</sup> and references therein). This potential frustration of the triplet motion favors the appearance of magnetization plateaus in VBC models.<sup>90,75,91,92,93,94</sup> This aspect was briefly discussed in the lecture notes published by the authors.<sup>95</sup>

#### 5.3.4.2. *With spontaneous lattice symmetry breaking*

In the previous models the (explicit) VBC phases do not break any lattice symmetry. They can be directly related to the geometry and relative strength of the couplings. In more symmetric situations with frustration, spontaneously symmetry breaking VBC can appear as a way to overcome this frustration by taking full advantage of the quantum fluctuations. This is probably the case in the  $J_1$ - $J_3$  model on the square lattice for intermediate  $J_3/J_1 \sim 0.6$ ,<sup>96</sup> in the  $J_1$ - $J_2$  model on the hexagonal lattice for intermediate  $J_2/J_1 \sim 0.4$ ,<sup>97</sup> and in the Heisenberg model on the checkerboard lattice.<sup>98,99,100,101,102,103</sup> In the two first cases the ground-states are dressed columnar VBC of dimers. Translation and  $C_4$  (resp.  $C_3$  only) symmetries of the lattice are spontaneously broken. The ground-state is 4 (resp. 3) times degenerate. Spin-spin correlations decrease exponentially with the system size. All excitations are gapped. Contrary to the  $J_1$ - $J_2$  model on the square lattice, exact diagonalizations<sup>96,97,99</sup> give a rather straightforward information on these systems where the correlation lengths are small enough (far enough from the critical points which limit the boundary of the VBC phases).

The spin- $\frac{1}{2}$  Heisenberg model on the checker board lattice, which can also be seen as a planar lattice of corner sharing tetrahedrons (see Fig. 5.2), has received the largest attention for different reasons.<sup>104,105,98,101,100,99,102,103</sup> The problem has classically a continuous local degeneracy: the Hamiltonian can be rewritten as the sum of the squares of the total spin of each tetrahedron, and every configuration with a zero spin on each tetrahedron is a ground-state. Classically this

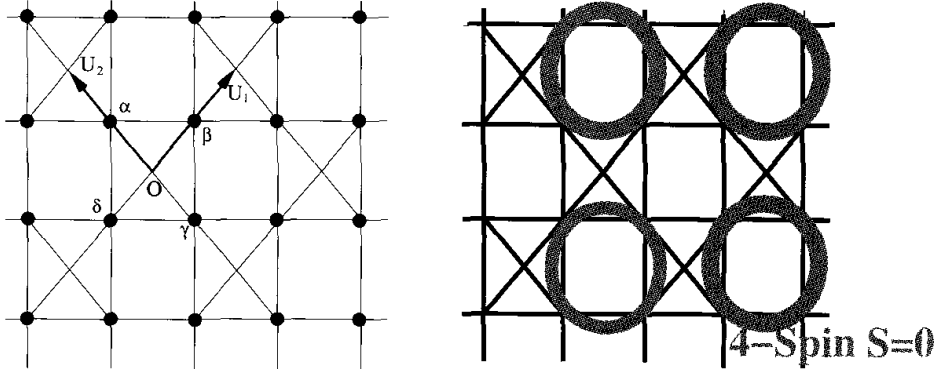


Fig. 5.2. Left: the checkerboard lattice. The spins sit at the vertices shown by bullets, all couplings are identical,  $\mathbf{u}_1$ ,  $\mathbf{u}_2$  are the unit vectors of the Bravais lattice. Right: the ground-states of the Heisenberg model on the checker board lattice are translational symmetry breaking VBC of 4-spin plaquettes on the uncrossed squares.

problem shares this property with the Heisenberg model on the kagome, pyrochlore<sup>106,107</sup>, garnet<sup>108</sup> and pyrochlore slab<sup>109</sup> lattices (these lattices made of corner sharing “simplexes” with 2, 3 or 4 spins each were dubbed “bisimplex” lattices by Henley<sup>110</sup>).

The quantum spin- $\frac{1}{2}$  antiferromagnet on the kagome lattice has been found to be quite specific with a small gap (if any) toward triplet excitations and an anomalous density of gapless low-lying singlets excitations (see §5.7).

The quantum scenario on the checkerboard lattice is quite different. The ground-state is a (dressed) product of 4-spin  $S = 0$  plaquettes on uncrossed squares: this state breaks translational symmetry but not  $C_4$  (the point group being defined at the center of an empty plaquette). It has a two fold degeneracy in the thermodynamic limit: this is easily seen in the symmetries and finite size scaling of the low lying levels of exact spectra.<sup>99</sup> The choice of the 4-spin  $S = 0$  states on the uncrossed squares corresponds to the most stable local configuration. The product of  $S = 0$  quadruplets is only weakly renormalized in the exact ground-state.<sup>99</sup>

Excitations of this model have been studied in different approaches, exact diagonalizations<sup>111</sup>, series expansions,<sup>101</sup> real space renormalization transformation.<sup>102</sup> All the excitations (singlet and triplet) are gapped. The triplet excitations originate from the triplet excitation of an uncrossed plaquette, they are weakly dispersive with a large gap. The singlet excitations cannot be described so simply: from exact diagonalizations data one can suspect that some of these excitations come from the reorganization of two adjacent triplet on crossed squares. The Contractor Renormalization

(CORE) method of Berg *et al.*<sup>102</sup> on the other hand suggests that these excitations are domain walls between the two translated plaquette-VBC ground-states.

### 5.3.5. Methods

Spin waves<sup>69</sup> and Schwinger bosons<sup>88,70</sup> are simple approximations to study the phase diagram of a quantum frustrated magnet. But the first method only gives an approximate knowledge on the range of existence of the Néel phases, and it is rather difficult to include the effect of fluctuations beyond the mean-field approximation within the Schwinger-Boson formulation. As discussed in the section devoted to large- $N$  approaches (§5.4), spontaneous lattice symmetry breaking are very likely to be due to topological effects (Berry phase of instantons) which cannot be captured by the mean-field state. This probably explains why no spontaneous VBC has ever been found (to our knowledge) in Schwinger-Boson calculations.<sup>h</sup> For unfrustrated problems, as the Heisenberg model on the  $\frac{1}{5}$ -depleted square lattice,<sup>71</sup> QMC is considered as the method which can give benchmarks for other approaches.

Although VBC are naturally described with the help of spin- $\frac{1}{2}$  valence-bonds, the appearance of such states in the low-spin limit can sometimes be anticipated from an appropriate large- $S$  approach. An example is given in the work of Tchernyshyov *et al.*<sup>103</sup> (see also a previous paper by Henley<sup>110</sup>) on the checkerboard Heisenberg model. In this model, when both couplings (square lattice bonds and diagonal bonds) are equal, ground-state has a continuous local degeneracy. However leading  $1/S$  corrections select collinear states out of this huge manifold.<sup>110</sup> There remains an exponential number of such states and they do not have any magnetic order. However they exhibit long-ranged *bond* order and a spontaneous symmetry breaking<sup>103</sup> which is analogous to the one observed numerically in the spin- $\frac{1}{2}$  case.

For frustrated problems, exact diagonalizations can be useful tools in situations where the system is not too close from a critical point, that is when the correlations length is not too large. Successful applications of exact diagonalizations methods to 2D Heisenberg magnets realizing a VBC include studies of the  $J_1-J_3$  model on the square lattice,<sup>96</sup>  $J_1-J_2$  model on the hexagonal lattice,<sup>97</sup> Heisenberg model on the checkerboard lattice.<sup>99</sup> In

---

<sup>h</sup>It seems however that spontaneous VBC naturally arise in large- $N$  approaches with fermionic representation of  $SU(N)$  when  $1/N$  corrections are considered (see section 5.5.2).

such situations analysis of the quasi degeneracy of the low-lying levels of the spectra and of their finite-size scaling gives an unbiased and direct informations on the symmetry breakings in the thermodynamic limit.<sup>99</sup> However the boundaries of the phases and the quantum critical points cannot be accurately determined with this method. The series expansions described in the previous section appears to be a powerful approach to determine phase boundaries.<sup>112,74</sup> If the spin-spin correlation length is not very short, as it is the case in the  $J_1-J_2$  model on the square lattice for  $J_2/J_1 \sim 0.5$ ,<sup>37</sup> it is very difficult to decide from exact diagonalizations between a VBC, a critical phase or an RVB SL.

Concerning excitations, exact diagonalizations give the gaps in each sector and provide a crude approximation of the dispersion laws of the first excitations. The large-scale nature of the excitations (as for examples domain walls excitations) can escape this method. The semi-analytical approaches which can be used for the study of the excitations of the VBC, all use as a basic departure point the excitations of a local cluster of spins conveniently renormalized by perturbation<sup>73,101</sup> or effective renormalization technique.<sup>102</sup> Contrary to exact diagonalizations these methods are not limited by finite-size effects but the results can be biased by the departure point.<sup>101,102</sup>

### 5.3.6. Summary of the properties of VBC phases

The generic features of VBC (whatever the dimensionality of the lattice) are:

- A spin gap, no  $SU(2)$  symmetry breaking and short-ranged spin-spin correlations,
- Long-ranged order in dimer-dimer and/or larger  $S = 0$  plaquettes. The coupling of this order to lattice distortions is probable in experimental realizations of spontaneous VBC.
- In *spontaneous* VBC phases the ground-state is degenerate. From the theoretical point of view the discrete symmetry of the order parameter of the VBC which spontaneously breaks a lattice symmetry may give birth to a finite temperature Ising-like transition.<sup>14</sup> Simultaneity between this transition and a possible structural transition is likely when the couplings of the spins to the lattice degrees of freedom (phonons) is considered.<sup>113</sup>
- VBC have gapped excitations, in the  $S = 0$  sector as well as in other  $S$  sectors. A wide zoology of modes is to be expected as well

as continua associated to multi-particle excitations or scattering of domain walls (in the case of a spontaneous symmetry breaking of the ground-state). In two dimensions all these excitations have integer spins (the ordered back-ground inducing a confinement of the spin- $\frac{1}{2}$  excitations)

Frustration on the square lattice or more generally on bipartite lattices is often overcome by VBC phases. The appearance of VBC in triangular geometries is possible in principle but there is up to now no examples of such phases in pure spin- $\frac{1}{2}$  models (in Sec. 5.5 examples will be given within the framework of quantum dimer models).

It has been advocated in the large- $N$  approaches (see section 5.4) that, at least in two dimensions, collinear spin-spin correlations generically lead to VBC or VBS and only non-collinear spin-spin correlations can give birth to RVB SL with unconfined spin- $\frac{1}{2}$  excitations. The present knowledge of  $SU(2)$  phase diagrams supports this prediction. The VBC found so far numerically in  $SU(2)$  spin models appear to be in regions of parameter space where the spin-spin correlations are characterized by some short-ranged collinear order in the large- $S$  limit. The  $J_1-J_2$  model on the honeycomb lattice has a classical incommensurate phase in the regime of high frustration and there are some evidences that in the quantum phase diagram the collinear phase is separated from the columnar VBC phase by a RVB SL.<sup>97</sup> The multiple-spin exchange (MSE) model on the triangular lattice is also believed to be a RVB SL<sup>114</sup> and the corresponding classical ground-states generically have non-coplanar spin configurations. Capriotti *et al.*<sup>37</sup> argued that the spin- $\frac{1}{2}$  square lattice  $J_1-J_2$  model could be a RVB SL. If confirmed, this would be the first counter-example to the general rule explained above (The Heisenberg model on the pyrochlore lattice might be an other counter-example<sup>102</sup>).

#### 5.4. Large- $N$ methods

Introduced by Affleck,<sup>115</sup> Affleck and Marston,<sup>116</sup> Arovas and Auerbach<sup>117</sup> and Read and Sachdev<sup>118,119,120</sup> in the context of spin models, large- $N$  approaches are powerful methods to investigate quantum antiferromagnets. When  $N$  is taken to infinity many of these models can be solved by saddle point methods and finite- $N$  corrections can be, at least in principle, explored in a controlled way. A success of these approaches is that they can describe the phenomenology of a large variety of phases encountered in quantum magnets : Magnetic LRO (possibly with order by disorder selection) as

well as phases dominated by short-ranged valence-bonds: VBC, VBS and RVB liquids. One crucial result (due to Read and Sachdev<sup>118,119,120,121,122</sup>) concerning these three later phases is that the analysis of finite- $N$  corrections to some large- $N$  formulations ( $Sp(N)$  for instance, see below) provides a general criterion to decide which of these three phase should appear in a given model.

This criterion is the following in 2D: if the (large- $N$  equivalent of the) “spin”  $S$  at each site matches the lattice coordination number  $z$  by  $2S = 0 \bmod z$  a VBS is to be expected. If it is not the case (as for a spin- $\frac{1}{2}$  model on the square lattice) one should look at the local spin-spin correlations. If they are reminiscent of a collinear order, a VBC with spontaneous translation symmetry breaking is expected whereas non-collinear short-ranged correlation generically give rise to a RVB phase without any broken symmetry and deconfined spinon excitations. These results are of course based on a large- $N$  generalization of the original spin model and there is no guaranty at all that these rules should always apply to  $SU(2)$  models. To our knowledge they have however not been manifestly found in error up to now.<sup>i</sup> In the following we will present some of the important reasoning steps leading to this result.

#### 5.4.1. Bond variables

The  $SU(2)$  algebra of a spin  $S$  at one site can be represented by 2 species of particles  $a_\sigma^\dagger$  (with  $\sigma = \uparrow, \downarrow$ ), provided that the total number of particles on one site is constrained to be  $a_\uparrow^\dagger a_\uparrow + a_\downarrow^\dagger a_\downarrow = 2S$ . The raising operator  $S^+$  (resp.  $S^-$ ) is simply represented by  $a_\uparrow^\dagger a_\downarrow$  (resp.  $a_\downarrow^\dagger a_\uparrow$ ). These particles can be chosen to be fermions (Abrikosov fermions) or bosons (Schwinger bosons). These particles carry a magnetization  $\pm \frac{1}{2}$  since  $S^z = \frac{1}{2}(a_\uparrow^\dagger a_\uparrow - a_\downarrow^\dagger a_\downarrow)$ . For this reason they are often called *spinons*. The Heisenberg interaction is a quartic interaction for these particles:

$$\vec{S}_i \cdot \vec{S}_j = S^2 - \frac{1}{2} A_{ij}^\dagger A_{ij} \quad (10)$$

with the bond operator  $A_{ij}$  defined by:

$$A_{ij} = a_{j\downarrow} a_{i\uparrow} - a_{j\uparrow} a_{i\downarrow} \quad (11)$$

Acting on the vacuum,  $A_{ij}^\dagger$  creates a spin singlet on the bond  $(ij)$ . Physically  $A_{ij}^\dagger A_{ij}$  measures the number of singlets on that bond and Eq. 10 shows

---

<sup>i</sup>The spin- $\frac{1}{2}$  kagome antiferromagnet might however be such an example. See section 5.7.

that the antiferromagnetic Heisenberg interaction just tries to maximize that number.

The idea of large- $N$  methods is to generalize the  $SU(2)$  symmetry of the spin- $S$  algebra to a larger group  $SU(N)$  (or  $Sp(N)$ ) by letting the index  $\sigma$  go from 1 to  $N$  (or  $2N$ ). The  $SU(N)$  (or  $Sp(N)$ ) generalization of the Heisenberg model is solved by a saddle point calculation of the action. The  $N = \infty$  limit is very similar to a mean-field decoupling of the four-body interaction of the physical  $SU(2)$  model:  $A_{ij}^\dagger A_{ij} \simeq A_{ij}^\dagger \langle A_{ij} \rangle + \langle A_{ij}^\dagger \rangle A_{ij} - |\langle A_{ij} \rangle|^2$ .

#### 5.4.2. $SU(N)$

The generalization of the Heisenberg model to such a symmetry group depends only on the choice of the irreducible representation of  $SU(N)$  according to which the “spin” operators transform (and not on the choice of fermions or bosons to implement the representation). For  $SU(2)$  this amounts to specify the magnitude  $S$  of the spin. For  $SU(N)$  irreducible representations are labeled by Young tableaux. The case of a general rectangular tableau with  $n_c$  columns and  $m$  rows was discussed by Read and Sachdev<sup>123</sup> and  $n_c$  appears to continue to play a role similar to  $2S$  in the large- $N$  phase diagrams.<sup>j</sup> In this review we will focus on a slightly different large- $N$  generalization of the  $SU(2)$  model which is both able to deal with frustration and magnetic states.

#### 5.4.3. $Sp(N)$

To perform a large- $N$  extension of *frustrated* Heisenberg models one has to use either fermions<sup>116</sup> or bosons with an  $Sp(N)$  symmetry. The latter seems to produce phase diagrams that closely resemble the  $SU(2)$  problems and we will focus on this representation which was introduced by Read and Sachdev.<sup>120</sup> The presentation below is largely inspired from their papers.<sup>118,119,120,121,122</sup>

---

<sup>j</sup>Taking the limit  $N \rightarrow \infty$  with  $m$  fixed of order 1 and  $n_c \sim N$  is most conveniently done with bosons  $b_{\alpha p}^\dagger$  where  $\alpha = 1 \dots N$  is the  $SU(N)$  index, while  $p = 1 \dots m$  label the different “colors”. There are therefore  $Nm$  kinds of bosons. On the other hand it is convenient to use  $n_c$  “colors” of fermions (still with an  $SU(N)$  index) to deal with the case  $n_c \sim \mathcal{O}(1)$  and  $m \sim N$ . Bosonic representations with  $n_c \sim N$  are appropriate to describe magnetically ordered phases<sup>117</sup> but cannot be used for frustrated models (such a representation is not self-conjugate). On the other hand fermionic representations, such as the  $m = N/2$  and  $n_c = 1$  one,<sup>116,124</sup> can be used on any lattice but they do not display magnetically ordered phases and tend to favor dimerized states.<sup>116,123,124</sup>

We now have  $2N$  flavors of bosons at each site:  $b_{i,\sigma}$  with  $\sigma = 1..2N$  and we define an  $Sp(N)$ -invariant bond operator:

$$A_{ij} = \sum_{\sigma, \sigma'=1..2N} \mathcal{J}_{\sigma, \sigma'} b_i^\sigma b_j^{\sigma'} \quad (12)$$

where the  $2N \times 2N$  antisymmetric tensor  $\mathcal{J}$  is block diagonal

$$\mathcal{J} = \begin{bmatrix} 0 & 1 & & & \\ -1 & 0 & & & \\ & & \ddots & & \\ & & & 0 & 1 \\ & & & -1 & 0 \end{bmatrix} \quad (13)$$

and generalizes the  $SU(2)$  antisymmetric tensor  $\epsilon_{ij}$  ( $SU(2)$  is identical to  $Sp(1)$ ). Up to some constant the  $Sp(N)$  Hamiltonian is

$$\mathcal{H} = -\frac{1}{N} \sum_{ij} J_{ij} A_{ij}^\dagger A_{ij} \quad (14)$$

with the constraints

$$\forall i \quad \sum_{\sigma=1}^{2N} b_{i\sigma}^\dagger b_{i\sigma} = n_c \quad (15)$$

$n_c = 2S$  in the  $SU(2)$  case and  $n_c/N = \kappa$  will be kept constant when taking the large- $N$  limit. The partition function can be represented by an imaginary time functional integral:

$$Z = \int \mathcal{D}[\lambda_i, b_i^\sigma, b_i^{\dagger\sigma}] \exp \left( - \int_0^\beta (L_0 + \mathcal{H}) d\tau \right) \quad (16)$$

$$L_0 = \sum_{i\sigma} b_i^{\dagger\sigma} (\partial_\tau + i\lambda_i) b_{i\sigma} - iN\kappa \sum_i \lambda_i \quad (17)$$

The  $\lambda_i(\tau)$  are Lagrange multipliers that enforce the constraint Eq. 15 at every site. Bond degrees of freedom  $Q_{ij}$  are introduced in order to decouple the bosons (Hubbard-Stratonovitch). The partition function is now

$$Z = \int \mathcal{D}[Q_{ij}, \bar{Q}_{ij}, \lambda_i, b_i^\sigma, b_i^{\dagger\sigma}] \exp \left( - \int_0^\beta (L_0 + L_1) d\tau \right) \quad (18)$$

with

$$L_1 = \sum_{ij} \left[ N \frac{|Q_{ij}|^2}{J_{ij}} - (A_{ij}^\dagger Q_{ij} + \text{h.c.}) \right], \quad (19)$$

so that a Gaussian integration of the  $Q_{ij}$  gives back Eq. 16. The bond variable are  $Sp(N)$  invariant and they can take non-zero expectation values at a mean-field level without breaking the  $Sp(N)$  symmetry. As we explain below, they are however not *gauge-invariant*.

#### 5.4.3.1. Gauge invariance

An important property of Eq. 18 is the  $U(1)$  gauge invariance associated to the following transformations:

$$b_{i\sigma} \rightarrow b_{i\sigma} e^{i\phi_i} \quad (20)$$

$$Q_{ij} \rightarrow Q_{ij} e^{i(\phi_i + \phi_j)} \quad (21)$$

$$\lambda_i \rightarrow \lambda_i - \partial_\tau \phi_i \quad (22)$$

where  $\phi_i(\tau)$  are arbitrary site- and imaginary-time-dependent angles. This gauge invariance comes from the conservation of the local boson number and reflects the fact the magnitude of the spin is constant at each site. If we focus on the phase degrees of freedom of the bond variables, the Eq. 18 describes a system of charge-1 bosons coupled to a  $U(1)$  lattice gauge theory.<sup>125,126</sup> These gauge degrees of freedom play a crucial role in the analysis of the fluctuations about mean-field solutions.

*Effective action for the bond variables* —The boson degrees of freedom can be integrated out to give an effective action for the bond variables:

$$Z = \int \mathcal{D}[Q_{ij}, \bar{Q}_{ij}, \lambda_i] \exp(-S^{\text{eff}}) \quad (23)$$

$$S^{\text{eff}} = N \int_0^\beta \left[ \sum_{ij} \frac{|Q_{ij}|^2}{J_{ij}} - i\kappa \sum_i \lambda_i \right] - N \text{Tr} \log G \quad (24)$$

where  $G^{-1}$  is the quadratic form which couples the bosons in Eq. 18 (propagator). It depends on the bond variables and on  $\lambda_i$ . We may write formally  $G^{-1} = \partial_\tau - i\lambda - Q$ . The term  $N \text{Tr} \log G$  is the free energy of the bosons in presence of the bond fields. By construction the action  $S^{\text{eff}}$  is gauge-invariant with respect to the transformations of Eqs. 20–22. So far this is an exact formulation of the original model for arbitrary  $N$ .

#### 5.4.3.2. Mean-field ( $N = \infty$ limit)

Since  $N$  factorizes (no flavor index is left in Eq. 24),  $Z$  is dominated by the saddle point of  $S^{\text{eff}}$  when  $N$  is large. For simple models such as the

first-neighbor antiferromagnet on the cubic lattice (any space dimension), the saddle point can be determined analytically. The  $N = \infty$  limit is almost equivalent to the Schwinger-boson mean-field theory.<sup>127,128</sup> This can otherwise be done numerically.<sup>k</sup> In this large- $N$  limit, two kinds of mean-field solutions can appear. For large enough  $\kappa$  the bosons condense at some wave-vector, the spectrum of the mean-field Hamiltonian is gapless. This corresponds physically to Néel long-range order. On the other hand, for smaller  $\kappa$  (smaller “spin”) the mean field Hamiltonian is gapped and the ground-state preserves the  $Sp(N)$  symmetry. Fluctuations around the saddle point are not expected to change drastically the Néel ordered phases but they play an important role in the physics of  $Sp(N)$  symmetric phases. The following is a brief discussion of the effects of fluctuations in these non-magnetic phases.

#### 5.4.3.3. Fluctuations about the mean-field solution

At the mean-field level described above some  $Q_{ij}$  acquire a (static in all known cases) non-zero expectation value:  $\langle Q_{ij} \rangle = \bar{Q}_{ij}$ . For this reason such a state spontaneously breaks the local gauge invariance of Eqs. 20,21 and 22. However this does not mean that the gauge degrees are all gapped and do not play any role at low energy. In fact, as remarked by Read and Sachdev, depending on the *geometry* of the lattice defined by the bonds where  $Q_{ij} \neq 0$ , some long-wavelength gapless gauge excitations survive and the associated fluctuations must be taken into account. More precisely, the fluctuations of the bond variables about the saddle point are decomposed into an amplitude and a phase

$$Q_{ij} = (\bar{Q}_{ij} + q_{ij}) \exp(i\theta_{ij}) \quad (25)$$

and we expand  $S_{\text{eff}}$  with these new variables. Two cases must then be considered:

- i) The lattice made of the sites connected by non-zero  $\bar{Q}_{ij}$  bonds is bipartite. This is automatically the case if the original lattice

---

<sup>k</sup>To our knowledge, all the saddle points considered so far are static (expectation values of the  $Q_{ij}$  are time-independent) and the corresponding  $\langle Q_{ij} \rangle$  could all be made real with an appropriate gauge transformation. There is no chiral order and the time-reversal symmetry is unbroken. The (oriented) sum of the complex phases of the bond variables around a plaquette defines a  $U(1)$  flux. This flux is related to the solid angle formed by the spins and it vanishes in collinear as well as in coplanar states. In such cases the phases can be therefore be gauged away and the  $\langle Q_{ij} \rangle$  can be made real. For this reason complex bond variables are usually not observed.<sup>129</sup>

defined by bonds where the exchange  $J_{ij} \neq 0$  is bipartite. This can also be true if the original lattice is a non-bipartite lattice but some bonds have  $\bar{Q}_{ij} = 0$  so that the remaining lattice is bipartite. This is the case, for instance, in the  $J_1-J_2$  model on the square lattice,<sup>120</sup> in some regions of the phase diagram of the Shastry-Sutherland model<sup>89</sup> and in on the checkerboard Heisenberg model.<sup>104</sup> Such configurations of the bond variables give *collinear* spin structures: spin-spin correlations can either be long-ranged (large  $\kappa$ , Néel phase) or short-ranged but in both cases the magnetic structure factor is peaked at a simple wave-vector  $\mathbf{k}_0$  such that  $2\mathbf{k}_0$  is a reciprocal lattice vector ( $k_0 = (\pi, 0)$ ,  $k_0 = (0, \pi)$  or  $k_0 = (\pi, \pi)$  in square geometries).

- ii) The lattice made of the sites connected by non-zero  $\bar{Q}_{ij}$  bonds is not bipartite. This happens in some phases of the  $J_1-J_2-J_3$  model on the square lattice,<sup>120</sup> on the triangular or kagome lattices<sup>130</sup>, in the Shastry-Sutherland model for some values of the exchange parameters<sup>89</sup> and on an anisotropic triangular lattice.<sup>131</sup> Such mean-field states generically have planar but non-collinear spin-spin correlations.

It is simple to check that case i) preserve a *global* continuous symmetry while such a symmetry is absent in ii). Consider the following *global* gauge transformation in case i) :

$$b_{i\sigma} \rightarrow b_{i\sigma} e^{i\phi} \quad b_{j\sigma} \rightarrow b_{j\sigma} e^{-i\phi} \quad (26)$$

$$Q_{ii'} \rightarrow Q_{ii'} e^{2i\phi} \quad Q_{jj'} \rightarrow Q_{jj'} e^{-2i\phi} \quad (27)$$

$$Q_{ij} \rightarrow Q_{ij} \quad (28)$$

where  $i, i'$  belongs to sublattice  $A$  and  $j, j'$  belongs to sublattice  $B$ . This transformation does not change the mean-field parameters  $\bar{Q}_{ij}$ . The only fields affected by this transformation are those connecting two sites on the same sublattice.<sup>1</sup> They have a zero expectation values in case i) (or do not even exist if the physical lattice is itself bipartite). For this reason it is possible to make low-energy (and long-wavelength) gapless gauge excitations about the saddle-point by replacing the global staggered phase shift  $\phi$  of Eq. 26 by a slowly varying (staggered)  $\theta_{ij}$  (Eq. 25). A gradient expansion

<sup>1</sup>In a gauge theory language the fields  $Q_{ii'}$  (resp.  $Q_{jj'}$ ) of Eq. 27 transform like a charge-2 scalar for the  $U(1)$  gauge field. Instead, from Eq. 26, the bosons (spinons) carry a charge 1.

of the effective action performed at the appropriate points in the Brillouin zone for the phase fluctuations only involves gradients of  $\theta$ . The corresponding action is that of  $U(1)$  lattice gauge theory coupled to charge-1 boson (spinons).

#### 5.4.3.4. Topological effects - instantons and spontaneous dimerization

So far only small fluctuations around the saddle point were considered and the contribution of topologically non-trivial gauge-field configurations were ignored. Consequently, the magnitude of the “spin”  $n_c/2$  was a continuous parameter and *the information about the integer or half-integer (for instance) character of  $S$  as disappeared*. From Haldane’s work on quantum spin chains and non-linear sigma models<sup>132</sup> it is well known that Berry phases in spin systems give rise to topological terms in the low-energy effective action which can play a crucial role depending on the parity of  $2S$ .

In non-linear sigma models in 2+1 dimensions the Berry phase vanishes for configurations which are smooth on the scale of the lattice spacing<sup>133,134</sup> (unlike the 1+1 dimensional case). However “hedgehog” space-time singularities<sup>133</sup> give non-trivial Berry phases. Read and Sachdev found that the closely related instantons of the effective  $U(1)$  gauge theory described before<sup>m</sup> also play a crucial role in the physics of the  $Sp(N)$  (as well as  $SU(N)$ ) spin models.

The Berry phase associated to such a singular configuration depends on details of the lattice geometry. In the short-range ordered  $(\pi, \pi)$  phase of the square lattice antiferromagnet this Berry phase is a multiple of  $in_c\pi/2$ . Although dealing with a gas of interacting ( $1/r$  Coulomb-like potential) instantons is a difficult problem (see Ref. <sup>119</sup> and references therein), we can guess that the physics will depend on  $n_c \bmod 4$ . A detailed analysis<sup>119</sup> shows that when  $n_c \neq 0 \bmod 4$  the instantons condense and *spontaneously break the lattice translation symmetry*. This generates a static electric field for the  $U(1)$  gauge field. Since the electric field is coupled to the difference of amplitudes of the bond variables, such state acquires spatially inhomogeneous expectation values of the bond variables, *it is a VBC and spinons are confined in pairs*. In the  $J_1-J_2$  model around  $J_2/J_1 \simeq 0.5$  the mean-field state is short-range ordered with correlations peaked at  $(\pi, \pi)$ . A columnar dimerized state is predicted by Read and Sachdev from this analysis of the

---

<sup>m</sup>In that gauge theory associated to the phases of the link variables an instanton corresponds to a tunneling event during which the total magnetic field piercing the lattice is changed by  $\pm 2\pi$ .

fluctuations, in agreement with a number of numerical works on the  $SU(2)$   $J_1-J_2$  spin- $\frac{1}{2}$  model.

In a recent work by Harada, Kawashima and Troyer<sup>135</sup> the phase diagram of the (first neighbor - unfrustrated)  $SU(N)$  antiferromagnet on the square lattice with  $n_c = 1$  was found to be in complete agreement with Read and Sachdev's predictions. They showed by quantum Monte Carlo simulations that for  $N \leq 4$  the systems is Néel ordered whereas it is a columnar VBC for  $N > 5$ . This provides an additional support to the field theory arguments described above. It also underlines that the mechanism of spontaneous symmetry breaking and formation of a VBC may come from quantum fluctuations only and that frustration is not always required (although it clearly enhances quantum fluctuations).

On the other hand when  $n_c = 0 \bmod 4$  the analysis of Read and Sachdev shows that fluctuations should not bring any broken lattice symmetry. Spinons are also confined and this state closely resembles the valence-bond solid (VBS) proposed by Affleck *et al.*<sup>61</sup> as a possible ground-state when the spin  $S$  matches the coordination number  $z$  according to  $2S = 0 \bmod z$  (see §5.3.3).

#### 5.4.3.5. Deconfined phases

Now we suppose that, starting from a mean-field solution with collinear correlations (case i), a parameter of the original spin model is varied so that the mean field solution is changed and some bonds  $Q_{ii'}$  ( $i$  and  $i'$  belong to the same sublattice) acquire a non zero expectation value (case ii). In the framework of square lattice antiferromagnets, a finite third-neighbor coupling ( $J_3$ ) would be needed.<sup>120</sup> From the point of view of the long-wavelength gauge fluctuations (related to the continuum limit of the phases  $\theta_{ij}$ ) discussed above, the appearance of  $\bar{Q}_{ii'} \neq 0$  is equivalent to the condensation of a (Higgs) boson of charge 2. This is a spontaneous break down of the global  $U(1)$  staggered symmetry of Eqs. 26–28 down to a  $\mathbb{Z}_2$  one since the field  $Q_{ii}$  is not invariant under Eq. 27 except if  $\phi = 0$  or  $\pi$ . Based on results of Fradkin and Shenker<sup>136</sup> concerning confinement in compact lattice gauge theories coupled to matter, Read and Sachdev argued that this Higgs mechanism suppresses the low-energy gauge fluctuations and liberate the spinons. This confinement transition is described by a  $\mathbb{Z}_2$  gauge theory. The suppression of the  $U(1)$  gauge fluctuations also forbids the condensation of

instantons discussed above and the ground-state remains unique<sup>n</sup> and *bond variables have uniform expectation values. It is a genuine SL without any broken symmetry and deconfined spinons.*

### 5.5. Quantum dimer models

In a previous section (§5.3) we showed that pairing spins- $\frac{1}{2}$  into singlets at short distances is a rather natural way to overcome frustration in Heisenberg antiferromagnets. QDM are defined in the Hilbert space of nearest-neighbor valence-bond (or dimer) coverings of the lattice. By construction these models focus on the dynamics in the singlet space and ignore magnetic (gapped magnons or gapped spinons) excitations. For this reason they are (a priori) not appropriate to describe the physics of spin systems where magnetic excitations are gapless.

The Hamiltonian of a QDM usually contains kinetic as well as potential energy terms for these dimers. Such Hamiltonians can often be simpler than their spin parents and are amenable to several analytic treatments because of their close relations to classical dimer problems,<sup>137,138,139</sup> Ising models and  $\mathbb{Z}_2$  gauge theory.<sup>140,141,142</sup> These models can offer simple descriptions of VBC<sup>143</sup> as well as RVB liquids.<sup>144,141</sup> It is in particular possible to write down some QDM that have a simple and exact VBC ground-state with spontaneous broken symmetries (such as Rokhsar and Kivelson's model on the square lattice<sup>143</sup> with attractive potential energy only - in which case the exact ground-state is very simple). Simple solvable QDM which have a dimer-liquid ground-state can also be constructed.<sup>141</sup>

#### 5.5.1. Hamiltonian

The first QDM was introduced by Rokhsar and Kivelson.<sup>143</sup> It is defined by an Hamiltonian acting in the Hilbert space of first-neighbor dimer (valence-bonds) coverings of the square lattice and reads:

$$\mathcal{H} = \sum_{\text{Plaquette}} [-J(|\bullet\bullet\rangle\langle\bullet\bullet| + \text{H.c.}) + V(|\bullet\bullet\rangle\langle\bullet\bullet| + |\bullet\bullet\rangle\langle\bullet\bullet|)] \quad (29)$$

Flipping two parallel dimers around a square plaquette is the simplest dimer move on the square lattice and the  $J$  terms precisely represent such dynamics. The  $V$  terms are diagonal in the dimer basis and account for an

---

<sup>n</sup>Except for a discrete topological degeneracy.

attraction or repulsion between nearest-neighbor dimers. These are the two *most local* terms (respecting all lattice symmetries) which can be considered.<sup>a</sup>

### 5.5.2. Relation with spin- $\frac{1}{2}$ models

There exists different interesting mappings between frustrated Ising models and QDM.<sup>145,142</sup> Here, however, we focus on the relations between QDM and  $SU(N)$  (or  $Sp(N)$ ) spin models in which dimers are related to singlet valence-bonds.

*Overlap expansion.* — A valence-bond state (product of two-spin singlets - belongs to the spin- $\frac{1}{2}$  Hilbert space) can be associated to any dimer covering.<sup>b</sup> Two such valence-bond states  $|a\rangle$  and  $|b\rangle$  are not orthogonal but, as first discussed by Sutherland<sup>146</sup> their overlap decays exponentially with the length  $L$  of the loops of their transition graphs (defined in §5.5.3.1) as  $|\langle a|b\rangle| = 2^{1-L/2}$ . Rokhsar and Kivelson<sup>143</sup> introduced a formal expansion parameter  $x$  and replaced  $|\langle a|b\rangle|$  by  $2x^L$ . Their idea is that although  $x = \frac{1}{\sqrt{2}}$  for physical  $SU(2)$  spins, the physics of some models may be captured by the first orders of a small  $x$  expansion. Truncating this expansion to order  $x^n$  gives an effective Hamiltonian which contains *local* terms involving at most  $n$  dimers.<sup>c</sup> In this approach the dimer states of the QDM are in one-to-one correspondence with *orthogonalized* valence-bonds in the spin Hilbert space.<sup>d</sup>

*Fluctuations about large- $N$  saddle points.* — From the argument above it could seem that the connection between spin- $\frac{1}{2}$  models and QDM relies on a variational approximation: the spin Hilbert space is restricted to the nearest-neighbor valence-bond subspace. This connection is in fact prob-

<sup>a</sup>They were originally derived<sup>143</sup> as the lowest order terms of a formal overlap expansion (see §5.5.2 below) of the Heisenberg. In that calculation  $J \sim x^4$  and  $V \sim x^8$ . Notice that a three-dimer kinetic term (extending over two neighboring plaquettes) is generated at order  $x^6$  and is not included in Eq. 29.

<sup>b</sup>There is however a sign ambiguity (a valence-bond is antisymmetric under the exchange of both spins) that can be fixed by choosing an orientation on every bond.

<sup>c</sup>The *signs* of the non-diagonal (kinetic) terms of the effective QDM obtained by such small  $x$  expansion depends on the sign convention which was chosen to map valence-bonds to dimers. An important question is to know whether, at least at the lowest non-trivial order, a sign convention giving the same sign for all kinetic terms exists (as in Eq. 29). This is the case on the square<sup>143</sup> and triangular lattices.<sup>144</sup>

<sup>d</sup>This implicitly assumes that the valence-bond states are linearly independent. This can be demonstrated on the square lattice and appears to be the case on the triangular and kagome lattices for large enough sizes. The operator which orthogonalizes the valence-bond basis into the dimer basis is  $\Omega^{-1/2}$  where  $\Omega_{a,b} = \langle a|b\rangle$  is the overlap matrix.

ably deeper, as some theories describing fluctuations about some large- $N$  saddle points ( $1/N$  corrections) are equivalent to (generalized) QDM. This mapping was discussed by Read and Sachdev<sup>123</sup> for representation with  $m = 1$  (number of rows in the Young tableau of the  $SU(N)$  representation),  $N \rightarrow \infty$  and  $n_c \sim \mathcal{O}(1)$ , it leads to a *generalized* QDM where  $n_c$  dimers emanate from each site. A QDM also describes  $1/N$  corrections in the case of the fermionic<sup>e</sup>  $SU(N)$  generalization<sup>116,124</sup> of the Heisenberg model:

$$\begin{aligned} \mathcal{H} &= \frac{1}{N} \sum_{ij} J_{ij} : B_{ij}^\dagger B_{ij} : \\ &= -\frac{1}{N} \sum_{ij} J_{ij} B_{ij}^\dagger B_{ij} + \text{cst} \end{aligned} \quad (30)$$

$$\text{where } B_{ij} = \sum_{\sigma=1}^N c_{j\sigma}^\dagger c_{i\sigma} \quad (31)$$

and where the  $c_{i\sigma}$  are  $N$  flavors of fermions satisfying a constraint similar to Eq. 15 :

$$\sum_{\sigma=1}^N c_{i\sigma}^\dagger c_{i\sigma} = N/2 \quad (32)$$

Rokhsar showed<sup>124</sup> that in the  $N \rightarrow \infty$  limit “dimerized states” (or Peierls states) becomes exact ground-states of Eq. 30 for a large class of models.<sup>f</sup> Quite naturally,  $1/N$  corrections will induce a dynamics into this subspace of dimerized states; it can be described by a QDM (with kinetic energy terms only at this order). At lowest order, on the square lattice, a kinetic term identical to the  $J$  term in Eq. 29 is generated and naturally favors a columnar or resonating-plaquette crystal (in agreement with a number of works on the spin- $\frac{1}{2}$  model). The same arguments were discussed for the kagome lattice.<sup>147</sup> In that case the leading  $1/N$  corrections to the fermionic saddle point generate three-dimer moves around hexagons and stabilize a

<sup>e</sup>Young tableau with  $n_c = 1$  column and  $m = N/2$  rows.

<sup>f</sup>Let  $J_0$  be the largest value of the  $J_{ij}$ . Each dimerization (no site is left empty) where only bonds where  $J_{ij} = J_0$  are occupied is a ground-state. Here a “dimer” between two neighbors  $i$  and  $j$  consists of a  $SU(N)$  singlet made with  $N$  fermions (one of each flavor) hopping back and forth between  $i$  and  $j$ . It is constructed from  $\prod_{\sigma=1}^N (c_{i\sigma}^\dagger + c_{j\sigma}^\dagger) |0\rangle$ , by projecting out the components which do not satisfy Eq. 32. Notice however that in the  $N \rightarrow \infty$  limit the relative fluctuations of the total number of fermion on each site are of order  $1/\sqrt{N}$  and can be neglected.

crystal of resonating hexagons.<sup>g</sup> This formalism was also applied to the checkerboard model<sup>98</sup> to conclude to the presence of a VBC phase.

### 5.5.3. Square lattice

The phase diagram of the Rokhsar and Kivelson's square lattice QDM is shown Fig. 5.3. Since a change in the signs of the basis dimer configurations can change  $J$  into  $-J$  (see Ref. <sup>143</sup>) we will choose  $J > 0$  without loss of generality.

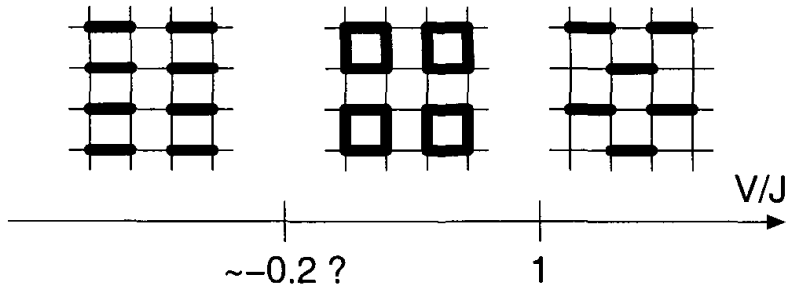


Fig. 5.3. Schematic phase diagram of the the square lattice QDM. The possible location of an intermediate plaquette phase is taken from the work of Leung *et al.*<sup>148</sup>

#### 5.5.3.1. Transition graphs and topological sectors

In order to understand the particularities of QDM on bipartite lattices it is useful to describe how the set of dimer coverings splits into *topological sectors*. To do so we first have to define transition graphs: the transition graph of two dimer coverings  $c$  and  $c'$  is obtained by superimposing  $c$  and  $c'$  on the top of each other; it defines a set of non-intersecting loops covering the lattice. On each bond where the dimers of  $c$  and  $c'$  match, a trivial loop of length 2 is obtained. When the lattice is bipartite (two sublattices  $A$  and  $B$ ) these loops can be *oriented* in the following way: any dimer belonging to  $c$  is oriented from  $A$  to  $B$  and dimers of  $c'$  are oriented  $B \rightarrow A$ . The transition graph is then made of loops of the type  $A \rightarrow B \rightarrow A \rightarrow B \dots$ . With periodic boundary conditions two winding numbers<sup>143</sup>  $-L/2 \leq \Omega_x, \Omega_y \leq L/2$  are associated to such a transition graph ( $L \times L$  sites).  $\Omega_x$  (resp.  $\Omega_y$ ) is the net number of topologically non-trivial loops

<sup>g</sup>To our knowledge however there is no clear evidence of such ordering in the spin- $\frac{1}{2}$  case.

(clockwise minus counterclockwise) encircling the torus in the  $x$  (resp.  $y$ ) direction.

Dimer coverings can be grouped into different *topological sectors*. By definition two dimer coverings belong to the same sector if they can be transformed into each other by repeated actions of *local* dimer moves (the transition graph associated to each movement does not wind around the whole system if it has periodic boundary conditions). On the square lattice two-dimer moves are sufficient to connect any two states in the same sector; that is the Hamiltonian Eq. 29 is ergodic within each topological sector. In a torus geometry,  $c$  and  $c'$  belongs to the same sector if and only if their transition graph has winding numbers  $\Omega_x = \Omega_y = 0$ . The different topological sectors can be labeled by their winding numbers with respect to some reference columnar configuration. Their number is of order  $\mathcal{O}(L^2)$  for a system of linear size  $L$ .

### 5.5.3.2. Staggered VBC for $V/J > 1$

When  $V$  is sufficiently large the system tries to minimize the number of parallel dimers. The staggered configuration shown Fig. 5.3 has no such *flippable plaquette*. It is always a zero-energy eigenstate of Eq. 29 and becomes a ground-state for  $J \geq V$ . It breaks several lattice symmetries (four-fold degenerate) and is a VBC.

The expectation value of the energy per plaquette satisfies  $\min(0, V - J) \leq E_0/N_p \leq \max(0, V + J)$ . For  $V/J > 1$  this gives  $0 \leq E_0/N_p$  and any zero-energy state saturates this lower bound and is therefore a ground-state. One should however notice that it is possible to make zero-energy domain walls in this VBC since the state shown Fig. 5.4 is also annihilated by the Hamiltonian. No local dimer movement can take place in the staggered VBC (with or without domain walls). Each of these states form a topological sector with a single configuration which has  $|\Omega_x| + |\Omega_y| = L/2$  with respect to a columnar state.

### 5.5.3.3. Columnar crystal for $V < 0$

When parallel dimers attract each other the system tries to maximize the number of flippable plaquettes. Columnar configurations as shown on the left side of Fig. 5.3 do maximize this number. Such a VBC is exactly realized for  $V < 0$  and  $J = 0$ . Elementary excitations consist of a pair of (say) vertical dimers in a background of vertical columns of horizontal dimers. Such excitations are gapped ( $\Delta E = 2|V|$ ) and this VBC phase will survive

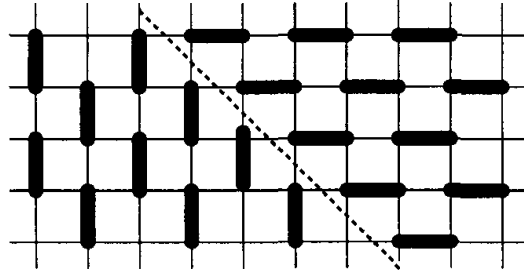


Fig. 5.4. Domain wall in a staggered VBC.

to the inclusion of a finite  $J$  term. Notice that unlike the staggered VBC presented in the previous paragraph the columnar dimer configuration is not an exact eigenstate when  $J \neq 0$ . The exact diagonalizations data of Leung *et al*<sup>148</sup> suggest that the columnar phase may disappear around a critical value  $V/J \simeq -0.2$ .

#### 5.5.3.4. Plaquette phase

When the kinetic energy dominates ( $|V| \ll J$ ) the system will try to maximize the number of resonating plaquettes  $| \rangle + | = \rangle$ . This can be achieved through the resonating plaquette crystal shown Fig. 5.3 and the numerical work (exact diagonalizations up to  $8 \times 8$  sites) of Leung *et al*<sup>148</sup> suggest that this phase is realized in an interval  $-0.2 \leq V/J \leq 1$ . Although this model would not suffer from the fermion sign problem we are not aware of any QMC simulation on this model.

#### 5.5.3.5. Rokhsar-Kivelson point

The point  $J = V$  (Rokhsar-Kivelson (RK) point) plays a special role. As remarked by Rokhsar and Kivelson<sup>143</sup> the equal-amplitude superposition of all dimerizations in a given topological sector is an exact ground-state. When  $J = V$  the Hamiltonian can be written as a sum of projectors:

$$\mathcal{H}_{J=V=1} = \sum_p |\Psi_p\rangle \langle \Psi_p| \quad (33)$$

$$|\Psi_p\rangle = |\bullet\bullet\rangle - |\bullet\bullet\rangle \quad (34)$$

The linear superposition of all dimer coverings belonging to a given sector  $\Omega$

$$|0\rangle = \sum_{c \in \Omega} |c\rangle \quad (35)$$

is annihilated by Eq. 33 and is therefore a ground-state. The argument is the following. Consider a plaquette  $p$  and a configuration  $|c\rangle$ . If  $|c\rangle$  has one or no dimer at all on the edges of  $p$  we have  $(\Psi_p|c\rangle = 0)$ . If two dimers are present, then there exists a configuration  $|c'\rangle$  in the same sector which only differ from  $|c\rangle$  by a two-dimer flip on  $p$ . In such a case the combination  $|c\rangle + |c'\rangle$  is again orthogonal to  $|\Psi_p\rangle$ . This shows that  $H|0\rangle = 0$ .

When open boundary conditions are considered (this restricts the topological sector to  $\Omega_x = \Omega_y = 0$ ) the RK state is the linear combination of an exponential number of configurations.<sup>h</sup> This is very different from the crystalline states considered so far where some periodic configurations were favored and it closely resembles Anderson's RVB picture. As we shall see this RK state is not a “true” liquid on the square lattice since dimer-dimer correlations are not short-ranged but algebraically decaying ( $\sim 1/r^2$ ) with distance. The calculation of dimer-dimer correlations in the RK state (Eq. 35) maps onto a *classical* dimer problem solved by Kasteleyn,<sup>137,139</sup> Fisher<sup>138</sup> and Fisher and Stephenson.<sup>149</sup> From this Rokhsar and Kivelson<sup>143</sup> constructed gapless excitations (in single-mode approximation) which dispersion relation vanishes as  $\mathbf{k}^2$  at small momentum (the origin is taken at  $(\pi, \pi)$ ). Quoting Rokhsar and Kivelson,<sup>143</sup> these excitations (dubbed “resonons”) are the *Goldstone mode of the gauge symmetry which allows the phases of the different topological sectors to be varied without changing the energy*. Another mode of gapless excitations (around  $(\pi, 0)$  and  $(0, \pi)$  in the Brillouin zone), specific to the fact that the ground-state has critical (algebraic) dimer-dimer correlations, was recently discovered.<sup>150</sup>

The QDM on the square lattice is thus believed to be ordered (VBC) everywhere except at the RK point ( $J = V$ ) where it has quasi long-ranged (critical) dimer-dimer correlations.

#### 5.5.4. Hexagonal lattice

The QDM on the honeycomb lattice was studied by Moessner, Sondhi and Chandra,<sup>151</sup> in particular with Monte Carlo simulations. The phase diagram is very similar to the square lattice-case discussed above. It possesses three crystalline phases (Fig. 5.5) and has algebraically decaying dimer-dimer correlations at the Rokhsar Kivelson point (where the ground-state in each sector has the same form as Eq. 35). The absence of liquid phase (with exponentially decaying  $2n$ -mer- $2n$ -mer correlations) is believed to

---

<sup>h</sup>This is also true for periodic boundary conditions provided the two winding numbers do not scale like the linear size  $L$ .

prevail in bipartite lattices. This relation between the absence of a deconfined dimer liquid phase<sup>i</sup> and the bipartite character of the lattice as been discussed by several authors<sup>152</sup> and is related to the possibility of a *height representation*<sup>153</sup> of dimer coverings when the lattice is bipartite.<sup>j</sup>

$$\begin{aligned} \mathcal{H} = & -J \sum_h \left( \left| \begin{array}{c} \bullet & \bullet \\ \diagup & \diagdown \\ \bullet & \bullet \end{array} \right\rangle \left\langle \begin{array}{c} \bullet & \bullet \\ \diagdown & \diagup \\ \bullet & \bullet \end{array} \right| + \text{H.c.} \right) \\ & + V \sum_h \left( \left| \begin{array}{c} \bullet & \bullet \\ \diagup & \diagdown \\ \bullet & \bullet \end{array} \right\rangle \left\langle \begin{array}{c} \bullet & \bullet \\ \diagdown & \diagup \\ \bullet & \bullet \end{array} \right| + \left| \begin{array}{c} \bullet & \bullet \\ \diagdown & \diagup \\ \bullet & \bullet \end{array} \right\rangle \left\langle \begin{array}{c} \bullet & \bullet \\ \diagup & \diagdown \\ \bullet & \bullet \end{array} \right| \right) \quad (36) \end{aligned}$$

Fouet *et al.*<sup>97</sup> studied the spin- $\frac{1}{2}$   $J_1-J_2-J_3$  model on the hexagonal lattice by exact diagonalizations and found evidences of a staggered VBC of the type predicted for  $V/J > 1$  by Moessner *et al.*<sup>151</sup> in the QDM. Other phases (Néel ordered phase and a possible short-range RVB SL) are also present in the spin- $\frac{1}{2}$  model.<sup>97</sup>

### 5.5.5. Triangular lattice

The most local dimer Hamiltonian on the triangular lattice contains kinetic and potential two-dimer terms on each rhombus; it was studied by Moessner

<sup>i</sup>Bipartiteness seems to forbid deconfinement but not short-ranged dimer-dimer correlations. The 4-8 lattice (squares and octogons) is an example where dimer-dimer correlations are short-ranged. We thank R. Moessner for pointing this to us. On this lattice the equal-amplitude superposition of all coverings would be similar to an explicit VBC wave-function (thus confining). Such situations are only possible when the number of sites is even in the unit cell.

<sup>j</sup>Consider a bipartite lattice with coordination number  $z$ . For each dimer covering we can associate integers (heights) on the dual lattice by the following rule. Set the height to be zero on a plaquette at the origin. The height is then defined on the whole lattice by turning clockwise (resp. counterclockwise) around sites of the  $A$ -sublattice (resp.  $B$ -sublattice) and changing the height by  $z-1$  when crossing a dimer and by  $-1$  when crossing an empty bond. It is simple to check the difference of heights  $\delta h(x) = h_1(x) - h_2(x)$  between two dimerizations is constant inside each loop of their transition graph. Notice that the loops of a transition graph can be naturally oriented on a bipartite lattice. Then,  $\delta h(x)$  changes by  $+z$  (resp.  $-z$ ) when crossing a clockwise (resp. counterclockwise) loop of the transition graph. Columnar dimerizations have an averaged height which is flat and staggered ones have the maximum tilt. The winding numbers  $(\Omega_x, \Omega_y)$  correspond to the average height difference between both sides of the sample. The kinetic energy terms of Eqs. 29 and 36 change the height of the corresponding plaquette by  $\pm z$  and the potential terms ( $V > 0$ ) favor tilted configurations.

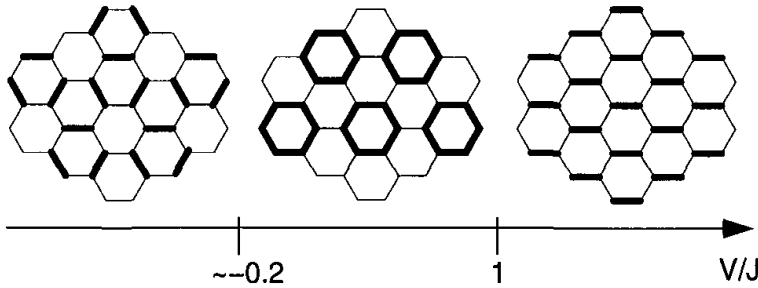


Fig. 5.5. Phase diagram of the hexagonal QDM obtained by Moessner *et al.*<sup>151</sup> Although the VBC shown for  $V < 0$  do not have all dimers parallel to the same direction it is equivalent to the columnar VBC found in the square lattice QDM because it maximizes the number of flippable plaquettes. It also corresponds to the ordering pattern predicted in the large- $N$  theory of Ref. <sup>119</sup> As for the VBC obtained for  $V/J > 1$ , it is the hexagonal counterpart of the *staggered* VBC of the square lattice (no flippable plaquette, exact eigenstate and maximum tilt in a height representation).

and Sondhi:<sup>144</sup>

$$\begin{aligned} \mathcal{H} = & -J \sum_r \left( \left| \begin{array}{cc} \bullet & \bullet \\ \bullet & \bullet \end{array} \right\rangle \left\langle \begin{array}{cc} \bullet & \bullet \\ \bullet & \bullet \end{array} \right| + \text{H.c.} \right) \\ & + V \sum_r \left( \left| \begin{array}{cc} \bullet & \bullet \\ \bullet & \bullet \end{array} \right\rangle \left\langle \begin{array}{cc} \bullet & \bullet \\ \bullet & \bullet \end{array} \right| + \left| \begin{array}{cc} \bullet & \bullet \\ \bullet & \bullet \end{array} \right\rangle \left\langle \begin{array}{cc} \bullet & \bullet \\ \bullet & \bullet \end{array} \right| \right) \end{aligned} \quad (37)$$

where the sums run over all rhombi  $r$  of the lattice (with three possible orientations). This model was shown to possess (at least) three crystalline phases, including a columnar and staggered one (Fig. 5.6) as in the two previous examples. An additional VBC (with resonating diamonds plaquettes) with a large unit cell (12 sites) was also predicted around  $V = 0$ . When  $V < 0$  and  $J = 0$  the ground-state is highly degenerate since it is possible, from an ordered columnar configuration, to shift all the dimers along any straight line without changing the number of flippable plaquettes (contrary to the square lattice case). However, an infinitesimal  $J$  is expected to lift this degeneracy and to order the ground-state in a columnar way.

The phenomenology of these ordered phases is that of usual VBC and we refer to the original paper<sup>144</sup> for details.

### 5.5.5.1. RVB liquid at the RK point

The new physics of this model appears through the existence of a *liquid* phase in the interval  $0.7 \lesssim V/J \leq 1$ . As for the two previous QDM the ground-states are exactly known at the RK point  $J = V$ . As before dimer-dimer correlations are obtained exactly at this point by a Pfaffian

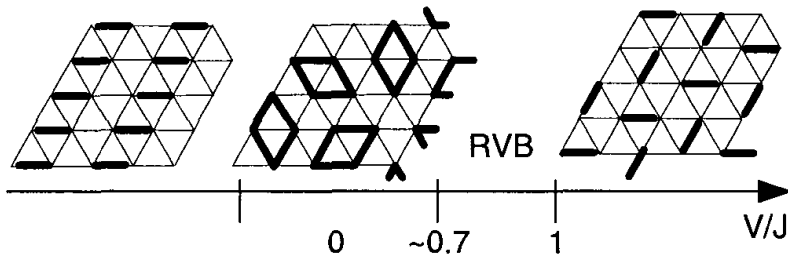


Fig. 5.6. Phase diagram of the triangular lattice QDM obtained by Moessner and Sondhi.<sup>144</sup>

calculation<sup>144,154,155</sup> but the result shows a *finite* correlation length. From their Monte Carlo simulations Moessner *et al.*<sup>144</sup> argued that the spectrum is gapped at the RK point and that this gap persists down to  $V/J \simeq 2/3$ , that is over a finite range of coupling. This picture is consistent with the exact diagonalizations performed on this model.<sup>156,157</sup>

#### 5.5.5.2. Topological order

When the lattice is not bipartite the loops of a transition graph can no longer be oriented. The winding numbers  $\Omega_x$  and  $\Omega_y$  are now defined as the (positive) number of non-trivial loop around  $x$  and  $y$  in the transition graph with a reference configuration (say columnar). These two integers are not conserved by local dimer moves. They are however *conserved modulo two*, which leaves only four sectors.<sup>k</sup> Consequently *the dimer liquid ground-state is four-fold degenerate* at the RK point. This degeneracy holds exactly at the RK point even on finite-size samples but it is expected to hold in the thermodynamic limit in the whole liquid phase ( $0.7 \lesssim V/J \leq 1$ ).

Conventional orders are often associated to a spontaneously broken symmetry and lead to ground-state degeneracies in the thermodynamic limit. The four-fold degeneracy discussed above is the signature of some kind of order, called topological order.<sup>158</sup> The peculiarity of this order is that it is not associated to any local order parameter: a local observable cannot decide whether a given dimerization is in one sector or another. The existence of topological order is intimately associated to the fractionalized nature of the elementary excitations (see below). In the case of a RVB dimer liquid

<sup>k</sup>The two-dimer moves included in Eq. 37 are not sufficient to guarantee ergodicity with each of the four sectors. Staggered states (12-fold degenerate - not  $\mathcal{O}(L)$  like on the square lattice) have no flippable plaquette but can be connected to other states with four-dimer moves.<sup>144</sup>

these excitations have been known to be *Ising vortices* for a long time<sup>159,160</sup> (dubbed *visons* in the recent literature<sup>161,162</sup>). We will now discuss these excitations in more details in the framework of a QDM which realizes the same dimer liquid phase but for which not only the ground-state but all the eigenstates are known exactly.

### 5.5.6. Solvable QDM on the kagome lattice

An exactly solvable QDM on the kagome lattice was introduced by D. Serban, V. Pasquier and one of us.<sup>141</sup> It offers a very simple and explicit realization of the ideas discussed above (visons, topological order etc.).

#### 5.5.6.1. Hamiltonian

The kagome lattice QDM introduced in Ref. <sup>141</sup> contains only kinetic terms and has no external parameter. The Hamiltonian reads:

$$\mathcal{H} = - \sum_h \sigma^x(h) \quad (38)$$

$$\text{where } \sigma^x(h) = \sum_{\alpha=1}^{32} |d_\alpha(h)\rangle \langle \bar{d}_\alpha(h)| + \text{H.c} \quad (39)$$

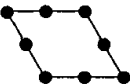
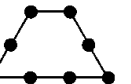
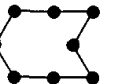
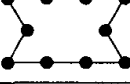
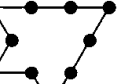
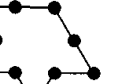
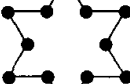
The sum runs over the 32 loops on the lattice which enclose a single hexagon and around which dimers can be moved (see Table 5.1 for the 8 inequivalent loops). The shortest loop is the hexagon itself, it involves 3 dimers. 4, 5 and 6-dimers moves are also possible by including 2, 4 and 6 additional triangles (the loop length must be even). The largest loop is the star. For each loop  $\alpha$  we associate the two ways dimers can be placed along that loop:  $|d_\alpha(h)\rangle$  and  $|\bar{d}_\alpha(h)\rangle$ . Notice that  $\sigma^x(h)$  measures the relative phases of dimer configurations displaying respectively the  $d_\alpha(h)$  and  $\bar{d}_\alpha(h)$  patterns in the wave function.

#### 5.5.6.2. RK ground-state

As for the QDM discussed previously the ground-state of this Hamiltonian is the equal amplitude superposition of all dimer coverings belonging to a given topological sector (as on the triangular lattice there are four sectors). This can be readily shown by writing  $\mathcal{H}$  as a sum of projectors:

$$\mathcal{H} = -N_h + \sum_h \sum_{\alpha=1}^{32} [ |d_\alpha(h)\rangle - |\bar{d}_\alpha(h)\rangle ] [ \langle d_\alpha(h)| - \langle \bar{d}_\alpha(h)| ] \quad (40)$$

Table 5.1. The 8 different classes of loops which can surround an hexagon of the kagome lattice. Including all possible symmetries we find 32 possible loops. The first column indicates the number of dimers involved in the coherent motion around the hexagon.

3			
4			
5			
6			

where  $N_h$  is the number of hexagons on the lattice. When expanding the products the diagonal terms give a simple constant since

$$\sum_{\alpha=1}^{32} |d_\alpha\rangle \langle d_\alpha| + |\bar{d}_\alpha\rangle \langle \bar{d}_\alpha| = 1 \quad (41)$$

This reflects the fact that, for any dimerization, the dimers on hexagon  $h$  match *one and only one* of the  $2 \times 32$  patterns  $\{d_\alpha, \bar{d}_\alpha\}$ .

Unlike the square or triangular case, the RK ground-states  $|0\rangle = \sum_{c \in \Omega} |c\rangle$  are not degenerate with some staggered VBC.<sup>1</sup> This means that the Hamiltonian of Eq. 38 is not at a phase transition to a VBC. As we will explain it is *inside* a liquid RVB phase.

The RK wave-function can be viewed as dimer condensate. It is similar to the ground-state of liquid  $^4\text{He}$  which has the same positive amplitude for any configuration and its permuted images.<sup>163</sup> An important difference, however, is that the QDM state is incompressible and cannot sustain acoustic phonons. This can be related to the fact that the  $U(1)$  symmetry of the Bose liquid is absent in the QDM on non-bipartite lattices. It is replaced instead by a discrete  $\mathbb{Z}_2$  gauge symmetry (see §5.5.6.7 below).

<sup>1</sup>Because resonances loops of length up to 12 are present the dynamics is ergodic in each of the four topological sectors.<sup>141</sup>

### 5.5.6.3. Ising pseudo-spin variables

The kinetic energy operators  $\sigma^x$  defined in Eq. 39 commute with each other. This is obvious when two such operators act on remote hexagons but it also holds for neighboring ones. This property can easily be demonstrated with the help of the arrow representation of dimer coverings introduced by Zeng and Elser.<sup>164</sup> This mapping of kagome dimerizations to arrows on the bonds of the honeycomb lattice is illustrated Fig. 5.7. Each arrow has two possible directions: it points toward the interior of one of the two neighboring triangles. If site  $i$  belongs to a dimer  $(i, j)$  its arrow must point toward the triangle the site  $j$  belongs to. A dimer covering can be constructed from any arrow configuration provided that the number of outgoing arrows is odd (1 or 3) on every triangle.

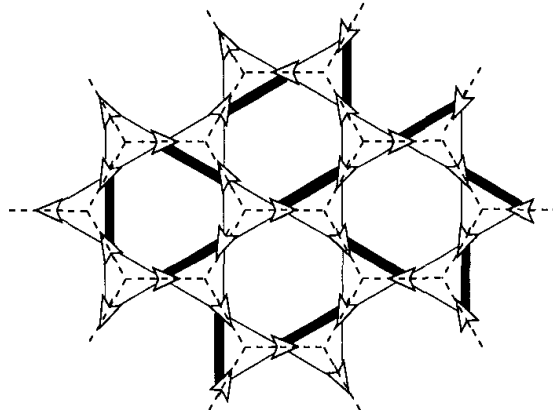


Fig. 5.7. A dimer covering on the kagome lattice and the corresponding arrows. Dashed lines: honeycomb lattice.

The operators  $\sigma^x$  have a particularly simple meaning in terms of the arrow degrees of freedom:  $\sigma^x(h)$  flips the 6 arrows sitting on  $h$ .<sup>m</sup> It is then clear that the  $\sigma^x$  commute and that  $\sigma^x(h)^2 = 1$ . In fact these operators can be used as Ising pseudo-spin variables and the Hamiltonian now describes non-interacting pseudo-spins in a uniform magnetic field pointing in the  $x$  direction. In the ground-state we have  $\sigma^x(h) = 1$  on every hexagon.

<sup>m</sup>Flipping all the arrows around any closed loop (such as around an hexagon) preserves the local constraint imposed on arrow configurations. Flipping the arrows around a topologically non-trivial loop changes the topological sector.

#### 5.5.6.4. Dimer-dimer correlations

The ground-state is the most possible disordered dimer liquid as the dimer-dimer correlations strictly vanish beyond a few lattice spacings. Such correlations can be computed by the Pfaffian method. On the kagome lattice the determinant of the Kasteleyn matrix (which is directly related to the partition function of the classical dimers problem) is exactly constant in Fourier space.<sup>165</sup> Since dimer-dimer correlations are obtained from the Fourier transform of the inverse of this determinant, they turn out to be strictly zero beyond a few lattice spacings (as soon as the two bonds do not touch a common triangle).<sup>141</sup> This result can also be obtained by a simpler argument<sup>141,166</sup> using the  $\sigma^x$  operators. This result is related to the kagome geometry.<sup>n</sup> This absence of long-ranged dimer-dimer correlations demonstrates that the RK state is a dimer liquid and that it breaks no lattice symmetry.

On the triangular lattice, even at high temperature, dimer-dimer correlations decay exponentially with distance but these correlations remain *finite* at any distance. On the square lattice such correlations are even larger because they decay only as a power law. This means that the infinite hard-core dimer repulsion makes QDM non-trivial even at infinite temperature; dimers cannot be free when they are fully-packed. From this point of view we see that the kagome lattice is particular: it is as close as possible to a free dimer gas, except for non-trivial correlations over a few lattice spacings. This is a reason why dimer coverings on the kagome lattice can be handled with independent pseudo-spin variables and why the RK state on this lattice is the most possible disordered RVB liquid.

#### 5.5.6.5. Visons excitations

The  $\sigma^x$  operators can be simultaneously diagonalized but they must satisfy the global constraint  $\prod_h \sigma^x(h) = 1$  since this product flips every arrow *twice*. It must therefore leave all dimerizations unchanged. The lowest excitations have therefore an energy 4 above the ground-state and they are made of a *pair* of hexagons  $a$  and  $b$  in a  $\sigma^x(a) = \sigma^x(b) = -1$  state.  $a$  and  $b$  are the locations of two Ising vortices (or *visons*<sup>161,162</sup>). As remarked before this means that the relative phases of the configurations with  $d_\alpha(h)$  and  $\bar{d}_\alpha(h)$  patterns have now changed sign. The corresponding wave-function is

---

<sup>n</sup>The model of Eq. 38 can be generalized to any lattice made of corner-sharing triangles.<sup>141</sup>

obtained in the following way. Consider a string  $\Omega$  which goes from  $a$  to  $b$  (see Fig. 5.8) and let  $\Omega(a, b)$  be the operator which measures the parity  $\pm 1$  of the number of dimers crossing that string.  $\Omega(a, b)$  commutes with all  $\sigma^x(h)$ , except for the ends of the string:  $\sigma^x(a)\Omega(a, b) = -\Omega(a, b)\sigma^x(a)$ . A dimer move changes the sign of  $\Omega(a, b)$  if and only if the associated loop crosses the string an odd number of times, which can only be done by surrounding one end of the string. This shows that  $\Omega(a, b)$  flips the  $\sigma^x$  in  $a$  and  $b$ .<sup>o</sup> As the RK ground state  $|0\rangle$ ,  $\Omega(a, b)|0\rangle$  is a linear combination of all dimer configurations belonging to one sector. However the amplitudes are now 1 and  $-1$  depending on the number of dimers crossing  $\Omega$ . This wave-function therefore has nodes, it is an excited state of energy 4 with two vortices in  $a$  and  $b$ . It is easy to see that a different choice  $\Omega'$  for the string connecting  $a$  and  $b$  gives the same state up to a global sign which depends on the parity of the number of kagome sites enclosed by  $\Omega \cup \Omega'$ .

These vortex excitations carry a  $\mathbb{Z}_2$  charge since attempting to put two vortices on the same hexagon does not change the state. Such excitations are not local in terms of the dimer degrees of freedom. Indeed, determining the sign of a given dimerization in a state with two vortices which are far apart requires the knowledge of the dimer locations along the whole string connecting the two vortex cores. In this model the vortices appear to be static and non-interacting. This is a particularity of this solvable model but the existence of gapped vison excitations is believed to be a robust property of RVB liquids. In more realistic models the vortices will acquire a dynamics and a dispersion relation but will remain gapped.<sup>p</sup> They will also have some interactions with each other but should remain *deconfined*. This property is particularly clear in the kagome QDM: vortices are necessarily created by pairs but the energy is independent of their relative distances.

The Ising vortices also offer a simple picture of the topological degeneracy. Consider a ground-state  $|+\rangle$  of the model which lives in the sector where the winding number  $\Omega_y$  (with respect to some arbitrary but fixed dimerization) is even. Another ground-state  $|-\rangle$  is obtained in the odd- $\Omega_y$  sector. Now consider the combination  $|0\rangle = |+\rangle + |-\rangle$  and apply the operator  $\Omega(0, L_x)$  corresponding to a closed loop surrounding the torus in the  $x$  direction. This amounts to creating a pair of nearby vortices at the origin, taking one of them around the torus in the  $x$  direction and annihilating them.

<sup>o</sup>Up to a global sign (reference dependent)  $\Omega(a, b)$  is equal to  $\sigma^z(a)\sigma^z(b)$  where the  $\sigma^z$  operators are those introduced by Zeng and Elser.

<sup>p</sup>It is possible to add potential energy terms to Eq. 38 to drive the system outside of the liquid phase and this transition corresponds to a vison condensation.

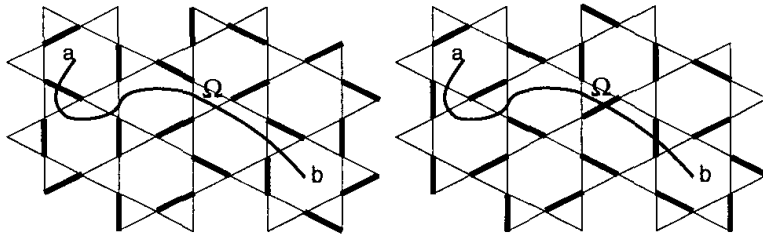


Fig. 5.8. A pair of visons (located in  $a$  and  $b$ ) is created by applying to the RK wavefunction a factor  $(-1)$  for each dimer crossing the string  $\Omega$ . The dimerization shown there on the left appears in the linear superposition of the two-vison state with the sign  $-1$  whereas the one on the right has the sign  $+1$ .

This can also be viewed as the creation of a vison in one hole of the torus (with no energy cost). It is simple to check that  $\Omega(0, L_x)|0\rangle = |+\rangle - |-\rangle$  (up to an irrelevant global sign). This provides a simple relation between the vison-pair creation operator and the existence of two topologically distinct ground-states  $|+\rangle + |-\rangle$  and  $|+\rangle - |-\rangle$ .

#### 5.5.6.6. Spinons deconfinement

We assume that dimers represent “dressed” singlet valence-bonds, as in the overlap expansion (§5.5.2). Since the Hilbert space is made of fully-packed dimer coverings the model of Eq. 38 only describes spin-singlet states. However, as any QDM, it can be extended to include static holes or spinons. Configurations with unpaired sites (spinon or holon) are now allowed but the kinetic terms of the original Hamiltonian which loop passes on an empty site gives zero. Consider a system with two static spinons in  $x$  and  $y$ . As on the square<sup>143</sup> and triangular lattices<sup>144</sup> at the RK point the exact ground-state  $|x, y\rangle$  remains the sum of all dimer coverings and the ground-state energy is independent of the distance between the two spinons (except at very short distance if they belong to a common hexagon). This is a first indication that RVB *spin* liquid has deconfined spin- $\frac{1}{2}$  excitations (spinons). In the QDM language these excitations are simply unpaired sites in a dimer liquid background. Such unpaired sites are necessarily created by pairs but they can then propagate freely (no attractive potential) when they are sufficiently far apart.

Another calculation allows to test the deconfinement properties of a dimer liquid. We consider the state  $|\psi\rangle = \sum_{\mathbf{r} \neq 0} |0, \mathbf{r}\rangle$  where  $|0, \mathbf{r}\rangle$  is the (un-normalized) ground-state with two spinons in  $0$  and  $\mathbf{r}$ . The probability to find a spinon in  $\mathbf{r}$  in the  $|\psi\rangle$  can be obtained by the relatively involved

calculation of the monomer correlation<sup>q</sup> with Pfaffians. On the square lattice this probability goes to zero as  $1/\sqrt{r}$ .<sup>149</sup> This shows that the second spinon is (quasi-) confined in the vicinity of the first one on the square lattice because escaping far away represents a large “entropy” cost in the dimer background. On the triangular lattice it goes exponentially to a constant.<sup>154</sup> This result is a signature of deconfinement. In fact the same signature can be obtained on the kagome lattice without any technical calculation since the monomer correlation is exactly 1/4 at any distance.<sup>167</sup>

If unpaired sites are allowed one can describe spinons or holons. Unfortunately in the presence of simple kinetic energy terms for these objects the model can no longer be solved. However one can consider a static spinon and its interaction with visons: when the spinon is adiabatically taken around a vison the dimers are shifted along a path encircling the vison. Because the vison wave-function is particularly simple in this model it is easy to check that this multiplies the wave-function by a factor  $-1$ . This is the signature of a long-ranged statistical interaction<sup>160,159</sup> between visons and spinons (or holons). In more realistic models, as long as the visons are gapped excitations the spinons are expected to be deconfined. On the other hand if the visons condense their long-ranged statistical interaction with spinons frustrates their motion. This is no longer true if they propagate in *pairs*, in which case they are not sensitive any more to visons (see Ref. <sup>141</sup> for an extension of the present QDM with a vison condensation). This simple physical picture illustrates the relation between vison condensation and spinon confinement.

#### 5.5.6.7. $\mathbb{Z}_2$ gauge theory

The forces responsible for confinement are usually associated to gauge fields and their fluctuations. Whereas  $U(1)$  compact gauge theories are generically confining in  $2+1$  dimensions,<sup>168,136</sup>  $\mathbb{Z}_2$  gauge theories are known to possess deconfined phases.<sup>169</sup> For this reason some attention has been paid to the connections between  $\mathbb{Z}_2$  theories and fractionalized phases in 2D electronic systems.<sup>161</sup>

It is known<sup>140</sup> that QDM can be obtained as special limits of  $\mathbb{Z}_2$  gauge theories, the gauge variable being the dimer number on a bond. However, on the kagome lattice this connection can be made exact and completely

---

<sup>q</sup>Ratio of number of dimer coverings with two holes in 0 and  $\mathbf{r}$  to the number without hole.

explicit since there is a one to one correspondence between dimer coverings and physical states (*i.e.* gauge-invariant) of a  $\mathbb{Z}_2$  gauge theory.<sup>141</sup> In this mapping the gauge fields are Ising variables living on the link of the honeycomb lattice (*i.e.* kagome sites) and are constructed from the arrows described previously. As for the constraints of gauge invariance they correspond to the odd parity of the number of outgoing arrows on every triangles. The  $\sigma^x$  operator used to define a solvable QDM translate into a gauge-invariant plaquette operator for the gauge degrees of freedom (product of the Ising gauge variables around an hexagon). With this mapping the visons appear to be vortices in the  $\mathbb{Z}_2$  gauge field and the solvable model of Eq. 38 maps to the deconfined phase of the gauge theory (precisely at infinite temperature).

### 5.5.7. A QDM with an extensive ground-state entropy

So far we have discussed QDM that realize either spontaneous VBC, critical states or RVB liquids. We wish to mention here that these three scenarios may not be the only possible ground-states for QDM. In particular, a QDM on the kagome lattice with an extensive ground-state entropy was recently discussed.<sup>170</sup> This model was introduced from the observation that the dimer kinetic energy terms arising from an overlap expansion (§5.5.2) generally have non trivial *signs* as soon as resonance loops of *different lengths* are considered. It was then realized that such signs (which make the QDM no longer appropriate for QMC simulations) can lead to qualitatively new phases, different from VBC or RVB liquids. The Hamiltonian introduced in Ref. <sup>170</sup> is similar to that of Eqs. 38-39 except that each resonance loop  $\alpha$  is now included with a *sign*  $(-1)^{n_\alpha}$  where  $n_\alpha = 3, \dots, 6$  is the number of dimers involved:

$$\mathcal{H} = \sum_h (-1)^{n_\alpha} [ |d_\alpha(h)\rangle\langle\bar{d}_\alpha(h)| + |\bar{d}_\alpha(h)\rangle\langle d_\alpha(h)| ] \quad (42)$$

These signs are precisely those appearing in the overlap expansion (at the order of one hexagon) of the Heisenberg model on the kagome lattice. This expansion was carried out by Zeng and Elser<sup>171</sup> in an insightful paper which laid the basis of the analysis of the kagome antiferromagnet in the first neighbor valence-bonds subspace.

Although not exactly solvable, the Hamiltonian of Eq. 42 was shown to be a dimer liquid (short-ranged dimer-dimer correlation) and to have a huge ground-state degeneracy  $\sim 2^{N/6} = 1.122^N$  ( $N$  is the number of kagome sites). In addition, several numerical indications pointed to a critical

behavior of this system,<sup>170</sup> with a possible algebraic decay of energy-energy correlations.<sup>r</sup> It was argued that the effective QDM describing the singlet dynamics of the spin- $\frac{1}{2}$  Heisenberg antiferromagnet on the kagome lattice could be *close* (in parameter space) to Eq. 42. If correct, this sheds light on the very large density of singlet states observed at low energy in the numerical spectra of that spin model (see Sec. 5.7).

## 5.6. Multiple-spin exchange models

### 5.6.1. Physical realizations of multiple-spin interactions

#### 5.6.1.1. Nuclear magnetism of solid $^3\text{He}$

Solid  $^3\text{He}$  was the first magnetic system in which the importance of MSE interactions was recognized.<sup>172,173,174</sup> Due to the large zero-point motion of the atoms about their mean positions, tunneling events during which 2, 3 or 4 atoms exchange their positions in a cyclic way are frequent. These processes generate an effective interaction between the (nuclear) spins which can be written

$$\mathcal{H} = \sum_P -J_P(-1)^P (P_{\text{spin}} + P_{\text{spin}}^{-1}) \quad (43)$$

where the sum runs over permutations  $P$ ,  $J_P > 0$  is the exchange frequency of the associated tunneling process (in real space) and  $P_{\text{spin}}$  acts on the Hilbert space of spin- $\frac{1}{2}$  located on the site of the crystal. The sign  $-(-1)^P$  depends of the signature of the permutation  $P$  and is a consequence of the Pauli principle. For a *cyclic* permutation involving  $n$  spins this sign is just  $(-1)^n$  and is responsible for the ferromagnetic character of processes involving an odd number of spins. For spin- $\frac{1}{2}$  particles, two and three-spin exchange terms reduce to the familiar Heisenberg interaction:

$$P_{12} = 2\vec{S}_1 \cdot \vec{S}_2 + \frac{1}{2} \quad (44)$$

$$P_{123} + P_{321} = P_{12} + P_{23} + P_{31} - 1 \quad (45)$$

but this is no longer true for  $n \geq 4$ :

$$P_{1234} + P_{4321} = P_{12}P_{34} + P_{14}P_{23} - P_{13}P_{24} + P_{13} + P_{24} - 1 \quad (46)$$

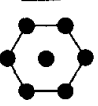
which can be expressed (thanks to Eq. 44) as a sum of terms with two and four Pauli matrices.

---

<sup>r</sup>Notice that a one-dimensional analog of Eq. 42 can be defined and exactly maps onto the Ising chain in transverse field at its critical point.

$^3\text{He}$  can form solid atomic mono-layers with a triangular geometry when adsorbed on a graphite substrate at ultra low temperatures (milli Kelvin range). This 2D magnet has been studied for a long time (see Refs. <sup>175,176</sup> and references therein) and the importance of MSE interactions involving up to six atoms has now been recognized.<sup>177,178</sup> The exchange frequencies of the most important processes have been computed by Path Integral Monte Carlo (PIMC)<sup>179,180,181,182</sup> (analytic WKB calculations have also been carried out<sup>177,183</sup>) as a function of the density. The proposed MSE Hamiltonian describing the magnetic properties of this 2D quantum crystal reads

$$\mathcal{H} = (J_2 - 2J_3) \sum P_{12} + J_4 \sum (P_{1\dots 4} + \text{H.c}) \quad (47)$$


$$- J_5 \sum (P_{1\dots 5} + \text{H.c}) + J_6 \sum (P_{1\dots 6} + \text{H.c})$$


where Eq. 45 was used to absorb the three-spin terms into an effective first-neighbor Heisenberg exchange  $J_2^{\text{eff}} = J_2 - 2J_3$ . At high density the hard-core potential between Helium atoms only leaves three-body exchanges possible ( $J_3 \gg J_{n\neq 3}$ ) and Eq. 48 reduces to a first neighbor Heisenberg *ferromagnet*,<sup>184</sup> as observed experimentally for the first time by Franco *et al.*<sup>185</sup> in high-density layers. On the other hand the second layer solidifies at lower density and higher order exchange terms cannot be ignored.<sup>s</sup> PIMC simulations<sup>182</sup> and high-temperature fits of the experimental data<sup>178</sup> showed that the relative strength of two- and four-spin terms if roughly  $J_2^{\text{eff}}/J_4 \sim -2$  in the low-density second layer solid. The  $J_2-J_4$  model was studied by exact diagonalizations in this region of parameter space and evidences for a short-ranged RVB SL phase with no broken symmetry were obtained.<sup>186,114,187</sup> The ultra-low temperature measurements of specific heat<sup>188</sup> and uniform susceptibility<sup>189</sup> are not incompatible with such a spin liquid phase but the spin gap, if any, has not yet been observed and should be smaller than  $100\mu\text{K}$ .

<sup>s</sup>The first layer is then so dense that exchange is strongly suppressed. The first layer can also be replaced by an  $^4\text{He}$  or HD mono-layer.

### 5.6.1.2. Wigner crystal

The Wigner crystal is another fermionic solid with a triangular geometry where MSE interactions can play an important role. At very low density the Coulomb energy dominates, the crystal is almost classical and MSE interactions are very small. Exchange frequencies  $J_P$  can be computed in this regime by a semi-classical (WKB) approximation<sup>177,190,191</sup> and, as for the high density solid of  $^3\text{He}$ , three-body exchanges dominate and give rise to ferromagnetism. However, at higher density and close to melting, PIMC calculations of the exchange frequency<sup>192</sup> showed that the magnetism may be described by a MSE model with parameters ( $J_2^{\text{eff}}$  and  $J_4$ ) close to those where the triangular MSE model is expected to be a RVB SL. Unlike the  $^3\text{He}$  case, the particles (electrons) are charged and an external magnetic field has also an orbital effect, it introduces complex phases in the exchange energies:  $P + P^{-1} \rightarrow e^{i\alpha}P + e^{-i\alpha}P^{-1}$  where the angle  $\alpha = 2\pi\phi/\phi_0$  is proportional to the magnetic flux  $\phi$  passing through the area enclosed by the exchange trajectory and  $\phi_0$  is the unit flux quantum. This can give rise to very rich phase diagrams<sup>192,191</sup> where complex MSE terms compete with the Zeeman effect (see Ref. <sup>193</sup> for some early experimental attempts to explore this physics).

### 5.6.1.3. Cuprates

The possibility of significant four-spin exchange around square Cu plaquettes in copper oxide compounds was first suggested by Roger and Delrieu.<sup>194</sup> They interpreted the anomalously large width of Raman scattering spectra as a signature of four-spin exchange in this copper oxide superconductor. The importance of these MSE interactions in  $\text{CuO}_2$  planes ( $J_4 \sim 0.25J_2$ ) has then been emphasized by a number of groups and in different materials and by different experimental and theoretical approaches.<sup>195,196,197,198</sup> Four-spin plaquette ring exchange also plays a significant role in ladder compounds.<sup>199,200,201,202</sup> For instance, exchange parameters with values  $J_{\text{rung}} = J_{\text{leg}} = 110$  meV and  $J_{\text{ring}} = 16.5$  meV were proposed for  $\text{La}_6\text{Ca}_8\text{Cu}_{24}\text{O}_{41}$  based on the dispersion relation of magnetic excitations.<sup>199,200</sup>

## 5.6.2. Two-leg ladders

Numerous works were devoted to ladder models with four-spin interactions. These include general bi-quadratic interactions as well as models with ring-

exchange terms. We will only discuss here the simplest of these MSE models:

$$\begin{aligned} \mathcal{H} = & J \sum_n \left( \vec{S}_{n,1} \cdot \vec{S}_{n,2} + \vec{S}_{n,1} \cdot \vec{S}_{n+1,1} + \vec{S}_{n,2} \cdot \vec{S}_{n+1,2} \right) \\ & + K \sum_{\square} (P_{1234} + H.c) \end{aligned} \quad (48)$$

Thanks to several studies<sup>200,203,204,205</sup> the phase diagram of this Hamiltonian is now rather well understood and five different phases were identified.

- **Ferromagnetic phase.** The ground-state is fully polarized. This phase includes the  $(J = -1, K = 0)$  and the  $(J = 0, K = -1)$  points.
- **Rung-singlet phase.** This phase includes the ground-state of the ladder without MSE term ( $J = 1, K = 0$ ). The spectrum is gapped and the ground-state is unique. A moderate  $K/J \gtrsim 0.23 \pm 0.03$  destroys this phase<sup>200,206,207,205</sup> in favor of the VBC below.
- **Staggered VBC** with dimers on the legs. In one of the two degenerate ground-states the dimerized bonds are  $(2n, 1) - (2n+1, 1)$  and  $(2n+1, 2) - (2n+2, 2)$ . The VBC disappears for  $K/J \gtrsim 0.5$ .<sup>205</sup> Such a staggered VBC was first predicted in the framework of a ladder with bi-quadratic interaction by Nersesyan and Tsvelik.<sup>59</sup> Using Matrix-Product Ansatz, Kolezhuk and Mikeska<sup>60</sup> constructed models which are generalizations of Eq. 48 and which have exact ground-state with long-ranged staggered dimer correlations. In this phase the magnetic excitations are very different from the magnon excitations of the rung-singlet phase above. Here the excitations do not form well-defined quasi-particles but a continuum made of pairs of domain walls connecting two dimerized ground-states.<sup>59,60</sup>
- **Scalar chirality phase.** The order parameter is  $\langle \vec{S}_{n,1} \cdot (\vec{S}_{n,2} \times \vec{S}_{n+1,2}) \rangle$  and it spontaneously breaks the time-reversal symmetry and translation invariance. The ground-state is two-fold degenerate up to the next transition at  $K/J \simeq 2.8 \pm 0.3$ .<sup>205</sup> There exists a duality transformation<sup>204,208</sup> which maps the scalar chirality order parameter onto the dimer order parameter of the VBC above.<sup>t</sup> Applying such a transformation to the exact VBC ground-states mentioned above, models with an exactly known ground-state and scalar chirality LRO can be constructed.<sup>204,208</sup> Although chiral SL have been much discussed in the literature, this is to our knowledge

---

<sup>t</sup>The Hamiltonian of Eq. 48 is self-dual at  $2K = J$ .

the first realization of such a phase in a SU(2) symmetric spin- $\frac{1}{2}$  model.

- **Short-ranged ordered phase with vector-chirality correlations.** The strongest correlations are  $\langle (\vec{S}_{n,1} \times \vec{S}_{n,2}) \cdot (\vec{S}_{n',1} \times \vec{S}_{n',2}) \rangle$  but they remain short-ranged. The spectrum is gapped and the ground-state is unique. This phase includes the pure  $K = 1$  model where  $J = 0$ . This phase is related by the duality transformation discussed above to the rung-singlet phase.<sup>208</sup> This transformation indeed relates the Néel correlations  $\langle (\vec{S}_{n,1} - \vec{S}_{n,2}) \cdot (\vec{S}_{n',1} - \vec{S}_{n',2}) \rangle$  (which are the strongest ones in the rung-singlet phase) to the vector-chirality correlations. Close to the ferromagnetic phase ( $J < 0$ ) one observes a crossover to a region where the strongest correlations are ferromagnetic spin-spin correlations along the legs and antiferromagnetic along the rungs.<sup>205</sup>

### 5.6.3. MSE model on the square lattice

The phase diagram of the Hamiltonian 48 on the *two-dimensional square-lattice* has been recently studied by Läuchli<sup>209</sup> by exact diagonalizations. Néel, ferromagnetic, columnar VBC and staggered VBC phases were identified, as in the ladder model above. In addition, a nematic phase characterized by long-ranged vector chirality correlations (alternating spin currents) was found around the  $K = 1$ ,  $J = 0$  point. To our knowledge this could be the first microscopic realization of a nematic order in a two-dimensional spin- $\frac{1}{2}$  model.

### 5.6.4. RVB phase of the triangular $J_2$ - $J_4$ MSE

Because of its relevance to solid  $^3\text{He}$  films and Wigner crystals, the MSE model on the triangular lattice has been the subject of many studies.<sup>210,211,212,213,186,114,187</sup> We will discuss here some properties of the simplest MSE model with up to four-spin cyclic exchange interactions ( $J_2 - 2J_3$  and  $J_4$  only in Eq. 48). The classical phase diagram (Fig. 5.9) of this model has been studied by Kubo and collaborators<sup>210,211</sup> and the quantum one has been roughly scanned in Ref.<sup>187</sup>: we will mainly focus on the short-ranged RVB spin liquid (see Fig. 5.9), which might be *the first RVB SL encountered in an SU(2)-symmetric spin model*.

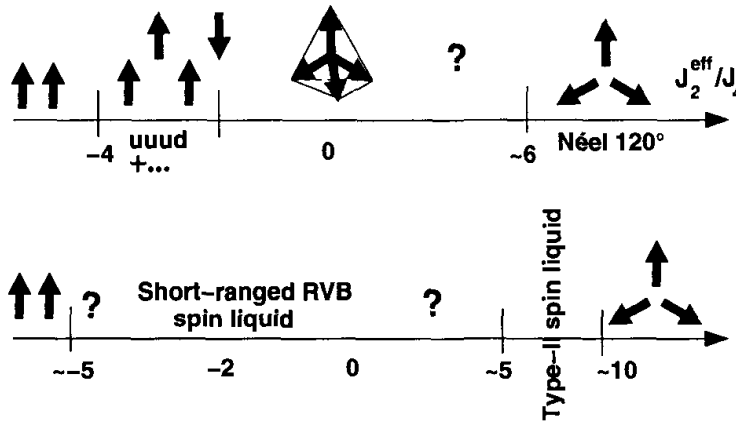


Fig. 5.9. Classical (top) and quantum (bottom) phases of the  $J_2 - J_4$  MSE Hamiltonian. The classical model was studied by Kubo and Momoi<sup>210</sup> and is based on a variational approach. The quantum phase diagram is the simplest scenario compatible with the exact diagonalizations data of Refs. <sup>186,114,187</sup>. While not completely understood, in the type-II spin-liquid region the spectra are characterized by a very large number of singlet excitations below the first triplet state. This is not the case in the RVB phase.

#### 5.6.4.1. Non-planar classical ground-states

It is well-known that an Heisenberg model (with possible second-neighbors, third-neighbors, ... interactions) on a Bravais lattice always admits a planar helical ground-state at the classical level. This is no longer true when MSE are present and finding the classical ground-state for arbitrary  $J_2$  and  $J_4$  is an unsolved problem. A mean-field phase diagram was obtained for the classical model<sup>210</sup> but very few exact results are known. In the neighborhood of  $J_4 = 1$ ,  $J_2 = 0$  the classical ground-state is known to be a four-sublattice configurations with magnetizations pointing toward the vertices of a regular tetrahedron.<sup>210</sup> This is a quite interesting model where the ground-state spontaneously breaks a discrete Ising symmetry associated to the sign of the triple product  $\vec{S}_1 \cdot (\vec{S}_2 \times \vec{S}_3)$  around a triangle. This broken symmetry gives rise to a finite-temperature phase transition which has been observed in Monte Carlo simulations.<sup>211</sup> This phenomena is similar to the transition predicted in the  $(\pi, 0)$  phase of the  $J_1 - J_2$  model on the square lattice.<sup>14</sup>

#### 5.6.4.2. Absence of Néel LRO

The classical ground-states at  $J_4 = 1$ ,  $J_2 = 0$  are tetrahedral configurations. Although this phase appears to be stable within the framework of linear spin-wave calculations<sup>211</sup> or Schwinger-Boson mean-field theory,<sup>212</sup> exact diagonalizations indicate that the magnetic LRO is washed out by quantum

fluctuations.<sup>211,114</sup> The chiral order predicted to survive at long distances and finite temperatures<sup>211</sup> in the classical system for  $J_2 = 0$  is also likely to be washed out by quantum fluctuations.<sup>114</sup>

When  $J_2 = 1$  a relatively small amount of  $J_4 \sim 0.1$  is sufficient to destroy the three-sublattice Néel LRO realized by the first-neighbor Heisenberg model.<sup>187</sup> The nature of the phase on the other side of this transition is not settled but the finite-size spectra display a large density of singlet excitations at low energy which could be reminiscent of the kagome situation.<sup>187</sup>

From exact diagonalizations (up to 36 sites) no sign of Néel LRO could be found at  $J_4 = 1, J_2 = -2$ .<sup>186,114</sup> In addition, the finite-size analysis showed that the spin-spin correlation length is quite short at  $J_2 = -2$  and  $J_4 = 1$  and a spin gap of the order of  $\Delta \sim 0.8$  exists at this point. Much of the numerical effort to elucidate the nature of the MSE ground-state was concentrated on this point because it is close to the parameters realized in low-density  $^3\text{He}$  films (when higher order exchanges are neglected).

#### 5.6.4.3. Local singlet-singlet correlations - absence of lattice symmetry breaking

Having excluded the possibility of a Néel ordered ground-state at  $J_4 = 1, J_2 = -2$  it is natural to look for a possible VBC. Because of the complexity of the MSE Hamiltonian it is not clear what kind of spatial order should be favored. From the analysis of dimer-dimer correlations (see Fig. 5.10) it appears that parallel valence-bonds repel each-other at short distance. This is similar to what is observed in the staggered phase of the  $J_2-J_4$  MSE ladder and square-lattice models. For this reason it appears that a plausible VBC would be the staggered VBC encountered in the triangular QDM for  $V > J$  (§5.5.5). However this scenario seems difficult to reconcile with the weakness of dimer-dimer correlations.<sup>114</sup> In addition, the low-energy singlet states and their quantum numbers<sup>214</sup> do not reflect the 12-fold quasi-degeneracy that should be present if the system was to spontaneously break some lattice symmetry according to a staggered VBC pattern. Small systems usually *favor* ordered phases because low-energy and long-wavelength fluctuations that could destabilize an ordered state are reduced compared to larger systems. From the fact that the finite-size spectra do not show the signatures of a staggered VBC symmetry breaking it is unlikely that the MSE model could develop a VBC of this kind in the thermodynamic limit.

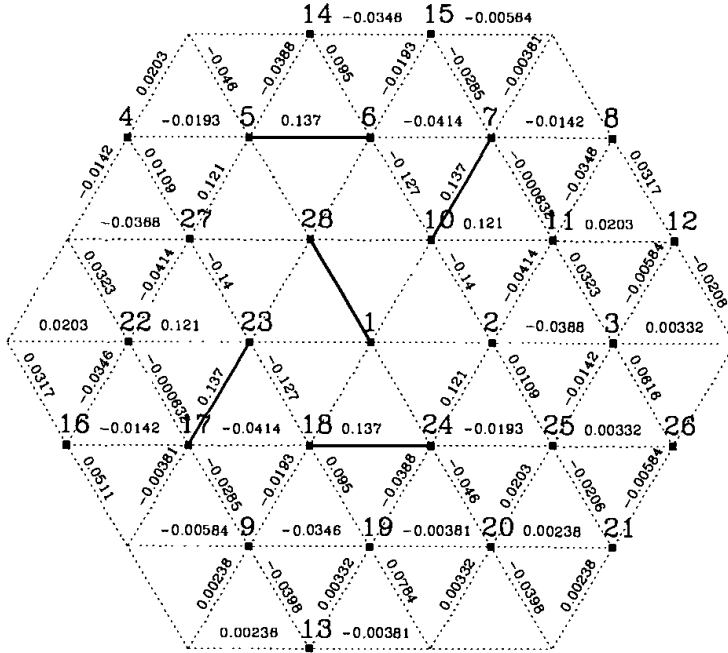


Fig. 5.10. Dimer-dimer correlations in the ground-state of the  $J_2$ - $J_4$  MSE model on the triangular lattice (28 sites) at  $J_2 = -2$ ,  $J_4 = 1$  (from Ref. <sup>114</sup>). Numbers are proportional to  $\langle \hat{d}_0 \hat{d}_x \rangle - \langle \hat{d}_0 \rangle \langle \hat{d}_x \rangle$  where the operator  $\hat{d}_x$  projects onto the singlet space of the bond  $x$  and  $\hat{d}_0$  refers to the reference bond (1, 28). These results shows a clear tendency for repulsion between parallel dimers.

#### 5.6.4.4. Topological degeneracy and Lieb-Schultz-Mattis theorem

Because no VBC phase could be identified in the MSE model at  $J_4 = 1$ ,  $J_2 = -2$  the numerical data were compared with the predictions of an RVB liquid scenario.

In one dimension a famous theorem due to Lieb, Schultz and Mattis<sup>215</sup> (LSM) states that in a one-dimensional spin system with an half-integer spin in the unit cell there is at least one excited state collapsing to the ground-state in the thermodynamic limit (periodic boundary conditions). There are in fact several arguments suggesting that this theorem might, at least to some extent, also apply to higher dimensions.<sup>216,217,157,218,219</sup> If that is the case a gapped system with an odd integer spin in the unit cell must have a degenerate ground-state. The simplest scenario to explain this degeneracy is a translation symmetry breaking. One could think that this would rule out the possibility of any (translation invariant) RVB liquid in such models. This is incorrect because a ground-state degeneracy can have

a topological origin on a system with periodic boundary conditions, as we discussed in the framework of QDM (§5.5). Such a phase is characterized by a four-fold topological ground-state degeneracy when the system is on a torus. That degeneracy allows the system to fulfill LSM's requirement without any spontaneous translation symmetry breaking.<sup>157</sup>

On a finite-size system the topological degeneracy is only approximate but some constraints exist for the quantum numbers (momentum in particular) of the quasi-degenerate multiplet.<sup>157</sup> A system with periodic boundary conditions with an even number of sites but an *odd number of rows* is expected to have two ground-states with differ by a momentum  $\pi$  in the direction parallel to the rows, in close analogy to the the LSM theorem in dimension one. The numerical spectra of the MSE model exhibit a set of three singlet energy levels collapsing onto the ground-state when the system size is increased<sup>114</sup> and their quantum number turn out to be consistent with the constraints derived from the general RVB picture.<sup>157</sup>

#### 5.6.4.5. Deconfined spinons

The SL phase described above is expected to have deconfined spinons ( $S = \frac{1}{2}$  excitations). These excitations should show up as an incoherent continuum in the spin-spin dynamical structure factor. However such a feature would probably be rather difficult to observe on small 2D lattices, in particular due to the small number of inequivalent  $\mathbf{k}$ -vectors in the Brillouin zone. On the other hand, the binding energy of two spinons can be evaluated by comparing the ground-state energy and the first magnetic excitation energy on even and odd samples. In the case of the MSE model at  $J_4 = 1, J_2 = -2$  the results show the existence of a bound-state (it is more favorable to put two spinons in the same small sample than in separate ones, which is not surprising) but this *does not mean that the spinons are confined* (contrary to the conclusions of Ref. <sup>114</sup>). Interestingly this binding energy seems to go to zero for the largest available sizes (Fig. 5.11): this might indicate the absence of attraction between spinons for large enough separation and an asymptotic deconfinement.

It is important to stress here that the RVB SL phase discussed here (and its QDM counterparts of §5.5.5 and §5.5.6) is not the only way to spinon deconfinement in 2D. There is at least another scenario, inherited from one dimension, which is the *sliding Luttinger liquid*. Indeed, the Luttinger liquid behavior and the one-dimensional critical behavior of magnetic chains seem to be robust to small (or moderate) *frustrating transverse couplings between*

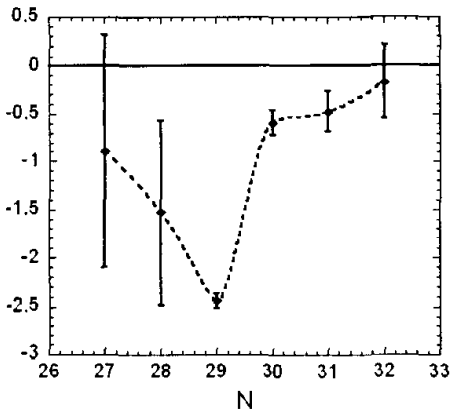


Fig. 5.11. Spinons binding energy as a function of the system size in the MSE model at  $J_2 = -2$  and  $J_4 = 1$ . The vertical bars correspond to the range of values found for different sample shapes.

chains, as observed both in theoretical<sup>220,221,222,223,224,225,226</sup> and numerical approaches.<sup>100</sup> This regime between one and two dimensions which may have been observed in  $\text{Cs}_2\text{CuCl}_4$ <sup>227</sup> is the subject of a number of recent studies.<sup>223,224</sup>

### 5.6.5. Other models with MSE interactions

Multiple-spin interactions are present in a number of models that were found to exhibit fractionalization or an RVB liquid ground-state. Well known examples of MSE interactions with an Ising symmetry are  $\mathbb{Z}_2$  gauge theories, where the gauge invariant plaquette term is a product of Pauli matrices  $\prod_i \sigma_i^z$ . Such theories have a deconfined phase in 2+1 dimension<sup>169</sup> and their relevance to fractionalized phases of 2D electronic systems has been pointed out by Senthil and Fisher.<sup>161</sup> The connexion between  $\mathbb{Z}_2$  gauge theories and QDM was mentioned in §5.5.6.7. Some MSE spin models with an Ising symmetry and a fractionalized ground-state were discussed by Kitaev,<sup>228</sup> Nayak and Shtengel.<sup>229</sup> In the other limit of a  $U(1)$  (or  $XY$ ) symmetry several models have been studied. Recent examples are based upon the spin- $\frac{1}{2}$  four-spin XY ring exchange interaction<sup>230,231,232,233</sup>

$$\mathcal{H} = -K \sum_{\langle i j k l \rangle} (S_i^+ S_j^- S_k^+ S_l^- + \text{H.c.}) \quad (49)$$

which is the  $XY$  analog of the  $SU(2)$  MSE interaction  $P_{1234} + \text{H.c.}$

## 5.7. Antiferromagnets on the kagome (and related) lattices

In RVB SL phases described in §5.5.5, §5.5.6 and §5.6.4 *singlet excitations (visons) are gapped*. In the  $\mathbb{Z}_2$  gauge theory approach this gap is essential for the consistency of the theory.<sup>161,162</sup> The gauge-field quasi particles are vortices of the gauge field and carry a unit  $\mathbb{Z}_2$  gauge flux but no spin. As illustrated in §5.5.6.6 in the framework of a simple QDM, visons have long-ranged interaction with spinons. If the spectrum of these visons has a gap then the spinons are unconfined and the phase is “fractionalized”. If they condense, the long range interaction between them and the spinons frustrate the motions of the latter which remained confined. The gap in the singlet sector (above the topological degeneracy) is thus a crucial ingredient of these RVB SL. At the end of this section we will show how the spin- $\frac{1}{2}$  first-neighbor Heisenberg model on the kagome lattice represents an enigma with respect to this scheme (as well as the QDM described in Sec. 5.5.7). We begin the section by a review of the properties of various models on the kagome lattice, which topology is the source of an extreme frustration, and, in many models, source of an extensive degeneracy of the ground-state.

### 5.7.1. Miscellaneous models on the kagome lattice

There has been a large number of studies devoted to different antiferromagnetic models on the kagome lattice. The nearest-neighbor Ising model on such a lattice is disordered, its entropy per site is very large  $S_{\text{kag}}^{\text{Ising}} = 0.502$ , more than half the independent spin value, much larger than the triangular lattice value  $S_{\text{tri}}^{\text{Ising}} = 0.323$  and of the order of Pauling approximation for independent triangles  $S_{\text{Pauling}} = 0.501$ .<sup>234</sup> This suggests that the correlations in this system are very weak: the model remains disordered at all temperatures.<sup>235,236</sup> Moessner and Sondhi have studied this Ising model in a transverse magnetic field (the simplest way to include some quantum fluctuations in the model): the model fails to order for any transverse field, at any temperature.<sup>145,237</sup>

The nearest-neighbor classical Heisenberg model on the kagome lattice has also a huge ground-state degeneracy. This property is easy to understand and holds on different lattices with corner sharing units such as the checkerboard lattice or the three dimensional pyrochlore lattice (Moessner and Chalker<sup>106,107</sup>). On all these lattices the nearest-neighbor Heisenberg Hamiltonian can be written as the sum of the square of the total spin  $\vec{S}_\alpha$  of individual units  $\alpha$  (a tetrahedron in the 2-d and 3-d pyrochlore cases and a triangle for the kagome lattice), which share only one vertex. Classical

ground-states are obtained whenever  $\forall \alpha \vec{S}_\alpha = \vec{0}$ . This condition fixes the relative positions of the three classical spins of a triangle at 120 degrees from each other in a plane. But it does not fix the relative orientation of the plane of a triad with respect to the planes of triads on corner sharing triangles: the model has a continuous local degeneracy<sup>238,236</sup> at  $T = 0$ .<sup>u</sup> Thermal fluctuations select coplanar configurations.<sup>238,236,240</sup> The possibility of long-range order in spin-spin correlations at very low temperature has been discussed without any definitive conclusion.<sup>236,241</sup> The order parameter of the planar phase is defined by the local helicity (sometimes called vectorial chirality) :

$$\vec{\zeta} = \vec{S}_1 \times \vec{S}_2 + \vec{S}_2 \times \vec{S}_3 + \vec{S}_3 \times \vec{S}_1 \quad (50)$$

where the three sites define a triangle. This kind of order is sometimes called *nematic* by analogy to liquid crystals. The existence of such an order parameter might be related to the instability of the classical Heisenberg model on the kagome lattice to Dzyaloshinsky-Moriya interactions.<sup>242,243</sup> The classical model has a large density of low-lying excitations at low temperature.<sup>244</sup>

### 5.7.2. Spin- $\frac{1}{2}$ Heisenberg model on the kagome lattice: an extreme play-ground for “quantum fluctuations”

The nearest-neighbor spin- $\frac{1}{2}$  quantum Heisenberg model on the kagome lattice has equally been the object of many studies<sup>245,246,247,248,171,249,250,251,252,253,254</sup> From these studies the following important facts have emerged :

#### 5.7.2.1. Ground-state energy per spin

The Heisenberg model on the kagome lattice has an extremely low energy per bond ( $\langle \mathbf{S}_i \cdot \mathbf{S}_j \rangle \simeq -0.44$ )  $\sim 87\%$  of the energy per bond in an isolated triangle. On this lattice the energy per bond of the spin- $\frac{1}{2}$  system is much lower than the classical energy  $\frac{E_{qu.}}{E_{cl.}} \sim 1.74$ , a ratio much larger than in any other 2D magnet, that can only be compared to the value obtained for the Bethe chain (1.77). The kagome lattice is the 2D lattice which offers the largest stabilization due to quantum fluctuations.

---

<sup>u</sup>Counting the *planar* ground-states amounts to determine in how many ways one can associate one of the three letters *A*, *B* and *C* to each site so that each triangle has spins along the three different orientations. This already represents an extensive entropy.<sup>239,236</sup>

### 5.7.2.2. Correlations

The ground-state is disordered.<sup>255</sup> Within accuracy of the finite-size numerical computations, spin-spin correlations,<sup>248</sup> dimer-dimer correlations (Fig. 5.12), chirality-chirality correlations<sup>246</sup> are short-ranged, which is consistent with the previous point and series expansion results.<sup>256</sup>

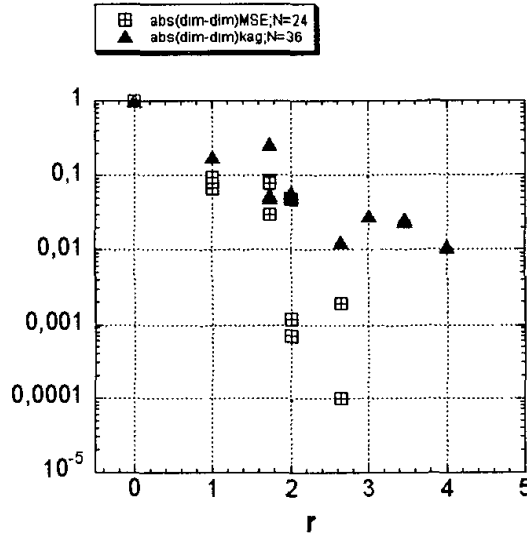


Fig. 5.12. Dimer-dimer correlations in the ground-state of the kagome Heisenberg model (black triangles) and in the MSE model discussed in §5.6.4 (open symbols) versus distance. Although the decrease of these correlations is weaker in the KH model than in the MSE model, it seems nevertheless roughly exponential in the first two decades, as the spin-spin correlations are.<sup>246,248</sup>

### 5.7.2.3. Spin-gap

There is plausibly a spin-gap of the order of  $1/20^{\text{th}}$  of the coupling constant.<sup>250</sup> In view of the smallness of this spin-gap with regards to the available sizes caution is necessary. The above conclusion was drawn from the value of the *microscopic* spin gap  $E_0(S = S_{\min} + 1) - E_0(S = S_{\min})$  on exact spectra of samples with up to 36 spins,<sup>250</sup> where  $E_0(S)$  is the lowest energy in the  $S$  sector, and  $S_{\min} = 0$  or  $\frac{1}{2}$  depending on the parity of the total number of spins. The finite-size effects on these results are an order of magnitude smaller than in a Néel ordered antiferromagnet. Nevertheless they are still not negligible for these sizes. An alternative determination of the spin-gap can be obtained along the following line. The lowest exact

eigenstate in each total spin sector  $S$  of a  $N$  spins sample defines the energy per spin  $e$  at  $T = 0$  as a function of its magnetization  $m = S/(N/2)$ . For low positive values of the magnetization, one can fit  $e(m)$  to the phenomenological law:<sup>v</sup>

$$e(m) = e(0) + am + bm^2/2 + \mathcal{O}(m^3) \quad (51)$$

$a$  and  $b$  are intensive quantities which depend on  $N$  but should converge to some (possibly zero) value when  $N \rightarrow \infty$ . This point of view is important because for an infinite system the thermodynamic function  $e(m) = \lim_{N \rightarrow \infty} E(S = mN/2)/N$  can be measured (through the zero temperature magnetization curve), but not  $E(S \sim \mathcal{O}(1))$ . The physical significance of Eq. 51 is clear:  $a$  measures half the spin gap (in a thermodynamic sense, that is the magnetic field  $H_c$  required to magnetize the system at zero temperature) and

$$b = \frac{\partial^2 e}{\partial m^2} = \chi^{-1} \quad (52)$$

where  $\chi$  is the homogeneous susceptibility of the medium for fields larger than the critical field  $H_c = a$ . This determination of the *thermodynamic* spin gap leads to a renormalization of the raw data<sup>250</sup> for small sizes (see Fig. 5.13). A linear extrapolation versus  $1/N$  (which should give a lower bound of the spin-gap) leads to the value 0.06 for the spin gap ( $e_\infty = -0.4365$  and  $\chi_\infty = 0.34$ ). This determination is in agreement with the direct extrapolation of the microscopic gap  $E_0(S = S_{min} + 1) - E_0(S = S_{min})$ . For  $N = 36$  at the smallest non-zero magnetization, the linear term of equation (51) is 90% of the quadratic term: this is an estimate of the degree of confidence on the existence of a spin-gap.

#### 5.7.2.4. An exceptional density of low lying excitations in the singlet sector

Whatever the ultimate fate of the spin gap a big surprise emerges from the exact spectra: the probable absence of gap in the singlet sector and the anomalous density of low energy states adjacent to the ground-state. Let us first comment the second point in details: even on the smallest size spectra the low lying states appear contiguous to the ground-state and the spectra

---

<sup>v</sup>This phenomenological form cannot extend below  $m = 0$  and beyond  $m = 1/3$  because at both magnetizations an angular point appears in  $e(m)$  with a discontinuity of the first derivative signaling a magnetization plateau.<sup>257,258</sup> This is discussed in more details in our lectures notes.<sup>95</sup>

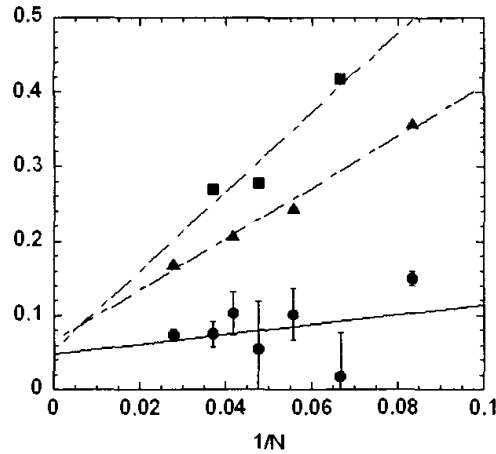


Fig. 5.13. Finite size scaling of the spin gap in the spin- $\frac{1}{2}$  Heisenberg model  $\mathcal{H} = \sum_{\langle i,j \rangle} \mathbf{S}_i \cdot \mathbf{S}_j$  on the kagome lattice. Triangles (resp. squares) are the raw results of the microscopic spin gap in the even (resp. odd) samples. Bullets represent the “thermodynamic” spin gap, they are obtained by the procedure described in the text (errors bars come from the rms uncertainty in the fits).

are extremely dense. The number of singlet levels in the spin-gap (taken as a natural energy band-width of the problem) increases exponentially fast with  $N$  as  $\sim 1.15^N$  as far as the  $N \leq 36$  systems are concerned (see Fig. 5.14). This property remains (and can be checked on larger systems) when the Hilbert space is restricted to that of first-neighbor valence-bond coverings.<sup>253,170</sup>

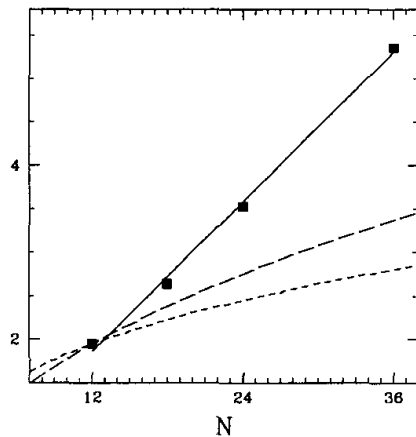


Fig. 5.14. Logarithm of the number of singlet states in the spin gap versus sample size (black squares). The short dashed and long dashed curves display the theoretical law (Eq. 54 with  $d = 2$ ) (short dashes:  $p = 1$ , long dashes:  $p = 2$ ).

Some remarks are necessary to fully appreciate this property. The  $2^N$  states of the system are stretched on an energy scale of the order of  $NJ$  where  $J$  is the coupling constant of the Hamiltonian. This implies that on most of the spectrum the density of states increases exponentially with  $N$ . If we specialize to the  $S = 0$  sector as we will do below, the picture is not very different: the number of states is  $C_{\frac{N}{2}}^N - C_{\frac{N}{2}-1}^N \sim \mathcal{O}(\frac{2^N}{N})$  and here too, in most of the spectrum the density is exponentially increasing with  $N$ . But in all the phases that we have studied up to now, the nature of the ground-state and of the low lying excitations leads to a different behavior at the bottom of the spectrum. The ground-state degeneracy is  $\mathcal{O}(1)$  in VBC, VBS and in the RVB SL (of the type discussed in §5.5.6 and §5.6.4 for instance) and it is  $\mathcal{O}(N^p)$  in Néel ordered states with  $p$  sublattices. In all these situations the low-lying excitations are described as modes or quasi-particles. Let us suppose that single-particle excitations have a dispersion law:

$$\omega(\mathbf{k}) \sim k^p. \quad (53)$$

In a  $d$ -dimensional system the total internal energy increases with temperature as  $E \sim NT^{(p+d)/p}$ , the specific heat as  $C_v \sim NT^{d/p}$  as well as the entropy  $S \sim NT^{d/p}$ . In a micro-canonical point of view the density of states  $\rho(E)$  or a large enough system is simply related to the entropy by  $S = \log(\rho(E))$ . Since  $S \sim NT^{d/p} = N(E/N)^{d/(p+d)}$  we obtain

$$\log(\rho(E)) \propto N^{\frac{p}{p+d}} \quad (54)$$

As an example, let us consider the Rokhsar Kivelson QDM on the square lattice at the quantum critical point (Sec. 5.5): the dispersion law of the so-called resonons is quadratic around  $\mathbf{Q} = (\pi, \pi)$ , the logarithm of the number of states increases as  $N^{1/2}$  (long dashes of Fig. 5.14).

Even with such many-particle excitations one would expect a number of levels increasing more slowly than in the numerical spectra. Infinitely soft low-energy modes ( $p \rightarrow \infty$ ), are necessary to recover a density of low-lying levels growing as  $\sim \alpha^N$ . It is still unclear if we can do a connection between the “zero modes” of the classical model at  $T = 0$  and this picture. And we cannot completely indulge ourselves in saying that quantum fluctuations are unable to lift the classical degeneracy as quantum fluctuations seem to open a spin gap.

A physical consequence of this exceptional density of low lying singlets can be observed in the specific heat: at low temperature the specific heat of this spin system is unusually large, with a double peak

structure,<sup>255,259,260,261</sup> insensitive to relatively large magnetic fields.<sup>252</sup> This is easily understood if we suppose that in this energy range there is a large density of singlet states.<sup>252</sup> This result is to be compared to the experimental results of Ramirez *et al.*<sup>262</sup> on  $\text{SrCr}_{9p}\text{Ga}_{12-9p}\text{O}_{19}$  (notice however that it is a spin- $\frac{3}{2}$  compound and that numerical calculations were performed on the spin- $\frac{1}{2}$  model) where the specific heat around 5 K has an extremely low sensitivity to magnetic fields up to 10 Tesla, whereas the homogeneous susceptibility in this range of temperature is probably very low if we notice that it turns down around 50K.<sup>263</sup>

#### 5.7.2.5. Absence of gap in the singlet sector

Up to  $N = 36$  sites there is no evidence of a possible gap in the singlet spectrum: this is an exceptional phenomenon in quantum mechanics of small systems where discretization is usually the rule.

It has been advocated in recent papers<sup>264,265</sup> that the ground-state of this model could break the translational symmetry and be a VBC. The first proposed crystal<sup>264</sup> is made of resonating *stars* with 6 dimers. The corresponding unit cell has 12 spins. The second VBC<sup>265</sup> is made of resonating (trimerized) *hexagons* and was already discussed as the most reasonable crystal (if any is realized in this system, which we think is not clear at all) by Marston and Zeng<sup>147</sup> and Zeng and Elser.<sup>171</sup> This later VBC has a unit cell with 36 sites. In both scenarios it is the energy gain obtained by *local resonances* (involving respectively 6 and 3 valence-bonds) which drives the system toward a VBC. From the energy point of view the star VBC is (by far) less realistic since it involves a much longer resonance loop.<sup>w</sup> This resonance loop involving 6 valence-bonds around a star has a vanishing amplitude at the lowest non-trivial order of the overlap expansion in the RVB subspace, as was shown by Zeng and Elser.<sup>171</sup> To our opinion there is no reason to think that the physics of the kagome model can be described from the limit of weakly coupled stars. On the other hand, in the approximation where only the shortest resonance loops are present, the model was indeed found to be in the *hexagon* VBC phase, as re-discovered recently from a different point of view.<sup>265</sup> A crucial (numerical) result of Zeng and Elser<sup>171</sup> is however that this VBC *melts* when higher order resonances loops are included.

<sup>w</sup>Notice also that the gap associated to the star VBC is predicted to be of the order of 1/10 of  $J$ ,<sup>264</sup> which is 10 times larger than the largest distance between two consecutive levels in the spectrum of the  $N = 36$  sample.

We have studied the 36-sites sample which can accommodate these two VBC: the low-lying levels of the spectrum do not give a clear picture of the supposed to be VBC. The eigenstates with the quantum numbers corresponding to these two VBC are not the lowest energy levels in the spectrum. No gap is seen in the spectrum, the largest distance between two consecutive states is  $10^{-2}$  and seems distributed at random, whereas the average distance between two consecutive states in the 50 first states is:  $2.510^{-3}$ . It has been argued that long wave-length quantum fluctuations (almost absent in the  $N = 36$  sample which contains only two resonating hexagons or three stars) could eventually restore the order. We think that this is incorrect. In a VBC it is *local resonances* which favor the crystal and longer resonances which tend to reduce the order parameter and which could eventually destabilize it. Long-wavelength will tend to restore a larger ground-state symmetry (reducing the degeneracy). From this point of view it is unlikely that a VBC pattern will appear in larger systems if it is not apparent in the smallest systems (provided that boundary conditions do not frustrate the corresponding VBC). We thus consider that up to now numerical results do not support the claims of a star or hexagon VBC ground-state in this model.

If the hexagon VBC was however realized the important question would probably be why the associated gap is so tiny, certainly smaller than  $10^{-3}$ . A natural scenario would be that of a very close proximity to a quantum critical point, but that critical point remains to be identified. A third possibility would be that of a system with a true extensive entropy at zero temperature. This is less likely in our opinion since (up to now) only models with simple (if not trivial) local symmetries were found to have such ground-state entropy (Ising antiferromagnet on the triangular lattice for instance or the QDM of §5.5.7) and this entropy is usually sent to (possibly small but) finite temperatures by almost any perturbation.

#### 5.7.2.6. Anomalous density of states in other spin sectors

An anomalous density of low lying states is equally observed in the spin  $\frac{1}{2}$  sector (where the law could be fitted to  $N^{1.15^N}$ ), in the spin 1 sector as well as in other sectors with larger total spin. It should be noticed that such a density of states implies the absence of an intrinsic energy scale for the low lying excitations: a phenomenon that has been observed in inelastic neutron scattering (Ref. <sup>266</sup> and Refs. therein) and theoretically in the imaginary part of the dynamic susceptibility calculated within the dynamical mean

field theory (Georges *et al.*<sup>267</sup>). A high spin susceptibility just above the spin gap is not excluded in the spin- $\frac{1}{2}$ .<sup>268</sup>

The global picture of this phase is thus that of a SL with no long-ranged correlations in any local observable, and an large entropy of singlets at  $T \ll J$ , which is a manifestation of the extraordinary large density of states in each  $S$  subspace.

### 5.7.3. Nearest-neighbor RVB description of the spin- $\frac{1}{2}$ kagome antiferromagnet

Considering a supposed-to-be large spin-gap, Zeng and Elser<sup>171</sup> proposed a description of the ground-state and low-lying excitations of the kagome model in the basis of next neighbor valence bonds. They analyzed in this context the dimer dynamics and showed on a  $N = 36$  sample that the hexagon VBC –favored by the shortest (three-)dimer moves– melts when introducing higher order tunneling. Mila and Mambrini<sup>251,253</sup> confirmed that this reduced Hilbert space of next neighbor valence bonds captures some of the most perplexing features of this magnet and specifically the absence of (measurable) gap in the singlet sector and the exponential number of singlets. One of us, D. Serban and V. Pasquier<sup>170</sup> have elaborated on this work and on Zeng and Elser’s approach and proposed a QDM with an extensive zero-point entropy and critical (energy-energy<sup>x</sup>) correlations (see §5.5.7). All these results point to an absence of an intrinsic low-energy scale. This feature is typical of a critical state, but as seen in the above discussion, the simple RK picture does not seem to fit nicely to the exact diagonalization data: may be the available sizes are too small or the behavior of this quantum system corresponds to something completely new. Some recent numerical results<sup>254</sup> (in the full spin- $\frac{1}{2}$  Hilbert space as well as in the RVB subspace) showed that (static) non-magnetic impurities (holes) experience an unexpected *repulsion* in this system and that no significant magnetic moment is created in the vicinity of the impurities. It has been argued<sup>269</sup> that static non-magnetic impurities are useful to detect a possible spinon deconfinement in two-dimensional antiferromagnets. From this point of view the results mentioned above suggest such a deconfinement.

---

<sup>x</sup>Dimer-dimer correlations are short-ranged in this model.

### 5.7.4. Experiments in compounds with kagome-like lattices

The low temperature specific heat of  $\text{SrCr}_9\text{Ga}_{12}\text{O}_{19}$  (the magnetic chromium ion has a spin  $3/2$ ) is apparently dominated by singlet states.<sup>262</sup> The magnetic excitations of this compound as seen by muons can be described as spins  $\frac{1}{2}$  itinerant in a sea of singlets.<sup>270</sup> The non-linear spin susceptibility of  $\text{SrCr}_9\text{Ga}_{12}\text{O}_{19}$  exhibits a very large increase at about 5 K, reminiscent of spin glasses,<sup>271</sup> but neutrons and muons show that a very significant fraction of the spins are not frozen below this temperature and exhibit still very rapid fluctuations.<sup>272</sup> The same phenomena have been observed in two jarosites that are equally good models of kagome antiferromagnets with half-odd-integer spin per unit cell.<sup>273,274</sup>

### 5.7.5. “Haldane’s conjecture”

Whereas the classical Heisenberg model on the kagome, checkerboard and pyrochlore lattices share the properties of local continuous degeneracy and disorder at  $T = 0$ , their quantum counterparts are quite different. As it has been explained in Sec. 5.3, the Heisenberg model on the checkerboard lattice has an ordered VBC with gaps to all excitations. In contrast to the case of the  $S = \frac{1}{2}$  Heisenberg model on the kagome lattice, recent results from Hida<sup>66</sup> show that there is a large gap to all excitations in the  $S = 1$  Heisenberg model on this same lattice, in agreement with experiments.<sup>275,276,277</sup>

Less is known on the ground-state of the Heisenberg model on the three-dimensional pyrochlore lattice: Canals and Lacroix<sup>278</sup> have shown that the spin-spin correlations are short ranged and they have observed that on a 16-sites spectrum the first excitations are singlet ones. Fouet *et al.* have computed the spectrum of a 32-sites pyrochlore sample,<sup>99</sup> this work confirms that the first excitations are still singlets for this size. There is plausibly a degeneracy of the ground-state in the thermodynamic limit but no evidence of a closing of the gap above: the system may therefore be a VBC. A first description of the singlet sector was proposed by Harris, Berlinsky and Bruder<sup>279</sup> and was developed further by Tsunetsugu.<sup>280,281</sup> It starts from the limit of weakly-coupled tetrahedron (and thus breaks some spatial symmetries). The ground-state of an isolated tetrahedron is two-fold degenerate and can be described by an Ising pseudo-spin. An effective Hamiltonian describing the interactions between these pseudo-spins was written<sup>279</sup> and analyzed in a semi-classical approximation. It was concluded that the system maybe a VBC. It was argued by Tsunetsugu that a soft mode could exist in the singlet sector.<sup>281</sup> The CORE approach of

Berg *et al.*<sup>102</sup> seems more appropriate to deal with these systems where dimerization is probably the dominant phenomenon. They treated larger units (block of four tetrahedron) and concludes to the existence of a VBC with a larger unit cell than the one predicted before<sup>279,280,281</sup> and a small singlet gap.

All these results seem to confirm a 2D version of Haldane's conjecture: among these frustrated systems with local continuous degeneracies in the classical limit, the spin- $\frac{1}{2}$  kagome antiferromagnet is the only system to have an half-odd integer spin in the unit cell. It is maybe not by chance that it is the only one with gapless excitations.<sup>y</sup> The spin- $\frac{1}{2}$  Heisenberg model on the checkerboard lattice or on the pyrochlore lattice and the spin-1 Heisenberg model on the kagome lattice have integer spins in the unit cell and quantum fluctuations lead to gapful excitations. It is also interesting to note that these results are consistent with a generalization of the LSM theorem in dimension two.<sup>216,217,157,218,219</sup>

An interesting analysis of Von Delft and Henley<sup>282</sup> supports this conjecture. These authors studied the collective tunnelling of a small cluster of spins between two spin configurations that are degenerate in the classical limit. They found that for half-odd-integer spins the tunnelling amplitude for a cluster of six spins around an hexagon (and on other larger loops) is exactly zero because of destructive interferences between different symmetry-related instantons. For small integer spins the interference is constructive and the tunnel amplitude and the tunnel splitting are large: this is consistent with numerical results which gives a large gap for the  $S = 1$  kagome antiferromagnet, and small gaps (if any) in the spin- $\frac{1}{2}$  system.

## 5.8. Conclusions

We conclude by summarizing some properties –and related open questions– of the different phases discussed in this review.

The properties of these phases are summarized in Table 5.2. Semi-classical phases with Néel long-ranged order, magnons as gapless excitations, do exist in spin- $\frac{1}{2}$  2D systems with moderate frustration: the Heisenberg model on the triangular lattice is the most explicit example, with a sublattice magnetization about one half of the classical value.<sup>2</sup> The ground-state degeneracy is in the thermodynamic limit a power of  $N$ .

---

<sup>y</sup>The SCGO compound with 7 spins 3/2 by unit cell belongs to the same category and as also gapless excitations.<sup>262</sup>

An increased frustration, lower coordination number or smaller spin lead to quantum phases, with a ground-state of higher symmetry, no long ranged order in spin-spin correlations, a spin gap and the restored  $SU(2)$  symmetry. Two main alternatives are then opened: the VBC or VBS phases on one hand, the RVB SL on the other. RVB SL and VBC (as well as VBS) first requires the formation of local singlets. When a particular local resonance pattern dominates the dynamics of the Hamiltonian the system will try to maximize the number of occurrence of this pattern. This is usually achieved by a regular arrangement, that is a VBC. When no such pattern dominates the system may form a translation invariant RVB SL. In the first case the ground-state can be qualitatively described by one ordered configuration of singlets dressed by small fluctuations. In the RVB SL the amplitudes of the wave-function are distributed over an exponentially large number of configurations. These ground-states lead to very different excitations:  $\Delta S = 1$  gapped magnons in the first case (and  $\Delta S = 0$  domain-wall excitations), gapped  $\Delta S = 0$  visons and gapped  $\Delta S = \frac{1}{2}$  unconfined spinons in the second case.

In agreement with the large- $N$  results (Sec. 5.4), VBC or VBS phases appear in general in quantum situations where the large- $S$  classical limit displays collinear order <sup>a</sup>, whereas up to now RVB SL phases have only be encountered in range of parameters were the classical solutions are non collinear (MSE<sup>186,114</sup> and  $J_1-J_2$  on the honeycomb lattice<sup>97</sup>).

These states obey the 2D extension of LSM theorem: if  $2S$  is odd in the unit cell and if excitations are gapped there is a ground-state degeneracy in the thermodynamic limit (with periodic boundary conditions). However the origin of the degeneracy differs in the two types of quantum phases. In the VBC phases the degeneracy is associated to spontaneously broken translation symmetry whereas in the RVB SL the degeneracy has a topological origin. In the VBS (or explicit VBC) the ground-state is unique but  $2S$  is even in the unit cell. As in one dimension the LSM theorem seems to play an important role and a formal proof of its validity in 2D is perhaps very close, if not achieved.<sup>218</sup> A RVB SL may have been observed numerically in a spin- $\frac{1}{2}$  model on the hexagonal lattice.<sup>97</sup> From the point of view of large- $N$  and QDM approaches a topological degeneracy is expected in such a SL. Interestingly that degeneracy is not imposed by the 2D extension of LSM's theorem and has not been detected.<sup>97</sup>

These paradigms are relatively well understood, at least on the qualita-

---

<sup>a</sup>We have discussed some possible counter examples in section 3. 6

tive level. They also appear naturally in the broader context of the classification of Mott insulators.<sup>283</sup> However several kinds of 2D frustrated magnets do not fall in these simple classes and many open questions remain.

This review was restricted to  $SU(2)$  invariant Hamiltonians. Whereas the Ising limit has been much studied, the differences between quantum XY and Heisenberg models have received much less attention.

Chiral SL have not been discussed in this review. They are characterized by a broken time-reversal symmetry. This possibility has been studied intensely since the 80's.<sup>284,285,286,4</sup> To the best of our knowledge it has not yet been identified in a realistic 2D model.<sup>b</sup>

The issue of quantum phase transitions in frustrated antiferromagnet is also an active topic that is not presented in this review. Many properties of these critical points are still unknown, not to mention the fascinating problems associated with (quenched) disorder.

Limited by place (and competence) we have not discussed in details the works done on spatially anisotropic models. This field which is in between one (review by P. Lecheminant in this book) and 2D is extremely flourishing tackled by bosonization and large- $N$  methods.

To conclude we would like to emphasize that new analytical and/or numerical methods are highly desirable to proceed in the analysis of the two emblematic problems by which we have opened and closed this review: the  $J_1-J_2$  model on the square lattice and the spin- $\frac{1}{2}$  Heisenberg model on the kagome (and pyrochlore) lattices. In both of these problems a consensus remains to be obtained.

## Acknowledgments

It would have been difficult to thank individually many of our colleagues cited in references with whom we had numerous and fruitful discussions – many thanks to all of them. It is also a pleasure to thank our close collaborators B. Bernu, V. Pasquier, D. Serban and P. Sindzingre, this review owes much to them. We are also grateful to C. Henley, A. Honecker, R. Moessner and O. Tchernyshyov for their insightful comments on the manuscript.

## References

1. E. Manousakis, Rev. Mod. Phys. **63**, 1 (1991).

---

<sup>b</sup>An example was recently discovered in one dimension: the scalar-chirality phase of the spin ladder model with 4-spin MSE interactions (see §5.6.2).

2. B. Bernu, P. Lecheminant, C. Lhuillier and L. Pierre, Phys. Rev. B **50**, 10048 (1994).
3. Proceedings of the *Highly Frustrated Magnetism 2000* conference, published in J. Can. Phys. **79**, (2001).
4. E. Fradkin, *Field Theories of Condensed Matter Systems*, Addison-Wesley (1998).
5. A. Auerbach, *Interacting electrons and Quantum Magnetism*, Springer-Verlag, Berlin Heidelberg New York, 1994.
6. A. M. Tsvelik, *Quantum Field Theory in Condensed Matter Physics* Cambridge University Press (1996).
7. S. Sachdev, *Quantum Phase Transitions*, Cambridge U. Press, New York (1999).
8. J. M. Luttinger and L. Tisza, Phys. Rev. **70**, 954 (1946).
9. P. Chandra and B. Douçot, Phys. Rev. B **38**, 9335 (1988).
10. J. Villain, R. Bidaux, J. P. Carton and R. Conte, J. Phys. (Paris) **41**, 1263 (1980).
11. E. Shender, Sov. Phys. JETP **56**, 178 (1982).
12. C. L. Henley, Phys. Rev. Lett. **62**, 2056 (1989).
13. A. Moreo, E. Dagotto, T. Jolicœur and J. Riera, Phys. Rev. B **42**, 6283 (1990).
14. P. Chandra, P. Coleman, and A. Larkin, Phys. Rev. Lett. **64**, 88 (1990).
15. R. R. P. Singh, W. Zheng, J. Oitmaa, O. P. Sushkov, C. J. Hamer, Phys. Rev. Lett. **91**, 017201 (2003).
16. G. Misguich, B. Bernu and L. Pierre, Phys. Rev. B **68**, 113409 (2003).
17. C. Weber, L. Capriotti, G. Misguich, F. Becca, M. Elhajal and F. Mila, Phys. Rev. Lett. **91**, 177202 (2003).
18. T. Jolicœur, E. Dagotto, E. Gagliano and S. Bacci, Phys. Rev. B **42**, 4800 (1990).
19. A. Chubukov and T. Jolicœur, Phys. Rev. B **46**, 11137 (1992).
20. S. E. Korshunov, Phys. Rev. B **47**, 6165 (1993).
21. P. Lecheminant, B. Bernu, C. Lhuillier and L. Pierre, Phys. Rev. B **52**, 6647 (1995).
22. R. Melzi *et al.*, Phys. Rev. Lett. **85**, 1318 (2000).
23. R. Melzi *et al.*, Phys. Rev. B **64**, 024409 (2001).
24. H. Rosner *et al.*, Phys. Rev. Lett. **88**, 186405 (2002).
25. H. Rosner *et al.*, Phys. Rev. B **67**, 014416 (2003).
26. D. J. Klein, J. Phys. A: Math. Gen. **15**, 661 (1982).
27. C. K. Majumdar and D. K. Ghosh, J. Math. Phys. **10**, 1399 (1969).
28. R. R. P. Singh, M. P. Gelfand and D. A. Huse, Phys. Rev. Lett. **61**, 2484 (1988).
29. M. P. Gelfand, R. R. P. Singh and D. A. Huse, J. Stat. Phys. **59**, 1093 (1990).
30. Zheng Weihong, J. Oitmaa, and C. J. Hamer, Phys. Rev. B **43**, 8321 (1991).
31. J. Oitmaa and Zheng Weihong, Phys. Rev. B **54**, 3022 (1996).
32. M. P. Gelfand, R. R. P. Singh and D. A. Huse, Phys. Rev. B **40**, 10801 (1989).

33. M. P. Gelfand, Phys. Rev. B **42**, 8206 (1990).
34. R. R. P. Singh, Zheng Weihong, C. J. Hamer, and J. Oitmaa, Phys. Rev. B **60**, 7278 (1999).
35. V. N. Kotov, J. Oitmaa, O. Sushkov and Zheng Weihong, Phil. Mag. B **80**, 1483 (2000).
36. M. E. Zhitomirsky and K. Ueda, Phys. Rev. B **54**, 9007 (1996).
37. L. Capriotti, F. Becca, A. Parola, and S. Sorella, Phys. Rev. Lett. **87**, 097201 (2001).
38. O. P. Sushkov, J. Oitmaa, and Zheng Weihong, Phys. Rev. B **66**, 054401 (2002).
39. O. P. Sushkov, J. Oitmaa, and Zheng Weihong, Phys. Rev. B **63**, 104420 (2001).
40. M. S. L. du Croo de Jongh, J. M. J. Van Leeuwen, and W. Van Saarloos, Phys. Rev. B **62**, 14844 (2000).
41. E. Dagotto and A. Moreo, Phys. Rev. B **39**, 4744 (1989), Phys. Rev. Lett. **63**, 2148 (1989).
42. F. Figueirido *et al.*, Phys. Rev. B **41**, 4619 (1990).
43. D. Poilblanc, E. Gagliano, S. Bacci and E. Dagotto, Phys. Rev. B, **43** 10970 (1991).
44. H. J. Schulz, T. A. L. Ziman, Europhys. Lett. **18**, 355 (1992). T. Einarsson and H. J. Schulz, Phys. Rev. B **51**, 6151 (1995).  
H. J. Schulz, T. A. L. Ziman, D. Poilblanc, J. Physique I **6**, 675 (1996).
45. S. Chakravarty, B. I. Halperin and D. R. Nelson, Phys. Rev. B **39**, 2344 (1989). H. Neuberger and T. Ziman, Phys. Rev. B **39**, 2608 (1989).  
D. Fisher, Phys. Rev. B **39**, 11783 (1989). T. Einarsson and H. Johannesson, Phys. Rev. B **43**, 5867 (1991). P. Hasenfratz and F. Niedermayer, Z. Phys. B. Condens. Matter **92**, 91 (1993).
46. A. W. Sandvik, Phys. Rev. B **56**, 11678 (1997).
47. S. Sorella, Phys. Rev. Lett. **80**, 4558 (1998).
48. S. Sorella, Phys. Rev. B **64**, 024512 (2001).
49. S. White, Phys. Rev. Lett. **69**, 2863 (1992).
50. S. White, Phys. Rev. B **48**, 10345 (1993).
51. T. Giamarchi and C. Lhuillier, Phys. Rev. B **43**, 12943 (1991).
52. B. Shastry and B. Sutherland, Phys. Rev. Lett. **47**, 964 (1981).
53. F. Haldane, Phys. Rev. B **25**, 4925 (1982).
54. I. Affleck, J. Phys. Cond. Matt. **1**, 3047 (1989).
55. H. Yokoyama and Y. Saiga, J. Phys. Soc. Jpn. **66**, 3617 (1997).
56. T. Nakamura and S. Takada, Phys. Rev. B **55**, 14413 (1997).
57. D. Augier, E. Sorensen, J. Riera, and D. Poilblanc, Phys. Rev. B **60**, 1075 (1999).
58. E. Dagotto and T. M. Rice, Science **271**, 618 (1996).
59. A. A. Nersesyan and A. M. Tsvelik, Phys. Rev. Lett. **78**, 3939 (1997).
60. A. K. Kolezhuk and H.-J. Mikeska, Int. J. Mod. Phys. B **12**, 2325 (1998).  
Phys. Rev. Lett. **80**, 2709 (1998). Phys. Rev. B **56**, 11380 (1997).
61. I. Affleck, T. Kennedy, E. Lieb, and H. Tasaki, Phys. Rev. Lett. **59**, 799 (1987).

62. I. Affleck, T. Kennedy, E. H. Lieb, and H. Tasaki, *Commun. Math. Phys.* **115**, 477 (1988).
63. M. den Nijs and K. Rommelse, *Phys. Rev. B* **40**, 4709 (1989).
64. T. Kennedy and H. Tasaki, *Phys. Rev. B* **45**, 304 (1992).
65. T. Jolicœur, private communication.
66. K. Hida, *J. Phys. Soc. Jpn.* **69**, 4003 (2000).
67. Y. Yamashita and K. Ueda, *Phys. Rev. Lett.* **85**, 4960 (2000).
68. N. Katoh and M. Imada, *J. Phys. Soc. Jpn.* **63**, 4529 (1994). M. Troyer, H. Tsunetsugu, and D. Wuertz, *Phys. Rev. B* **50**, 13515 (1994). S. Taniguchi *et al.*, *J. Phys. Soc. Jpn.* **64**, 2758 (1995). K. Kodama *et al.*, *J. Phys. Soc. Jpn.* **65**, 1941 (1996). Y. Fukumoto and A. Oguchi, *J. Phys. Soc. Jpn.* **65**, 1440 (1996). K. Kodama *et al.*, *J. Phys. Soc. Jpn.* **66**, 793 (1997). T. Miyasaki and D. Yoshioka, *J. Phys. Soc. Jpn.* **65**, 2370 (1996). T. Ohama, H. Yasuoka, M. Isobe, and Y. Ueda, *J. Phys. Soc. Jpn.* **66**, 23 (1997).
69. K. Ueda, H. Kontani, M. Sigrist, and P. A. Lee, *Phys. Rev. Lett.* **76**, 1932 (1996).
70. M. Albrecht and F. Mila, *Phys. Rev. B* **53**, 2945 (1996).
71. M. Troyer, H. Kontani, and K. Ueda, *Phys. Rev. Lett.* **76**, 3822 (1996).
72. S. Sachdev and N. Read, *Phys. Rev. Lett.* **77**, 4800 (1996).
73. O. A. Starykh *et al.*, *Phys. Rev. Lett.* **77**, 2558 (1996).
74. Zheng Weihong *et al.*, *Phys. Rev. B* **55**, 11377 (1997).
75. H. Kageyama *et al.*, *Phys. Rev. Lett.* **82**, 3168 (1999).
76. H. Nojiri *et al.*, *J. Phys. Soc. Jpn.* **68**, 2906 (1999).
77. S. Miyahara and K. Ueda, *Phys. Rev. Lett.* **82**, 3701 (1999).
78. H. Kageyama *et al.*, *Phys. Rev. Lett.* **84**, 5876 (2000).
79. A. Koga and N. Kawakami, *Phys. Rev. Lett.* **84**, 4461 (2000).
80. E. Müller-Hartmann, R. R. P. Singh, C. Knetter, and G. S. Uhrig, *Phys. Rev. Lett.* **84**, 1808 (2000).
81. K. Totsuka, S. Miyahara, and K. Ueda, *Phys. Rev. Lett.* **86**, 520 (2001).
82. A. Läuchli, S. Wessel, and M. Sigrist, *Phys. Rev. B* **66**, 014401 (2002).
83. K. Kodama *et al.*, *Science* **298**, 395 (2002).
84. S. Miyahara and K. Ueda, *J. Phys.: Condens. Matter* **15**, R327-R366 (2003).
85. B. Shastry and B. Sutherland, *Physica B (Amsterdam)* **108**, 1069 (1981).
86. O. Cepas, T. Ziman, Proceedings of the conference in Fukuoka, Nov. 2001, to appear in Fukuoka University Press [cond-mat/0207191]. O. Cepas, T. Sakai, T. Ziman, *Progr. Theor. Phys. Suppl.* **145**, 43 (2002).
87. W. Zheng, J. Oitmaa, and C. J. Hamer *Phys. Rev. B* **65**, 014408 (2002).
88. M. Albrecht and F. Mila, *Europhys. Lett.* **34**, 145 (1996).
89. C. H. Chung, J. B. Marston, and S. Sachdev, *Phys. Rev. B* **64**, 134407 (2001).
90. Y. Fukumoto and A. Oguchi, *J. Phys. Soc. Jpn.* **68**, 3655 (1999).
91. T. Momoi and K. Totsuka, *Phys. Rev. B* **61**, 3231 (2000).
92. T. Momoi and K. Totsuka, *Phys. Rev. B* **62**, 15067 (2000).
93. S. Miyahara and K. Ueda, *Phys. Rev. B* **61**, 3417 (2000).
94. G. Misguich, T. Jolicœur, and S. M. Girvin, *Phys. Rev. Lett.* **87**, 097203 (2001).

95. C. Lhuillier and G. Misguich, in *High Magnetic Fields*, edited by C. Berthier, L. Levy, and G. Martinez (Springer, Berlin, 2002), pp. 161–190, [cond-mat/0109146].
96. P. W. Leung and N. Lam, Phys. Rev. B **53**, 2213 (1996).
97. J.-B. Fouet, P. Sindzingre, and C. Lhuillier, Eur. Phys. J. B **20**, 241 (2001).
98. B. Canals, Phys. Rev. B **65**, 184408 (2002).
99. J.-B. Fouet, M. Mambrini, P. Sindzingre, and C. Lhuillier, Phys. Rev. B **67**, 054411 (2003).
100. P. Sindzingre, J. B. Fouet, and C. Lhuillier, Phys. Rev. B **66**, 174424 (2002).
101. W. Brenig and A. Honecker, Phys. Rev. B **65**, 140407R (2002).
102. E. Berg, E. Altman, and A. Auerbach, Phys. Rev. Lett. **90**, 147204 (2003).
103. O. Tchernyshyov, O. A. Starykh, R. Moessner and A. G. Abanov, Phys. Rev. B **68**, 144422 (2003).
104. R. Moessner, Oleg Tchernyshyov and S. L. Sondhi, cond-mat/0106286.
105. S. Palmer and J. .T. Chalker, Phys. Rev. B **64**, 094412 (2002).
106. R. Moessner and J. T. Chalker, Phys. Rev. B **58**, 12049 (1998).
107. R. Moessner and J. T. Chalker, Phys. Rev. Lett. **80**, 2929 (1998).
108. O. A. Petrenko and D. McK. Paul, Phys. Rev. B **63**, 024409 (2001).
109. Hikaru Kawamura and Takuya Arimori, Phys. Rev. Lett. **88**, 077202 (2002)
110. C. L. Henley, Can. J. Phys. (Canada) **79**, 1307 (2001). [cond-mat/0009130]
111. J.-B. Fouet, Ph.D. thesis, Université Cergy Pontoise, 2003.
112. M. P. Gelfand *et al.*, Phys. Rev. Lett. **77**, 2794 (1996).
113. F. Becca and F. Mila, Phys. Rev. Lett. **89**, 037204 (2002).
114. G. Misguich, C. Lhuillier, B. Bernu and C. Waldtmann, Phys. Rev. B **60**, 1064 (1999).
115. I. Affleck, Phys. Rev. Lett. **54**, 966 (1985).
116. I. Affleck and J. Marston, Phys. Rev. B **37**, 3774 (1988).
117. D. Arovas and A. Auerbach, Phys. Rev. B **38**, 316 (1988).
118. N. Read and S. Sachdev, Phys. Rev. Lett. **62**, 1694 (1989).
119. N. Read and S. Sachdev, Phys. Rev. B **42**, 4568 (1990).
120. N. Read and S. Sachdev, Phys. Rev. Lett. **66**, 1773 (1991).
121. S. Sachdev and N. Read, Int. J. Mod. Phys. **5**, 219 (1991).
122. S. Sachdev in *Low Dimensional Quantum Field Theories for Condensed Matter Physicists* edited by Y. Lu, S. Lundqvist, and G. Morandi, World Scientific, Singapore, 1995. cond-mat/9303014.
123. N. Read and S. Sachdev, Nucl. Phys. B **316**, 609 (1989).
124. D. Rokhsar, Phys. Rev. B **42**, 2526 (1991).
125. K. G. Wilson, Phys. Rev. D **10**, 2445 (1974).
126. R. Balian, J. M. Drouffe, and C. Itzykson, Phys. Rev. D **10**, 3376 (1974), Phys. Rev. D **11**, 2098 (1975), Phys. Rev. D **11**, 2098 (1975).
127. D. P. Arovas and A. Auerbach, Phys. Rev. B **38**, 316 (1988). A. Auerbach and D. P. Arovas, Phys. Rev. Lett. **61**, 617 (1988). J. E. Hirsch and S. Tang, Phys. Rev. B **39**, 2850 (1989).
128. H. A. Ceccatto, C. J. Gazza, and A. E. Trumper, Phys. Rev. B **47**, 12329 (1993). A. E. Trumper, L. O. Manuel, C. J. Gazza, and H. A. Ceccatto Phys. Rev. Lett. **78**, 2216 (1997).

129. We thank O. Tchernyshyov for pointing us this physical interpretation of the  $U(1)$  flux.
130. S. Sachdev, Phys. Rev. B **45**, 12377 (1992).
131. C. H. Chung and J. B. Marston and Ross H. McKenzie, J. Phys.: Condens. Matter **13**, 5159 (2001).
132. F. D. M. Haldane, Phys. Lett. **93A**, 464 (1983);  
Phys. Rev. Lett. **50**, 1153 (1983).
133. F. D. M. Haldane, Phys. Rev. Lett. **61**, 1029 (1988).
134. X. G. Wen and A. Zee, Phys. Rev. Lett. **61**, 1025 (1988). E. Fradkin and M. Stone, Phys. Rev. B **38**, 7215 (1988). T. Dombre and N. Read, Phys. Rev. B **38**, 7181 (1988).
135. K. Harada, N. Kawashima, and M. Troyer, Phys. Rev. Lett. **90**, 117203 (2003).
136. E. Fradkin and S. H. Shenker, Phys. Rev. D **19**, 3682 (1979).
137. P. W. Kasteleyn, Physica **27**, 1209 (1961).
138. M. E. Fisher, Phys. Rev. **124**, 1664 (1961).
139. P. W. Kasteleyn, J. of Math. Phys. **4**, 287 (1963).
140. R. Moessner, S. L. Sondhi, E. Fradkin, Phys. Rev. B **65**, 024504 (2002).
141. G. Misguich, D. Serban, V. Pasquier, Phys. Rev. Lett. **89**, 137202 (2002).
142. R. Moessner, S. L. Sondhi, Phys. Rev. B **68**, 054405 (2003).
143. D. S. Rokhsar and S. A. Kivelson, Phys. Rev. Lett. **61**, 2376 (1988).
144. R. Moessner and S. L. Sondhi, Phys. Rev. Lett. **86**, 1881 (2001).
145. R. Moessner, S. L. Sondhi, and P. Chandra, Phys. Rev. Lett. **84**, 4457 (2000).
146. B. Sutherland, Phys. Rev. B **37**, 3786 (1988).
147. J. B. Marston, C. Zeng, J. Appl. Phys. **69**, 5962 (1991).
148. P. W. Leung, K. C. Chiu and K. J. Runge, Phys. Rev. B **54**, 12938 (1996).
149. M. E. Fisher and J. Stephenson Phys. Rev. **132**, 1411 (1963).
150. R. Moessner and S. L. Sondhi, Phys. Rev. B **68**, 184512 (2003). See Appendix B concerning the square-lattice QDM.
151. R. Moessner, S. L. Sondhi and P. Chandra, Phys. Rev. B **64**, 144416 (2001).
152. D. A. Huse, W. Krauth, R. Moessner and S. L. Sondhi, Phys. Rev. Lett. **91**, 167004 (2003) and references therein.
153. L. S. Levitov, Phys. Rev. Lett. **64**, 92 (1990),  
C. L. Henley, J. Stat. Phys. **89**, 483 (1997).
154. P. Fendley, R. Moessner and S. L. Sondhi, Phys. Rev. B **66**, 214513 (2002).
155. A. Ioselevich, D. A. Ivanov and M. V. Feigelman, Phys. Rev. B **66**, 174405 (2002).
156. L. B. Ioffe, M. V. Feigel'man, A. Ioselevich, D. Ivanov, M. Troyer, G. Blatter, Nature **415**, 503 (2002).
157. G. Misguich, C. Lhuillier, M. Mambrini, P. Sindzingre, Eur. Phys. J. B **26**, 167 (2002).
158. X. G. Wen, Phys. Rev. B **44**, 2664 (1991).
159. S. Kivelson, Phys. Rev. B **39**, 259 (1989).
160. N. Read and B. Chakraborty, Phys. Rev. B **40**, 7133 (1989).
161. T. Senthil and M. P. A. Fisher, Phys. Rev. B **62**, 7850 (2000).

162. T. Senthil and M. P. A. Fisher, Phys. Rev. Lett. **86**, 292 (2001); Phys. Rev. B **63**, 134521 (2001).
163. R. P. Feynman, Phys. Rev. **90**, 1116 (1952), Phys. Rev. **91**, 1291 (1953).
164. V. Elser and C. Zeng, Phys. Rev. B **48**, 13647 (1993).
165. A. J. Phares and F. J. Wunderlich, Nuovo Cimento B **101**, 653 (1988).
166. See §V.E.6 of Ref.<sup>170</sup>
167. This follows from the independence of the arrow variables, see §V.B of Ref.<sup>170</sup>
168. A. M. Polyakov, *Gauge Fields and Strings*, (Harwood Academic, New York, 1987).
169. J. B. Kogut, Rev. Mod. Phys. **51**, 659 (1979).
170. G. Misguich, D. Serban and V. Pasquier, Phys. Rev. B **67**, 214413 (2003).
171. C. Zeng and V. Elser, Phys. Rev. B **51**, 8318 (1995).
172. D. J. Thouless, Proc. Phys. Soc. London **86**, 893 (1965).
173. M. Roger, J. H. Hetherington, and J. M. Delrieu, Rev. Mod. Phys. **55**, 1 (1983).
174. M. C. Cross and D. S. Fisher, Rev. Mod. Phys. **57**, 881 (1985).
175. D. S. Greywall and P. A. Busch, Phys. Rev. Lett. **62**, 1868 (1989).  
D. S. Greywall, Phys. Rev. B **41**, 1842 (1990).
176. H. Godfrin and R. E. Rapp, Adv. Phys. **44**, 113 (1995).
177. M. Roger, Phys. Rev. B **30**, 6432 (1984).
178. M. Roger, C. Bäuerle, Yu. M. Bunkov, A.-S. Chen, and H. Godfrin, Phys. Rev. Lett. **80**, 1308 (1998).
179. D. M. Ceperley and G. Jacucci, Phys. Rev. Lett. **58**, 1648 (1987).
180. B. Bernu, D. Ceperley, and C. Lhuillier, J. Low Temp. Phys. **89**, 589 (1992).
181. D. M. Ceperley, Rev. Mod. Phys. **67**, 279 (1995).
182. B. Bernu and D. Ceperley, in *Quantum Monte Carlo Methods in Physics and Chemistry*, edited by M. P. Nightingale and C. J. Umrigar (Kluwer, Dordrecht, The Netherlands, 1999).
183. H. Ashizawa and D. S. Hirashima, Phys. Rev. B **62**, 9413 (2000).
184. J. M. Delrieu, M. Roger, J. H. Hetherington, J. Low Temp. Phys. **40**, 71 (1980).
185. H. Franco, R. E. Rapp and H. Godfrin, Phys. Rev. Lett. **57**, 1161 (1986).
186. G. Misguich, B. Bernu, C. Lhuillier, and C. Waldtmann, Phys. Rev. Lett. **81**, 1098 (1998).
187. W. LiMing, G. Misguich, P. Sindzingre, and C. Lhuillier, Phys. Rev. B **62**, 6372 (2000).
188. K. Ishida, M. Morishita, K. Yawata, and H. Fukuyama, Phys. Rev. Lett. **79**, 3451 (1997).
189. E. Collin *et al.*, Phys. Rev. Lett. **86**, 2447 (2001).
190. M. Katano and D. S. Hirashima, Phys. Rev. B **62**, 2573 (2000).
191. D. S. Hirashima and K. Kubo, Phys. Rev. B **63**, 125340 (2001).
192. B. Bernu, L. Candido, and D. M. Ceperley Phys. Rev. Lett. **86**, 870 (2001).
193. T. Okamoto and S. Kawaji, Phys. Rev. B **57**, 9097 (1998).
194. M. Roger and J. M. Delrieu, Phys. Rev. B **39**, 2299 (1989).
195. S. Sugai *et al.*, Phys. Rev. B **42**, 1045 (1990).

196. R. Coldea *et al.*, Phys. Rev. Lett. **86**, 5377 (2001).
197. E. Müller-Hartmann and A. Reischl, Eur. Phys. J. B **28**, 173 (2002).
198. A. A. Katanin, and A. P. Kampf, Phys. Rev. B **67**, 100404R (2003).
199. M. Matsuda *et al.*, Phys. Rev. B **62**, 8903 (2000).
200. S. Brehmer *et al.*, Phys. Rev. B **60**, 329 (1999).
201. K. P. Schmidt, C. Knetter and G. S. Uhrig, Europhys. Lett. **56**, 877 (2001).
202. A. Göling *et al.*, Phys. Rev. B **67**, 052403 (2003).
203. M. Müller, T. Vekua, and H.-J. Mikeska, Phys. Rev. B **66**, 134423 (2002).
204. T. Hikihara, T. Momoi, and X. Hu, Phys. Rev. Lett. **90**, 087204 (2003).
205. A. Läuchli, G. Schmid, and M. Troyer, Phys. Rev. B **67**, 100409R (2003).
206. Y. Honda and T. Horiguchi, cond-mat/0106426.
207. K. Hijii and K. Nomura Phys. Rev. B **65**, 104413 (2002).
208. T. Momoi, T. Hikihara, M. Nakamura, Xiao Hu, Phys. Rev. B **67**, 174410 (2003).
209. A. Läuchli, talk given at the *Highly Frustrated Magnetism 2003* conference, Grenoble, France (August 2003).
210. K. Kubo and T. Momoi, Z. Phys. B **103**, 485 (1997).
211. T. Momoi, K. Kubo, and K. Niki, Phys. Rev. Lett. **79**, 2081 (1997).
212. G. Misguich, B. Bernu, and C. Lhuillier, J. Low Temp. Phys. **110**, 327 (1998).
213. K. Kubo, H. Sakamoto, T. Momoi, and K. Niki, J. Low Temp. Phys. **111**, 583 (1998).
214. A 16- and a 32-site triangular lattices which do not frustrate the staggered VBC were investigated. In both cases some of the irreducible representations of the space group required to break the appropriate lattice symmetries are very high in the spectrum. C. Lhuillier and G. Misguich (unpublished).
215. E. H. Lieb, T. D. Schultz, D. C. Mattis., Ann. Phys. (N.Y.) **16**, 407 (1961).
216. I. Affleck and E. Lieb, Lett. Math. Phys. **12**, 57 (1986).
217. M. Oshikawa, Phys. Rev. Lett. **84**, 1535 (2000).
218. M. B. Hastings, Phys. Rev. B **69**, 104431 (2004).
219. M. Oshikawa, Phys. Rev. Lett. **90**, 236401 (2003).
220. A. A. Nersesyan, A. O. Gogolin, and F. H. L. Essler, Phys. Rev. Lett. **81**, 910 (1998).
221. P. Azaria *et al.*, Phys. Rev. Lett. **81**, 1694 (1998).
222. V. J. Emery, E. Fradkin, S. A. Kivelson and T. C. Lubensky, Phys. Rev. Lett. **85**, 2160 (2000).
223. M. Bocquet, F. Essler, A. M. Tsvelik and A. O. Gogolin, Phys. Rev. B **64**, 094425 (2001), M. Bocquet, Phys. Rev. B **65**, 1884415 (2001).
224. A. Vishwanath and D. Carpentier, Phys. Rev. Lett. **86**, 676 (2001).
225. S. Sachdev and K. Park, Annals of Physics (N.Y.), **58**, 298 (2002).
226. O. A. Starykh and R. R. P. Singh and G. C. Levine, Phys. Rev. Lett. **88**, 167203 (2002).
227. R. Coldea, D. A. Tennant, A. M. Tsvelik, and Z. Tyliczynski, Phys. Rev. Lett. **86**, 1335 (2001).
228. A. Kitaev, Annals Phys. **303**, 2 (2003). [quant-ph/9707021]
229. C. Nayak and K. Shtengel, Phys. Rev. B **64**, 064422 (2001).

230. L. Balents, M. P. A. Fisher, and S. M. Girvin, Phys. Rev. B **65**, 224412 (2002).
231. A. Paramekanti, L. Balents, and M. P. A. Fisher Phys. Rev. B **66**, 054526 (2002).
232. A. W. Sandvik, S. Daul, R. R. P. Singh, and D. J. Scalapino, Phys. Rev. Lett. **89**, 247201 (2002).
233. T. Senthil and O. Motrunich, Phys. Rev. B **66**, 205104 (2002).
234. L. Pauling, in *The nature of the chemical bond* (Cornell University Press, Ithaca, 1938).
235. K. Kano and S. Naya, Prog. in Theor. Phys. **10**, 158 (1953).
236. D. Huse and A. Rutenberg, Phys. Rev. B **45**, 7536 (1992).
237. R. Moessner and S. L. Sondhi, Phys. Rev. B **63**, 224401 (2001).
238. J. Chalker, P. C. W. Holdsworth, and E. F. Shender, Phys. Rev. Lett. **68**, 855 (1992).
239. R. J. Baxter, J. Math. Phys. **11**, 784 (1970).
240. I. Richter, P. Chandra, and P. Coleman, Phys. Rev. B **47**, 15342 (1993).
241. J. Reimers and A. Berlinsky, Phys. Rev. B **48**, 9539 (1993).
242. M. Elhajal, Ph. D. thesis, Université Joseph Fourier. Grenoble. France, 2002.
243. M. Elhajal, B. Canals, and C. Lacroix, Phys. Rev. B **66**, 014422 (2002).
244. A. Keren, Phys. Rev. Lett. **72**, 3254 (1994).
245. V. Elser, Phys. Rev. Lett. **62**, 2405 (1989).
246. J. Chalker and J. Eastmond, Phys. Rev. B **46**, 14201 (1992).
247. S. Sachdev, Phys. Rev. B **45**, 12377 (1992).
248. P. Leung and V. Elser, Phys. Rev. B **47**, 5459 (1993).
249. P. Lecheminant *et al.*, Phys. Rev. B **56**, 2521 (1997).
250. C. Waldtmann *et al.*, Eur. Phys. J. B **2**, 501 (1998).
251. F. Mila, Phys. Rev. Lett. **81**, 2356 (1998).
252. P. Sindzingre *et al.*, Phys. Rev. Lett. **84**, 2953 (2000).
253. M. Mambrini and F. Mila, Eur. Phys. J. B **17**, 651 (2001).
254. S. Dommange, M. Mambrini, B. Normand and F. Mila, Phys. Rev. B **68**, 224416 (2003).
255. C. Zeng and V. Elser, Phys. Rev. B **42**, 8436 (1990).
256. R. Singh and D. Huse, Phys. Rev. Lett. **68**, 1766 (1992).
257. K. Hida, J. Phys. Soc. Jpn. **70**, 3673 (2001).
258. D. C. Cabra, M. D. Grynberg, P. C. W. Holdsworth, P. Pujol, Phys. Rev. B **65**, 094418 (2002).
259. N. Eltsner and A. P. Young, Phys. Rev. B **50**, 6871 (1994).
260. T. Nakamura and S. Miyashita, Phys. Rev. B **52**, 9174 (1995).
261. P. Tomczak and J. Richter, Phys. Rev. B **54**, 9004 (1996).
262. A. P. Ramirez, B. Hessen, and M. Winkelmann, Phys. Rev. Lett. **84**, 2957 (2000).
263. P. Mendels *et al.*, Phys. Rev. Lett. **85**, 3496 (2000).
264. A. V. Syromyatnikov and S. V. Maleyev, Phys. Rev. B **66**, 132408 (2002).
265. P. Nikolic and T. Senthil, cond-mat/0305189.
266. T. Mondelli *et al.*, Physica B **284**, 1371 (2000).
267. A. Georges, R. Siddhartan and S. Florens, Phys. Rev. Lett. **87**, 277203

- (2001).
- 268. C. Lhuillier and P. Sindzingre, in *Quantum properties of Low dimensional antiferromagnets*, edited by Y. Ajiro and J. P. Boucher (Kyushu University Press, Fukuoka, Japan, 2002), p. 111.
  - 269. S. Sachdev and M. Vojta, Proceedings of the XIII International Congress on Mathematical Physics, July 2000, London. A. Fokas, A. Grigoryan, T. Kibble, and B. Zegarlinski eds, International Press, Boston (2001) [cond-mat/0009202].
  - 270. Y. Uemura *et al.*, Phys. Rev. Lett. **73**, 3306 (1994).
  - 271. A. Ramirez, G. P. Espinosa, and A. S. Cooper, Phys. Rev. Lett. **64**, 2070 (1990).
  - 272. S.-H. Lee *et al.*, Europhys. Lett. **35**, 127 (1996).
  - 273. A. Keren *et al.*, Phys. Rev. B **53**, 6451 (1996).
  - 274. A. S. Wills *et al.*, Europhys. Lett. **42**, 325 (1998).
  - 275. K. Awaga *et al.*, Phys. Rev. B **49**, 3975 (1994).
  - 276. N. Wada *et al.*, J. Phys. Soc. Jpn. **66**, 961 (1997).
  - 277. I. Watanabe *et al.*, Phys. Rev. B **58**, 2438 (1998).
  - 278. B. Canals and C. Lacroix, Phys. Rev. Lett. **80**, 2933 (1998).
  - 279. A. B. Harris, A. J. Berlinsky and C. Bruder, J. Appl. Phys. **69**, 5200 (1991).
  - 280. H. Tsunetsugu, J. Phys. Soc. Jpn. **70**, 640 (2001).
  - 281. H. Tsunetsugu, Phys. Rev. B **65**, 024415 (2002).
  - 282. J. V. Delft and C. L. Henley, Phys. Rev. Lett. **69**, 3236 (1992), Phys. Rev. B **48**, 965 (1993).
  - 283. S. Sachdev, Annals Phys. **303**, 226 (2003) [cond-mat/0211027] and Rev. Mod. Phys. **75**, 913 (2003).
  - 284. X. Wen, F. Wilczek, and A. Zee, Phys. Rev. B **39**, 11413 (1989).
  - 285. V. Kalmeyer and R. Laughlin, Phys. Rev. Lett. **59**, 2095 (1987), Phys. Rev. B **39**, 11879 (1989).
  - 286. K. Yang, L. Warman, and S. M. Girvin, Phys. Rev. Lett. **70**, 2641 (1993).

Table 5.2. Different phases encountered in  $SU(2)$ -symmetric frustrated models in 2D

Phase	$2S/\text{cell}$	Order	Degeneracy	Broken sym.	Excitations	Thermo.	Examples
Néel AF p-sublattice	any	spin-spin LRO	$\mathcal{O}(N^P)$	$SU(2)$ Translations Point group	Gapless magnons (spin waves)	$C_v \sim T^2$ $\chi \sim cst$	Spin- $\frac{1}{2}$ triangular Heisenberg AF
VBC (§5.3) (spontaneous)	odd	singlet-singlet LRO coll. spin-spin SRO	$> 1$	Translations Point group	Gapped magnons	$C_v$ and $\chi$ activated	Honeycomb $J_1-J_2$ Checkerboard Square $J_1-J_2$ ?
VBC (§5.3) (explicit)	even	None	1	None	Gapped magnons	$C_v$ and $\chi$ activated	$\text{SrCu}_2(\text{BO}_3)_2$ $\text{CaV}_4\text{O}_9$
VBS (§5.3.3)	even	“String” LRO	1	None	Gapped magnons Edge excitations	$C_v$ and $\chi$ activated	AKLT Hamiltonians $S = 1$ kagome AF ?
RVB SL (§5.5 §5.5.6, §5.6.4)	odd	Topological non-coll. SRO	4 (torus)	None	Gapped spinons Gapped visons	$C_v$ and $\chi$ activated	MSE (§5.6) QDM on triangular and kagome lattices
Kagome (§5.7) Heisenberg AF	3	None ?	$\sim 1.15N$ ?	None ?	Gapped triplets ? Gapless singlets	$C_v \sim T^\alpha$ ? $\chi$ activated	

This table summarizes the properties of some important phases encountered in 2D frustrated magnets.  $S$  is the value of the spin on each site. “Order” refers to the nature of the long-ranged correlations (if any). The ground-state degeneracy in the limit of an infinite system (with periodic boundary conditions) is indicated in the fourth column, except for RVB SL it is related to the spontaneously broken symmetries mentioned in the next column. Elementary excitations and the low-temperature behavior of the specific heat ( $C_v$ ) and uniform susceptibility ( $\chi$ ) are given in column six. The last column gives some examples of theoretical or experimental realizations of these phases. The six families of systems presented here of course do not exhaust all possibilities. The results which are plausible but still debated (concerning the spin- $\frac{1}{2}$  Heisenberg antiferromagnet on the kagome lattice in particular) are indicated by question marks. Some authors classify all the systems with gapped excitations in a loose category of “quantum disordered systems”, alluding to the absence of Néel long-ranged order. It is a rather unhappy appellation for VBC (which obviously have some order) and in fact for most of the quantum systems with a gap. In classical statistical physics “disorder” is associated to entropy, which is not the case in these gapped systems at  $T = 0$ .

# CHAPTER 6

## ONE-DIMENSIONAL SPIN LIQUIDS

P. Lecheminant

*Laboratoire de Physique Théorique et Modélisation, CNRS UMR 8089,  
Université de Cergy-Pontoise, 5 mail Gay-Lussac, Neuville sur Oise,  
95301 Cergy-Pontoise Cedex, France*

This chapter is intended as a brief overview of some of the zero-temperature quantum spin liquid phases with unbroken SU(2) spin symmetry that have been found in one dimension. The main characteristics of these phases are discussed by means of the bosonization approach. A special emphasis is laid on the interplay between frustration and quantum fluctuations in one dimension.

### 6.1. Introduction

A central issue in the study of strongly correlated systems is the classification of all possible Mott insulating phases at zero temperature. The general strategy for describing the possible phases associated with the spin degrees of freedom (the so-called “quantum magnetism”) of Mott insulators consists of analysing localized spin models such as the antiferromagnetic (AF) Heisenberg model:

$$\mathcal{H} = J \sum_{\langle i,j \rangle} \vec{S}_i \cdot \vec{S}_j + \dots, \quad (1)$$

where  $\vec{S}_i$  are quantum spin- $S$  operators on sites  $i$  of a lattice, and the sum  $\langle i,j \rangle$  is over the nearest neighbor sites with an antiferromagnetic exchange ( $J > 0$ ); the ellipsis represents additional terms like second-neighbor competing exchange interaction or ring exchange that can be eventually added to the Heisenberg Hamiltonian (1). Generically, the ground state of the model (1) without these additional terms displays long-range Néel ordering ( $\langle \vec{S}_i \rangle \neq \vec{0}$ ) which breaks spontaneously the SU(2) symmetry of the

lattice Hamiltonian (1). The low-energy excitations are gapless spin-waves (i.e. magnons) as expected when a continuous symmetry is spontaneously broken.

A central focus of quantum magnetism over the years, starting from the proposal made by Anderson<sup>1</sup>, has been the search for a spin liquid behavior i.e. a phase with no magnetic long-range Néel order. Spin liquids phases are expected to be stabilized in low dimensions or in presence of frustration, i.e. in situations where quantum fluctuations can strongly suppress magnetism. It gives rise to rich physics with exotic low-energy excitations which require in most cases the use of non-perturbative techniques to fully determine its properties. In the two-dimensional case, different spin liquid phases have been found and display bond ordering or topological ordering (for a review see for instance Refs. <sup>2,3</sup> and references therein). An interesting attempt to develop a systematic classification of two-dimensional spin liquids has also recently been explored by Wen<sup>4</sup>.

In one dimension, the quantum analog of the Mermin-Wagner<sup>5</sup> theorem shows that quantum fluctuations always disorder the ground state in systems with a continuous symmetry. The generic situation in one dimension is thus to have a spin liquid phase. The one dimensional case is also extremely favorable since several non-perturbative techniques are available to fully characterize the physical properties of different spin liquids. These powerful techniques include integrability, conformal field theory (CFT)<sup>6,7</sup>, the bosonization approach<sup>8,9,10</sup>, and numerical calculations such as the density matrix renormalization group (DMRG) approach<sup>11</sup>. The determination of the properties of spin liquids is not a purely academic problem since many physical realizations of spin chains have been synthesized over the years. The reader may consult for instance the recent reviews<sup>12,13</sup> on experiments in quasi-one dimensional spin systems.

The main questions in the study of one-dimensional spin liquids are in order: What are the different spin liquid phases available at zero-temperature? What are the different physical properties of these spin liquids? What is the nature of the quantum phase transition<sup>14</sup> between two different spin liquids? Last but not least, the problem of dimensional crossover, i.e. the fate of the spin liquid as the two dimensional case is reached is also a central topic. In particular, is it possible to stabilize a spin liquid phase in  $d = 2$  starting from the  $d = 1$  case?

In this work, we shall mainly be concerned with the two first questions for spin liquids with unbroken SU(2) spin symmetry. Using the bosonization approach, we shall discuss some of the physical properties of spin liquids

that have been found in spin chains, spin ladders with or without frustration. An important question related to this problem is how can one classify all these 1D spin liquid phases at  $T = 0$ ? A first distinction concerns the existence or absence of a spectral gap in the model. In a gapless system (critical spin liquid), one has quasi-long range Néel order. The leading asymptotics of spin-spin correlation functions display a power law behavior with an exponent characterized by a well defined underlying CFT<sup>15</sup>. In contrast, in a spin liquid phase with a spectral gap, spin-spin correlation functions have an exponential decay with the distance due to the existence of a finite correlation length  $\xi$ :  $\langle \vec{S}_i \cdot \vec{S}_j \rangle \sim \exp(-|i - j|/\xi)$ . At this point, it is worth stressing that two gapful spin liquid phases sharing the same thermodynamic properties (typically a thermal activation law at low T) may display very different behaviors in other physical quantities of interest such as, for instance, dynamical or optical properties. It is thus necessary to make a scrutiny analysis of the properties of the phase before elaborating a complete classification. Let us first consider the ground state of a gapful spin liquid phase. A (discrete) symmetry might be spontaneously broken in the ground state resulting on a ground-state degeneracy. The spin liquid phase may display also an hidden topological order<sup>16</sup> which manifests itself in a ground-state degeneracy which depends on the nature of boundary conditions (BC) used i.e. periodic or open BC. The resulting chain-end (edge) excitations in the open BC case can be observed in the NMR profile of a spin chain compound doped with non-magnetic impurities like Zn or Mg. Another important distinction between two spin liquids relies on the quantum number carried by elementary excitations. The fractionalized or integer nature of this quantum number has crucial consequences in the dynamical structure factor of the system which directly probes the elementary nature of the spin-flip. A sharp spectral peak, characteristic of a well defined  $S = 1$  mode, or a broad (incoherent background) feature in the dynamical structure factor can be seen in inelastic neutron scattering experiments. Finally, an interesting question is the existence or not of bound states in the energy spectrum below the two-particle continuum. Spin liquid phases may then be distinguished at this level which is also an important fact from the experimental point of view since observation of magnetic singlet bound states can be realized through light scattering experiments<sup>13</sup>. This classification is certainly far from being complete but it enables us to distinguish between several spin liquid phases and investigate the nature of the quantum phase transition between them.

This chapter is organized as follows: We present, in Section 2, the dif-

ferent spin liquid phases that occur in unfrustrated spin chains and spin ladders. The main effects of frustration in one-dimensional spin liquids are described in Section 3. In particular, we shall observe that frustration plays its trick by allowing deconfined spinons (carrying fractional  $S = 1/2$  quantum number) as elementary excitations and it provides a non-trivial source of incommensurability. Finally, our concluding remarks are given in Section 4.

## 6.2. Unfrustrated spin chains

The paradigmatic model to investigate the properties of 1D quantum magnets in absence of frustration is the AF Heisenberg spin chain given by the Hamiltonian:

$$\mathcal{H} = J \sum_i \vec{S}_i \cdot \vec{S}_{i+1}, \quad (2)$$

where  $\vec{S}_i$  is a spin- $S$  operator at the  $i$ th site of the chain and the exchange interaction is antiferromagnetic:  $J > 0$ . In the classical limit, the model displays Néel long-range order:  $\vec{S}_i \sim S(-1)^i \vec{n}$ ,  $\vec{n}$  being an unit vector with an arbitrary fixed orientation in spin space. This solution breaks the SU(2) symmetry of the model (2) down to U(1). Corresponding to this symmetry breaking scheme, there are two Goldstone modes which propagate with the same velocity (Lorentz invariance in the low-energy limit). In the language of CFT<sup>7</sup>, it corresponds to a field theory with central charge  $c = 2$  ( $c = 1$  being the central charge of a free massless boson field). Physically, these Goldstone modes are nothing but a doublet of gapless spin waves modes associated with slow modulations in the orientation of the vector  $\vec{n}$  which represents the order parameter of the Néel magnetic structure. In the quantum case, this Néel solution in one dimension is destabilized by strong quantum fluctuations no matter how large  $S$  is: a spin liquid phase is formed.

### 6.2.1. Spin-1/2 Heisenberg chain

In the ultra quantum limit i.e.  $S = 1/2$ , the nature of the spin liquid phase can be fully determined since the model (2) is exactly solvable for  $S = 1/2$  by means of the Bethe ansatz approach. In particular, starting with Bethe's seminal work<sup>17</sup>, a host of exact results have been obtained over the years for ground state properties<sup>18</sup>, magnetic susceptibility<sup>19</sup>, thermodynamics<sup>20</sup>, excitation spectrum<sup>21,22</sup>, and correlation functions<sup>23</sup>.

The model displays quantum criticality properties which belong to the Wess-Zumino-Novikov-Witten (WZNW)  $\text{su}(2)_1$  universality class<sup>15</sup>. The low-energy limit of the spin-1/2 AF Heisenberg chain (2) is described by the  $\text{su}(2)_1$  WZNW CFT with central charge  $c = 1$  perturbed by marginally irrelevant current-current interaction<sup>15,24</sup>. The resulting Hamiltonian density reads as follows:

$$\mathcal{H}_{\text{eff}} = \frac{2\pi v}{3} \left( \vec{J}_L^2 + \vec{J}_R^2 \right) + \lambda \vec{J}_R \cdot \vec{J}_L, \quad (3)$$

where  $\vec{J}_R$  and  $\vec{J}_L$  are respectively the right and left  $\text{su}(2)_1$  currents which generate the  $\text{su}(2)_1$  WZNW CFT<sup>25</sup>; these currents satisfy the  $\text{su}(2)_1$  Kac-Moody commutation relations:

$$[J_{R,L}^a(x), J_{R,L}^b(y)] = \mp \frac{i\delta^{ab}}{4\pi} \delta'(x-y) + i\epsilon^{abc} J_{R,L}^c(x) \delta(x-y). \quad (4)$$

In Eq. (3),  $v$  is the spin velocity and  $\lambda < 0$  so that the last contribution is a marginally irrelevant term that renormalizes to zero in the far infrared (IR) limit. This perturbation accounts for logarithmic corrections in the spin-spin correlation<sup>26</sup> which is exactly known<sup>27</sup> in the long-distance limit:

$$\langle \vec{S}_0 \cdot \vec{S}_r \rangle \underset{r \gg 1}{\simeq} \frac{(-1)^r}{(2\pi)^{3/2}} \frac{(\ln r)^{1/2}}{r}. \quad (5)$$

The most striking feature of this spin liquid phase stems from the nature of its elementary excitations. They have been elucidated by Faddeev and Takhtajan<sup>22</sup> within the Bethe ansatz approach and consist of fractional  $S = 1/2$  massless excitations called spinons. The lowest excitations are fourthfold degenerate and correspond to a triplet ( $S = 1$ ) and a singlet ( $S = 0$ ). The resulting energy spectrum is a continuum in  $(k, \omega)$  space between a lower boundary (the des Cloizeaux-Pearson dispersion relation<sup>21</sup>)  $\omega_{\text{dcp}} = \pi J |\sin k|/2$  ( $-\pi < k \leq \pi$ ) and an upper boundary  $\omega_u = \pi J |\sin(k/2)|$  (see Fig. 6.1). The central point of the analysis is that this continuum can be interpreted as being made up of two spin-1/2 excitations (spinons) with the dispersion:

$$\omega_{\text{spinon}} = \frac{\pi J}{2} \sin k, \quad (6)$$

with  $0 < k < \pi$ . A spinon has thus a wave-vector restricted to only half of the Brillouin zone. A triplet (or singlet) excitation with momentum  $k$  is then described by two spinons with momenta  $k_1$  and  $k_2$  ( $0 < k_1 \leq k_2 < \pi$ ) such that:  $\omega(k) = \omega_{\text{spinon}}(k_1) + \omega_{\text{spinon}}(k_2)$  with  $k = k_1 + k_2$  (respectively  $k = k_1 + k_2 - 2\pi$ ) if  $0 < k \leq \pi$  (respectively  $-\pi < k < 0$ ). It corresponds

to a two-parameter continuum  $\omega(k) = \pi J \sin(k/2) \cos(k/2 - q_1)$  with  $0 < q_1 < k/2$  for  $0 < k < \pi$  and  $\pi + k < q_1 < \pi + k/2$  for  $-\pi < k < 0$  which identifies with the continuum of the spin-1/2 AF Heisenberg chain.

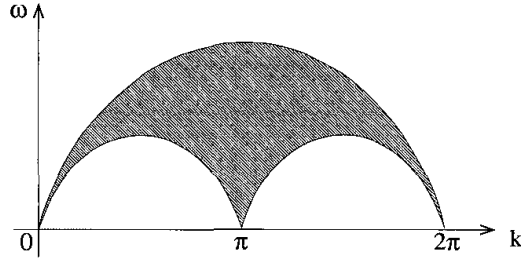


Fig. 6.1. Two-spinon continuum of the spin-1/2 AF Heisenberg chain.

A magnon excitation carrying  $S = 1$  quantum number is thus no longer an elementary excitation in this model but is fractionalized into two spinons. One important experimental signature of these spinons is the absence of any sharp peak in the dynamical susceptibility structure factor since a single spin-flip generates a triplet excitation which is not elementary here but made up of two spinons. The spectral density is then a convolution of the spectral densities of the individual spinons. These spinons have fascinating properties in particular they obey semion statistics intermediate between bosons and fermions<sup>28</sup> as it can be seen by the study of the elementary excitations of the Haldane-Shastry model<sup>29</sup> which belongs to the same universality class as the spin-1/2 AF Heisenberg chain. An heuristic way to describe the spinons is to consider an anisotropic XXZ version of the Heisenberg model (2):

$$\mathcal{H}_{\text{XXZ}} = J_z \sum_i S_i^z S_{i+1}^z + \frac{J_\perp}{2} \sum_i (S_i^+ S_{i+1}^- + S_i^- S_{i+1}^+) . \quad (7)$$

This model is still integrable and the ground state is two-fold degenerate for  $J_z > J_\perp$  as the result of the spontaneous breaking of a discrete  $Z_2$  symmetry. In this regime, a spectral gap is opened and the elementary excitations are massive spinons. A simple way to understand these properties is to consider the Ising limit when  $J_z \gg J_\perp$  where the ground state reduces to the two Néel ordered states:  $\uparrow \downarrow \uparrow \downarrow \uparrow \downarrow \dots$  and  $\downarrow \uparrow \downarrow \uparrow \downarrow \uparrow \dots$ . The elementary excitations are massive kinks which carry  $\Delta S^z = \pm 1/2$  quantum number and interpolate between these two ground states:  $\uparrow \downarrow \uparrow \downarrow \uparrow \times \uparrow \downarrow \uparrow \dots$ . The composite nature of a magnon excitation can then be readily seen by starting from

a ground state and apply a single spin-flip on it to obtain the configuration:  $\uparrow\downarrow\uparrow\downarrow\downarrow\downarrow\uparrow\downarrow\uparrow\downarrow$ . Applying the exchange  $J_{\perp}$  interaction of the model (7) on this state, this magnon excitation with  $\Delta S^z = -1$  is in fact made up of two kinks of the Néel order i.e. two spinons:  $\uparrow\downarrow \times \downarrow\uparrow\downarrow\uparrow\downarrow \times \downarrow\uparrow\downarrow$ . At the transition  $J_z = J_{\perp}$  (isotropic limit), the ground state is disordered by “condensation” of these kinks and the low-lying excitations carrying  $\Delta S^z = \pm 1/2$  are transmuted from gapful kinks to gapless spinons. Magnons are still built as pairs of these spinons and have a gapless energy spectrum.

This remarkable production of two particles from a single spin-flip has been explored in inelastic neutron scattering measurements on quasi-1D compounds that are good experimental realizations of the model (2). The first clear evidence of spinons comes from neutron experiments<sup>30</sup> on  $\text{KCuF}_3$  that found a continuum of magnetic excitations consistent with that expected from unbound spinons pair. The spinon continuum has also been observed in several other realizations of the spin-1/2 AF Heisenberg chain as the copper benzoate  $\text{Cu}(\text{C}_6\text{D}_5\text{COO})_2 \cdot 3\text{D}_2\text{O}$ <sup>31</sup>,  $\text{BaCu}_2\text{Si}_2\text{O}_7$ <sup>32</sup>, and  $\text{Cu}(\text{C}_4\text{H}_4\text{N}_2)(\text{NO}_3)_2$ <sup>33</sup>.

### 6.2.2. Haldane's conjecture

After the elucidation of the elementary excitations of the spin-1/2 AF Heisenberg chain by Faddeev and Takhtajan<sup>22</sup> in the early eighties, a central question of 1D quantum magnetism concerns the stability of the spinons. What is the fate of these exotic excitations upon switching on small deviations from the model (2)? Do these additional terms lead to a confinement of the spinons or do they still remain deconfined?

A simple modification of the spin-1/2 AF Heisenberg chain (2) is not to add perturbations but to change the Hilbert space namely to consider the general spin- $S$  case. The resulting model is no longer integrable and one has to resort to approximate methods to describe its physical properties. This question has lead to one of the most profound result in the field of 1D quantum magnetism: the difference between integer and half-integer spins AF Heisenberg chains predicted by Haldane<sup>34</sup>. Integer spin chains are incompressible spin liquids with a finite gap (the so-called Haldane gap) in the energy spectrum. In that case, the spinons are confined and the elementary excitations of the model are massive (optical)  $S = 1$  magnons. In contrast, for half-integer spins, the model displays quantum criticality with similar universal properties as the  $S = 1/2$  case that are described by the  $\text{su}(2)_1$  WZNW universality class. The elementary excitations are still,

in this case, gapless spinons.

This remarkable distinction between integer and half-integer spins, historically called Haldane's conjecture, has been obtained by means of a semi-classical analysis of the model with a special emphasis on the topological nature of the order parameter fluctuations. For a review of this approach, the reader may consult the reviews<sup>35,24</sup> and the books<sup>36,37,14</sup>. In the large  $S$  limit, the Euclidean action that describes the low-energy properties of the spin- $S$  AF Heisenberg chain reads as follows

$$\mathcal{S}_{\text{eff}} = \frac{v}{2g} \int d\tau dx \left[ \frac{1}{v^2} (\partial_\tau \vec{n})^2 + (\partial_x \vec{n})^2 \right] + i 2\pi S \mathcal{Q}(\vec{n}), \quad (8)$$

where  $v = 2JS$ ,  $g = 2/S$ , and  $\vec{n}$  is the order parameter of the Néel collinear state. The second contribution in Eq. (8) is a topological term since  $\mathcal{Q}(\vec{n}) = \int d\tau dx \vec{n} \cdot (\partial_\tau \vec{n} \wedge \partial_x \vec{n})/4\pi$  is an integer, called the Pontryagin index, which measures the number of times the spin configuration  $\vec{n}(x, \tau)$  covers the surface of the unit sphere  $S^2$ . In more mathematical terms, the configurations  $\vec{n}(x, \tau)$ , with fixed boundary conditions at infinity, are mappings of the sphere  $S^2$  onto  $S^2$  with homotopy classes classified by an integer  $\Pi_2(S^2) = \mathbb{Z}$ , which is nothing but the Pontryagin index  $Q$ . For integer spin chains, the term  $2\pi S \mathcal{Q}(\vec{n})$  in Eq. (8) has no effect on the path integral of the model and can be discarded. The effective action (8) reduces then to the one of the two-dimensional O(3) non-linear sigma model which is a massive integrable field theory<sup>38,39</sup>. The exact low-energy spectrum of this field theory consists of a massive bosonic triplet with mass  $m \sim e^{-2\pi/g}$  and it exhibits no bound states. The AF Heisenberg chain with integer spin is thus expected to have low-lying triplet excitations with a gap that scales as  $\Delta \sim ve^{-\pi S}$  when  $S$  is large.

In the case of half-integer spins, the topological term in Eq. (8) manifests itself in the path integral through a phase factor  $(-1)^{\mathcal{Q}}$  which gives rise to quantum interference between topologically distinct paths in space-time of the order parameter field  $\vec{n}(x, \tau)$ . It turns out that this process protects the model from a dynamically generated mass gap by quantum fluctuations and, in contrast, it leads to a non-perturbative massless flow towards an IR conformally invariant fixed point<sup>40,41,42</sup> which belongs to the  $\text{su}(2)_1$  WZNW universality class. Since this fixed point describes also the universal properties of the spin-1/2 AF Heisenberg chain, all half-integer spin chains should exhibit the same type of emerging quantum criticality with for instance spin-spin correlations that decay according to the power law behavior (5).

### 6.2.3. Haldane spin liquid: spin-1 Heisenberg chain

The simplest incompressible one-dimensional spin liquid phase corresponds to the spin-1 AF Heisenberg chain. The existence of a Haldane gap in this model has generated an intense activity over the years after its prediction. It has been confirmed numerically from exact diagonalizations on finite samples<sup>43</sup>, quantum Monte-Carlo methods<sup>44</sup>, transfert matrix computations<sup>45</sup>, and finally from DMRG calculations<sup>11,46</sup>. In particular, this latter technique predicts a gap  $\Delta = 0.41050(2)J$  and a correlation length  $\xi \simeq 6.03(1)$  lattice spacings. From the experimental point of view, several Haldane compounds have been synthesized over the years (see for instance Ref.<sup>12</sup> for a recent review). The two most studied compounds are CsNiCl<sub>3</sub><sup>47</sup> and Ni(C<sub>2</sub>H<sub>8</sub>N<sub>2</sub>)<sub>2</sub>NO<sub>2</sub>(ClO<sub>4</sub>) (NENP)<sup>48</sup> where spin-1 local moments are provided by Ni<sup>2+</sup> ions. In particular, inelastic neutron scattering experiments on NENP<sup>48,49</sup> confirm the existence of the Haldane gap. This energy gap has also been observed in several other quasi-1D spin-1 materials as (CH<sub>3</sub>)<sub>4</sub>NNi(NO<sub>2</sub>)<sub>3</sub><sup>50</sup>, AgVP<sub>2</sub>S<sub>6</sub><sup>51</sup>, and Y<sub>2</sub>BaNiO<sub>5</sub><sup>52,53</sup> which is probably the best realization of the spin-1 AF Heisenberg chain. Finally, it is worth noting that the recent compounds Ni(C<sub>5</sub>D<sub>14</sub>N<sub>2</sub>)<sub>2</sub>N<sub>3</sub>(PF<sub>6</sub>) (NDMAP)<sup>54</sup> and Ni(C<sub>5</sub>H<sub>14</sub>N<sub>2</sub>)<sub>2</sub>N<sub>3</sub>(ClO<sub>4</sub>) (NDMAZ)<sup>55</sup> enable to investigate experimentally the high magnetic field properties of the spin-1 Heisenberg chain<sup>56</sup>. From the theoretical point of view, several methods have been introduced to shed light on the nature of the mechanism of the Haldane-gap phenomena and to determine the main characteristics of this incompressible spin liquid phase. These approaches are the non-linear sigma model field theory obtained in the large spin limit<sup>34,35</sup>, the valence bond state (VBS) description<sup>57</sup>, the Majorana fermions method<sup>58</sup>, and the restricted Hilbert space approach<sup>59,60</sup>.

Probably, the simplest and most appealing approach to study the physical properties of the spin-1 AF Heisenberg chain consists to add a biquadratic interaction to the model (2):

$$\mathcal{H}_\beta = J \sum_i \left[ \vec{S}_i \cdot \vec{S}_{i+1} + \beta (\vec{S}_i \cdot \vec{S}_{i+1})^2 \right]. \quad (9)$$

One of the main interest of this extended Heisenberg model is that for  $\beta = 1/3$ , the so-called AKLT point<sup>57</sup>, the model has an exactly solvable ground state which captures the main characteristics of the Haldane spin liquid phase. At this special point, the Hamiltonian (9) is equivalent to the sum of projection operators  $P_2(i, i+1)$  that project onto the spin-2

contribution for every pair of nearest-neighbor spins:

$$\mathcal{H}_{AKLT} = \mathcal{H}_{\beta=1/3} = 2J \sum_i \left[ P_2(i, i+1) - \frac{1}{3} \right]. \quad (10)$$

From this structure, the ground state of this model can be constructed exactly using nearest-neighbor valence bonds. Following Affleck and coworkers pionneer work <sup>57</sup>, each original  $S = 1$  spin is written as two spin-1/2 variables in a triplet state. The ground state is then obtained by coupling into a singlet state all nearest-neighbor spin-1/2, thus forming a crystalline pattern of valence bonds (see Fig. 6.2). This state is called the valence-

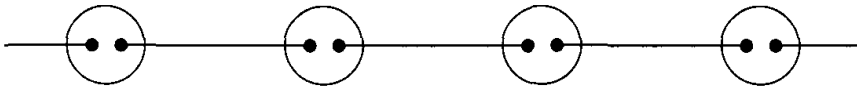


Fig. 6.2. VBS state in a chain with periodic boundary conditions.

bond-solid (VBS) state. For periodic BC and an even number of sites, this VBS state is the unique ground state and does not break the translation symmetry of the Hamiltonian (10). It can also be shown rigorously <sup>57</sup> that the AKLT model has a spectral gap whose value has been computed numerically:  $\Delta \simeq 0.7J$  <sup>61</sup>. In addition, the authors of Ref. <sup>57</sup> have also been able to show that the spin-spin correlation function decays exponentially with the distance with a finite correlation length equals to  $\xi = 1/\ln 3$  lattice spacings. The VBS state is therefore the simplest incompressible spin liquid phase with a unique ground state and a gap to all excitations.

Despite the exponential decay of correlations in this spin liquid phase, there is a subtle form of hidden AF ordering. This hidden order was first discovered by den Nijs and Rommelse <sup>62</sup> using an equivalence of the spin-1 chain to a two-dimensional restricted solid-on-solid model and also later by Tasaki <sup>63</sup> by means of a geometrical approach. A simple way to exhibit this hidden AF ordering is to look at the VBS state written in the conventional  $S^z$  representation. A typical configuration has the following structure: ..0↑0..0↓↑↓0↓0..0↑0.., i.e. each ↑ ( $S_n^z = +1$  state) is followed by ↓ ( $S_n^z = -1$  state) with an arbitrary number of 0 states ( $S_n^z = 0$  state) between and vice versa. If we ignore the spins with  $S_n^z = 0$  state then the remaining spins display a perfect long-range spin-1/2 Néel ordering: ↑↓↑↓↑↓ ... The VBS state has thus a perfect dilute AF Néel order. Because of the arbitrary

number of  $S_n^z = 0$  sites inserted between  $S_p^z = \pm 1$  sites, the long-range AF order is invisible in the spin-spin correlation function which has an exponential decay. However, this hidden order becomes manifest in the non-local string order parameter introduced by den Nijs and Rommelse<sup>62</sup> and defined by

$$\mathcal{O}_{\text{string}}^\alpha = - \lim_{|i-j| \rightarrow +\infty} \langle S_i^\alpha \exp \left( i\pi \sum_{k=j+1}^{i-1} S_k^\alpha \right) S_j^\alpha \rangle, \quad (11)$$

with  $\alpha = x, y, z$ . In the VBS ground-state, this order parameter can be computed exactly<sup>62</sup>:  $\mathcal{O}_{\text{string}}^\alpha = 4/9$  i.e. this object exhibits long-range order in the VBS phase. The existence of such a hidden order is essential to the basic mechanism of the Haldane gap: breaking this topological order to create an excitation costs a finite energy gap. The properties of this dilute AF order was further elucidated by Kennedy and Tasaki<sup>64</sup>. They were able to show, using a non-local unitary transformation, that the long-range order  $\mathcal{O}_{\text{string}}^\alpha \neq 0$  and the Haldane gap are related to a spontaneous breaking of a hidden  $Z_2 \times Z_2$  symmetry. In particular, the string order parameter becomes the usual local ferromagnetic order parameter under this non-local unitary transformation. Another important consequence of this broken  $Z_2 \times Z_2$  symmetry is the existence of a quasi-degeneracy of four lowest energy levels for a finite-size chain. This can also be understood within the VSB state since for open BC the AKLT model (10) has exactly four ground states with the existence of two spin-1/2 degrees of freedom that are unpaired at each end of the chain (see Fig. 6.3). Three of these states constitute a spin

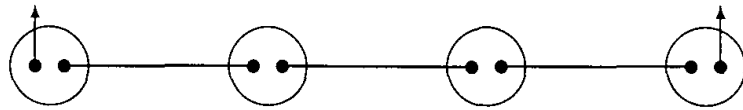


Fig. 6.3. VBS state with open boundary conditions; unpaired bonds are left at the boundaries resulting into two free spin-1/2 objects at the edges.

triplet whereas the last one is a spin singlet.

Beside the fact that only the ground state of the Hamiltonian (10) is known exactly, the AKLT approach is also very useful to describe low-lying excitations of the model through a variational approach starting from the VBS state. A first approach<sup>65</sup> consists to create a “magnon” excitation by

applying a spin-flip on the VBS ground state ( $|VBS\rangle$ ):

$$|k\rangle = \frac{1}{\sqrt{N}} \sum_{j=1}^N \exp(ikj) S_j^+ |VBS\rangle, \quad (12)$$

$N$  being the system size. It is very tempting to interpret this excitation as a standard  $S = 1$  magnon i.e. an excitation which modifies only locally the AF Néel order. In fact, the trial wave function (12) does not describe a magnon excitation of the perfect hidden Néel order of the VBS state but it has instead a solitonic nature<sup>61</sup>. Indeed, in the  $S^z$  representation, a typical configuration that appears in  $S_j^+ |VBS\rangle$  has the following structure:  $\dots 0 \uparrow 0 \dots 0 \downarrow 0 \uparrow 0 \downarrow 0 \dots 0 \uparrow 0 \dots$ . Removing the 0 states, this configuration becomes  $\uparrow \downarrow \uparrow \downarrow \uparrow \dots$  i.e. a soliton or domain wall which destroys non-locally the AF Néel long-range order. An alternative approach to describe the elementary excitations of the AKLT (10) model is to start from the VBS state and to promote the spins of the link  $(j, j + 1)$  into a triplet state  $|\Phi_j^a\rangle$ <sup>66,61,67</sup>. This low-lying excitation carrying momenta  $k$  describes a moving triplet bond, usually called crackion, and it is defined by

$$|\Phi^a(k)\rangle = \frac{1}{\sqrt{N}} \sum_{j=1}^N \exp(ikj) |\Phi_j^a\rangle. \quad (13)$$

In fact, the two approaches (12) and (13) are related and describe the same dispersion relation for the triplet excitation<sup>61</sup>. The solitonic nature of the excitation (13) becomes manifest by considering open boundary conditions and the non-local unitary transformation introduced by Kennedy and Tasaki<sup>64</sup>. In that case, the trial excited wave function corresponds to a domain wall that interpolates between two of the four possible ground states<sup>61</sup>.

One of the main success of this VBS approach stems from the fact that the properties of the VBS state are not special to the AKLT point (10) but have a larger extent. This model turns out to be smoothly connected to the spin-1 Heisenberg chain in the sense that they share the same physical properties. In this respect, numerical investigations<sup>68,69,70,71,72,73,74</sup> of the phase diagram of the bilinear-biquadratic spin-1 Hamiltonian (9) have revealed that this model with  $|\beta| < 1$  belongs to a same phase, the Haldane phase, whose main characteristics are well described by the VBS state. In particular, the origin of the Haldane gap in the spin-1 Heisenberg chain is a consequence of a hidden  $Z_2 \times Z_2$  broken symmetry as for the AKLT model (10). At the Heisenberg point  $\beta = 0$ , the hidden AF Néel ordering is no

longer perfect as at the AKLT point. It is only locally destroyed so that there is still long-range order at  $\beta = 0$  with a non-zero string order parameter (11) but smaller than at the AKLT point:  $\mathcal{O}_{\text{string}}^{\alpha} \simeq 0.374$ <sup>70,71,46</sup>. A second consequence of the spontaneous breaking of the  $Z_2 \times Z_2$  symmetry is the two almost free  $S = 1/2$  degrees of freedom at the ends of a finite chain with open BC. At the Heisenberg point, exact diagonalizations<sup>68</sup> of finite open samples with an even number of sites have shown that the ground state is a singlet and the existence of an exponentially low-lying triplet state (the so-called Kennedy triplet) in the Haldane gap. This leads to a fourfold ground-state degeneracy in the thermodynamic limit which can be simply understood by means of the VBS description of Fig. 6.3 as described above. The existence of these two  $S = 1/2$  edge states is a robust and striking property of the Haldane spin liquid phase and they are present in the whole region  $|\beta| < 1$  of the bilinear-biquadratic spin-1 model<sup>73,74</sup>. The physical properties of these  $S = 1/2$  chain-boundary excitations in the open spin-1 chain have been investigated in detail numerically<sup>46,75,76,77,78,79,73,74,80</sup> and also analytically<sup>81,82,83</sup>. Remarkably enough, this liberation of fractional spin-1/2 degrees of freedom in a spin-1 Heisenberg chain has been observed experimentally in the spin-1 compound NENP cut by non-magnetic impurities ( $Zn^{2+}$  or  $Mg^{2+}$ )<sup>84,85</sup> and also doped with magnetic ions ( $Cu^{2+}$ )<sup>86</sup>. In particular, these spin-1/2 chain-boundary excitations reveal itself as satellite peaks in the NMR profile of the Mg-doped  $Y_2BaNiO_5$ <sup>87</sup>. A very recent inelastic neutron scattering experiments<sup>88</sup> further probe the microscopic structure of these edge states through the wave-vector dependence of the Zeeman resonance.

#### 6.2.4. General spin- $S$ case

For higher spin- $S$  value ( $S > 1$ ), the difference between integer-spin and half-integer AF Heisenberg chains has been explained within the semiclassical analysis pionnered by Haldane<sup>34,35</sup> and also by means of the Abelian<sup>89</sup> and non-Abelian<sup>40,90</sup> bosonization approaches. The Haldane's conjecture for  $S > 1$  has also been investigated numerically and experimentally over the years.

The numerical studies<sup>91,92,93,94</sup> of the  $S = 3/2$  AF Heisenberg chain report that the model displays a critical behavior that belongs to the same universality class as the  $S = 1/2$  Heisenberg chain. Several quasi-1D AF compounds with spin 3/2 have been found like  $CsVBr_3$ ,  $CsVCl_3$ <sup>95,96</sup>, and  $AgCrP_2S_6$ <sup>97</sup>. In particular, the uniform susceptibility of the spin-

$3/2$   $\text{AgCrP}_2\text{S}_6$  material measured experimentally<sup>97</sup> is consistent with the result for spin- $1/2$ , i.e. confirming the universal behavior of half-integer spins. In the  $S = 2$  case, the existence of a Haldane gap has been established in various quantum Monte-Carlo approaches<sup>98</sup> and in DMRG calculations<sup>99,100,101</sup>. In the thermodynamic limit, a finite gap of  $\Delta = 0.085(5)J$  and a finite correlation length  $\xi = 49(1)$  lattice spacings have been found in DMRG<sup>100</sup>. Several Haldane spin-2 compounds have been discovered over the years (see Ref.<sup>12</sup> for a review) like  $\text{CsCrCl}_3$  and  $(2,2'$ -bipyridine)trichloromanganase(III) ( $\text{MnCl}_3(\text{bipy})$ )<sup>102</sup>. Experiments<sup>102</sup> on this last compound report the existence of a gap  $\Delta/J = 0.07 \pm 0.02$  which is in good agreement with the numerical results.

Integer  $S > 1$  spin chains share similar properties as the  $S = 1$  case. In particular, there is still a hidden AF order in the integer  $S > 1$  case. A non-local string order parameter that measures this topological order has been proposed by Oshikawa<sup>103</sup>:

$$\mathcal{O}_{\text{string}}^{\alpha} \left( \frac{\pi}{S} \right) = - \lim_{|i-j| \rightarrow +\infty} \langle S_i^{\alpha} \exp \left( i\pi/S \sum_{k=j+1}^{i-1} S_k^{\alpha} \right) S_j^{\alpha} \rangle, \quad (14)$$

where  $\alpha = x, y, z$ . This order parameter can be exactly computed in spin- $S$  generalization of the VBS state<sup>103,104</sup> and numerically for the Heisenberg chain<sup>105,99,100</sup>. For instance, in the spin-2 case, DMRG calculations<sup>100</sup> found  $\mathcal{O}_{\text{string}}^{\alpha}(\pi/2) = 0.726(2)$ . However, the full characterization of the hidden AF order for integer spin  $S > 1$  is less clear than for  $S = 1$  where, as seen above, it is related to a broken  $Z_2 \times Z_2$  symmetry. In fact, the nature of the hidden symmetry breaking is still an open problem for  $S > 1$ . Insight on this issue might be gained by studying the structure of edge states of open integer spin- $S$  chains. Higher- $S$  VBS states with open BC have  $(S+1)^2$ -fold degenerate ground states with the presence of two free  $S/2$  degrees of freedom at each end of the chain in close parallel to the  $S = 1$  case (see Fig. 6.3). A non-linear sigma model approach<sup>106</sup> of the open spin- $S$  Heisenberg chain reveals the existence of spin- $S/2$  edge states in the integer spin case. These results lead us to expect that  $Z_{2S} \times Z_{2S}$  might be a good candidate to describe the hidden symmetry breaking scheme in the integer spin- $S$  case. In the  $S = 2$  case, the approximate nine-fold degeneracy of the ground state of finite open chains have been observed numerically<sup>77,99,100</sup> by DMRG. The presence of these spin-1 chain-end excitations has also been confirmed experimentally in the ESR study of the spin-2 Haldane compound  $\text{CsCrCl}_3$  doped with non-magnetic  $\text{Mg}^{2+}$  ions<sup>107</sup>.

The liberation of these fractional spin- $S/2$  degrees of freedom when non-magnetic impurities are introduced in integer spin- $S$  AF Heisenberg chain is a remarkable fact. It stems from the presence of a non-trivial topological ordering in the ground state of the spin- $S$  chain. In this respect, the existence of these edge states opens the possibility to make a distinction between spin- $S$  Haldane liquid phases. These massive spin liquid phases share the same thermodynamics properties but have for instance different chain-end ESR response due to the special nature of their edge states. In fact, this topological distinction between gapped spin liquid phases can also be applied to the massless case. All half-integer AF Heisenberg spin chains have the same bulk universal properties described by an IR fixed point which belongs to the  $\text{su}(2)_1$  WZNW universality class. However, the ground state of half-integer spin chains still sustains a topological ordering. Indeed, by means of a non-linear sigma model approach, Ng<sup>106</sup> has given evidence that edge states with fractionalized quantum number  $(S - 1/2)/2$  exist in open half-integer spin- $S$  AF Heisenberg chain. This interesting result has been confirmed numerically by examining open spin chains with spins up to  $S = 9/2$  by DMRG<sup>77,108</sup>. Recently, a numerical investigation<sup>109</sup> of the non-local string order parameter (14) directly reveals the presence of a topological order in half-integer spin- $S$  AF Heisenberg chains. The existence of this hidden topological order (or the related chain-end excitations) leads to a topological distinction between gapless spin liquid phases with the same emerging quantum criticality.

### 6.2.5. Two-leg spin ladder

A further impetus for the study of low-dimensional spin systems was given by the discovery of spin-ladder materials one decade ago<sup>110</sup>. These systems consist of a finite number ( $n_{\text{leg}}$ ) of spin-1/2 AF Heisenberg chains coupled by a transverse exchange interaction  $J_{\perp}$ . The Hamiltonian of this model reads as follows

$$\mathcal{H}_{n_{\text{leg}}} = J_{\parallel} \sum_i \sum_{a=1}^{n_{\text{leg}}} \vec{S}_{a,i} \cdot \vec{S}_{a,i+1} + J_{\perp} \sum_i \sum_{a=1}^{n_{\text{leg}}-1} \vec{S}_{a,i} \cdot \vec{S}_{a+1,i}, \quad (15)$$

where  $\vec{S}_{a,i}$  is a spin-1/2 operator at site  $i$  on the  $a$ -th chain and the in-chain exchange  $J_{\parallel}$  is antiferromagnetic ( $J_{\parallel} > 0$ ). One of the main interest of these spin ladders stems from the fact that they are intermediate objects between 1D and 2D systems. Moreover, these quasi-1D systems share many properties with the cuprates and, because of their relative simplicity, may

provide some insights on mechanisms behind high- $T_c$  superconductivity.

Despite this original motivation to study spin ladders, these systems display striking properties which make them interesting by themselves in the field of 1D quantum magnetism. In particular, in close parallel to the qualitative difference between integer and half-integer AF Heisenberg spin chains, the universal properties of spin ladders (15) with open boundary conditions in the transverse direction strongly depend on the parity of the number of legs  $n_{\text{leg}}$ <sup>111,112,113,114,115</sup>. Ladders with even number of legs are spin liquids with a finite gap in the excitation spectrum and exponentially decaying spin-spin correlations. The original massless spinons of the spin-1/2 chains get confined by the interchain coupling to form coherent optical spin-1 magnon excitations. Upon doping, these ladders display quasi-long-range superconducting pairing correlations with an approximate d-wave symmetry<sup>110</sup>. In contrast, odd-legged ladders have a gapless spectrum which is characterized by a central charge  $c = 1$  corresponding to an effective  $S = 1/2$  AF Heisenberg spin chain. Upon doping, odd-legged ladders exhibit a metallic behavior typical of a Luttinger liquid<sup>116</sup>. This difference on the energy spectrum of the spin ladders depending on the parity of  $n_{\text{leg}}$  is strongly reminiscent of the Haldane conjecture for AF Heisenberg spin chains with  $S = n_{\text{leg}}/2$ . It can be simply understood from the fact that in the strong ferromagnetic rung coupling limit the spin ladder (15) is indeed equivalent to a single  $S = n_{\text{leg}}/2$  AF Heisenberg chain.

Several spin ladders materials have been discovered over the years. The family of compounds  $\text{Sr}_{n-1}\text{Cu}_{n+1}\text{O}_{2n}$  approximately realize ladders with  $n_{\text{leg}} = (n+1)/2$ ,  $n = 3, 5, 7..$  legs<sup>111</sup>. The even-odd scenario in ladders was confirmed experimentally from susceptibility and muons resonance measurements on this compound with  $n = 3$  and  $n = 5$ <sup>117,118</sup>. The existence of a spin gap in the two-leg case ( $n_{\text{leg}} = 2$ ) was found in experiments on the two-leg compounds  $\text{A}_{14}\text{Cu}_{24}\text{O}_{41}$  ( $\text{A}_{14} \equiv \text{La}_6\text{Ca}_8$ ,  $(\text{Sr},\text{La},\text{Ca})_{14}$ )<sup>119</sup>,  $\text{Cu}_2(\text{C}_5\text{H}_{12}\text{N}_2)_2\text{Cl}_4$ <sup>120,121</sup>,  $(\text{C}_5\text{H}_{12}\text{N})_2\text{CuBr}_4$ <sup>122</sup> and the organic compound BIP-BNO<sup>123</sup>. However, it is worth noting that additional interactions are required to fully describe these materials such as for instance a non-negligible ring exchange for the compound  $\text{A}_{14}\text{Cu}_{24}\text{O}_{41}$ <sup>124,125</sup> or a small diagonal interchain exchange interaction for  $\text{Cu}_2(\text{C}_5\text{H}_{12}\text{N}_2)_2\text{Cl}_4$ <sup>120,121</sup>.

The existence of a spin gap in the two-leg case can be anticipated by considering a strong-coupling analysis of the model (15) with  $n_{\text{leg}} = 2$ . In the limit of strong AF interchain coupling  $J_{\perp} \gg J_{\parallel}$ , the ground state consists of singlet bonds formed across the rungs of the ladder, with triplet excitations separated by a large energy gap of order  $J_{\perp}$ . Perturbations in

small  $J_{\parallel}$  will cause these singlet bonds to resonate and the triplet excitations form a band with bandwidth  $\sim J_{\parallel}$  but the spectral gap survives<sup>126</sup>. In the strong ferromagnetic interchain  $-J_{\perp} \gg J_{\parallel}$  coupling case, local spins  $S = 1$  associated with each rung of the ladder are formed leading thus to a spin-1 AF Heisenberg chain with a non-zero Haldane gap in the energy spectrum. The cross-over between strong and weak coupling limits has been carefully analysed in numerical calculations<sup>127,128,129,130</sup>. It turns out that the ground state in the two strong-coupling limits  $|J_{\perp}|/J_{\parallel} \gg 1$  evolves adiabatically with increasing  $J_{\parallel}$ . The spin gap survives for arbitrarily large  $J_{\parallel}/|J_{\perp}|$  and finally vanishes for  $J_{\perp} = 0$ , i. e. when the two spin-1/2 AF Heisenberg chains are decoupled. The critical point  $J_{\perp} = 0$  separates thus two strong-coupling massive phases: a rung-singlet phase for  $J_{\perp} > 0$  and a phase with  $J_{\perp} < 0$  which is smoothly connected to the Haldane phase of the spin-1 chain.

The opening of the spin gap upon switching on the interchain coupling can be investigated by means of the bosonization approach<sup>131,132,89</sup>. In particular, the field theory that accounts for the massless spinon-optical magnon transmutation, when  $J_{\perp}$  is small, corresponds to an  $\text{SO}(3) \times \text{Z}_2$  symmetric model of four massive Majorana (real) fermions<sup>132,133</sup> i.e. four off-critical 2D Ising models (for a review see for instance the book<sup>10</sup>). The resulting low-energy field theory is described by the following Hamiltonian density<sup>132,133</sup>:

$$\begin{aligned} \mathcal{H}_{n_{\text{leg}}=2} = & -\frac{iv_t}{2} \left( \vec{\xi}_R \cdot \partial_x \vec{\xi}_R - \vec{\xi}_L \cdot \partial_x \vec{\xi}_L \right) - im_t \vec{\xi}_R \cdot \vec{\xi}_L \\ & - \frac{iv_s}{2} \left( \xi_R^0 \partial_x \xi_R^0 - \xi_L^0 \partial_x \xi_L^0 \right) - im_s \xi_R^0 \xi_L^0 + \mathcal{H}_{\text{marg}}, \end{aligned} \quad (16)$$

where  $\vec{\xi}_{R,L}$  are a triplet of right and left-moving Majorana fermions that describe the  $S = 1$  low-lying excitations of the two-leg spin ladder and the Majorana fermion  $\xi_{R,L}^0$  accounts for the singlet excitation. The masses of these real fermions are given by in the weak coupling limit:  $m_t = J_{\perp} \lambda^2 / 2\pi$  and  $m_s = -3J_{\perp} \lambda^2 / 2\pi$ ,  $\lambda$  being a non-universal constant. These triplet and singlet massive Majorana fermions are weakly coupled by a marginal perturbation associated to the last term of Eq. (16):

$$\mathcal{H}_{\text{marg}} = \frac{g_1}{2} \left( \vec{\xi}_R \cdot \vec{\xi}_L \right)^2 + g_2 \vec{\xi}_R \cdot \vec{\xi}_L \xi_R^0 \xi_L^0, \quad (17)$$

with  $g_1 = -g_2 = \pi a_0 J_{\perp} / 2$ ,  $a_0$  being the lattice spacing. The model (16), derived in the weak coupling limit  $|J_{\perp}| \ll J_{\parallel}$ , is expected to have a larger extent and to capture in fact the low-energy properties of the two-leg spin

ladder for arbitrary  $J_{\perp}$  with a suitable redefinition of the masses  $m_{s,t}$ , velocities  $v_{s,t}$ , and coupling constants  $g_{1,2}$ . This stems from the continuity between the weak- and strong-coupling limits in the two-leg spin ladder observed numerically<sup>127,128,129,130</sup>. In addition, in the strong ferromagnetic rung limit  $-J_{\perp} \gg J_{\parallel}$ , the singlet excitation described by the Majorana fermion  $\xi_{R,L}^0$  are frozen ( $|m_s| \rightarrow \infty$ ) so that the low-energy properties of the model (16) are governed by the triplet magnetic excitations corresponding to the fermions  $\vec{\xi}_{R,L}$ . The resulting model coincides with the low-energy field theory of the spin-1 AF Heisenberg chain obtained by Tsvelik<sup>58</sup> by perturbing around the Babujian-Takhtajan<sup>134</sup> integrable point of the bilinear-biquadratic spin-1 chain (9) with  $\beta = -1$ . The Hamiltonian (16) correctly thus captures the low-energy properties of the two-leg spin ladder in the limit  $-J_{\perp} \gg J_{\parallel}$  where it reduces to the spin-1 AF Heisenberg chain.

Despite of its apparent simplicity, the model (16) is not an integrable field theory and takes the form a massive  $\text{SO}(3) \times \text{Z}_2$  Gross-Neveu model<sup>135</sup>. However, the leading behavior of the physical quantities of the two-leg spin ladder can be determined by treating the marginal contribution (17) perturbatively. As shown in Ref.<sup>132</sup>, this term leads to a renormalization of the masses and velocities so that the low-energy description (16) simply reduces to four independent massive Majorana fermions, i.e. four decoupled off-critical 2D Ising models. This mapping onto off-critical 2D Ising models can then be exploited to derive the low-energy properties of the two-leg spin ladder such as, for instance, the spectrum of elementary excitations, low-T thermodynamics and the leading asymptotics of spin-spin correlation functions. To this end, one needs to express the spin operators  $\vec{S}_{a,i}$  in terms of the Ising fields. In the continuum limit, the spin densities separate into the smooth and staggered parts<sup>40</sup>:  $\vec{S}_a(x) = \vec{J}_{aL}(x) + \vec{J}_{aR}(x) + (-1)^{x/a_0} \vec{n}_a(x)$ . The chiral  $\text{su}(2)_1$  currents, uniform parts of the spin densities, can be written locally in terms of the Majorana fermions<sup>132,136</sup>:

$$\vec{J}_{aR,L} = -\frac{i}{4} \vec{\xi}_{R,L} \wedge \vec{\xi}_{R,L} + i \frac{\tau_a}{2} \vec{\xi}_{R,L} \xi_{R,L}^0, \quad (18)$$

with  $\tau_1 = +1$  and  $\tau_2 = -1$ . In contrast, the staggered magnetizations  $\vec{n}_a$  are non-local in terms of the underlying fermions and express in terms of the order ( $\sigma_a$ ) and disorder ( $\mu_a$ ) of the Ising models<sup>58,132,136</sup>.

$$\begin{aligned} \vec{n}_+ &\sim (\mu_0 \mu_1 \sigma_2 \sigma_3, \mu_0 \sigma_1 \mu_2 \sigma_3, \mu_0 \sigma_1 \sigma_2 \mu_3) \\ \vec{n}_- &\sim (\sigma_0 \sigma_1 \mu_2 \mu_3, \sigma_0 \mu_1 \sigma_2 \mu_3, \sigma_0 \mu_1 \mu_2 \sigma_3), \end{aligned} \quad (19)$$

where  $\vec{n}_{\pm} = \vec{n}_1 \pm \vec{n}_2$ . Due to the existence of non-zero masses  $m_{s,t}$  for the fermions in Eq. (16), all related Ising models are non-critical. A spectral

gap is thus present in the two-leg spin ladder for all signs of the interchain interaction  $J_{\perp}$  and it opens linearly with  $J_{\perp}$  in the weak coupling limit. In addition, the Ising description (18,19) of the spin densities allows the calculation of the leading asymptotics of spin-spin correlations using exact results of the two-point function of a non-critical Ising model. Since the signs of the triplet and singlet masses are always opposite in Eq. (16), it can be shown<sup>132</sup> that the dynamical spin susceptibility displays a sharp single-magnon peak near  $q = \pi/a_0$  and  $\omega = |m_t|$  which reflects the elementary nature of the triplet excitations for all signs of  $J_{\perp}$ .

In this respect, the spin liquid phase of the two-leg spin ladder is very similar to the Haldane phase of the spin-1 chain. However, it has been stressed recently that the phase with  $J_{\perp} < 0$ , smoothly connected to the Haldane phase of the spin-1 chain, and the rung-singlet phase for  $J_{\perp} > 0$  are, in fact, topologically distinct gapped phases<sup>137</sup>. The distinction is intimately related to the short-range valence bond structure of their ground states. In close parallel to the classification of short-range valence bond configurations on a two-dimensional square lattice<sup>138</sup>, two different topological classes can be defined in the one-dimensional case by counting the number  $Q_y$  of valence bonds crossing an arbitrary vertical line<sup>137</sup>. In the case of the rung-singlet phase,  $Q_y$  is always even while it is odd for the Haldane phase with  $J_{\perp} < 0$ . Two different non-local string order parameters can then be defined in connection to this topological distinction<sup>129,130,137</sup>:

$$\begin{aligned}\mathcal{O}_{\text{even}}^{\alpha} &= -\lim_{|i-j| \rightarrow +\infty} \langle (S_{1,i+1}^{\alpha} + S_{2,i}^{\alpha}) e^{i\pi \sum_{k=j+1}^{i-1} (S_{1,k+1}^{\alpha} + S_{2,k}^{\alpha})} (S_{1,j+1}^{\alpha} + S_{2,j}^{\alpha}) \rangle \\ \mathcal{O}_{\text{odd}}^{\alpha} &= -\lim_{|i-j| \rightarrow +\infty} \langle (S_{1,i}^{\alpha} + S_{2,i}^{\alpha}) e^{i\pi \sum_{k=j+1}^{i-1} (S_{1,k}^{\alpha} + S_{2,k}^{\alpha})} (S_{1,j}^{\alpha} + S_{2,j}^{\alpha}) \rangle,\end{aligned}\quad (20)$$

with  $\alpha = x, y, z$ . The Haldane and rung-singlet phases are then characterized by  $\mathcal{O}_{\text{odd}}^{\alpha} \neq 0$ ,  $\mathcal{O}_{\text{even}}^{\alpha} = 0$ , and by  $\mathcal{O}_{\text{even}}^{\alpha} \neq 0$ ,  $\mathcal{O}_{\text{odd}}^{\alpha} = 0$  respectively. The order parameters (20) reveal also the difference nature of the hidden AF Néel order in the Haldane phase (non-zero triplet states along the rung) and in the rung-singlet phase (non-zero triplet states along the diagonal)<sup>129,130,137</sup>. This topological difference can be discussed in light of the Ising description (19) of the two-leg spin ladder. The string order parameters (20) can be expressed in terms of the order and disorder Ising operators<sup>139</sup>:  $\mathcal{O}_{\text{odd}}^z \sim \langle \sigma_1 \rangle^2 \langle \sigma_2 \rangle^2$  and  $\mathcal{O}_{\text{even}}^z \sim \langle \mu_1 \rangle^2 \langle \mu_2 \rangle^2$ . For a ferromagnetic (respectively antiferromagnetic) interchain coupling, the Ising models in the triplet sector are in their ordered (respectively disordered) phases so that  $\mathcal{O}_{\text{odd}}^z \neq 0$  and  $\mathcal{O}_{\text{even}}^z = 0$  (respectively  $\mathcal{O}_{\text{odd}}^z = 0$  and  $\mathcal{O}_{\text{even}}^z \neq 0$ ). In this Ising description, the phases with  $J_{\perp} > 0$  and  $J_{\perp} < 0$  are thus simply re-

lated by a Kramers-Wannier duality transformation on the underlying Ising models.

The topological distinction between these two phases becomes manifest when analysing the ground-state degeneracy depending on the nature of BC used. In the open BC case, as noted by the authors of Ref. <sup>137</sup>, ground states of gapped spin liquid states characterized by an odd value of  $Q_y$  have spin-1/2 edge states, while these end states disappear when  $Q_y$  is even. The existence of these  $S = 1/2$  chain-end degrees of freedom leads to a ground-state degeneracy in a two-leg spin ladder with open BC. In the Haldane phase of the ladder with  $J_\perp < 0$ , finite open chains with an even number of sites have a singlet ground-state with an exponentially low-lying triplet in the spin gap resulting on a fourfold ground-state degeneracy in the thermodynamic limit. In contrast, the ground state in the rung-singlet phase is always unique whether open or periodic BC are used: no low-lying triplet states are found inside the spin gap in open ladder with  $J_\perp > 0$  and an even number of sites. In this respect, the rung-singlet phase with  $J_\perp > 0$ , in contrast to the  $J_\perp < 0$  case, is not equivalent to the Haldane phase characterized by  $S = 1/2$  chain-end excitations even though they share similar properties such as the presence of a spin gap, and a non-zero string order parameter. The existence or absence of spin-1/2 edge states in the open two-leg spin ladder can also be discussed within the Ising model description (16) <sup>83</sup>. In particular, the fourfold ground-state degeneracy of the open two-leg ladder with a ferromagnetic interchain coupling can be obtained within this approach. Indeed, for  $J_\perp < 0$ , the three Ising models for the triplet sector are all in their ordered phases while the Ising model for the singlet degrees of freedom belongs to its disorder phase so that  $\langle \sigma_i \rangle \neq 0$  ( $i = 1, 2, 3$ ) and  $\langle \sigma_0 \rangle = 0$ . In that case, each Ising model in the triplet sector has a doubly degenerate ground state which gives thus an eightfold degeneracy. However, there is a redundancy in the Ising description since the triplet Hamiltonian in Eq. (16), the total uniform and staggered magnetizations in Eqs. (18,19) are all invariant under the transformation:  $\xi_{R,L}^i \rightarrow -\xi_{R,L}^i$ ,  $\mu_i \rightarrow \mu_i$ , and  $\sigma_i \rightarrow -\sigma_i$ ,  $i = 1, 2, 3$ . This leads to a physical fourfold ground-state degeneracy as it should be in the Haldane phase. Another advantage of this Ising model description is to make explicit the spontaneous breaking of a hidden  $Z_2 \times Z_2$  symmetry associated to the ground-state degeneracy for  $J_\perp < 0$ . The existence of this hidden symmetry can also be revealed with help of a non-local unitary transformation on the lattice spins of the two-leg ladder <sup>140</sup> as in the spin-1 AF Heisenberg chain <sup>64</sup>.

Finally, the Haldane and rung-singlet phases of the two-leg spin ladder

can also be distinguished by their optical properties. In the rung-singlet phase, the existence of singlet or triplet two-magnon bound states below the two-magnon continuum has been predicted theoretically by a number of groups<sup>141,142,143,144</sup>. Recently, the singlet two-magnon bound state has been observed in the optical conductivity spectrum of the compound  $(\text{La,Ca})_{14}\text{Cu}_{24}\text{O}_{41}$ <sup>145</sup> which contains layers with  $\text{Cu}_2\text{O}_3$  two-leg spin ladder with  $J_\perp > 0$ . On the contrary, it is expected that for a ferromagnetic interchain coupling no bound states are present below the two-particle continuum as in the spin-1 AF Heisenberg chain<sup>46</sup>. The existence of bound states in the two-leg spin ladder can be discussed in the context of the field theory approach (16). Indeed, the marginal term (17) plays its trick by giving rise to an effective interaction between the magnon excitations. In the AF interchain case, the contribution (17) is in fact marginal relevant and the interaction between magnons are attractive. The presence of bound states in this case can be argued qualitatively as a result of this attractive interaction. The Hamiltonian (17) takes the form of a  $\text{SO}(4)$  Gross-Neveu model up to irrelevant contributions and a duality transformation  $\xi_R^0 \rightarrow -\xi_R^0$  in the singlet sector. The latter model is integrable<sup>38</sup> and, for  $J_\perp > 0$ , the low-lying excitations are massive kinks and anti-kinks interpolating between the two degenerate ground states resulting from the spontaneous symmetry breaking of the  $Z_2$  symmetry:  $\xi_R^a \xi_L^a \rightarrow -\xi_R^a \xi_L^a$ ,  $a = 0, \dots, 3$ . The mass terms in the full Hamiltonian (16) break explicitly this  $Z_2$  symmetry and the ground-state degeneracy is lifted so that kink configurations are no longer asymptotic states of the field theory. The situation is in close parallel to the two-dimensional Ising model in its low-temperature phase upon switching on a magnetic field. The mass terms are then expected to induce a linear confining potential between the kinks giving rise to a sequence of bound states. In contrast, when  $J_\perp < 0$ , the perturbation (17) is a marginal irrelevant contribution and the spectrum of the model (16) consists of massive fermions and their multiparticle excitations.

#### 6.2.6. Non-Haldane spin liquid

The Haldane and rung-singlet phases of the two-leg spin ladder are not the only possible gapped spin-liquid states available in 1D unfrustrated quantum magnets. In this respect, Nersesyan and Tsvelik<sup>133</sup> have discussed the example of a gapped spin liquid phase without any coherent magnon excitations. The spectral function of this state displays a broad feature rather than a single sharp magnon peak. Such a spin liquid can be stabilized

by the introduction of a four-spin interchain interaction that couples two spin-1/2 AF Heisenberg chains:

$$\mathcal{H}_{\text{so}} = J \sum_i \sum_{a=1}^2 \vec{S}_{a,i} \cdot \vec{S}_{a,i+1} + K \sum_i (\vec{S}_{1,i} \cdot \vec{S}_{1,i+1}) (\vec{S}_{2,i} \cdot \vec{S}_{2,i+1}). \quad (21)$$

The biquadratic interaction represents an interchain coupling for the spin-dimerization operators ( $\epsilon_{a,i} \sim (-1)^i \vec{S}_{a,i+1} \cdot \vec{S}_{a,i}$ ) of each chain which can be effectively generated by spin-phonon interaction. A second motivation to investigate the effect of this four-spin interaction stems from orbital degeneracy. In most of transition metal compounds, in addition to the usual spin degeneracy, the low-lying electron states are also characterized by orbital degeneracy<sup>146</sup>. A starting point to study magnetic properties of magnetic insulators with Jahn-Teller ions is the two-band Hubbard-like models. At quarter-filling (one electron per atom), this system is a Mott insulator in the limit of strong Coulomb interaction and the state of each ion can be characterized by a spin degrees of freedom  $\vec{S}_{1,i}$  and an orbital state described by a pseudo-spin-1/2  $\vec{S}_{2,i}$ . In the large Coulomb repulsion limit, the simplest Hamiltonian that describes the competition between spin and orbital degrees of freedom in one dimension reduces to the spin-orbital model (21). In particular, this model has been introduced by Pati et al.<sup>147</sup> to explain the unusual magnetic properties of the quasi-one-dimensional spin gapped material  $\text{Na}_2\text{Ti}_2\text{Sb}_2\text{O}$ <sup>148</sup>.

The spin-orbital model (21) is unfrustrated for  $K < 0$  whereas the frustration manifests itself in the antiferromagnetic case  $K > 0$  only in the intermediate regime  $K \simeq J$  as we shall see later. The Hamiltonian (21) is invariant under independent SU(2) rotations in the spin ( $\vec{S}_1$ ) and orbital ( $\vec{S}_2$ ) spaces. For generic couplings, the model (21) is thus  $SU(2) \times SU(2) \times Z_2$  symmetric, the additional Ising symmetry being the exchange between the spins  $\vec{S}_1$  and  $\vec{S}_2$ . In the weak coupling limit  $|K| \ll J$ , this underlying SO(4) symmetry of the spin-orbital model (21) is reflected in the form of its low-energy Hamiltonian density which is described in terms of four massive Majorana fermions<sup>133,149</sup>:

$$\mathcal{H}_{\text{so}} \simeq -\frac{iv}{2} \sum_{a=0}^3 (\xi_R^a \partial_x \xi_R^a - \xi_L^a \partial_x \xi_L^a) - im \sum_{a=0}^3 \xi_R^a \xi_L^a, \quad (22)$$

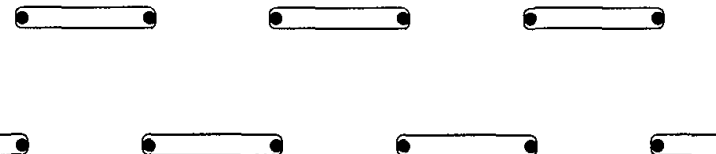
with  $m = \alpha K$ ,  $\alpha$  being a positive non-universal constant. In Eq. (22), a marginal contribution, similar to Eq. (17), has been neglected. In contrast to the low-energy description (16) of the standard two-leg spin ladder, the triplet and singlet Majorana modes become equally important here as a

consequence of the SO(4) symmetry of the spin-orbital model (21). The resulting low-energy properties of the model can then be determined by this mapping onto four off-critical 2D Ising models. As the staggered magnetizations (19), the spin dimerization fields  $\epsilon_{1,2}$  can be expressed in terms of the order and disorder operators of the underlying Ising models:

$$\epsilon_a \sim \mu_1 \mu_2 \mu_3 \mu_0 \pm \tau_a \sigma_1 \sigma_2 \sigma_3 \sigma_0, \quad (23)$$

with  $\tau_1 = 1$  and  $\tau_2 = -1$ . For an AF biquadratic coupling ( $K > 0$ ), the four Ising models belong to their ordered phases so that the model (22) enters a spontaneously dimerized phase with a finite gap and  $\langle \epsilon_1 \rangle = -\langle \epsilon_2 \rangle = \pm |\epsilon_0|$ . The ground state is thus two-fold degenerate and dimerizes with an alternating pattern as shown in Fig. 6.4 (a). In contrast, in the ferromagnetic

(a)



(b)

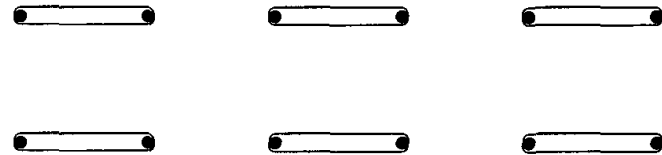


Fig. 6.4. Ground states of the spin-orbital model in the weak coupling limit  $|K| \ll J$ . The bonds indicate a singlet pairing between the spins. (a) Alternating dimerization for  $K > 0$ ; (b) in-phase dimerization for  $K < 0$ . In each case, a second ground state is obtained by applying the one-step translation symmetry on each chain to the states depicted here.

$K < 0$  case, the dimerization is now in-phase between the two chains:  $\langle \epsilon_1 \rangle = \langle \epsilon_2 \rangle = \pm |\epsilon_0|$  as depicted by Fig. 6.4 (b). A first distinction between this gapped spin liquid state and the Haldane and rung-singlet phases of the two-leg spin ladder stems from the ground-state degeneracy and the fact that the lattice translation symmetry is spontaneously broken in the

ground states of Fig. 6.4. A more drastic difference appears at the level of the low-lying excitations. Indeed, the elementary excitations of the spin-

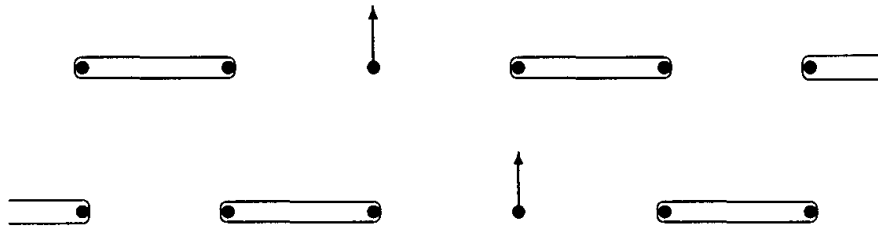


Fig. 6.5. Triplet excitation of the alternating dimerization described in terms of a pair of dimerization kinks of each chain.

orbital model are neither optical magnons nor massive spinons but a pair of propagating massive triplet or singlet kinks connecting two spontaneously dimerized ground states<sup>133</sup>. An example of such a triplet excitation is described in Fig. 6.5 for the staggered dimerization phase with  $K > 0$ . The composite nature of the  $S = 1$  excitation reveals itself in the dynamical structure factor of the model which can be determined using the Ising description (19) of the total and relative staggered magnetizations<sup>133</sup>. The dynamical magnetic susceptibility displays a two-particle threshold instead of a sharp magnon peak near  $q = \pi/a_0$  as in the two-leg spin ladder or the spin-1 chain. This incoherent background in the dynamical structure factor leads to a new gapped spin liquid phase in unfrustrated quantum magnetism without any coherent magnon excitations. In this respect, this state has been called non-Haldane spin liquid by Nersesyan and Tsvelik<sup>133</sup>. The existence of this spin liquid phase has been confirmed non-perturbatively at two special points in the phase diagram of the spin-orbital model (21). At  $J = 3K/4$ , the ground state is exactly known<sup>150</sup> and is a product of checkerboard-ordered spin and orbital singlets as in Fig. 6.4 (a) obtained in the weak coupling limit. At  $K = -4J$ , the model is exactly solvable and the ground-state energy and triplet energy gap have been determined exactly<sup>151</sup>. The system has two spontaneously dimerized ground states and belongs to the class of non-Haldane spin liquid.

Finally, it is worth noting that the alternating and in-phase dimerization phases can be distinguished in close parallel to the topological distinction between the two gapped phases of the two-leg spin ladder. Using the topological criterion of Kim et al.<sup>137</sup>, one observes from Fig. 6.4 that the number  $Q_y$  of valence bonds crossing a vertical line is odd (respectively

even) for the staggered (respectively in-phase) dimerization. The two non-Haldane spin liquid phases with  $K > 0$  and  $K < 0$  belong thus to two different topological classes. This difference becomes manifest when investigating the structure of the edge states of the two phases with open BC. The physical properties of these boundary excitations of the semi-infinite spin-orbital model (21) can be determined by means of the Ising mapping (22) of the weak coupling limit similarly to the cut two-leg ladder<sup>83</sup>. For  $K < 0$ , such edge states are absent whereas, in the  $K > 0$  case, two spin-1/2 chain-end excitations are expected<sup>152</sup>.

### 6.3. Frustration effects

In this section, we shall review some of the main aspects of the interplay between frustration and quantum fluctuations in AF spin chains and spin ladders. The natural question is whether frustration can stabilize new types of spin liquid phases with exotic spin excitations not encountered in Section 2. The paradigmatic model to analyse the effect of frustration in spin chains is the  $J_1 - J_2$  spin-1/2 Heisenberg chain with Hamiltonian:

$$\mathcal{H} = J_1 \sum_i \vec{S}_i \cdot \vec{S}_{i+1} + J_2 \sum_i \vec{S}_i \cdot \vec{S}_{i+2}, \quad (24)$$

where the next-nearest neighbor coupling  $J_2 > 0$  is a competing AF interaction which introduces frustration. This model can also be viewed as a frustrated two-leg spin ladder where the spin chains are coupled in a zigzag way as shown in Fig. 6.6. Let us first discuss some of the main characteristics of frustration in 1D spin systems by means of a semiclassical approach.

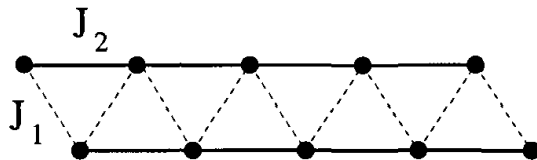


Fig. 6.6. Two-leg zigzag ladder.

#### 6.3.1. Semiclassical analysis

Classically, one of the main effect of frustration is to favor non-collinear magnetic ordering where the spins lie in a plane rather than along a single

direction as in unfrustrated spin systems:

$$\vec{S}_i = S \cos(\vec{Q} \cdot \vec{r}_i) \vec{n}_1 + S \sin(\vec{Q} \cdot \vec{r}_i) \vec{n}_2, \quad (25)$$

where  $\vec{r}_i$  is the spatial location of the site  $i$  and  $\vec{n}_{1,2}$  are two mutually orthogonal fixed vectors in spin space with unit length. The magnetic structure corresponding to the ordering (25) is a circular spiral with a pitch angle related to the wave-vector  $\vec{Q}$  which is, in general, incommensurate. In the case of the  $J_1 - J_2$  chain (24), the spiral ground state is stabilized when  $J_2/J_1 > 1/4$ . The spins are arranged in a canted configuration in which each spin makes an angle  $\alpha$  with its predecessor such that  $\cos \alpha = -J_1/4J_2$ . The classical ground state of the model is doubly degenerate since the spin configurations (25) can turn clockwise and counterclockwise with the same energy along the spiral axis  $\vec{n}_3 = \vec{n}_1 \wedge \vec{n}_2$ . A  $Z_2$  discrete symmetry characterized by this right- and left-handed chirality is thus spontaneously broken in this helical structure. A corresponding chiral ordering<sup>153</sup> can be defined and detected by the chiral order parameter:  $\langle (\vec{S}_i \wedge \vec{S}_{i+1}) \cdot \vec{n}_3 \rangle \neq 0$ . In contrast to the Néel state of unfrustrated magnets, the SU(2) spin rotation of the Heisenberg Hamiltonian is completely broken in the non-collinear state (25). Three Goldstone or spin-wave modes are thus expected here from this spontaneous symmetry breaking scheme. It leads to a CFT with central charge  $c = 3$  with extended criticality in comparison to the unfrustrated case ( $c = 2$ , see Section 2). A second distinction stems from the spin-wave calculation<sup>154</sup> for non-collinear ordered states which reports the presence of two different spin-wave velocities. Therefore, the low-energy field theory describing canted magnets is expected to be non-Lorentz invariant. To identify this effective field theory, one needs to define a suitable order parameter for canted magnets. The long-wavelength fluctuations of the spin configurations (25) can be captured by introducing a two-component complex field  $z_a, a = 1, 2$  of unit modulus ( $|z_1|^2 + |z_2|^2 = 1$ ) such that<sup>2</sup>:

$$\vec{n}_1 + i\vec{n}_2 = \epsilon_{ac} z_c \vec{\sigma}_{ab} z_b, \quad (26)$$

where  $\epsilon_{ab}$  is the standard antisymmetric tensor and  $\vec{\sigma}$  is a vector formed by the Pauli matrices. It is indeed straightforward to see that this identification (26) correctly reproduces the constraints:  $\vec{n}_1^2 = \vec{n}_2^2 = 1$  and  $\vec{n}_1 \cdot \vec{n}_2 = 0$  if the two-component complex field  $z_a$  belongs to the three-dimensional surface of the unit sphere in four dimensions denoted by  $S^3$ . Moreover, it is worth noting that the field  $z = (z_1, z_2)$  transforms like a  $S = 1/2$  spinor under spin rotations. The representation (26) is double-valued since  $z$  and  $-z$

describe the same non-collinearly ordered state. The order parameter space corresponding to canted magnets (25) is thus  $S^3/Z_2$ .

A crucial consequence of this identification is that the order parameter allows topologically nontrivial vortices having a  $2\pi$  circulation since  $\pi_1(S^3/Z_2) = Z_2$ <sup>155</sup>. Upon encircling such a  $Z_2$  vortex, called now a vison<sup>156</sup>, by a closed loop, the value of the spinor complex field  $z = (z_1, z_2)$  changes smoothly from  $z$  to  $-z$ , i.e. two points diametrically opposed on the surface of a sphere  $S^3$ . The existence of these stable vison defects reveals itself in the semiclassical description of frustrated spin chains like the  $J_1 - J_2$  Heisenberg chain (24). In particular, in sharp contrast to unfrustrated spin chains, no Pontryagin topological term has been found in the effective action that describes the low-energy properties of the  $J_1 - J_2$  Heisenberg chain<sup>157,158</sup> and two-dimensional frustrated Heisenberg antiferromagnets<sup>159</sup> in the large spin limit. This stems from the very special topological nature of the order parameter for canted magnets which has a trivial second homotopy group:  $\pi_2(S^3/Z_2) = 0$ <sup>155</sup>. However, there is still a subtle distinction between half-integer and integer spins in the  $J_1 - J_2$  Heisenberg chain<sup>160,157</sup> related to the existence of stable visons. A Berry phase calculation<sup>157,160,161,162</sup> shows that tunneling between sectors with different  $Z_2$  topological number is possible for integer spins but not for half-integer spins due to cancellation between pairs of paths. The ground state of the  $J_1 - J_2$  model is thus non-degenerate for integer spins and two-fold degenerate (two different sectors non-coupled by tunneling effect) for half-integer spins. The quantum number carried by elementary excitations depends also strongly on the nature of the spins<sup>160</sup>. In the half-integer case, there is an energy gap towards the creation of  $Z_2$  visons so that these topological defects are strongly suppressed. The low-energy excitations are then described by the spinor field  $z = (z_1, z_2)$  of Eq. (26) which is free to propagate in absence of visons and carries a  $S = 1/2$  quantum number under spin rotations. Neglecting anisotropy, the Euclidean effective action that governs the leading low-energy properties of the  $J_1 - J_2$  chain for half-integer spins is the  $SU(2) \times SU(2)$  principal chiral model defined by

$$\mathcal{S}_G = \frac{v}{2g} \int dx d\tau \text{Tr} (\partial_\mu G^\dagger \partial_\mu G), \quad (27)$$

where  $G$  is a  $SU(2)$  matrix formed by the two complex fields  $z_{1,2}$ . This field theory<sup>163,164</sup> is integrable and its low-energy spectrum consists of massive excitation with  $S = 1/2$  quantum number i.e. massive deconfined spinons. In contrast, in the integer spin case, the visons now proliferate in

the ground state so that the spinor field  $z = (z_1, z_2)$  cannot any longer be defined as single-valued configurations. The suitable fields that describe the low-energy excitations of the  $J_1 - J_2$  chain with integer spins are bilinear of  $z$  and correspond to the  $\vec{n}_{1,2}$  fields of Eq. (26). In that case, neglecting anisotropy, the effective field theory that captures the leading low-energy properties of the frustrated spin chain with integer spins is the non-linear sigma model  $\text{SO}(3) \times \text{SO}(3)$  with action:

$$S_R = \frac{v}{2g} \int dx d\tau \text{Tr} (\partial_\mu R^{-1} \partial_\mu R), \quad (28)$$

where  $R$  is a rotation matrix made of the triplet vectors  $\vec{n}_{1,2}$  and  $\vec{n}_3 = \vec{n}_1 \wedge \vec{n}_2$ . The low-lying spectrum of this field theory can be determined by a large N approach<sup>157,158</sup> or by means of a strong-coupling analysis<sup>160</sup>: it consists of a triplet of  $S = 1$  massive magnons. In the integer spin case, the spinons are thus expected to be confined into optical magnons.

An important prediction, obtained in this semiclassical description, is thus the existence of a gapped spin liquid phase for half-integer spins with a two-fold degenerate ground state and massive deconfined spinons. Such a state is stabilized by frustration and represents a spin liquid phase not encountered in Section 2. We shall now consider the ultra-quantum case with  $S = 1/2$  where a combination of numerical and field theoretical techniques can be used to fully determine the main characteristics of this spin liquid phase.

### 6.3.2. Spin liquid phase with massive deconfined spinons

The phase diagram of the spin-1/2  $J_1 - J_2$  Heisenberg chain (24) has been studied extensively over the years after the bosonization analysis of Haldane<sup>165</sup>. This problem is not also a purely academic question since inorganic compounds such as  $\text{CuGeO}_3$ <sup>166,167</sup> or  $\text{LiV}_2\text{O}_5$ <sup>168</sup> can be considered as prototypes of the spin-1/2  $J_1 - J_2$  chain (24). In particular, values such as  $J_1 \simeq 160$  K and  $J_2/J_1 \simeq 0.36$  have been proposed for  $\text{CuGeO}_3$ <sup>169</sup>. In addition, the quasi-1D compound  $\text{SrCuO}_2$  contains a collection of spin-1/2 Heisenberg chains assembled pairwise in an array of weakly coupled zigzag ladders<sup>170,171</sup>. These zigzag ladders are built from corner-sharing Cu-O chains with an exchange  $J_2$  staked pairwise in edge-sharing geometry. The frustrating interaction  $J_1$  between the chains (see Fig. 6.6) stems from the nearly  $90^\circ$  Cu-O-Cu bonds and is expected to be weak<sup>170</sup>. Finally, two other possible realizations of the spin-1/2  $J_1 - J_2$  chain (24) have been recently proposed: the compound  $(\text{N}_2\text{H}_5)\text{CuCl}_3$  which can be

described as a two-leg zigzag spin ladder with  $J_1/J_2 \simeq 0.25$ <sup>172</sup> and Cu[2-(2-aminomethyl)pyridine]Br<sub>2</sub> with a ratio  $J_2/J_1 \simeq 0.2$ <sup>173</sup>.

A starting point for investigating the phase diagram of the spin-1/2  $J_1 - J_2$  chain (24) is to consider the weak coupling limit when  $J_2 \ll J_1$ . This enables us to study the stability of the massless spinons of the spin-1/2 AF Heisenberg chain upon switching on a small next-nearest-neighbor frustrating interaction  $J_2$ . In this weak-coupling regime, the low-energy effective Hamiltonian density of the model reads as follows<sup>165</sup>:

$$\mathcal{H}_{\text{eff}} = \frac{2\pi v}{3} \left( \vec{J}_L^2 + \vec{J}_R^2 \right) + \gamma \vec{J}_L \cdot \vec{J}_R, \quad (29)$$

where  $\vec{J}_{L,R}$  are the left and right su(2)<sub>1</sub> currents that generate the su(2)<sub>1</sub> quantum criticality of the spin-1/2 AF Heisenberg chain. The low-energy physics of the model are thus mainly determined by the marginal current-current interaction of Eq. (29) with coupling constant  $\gamma \simeq J_2 - J_{2c}$ ,  $J_{2c}$  being a non-universal positive constant. For a small value of  $J_2$ , one has  $\gamma < 0$  so that the interaction in Eq. (29) is a marginal irrelevant contribution. The low-energy physics of the  $J_1 - J_2$  chain is thus identical to that of the spin-1/2 AF Heisenberg chain which is governed by the su(2)<sub>1</sub> fixed point with additional logarithmic corrections introduced by the current-current interaction. In this respect, frustration plays no important role in the regime  $J_2 < J_{2c}$  and the spin-1/2 Heisenberg phase with massless spinons is stable upon switching on a small value of  $J_2$ . However, for  $J_2 > J_{2c}$  ( $\gamma > 0$ ), the current-current interaction becomes marginal relevant and a strong coupling regime develops with a dynamically generated spectral gap. A phase transition of Berezinskii-Kosterlitz-Thouless (BKT) type<sup>174</sup> occurs at  $J_2 = J_{2c}$  which separates the gapless spin-1/2 Heisenberg phase from a fully massive region. The actual value of the transition has been determined numerically by different groups to be:  $J_{2c} \simeq 0.2411 J_1$ <sup>175,176,177,178</sup>. At this point, it is worth noting that the quasi-1D material Cu[2-(2-aminomethyl)pyridine]Br<sub>2</sub> can be described by a spin-1/2  $J_1 - J_2$  Heisenberg chain with  $J_2/J_1 \simeq 0.2$ <sup>173</sup> and should thus belong to the critical Heisenberg phase with  $J_2 < J_{2c}$ . The absence of a spin gap for this compound has been reported experimentally<sup>173</sup>.

The main characteristics of the strong coupling massive phase with  $J_2 > J_{2c}$  can be determined from Eq. (29). The field theory (29) is indeed integrable and corresponds to a chiral Gross-Neveu model or a non-Abelian version of the Thirring model with a SU(2) symmetry. The low-energy excitations of the model (29) are a massive doublet (massive spinons) with

mass  $m \sim a_0^{-1} \exp(-2\pi/\gamma)$ <sup>179,180</sup>. A striking effect of frustration is thus the formation of a mass for the spinons of the spin-1/2 AF Heisenberg chain without confining them into  $S = 1$  excitations as in the two-leg spin ladder. A second consequence of frustration is the presence of spontaneously dimerization in the model. A simple way to exhibit this dimerization is to use the bosonization approach to express the Hamiltonian (29) in terms of a  $\beta^2 = 8\pi$  sine-Gordon model<sup>165</sup>:

$$\mathcal{H}_{\text{eff}} = \frac{v}{2} \left[ (\partial_x \Phi)^2 + (\partial_x \Theta)^2 \right] + \frac{\gamma}{2\pi} \partial_x \Phi_R \partial_x \Phi_L - \frac{\gamma a_0^2}{4\pi^2} \cos \sqrt{8\pi} \Phi, \quad (30)$$

where  $\Phi_{R,L}$  are the chiral components of the bosonic field  $\Phi$  ( $\Phi = \Phi_R + \Phi_L$ ) and  $\Theta$  is its dual field ( $\Theta = \Phi_L - \Phi_R$ ). The SU(2) invariance of the model (30) is hidden in the structure of the interaction with a single coupling constant and the fact that the bosonic field  $\Phi$  is compactified on a circle with a special radius  $R = 1/\sqrt{2\pi}$  consistent with the SU(2) symmetry. This compactification leads to the following identification:

$$\Phi \sim \Phi + 2\pi R n = \Phi + n\sqrt{2\pi}, \quad (31)$$

$n$  being integer. In the phase with  $J_2 > J_{2c}$ , one has  $\gamma > 0$  so that the bosonic field is pinned at one of its minima:  $\langle \Phi \rangle = p\sqrt{\pi/2}$ ,  $p$  being integer. However, by taking into account the identification (31), the  $\beta^2 = 8\pi$  sine-Gordon model (30) has only two inequivalent ground states with  $\langle \Phi \rangle = 0$  and  $\langle \Phi \rangle = \sqrt{\pi/2}$ . This two-fold degeneracy can be interpreted as resulting from the spontaneous breaking of a discrete  $Z_2$  symmetry. This symmetry identifies with the one-step translation symmetry ( $T_{a_0}$ ) which is described by the following shift on the bosonic field<sup>24</sup>:  $\Phi \rightarrow \Phi + \sqrt{\pi/2}$ . This symmetry is spontaneously broken in the phase  $J_2 > J_{2c}$  and the two ground-state field configurations are connected by this translation symmetry. An order parameter designed to characterize this phase is the spin dimerization operator  $\epsilon_n = (-1)^n \vec{S}_n \cdot \vec{S}_{n+1}$  which admits the following bosonic representation in the continuum limit  $\epsilon \sim \cos \sqrt{2\pi} \Phi$ <sup>24,10</sup>. This operator changes sign under the lattice translation symmetry and has a non-zero expectation value  $\langle \epsilon \rangle \neq 0$  in the two ground states of the  $\beta^2 = 8\pi$  sine-Gordon model (30).

For  $J_2 > J_{2c}$ , frustration stabilizes thus a gapful spontaneously dimerized phase which is characterized by a two-fold degenerate ground state and a spontaneous breaking of the lattice translation symmetry. The elementary excitations of this phase are massive spinons that carry  $S = 1/2$  quantum number and identify with the kinks of the underlying dimerization. A simple way to understand the emergence of these deconfined spinons is to consider the Majumdar-Ghosh (MG)<sup>181</sup> point at  $J_2 = J_1/2$  where the

ground state of the lattice model (24) is exactly known. This MG point for the spontaneously dimerized phase plays a similar role than the AKLT point (10) for describing the main properties of the Haldane phase in the phase diagram of the spin-1 bilinear-biquadratic chain (9). For  $J_2 = J_1/2$ , the Hamiltonian (24) takes the following form up to a constant:

$$\mathcal{H}_{\text{MG}} = \frac{3J_1}{4} \sum_i P_{3/2}(i-1, i, i+1), \quad (32)$$

where  $P_{3/2}(i-1, i, i+1)$  projects the total spin of the three spins located at sites  $i-1, i, i+1$  onto the  $S = 3/2$  subspace. For an even number of sites  $N$  and periodic BC, the ground state of the MG model (32) is two-fold degenerate and corresponds to the two singlet states:

$$\begin{aligned} |\Phi_1\rangle &= [1, 2] [3, 4] \dots [N-1, N] \\ |\Phi_2\rangle &= [2, 3] [4, 5] \dots [N, 1], \end{aligned} \quad (33)$$

where  $[i, i+1]$  denotes a singlet bond between the spins at the  $i$  and  $i+1$  sites. The two ground states (33) are represented in Fig. 6.7. The lattice

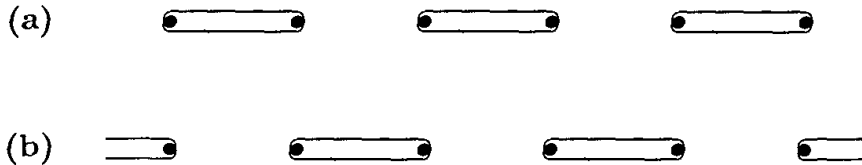


Fig. 6.7. The two dimerized ground states at the Majumdar-Ghosh point; (a)  $|\Phi_1\rangle$ , (b)  $|\Phi_2\rangle$ .

translation symmetry  $T_{a_0}$  is broken in the two ground states (33) and it exchanges them:  $T_{a_0}|\Phi_{1,2}\rangle = |\Phi_{2,1}\rangle$ . The existence of gap in the MG model (32) has been shown rigorously by Affleck et al.<sup>57</sup> and the spin-spin correlation function can be determined exactly at the MG point<sup>182</sup>:

$$\langle \vec{S}_i \cdot \vec{S}_j \rangle = \frac{3}{4} \delta_{i,j} - \frac{3}{8} \delta_{|i-j|,1}. \quad (34)$$

This correlation function is thus zero for distance larger than one lattice spacing. The ground-state degeneracy and the spontaneous breaking of a

discrete  $Z_2$  symmetry suggest the existence of topological excitations which interpolate between the two ground states (33). These kink excitations can be viewed as the insertion of a spin-1/2 in a sea of singlet valence bond states as shown in Fig. 6.8. This spin-1/2 excitation (spinon) is nothing but a domain wall between the two states (33). For periodic BC, these kinks

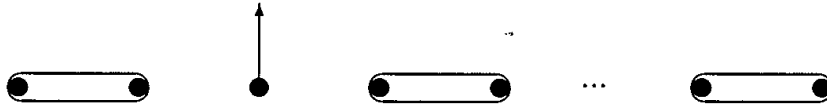


Fig. 6.8. Dimerization kink (spinon) with  $S = 1/2$  quantum number.

states appear always in pairs (see Fig. 6.9) and the low-lying excitations of the MG model can be built starting from the state<sup>182</sup>:

$$|p, m\rangle = [1, 2] \dots [2p - 3, 2p - 2] \alpha_{2p-1} [2p, 2p + 1] \dots [2m - 2, 2m - 1] \alpha_{2m} [2m + 1, 2m + 2] \dots [N - 1, N], \quad (35)$$

where  $\alpha_{2p-1}$  and  $\alpha_{2m}$  denote spin-1/2 states located at the sites  $2p - 1$  and  $2m$  respectively. A variational approach of the low-lying excitations<sup>182,183</sup> can then be done by considering a linear combination of states (35) and it leads to a triplet and singlet continuum spin excitations. In particular,



Fig. 6.9. Spin-1 excitation built from two spinons.

the dispersion relation of a massive spinon, obtained within this approach, takes the form<sup>182</sup>:

$$\epsilon(k) = \frac{5J_1}{8} + \frac{J_1}{2} \cos(2ka_0). \quad (36)$$

This dispersion relation has been verified numerically by exact diagonalizations<sup>184</sup>. Finally, as shown by Caspers and Magnus<sup>185</sup>, there are additional

exact singlet and triplet bound-states at momentum  $k = \pi/2a_0$  which are degenerate with energy  $E = J_1$ . Exact diagonalization and DMRG calculations<sup>184</sup> have confirmed the existence of these bound-states for a small range of momenta close to  $k = \pi/2a_0$  in the region  $J_2 \geq J_1/2$ .

In summary, the spontaneously dimerized phase for  $J_2 > J_{2c}$  represents a distinct spin liquid phase stabilized by frustration. The main distinction, from the spin liquid phases of the two-leg spin ladder and spin-orbital model, originates in the fractionalized nature of the quantum number carried by elementary excitations. In particular, instead of a sharp  $S = 1$  magnon peak as in the two-leg spin ladder, the dynamical structure factor of the model in this dimerized phase displays an incoherent background with additional bound-states features. The main difference between the dimerized phase of Fig. 6.7 and the staggered dimerization phase of the spin-orbital model (21) stems from the nature of the low-lying excitations. In the latter phase, the excitations are a pair of propagating massive triplet kinks, as described above, whereas here the elementary excitations are massive spinons.

This dimerized phase, with deconfined massive spinons excitations, extends in the entire region with  $J_2 > J_{2c}$  as it has been shown numerically. Fig. 6.10 represents the evolution of the spin gap  $\Delta$ , computed by DMRG<sup>178</sup>, as function of the next-nearest neighbor interaction  $J_2$ . As depicted by

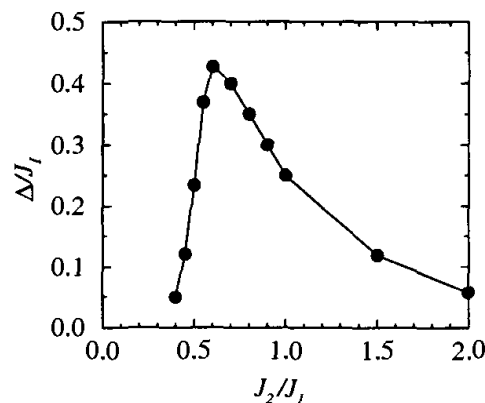


Fig. 6.10. Evolution of the spin gap, computed by DMRG, as a function of  $J_2$  for  $J_2 > J_{2c}$ ; taken from Ref. 178.

Fig. 6.10, the spin gap is maximum for  $J_2/J_1 \simeq 0.6$  and decreases to zero in the large  $J_2$  limit. The absence of a spin gap in this regime can be easily

understood since for  $J_2 \gg J_1$ , the  $J_1 - J_2$  spin chain can be better viewed as a two-leg zigzag ladder (see Fig. 6.6). In the limit  $J_2 \rightarrow +\infty$ , the two spin-1/2 Heisenberg chains are decoupled so that the model is critical:  $\Delta = 0$ . From the results of Fig. 6.6, it is very tempting to conclude that the whole region with  $J_2 > J_{2c}$  describes a single phase. However, a subtle qualitative change occurs in the model at the level of spin correlation functions after the MG point in close parallel to the Haldane phase of the spin-1 bilinear-biquadratic chain (9) just after the AKLT point (10)<sup>72,186,187</sup>. Indeed, an incommensurate behavior develops in the real-space spin-spin correlation function for  $J_2 > J_1/2$ <sup>176,188,178,189,190</sup>. This incommensurability can be interpreted as a quantum signature of the spiral structure of the classical ground state of the  $J_1 - J_2$  spin chain for  $J_2 > J_1/4$ . After the MG point, the leading asymptotic of the spin-spin correlation function behaves as

$$\langle \vec{S}_i \cdot \vec{S}_{i+r} \rangle \sim \frac{1}{r^{1/2}} \cos(q r a_0) \exp(-ra_0/\xi), \quad (37)$$

where the oscillation factor depends on  $J_2/J_1$ . In parallel to the classification of commensurate-incommensurate transitions in Ising spin systems<sup>191</sup>, the MG point, as the AKLT point (10), is a disorder point of the first kind<sup>72</sup>. The momentum  $q_{\max}$  which maximizes the static structure factor (Fourier transform of the spin-spin correlation function) becomes incommensurate not at the MG point but slightly after  $J_{2L} \simeq 0.5206J_1$ <sup>188</sup> at a Lifshitz point<sup>72</sup>. For  $J_2 > J_{2L}$ , the static structure factor displays a double peak structure rather than a single peak. The low-lying excitations are then characterized by an incommensurate momenta  $q_{\max} \neq \pi/a_0$ . In contrast to the classical case, it is worth noting that the BKT phase transition between the critical and dimerized phases and the onset of incommensurability at the Lifshitz point occur at different points of the phase diagram,  $J_{2c} \simeq 0.2411J_1$  and  $J_{2L} \simeq 0.5206J_1$  respectively. Though no real phase transition occurs for  $J_2 > J_{2c}$  in the model, the dimerized phase in the region  $J_2 > J_{2L}$  can be distinguished from that at  $J_{2c} < J_2 < J_{2L}$  due to the existence of this incommensurability. In this respect, the spontaneously dimerized phase for  $J_2 > J_{2L}$  with deconfined massive spinons and incommensurate correlations represents a remarkable 1D spin liquid phase stabilized by frustration.

This incommensurability induced by frustration is, in fact, quite general in 1D and not restricted to the spin-1/2 case. In particular, this phenomenon appears also in the spin-1 case. The zero-temperature phase diagram of the spin-1  $J_1 - J_2$  Heisenberg chain (24) has been investigated numerically<sup>192,158,193,194,195,196</sup> and a spectral gap exists for all finite value of  $J_2$ . A

first-order transition occurs at  $(J_2/J_1)_T \simeq 0.744$ <sup>194</sup> separating a Haldane phase from a double Haldane phase<sup>194,195,196</sup>. The quantum number carried by elementary excitations is  $S = 1$  in full agreement with the semiclassical approach<sup>160</sup> described above. Frustration plays its trick here by giving rise to a similar onset of incommensurability as in the spin-1/2 case. A disorder point of the first kind occurs at  $(J_2/J_1)_D \simeq 0.284$  together with a Lifshitz point  $(J_2/J_1)_L \simeq 0.3725$ <sup>194</sup> after which the static structure factor develops a two-peak structure.

### 6.3.3. Field theory of spin liquid with incommensurate correlations

Frustration represents thus a novel mechanism in one dimension for generating incommensurability as external magnetic fields or Dzyaloshinskii-Moriya interaction<sup>197</sup>. The zigzag ladder representation (Fig. 6.6) of the  $J_1 - J_2$  model enables one to investigate, by a weak coupling approach  $J_1 \ll J_2$ , the main characteristics of frustration and to shed light on the mechanism that gives rise to incommensurate correlations in the large  $J_2$  regime. In the spin-1/2 case, the onset of incommensurability and the presence of deconfined massive spinons might be understood starting from the limit where the two spin-1/2 AF Heisenberg chains are decoupled.

The continuum limit of the  $S = 1/2$  two-leg zigzag ladder has been analysed by several groups<sup>178,136,198,199,200,201,202</sup>. The interacting part of the Hamiltonian density of the low-energy field theory reads as follows:

$$\mathcal{H}_{\text{int}} \simeq g_1 \left( \vec{J}_{1L} \cdot \vec{J}_{2R} + \vec{J}_{2L} \cdot \vec{J}_{1R} \right) + g_2 \vec{n}_1 \cdot \partial_x \vec{n}_2, \quad (38)$$

where  $\vec{J}_{a,L,R}$  ( $a = 1, 2$ ) are the left-right  $\text{su}(2)_1$  currents corresponding to the continuum description of the  $a$ th spin-1/2 AF Heisenberg chain. In Eq. (38),  $\vec{n}_a$  denotes the staggered magnetization of the spin density of the chain with index  $a = 1, 2$ . In the continuum limit, this  $\vec{n}_a$  field identifies with the vector part of the primary field, with scaling dimension  $\Delta_n = 1/2$ , of the  $\text{su}(2)_1$  WZNW CFT transforming according to the fundamental representation of  $\text{SU}(2)$ <sup>15,40,24,10</sup>. In this continuum description, frustration suppresses geometrically the standard backscattering contribution  $\vec{n}_1 \cdot \vec{n}_2$  which governs the low-energy physics of the two-leg spin ladder. This term represents a strongly relevant perturbation of scaling dimension 1. It corresponds to the energy operators of the underlying Ising models of the low-energy description (16) of the two-leg spin ladder<sup>89,132</sup>. As seen in Section 2, this backscattering contribution leads to the formation of a spin gap in

this model as well as the confinement of the original massless spinons into optical magnons. In presence of frustration, the interacting part (38) is now only marginal relevant and consists of two terms of different nature. The first one, with coupling constant  $g_1$ , is a current-current interaction similar to that which appears in the effective field theory (29) of the spin-1/2  $J_1-J_2$  Heisenberg chain in the weak coupling limit  $J_2 \ll J_1$ . The second marginal contribution in Eq. (38), called twist term<sup>199</sup>,  $\mathcal{O}_{\text{twist}} = \vec{n}_1 \cdot \partial_x \vec{n}_2$  is a novel parity-breaking perturbation which contains the staggered magnetizations of each chain and also a spatial derivative. In contrast to the current-current perturbation, this twist term is not a scalar under the Lorentz transformation in 1 + 1 dimensions but behaves as a vector. In the CFT jargon, this kind of perturbation is characterized by a non-zero conformal spin  $S = \pm 1$  together with its scaling dimension  $\Delta = 2$ . In fact, this twist perturbation has been forgotten in the first bosonization analysis of the two-leg zigzag spin ladder<sup>178,136</sup>. It has been discovered by Nersesyan et al.<sup>199</sup> and independently by Allen<sup>198</sup>. It is interesting to observe that a similar operator appears in the effective field theory approach to the spin-1 two-leg zigzag ladder in the large  $J_2$  limit<sup>203</sup>. This twist perturbation is thus the hallmark of frustration in the low-energy description of frustrated spin ladders with zigzag interchain interaction.

The effect of such a non-zero conformal spin perturbation is non-trivial since the usual irrelevant versus relevant criterion of perturbative field theory does not hold for such a non-scalar contribution (see for instance the discussion in the book<sup>10</sup>). In the case of a  $S = \pm 1$  perturbation, it is expected that the generic effect of this contribution is the onset of incommensurability. In this respect, a simple example of incommensurability arising from such a perturbation is the spin-1/2 XXZ Heisenberg chain in a magnetic field along the z-axis. The Hamiltonian density of this model, obtained within the bosonization approach, reads as follows<sup>204</sup>:

$$\mathcal{H} = \frac{v}{2} \left[ (\partial_x \Phi)^2 + (\partial_x \Theta)^2 \right] - g \cos \beta \Phi - h \partial_x \Phi. \quad (39)$$

Here the  $S = \pm 1$  perturbation is described by the uniform part of the spin density  $\partial_x \Phi$ . It is well known that in this model, when the magnetic field  $h$  is increased, a commensurate-incommensurate phase transition takes place with the appearance of an incommensurate phase with critical correlation functions<sup>205,206,207,208</sup>. This transition occurs for a finite or vanishing magnetic field depending on the relevance or irrelevance of the  $\cos \beta \Phi$  term. A similar incommensurability generated by a  $S = \pm 1$  conformal spin perturbation occurs in the spin-1/2 XXZ Heisenberg chain in a transverse

magnetic field<sup>209,210,211</sup>, in a model of two spinless Luttinger chains weakly-coupled by a single-particle interchain hopping<sup>212,209,213</sup>, and in the quantum axial next-to-nearest neighbor Ising (ANNNI) chain in a transverse magnetic field<sup>214</sup>. Finally, it is important to note that there exists some exactly solvable CFT models perturbed by  $S = \pm 1$  conformal spin term for which the presence of incommensurability can be shown non-perturbatively<sup>215,216</sup>.

All these results suggest that the twist term  $\mathcal{O}_{\text{twist}} = \vec{n}_1 \cdot \partial_x \vec{n}_2$ , as proposed by Nersesyan et al.<sup>199</sup>, should be at the origin of the incommensurability found numerically in the spin-1/2  $J_1 - J_2$  Heisenberg chain (24) when  $J_2 > 0.52J_1$ . To this end, this twist term and the current-current interaction of Eq. (38) can be expressed in terms of the four Majorana fermions  $\xi_{R,L}^a, a = 0, 1, 2, 3$  of the continuum limit (16) of the standard two-leg spin ladder<sup>198,199</sup>. In particular, the current-current interaction is built from of the following tensor:  $\mathcal{O}_{cc}^{ab} = \xi_R^a \xi_L^a \xi_R^b \xi_L^b$  with  $a, b = 0, 1, 2, 3$  and  $a \neq b$ . The twist perturbation is also local in terms of these Majorana fermions but with a different structure. A typical term that enters its expression is  $\mathcal{O}_{\text{twist}}^{abcd} = \xi_R^a \xi_L^b \xi_L^c \xi_L^d$  with  $a, b, c, d = 0, 1, 2, 3$  and  $a \neq b \neq c \neq d$ . The non-zero conformal spin of this twist term is reflected here by the different number of right and left fermions in this expression. The field theory (38), expressed in terms of these four Majorana fermions, turns out not to be integrable. The renormalization group (RG) flow analysis reveals that the current-current interaction and the twist term are equally important in the IR limit. They reach a strong coupling regime simultaneously with a fixed ratio<sup>198,201,202</sup>. The nature of this strong coupling regime is still an open problem since the emerging IR field theory is not integrable and one cannot disentangle the effect of the two interactions of Eq. (38). However, it is very tempting to explain the main characteristics of the spontaneously dimerized phase with incommensurate correlation of the spin-1/2  $J_1 - J_2$  Heisenberg chain in the large  $J_2$  limit from these two contributions. On one hand, the current-current contribution of Eq. (38), equivalent to two decoupled SU(2) Thirring model, has similar properties as the field theory (29) obtained in the weak coupling regime  $J_2 \ll J_1$ . The spontaneously dimerization and the existence of massive deconfined spinons should result from this interaction. In fact, this current-current interaction appears alone, without a twist term, in the continuum limit of a frustrated two-leg spin ladder with crossings along a special line of the couplings<sup>201</sup>. It has been shown that this model, in the weak coupling limit, is characterized by a weak spontaneously dimerization with massive spinons as elementary

excitations<sup>201</sup>. Finally, as already stressed, the twist perturbation of Eq. (38) should be at the origin of the incommensurability in the large  $J_2$  limit<sup>199</sup>. In this respect, the effect of the twist term of the two-leg zigzag ladder has been analysed within a RPA approach and it leads indeed to some incommensurability behavior in the spin-spin correlation function<sup>217</sup>.

A simple way to disentangle the effects of the current-current interaction and the twist perturbation is to introduce an exchange anisotropy which makes the twist contribution more relevant in the RG sense<sup>199</sup>. The extreme case is the XY version of the spin-1/2  $J_1 - J_2$  Heisenberg chain with Hamiltonian:

$$\mathcal{H}_{\text{XY}} = J_1 \sum_n (S_n^x S_{n+1}^x + S_n^y S_{n+1}^y) + J_2 \sum_n (S_n^x S_{n+2}^x + S_n^y S_{n+2}^y). \quad (40)$$

In the ladder limit when  $J_2 \gg J_1$ , the low-energy physics of this model can be analysed by means of the bosonization approach. Introducing two bosonic fields  $\Phi_{\pm}$ , the resulting bosonic Hamiltonian density of the model reads as follows<sup>199</sup>:

$$\mathcal{H}_{\text{XY}} \simeq \frac{v}{2} \sum_{a=\pm} \left( (\partial_x \Phi_a)^2 + (\partial_x \Theta_a)^2 \right) + g \partial_x \Theta_+ \sin \left( \sqrt{2\pi} \Theta_- \right), \quad (41)$$

where  $\Theta_{\pm}$  are the dual fields associated to the bosonic fields  $\Phi_{\pm}$ . The Hamiltonian (41) describes a nontrivial field theory with a relevant  $S = \pm 1$  conformal spin twist perturbation with scaling dimension  $\Delta_g = 3/2$ . In this strong anisotropic XY case, the current-current perturbation is less dominant and can be safely neglected to derive the nature of the phase of the model when  $J_2 \gg J_1$ . The presence of incommensurability in the system can then be found using a mean-field analysis of the model by decoupling the two pieces of the twist term of Eq. (41). In particular, the leading asymptotic behavior of the transverse spin-spin correlation functions of the model obtained by this mean-field approach is given by<sup>199</sup>:

$$\langle S_1^\dagger(x) S_a^-(0) \rangle \sim \frac{\exp(iqx)}{|x|^{1/4}}, \quad a = 1, 2, \quad (42)$$

which displays an incommensurate critical behavior with an oscillating factor:  $q - \pi/a_0 \sim (J_1/J_2)^2$ . The physical picture that emerges from this mean-field analysis is the existence of a critical spin nematic phase that preserves the U(1) and time-reversal symmetries and displays long-range chiral ordering in its ground state:  $\langle (\vec{S}_{n+1} \wedge \vec{S}_n)_z \rangle \neq 0$ . It is important to note that this spin nematic phase does not break the time-reversal symmetry but spontaneously breaks a  $Z_2$  symmetry of the model which is a

tensor product of a site-parity and link-parity symmetries on the two chains:  $P_L^{(1)} \times P_S^{(2)}$ . The z-component of the spin current  $J_{as}^z$  associated to the  $a$ th spin-1/2 XY chain ( $a = 1, 2$ ) takes a non-zero expectation value in the ground state of the mean field Hamiltonian <sup>199</sup>:

$$\langle J_{1s}^z \rangle = \langle J_{2s}^z \rangle = -\frac{v}{\sqrt{2\pi}} \langle \partial_x \Theta_+ \rangle \neq 0. \quad (43)$$

As a result, this produces a picture of local nonzero spin currents polarized along the z-anisotropy axis circulating around the triangular plaquettes of the two-leg zigzag spin ladder. This phase has been first found numerically by Nishiyama <sup>218</sup>, who has investigated the existence of chiral order of the Josephson ladder with half a flux quantum per plaquette. It has also been obtained by Hikihara et al. <sup>219</sup> by means of the DMRG approach and by Vieira et al. <sup>220</sup> using exact diagonalization calculations. This critical incommensurate phase is the quantum analogue of the classical spiral phase with chiral ordering <sup>153</sup>. It is thus natural to expect that this phase is not restricted to the spin-1/2 case but should exist in the range of parameters of the model (40) in the general spin case. Indeed, the existence of this critical spin nematic phase in the spin-S case has been shown numerically for  $S = 1, 3/2, 2$  <sup>219,221</sup>, by means of a semiclassical method <sup>222</sup>, and finally by the Abelian bosonization approach <sup>223</sup> of a general spin  $S$  introduced by Schulz <sup>89</sup>.

#### 6.3.4. Extended criticality stabilized by frustration

In addition to incommensurability, a second characteristic of classical canted magnets is the presence of three gapless spin-wave modes instead of two as in the Néel colinear state. An interesting question is whether frustration can lead to new type of emerging quantum criticality not encountered in unfrustrated spin chains or ladders. In this last case, the critical behavior of half-integer AF Heisenberg spin chains or odd-legged spin ladders is characterized by one gapless bosonic mode i. e. by a CFT with central charge  $c = 1$ . As it has already been pointed out in the previous section, a striking effect of frustration in the continuum limit stems from the fact that the low-energy effective field theory is mainly governed by marginal interactions. New type of IR critical behaviors may result from the delicate balance between these marginal perturbations. In the following, we shall give some examples of critical phases and quantum critical points with extended criticality stabilized by frustration in 1D spin systems.

### 6.3.4.1. Critical phases with $SU(N)$ quantum criticality

A first example of a system with extended criticality is the 1D spin-orbital model (21) in a regime where frustration reveals itself  $K \sim J$ . At the special point  $J = K/4$ , the Hamiltonian (21) can be expressed in terms of a product of two-body permutation operator in  $S_1$  and  $S_2$  subspaces:

$$\begin{aligned}\mathcal{H}_{\text{so}} &= J \sum_i \left( 2\vec{S}_{1,i} \cdot \vec{S}_{1,i+1} + \frac{1}{2} \right) \left( 2\vec{S}_{2,i} \cdot \vec{S}_{2,i+1} + \frac{1}{2} \right) \\ &= J \sum_i P_{i,i+1}^{(S_1=1/2)} P_{i,i+1}^{(S_2=1/2)}.\end{aligned}\quad (44)$$

Since this Hamiltonian exchanges both  $\vec{S}_{1,i}$  and  $\vec{S}_{2,i}$  spins at the same time, the spin-orbital model at  $J = K/4$  is not only  $SU(2) \times SU(2)$  symmetric but actually has an enlarged  $SU(4)$  symmetry which unifies the spin and orbital degrees of freedom<sup>224,225,226</sup>. More precisely, the Hamiltonian (44) can be recasted as an AF Heisenberg spin chain with  $SU(4)$  spins up to a constant:

$$\mathcal{H}_{\text{SU}(4)} = J \sum_i \sum_{A=1}^{15} T_i^A T_{i+1}^A,\quad (45)$$

where  $T^A$  are the 15 generators belonging to the fundamental representation of  $SU(4)$ . This model is exactly solvable by means of the Bethe ansatz<sup>227</sup> and its low-energy spectrum consists of three gapless spinons with wave vectors  $\pm\pi/2a_0$  and  $\pi/a_0$ <sup>227,228</sup>. As shown by Affleck<sup>229</sup>, the critical theory corresponds to the  $\text{su}(4)_1$  WZNW model with central charge  $c = 3$  (three massless bosonic modes). The existence of this quantum critical point with a  $SU(4)$  symmetry allows us to study the spin-orbital model (21) by a continuum description in an intermediate coupling regime  $J \sim K$  where frustration shows off. In this respect, it is important to notice that, according to the Zamolodchikov's  $c$  theorem<sup>230</sup>, the  $SU(4)$  critical point with central charge  $c = 3$  cannot be reached by a RG trajectory starting from the decoupling limit ( $K = 0$ ) of two spin-1/2 AF Heisenberg chains with total central charge  $c = 2$ . Stated differently, the physics in the neighborhood of the  $SU(4)$  point cannot be understood in terms of weakly coupled  $S = 1/2$  Heisenberg chains. The strategy to tackle with this intermediate coupling regime is to start from the  $SU(4)$  Hubbard chain at quater-filling and apply the bosonization approach to obtain the continuum description of the spin densities  $\vec{S}_{1,2}(x)$  at the  $SU(4)$  point in the large Coulomb repulsion limit. The low-energy field theory which describes small deviations

from the SU(4) symmetric point can then be derived<sup>231,232</sup>. The resulting effective Hamiltonian density associated to the symmetry breaking scheme  $SU(4) \rightarrow SU(2) \times SU(2)$  of the spin-orbital model (21) reads as follows<sup>231</sup>:

$$\begin{aligned} \mathcal{H}_{\text{eff}} = & -\frac{iv_s}{2} \left( \vec{\xi}_{sR} \cdot \partial_x \vec{\xi}_{sR} - \vec{\xi}_{sL} \cdot \partial_x \vec{\xi}_{sL} \right) - \frac{iv_o}{2} \left( \vec{\xi}_{oR} \cdot \partial_x \vec{\xi}_{oR} - \vec{\xi}_{oL} \cdot \partial_x \vec{\xi}_{oL} \right) \\ & + g_1 \left( \vec{\xi}_{sR} \cdot \vec{\xi}_{sL} \right)^2 + g_2 \left( \vec{\xi}_{oR} \cdot \vec{\xi}_{oL} \right)^2 + g_3 \left( \vec{\xi}_{sR} \cdot \vec{\xi}_{sL} \right) \left( \vec{\xi}_{oR} \cdot \vec{\xi}_{oL} \right), \end{aligned} \quad (46)$$

where  $\vec{\xi}_{sR,L}$  and  $\vec{\xi}_{oR,L}$  are two triplet of Majorana fermions which act respectively in the spin and orbital sectors. In Eq. (46), we have considered a more general situation than the model (21) by allowing the exchange in spin ( $J_1$ ) and orbital ( $J_2$ ) channels to be different: the three coupling constants  $g_i$  are independent. The interaction of the low-energy field theory (46) is marginal and describes two SO(3) Gross-Neveu<sup>135</sup> models marginally coupled. This field theory is not integrable so that one has to recourse to perturbation theory to elucidate the phase diagram of the spin-orbital model in the vicinity of the SU(4) symmetric point. In fact, the all-order beta functions of the field theory (46) can be determined using the approach of Gerganov et al.<sup>233</sup>. These authors have computed the all-order beta functions of a general model with anisotropic current-current interactions in a special minimal scheme prescription. The model (46) can be viewed as a current-current interaction corresponding to the symmetry breaking scheme  $SU(6) \rightarrow SU(3) \times SU(3)$ . The application of the general formula given in Ref.<sup>233</sup> confirms the conclusions derived from the one-loop calculation<sup>231,232</sup> which reveals the existence of two phases with different remarkable properties.

A first phase, for  $J_1 \simeq J_2 > K/4$ , has a spectral gap and the ground state has a similar staggered dimerization as the weak-coupling phase of Fig. 6.4. Provided the anisotropy is not too large  $J_1 \neq J_2$  in the vicinity of the SU(4) symmetric point, the massive phase displays an approximate  $SU(6) \sim SU(4)$  enlarged symmetry. Indeed, by neglecting the velocity anisotropy in Eq. (46), the RG equations reveal a flow to strong coupling along a symmetric ray described by the Hamiltonian density<sup>231</sup>:

$$\begin{aligned} \mathcal{H}_{\text{IR}} \simeq & -\frac{iv_*}{2} \left( \vec{\xi}_{sR} \cdot \partial_x \vec{\xi}_{sR} - \vec{\xi}_{sL} \cdot \partial_x \vec{\xi}_{sL} + \vec{\xi}_{oR} \cdot \partial_x \vec{\xi}_{oR} - \vec{\xi}_{oL} \cdot \partial_x \vec{\xi}_{oL} \right) \\ & + g_* \left( \vec{\xi}_{sR} \cdot \vec{\xi}_{sL} - \vec{\xi}_{oR} \cdot \vec{\xi}_{oL} \right)^2, \end{aligned} \quad (47)$$

with  $g_* > 0$  so that after a duality transformation on the chiral fermions  $\vec{\xi}_{oR} \rightarrow -\vec{\xi}_{oR}$ , the Hamiltonian (47) takes the form of a SO(6) Gross-Neveu

model which is a massive integrable field theory. Its spectrum is known and consists of the fundamental fermion, with mass  $M$ , together with a kink and anti-kink with mass  $m_{\text{kink}} = M/\sqrt{2}$ <sup>38</sup>. The initial model (46),  $SU(2) \times SU(2)$  symmetric, acquires thus in the IR limit an enlarged  $SO(6)$  symmetry. In more physical terms, the spin and orbital degrees of freedom are unified and described by a same multiplet with six components. A similar example of symmetry restauration by interactions is the emergence of a  $SO(8)$  symmetry in weakly-coupled two-leg Hubbard ladder at half-filling<sup>234</sup> and in the  $SU(4)$  Hubbard chain at half-filling<sup>235</sup>. The nature of the strong-coupling phase of Eq. (47) can be elucidated by observing that the interacting part of the field theory (47) is:  $\mathcal{H}_{\text{IR}}^{\text{int}} = -g_* \mathcal{O}_{\text{SD}}^2$ ,  $\mathcal{O}_{\text{SD}}$  being the continuum limit of the staggered dimerization operator:

$$\mathcal{O}_{\text{SD}} = i(\vec{\xi}_{sR} \cdot \vec{\xi}_{sL} - \vec{\xi}_{oR} \cdot \vec{\xi}_{oL}) \sim (-1)^n (\vec{S}_{1,n+1} \cdot \vec{S}_{1,n} - \vec{S}_{2,n+1} \cdot \vec{S}_{2,n}). \quad (48)$$

In the IR limit, the strong-coupling phase is thus characterized by  $\langle \mathcal{O}_{\text{SD}} \rangle = \pm \Delta_0 \neq 0$ , i.e. a staggered dimerized phase which breaks spontaneously the translation symmetry (see Fig. 6.4).

The second phase with  $J_1 \simeq J_2 < K/4$  has striking properties. All couplings in Eq. (46) flow to zero in the IR limit and the interaction is marginal irrelevant. The six Majorana fermions are thus massless and the phase displays extended quantum criticality characterized by a central charge  $c = 3$ . Spin-spin correlation functions decay algebraically with exponent  $3/2$  and exhibit a four-site periodicity ( $2k_F = \pi/2a_0$ ). The critical behavior at the

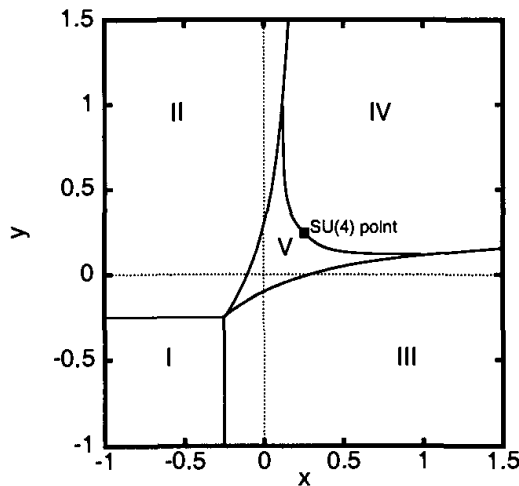


Fig. 6.11. Phase diagram of the spin-orbital model obtained by DMRG;  $x = J_2/K$  and  $y = J_1/K$ ; taken from Ref. 232.

SU(4) point (45) extends to a finite region of the phase diagram of the spin-orbital model. In this respect, this remarkable gapless phase with extended quantum criticality  $c = 3$  represents a new universality class, stabilized by frustration, in spin chains and spin ladders. It is worth noting that this phase has a maximum of gapless modes allowed by the classical structure of a spiral (three Goldstone modes).

The phase diagram of the anisotropic spin-orbital model (21) with  $J_1 \neq J_2$  has been investigated numerically by means of the DMRG technique<sup>147,236,232</sup>. Figure 6.11 represents the resulting  $T = 0$  phase diagram obtained in Refs.<sup>236,232</sup>. In phase I, both spin and orbital degrees of freedom are in fully polarized ferromagnetic states. In phase II, the orbital degrees of freedom are still in a ferromagnetic state whereas the spin degrees of freedom are now critical (criticality of a spin-1/2 AF Heisenberg chain) and vice versa in phase III. Phase IV corresponds to the staggered dimerized phase of Fig. 6.4 while phase V is the  $c = 3$  gapless phase with extended quantum criticality. In fact, this critical phase has been first discovered only along a special line  $-K/4 < J_1 = J_2 < K/4$  in the DMRG calculation of Pati et al.<sup>147</sup>. Additional DMRG works<sup>236,232</sup> have shown the existence of this gapless phase in an extended region (Phase V) of the phase diagram (Fig. 6.11).

A second model which displays extended quantum criticality induced by frustration is the spin-1 bilinear-biquadratic chain (9) with a biquadratic coupling constant  $\beta > 1$ . In this regime, frustration manifests itself and the classical ground state is an incommensurate spiral. The Haldane phase of the spin-1 bilinear-biquadratic chain (9) with  $|\beta| < 1$  ends at the integrable point with  $\beta = 1$ , the so-called Uimin-Lai-Sutherland<sup>237,227</sup> point. This model can be expressed in terms of SU(3) spins and takes the form of a SU(3) AF Heisenberg spin chain:

$$\mathcal{H}_{\text{SU}(3)} = J \sum_i \sum_{A=1}^8 T_i^A T_{i+1}^A, \quad (49)$$

where  $T^A$  are the 8 generators belonging to the fundamental representation of SU(3). This model is exactly solvable by means of the Bethe ansatz<sup>237,227</sup> and its low-energy spectrum consists of two gapless spinons with wave vectors  $\pm 2\pi/3a_0$ <sup>227</sup>. As shown by Affleck<sup>229</sup>, the critical theory corresponds to the  $\text{su}(3)_1$  WZNW model with central charge  $c = 2$  (two massless bosonic modes). The existence of this quantum critical point with a SU(3) symmetry allows to study the spin-1 bilinear-biquadratic chain (9) in the vicinity of  $\beta \simeq 1$  by means of a field theory approach<sup>238</sup>. The low-energy effective

field theory is described by marginal current-current interactions associated to the symmetry breaking scheme  $SU(3) \rightarrow SU(2)$ <sup>238</sup>. The one-loop RG flow near  $\beta \simeq 1$  reveals the existence of two distinct phases. On one hand, a phase with a dynamical mass generation when  $\beta < 1$  which signals the onset of the Haldane phase. On the other hand, a massless phase for  $\beta > 1$  where interactions are marginal irrelevant. The  $SU(3)$  quantum criticality of the Uimin-Lai-Sutherland point, with two gapless bosonic modes, extends to a finite region of the phase diagram of the generalized spin-1 Heisenberg chain (9). This massless phase has been first predicted in a numerical investigation of this model by Fáth and Sólyom<sup>239</sup> and confirmed recently by means of a DMRG analysis<sup>240</sup>. This massless phase with approximate  $SU(3)$  symmetry, stabilized by frustration, is similar in spirit to the previous  $SU(4)$  massless phase of the spin-orbital model (21). Finally, it is worth noting that this  $c = 2$  massless phase appears also in the phase diagram of the so-called spin tube model, a three-leg spin ladder with frustrated periodic interchain interaction, in a magnetic field<sup>241</sup>.

#### 6.3.4.2. Chirally stabilized critical spin liquid

Frustration can also induce an exotic quantum critical point in frustrated spin ladders. A possible lattice realization of this phenomenon is a model (see Fig. 6.12) of three  $S = 1/2$  AF Heisenberg spin chains weakly coupled by on-rung  $J_{\perp}$  and plaquette-diagonal  $J_{\times}$  interchain interactions<sup>242</sup>. The Hamiltonian of this model reads as follows:

$$\begin{aligned} \mathcal{H}_{\times} = & J_{\parallel} \sum_i \sum_{a=1}^3 \vec{S}_{a,i} \cdot \vec{S}_{a,i+1} + J_{\perp} \sum_i \vec{S}_{2,i} \cdot (\vec{S}_{1,i} + \vec{S}_{3,i}) \\ & + J_{\times} \sum_i \left[ (\vec{S}_{1,i} + \vec{S}_{3,i}) \cdot \vec{S}_{2,i+1} + (\vec{S}_{1,i+1} + \vec{S}_{3,i+1}) \cdot \vec{S}_{2,i} \right]. \end{aligned} \quad (50)$$

In the continuum limit with  $J_{\perp}, J_{\times} \ll J_{\parallel}$ , the Hamiltonian of the lattice model (50) takes the form:

$$\begin{aligned} \mathcal{H}_{\times} = & \frac{2\pi v}{3} \sum_{a=1}^3 \left( \vec{J}_{aR}^2 + \vec{J}_{aL}^2 \right) + \tilde{g} \vec{n}_2 \cdot (\vec{n}_1 + \vec{n}_3) \\ & + g \left[ \vec{J}_{2R} \cdot (\vec{J}_{1L} + \vec{J}_{3L}) + \vec{J}_{2L} \cdot (\vec{J}_{1R} + \vec{J}_{3R}) \right], \end{aligned} \quad (51)$$

with  $g = a_0(J_{\perp} + 2J_{\times})$  and  $\tilde{g} = a_0(J_{\perp} - 2J_{\times})$ . In Eq. (51),  $\vec{J}_{aR,L}$  ( $a = 1, 2, 3$ ) are the right and left chiral  $su(2)_1$  currents which accounts for the low-energy description of the uniform part of the spin density of

the  $a$ th spin-1/2 chain. It is interesting to note that in Eq. (51), there is no marginally relevant twist perturbation  $\vec{n}_1 \cdot \partial_x \vec{n}_2$  which appears in the continuum description of the two-leg spin ladder with a small zigzag inter-chain coupling (38). The two interaction terms in Eq. (51) are of different

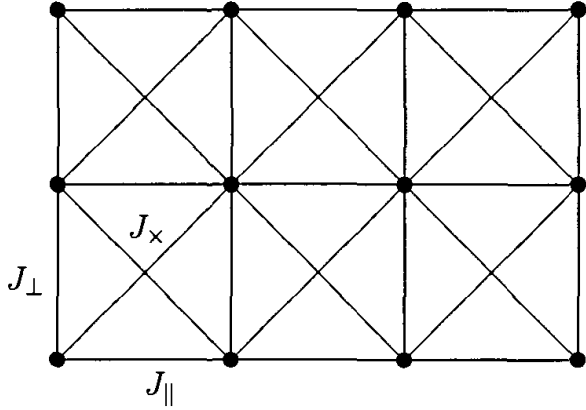


Fig. 6.12. Three-leg spin ladder with crossings.

nature. On one hand, the first contribution, with coupling constant  $\tilde{g}$ , is a strongly relevant perturbation with scaling dimension  $\Delta_{\tilde{g}} = 1$ . On the other hand, the second term is a current-current interaction which is only marginal and, as long as  $\tilde{g}$  is not too small, can be discarded. As a result, for generic values of  $g$  and  $\tilde{g}$ , the low-energy physics of the model (50) will be essentially that of the standard three-leg ladder, and frustration will play no role (except for renormalization of mass gaps and velocities). The important point here is that in contrast with non-frustrated ladders, the two coupling constants  $g, \tilde{g}$  can vary independently, and there exists a vicinity of the line  $J_{\perp} = 2J_x$  ( $\tilde{g} = 0$ ) where the low-energy properties of the model are mainly determined by current-current interchain interaction.

Along the special line  $J_{\perp} = 2J_x$ , the low-energy effective Hamiltonian (51) simplifies as follows<sup>242</sup>:

$$\begin{aligned} \mathcal{H}_x = & -\frac{iv}{2} (\xi_R^0 \partial_x \xi_R^0 - \xi_L^0 \partial_x \xi_L^0) + \frac{2\pi v}{3} (\vec{J}_{2R}^2 + \vec{J}_{2L}^2) \\ & + \frac{\pi v}{2} (\vec{I}_R^2 + \vec{I}_L^2) + g \left[ \vec{J}_{2R} \cdot \vec{I}_L + \vec{J}_{2L} \cdot \vec{I}_R \right], \end{aligned} \quad (52)$$

where  $\xi_{R,L}^0$  are Majorana fermions which are associated to the  $Z_2$  ( $1 \rightarrow 3$ ) discrete interchange symmetry between the surface chains labelled  $a = 1, 3$  in the lattice model (50); the total chiral current of the surface chains is noted  $\vec{I}_{R,L} = \vec{J}_{1R,L} + \vec{J}_{3R,L}$  and corresponds to a  $\text{su}(2)_2$  WZNW current.

The Hamiltonian (52) has an interesting structure. First, the Majorana fermions  $\xi_{R,L}^0$  do not participate in the interaction and remain thus critical in the IR limit. These massless degrees of freedom can be interpreted as an effective two-dimensional Ising model at  $T = T_c$  which accounts for singlet excitations between the surface chains. All non-trivial physics of the model is incorporated in the current-current dependent part of the Hamiltonian (52), denoted by  $\mathcal{H}_{cc}$ , which describes marginally coupled  $\text{su}(2)_1$  and  $\text{su}(2)_2$  WZNW models. Moreover, this Hamiltonian separates into two commuting and *chirally asymmetric* parts:  $\mathcal{H}_{cc} = \mathcal{H}_1 + \mathcal{H}_2$ ,  $([\mathcal{H}_1, \mathcal{H}_2] = 0)$ , where

$$\mathcal{H}_1 = \frac{\pi v}{2} \vec{I}_R^2 + \frac{2\pi v}{3} \vec{J}_{2L}^2 + g \vec{I}_R \cdot \vec{J}_{2L}, \quad (53)$$

and  $\mathcal{H}_2$  is obtained from  $\mathcal{H}_1$  by inverting chiralities of all the currents. The model (53) is integrable by means of the Bethe-ansatz approach<sup>163,243</sup>. A simple RG analysis shows that, at  $g > 0$ , the interaction is marginally relevant. Usually the development of a strong coupling regime is accompanied by a dynamical mass generation and the loss of conformal invariance in the strong coupling limit. However, here due to the chiral asymmetry of  $\mathcal{H}_1$ , it turns out that the effective interaction flows towards an intermediate fixed point where conformal invariance is recovered with a smaller central charge. This critical behavior has been identified as the universality class of chirally stabilized fluids, introduced by Andrei, Douglas, and Jerez<sup>243</sup>. In the case of the model (53), the symmetry of the IR fixed point, obtained from the Bethe-ansatz analysis<sup>243</sup>, turns out to be  $\text{su}(2)_1|_R \times \text{Z}_2|_L$ . This result can also be derived using a Toulouse point approach<sup>242</sup>. As a whole, taking into account of the contribution of the Majorana fermions  $\xi_{R,L}^0$ , the model (52) displays critical properties characterized by a fixed point with a  $\text{su}(2)_1 \times \text{Z}_2 \times \text{Z}_2$  symmetry and a  $c = 2$  central charge. This emerging quantum criticality can be interpreted as the criticality resulting from an effective  $S = 1/2$  AF Heisenberg chain and two decoupled critical Ising models. Frustration, introduced by the diagonal exchange interaction  $J_x$ , shows up in a non-trivial way by stabilizing a quantum critical point with central charge  $c = 2$ . This IR behavior differs from the standard  $c = 1$  quantum criticality in unfrustrated three-leg spin ladder by the two gapless non-magnetic, singlet, degrees of freedom described by the Ising models. The physical properties of the model at this  $c = 2$  critical point can be determined by a Toulouse point approach of the model (52)<sup>242</sup>. The slowest spin-spin correlation functions of the model at the IR critical point correspond to the staggered correlations between the spins of the surface chains which decay with a universal exponent  $3/2$ . As a consequence, the low-

temperature dependence of the NMR relaxation rate scales as  $1/T_1 \sim \sqrt{T}$  in contrast to  $1/T_1 \sim \text{const}$  for the spin-1/2 AF Heisenberg chain<sup>10</sup>. The  $c = 2$  quantum critical point, induced by frustration, describes thus a new universality class in spin ladders. In addition, the Toulouse point analysis enables us to investigate the effect of the neglected backscattering term  $\vec{n}_2 \cdot (\vec{n}_1 + \vec{n}_3)$  of the model (51) in the vicinity of the line  $\tilde{g} = 0$ . The main effect of this operator is to open a spectral gap in the Ising degrees of freedom of the  $c = 2$  fixed point but has no dramatic effect on the effective  $S = 1/2$  AF Heisenberg chain. The  $c = 2$  IR fixed point is thus unstable with respect to the interchain backscattering term and the model (51) will display IR critical properties governed by the  $c = 1$  fixed point of the three-leg spin ladder or the  $S = 1/2$  AF Heisenberg spin chain.

Finally, it is worth noting that the zero-temperature phase diagram of the three-leg spin ladder with crossings (50) has been recently investigated by means of the DMRG approach<sup>244</sup>. Two critical phases have been found corresponding to the  $S = 3/2$  AF Heisenberg chain and the three-leg spin ladder. Frustration, introduced through the diagonal interchain interaction  $J_x$ , induces a quantum phase transition between these two critical phases belonging to the standard  $c = 1$  universality class. At large  $J_x$ , the transition has been found to be of first order. In the weak coupling regime, the transition occurs at  $J_\perp = 2J_x$  when  $J_x < 0.8J_\parallel$  in full agreement with the field theoretical description (51) of the model. Extended DMRG calculations are required to fully characterize the nature of the phase boundary at  $J_\perp = 2J_x$  in the weak coupling regime in particular to verify the chiral spin liquid behavior with  $c = 2$  criticality proposed in Ref.<sup>242</sup>.

#### 6.4. Concluding remarks

The suppression of magnetism by quantum fluctuations in one dimension gives rise to a large variety of zero-temperature spin liquid phases with striking different physical properties. The canonical examples are the emerging quantum criticality of the spin-1/2 AF Heisenberg chain, controlled by gapless elementary excitations with fractional quantum numbers (spinons), and the formation of an incompressible Haldane spin liquid phase in the spin-1 case with optical  $S = 1$  magnon excitations. Several other types of incompressible spin liquid phases can be stabilized with different dynamical or optical properties. A distinct spin liquid behavior may be revealed in the form of the dynamical structure factor with the presence or not of a sharp spectral peak which directly probes the elementary nature of

the triplet excitation of the phase. In this respect, the staggered dimerized phase of the two-leg spin ladder with a biquadratic interchain exchange represents a non-Haldane spin liquid phase even though a spectral gap is formed by quantum fluctuations. The main difference between this phase and the Haldane phase of the spin-1 Heisenberg chain stems from the composite nature of the spin-flip  $S = 1$  excitation due to the presence of a two-particle threshold in the dynamical structure factor instead of a sharp magnon peak. Two gapped spin liquid phases can also be distinguished at the level of the topology of the short-range valence bond description of their ground states. A spin liquid phase may exhibit a ground-state degeneracy depending on the nature of boundary conditions used. In particular, for open boundary conditions, chain-end spin excitations can result from this ground-state degeneracy leading to well defined satellite peaks in the NMR profile of the system doped with non-magnetic impurities. An example of this topological distinction between two gapped phases is provided by the two-leg spin ladder. In the Haldane phase of the open two-leg ladder with a ferromagnetic rung interchain  $J_{\perp} < 0$ ,  $S = 1/2$  edge states are formed whereas these chain-end excitations disappear in the rung singlet phase of the ladder with  $J_{\perp} > 0$ .

Frustration, i.e. the impossibility to satisfy simultaneously every pairwise interaction, can induce additional types of spin liquid phases with exotic properties. In the spin-1/2 case, one of the most striking effect of frustration is the stabilization of a spontaneously dimerized phase with massive deconfined spinon excitations. Frustration represents thus a direct route to fractionalization. The existence of these deconfined spinon excitations has important consequences, as for instance, in the study of doping effects of such a spin liquid phase with non-magnetic impurities. On general grounds, it is expected that no free spin degrees of freedom are generated around non-magnetic impurities due to the presence of deconfined spinons<sup>245</sup>. In the case of the spontaneously dimerized phase of the spin-1/2  $J_1$ - $J_2$  Heisenberg chain, the absence of induced free spin degrees of freedom or edge states has been shown recently<sup>246</sup>. A second remarkable effect of frustration is the onset of incommensurability in spin chains whose classical ground state has a spiral structure. In this respect, frustration is a novel mechanism in one dimension for generating incommensurate behavior as external magnetic fields or Dzyaloshinskii-Moriya interaction. An example of such a spin liquid phase with incommensurate correlation is the quantum  $J_1 - J_2$  Heisenberg chain in the large next-nearest neighbor limit. When the SU(2) symmetry of this model is explicitly broken, an incommensurate

phase is produced by frustration with local non-zero spin currents, polarized along the anisotropic axis, circulating around triangular plaquettes. This phase is the quantum signature of the classical spiral phase induced by frustration. Finally, a last effect of frustration, discussed in this review, is the possible realization of a new type of emerging quantum criticality in spin chains and ladders. In the continuum description, the low-energy effective field theory of a frustrated spin chain is mainly governed by marginal interactions. An extended IR critical behavior characterized by a CFT with central charge  $c > 1$  may result from the delicate balance between these marginal contributions.

Regarding perspectives, a natural question to raise is the existence of a novel 1D spin liquid phase with unbroken SU(2) spin symmetry which displays physical properties not described in this review. In particular, an interesting possibility is the realization of a 1D version of the chiral spin liquid phase<sup>247</sup> which breaks spontaneously the time-reversal symmetry. In fact, such a phase has been identified recently in the phase diagram of the two-leg spin ladder with a four-spin cyclic exchange<sup>248,249</sup>. In the large ring-exchange limit, a spin liquid phase characterized by a non-zero scalar-chirality operator  $\langle \vec{S}_{1,i} \cdot (\vec{S}_{2,i} \wedge \vec{S}_{1,i+1}) \rangle$ , breaking both parity and time-reversal symmetries, has been found in DMRG calculations<sup>248,249</sup>. Using duality arguments, the authors of Ref.<sup>249</sup> have also exhibited several spin ladder models with exact ground-state which display spontaneous breaking of the time-reversal symmetry. Finally, a central issue is the possibility to stabilize a two-dimensional SU(2)-invariant spin liquid phase with exotic properties starting from the one-dimensional limit. Recently, a model of two-dimensional frustrated spin system with SU(2) spin symmetry and strong spatially anisotropy has been introduced by Nersesyan and Tsvelik<sup>250</sup>. This model can also be interpreted as a collection of weakly coupled spin chains. It has been shown that, in the limit of infinite number of chains, this system displays a spin liquid phase with massive deconfined fractional spin-1/2 excitations (spinons)<sup>250</sup>. The existence of spinons in two-dimensional spin systems has also been found in a crossed-chain model<sup>251</sup> which is a 2D anisotropic version of the pyrochlore lattice. Remarkably enough, for a range of coupling constants<sup>251,252</sup>, this system is a non-dimerized spin liquid with deconfined gapless spinons as elementary excitations. This spin liquid phase, stabilized by frustration, is an example of a SU(2) version of a sliding Luttinger liquid phase<sup>253</sup>. We hope that other two-dimensional spin liquid phases with exotic properties will be reported in the near future.

## Acknowledgments

We would like to thank D. Allen, P. Azaria, E. Boulat, B. Douçot, F. H. L. Essler, Th. Giamarchi, Th. Jolicoeur, A. A. Nersesyan, E. Orignac, T. T. Truong, and A. M. Tsvelik for helpful discussions and their interest in this work.

## References

1. P. W. Anderson, *Mater. Res. Bull.* **8**, 153 (1973); *Science* **235**, 1196 (1987).
2. S. Sachdev and K. Park, *Ann. Phys.* **298**, 58 (2002); S. Sachdev, *ibid.* **303**, 226 (2003).
3. C. Lhuillier and G. Misguich, Frustrated quantum magnets, in *High Magnetic fields*, edited by C. Berthier, L. P. Lévy, and G. Martinez, p 161 (Lecture Notes in Physics Vol 595, Springer, 2002); arXiv: cond-mat/0109146; See also, G. Misguich and C. Lhuillier, Frustration in two-dimensional quantum antiferromagnets, in this volume, arXiv: cond-mat/0310405.
4. X. G. Wen, *Phys. Rev. B* **65**, 165113 (2002).
5. N. D. Mermin and H. Wagner, *Phys. Rev. Lett.* **17**, 1307 (1968).
6. A. A. Belavin, A. M. Polyakov, and A. B. Zamolodchikov, *Nucl. Phys. B* **241**, 333 (1984).
7. P. Di Francesco, P. Mathieu, and D. Sénéchal, *Conformal Field Theory* (Springer-Verlag, New York, 1997).
8. A. Luther and I. Peschel, *Phys. Rev. B* **9**, 2911 (1974).
9. S. Coleman, *Phys. Rev. B* **11**, 2088 (1975).
10. A. O. Gogolin, A. A. Nersesyan, and A. M. Tsvelik, *Bosonization and Strongly Correlated Systems* (Cambridge University Press, Cambridge, 1998).
11. S. R. White, *Phys. Rev. Lett.* **69**, 2863 (1992); *Phys. Rev. B* **48**, 10345 (1993).
12. M. Yamashita, T. Ishii, and H. Matsuzaka, *Coord. Chem. Rev.* **198**, 347 (2000).
13. P. Lemmens, G. Güntherodt, and C. Gros, *Phys. Rep.* **375**, 1 (2003).
14. S. Sachdev, *Quantum Phase Transitions* (Cambridge University Press, Cambridge, 1999).
15. I. Affleck, *Phys. Rev. Lett.* **55**, 1355 (1985); *Nucl. Phys. B* **265**, 409 (1986).
16. X. G. Wen, *Adv. in Phys.* **44**, 405 (1995).
17. H. Bethe, *Z. Phys.* **71**, 205 (1931).
18. L. Hulthén, *Ark. Mat., Astron. Fys.* **26A**, 1 (1938).
19. R. B. Griffiths, *Phys. Rev.* **133**, A768 (1964); C. N. Yang and C. P. Yang, *Phys. Rev.* **150**, 327 (1966); S. Eggert, I. Affleck, and M. Takahashi, *Phys. Rev. Lett.* **73**, 332 (1994); S. Lukyanov, *Nucl. Phys. B* **522**, 533 (1998); A. Klümper and D. C. Johnston, *Phys. Rev. Lett.* **84**, 4701 (2000).
20. M. Takahashi, *Thermodynamics of One-Dimensional Solvable Models* (Cambridge University Press, Cambridge, 1999).
21. J. des Cloizeaux and J. J. Pearson, *Phys. Rev.* **128**, 2131 (1962).

22. L. D. Faddeev and L. A. Takhtajan, *Phys. Lett. A* **85**, 375 (1981).
23. A. Luther and I. Peschel, *Phys. Rev. B* **9**, 2911 (1974); A. H. Bougourzi, M. Couture, and M. Kacir, *ibid.* **54**, 12669 (1996); A. Abada, A. H. Bougourzi, and B. Si-Lakhal, *Nucl. Phys. B* **497**, 733 (1997); N. Kitanine, J. M. Maillet, and V. Terras, *ibid.* **554**, 647 (1999).
24. I. Affleck, *Field theory methods and quantum critical phenomena*, in Les Houches, session XLIX, *Champs, Cordes et Phénomènes critiques* (Elsevier, New-York, 1989).
25. V. G. Knizhnik and A. B. Zamolodchikov, *Nucl. Phys. B* **247**, 83 (1984).
26. I. Affleck, D. Gepner, H. J. Schulz, and T. Ziman, *J. Phys. A* **22**, 511 (1989); R. R. P. Singh, M. E. Fisher, and R. Shankar, *Phys. Rev. B* **39**, 2562 (1989); T. Giamarchi and H. J. Schulz, *ibid.*, 4620 (1989).
27. I. Affleck, *J. Phys. A* **31**, 4573 (1998); T. Hikihara and A. Furusaki, *Phys. Rev. B* **58**, R583 (1998); S. Lukyanov and V. Terras, *Nucl. Phys. B* **654**, 323 (2003).
28. F. D. M. Haldane, *Phys. Rev. Lett.* **66**, 1529 (1991).
29. F. D. M. Haldane, *Phys. Rev. Lett.* **60**, 635 (1988); B. S. Shastry, *ibid.*, 639 (1988).
30. S. E. Nagler, D. A. Tennant, R. A. Cowley, T. G. Perring, and S. K. Satija, *Phys. Rev. B* **44**, 12361 (1991); D. A. Tennant, T. G. Perring, R. A. Cowley, and S. E. Nagler, *Phys. Rev. Lett.* **70**, 4003 (1993); D. A. Tennant, R. A. Cowley, S. E. Nagler, and A. M. Tsvelik, *Phys. Rev. B* **52**, 13368 (1995).
31. D. C. Dender, D. Davidović, D. H. Reich, C. Broholm, K. Lefmann, and G. Aeppli, *Phys. Rev. B* **53**, 2583 (1996).
32. I. Tsukada, Y. Sasago, K. Uchinokura, A. Zheludev, S. Maslov, G. Shirane, K. Kakurai, and E. Ressouche, *Phys. Rev. B* **60**, 6601 (1999).
33. P. R. Hammar, M. B. Stone, D. H. Reich, C. Broholm, P. J. Gibson, M. M. Turnbull, C. P. Landee, and M. Oshikawa, *Phys. Rev. B* **59**, 1008 (1999).
34. F. D. M. Haldane, *Phys. Rev. Lett.* **50**, 1153 (1983); *Phys. Lett. A* **93**, 464 (1983).
35. I. Affleck, *J. Phys. Condens. Matter* **1**, 3047 (1989).
36. E. Fradkin, *Field Theories of Condensed Matter Systems* (Addison-Wesley, 1991).
37. A. Auerbach, *Interacting Electrons and Quantum Magnetism*, (Springer-Verlag, New York, 1994).
38. A. B. Zamolodchikov and Al. B. Zamolodchikov, *Ann. Phys.* **120**, 253 (1979).
39. P. B. Wiegmann, *Phys. Lett. B* **152**, 209 (1985).
40. I. Affleck and F. D. M. Haldane, *Phys. Rev. B* **36**, 5291 (1987).
41. R. Shankar and N. Read, *Nucl. Phys. B* **336**, 457 (1990).
42. A. B. Zamolodchikov and Al. B. Zamolodchikov, *Nucl. Phys. B* **379**, 602 (1992).
43. R. Botet and R. Jullien, *Phys. Rev. B* **27**, 613 (1983); R. Botet, R. Jullien, and M. Kolb, *ibid.* **28**, 3914 (1983); M. Kolb, R. Botet, and R. Jullien, *J. Phys. A* **16**, L673 (1983); U. Glaus and T. Schneider, *Phys. Rev. B* **30**, 215 (1984); J. B. Parkinson and J. C. Bonner, *ibid.* **32**, 4703 (1985); H. J. Schulz

- and T. A. L. Ziman, *ibid.* **33**, 6545 (1986); A. Moreo, *ibid.* **35**, 8562 (1987); T. Sakai and M. Takahashi, *ibid.* **42**, 1090, 4537 (1990); O. Golinelli, T. Jolicoeur, and R. Lacaze, *ibid.* **46**, 10854 (1992); S. Haas, J. Riera, and E. Dagotto, *ibid.* **48**, 3281 (1993); M. Kaburagi, I. Harada, and T. Tonegawa, *J. Phys. Soc. Jpn.* **62**, 1848 (1993); T. Sakai and M. Takahashi, *ibid.* **63**, 755 (1994).
44. M. P. Nightingale and H. W. Blöte, *Phys. Rev. B* **33**, 659 (1986); M. Marcu and J. Müller, *Phys. Lett. A* **119**, 469 (1987); M. Takahashi, *Phys. Rev. B* **38**, 5188 (1988); *Phys. Rev. Lett.* **62**, 2313 (1989); K. Nomura, *Phys. Rev. B* **40**, 2421 (1989); S. Liang, *Phys. Rev. Lett.* **64**, 1597 (1990); J. Deisz, M. Jarrell, and D. L. Cox, *Phys. Rev. B* **42**, 4869 (1990); S. V. Meshkov, *ibid.* **48**, 6167 (1993); S. Miyashita and S. Yamamoto, *ibid.*, 913 (1993); J. Deisz, M. Jarrell, and D. L. Cox, *ibid.*, 10227 (1993).
  45. K. Kubo and S. Takada, *J. Phys. Soc. Jpn.* **55**, 438 (1986); K. Betsuyaku, *Phys. Rev. B* **34**, 8125 (1986); K. Kubo, *ibid.* **46**, 866 (1992).
  46. S. R. White and D. A. Huse, *Phys. Rev. B* **48**, 3844 (1993); E. S. Sorensen and I. Affleck, *Phys. Rev. Lett.* **71**, 1633 (1993); *Phys. Rev. B* **49**, 15771 (1994).
  47. W. J. L. Buyers, R. M. Morra, R. L. Armstrong, M. J. Hogan, P. Gerlach, and K. Hirakawa, *Phys. Rev. Lett.* **56**, 371 (1986); M. Steiner, K. Kakurai, J. K. Kjems, D. Petitgrand, and R. Pynn, *J. Appl. Phys.* **61**, 3953 (1987); R. M. Morra, W. J. L. Buyers, R. L. Armstrong, and K. Hirakawa, *Phys. Rev. B* **38**, 543 (1988); Z. Tun, W. J. L. Buyers, R. L. Armstrong, K. Hirakawa, and B. Briat, *ibid.* **42**, 4677 (1990); I. A. Zaliznyak, L. P. Regnault, and D. Petitgrand, *ibid.* **50**, 15824 (1994).
  48. J. P. Renard, M. Verdaguer, L. P. Regnault, W. A. C. Erkelens, J. Rossat-Mignod, and W. G. Stirling, *Europhys. Lett.* **3**, 949 (1987).
  49. J. P. Renard, M. M. Verdaguer, L. P. Regnault, W. A. C. Erkelens, J. Rossat-Mignod, J. Ribas, W. G. Stirling, and C. Vettier, *J. Appl. Phys.* **63**, 3538 (1988); L. P. Regnault, C. Vettier, J. Rossat-Mignod, and J. P. Renard, *Physica B* **156-157**, 247 (1989); *ibid.* **180-181**, 188 (1992); S. Ma, C. Broholm, D. H. Reich, B. J. Sternlieb, and R. W. Erwin, *Phys. Rev. Lett.* **69**, 3571 (1992); L. P. Regnault, I. Zaliznyak, J. P. Renard, and C. Vettier, *Phys. Rev. B* **50**, 9174 (1994); S. Ma, D. H. Reich, C. Broholm, B. J. Sternlieb, and R. W. Erwin, *ibid.* **51**, 3289 (1995).
  50. V. Gadet, M. Verdaguer, V. Briois, A. Gleizes, J. P. Renard, P. Beauvillain, C. Chappert, T. Goto, K. Le Dang, and P. Veillet, *Phys. Rev. B* **44**, 705 (1991).
  51. H. Mutka, C. Payen, P. Molinié, J. L. Soubeyroux, P. Colombet, and A. D. Taylor, *Phys. Rev. Lett.* **67**, 497 (1991).
  52. J. Darriet and J. P. Renard, *Solid State Commun.* **86**, 409 (1993); T. Sakaguchi, K. Kakurai, T. Yokoo, and J. Akimitsu, *J. Phys. Soc. Jpn.* **65**, 3025 (1996).
  53. G. Xu, J. F. Ditusa, T. Ito, K. Oka, H. Takagi, C. Broholm, and G. Aepli, *Phys. Rev. B* **54**, R6827 (1996).
  54. Z. Honda, H. Askawa, and K. Katsumata, *Phys. Rev. Lett.* **81**, 2566 (1998);

- Y. Chen, Z. Honda, A. Zheludev, C. Broholm, K. Katsumata, and S. M. Shapiro, *ibid.* **86**, 1618 (2001).
55. Z. Honda, K. Katsumata, H. Aruga Katori, K. Yamada, T. Ohishi, T. Manabe, and M. Yamashita, *J. Phys. Condens. Matter* **9**, L83 (1997).
  56. A. Zheludev, Z. Honda, K. Katsumata, R. Feyerherm, and K. Prokes, *Europhys. Lett.* **55**, 868 (2001); A. Zheludev, Z. Honda, Y. Chen, C. L. Broholm, K. Katsumata, and S. M. Shapiro, *Phys. Rev. Lett.* **88**, 077206 (2002).
  57. I. Affleck, T. Kennedy, E. H. Lieb, and H. Tasaki, *Phys. Rev. Lett.* **59**, 799 (1987); *Commun. Math. Phys.* **115**, 477 (1988).
  58. A. M. Tsvelik, *Phys. Rev. B* **42**, 10499 (1990).
  59. G. Gómez-Santos, *Phys. Rev. Lett.* **63**, 790 (1989).
  60. H.-J. Mikeska, *Europhys. Lett.* **19**, 39 (1992).
  61. G. Fáth and J. Sólyom, *J. Phys. Condens. Matter* **5**, 8983 (1993).
  62. M. den Nijs and K. Rommelse, *Phys. Rev. B* **40**, 4709 (1989).
  63. H. Tasaki, *Phys. Rev. Lett.* **66**, 798 (1991).
  64. T. Kennedy and H. Tasaki, *Phys. Rev. B* **45**, 304 (1992); *Commun. Math. Phys.* **147**, 431 (1992).
  65. D. P. Arovas, A. Auerbach, and F. D. M. Haldane, *Phys. Rev. Lett.* **60**, 531 (1988).
  66. S. Knabe, *J. Stat. Phys.* **52**, 627 (1988).
  67. R. Scharf and H.-J. Mikeska, *J. Phys. Condens. Matter* **7**, 5083 (1995).
  68. T. Kennedy, *J. Phys. Condens. Matter* **2**, 5737 (1990).
  69. K. Chang, I. Affleck, G. W. Hayden, and Z. G. Soos, *J. Phys. Condens. Matter* **1**, 153 (1989); E. S. Sorensen and A. P. Young, *Phys. Rev. B* **42**, 754 (1990); J. Deisz, *ibid.* **46**, 2885 (1992).
  70. S. M. Girvin and D. P. Arovas, *Phys. Scr. T* **27**, 156 (1989); D. P. Arovas and S. M. Girvin, *Recent Progress in Many-Body Theories*, Vol **3**, 315 (Plenum Press, New York, 1992).
  71. Y. Hatsugai and M. Kohmoto, *Phys. Rev. B* **44**, 11789 (1991); K. Kubo, *ibid.* **46**, 866 (1992); F. Alcaraz and Y. Hatsugai, *ibid.*, 13914 (1992);
  72. U. Schollwöck, T. Jolicoeur, and T. Garel, *Phys. Rev. B* **53**, 3304 (1996); O. Golinelli, T. Jolicoeur, and E. S. Sorensen, *Eur. Phys. J. B* **11**, 199 (1999).
  73. E. Polizzi, F. Mila, and E. S. Sorensen, *Phys. Rev. B* **58**, 2407 (1998).
  74. S.-W. Tsai and J. B. Marston, *Phys. Rev. B* **62**, 5546 (2000).
  75. S. Miyashita and S. Yamamoto, *Phys. Rev. B* **48**, 913, 9528 (1993); *ibid.* **51**, 3649 (1995).
  76. M. Kaburagi, I. Harada, and T. Tonegawa, *J. Phys. Soc. Jpn.* **62**, 1848 (1993).
  77. S. Qin, T. K. Ng, and Z. B. Su, *Phys. Rev. B* **52**, 12844 (1995).
  78. Ö. Legeza, G. Fáth, and J. Sólyom, *Phys. Rev. B* **55**, 291 (1997); Ö. Legeza and J. Sólyom, *ibid.* **59**, 3606 (1999).
  79. C. D. Batista, K. Hallberg, and A. A. Aligia, *Phys. Rev. B* **58**, 9248 (1998); *ibid.* **60**, R12553 (1999).
  80. F. Alet and E. S. Sorensen, *Phys. Rev. B* **62**, 14116 (2000).
  81. P. Mitra, B. Halperin, and I. Affleck, *Phys. Rev. B* **45**, 5299 (1992).
  82. E. S. Sorensen and I. Affleck, *Phys. Rev. B* **49**, 15771 (1994).

83. P. Lecheminant and E. Orignac, *Phys. Rev. B* **65**, 174406 (2002).
84. S. H. Glarum, S. Geschwind, K. M. Lee, M. L. Kaplan, and J. Michel, *Phys. Rev. Lett.* **67**, 1614 (1991).
85. T. Goto, S. Satoh, Y. Matsumata, and M. Hagiwara, *Phys. Rev. B* **55**, 2709 (1997).
86. M. Hagiwara, K. Katsumata, I. Affleck, B. I. Halperin, and J. P. Renard, *Phys. Rev. Lett.* **65**, 3181 (1990).
87. F. Tedoldi, R. Santachiara, and M. Horvatić, *Phys. Rev. Lett.* **83**, 412 (1999).
88. M. Kenzelmann, G. Xu, I. A. Zaliznyak, C. Broholm, J. F. DiTusa, G. Aeppli, T. Ito, K. Oka, and H. Takagi, *Phys. Rev. Lett.* **90**, 087202 (2003).
89. H. J. Schulz, *Phys. Rev. B* **34**, 6372 (1986).
90. D. C. Cabra, P. Pujol, and C. von Reichenbach, *Phys. Rev. B* **58**, 65 (1998).
91. A. Moreo, *Phys. Rev. B* **35**, 8562 (1987); C. C. Alcaraz and A. Moreo, *ibid.* **46**, 2896 (1992).
92. T. Ziman and H. J. Schulz, *Phys. Rev. Lett.* **59**, 140 (1987).
93. K. Hallberg, X. Q. G. Wang, P. Horsch, and A. Moreo, *Phys. Rev. Lett.* **76**, 4955 (1996).
94. J. Lou, J. Dai, S. Qin, Z. Su, and L. Yu, *Phys. Rev. B* **62**, 8600 (2000).
95. M. Niel, C. Cros, G. Le Flem, M. Pouchard, and P. Hagenmuller, *Physica B* **86-88**, 702 (1977).
96. S. Itoh, K. Kakurai, Y. Endoh, and H. Tanaka, *Physica B* **213-214**, 161 (1995).
97. H. Mutka, C. Payen, and P. Molinié, *Europhys. Lett.* **21**, 623 (1993).
98. N. Hatano and M. Suzuki, *J. Phys. Soc. Jpn.* **62**, 1346 (1993); S. V. Meshkov, *Phys. Rev. B* **48**, 6167 (1993); J. Deisz, M. Jarell, and D. L. Cox, *ibid.* **48**, 10227 (1993); G. Sun, *ibid.* **51**, 8370 (1995); S. Yamamoto, *Phys. Rev. Lett.* **75**, 3348 (1995).
99. Y. Nishiyama, K. Totsuka, N. Hatano, and M. Suzuki, *J. Phys. Soc. Jpn.* **64**, 414 (1995).
100. U. Schollwöck and T. Jolicoeur, *Europhys. Lett.* **30**, 493 (1995); U. Schollwöck, O. Golinelli, and T. Jolicoeur, *Phys. Rev. B* **54**, 4038 (1996).
101. S. Qin, Y.-L. Liu, and L. Yu, *Phys. Rev. B* **55**, 2721 (1997); S. Qin, X. Wang, and L. Yu, *ibid.* **56**, R14251 (1997).
102. G. E. Granroth, M. W. Meisel, M. Chaparala, T. Jolicoeur, B. H. Ward, and D. R. Talham, *Phys. Rev. Lett.* **77**, 1616 (1996).
103. M. Oshikawa, *J. Phys. Condens. Matter* **4**, 7469 (1992).
104. K. Totsuka and M. Suzuki, *J. Phys. Condens. Matter* **7**, 1639 (1995).
105. Y. Hatsugai, *J. Phys. Soc. Jpn.* **61**, 3856 (1992).
106. T.-K. Ng, *Phys. Rev. B* **50**, 555 (1994).
107. H. Yamazaki and K. Katsumata, *Phys. Rev. B* **54**, R6831 (1996).
108. J. Lou, S. Qin, T.-K. Ng, and Z. Su, *Phys. Rev. B* **65**, 104401 (2002).
109. S. Qin, J. Lou, L. Sun, and C. Chen, *Phys. Rev. Lett.* **90**, 067202 (2003); J. Lou, S. Qin, and C. Chen, *Phys. Rev. Lett.* **91**, 087204 (2003); C. Chen, *Phys. Lett. A* **317**, 135 (2003).
110. For reviews see E. Dagotto and T. M. Rice, *Science* **271**, 618 (1996); T. M. Rice, *Z. Phys. B* **103**, 165 (1997); E. Dagotto, *Rep. Prog. Phys.* **62**, 1525

- (1999).
111. S. Gopalan, T. M. Rice, and M. Sigrist, *Phys. Rev. B* **49**, 8901 (1994).
  112. S. R. White, R. M. Noack, and D. J. Scalapino, *Phys. Rev. Lett.* **73**, 886 (1994).
  113. B. Frischmuth, B. Ammon, and M. Troyer, *Phys. Rev. B* **54**, R3714 (1996); B. Frischmuth, S. Haas, G. Sierra, and T. M. Rice, *ibid.* **55**, R3340 (1997).
  114. A. G. Rojo, *Phys. Rev. B* **53**, 9172 (1996).
  115. G. Sierra, *J. Phys. A* **29**, 3299 (1996).
  116. For a review, see for instance: J. Voit, *Rep. Prog. Phys.* **58**, 977 (1995); H. J. Schulz, G. Cuniberti, and P. Pieri, *Lecture notes of the Chia Laguna summer school*, (Springer Verlag, 1997); arXiv: cond-mat/9807366.
  117. M. Azuma, Z. Hiroi, M. Takano, K. Ishida, and Y. Kitaoka, *Phys. Rev. Lett.* **73**, 3463 (1994).
  118. K. Kojima, A. Keren, G. M. Luke, B. Nachumi, W. D. Wu, Y. J. Uemura, M. Azuma, and M. Takano, *Phys. Rev. Lett.* **74**, 2812 (1995).
  119. S. A. Carter, B. Batlogg, R. J. Carla, J. J. Krajewski, W. F. Peck Jr., and T. M. Rice, *Phys. Rev. Lett.* **77**, 1378 (1996); R. S. Eccleston, M. Uehara, J. Akimitsu, H. Eisaki, N. Motoyama, and S.-I. Uchida, *ibid.* **81**, 1702 (1998); T. Imai, K. R. Thurber, K. M. Shen, A. W. Hunt, and F. C. Chou, *ibid.*, 220 (1998); M. Takigawa, N. Motoyama, H. Eisaki, and S. Uchida, *Phys. Rev. B* **57**, 1124 (1998); L. P. Regnault, A. H. Moudden, J. P. Boucher, E. Lorenzo, A. Hiess, A. Vietkin, and A. Revcolevschi, *Physica B* **259-261**, 1038 (1999); A. Glozar, G. Blumberg, B. S. Dennis, B. S. Shastry, N. Motoyama, H. Eisaki, and S. Uchida, *Phys. Rev. Lett.* **87**, 197202 (2001).
  120. C. A. Hayward, D. Poilblanc, and L. P. Lévy, *Phys. Rev. B* **54**, R12649 (1996); G. Chaboussant, P. A. Crowell, L. P. Lévy, O. Piovesana, A. Madouri, and D. Mailly, *ibid.* **55**, 3046 (1997); G. Chaboussant, M.-H. Julien, Y. Fagot-Revurat, L. P. Lévy, C. Berthier, M. Horvatić, and O. Piovesana, *Phys. Rev. Lett.* **79**, 925 (1997); G. Chaboussant, Y. Fagot-Revurat, M.-H. Julien, M. E. Hanson, C. Berthier, M. Horvatić, L. P. Lévy, and O. Piovesana, *ibid.* **80**, 2713 (1998).
  121. P. R. Hammar, D. H. Reich, C. Broholm, and F. Trouw, *Phys. Rev. B* **57**, 7846 (1998).
  122. B. C. Watson *et al.*, *Phys. Rev. Lett.* **86**, 5168 (2001).
  123. K. Katoh, Y. Hosokoshi, K. Inoue, and T. Goto, *J. Phys. Soc. Jpn.* **69**, 1008 (2000); K. Katoh, Y. Hosokoshi, K. Inoue, M. I. Bartashevich, H. Nakano, and T. Goto, *J. Phys. Chem. Sol.* **63**, 1277 (2002).
  124. S. Brehmer, H.-J. Mikeska, M. Müller, N. Nagaosa, and S. Uchida, *Phys. Rev. B* **60**, 329 (1999); M. Matsuda, K. Katsumata, R. S. Eccleston, S. Brehmer, and H.-J. Mikeska, *ibid.* **62**, 8903 (2000).
  125. T. S. Nunner, P. Brune, T. Kopp, M. Windt, and M. Grüninger, *Phys. Rev. B* **66**, 180404 (2002).
  126. T. Barnes, E. Dagotto, J. Riera, and E. S. Swanson, *Phys. Rev. B* **47**, 3196 (1993).
  127. K. Hida, *J. Phys. Soc. Jpn.* **60**, 1347 (1991); *ibid.* **64**, 4896 (1995).
  128. H. Watanabe, *Phys. Rev. B* **50**, 13442 (1994); *ibid.* **52**, 12508 (1995).

129. Y. Nishiyama, N. Hatano, and M. Suzuki, *J. Phys. Soc. Jpn.* **64**, 1967 (1995).
130. S. R. White, *Phys. Rev. B* **53**, 52 (1996).
131. S. P. Strong and A. J. Millis, *Phys. Rev. Lett.* **69**, 2419 (1992); *Phys. Rev. B* **50**, 9911 (1994).
132. D. G. Shelton, A. A. Nersesyan, and A. M. Tsvelik, *Phys. Rev. B* **53**, 8521 (1996).
133. A. A. Nersesyan and A. M. Tsvelik, *Phys. Rev. Lett.* **78**, 3969 (1997); *Errata* **79**, 1171 (1997).
134. L. Takhtajan, *Phys. Lett. A* **87**, 479 (1982); J. Babujian, *ibid.* **90**, 479 (1982).
135. D. J. Gross and A. Neveu, *Phys. Rev. D* **10**, 3235 (1974).
136. D. Allen and D. Sénéchal, *Phys. Rev. B* **55**, 299 (1997).
137. E. H. Kim, G. Fáth, J. Sólyom, and D. J. Scalapino, *Phys. Rev. B* **62**, 14965 (2000); G. Fáth, Ö. Legeza, and J. Sólyom, *ibid.* **63**, 134403 (2001).
138. N. Read and B. Chakraborty, *Phys. Rev. B* **40**, 7133 (1989).
139. M. Nakamura, *Physica B* **329-333**, 1000 (2003).
140. S. Takada and H. Watanabe, *J. Phys. Soc. Jpn.* **61**, 39 (1992).
141. K. Damle and S. Sachdev, *Phys. Rev. B* **57**, 8307 (1998).
142. O. P. Sushkov and V. N. Kotov, *Phys. Rev. Lett.* **81**, 1941 (1998); V. N. Kotov, O. P. Sushkov and R. Eder, *Phys. Rev. B* **59**, 6266 (1999).
143. C. Jurecka and W. Brenig, *Phys. Rev. B* **61**, 14307 (2000).
144. S. Trebst, H. Monien, C. J. Hamer, Z. Weihong, and R. R. P. Singh, *Phys. Rev. Lett.* **85**, 4373 (2000); W. Zheng, C. J. Hamer, R. R. P. Singh, S. Trebst, and H. Monien, *Phys. Rev. B* **63**, 144410 (2001).
145. M. Windt, M. Grüninger, T. Nunner, C. Knetter, K. P. Schmidt, G. S. Uhrig, T. Kopp, A. Freimuth, U. Ammerahl, B. Büchner, and A. Revcolevschi, *Phys. Rev. Lett.* **87**, 127002 (2001).
146. K. I. Kugel and D. I. Khomskii, *Sov. Phys. Usp.* **25**, 231 (1982).
147. S. K. Pati, R. R. P. Singh, and D. I. Khomskii, *Phys. Rev. Lett.* **81**, 5406 (1998).
148. E. Axtell, T. Ozawa, S. Kauzlarich, and R. R. P. Singh, *J. Solid State Chem.* **134**, 423 (1997).
149. E. Orignac, R. Citro, and N. Andrei, *Phys. Rev. B* **61**, 11533 (2000).
150. A. K. Kolezhuk and H.-J. Mikeska, *Phys. Rev. Lett.* **80**, 2709 (1998); A. K. Kolezhuk, H.-J. Mikeska, and U. Schollwöck, *Phys. Rev. B* **63**, 064418 (2000).
151. M. J. Martins and B. Nienhuis, *Phys. Rev. Lett.* **85**, 4956 (2000).
152. P. Lecheminant and E. Orignac, unpublished.
153. J. Villain, *J. Phys. Fr.* **38**, 385 (1977); Chiral order in Helimagnets, proceedings of the 13th IUPAP Conference on Statistical Physics, edited by C. Weil, D. Cabid, C. G. Kuper, and I. Riess (1978).
154. T. Jolicoeur and J. C. Le Guillou, *Phys. Rev. B* **40**, 2727 (1989).
155. See for instance, N. D. Mermin, *Rev. Mod. Phys.* **51**, 591 (1979).
156. T. Senthil and M. P. A. Fisher, *Phys. Rev. B* **62**, 7850 (2000).
157. S. Rao and D. Sen, *Nucl. Phys. B* **424**, 547 (1994); *J. Phys. Condens. Matter* **9**, 1831 (1997).

158. D. Allen and D. Sénéchal, *Phys. Rev. B* **51**, 6394 (1995).
159. T. Dombre and N. Read, *Phys. Rev. B* **39**, 6797 (1989).
160. F. D. M. Haldane, talk at the workshop New Theoretical Approaches to Strongly Correlated Systems, Cambridge (2000); F. D. M. Haldane, *Phys. Rev. Lett.* **61**, 1029 (1988).
161. J. von Delft and C. L. Henley, *Phys. Rev. Lett.* **69**, 3236 (1992); *Phys. Rev. B* **48**, 965 (1992).
162. D. Loss, D. P. DiVincenzo, and G. Grinstein, *Phys. Rev. Lett.* **69**, 3232 (1992).
163. A. M. Polyakov and P. B. Wiegmann, *Phys. Lett.* **131 B**, 121 (1983); *ibid.* **141**, 223 (1984).
164. E. Ogievetsky, N. Reshetikhin, and P. B. Wiegmann, *Nucl. Phys. B* **280**, 45 (1987).
165. F. D. M. Haldane, *Phys. Rev. B* **25**, 4925 (1982); Errata *ibid.* **26**, 5257 (1982).
166. M. Hase, I. Terasaki, and K. Uchinokura, *Phys. Rev. Lett.* **70**, 3651 (1993).
167. For a review, see for instance: J. P. Boucher and L. P. Regnault, *J. Phys. I* **6**, 1939 (1996).
168. M. Isobe and Y. Ueda, *J. Phys. Soc. Jpn.* **65**, 3142 (1996); N. Fujiwara, H. Yasuoka, M. Isobe, Y. Ueda, and S. Maegawa, *Phys. Rev. B* **55**, R11945 (1997).
169. G. Castilla, S. Chakravarty, and V. J. Emery, *Phys. Rev. Lett.* **75**, 1823 (1995); J. Riera and A. Dobry, *Phys. Rev. B* **51**, 16098 (1995).
170. M. Matsuda and K. Katsumata, *J. Mag. Mag. Mat.* **140-144**, 1671 (1995); M. Matsuda, K. Katsumata, K. M. Kojima, M. Larkin, G. M. Luke, J. Merrin, B. Nachumi, Y. J. Uemura, H. Eisaki, N. Motoyama, S. Uchida, and G. Shirane, *Phys. Rev. B* **55**, R11953 (1997).
171. N. Motoyama, H. Eisaki, and S. Uchida, *Phys. Rev. Lett.* **76**, 3212 (1996).
172. N. Maeshima, M. Hagiwara, Y. Narumi, K. Kindo, T. C. Kobayashi, and K. Okunishi, *J. Phys. Condens. Matter* **15**, 3607 (2003).
173. H. Kikuchi, H. Nagasawa, Y. Ajiro, T. Asano, and T. Goto, *Physica B* **284-288**, 1631 (2000).
174. V. L. Berezinskii, *Sov. Phys. JETP* **34**, 610 (1972); J. M. Kosterlitz and D. J. Thouless, *J. Phys. C* **6**, 1181 (1973); J. M. Kosterlitz, *ibid.* **7**, 1046 (1974).
175. K. Okamoto and K. Nomura, *Phys. Lett. A* **169**, 433 (1992); K. Nomura and K. Okamoto, *J. Phys. A* **27**, 5773 (1994).
176. R. Chitra, S. Pati, H. R. Krishnamurthy, D. Sen, and S. Ramasesha, *Phys. Rev. B* **52**, 6581 (1995).
177. S. Eggert, *Phys. Rev. B* **54**, 9612 (1996).
178. S. White and I. Affleck, *Phys. Rev. B* **54**, 9862 (1996).
179. N. Andrei and J. H. Lowenstein, *Phys. Rev. Lett.* **43**, 1698 (1979); *Phys. Lett. B* **90**, 106 (1980).
180. A. A. Belavin, *Phys. Lett. B* **87**, 117 (1979).
181. C. K. Majumdar and D. K. Ghosh, *J. Math. Phys.* **10**, 1388, 1399 (1969).
182. B. S. Shastry and B. Sutherland, *Phys. Rev. Lett.* **47**, 964 (1981).

183. W. J. Caspers, K. M. Emmett, and W. Magnus, *J. Phys. A* **17**, 2687 (1984).
184. E. Sorensen, I. Affleck, D. Augier, and D. Poilblanc, *Phys. Rev. B* **58**, R14701 (1998).
185. W. J. Caspers and W. Magnus, *Phys. Lett. A* **88**, 103 (1982).
186. G. Fáth and A. Süto, *Phys. Rev. B* **62**, 3778 (2000).
187. K. Nomura, *J. Phys. Soc. Jpn.* **72**, 476 (2003).
188. R. Bursill, G. A. Gehring, D. J. J. Farnell, J. B. Parkinson, T. Xiang, and C. Zeng, *J. Phys. Condens. Matter* **7**, 8605 (1995).
189. S. Watanabe and H. Yokoyama, *J. Phys. Soc. Jpn.* **68**, 2073 (1999).
190. A. A. Aligia, C. D. Batista, and F. H. L. Essler, *Phys. Rev. B* **62**, 3259 (2000).
191. J. Stephenson, *Can. J. Phys.* **47**, 2621 (1969); *ibid.* **48**, 1724, 2118 (1970); *J. Math. Phys.* **12**, 420 (1970).
192. T. Tonegawa, M. Kaburagi, N. Ichikawa, and I. Harada, *J. Phys. Soc. Jpn.* **61**, 2890 (1992).
193. S. Pati, R. Chitra, D. Sen, H. R. Krishnamurthy, and S. Ramasesha, *Europhys. Lett.* **33**, 707 (1996).
194. A. Kolezhuk, R. Roth, and U. Schollwöck, *Phys. Rev. Lett.* **77**, 5142 (1996); *Phys. Rev. B* **55**, 8928 (1997).
195. R. Roth and U. Schollwöck, *Phys. Rev. B* **58**, 9264 (1998).
196. A. Kolezhuk and U. Schollwöck, *Phys. Rev. B* **65**, 100401 (2002).
197. I. Dzyaloshinskii, *J. Phys. Chem. Solids* **4**, 241 (1958); T. Moriya, *Phys. Rev. Lett.* **4**, 228 (1960); *Phys. Rev.* **120**, 91 (1960).
198. D. Allen, PhD thesis, Sherbrooke university, 1998.
199. A. A. Nersesyan, A. O. Gogolin, and F. H. L. Essler, *Phys. Rev. Lett.* **81**, 910 (1998).
200. D. C. Cabra, A. Honecker, and P. Pujol, *Eur. Phys. J. B* **13**, 55 (2000).
201. D. Allen, F. H. L. Essler, and A. A. Nersesyan, *Phys. Rev. B* **61**, 8871 (2000).
202. C. Itoi and S. Qin, *Phys. Rev. B* **63**, 224423 (2001).
203. D. Allen and D. Sénechal, *Phys. Rev. B* **61**, 12134 (2000).
204. R. Chitra and T. Giamarchi, *Phys. Rev. B* **55**, 5816 (1997).
205. G. I. Dzhaparidze and A. A. Nersesyan, *JETP Lett.* **27**, 334 (1978); *J. Low. Temp. Phys.* **37**, 95 (1979).
206. V. L. Pokrovsky and A. L. Talapov, *Phys. Rev. Lett.* **42**, 65 (1979); *Sov. Phys. JETP* **51**, 134 (1980).
207. H. J. Schulz, *Phys. Rev. B* **22**, 5274 (1980).
208. Y. Okwamoto, *J. Phys. Soc. Jpn.* **49**, 8 (1980).
209. A. A. Nersesyan, A. Luther, and F. V. Kusmartsev, *Phys. Lett. A* **176**, 363 (1993).
210. D. V. Dmitriev, V. Ya. Krivnov, and A. A. Ovchinnikov, *Phys. Rev. B* **65**, 172409 (2002); D. V. Dmitriev, V. Ya. Krivnov, A. A. Ovchinnikov, and A. Langari, *JETP* **95**, 538 (2002).
211. A. Dutta and D. Sen, *Phys. Rev. B* **67**, 094435 (2003).
212. A. A. Nersesyan, *Phys. Lett. A* **153**, 49 (1991); A. A. Nersesyan, A. Luther, and F. V. Kusmartsev, *JETP Lett.* **55**, 692 (1992).

213. P. Fendley and C. Nayak, *Phys. Rev. B* **63**, 115102 (2001).
214. D. Allen, P. Azaria, and P. Lecheminant, *J. Phys. A* **34**, L305 (2001).
215. J. L. Cardy, *Nucl. Phys. B* **389**, 577 (1993).
216. A. M. Tsvelik, *Nucl. Phys. B* **612**, 479 (2001).
217. D. Allen, private communication and unpublished.
218. Y. Nishiyama, *Eur. Phys. J. B* **17**, 295 (2000).
219. T. Hikihara, M. Kaburagi, and H. Kawamura, *Phys. Rev. B* **63**, 174430 (2001); *Prog. Theor. Phys. Suppl.* **145**, 58 (2002).
220. P. D. Sacramento and V. R. Vieira, *J. Phys. Condens. Matter* **14**, 591 (2002); V. R. Vieira, N. Guihery, J. P. Rodriguez, and P. D. Sacramento, *Phys. Rev. B* **63**, 224417 (2001).
221. M. Kaburagi, H. Kawamura, and T. Hikihara, *J. Phys. Soc. Jpn.* **68**, 3185 (1999); T. Hikihara, M. Kaburagi, H. Kawamura, and T. Tonegawa, *ibid.* **69**, 259 (2000).
222. A. K. Kolezhuk, *Phys. Rev. B* **62**, R6057 (2000); *Prog. Theor. Phys. Suppl.* **145**, 29 (2002).
223. P. Lecheminant, T. Jolicoeur, and P. Azaria, *Phys. Rev. B* **63**, 174426 (2001); T. Jolicoeur and P. Lecheminant, *Prog. Theor. Phys. Suppl.* **145**, 23 (2002).
224. Y. Q. Li, M. Ma, D. N. Shi, and F. C. Zhang, *Phys. Rev. Lett.* **81**, 3527 (1998).
225. Y. Yamashita, N. Shibata, and K. Ueda, *Phys. Rev. B* **58**, 9114 (1998).
226. B. Frischmuth, F. Mila, and M. Troyer, *Phys. Rev. Lett.* **82**, 835 (1999).
227. B. Sutherland, *Phys. Rev. B* **12**, 3795 (1975).
228. Y.-Q. Li, M. Ma, D.-N. Shi, and F.-C. Zhang, *Phys. Rev. B* **60**, 12781 (1999).
229. I. Affleck, *Nucl. Phys. B* **305**, 582 (1988).
230. A. B. Zamolodchikov, *JETP Lett.* **43**, 730 (1986).
231. P. Azaria, A. O. Gogolin, P. Lecheminant, and A. A. Nersesyan, *Phys. Rev. Lett.* **83**, 624 (1999); P. Azaria, E. Boulat, and P. Lecheminant, *Phys. Rev. B* **61**, 12112 (2000).
232. C. Itoi, S. Qin, and I. Affleck, *Phys. Rev. B* **61**, 6747 (2000).
233. B. Gerganov, A. Leclair, and M. Moriconi, *Phys. Rev. Lett.* **86**, 4753 (2001); A. Leclair, *Phys. Rev. B* **64**, 045329 (2001).
234. H.-H. Lin, L. Balents, and M. P. A. Fisher, *Phys. Rev. B* **58**, 1794 (1998).
235. R. Assaraf, P. Azaria, E. Boulat, M. Caffarel, and P. Lecheminant, arXiv: cond-mat/0310090.
236. Y. Yamashita, N. Shibata, and K. Ueda, *J. Phys. Soc. Jpn.* **69**, 242 (2000).
237. G. V. Uimin, *JETP Lett.* **12**, 225 (1970); C. K. Lai, *J. Math. Phys.* **15**, 1675 (1974).
238. C. Itoi and M.-H. Kato, *Phys. Rev. B* **55**, 8295 (1997).
239. G. Fáth and J. Sólyom, *Phys. Rev. B* **44**, 11836 (1991); *ibid.* **47**, 872 (1993).
240. A. Läuchli, G. Schmid, and S. Trebst, cond-mat/0311082.
241. R. Citro, E. Orignac, N. Andrei, C. Itoi, and S. Qin, *J. Phys. Condens. Matter* **12**, 3041 (2000).
242. P. Azaria, P. Lecheminant, and A. A. Nersesyan, *Phys. Rev. B* **58**, R8881 (1998); P. Azaria and P. Lecheminant, *Nucl. Phys. B* **575**, 439 (2000).

243. N. Andrei, M. Douglas, and A. Jerez, *Phys. Rev. B* **58**, 7619 (1998).
244. X. Wang, N. Zhu, and C. Chen, *Phys. Rev. B* **66**, 172405 (2002).
245. S. Sachdev and M. Vojta, in Proceedings of the XIII International Congress on Mathematical Physics, edited by A. Fokas, A. Grigoryan, T. Kibble, and B. Zegarlinski, (International Press, Boston, 2001); arXiv: cond-mat/0009202.
246. B. Normand and F. Mila, *Phys. Rev. B* **65**, 104411 (2002).
247. X. G. Wen, F. Wilczek, and A. Zee, *Phys. Rev. B* **39**, 11413 (1989).
248. A. Läuchli, G. Schmid, and M. Troyer, *Phys. Rev. B* **67**, 100409(R) (2003).
249. T. Hikihara, T. Momoi, and X. Hu, *Phys. Rev. Lett.* **90**, 087204 (2003); T. Momoi, T. Hikihara, M. Nakamura, and X. Hu, *Phys. Rev. B* **67**, 174410 (2003).
250. A. A. Nersesyan and A. M. Tsvelik, *Phys. Rev. B* **67**, 024422 (2003); F. A. Smirnov and A. M. Tsvelik, *ibid.* **68**, 144412 (2003); M. J. Bhaseen and A. M. Tsvelik, *ibid.* **68**, 094405 (2003).
251. O. A. Starykh, R. R. P. Singh, and G. C. Levine, *Phys. Rev. Lett.* **88**, 167203 (2002); R. R. P. Singh, O. A. Starykh, and P. J. Freitas, *J. Appl. Phys.* **83**, 7387 (1998).
252. P. Sindzingre, J.-B. Fouet, and C. Lhuillier, *Phys. Rev. B* **66**, 174424 (2002).
253. V. J. Emery, E. Fradkin, S. A. Kivelson, and T. C. Lubensky, *Phys. Rev. Lett.* **85**, 2160 (2000); A. Vishwanath and D. Carpentier, *Phys. Rev. Lett.* **86**, 676 (2001); R. Mukhopadhyay, C. L. Kane, and T. C. Lubensky, *Phys. Rev. B* **63**, 081103 (2001); *ibid.* **64**, 045120 (2001); S. L. Sondhi and K. Yang, *ibid.* **63**, 054430 (2001).

## CHAPTER 7

### SPIN ICE

Steven T. Bramwell

*University College London, Department of Chemistry, 20 Gordon Street, London  
WC1H 0AJ, U.K.*

Michel J. P. Gingras

*Department of Physics, University of Waterloo, Waterloo, Ontario, N2L 3G1,  
Canada.*

*and*

*Canadian Institute for Advanced Research, 180 Dundas Street West, Toronto,  
Ontario, M5G 1Z8, Canada.*

Peter C. W. Holdsworth

*Laboratoire de Physique, Ecole Normale Supérieure, 46 Avenue d'Italie, F-69634  
Lyon Cedex 07, France.*

Pauling's model of hydrogen disorder in water ice represents the prototype of a frustrated system. Over the years it has spawned several analogous models, including Anderson's model antiferromagnet and the statistical "vertex" models. Spin Ice is a sixteen vertex model of "ferromagnetic frustration" that is approximated by real materials, most notably the rare earth pyrochlores  $\text{Ho}_2\text{Ti}_2\text{O}_7$ ,  $\text{Dy}_2\text{Ti}_2\text{O}_7$  and  $\text{Ho}_2\text{Sn}_2\text{O}_7$ . These "spin ice materials" have the Pauling zero point entropy and in all respects represent almost ideal realisations of Pauling's model. They provide experimentalists with unprecedented access to a wide variety of novel magnetic states and phase transitions that are located in different regions of the field-temperature phase diagram. They afford theoreticians the opportunity to explore many new features of the magnetic interactions and statistical mechanics of frustrated systems. This chapter is a comprehensive review of the physics - both experimental and theoret-

ical - of spin ice. It starts with a discussion of the historic problem of water ice and its relation to spin ice and other frustrated magnets. The properties of spin ice are then discussed in three sections that deal with the zero field spin ice state, the numerous field-induced states (including the recently identified “kagomé ice”) and the magnetic dynamics. Some materials related to spin ice are briefly described and the chapter is concluded with a short summary of spin ice physics.

**Keywords:** Spin ice, water ice, frustration, frustrated ferromagnetism, zero point entropy, vertex models, Ising model, specific heat, magnetization, neutron scattering, dipolar interactions, Ewald summation, Monte Carlo simulations, spin dynamics, AC-susceptibility, neutron spin echo, quantum tunneling, magnetic relaxation, liquid-gas transition, Kastelyn transition.

## 7.1. Introduction

Pauling’s model of the hydrogen structure of water ice, with its characteristic property of zero point entropy, stands as a canonical model of disorder in condensed matter<sup>1</sup>. Magnetic models with similar properties were developed half a century ago by Wannier<sup>2</sup> and Anderson<sup>3</sup>, who demonstrated how zero point entropy could arise in Ising model antiferromagnets with triangular<sup>2</sup> or tetrahedral geometry<sup>3</sup>. These antiferromagnetic systems would now be described as “geometrically frustrated” as their lattice geometry means that they are unable to satisfy the local minimum energy conditions (although the concept of frustration first arose from spin glass research where it is usually associated with random chemical disorder<sup>6</sup>). However, despite the historic role of Pauling’s model in magnetism research, it is only relatively recently that its magnetic equivalent has been realised in the laboratory. “Spin ice”<sup>4,5</sup> – a microscopic mapping of Pauling’s model onto a *ferromagnetic*, rather than an antiferromagnetic system – is approximated almost ideally by the so-called “spin ice materials”. These systems finally provide concrete experimental examples of the basic models of magnetic frustration envisaged by Wannier and Anderson and of the more generalised ice-type models that have been studied theoretically for many years<sup>7,8</sup>.

The prototypical spin ice materials  $\text{Ho}_2\text{Ti}_2\text{O}_7$  and  $\text{Dy}_2\text{Ti}_2\text{O}_7$  are oxides with the pyrochlore structure in which the  $\text{Ti}^{4+}$  ions are non-magnetic and the trivalent rare earth ions occupy a face centered cubic lattice of corner-linked tetrahedra, as shown in Fig. 7.1. They are highly crystalline electrical insulators with band gaps of the order of optical frequencies. The crystal field on the rare earth ions is much stronger than the (effectively ferromagnetic) dipole interaction that in turn largely dominates the superexchange (thought to be weakly antiferromagnetic). The single ion ground state is a doublet, composed almost entirely of free ion sub levels with the maximum  $M_J = \pm J$ <sup>a</sup>, with the first group of excited crystal field states lying some 300 K above the ground state. This gives rise to strong single ion anisotropy that at low temperature constrains the atomic magnetic moment (henceforth “spin”) parallel to its local quantization axis, a member of the  $\langle 111 \rangle$  set.<sup>b</sup> Consequently, in terms of its static properties, each moment behaves like a classical Ising spin lying parallel to the axis that connects the center of the elementary tetrahedron of the pyrochlore lattice to its vertex.

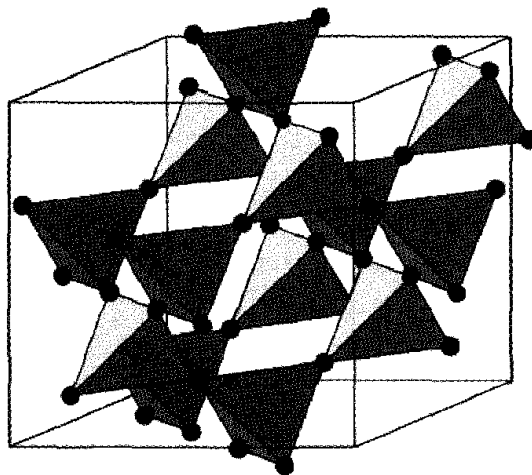


Fig. 7.1. The pyrochlore lattice occupied by the rare earth ions in the spin ice materials

<sup>a</sup>The total angular momentum of the free rare earth ion is characterised by two quantum numbers  $J$  and  $M_J$ , which takes the values  $J, J - 1 \dots - J$ . The observable magnetic moment is  $\mu_z = -g_J\mu_B M_J$  where  $g_J$  is the Landé g-factor and  $z$  denotes the quantization axis.  $M_J = \pm J$  therefore corresponds to a moment  $\mp g_J\mu_B J$

<sup>b</sup>We adopt the standard crystallographic convention that [...] refers to the indices of a single lattice direction and  $\langle \dots \rangle$  refers to the set of all equivalent lattice directions.

When one adds ferromagnetic spin-spin coupling to this model of  $\langle 111 \rangle$  Ising spins, the ground state of a single tetrahedron is determined by the condition that two spins must point “in” and two must point “out” of each tetrahedron. This “two in, two out” rule minimizes only four of the six pairwise interactions, which is the best that can be achieved given the tetrahedral geometry. Hence, spin ice is frustrated. The ground state rules for spin ice are equivalent to the rules that control local hydrogen arrangements in Pauling’s model of water ice. In fact, the mapping of the  $\langle 111 \rangle$  Ising ferromagnet onto Pauling’s model is precise if one considers cubic ice, the spins playing the role of proton displacement vectors located at the mid-points of the oxide-oxide lines of contact (see Fig. 7.2). The remarkable fact is that this scenario actually occurs in the spin ice materials, to an excellent approximation. Like water ice they have zero point entropy and there are also analogies in the dynamics. However, unlike water ice, the spin ice materials are ideal systems for both experimental and theoretical study: samples are easy to handle, the Hamiltonian is simple, well-established and tractable, magnetic fields can be applied that far exceed in relative magnitude any electric fields that can be applied to water ice; spin dynamics are fast compared to proton dynamics, and so forth ... In fact, studies of spin ice materials have started to reveal much new physics that might in principle be observed in ice itself, were it more amenable to experiment. It could thus be argued that spin ice has already replaced water ice as the canonical realization of an “ice-type” model.

Whatever its ultimate significance, the spin ice phenomenon provides an ideal system for the combined experimental and theoretical approach to the statistical mechanics of frustrated systems, as well as an interesting new type of magnetic material. The purpose of this review is to describe the current state of experimental and theoretical work on spin ice, to identify the main trends for future research, and to assess the significance of the new physics revealed. It is not primarily a comparison of spin ice and water ice, although we do describe the historic problem of water ice in Section 7.2.1. Nor is it an attempt to put spin ice in the general context of frustrated magnetism, although we briefly allude to this in Section 7.2.5. It is hoped that this review will be of interest to those who know nothing of spin ice as well as workers in the field who are seeking an overview. We note two previous reviews of spin ice<sup>9,10</sup> and that spin ice has been discussed in the generally broader context of frustrated materials and related phenomena<sup>11,12</sup>.

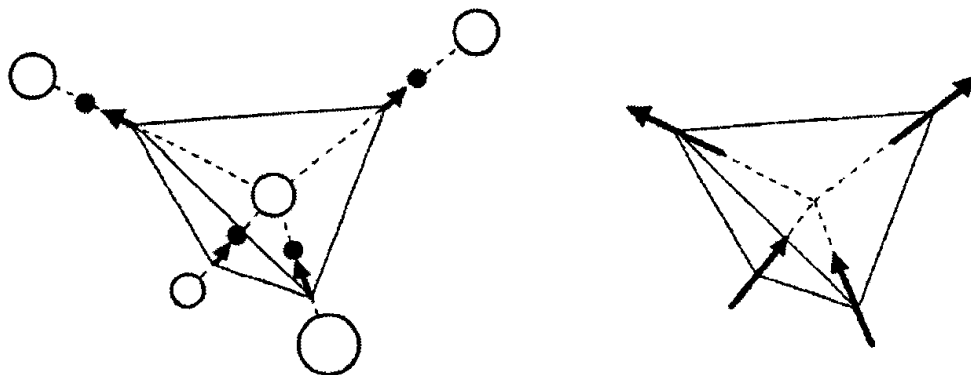


Fig. 7.2. Illustration of the equivalence of the water ice rule “two protons near, two protons far” and the spin ice rule “two spins in, two spins out”. The diagram (left) illustrates a water molecule in the tetrahedral coordination of the ice structure (oxides are denoted by open circles, protons by filled circles). The proton positions are located by displacement vectors that occupy a lattice of linked tetrahedra. In spin ice (right) the displacement vectors are replaced by rare earth moments (“spins”) occupying the pyrochlore lattice (Fig. 7.1), which is the dual lattice (i.e. the lattice formed by the mid-points of the bonds) of the oxide lattice in cubic ice.

## 7.2. From Water Ice to Spin Ice

### 7.2.1. Pauling’s Model

Ice is the paradigm for disordered systems, not least because of the experimental evidence it shows for the apparent violation of the third law of thermodynamics. A series of quite remarkable experiments terminated, in 1936, with Giauque and Stout’s paper “*The Entropy of Water and the Third Law of Thermodynamics. Heat Capacity of Ice from 15 to 273 K.*”<sup>13</sup>. In their paper Giauque and Stout reported calorimetric measurements on water through the freezing and vaporization transitions up to the high temperature gas phase. The entropy was calculated by integrating the heat capacity and adding the latent heat contributions; the low temperature measurements being extrapolated to zero, using Debye’s then recently derived formula<sup>14</sup>. The resulting entropy,  $S_1 = 44.28 \text{ Cal/deg}\cdot\text{mol}$ , was compared with a second estimate,  $S_2 = 45.10 \text{ Cal/deg}\cdot\text{mol}$ , calculated using the statistical mechanics of an ideal gas, with internal energy levels taken from spectroscopic measurements. The two values were found to disagree by  $S_0 = 0.82 \pm 0.05 \text{ Cal/deg}\cdot\text{mol}$ . The difference was famously accounted for, to an excellent approximation, by Pauling<sup>1</sup>, who showed that ice pos-

sesses a finite entropy (estimated as 0.81 Cal/deg.mol) at zero temperature due to the configurational disorder intrinsic to the proton system.

The ice problem is a classic example of how the separation of energy scales can leave certain classes of internal degrees of freedom as irrelevant and frustrated bystanders in the energy minimization process. Here, the chemical binding energy of the water molecule is so strong (221 kCal/mol) that it is left essentially unchanged in the solid condensed phase. As a result, the ground state configuration does not minimize the electrostatic energy of a neutral ensemble of  $O^{2-}$  and  $H^+$  ions. Rather, in the hexagonal ("wurtzite") and cubic ("sphalerite") ice phases<sup>15</sup>, the oxygen ions form an open tetrahedral structure, whose 109 degree angles conform closely to that encompassing the H – O – H bonds of an isolated water molecule. In the wurtzite phase the O – O bond length is 2.76 Å, while the O – H bond in the water molecule measures only 0.96 Å. As the internal  $H_2O$  molecular structure is maintained, the minimum energy position is not half way between the two oxide ions. Instead, there are two equivalent positions for a proton lying on the O – O line of contact<sup>1</sup>. With the four-fold oxygen co-ordination there is one proton per O – O "bond". The constraint of  $H_2O$  molecular integrity therefore leads to the "ice rules" for a ground state configuration: for each oxygen two protons must be in the near position and two in the far position. From an electrostatic point of view the protons would like to be as far apart as possible. The ice rules therefore frustrate the effective proton-proton interaction.

The ice rules were enunciated by Bernal and Fowler in 1933<sup>16</sup>. In that period X-ray diffraction could only determine the oxygen structure, but Bernal and Fowler argued that the hydrogens must lie along the oxygen-oxygen lines of contact. They proposed an ordered proton structure, undoubtedly presuming that this would be the case. However, around that time Giauque and co-workers first established the probable existence of a zero point entropy<sup>17</sup>. This led Pauling to his proposal (published in 1935) that the open tetrahedral structure of ice affords many equivalent ways of satisfying the ice rules. Pauling went on to approximately calculate the associated configurational entropy in the following way: consider one mole of ice, containing a number  $N$  of  $O^{2-}$  ions. Each O – O bond can be taken as having two proton positions, which gives  $2^{2N}$  possible configurations. Out of the 16 possible configurations associated with each oxygen, ten are energetically unfavourable: the  $OH_4^{2+}$  configuration, the 4  $OH_3^+$  configurations, the 4  $OH^-$  configurations and the  $O^{2-}$  configuration. This leaves the six configurations that satisfy the Bernal-Fowler rules as

the allowed local proton configurations around each oxygen ion. An upper bound on the number of ground state configurations is therefore estimated as  $\Omega \leq 2^{2N}(6/16)^N = (3/2)^N$ . The corresponding configurational entropy,  $S_0 = k_B \ln(\Omega) = Nk_B \ln(3/2) = 0.81 \text{ Cal/deg}\cdot\text{mol}$  is in remarkable agreement with the missing entropy in Giauque and Stout's experiment,  $0.82 \pm 0.05 \text{ Cal/deg}\cdot\text{mol}$ . Although Pauling's calculation neglects both the global constraint on the number of protons and the local constraints coming from closed loops on the Wurtzite lattice, it has been subsequently shown to be accurate to  $1 - 2\%$ <sup>18</sup>.

### 7.2.2. Why is the Zero Point Entropy not Zero?

Pauling's model assumes then that the protons remain in disordered configurations consistent with the Bernal-Fowler rules. The proton disorder has been confirmed by neutron scattering on deuterated, or heavy ice<sup>19</sup>. Remarkably, it seems that the calorimetry results do not require an ergodic exploration of the ground state configurations. Even in Giauque and Stout's original paper it is remarked that the response time of the sample goes through a maximum at around 100 K, corresponding to a freezing of the proton degrees of freedom. It seems then that the system settles essentially into a single ground state and does not evolve in time over the manifold of possible states. However, as there are no long range correlations, it is self averaging. That is, no information is transmitted over macroscopic distances and the sample behaves itself as a Gibbs ensemble of equivalent states. This interpretation is in strong contrast with the case of spin glasses, where despite high (quasi-)ground state degeneracy, each state requires collective organization.

This might seem paradoxical: if ice (or spin ice) freezes into a particular ice-rules state, this seems just as definite a molecular (spin) arrangement as an ordered state. So why is the ground state entropy not zero in both cases? The question can be answered at several levels: if the sample were cut into many sub-samples, subsequent measurements on one of these would give no information about the microscopic state of the other sub-samples. The opposite is true of a system that has collectively broken symmetry to find a long range ordered state. The excitation spectrum above the ground states, constituting the specific heat, must reflect this difference in information: for ice, this is confirmed by Giauque and Stout's experiment. Another very simple example is an Ising paramagnetic system in zero magnetic field. All  $2^N$  configurations have zero energy. At all temperatures  $C_H$  would be

zero and all entropy measurements would give  $\Delta S = 0$ . The ground state entropy is then very trivially  $S_0 = Nk_B \ln(2)$ . The simplest models of ice and spin ice are somewhere between this trivial example and an ordered system: they allow zero energy excitations, not of single particles, but of a small number of particles. What about the lack of dynamics? Given the self averaging, dynamics are not needed: an ergodic system and a Gibbs ensemble give identical results. Discussions of the definition of entropy in this context can be found in Rushbrooke<sup>20</sup> and Mayer and Mayer<sup>21</sup>.

Following Giauque and Stout's experiment and Pauling's explanation one might still ask the question, can the third law really be violated in practice? A highly degenerate ground state structure would be expected to be extremely susceptible to perturbations. Hence, there should always be some interaction - further neighbour exchange, electric or magnetic dipole, external fields, quantum fluctuations (i.e. proton or spin tunneling) etc. - that lifts the degeneracy, giving finally a single preferred state and no anomaly. This is certainly true and we will see an explicit example of it later, in the case of the spin ice model, when dipolar interactions are considered. However, experimentally this is not what is observed either in water ice, or in the magnetic analogues discussed in this review. The evidence is that the third law does not apply to these systems on the time scale of any conceivable experiment. Rushbrooke has therefore described the observed zero point entropy as a "practical entropy", to logically distinguish it from the entropy of the expected (but unobserved) equilibrium state<sup>20</sup>.

We can now recognize such degeneracy as a standard consequence of having frustrated degrees of freedom. Pauling's model of two proton positions per bond is Ising-like and the frustration can be described by a nearest neighbour exchange term. Many such model systems have been studied, as described below in Section 7.2.3 and elsewhere in this book. The recently discovered spin ice materials<sup>4</sup> provide an important experimental connection between these models and water ice. This is well illustrated by Ramirez *et al.*'s calorimetry experiment on the spin ice material  $Dy_2Ti_2O_7$ <sup>22</sup>, in which Pauling's ground state entropy was measured using a procedure analogous to that used by Giauque and Stout.

### 7.2.3. Generalizations of Pauling's Model

#### 7.2.3.1. Wannier's Model

In an elegant 1950 paper, Wannier<sup>2</sup> investigated the statistical mechanics of antiferromagnetically coupled Ising spins on a triangular lattice, using

the then recently developed methods of Kaufmann and Onsager. His main conclusion, that “*The system is disordered at all temperatures and possesses no Curie point.*” probably represents the first published recognition of frustrated magnetism. The ground state of the model is macroscopically degenerate: it has two spins up and one down (or vice versa) per triangle and has zero point entropy  $0.323 Nk_B$ , where  $N$  is the number of spins.

### 7.2.3.2. Anderson’s Model

Anderson<sup>3</sup> considered the problem of cation ordering in inverse spinels and magnetic ordering in normal spinels. To a first approximation both these problems map onto the antiferromagnetic Ising model on the B-site spinel lattice, which is identical to the pyrochlore lattice, Fig. 7.1. The task is to place + and – signs on this lattice in the ratio 1:1, such that the number of +/– pairs is maximized. This condition is fulfilled with two + and two – signs per tetrahedron. The tetrahedra of the spinel lattice are arranged on the same lattice as the oxide ions in cubic ice. The spinel lattice consists of alternate “up” and “down” tetrahedra, so the Pauling ice rules are recovered if a + sign represents “proton in” on an up tetrahedron and “proton out” on a down tetrahedron, and vice-versa for a – sign. The model therefore has the Pauling zero point entropy and represents one of the first examples of what now would be called a geometrically frustrated antiferromagnet, predated only by Wannier’s model (see above). As regards to the spinel systems, Anderson calculated the Coulomb (Madelung) energies of ordered phases and concluded that the energy advantage  $\Delta U$  of adopting one of these was only a few per cent of the near neighbour energy, implying a transition at a temperature  $T_c \propto \Delta U / \Delta S$  (where  $\Delta S \approx S_0$ , the zero point entropy). Because  $T_c$  is a low temperature, the experimental dynamics might be too slow to equilibrate the system, leading to observable ionic disorder. This is born out experimentally both in the spinels and the pyrochlore fluorides of general formula  $AXYF_6$  (e.g.  $CsMnFeF_6$ ), which have a fully disordered pyrochlore lattice of X and Y ions even in highly annealed samples. It is interesting to note that Anderson also considered different ratios of X and Y ions, including the ratio 3:1, a situation that maps onto the “kagomé ice” model discussed in Section 7.4.5 as well as onto Wannier’s model<sup>2</sup>.

In the context of frustration, Anderson’s model is important as a paradigm for geometrical frustration on lattices built on corner-sharing simplex units (triangles or tetrahedra), typified by the pyrochlore and kagomé lattices. The idea was revived twenty years later by Villain<sup>23</sup>, who dis-

cussed the properties of the pyrochlore Heisenberg antiferromagnet, heralding many years of research into frustrated antiferromagnetic materials. As remarked by Anderson himself, this model shares with the Ising antiferromagnet the property of a disordered ground state: in this case a spin liquid or cooperative paramagnet<sup>23,24</sup>. The Heisenberg antiferromagnet model is realistic, being approximated by several real magnetic materials, for example  $\text{CsNiCrF}_6$  and  $\text{CsMnFeF}_6$ <sup>25,26</sup>. In contrast there are no known realizations of Anderson's Ising antiferromagnet. The reasons for this are discussed in Section 7.2.3.4 below.

#### 7.2.3.3. *Vertex Models*

In the 1960's and 1970's models of ferroelectrics derived from the Pauling ice model became of great interest, as, in two dimensions at least, their properties could often be calculated exactly<sup>7,8</sup>. These became known as "vertex models". A vertex is a local configuration of displacement vectors that has a definite energy: for example "four protons in" would constitute a single vertex. The phase diagram of the models could be mapped out in terms of the weighting of these vertices, which for real systems are determined by their Gibbs-Boltzmann probabilities (which can be controlled to some extent by the application of an external field). A landmark calculation was Baxter's exact solution of the eight vertex model in two dimensions which is equivalent to a Pauling model that includes the  $\text{OH}_4^{2+}$  and  $\text{O}^{2-}$  configurations along with the six ice-rule states, to make eight in total.

Some mappings of vertex models onto Ising models have previously been proposed. For example the two dimensional eight vertex model can be mapped alternatively onto Ising models with two and four spin interactions or Ising models with further neighbour interactions: see Ref. [7] for details.

#### 7.2.3.4. *Possibility of Realizing Magnetic Vertex Models*

From the above discussion, it should be clear that it is usually possible to map an ice-type or vertex model onto a magnetic system. The problem is that the magnetic models so derived are often rather unrealistic. This is exemplified by the absence of any reported examples of Anderson's antiferromagnet in nearly fifty years since its publication<sup>3</sup>. This fact may be understood by the following argument. The occurrence of Ising-like variables in real magnetic materials is always associated with magnetocrystalline anisotropy arising from the combined effect of the local crystal field and spin orbit coupling. The local magnetic moments therefore always

have a symmetry compatible with the local point symmetry of the crystal structure, which means that practical Ising magnets require a unique crystallographic axis. The simplest model for Ising-like spins in the cubic pyrochlore symmetry is with *local* easy axes defined by the four local axes of point symmetry, each a different member of the  $\langle 111 \rangle$  set. In this case the crystal fields themselves frustrate the exchange interaction as they inhibit parallel or antiparallel nearest neighbour spin configurations. Within this restricted phase space the physics resulting from ferromagnetic and anti-ferromagnetic couplings are reversed, compared to simple (uniaxial) Ising models<sup>4,5,27,28</sup>. Counter-intuitively the antiferromagnet behaves as an Ising ferromagnet, and does *not* have a macroscopically degenerate ground state<sup>5</sup>. It is rather, *ferromagnetically* coupled spin ice that maps onto Pauling's model<sup>1</sup> and hence onto Anderson's model<sup>3</sup>. In this sense spin ice *is* the experimental realization of Anderson's antiferromagnet. However it should be noted that ferromagnetic spin ice has a much richer experimental phenomenology than the antiferromagnetic Ising model: this is because a laboratory field can couple to many order parameters in the ferromagnetic system which is not possible in its antiferromagnetic counterpart. Thus the interesting physics of spin ice in an applied field (described in Section 7.4) is not an immediately obvious property of the Ising antiferromagnet. Hence we have an example where two equivalent statistical mechanical model systems (spin ice and Anderson's antiferromagnet) are very different from the experimental point of view.

The symmetry argument used above does not apply to Wannier's antiferromagnet (the Ising model on the triangular lattice)<sup>2</sup> because the normal to the triangular net defines a unique axis. Although there are examples of Ising-like triangular antiferromagnets, such as  $\text{CsCoCl}_3$ <sup>29</sup>, it appears that no realisations of the Wannier zero point entropy have yet been found. However, we describe later in Section 7.4.5.1, how spin ice in a magnetic field applied on [111] maps on to the ground state of Wannier's model antiferromagnet<sup>2</sup> and may thus be considered its experimental realisation.

It is also evident that spin ice provides the first truly ideal realisation of a vertex model in magnetism: the previous mappings of vertex models onto magnetic Ising models are either not very realistic or not very well represented experimentally. In fact, spin ice is a 16-vertex model with the 16 vertices corresponding to the  $2^4$  spin configurations of a single tetrahedron. The beauty of spin ice is that the experimentalist has significant power to selectively control the statistical weights of the vertices, via the application of an external field along several of the principal symmetry axes, for example

[100], [110], [111] and [211]. This remarkable feature of spin ice, which is explored further in Section 7.4, means that one finally has a system that connects comprehensively to the theory of vertex models. It is hoped that this property might re-invigorate interest in exact analysis of such systems (see for example <sup>30</sup>).

#### **7.2.4. Spin Ice**

As often happens, the appropriate labeling of a new scientific phenomenon can contribute to the process of unravelling its origin and understanding it. This appears to have been the case for “spin ice”. The name “spin ice” and the concept of frustrated ferromagnetism was initially proposed in Ref. [4]. Specifically, Ref. [4] introduced the “spin ice model”, that is the  $\langle 111 \rangle$  Ising pyrochlore ferromagnet (now known as the near neighbour spin ice model) in order to explain diverse experiments on holmium titanate,  $\text{Ho}_2\text{Ti}_2\text{O}_7$ . It is relevant in the context of this review to first discuss why the experimental results demanded the invention of the spin ice model.

##### *7.2.4.1. Definition of the Spin Ice Model and its Application to $\text{Ho}_2\text{Ti}_2\text{O}_7$*

The first evidence of magnetic frustration in  $\text{Ho}_2\text{Ti}_2\text{O}_7$  came from a muon spin relaxation ( $\mu SR$ ) experiment performed at the ISIS facility in 1996 <sup>31</sup> (and reported briefly as part of <sup>32</sup>). The initial hypothesis being tested was that  $\text{Ho}_2\text{Ti}_2\text{O}_7$  was a geometrically frustrated antiferromagnet, which might not magnetically order down to the lowest measurable temperatures.  $\mu SR$  is a sensitive measure of magnetic order as an ordered spin structure will often produce a well-defined and narrow distribution of dipolar fields at the muon stopping site, giving rise to characteristic precessional oscillations in the relaxation signal. In zero applied magnetic field  $\text{Ho}_2\text{Ti}_2\text{O}_7$  showed no such oscillations; but after the application and removal of a field, oscillations were found to be “frozen” into the signal. This effect (see Section 7.3.1.2) was reminiscent of spin glass behaviour and consistent with the hypothesis of frustrated antiferromagnetism. However, careful magnetization measurements on single crystal samples performed in order to estimate the Curie-Weiss temperature,  $\theta_{\text{CW}}$ , found that  $\theta_{\text{CW}}$  depended strongly on sample shape, indicative of a large demagnetization factor. Estimation of the latter, combined with measurements on quasi-ellipsoidal samples of different aspect ratio <sup>33</sup>, fixed the Curie-Weiss temperature accurately at  $\theta_{\text{CW}} = 1.9 \pm 0.1 \text{ K}$  <sup>4,32</sup>. The surprise was that this value is *ferromagnetic*:

the Curie-Weiss temperature is a robust measure of the sum of pairwise coupling energies experienced by a spin, so  $\text{Ho}_2\text{Ti}_2\text{O}_7$  could be thought of as having predominantly ferromagnetic spin-spin interactions. At first sight this was inconsistent with the  $\mu SR$  result, so in order to get a more detailed microscopic picture of  $\text{Ho}_2\text{Ti}_2\text{O}_7$ , several neutron scattering experiments were performed on a large single crystal. In zero applied field these measurements confirmed the  $\mu SR$  result of no magnetic order down to 50 mK, but the build up of diffuse scattering near to the Brillouin zone centers in reciprocal space was again more characteristic of ferromagnetic than antiferromagnetic correlations. In an applied field the dramatic growth of Bragg peaks indicated the restoration of magnetic order. The relaxation of these peaks confirmed the history dependence already noted in the  $\mu SR$  experiment, while their positions at the  $\mathbf{Q} = \mathbf{0}$  and  $\mathbf{Q} = \mathbf{X}$  points of the Brillouin zone were again curiously indicative of both ferromagnetic and antiferromagnetic ordering patterns in a field.

In the meantime an analysis of powder magnetization measurements had confirmed, as found by previous authors (see Section 7.2.4.3), that  $\text{Ho}^{3+}$  could be represented to a good approximation by an Ising ground state doublet with large moment. By analogy with  $\text{LiHoF}_4$ <sup>34</sup> and the single-molecule magnets<sup>35</sup> (which have large Ising-like spins), this suggested a picture of Ising spins fixed along the local quantization axis: in this case the trigonal  $\langle 111 \rangle$  axes that connect the vertices of each tetrahedron to its center.

Thus, at the most basic level of approximation, the experiments demanded a model with  $\langle 111 \rangle$  spins and near neighbour ferromagnetic coupling<sup>4</sup>. Of course, this is a phenomenological approach that does not inquire as to the nature of the coupling: subsequent refinements have taken a more microscopic starting point that invokes realistic dipolar and exchange interactions<sup>36,37</sup> (see Section 7.3.2). For the  $\langle 111 \rangle$  Ising ferromagnet, simple calculation showed that the ground state of a single tetrahedron of spins is the configuration with two spins pointing in and two pointing out. As Anderson had shown the pyrochlore lattice to be the dual lattice (i.e. the lattice formed by the mid points of the bonds) of cubic ice, “two spins in, two spins out” was therefore found to correspond to the ice rules, and the nearest neighbour  $\langle 111 \rangle$  Ising ferromagnet was mapped directly onto the Pauling ice model. Hence it was christened the “spin ice” model<sup>4</sup>. This model not only provided a natural explanation of the unexpected absence of magnetic order in ferromagnetic  $\text{Ho}_2\text{Ti}_2\text{O}_7$ , but also gave a good description of its detailed magnetic properties. In particular, it was demon-

strated in Ref. [4] that numerical simulations of the model were consistent with both the bulk magnetization measurements and the zero field diffuse neutron scattering arising from the disordered spin structure. Furthermore, the field-induced ordering patterns matched well with the predictions of the model. At  $T \sim 0.3$  K, the zero field magnetic state of  $\text{Ho}_2\text{Ti}_2\text{O}_7$  was thus established to approximate an ice-rules state, and the implication was that it should have the Pauling zero point entropy<sup>4</sup>.

#### *7.2.4.2. Identification of Spin Ice Materials*

Following the initial proposal of spin ice in  $\text{Ho}_2\text{Ti}_2\text{O}_7$ <sup>4</sup>, it was suggested<sup>38</sup>, on the basis of similar magnetization properties, that  $\text{Dy}_2\text{Ti}_2\text{O}_7$  and  $\text{Yb}_2\text{Ti}_2\text{O}_7$  were also spin ices. This prediction was later born out for the Dy material<sup>22</sup> but not for the Yb material<sup>40,41</sup>. An early, and important experimental result was the direct measurement of the predicted zero point entropy in  $\text{Dy}_2\text{Ti}_2\text{O}_7$  by Ramirez and co-workers<sup>22</sup>, discussed further in Section 7.3.1.1. Some confusion subsequently arose from the suggestion<sup>36,39</sup> that  $\text{Ho}_2\text{Ti}_2\text{O}_7$  may have a partially ordered ground state and may not be spin ice. This idea arose as a theoretical interpretation of a Schottky-like increase of the heat capacity below 0.6 K. It implied that the neutron scattering experiments of Ref. [4], that had ruled out such a state, were in error. However, later neutron measurements<sup>42,43</sup> confirmed the correctness of Ref. [4] and again ruled out the ordered spin structure proposed in Ref. [36] below 0.6 K. In fact the low temperature specific heat rise had previously been observed in isostructural  $\text{Ho}_2\text{GaSbO}_7$  and attributed to the freezing out of the nuclear spins<sup>44</sup>. Analysis of the specific heat with subtraction of the nuclear contribution<sup>42,45,46</sup> finally established the Pauling entropy for  $\text{Ho}_2\text{Ti}_2\text{O}_7$  (see Section 7.3.1.1). It is now clear from the combination of bulk and microscopic measurements discussed in this review, that both  $\text{Ho}_2\text{Ti}_2\text{O}_7$  and  $\text{Dy}_2\text{Ti}_2\text{O}_7$  as well as  $\text{Ho}_2\text{Sn}_2\text{O}_7$ <sup>47</sup> are spin ice materials with the Pauling zero point entropy, and that their similarities are much greater than their differences. The principal difference in fact relates to the hyperfine effect, which is much stronger in the Ho materials than in the Dy materials (see next section). Other possible realizations of spin ice are mentioned in Section 7.6.

#### *7.2.4.3. Basic Properties of the Spin Ice Materials*

The spin ice titanates or stannates can be prepared as high quality powder samples by ceramic techniques<sup>48,49</sup>. The titanates, but not the stannates,

can also be prepared as large single crystals either by flux methods<sup>50</sup> or by the floating zone technique<sup>51,52</sup>. The flux grown crystals have an octahedral habit, typically slightly flattened along [111], while the higher quality crystals are of a translucent brown to amber colour.

The spin ice materials adopt the cubic pyrochlore structure, space group Fd $\bar{3}$ m. This structure has the rare earth ion on the 16d site, Fig. 7.1, Ti or Sn on 16c (forming another pyrochlore lattice), an oxygen on 48f and another on 8b. The cubic lattice parameter is about 10.1 Å for Ho<sub>2</sub>Ti<sub>2</sub>O<sub>7</sub> and Dy<sub>2</sub>Ti<sub>2</sub>O<sub>7</sub> and about 10.4 Å for Ho<sub>2</sub>Sn<sub>2</sub>O<sub>7</sub>. For the latter compound the x parameter for the 48f site is 0.3368(5)<sup>47</sup>. The point symmetry at the rare earth site is defined by the local trigonal axis, a member of the ⟨111⟩ cubic direction set, that connects the centre of the elementary tetrahedron with its vertex. An 8b oxygen lies at the centre of each tetrahedron. The rare earth is coordinated by two such oxygen ions that lie along the trigonal axis. The coordination shell is then completed by six more oxygens at a slightly greater distance from the central ion that form a puckered hexagon with its rotation axis along the local trigonal axis.

The crystal fields of the spin ice materials have been considered in various works<sup>4,39,44,53,54,55,56,57</sup>. A detailed neutron scattering investigation by Rosenkranz *et al.* established the energy level scheme for Ho<sup>3+</sup> in Ho<sub>2</sub>Ti<sub>2</sub>O<sub>7</sub> (see Fig. 7.3<sup>39</sup>). Most authors agree that the ground state of Ho<sup>3+</sup> in Ho<sub>2</sub>Ti<sub>2</sub>O<sub>7</sub> is an almost pure |±8⟩ doublet and that of Dy<sup>3+</sup> in Dy<sub>2</sub>Ti<sub>2</sub>O<sub>7</sub> is an almost pure |±15/2⟩ Kramers doublet. However, the crystal field symmetry allows admixture of some other |J, M<sub>J</sub>⟩ states (with M<sub>J</sub> ≠ J) into the ground state doublet. Estimates of the degree of admixture differ. Ref. [55] reports, on the basis of fitting low field susceptibility curves between 77 K and 300 K, that the ground state doublet of Ho<sup>3+</sup> in Ho<sub>2</sub>Ti<sub>2</sub>O<sub>7</sub> includes 12 % of other states. However, the crystal field parameters derived in Ref. [55] deviate substantially from those found by Rosenkranz *et al.* using inelastic neutron scattering techniques<sup>39</sup>, which suggest a smaller admixture and should probably be considered to be the more accurate results. There is no available neutron scattering study of Dy<sub>2</sub>Ti<sub>2</sub>O<sub>7</sub>, but magnetization studies<sup>54</sup> find evidence of a slightly lower magnetic moment than expected for pure |±15/2⟩. Rosenkranz *et al.*<sup>39</sup> and Qiu<sup>57</sup> have estimated the crystal field scheme for Dy<sub>2</sub>Ti<sub>2</sub>O<sub>7</sub> using the crystal field parameters of Ho<sub>2</sub>Ti<sub>2</sub>O<sub>7</sub> with a correction for the different radial integrals of Dy<sup>3+</sup><sup>57</sup>. This approach finds that the ground state doublet is 99% |±15/2⟩. In all the spin ice materials, the first excited crystal field levels are the order of 300 K above the ground state. At elevated temperatures Ho<sub>2</sub>Ti<sub>2</sub>O<sub>7</sub> and Dy<sub>2</sub>Ti<sub>2</sub>O<sub>7</sub> show significant

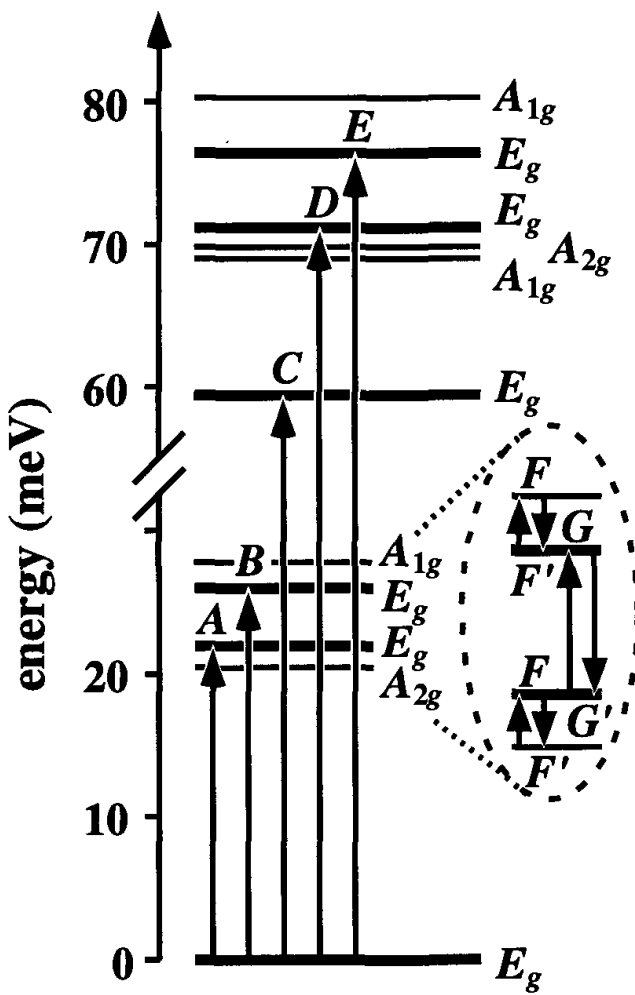


Fig. 7.3.  $\text{Ho}_2\text{Ti}_2\text{O}_7$ : Single ion energy level scheme (from Ref. [39]). The arrows indicate transitions observed by neutron scattering.

magnetostriiction<sup>53</sup> and quite large dielectric constants. However, there is no evidence of anomalous effects at the low temperatures where spin ice behaviour occurs. The dielectric properties have been studied in detail by Mamsurova *et al.*<sup>58</sup>, who conclude that anomalies observed at  $\sim 40$  K and  $\sim 80$  K are associated with defects: it seems likely that samples prepared at high temperature are slightly oxygen-deficient and contain a small amount ( $\sim 0.25\%$ ) of magnetic  $\text{Ti}^{3+}$  or  $\text{Ti}^{2+}$ . Once again these do not seem to significantly affect the low temperature properties.

Natural Dy has a mixture of isotopes while Ho is a single isotope  $^{165}\text{Ho}$ . Nuclear-electronic hyperfine coupling is particularly strong in the Ho materials ( $\sim 0.35$ ) K<sup>42,44,56</sup>, but very small ( $< 50$  mK) in  $\text{Dy}_2\text{Ti}_2\text{O}_7$ , as

evidenced by an absence of a contribution to the heat capacity<sup>22</sup>. The specific heat behaviour of the spin ice materials is discussed further in Section 7.3.1.1. That of Dy<sub>2</sub>Ti<sub>2</sub>O<sub>7</sub> was previously considered in Refs. [44,59]; it is interesting to note that Blöte *et al.*<sup>44</sup> noted a shortfall in entropy, now understood to result from the macroscopic degeneracy of the spin ice state.

Basic magnetic characterisation of powder samples of the spin ice materials is described in Refs. [44,54,60,61,62,63]. The magnetic susceptibility in general shows a very small Curie-Weiss temperature, which must be carefully corrected for the strong demagnetizing factor: for a spherical or powder sample this correction amounts to adding 1.4 K to the value estimated from the raw data. Note that some experimental reports do not make this important correction. Accurate estimates on single crystal samples of the corrected values are  $\theta_{\text{CW}} = 1.9$  K for Ho<sub>2</sub>Ti<sub>2</sub>O<sub>7</sub><sup>4</sup> and 1.2 K for Dy<sub>2</sub>Ti<sub>2</sub>O<sub>7</sub><sup>54,64</sup>. The value 1.8 K for Ho<sub>2</sub>Sn<sub>2</sub>O<sub>7</sub><sup>65</sup> has been estimated from measurements on a powder sample. The dipolar interaction alone, assuming a full classical moment, would yield  $\sim 3$ K, so the shortfall has been ascribed to antiferromagnetic superexchange coupling<sup>37</sup>. Assuming that this hypothesis is correct (there may be other possible reasons for the shortfall including lower than expected magnetic moments), one can obtain a self consistent description of the mean magnetic coupling energy in the spin ice materials. For example, the antiferromagnetic superexchange can alternatively be estimated by specific heat methods, as described in Section 7.3.1.1.

## 7.2.5. Spin Ice as a Frustrated Magnet

### 7.2.5.1. Frustration and Underconstraining

The macroscopically degenerate ground states that are characteristic of frustrated systems can be understood in terms of underconstraining arguments<sup>66</sup>. That is, in terms of the difference between the number of constraints necessary to determine a ground state and the number of degrees of freedom that the system possesses. In an unfrustrated system, the two differ by a microscopic number at most. For example, in a classical ferromagnet, fixing the two independent directions of the first spin,  $S_1^x, S_1^y$ , the ground state configuration is satisfied only by satisfying the  $2(N - 1)$  microscopic constraints  $S_i^x = S_1^x, S_i^y = S_1^y$ . Once satisfied, the ground state is uniquely defined. For discrete systems, enumeration of the degeneracy can be cast in a similar language. For example, for Anderson's Ising pyrochlore antiferromagnet, the ground state condition is undercon-

strained, demanding only that the total magnetization of the four Ising spins on each tetrahedron be zero. Six of the  $2^4 = 16$  possible spin configurations satisfy this condition. Counting  $2^4$  configurations for each tetrahedron gives, for a system of  $N$  spins and  $N/2$  tetrahedra, a total number of microstates,  $\tilde{\Omega}_T = 2^{2N}$ , which greatly overestimates the exact total,  $\Omega_T = 2^N$ . This is because the spins are shared between two tetrahedra, so that the configurations on each tetrahedron are not independent. Following a Pauling-like argument; allocating  $2^2 = 4$  states per tetrahedron and assuming that  $6/16$  of them satisfy the constraint, leads to a ground state degeneracy  $\Omega_0 = \{2^2(6/16)\}^{N/2} = (3/2)^{N/2}$ . The corresponding entropy  $S_0 = k_B \ln(\Omega_0) = (Nk_B/2) \ln(3/2)$  is of course just Pauling's original result. In the mapping from ice to Anderson's antiferromagnet, or alternatively to spin ice,  $N$  oxygen ions lead to  $2N$  spins and we recover the Pauling entropy.

The macroscopic degeneracy can therefore be expressed in terms of the number of unconstrained degrees of freedom, or in the case of discrete symmetry, in terms of a local, unconstrained phase space. These Pauling type arguments that neglect collective constraints coming, for example, from closed loops in the lattice, give an upper bound to the ground state entropy. For corner sharing, or tetrahedral systems, as has been shown both experimentally and numerically, this upper bound is an excellent approximation to the true ground state entropy. A more detailed discussion, applied to continuous spin systems can be found in Ref. [66].

#### 7.2.5.2. $\langle 111 \rangle$ Pyrochlore Models

As discussed above, the pyrochlore structure is remarkable in that its "natural" magnetic Ising variables (i.e. those consistent with point symmetry) are fully frustrated only when the near neighbour interactions are *ferromagnetic*. With antiferromagnetic coupling these variables remain unfrustrated by the interaction and the system orders magnetically. This situation is the opposite to the case of the Heisenberg model on the pyrochlore lattice, where the antiferromagnet is highly frustrated and the ferromagnet is not<sup>5,27,66</sup>.

The contrasting behaviour of the Ising and Heisenberg models makes it interesting to inquire as to the behaviour of the "intermediate" case of continuous spins, with local easy-axis (Ising-like) anisotropy. The case of ferromagnetic coupling has been discussed in Ref. [67]. The macroscopic spin ice degeneracy is found to be lifted in favour of a particular state

with  $q = 0$  long range order, where  $q$  is the reciprocal lattice vector of the underlying Bravais lattice. Relaxing the spins continuously away from the  $\langle 111 \rangle$  crystal field directions one gains exchange energy at the cost of crystal field energy. As the gain goes linearly with the relaxation, while the loss goes quadratically the modified minimum energy states are distorted away from the  $q = 0$  spin ice state. This maximizes the energy gain and hence the distorted state becomes the unique ground state. This model is discussed further in Section 7.4.1.1.

In the case of easy axis crystal fields and antiferromagnetic coupling, the system has the ordered ground state of the  $\langle 111 \rangle$  Ising model, the so called  $\text{FeF}_3$  (“all in – all out”) structure, observed experimentally in this material<sup>68,69</sup>. This state has global two-fold symmetry and for strong crystal fields there is a second order Ising-like phase transition<sup>27</sup>. For weaker fields there is a first order phase transition. This is separated from the second order transition by a tri-critical point with critical exponents that differ from those of the three dimensional Ising model<sup>70</sup>.

One can also consider the case of easy-plane or XY spins, i.e. spins that lie in the planes perpendicular to the local  $\langle 111 \rangle$  trigonal axes<sup>71,72,73</sup>. This case is closer to the Hesienberg model in that the antiferromagnet has a highly degenerate ground state. However, the ground state entropy is sub-extensive and there is a fluctuation driven, or “order by disorder”<sup>23</sup> transition to a long range ordered state, observed in the material  $\text{Er}_2\text{Ti}_2\text{O}_7$ <sup>71,72</sup>. With ferromagnetic coupling one finds a transition to an ordered ferromagnetic state with canted spins<sup>73</sup>.

### 7.3. Properties of the Zero Field Spin Ice State

#### 7.3.1. Experimental Properties

##### 7.3.1.1. Heat Capacity: Zero Point Entropy

The key thermodynamic characteristic of the spin ice state is its nonzero Pauling entropy,  $S_0$ , with  $S_0 \approx (Nk_B/2) \ln(\frac{3}{2})^1$ . Ramirez and co-workers<sup>22</sup> directly investigated this property via experimental measurements of the heat capacity of  $\text{Dy}_2\text{Ti}_2\text{O}_7$ .

The experimental procedure used in Ref. [22] closely followed the one used by Giauque in 1935 in his determination of the residual entropy of water ice<sup>13</sup>. At temperatures below 10 K, the specific heat contribution from phonons in  $\text{Dy}_2\text{Ti}_2\text{O}_7$  is sufficiently small to allow one to measure the magnetic contribution that develops as the paramagnetic regime  $T < \theta_{\text{CW}}$  is entered upon cooling. The top panel of Fig. 7.4 shows the magnetic

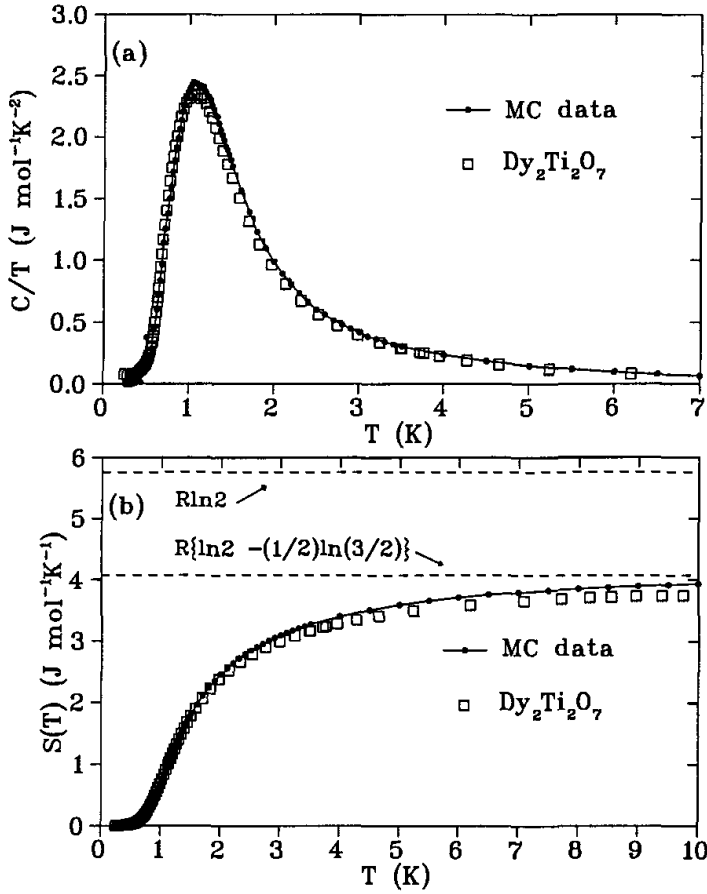


Fig. 7.4.  $\text{Dy}_2\text{Ti}_2\text{O}_7$ : (a) Specific heat and (b) entropy versus temperature, measured by Ramirez *et al.* (Ref. [22]). This quantity corresponds to  $\delta S$  of equation 1 and shows evidence of the Pauling zero point entropy. The data are compared to that calculated by Monte Carlo simulations of the dipolar spin ice model (Ref. [37]) with exchange  $J_{nn} = -1.24$  K and dipolar coupling  $D_{nn} = 2.35$  K (see Section 7.3.2).

specific heat of  $\text{Dy}_2\text{Ti}_2\text{O}_7$  from a temperature  $T = 7$  K down to 300 mK. One observes a rise of the specific heat upon cooling with a broad maximum around  $T_{\text{peak}} \sim 1.2$  K. This growth of the specific heat indicates the build-up of magnetic correlations and removal of magnetic entropy as the system is cooled. The broad maximum and the absence of a sharp feature in  $C_H(T)$  is a strong indication that the system does not develop long range magnetic order via a thermodynamic phase transition. The magnetic specific heat drops rapidly below  $T_{\text{peak}}$ , essentially vanishing below  $T_{\text{min}} \sim 400$  mK. This indicates that the spins freeze as the temperature is lowered below  $T_{\text{peak}}$  and that all thermal spin fluctuations have ceased below  $T_{\text{min}}$ . The entropy removed from the system upon cooling can be determined from the

heat capacity measurements using the thermodynamic relationship

$$\delta S \equiv S(T_2) - S(T_1) = \int_{T_1}^{T_2} \frac{C_H(T)}{T} dT \quad (1)$$

where  $\delta S$  is the entropy difference between temperatures  $T_2$  and  $T_1$ . Since there are two possible spin orientations per degree of freedom, the molar spin entropy in the high temperature paramagnetic regime ( $T \gg \theta_{\text{CW}}$ ) is  $R \ln(2)$  ( $R$  is the molar gas constant,  $R = 8.3145 \text{ J mol}^{-1} \text{ K}^{-1}$ ). The bottom panel of Fig. 7.4, taken from Ref. [22], shows the temperature dependence of  $\delta S$  as  $T$  is increased from 400 mK to 10K. The lower panel of Fig. 7.4 shows that the entropy recovered upon warming the system is about  $3.9 \text{ J mol}^{-1} \text{ K}^{-1}$ , a value that is considerably less than the value  $R \ln(2) \approx 5.76 \text{ J mol}^{-1} \text{ K}^{-1}$ . The difference,  $1.86 \text{ J mol}^{-1} \text{ K}^{-1}$ , is close to the Pauling estimate for the ground state entropy associated with the extensive ground state degeneracy of spin ice:  $S_0 = (R/2) \ln(3/2) = 1.68 \text{ mol}^{-1} \text{ K}^{-1}$ , which includes a factor of 2 to account for the mapping the mapping of 1 mole of ice onto 2 moles of spin ice (see Section 7.2.5.1). This result is consistent with the interpretation that the state reached upon cooling from the paramagnetic phase down to  $T \sim 400 \text{ mK}$  in  $\text{Dy}_2\text{Ti}_2\text{O}_7$  carries extensive entropy close to  $S_0$  and obeys the ice rules.

The experiment of Ramirez *et al.*, apart from the cryogenics involved, is thus somewhat simpler than the original experiment on ice: given the separation of energy scales between the effective coupling,  $\sim O(1) \text{ K}$ , and the crystal field strength,  $\sim O(100) \text{ K}$ , one can assume, to a good approximation, that at  $\sim O(10) \text{ K}$ , there are uncorrelated Ising degrees of freedom, with molar entropy  $S = R \ln(2)$ . Unlike water ice, the spin ice state is reached from the high temperature uncorrelated phase without passing through gas-liquid or liquid-solid transitions. Furthermore, spin ice offers a second test of the zero point entropy, unavailable in water ice: the application of a magnetic field to restore long range order. For example, a field applied along the [100] direction lifts the degeneracy in favour of a non-collinear ferromagnetic state <sup>38</sup>. Repeating the experiment in a field, one would therefore expect to recuperate the missing entropy. Despite performing the experiment on a powder sample of  $\text{Dy}_2\text{Ti}_2\text{O}_7$  and of the loss of ergodicity at low temperature (which one might now expect to hinder the process of the selection of a unique state) this change in behaviour was qualitatively confirmed <sup>22</sup>.

A demonstration, via heat capacity measurements, that the low temperature disordered state attained by  $\text{Ho}_2\text{Ti}_2\text{O}_7$ <sup>4</sup> indeed has zero point

entropy, proved to be less straightforward than for  $Dy_2Ti_2O_7$ <sup>45</sup>, causing some confusion as to the true nature of the low temperature state attained<sup>36,74</sup>. The temperature dependence of  $C_H(T)$  for  $Ho_2Ti_2O_7$  (Fig. 7.5) is significantly different from that of  $Dy_2Ti_2O_7$  (Fig. 7.4). Firstly, there is

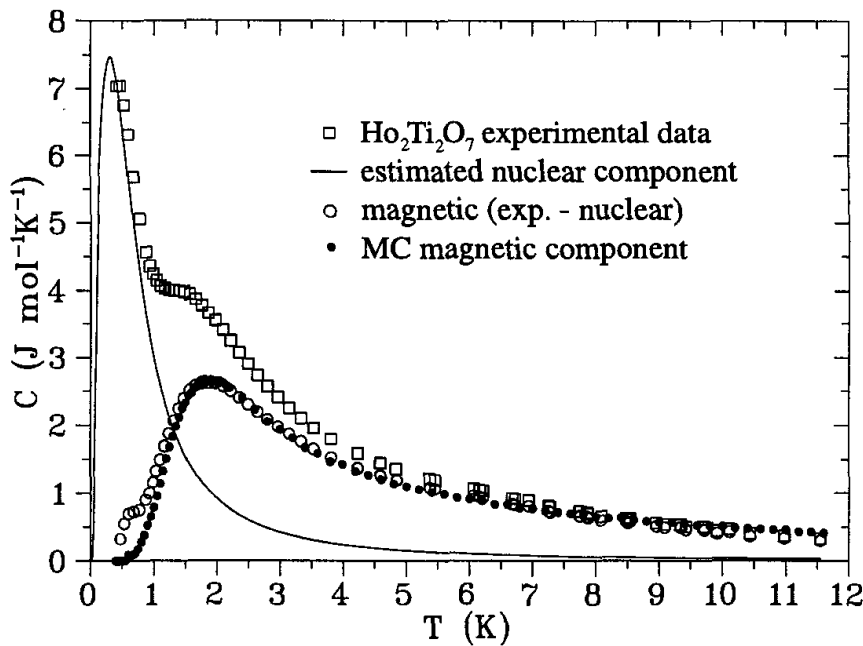


Fig. 7.5.  $Ho_2Ti_2O_7$ : The total specific heat is shown by the empty squares and the expected nuclear contribution by the solid line. The electronic contribution has been estimated by subtracting these two curves (open circles). Near to 0.7 K this subtraction is prone to a large error (see text). Dipolar spin ice simulation results are indicated by the filled circles (from Ref. [42]).

no broad maximum, and at a temperature close to  $T \sim 0.6$  K, the specific heat rises, followed by a sudden freezing-out and loss of thermal equilibrium<sup>36</sup>. The behaviour of  $Ho_2Ti_2O_7$  was interpreted by some authors as an indication for some kind of partial ordering transition, rather than spin ice behaviour<sup>36,74</sup>. However, the holmium ion is somewhat atypical in that it possesses a particularly large hyperfine coupling between the nuclear spins and electronic spins. The importance of this term had previously been commented by Blöte *et al.* in earlier heat capacity measurements on isostructural  $Ho_2GaSbO_7$ <sup>44</sup>. In fact,  $Ho^{3+}$  materials commonly have large nuclear-electronic coupling<sup>75,76</sup>; for example, this has proved to be of importance in the quantitative calculation of the transverse field versus temperature phase diagram in the dipolar Ising ferromagnet  $LiHoF_4$ <sup>77</sup>. The hyperfine interaction leads to a Shottky nuclear specific heat anomaly at  $T_{nuc}$ . To isolate the

electronic component from the low temperature  $C_H(T)$  in  $\text{Ho}_2\text{Ti}_2\text{O}_7$ , one therefore has to first remove the nuclear contribution<sup>45</sup> (see also<sup>55</sup>). In a different study<sup>42</sup>, the specific heat of  $\text{Ho}_2\text{Ti}_2\text{O}_7$  was measured on a single crystal rather than a powder sample, making thermal equilibration easier at low temperature<sup>36</sup>. The low temperature magnetic specific heat (with phonon contribution subtracted) of a  $\text{Ho}_2\text{Ti}_2\text{O}_7$  single crystal is shown by the open squares in Fig. 7.5. One can discern a shoulder in the data around a temperature of  $T_{\text{cr}} \approx 1.5$  K. This shoulder is indicative of a change of regime in the nature of the thermal excitations from  $T > T_{\text{cr}}$  to  $T < T_{\text{cr}}$ . The nuclear hyperfine contribution, which can be estimated from measurements on  $\text{Ho}_2\text{GaSbO}_7$ <sup>44</sup>, is shown by the solid line. Subtracting this from the above data gives an estimate for the electronic contribution. This is shown by the open circles in Fig 7.5, which now bears a strong resemblance to the  $C_H(T)$  data above for  $\text{Dy}_2\text{Ti}_2\text{O}_7$  in Fig. 7.4a. One can see a kink in the subtracted data around a temperature of 600 mK. The kink has been argued to be an artifact of the data manipulation (i.e. subtraction of estimated hyperfine contribution to the specific heat) and not an indication of any real rapid change in the electronic spin configuration. This conclusion is supported by neutron scattering results at 50 mK, which show no sign of the spin-spin correlations building up above those found in Monte Carlo simulations<sup>42</sup>. The temperature integration of the electronic contribution of  $C_H(T)$  for  $\text{Ho}_2\text{Ti}_2\text{O}_7$  in Fig. 7.6 shows convincingly a residual entropy close to the Pauling value ( $S_0$ )<sup>46</sup>. Similarly, the zero point entropy is released by the application of a magnetic field of 1 T. These results confirm that the low temperature disordered magnetic state of  $\text{Ho}_2\text{Ti}_2\text{O}_7$  is indeed a spin ice state, just as in the case of  $\text{Dy}_2\text{Ti}_2\text{O}_7$ .

### 7.3.1.2. Low Field Magnetic Susceptibility: Spin Freezing

The first magnetization study of the spin ice regime was performed by Matsuhira *et al.* on polycrystalline samples of  $\text{Ho}_2\text{Sn}_2\text{O}_7$  and  $\text{Ho}_2\text{Ti}_2\text{O}_7$  at temperatures down to  $T = 100$  mK<sup>65</sup>. Below the spin ice freezing temperature of  $\text{Ho}_2\text{Sn}_2\text{O}_7$  there is a very pronounced divergence between the field cooled (FC) and zero field cooled (ZFC) magnetization (see Fig. 7.7). In the history dependent regime there is strong magnetic hysteresis (Fig. 7.7) and a remanent moment can be frozen into the sample. This remanence had previously been observed on single crystalline  $\text{Ho}_2\text{Ti}_2\text{O}_7$  using  $\mu\text{SR}$ <sup>32</sup> and neutron scattering<sup>4</sup>. It is clear from these studies that the spin ice state is frozen, at least as far as major magnetic reorientations are

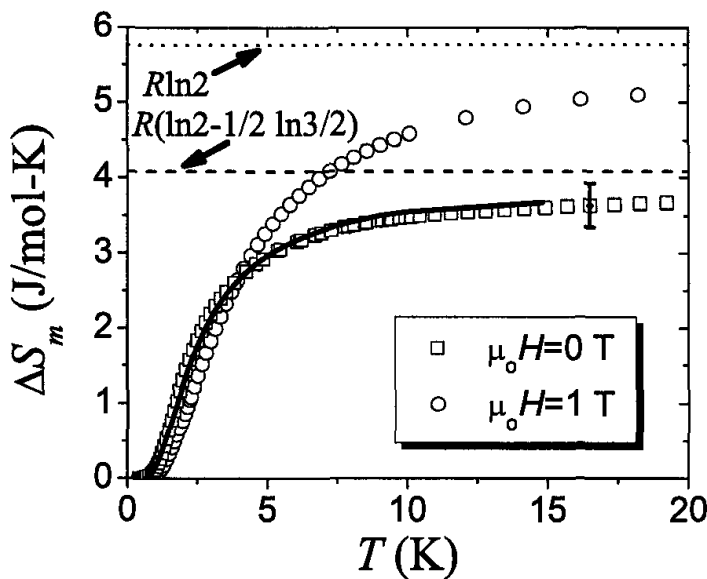


Fig. 7.6.  $\text{Ho}_2\text{Ti}_2\text{O}_7$ : magnetic entropy versus temperature (from Ref. [46]), showing the existence of a Pauling zero point entropy and its removal by an applied field. The solid line is the prediction of the near-neighbour spin ice model of Ref. [5].

concerned (however, see Section 7.5). Very recently, low temperature hysteresis curves have been reported for powder samples of  $\text{Dy}_2\text{Ti}_2\text{O}_7$ , again confirming the frozen nature of the spin ice state<sup>78</sup>. It should be noted, as discussed below in Section 7.5, that the static frozen nature of spin ice is firmly established only as regards major reorientations of the magnetization: there is evidence that some local spin dynamics persists to the lowest measured temperatures<sup>79,80</sup>.

### 7.3.1.3. Spin Arrangement Observed by Neutron Scattering

The neutron scattering from all the spin ice materials is, at low temperatures, within the energy resolution of most conventional neutron spectrometers (but see Section 7.5.3.2). The measured scattering patterns therefore measure the static spin correlations. Zero field neutron scattering<sup>4,42,43</sup> on  $\text{Ho}_2\text{Ti}_2\text{O}_7$  in the millikelvin range reveals broad diffuse features. In the  $hh\ell$  plane of reciprocal space these are centered around  $(001)$ ,  $(003)$ ,  $(110)$  and  $(3/2, 3/2, 3/2)$  (see Fig. 7.8). These features are predicted qualitatively by the near neighbour spin ice model<sup>4</sup>, but there are clear differences of detail, particularly as regards the shape of the features. A very recently reported study of  $\text{Dy}_2\text{Ti}_2\text{O}_7$ <sup>81</sup> has similarly confirmed the qualitative relevance of the near neighbour model, but again differences in detail. For a description

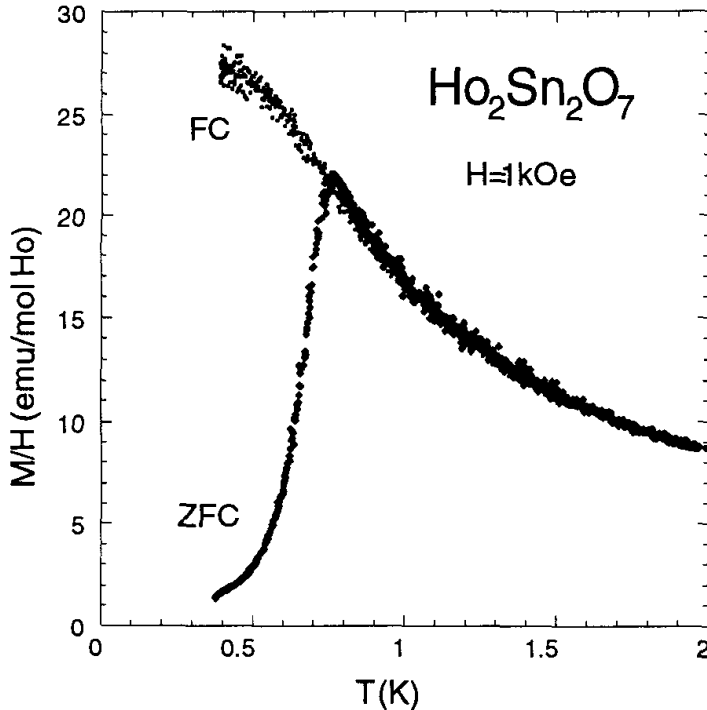


Fig. 7.7.  $\text{Ho}_2\text{Sn}_2\text{O}_7$ : magnetization versus temperature for a polycrystalline sample, showing a pronounced splitting between field-cooled (FC) and zero field cooled (ZFC) data (Ref. [65]).

of these differences one must turn to the dipolar spin ice model discussed in Section 7.3.2.  $\text{Ho}_2\text{Sn}_2\text{O}_7$  has only been studied as a powder, but again the necessity of considering the dipolar interaction is evident<sup>47</sup>.

### 7.3.2. Microscopic Theories and Experimental Tests

#### 7.3.2.1. Near-Neighbour Spin Ice Model: Successes and Failures

From the above discussion, we have seen that the near neighbour model<sup>4,5</sup>, when applied to  $\text{Ho}_2\text{Ti}_2\text{O}_7$ ,  $\text{Dy}_2\text{Ti}_2\text{O}_7$  and  $\text{Ho}_2\text{Sn}_2\text{O}_7$ , correctly predicts the existence of the spin ice state, its frozen nature and the existence and magnitude of its zero point entropy. Considering the low-field experiments, bulk measurements do not demand a higher level theory. However, the need arises when one considers the neutron scattering experiments of Fig. 7.8, for example. Similarly, we shall see later that the near neighbour model qualitatively captures the behaviour of spin ice in an applied field remarkably well, but for a detailed quantitative understanding a more accurate magnetic Hamiltonian is required. The main improvement that has been studied to date is the inclusion of the full dipolar interaction between two

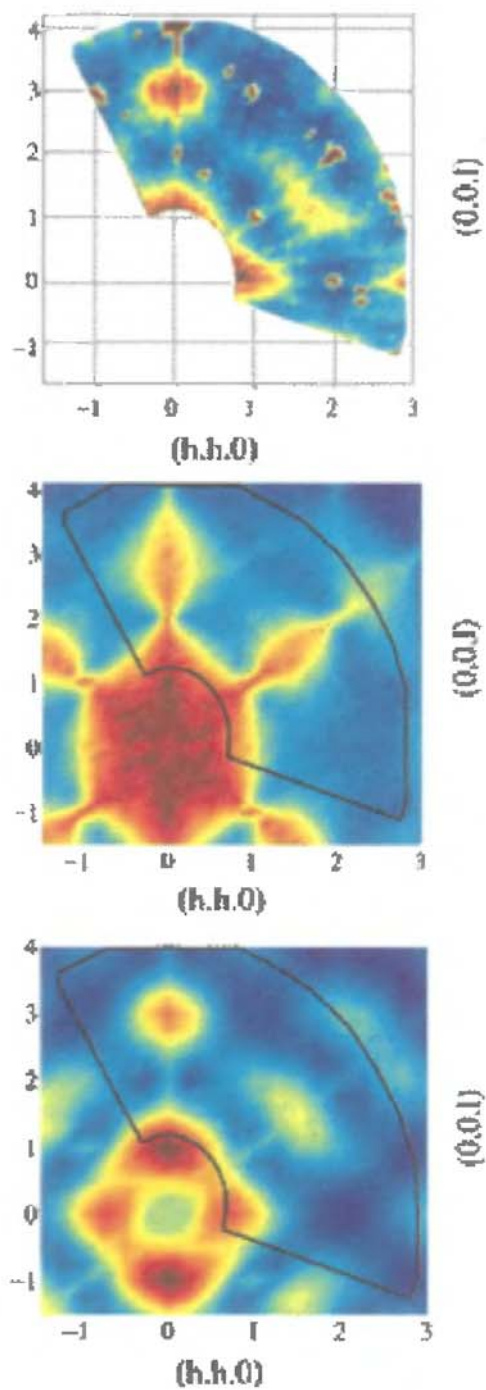


**Fig. 7.8.**  $\text{Ho}_2\text{Ti}_2\text{O}_7$ : Neutron scattering in the  $hh\bar{l}$  plane showing experimental data (upper panel; the sharp spots are nuclear Bragg scattering with no magnetic component), compared with Monte Carlo simulations of the near neighbour spin ice model (middle panel) and dipolar model (lower panel) (Ref. [42]). Blue indicates the weakest and red-brown the strongest intensity.

idealised magnetic moments, with the addition of a phenomenological near neighbour exchange term. This model was first suggested by Siddharthan *et al.*<sup>36</sup> and has become known as the “dipolar spin ice model”. It is to this model that we now turn.

### 7.3.2.2. The Problem of Treating the Dipolar Interaction

Consider the simple theoretical model of  $\langle 111 \rangle$  Ising spins interacting via nearest neighbour ferromagnetic exchange. We emphasized above how the simplicity of this model gives rise to Bernal-Fowler ice-rules for the Ising spins. This leads to underconstrained conditions for the minimum energy states, which consequently results in a macroscopic ground state degeneracy. As discussed above, the experimental evidence for spin ice behaviour has so far been established in rare-earth compounds which possess ideal Ising-like spins with large magnetic moments of approximately  $\mu \approx 10\mu_B$ . These interact via long range dipole-dipole interactions. The strength of the dipole-dipole energy,  $D$ , for nearest-neighbour spins can be estimated using the formula

$$D = \frac{\mu_0}{4\pi} \frac{\mu^2}{r_{nn}^3} \quad (2)$$

where  $r_{nn}$  is the nearest-neighbour distance. Taking  $r_{nn} = (a/4)\sqrt{2}$ , where  $a \sim 10\text{\AA}$  is the size of the conventional cubic unit cell, we get  $D \sim 1.4$  K. The Curie-Weiss temperature,  $\theta_{CW}$ , as determined via magnetic susceptibility measurements, is a measure of the overall magnetic energy scale in a system. In view of the experimental fact that  $\theta_{CW}$  in the spin ice materials is the order of  $\sim 10^0$  K, the dipolar interactions are therefore a sizeable contribution to the overall energy scale. The Hamiltonian for magnetic dipole-dipole interactions,  $H_{dd}$  is:

$$H_{dd} = Dr_{nn}^3 \sum_{i>j} \frac{\mathbf{S}_i^{\hat{z}_i} \cdot \mathbf{S}_j^{\hat{z}_j}}{|\mathbf{r}_{ij}|^3} - \frac{3(\mathbf{S}_i^{\hat{z}_i} \cdot \mathbf{r}_{ij})(\mathbf{S}_j^{\hat{z}_j} \cdot \mathbf{r}_{ij})}{|\mathbf{r}_{ij}|^5}, \quad (3)$$

where  $\mathbf{S}_i = S_i \hat{z}_i$  are three-component classical spin vectors of unit length  $|\mathbf{S}_i| = 1$  pointing along the local trigonal  $\langle 111 \rangle$  axes with  $\mu_i = \mu \mathbf{S}_i$ . The size of the magnetic moment,  $\mu$ , is absorbed in the definition of  $D$  which sets the energy scale for the dipolar interactions. In general, one expects that in magnetic rare-earth insulators there exist exchange interactions as well as magnetic dipolar interactions. A suitable starting point is therefore the Hamiltonian,  $H$ , where both long range dipolar interactions and nearest

neighbour exchange with exchange constant,  $J$ , are considered:

$$H = -J \sum_{\langle ij \rangle} \mathbf{S}_i^{\hat{z}_i} \cdot \mathbf{S}_j^{\hat{z}_j} + D r_{nn}^3 \sum_{i>j} \frac{\mathbf{S}_i^{\hat{z}_i} \cdot \mathbf{S}_j^{\hat{z}_j}}{|\mathbf{r}_{ij}|^3} - \frac{3(\mathbf{S}_i^{\hat{z}_i} \cdot \mathbf{r}_{ij})(\mathbf{S}_j^{\hat{z}_j} \cdot \mathbf{r}_{ij})}{|\mathbf{r}_{ij}|^5}. \quad (4)$$

The Hamiltonian  $H$  is presumably more realistic and relevant to real rare-earth materials than the nearest-neighbour spin Hamiltonian defined in Ref. [4], so the first question to understand is under what circumstances, if any, it allows for spin ice behaviour, as signaled by a zero point entropy.

First consider the contribution to  $H$  coming from first nearest neighbour spins. For nearest neighbour  $\langle 111 \rangle$  Ising spins  $\mathbf{S}_i$  on the pyrochlore lattice,  $\mathbf{S}_i \cdot \mathbf{S}_j = (-1/3)\sigma_i\sigma_j$  and  $(\mathbf{S}_i \cdot \mathbf{r}_{ij})(\mathbf{S}_j \cdot \mathbf{r}_{ij}) = -(2/3)\sigma_i\sigma_j$  for  $\mathbf{r}_{ij} = \mathbf{r}_{nn}$ , where we have now introduced Ising variables  $\sigma_i = \pm 1$  to represent the spin  $\mathbf{S}_i$  points along or antiparallel to the member of the  $\langle 111 \rangle$  set that defines the local point symmetry (see also <sup>27</sup>). Rewriting  $H$  in terms of  $\sigma_i$  and  $\sigma_j$  for the combined nearest-neighbour exchange and dipoles at nearest neighbour we have

$$H_{\text{eff}} = \sum_{\langle ij \rangle} J_{\text{eff}} \sigma_i \sigma_j \quad (5)$$

where  $J_{\text{eff}} \equiv J_{nn} + D_{nn}$ . The effective Ising nearest-neighbour exchange is  $J_{nn} \equiv J/3$  and the effective Ising nearest-neighbour dipole coupling is  $D_{nn} \equiv 5D/3$ , with  $D > 0$ .

To avoid confusion we briefly comment on the sign convention in Eqn. 5, as well as the definitions of  $J_{nn}$ ,  $D_{nn}$  and  $J_{\text{eff}}$ . Eqn. 5 is a mapping of the ferromagnetic spin ice Hamiltonian of Refs. [4,5] on to an antiferromagnetic Ising model (equivalent to Anderson's <sup>3</sup>). A mapping of this sort was discussed by Moessner <sup>27</sup>. In the case of Eqn. 5, the absence of the usual minus sign in front of Hamiltonian is intentional: it allows one to preserve the positive (ferromagnetic) sign of the interaction  $J_{\text{eff}}$ . Furthermore, elimination of the vector spins of the spin ice model and their replacement with global scalar Ising variables,  $\sigma_i$ , absorbs the full magnitude of the interaction energy into  $J_{\text{eff}}$ , allowing a transparent discussion of its magnitude (however, it should be noted that Eqn. 5 is of no utility when discussing field-induced states, where it is essential to preserve the vector nature of the spins).

From Eqn. 5 one can construct a very simple nearest-neighbour criterion for spin ice behaviour. For  $J_{\text{eff}} > 0$ , one has an effective antiferromagnetic nearest neighbour model for the  $\sigma_i$  variables which extensive degeneracy.

For  $J_{\text{eff}} < 0$ , i.e. for  $J$  antiferromagnetic and  $J < -5D$ , one has two unique ground states related by global symmetry that corresponds to all spins pointing in or out of a tetrahedral unit<sup>5,27,72</sup>. This corresponds to the magnetic structure of  $\text{FeF}_3$  alluded to above, and which orders at finite temperature<sup>37</sup>. This simple argument therefore predicts that materials with antiferromagnetic exchange  $J$  ( $J < 0$ ) should display spin ice behaviour provided  $J > -5D$ . For example, as we will discuss in more detail below,  $\text{Dy}_2\text{Ti}_2\text{O}_7$  has  $J \approx -3.72$  K,  $D \approx 1.41$  K ( $J_{\text{eff}} \approx 1.1$  K) while  $\text{Ho}_2\text{Ti}_2\text{O}_7$  has  $J \approx -1.65$  K,  $D \approx 1.41$  ( $J_{\text{eff}} \approx 1.8$  K), hence satisfying the nearest neighbour spin ice criterion,  $J_{\text{eff}} > 0$ . As discussed in the next section, the criterion  $J_{\text{eff}} = J/3 + 5D/3 > 0$  for spin ice behaviour is not exact when considering long range dipole-dipole interactions. In that case the condition for spin ice behaviour is  $J_{\text{nn}}/D_{\text{nn}} > -0.905$ , giving  $J_{\text{eff}}/D_{\text{nn}} > 0.095$ <sup>37</sup>.

Let us now return to the dipolar contribution ( $H_{\text{dd}}$  in Eqn. 3), and comment on two important properties of the magnetic dipolar interaction. Firstly, it is long ranged and the truncation at nearest-neighbour would seem to be a gross approximation. Indeed, the magnitude of the dipolar coupling decays very slowly as  $1/r_{ij}^3$  i.e. as the third power of the distance  $r_{ij} \equiv |\mathbf{r}_{ij}|$  separating two magnetic moments  $\mu_i$  and  $\mu_j$ . Secondly, dipolar interactions are strongly anisotropic: they depend on the relative orientation of the interacting moments with respect to the separation vector  $\mathbf{r}_{ij}$  via the  $\mu_i \cdot \mathbf{r}_{ij}$  terms in Eqn. 3. Dipolar couplings are complicated interactions because of the combination of these two features. In contrast, spin ice behaviour and extensive degeneracy is intimately tied to the existence of Bernal-Fowler ice-rules which themselves arise from the overwhelming simplicity of a nearest-neighbour model.

These considerations lead to a first and very interesting question regarding the origin of spin ice behaviour in dipole-coupled rare-earth materials: how is it that the seemingly “complicated” dipolar interactions allow for the emergence of ice rules and consequent extensive degeneracy? From a more technical perspective, one does generally expect that long range interactions beyond nearest-neighbour will combine with spin anisotropy to select a unique ordered ground state. For example, in the context of highly-frustrated antiferromagnets, it is known that exchange interactions beyond nearest-neighbour select a unique ground state in the classical Heisenberg antiferromagnet on the two-dimensional kagomé lattice<sup>82</sup>. Similarly, they typically select a unique ordering wave vector in classical Heisenberg pyrochlore antiferromagnets<sup>83</sup>. Of course, in all such cases, there exist combinations of the distance,  $r$ , dependent exchange,  $J(r)$ , where the classical

ground state selection is not complete<sup>82,83</sup>. However, this situation requires a fine-tuning of the  $J(r)$  that rarely occurs in real materials. It has been found that weak dipolar interactions in the pyrochlore lattice with antiferromagnetically coupled Heisenberg spins lead to a unique ordered ground state (apart from a finite number of discrete symmetry related states)<sup>84,85</sup>.

Having mentioned a number of examples where interactions beyond nearest-neighbour can give rise to ordered ground state selection, we return to the question of the distance dependence of the dipolar contribution to Hamiltonian Eqn. 4. For example, the second nearest neighbour distance is  $\sqrt{3}$  times larger than the nearest neighbour distance, and one then has a second nearest neighbour energy scale,  $D_{\text{nnn}} \sim 0.2D_{\text{nn}}$ . This implies an important perturbation compared to  $J_{\text{eff}} = J_{\text{nn}} + D_{\text{nn}}$ , especially in the context of antiferromagnetic (negative)  $J_{\text{nn}}$ , where  $J_{\text{eff}} < D_{\text{nn}}$ . Specifically, for  $\text{Dy}_2\text{Ti}_2\text{O}_7$ , the second nearest neighbour energy scale is a large proportion of the total energy. One would therefore naturally expect dipolar interactions beyond nearest neighbour to cause the different ice-rule states to have different energies. This would break the degeneracy of the spin ice manifold and cause long range order below a critical temperature  $T_N \sim O(D_{\text{nn}})$ . Thus, there arises the original puzzle posed by the spin ice materials that can be summarized by two questions:

- Is the experimental observation of spin ice behaviour consistent with dominant long range dipolar interactions?
- If so, then why is spin ice behaviour maintained in the presence of these interactions when one would expect them to lead to long range order below a temperature  $T_c$  of order  $D_{\text{nn}}$ ?

This issue was first investigated by Siddharthan and collaborators who used classical Monte Carlo simulations to investigate the thermodynamic properties of Hamiltonian  $H$ , Eqn. 4, with the dipolar interaction truncated at the fifth<sup>36</sup> and twelfth<sup>74</sup> nearest neighbour. We recall that at the nearest neighbour level, a positive  $J_{\text{eff}}$  gives rise to a two-in/two-out ground state on a single tetrahedron which results in a net magnetic moment for an isolated tetrahedron. It is therefore not obvious *a priori* that the long range part of the dipolar interactions in Hamiltonian 4 should not stabilize a ferromagnetic ground state. On the other hand, it is known from experiments that the spin ice state does not carry a net (bulk) magnetic moment at sufficiently large length scale. If the ground state of  $H$  is not ferromagnetic, the precise cancellation of the moment at large enough length scale is a delicate matter that arises from the large distance behaviour of

the dipolar interactions. Hence, precise handling of the long distance dependence is crucial and in such a situation, the dipolar interactions clearly need to be summed up to infinite distance. It is well known that dipole lattice summations are difficult to handle and are conditionally convergent. A standard technique to handle slowly convergent  $1/r^3$  dipolar interactions is the Ewald summation method<sup>86,87,88,89</sup>. This method has been successfully used to investigate the properties of dipolar fluids<sup>90,91</sup> as well as to understand the nature of critical phenomena in ferromagnets subject to long range magnetic dipole-dipole interactions<sup>92,93</sup>. Very roughly speaking, the Ewald summation method implements a mathematical construct that is akin to the Madelung construction used to calculate the electrostatic binding energy of ionic crystals. In the next section we describe the results obtained by Monte Carlo simulations of the dipolar spin ice Hamiltonian  $H$  (Eqn. 4) that uses the Ewald method.

### 7.3.2.3. The Ewald Monte Carlo

The reader is referred to Refs. [86,87,88,89] for a discussion of the Ewald method as implemented in a conventional Monte Carlo simulation. In essence, for a finite size cubic system of linear size  $L$  that contains  $L^3$  conventional pyrochlore cubic unit cells, hence  $16L^3$  spins, the Ewald summation method recasts the original direct real space dipole-dipole interaction in Eqn. 4 by an effective interaction where the image dipoles of those contained in the cell of size  $L$  are resummed to infinity. In this sense, the Ewald method enhances the tendency towards periodic long range order for “small”  $L$ . Once the Ewald interactions between Ising spins  $\sigma_i$  and  $\sigma_j$  that belong to the simulation cell have been calculated (and stored in a data structure), the Monte Carlo simulation proceeds using the conventional Metropolis algorithm.

To make quantitative contact with experimental results, one needs to know the numerical values of the parameters entering the Hamiltonian Eqn.4. Since the lattice structure is known from X-ray or neutron diffraction, the size  $a$  of the conventional cubic unit cell is known, and one knows the distance  $r_{ij}$  between spins. The only unknowns in Eqn. 4 are therefore the value of the nearest-neighbour exchange  $J$  and the magnitude of the magnetic moment  $\mu$ . For the rare-earth spin ice materials, the value of  $\mu$  is close to its maximum possible value given the Landé g-factor  $g_J$  and the total angular momentum quantum number  $J$  of the ion<sup>39</sup>. For example, for Dy<sup>3+</sup>  $g = 4/3$  and  $J = 15/2$  while for Ho<sup>3+</sup>  $g = 5/4$  and  $J = 8$ , giving

a value  $\mu \approx 10\mu_B$  in both cases. This gives an energy scale  $D$  close to 1.41 K for both  $\text{Ho}_2\text{Ti}_2\text{O}_7$  and  $\text{Dy}_2\text{Ti}_2\text{O}_7$  using a nearest-neighbour distance  $a\sqrt{2}/4$  with  $a \approx 10.1$  Å. This value of  $D$  (and  $D_{\text{nn}} = 5D/3 = 2.35$  K) is the value used in previous Monte Carlo simulations<sup>37,42</sup>.

Simulations on the dipolar spin ice model are carried out using the standard single spin flip Metropolis algorithm. To mimic the experimental conditions pertinent to real materials, the simulation sample is cooled slowly. At each temperature step, the system is equilibrated carefully, with various thermodynamic quantities of interest calculated. The single spin flip Metropolis algorithm is able to map out three different regions of the  $T$  vs  $J_{\text{nn}}/D_{\text{nn}}$  phase diagram shown in Fig. 7.9. Thermodynamic data indicates that when the nearest neighbour exchange is antiferromagnetic

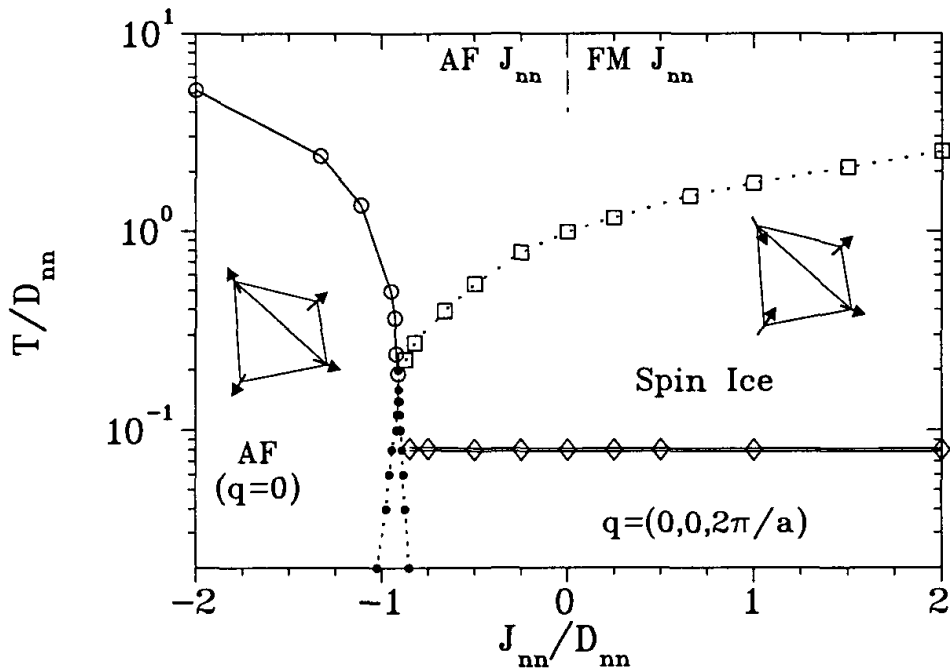


Fig. 7.9. Dipolar spin ice model: the phase diagram. The antiferromagnetic (AF) ground state is an all-spins-in or all-spins-out configuration for each tetrahedron for  $J_{\text{nn}}/D_{\text{nn}} < -0.905$ . For  $J_{\text{nn}}/D_{\text{nn}} > -0.905$  the system exhibits spin ice phenomenology as revealed by a broad specific heat peak at a temperature  $T_{\text{peak}}$  shown by the dashed lines (open squares). A loop Monte Carlo algorithm, that allows for better thermal equilibration than conventional Metropolis, reveals a transition to a long range ordered spin ice state with ordering wave vector  $\mathbf{q} = (0, 0, 2\pi/a)$  at a temperature  $T_c \approx 0.07D_{\text{nn}}$ . The region encompassed between the almost vertical dotted lines displays hysteresis in the long range ordered state selected ( $\mathbf{q} = 0$  vs.  $\mathbf{q} = (0, 0, 2\pi/a)$ ) as  $J_{\text{nn}}/D_{\text{nn}}$  is varied at fixed temperature  $T$  (from Refs. [94,95]).

and sufficiently large compared to the dipolar interactions ( $J_{nn} < 0$  and  $|J_{nn}| \gg D_{nn}$ ), the system undergoes a second order phase transition to an all-in–all-out ground state characterised by wave vector  $\mathbf{q} = 0$ . In the spin ice regime,  $J_{\text{eff}}/D_{\text{nn}} = 1 + J_{\text{nn}}/D_{\text{nn}} > 0.095$ , each specific heat data set for different  $J_{\text{nn}}$  shows qualitatively the same broad peak as observed in the nearest neighbour model<sup>38</sup> (see Fig. 7.10). The height,  $C_{\text{peak}}$ , and peak

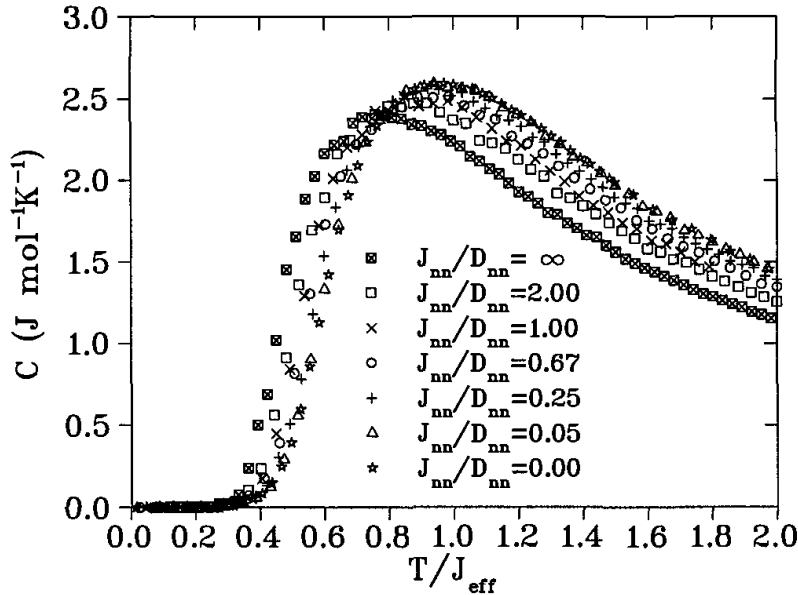


Fig. 7.10. Dipolar spin ice model: specific heat for system size  $L = 2$ , with temperature,  $T$ , re-scaled into units of the effective nearest neighbour interaction  $J_{\text{eff}} \equiv J_{\text{nn}} + D_{\text{nn}}$ .  $J_{\text{nn}}/D_{\text{nn}} = 0$  corresponds to purely dipolar interactions, while  $J_{\text{nn}}/D_{\text{nn}} = \infty$  corresponds to nearest neighbour ferromagnetic exchange only. Simulation runs for  $L = 4$  were also performed, but revealed no important finite size effects (from Ref. [95]).

temperature position,  $T_{\text{peak}}$ , show very little dependence on system size, for simulation cells of  $L = 2 - 6$ . However, both  $C_{\text{peak}}$  and  $T_{\text{peak}}$  are found to depend strongly on the ratio of  $J_{\text{nn}}/D_{\text{nn}}$ , as illustrated in Fig. 7.11.

By re-scaling the temperature scale for the specific heat corresponding to a number of different interaction parameters  $J_{\text{nn}}$  and  $D_{\text{nn}}$ , one can expose more clearly the dependence of the specific heat on the competition between the nearest neighbour exchange  $J_{\text{nn}}$  and the dipole-dipole interactions. In Fig. 7.10, this dependence is illustrated in the regime  $J_{\text{nn}}/D_{\text{nn}} > 0$ . The data show that in terms of an effective energy scale,  $J_{\text{eff}} \equiv J_{\text{nn}} + D_{\text{nn}}$ , the medium to long range effects of the dipolar interactions are in some sense “screened”, and one recovers qualitatively the short range physics of the nearest neighbour spin ice model. As  $J_{\text{nn}}$  becomes antiferromagnetic

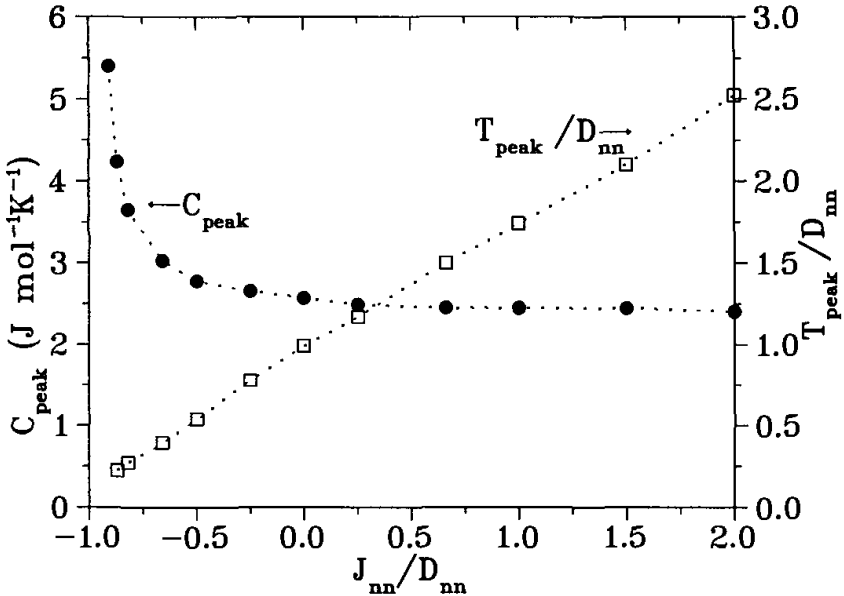


Fig. 7.11. Dipolar spin ice model: dependence of the simulated specific heat peak height  $C_{\text{peak}}$  and temperature  $T_{\text{peak}}$  on exchange and dipole-dipole interaction parameters. In this figure  $D_{nn}$  is set to 2.35K (from Refs. [37,95]).

(see  $C_{\text{peak}}$  vs  $J_{nn}/D_{nn}$  for  $J_{nn}/D_{nn} < 0$  in Fig. 7.11), the approximate collapse onto a single energy scale becomes less accurate, with the specific heat becoming dependent on  $J_{nn}/D_{nn}$ . It is within this regime that both  $\text{Ho}_2\text{Ti}_2\text{O}_7$  and  $\text{Dy}_2\text{Ti}_2\text{O}_7$  are expected to be realized, as we now discuss.

Since  $D_{nn}$  is calculated from Eqn. (2),  $J_{nn}$  must be determined from experimental data. By fitting either the height,  $C_{\text{peak}}$ , or the peak temperature,  $T_{\text{peak}}$ , of the specific heat curves of the Monte Carlo simulation to the experimental results<sup>22</sup>, one finds  $J_{nn} = -1.24\text{K}$  for  $\text{Dy}_2\text{Ti}_2\text{O}_7$ . The results of this fitting are illustrated in the top panel of Fig. 7.4a<sup>37</sup>. A fitting of the height or peak temperature of the experimental magnetic specific heat for  $\text{Ho}_2\text{Ti}_2\text{O}_7$  gives  $J_{nn} = -0.52\text{K}$  for this material<sup>42</sup>. As discussed above, a good fit of the electronic specific heat for  $\text{Ho}_2\text{Ti}_2\text{O}_7$  can also be achieved once the hyperfine contribution has been removed (See Fig. 7.5)<sup>42,45,46</sup>.

As discussed above, numerical integration of the specific heat divided by temperature can be performed to determine the entropy of both  $\text{Ho}_2\text{Ti}_2\text{O}_7$  and  $\text{Dy}_2\text{Ti}_2\text{O}_7$  (see Eqn. 1). The results for  $\text{Dy}_2\text{Ti}_2\text{O}_7$  are illustrated in Fig. 7.4b. The entropy recovered between  $T = 0.4\text{K}$ , where  $C_H(T)$  is very small, up to a temperature  $T = 10\text{K}$ , is  $S(T = 10\text{K}) - S(T \approx 0) \approx 3.930 \text{ J mol}^{-1} \text{ K}^{-1}$ . As we can see in Fig. 7.4b, the Monte Carlo data for  $S(T)$  at  $T = 10 \text{ K}$  is slightly below the Pauling's value  $R\{\ln(2) - (1/2)\ln(3/2)\}$ . To perform the calculation of the recovered entropy between  $T = 10 \text{ K}$  up

to  $T = \infty$ , one can extrapolate the temperature dependence of the specific heat  $C_H(T)$  for  $T > 10$  K by matching the Monte Carlo value of  $C_H(T)$  at  $T = 10$  K with the  $1/T^2$  high temperature paramagnetic temperature regime,  $C_H(T) = C_\infty/T^2$ . This gives a value  $C_\infty = 29.015 \text{ J mol}^{-1} \text{ K}$ , and an extra entropy of  $S(T = \infty) - S(T = 10) = 0.145 \text{ J mol}^{-1} \text{ K}^{-1}$ , hence a value  $S(T = \infty) - S(T \approx 0) = 4.075 \text{ J mol}^{-1} \text{ K}^{-1}$ , in exceedingly close agreement with Pauling's value,  $4.077 \text{ J mol}^{-1} \text{ K}^{-1}$ . Hence, the simulation with the appropriate experimental parameters retains Pauling's entropy  $S_0 = R/2\ln(3/2)$ , as is found experimentally for  $\text{Dy}_2\text{Ti}_2\text{O}_7$  and  $\text{Ho}_2\text{Ti}_2\text{O}_7$ .

While the above conventional Monte Carlo simulations of the model Hamiltonian for the spin ice compounds, Eqn. (4), yields a reasonably successful quantitative theory of bulk spin ice behaviour, there still remains the second question raised earlier in Section 7.3.2.2 as to why dipolar interactions, despite their anisotropic and long range nature, do not appear to lift the macroscopic degeneracy associated with the ice rules and select an ordered state at a temperature  $T \sim D_{\text{nn}}$ . As explained in the next section, as far as the simulations are concerned, the answer lies in the use of the single spin flip dynamics Monte Carlo algorithm which becomes inefficient at low temperatures deep in the spin ice state.

#### 7.3.2.4. Mean-Field Theory

The key question left unanswered by the above Monte Carlo simulations is in some sense the simplest one of all: are there preferred spin-spin correlations in dipolar spin ice within the ice-rule obeying low temperature state below  $T_{\text{peak}}$  that lead, in principle, to a long range ordered state?

The simplest approach to address this question is to calculate the wave vector ( $\mathbf{q}$ ) dependence of the static susceptibility,  $\chi(\mathbf{q})$ , in the paramagnetic phase<sup>83</sup>. There are several ways to do this. The simplest way is to perform a high-temperature series expansion of  $\chi(\mathbf{q})$ <sup>82</sup>. A more expeditive approach is to use mean field theory (or the random phase approximation). In this context, mean-field theory can be interpreted as a partial sum of an infinite number of diagrams in the high-temperature series expansion<sup>82</sup>. In the limit of very high temperature, the leading  $1/T$  correction of  $\chi(\mathbf{q})$  beyond the Curie behaviour is the same in both high-temperature series expansion and in mean-field theory. The aim of such a calculation is to identify the periodicity,  $\mathbf{q}_o$ , of the spatial modulation of the magnetization density that first becomes unstable as the temperature is decreased. Except for sufficiently simple spin Hamiltonians, such a calculation will not give

information about the ground state. A well known example is that of the ANNNI (anisotropic-next-nearest-neighbour Ising) model where there exist regions in exchange coupling parameter space where incommensurate soft-modes first appear upon cooling at  $T_c$ , but which immediately give way to a cascade of phase transitions to distinct states until one ultimately reaches a “simple” ground state<sup>96</sup>. If from the mean-field calculation, one can identify an ordering wave vector  $\mathbf{q}_o$  (and eigenvectors of the interacting susceptibility) for which the corresponding magnitude of the spins at each lattice site  $\mathbf{r}$ ,  $\mathbf{S}(\mathbf{r}) = 1$ , (the so-called “permanent moment structure”), then one has not only identified the critical mode at  $T_c$ , but also the ground state (unless the transition is pre-empted by a first order transition at a different  $\mathbf{q}$  than  $\mathbf{q}_o$  and a temperature  $T > T_c(\mathbf{q}_o)$ ).

The key step in the mean-field calculation is the determination of the Fourier transform of the spin-spin interactions  $\mathcal{J}_{\alpha\beta}^{ab}(i, j)$ . Indices  $i$  and  $j$  label the sites  $\mathbf{r}_i$  and  $\mathbf{r}_j$  occupied by spins  $\mathbf{S}(\mathbf{r}_i)$ ,  $\alpha$  and  $\beta$  label the spin components ( $\alpha = x, y, z$ ) and  $\mathcal{J}_{\alpha\beta}^{ab}(i, j)$  incorporates both exchange and dipolar interactions. The dependence on the spin components is due to anisotropy, as arises from the dipolar interactions. Finally, one introduces sub-lattice indices  $a$  and  $b$  that label the sublattices of the tetrahedral basis. Here there are four Bravais sublattices, chosen to have their origins on either an “up” or “down” tetrahedron (see Fig. 7.1). As a result of this, there are four branches for each  $\mathbf{q}$  value. Details of the calculations are presented in Refs. [97,98]. The mean-field critical temperature,  $T_c^{\text{mf}}$  is given by the largest eigenvalue,  $\lambda^r(\mathbf{q})$ , of  $\mathcal{J}_{\alpha\beta}^{ab}(\mathbf{q})$  over the whole Brillouin zone ( $r$  labels the four eigenvalues/modes at each  $\mathbf{q}$ ). More compactly,  $T_c = \max_{\mathbf{q}}\{\lambda^{\max}(\mathbf{q})\}$  where  $\{\lambda^{\max}(\mathbf{q})\}$  is the largest of the four eigenvalues ( $r = 1, 2, 3, 4$ ) at wave vector  $\mathbf{q}$ , and  $\max_{\mathbf{q}}$  indicates the global maximum of the spectrum of  $\{\lambda^{\max}\}$  over all  $\mathbf{q}$ . The value of  $\mathbf{q}$  for which  $\lambda^r(\mathbf{q})$  is maximum is the ordering wave vector  $\mathbf{q}_o$ .

It was shown in Ref. [97] that truncating the dipolar lattice sums in Eqn. 4 at ever increasing cut-off distance leads to the development of a very flat quasi-dispersionless spectrum for  $\lambda^{\max}(\mathbf{q})$  as the dipolar cut-off goes to infinity. Treating dipolar interactions via the Ewald method, where the long range dipolar interactions are not truncated, one finds a completely smooth and quasi-degenerate soft mode spectrum with a global maximum (critical mode) at  $\{001\}$ <sup>c</sup>: see Fig. 7.12<sup>98</sup>. Inspection of the corresponding eigenvectors of  $\mathcal{J}_{\alpha\beta}^{ab}(\mathbf{q})$  associated with the doubly degenerate critical mode

---

<sup>c</sup>{...} represents the set of symmetry-related reciprocal lattice points

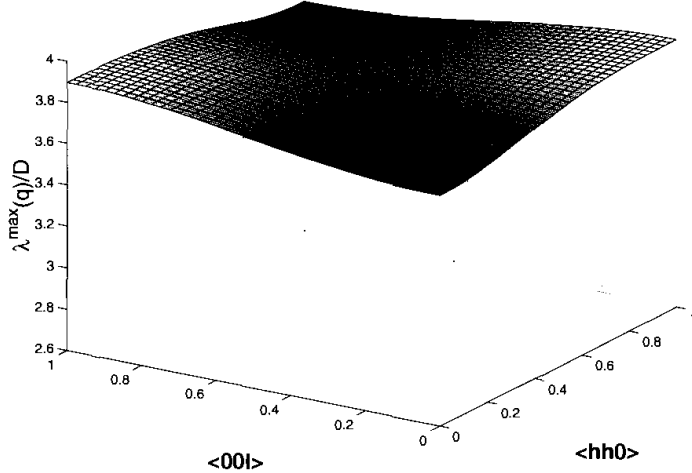


Fig. 7.12. Dipolar spin ice model: the scaled maximum eigenvalues,  $\lambda^{\max}(q)/D$ , in the  $(hhl)$  plane. The dipole-dipole interactions are treated with the Ewald approach. Here, the exchange coupling  $J$  was set to zero (from Ref. [98]).

at  $\{001\}$  indicates a two-in two-out spin ice structure, where the spins on sub-lattices  $a = 1, 3$  point opposite to those on sub-lattices  $a = 2, 4$  in a tetrahedral unit. Ref. [98] discusses how these soft modes can be used to reconstruct the long ranged ordered (permanent moment) structure, where the thermal local magnetization is the same on all sites, and which corresponds to the long range ordered spin ice state that develops at low temperature if ergodicity can be maintained in Monte Carlo simulations (see Section 7.3.2.5).

From mean-field theory, one can also determine the value of  $J_{nn}/D_{nn}$  at which the ordering changes from an “all-in–all-out”  $\mathbf{q} = 0$  state (i.e. from large negative antiferromagnetic  $J_{nn}$ ) to the  $(001)$  long range ordered spin ice state. It is found that the transition between the two states occurs at  $J_{nn}/D_{nn} = -0.905$ . This agrees with the value found in Monte Carlo simulations results for the transition between all-in–all-out  $\mathbf{q} = 0$  ordering and spin ice regime<sup>37</sup>, and agrees as well with zero temperature energy calculations of the all-in–all-out ground state versus the  $(001)$  state mentioned above.

Having obtained strong evidence from mean-field theory that there exists a well-defined, unique ordering wave vector in the long range dipolar spin ice model at the Gaussian mean-field level, one can proceed with the search for a transition to long range order in the model that is dynamically inhibited when using conventional single spin-flip Monte Carlo simulations.

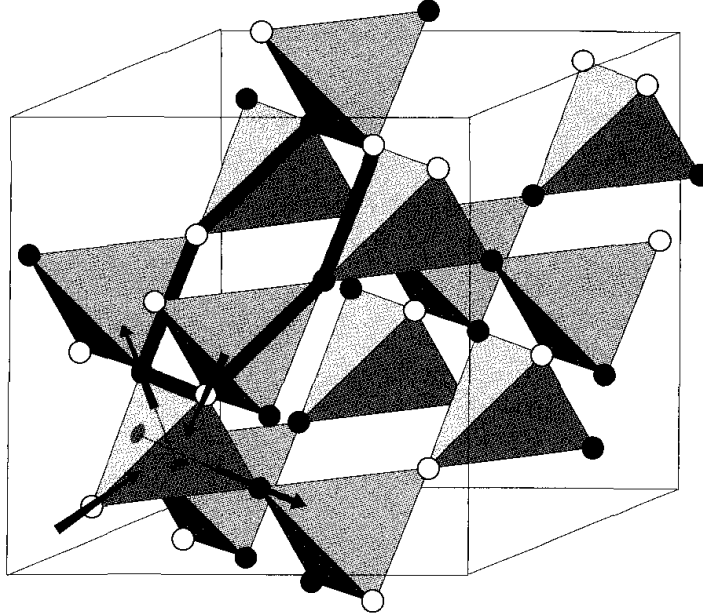


Fig. 7.13. The pyrochlore lattice, illustrating a spin ice state and a possible “loop move”. The lower left “downward” tetrahedron shows Ising spins as arrows. Each spin axis is along the local  $\langle 111 \rangle$  quantization axis, which goes from one site to the centre of the opposing triangular face (as shown by the disks) and meets with the three other  $\langle 111 \rangle$  axes in the middle of the tetrahedron. For clarity, black and white circles on the lattice points denote other spins. White represents a spin pointing into a downward tetrahedron while black is a spin point out. The entire lattice is shown in an ice-rules state (two black and two white sites for every tetrahedron). The hexagon (thick gray line) shows a minimal size loop move, which corresponds to reversing all colours (spins) on the loop to produce a new ice-rules state (from Ref. [99]).

#### 7.3.2.5. The Loop Monte Carlo

In order to investigate the low temperature ordering properties of dipolar spin ice, one needs a Monte Carlo algorithm with non-local updates that effectively bypass the energy barriers that separate nearly degenerate states and allow the simulation to explore the restricted ice-rules phase space that prevents ordering in the model<sup>94,95,99</sup>. Such an algorithm can then be used to explore and characterize the long range ordered state that arises out of ice-rules manifold and which is slightly energetically favoured by the long range dipolar interactions over an arbitrary ice-rule obeying state.

One first identifies the true zero energy modes that can take the near-

neighbour spin ice model from one spin ice state to another exactly degenerate ice state. An example of these zero modes, or loops, is shown in Fig. 7.13. An initial working hypothesis is that in the dipolar spin ice model, with interactions beyond nearest neighbour, the system freezes into a state that obeys the ice rules. This is indeed what is found in simulations: systems simulated using conventional single spin flips always freeze out in an ice-rules state with no “defects” that violate the ice rules. With interactions beyond nearest-neighbour, these loop moves become low energy excitations (quasi-zero modes) that can take the dipolar spin ice model from one ice-rules state to another without introducing spin defects. This allows all of the quasi-degenerate spin ice states to be sampled ergodically, and facilitates the development of a long range ordered state at low temperatures.

Barkema and Newman<sup>100,101</sup> proposed a loop algorithm that was originally designed for two dimensional square ice models within a Monte Carlo simulation. This scheme can be readily adapted to the three dimensional pyrochlore lattice. In the context of square ice, two types of loop algorithm, the so-called long and short loop algorithm, were investigated<sup>94</sup>. In the square ice model, each vertex on a square lattice has four spins associated with it. The vertices are analogous to tetrahedron centers. The ice rules correspond to “two spins pointing in, two spins pointing out” at each vertex. In the Barkema and Newman algorithm, a loop is formed by tracing a path through ice-rules vertices, alternating between spins pointing into and spins pointing out of the vertices. A “long loop” is completed when the path closes upon the same spin from which it started. A “short loop” is formed whenever the path traced by the loop encounters any other vertex (tetrahedron) already included in the loop – excluding the dangling tail of spins (Fig. 7.14).

The implementation of the Barkema and Newman loop algorithm for the three dimensional pyrochlore lattice spin ice problem proceeds as follows. In this system, the smallest complete loop that is a zero mode on the pyrochlore lattice consists of six spins (see Fig. 7.13). Such a loop in spin ice was previously identified in Ref. [5] and also by Pauling<sup>1</sup> in the context of water ice and Anderson<sup>3</sup> in the context of the spinel lattice. However using the above loop algorithm, much larger loops are possible. When used with the pyrochlore lattice (Fig. 7.13), such a loop must pass through two spins on each tetrahedron. A loop always “enters” a tetrahedron through an inward pointing spin and “leaves” a tetrahedron through an outward pointing spin. The periodic boundary conditions of the lattice create no difficulties. If one forms a closed loop in this manner, each spin on the loop

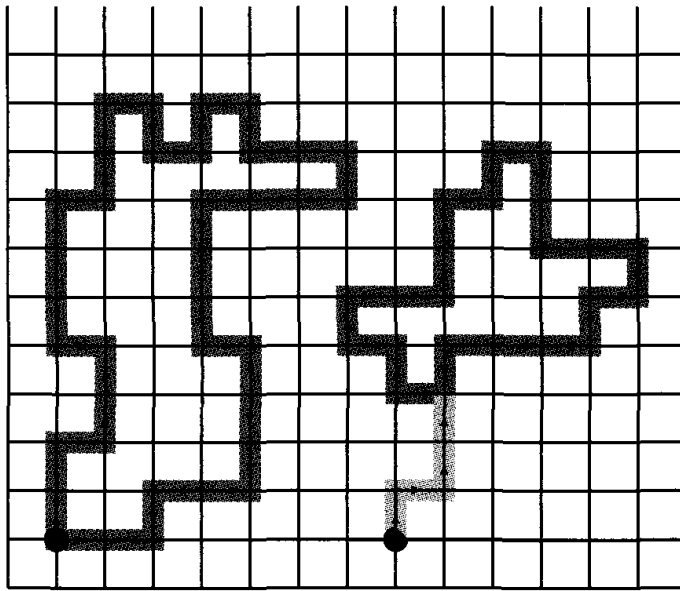


Fig. 7.14. Long and short loops formed by the Newman and Barkema algorithm (Refs. [100,101]) on a square ice lattice. Vertices are represented by points where lattice lines cross. Each vertex has two spins pointing in and two spins pointing out, however for clarity, only spins which are included in the loops are shown. Starting vertices are indicated by large black dots. On the left is an example of a long loop, which is completed when it encounters its own starting vertex. On the right is a short loop, which is complete when it crosses itself at any point. Dark gray lines outline completed loops. The excluded tail of the short loop is shown in light gray (from Refs. [94,95]).

is reversed, and the whole system stays in an ice-rules state. However, small increases or decreases in the dipole-dipole energy may arise due to small energy differences between the old and the new ice-rules state. These small energy changes caused by the loop moves are evaluated via a Metropolis algorithm within the Monte Carlo program<sup>100,101</sup>. Full details of the loop Monte Carlo simulation method are given in Refs [94,95]. Here, we only give a summary of the key results.

It was discussed in Refs. [94,95,99] that loop Monte Carlo simulations are successful in restoring ergodicity in simulations of dipolar spin ice. A main consequence of this restoration of ergodicity is the observation of a low temperature phase transition in the model. For example, as a first indication, a Monte Carlo loop simulation of  $\text{Dy}_2\text{Ti}_2\text{O}_7$  (using  $J_{\text{nn}} = -1.24$  K and  $D_{\text{nn}} = 2.35$  K) now shows a sharp peak in the specific heat at a temperature significantly below the spin ice peak (See Fig. 7.15). The feature in the specific heat and the abrupt drop in energy (see Fig. 7.16) at the same temperature gives compelling preliminary evidence that the

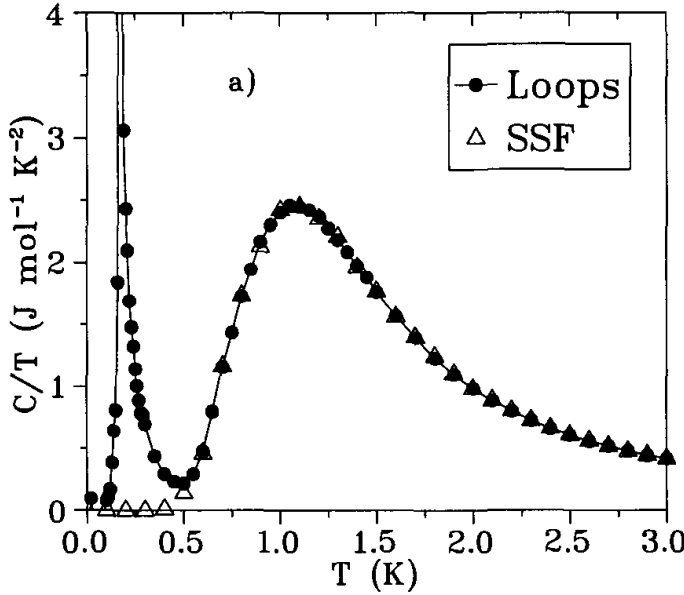


Fig. 7.15. Dipolar spin ice model: the low temperature magnetic specific heat calculated by numerical simulation for a system size  $L=4$  and with simulation parameters set for  $Dy_2Ti_2O_7$ . Closed circles are simulation data run with the short loop algorithm (Loops), open triangles are data obtained using the single spin flip (SSF) Metropolis algorithm. The broad feature in the specific heat at  $T \approx 1$  K indicates the rapid development of the spin ice rule obeying states. The sharp feature at  $T_c$  is the appearance of a phase transition to a ground state being made dynamically accessible via the non-local loop dynamics (from Refs. [94,95]).

loop algorithm is successful in allowing a phase transition to occur at a temperature of  $T_c \approx 0.18$  K. Also, the energy curve shows a discontinuous drop at  $T_c$  (i.e. latent heat) for large lattice sizes, suggesting a first order phase transition (Fig. 7.16). In the remainder of this section, we discuss the nature of the low temperature ordered state of dipolar spin ice and the phase transition that leads to it.

Direct inspection of the spin directions at  $T < 0.18$  K reveals that the long range ordered state obeys the ice rules, has zero magnetic moment per unit cell and is commensurate with the cubic pyrochlore unit cell (see Fig. 7.17). This state corresponds to the critical mode found in the mean-field calculation discussed above <sup>97,98</sup>. There are twelve symmetrically equivalent spin configurations for the ground state as explained below, two for each cubic axis ( $\langle 100 \rangle$ ) direction and their spin reversed states. The ordering wave vector  $\mathbf{q}_o$  lies parallel to one of the cubic axis directions, specifically  $\mathbf{q}_o = (0, 0, 2\pi/a)$  or one of its symmetrically equivalent (star) directions. To construct the ordered state, first consider a starting tetrahedron with its six possible ice-rules states. For a given ordering wave

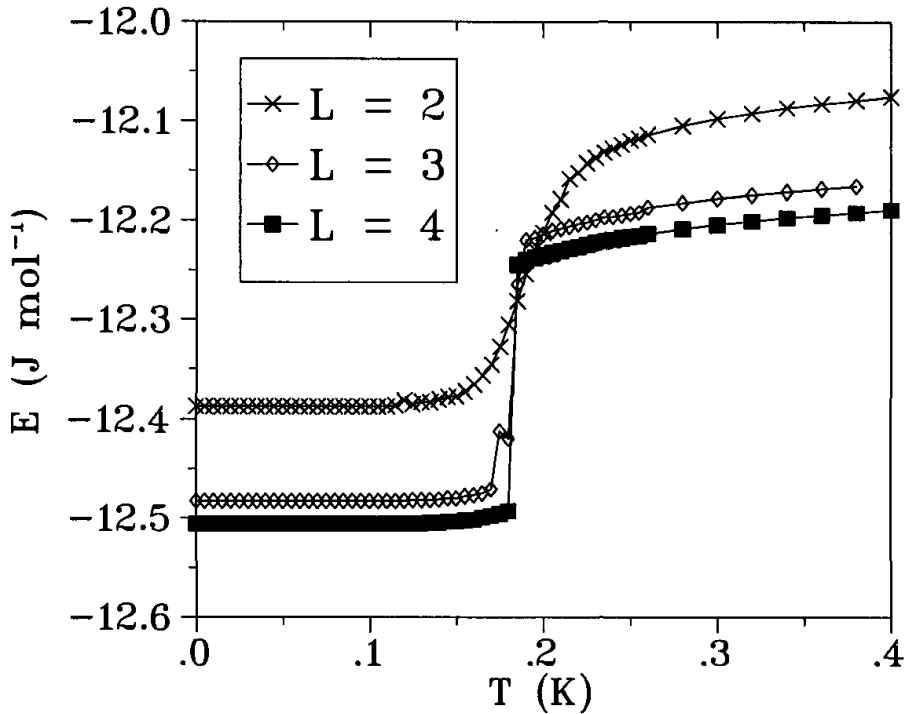


Fig. 7.16. Dipolar spin ice model: details of the loop Monte Carlo simulation energy near the transition for different system sizes (from Refs. [94,95]).

vector  $\mathbf{q}_o$ , this tetrahedron selects one of the four possible spin configurations (two independent configurations and their spin-reversals,  $S_i^a \rightarrow -S_i^a$ ) with a total magnetic moment for the tetrahedron perpendicular to  $\mathbf{q}_o$ . The entire ordered state may be described by planes (perpendicular to  $\mathbf{q}_o$ ) of such tetrahedra. The wavelength defined by this  $\mathbf{q}_o$  physically corresponds to antiferromagnetically stacked planes of tetrahedra, which means that a given plane has tetrahedra of reversed spin configuration with respect to the planes above and below it (i.e. those displaced by half of cubic unit cell constant). To describe this state we define the multi-component order parameter

$$\Psi_\alpha^m = \frac{1}{N} \left| \sum_{j=1}^{N/4} \sum_{a=1}^4 \sigma_j^a e^{(i\phi_a^m + i\mathbf{q}_\alpha \cdot \mathbf{R}_j)} \right|. \quad (6)$$

This type of labeling is natural given that the pyrochlore lattice can be viewed as an face centred cubic (FCC) lattice with a “downward” tetrahedral basis (Fig. 7.1). Thus  $j$  labels the FCC lattice points of the pyrochlore lattice, and the index  $a$  sums over the four spins that make the basis connected to each  $j$ . The index  $\alpha$  labels the three possible symmetry related

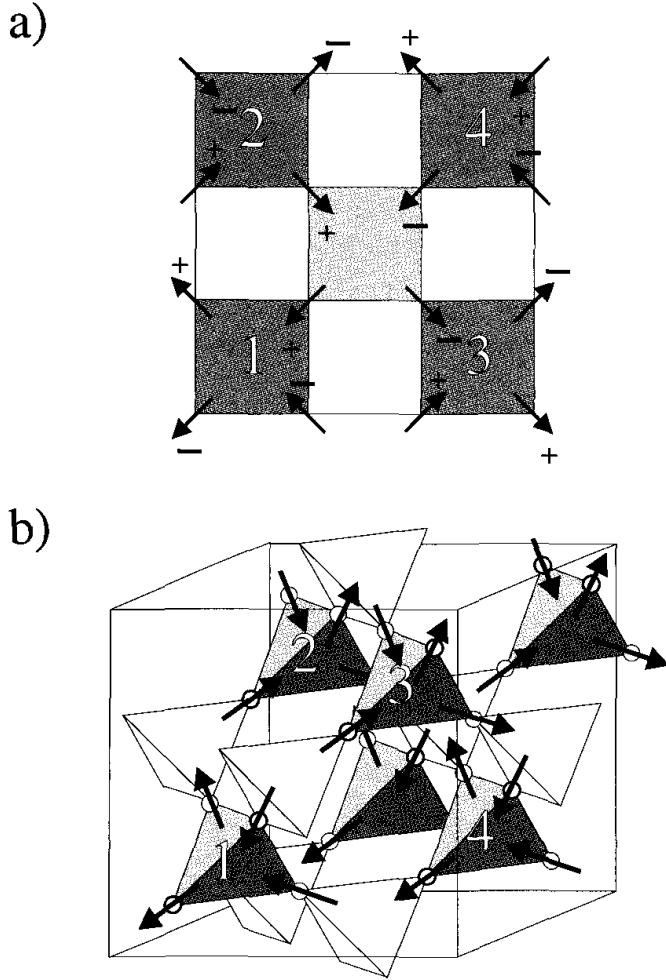


Fig. 7.17. Dipolar spin ice model: the long range ordered  $\mathbf{q} = (0, 0, 2\pi/a)$  ground state projected down the  $z$  axis (a); the four tetrahedra making up the cubic unit cell appear as dark gray squares. The light gray square in the middle does not represent a tetrahedron, but its diagonally opposing spins are in the same lattice plane. The component of each spin parallel to the  $z$  axis is indicated by a + and - sign. In perspective (b), the four tetrahedra of the unit cell are numbered to enable comparison with (a) (from Ref. [99]).

$q_o$  ordering wave vectors. For a given  $q_\alpha$ , as described above, there are two ice-rules configurations and their reversals which can each form a ground state. Thus  $m = 1, 2$  labels these possibilities with the phase factors  $\{\phi_a^m\}$ , describing the given configurations  $m$ . Each Ising variable  $\sigma_j^a$  has a value +1 or -1 when a spin points into or out of its downward tetrahedron  $j$ , respectively.

$\Psi_\alpha^m$  has six degenerate components, each of which can take on a value between 0 and 1. Upon cooling through the transition, the system selects

a unique ordered configuration, causing the corresponding component of  $\Psi_\alpha^m$  to rise to unity and the other five to fall to zero (provided the finite size system is simulated below the critical temperature over a time scale less than the ergodic time scale over which full spin symmetry would be restored). The component which rises to unity is equally likely to be any one of the six that are randomly selected by spontaneous symmetry breaking.

The average magnitude of the multi component order is defined as

$$\langle \Psi \rangle = \sqrt{\sum_{m=1}^2 \sum_{\alpha=1}^3 (\Psi_\alpha^m)^2}. \quad (7)$$

Figure 7.18 is a plot of this quantity versus temperature for three different system sizes. For  $T < T_c$  the different lattice sizes produce identical order parameters. By contrast,  $\langle \Psi \rangle$  for the smaller lattice size displays pronounced rounding near  $T_c$  and an increased residual value for large  $T$ . The larger lattice size produces an order parameter with a clear discontinuity at  $T_c$ . This discontinuity in the order parameter combined with the discontinuity of the total energy in Fig. 7.16 can be viewed as strong evidence for a first order transition.

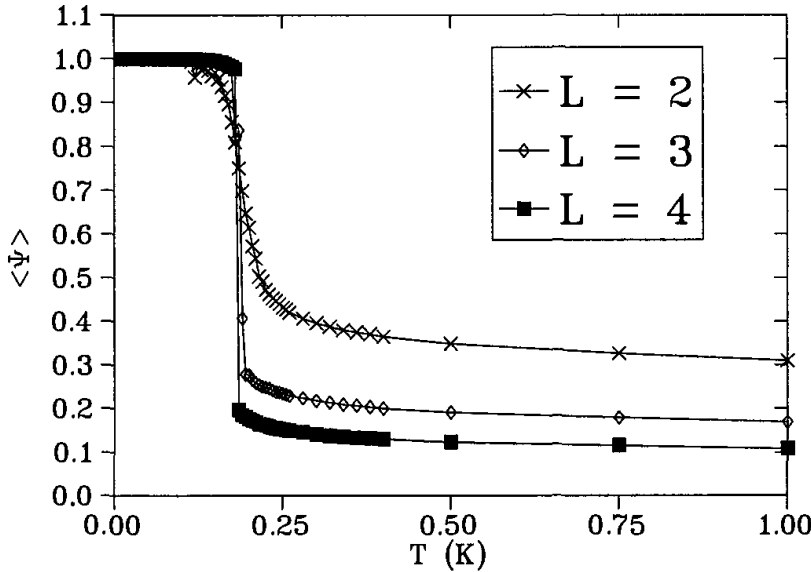


Fig. 7.18. Dipolar spin ice model: the  $\mathbf{q} = (0, 0, 2\pi/a)$  order parameter. Curves are shown for system size  $L = 2$ ,  $L = 3$ , and  $L = 4$  (from Ref. [99]).

The loop Monte Carlo simulation allows an estimate of the latent heat at the transition. Referring to Fig. 7.16, the energy discontinuity,  $\Delta E$ , as

read off this graph for  $L = 4$ , is

$$\Delta E \approx 0.248 \text{ J mol}^{-1}. \quad (8)$$

This behaviour is also consistent with the transition being first order. Below, we compare this  $\Delta E$  to the latent heat associated with the entropy jump at the transition and calculated through the finite size scaling of the height of the specific heat <sup>102</sup>:

$$C_{\text{peak}} \approx \frac{(\Delta E)^2}{4k_B T_c^2} L^d + a \quad (9)$$

where  $L^d$  is the system volume as before, and  $a$  is the y-intercept of the finite-size scaling graph of  $C_{\text{peak}}(L)$  vs  $L^3$ . To achieve good statistics of the finite-size scaling behaviour of the transition to long range order, one has to employ histogram methods and reweighting techniques discussed in Refs. [103,104,105] and employed in the present context in Refs. [94,95,99].

The  $L^3$  dependence of  $C_{\text{peak}}(L)$  in Fig. 7.19 shows that the finite size scaling is consistent with that expected for a first order transition. Also, as a second estimator of the latent heat, the slope of the  $L^3$  fit allows to determine  $\Delta E$  using Eqn. (9). One deduces a latent heat of

$$\Delta E = 0.245 \text{ J mol}^{-1}, \quad (10)$$

consistent with the value obtained in Fig. 7.16 (for the  $L = 4$  system) from reading directly off of the energy graph (see Eqn. (8)). From the estimate of the latent heat, one finds that the entropy jump at the transition at  $T_c \sim 0.18$  K is approximately  $\Delta E/T_c \approx 1.37 \text{ J/mol K}$ . Adding to this entropy jump the (small) amount of entropy removed between  $0 < T < T_c$ , and between  $T_c < T = \infty$ , one finds within 2% the full entropy expected for such an Ising system, that is  $R \ln(2) = 5.765 \text{ J mol}^{-1} \text{ K}^{-1}$  (see Fig. 7.20).

Taking all indicators together, one finds that that the transition to long range order at 180 mK recovers all residual Pauling entropy of the dipolar spin ice model. Thus one can assert that the degeneracy associated with the spin ice model, and the corresponding value of zero point entropy, is “naturally” lifted due to the internal perturbations beyond nearest neighbour within the long range dipole-dipole interactions, if equilibrium can be maintained at sufficiently low temperatures.

To summarize the results presented in this section, we refer the reader to the dipolar spin ice Monte Carlo phase diagram, Fig. 7.9. As illustrated in the Figure, the transition between the spin ice phase (which retains Pauling’s entropy) and the  $\mathbf{q}_o = (0, 0, 2\pi/a)$  ordered phase is independent of

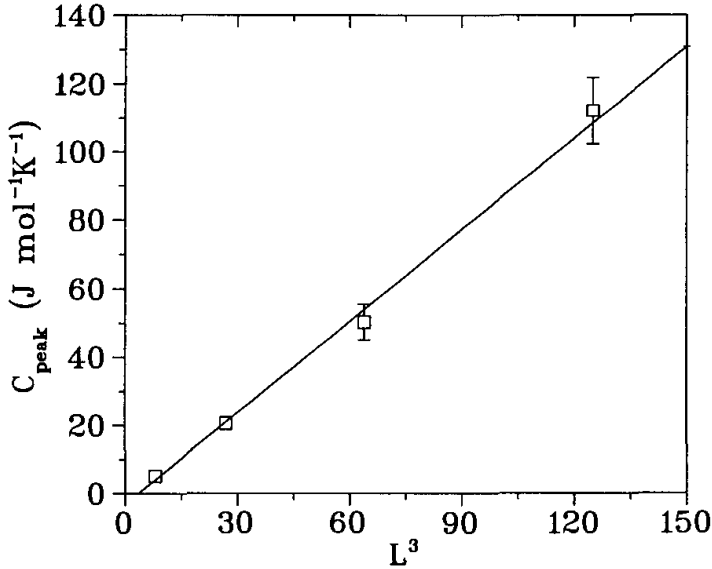


Fig. 7.19. Dipolar spin ice model: finite size scaling fit for the specific peak heights of the ordering transition observed in the loop Monte Carlo simulations. Data points represent the mean  $C_{\text{peak}}$  value for a given  $L$  averaged over ten simulations for each  $L$ . Error bars show one standard deviation (from Ref. [99]).

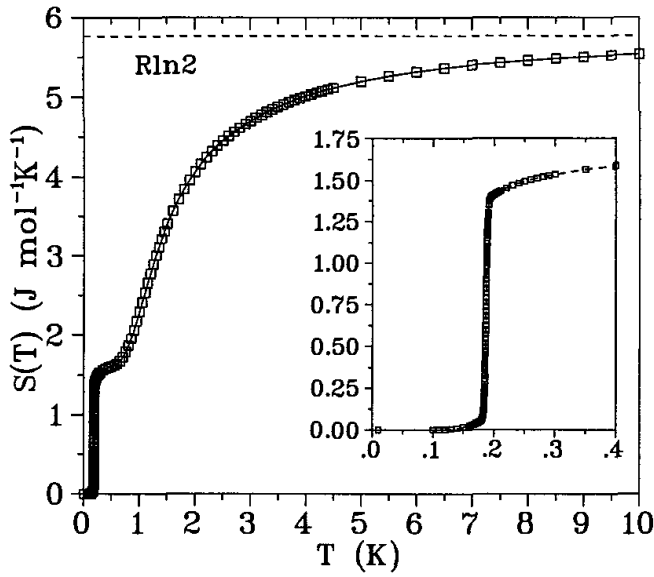


Fig. 7.20. Dipolar spin ice model: the entropy calculated by integrating the specific heat simulated by the loop Monte Carlo method. The entire value of entropy for the system ( $R \ln 2$ ) is recovered in the high temperature limit. The inset shows the details of the entropy recovered by the transition to long range order (from Refs. [94,95]).

the strength of  $J_{\text{nn}}$ . One finds that this first order line also partially follows the boundary between the antiferromagnetic ordered phase and the higher

temperature paramagnetic phase, and that a tricritical point separates these two regions of the line, that occurs near the value  $J_{\text{nn}}/D_{\text{nn}} \sim -1.1$ .

#### 7.3.2.6. Application of the Dipolar Model to Neutron Scattering Results

As mentioned in Section 7.3.1.3 above, elastic neutron scattering is a sufficiently detailed microscopic probe to identify corrections to the near neighbour spin ice model that are not required to describe the bulk properties. Referring to Fig. 7.8, of the several characteristic “blobs” of scattering observed in  $\text{Ho}_2\text{Ti}_2\text{O}_7$ , that centered at  $(0, 0, 3)$  is rounder in reality than predicted by the near neighbour model<sup>106</sup> and that centered at  $(3/2, 3/2, 3/2)$  is more elongated along  $[\bar{1}\bar{1}1]$ . As shown in the Figure, such differences are well accounted for by the dipolar model<sup>42</sup>. The description is quantitative<sup>42</sup>, as has been further confirmed by the neutron measurements of Kanada *et al.*<sup>43</sup>, who fitted the experimental scattering along  $hh0$  and  $00l$  at temperatures between 0.4 K and 50 K to the predictions of the dipolar model. Likewise, Kadowaki *et al.* fitted the experimental powder diffraction from  $\text{Ho}_2\text{Sn}_2\text{O}_7$  with the prediction of the dipolar model between  $T = 0.4$  K and 50 K<sup>47</sup>.

$\text{Dy}_2\text{Ti}_2\text{O}_7$  does not lend itself well to neutron studies as several of the natural Dy isotopes are strongly neutron-absorbing. This problem has been solved by Fennell *et al.*<sup>81,107</sup> who have prepared a single crystal of  $^{162}\text{Dy}_2\text{Ti}_2\text{O}_7$ , with greatly reduced absorption. A very recently reported comparison of experiment and theory has shown that the spin ice state at 0.3 K is reasonably well accounted for by the dipolar model, but that the differences between experiment and theory are much greater than for the Ho materials. In particular, there is enhanced magnetic scattering around the Brillouin zone boundaries that is not well accounted for by the dipolar model<sup>81</sup>.

#### 7.3.2.7. How Realistic is the Dipolar Model?

We have shown above how the dipolar model with single spin flip dynamics provides a good description of the elastic neutron scattering and bulk properties of the spin ice materials. It is also evident – especially from the latest neutron scattering results of Fennell *et al.*<sup>81</sup> – that the model is not perfect. As improvements to the model one could consider, for example, further neighbour exchange or a more accurate quantum mechanical description of the admixing of excited  $M_J$  levels into the ground state doublet<sup>77</sup>.

For example, it could be argued that it is better to consider, rather than Ising spins, Heisenberg spins with a strong uniaxial anisotropy  $D$  to force them along  $\langle 111 \rangle$ <sup>98</sup>. This model with ferromagnetic near neighbour exchange coupling was considered by Champion *et al.*<sup>67</sup> who found that it has an ordering transition to a ferromagnetic state with the spins canted off the local trigonal axis towards ferromagnetic alignment (the canting decreasing to zero as  $D \rightarrow 0$ ). The transition is first order for  $D/J > 5$  and second order for  $D/J < 5$ . Another related model, which combines dipolar interactions with g-factor anisotropy (but no exchange) has recently been considered by Chamberlain *et al.*<sup>108</sup> who numerically calculated the  $T = 0$  ground states as a function of anisotropy. For the Ising limit the ordered state identified by Melko *et al.*<sup>99</sup> is recovered, while for the Heisenberg limit a ground state similar to Champion's canted ferromagnetic state is found. It thus seems likely that the combination of dipolar interactions and non-Ising magnetic moments might result in a competition between these two ground states. However it should be emphasised that to date, only the dipolar spin ice model has received significant experimental support.

It is then relevant to ask, is the dipolar model sufficiently accurate to have identified a "true" ground state in the spin ice materials? Thus, as discussed in detail above, Melko *et al.*<sup>99</sup> showed that taking into account the correct long range dipolar interaction and implementing a special dynamics, the degeneracy is lifted, the system remains ergodic and the missing entropy is liberated through a low temperature phase transition. However, although thermodynamics as we know it is clearly saved in this way, experimentally there is no evidence of such a transition in the spin ice materials. Loss of ergodicity means that the spin ice materials behave, in this regard, much more like the idealised near neighbour spin ice model<sup>4</sup> than this essentially exact numerical calculation. It is of course possible that minor terms in the spin Hamiltonian are not yet correctly identified<sup>81</sup>, causing this disagreement between experiment and theory.

#### 7.4. Field-Induced Phases

In the Introduction we remarked how the (near neighbour) spin ice model is a sixteen vertex model in which the statistical weights of the vertices can be controlled by the application of a magnetic field along different symmetry directions. In experimental terms this gives the possibility of a remarkable degree of control over the physics of spin ice materials and in-field studies indeed have revealed many interesting new phenomena. In this section we

review both the theoretical and experimental aspects of spin ice behaviour in an applied field.

### 7.4.1. Theory

#### 7.4.1.1. Near Neighbour Model

The application of a magnetic field to the near neighbour spin ice model shows several interesting features. Monte Carlo calculations of magnetization curves for the three symmetry axes [100] [110] and [111] are shown in Fig. 7.21<sup>38</sup>. The magnetization per spin saturates at slightly different values depending on the field direction:  $1/\sqrt{3}$ ,  $1/\sqrt{6}$  and  $1/2$  of the spin length for [100], [110] and [111], respectively.

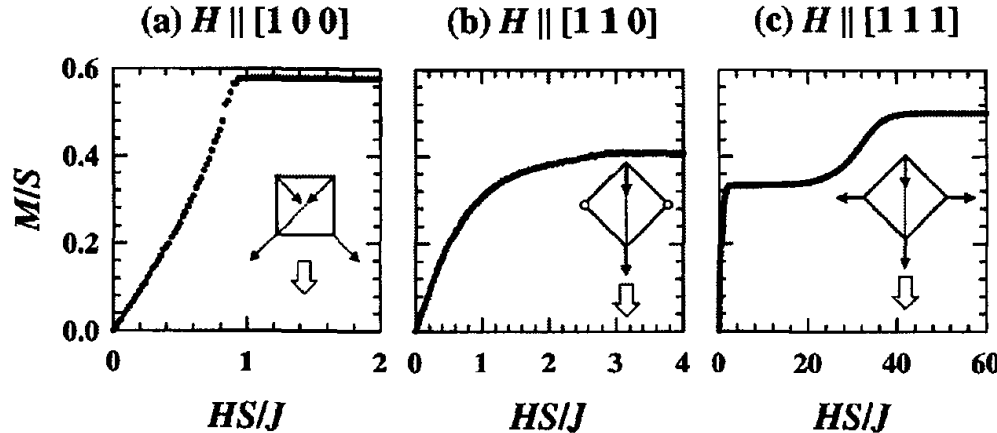


Fig. 7.21. Near neighbour spin ice model: Monte Carlo simulation results for the magnetization in an applied field for the three symmetry axes [100] [110] and [111] (Ref. [38]).

With the field applied along the 4-fold axis [100], all spins couple to the field and are saturated in a canted ferromagnetic state at high field. Barely visible on the simulated magnetization-field plot is a small jump in the magnetization near to saturation. This is in fact a first order phase transition which is more clearly visible as a spike in the specific heat. The relevant data, and the corresponding magnetic phase diagram are shown in Figs. 7.22 and 7.23. There are two lines of first order phase transitions terminating in a critical end point (note that this might still be first order<sup>109</sup>). The phase transition involves a jump in magnetization between two

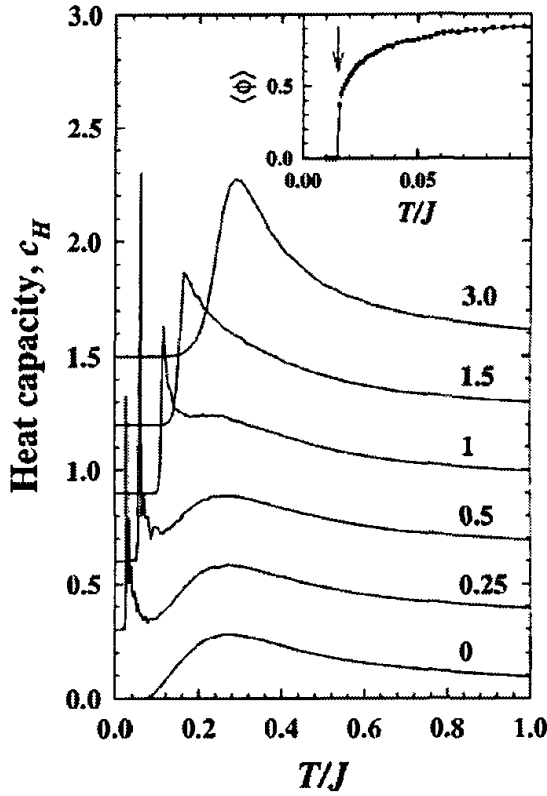


Fig. 7.22. Near neighbour spin ice model: Monte Carlo simulation results in a fields applied on [100], revealing a specific heat spike that indicates a line of first order phase transitions (see Fig. 7.23). The inset shows the “liquid-gas order parameter”  $\langle \Phi \rangle = m_l - m_g$  where  $m_l$  and  $m_g$  are the magnetizations above and below the critical line respectively (Ref. [38]).

phases of the same symmetry. In this case it is analogous to the liquid-gas transition which involves a jump in density. Such symmetry-sustaining phase transitions are known in ferroelectrics<sup>110</sup>, and the general shape can be justified by Landau theory with a negative fourth order term in the free energy expansion. An extension of the near neighbour spin ice model studied by Champion *et al.*<sup>67</sup> involves the use of continuous spins with strong  $\langle 111 \rangle$  anisotropy  $D$ , rather than Ising spins. In this model the [100] ferromagnetic state (with variable canting) becomes the ground state for all finite  $D$  and the corresponding zero-field ordering transition crosses over from second order at small  $D$  to first order at a triple point that marks the confluence of three lines of first order phase transitions. There is tricritical point at  $D/J \approx 5$  where the triple point disappears.

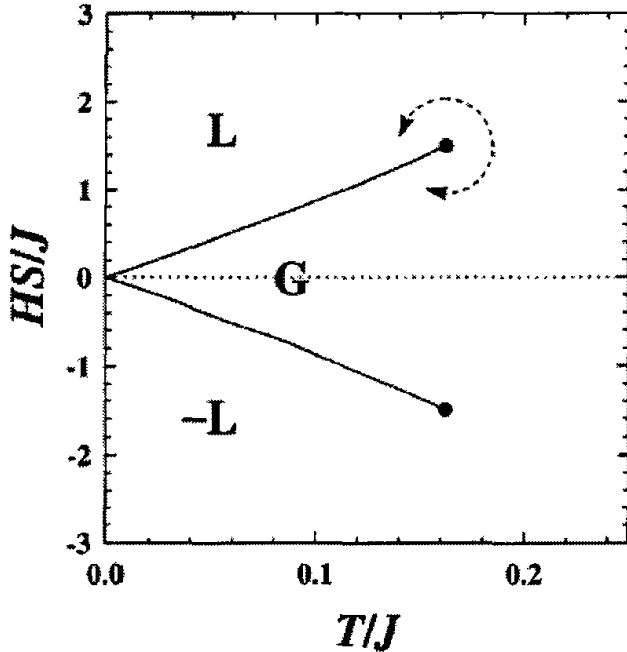


Fig. 7.23. Near neighbour spin ice model: magnetic phase diagram for a field applied along [100], emphasising the analogy with a liquid-gas system (Ref. [38]).

With a field applied along the 2-fold axis [110], now only two spins on each tetrahedron couple to the field, the other two remaining perpendicular (see inset of middle panel of Fig. 7.21). The former pair are aligned by the field into collinear “ $\alpha$ ” chains of canted spins, such that one spin points into and one out of each tetrahedron. Application of the ice rule means that the perpendicular spin pair must also be “one in, one out”, and hence align in collinear so-called  $\beta$  chains of canted spins oriented perpendicular to the field. However at the level of the near neighbour model these perpendicular chains are not energetically coupled together.

With the field along the 3-fold axis [111], there is an initial and rapid saturation of the magnetization to a “plateau” of  $1/3$  of the spin length, which is then followed by a second rise to full saturation (Fig. 7.21c). In this orientation one spin is parallel to the field while the other three can all couple to it. Hence the lowest energy state has three spins in and one out (or vice-versa, depending if it is an “up” or “down” tetrahedron). Hence the second rise in magnetization involves breaking the spin ice rules. As pointed out in Ref. [111], the plateau state has one spin aligned, and the other three fixed by the ice rules. This leads to the very interesting property

of retaining an extensive zero point entropy, as discussed further in Section 7.4.5.

#### 7.4.1.2. *Dipolar Model*

The simple nearest-neighbour model allows us to understand the constraints introduced by the applied magnetic field at the single-tetrahedron level. To discuss quantitatively the development of spin-spin correlations in an applied field, it is necessary to discuss the long range dipolar interactions.

Recent numerical work on the dipolar model in a field applied along [110] has found a transition to long range order at low temperatures for exchange and dipole-dipole coupling parameters appropriate for  $\text{Dy}_2\text{Ti}_2\text{O}_7$ <sup>112,113</sup>. Yoshida *et al.* have described the corresponding phase diagram<sup>106</sup>. Below 0.15 T the ground state is the theoretical zero field ordered state identified by Melko *et al.*<sup>99</sup> in which the  $\alpha$  and  $\beta$  chains (defined above) are three-dimensionally ordered in an antiferromagnetic way. However above  $\mu_0 H = 0.15$  T, the ground state is the  $Q = X$  state discussed by Harris *et al.*<sup>4</sup>, which has ferromagnetic  $\alpha$  chains. In the dipolar model, these are found to persist even above the temperature ( $\sim 1$  K) where the  $\beta$  chains disorder for  $\mu_0 H \rightarrow \infty$ . Thus, the principal difference between the near neighbour and dipolar models relates to the ordering of the  $\beta$  chains in the latter but not in the former.

#### 7.4.2. *Magnetization Measurements Above $T = 1K$*

It was first shown by Cornelius and Gardner<sup>46</sup> that the magnetization curves of  $\text{Ho}_2\text{Ti}_2\text{O}_7$  near 2 K bear a striking qualitative resemblance to the predictions of the near neighbour model<sup>38</sup>, although the saturation magnetizations measured in<sup>46</sup> were not in good agreement with the theory. This has recently been corrected by Petrenko *et al.*<sup>114</sup>, who re-measured the magnetization curves along the major symmetry directions [100] [110] and [001]. They found very good agreement with both the qualitative shape and saturation magnetization values of the near-neighbour spin ice model (see Fig. 7.24). In the mean time, Fukuzawa *et al.*<sup>64</sup> measured magnetization on single crystals of  $\text{Dy}_2\text{Ti}_2\text{O}_7$  (Fig. 7.25) and found excellent agreement with the predictions of the dipolar model which, at the temperatures considered, are qualitatively similar to those of the near neighbour model. The development of the [111] plateau state is a particularly noticeable feature of these curves. The plateau in  $\text{Dy}_2\text{Ti}_2\text{O}_7$  in Fig. 7.25 at 1.8 K is less visible than for  $\text{Ho}_2\text{Ti}_2\text{O}_7$  in Fig. 7.24 at 1.6 K since, as discussed above,  $\text{Ho}_2\text{Ti}_2\text{O}_7$

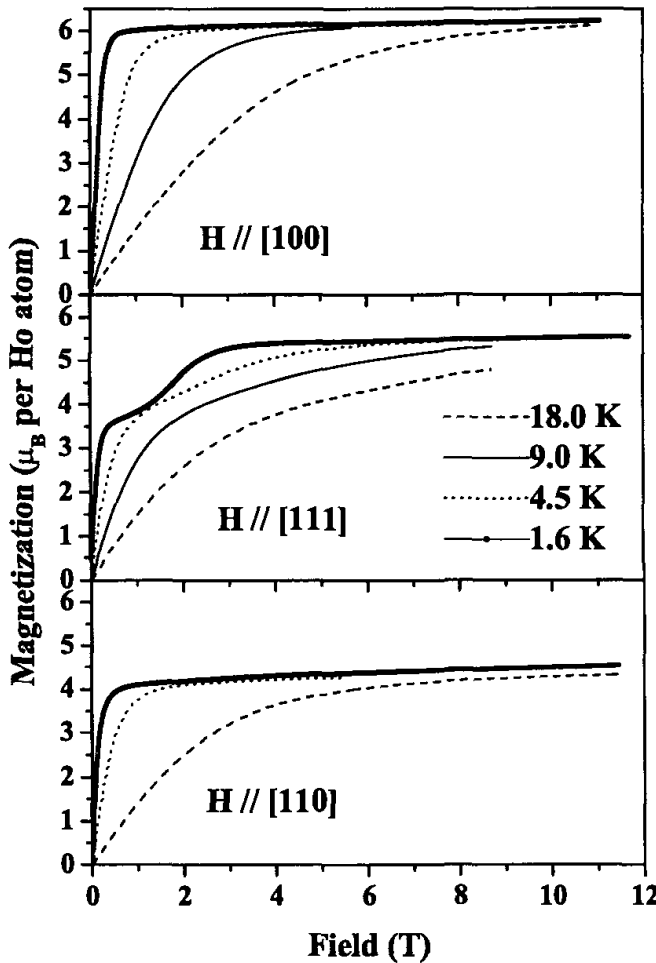


Fig. 7.24.  $\text{Ho}_2\text{Ti}_2\text{O}_7$ : Magnetization versus field curves (Ref. [114]), showing qualitative agreement with the theoretical predictions of Fig. 7.21.

enters the spin ice regime at  $T_{\text{peak}} \sim 1.9$  K while  $\text{Dy}_2\text{Ti}_2\text{O}_7$  is not yet really in the spin ice state at 1.8 K since it enters the spin ice regime below  $\sim T_{\text{peak}} \sim 1.2$  K.

#### 7.4.3. Bulk Measurements at Low Temperature

##### 7.4.3.1. [111] Direction

The most comprehensive bulk measurements in this regime are on the specific heat<sup>111,115,116</sup>. The application of a magnetic field generally results in a shift of the Schottky-like peak in the heat capacity to higher temperature as the energy cost of a spin flip is increased by the Zeeman splitting. The

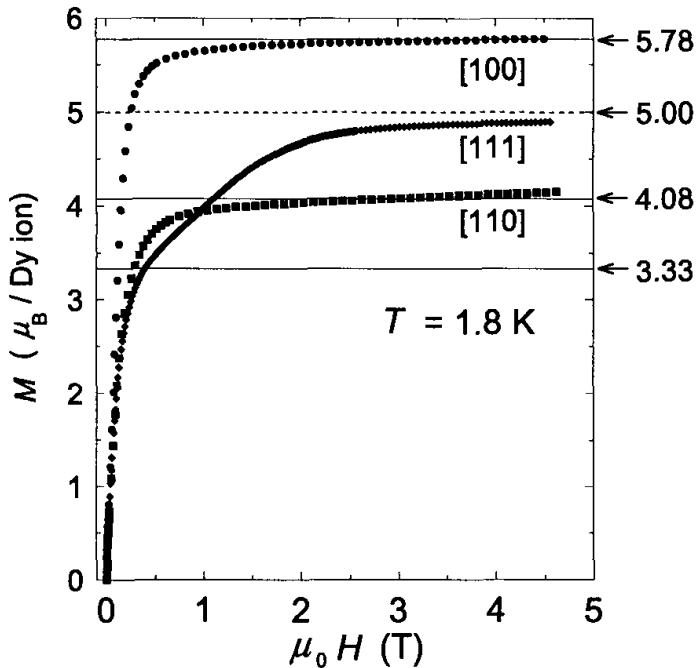


Fig. 7.25.  $\text{Dy}_2\text{Ti}_2\text{O}_7$ : Magnetization versus field curves (Ref. [64]), showing qualitative agreement with the theoretical predictions of Fig. 7.21. The curves have been justified in detail by a comparison with the dipolar spin ice model.

magnetic entropy can be determined by integrating the specific heat into the paramagnetic regime, as in Ref. [22]. This is particularly interesting when a field is applied along [111] such that the sample is in the plateau state (in reference to panel c of Fig. 7.21). Here one observes the entropy of “kagomé ice”, discussed below (Section 7.4.5.1). At high magnetic field ( $\sim 1$  T) it has been confirmed that all the entropy is eliminated, regardless of the direction of application of the field<sup>116</sup>. However, some anomalous effects have been noticed in the specific heat below 300 mK, that require further investigation<sup>117,118</sup>.

A significant paper by Sakakibara *et al.*<sup>119</sup> has examined the evolution of the bulk magnetization with the field applied along [111] at millikelvin temperatures. Remarkably, the increase in magnetization out of the plateau state to full saturation evolves into a first order transition below  $T_c = 0.36$  K, as shown in Fig. 7.26. As in the case of the predicted transition with field along [100]<sup>38</sup>, this transition with field along [111] is symmetry-sustaining and can be considered analogous to the liquid-gas transition. There is a line of first order transitions on the magnetization-field phase

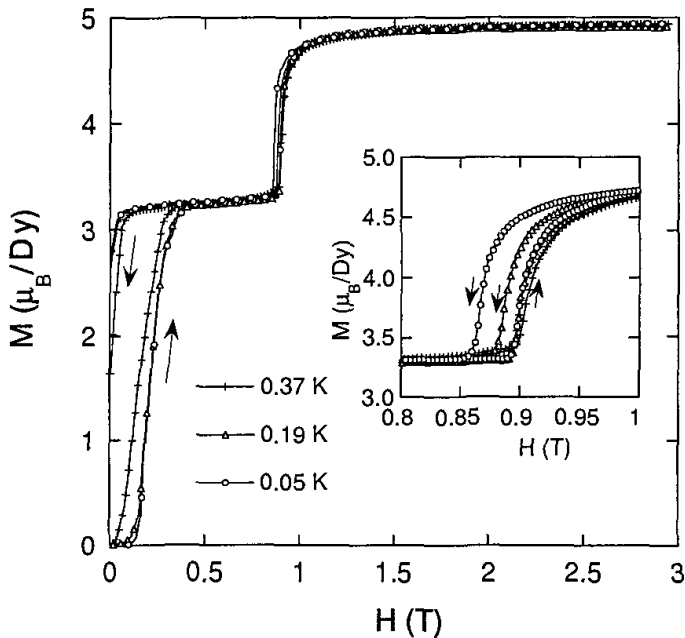


Fig. 7.26.  $\text{Dy}_2\text{Ti}_2\text{O}_7$ : Field applied along [111]. Magnetization versus field isotherms in the millikelvin temperature range showing the evolution of a first order phase transition between the magnetization plateau and saturation (Ref. [119]). Inset shows the field hysteresis around 0.9 T for the three temperatures that correspond to the main panel.

diagram with weak hysteresis. This line disappears at a critical point with divergent susceptibility at  $T_c = 0.36(2)$  K,  $H_c = 0.93$  T. The first-order line can be extrapolated to zero temperature at a finite field (0.905 T) (see Fig. 7.27.) The authors found that the phase transition lies outside the spin ice regime of very strong history dependence. It is this feature that makes the transition easily observable: although Harris *et al.*<sup>38</sup> predicted a liquid-gas type transition for the field applied on [100] rather than [111], it seems that any transition in the [100] direction would be affected by strong history dependence and thus be hard to establish with certainty (see Section 7.4.3.3). Further experimental results regarding this phase transition are discussed in Section 7.4.5.3.

The temperature and field dependence of the [111] phase transition may be calculated by a simple thermodynamic argument<sup>115</sup>. The molar entropy (per Dy) of the plateau state is  $S_k = 0.65 \text{ J K}^{-1} \text{ mol}^{-1}$  (see below) while its molar field energy is  $U_1 = -(10/3)\mu_B H N_A \text{ J mol}^{-1}$  (here  $N_A$  is Avogadro's number). That of the saturated state is zero and  $U_s = -(10/2)\mu_B H N_A \text{ J mol}^{-1}$  respectively. There is also an energy change in passing through the transition, arising from the combined exchange and dipolar couplings:

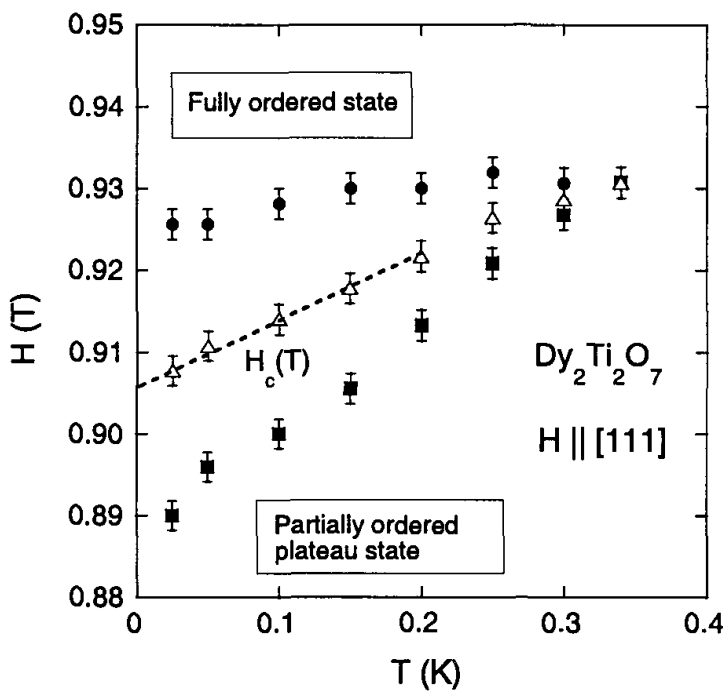


Fig. 7.27.  $\text{Dy}_2\text{Ti}_2\text{O}_7$ : Field applied along [111]. Magnetic phase diagram showing a line of first order phase transitions terminating in a critical end point (Ref. [119]).

$J_{\text{eff}} = J_{\text{nn}} + D_{\text{nn}} = 2.35 \text{ K} - 1.24 \text{ K} = 1.1 \text{ K}$  equivalent to  $U_0 = 1.1 \text{ K} k_B N_A$  ( $\text{J mol}^{-1}$ ). The molar Gibbs functions of the kagomé (k) and saturated (s) states are:

$$G_k = U_0 + U_1 - TS_k \quad (11)$$

$$G_s = U_s \quad (12)$$

Solving these equations gives a zero temperature transition at  $\mu_0 H = 0.98 \text{ T}$  and a slope of the first order line of  $\mu_0 dH_c/dT = 0.070 \text{ TK}^{-1}$ , in good agreement with the experimental values 0.905, 0.08 respectively. This argument suggests that the phase transition might be contained in the near neighbour spin ice model even though it was not observed in<sup>38</sup>. This point is discussed further in Section 7.4.5.3.

We finally mention a very recent report that has found another susceptibility peak at slightly higher fields than the first order line in  $Dy_2Ti_2O_7$ : currently the origin of this peak is not clear<sup>117,118</sup>.

#### 7.4.3.2. [110] Direction

A specific heat study of  $Dy_2Ti_2O_7$  in a magnetic field applied along [110] has been reported<sup>120</sup>. In this direction, as explained above, the system forms two sets of canted ferromagnetic chains: one in which the chains run parallel to the field and one in which the chains run perpendicular to it. These chains are conveniently labeled  $\alpha$  and  $\beta$  respectively<sup>120</sup>. The spins in the  $\alpha$  chains have a large component on the applied field and are pinned by it for sufficiently strong fields and sufficiently low temperature. The spins in the  $\beta$  chains are strictly perpendicular to the applied field. Hiroi *et al.*<sup>120</sup> argue that the  $\beta$  chains behave to a first approximation as an assembly of independent Ising ferromagnetic chains. In an applied field of  $\mu_0 H = B_0 = 1.5$  T they observe two peaks: one at  $\sim 7$  K which is ascribed to freezing of the spins on the  $\alpha$  chains, and a second at just above 1 K that is argued to arise from the development of correlations among the spins on the  $\beta$  chains. However this peak is much sharper than the Schottky-like peak expected for a one dimensional Ising model, even with the inclusion of further neighbour interactions. An experimentally deduced phase diagram<sup>120</sup> is shown in Fig. 7.28. Note that none of the phases indicated on the experimental phase diagram are fully ordered phases. This contrasts with the theoretical phase diagram for the dipolar spin ice model recently determined by Yoshida *et al.*<sup>112</sup> and discussed in Section 7.4.1.2 above.

#### 7.4.3.3. [100] Direction

Higashinaka *et al.* have reported a study of the specific heat of  $Dy_2Ti_2O_7$  in a magnetic field applied on [100]<sup>121</sup>. Unlike the numerical results of the near neighbour model (Figure 7.22), the experimental data revealed only one peak at all values of the applied field (0 - 5 T) in the temperature range  $T > 0.35$  K. A single Schottky-like peak was observed to shift to higher temperatures with increasing field, corresponding to a shift of the dominant energy scale from nearest neighbour ferromagnetic interactions to the Zeeman energy of a single spin. Despite the absence of any observed phase transition, it is perhaps premature to completely rule out the possibility of a “liquid-gas” phase transition of the type predicted for the near neighbour model (and actually observed with the field along [111]- see above) until these data have been extended to a lower temperature.

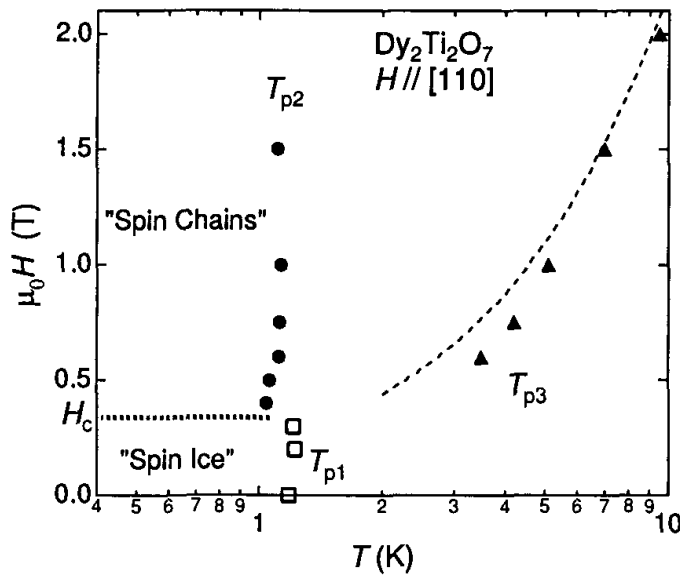


Fig. 7.28.  $\text{Dy}_2\text{Ti}_2\text{O}_7$ : phase diagram for a field applied along [110] showing three lines of specific heat maxima:  $T_{p1}$ ,  $T_{p2}$ ,  $T_{p3}$ , arising from spin ice freezing and formation of  $\beta$  and  $\alpha$  chains respectively (Ref. [120]). Note that none of the phases indicated are fully ordered phases.

#### 7.4.3.4. [211] Direction

The [211] direction bisects a triangular face of the elementary tetrahedron of the pyrochlore lattice. Therefore, for strong fields applied along [211], for each tetrahedron, three spins are frozen by the field and one spin is perpendicular to the field. One might again expect in this case a low temperature transition since 1/4 spins are decoupled from the external applied field. Such a field configuration was studied in Ref. [121]. No sign of a transition above 0.3 K was observed: only a broad specific heat anomaly around 1.7 K. Very recent theoretical work on the dipolar model by Ruff *et al.*<sup>113</sup> confirms that while a [211] field is perpendicular to one sublattice, there is an internal exchange plus dipolar field that enforces the ice rules, and which results in a Schottky anomaly at 1.7 K, as observed experimentally<sup>121</sup>. The same work<sup>113</sup> suggests that a detuning of the large field from perfect perpendicular alignment causes cancellation of this zero temperature internal exchange plus dipolar field, giving rise to a sharp crossover to a dipolar ferromagnetic ground state at a temperature of 0.6 K in the limit of large field<sup>113</sup>. This feature is a crossover and not a true phase transi-

tion since the component of the detuned field away from perfect alignment over compensates the exchange plus dipolar field at all nonzero temperatures. Consequently, the global symmetry is broken at all temperatures with the magnetization along the small detuned field component. The addition of a small third nearest-neighbour antiferromagnetic exchange coupling,  $J_3 = -0.02$  K, brings the transition down to 0.35 K, the temperature at which a feature is observed in powder specific heat experiments<sup>22</sup>. More experimental single crystal work is needed to demonstrate the validity of this detuned field idea and also its relevance to the powder specific heat experiment<sup>22</sup> discussed in the next section.

#### 7.4.3.5. Powder Measurements

In a sufficiently homogenous powder, an applied field couples to crystallites that collectively represent all crystallographic directions. Therefore powder measurements give some qualitative guide to the overall behaviour. Three notable features were found in powder specific heat measurements on  $\text{Dy}_2\text{Ti}_2\text{O}_7$  in a field<sup>22</sup>. Firstly, a sharp peak at 0.35 K that develops below 0.75 T, remains at the same temperature and to a large extent is unaffected in its shape up to fields of 7 T. Secondly, another feature at a temperature of 0.5 K first develops for a field of 1 T and has essentially disappeared above 3 T. Finally, a third feature is observed at 1.2 K that first develops at 0.5 T and remain noticeable up to 6 Tesla, although it is never as sharp as the 0.35 K sharp peak.

It was proposed in Ref. [22] that some of these three specific heat features might originate from microcrystals of the powder sample that are oriented along, for example, the [110] and [211] directions, such that a finite proportion of all the spins are perpendicular to the magnetic field. It currently appears that the 1.2 K feature in powder specific heat experiment may indeed be related to fields along  $\langle 110 \rangle$  directions<sup>112,113,120</sup>, while the origin of the 0.35 K feature is still in need of investigation<sup>113</sup>. It also seems that the 0.5 K feature is related to the kagomé ice physics that occur for a field aligned along a  $\langle 111 \rangle$  direction (see Section 7.4.5 below, dedicated to kagomé ice)<sup>117</sup>. In particular, a sharp specific heat peak at  $\sim 0.5$  K is observed for a field of  $B_c \sim 1$  T. This field corresponds to the critical field  $B_c$  for the zero temperature transition from the plateau state to the aligned state which breaks the ice rules (see Section 7.4.3.1).

#### 7.4.4. Neutron Scattering Results

##### 7.4.4.1. [110] Direction

As described above, the expectation from the near neighbour spin ice model is for parallel or  $\alpha$  chains to be “pinned” by the field, while uncorrelated perpendicular or  $\beta$  chains develop as a result of the ice rules. For both  $\text{Ho}_2\text{Ti}_2\text{O}_7$  and  $\text{Dy}_2\text{Ti}_2\text{O}_7$  neutron scattering<sup>4,57,107,122</sup> reveals the growth of Bragg peaks at the Brillouin zone centers, ( $Q = 0$ ), arising from the  $\alpha$  chains formed when the field is applied. The  $\beta$  chains separately give rise to broader peaks at the  $Q = X$  positions. The scattering from a crystal of  $^{162}\text{Dy}_2\text{Ti}_2\text{O}_7$  is illustrated in Figure 7.29. The  $Q = X$  peaks from the  $\beta$  chains are narrow (though not quite resolution limited) in the direction parallel to the  $\beta$  chain direction and much broader in the perpendicular direction. This indicates very long range correlations within the chains and much shorter range correlations between chains. The respective correlation lengths can be estimated by fitting the peak shape. They extend for 1200 Å and 16 Å at  $T = 0.05$  K,  $B_0 = 1.5$  T<sup>122</sup>.

Based on recent numerical work<sup>112,113</sup>, one would conclude that the correlations between  $\beta$  chains are induced by the long range dipolar interaction. It is found experimentally that the degree of order can be increased by annealing at elevated temperature ( $\sim 1$  K) or repetitive field-cycling at 50 mK<sup>122</sup>. However, true long range order is never established. It has been pointed out<sup>120,122</sup> that the  $\beta$  chains themselves occupy an almost undistorted triangular lattice, and hence the absence of true long range order might reflect the geometric frustration inherent to this system. At low temperature ( $\sim 50$  mK), for both  $\text{Ho}_2\text{Ti}_2\text{O}_7$  and  $\text{Dy}_2\text{Ti}_2\text{O}_7$ , the growth of Bragg peaks in an applied field is discontinuous, with at least two, and possibly several, abrupt jumps in the Bragg intensity as a function of field<sup>107,122</sup>. These may be indicative of first order phase transitions. It is also interesting to note that the  $Q = 0$  Bragg intensity shows hysteresis: the diffracted intensity is related to the square of the magnetization  $\vec{M}$ , so one observes something similar to  $\vec{M}^2$  versus  $B_0$ . The pristine<sup>d</sup> “magnetization” curve unusually lies outside the hysteresis loop measured after field cycling. Hence, the zero field cooled spin ice state is much harder to magnetize than the field-cycled state.

---

<sup>d</sup>i.e. the initial magnetization curve in the first quadrant of the hysteresis loop, with field increasing

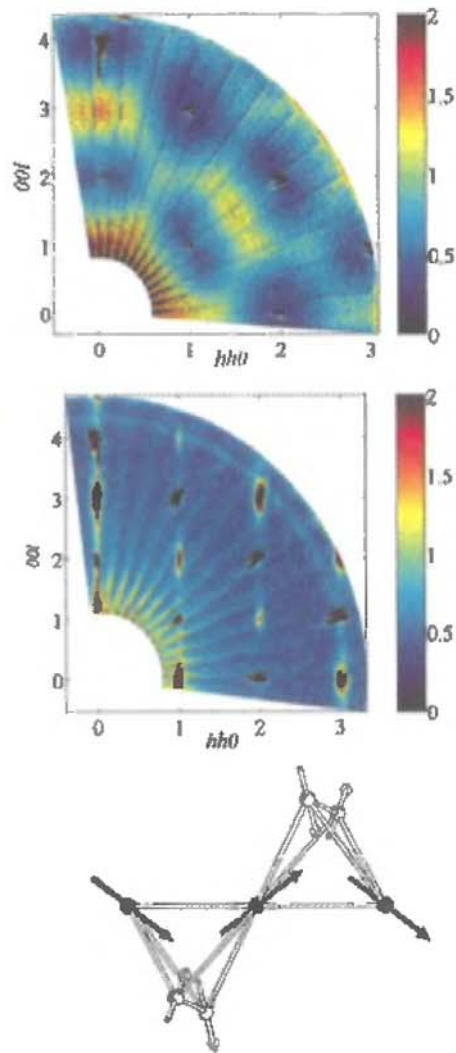


**Fig. 7.29.**  $\text{Dy}_2\text{Ti}_2\text{O}_7$ : Neutron scattering in the  $hhl$  plane in zero field and a field applied parallel to  $[1\bar{1}0]$  (i.e. perpendicular to the plane of this picture) (Ref. [122]). Blue is the lowest intensity, brown the highest. In zero field the Bragg peaks observed have no magnetic contribution. The figure illustrates the broad features of the zero field spin ice state (upper panel) replaced in an applied field of 1.5 T (middle panel) by strong magnetic Bragg scattering at the  $Q = 0$  positions ( $hkl$  all odd or all even) and broader scattering (extended along  $00l$ ) at the  $Q = X$  positions (the remaining positions with integer  $hkl$ ). These correspond to the  $\alpha$  and  $\beta$  chains respectively, as illustrated in the lower panel which is drawn in the same orientation (slightly offset for clarity) as the scattering map. Dark spins represent  $\beta$  chains, light spins represent  $\alpha$  chains.

For temperatures above 0.4 K, the neutron scattering of Refs. [57,107,122] and the bulk measurements of Ref. [120] are in reasonable agreement regarding the general features of the phase diagram shown in Figure 7.28. That is, there are four disordered regimes, as shown in the Figure. At higher temperatures ( $T > 4$  K) the integrated magnetic intensity of the (220) reflection of  $\text{Dy}_2\text{Ti}_2\text{O}_7$  collapses onto a single function of  $\mu_0 H/T$  showing that, in this temperature range, the spin-spin coupling is unimportant and the induced moment represents the paramagnetic response of single ions<sup>57</sup>.

#### 7.4.4.2. [100], [111] and [211] Directions

Fennell<sup>122</sup> has recently studied fields applied along the [100] direction, in  $\text{Dy}_2\text{Ti}_2\text{O}_7$  and [100], [111] and [211] directions in  $\text{Ho}_2\text{Ti}_2\text{O}_7$ .

On the application of a magnetic field to  $\text{Ho}_2\text{Ti}_2\text{O}_7$  and  $\text{Dy}_2\text{Ti}_2\text{O}_7$  along the easy [100] direction, the spins are ordered in a canted ferromagnetic state giving rise to Bragg peaks at the Brillouin zone centers ( $Q = 0$ ). Their intensity saturates above  $B_0 = 0.5$  T. Below  $T = 0.3$  K hysteresis is observed, and below 1.5 K, one or possibly two distinct jumps in the Bragg intensity develop as a function of field. It is possible that these are related to the predicted first order liquid-gas type transition<sup>38</sup> but this is hard to demonstrate convincingly because of the very strong history dependence. With the field along [111],  $\text{Ho}_2\text{Ti}_2\text{O}_7$  shows the expected two step saturation growth of  $Q = 0$  Bragg peaks below  $\sim 2$  K. With the field applied along [211] one spin is perpendicular to the field and the other three are “pinned” by it into a two-in, one-out configuration. The neutron Bragg intensities are consistent with processes that involve the ordering of the perpendicular spin according to the ice rules as a function of field or temperature.

#### 7.4.5. Kagomé Ice

The existence and characterisation of kagomé ice is one of the most remarkable recent developments in the physics of spin ice. Wills *et al.*<sup>123</sup> were the first to conceive of a two dimensional spin ice model (see below) while Matsuhira *et al.*<sup>111</sup> later formulated a similar model and applied it to the [111] plateau state of the spin ice materials; one should also mention the contribution of Higashinaka *et al.*<sup>116</sup>. In the context of this review, it therefore seems appropriate to start with the real pyrochlore materials with field along [111], and show how these relate to the idealised model of Wills *et al.*

#### 7.4.5.1. Basic Kagomé Ice Model and Mappings

Matsuhira *et al.*<sup>111</sup> pointed out that the [111] plateau state of spin ice, should, according to the ice rules, retain a zero point entropy. To see this, note that when projected along [111], the pyrochlore lattice can be considered as an assembly of kagomé lattice planes (i.e. planes of corner-linked triangles) decorated by spins alternately above and below the plane to form “up” and “down” tetrahedra (see Fig. 7.30). The plateau state corresponds to the alignment of the apical spin in each tetrahedron, so if the field is “up” then this spin points “out” on an up tetrahedron and “in” on a down tetrahedron. To obey the ice rules the remaining spins (three per tetrahedron) in the kagomé plane must adopt the configuration in-in-out or in-out-out on up and down tetrahedra respectively. This leaves an intra-tetrahedron degree of freedom analogous to that in Pauling’s model and leads to a zero point entropy. The “in-plane” spins do not lie precisely in the kagomé plane, leading to a slight energetic preference in the applied field for (say) in-in-out over out-in-in (because, depending on whether one is discussing an “up” or “down” tetrahedron, one of these will have a larger component on the field). However, it is assumed this effect is dominated by the ice rules. A kagomé ice state projected onto the [111] plane is illustrated in Fig. 7.31.

It is clear, therefore, that this situation closely resembles the idealised two-dimensional model defined by Wills *et al.*<sup>123</sup> and termed “kagomé spin ice”. In this model, one has spins on a kagomé lattice directed along the bisectors of the equilateral triangles and ferromagnetically coupled, as in spin ice itself. Wills *et al.* also considered the effect of magnetic fields and further neighbour interactions on this model and argued that the model might be relevant to vanadium jarosite materials.

The kagomé spin ice model of Wills *et al.* can be mapped on to the model of two A ions and one B ion occupying the kagomé lattice such that the number of AB interactions is maximized. As mentioned in Section 7.2.3.2, this model was considered by Anderson who mapped it onto Wannier’s solution of the triangular Ising antiferromagnet. To understand this mapping, place a lattice point at the center of every hexagon in the kagomé lattice and position  $+/-$  variables such that each triangle has, at random, either  $++-$  or  $-++$ . The new lattice is a triangular lattice with the  $+/-$  variables forming one of the many degenerate ground states of Wannier’s antiferromagnet. The kagomé lattice points lie on the mid-

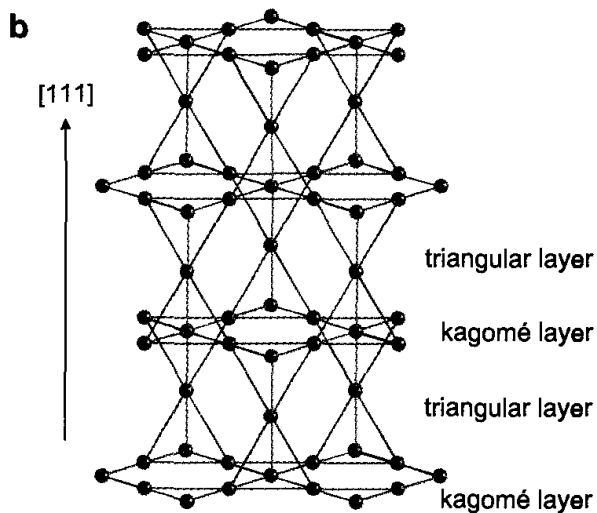


Fig. 7.30. Illustration of how the pyrochlore lattice can be regarded as an assembly of kagomé planes decorated by interstitial spins, when viewed along [111] (Ref. [111]).

points of the bonds of this triangular lattice, so if an  $+-$  bond is denoted A and a  $--$  or  $++$  bond denoted B, then the kagomé lattice is populated by A/B variables such that each triangle has AAB, as required. The merit

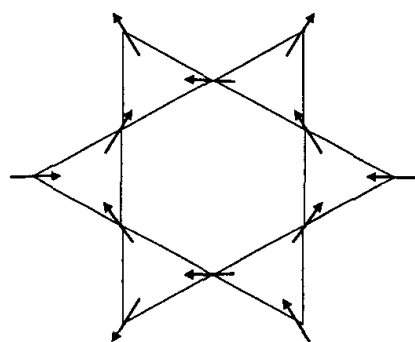


Fig. 7.31. A state of the kagomé spin ice model

of mapping on to Wannier's model is that the latter is exactly solved with intensive molar zero point entropy  $0.32306 R^2$ , which translates as 0.1077

R in Wills *et al.*'s model or 0.08077 R for kagomé ice on the pyrochlore lattice. This result can alternatively be obtained by mapping onto a model of dimers that populates the bonds of the honeycomb lattice occupied by the centers of the triangles<sup>124</sup>.

#### 7.4.5.2. Experimental Results: Specific Heat

Matsuhiro *et al.*<sup>111</sup> measured the zero point entropy of Dy<sub>2</sub>Ti<sub>2</sub>O<sub>7</sub> as a function of field applied on [111] by integrating the specific heat. They found that the entropy falls from approximately Pauling's value in zero field to the value  $0.8 \pm 0.1 \text{ JK}^{-1}$  per mole of Dy in the plateau state for applied fields between 0.25 and 0.75 T (see Fig. 7.32). This value was later refined to  $0.65 \pm 0.1$  by more detailed subtraction of a background from the specific heat<sup>115</sup>. This estimate corresponds to an entropy 0.078 R per mole of Dy, which is very close to the theoretical value 0.081 R (see previous section). These results constitute excellent evidence for the existence of the kagomé ice state in this material. The transition from the kagomé ice state with increasing magnetic field was discussed earlier in Section 7.4.3.1 and in the next section.

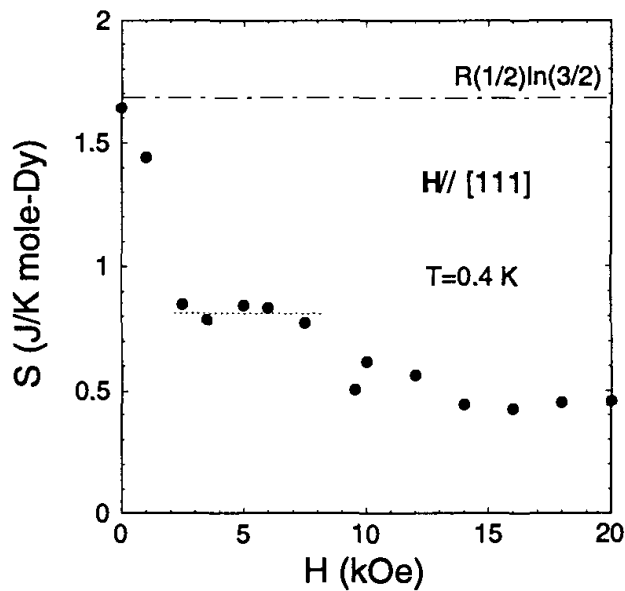


Fig. 7.32. Dy<sub>2</sub>Ti<sub>2</sub>O<sub>7</sub>: Specific heat versus applied field along [111] (from Ref. [111]) showing a value in the "plateau state" (dotted line) that is consistent with kagomé ice behaviour.

#### 7.4.5.3. Theory of the Kagomé Ice State: Kastelyn Transition

It is now well understood that the application of a magnetic field along the [111] direction in the spin ice compounds leads to two magnetization plateaux at low temperatures ( $T \ll J_{\text{eff}}$ ) and as a function of applied magnetic field. The plateau at strong field corresponds to the maximally polarized three in, one out state (in reference to an “up” tetrahedron). The entropy of the low field plateau (the kagomé ice state) is reduced compared to the zero field spin ice state, but is still extensive. Recent theoretical work by Moessner and Sondhi<sup>125</sup> and Isakov *et al.*<sup>126</sup> has revealed some remarkable features of spin ice in this regime. In Ref. [125] the available degrees of freedom, which in the low field plateau live on decoupled kagomé planes, are mapped to hard core dimers on a honeycomb lattice. The resulting two dimensional kagomé ice state is found to be critical. Small tilts of the applied field at low temperature away from perfect [111] alignment lead to a vanishing of the entropy and the termination of the critical phase by a “Kasteleyn” transition characterized by highly anisotropic scaling. Ref. [126] has considered the crossovers between the different plateau regimes from a point of view of (entropically) interacting defects. It was found in an analytical theory for the nearest-neighbour spin ice model, which covers most of the magnetization curve, that the entropy is non-monotonic as a function of applied field, and exhibits a giant spike at the low-field plateau to high-field plateau transition. In other words, the entropy becomes much larger than its kagomé ice value (even exceeding the Pauling value) before finally falling to zero.

In very recent experimental work, the existence of an entropy spike has been confirmed. Aoki *et al.*<sup>127</sup> have used magnetocaloric effect measurements to make a very accurate determination of the entropy of  $\text{Dy}_2\text{Ti}_2\text{O}_7$  as a function of field as one crosses the critical line in Fig. 7.27. The experimental data are illustrated in Fig. 7.33. Although the observed spike is large (reaching 1 J/K·mol Dy at  $T = 500$  mK), it is smaller than that predicted theoretically (2.4 J/K·mol Dy) for the near neighbour model and falls with decreasing temperature, also in contrast to the theory. As described in Section 7.4.3.1, the experimental transition is first order while in the near neighbour model it appears to be a crossover. Thus, one could speculate that here too, the differences between experiment and theory may be a consequence of long range dipolar couplings.

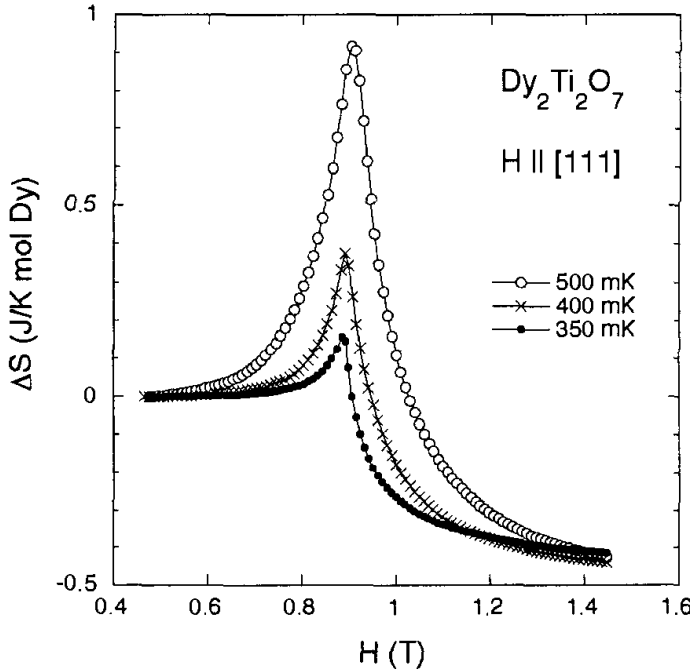


Fig. 7.33.  $\text{Dy}_2\text{Ti}_2\text{O}_7$ : change in entropy with a field along  $\langle 111 \rangle$  illustrating the giant entropy spike discussed in the text (Ref. [127]).

## 7.5. Spin Dynamics of the Spin Ice Materials

From an experimental perspective, the spin ice materials display extremely interesting dynamical properties, which are the subject of this section. We begin with some background to the experimental quantities of interest, before proceeding to describe the main experimental results.

### 7.5.1. Experimental Quantities of Interest

The purpose of this section is to briefly review, for the benefit of the non-expert reader, the quantities that are typically measured when probing the spin dynamics.

#### 7.5.1.1. Correlation Functions and Neutron Scattering

The thermal fluctuations of an equilibrium system may be specified by time and distance dependent correlation functions or equivalently by Fourier transformed correlation functions, depending on wave vector  $\mathbf{Q}$  and angular frequency  $\omega$ . The canonical experimental probe of a spin system is therefore neutron scattering, which in its conventional form can directly measure the spin correlation function  $S^{\alpha\beta}(\mathbf{Q}, \omega)$ , known in scattering the-

ory as the dynamic scattering function (here  $\alpha\beta = x, y, z$  specify the spin components). This function is defined as

$$S^{\alpha\beta}(\mathbf{Q}, \omega) = \frac{1}{2\pi N} \int \langle S^\alpha(-\mathbf{Q}, 0) S^\beta(\mathbf{Q}, t) \rangle \exp(i\omega t) dt \quad (13)$$

where  $\langle \dots \rangle$  is a thermal average, and  $S^\alpha(\mathbf{Q}, t)$  a Fourier spin component at time  $t$ . The dynamic scattering function contains a detailed microscopic description of the spin dynamics of a given system at equilibrium.

#### 7.5.1.2. Fluctuation-Dissipation Theorem and AC-Susceptibility

The diffuse part of  $S(\mathbf{Q}, \omega)$  (for compactness we have dropped the labels  $\alpha, \beta$ ) can be related by the fluctuation-dissipation theorem to the imaginary part of the generalized susceptibility  $\chi(\mathbf{Q}, \omega)$ , by the relation

$$S_{\text{diffuse}}(\mathbf{Q}, \omega) = \frac{\hbar}{\pi g^2 \mu_B^2} \frac{1}{1 - \exp(-\hbar\omega/k_B T)} \chi''(\mathbf{Q}, \omega). \quad (14)$$

This relationship expresses the very important fact that the linear response of a system magnetization  $M(\mathbf{Q}, \omega)$  to weak applied fields  $h(\mathbf{Q}, \omega)$  is completely determined by the equilibrium correlation functions. Physically this arises because, to first order in perturbation theory, the system does not distinguish between a perturbation to the spin structure caused by a thermal fluctuation and one caused by an external field. This is useful as it means that the equilibrium fluctuations can also be probed by the direct application of a laboratory field  $h(0, \omega)$ . Typically, one performs frequency dependent (AC) susceptibility measurements which directly yield both  $\chi'(0, \omega)$  and  $\chi''(0, \omega)$ . These two functions are inter-related by the Kramers-Kronig relations and so either contains a complete description of the response of the Fourier component  $M(0, \omega)$ . The advantage of AC-susceptibility is that it can probe a frequency range inaccessible to neutron scattering ( $< 10^6$  Hz) while its limitation is that it is a bulk measurement: information on the spatial correlations are averaged out of the problem.

#### 7.5.1.3. Spectral Shape Function

In practical terms it is convenient to separate statics and dynamics and consider a wave vector dependent susceptibility  $\chi(\mathbf{Q})$  and a normalized spectral shape function  $F(\mathbf{Q}, \omega)$ . The quantity  $\chi(\mathbf{Q})$  may be measured by collecting scattered neutrons of all energies, which under suitable conditions

is equivalent to integrating  $S(\mathbf{Q}, \omega)$  over  $\omega$ , while  $F(\mathbf{Q}, \omega)$  can be measured by examining the spectrum of scattered neutrons at fixed scattering vector  $\mathbf{Q}$ . The diffuse scattering function is written

$$S_{\text{diffuse}}(\mathbf{Q}, \omega) = \frac{kT}{g^2 \mu_B^2} \chi(\mathbf{Q}) \frac{\hbar\omega}{1 - \exp(-\hbar\omega/k_B T)} F(\mathbf{Q}, \omega). \quad (15)$$

The Fourier transform of  $F(\mathbf{Q}, \omega)$  is the quantity  $F(\mathbf{Q}, t)$ , a measure of how a spin component  $S(\mathbf{Q}, t)$  relaxes after a perturbation. It is equal to the “intermediate scattering function”,  $S(\mathbf{Q}, t)$  divided by its value at  $t = 0$ , and can be determined directly by the technique of neutron spin echo (NSE).

#### 7.5.1.4. Exponential Relaxation

The simplest type of relaxation occurs when a field is turned off at time  $t = 0$  and  $S(\mathbf{Q}, t)$  relaxes exponentially. With single ion dynamics there is no wave vector dependence, and the following relations apply:

$$F(\mathbf{Q}, t) = \exp(-\Gamma t) \quad (16)$$

$$S(Q, \omega) \approx k_B T \chi(Q) \frac{\Gamma}{\omega^2 + \Gamma^2} \quad (\text{assuming } k_B T \gg \hbar\omega) \quad (17)$$

$$\chi'(0, \omega) = \chi(0) \frac{\Gamma^2}{\omega^2 + \Gamma^2} \quad (18)$$

$$\chi''(0, \omega) = \chi(0) \frac{\omega\Gamma}{\omega^2 + \Gamma^2} \quad (19)$$

exponential relaxation of this sort is often assumed in phenomenological approaches and arises typically in diffusion problems, for example the case of Arrhenius relaxation across a barrier with attempt frequency  $\Gamma = \Gamma_0 \exp(-\Delta/k_B T)$ . It also arises in the analogous case of the electrical field response of non-interacting dipolar liquids (Debye relaxation). Departure from this form may be revealed by a Cole-Cole plot of  $\chi'$  vs  $\chi''$  which should be semicircular for pure exponential relaxation. A phenomenological extension of this concept is the Davidson-Cole formalism<sup>128,129</sup> which assumes  $\chi = \chi(0)/(1 + i\omega t_c)^\beta$ . The case  $\beta = 1$  corresponds to a single exponential relaxation while  $0 < \beta < 1$  corresponds to a distribution of exponential relaxation times with  $t_c$  being an upper cut off.

### 7.5.2. Differences Between $\text{Ho}_2\text{Ti}_2\text{O}_7$ and $\text{Dy}_2\text{Ti}_2\text{O}_7$

Early approaches to the spin dynamics of the spin ice materials were complicated by an apparent difference between  $\text{Ho}_2\text{Ti}_2\text{O}_7$  and  $\text{Dy}_2\text{Ti}_2\text{O}_7$ . It is now clear that the behaviour of the two materials is qualitatively the same, except perhaps in the very low temperature range where hyperfine coupling becomes important (see Section 7.5.5.2). Hence, in the following, we organize the discussion in a logical sense as a function of temperature range, rather than discussing the various spin ice materials individually.

### 7.5.3. Relaxation at High Temperature, $T \sim 15$ K and Above

#### 7.5.3.1. AC-Susceptibility ( $AC-\chi$ )

It came as a surprise in 2001 when two papers – by Matsuhira *et al.*<sup>130</sup> and Snyder *et al.*<sup>131</sup> – reported a peak in AC-susceptibility of polycrystalline  $\text{Dy}_2\text{Ti}_2\text{O}_7$  near to 15 K, suggestive of spin freezing, but at a temperature scale well above that expected for spin ice. This feature is henceforth referred to as “the 15 K peak” although it should be noted that its peak temperature shifts with frequency as illustrated in Figure 7.34. The frequency shift of the 15 K peak can be described by an Arrhenius law, with activation energy  $E_a = 220$  K<sup>130,131</sup>. It is accompanied by a semicircular Cole-Cole plot corresponding to a single exponential relaxation. An initial interpretation<sup>131</sup> was that the cooperative spin ice freezing was already occurring at this high temperature, but this interpretation was later shown to be inconsistent with direct microscopic measurement of the spin correlations<sup>79</sup> (see below). The 15 K peak is not clearly visible in the case of  $\text{Ho}_2\text{Ti}_2\text{O}_7$  but it can be revealed by the application of a magnetic field to single crystal samples<sup>79</sup>, giving an activation barrier of  $\sim 250$  K. The reason for the difference between  $\text{Ho}_2\text{Ti}_2\text{O}_7$  and  $\text{Dy}_2\text{Ti}_2\text{O}_7$  is discussed further in Section 7.34 below.

#### 7.5.3.2. Neutron Spin Echo (NSE)

Ehlers *et al.* used NSE to determine the microscopic origin of the high temperature spin dynamics of a polycrystalline sample of  $\text{Ho}_2\text{Ti}_2\text{O}_7$ , measured over a temperature range 0.3 K - 200 K<sup>79</sup>. Further experimental work extended this range to 800 K<sup>132</sup>. As expected from<sup>130,131</sup>, these experiments revealed a single exponential decay with approximate Arrhenius activation

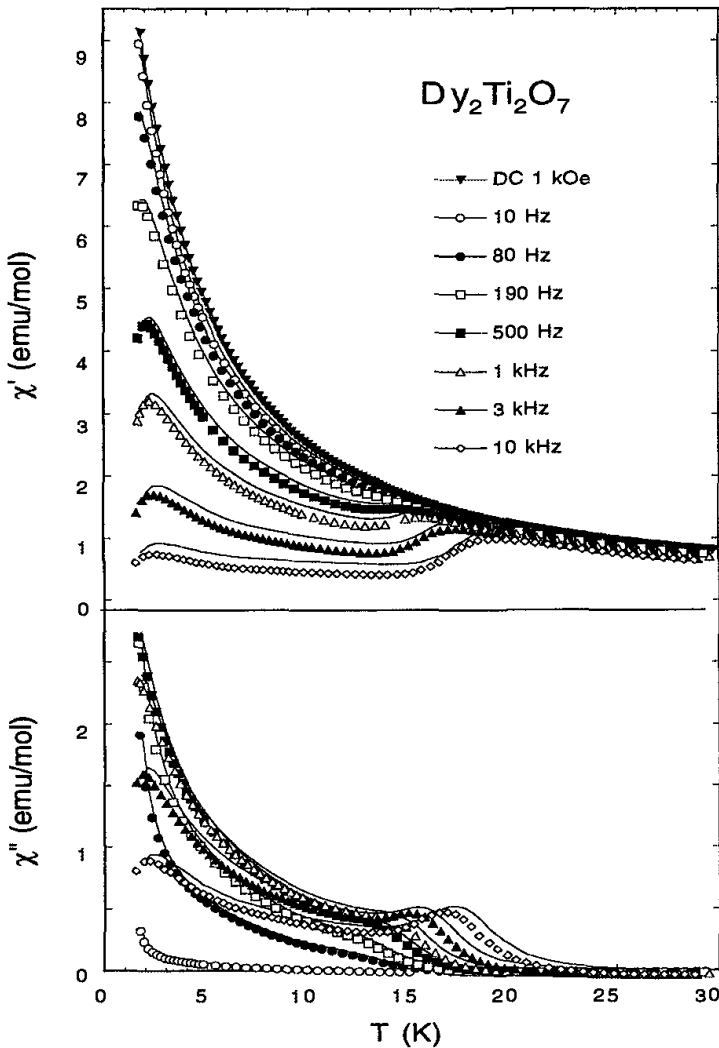


Fig. 7.34.  $\text{Dy}_2\text{Ti}_2\text{O}_7$ : AC-susceptibility (upper panel:  $\chi'$ , lower panel  $\chi''$ ) as a function of temperature at several frequencies, illustrating the “15 K peak” (Ref. [130]).

79.

$$F(\mathbf{Q}, t) = (1 - A) \exp(-\Gamma t) \quad (20)$$

with  $A = 0.09(1)$ ,  $\Gamma = 21.1(2) \times 10^{11} \exp(-\Delta/k_B T)$  Hz, and  $\Delta/k_B = 293(12)$  K.

The Arrhenius behaviour of the correlation function  $F(Q, t)$  at  $t = 1$  ns is illustrated in Fig. 7.35. The neutron scattering was found to be  $Q$ -independent ( $Q = |\mathbf{Q}|$ ) which establishes that the single exponential decay is a single-ion phenomenon. In view of its energy scale  $\Delta$  matching that of the first set of excited crystal field levels (see Fig. 7.3), it is almost certainly

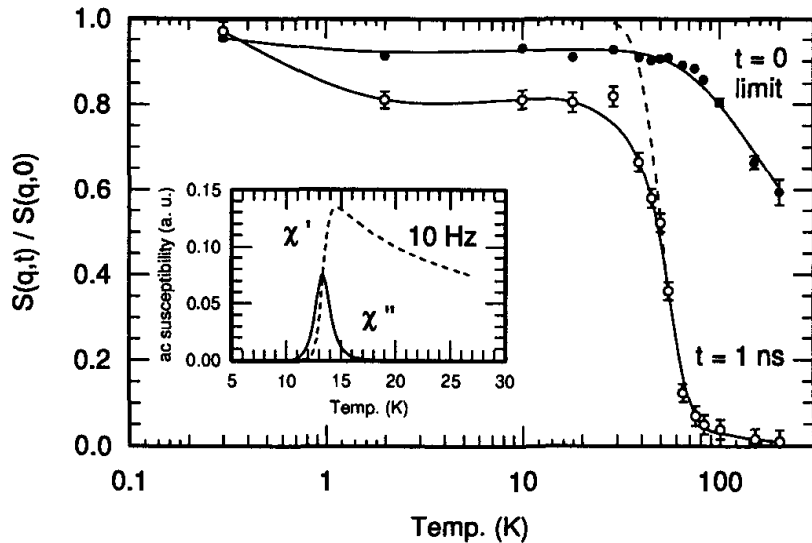


Fig. 7.35.  $\text{Ho}_2\text{Ti}_2\text{O}_7$ : Spin relaxation measured by neutron spin echo (NSE) (Ref. [132]) at  $t = 0$  and  $t = 1 \text{ ns}$ . Note the approximately athermal regime in the  $t = 1 \text{ ns}$  data below  $T = 15 \text{ K}$ . The blue dashed line represents Arrhenius kinetics and the inset the AC-susceptibility that corresponds to this approximation.

a spin reversal that involves promotion of a spin to these states followed by de-excitation. It would seem a reasonable assumption, as suggested in Ref. [79], that an analogous process occurs in  $\text{Dy}_2\text{Ti}_2\text{O}_7$ .

It is tempting to regard this process as activation over a quasiclassical barrier in a manner analogous to the large spin, single-molecule magnet “ $\text{Mn}_{12}$ ”<sup>35</sup>. In this system, the crystal field gives rise to a Stark-like<sup>e</sup> splitting of the  $|J, M_J\rangle$  levels giving a ladder of  $|\pm M_J\rangle$  states characterized by  $M_J = J, J - 1, \dots, 0$ . These states form what may be regarded as a quasiclassical barrier in that a classical spin reorientation involves surmounting the ladder of states in a sequential fashion. The spin ice materials share the property of an almost pure doublet ground state:  $|\pm 8\rangle$  and  $|\pm 15/2\rangle$  for Ho and Dy respectively. However, the excited states are generally complicated admixtures of other  $M_J$  levels, so at this point the analogy breaks down. Nevertheless, it should be realistic to regard the spin ice relaxation as a promotion to an excited level, a quantum spin rotation within that level and then de-excitation to give the net result of a spin flip. In this regard it would be useful to use the crystal field scheme of Rosenkranz *et al.*<sup>39</sup> to calculate the relaxation of the single ion system. It should also be noted

<sup>e</sup>The Stark effect of atomic spectroscopy involves the splitting of free-ion terms into  $|\pm M_J\rangle$  levels under the influence of a uniform electric field.

that the physical origin of the spin dynamics (i.e. the transition matrix element in the Fermi Golden rule) has not yet been established, although magnetoelastic interactions would appear to be a likely cause.

#### 7.5.3.3. *Origin of the 15 K AC-Susceptibility Peak*

As described above, the 15 K peak is observed in the low field AC susceptibility of  $\text{Dy}_2\text{Ti}_2\text{O}_7$  but not clearly in that of  $\text{Ho}_2\text{Ti}_2\text{O}_7$ . This alternate appearance and non-appearance of the 15 K peak in the spin ice materials contains a clue to its origin. The relaxation function of  $\text{Ho}_2\text{Ti}_2\text{O}_7$  determined by NSE in the frequency range  $10^9$ - $10^{12}$  Hz can be transformed to an AC-susceptibility (see section 5.1.4) and extrapolated to  $Q = 0$  and into the AC-susceptibility frequency window ( $\leq 10^5$  Hz). In that case it does predict a peak at 15 K and a rapid drop to zero below that temperature (see inset, Figure 7.35). Therefore both  $\text{Ho}_2\text{Ti}_2\text{O}_7$  and  $\text{Dy}_2\text{Ti}_2\text{O}_7$  exhibit a freezing of this “high temperature” relaxation process near to 15 K.

Why then does this freezing process give rise to a susceptibility peak in  $\text{Dy}_2\text{Ti}_2\text{O}_7$  but not in  $\text{Ho}_2\text{Ti}_2\text{O}_7$ ? We first observe that, mathematically, it is perfectly possible to formulate two relaxation functions of the same functional form but with slightly different parameters, one of which does give rise to a susceptibility peak and the other of which does not. In the present case, one should imagine the exponential decay function of the “high temperature” process ‘cut-off’ rather abruptly above some characteristic time  $t_c$ , which is approximately temperature-independent. As the temperature is lowered the exponential decay rate of the high temperature process decreases. If  $1/t_c$  lies to the low frequency side of the experimental (AC- $\chi$ ) frequency window there is a strong susceptibility peak because all the observed response is due to the high temperature process. However if  $1/t_c$  lies to the high frequency side, there is no peak as all the response is due to the low temperature process, characterised by  $t_c$ . Thus, to get a “no peak scenario” the form  $F(Q, t) = \exp(-E_a/k_B T)$  must be cut off in the range of frequencies that fall between the neutron and AC- $\chi$  experimental windows, and one can conclude that there is most likely an approximately temperature-independent relaxation process active in both  $\text{Ho}_2\text{Ti}_2\text{O}_7$  and  $\text{Dy}_2\text{Ti}_2\text{O}_7$  but with slightly different characteristic times. In agreement with this scenario, it has been found that the application of a magnetic field to  $\text{Ho}_2\text{Ti}_2\text{O}_7$  results in the clear appearance of the 15 K peak in this material<sup>79</sup>. The implication is that the applied field changes the rate of the low temperature process to bring  $t_c$  into the experimental window.

To summarise the argument, there are two distinct relaxation processes in the spin ice materials. these can be thought of as a high temperature thermally activated process and a lower temperature approximately athermal process. The slowing down of the high temperature process is observable as a “15 K peak” if the low temperature process is sufficiently slow to allow it to be visible. The rate of the low temperature process is characterised by a “cut off” in the spin relaxation function. The cut-off time scale  $t_c$  can be adjusted experimentally either by the application of a field, which drives it to lower frequency, revealing the 15 K peak, or possibly by doping with impurities (see below) which drives it to higher frequency, obscuring the 15 K peak. The simplest model consistent with these facts is a dynamical process that is approximately temperature-independent near 15 K, which is suppressed by an applied field<sup>79</sup>. At 15 K spin ice is strictly paramagnetic, with weak spin ice correlations starting to develop, but all spin configurations still highly populated. It has been suggested<sup>79</sup> that many spin configurations put an instantaneous strong transverse dipolar field on a given spin, giving rise to quantum mechanical tunneling dynamics, which take over from the Arrhenius dynamics below 15 K and are finally extinguished near 1 K, where the appropriate configurations are frozen out.

The NSE furnishes direct evidence for a quantum tunneling regime in that  $S(q, t = 1\text{ns})$  (Figure 7.35) becomes temperature independent below  $T = 15$  K before rising again (though not quite to unity - see below) as the build up of spin ice correlations occurs near to 2 K. Thus, it is established that the spin relaxation at 1 ns is approximately athermal over a broad temperature range which is evidence for a tunneling process. If this interpretation stands the test of time it represents a remarkably high temperature for such tunneling dynamics to be observed and also a remarkable case of tunneling induced by the dipolar interaction itself. The temperature scale is far in excess of that of  $\text{Mn}_{12}$ <sup>35</sup> or such systems as  $\text{LiHoF}_4$ <sup>34</sup>. The reason, of course, is the enormous crystal field splitting in the spin ice materials. However, if spin tunneling is involved it is not yet clear as to whether it can be thought of in terms of direct resonant transitions between essentially pure  $|\pm J\rangle$  states, or in terms of quantum rotations mediated by admixtures of other  $M_J$  states even in the absence of external or dipolar fields. Further evidence for tunneling is discussed in Section 7.5.4.2 below.

#### 7.5.4. Relaxation in the Range $1 \text{ K} \leq T \leq 15 \text{ K}$

In many ways this is the most interesting temperature range for the spin dynamics of the spin ice materials. As the temperature is lowered, single ion dynamics should give way to collective dynamics as the system organizes itself into the spin ice state. In this temperature range the spin-flip dynamics are mainly out of the dynamical range of neutron scattering techniques and one must rely on AC-susceptibility. However it is clear from neutron scattering that the static spin ice correlations develop strongly below about 1 K. These are characterised in the dynamics by a second susceptibility peak in this temperature range for  $\text{Ho}_2\text{Ti}_2\text{O}_7$ ,  $\text{Ho}_2\text{Sn}_2\text{O}_7$  and  $\text{Dy}_2\text{Ti}_2\text{O}_7$ , as illustrated in Fig. 7.36.

##### 7.5.4.1. AC-Susceptibility: Phenomenological Model

Assuming phenomenological Arrhenius dynamics, the frequency shift of the temperature of the “1K peak” corresponds to an activation energy of the order of 20 K in all three materials with an attempt frequency of the order  $10^{10}$  Hz. However, it is clear that below 15 K, there are multiple relaxation times in the samples, with strong deviations from a semicircular Cole-Cole plot. For  $\text{Dy}_2\text{Ti}_2\text{O}_7$ , Matsuhira *et al.*<sup>130</sup> used the Davidson-Cole formalism to reconstruct a distribution of relaxation times. These distributions broaden below  $T = 15 \text{ K}$ , with a range of frequencies below a rather sharp peak. This might indicate the relaxation of clusters, rather than single spins. However, it should be noted that while this phenomenological approach establishes that  $F(0, t)$  can be represented as a sum of exponentials; it does not necessarily mean that there really is a set of non-interacting Arrhenius-type processes in the sample. It has been pointed out by Cornelius that the crossover between a single time scale Arrhenius decay and multiple relaxation times is analogous to a transition from “strong” to “fragile” behaviour in glass-forming liquids<sup>133</sup>.

##### 7.5.4.2. AC-Susceptibility: Towards a Microscopic Model

Important evidence for the existence of the temperature regime of quantum tunneling suggested by Ehlers *et al.*<sup>79</sup>, has recently been provided by the discovery of a remarkable feature in the AC-susceptibility of polycrystalline  $\text{Dy}_2\text{Ti}_2\text{O}_7$ <sup>134</sup>. Initially, Snyder *et al.*<sup>134</sup> estimated the average relaxation time  $\tau$  in polycrystalline  $\text{Dy}_2\text{Ti}_2\text{O}_7$  from the maximum in  $\chi''$  and confirmed that this is approximately temperature independent below  $T = 15 \text{ K}$  (see

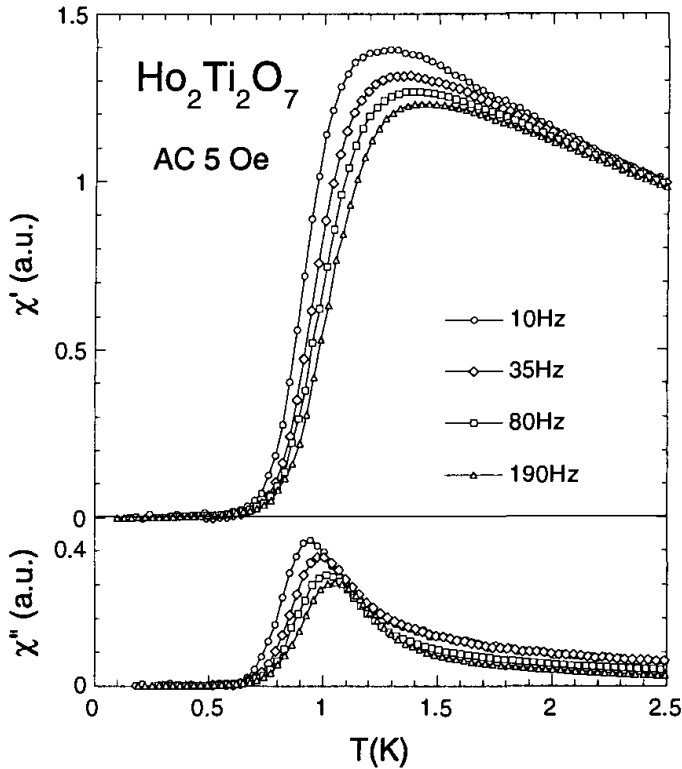


Fig. 7.36.  $\text{Ho}_2\text{Ti}_2\text{O}_7$ : AC-susceptibility measured on a powder sample showing the spin ice dynamical freezing (Ref. [65]).

inset, Fig. 7.37). As expected from Ref. [79],  $\tau$  increases (i.e. the tunneling slows) in strong applied fields due to Zeeman splitting. However, at weak fields,  $\tau$  was found to decrease, reaching a temperature dependent minimum at applied fields the order of a few kOe (see Fig. 7.37). This initial increase in tunneling rate has been interpreted as due to the presence of transverse field components as well as to the partial cancellation of the longitudinal field components. The latter effect moves towards restoring the degeneracy to the  $|\pm 15/2\rangle$  states.

It is clear that there is great scope for more experimental work on the spin dynamics in this regime, particularly by examining the effect of field direction on single crystal samples. There is also a need for a microscopic theory, particularly one that can justify the effective activation energy scale the order of 20 K, which although clearly connected with the dipolar forces, is not yet justified in detail.

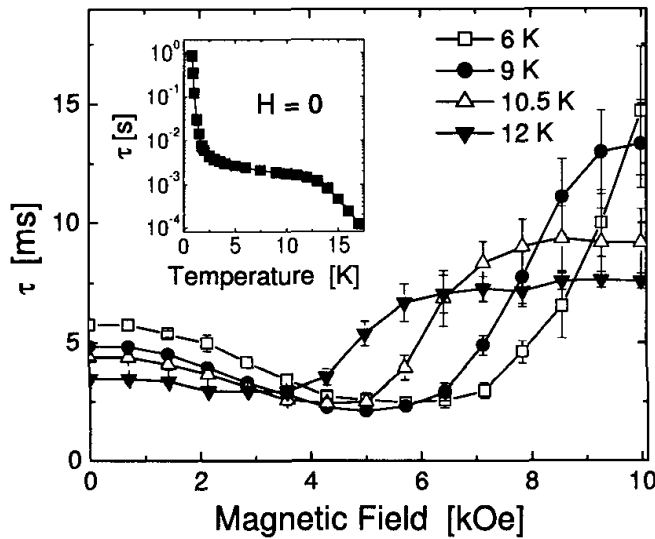


Fig. 7.37.  $\text{Dy}_2\text{Ti}_2\text{O}_7$ : Field dependence of the characteristic relaxation time measured by AC susceptibility, illustrating a minimum at finite applied field. The inset shows the estimated relaxation time versus temperature, illustrating a weakly temperature dependent regime ascribed to quantum tunneling (Ref. [134]).

### 7.5.5. Spin Dynamics in the Spin Ice Regime Below 1 K

#### 7.5.5.1. Slow Relaxation

It is now virtually certain that electron spin flip dynamics are exponentially frozen out below about 1 K in all the spin ice materials. This is dramatically confirmed by the DC-susceptibility measurement of Matsuhira *et al.* on polycrystalline  $\text{Ho}_2\text{Sn}_2\text{O}_7$  shown in Figure 7.7. Here one observes a massive splitting between field cooled (FC) and zero field cooled (ZFC) susceptibility and corresponding magnetic hysteresis loops. Magnetic hysteresis is also observed in  $\text{Ho}_2\text{Ti}_2\text{O}_7$  and  $\text{Dy}_2\text{Ti}_2\text{O}_7$ <sup>78</sup>. As mentioned above, after the application of a magnetic field, remanent moments can be frozen into the spin ice samples. Snyder *et al.*<sup>78</sup> have reported a comparison of the thermoremanent and isothermal-remanent magnetization of  $\text{Dy}_2\text{Ti}_2\text{O}_7$ <sup>78</sup>. The thermoremanent magnetization was prepared by cooling in field  $H$  and slowly reducing the field to zero. The isothermal remanent magnetization was prepared by cooling in a field, applying a field  $H$ , waiting to obtain almost complete relaxation, and then removing the field. In both cases the remanent magnetization was then measured as a function of time to determine its equilibrium value. The resulting differences (Fig. 7.38) shows that

the frozen spin ice state possesses the property of memory of its preparation in a manner similar to that displayed by spin glasses. Indeed, the data of Fig. 7.38 look strikingly similar to that for the spin glass system AuFe<sub>0.05</sub><sup>135</sup> (even though the spin ice freezing is certainly distinct from that of a spin glass as emphasised in Ref. [78]). Future studies of the slow relaxation or aging properties of the spin ice systems promise to be very interesting.

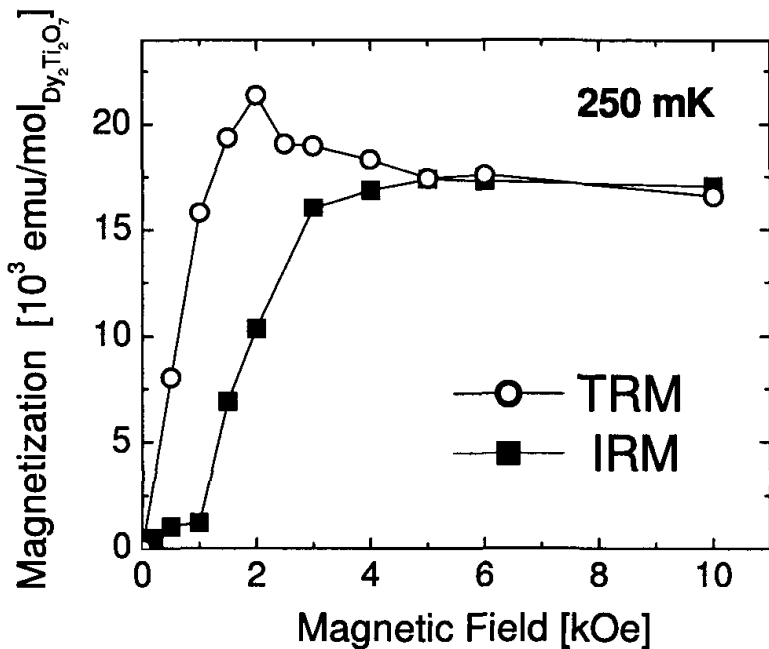


Fig. 7.38.  $\text{Dy}_2\text{Ti}_2\text{O}_7$ : Thermoremanent magnetization (TRM) and isothermal remanent magnetization (IRM) as a function of applied field at 250 mK (Ref. [78]).

### 7.5.5.2. Evidence for Residual Dynamics in the Frozen State

There is some evidence of residual dynamics in the spin ice materials existing down to the lowest measured temperatures. The NSE results mentioned above suggest a small component of very fast relaxation that is manifest in a finite constant  $A$  in Eqn. 20.  $\mu\text{SR}$  experiments also suggest spin dynamics in both  $\text{Ho}_2\text{Ti}_2\text{O}_7$  and  $\text{Dy}_2\text{Ti}_2\text{O}_7$ <sup>136</sup>. Since there are no spin flip dynamics at these temperatures it seems most likely that all residual dynamics can be attributed to hyperfine coupling to the nuclear spins which can induce a fast “wobble” or incoherent oscillation of the combined electronic-nuclear

spin around its local quantization axis<sup>79,136</sup>.

Bertin *et al.*<sup>80</sup> have suggested the remarkable possibility that the specific heat behaviour of Dy<sub>2</sub>Ti<sub>2</sub>O<sub>7</sub> is indicative of electron spin dynamics persisting to the lowest temperatures in this material. Basically, the anomalous absence of a nuclear specific heat in Dy<sub>2</sub>Ti<sub>2</sub>O<sub>7</sub> is attributed to electronic spin dynamics. However this argument would imply that Ho<sub>2</sub>Ti<sub>2</sub>O<sub>7</sub> (which has a full nuclear contribution<sup>42</sup>) is purely static, in apparent contravention of the NSE and  $\mu$ SR results. It is clear that more work is needed to fully understand these low temperature dynamical effects.

#### 7.5.6. Doped Spin Ice

The removal of protons in water ice by doping with KOH leads to a long range ordered state<sup>137</sup>. One interpretation of this is that proton dynamics are strongly restored in the doped samples allowing the system to locate its “true” ground state. Of course this idea cannot be proved or disproved as KOH-doped ice is not ice itself. It does, however, make it particularly interesting to examine the spin dynamics of spin ice materials in which spins have been removed by doping with non-magnetic impurities.

Snyder *et al.*<sup>131,138</sup> have reported AC-susceptibility measurements on polycrystalline Dy<sub>2-x</sub>Y<sub>x</sub>Ti<sub>2</sub>O<sub>7</sub> with x up to 0.4. The doping of spin ice has, broadly speaking, the opposite effect of applying a field leading to the “disappearance” of the 15 K peak, which was originally interpreted as a cooperative process. However, as shown in Ref. [79], the increase in susceptibility below 15 K on doping can only be interpreted as a decrease in  $F(Q, t)$  or a speeding up of dynamics at a given temperature. The fact that there is no change in the susceptibility at temperatures above the 15 K peak shows that the process freezing out at that temperature is itself not affected by doping: it is a single ion Arrhenius process, as confirmed by the fact that the parameters describing this peak do not change with x. As argued in section 5.2.3 the “disappearance” of the peak is due to the speeding up of a lower temperature relaxation process, which is now thought to involve quantum mechanical spin tunneling<sup>79,134</sup>. Very recently, Snyder *et al.*<sup>139</sup> have reported an extension of their study to include both Y and Lu dopants, and values of x up to x = 1.98 (i.e a magnetically very dilute sample). The notable conclusion of this work is that the 15 K peak, suppressed for x < 0.4, actually re-emerges for higher doping levels, whereupon it shifts up to  $\sim$ 22 K (x = 1.98). This suggests that the lower temperature quantum relaxation process is absent in very dilute samples

and that the crystal field changes with doping. It is a remarkable fact that the sample with  $x = 1.98$  (Y) appears practically static to ac-susceptibility below  $T \approx 20$  K. The latest results are argued to confirm the single-ion nature of the higher temperature relaxation process.

The speeding up of the low temperature dynamics on doping has also been observed on doped polycrystalline  $\text{Ho}_{2-x}\text{La}_x\text{Ti}_2\text{O}_7$  with  $x = 0.05$ <sup>79</sup>. Here, the lower temperature susceptibility peak shifts in a manner consistent with a 100 fold increase in relaxation rate. However such a dramatic speeding up is not observed in Yttrium doped  $\text{Ho}_2\text{Ti}_2\text{O}_7$ <sup>140</sup> which suggests that lattice distortions (or perhaps defects) play a role:  $\text{La}^{3+}$  is a much larger ion than  $\text{Ho}^{3+}$  whereas  $\text{Y}^{3+}$  is about the same size. In this system weak doping does not stabilize long range order at millikelvin temperatures nor does it significantly affect the entropy per spin<sup>79,140</sup>.

The possibility of a dilution-induced transition to long range order was investigated by Melko<sup>94</sup> using conventional spin flip Monte Carlo simulations. However, this preliminary result did not reveal any sign of a dilution-induced transition to long range order that might have been made accessible to single spin flip dynamics via the reduction of energy barriers. This result is consistent with the experimental observations described above. For sufficiently large  $x$ , one expects the degeneracy to be lifted by the random dilution<sup>23</sup> and the ground state of the system to become that of a dipolar Ising spin glass, akin to that of  $\text{LiHo}_{1-x}\text{Y}_x\text{F}_4$ <sup>141</sup>

### 7.5.7. Spin Ice Under Pressure

Water ice under applied pressure has fascinating physics, yielding many phases<sup>142</sup>. This makes the application of pressure to spin ice particularly interesting. Mirebeau and Goncharenko<sup>143</sup> have reported an elastic neutron scattering investigation of polycrystalline  $\text{Ho}_2\text{Ti}_2\text{O}_7$ , in applied pressures of up to 6 GPa at temperatures down to 1.4 K. At the lowest temperatures the dipolar spin ice correlations are clearly visible in the powder scattering pattern. However there is no discernable change at high pressure: the conclusion is that dipolar spin ice is stable under applied pressure. This contrasts with the behaviour of the spin liquid material  $\text{Tb}_2\text{Ti}_2\text{O}_7$  which orders magnetically under the application of pressure<sup>144</sup>.

## 7.6. Spin Ice Related Materials

The discussion in this Chapter has been highly focused on the currently best characterized spin ice materials,  $\text{Ho}_2\text{Ti}_2\text{O}_7$ ,  $\text{Dy}_2\text{Ti}_2\text{O}_7$  and  $\text{Ho}_2\text{Sn}_2\text{O}_7$  for

which strong evidence of spin ice phenomenology has been established based on bulk measurements and neutron scattering experiments. In addition, there are two other obvious candidates for spin ice behaviour:  $\text{Dy}_2\text{Sn}_2\text{O}_7$ ,<sup>62</sup>, which shows very similar AC-susceptibility behaviour to  $\text{Dy}_2\text{Ti}_2\text{O}_7$ , and  $\text{Ho}_2\text{GaSbO}_7$ , which (as already mentioned) has very similar specific heat properties to those of  $\text{Ho}_2\text{Ti}_2\text{O}_7$ .<sup>44</sup> We also note that Matsuhira *et al.*<sup>62</sup> have suggested that  $\text{Pr}_2\text{Sn}_2\text{O}_7$  might be a spin ice as judged by its bulk properties. If proved to be correct, this is particularly interesting as the dipole interaction is weak in this material: hence it might be an ideal realisation of near-neighbour, rather than dipolar spin ice.

Throughout this article we have used the term “spin ice material” to refer to materials that closely approximate the spin ice model as originally defined in<sup>4</sup>. But we have also explored the relationship between this model and the Heisenberg model antiferromagnet (see Section 7.2), which in one sense can be seen as an extension, by Anderson<sup>3</sup> and Villain<sup>23</sup>, of the concept originally introduced by Pauling<sup>1</sup>. Similarly, holmium and dysprosium titanates are themselves part of a larger series of rare earth titanates which have been extensively studied in recent years as model highly frustrated antiferromagnets (the stannates have been less studied). Hence, in this section, we briefly summarise the properties of these and other materials that are closely related to the spin ice family.

### 7.6.1. Rare Earth Titanates

Among the titanates, there is a gamut of materials that exhibit interesting magnetic behaviour that depends on the choice of the rare-earth trivalent ion, as different rare earth ions possess different type of anisotropy.  $\text{Gd}_2\text{Ti}_2\text{O}_7$  has  $L = 0$  and  $S = 7/2$  and will therefore have only very weak single-ion anisotropy. This system should be well described to a good approximation by a Heisenberg antiferromagnet where the crystal field is a weaker perturbation to the free ion state than are the long range dipole-dipole interactions.<sup>145</sup>  $\text{Gd}_2\text{Ti}_2\text{O}_7$  exhibits two transitions in zero applied field, at 1.1 K and 0.7 K, which have been seen in neutron scattering<sup>146</sup> and bulk measurements<sup>145,147</sup>, as well as a number of phase transitions in applied magnetic field<sup>147,148</sup>. Considering only antiferromagnetic exchange and dipolar interactions, the ground state of this idealised model is an ordered state with propagation vector  $k = 0$ <sup>84,85</sup> that is robust to quantum spin fluctuations<sup>85</sup>. However, this is not the ordered state observed in  $\text{Gd}_2\text{Ti}_2\text{O}_7$ <sup>146</sup>. Recent neutron scattering experiments<sup>149</sup> have

firmly established that the zero field state of  $\text{Gd}_2\text{Ti}_2\text{O}_7$ , described by the propagation vector  $\mathbf{k} = 1/2, 1/2, 1/2$ , is partially ordered between 0.7 K and 1.0 K, and fully ordered below 0.7 K in a four wave vector structure. Recent theoretical calculations<sup>150,151</sup> find consistency with the structure between 0.7 K and 1.0 K, but the 4- $k$  structure below 0.7 K has not yet been justified theoretically. There are open questions as to the dynamics of the Gd moments in  $\text{Gd}_2\text{Ti}_2\text{O}_7$ <sup>80</sup>.

Except for  $\text{Gd}_2\text{Ti}_2\text{O}_7$ , the other heavy rare earth  $\text{R}_2\text{Ti}_2\text{O}_7$  materials have strong single ion anisotropy.  $\text{Tb}_2\text{Ti}_2\text{O}_7$  is an antiferromagnetic material with a measured Curie-Weiss temperature  $\theta_{\text{CW}}$  of approximately -20 K. If treated as a  $\langle 111 \rangle$  Ising antiferromagnet (see Section 7.3.2.2) it has  $J \approx -2.64$  K and  $D \approx 0.48$  K, giving  $J_{\text{eff}} \approx -0.08$  K and should in principle order at approximately 1.2 K<sup>37</sup>; but in fact it does not display long range order down to a temperature of 60 mK<sup>152</sup>, and has been advanced as one of the paradigm materials displaying spin liquid (or collective paramagnetic) behaviour in three dimensions. There is, on the other hand, a report of glassy behaviour setting in below 70 mK<sup>153</sup>. Such glassy behaviour has also been reported in the related  $\text{Tb}_2\text{Nb}_2\text{O}_7$  compound below 0.8 K<sup>154</sup>. At the present time, the explanation as to why  $\text{Tb}_2\text{Ti}_2\text{O}_7$  fails to order down to 60-70 mK thus remains a puzzle<sup>155,156</sup>. This puzzle is made even more intriguing when it is noted that  $\text{Tb}_2\text{Ti}_2\text{O}_7$  orders at approximately 2 K under applied pressure in excess of 2 GPa<sup>144</sup>.

$\text{Er}_2\text{Ti}_2\text{O}_7$  and  $\text{Yb}_2\text{Ti}_2\text{O}_7$  have XY spins, which approximately lie perpendicular to the local trigonal axis.  $\text{Er}_2\text{Ti}_2\text{O}_7$  is an antiferromagnet while  $\text{Yb}_2\text{Ti}_2\text{O}_7$  has a small positive ferromagnetic  $\theta_{\text{CW}}$ .  $\text{Er}_2\text{Ti}_2\text{O}_7$  has a transition to long range order at 1.17 K, probably stabilised by an “order-by-disorder” mechanism<sup>71</sup>.  $\text{Yb}_2\text{Ti}_2\text{O}_7$  displays a sharp first order transition in the specific heat at approximately 0.24 K where static order was not initially observed<sup>40</sup>. However, this conclusion has recently been questioned, as neutron diffraction evidence for a transition to long range ferromagnetic order has been found<sup>41</sup>.

### 7.6.2. Other Pyrochlores Related to Spin Ice

$\text{Ho}_2\text{Ru}_2\text{O}_7$  has been advanced as another candidate spin ice material, but one in which the transition metal  $\text{Ru}^{4+}$  is magnetic, unlike  $\text{Ti}^{4+}$  in  $\text{Ho}_2\text{Ti}_2\text{O}_7$ <sup>157</sup>. However, recent neutron studies<sup>158</sup> have revealed that  $\text{Ho}_2\text{Ru}_2\text{O}_7$  has two magnetic transitions at  $T \sim 95$  K and  $T \sim 1.4$  K to long range ordered states involving the Ru and Ho sublattices, respectively.

Between these transitions, the Ho<sup>3+</sup> moments form short-ranged ordered spin clusters. The internal field provided by the ordered S=1 Ru<sup>4+</sup> moments disrupts the fragile spin ice state of the Ho<sup>3+</sup> moments, and drives them to develop long range order below 1.4 K <sup>158</sup>.

Departing from insulating materials and considering the manifestation of spin ice phenomenology within metallic pyrochlores, two materials are worth noting. In Nd<sub>2</sub>Mo<sub>2</sub>O<sub>7</sub> the spin ice-like correlations on the Nd<sup>3+</sup> sublattice perturb the metallic behaviour on the Mo sublattice to give a gigantic anomalous Hall effect <sup>159</sup>. We also note a very recent theoretical study of a “double exchange spin ice model” that may be relevant to this system <sup>160</sup>. Another example is Dy<sub>2</sub>Ir<sub>2</sub>O<sub>7</sub> which is also metallic, but where the Dy spins appear to be antiferromagnetically coupled, leading to a transition to long range order <sup>161</sup>.

There are many other chemical modifications that can be made on the rare earth titanate structure, by substituting two ions, with charges 3+ and 5+, on the Ti site. However, few of these have yet been tested for spin ice behaviour. One exception is Ho<sub>2</sub>(HoSb)O<sub>7</sub> <sup>162</sup> which shows complex non-collinear order below  $T_N \approx 2$  K.

## 7.7. Conclusions

We have tried to present a relatively comprehensive review of spin ice research which is, we hope, up to date at the time of writing; we apologise to any authors whose work we have inadvertently missed or misrepresented. The field is developing quickly, particularly in the area of spin dynamics and field-dependent properties and it is anticipated that some parts of this review will quickly become out of date! However, we hope it will be a useful account of the first seven years of spin ice research. We have mainly restricted our attention to the best characterised spin ice materials Ho<sub>2</sub>Ti<sub>2</sub>O<sub>7</sub>, Dy<sub>2</sub>Ti<sub>2</sub>O<sub>7</sub> and Ho<sub>2</sub>Sn<sub>2</sub>O<sub>7</sub>. We have not elaborated on many possible avenues for future research, which might include, for example, studies of epitaxial films: we note that these have already been prepared with other pyrochlores <sup>163</sup>.

Let us conclude by summarising some of the main features of spin ice physics. The near neighbour spin ice model is a 16-vertex model of frustrated ferromagnetism that is realised in several real materials. The model - and the materials - have zero point entropy in the ground state and the experimentalist has remarkable control of the statistical weightings of the “vertices” by applying a field to single crystals. This leads to many inter-

esting field-induced states including kagomé ice, with zero point entropy and the “spin chain” state which in simple terms can be thought of as a one dimensional Ising ferromagnet. Several interesting phase transitions are also observed, including “liquid-gas” type transitions and possibly the Kastelyn transition. Through various mappings, the spin ice materials can be considered ideal experimental realisations of some basic models of frustration: Anderson’s Ising antiferromagnet, Wannier’s triangular antiferromagnet and of course, Pauling’s ice model. The spin ice state represents a particular kind of frozen magnetic state with correlations of limited range. The high temperature dynamics include a crossover from thermally activated to quantum tunneling dynamics at a particularly high temperature (15 K), with the spin ice freezing process near 1 K apparently distinct from that of a conventional spin glass. The search for a detailed microscopic understanding of the spin ice materials has uncovered several new features of the dipolar interaction. For all these reasons, spin ice has proved to be a fruitful playground in which to explore, develop and challenge our overall understanding of frustrated spin systems.

### Acknowledgements

S.T.B. acknowledges funding from the EPSRC and thanks the E.N.S. Lyon for a Loadenbach Visiting Professorship (2003). M. J. P. G. acknowledges the following sources of funding: NSERC of Canada, Canada Research Chair Program, Research Corporation, Canada Foundation for Innovation, Canadian Institute for Advanced Research, Ontario Innovation Trust, Ontario Challenge Fund and Materials and Manufacturing Ontario.

We thank Andrew Cornelius, Georg Ehlers, Jason Gardner, Kazuyuki Matsuhira, Oleg Petrenko, Stephan Rosenkranz, Toshiro Sakakibara and Peter Schiffer for supplying figures and for permission to reproduce them. We thank Colin Broholm and Yiming Qiu for supplying a copy of his Ph.D. thesis (Ref. [57]).

It is a pleasure to thank our recent collaborators in the area of spin ice physics: Simon Banks, Daniel Cabra, Benjamin Canals, Dickon Champion, Andrew Cornelius, Adrian del Maestro, Byron den Hertog, Maxime Dion, Sarah Dunsiger, Georg Ehlers, Matt Enjalran, Bjorn Fåk, Tom Fenell, Mark Field, Hideto Fukazawa, Jason Gardner, Bruce Gaulin, John Greedan, Mark Green, Mark Harris, Ryuji Higashinaka, Ying-Jer Kao, Rob Kiefl, Philip King, Jorge Lago, Yoshi Maeno, Des McMorrow, Roger Melko, Isabelle Mirebeau, Roderich Moessner, Hamid Molavian, Martin Orendáč,

Bashir Ouladdiaf, Ivan Parkin, Oleg Petrenko, Pierre Pujol, Jacob Ruff, Zaher Salman, Fahad Shahabazi, Masae Shirai, Jeff Sonier, Ross Stewart, Andrea Taroni, Andrew Wills, and Taras Yavorskii. S. T. B. would particularly like to thank Mark Harris for an initial collaboration in this field. We have also benefitted from collaborations and discussions with many other people, too numerous to mention here; we thank all of them.

## References

1. L. Pauling, *J. Am. Chem. Soc.*, **57**, 2680 (1935).
2. G. H. Wannier, *Phys. Rev.*, **79**, 357 (1950); erratum *Phys. Rev. B*, **7**, 5017 (1973).
3. P. W. Anderson, *Phys. Rev.*, **102**, 1008 (1956).
4. M. J. Harris, S. T. Bramwell, D. F. McMorrow, T. Zeiske and K. W. Godfrey, *Phys. Rev. Lett.*, **79**, 2554 (1997).
5. S. T. Bramwell and M. J. Harris, *J. Phys. Condens. Matter*, **10**, L215 (1998).
6. G. Toulouse, *Commun. Phys.*, **2**, 115 (1977).
7. *Exactly Solved Models in Statistical Mechanics*. R. J. Baxter, Academic Press (1982).
8. E. H. Lieb and F. Y. Wu in *Phase Transitions and Critical Phenomena*, C. Domb and M. S. Green Eds, Academic Press, New York (1972).
9. S. T. Bramwell and M. J. P. Gingras, *Science*, **294**, 1495 (2001).
10. B. S. Shastry, *Physica B*, **329**, 1024 (2003).
11. A. P. Ramirez, C. L. Broholm, R. J. Cava and G. R. Kowach, *Physica B*, **280**, 290 (2000).
12. A. P. Ramirez, *Nature*, **421**, 483 (2003).
13. W. F. Giauque and J. W. Stout, *J. Am. Chem. Soc.*, **58**, 1144 (1936).
14. P. Debye, *Ann. der Physik*, **39**, 789 (1912).
15. *Models of Disorder: The Theoretical Physics of Homogeneously Disordered Systems*, J. M. Ziman, Cambridge University Press (1976).
16. J. D. Bernal and R. H. Fowler, *J. Chem. Phys.*, **1**, 515 (1933).
17. W. F. Giauque and M. F. Ashley, *Phys. Rev.*, **43**, 81 (1933).
18. J. F. Nagle, *J. Math. Phys.*, **7**, 1484 (1966).
19. E. O. Wollan, W. L. Davidson and C. G. Schull, *Phys Rev.*, **75**, 1348 (1949).
20. G. S. Rushbrooke, *Introduction to Statistical Mechanics*. Oxford University Press (1949).
21. J. E. Mayer and M. G. Mayer, *Statistical Mechanics (Second Ed.)*. J. Wiley (1977).
22. A. P. Ramirez, A. Hayashi, R. J. Cava, R. Siddharthan and B. S. Shastry, *Nature*, **399**, 333 (1999).
23. J. Villain, *Z. Phys. B*, **33**, 31 (1979).
24. R. Moessner and J. T. Chalker, *Phys. Rev. Lett.*, **80**, 2929 (1998).
25. M. J. Harris, M. P. Zinkin, Z. Tun, B. M. Wanklyn and I. P. Swainson, *Phys. Rev. Lett.*, **73**, 189 (1994).
26. M. J. Harris, M. P. Zinkin and T. Zeiske, *Phys. Rev. B*, **52**, R707 (1995).

27. R. Moessner, *Phys. Rev. B*, **57**, R5587 (1998).
28. A. J. Garcia-Adeva and D. L. Huber, *Phys. Rev. B*, **64**, 172403 (2001).
29. N. Mekata, *J. Phys. Soc. Japan*, **42**, 76 (1977).
30. G. I. Watson, *J. Stat. Phys.*, **94**, 1045 (1999).
31. M. J. Harris, S. T. Bramwell and P. J. C. King, unpublished.
32. M. J. Harris, S. T. Bramwell, T. Zeiske, D. F. McMorrow and P. J. C. King, *J. Magn. Magn. Mater.*, **177**, 757 (1998).
33. S. T. Bramwell, unpublished.
34. D. Bitko, T. F. Rosenbaum and G. Aeppli, *Phys. Rev. Lett.*, **77**, 940 (1996).
35. J. R. Friedman, M. P. Sarachik, J. Tejada and R. Ziolo, *Phys. Rev. Lett.*, **76**, 3830 (1996).
36. R. Siddharthan, B. S. Shastry, A. P. Ramirez, A. Hayashi, R. J. Cava and S. Rosenkranz, *Phys. Rev. Lett.*, **83**, 1854 (1999).
37. B. C. den Hertog and M. J. P. Gingras, *Phys. Rev. Lett.*, **84**, 3430 (2000).
38. M. J. Harris, S. T. Bramwell, P. C. W. Holdsworth and J. D.M. Champion, *Phys. Rev. Lett.*, **81**, 4496 (1998).
39. S. Rosenkranz, A. P. Ramirez, A. Hayashi, R. J. Cava, R. Siddharthan and B. S. Shastry, *J. Appl. Phys.*, **84**, 5914 (2000).
40. J. A. Hodges, P. Bonville, A. Forget, A. Yaouanc, P. Dalmas de Reotier, G. André, M. Rams, K. Krolas, C. Ritter, P.C.M. Gubbens, C.T. Kaiser, P.J.C. King and C. Baines, *Phys. Rev. Lett.*, **88**, 077204 (2002).
41. Y. Yasui, M. Soda, S. Iikubo, M. Ito, M. Sato, N. Hamaguchi, T. Matsushita, N. Wada, T. Takeuchi, N. Aso and K. Kakurai, *J Phys. Soc. Japan*, **72**, 3014 (2003).
42. S. T. Bramwell, M. J. Harris, B. C. den Hertog, M. J. P. Gingras, J. S. Gardner, D. F. McMorrow, A. R. Wildes, A. L. Cornelius, J. D. M. Champion, R. G. Melko and T. Fennell, *Phys. Rev. Lett.*, **87**, 047205 (2001).
43. M. Kanada, Y. Yasui, Y. Kondo, S. Iikubo, M. Ito and M. Harashina, M. Sato, H. Okumura, K. Kakurai and H. Kadowaki, *J. Phys. Soc. Japan*, **71**, 313 (2002).
44. H. W. J. Blöte, R. F. Wielinga and W. J. Huiskamp, *Physica*, **43**, 549 (1969).
45. B. C. den Hertog, M. J. P. Gingras, S. T. Bramwell, M. J. Harris, cond-mat/9912220 (1999).
46. A. L. Cornelius and J. S. Gardner, *Phys. Rev. B*, **64**, 060406 (2001).
47. H. Kadowaki, Y. Ishii, K. Matsuhira and Y. Hinatsu, *Phys. Rev. B*, **65**, 144421 (2002).
48. R. S. Roth, *J. Res. Natl. Bur. Stand.*, **56**, 17 (1956).
49. O. Knop, F. Brisse, L. Castelliz and Sutarno, *Can J. Chem.*, **43**, 2812 (1965).
50. B. M. Wanklyn et al, *J. Mater. Sci.*, **3**, 395 (1968).
51. G. Balakrishnan, O. A. Petrenko, M. R. Lees and D. McK. Paul, *J Phys. Condens. Matter*, **10**, L723 (1998).
52. J. S. Gardner, B. D. Gaulin and D. McK. Paul, *J. Cryst. Growth*, **191**, 740 (1998).
53. L. G. Mamsurova, K. K. Pukhov, N. G. Trusevich and L. G. Shcherbakova, *Sov. Phys. Solid State*, **27**, 1214 (1985).

54. S. T. Bramwell, M. N. Field, M. J. Harris and I. P. Parkin, *J. Phys. Condens. Matter*, **12**, 483 (2000).
55. Y. M. Jana and D. Ghosh, *Phys. Rev. B*, **61**, 9657 (2000).
56. Y. M. Jana, A. Sengupta and D. Ghosh, *J. Magn. Magn. Mater.*, **248**, 7 (2002).
57. Y. Qiu, Ph.D. Thesis, John Hopkins University, 2002.
58. L. G. Mamsurova, K. S. Pigal'skii, N. G. Trusevich and L. G. Shcherbakova, *Sov. Phys. Solid State*, **27**, 978 (1985).
59. D. J. Flood, *J. Appl. Phys.*, **45**, 4041 (1974).
60. J. D. Cashion, A. H. Cooke, M. J. M. Leask, T. L. Thorpe and M. R. Wells, *J. Mater. Sci.*, **3**, 402 (1968).
61. V. Bondah-Jagalu and S. T. Bramwell, *Can. J. Phys.*, **79**, 1381 (2001).
62. K. Matsuhira, Y. Hinatsu, K. Tenya, H. Amitsuka and T. Sakakibara, *J. Phys. Soc. Japan*, **71**, 1576 (2002).
63. T. Katsufuji, *Phys. Rev. B*, **69**, 064422 (2004).
64. H. Fukazawa, R. G. Melko, R. Higashinaka, Y. Maeno and M. J. P. Gingras, *Phys. Rev. B*, **65**, 054410 (2002).
65. K. Matsuhira, Y. Hinatsu, K. Tenya and T. Sakakibara, *J. Phys. Condens. Matter*, **12**, L649 (2000).
66. R. Moessner and J. T. Chalker, *Phys. Rev. B*, **58**, 12049 (1998).
67. J. D. M. Champion, S. T. Bramwell, P. C. W. Holdsworth and M. J. Harris, *Europhys. Lett.*, **57**, 93 (2002).
68. G. Ferey, R. de Pape, M. Leblanc, J. Pannetier, *Rev. Chim. Minerale*, **23**, 474 (1986).
69. J. N. Reimers, J. E. Greedan and M. Bjorgvinsson, *Phys. Rev. B*, **45**, 7295 (1992).
70. P. C. W. Holdsworth, unpublished.
71. J. D. M. Champion, M. J. Harris, P. C. W. Holdsworth, A. S. Wills, G. Balakrishnan, S. T. Bramwell, E. Čižmár, T. Fennell, J. S. Gardner, J. Lago, D. F. McMorrow, M. Orendáč, A. Orendáčová, D. M<sup>c</sup>K. Paul, R. I. Smith, M. T. F. Telling and A. Wildes, *Phys. Rev. B*, **68**, 020401 (2003).
72. S. T. Bramwell, M. J.P. Gingras and J. N. Reimers, *J. Appl. Phys.*, **75**, 5523 (1994).
73. J. D. M. Champion, Ph. D. Thesis, London University, 2001.
74. R. Siddharthan, B. S. Shastry and A. P. Ramirez, *Phys. Rev. B*, **63**, 184412 (2001).
75. B. Bleaney, F. N. H. Robinson, M. R. Wells, *Proc. R. Soc. Lond. A*, **362**, 179 (1978).
76. K. Ram and K. K. Sharma, *J. Phys. C.: Solid State Phys.*, **18**, 619 (1985).
77. P. B. Chakraborty, P. Henelius, H. Kjonsberg, A. W. Sandvik and S. M. Girvin, cond-mat/0402051 (2004).
78. J. Snyder, B. G. Ueland, J. S. Slusky, H. Karunadasa, R. J. Cava and P. Schiffer, *Phys. Rev. B*, **69**, 064414 (2004).
79. G. Ehlers, A.L. Cornelius, M. Orendáč, M. Kajnakova, T. Fennell, S. T. Bramwell and J. S. Gardner, *J. Phys. Condens. Matter*, **15**:L9 (2003).
80. E. Bertin, J. A. Hodges, J.-P. Bouchaud, J.P. Sanchez P. Bonville and

- P. Vuillet, *Eur. Phys. J., B* **27**, 347 (2002).
81. T. Fennell, O. A. Petrenko, B. Fåk and S. T. Bramwell, M. Enjalran, T. Yavors'kii, M. J. P. Gingras, R. G. Melko and G. Balakrishnan, cond-mat/0404594 (2004).
  82. A.B. Harris, C. Kallin and A.J. Berlinsky, *Phys. Rev. B*, **45**, 2899 (1992).
  83. J. N. Reimers, A. J. Berlinsky and A. C. Shi, *Phys. Rev. B*, **43**, 865 (1991).
  84. S. E. Palmer and J. T. Chalker, *Phys. Rev. B*, **62**, 4888 (2000).
  85. A. G. Del Maestro and M. J.P. Gingras, *J. Phys. Condens. Matter*, **16**, 3339 (2004).
  86. P. P. Ewald, *Ann. Physik*, **64**, 253 (1921).
  87. S. W. de Leeuw, J. W. Perram and E. R. Smith, *Ann. Rev. Phys. Chem.*, **37**, 245 (1986).
  88. M. Born and Huang, *Dynamical Theory of Crystal Lattices*. Oxford University Press (1968).
  89. *Principles of the Theory of Solids* (2nd ed.), J. M. Ziman, Cambridge University Press, Cambridge (1972).
  90. P. J. Camp, J. C. Shelley and G. N. Patey, *Phys. Rev. Lett.*, **84**, 115 (2000).
  91. G. Ayton, M. J. P. Gingras and G. N. Patey, *Phys. Rev. Lett.*, **75**, 2360 (1995).
  92. A. Aharony and M.E. Fisher, *Phys. Rev. B*, **8**, 3323 (1973).
  93. *Phase Transitions and Critical Phenomena Vol. 3*, Domb and Green, editors, Academic Press London (1974).
  94. R. G. Melko, *M. Sc. Thesis, University of Waterloo* (2001).
  95. R. G. Melko, M. Enjalran, B. C. den Hertog and M. J. P. Gingras, cond-mat/0308282 (2003).
  96. W. Selke, *Phys. Rep.*, **170**, 213 (1988).
  97. M. J. P. Gingras and B. C. den Hertog, *Can. J. Phys.*, **79**, 1339 (2001).
  98. M. Enjalran and M. J. P. Gingras. cond-mat/0307151 (2003).
  99. R. G. Melko, B. C. den Hertog and M. J. P. Gingras, *Phys. Rev. Lett.*, **87**, 067203 (2001).
  100. G. T. Barkema and M. E. J. Newman, *Phys. Rev. E*, **57**, 1155 (1998).
  101. M. E. J. Newman and G. T. Barkema, *Monte Carlo Methods in Statistical Physics*. Clarendon Press, Oxford (1999).
  102. *Monte Carlo Simulation in Statistical Physics*, K. Binder and D. W. Heermann, Springer, Germany (1997).
  103. B. A. Berg and T. Neuhaus, *Phys. Rev. Lett.*, **68**, 9 (1992).
  104. U. H. E. Hansmann and Y. Okamoto, *Physica A*, **212**, 415 (1994).
  105. A. M. Ferrenberg and R. H. Swendsen, *Phys. Rev. Lett.*, **61**, 2635 (1998).
  106. S. Yoshida, K. Nemoto and K. Wada, *J. Phys. Soc. Japan*, **71**, 948 (2002).
  107. T. Fennell, O. A. Petrenko and G. Balakrishnan, S. T. Bramwell, J. D. M. Champion, B. Fåk, M. J. Harris and D. McK. Paul, *Appl. Phys. A: Mat. Sci. Proc.*, **74**:S889 (2002).
  108. S. L. Chamberlain, S. T. Hess and L. R. Corruccini, *Physics Letters A*, **323**, 310 (2004).
  109. M. E. Fisher and A N. Berker, *Phys. Rev. B*, **26**, 2507 (1982).
  110. T. Mitsui, I. Tatsuzaki and E. Nakamura, *An Introduction to the Physics of*

- Ferroelectrics and Related Phenomena.* Gordon and Breach Science Publishers, 1976.
111. K. Matsuhira, Z. Hiroi, T. Tayama, S. Takagi and T. Sakakibara, *J. Phys. Condens. Matter*, **14**:L559 (2002).
  112. S. Yoshida, K. Nemoto and K. Wada, cond-mat/0403762 (2004).
  113. J. P. C. Ruff, R. G. Melko and M. J. P. Gingras, unpublished.
  114. O. Petrenko, G. R. Lees and G. Balakrishnan, *Phys. Rev. B*, **68**, 012406 (2003).
  115. Z. Hiroi, K. Matsuhira, S. Takagi, T. Tayama and T. Sakakibara, *J. Phys. Soc. Japan*, **72**, 411 (2003).
  116. H. Fukazawa, R. Higashinaka and Y. Maeno, *Phys. Rev. B*, **68**, 014415 (2003).
  117. R. Higashinaka, H. Fukazawa, K. Deguchi and Y. Maeno, *J. Phys. Condens. Matter*, **14**:S679 (2004).
  118. R. Higashinaka, H. Fukuzawa, K. Deguchi and Y. Maeno, cond-mat/0406307 (2004)
  119. T. Sakakibara, T. Tayama, Z. Hiroi, K. Matsuhira and S. Takagi, *Phys. Rev. Lett.*, **90**, 207205 (2003).
  120. Z. Hiroi, K. Matsuhira and M. Ogata, *J. Phys. Soc. Japan*, **72**, 3045 (2003).
  121. R. Higashinaka, H. Fukazawa and Y. Maeno, *Physica B*, **329**, 1040 (2003).
  122. T. Fennell, *Ph. D. Thesis, University of London* (2003)..
  123. A. S. Wills, R. Ballou and C. Lacroix, *Phys. Rev. B*, **66**, 144407 (2002).
  124. M. Udagawa, M. Ogata and Z. Hiroi, *J. Phys. Soc. Japan*, **71**, 2365 (2002).
  125. R. Moessner and S. L. Sondhi, *Phys. Rev. B*, **68**, 064411 (2003).
  126. S. V. Isakov, K. S. Raman, R. Moessner and S. L. Sondhi, cond-mat/0404417 (2004).
  127. H. Aoki, T. Sakakibara, K. Matsuhira and Z. Hiroi, *J. Phys. Soc. Japan* (to be published, 2004).
  128. D. W. Davidson and R. H. Cole, *J. Chem. Phys.*, **18**, 1417 (1950).
  129. D. W. Davidson and R. H. Cole, *J. Chem. Phys.*, **19**, 1484 (1951).
  130. K. Matsuhira, Y. Hinatsu and T. Sakakibara, *J. Phys. Condens. Matter*, **13**:L737, 2001.
  131. J. Snyder, J. S. Slusky, R. J. Cava and P. Schiffer, *Nature*, **413**, 48 (2001).
  132. G. Ehlers, A. L. Cornelius, T. Fennell, M. Koza and S. T. Bramwell and J. S. Gardner, *J. Phys. Condens. Matter*, **16**:S635 (2004).
  133. A. L. Cornelius, private communication (2004).
  134. J. Snyder, B. G. Ueland, J. S. Slusky, H. Karunadasa, R. J. Cava, A. Mizel and P. Schiffer, *Phys. Rev. Lett.*, **91**, 107201 (2004).
  135. J. L. Tholence and R. Tournier, *J. Phys. (Paris)*, **35**:C4 (1974).
  136. J. Lago and S. R. Dunsiger, unpublished.
  137. Y. Tajima, T. Matsuo and H. Sugo, *Nature*, **299**, 1810 (1982).
  138. J. Snyder, J. S. Slusky, R. J. Cava and P. Schiffer, *Phys. Rev. B*, **66**, 064432 (2002).
  139. J. Snyder, B. G. Ueland, A. Mizel, J. S. Slusky, H. Karunadasa, R. J. Cava and P. Schiffer, cond-mat/0405233 (2004) .
  140. M. Orendáč *et al.*, to be published (2004).

141. D. H. Reich, B. Ellman, J. Yang, T. F. Rosenbaum, G. Aeppli and D. P. Belanger *Phys. Rev. B* **42**, 4631 (1990).
142. R. F. Whitworth and V. F. Petrenko, editors, *Physics of Ice*. Oxford University Press (2002).
143. I. Mirebeau and I. Goncharenko, *J. Phys. Condens. Matter*, **16**:S653 (2004).
144. I. Mirebeau, I. N. Goncharenko, P. Cadavez-Pares, S.T. Bramwell, M. J. P. Gingras and J. S. Gardner, *Nature*, **420**, 54 (2002).
145. N. P. Raju, M. Dion, M. J. P. Gingras, T.E. Mason and J. E. Greedan, *Phys. Rev. B*, **59**, 14489 (1999).
146. J. D. M. Champion, A. S. Wills, T. Fennell, S. T. Bramwell, J. S. Gardner and M. A. Green, *Phys. Rev. B*, **64**, 140407(R) (2001).
147. A. P. Ramirez, B. S. Shastry, A. Hayashi, D. A. Huse, J. J. Krajewski and R. J. Cava, *Phys. Rev. Lett.*, **89**, 067202 (1999).
148. O. Petrenko, G. R. Lees, G. Balakrishnan and D. McK. Paul, cond-mat/0309405 (2004).
149. J. R. Stewart, G. Ehlers, A. S. Wills, S. T. Bramwell and J. S. Gardner, *J. Phys. Condens. Matter*, **16**, L321 (2004).
150. M. Enjalran and M. J. P. Gingras, cond-mat/0307152 (2003).
151. O. Cépas and B. Sriram Shastry, *Phys. Rev. B*, **69**, 184402 (2004).
152. J. S. Gardner, A. Keren, G. Ehlers, C. Stock, E. Segal, J. M. Roper, B. Fåk, M. B. Stone, P. R. Hammar, D. H. Reich and B. D. Gaulin, *Phys. Rev. B*, **68**, 180401 (2003).
153. G. Luo, S.T. Hess and L. R. Corruccini, *Phys. Lett. A*, **291**, 306 (2001).
154. Y. M. Jana, Y. M. O. Sakai, R. Higashinaka, H. Fukazawa, Y. Maeno, P. Dasgupta and D. Ghosh, *Phys. Rev. B*, **68**, 174413 (2003).
155. M. Enjalran, M. J. P. Gingras, Y.-J. Kao, A. Del Maestro and H. R. Molavian, *J. Phys. Condens. Matter*, **16**, S673 (2004).
156. Y.-J. Kao, M. Enjalran, A. del Maestro, H. L. Malavian and M. J. P. Gingras, *Phys. Rev. B*, **68**, 172407 (2003).
157. C. Bansal, H. Kawanaka and H. Bando and Y. Nishihara, *Phys. Rev. B*, **420**, 052406 (2002).
158. C. R. Wiebe, J. S. Gardner, S.-J. Kim, G. M. Luke and A. S. Wills, B. D. Gaulin, J. E. Greedan, I. Swainson, Y. Qiu and C. Jones, cond-mat/0404235 (2004).
159. Y. Taguchi, Y. Oohara, H. Yoshizawa, H. Yoshizawa, N. Nagaosa and Y. Tokura, *Science*, **291**, 2573 (2001).
160. Y. Shimomura, S. Miyahara and N. Fukuzawa, cond-mat/0406366 (2004)
161. D. Yanagishima and Y. Maeno, *J. Phys. Soc. Japan*, **70**, 2880 (2001).
162. T. Fennell, S. T. Bramwell and M. A. Green, *Can J. Phys.*, **79**, 1415 (2001).
163. J. Nishimura, T. Fukumura, M. Ohtani, Y. Taguchi and M. Kawasaki, I. Ohkubo, H. Koinuma, H. Ohguchi, K. Ono, M. Oshima and Y. Tokura, *Appl. Phys. Lett.*, **82**, 1571 (1998).

## CHAPTER 8

# EXPERIMENTAL STUDIES OF FRUSTRATED PYROCHLORE ANTIFERROMAGNETS

Bruce D. Gaulin

*Department of Physics and Astronomy,  
Canadian Institute for Advanced Research, McMaster University  
Hamilton, ON, L8S 4M1, Canada  
E-mail: gaulin@mcmaster.ca*

Jason S. Gardner

*Physics Department, Brookhaven National Laboratory,  
Upton, New York 11973-5000 &  
NIST Center for Neutron Research,  
National Institute of Standards and Technology,  
Gaithersburg, Maryland 20899-8562*

Much recent experimental progress has been made in the study of magnetic materials made up of antiferromagnetically-coupled magnetic moments residing on networks of corner-sharing tetrahedra. Such networks of magnetic moments display phenomena known broadly as geometric frustration. They are found in nature in a variety of cubic pyrochlore, spinel and Laves phase materials, with the magnetic moments arising from either rare earth or transition metal electrons. Typically, the rare earth moments are relatively large and are only weakly coupled by exchange, such that the competition between antiferromagnetic exchange and dipolar interactions is important. Antiferromagnetic exchange interactions are stronger in transition metal-based materials, and the manifestation of geometrical frustration is different. This review focusses on experimental progress in this area from the last ten years primarily due to neutron scattering studies.

### 8.1. Introduction

It is now well appreciated that the combination of antiferromagnetic interactions and certain lattice symmetries lead to phenomena known broadly as geometrical frustration.<sup>1</sup> The system under question cannot simultaneously satisfy all of its near neighbour pairwise exchange interactions and the resulting ground state can have a large degeneracy. This situation is illustrated schematically in Fig. 8.1a and 8.1b. Figure 8.1a shows two antiferromagnetically-coupled spins on a triangle and the frustration which arises if their ground state configuration requires nearest neighbour spins to be antiparallel. The tetrahedron, shown in Fig. 8.1b is to three dimensions what the triangle is to two dimensions, and a related degeneracy is relevant to finding a ground state arrangement for four near neighbour spins at the vertices of a tetrahedron.

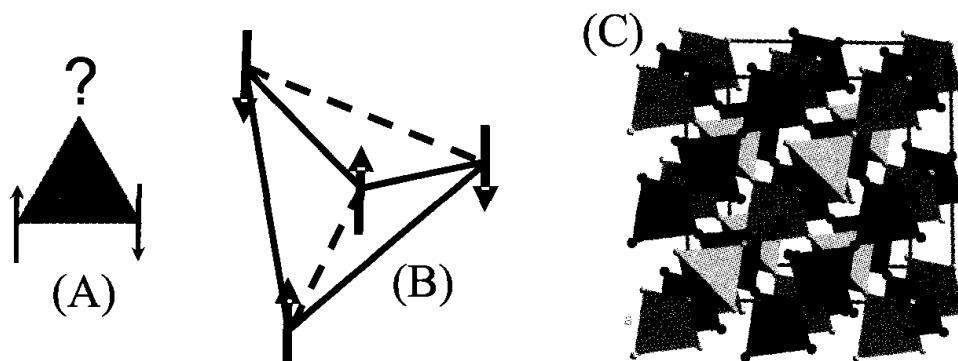


Fig. 8.1. (A) Two of three Ising spins located on a triangular unit can form an up-down pair, while the spin at the apex is frustrated. (B) Ising spins on a tetrahedron showing four satisfied (antiferromagnetic) and two frustrated (ferromagnetic) bonds. (C) The oxide pyrochlore unit cell showing the A (light) and B (dark) metal sublattices, each of which independently forms a network of corner sharing tetrahedra.

Such assemblies of interacting spins with triangular and tetrahedral coordination are in fact common in nature. In two dimensions one can form a network of edge-sharing triangles, giving rise to the familiar triangular lattice, which forms the basal plane of all hexagonal crystals. One can also form a network of corner-sharing triangles resulting in the kagomé lattice, which while relatively rare, is still manifest in a variety of quasi-two-dimensional crystal structures. One can also imagine more complicated assemblies of triangular plaquettes, such as the “Maple Leaf” lattice,<sup>2</sup> wherein every spin has five-fold coordination in two dimensions; however to date such struc-

tures have not been exhibited in real materials.

In three dimensions, a network of edge-sharing tetrahedra results in the familiar face centred cubic lattice, while networks of corner-sharing tetrahedra constitute sublattices of the cubic pyrochlore, spinel and Laves phase materials, all of which are relatively common.

In the context of magnetism in solids, this type of problem was considered theoretically first by Wannier<sup>3</sup> who showed that the thermodynamics of the classical Ising antiferromagnet on a two dimensional triangular lattice was qualitatively different from that of the corresponding ferromagnet. Theoretical treatment of the problem of classical spins with antiferromagnetic interactions on a lattice of corner-sharing tetrahedra was considered by both Anderson<sup>4</sup> and Villain,<sup>5</sup> the latter of whom coined the term "cooperative paramagnet" to describe the resulting low temperature state.

This type of phenomena, however, is not restricted to antiferromagnetism or even to magnets, but arises much more generally in interacting cooperative systems. It arises, for example in both hydrogen ordering in solid H<sub>2</sub>O<sup>6</sup> and in the corresponding problem in magnetism, spin ice,<sup>7</sup> which arises in the presence of *ferromagnetism* and tetrahedrally-coordinated spins (phenomena considered separately in this volume by Bramwell, Gingras and Holdsworth).

## 8.2. Pyrochlore Lattices

The cubic oxide pyrochlores crystallize into the space group Fd $\bar{3}m$ <sup>8</sup> and have the chemical composition A<sub>2</sub>B<sub>2</sub>O<sub>7</sub>, where the A sublattice is often occupied by a trivalent rare earth ion and the B sublattice by a tetravalent transition metal ion. Both the A and B sublattices, independently, form a network of corner-sharing tetrahedra, as shown in Fig. 8.1c. The A and B networks are shifted relative to each other along the cubic [111] direction.

As either of the rare earth or the transition metal site may possess a magnetic moment, it is possible for pyrochlores to exist in which either the A sublattice is magnetic, as occurs in Tb<sub>2</sub>Ti<sub>2</sub>O<sub>7</sub><sup>9</sup> for example, or the B sublattice is, as occurs in Y<sub>2</sub>Mo<sub>2</sub>O<sub>7</sub>.<sup>10</sup> It is also possible for both sublattices to be simultaneously magnetic, as occurs in Tb<sub>2</sub>Mo<sub>2</sub>O<sub>7</sub>,<sup>11</sup> or for neither to be magnetic, as occurs in Y<sub>2</sub>Ti<sub>2</sub>O<sub>7</sub><sup>12</sup> for example.

The local chemical environment around the A and B sites is not the same, with the A site being eight-fold coordinated by a distorted cube of O<sup>2-</sup> ions, while the B site is coordinated within BO<sub>6</sub> octahedra.<sup>8</sup> This local structure can profoundly influence the magnetism in these compounds,

particularly for the rare earth moment at the A site. The nature of the distortion of the oxygen environment determines the crystalline electric field splittings relevant to the rare earth ion, which in turn determine the nature of the rare earth magnetic moment and its anisotropies. The transition metal moment tends to be spin only, due to quenching of its orbital magnetic moment.

The rare earth magnetic moments at the A site of the pyrochlores interact with each other via rather weak exchange in insulating pyrochlores. This is due to the fact that the 4f electrons are relatively localized and shielded from the neighbouring electronic environment by their 5s and 5p electrons. The electronic overlap which drive superexchange interactions are therefore weak and near neighbour exchange is typically  $\sim 10$  K or less in such rare earth magnets. The orbitally quenched moments in transition metal-based pyrochlores interact much more strongly as the d-electrons are more extended and the overlap and resulting exchange can be an order of magnitude or more stronger than in the insulating rare earth based pyrochlores.

Metallic pyrochlores also exist, and some of these relax the condition that the A site be occupied by a rare earth atom. For example, much recent attention has focussed on  $\text{Cd}_2\text{Re}_2\text{O}_7$ <sup>13</sup> and  $\text{Cd}_2\text{Os}_2\text{O}_7$ ,<sup>14</sup> as  $\text{Cd}_2\text{Re}_2\text{O}_7$  has been found to be superconducting at low temperatures ( $\sim 1\text{-}2$  K) and  $\text{Cd}_2\text{Os}_2\text{O}_7$  undergoes an intriguing metal-insulator transition at relatively high temperatures. There is also very interesting metal-insulating behavior observed across the  $\text{RE}_2\text{Mo}_2\text{O}_7$  series, where RE is a rare earth ion.<sup>15</sup> In this family of materials the conductivity changes from metallic to insulating as the RE atom moves from the light rare earths to the heavy rare earths. Very recently, superconductivity has also been discovered in so-called  $\beta$ -pyrochlores  $\text{KO}_{\text{s}}\text{Os}_2\text{O}_6$ <sup>16</sup> and  $\text{RbOs}_2\text{O}_6$ ,<sup>17</sup> at  $\sim 9.6$  and 6.3 K respectively. These metals also crystallize in the cubic space group  $\text{Fd}\bar{3}\text{m}$  with Os occupying sites on a network of corner sharing tetrahedra.

The network of corner-sharing tetrahedra also forms within the cubic spinels<sup>18</sup> which also crystallize in the space group  $\text{Fd}\bar{3}\text{m}$ . These materials often have the chemical composition  $\text{AB}_2\text{O}_4$ , and the B site sublattice also takes on the pyrochlore lattice. In insulating spinels where the A site is divalent, such as  $\text{Zn}^{2+}$  or  $\text{Mg}^{2+}$ , the B site can be a trivalent magnetic transition metal ion, such as  $\text{Cr}^{3+}$  in  $\text{ZnCr}_2\text{O}_4$ . These materials are Mott insulators and, as in the case of the transition metal ions on the pyrochlore lattice, the antiferromagnetic interactions between the B site ions are relatively strong.

In the case where the A site is monovalent, such as  $\text{Li}^{1+}$  in  $\text{LiV}_2\text{O}_4$ ,<sup>19</sup>

a narrow band metal results within non-integral valence on the transition metal at the B site, in this example the V site. Although the straightforward conditions for geometrical frustration due to near neighbour antiferromagnetic interactions are not obviously relevant to the metallic magnet, interesting heavy fermion behaviour is observed in this material which has been proposed as a consequence of the frustrated magnetic interactions.<sup>20</sup>

At low temperatures the insulating cubic spinel magnets often distort to tetragonal symmetry,<sup>21</sup> and thus the “full” frustration of the pyrochlore lattice can be partially relieved. Recent neutron scattering work has proposed that this distortion is in fact driven by the geometric frustration in a manner akin to the spin-Peierls transitions<sup>22</sup> in quasi-one-dimensional  $s=1/2$  antiferromagnetic materials.

The coupling between lattice and magnetic degrees of freedom in pyrochlore antiferromagnets has been examined theoretically by Tchernyshyov *et al.*<sup>23</sup> Their work shows that a Jahn-Teller-like distortion of the tetrahedra can lower the overall energy of the coupled lattice and magnetism, and result in appropriately dimerized phases similar to experimental observations.<sup>22</sup>

The same pyrochlore sublattice also appears in cubic Laves phase materials such as YMn<sub>2</sub>,<sup>24</sup> where the Mn atoms reside on it in its high temperature, paramagnetic phase. This metal undergoes a strongly first order magnetic phase transition to a long period modulated magnetic structure with an accompanying lattice distortion. The phase transitions can be suppressed with minor alloying, of Sc at the Y site<sup>25</sup> for example, or with applied pressure.<sup>26</sup>

In what follows, we will review progress that has been made primarily through neutron scattering studies on some of the simplest such systems described by antiferromagnetically-coupled spins on the pyrochlore lattice. These will include the insulating pyrochlores Tb<sub>2</sub>Ti<sub>2</sub>O<sub>7</sub> and Y<sub>2</sub>Mo<sub>2</sub>O<sub>7</sub>, as well as the insulating spinel ZnCr<sub>2</sub>O<sub>4</sub>. This survey is clearly not comprehensive, but rather selective on systems for which our experimental understanding is relatively mature, and representative of the richness in low temperature ground states that are displayed under the umbrella of geometrical frustration.

### 8.3. Neutron Scattering Techniques

The complete experimental characterization of magnetic materials requires that an array of advanced experimental techniques be applied to the new

materials. Beyond basic structural characterization (typically x-ray diffraction) susceptibility, magnetization and heat capacity measurements are usually required to establish the fundamental magnetic properties of the materials. Metallic materials and materials where itinerant charge degrees of freedom are of interest also require an understanding of transport and Fermi surface properties. To make further progress, microscopic probes of magnetism must be employed, including NMR,  $\mu$ SR and neutron scattering.

Of these experimental probes, neutron scattering is the only one capable of providing information on the static and dynamic behaviour of the magnetic system as a function of wavevector spanning the entire Brillouin zone, and as a function of frequency covering spin dynamics on time scales from  $10^{-9}$  seconds to  $10^{-13}$  seconds. For this reason, neutron scattering is often regarded as an essential probe in the understanding of magnetic systems.

The neutron is, of course, electrically neutral, but carries a spin 1/2 magnetic moment. As such neutron scattering is a weak probe of matter, in the sense that neutrons penetrate deeply into most materials and large volumes of material are often needed to carry out neutron experiments, especially inelastic neutron scattering experiments. It is also a weak probe of matter in the sense that the scattering cross section can be described within the Born Approximation and Fermi's Golden Rule. This is a significant advantage as it means that theoretical calculations can be compared directly to the relevant neutron scattering measurements.

The double differential scattering cross section describing the relative magnetic neutron scattering into an element of solid angle  $d\Omega$  and with the scattered neutron having a final energy between  $E_f$  and  $E_f + dE_f$  can be written as:

$$\frac{d^2\sigma}{d\Omega_f dE_f} = \frac{N}{\hbar} \frac{k_f}{k_i} p^2 e^{-2W} \Sigma_{\alpha\beta} (\delta_{\alpha,\beta} - \hat{Q}_\alpha \hat{Q}_\beta) S^{\alpha\beta}(\mathbf{Q}, \omega) \quad (1)$$

Here  $k_i$  and  $k_f$  are the initial and scattered neutron wavevectors;  $p = \frac{\gamma r_0}{2} g f(\mathbf{Q})$  where  $\gamma$  is the gyromagnetic ratio of the neutron,  $r_0$  is the classical electron radius,  $g$  is the Lande  $g$  factor, and  $f(\mathbf{Q})$  is the magnetic form factor appropriate to the magnetic moment density of the atom; and  $e^{-2W}$  is the Debye-Waller factor.

The physics of the spins, and more generally the magnetic moments, is contained in:

$$S^{\alpha\beta}(\mathbf{Q}, \omega) = \frac{1}{2\pi} \int_{-\infty}^{\infty} dt e^{-i\omega t} \Sigma_l e^{(i\mathbf{Q}\cdot\mathbf{r}_l)} \langle S_0^\alpha S_l^\beta(t) \rangle \quad (2)$$

The  $\Sigma_{\alpha\beta}(\delta_{\alpha,\beta} - \hat{Q}_\alpha \hat{Q}_\beta) S^{\alpha\beta}(\mathbf{Q}, \omega)$  term in Eq. 1 ensures that the neutron scattering cross section is sensitive to only those components of moment which lie in a plane perpendicular to  $\mathbf{Q}=\mathbf{k}_i-\mathbf{k}_f$ , therefore the neutron scattering experiment directly measures the Fourier transform in space and time of this spin pair correlation function.

Integrating over all energy and over a complete Brillouin zone gives rise to the sum rule:

$$\int_{-\infty}^{\infty} d\omega \int_{BZ} d\mathbf{Q} S^{\alpha\beta}(\mathbf{Q}, \omega) \sim S(S+1)\delta_{\alpha\beta} \quad (3)$$

This relation implies that the total magnetic scattering scales as the size of the moment with  $S(S+1)$ , and that systems with suppressed magnetic ordering and therefore suppressed ordered magnetic moments necessarily exhibit enhanced inelastic scattering so as to satisfy the above sum rule. Excellent comprehensive reviews of neutron scattering exist and are referenced for the interested reader.<sup>27</sup>

#### 8.4. Cooperative Paramagnetism in $\text{Tb}_2\text{Ti}_2\text{O}_7$

The insulating rare earth pyrochlore  $\text{Tb}_2\text{Ti}_2\text{O}_7$  is a well studied system where the A-site  $\text{Tb}^{3+}$  ions are magnetic due to the partially-filled 4f shell, while the B-site  $\text{Ti}^{4+}$  ion is nonmagnetic. Like most of the  $\text{A}_2\text{B}_2\text{O}_7$  pyrochlores, the conventional cubic unit cell, shown in Fig. 1c, has cube edge dimensions of  $a \sim 10.1$  Å. The crystallographic structure of this material has been very carefully studied<sup>28</sup> and it is characterized as an (almost) disorder-free cubic pyrochlore.

It is often the case that new materials are first studied in polycrystalline form, as that is the form in which they are first prepared. If the material is of sufficient interest, an effort will generally be made to produce high quality single crystals, although this may ultimately prove to be difficult or impossible. The experimental study of the cubic pyrochlore  $\text{Tb}_2\text{Ti}_2\text{O}_7$  follows this path, with initial measurements performed on polycrystalline materials and later more sophisticated measurements made on single crystals.

Powder neutron diffraction measurements on  $\text{Tb}_2\text{Ti}_2\text{O}_7$ <sup>9</sup> taken at 2.5 K are shown in the top panel of Fig. 8.2 and these results clearly feature two

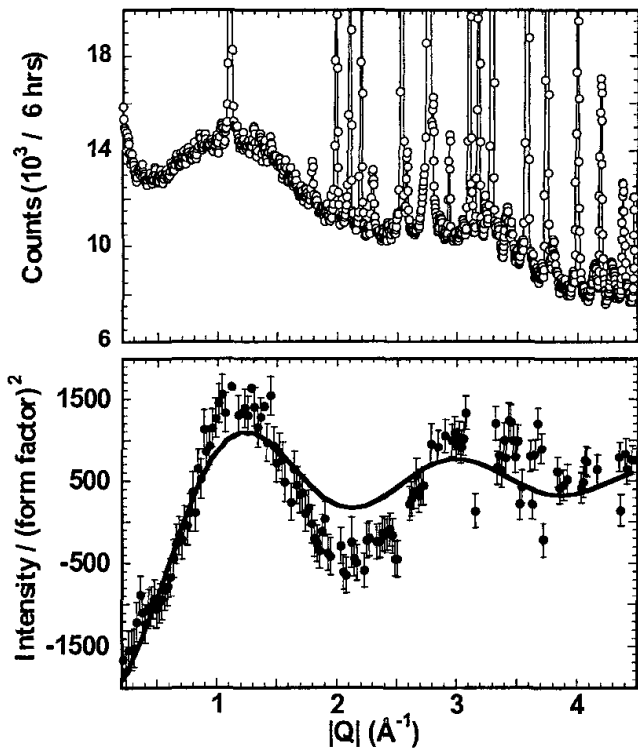


Fig. 8.2. Neutron powder diffraction data taken on  $\text{Tb}_2\text{Ti}_2\text{O}_7$  at  $2.5 \text{ K}$  is shown.<sup>9</sup> The upper panel shows the raw data while the lower panel shows the same data after a data set at  $T=100 \text{ K}$  (representing the nuclear scattering background) has been subtracted from it (see text).

distributions of scattering. One of these consists of sharp nuclear Bragg peaks, narrow in  $Q$ , due to the crystalline order in the material. But a second diffuse, liquid-like component is also clearly visible and is attributed to magnetic short range order.

Although the general trend of the diffuse scattering is clear in the raw data, the isolation of this magnetic scattering is not completely straightforward. In principle, the best method for accomplishing this is to use neutron polarization analysis.<sup>29</sup> However this method involves large trade-offs in intensity, and is not routinely employed for that reason. A substitute method is to subtract a high temperature data set from a low temperature data set. Assuming that the magnetic scattering is  $Q$ -independent at high temperatures, and that the nuclear scattering shows little temperature dependence, the resulting net scattered intensity can be attributed to magnetism.

The bottom panel of Fig. 8.2 shows just such a subtraction with a  $T=100 \text{ K}$  data set subtracted from the  $T=2.5 \text{ K}$  data set that is shown

in the upper panel. This data has been corrected for the magnetic form factor appropriate to  $Tb^{3+}$  and fit to a theoretical model for short range isotropic spin correlations over a few near neighbour distances. The theoretical form<sup>30</sup> used in the fit to the data in the bottom panel of Fig. 8.2 is appropriate to spin correlations existing over near neighbour distances only. It is clear from the bottom panel of Fig. 8.2, that this simple form for the scattering places the peaks and valleys in  $S(Q)$  at the correct positions in  $Q$ , but that the quantitative fit is imperfect. Nonetheless, as the width of the scattering is also roughly accounted for by this model with only near neighbour spin correlations, we can conclude that the spin correlations at  $T=2.5$  K in this material are of very short range.

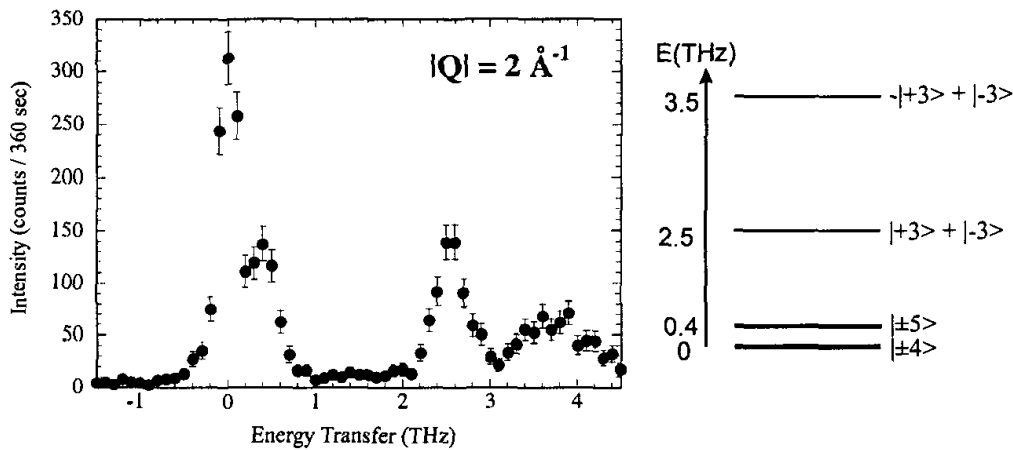


Fig. 8.3. A constant  $|Q|$  scan ( $2 \text{ \AA}^{-1}$ ) at 11 K from polycrystalline  $Tb_2Ti_2O_7$  is shown. At  $\sim 3.8$  THz, the magnetic scattering is contaminated by an optical phonon branch. The proposed crystalline electric field level scheme and the major components of the eigenstates derived from these measurements are shown on the right.<sup>33</sup>

These magnetic  $S(Q)$  results obtained here on  $Tb_2Ti_2O_7$  are similar to the results of the magnetic  $S(Q)$  derived from measurements on powder  $Tb_2Mo_2O_7$  samples,<sup>31</sup> wherein both the  $Tb^{3+}$  and  $Mo^{4+}$  sites are magnetic. In the  $Tb_2Mo_2O_7$  case a short range order peak is present near  $2 \text{ \AA}^{-1}$ , in addition to those seen in Fig. 8.2 near 1 and  $3 \text{ \AA}^{-1}$ . This indicates an interaction between the two A and B frustrated pyrochlore sublattices. Single crystal measurements of the magnetic  $S(Q)$  along high symmetry directions in  $CsNiCrF_6$ <sup>32</sup> also possess very similar characteristics to those seen in Fig. 8.2, although in this  $CsNiCrF_6$  case, two magnetic species,  $Ni^{2+}$  and  $Cr^{3+}$ , are randomly distributed over a single pyrochlore sublattice.

Inelastic scattering experiments were also carried out on polycrystalline  $\text{Tb}_2\text{Ti}_2\text{O}_7$ <sup>33</sup> and a typical scan at  $Q=2 \text{ \AA}^{-1}$  is shown in Fig. 8.3. Three bands of excitations are clearly observed near 0.37, 2.53, and 3.50 THz. As the excitations in this powder sample are relatively sharp in energy, they must originate from relatively dispersionless excitations. Their dispersion as a function of modulus of  $Q$ , was explicitly mapped<sup>33</sup> out and is shown in Fig. 8.4. Indeed, at temperatures above 30 K, there is very little dispersion in any of the three branches of magnetic excitations, a characteristic of crystalline electric field levels associated with the rare earth site. A weak, but very interesting dispersion develops in the lowest energy band near 0.37 THz  $\sim 20$  K, at temperatures below  $\sim 20$  K, as can be seen in the bottom panel of Fig. 8.4. This dispersion is such that the energy of the excitation is lowest at those wavevectors for which the magnetic structure factor,  $S(Q)$ , is maximum. This behaviour is very reminiscent of the roton minimum in the single particle excitation spectrum of liquid  $^4\text{He}$ .<sup>34</sup>

A crystalline electric field (CEF) level scheme appropriate to the  $^7\text{F}_6$

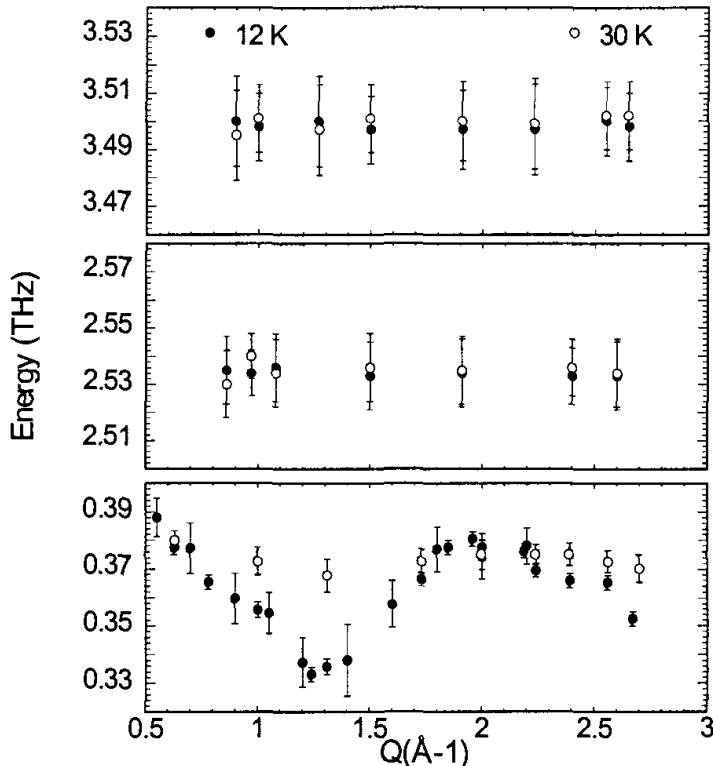


Fig. 8.4. The dispersion relation for the three lowest lying excitations in  $\text{Tb}_2\text{Ti}_2\text{O}_7$ . In the bottom panel, an unusual partial softening of the lowest energy excitation at  $|Q| \sim 1.2 \text{ \AA}^{-1}$  is seen below 20 K.<sup>33</sup>

configuration of  $\text{Tb}^{3+}$  in the A site environment of  $\text{Tb}_2\text{Ti}_2\text{O}_7$  was worked out on the basis of these inelastic measurements.<sup>35</sup> With  $J=6$ , the ground state and first excited states are both doublets, with two singlets at much higher energies, as shown schematically in Fig. 8.3. The ground state doublet is made up primarily of  $J^z$  eigenstates  $|\pm 4\rangle$  and  $|\pm 1\rangle$  and the first excited doublet of  $J^z$  eigenstates  $|\pm 5\rangle$  and  $|\pm 2\rangle$ . One of the other two singlets corresponds exclusively to  $|\pm 6\rangle$  and  $|\pm 3\rangle$ , while the remaining singlet corresponds to  $|\pm 6\rangle$ ,  $|\pm 3\rangle$ , and  $|0\rangle$ . Note that within this CEF scheme the ground state is connected to all these low lying excited states by  $\langle A|S^+|0\rangle$  and  $\langle A|S^-|0\rangle$  matrix elements, and thus all these transitions are expected to be visible with neutron spectroscopy, which obeys such a dipole selection rule.

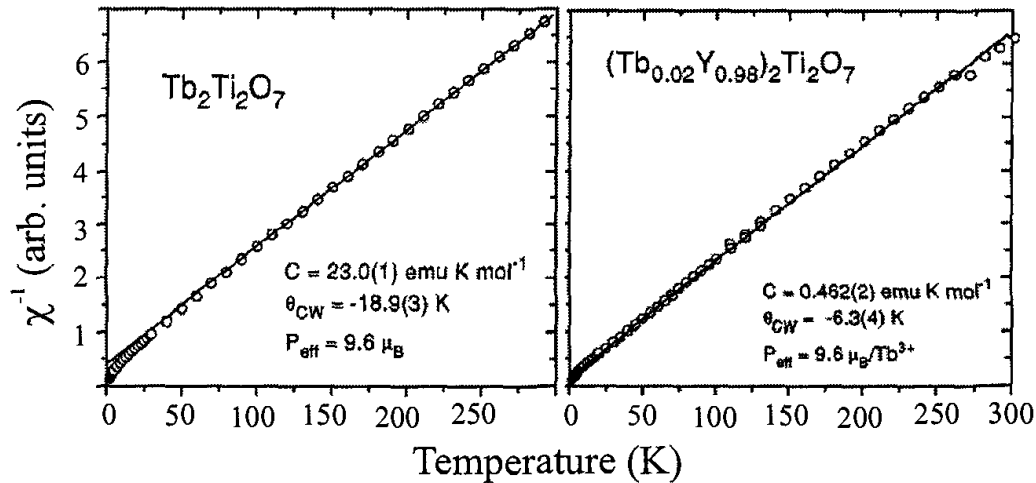


Fig. 8.5. The temperature dependence of the inverse susceptibility of the  $\text{Tb}_2\text{Ti}_2\text{O}_7$  and a magnetically diluted sample,  $(\text{Tb}_{0.02}\text{Y}_{0.98})_2\text{Ti}_2\text{O}_7$ , intended to isolate  $\text{Tb}^{3+}$  magnetic moments.<sup>35</sup>

Such a CEF scheme implies that the *ground state moment* (as opposed to the full paramagnetic moment), of the  $\text{Tb}^{3+}$  is  $\sim 5 \mu_B$ . Also, were the excited state doublet at  $\Delta \sim 20$  K, separated from the ground state by a significantly greater energy, then the moment would be considered to be an extreme Ising moment, ie. capable of pointing only along local  $<111>$  directions; that is either into or out of the tetrahedra. We will return to this issue later.

The CEF excitations provide information as to the size and anisotropy of the local  $\text{Tb}^{3+}$  moments. However, the nature of the magnetic interactions between the moments must be derived from magnetic suscep-

tibility measurements, as shown in Fig. 8.5<sup>35</sup> for both  $\text{Tb}_2\text{Ti}_2\text{O}_7$  and  $(\text{Tb}_{0.02}\text{Y}_{0.98})_2\text{Ti}_2\text{O}_7$ . As can be seen, Curie-Weiss fits to the high temperature susceptibility give a paramagnetic moment of  $9.6 \mu_B/\text{Tb}^{3+}$ , very close to the 9.72 value appropriate to the  $^7\text{F}_6$  free ion value. The Curie-Weiss temperature which parametrizes the average magnetic interactions is obtained from the T-intercept of the Curie-Weiss fit at high temperatures: this is clearly negative for both  $\text{Tb}_2\text{Ti}_2\text{O}_7$  and  $(\text{Tb}_{0.02}\text{Y}_{0.98})_2\text{Ti}_2\text{O}_7$  indicating antiferromagnetic exchange interactions. Magnetically dilute  $(\text{Tb}_{0.02}\text{Y}_{0.98})_2\text{Ti}_2\text{O}_7$  would be expected to be representative of a non-interacting system, and consequently the Curie-Weiss temperature derived from its analysis is attributed to crystal field and non-exchange contributions to  $\Theta_{CW}$ . For that reason the  $\Theta_{CW}$ , which we attribute to magnetic interactions in  $\text{Tb}_2\text{Ti}_2\text{O}_7$  is the difference between the  $\Theta_{CW}$  for each of  $\text{Tb}_2\text{Ti}_2\text{O}_7$  and  $(\text{Tb}_{0.02}\text{Y}_{0.98})_2\text{Ti}_2\text{O}_7$ ; that is:

$$\Theta_{CW}(\text{Tb}_2\text{Ti}_2\text{O}_7) - \Theta_{CW}((\text{Tb}_{0.02}\text{Y}_{0.98})_2\text{Ti}_2\text{O}_7) \sim -13K \quad (4)$$

Together with an estimate for the contribution of the magnetic dipole interactions to  $\Theta_{CW}$ , an estimate for the exchange contribution to  $\Theta_{CW}$  is in the range from -10.6 to -14.2 K and it is antiferromagnetic.

Relatively large single crystals of  $\text{Tb}_2\text{Ti}_2\text{O}_7$  could be grown using floating zone image furnace techniques,<sup>36</sup> and the resulting single crystals enabled a series of experiments which could probe the four dimensional dynamic structure factor  $S(\mathbf{Q}, \hbar\omega)$ . The left panel of Fig. 8.6 shows the difference between  $S(\mathbf{Q}) = \int S(\mathbf{Q}, \hbar\omega) d\omega$  measured at  $T=9$  K and that measured at  $T=100$  K,<sup>33</sup> within the  $(h,h,l)$  plane in reciprocal space. Once again a difference between a low and high temperature data set is employed to isolate the magnetic structure factor. For cubic crystals, this  $(h,h,l)$  plane in reciprocal space is often employed in neutron scattering studies as it contains the  $(0,0,l)$ ,  $(h,h,0)$ , and  $(h,h,h)$  high symmetry directions.

One clearly observes a “checkerboard” pattern to the scattering, with diffuse scattering covering entire Brillouin zones. This indicates spin correlations on a length scale small compared to the dimensions of the unit cell  $\sim 10.2 \text{ \AA}$ , consistent with the near-neighbour spin correlations estimated from the data on the powder samples. However, the single crystal data is clearly *not* isotropic in reciprocal space, explaining the quantitative failure of the simple isotropic model for the structure factor shown as the solid line in the bottom panel of Fig. 8.2.

The temperature dependence to this diffuse  $S(\mathbf{Q})$ <sup>33</sup> extends to re-

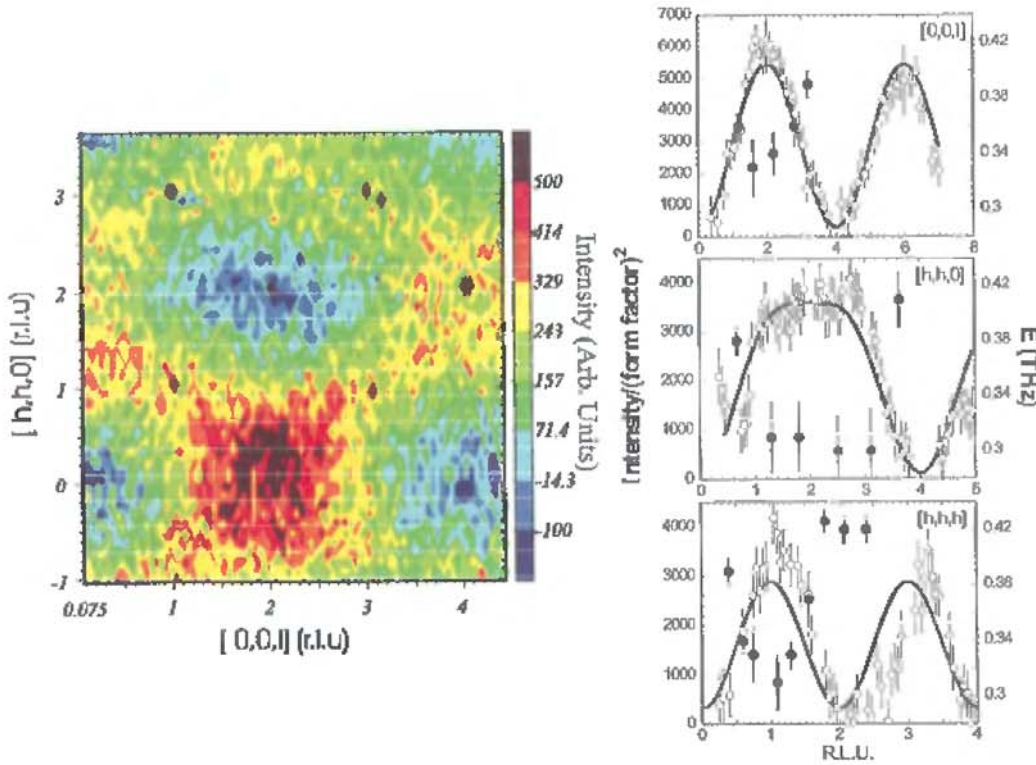


Fig. 8.6. Left panel: The diffuse magnetic scattering from a single crystal of  $\text{Tb}_2\text{Ti}_2\text{O}_7$  in the  $(h,h,l)$  plane is shown. Right panel: Cuts through the diffuse scattering (open circles) along high symmetry directions  $(0,0,l)$ ,  $(h,h,0)$  and  $(h,h,h)$  are shown along with the dispersion of the lowest lying magnetic excitation (closed circles) mode at 4 K. The diffuse scattering intensity scale is on the left side of the panel, while the energy scale of the lowest magnetic excitation is on the right side of the panel.<sup>33</sup>

markably high temperatures as is shown in Fig. 8.7. Here we show  $S(Q=(0,0,2.25))$  as a function of temperature. This wavevector was chosen for study as it is quite close to the peak in the diffuse scattering near  $(0,0,2)$ , but far enough removed to be free of any spurious scattering effects due to, for example, higher order wavelength contamination of the neutron beam. One sees a dramatic upturn to the temperature dependence below  $\sim 25$  K, but the diffuse scattering continues to evolve with temperature until at least 100 K. It was for this reason that the T=100 K data set was used in the subtraction of the data sets shown in Fig. 8.6. The temperature scale of  $\sim 25$  K corresponds to the energy scale on which the excited state doublet is populated and develops the dispersion seen in the bottom panel of Fig. 8.4.

With a high quality single crystal, the dispersion of the low lying  $\hbar\omega \sim 0.33$  THz magnetic excitation can be studied as a function of  $Q$ ,<sup>33</sup> as op-

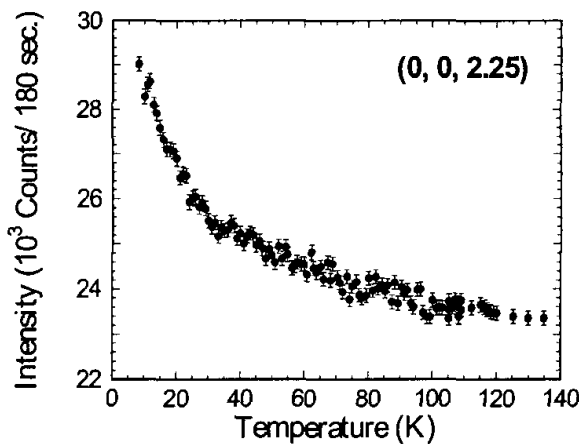


Fig. 8.7. The temperature dependence of the diffuse scattering as measured at  $(0,0,2.25)$ , close to the peak in the magnetic diffuse scattering at  $\mathbf{Q}=(0,0,2)$ .<sup>33</sup>

posed to modulus of  $\mathbf{Q}$  derived from powder samples. One sees the development of dispersion for temperatures below  $\sim 25$  K, as was observed in powders.<sup>9</sup> This low temperature dispersion is plotted along the three high symmetry directions within the  $(h,h,l)$  plane in Fig. 8.6, on which are overlaid cuts of  $S(\mathbf{Q})$  along  $(0,0,l)$  (top),  $(h,h,0)$  (middle), and  $(h,h,h)$  (bottom). We see that the minima in the dispersion of this low lying magnetic mode correspond exactly with peaks in  $S(\mathbf{Q})$ , even though  $S(\mathbf{Q})$  is anisotropic in  $\mathbf{Q}$ ; that is even though it displays the “checkerboard” pattern within the  $(h,h,l)$  plane of reciprocal space.

Related  $S(\mathbf{Q})$  and  $S(\mathbf{Q}, \hbar\omega)$  measurements have been carried out to

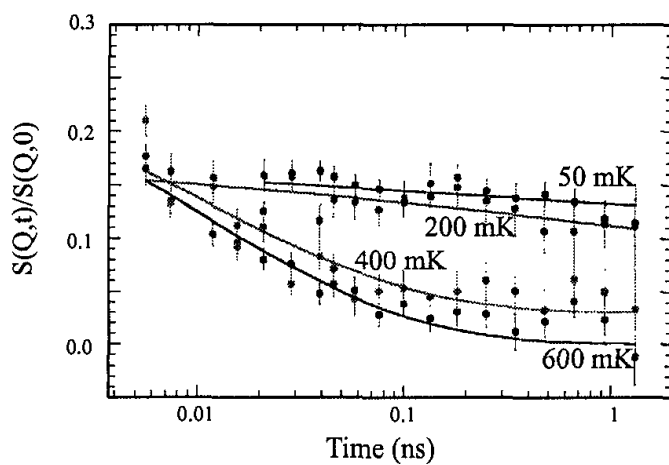


Fig. 8.8. The normalized, intermediate scattering function measured with neutron spin echo techniques at several temperatures from polycrystalline  $Tb_2Ti_2O_7$ .<sup>37</sup>

much lower temperatures, as low as 0.07 K.<sup>9,37</sup> Remarkably the magnetic  $S(Q)$  remains largely the same as the checkerboard pattern observed at 9 K and shown in Fig. 8.6. As we will discuss below, the absence of a phase transition down to these very low temperatures is surprising, and ultimately enigmatic.

Neutron spin echo<sup>37,39</sup> and  $\mu$ SR<sup>9,40</sup> measurements have also been carried out to similarly low temperatures to probe the fluctuating nature of the magnetic moments. The normalized intermediate scattering function  $S(Q,t)/S(Q,0)$  measured in neutron spin echo from powder samples is shown in Fig. 8.8.<sup>37</sup> Above  $\sim 0.3$  K,  $S(Q,t)/S(Q,0)$  decays with time on the time scale of 0.01 to 1 ns, consistent with  $\frac{1}{T_1}$   $\mu$ SR measurements which show fluctuating moments down to at least 0.05 K.<sup>9</sup> Below  $T=0.3$  K, the time dependence of  $S(Q,t)/S(Q,0)$  flattens out, indicating a population of frozen magnetic moments. However a large majority of the magnetic moments remain fluctuating below 0.3 K as the normalized  $S(Q,t)/S(Q,0)$  is not observed any higher than  $\sim 0.2$  for any times within the neutron spin echo time window. Susceptibility measurements also indicate freezing below  $\sim 0.3$  K.<sup>37,41</sup> We attribute this partial spin freezing to a small subset of magnetic moments distributed near a small number of defects.

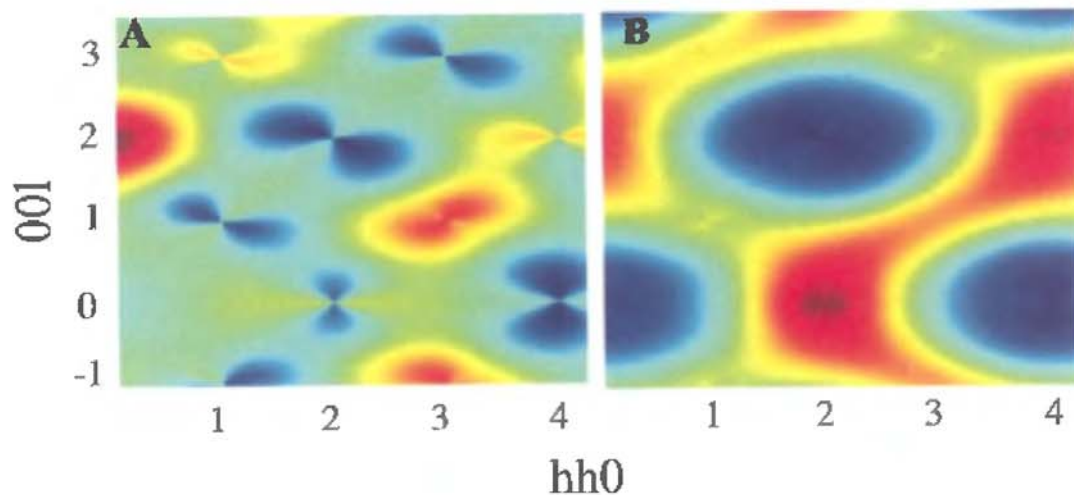


Fig. 8.9. Two theoretical models<sup>38</sup> of the diffuse magnetic scattering in the  $(h,h,l)$  plane of  $Tb_2Ti_2O_7$ . The left panel shows a calculation assuming extreme Ising moments, while the right panel incorporates the finite gap to the lowest lying magnetic excitations which tends to restore spin isotropy to the system. The calculation in the right panel is a good descriptor of the measured  $S(Q)$  shown in Fig. 8.6.

Evidence for spin freezing was also found independently in neutron scattering experiments performed on other single crystal samples.<sup>42</sup> In this case, hysteresis is observed in the scattering near (0,0,2) at temperatures less than  $\sim 1.7$  K. However, as in the samples described above, most of the scattering remains diffuse in nature even below 1.7 K.

From an experimental point of view  $Tb_2Ti_2O_7$  is well characterized, at least in zero applied magnetic field. It is appropriate to then ask, how consistent is the information which has been derived from the different measurements. That is how well do we understand the low temperature properties of this frustrated magnetic material?

The most striking experimental feature of  $Tb_2Ti_2O_7$  is that most of the  $Tb^{3+}$  moments remain dynamic to temperatures as low as 0.05 K. As discussed at length by Kao *et al.*,<sup>38</sup> this is not what one would conclude for antiferromagnetically coupled spins with strong [111] anisotropy. In this case, the ground state is in fact not degenerate, and a non-collinear Néel state is expected with all spins pointing into a tetrahedron, and all spins pointing out of the neighbouring tetrahedra. Interesting, this is in contrast to the “spin ice” ferromagnet with strong local [111] anisotropy, which does display a macroscopic degeneracy at low temperatures. Given estimates for  $\Theta_{CW}$  and contributions from dipolar interactions in  $Tb_2Ti_2O_7$ , an ordering temperatures of  $T_N \sim 1$  K is expected into a non-collinear Néel state.

However, the measured magnetic structure factor  $S(\mathbf{Q})$  shown in Fig. 8.6, *cannot* be accounted for by antiferromagnetically-coupled spins in the presence of strong local <111> anisotropy. This is explicitly shown in the left panel of Fig. 8.9 wherein the calculation of  $S(\mathbf{Q})$  including appropriate antiferromagnetic exchange, long range dipolar interactions, and strong local <111> anisotropy is presented. Clearly this calculation does not describe the experimental measurement on  $Tb_2Ti_2O_7$  shown in Fig. 8.6 at all.

In fact Gardner *et al.*<sup>33</sup> have shown that a remarkably simple calculation on the basis of extreme near-neighbour correlations only, can reproduce most of the features of the experimentally determined  $S(\mathbf{Q})$ . As this calculation assumes no spin direction, it implies an isotropy to the local spin structure at odds with the local <111> anisotropy assumed to be relevant on the basis of the CEF measurements shown in Fig. 6. Yasui *et al.*<sup>42</sup> also attempted to model their measured  $S(\mathbf{Q})$  on the basis of proposed spin correlations over two interconnected tetrahedra connected by a single, central spin (that is over a seven spin cluster). These results were also at odds with a picture in which the spins are restricted to point along local <111> directions.

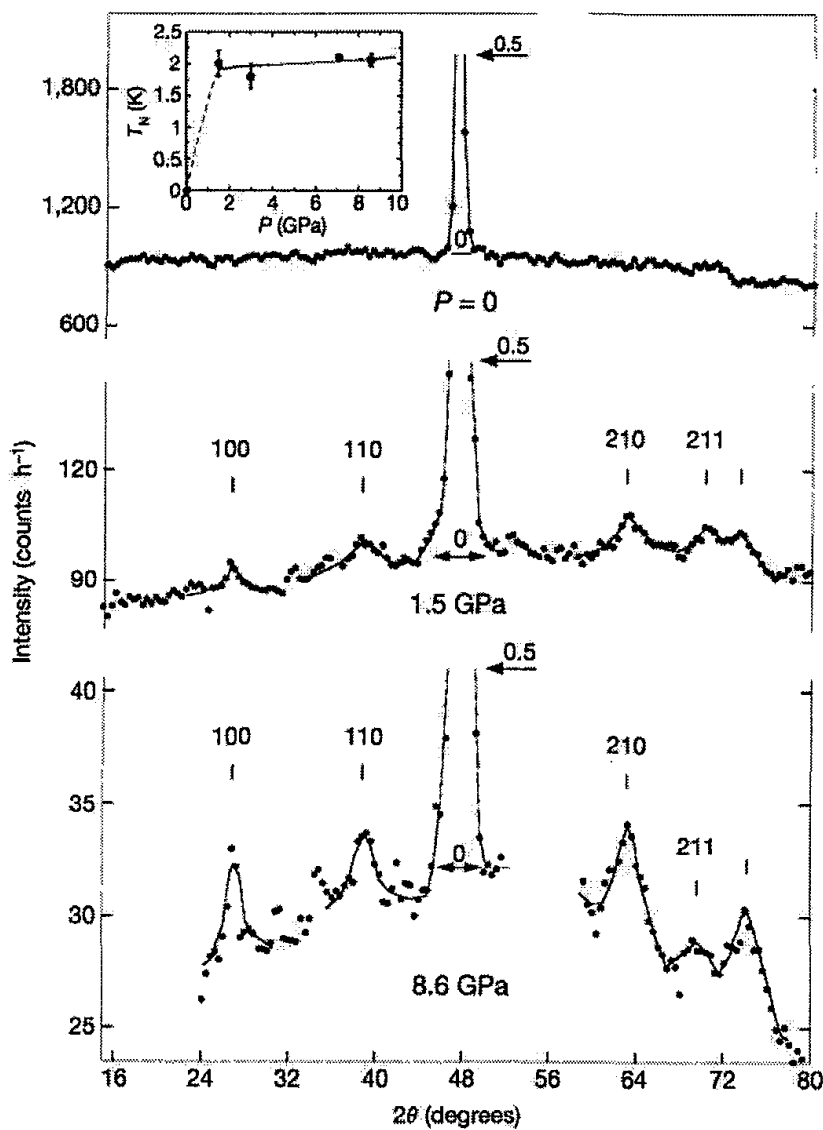


Fig. 8.10. Pressure induced magnetic Bragg scattering from polycrystalline  $\text{Tb}_2\text{Ti}_2\text{O}_7$  at  $<2$  K. The data shows the pressure evolution of static correlations in the cooperative paramagnet. The inset depicts the pressure dependence of the transition temperature.<sup>43</sup>

However Kao *et al.*<sup>38</sup> went much further, and incorporated the finite and relatively small energy gap ( $\sim 20$  K) separating the ground state doublet from the excited state doublet in  $\text{Tb}_2\text{Ti}_2\text{O}_7$  using a random phase approximation. The inclusion of the effect of this low lying excited state restores the spin isotropy to the problem, and gives rise to a calculated  $S(\mathbf{Q})$  which now includes the effects of the antiferromagnetic exchange, the long range

dipolar interactions, as well as the details of the CEF scheme to produce the calculated magnetic  $S(\mathbf{Q})$  shown in the right panel of Fig. 8.9. This new calculation is clearly an excellent descriptor of the measured  $S(\mathbf{Q})$ , and represents a significant step forward in our detailed understanding of this material. However, it still leaves the problem as to why  $Tb_2Ti_2O_7$  fails to achieve long range order near 1 K?

Indeed, recent measurements by Mirebeau *et al.*<sup>43</sup> have shown that polycrystalline  $Tb_2Ti_2O_7$  does indeed achieve long range magnetic order near 2 K, but only under hydrostatic pressure exceeding  $\sim 1$  GPa. Powder neutron diffraction data as a function of pressure is shown in Fig. 8.10. Weak magnetic Bragg peaks can be seen to arise out of a flat background at applied pressures of 1.5 GPa and above. This remarkable experiment also shows that even under the conditions of applied hydrostatic pressure, the antiferromagnetic order coexists with spin liquid like fluctuations; that is that considerable diffuse scattering remains even in the presence of the magnetic Bragg peaks. This study indicates that  $Tb_2Ti_2O_7$  is close to an instability to Néel order, as theoretical analysis suggests it should be. However in the absence of an external perturbation it remains in an enigmatic spin liquid to very low temperatures. Clearly future work looking at the stability of the spin liquid state to other external perturbations such as unidirectional stress and magnetic fields will be important for further progress in understanding this remarkable material.

### 8.5. The Spin Glass Ground State in $Y_2Mo_2O_7$

The pyrochlore  $Y_2Mo_2O_7$  is a well studied system<sup>10,44,45,46,47,48,49,50,51</sup>, wherein magnetic  $Mo^{4+}$  moments reside at the B-site in the pyrochlore structure.<sup>8</sup> As was the case with  $Tb_2Ti_2O_7$ , the conventional unit cell shown in Fig. 1c, has dimensions such that a cube edge is  $\sim 10.2$  Å. The structure of  $Y_2Mo_2O_7$  has complexities which we will discuss below. However these are relatively subtle, and our starting point in the description of  $Y_2Mo_2O_7$  is of antiferromagnetically-coupled  $Mo^{4+}$  moments which interact on a network of corner-sharing tetrahedra. To date  $Y_2Mo_2O_7$  has been produced only as polycrystalline material, and thus a more limited set of measurements can be carried out than was the case in  $Tb_2Ti_2O_7$ .

High temperature susceptibility measurements, in the range from 300 K - 1000 K, on  $Y_2Mo_2O_7$  yield a large Curie-Weiss temperature of  $\Theta_{CW} \sim -200$  K and an effective paramagnetic magnetic moment of  $2.55 \mu_B/Mo$  indicating strong antiferromagnetic coupling between  $S=1$

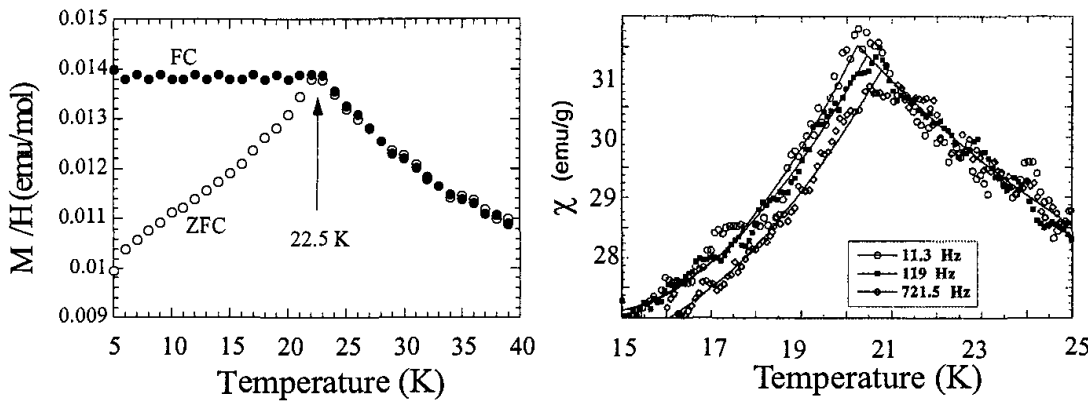


Fig. 8.11. Left: Static magnetic susceptibility of  $\text{Y}_2\text{Mo}_2\text{O}_7$  revealing the history dependent signature of a spin-glass-like transition.<sup>45</sup> Right: The frequency dependence of the AC susceptibility is shown.<sup>46</sup>

$\text{Mo}^{4+}$  moments.<sup>44</sup> Thus relatively strong exchange interactions are present in  $\text{Y}_2\text{Mo}_2\text{O}_7$ , in contrast to those discussed above between rare earth  $\text{Tb}^{3+}$  moments in  $\text{Tb}_2\text{Ti}_2\text{O}_7$ .<sup>9</sup> The paramagnetic moment in  $\text{Y}_2\text{Mo}_2\text{O}_7$  is close to that expected for orbitally-quenched  $\text{Mo}^{4+}$  magnetic moments:  $g\sqrt{S(S+1)} = 2.8\mu_B$ .

As shown in the left panel of Fig. 8.11 the DC magnetic susceptibility shows a clear break between the field-cooled (FC) and zero-field-cooled (ZFC) susceptibilities below  $T_g \sim 22$  K. This difference between the magnetic susceptibilities as measured under different protocols is typical of chemically-disordered spin glasses, such as CuMn, EuSrS and CdMnTe.

Further study of the non-linear DC-susceptibility<sup>47</sup> as well as AC-susceptibility measurements<sup>46</sup> confirm the spin glass nature of the low temperature ground state in  $\text{Y}_2\text{Mo}_2\text{O}_7$ . AC-susceptibility data is shown in right panel of Fig. 8.11 at frequencies ranging from 11.3 to 721 Hz. This data shows a clear peak whose position moves to lower temperatures with decreasing frequency, again typical of chemically disordered spin glasses. (This data indicates a slightly lower  $T_g$ , likely due to the absolute calibration of the thermometry).

It is well appreciated that chemically-disordered spin glasses display critical divergences associated with their *non-linear* susceptibility,<sup>52</sup> as opposed to the divergences which characterize the susceptibility or staggered susceptibility in conventional ferromagnets and antiferromagnets undergoing critical phase transitions. Nonlinear susceptibility measurements on  $\text{Y}_2\text{Mo}_2\text{O}_7$ <sup>47</sup> shows such static critical behaviour, parameterised in terms of critical ex-

ponents  $\gamma \sim 2.8$ ,  $\beta \sim 0.8$ , and  $\delta \sim 4.7$ , and is consistent with an underlying thermodynamic phase transition to the spin glass state near 22 K. These critical exponents are typical of three dimensional spin glasses. The scaling analysis of the non-linear DC-susceptibility data is shown in Fig.8.12.

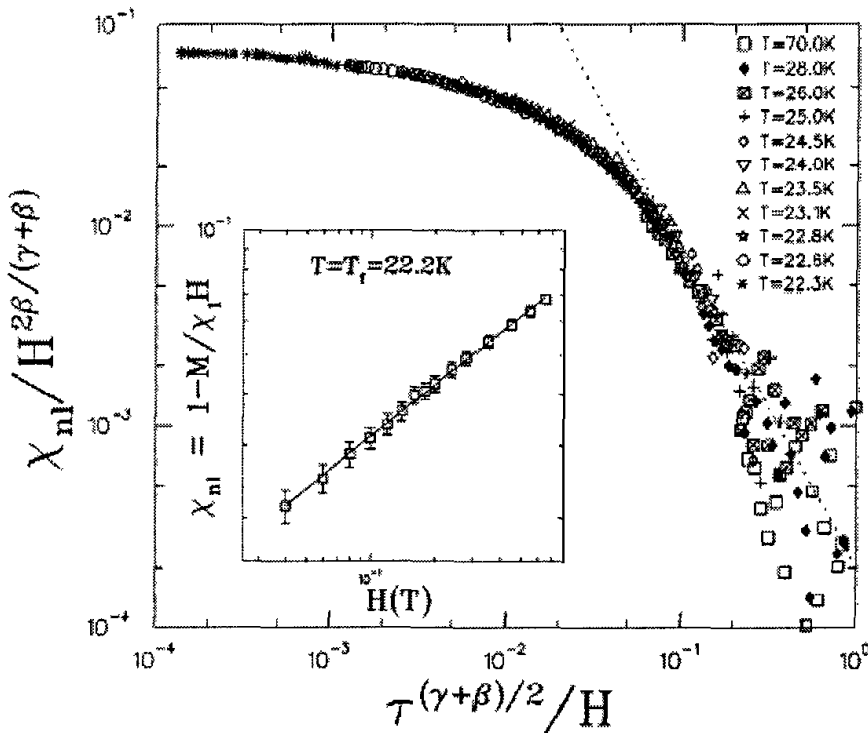


Fig. 8.12. The scaling behaviour of the non-linear DC susceptibility of  $\text{Y}_2\text{Mo}_2\text{O}_7$  is shown as a function of both magnetic field strength and temperature. The inset shows the field dependence of the nonlinear DC susceptibility at  $T_f = T_g = 22.2$  K.<sup>47</sup>

Neutron scattering measurements<sup>45</sup> were performed on the SPINS triple axis spectrometer located on a cold neutron guide at the NIST Center for Neutron Research. The  $|Q|$  dependence of the elastic neutron scattering from the powder sample is shown in Fig.8.13A. These measurements employed neutrons with constant scattered energy of 5.1 meV. Figure 8.13A shows the difference between low temperature elastic neutron scattering taken at  $T=1.4$  K and that taken at a relatively high temperature, 50 K. One clearly observes a diffuse peak in the elastic scattering centred at  $|Q| \sim 0.44 \text{ \AA}^{-1}$ . For reference, a horizontal bar on the same plot indicates the resolution width of Bragg peaks measured using the SPINS spectrometer in this configuration. The breadth of the diffuse scattering clearly exceeds the res-

olution width, indicative of a finite and relatively short correlation length. The energy resolution of the nominally elastic scattering experiment sets the time scale on which the measured spin correlations are static. For the present set of measurements this is  $\tau > \frac{\hbar}{\Delta E} = 3ps$ .

This diffuse scattering is quite different from that observed in  $Tb_2Ti_2O_7$ , where the first peak in the diffuse magnetic scattering appears at  $|Q| \sim 1.2 \text{ \AA}^{-1}$  (see Fig.8.2). In the case of  $Y_2Mo_2O_7$ , the peak in the diffuse scattering appears at  $Q \sim 0.44 \text{ \AA}^{-2}$ . We understand this position of the peak in the diffuse scattering as being given by  $\sim 2\pi/d(110)$ , where  $d(110) \sim \sqrt{2} \times 10.2 \text{ \AA}$  is the face diagonal of a conventional cubic unit cell. Such a local periodicity permits a four sublattice local structure along [110], which is shown schematically in the inset to Fig.8.13A.

The moment direction associated with each of the four sublattices cannot be known given the only information available is that associated with the peak of the diffuse magnetic scattering. However the constraint  $\sum_i S_i = 0$  is implied by the vanishing of the magnetic scattering as  $Q$  goes to zero. We therefore represent each of the four sublattices by a different colour and enforce the  $\sum_i S_i = 0$  constraint by requiring that each tetrahedron is colour neutral.

The half width at half maximum of this diffuse magnetic scattering gives rise to a correlation length which we set as  $\xi \sim 1/\text{HWHM} \sim 5 \text{ \AA}$ . This is consistent with a “cluster glass” spin configuration below  $T_g \sim 22 \text{ K}$ , in which locally ordered conventional unit cells of the type shown in the inset to Fig.8.13A, are incoherently correlated with each other.

The fraction of the total magnetic moment which participate in this spin glass state can be estimated from this neutron scattering experiment. The magnitude of the frozen, staggered magnetization is derived by integrating the elastic magnetic scattering data and comparing it to nuclear scattering whose intensity can be calculated. This analysis produces the estimate that  $2/3$  of the  $Mo^{4+}$  moment is frozen at low temperatures. This is an unusually small fraction of the total spin population participating in the ordered state of a three dimensional magnet in the limit  $T/\Theta_{CW} \rightarrow 0$ .

The temperature dependence of the elastic scattering at  $|Q| \sim 0.44 \text{ \AA}^{-1}$  is shown in Fig.8.13B. Interestingly, the temperature dependence falls off as expected as the temperature is raised, however  $T_g$  is given roughly by the inflection point on this curve, not by where the intensity becomes temperature-independent. This approximately temperature independent regime only occurs for temperatures greater than  $\sim 50 \text{ K}$ , more than twice  $T_g$ .

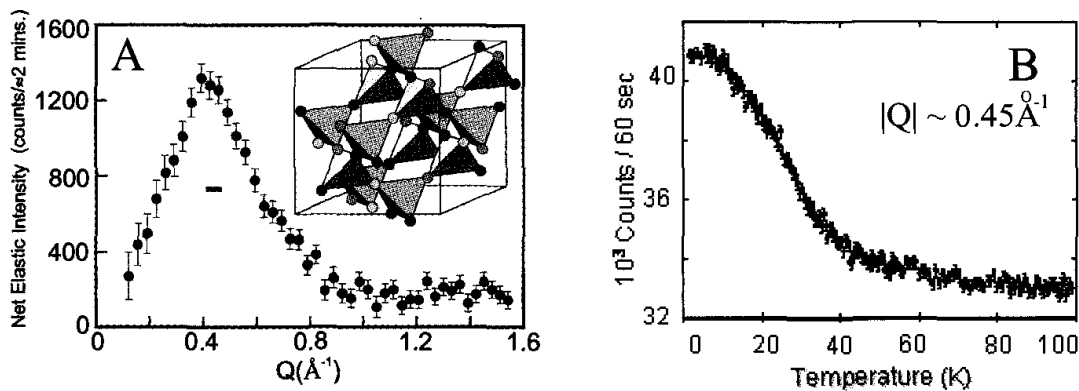


Fig. 8.13. (A) The  $|Q|$  dependence of the elastic magnetic scattering from  $\text{Y}_2\text{Mo}_2\text{O}_7$  at 1.5 K, obtained by subtracting a 50 K data set from a 1.5 K data set. The proposed four sublattice spin arrangement for short range correlations in  $\text{Y}_2\text{Mo}_2\text{O}_7$ , consistent with the data is shown in the inset. (B) The temperature dependence of the peak of the elastic scattering at  $|Q|=0.45 \text{ \AA}^{-1}$  is shown.<sup>45</sup>

Inelastic neutron scattering measurements were also performed at the maximum in the diffuse scattering,  $|Q| \sim 0.44 \text{ \AA}^{-1}$ . This data is shown in both a colour contour map in the top panel of Fig.8.14, where the intensity scale is linear, and in the bottom panel of Fig.8.14, where a subset of the same data is plotted on a semilog scale. The colour contour map shows clearly that the inelastic scattering collapses into the elastic position at  $T_g \sim 22 \text{ K}$ , indicating that the spins have frozen on the time scale of the neutron measurements, even though the spatial correlations correspond to a correlation length of only approximately 5  $\text{\AA}$ . What is also striking about the colour contour map in the top panel of Fig.8.14, is that strong temporal correlations begin as high as  $50 \text{ K} \sim 2 \times T_g$ , which would represent a very wide “critical” regime for conventional critical phenomena near continuous phase transitions. This is similar to what was concluded on the basis of the elastic magnetic scattering alone (Fig.8.13B).

It is straightforward to integrate the inelastic scattering, thus measuring  $\int_{-3\text{meV}}^{3\text{meV}} S(Q=0.44 \text{ \AA}, \hbar\omega) d\omega$  in  $\text{Y}_2\text{Mo}_2\text{O}_7$ , and this is shown in the top panel of Fig.8.15. This integral excludes the elastic scattering, and it is pleasing to see that its temperature dependence assumes the complement of the nominally elastic magnetic scattering in  $\text{Y}_2\text{Mo}_2\text{O}_7$  shown in Fig.8.13. Again in this case,  $T_g$ , is given by the inflection point on the temperature dependence of this inelastic scattering.

This energy dependence of the inelastic scattering could be fit to a simple form of  $S(Q=0.44 \text{ \AA}^{-1}, \hbar\omega)$  and consequently a simple form of the

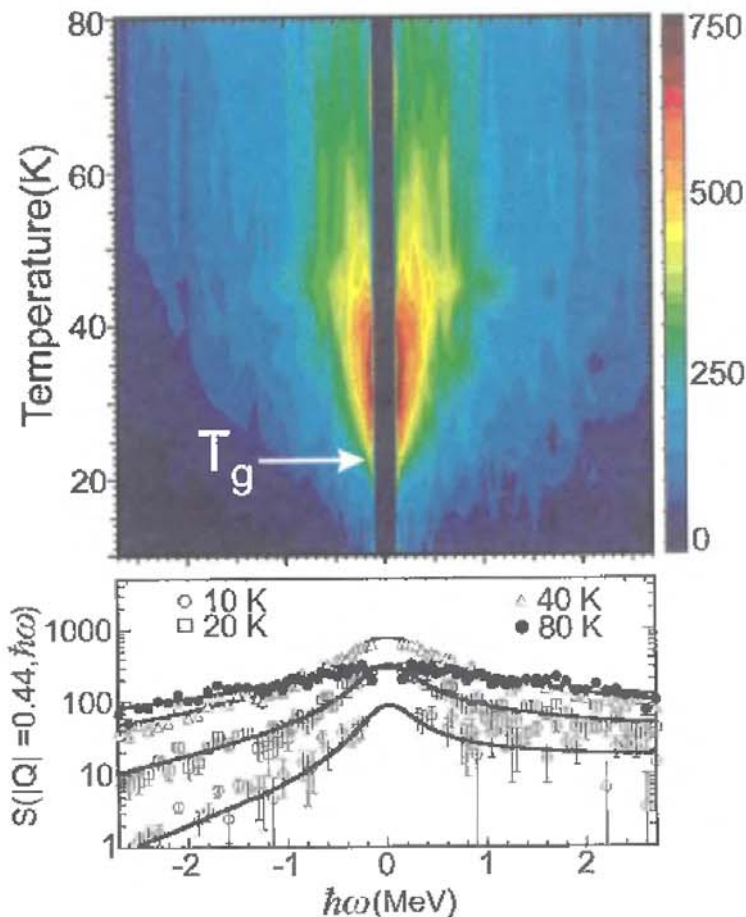


Fig. 8.14. The normalised, background subtracted inelastic scattering data for  $S(Q,\omega)$  from  $\text{Y}_2\text{Mo}_2\text{O}_7$ . The contour plot is produced from twelve data sets between 10 and 80 K similar to those shown in the bottom panel. The bottom panel shows the selected data sets from those in the top panel, but on a semilog scale and plotted with fits to the data which parameterise the inelastic scattering and which are described in detail in the text.<sup>45</sup>

imaginary part of the dynamic susceptibility,  $\chi''(\hbar\omega)$ :

$$S(Q = 0.44 \text{ \AA}^{-1}, \hbar\omega) = \frac{1}{\pi} \chi''(\hbar\omega) [1 + n(\hbar\omega)] \quad (5)$$

with

$$\chi''(\hbar\omega) = \chi_o \arctan\left(\frac{\hbar\omega}{\Gamma}\right) \quad (6)$$

The fits shown in the bottom panel of Fig. 8.14 incorporate an appropriate instrumental resolution-convolution of this theoretical form for  $S(Q=0.44 \text{ \AA}^{-1}, \hbar\omega)$  to the inelastic scattering data. The description is clearly very good, and this allows us to extract the measured relaxation rate,  $\Gamma$  from the data. This is shown in the bottom panel of Fig. 8.15 as a

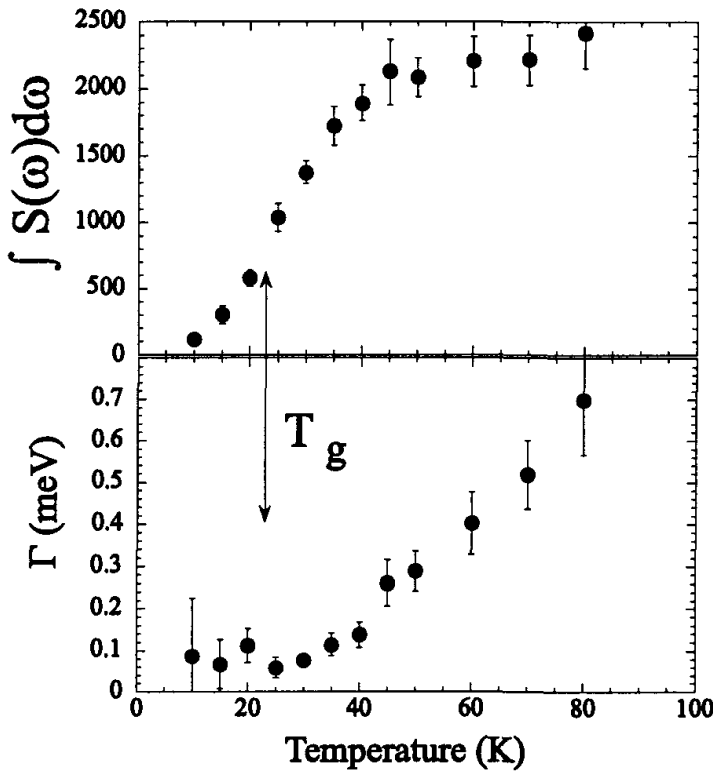


Fig. 8.15. Results from the fits shown in bottom panel of Fig.8.14 to the inelastic data as described in the text. The top panel shows the integrated inelastic scattering as a function of temperature. The bottom panel shows the temperature dependence of the relaxation rate.<sup>45</sup>

function of temperature. The spin freezing transition at  $T_g \sim 22$  K corresponds to the point at which the relaxation rate goes to zero.

The spin glass ground state in  $Y_2Mo_2O_7$  is certainly well characterised but the question as to what drives the formation of such a state remains not fully addressed. In fact many geometrically frustrated antiferromagnets possess low temperature states which are spin glass-like, or which possess substantial glassy characteristics. This is true, for example, in the case of the well studied kagomé-like (or “pyrochlore-slab”) material  $SrCr_{9-p}Ga_{12-9p}O_{19}$ ,<sup>53</sup> as well as for the site-random pyrochlore  $CsNiCrF_6$ ,<sup>54</sup> where Ni and Cr ions randomly populate a single pyrochlore sublattice. However, in these latter two examples, there is rather obvious chemical disorder present, and thus one is not surprised that a spin glass state occurs at low temperatures, as frustration and disorder are traditional building blocks for a spin glass state.

Of course, all real materials are imperfect at some level. In the case

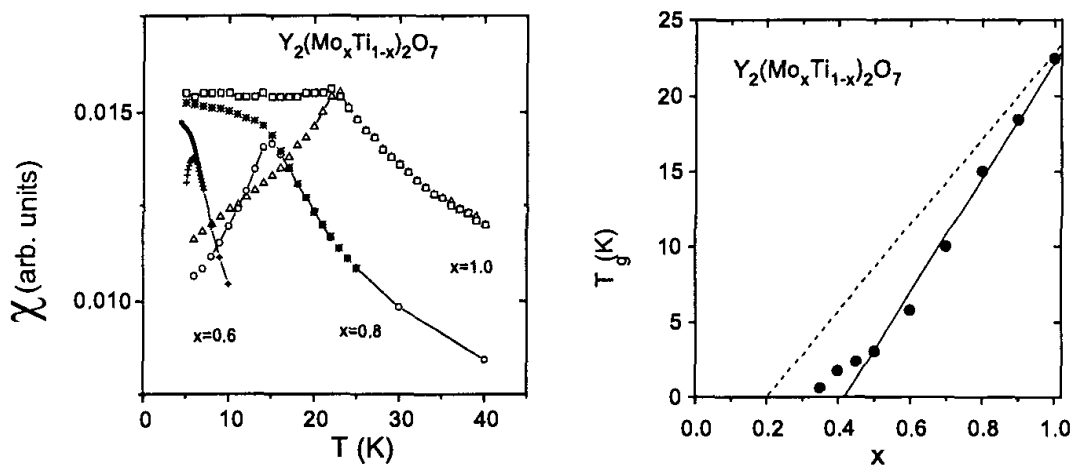


Fig. 8.16. Static susceptibility of  $\text{Y}_2(\text{Mo},\text{Ti})_2\text{O}_7$ . It is clear that when the magnetic sublattice is diluted, the freezing temperature,  $T_g$ , is reduced.<sup>49</sup>

of  $\text{Y}_2\text{Mo}_2\text{O}_7$ , the chemical imperfections are much more subtle than those discussed above for  $\text{SrCr}_{9-p}\text{Ga}_{12-9p}\text{O}_{19}$  or for  $\text{CsNiCrF}_6$ . Standard neutron and x-ray powder diffraction refinements of the structure of  $\text{Y}_2\text{Mo}_2\text{O}_7$  show a well ordered crystallographic lattice,<sup>48</sup> with the only potential indication of inhomogeneity residing in a root-mean-square displacement parameter for the  $\text{Mo}^{4+}$  site which is about 40% greater than that describing atomic displacements in other pyrochlores which are believed to be chemically well ordered.

While it is not easy to improve the crystalline perfection in  $\text{Y}_2\text{Mo}_2\text{O}_7$ , one can systematically study material containing more disorder. Interestingly the intentional introduction of disorder to  $\text{Y}_2\text{Mo}_2\text{O}_7$  in the form of substituting diamagnetic  $\text{Ti}^{4+}$  for magnetic  $\text{Mo}^{4+}$  does not enhance the spin glass state. Rather it causes the spin glass state to behave as if it were any other ordered magnetic state.<sup>49</sup> As can be seen in Fig. 8.16,  $T_g$  drops to zero in an almost linear fashion, near 60% substitution. This percolation threshold for the spin glass state is very close to that expected for site dilution on the three dimensional pyrochlore lattice, and thus, somewhat counterintuitively, the spin glass state behaves as any other ordered state would behave on dilution.

More sophisticated structural analysis does report evidence for chemical inhomogeneity in  $\text{Y}_2\text{Mo}_2\text{O}_7$ . This evidence is in the form of both XAFS<sup>50</sup> analysis of  $\text{Mo}^{4+}$ - $\text{Mo}^{4+}$  pair distances, as well as the  $^{89}\text{Y}$  NMR<sup>51</sup> spectrum which provides evidence for discrete lattice distortions. The  $^{89}\text{Y}$  NMR spectrum from  $\text{Y}_2\text{Mo}_2\text{O}_7$  is shown at two temperatures, both well above  $T_g$ ,

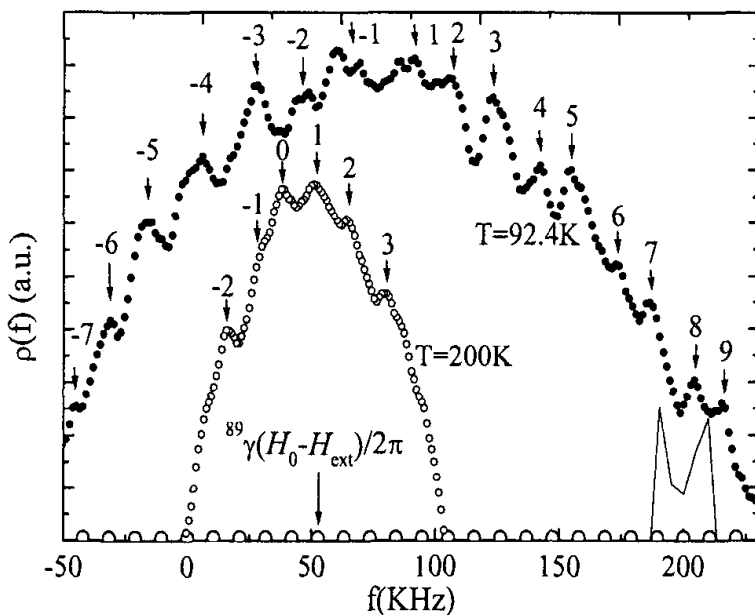


Fig. 8.17.  $^{89}\text{Y}$ -NMR data from  $\text{Y}_2\text{Mo}_2\text{O}_7$  at 200 and 92 K is shown. The very detailed structure as a function of frequency on top of the usual Gaussian peak is interpreted in terms of local distortions of the  $\text{Mo}^{4+}$  sublattice.<sup>51</sup>

in Fig.8.17. Multiple peaks as a function of frequency are evident, and this work speculates that these are due to subtle lattice distortions which may relieve the magnetic frustration, thereby lowering the overall free energy in  $\text{Y}_2\text{Mo}_2\text{O}_7$ .

As was previously mentioned recent theoretical analysis<sup>23</sup> has also investigated the role of magnetoelastic coupling in generating “order by disorder” in pyrochlore antiferromagnets. While not necessarily relevant to the analysis of  $\text{Y}_2\text{Mo}_2\text{O}_7$ , structural phase transitions are known to occur within the cubic pyrochlores which lower the translation symmetry of the lattice. One such well studied example is the superconducting pyrochlore  $\text{Cd}_2\text{Re}_2\text{O}_7$ <sup>55</sup> which transforms to a tetragonal subgroup of the  $\text{Fd}\bar{3}\text{m}$  pyrochlore lattice. This material is apparently non-magnetic, but the point remains that lattice and magnetic degrees of freedom are coupled.

### 8.6. Composite Spin Degrees of Freedom and Spin-Peierls-like Ground State in the Frustrated Spinel $\text{ZnCr}_2\text{O}_4$

As mentioned in section 2, the pyrochlore lattice of corner sharing tetrahedra is also found on the B-sublattice of the cubic spinels with the chemical composition  $\text{AB}_2\text{O}_4$ . In insulators of this form, it is common for the B-site to be occupied by a trivalent transition metal ion, which opens up the possibility of “another flavour” of antiferromagnetism on the pyrochlore lattice. Perhaps the best investigated example of such a compound is  $\text{ZnCr}_2\text{O}_4$ .<sup>18</sup> Lee *et al.*<sup>56</sup> have extensively studied this material using neutron scattering techniques, again using the SPINS cold triple axis spectrometer at NIST. Their results reveal yet another ground state, distinct from either the cooperative paramagnet which  $\text{Tb}_2\text{Ti}_2\text{O}_7$  displays, or the spin glass ground state which  $\text{Y}_2\text{Mo}_2\text{O}_7$  displays, as a consequence of geometrical frustration. In the case of the  $\text{Cr}^{3+}$  magnetic moments in  $\text{ZnCr}_2\text{O}_4$ , the ground state is based on nanoscale, hexagonal rings of correlated spins. Lee and coworkers showed that this frustrated spinel undergoes a strongly first order phase transition at 12.5 K from a cubic spin liquid with a gapless spin excitation spectrum, to a tetragonal Néel state with a local spin resonance at finite energy: 4.5 meV. Lee *et al.* make the reasonable argument that such a phase transition, with coupled spin and lattice degrees of freedom, possesses striking similarities to the spin-Peierls phase transition known to be relevant to quasi-one-dimensional, quantum antiferromagnets.

As was the case in the study of  $\text{Tb}_2\text{Ti}_2\text{O}_7$ , initial measurements on  $\text{ZnCr}_2\text{O}_4$  were performed on polycrystalline materials. Later, when single crystal samples were available, a more sophisticated analysis was allowed. The initial measurements on polycrystalline materials are surveyed in Fig. 8.18. The bottom panel shows the temperature dependence of the magnetic Bragg scattering on entering the Néel state in  $\text{ZnCr}_2\text{O}_4$  as well as the accompanying lattice strain as the crystal simultaneously distorts from its cubic high temperature structure to the tetragonal low temperature structure. The abrupt temperature dependence associated with both the magnetic and structural phase transitions are as expected for a strongly discontinuous or first order phase transition.

The top panel of Fig. 8.18 shows the inelastic neutron scattering from polycrystalline  $\text{ZnCr}_2\text{O}_4$  at a modulus of wavevector,  $Q=1.5 \text{ \AA}^{-1}$ . Strong quasielastic magnetic neutron scattering is observed near this wavevector above  $T_N$ . On lowering the temperature below  $\sim 12.5$  K, this magnetic

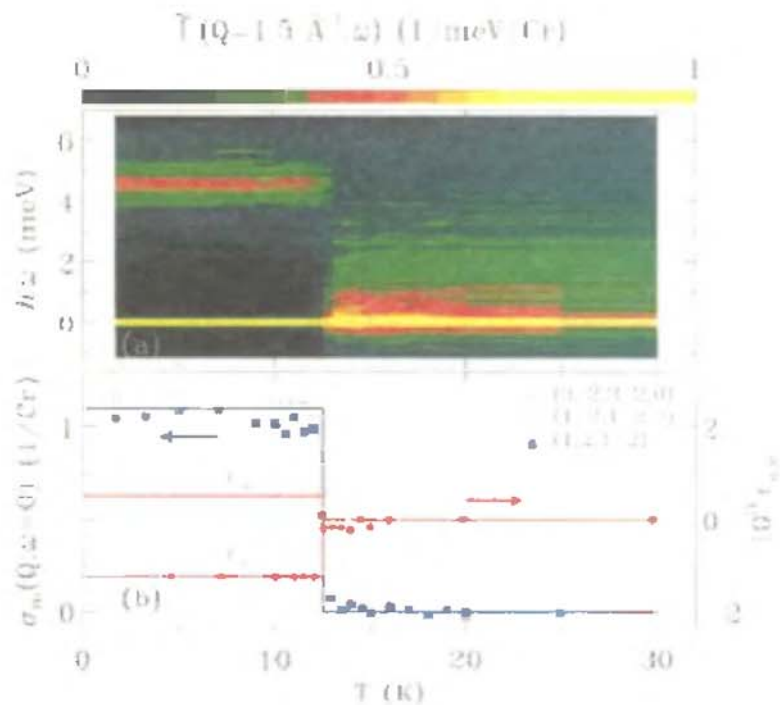


Fig. 8.18. (top) A colour image of constant- $Q$  scans measured on a polycrystalline sample of  $\text{ZnCr}_2\text{O}_4$  using a triple axis spectrometer as a function of temperature.<sup>56</sup> (bottom) The temperature dependence of the magnetic Bragg scattering (squares) and the lattice strain along  $a$  and  $c$  (circles) show abrupt temperature dependencies characteristic of a strongly discontinuous phase transition.

scattering becomes localized into an inelastic resonance. The top panel of Fig. 8.18 clearly shows that the inelastic magnetic resonance itself develops abruptly, at 4.5 meV upon cooling through the first order phase transition.

This powder-averaged magnetic inelastic scattering can be quantitatively analysed and Lee *et al.* showed that the spectral weight of the resonance accounts for roughly 22% of the total fluctuating moment in Cr. Very interestingly, they also showed that the inelastic scattering which was centered at  $Q=1.5 \text{ \AA}^{-1}$  was broad in wavevector space, characterized by a half width at half maximum of  $\kappa=0.48 \text{ \AA}^{-1}$ . This indicates the presence of a resonating spin cluster, rather than individual spins or single tetrahedra, as the origin for the inelastic magnetic resonance.

This study also pointed out very interesting analogies between the phase transition observed in  $\text{ZnCr}_2\text{O}_4$ , and that characterizing the spin Peierls transition in quasi-one dimensional quantum antiferromagnets such as  $\text{CuGeO}_3$ .<sup>58</sup> There are differences between the phenomena in  $\text{ZnCr}_2\text{O}_4$  and that of spin-Peierls systems; notably the order of the transition and

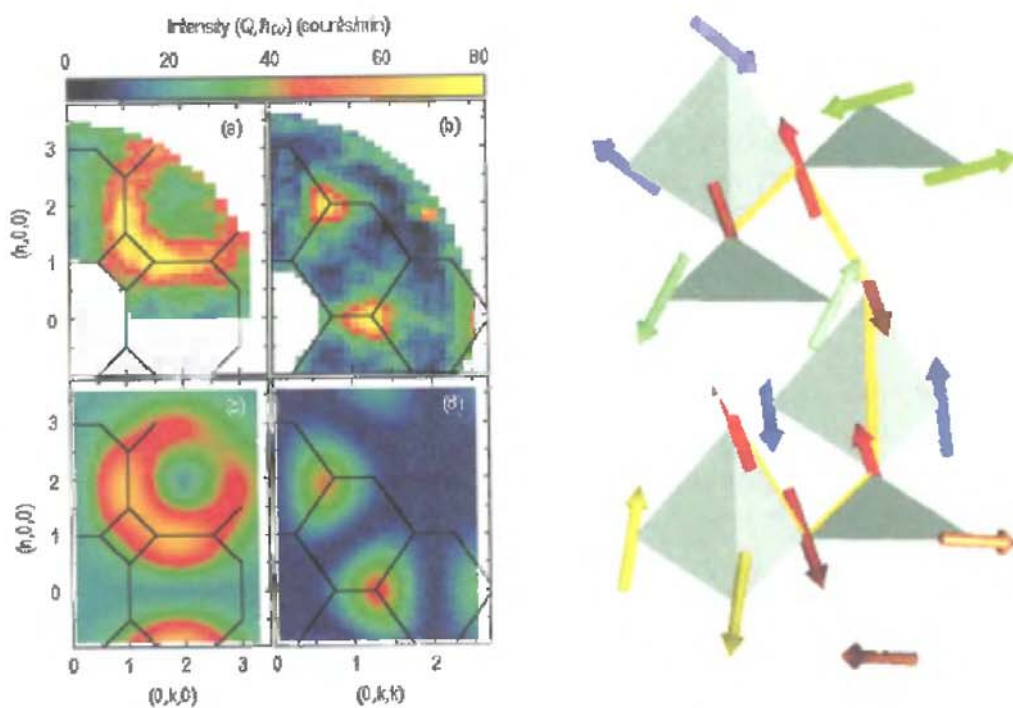


Fig. 8.19. Left Panel: (a and b) Colour maps of inelastic scattering at  $\hbar\omega = 1\text{ meV}$  for two high symmetry planes in a single crystal of  $\text{ZnCr}_2\text{O}_4$  at 15 K. (c and d) The calculated form factor for correlated antiferromagnetic hexagons similar to those shown schematically in the right panel. Right panel: One hexagon and the associated six tetrahedra used as the basis for the diffuse scattering calculations on which the form factors shown on the left hand side (c and d).<sup>57</sup>

the nature of the low temperature ground state. However the similarities related to the coupling between lattice and spin degrees of freedom such that a finite energy magnetic resonance appears below the phase transition and with it, a concomitant lowering of the magnetic energy of the system. The analogous phenomena in a spin-Peierls system occurs through a lattice dimerisation and the development of a magnetic singlet-triplet energy gap.

A subsequent neutron scattering study on single crystal  $\text{ZnCr}_2\text{O}_4$  revealed substantially more detail as to the nature of the correlated spin clusters. Lee *et al.*<sup>57</sup> were able to determine the magnetic dynamic form factor within two planes of reciprocal space, work which required single crystals, and which is shown in Fig. 8.19 (a and b). These data show the  $\mathbf{Q}$  dependence of the quasielastic scattering at  $\hbar\omega=1\text{ meV}$  and  $T=15\text{ K}$ , above  $T_N$ , in the  $(h,k,0)$  and  $(h,k,k)$  planes of reciprocal space. One sees broad maxima at the Brillouin zone boundaries, signaling the emergence of confined nano-scale spin clusters. Unlike the scattering due to single correlated tetrahedra observed in the pyrochlore  $\text{Tb}_2\text{Ti}_2\text{O}_7$ ,<sup>33</sup> the scattering

shown in Fig. 8.19 require larger correlated units to account for the details of the  $\mathbf{Q}$ -dependence of this inelastic scattering.

It was found that the scattering was well described by antiferromagnetic hexagonal spin loops, made up of six tetrahedra where two spins from each tetrahedron occupy the vertices of the loop. The remaining two spins of a given tetrahedron belong to a different hexagon, thereby allowing the assignment of all the spins on the magnetic sublattice to hexagons simultaneously, and producing  $N/6$  weakly interacting degrees of freedom, from the  $N$  original spins. The calculated dynamic form factor for such a correlated nanoscale spin structure is shown in figure 8.19 (c and d) for each of the two planes studied. In this manner,  $ZnCr_2O_4$  is convincingly shown at low temperatures to be comprised of weakly interacting hexagonal spin-loops.

## 8.7. Conclusions and Outlook

We have reviewed experimental progress in understanding three of the many magnetic materials which are known to combine antiferromagnetism and tetrahedral local geometries. Even within this subset of three frustrated materials, we find quite different exotic ground states: the enigmatic co-operative paramagnetic ground state of  $Tb_2Ti_2O_7$ ; the spin glass ground state of  $Y_2Mo_2O_7$ ; and the composite spin degrees of freedom and distorted pyrochlore lattice in  $ZnCr_2O_4$ . Aesthetically, we may well wish for a form of universal behaviour in systems which, at least at first glance, have so much in common. However it is also very rewarding to appreciate the richness of the complex ground states which geometrical frustration has enabled in these real materials. There seems little doubt that this richness will continue as a theme in the elucidation of the physical properties of geometrically frustrated magnets in the near future. There is also little doubt that the production of single crystal materials in pristine form, as well as access to the most advanced instrumentation for neutron scattering and other advanced characterization will continue to be extremely important in our ability to study and ultimately understand such novel materials.

## Acknowledgments

This work was supported at McMaster University by NSERC of Canada and by the Canadian Institute for Advanced Research. It was supported at Brookhaven National Laboratory by the U.S. Department of Energy under contracts DE-AC02-98CH10886. It is a pleasure to thank our many colleagues and collaborators who have contributed to our involvement in

this work. These include: D.P. Belanger, A.J. Berlinsky, C.L. Broholm, W. Buyers, M.F. Collins, G. Ehlers, M.J.P. Gingras, I.N. Goncharenko, J.E. Greedan, A. Harrison, C. Kallin, H. Kawamura, A. Keren, S.-H. Lee, G.M. Luke, T.E. Mason, M. Mao, M. Mekata, I. Mirebeau, R. Moessner, N. Raju, A.P. Ramirez, J.N. Reimers, P. Schiffer, C.V. Stager, J.L. Thollence, Y.J. Uemura. Finally, we are indebted to A.A.M. Gaulin and K.M. Hughes for a critical reading of the manuscript.

## References

1. for reviews see: *Magnetic Systems with Competing Interactions*, edited by H.T. Diep (World Scientific, Singapore, 1994); P. Shiffer and A.P. Ramirez, *Commun. Cond. Mat. Phys.*, **18**, 21 (1996); M.J.P. Gingras, eds., *Can. J. Phys.* **79**, (2001).
2. Z. F. Wang and B. W. Southern, *Phys. Rev. B* **68**, 094419 (2003).
3. G.H. Wannier, *Phys. Rev.* **79**, 357 (1950).
4. P.W. Anderson, *Phys. Rev.* **102**, 1008 (1956).
5. J. Villain, *Z. Phys. B* **33**, 31 (1979).
6. L. Pauling, *J. Am. Chem. Soc.* **57**, 2680 (1935).
7. S.T. Bramwell and M.J.P. Gingras, *Science* **294**, 1495 (2001).
8. M.A. Subramanian, G. Aravamudan, and G.V. Subba Rao, *Prog. Solid State Chem.* **15**, 55 (1983).
9. J.S. Gardner, S.R. Dunsiger, B.D. Gaulin, M.J.P. Gingras, J.E. Greedan, R.F. Kiefl, M.D. Lumsden, W.A. MacFarlane, N.P. Raju, J.E. Sonier, I. Swainson and Z. Tun, *Phys. Rev. Lett.* **82**, 1012 (1999).
10. J.E. Greedan, M. Sato, Y. Xu and F.S. Razavi, *Solid State Comm.* **59**, 895 (1986).
11. J.E. Greedan, J.N. Reimers, S.L. Penny and C.V. Stager, *J. App. Phys.* **67**, 5967 (1990).
12. D. Goldschmidt and H.L. Tuller, *Phys. Rev. B* **34**, 5558 (1986).
13. H. Sakai, K. Yoshimura, H. Ohno, H. Kato, S. Kambe, R.E. Walstedt, T.D. Matsuda and Y. Haga, *J. Phys.: Cond. Matt.* **13**, L785 (2001).
14. D. Mandrus, J.R. Thompson, R. Gaal, L. Forro, J.C. Bryan, B.C. Chakoumakos, L.M. Woods, B.C. Sales, R.S. Fishman and V. Keppens, *Phys. Rev. B* **63**, 195104 (2001).
15. T. Katsufuji, H.Y. Hwang and S.W. Cheong, *Phys. Rev. Lett.* **84**, 1998 (2000).
16. S. Yonezawa, Y. Muraoka, Y. Matsushita and Z Hiroi, *J. Phys.: Cond. Matt.* **16**, L9 (2004).
17. S. Yonezawa, Y. Muraoka, Y. Matsushita and Z Hiroi, *J. Phys. Soc. Jpn.* **73**, 819 (2004).
18. F. Leccabue, C. Pelosi, E. Agostinelli, V. Fares, D. Fiorani and E. Parazzzo, *J. Crystal Growth* **79**, 410 (1986).
19. S. Kondo, D.C. Johnston, C.A. Swenson, F. Borsa, A.V. Mahajan, L.L. Miller, T. Gu, A.I. Goldman, M.B. Maple, D.A. Gajewski, E.J. Freeman,

- N.R. Dilley, R.P. Dickey, J. Merrin, K. Kojima, G.M. Luke, Y.J. Uemura, O. Chmaissem and J.D. Jorgensen, *Phys. Rev. Lett.* **78**, 3729 (1997).
20. S.H. Lee, Y. Qiu, C. Broholm, Y. Ueda and J.J. Rush, *Phys. Rev. Lett.* **86**, 5554 (2001).
  21. R.L. Millard, R.C. Peterson and B.K. Hunter, *Am. Mineral* **80**, 885 (1995).
  22. S.H. Lee, C. Broholm, T.H. Kim, W. Ratcliff and S.W. Cheong, *Phys. Rev. Lett.* **84**, 3718 (2000).
  23. O. Tchernyshyov, R. Moessner and S. L. Sondhi, *Phys. Rev. B* **66**, 064403 (2002).
  24. R. Cywinski, S.H. Kilcoyne and C.A. Scott, *J. Phys.: Cond. Matt.* **3**, 6473 (1991).
  25. R. Ballou, E. LelievreBerna and B. Fåk, *Phys. Rev. Lett.* **76**, 2125 (1996).
  26. G.M. Kalvius, E. Schreier, M. Ekstrom, O. Hartmann, S. Henneberger, A. Kratzer, R. Wappling, E. Martin, F.J. Burghart, R. Ballou, J. Deportes and C. Niedermayer, *Hyp. Int.* **128**, 275 (2000).
  27. L. Price and K. Skold Eds., *Methods of Experimental Physics, Neutron Scattering, Vol. 23, Parts A,B,C,D* (Academic Press, 1987) and G. Shirane, S.M. Shapiro, and J.M. Tranquada *Neutron Scattering with a Triple Axis Spectrometer*, (Cambridge University Press, 2002).
  28. S. W. Han, J. S. Gardner and C. H. Booth, *Phys. Rev. B* **69**, 024416 (2004).
  29. R. M. Moon, T. Riste and W. C. Koehler, *Phys. Rev.* **181**, 920 (1969).
  30. E. F. Bertaut and P. Burlet, *Solid State Commun.* **5**, 279 (1967).
  31. B. D. Gaulin, J.N. Reimers, T. E. Mason, J. E. Greedan and Z. Tun, *Phys. Rev. Lett.* **69**, 3244 (1992).
  32. M. J. Harris, M. P. Zinkin, Z. Tun, B. M. Wanklyn and I. P. Swainson, *Phys. Rev. Lett.* **73**, 189 (1994).
  33. J. S. Gardner, B. D. Gaulin, A. J. Berlinsky, P. Waldron, S. R. Dunsiger, N. P. Raju and J. E. Greedan, *Phys. Rev. B* **64**, 224416 (2001).
  34. H. R. Glyde and E. C. Svensson, *Methods of Experimental Physics* **23**, 303 (Academic Press, San Diego, 1987).
  35. M. J. P. Gingras, B. C. den Hertog, M. Faucher, J. S. Gardner, S. R. Dunsiger, L. J. Chang, B. D. Gaulin, N. P. Raju, and J. E. Greedan, *Phys. Rev. B* **62**, 6496 (2000).
  36. J.S. Gardner, B.D. Gaulin and D.M<sup>c</sup>K. Paul, *J. Crystal Growth* **191**, 740 (1998).
  37. J. S. Gardner, A. Keren, G. Ehlers, C. Stock, Eva Segal, J. M. Roper, B. Fåk, P. R. Hammar, M. B. Stone, D. H. Reich and B. D. Gaulin, *Phys. Rev. B* **68**, 134410 (2003).
  38. Y. J. Kao, M. Enjalran, A. Del Maestro, H. R. Molavian, M. J. P. Gingras, *Phys. Rev. B* **68**, 172407 (2003).
  39. J. S. Gardner, G. Ehlers, S. T. Bramwell and B. D. Gaulin, *J. Phys.: Condens. Matter* **16**, S643 (2004).
  40. A. Keren, J. S. Gardner, G. Ehlers, A. Fukaya, E. Segal and Y. J. Uemura, *Phys. Rev. Lett.* **92**, 107204 (2004).
  41. G. Luo, S. T. Hess and L. R. Corruccini, *Physics Letters A* **291**, 306 (2001).
  42. Y. Yasui, M. Kanada, M. Ito, H. Harashina, M. Sato, H. Okumura, K.

- Kakurai and H. J. Kadowaki, *Phys. Soc. Jpn.* **71**, 599 (2002).
- 43. I. Mirebeau, I. N. Goncharenko, P. Cadavez-Peres, S. T. Bramwell, M. J. P. Gingras and J. S. Gardner, *Nature* **420**, 54 (2002).
  - 44. N. P. Raju, E. Gmelin and R. K. Kremer, *Phys. Rev. B* **46**, 5405 (1992) and D. Walton, A. McCleary, C. V. Stager and N. P. Raju, *Phys. Rev. B* **59**, 135 (1999).
  - 45. J. S. Gardner, B. D. Gaulin, S.-H. Lee, C. Broholm, N. P. Raju and J. E. Greedan, *Phys. Rev. Lett.* **83**, 211 (1999).
  - 46. J. L. Thollence and B.D. Gaulin, unpublished.
  - 47. M. J. P. Gingras, C.V. Stager, N. P. Raju, B. D. Gaulin and J. E. Greedan, *Phys. Rev. Lett.* **78**, 947 (1997).
  - 48. J. N. Reimers, J. E. Greedan and M. Sato, *J. Solid State Chem.* **72**, 390 (1988).
  - 49. N. P. Raju et al., to be published.
  - 50. C. H. Booth, J. S. Gardner, G. H. Kwei, R. H. Heffner, F. Bridges and M. A. Subramanian *Phys. Rev. B* **62**, R755 (2000).
  - 51. A. Keren and J. S. Gardner, *Phys. Rev. Lett.* **87**, 177201 (2001).
  - 52. K. Binder and A. P. Young, *Rev. of Mod. Phys.* **58**, 801 (1986); J. A. Mydosh *Spin Glasses: An Experimental Introduction*, (Taylor and Francis, 1993).
  - 53. X. Obradors A. Labarta, A. Isalgue, J. Tejada, J. Rodriguez and M. Pernet, *Solid State Commun.* **65**, 189 (1988).
  - 54. M. J. Harris and M. P. Zinkin, *Mod. Phys. Lett. B* **10**, 417 (1996).
  - 55. J. P. Castellan, B. D. Gaulin, J. van Duijn, M. J. Lewis, M. D. Lumsden, R. Jin, J. He, S. E. Nagler and D. Mandrus, *Phys. Rev. B* **66**, 134528 (2002).
  - 56. S.-H. Lee, C. Broholm, T. H. Kim, W. Radcliff II, and S.-W. Cheong, *Phys. Rev. Lett.* **84**, 3718 (2000).
  - 57. S.-H. Lee, C. Broholm, W. Radcliff II, G. Gasparovic, Q. Huang, T. H. Kim, and S.-W. Cheong, *Nature* **418**, 856 (2002).
  - 58. see for example: K. Uchinokura, *J. Phys.: Condens. Matter* **14**, R195 (2002)



## CHAPTER 9

### RECENT PROGRESS IN SPIN GLASSES

N. Kawashima<sup>1</sup> and H. Rieger<sup>2</sup>

*Department of Physics, Tokyo Metropolitan University,*

*<sup>1</sup> Hachioji, Tokyo 192-0397, Japan*

*E-mail: nao@phys.metro-u.ac.jp*

*<sup>2</sup> Theoretische Physik, Universität des Saarlandes,*

*66041 Saarbrücken, Germany*

*E-mail: H.Rieger@mx.uni-saarland.de*

We review recent findings on spin glass models. Both the equilibrium properties and the dynamic properties are covered. We focus on progress in theoretical, in particular numerical, studies, while its relationship to real magnetic materials is also mentioned.

The motivation that pulls researchers toward spin glasses is possibly not the potential future use of spin glass materials in “practical” applications. It is rather the expectation that there must be something very fundamental in systems with randomness and frustration. It seems that this expectation has been acquiring a firmer ground as the difficulty of the problem is appreciated more clearly. For example, a close relationship has been established between spin glass problems and a class of optimization problems known to be *NP-hard*. It is now widely accepted that a good (i.e. polynomial) computational algorithm for solving any one of *NP-hard* problems most probably does not exist. Therefore, it is quite natural to expect that the Ising spin glass problem, as one of the problem in the class, would be very hard to solve, which indeed turns out to be the case in a vast number of numerical studies. None the less, it is often the case that only numerical studies can decide whether a certain hypothetical picture applies to a given instance.

Consequently, the major part of what we present below is inevitably a description of the current status of spin glass studies, what is being said and done on the issue, rather than an account of established facts. In what follows, we put an emphasis on the theoretical and the numerical progress achieved in the field in the last decade. We mention older theoretical and experimental works only when it is necessary for readers to be able to follow current topics without reading through many other articles. Many of the important older works and experimental results, therefore, have been left out. For a review on these, the readers are referred to [1], [2], [3], [4], and [5].

The present chapter is organized as follows. In section 9.1, we first give a brief overview of two well-known paradigms on spin glasses and summarize the predictions derived from them. Then, in the subsequent sections 9.2, 9.3 and 9.4, we discuss equilibrium properties of Ising spin glass models. In particular, in section 9.3, a recent active debate, as to which paradigm is appropriate for realistic short-range spin glass models in three dimensions, is presented. Then, we proceed with the dynamical properties in section 9.5 to examine these paradigms on a different ground. In this section, an emphasis is put on aging phenomena while some other non-equilibrium properties are also discussed. Models with continuous degrees of freedom as well as the Potts spin glass models are mentioned in section 9.6. The effects of weak disorder discussed in section 9.7 provide us with a set of interesting issues quite different from those arising from strong disorder dealt with in the preceding sections. Several exact relations can be found and play an important role in shedding light on the issue under debate. Finally, we see in section 9.8 what results from the interplay between quantum fluctuations and randomness in spin glasses.

### **9.1. Two Pictures**

The equilibrium properties of Ising spin-glass models in finite dimensions have been investigated mainly through developments of working hypotheses and numerical techniques. In principle, we can judge which working hypothesis is correct by numerical computations. The working hypotheses are often called “pictures”. Among various pictures, unarguably the most frequently mentioned are the replica-symmetry-breaking (RSB) and the droplet picture. In fact, the dichotomy between these two has been the central issue in the spin glass research for more than a decade. However, it is rather difficult to perform a conclusive numerical test in the three dimensional-

case. One thing that renders the test so difficult is that the lower critical dimension appears to be close to three. Another factor is, as mentioned in the introduction, that there is no polynomial algorithm for obtaining the ground state of a given instance in three (and higher) dimension. Therefore, the best we can do at present is to summarize on-going arguments, discriminating what has been established from what has not, and presenting the most important numerical evidences. We try to do these in what follows.

It should also be pointed out that most of the “pictures” are asymptotic theories which are supposed to be correct only for large systems. In contrast to most regular systems the utility of an asymptotic theory for glassy systems cannot be taken for granted. It was pointed out<sup>6</sup> that in most real spin glass materials the typical length scale of an equilibrated domain within the experimental time scale may not exceed a small number of lattice spacings. If this is the case, considering the numerical evidence of the existence of large corrections to scaling, it can happen that the asymptotically correct theory fails to explain experimental results. The fact that many experiments on spin glasses, those at temperatures below the transition in particular, are not performed in equilibrium implies that an equilibrium theory may not be appropriate. Some attempts to construct a theory for a realistic time and length scales are reviewed in section 9.5.

### 9.1.1. Mean-Field Picture

We start with a brief description of the two pictures mentioned above in the present and the next subsection. We do not, however, intend to repeat the whole history of the development of each picture or discuss every technical detail. The reader may find a complete description of these pictures in a number of review articles.<sup>1,2,7,8,9,10</sup>

The RSB picture or the mean-field picture is based on Parisi’s solution<sup>11,12,13,14</sup> of the Sherrington-Kirkpatrick (SK) model<sup>15</sup> and its interpretation in terms of a multitude of thermodynamic states [16,17]. The SK model of  $N$  Ising spins,  $S_i$ , is defined by the Hamiltonian

$$H = - \sum_{(i,j)} J_{ij} S_i S_j$$

where the summation is taken over all  $N(N - 1)/2$  pairs of spins  $(i, j)$  with  $i \neq j$ . The coupling constants  $J_{ij}$  are quenched Gaussian random variables with zero mean and variance  $J/N$  where  $J$  is a positive constant of  $\mathcal{O}(1)$  that sets the energy scale. In [15], the replica method was used in which  $n$  identical copies (replicas) of the system are introduced to perform the

disorder average of the free energy:  $-\beta F = [\ln Z]_{\text{av}} = \lim_{n \rightarrow 0} ([Z^n]_{\text{av}} - 1)/n$ . They found a solution of the mean-field equations using a replica symmetric Ansatz (see below). This solution has a phase transition and the transition point is located at the temperature  $T_c = J$ . Below this temperature, the order parameter

$$q_{\text{EA}} = q^{\alpha\beta} \equiv \frac{1}{N} \sum_i S_i^\alpha S_i^\beta \quad (1)$$

has a non-zero value where indices  $\alpha$  and  $\beta$  specify replicas. The replica symmetric Ansatz means that only solutions to the mean-field equations with  $q^{\alpha\beta}$  being independent of  $\alpha$  and  $\beta$  (before taking the limit  $n \rightarrow 0$ ) are allowed. However, this solution did not describe the low temperature phase correctly since the entropy predicted by this solution became negative at low temperatures.

In [18] a different approach was taken for the SK model. They constructed a set of equations (called the TAP equations) that expresses the equation of state for each bond-realization of the SK model in terms of the local magnetization,  $m_i = \langle S_i \rangle$ . They studied the eigen-modes of the stability matrix of stable solutions of the TAP equations and found that the spectrum of the eigen-values extends down to zero, suggesting that the solutions are only marginally stable in the thermodynamic limit. Furthermore, the stability matrix in the replica space, i.e., the second derivatives of the free energy with respect to the replica order parameters,  $q^{\alpha\beta}$ , was examined.<sup>19</sup> It turned out that the replica symmetric solution is stable only in the paramagnetic phase and becomes unstable below the phase boundary called the AT line in the  $T$ - $H$  plane. Therefore, the SK solution is correct above the AT line whereas it is not below the AT line.

To find the correct solution of the SK model below the AT line the replica symmetry had to be broken. The way the symmetry is to be broken is, however, highly non-trivial. A solution, called the Parisi solution, was proposed<sup>11,12,13,14</sup> based on a novel metric structure of the replica-index space. It has now been proved with acceptable mathematical rigor that the solution is exact.<sup>20</sup> In the Parisi solution, a metric structure is introduced in the replica-index space and it is assumed that the overlap  $q$  between two replicas depends only on the distance between the two in this index space. As a result, the order parameter is actually not a single number, in contrast to the EA order parameter  $q_{\text{EA}}$ , but a function  $q(x)$  ( $0 \leq x \leq 1$ ), where  $x$  is a suitable parameterization of the distance between two replica indices. A remarkable feature of Parisi's solution below the AT line was that  $q(x)$

varies continuously as a function of  $x$ .

The order-parameter function  $q(x)$  first appeared to be a mathematical artifact, but its physical meaning was later clarified<sup>14</sup> by relating  $q(x)$  to the probability distribution  $P(q)$  of the overlap  $q$  between *pure states*, rather than the replicas. A pure state is defined as an extremal equilibrium distribution in the thermodynamic limit that cannot be expressed as a linear combination of any other distributions. Denoting the inverse function of  $q(x)$  as  $x(q)$ , it was found that

$$x(q) = \int_{-\infty}^q dq' P(q'). \quad (2)$$

Here, the overlap distribution  $P(q)$  is formally (and somewhat symbolically) defined as

$$P(q) = \sum_{\alpha, \beta} P_\alpha P_\beta \delta(q - q^{\alpha\beta}). \quad (3)$$

Here the indices  $\alpha$  and  $\beta$  specify pure states, not replicas,  $q_{\alpha\beta}$  is the overlap between the two pure states  $\alpha$  and  $\beta$ , and  $P_\alpha$  is the probability for the system to be in the pure state  $\alpha$ .

Equation (2) may provide a way to investigate the structure of the space of the equilibrium distributions with the replica method. We can conclude, for instance, that more than one pure state exists and the overlap between two pure states varies depending on the particular pair of states if  $q(x)$  is not constant. If  $q(x)$  changes continuously in a finite range of  $x$ , as in Parisi's solution for the SK model, there must even be an infinite number of pure states. Simply stated, the RSB picture for systems in finite dimensions with short range interactions consists of the hypothesis that there are infinitely many pure states with varying overlaps and various predictions derived from the hypothesis.

The definition (3) of  $P(q)$ , however, must be taken with caution since the existence of pure states as a well-defined thermodynamic limit is not clear for disordered systems. In fact, it was shown<sup>16,17</sup> that  $P_J(q)$  for a bond realization  $J$  depends on  $J$  even in the thermodynamic limit. As discussed below, this means<sup>21</sup> that a unique thermodynamic limit of  $P_J(q)$  with fixed bond realization  $J$  does not exist. Therefore, the order parameter,  $q(x)$ , is not self-averaging for the SK model, in striking contrast to homogeneous systems.

Because of this subtle nature of the order parameter, the exact implication of the RSB picture for more realistic spin glass models in finite dimensions is somewhat ambiguous and has been a subject of debates.<sup>9,10</sup> One

focus is the interpretation of the numerical result for finite systems. The definition of  $q$  and  $P(q)$  often used in numerical simulations is based on the overlap between two spin configurations,  $S$  and  $S'$ , independently chosen from the equilibrium distribution of the same bond realization. Namely,

$$\begin{aligned} q(S, S') &\equiv \frac{1}{N} \sum_{i=1}^N S_i S'_i, & P(q; L) &\equiv [P_J(q; L)], \\ P_J(q; L) &\equiv \sum_S \sum_{S'} P_J(S; L) P_J(S'; L) \delta(q - q(S, S')) \end{aligned} \quad (4)$$

where  $P_J(S; L)$  is the normalized Boltzmann weight of the spin configuration  $S$  in a system of the linear size  $L$  with the bond configuration  $J$ . Throughout this article, unless stated otherwise, the angular bracket  $[\dots]$  denotes the bond-configuration average with the distribution  $P(J) = \prod_{(ij)} P_1(J_{ij})$ , where the single-bond distribution  $P_1$  is independent of  $(ij)$ . The following link-overlap and its distribution are also often discussed recently:

$$\begin{aligned} q_l(S, S') &\equiv \frac{1}{N_l} \sum_{(ij)} S_i S_j S'_i S'_j, & P(q_l; L) &\equiv [P_J(q_l; L)], \\ P_J(q_l; L) &\equiv \sum_S \sum_{S'} P_J(S; L) P_J(S'; L) \delta(q_l - q_l(S, S')) , \end{aligned} \quad (5)$$

where the summation concerning  $(ij)$  is over all the pairs of nearest neighbor spins, and  $N_l$  is the total number of the pairs in the system.

The following is the list of features that follows from the RSB picture.

- (1) The overlap distribution,  $P(q; L)$ , converges to a function  $P(q)$  that has a continuous part in the limit of  $L \rightarrow \infty$ . In particular,  $P(0; L)$  converges to a finite value  $P(0) > 0$ .
- (2) Some quantities, such as  $P_J(q; L)$ , are non-self-averaging, i.e., a unique thermodynamic limit does not exist for a fixed bond realization.
- (3) The bond-averaged link-overlap distribution  $P(q_l; L)$  is not  $\delta(q_l)$  in the thermodynamic limit, i.e., its width converges to a finite value.
- (4) Global excitations with the energy cost of  $\mathcal{O}(1)$  exist.
- (5) A change in the boundary conditions generally affects spins located far away from the boundary.

### 9.1.2. *Droplet Picture*

Another well-known picture<sup>22,23,24,25,26</sup> is based on a scaling hypothesis on local excitations and produces markedly different conclusion for various

quantities, in particular,  $P(q)$ . The basic assumption in this picture is that even below the transition temperature in zero magnetic field there are only two pure states that are mapped to each other by the total inversion of spins as in the homogeneous ferromagnets. Then, several scaling properties are assumed for compact excitations with varying size, which are called *droplets*. To be specific, a droplet of the scale  $l$  has a typical excitation free energy  $\epsilon_l \sim \Upsilon l^\theta$ , where  $\theta$  is called the droplet exponent. Since this exponent relates the energy scale to the length, similar to the stiffness exponent  $\theta_S$  that relates the domain wall excitation energy to the system size, the simplest assumption is to identify  $\theta$  with the stiffness exponent  $\theta_S$ .

Among various results derived from this picture, of particular importance are the scaling forms of the correlation functions.<sup>24,23</sup> For example, it is predicted for models with a continuous bond distribution and with no magnetic field that the following asymptotic form should apply:

$$[\langle S_i S_j \rangle^2] - [\langle S_i \rangle^2][\langle S_j \rangle^2] \sim T/\Upsilon R^\theta \quad (6)$$

near zero temperature, where  $R$  is the distance between site  $i$  and site  $j$  and the thermal average  $\langle \dots \rangle$  is taken in a single pure state (if there are two). It follows that the variance of the distribution function  $P(q; L)$  defined in (4) (more strictly, the variance of  $P(|q|; L)$ ) decreases as the system size increases:

$$(\Delta q)^2 \equiv [\langle q^2 \rangle] - [\langle |q| \rangle]^2 \propto L^{-\theta} \rightarrow 0.$$

Therefore, when  $P(q)$  is defined as the thermodynamic limit of  $P(q; L)$ , it consists of a pair of delta peaks at  $q = \pm q_{EA}$ .

For the models with discrete energy levels, such as the  $\pm J$  model, the scaling form of the correlation function near  $T = 0$  must be modified. However, it is widely believed that the discretized nature of the energy level is not relevant at finite temperatures and the behavior is qualitatively the same as the one of the models with continuous energy levels.

Below, we list the defining properties of the droplet picture together with some predictions derived from it.

- (1) The distribution of the excitation free energy of droplets of the scale  $l$ ,  $P(\epsilon_l)$ , is continuous down to zero energy.
- (2)  $P(\epsilon_l)$  has the typical energy scale  $\Upsilon l^\theta$  with  $\Upsilon$  being an  $\mathcal{O}(1)$  constant. Specifically,  $P(\epsilon_l)$  has the scaling form

$$P(\epsilon_l) \sim \frac{1}{\Upsilon l^\theta} \tilde{P}\left(\frac{\epsilon_l}{\Upsilon l^\theta}\right).$$

- (3)  $P(q)$  is self-averaging and it consists of a pair of delta peaks below the transition temperature.
- (4) Since  $P(0; L)$  is proportional to the excitation probability of a droplet that contains approximately one half of all the spins, for a system with

condition. The stiffness exponent  $\theta_S$  is then determined by the asymptotic size-dependence of the stiffness,  $\Delta F$ :

$$\Delta F \propto L^{\theta_S}.$$

According to [23], when the distribution of coupling constants is continuous and has a non-zero weight at  $J = 0$ , whether a phase transition takes place at a finite temperature or not is determined by the sign of the stiffness exponent. If it is positive, the zero temperature phase is strongly ordered, leading to a finite-temperature phase transition, whereas otherwise the order is fragile and infinitesimal thermal fluctuations would destroy it, leading to criticality at zero temperature. Numerical computations of the ground states of finite systems in two dimensions were carried out<sup>23,28,29</sup> for estimating the stiffness exponent at  $T = 0$ . For the Gaussian distribution of the bonds, it turned out that  $\theta_S \sim -0.3$ . At present, one of the most accurate and reliable estimates of the stiffness exponent is given in [30] as  $\theta_S = -0.282(2)$  for the Gaussian bond distribution with periodic/anti-periodic boundary condition. Due to the negative value of the stiffness exponent, it is widely believed that there is no finite temperature transition in this model and that the system is critical at zero-temperature.

The stiffness exponent of  $\pm J$  model, on the other hand, is much closer to the marginal value, 0. It was estimated,<sup>31</sup> with the assumption of the power-law dependence of the stiffness on the system size, as

$$\theta_S = -0.060(4),$$

while the possibility of  $\theta_S = 0$  was not ruled out. The possibility of the stiffness exponent being zero was strongly suggested by another ground state computation.<sup>30</sup>

Recently, it was pointed out that the stiffness exponent have to be interpreted differently for  $\pm J$  models. Amoruso *et al.*<sup>32</sup> carried out a renormalization calculation using the Migdal-Kadanoff method. They found that the stiffness exponent, calculated within this approximation, is zero in any dimension lower than the lower critical dimension. This finding suggests that the stiffness exponent being zero does not necessarily imply that the system is exactly at the lower critical dimension. This type of dimensional dependence of the stiffness exponent was observed only for the class of the bond distribution for which the discretized nature of the coupling constant is not smeared out by the renormalization. Since the  $\pm J$  bond distribution falls into this class, the above-mentioned numerical estimates,  $\theta_S \sim 0$ , may only mean that the lower-critical dimension is two *or above*. For the  $\pm J$  model,

however, even the possibility of a finite temperature phase transition was suggested,<sup>33</sup> as we discuss in greater detail further below.

### 9.2.2. *Droplet Argument for Gaussian-Coupling Models*

For two dimensional systems with a symmetric ( $P(J) = P(-J)$ ) and continuous bond distribution, it was argued<sup>23</sup> that there is only one independent critical exponent. In other words, all critical indices are related to the stiffness exponent via scaling laws. We consider the following finite size scaling form of the singular part of the free energy  $F_s$ ,

$$\Phi(T, H, L) \equiv \beta F_s = -[\log Z] \sim \phi(TL^y, HL^{y_h}).$$

The condition that the total magnetization  $[M] \equiv \lim_{H \rightarrow 0} \partial F_s / \partial H$  is proportional to  $L^{d/2}$  at  $T = 0$  relates  $y$  to  $y_h$  via

$$y_h = y + \frac{d}{2}.$$

Then, by differentiating  $\Phi$  with respect to  $T$  and  $H$ , we can express any critical index by  $y$ . For example, the magnetization per spin depends on the magnetic field as  $m = L^{-d} M \sim L^{-\frac{d}{2}} \sim H^{\frac{d}{2y_h}}$ , which means that the exponent  $\delta$  appearing in the scaling of the magnetization with the magnetic field is  $\delta = 1 - 2y/d$ . The non-linear susceptibility  $\chi_2 \equiv L^{-d} \partial^3 M / \partial H^3$  at  $H = 0$  depends on the temperature as  $\chi_2 \sim T^{-\gamma_2}$  with  $\gamma_2 = 3 + \frac{d}{y}$ . Since the spin glass susceptibility  $\chi_{SG}$  at  $H = 0$  is related to  $\chi_2$  as  $\chi_{SG} \equiv L^{-d} \sum_{i,j} [\langle S_i S_j \rangle^2] = T^3 \chi_2$ , the corresponding exponent is  $\gamma_{SG} = d/y$ . Similarly, the specific heat exponent can be expressed as  $\alpha = -d/y$ . As for the exponent  $\eta_{SG}$ , that characterizes the asymptotic form of the two-point spin glass correlation function  $[\langle S_i S_j \rangle^2] \sim R_{ij}^{d-2+\eta_{SG}}$ , we have  $2 - \eta_{SG} = y\gamma_{SG}$ , which yields  $\eta_{SG} = 2 - d$ . This is consistent with the fact that the correlation function does not decay at zero-temperature.

### 9.2.3. *Droplets in Gaussian-Coupling Models: Numerics*

As mentioned above, one naturally expects<sup>24</sup> that the exponent  $-y$  is identical to the stiffness exponent  $\theta_S$  since both the exponents relate the energy scale to the length scale. However, the estimates of various critical exponents<sup>34,35,36,38,39</sup> based on the system size up to  $L \sim 50$  seem to satisfy the scaling relation with  $y \sim 0.5$  rather than  $y = -\theta_S \sim 0.3$ .

In order to check if  $y$  coincides with  $-\theta$ , a direct numerical estimate of the droplet excitation exponent  $\theta$  was carried out using a heuristic op-

timization procedure<sup>40,41</sup> applied to the EA model with a Gaussian bond-distribution in two dimensions. For each realization of the model, the ground state spin-configuration was computed with free boundary condition. Then, the spins on the boundary were fixed as they were in the original ground state whereas the spin at the center was fixed in the opposite direction. These constraints lead to a new ground state that is identical to the old one on the boundary but differs from it in the vicinity of the central spin by a droplet of flipped spins around the center. The droplet is typically as large as the system itself. The system-size dependence of the droplet volume  $V$  and the droplet excitation energy  $E$  could be described well by the scaling law

$$V(L) \propto L^{d_D}, \quad \text{and} \quad E(L) \propto (V(L))^{\theta/d_D}$$

with

$$d_D = 1.80(2), \quad \text{and} \quad -\theta = 0.47(5)$$

for the range of the system size  $5 \leq L \leq 49$ . In particular, the value of  $-\theta$  agreed with most of the previous estimates of  $y$ . This can be understood also within the droplet theory because all scaling forms derived by droplet arguments are identical to what one can get via the ordinary finite size scaling by identifying  $\theta$  and  $-y$ .

However, a recent computation<sup>42</sup> demonstrates the presence of a cross-over in the droplet excitation energy. They performed essentially the same calculations as the one described above for larger systems (up to  $L = 160$ ). and argued that there may be a correction term due to the self-interaction of the surface of the droplets and that the droplet excitation energy has the form

$$\Delta E(L) \sim AL^\theta + BL^{-\omega}$$

with  $\omega > |\theta_D|$ . The numerical data could be well fitted by

$$-\theta_D = 0.29, \quad \text{and} \quad \omega = 0.97(5).$$

as is shown in Fig.9.1(a). The fact that the estimate of the droplet exponent now becomes close to the stiffness exponent indicates the validity of the simplest scenario. However, the result on the fractal dimension of droplets seems to suggest the contorary; their result appears to confirm the previous result  $d_D \sim 1.8$  (Fig.9.1(b)). While this may be another transient behavior, the problem of compactness of the droplets remains open in the two-dimensional system.

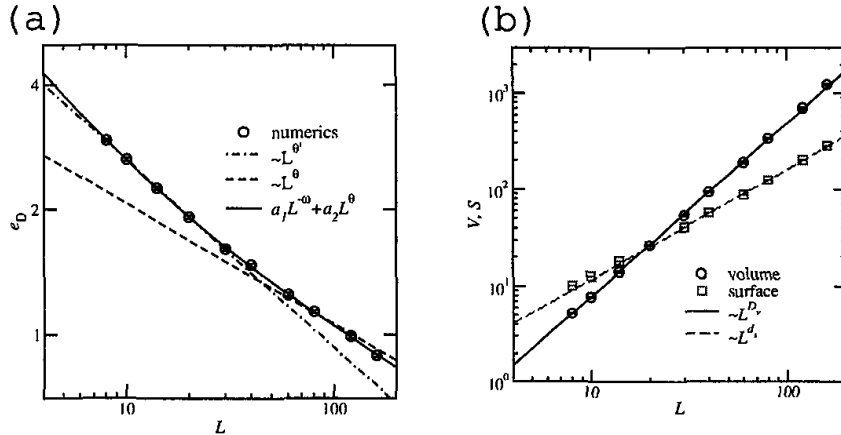


Fig. 9.1. (a) The droplet energy as a function of the system size. The two dashed straight lines represent the algebraic dependences  $L^{-0.47}$  for smaller systems and  $L^{-0.29}$  for larger ones, respectively. The solid curve is a fitting function (see text). (b) The volume and surface of the droplets. (From [42].)

The same model was studied in [43] and then in [44] at zero-temperature using a different approach. For each realization of the model, the ground state for periodic boundary condition was compared with the ground state for another set of boundary conditions, such as anti-periodic and random boundary conditions. (In the latter, half of the bonds across the boundary are chosen at random and inverted while the other half are kept unchanged.) The authors of [44] argued that in the RSB picture the change in the boundary condition would induce an excitation whose surface-to-volume ratio should not diminish as the system size increases, whereas in the droplet picture it should decrease down to zero. Therefore, we can differentiate between the two pictures by applying a boundary condition that induces a domain wall in the system and focusing on a small box located at the center of the system. If the probability of having the domain wall crossing this part is finite even in the thermodynamic limit, it would indicate the validity of the RSB picture. On the other hand, it should decrease to zero if the droplet picture is valid.

They performed a calculation of exact ground states of many instances of the EA model in two dimensions with the Gaussian bond distribution. The system size explored was up to  $L = 30$ . They considered a box of the linear size of  $L_{\text{box}} = 2$  located at the center of the system, and measured the distribution of the overlap  $q_{\text{box}}$  on this box:

$$q_{\text{box}}^{\alpha\beta} \equiv \frac{1}{L_{\text{box}}^d} \sum_{i \in \text{"box"}} S_i^\alpha S_i^\beta$$

where  $\alpha$  and  $\beta$  are the indices specifying real replicas. If the boundary passes the box with a finite probability, the distribution of  $q_{\text{box}}^{\alpha\beta}$  should have a finite weight around  $q_{\text{box}}^{\alpha\beta} = 0$ . This weight turned out to be decreasing with the power of  $-0.7$  as a function of the system size. Based on this result, they concluded that the zero-temperature structure of the two-dimensional EA model is trivial, i.e., only two pure states exist. (See Fig.9.4.)

#### 9.2.4. Finite-Temperature Transition?

There are some numerical results<sup>33</sup> of Monte Carlo simulation on the  $\pm J$  model that suggest the existence of a phase transition at a finite temperature. Specifically, the overlap distribution  $P(q; L)$  and the binder parameter  $g$  were computed. The estimates of the Binder parameter

$$g_q \equiv \frac{1}{2} \left( 3 - \frac{[\langle q^4 \rangle]}{[\langle q^2 \rangle]^2} \right) \quad (9)$$

as a function of the temperature for various system sizes appeared to have a common crossing point. The finite-size-scaling plot seems better when a finite transition temperature  $T_c \sim 0.24J$  was assumed instead of zero transition temperature. Their estimate for the critical indices of this finite temperature transition are  $\nu \sim 1.8$  and  $\eta \sim 0.2$ . The overlap distribution  $P(q; L)$  could be nicely scaled with the same  $\eta$  but with a slightly higher temperature  $T_c \approx 0.29J$ . Similar results were obtained<sup>45</sup> for an asymmetric bond distribution.

Numerical evidences suggest that the stiffness exponent of the two-dimensional  $\pm J$  model is non-positive, as discussed in subsection 9.2.1, which indicates that the lower critical dimension of the  $\pm J$  model is equal to or greater than two. Now, if a spin-glass transition takes place at a finite temperature as suggested, it means that the lower critical dimension is not greater than two. Therefore the only scenario consistent with all the available numerical and analytical results is that the lower-critical dimension is exactly two and that the stiffness exponent is exactly zero in two dimensions. More evidences, however, appear to be necessary to settle this issue beyond reasonable doubts.

### 9.3. Equilibrium Properties of Three-Dimensional Models

The problem of spin glasses in three dimensions is the central topic of the field. Whereas the RSB nature of the low-temperature phase in four dimensions is much less controversial, the nature of the low-temperature phase in three dimensions still remains the subject of an active debate.

Below we present a number of numerical results. Because of the severe technical limitations for three dimensional cases, all the results obtained are for small systems, typically up to the linear size of about 10 lattice spacings or slightly more. Therefore, many important issues are left open, in particular the question as to what picture yields the correct description of the low-temperature phase of the EA model, which is the main subject of subsection 9.3.3 through subsection 9.3.8.

### 9.3.1. Finite Temperature Transition?

Even the very existence of a phase transition at finite temperature was not easy to establish. An evidence of the existence was obtained through the calculation of the domain wall energy at zero-temperature,<sup>29</sup> in which a positive estimate for the stiffness exponent was obtained. However, the system size was rather limited ( $L \leq 8$ ) and the estimated value of the stiffness exponent was small ( $\theta \sim 0.2$ ). Therefore, this finding about the stiffness exponent alone was not sufficient to establish the existence of a finite-temperature phase transition. Finite temperature approaches could not settle the issue, either. For example, while Monte Carlo simulations<sup>46,47</sup> strongly suggested the existence of a transition at a finite temperature, they could not rule out the possibility of zero-temperature singularity with an exponentially diverging correlation length; it was suggested<sup>48</sup> that all existing data at that time (namely 1994) were consistent with both hypotheses:  $T_c > 0$  and  $T_c = 0$ . In particular, the simulation results of [48] for the spin-glass susceptibility could be fitted by a functional form consistent with a zero-temperature singularity,  $\chi_{\text{SG}} = 1 + A/(T - T_c)^\gamma$ , just as well as the one consistent with a finite-temperature transition  $\chi_{\text{SG}} = A(e^{(B/T)^p} - 1) + C$ .

However, another set of Monte-Carlo results<sup>49</sup> showed beyond reasonable doubts the existence of a finite temperature transition in the  $\pm J$  model in three dimensions. Specifically, it demonstrated that the Binder parameter curves for different system sizes cross at the same point (Fig.9.2) near

$$T \sim 1.1, \quad \text{and} \quad g_{\text{sg}} \sim 0.75.$$

With the assumption of the algebraic singularity at the critical point, the critical temperature and the critical indices were estimated as

$$T_c = 1.11(4), \quad \nu = 1.7(3), \quad \text{and} \quad \eta = -0.35(5).$$

These estimates were consistent with previous ones<sup>46</sup> and confirmed by other simulations as presented in Table 9.1.

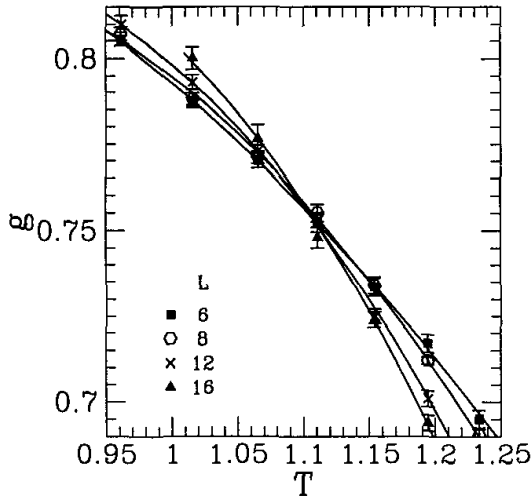


Fig. 9.2. The Binder parameter vs temperature for the  $\pm J$  model in three dimensions. (From [49].)

A Monte Carlo simulation for larger system sizes<sup>50</sup> clarified the issue further. The results of the correlation length and the spin-glass susceptibility were extrapolated to the infinite system-size limit via finite size scaling, and were well fitted by a curve representing an algebraic divergence at a finite temperature. While the existence of a finite temperature phase transition could be concluded from this result, the nature of the singularities at the critical point could not unambiguously be settled. (The singularity could be an essential rather than an algebraic singularity.) In the next subsection, we present other numerical results concerning the nature of the critical point.

### 9.3.2. Universality Class

Early Monte Carlo simulations such as [46] indicated a scenario that the system stays critical in the whole low temperature region. Namely, these data could be explained by a line of critical points terminating at  $T_c = 1.2$ , similar to the Berezinskii-Kosterlitz-Thouless transition in the two-dimensional XY ferromagnet. The conclusion of [50] on this issue was similar, while it was suggested that a finite-temperature transition with a algebraic divergence is most likely. With the assumption of the algebraic divergence, the critical parameters were estimated to be consistent with previous ones mentioned above. However, the data were also consistent with an exponential divergence as in the BKT transition.

A large-scale Monte Carlo simulation<sup>51</sup> clarified the issue of the nature of the phase transition. Using special purpose machines and parallel tempering method<sup>52,53</sup> the authors succeeded to equilibrate the  $\pm J$  model of sizes up to  $L = 20$  down to a temperature low enough to cover a sufficiently large region around the transition point. They obtained various results consistent with an ordinary second order phase transition. For example, they observed a clear crossing in the effective correlation length<sup>54</sup>  $\xi(L)$  divided by the system size  $L$ . (They defined the effective correlation length as  $\xi^2(L) \equiv \tilde{k}_m^{-2}(C_q(0)/C_q(\mathbf{k}_m) - 1)$ , where  $C_q(\mathbf{k})$  is the static structure factor,  $\mathbf{k}_m$  is the smallest non-zero wave number compatible to the boundary condition, and  $\tilde{k}^2 \equiv 4(\sin^2(k^x/2) + \sin^2(k^y/2) + \sin^2(k^z/2))$ .)

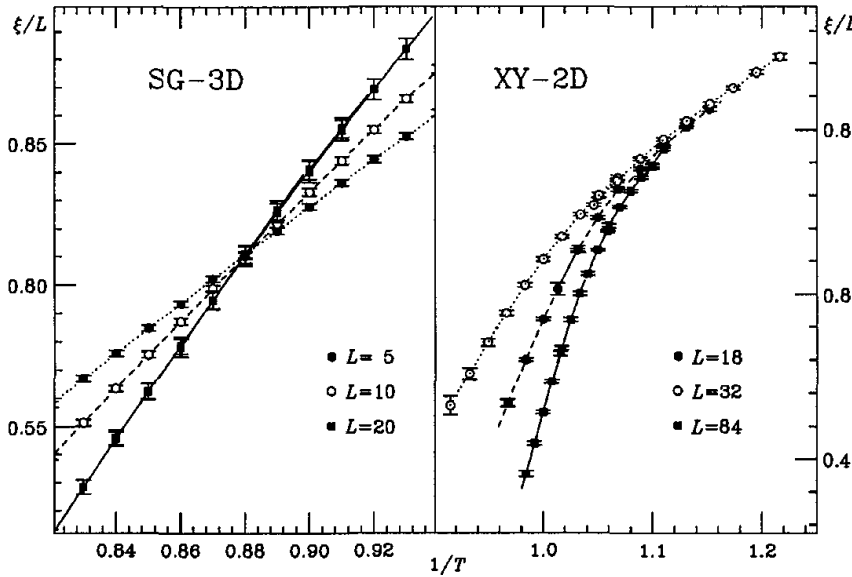


Fig. 9.3. The effective correlation length divided by the system size. The left panel is for the  $\pm J$  model in three dimensions whereas the right panel is for the  $XY$  model in two dimensions. (From [51].)

The scaling dimension of the effective correlation length is zero; the curves for various system sizes should intersect at the same point similar to the Binder parameter. Indeed, it shows a common intersection point as in the right panel of Fig. 9.3. This is in marked contrast to what we typically see in a BKT type transition, which is shown in the right panel of Fig. 9.3 for comparison. From this result one concludes that the phase transition is an ordinary second-order one. For the critical temperature and the indices, again, see Table 9.1.

The results of [51] provided also indications in favor of an RSB nature of the system below the critical temperature. Namely, the estimates of a quantity called the  $G$ -parameter seems to have a finite value even below the critical point. The  $G$ -parameter is defined<sup>55</sup> as

$$G \equiv \frac{[\langle q^2 \rangle^2] - [\langle q^2 \rangle]^2}{3[\langle q^2 \rangle]^2 - [\langle q^4 \rangle]}.$$

The numerator is finite only if the sample-to-sample dependence of  $P(q)$  does not vanish, while the denominator can be finite even if there is no sample dependence. Therefore, a observed non-vanishing value of  $G$  implies that  $P(q)$  is not self-averaging.

However, there are a number of evidences by other groups that can be interpreted otherwise, namely, in favor of the absence of an RSB nature of the low temperature phase, as we discuss below.

### 9.3.3. Low-Temperature Phase of the $\pm J$ Model

There is a very active debate on the nature of the low-temperature phase of three dimensional spin glass models. In the following few subsections, we review various theories, arguments and numerical calculations that were made or done with the ultimate aim to clarify the issue. But none of the pictures, RSB, droplet, or others, could be established so far. Nonetheless, the debate itself is interesting and each picture is worth being scrutinized with detailed numerical calculations. While the common belief is that the  $\pm J$  model and the Gaussian-coupling model show essentially the same physics at finite temperature, we present them separately since many of the computations are done at zero temperature where the two may differ. The  $\pm J$  model is discussed in the present subsection and the Gaussian-coupling model in the next.

A finite temperature simulation on the  $\pm J$  model was performed<sup>77</sup> using the replica exchange Monte Carlo simulation<sup>53</sup> for  $\pm J$  model reaching down to  $T = 0.2$  for the system size up to  $L = 10$ . The integrated overlap probability distribution

$$x(1/2) \equiv \int_0^{1/2} dq P(q)$$

was computed as a function of the temperature and the system size. Inspired by [78], the scaling —  $x(1/2)$  being proportional to  $L^\lambda$  for small  $L$  and to  $L^\theta$  for larger  $L$  — was assumed. In other words,

$$x(1/2) = TL^{-\theta} f(TL^\lambda)$$

Table 9.1. The estimates of the critical temperature and the exponents for the three dimensional spin glass models. The entries are categorized into three groups according to the anisotropy: easy-axis (top), isotropic (middle), and easy-plane (bottom). The entries with “\*\*” are not quoted in the original paper but estimated through the scaling relations by the present authors. The entries with “<sup>c</sup>” are for the chiral glass transition. . .

Authors	Material/Model	$T_c/J$	$\nu$	$\eta$	$\beta$	$\gamma$	$z$
Gunnarsson <i>et al.</i> <sup>56</sup>	FeMnTiO	—	1.7	-0.35	0.54	4.0(3)	6.2
Ogielski <sup>47</sup>	Ising, $\pm J$	1.175(25)	1.3(1)	-0.22(5)	0.5	2.9(3)	6.0(5)
Bhatt-Young <sup>46</sup>	Ising, $\pm J$	1.2 <sub>-0.2</sub> <sup>0.1</sup>	1.3(3)	-0.3(2)	0.46*	3.2	—
Singh-Chakravarty <sup>57</sup>	Ising, $\pm J$	1.2(1)	—	—	—	2.9(5)	—
Bhatt-Young <sup>58</sup>	Ising, Gaussian	0.9	1.6(4)	-0.4(2)	—	—	—
Kawashima-Young <sup>49</sup>	Ising, $\pm J$	1.11(4)	1.7(3)	-0.35(5)	0.55*	4.0*	—
Iniguez <i>et al.</i> <sup>59</sup>	Ising, Gaussian	1.02(5)	1.5(3)	—	—	—	—
Marinari <i>et al.</i> <sup>60</sup>	Ising, Gaussian	0.98(5)	2.00(15)	-0.36(6)	0.64*	4.72*	—
Berg-Janke <sup>61</sup>	Ising, $\pm J$	0.88	—	-0.37(4)	—	—	—
Palassini-Caracciolo <sup>50</sup>	Ising, $\pm J$	1.156(15)	1.8(2)	-0.26(4)	0.65*	4.1(5)	—
Mari-Campbell <sup>62</sup>	Ising, $\pm J$	1.19(1)	1.33(5)	-0.22(2)	0.52*	2.95(15)	—
Ballesteros <i>et al.</i> <sup>51</sup>	Ising, $\pm J$	1.138(10)	2.15(15)	-0.337(15)	0.73*	5.0*	—
Mari-Campbell <sup>63</sup>	Ising, $\pm J$	1.195(15)	1.35(10)	-0.225(25)	0.55*	2.95(30)	5.65(15)
Nakamura <i>et al.</i> <sup>64</sup>	Ising, $\pm J$	1.17(4)	1.5(3)	-0.4(1)	0.45*	3.6(6)	6.2(2)
de Courtenary <i>et al.</i> <sup>65</sup>	CuMn,AgMn	—	1.4*	0.4*	1.0(1)	2.2(1)	—
Bouchiat <sup>66</sup>	AgMn	—	1.4*	0.4*	1.0(1)	2.2(2)	—
Levy-Ogielski <sup>67</sup>	AgMn	—	1.3(2)	0.4*	0.9(2)	2.1(1)	5.5
Simpson <sup>68</sup>	CuAlMn	—	1.3*	0.5*	1.0*	1.9*	—
Coles-Williams <sup>69</sup>	PdMn	—	1.3*	0.4*	0.90(15)	2.0(2)	—
Vincent-Hamman <sup>70</sup>	CdCrInS	—	1.25(25)	0.2*	0.75(10)	2.3(4)	5.5
Kawamura <sup>71</sup>	Heisenberg, Gaussian	0.157(10) <sup>c</sup>	—	—	1.1(1) <sup>c</sup>	—	—
Hukushima-Kawamura <sup>72</sup>	Heisenberg, Gaussian	0.160(5) <sup>c</sup>	1.2 <sup>c</sup>	0.8 <sup>c</sup>	1.1(1) <sup>c</sup>	1.5(3) <sup>c</sup>	—
Matsubara <i>et al.</i> <sup>73</sup>	Heisenberg, $\pm J$	0.18	—	—	—	—	—
Nakamura-Endoh <sup>74</sup>	Heisenberg, $\pm J$	0.21 <sup>+0.01</sup> <sub>-0.03</sub>	1.1(2)	0.3*	0.72(6)	1.9(4)	4.5
Lee-Young <sup>75</sup>	Heisenberg, Gaussian	0.16(2)	1.1(2)	—	—	—	—
Nakamura <i>et al.</i> <sup>64</sup>	Heisenberg, $\pm J$	0.20(2)	0.8(2)	-0.3(3)	—	1.9(5)	6.2(5)
Kawamura-Li <sup>76</sup>	XY, $\pm J$	0.39(3) <sup>c</sup>	1.2(2) <sup>c</sup>	0.15(20) <sup>c</sup>	—	—	7.4(10) <sup>c</sup>
Lee-Young <sup>75</sup>	XY, Gaussian	0.34(2)	1.2(2)	—	—	—	—
Nakamura <i>et al.</i> <sup>64</sup>	XY, $\pm J$	0.43(3)	—	-0.4(2)	—	—	6.8(5)

was assumed. The fitting to the numerical results worked nicely with  $\theta = 0$  yielding

$$\lambda = 0.9(1),$$

whereas a fitting with  $\theta = 0.2$ , the droplet prediction, turned out to be significantly worse. The estimate of  $\lambda$  is considerably smaller than a preceding estimate<sup>79</sup> while consistent with the value  $\lambda = 0.72(12)$  in [80].

Zero-temperature calculations offer a powerful alternative to the finite temperature approach with Monte Carlo simulations, because one might expect that the differences between the two scenarios should be more prominent at lower temperature, and much better methods are available for systems at zero-temperature than for a very low but finite temperature. For three dimensional models, most methods for solving zero-temperature problems are based on heuristic optimization since no good exact method is available due to the NP-hardness of the problem. A computation of the ground states of the  $\pm J$  Ising model up to  $L = 14$  was done<sup>81,82</sup> with a heuristic algorithm called the cluster-exact approximation method.<sup>83</sup> Later the computation was redone,<sup>79,84</sup> in order to fix the problem of the biased sampling.<sup>85</sup> It was found that the width of the overlap distribution,  $P(q)$ , decreases as the system becomes larger, indicating the triviality of  $P(q)$ . The validity of the ultra-metric relation,  $q_{12} = q_{23} < q_{31}$ , was also examined, where  $q_{ij}$ 's are the overlaps among three randomly chosen ground states. The numerical results indicated that the ultra-metric relation holds for a typical triplet of ground states with relatively large mutual distances. However, it was also found that the contribution from these triplets to  $P(q)$ , which constitutes the “non-trivial” (i.e., continuous) component of  $P(q)$ , decreases as the system becomes larger. In fact, the integrated weight of  $P(q)$  systematically decreased toward zero as

$$x(q) \equiv \int_{-q}^q dq P(q) \propto L^{-\lambda}$$

with  $\lambda = 1.25(5)$  for  $q = 0.5$ . This indicated a trivial structure of  $P(q)$  at zero temperature. As for the exponent  $\lambda$ , a different estimate was obtained<sup>77</sup> as mentioned below.

The authors of [78] considered  $P(q)$  for the  $\pm J$  model at  $T = 0$ , and pointed out that the ground state space may be dominated by a single valley or a single pure state no matter which picture is valid. They argued that even if there are multiple valleys in the energy landscape of the discrete energy model, the distribution of the overlap  $P(q)$  may still be trivial,

indicating that it is impossible to discriminate between the two scenarios by a computation of  $P(q)$  such as the one mentioned above.

The underlying assumption of the argument is the many-valley structure in the phase space and the sponge-like structure of low-lying excitations in the real space. (The latter is further discussed below in subsection 9.3.6 and subsection 9.3.7.) A droplet typically has a finite volume and when flipped it takes a state in a valley to another state in the same valley. In contrast, a typical sponge-like cluster is supposed to occupy a finite fraction of the whole system and flipping it generally causes a transition from one valley to another.

This argument is based on an estimate of the entropy by counting zero-energy excitations from a particular ground state. In general, the continuous part of  $P(q)$ , if any, is caused by excitations of various scales whose excitation free energies are smaller than the temperature. In particular, at zero temperature, it is caused by zero-energy “excitations”. They argued that  $P(q)$  has a trivial structure even if there are multiple valleys. To see this, it suffices to consider the case of two valleys. Each valley contributes to  $P(q)$  according to its weight that is the number of distinct spin configurations in the valley. This number is roughly the same as the number of zero-energy droplets. We can choose two representative configurations, one from each valley, that can be transformed to each other by flipping a sponge-like cluster. Then, the zero-energy droplet excitations in one configuration differ from those in the other configuration only on (or near) the boundary of the sponge-like cluster. Therefore, if  $A$  is the area of the surface of the sponge-like cluster, the droplets differ only at  $A$  positions. This difference results in the entropy difference of  $\mathcal{O}(A^{1/2})$ . (The power 1/2 comes from the assumption that the number of the droplet-like excitation located on the surface is a random variable.) It follows that the contribution (to the continuous part of  $P(q)$ ) from one valley differs from that from the other typically by a factor  $e^{\pm(\text{const}) \times A^{1/2}}$ . We now see that almost certainly  $P(q)$  is dominated by a contribution from a single valley in the thermodynamic limit where  $A \rightarrow \infty$ , leading to a trivial structure in  $P(q)$ . It is clear that the presence of more than two valleys does not affect the result as long as the number of valleys does not grow too fast as the system size increases. Based on this result, they argued that a trivial  $P(q)$  for the  $\pm J$  model in three dimensions at  $T = 0^{84}$  does not necessarily indicate the absence of the RSB.

However, it is not known how the number of valleys depends on the system size. It is not too unrealistic to assume that the number of valleys

grows faster than or proportional to the number of spins,  $N$ . If so, a typical minimum entropy difference between two valleys would be less than  $A^{1/2}/N < N^{-1/2} \rightarrow 0$ . Therefore, it is not clear if this argument really invalidates the numerical evidence in [84] for triviality of the energy landscape structure.

### 9.3.4. Low-temperature Phase of the Gaussian-Coupling Model

The ground state of models with the Gaussian bond distribution, is unique up to a trivial degeneracy due to the  $Z_2$  symmetry. However, it is still possible to extract useful information about low-lying excitations from zero-temperature computations. The authors of [86] attempted to use the same strategy that they used for two dimensional models with the Gaussian bond distribution<sup>44</sup> (see subsection 9.2.3) to discriminate between the two scenarios in three dimensions. They estimated the probability of a domain-wall passing through a small imaginary box placed inside the system. A clear decreasing behavior as a function of the system size was found, in favor of the droplet picture. However, the amount of the total decrease that they could observe by changing the system size was only of a factor of 1.3 or 1.4, due to a severe system size limitation. (In the case of two dimensions, the same quantity varies by almost an order of magnitude as can be seen in Fig.9.4.)

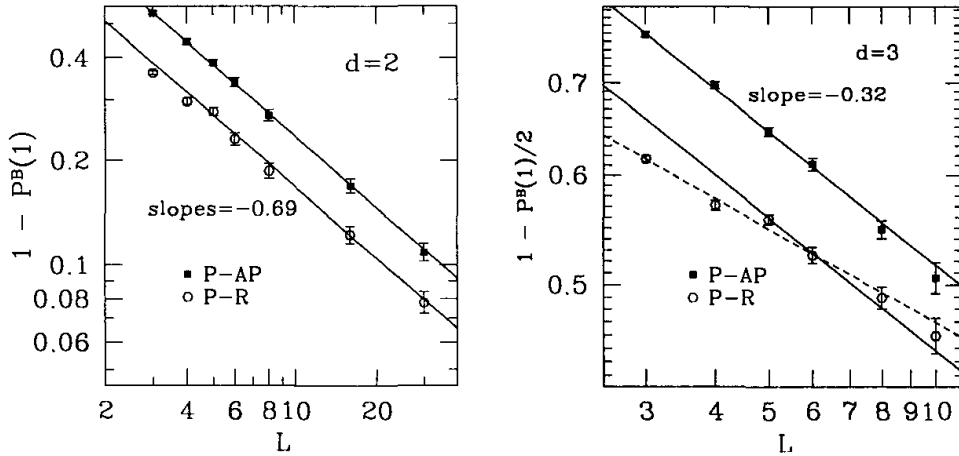


Fig. 9.4. The probability of a domain wall passing through the box. The left panel is for the EA model with the Gaussian bond distribution in two dimensions at  $T = 0$  and  $H = 0$ , whereas the right panel is for the same model in three dimensions. (From [86].)

In addition to the response to the boundary condition, the effect of a weak perturbation applied to the whole system was also examined.<sup>87</sup> The perturbation was chosen in favor of the excited states against the ground state. For each bond realization, they first obtained the ground state, which we denote  $\{S_i^{(0)}\}$ . Then to each coupling constant  $J_{ij}$  the following perturbation was added

$$\Delta J_{ij} \equiv -\Delta J S_i^{(0)} S_j^{(0)}.$$

where  $\Delta J \equiv \epsilon/N_{\text{bond}}$  was chosen to be of  $\mathcal{O}(L^{-d})$ . With this perturbation the ground state energy is increased, exactly, by  $\epsilon$ , whereas excited state energies are changed according to its similarity to the ground state. Therefore by adjusting the amplitude of the perturbation and examining the overlap between the original ground state and the ground state of the perturbed system, one may obtain some information about the excitations.

The RSB picture predicts the existence of many spin states that are local minima of the Hamiltonian. These states differ from the ground state by only an infinitesimal amount of energy per spin but differ by a macroscopic number of spins such that the average Hamming distance between them (normalized by the system size) converges to some finite value in the large system size limit. This means for the bulk perturbation considered in [87] that the overlap between the two such minima, the one with the perturbation and the other without, should be truly smaller than unity in the thermodynamic limit, no matter how small the perturbation may be. Therefore in the RSB picture,  $1 - [q]$  should be finite where  $q$  is the overlap between the two minima. On the other hand, in the droplet picture,  $1 - [q]$  should depend on the system size by a power-law being characterized by the droplet energy exponent  $\theta$  and an exponent related to the geometrical properties of the excitations. To be specific, since  $1 - [q]$  is dominated by the contribution from droplets whose linear size is comparable to the system size  $L$ , it is roughly equal to the volume fraction of a typical droplet of size  $L$  multiplied by the probability of such a droplet being excited. Namely,

$$1 - [q] \propto \frac{L^{d_v}}{L^d} \times \frac{\Delta_L}{\epsilon_L} \quad (10)$$

where  $\Delta_L$  is the energy gain by the droplet excitation due to the perturbation and  $\epsilon_L$  is the droplet excitation energy without the perturbation. If the droplets are compact, as assumed in [87], only the second factor matters since  $d_v = d$ . For  $\Delta_L$ , the authors of [87] assumed that  $\epsilon \sim \mathcal{O}(1)$  when integrated over the whole system, which is equivalent to setting  $\Delta_L \propto L^{-d+d_s}$

where  $d_s$  is the fractal dimension of the boundary of droplets. Based on this, the following scaling form for the overlap was proposed [87]:

$$v(\epsilon, L) \equiv 1 - [q] \sim \tilde{V}(\epsilon/L^{d-d_s-\theta}). \quad (11)$$

For the link overlap  $q_l$ , a similar argument yields

$$s(\epsilon, L) \equiv 1 - [q_l] \sim L^{-(d-d_s)} \tilde{S}(\epsilon/L^{d-d_s-\theta}). \quad (12)$$

In the system size range that could be explored, (namely,  $L \leq 8$ ), the numerical results for  $[q]$  and  $[q_l]$  shows that  $v(\epsilon, L)$  and  $s(\epsilon, L)$  obeys the power law and decreases to zero as the system size increases, contradicting the RSB picture. However, fitting the numerical results to the forms (11) and (12) yielded

$$d - d_s = 0.42(2), \quad \text{and} \quad d - d_s + \theta = 0.44(2).$$

This implies

$$\theta = 0.02(3).$$

The difference between the value and the stiffness exponent ( $\sim 0.2$ ) obtained from the domain wall calculation is statistically significant, i.e., the result contradicts not only to the RSB picture but also to the droplet picture unless this seeming contradiction is caused by a large correction to scaling.

Concerning the possible source of the correction, two arguments<sup>88,89,42</sup> were presented to explain the inconsistency observed in numerical results within the framework of the droplet argument. It was pointed out<sup>88</sup> that if one assumes a “clean” scaling with no correction for the droplet excitation energy, the contribution from small droplets gives rise to a correction to scaling in quantities such as the spin-glass susceptibility and the magnetic susceptibility. The droplet excitation energy computed with the condition used in [40,41] and the link overlap computed in [87] may have been affected by such a correction to scaling. Another possible source of a correction to scaling is the interaction between domain walls. It was argued<sup>89,42</sup> that the energy of a domain wall may be increased by the presence of another domain wall and that the energy shift due to this interaction may have the form  $l^{-\omega'}$  where  $l$  is the distance between two domain walls. Similarly, a “self-interaction” of the domain wall may give rise to a correction to scaling in the droplet excitations as  $E = Al^\theta + Bl^{-\omega}$ . In this case  $l$  stands for the size of the droplets. As the correction-to-scaling exponent due to this mechanism, the authors of [89] quoted the value  $\omega \sim 0.13(2)$ <sup>90</sup>.

In response to some reports (see the following paragraphs in the present section) contradicting to their conclusion, the authors of [91] further pursued the ground state nature of the three dimensional system with the Gaussian bond-distribution, along the same line as their own preceding calculation.<sup>87</sup> This time, however, larger systems ( $L = 12$ ) were dealt with the branch-and-cut algorithm.<sup>92</sup> This algorithm guarantees that the states found are the true ground states. In addition, a greater care was taken for various possibilities of fitting functions and different sources of corrections to scaling. Specifically, they considered a few different fitting functions for size dependent quantities such as the link overlap and the box overlap. Fitting functions consistent with the droplet, the TNT, and the RSB scenario, respectively, were considered. (For the TNT scenario, see subsection 9.3.6 and subsection 9.3.7 below.) It was found that the size dependence of the surface-to-volume ratio, i.e.,  $1 - q_1$ , could be explained by any one of three pictures, and also that the size dependence of the box overlap could be explained by any one of three pictures. The estimates of the exponent  $\mu \equiv d - d_s + \theta$  turned out to depend on the boundary condition. With the free boundary condition, the estimates are  $d - d_s = 0.44(3)$ ,  $\mu = 0.63(3)$ , and  $\theta = 0.19(6)$ , whereas for the periodic boundary condition, they are  $d - d_s = 0.43(2)$ ,  $\mu = 0.42(3)$ , and  $\theta = -0.01(3)$ . The latter set of values are consistent with their preceding estimates<sup>87</sup> whereas the former are not.

Another set of numerical results, presented in [93,94,95] seems to contradict to the results of [87,86] presented above. As for the calculation based on the small imaginary box placed at the center of the system, it was argued<sup>93</sup> that the probability of the state inside the box being affected by the change in the boundary condition should obey the scaling

$$P_{\text{change}}(L_{\text{box}}, L) \sim g(L_{\text{box}}/L), \quad (13)$$

if the droplet argument is correct. However, the numerical results in [93] for  $L_{\text{box}} = 2, 3, 4$  and  $L = 12$  did not fit in this scaling.

In [93], the scaling property of the domain wall induced by the anti-periodic boundary condition in the  $x$ -direction was also examined. In particular, the probability of the domain wall not intersecting a plane perpendicular to the  $x$  axis was measured. It was found that the non-intersecting probability approaches zero as the system size increases:

$$P_L(\text{"The domain wall does not intersect the plane."}) \propto L^{-\gamma},$$

with  $\gamma = 1.5 - 2.0$ . Based on this observation they suggested that the domain wall is space filling, i.e.,  $d = d_s$ .

In [94,95], zero-temperature calculations were performed with the conditions analogous to the ones in [86] and [87]. In [94], the effect of the anti-periodic boundary conditions, which were imposed in the  $x$  direction, was compared with the periodic one. The links perpendicular to the  $yz$  plane were treated separately from those parallel to the  $yz$  plane. The result of the link overlap for the perpendicular links,  $q_P$ , and that for the transverse ones,  $q_T$ , are shown in Fig.9.5(a). Both kinds of the link over-

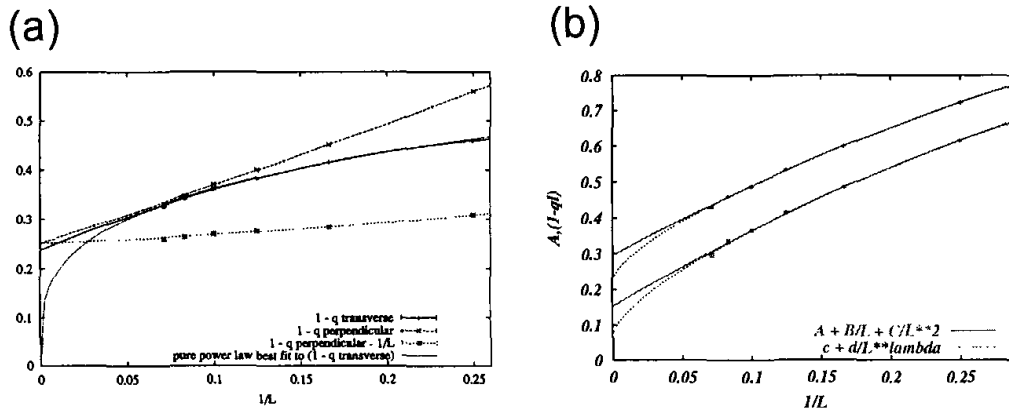


Fig. 9.5. (a) The link-overlap for the perpendicular links,  $q_P$ , and that for the transverse ones,  $q_T$ , between the two ground states with and without a twist in the boundary, and (b) the link-overlap (subtracted from unity) between the two ground states with and without a bulk perturbation. (The lower set of data is for the average link-overlap, whereas the upper one is for the link-overlap restricted to those pairs of states which have zero mutual overlaps. For each set of data, the upper fitting curve is a second order polynomial in  $1/L$  and the lower one is a fractional power in  $1/L$  with an additional constant term.) For both (a) and (b), the model is the three-dimensional EA model with the Gaussian bond distribution at zero temperature. (From (a) [94] and (b) [95].)

lap can be fitted well by second order polynomials in  $1/L$  as shown in the figure. From the zero-th order term, they concluded that

$$\lim_{L \rightarrow \infty} 1 - q_l = 0.245(15),$$

in contrast to the droplet prediction  $1 - q_l \rightarrow 0$ .

In [95], the effect of the bulk perturbation at zero temperature was studied. The perturbation was the same as the one considered in [87]. The link overlap,  $q_l(q)$ , was computed as a function of the bulk overlap,  $q$ . In addition to the average link-overlap,  $q_l(L)$ , attention was paid to the quantity  $A(L) \equiv 1 - q_l(q=0)$ , where  $q_l(q=0)$  is the link overlap between two states that have zero overlap. In the droplet picture, both quantities should converge to 0 as  $L$  goes to infinity. The numerical results are shown

in Fig.9.5(b). It was found that in both cases of the boundary and the bulk perturbations, the size dependence of the surface-to-volume ratio of the domain wall, i.e.,  $1 - q_l$  can be fitted by a polynomial in  $1/L$  with a finite constant term, consistent with the RSB picture.

Concerning the results presented in [93], it was pointed out<sup>96</sup> that the probability  $P_{\text{change}}$  is subject to a strong correction to scaling and that, taking such a correction term into account, the data presented in [93] can be fitted reasonably well with the scaling form (13). It was also pointed out that even the two dimensional data, which is believed to obey (13), could not be fitted by this scaling form without a similar correction term. As for the non-intersecting probability of the domain wall with the plane, it was simply pointed out that the observation in [93] does not necessarily imply  $d = d_s$  because the observed behavior can be caused by domain walls that are rough but not space filling. In addition, as already mentioned above, their latest calculation<sup>91</sup> suggests that we have not yet accumulated numerical evidences sufficient to decide between the possible scenarios.

Before concluding this subsection, let us mention what is known about the geometrical nature of droplets. For this issue, a zero-temperature calculation was performed.<sup>90</sup> Using an efficient heuristic algorithm, the authors of [90] obtained ground states of three dimensional systems of the size  $L = 6$  and  $L = 10$ . For each sample, they first obtained the ground state. Then, a center of the excitation is chosen randomly. They searched for the droplets of various sizes including the central spin. In their calculation, a droplet was defined as the cluster of spins of the smallest excitation energy among those which have a given volume. In spite of the limited system size, they succeeded in obtaining system-size independent numerical results. They found that the linear scale of the droplets is described by

$$R(v) \propto v^b \quad (b \sim 0.5),$$

whereas the volume dependence of the excitation energy obeys

$$E(v) \propto v^a \quad (a \sim -0.06).$$

The first relation means that the droplets are roughly two dimensional fractal objects rather than compact ones. The second relation is rather surprising, since at first glance it might seem to contradict the existence of the finite-temperature phase transition. They claimed that this does not necessarily mean the absence of the phase transition because the basic assumption of the droplet argument may not be valid. Another possible

source of the discrepancy may be the definition of the droplet with the very restrictive fixed-volume constraint.

### 9.3.5. Effect of Magnetic Fields

Whereas the RSB picture predicts the persistence of the spin glass phase against a small but finite magnetic field, the droplet-picture predicts the contrary — the absence of the spin glass phase at any finite magnetic field. Therefore, one of the possible ways to distinguish between the two scenarios may be found in the behavior of short-range models in a finite magnetic fields. However, it is rather hard to perform this task near the critical temperature (of the zero-field case). This difficulty is not only because the dynamics near the critical point is slow but also because the critical value of the magnetic field predicted by the mean-field type argument is small. To avoid at least the latter difficulty, a zero-temperature calculation was performed.<sup>97</sup> Using a heuristic optimization algorithm, the ground state of the three dimensional EA model was computed with the Gaussian bond distribution up to  $L = 12$  with various uniform magnetic fields.

In addition to the magnetic field, also some constraints were imposed at the same time to probe low-lying excitations. For example, a spin may be forced to be opposite to its natural direction in the original ground state with no constraint. Then, the lowest-energy excitation among those which include the chosen spin is excited. In the RSB picture, where there are infinite number of states different from each other by a finite fraction of spins within an  $\mathcal{O}(1)$  window of excitation energy, such a excitation should typically contain a finite fraction of all spins. (See also subsection 9.3.6 and subsection 9.3.7 below.) Therefore, the volume of excited cluster tends to infinity with increasing system size. On the other hand, in the droplet scenario, the influence of the forced spin cannot reach beyond the distance determined by the magnetic field  $H$  as

$$l(H) \propto H^{-2/(d-2\theta)}.$$

Therefore, when the system size is increased beyond this length, the size of the excited clusters should stay constant independent of the system size. Some results of computation along this line of consideration were presented in [97]. They demonstrate the fragility of the ground state in a magnetic field. For example, the forced spin-flip typically drags as much as 30 percents of all spins at  $H = 0.2$  for  $L = 12$ . The size of the excited cluster generally increases as the system size increases. However, neither a saturation nor a proportionality to  $L^d$  could be identified clearly.

Therefore, they tried another constraint where signs of an array of bonds along a plane are switched. This corresponds to imposing the anti-periodic boundary condition to the system. In the RSB picture, the resulting excitation again should extend to the whole system, whereas in the droplet scenario, it should not for systems larger than  $l(H)$ . They measured the probability of the excitation wrapping around the system. It was found that the wrapping probability increases for  $H \leq 0.6$  as the system becomes larger whereas it decreases for  $H \geq 0.7$ . Based on this result they suggested that  $H_c$  is finite and is close to 0.65 at  $T = 0$ . While they did not exclude the possibility of  $H_c = 0$  considering the finite size corrections that may be present, their approach seems promising and it is probably worth putting more effort in this direction.

### 9.3.6. *Sponge-Like Excitations*

While the droplet picture presents a clear “real-space” image for the low-lying excitations, we have not discussed how low-lying excitations should look in the RSB picture. The authors of [98] discussed geometrical properties of low-lying excitations that are compatible with the RSB picture. They proposed that low-lying excitations may have a “sponge”-like shape. A sponge-like cluster has a characteristic length scale  $l_c$ . They argued that excitations smaller than this scale obey the droplet scaling whereas beyond this scale the droplet predictions do not apply. A sponge-like object is defined by the following properties.

- (1) It is a connected object, and so is its complement.
- (2) It occupies a finite fraction of the whole system’s volume.
- (3) It spans the whole system, and so does its complement.
- (4) It has a characteristic length scale different from the system-size and the lattice constant. When coarse-grained beyond this length scale, the object occupies the space uniformly whereas below this scale non-uniformity can be seen.
- (5) Its surface contains a finite fraction of its volume, i.e., the surface-to-volume ratio is finite and independent of the system size up to a finite size correction.

They argued that in finite dimensions, three for instance, there may be excitations of sponge-like clusters with excitation energy of  $\mathcal{O}(1)$ , independent of the system size. At the same time, the energy barrier that must be overcome in order to excite such a cluster diverges as the system size

increases. Namely, two pure states in the RSB picture can be transformed into one another by flipping spins in one or more of the sponge-like clusters. Since they occupy a finite fraction of the whole system, as soon as thermal fluctuations are introduced, they give rise to the non-trivial structure in the overlap distribution function,  $P(q)$ . In addition, because of the property (5), such excitations yield a non-trivial functional form for the link overlap distribution  $P(q_l)$ .

Obviously, the last two properties (4) and (5) above are closely related to each other, because the surface-to-volume ratio may be determined by the characteristic length scale as  $S/V \sim l_c^{-1}$ . It is important to estimate the length scale,  $l_c$ , in order to check the applicability of the picture to individual cases. An attempt was made<sup>99</sup> to estimate this ratio numerically by considering the EA spin glass model with a Gaussian bond distribution. For each bond realization, the ground state was obtained using a heuristic optimization technique. Then, the ground state search was performed once more, this time under the constraint that a pair of spins (chosen randomly) have the opposite relative orientation as compared to the one in the first ground state.

In the droplet picture, the difference of two ground states is supposed to be a droplet of a size that is smaller than the distance of the two chosen spins, whereas in the sponge picture it should be identified with a sponge if one of the chosen spin is included in the sponge and the other is not. In the sponge picture, such an event should happen with a finite and system-size-independent probability because at the scale larger than  $l_c$  the sponge is uniform and the fraction of the sponge is system-size-independent.

Calculations of the system up to  $L = 11$  were performed.<sup>99</sup> In order to check the property (3), the authors measured the probability of the event that the excited cluster spans the whole system. It was found that the probability does not show a strong system size dependence, indicating that large excitations with  $\mathcal{O}(1)$  excitation energy exists.

### 9.3.7. TNT Picture — Introduction of a New Scaling Length

However, their other findings<sup>99</sup> indicated that the sponge picture defined above does not exactly describe the model, either. Particularly disturbing was the result of the surface-to-volume ratio of the system-spanning clusters obtained by the procedure mentioned in subsection 9.3.6; the ratio decreases as a function of the system size. A power-law yielded a reasonable fit, i.e.

$S/V \propto L^{-0.3}$ , suggesting  $l_c$  (defined as the  $V/S$ ) tends to infinity in the limit  $L \rightarrow \infty$ . If one compares the ground state with the (sponge) excited state and focus on a small box located around the center of the system, the domain boundary  $S$  would never pass through this box in the infinite system size limit. The link-overlap is therefore always complete (i.e., 1) within the box. This is in agreement with the result<sup>86,87</sup> mentioned in subsection 9.3.4. The increase of the characteristic length  $l_c$  was also confirmed in [100]. It follows that the distribution of the link overlap should have a trivial delta-peak structure while that of the ordinary overlap may have a non-trivial structure. This new scenario with the new system-size-dependent scaling length  $l_c(L)$  is called<sup>99</sup> the ‘TNT’ scenario, an abbreviation of “Trivial  $P(q_l)$  and Non-Trivial  $P(q)$ ”.

A closely related calculation was done by the authors of [101], who performed a Monte Carlo simulation of the EA model with the Gaussian bond distribution. They reached rather low temperatures ( $T \sim 0.2J$ ) employing the exchange Monte Carlo method.<sup>53</sup> The overlap distribution  $P(q)$  was measured. The zero-overlap probability  $P(0)$  stays constant, in contrast to the prediction of the droplet picture ( $P(0) \propto L^{-\theta}$  with  $\theta \sim 0.2$ ), consistent with the RSB picture and the TNT picture. However, the temperature dependence of  $P(0)$  at a fixed system size agreed with the droplet picture, i.e.,  $P(0) \propto T$ . They also obtained the link-overlap distribution. Its width turned out to be proportional to  $L^{-\mu_l}$  where  $\mu_l$  was estimated as

$$\mu_l = 0.76(3)$$

from an extrapolation to  $T = 0$ . The TNT picture discussed above assumes the presence of excitations with size-independent energy, i.e.,  $\theta = 0$  whereas the surface-to-volume ratio of excited clusters goes to zero. Based on this picture together with the above estimate of  $\mu_l$ , they obtained (by setting  $\theta = 0$  in (8))

$$d - d_S = 0.38(2)$$

which is consistent with the zero-temperature calculation<sup>87</sup>  $d - d_S = 0.42(2)$ .

### 9.3.8. Arguments Supporting the Droplet Picture

In [102], the notion of pure states was re-examined for the disordered systems. The relationship between the appearance of  $P_J(q)$  and the number of pure states was discussed. It was suggested that  $P_J(q)$  is an erroneous indicator of the multiplicity of pure states. In the ferromagnetic

two-dimensional Ising model below the critical temperature, one has an example of  $P(q)$  being non-trivial while there are only two pure states. Namely, when the anti-periodic boundary condition is imposed in both the directions, because of the arbitrariness of the position of domain boundaries,  $P(q)$  includes a continuous part. On the other hand, in the three-dimensional random field model, one can see the case where  $P_J(q)$  consists of a single delta peak although there are two pure states. This is because the free-energy difference between the two pure states, one with  $\langle S_i \rangle = m > 0$  and the other with  $\langle S_i \rangle = -m$ , diverges being proportional to  $N^{1/2}$ . Therefore  $P_J(q)$  for a given sample consists of only one delta peak.

The argument was elaborated in [21,10], in which the authors exploited the translation ergodicity. They proved that any translationally invariant quantity measured for a particular bond realization  $J$  is equal to its bond configuration average, provided that the distribution of each bond is independent and spatially uniform. Since  $P_J(q)$  is obviously translationally invariant, it follows that  $P_J(q)$  is self-averaging, i.e., does not depend on  $J$ . This result is in contrast with what we know for the SK model. Furthermore, they argued that since  $P_J(q)$  is self-averaging it would be improbable that  $P_J(q)$  has a continuous part. The reason for this is that there are only countably many pure states and therefore  $P(q)$  consists of countably many delta peaks. Consequently, we would have to choose many but only countably many numbers from the interval  $-1 \leq q \leq 1$  to locate these delta functions. They argued that existence of such countably many “preferred” locations, yet independent of  $J$ , are very implausible. Their argument made it clear that we must be careful about using the notion of the pure state in the disordered systems.

However, it was pointed out<sup>103</sup> that the very existence of the pure states that was implicitly assumed in [21] is questionable. This means that the pure states that appear in (3) may have only a metaphoric meaning, and should not be taken too strictly for disordered systems. From this point of view, one may say that the non-existence of the unique thermodynamic limit, or, more specifically, a chaotic system-size dependence of various quantities may signify the RSB nature of the spin glass systems.

#### 9.4. Models in Four or Higher Dimensions

Numerical simulations are easier in four or higher dimensions than in three. This is presumably because  $d = 4$  is well separated from the lower critical dimension. The existence of a finite-temperature phase transition in four

dimensions was established already in an early numerical study<sup>58</sup> where a clear crossing in the Binder parameter, defined in (9), could be observed. The critical point was located at  $T_c = 1.75(5)$  and the critical exponents were estimated to be  $\nu = 0.8 \pm 0.15$  and  $\eta = -0.3 \pm 0.15$  for the Gaussian bond distribution. The scaling relation  $\gamma/\nu = 2 - \eta$  yields  $\gamma = 1.8(4)$  which agrees well with the result  $\gamma = 2.0(4)$  of a high-temperature series expansion<sup>104</sup> for the  $\pm J$  bond distribution. More precise estimates of the critical indices were obtained in [105]:

$$T_c = 1.80(1), \quad \nu = 0.9(1), \quad \eta = -0.35(5), \quad \text{and} \quad \gamma = 2.1(2).$$

Based on an off-equilibrium simulation, they also obtained an estimate of the EA order parameter below the critical point as a function of the temperature. A non-vanishing order parameter excludes the possibility that the transition is of the BKT-type. As for the nature of the low-temperature phase, the observation made in [106] that  $P(0)$  is system-size independent below the critical temperature indicates that the droplet picture is inappropriate for the four-dimensional spin glass. For a detailed discussion on other results obtained before 1997, the readers are referred to the review [103]. Here we only mention one of the latest computations for clarifying the nature of the low-temperature phase in four dimensions.

The replica exchange method was used in [101] to study the 4d spin glass model with a Gaussian bond distribution at rather low temperatures  $T \sim 0.2J \sim 0.1T_c$ . The zero-overlap probability  $P(0)$  was measured in four dimensions as well as in three. In both cases  $P(0)$  was found to be independent of the system size for a fixed temperature, and a roughly linearly dependent on the temperature for a fixed system size. The authors of [101] summarized their results as being consistent with the TNT picture mentioned above. They also estimated the exponent characterizing the size dependence of the variance of the link-overlap distribution, namely,  $\theta + 2(d - d_s)$  where  $d_s$  is the fractal dimension of droplet boundaries (see the discussion in subsection 9.3.4). The extrapolated value to the zero temperature was  $\theta + 2(d - ds) = 0.35(6)$  while they did not rule out the possibility of this value being zero.

For the ground state properties in four dimensions, we refer the reader to [107], in which the ground states of the model in four dimensions up to  $L = 7$  were computed. The stiffness exponent was estimated as  $\theta_s = 0.64(5)$ .

Although somewhat misplaced in this section on higher dimensional models we mention here the one-dimensional spin glass model with *long-range* interactions, i.e.  $J_{ij} = c_\sigma \epsilon_{ij}/r_{ij}^\sigma$ , where  $\epsilon_{ij}$  is a Gaussian random

number with zero mean and variance one and  $r_{ij}$  the Euclidean distance between spin  $i$  and  $j$  on a finite ring (of perimeter  $L$ ) embedded in the two-dimensional space. This system, on the borderline between finite-dimensional and mean field models, was studied in [108,109] for system sizes up to  $L = 512$ . Finite temperature simulations as well as the study of low-energy excitations yielded results that are inconsistent with the droplet picture but (partially) consistent with the TNT picture.

## 9.5. Aging

The out-of-equilibrium dynamics of spin glasses has become a very rich field in the recent years and an excellent review on the intensive theoretical work that has been performed on it until 1998 can be found in [110] and an overview over the experimental situation until that date can be found in [111,112]. Since then a number of interesting developments have occurred and we will focus on them with the prerequisites necessary to understand them. We start with the theoretical concept of a length scale that evolves in time and is flexible enough to account for a number of numerical and experimental results. Then we focus on two-time quantities that are typically measured experimentally and their behavior in various temperature protocols (i.e. aging histories) — showing effects like memory and rejuvenation. Finally we discuss the theory for violations of the fluctuation-dissipation theorem and the numerical and experimental evidences for it.

### 9.5.1. A Growing Length Scale During Aging?

Spin glasses have an order parameter which is (cum grano salis, i.e. disregarding the potential complications arising from a possible RSB)  $q_{EA} = [\langle S_i \rangle^2]$ . In comparison to structural glasses<sup>113</sup> this is a very lucky situation, not only as a starting point for equilibrium theory, which we have discussed in last sections, but also for non-equilibrium dynamics. An example is the common picture of the dynamical evolution of a system out of equilibrium quenched into the phase with non-vanishing  $q_{EA}$ , in which larger and larger regions of space become ordered.<sup>114</sup> Thus it appears natural to postulate a time-dependent length-scale  $L(t)$  for these equilibrated domains for spin glasses. We choose such a picture, motivated by coarsening systems,<sup>114</sup> as our starting point for reviewing the out-of-equilibrium dynamics of spin glasses.

Within the droplet theory<sup>115</sup> the slow out-of-equilibrium dynamics of a finite-dimensional spin glass is due to thermally activated growth of lo-

cally equilibrated regions. The growth of such regions is supposed to happen through domain wall movements as in the context of pinned domain walls in random field systems<sup>116</sup> or in elastic manifolds in a disordered environment<sup>117</sup> via a thermally activated process overcoming a free energy barrier. It is assumed that the typical energy barrier  $B_{L(t)}$  scales with the typical size  $L(t)$  of the domains reached after a time  $t$  as

$$B_{L(t)} \sim \Delta(L(t)/L_0)^\psi, \quad (14)$$

where  $\psi$  is the barrier exponent characteristic of the particular system under consideration and  $\Delta$  is some constant. Since the dynamics is activated, the typical time to overcome a barrier  $B$  grows exponentially with  $B/T$ ,  $T$  being the temperature;  $t_{L,\text{activated}} \sim \exp(B_L/k_B T)$ . Hence one would expect that after a time  $t$  domains of size

$$L(t) \sim \left( \frac{k_B T}{\Delta} \ln(t/\tau_0) \right)^{1/\psi} \quad (15)$$

are equilibrated ( $\tau_0$  being a microscopic time scale), i.e. the typical domain size grows logarithmically slowly with  $t$ . Numerically one can determine the typical domain size  $L(t)$  directly via the spatial two-replica correlation function

$$G(r, t) = \frac{1}{N} \sum_{i=1}^N \langle S_i^a(t) S_{i+r}^a(t) S_i^b(t) S_{i+r}^b(t) \rangle, \quad (16)$$

where  $a$  and  $b$  denote two replicas of the same system (i.e. the same disorder realization). For the first time this spatial correlation function was studied numerically for the two-dimensional EA spin glass model in [118], and for the 3d EA model in [119,120,121], later also in [122,123,124,125]. The extraction of the typical time-dependent domain-size,  $L(t)$ , from the correlation function  $G(r, t)$  given in (16) is itself a delicate issue. In the first studies in [119,118,120] the definition  $L_T(t) = \int dr G_T(r, t)$  was used where the subscript  $T$  signifies the temperature dependence. This form would be justified if  $G_T(r, t)$  is of a pure exponential form  $G_T(r, t) \sim \exp(-r/L_T(t))$ . Also a scaling form  $G_T(r, t) \sim \tilde{g}(r/L_T(t))$  has been checked in these early works using the length scale obtained via the integral method and a good data collapse was obtained for all parameter values (times and temperatures) used. A more flexible functional form was assumed in [121] that was also capable of fitting more accurate estimates of  $G_T(r, t)$  obtained later.<sup>123,126</sup>

$$G_T(r, t) \sim r^{-\beta(T)} \tilde{g}(r/L_T(t)). \quad (17)$$

The best-fit values of temperature exponent  $\beta(T)$  were found to be constant around 0.5 in three dimensions and decreasing from 1.6 to 0.9 in the temperature range 1.0 to 0.5 in four dimensions (where  $T_c \approx 1.8$ ). In [125] only the tail of  $G_T(r, t)$  was used to extract  $L_T(t)$  assuming a pure exponential form for it. All in all, these different forms do not cause large variations in the estimates of  $L_T(t)$ , the reason simply being that the typical domain sizes reached in the times  $t$  accessible to Monte-Carlo studies to date are only a few lattice spacings. It should be noted that these functional forms imply that  $G_T(r, t)$  decays to zero with the distance  $r$  even in the limit  $t \rightarrow \infty$ , whereas in the droplet theory one would expect a non-vanishing large distance limit:  $\lim_{r \rightarrow \infty} \lim_{t \rightarrow \infty} G_T(r, t) = q_{EA}^2(T) + \mathcal{O}(r^{-\theta})$ . Functional forms respecting such an asymptotic behavior can be also devised to fit the data of  $G_T(r, t)$  well.<sup>126</sup>

Suppose that we have now estimates of  $L(t)$  obtained in one way or the other from numerical simulations or from experiments. (Experimentally there is no straightforward way, by which one could possibly measure  $G(r, t)$  or its space and/or time Fourier transform via scattering or similar techniques. Still there is an interesting experimental development<sup>127</sup> on this point which we discuss further below.) When fitted to the logarithmic growth law (15) the estimated value of  $\psi$  was approximately 0.7<sup>120</sup> and was only acceptable if a finite offset length was introduced. However, a power law form with a temperature dependent exponent

$$L(t) \propto t^{\alpha(T)} \quad (18)$$

fits the data well, with  $\alpha(T) \approx 0.16 T/T_c$ .<sup>120,121</sup> This observation may indicate that we must replace the power-law length-dependence of the barriers (14) by the logarithmic dependence

$$B_{L(t)} \propto \Lambda \ln L(t) \quad (19)$$

as suggested in [128,129], or it may serve as a motivation to modify the simple domain growth picture discussed so far in a way that has been first discussed in [124], later also in [130,131,126,125]. The essential idea in these discussions is that the initial coarsening process is still influenced by critical fluctuations — which is plausible since (i) the temperature that are usually studied are not too far from the critical temperature  $T/T_c \geq 0.7$  and (ii) in the initial stage the equilibrated length scales are still very small.

Close to  $T_c$  the equilibrium correlation length is given by  $\xi(T) \sim L_0 |1 - T/T_c|^{-\nu}$ , and even at  $T < T_c$  the dynamics on length scales  $L < \xi$  might be dominated by critical fluctuations rather than activated processes.

Hence one might expect that as long as  $L < \xi$  the typical size of equilibrated domains grows with time  $t$  as  $L(t) \sim l_0(t/t_0)^{1/z}$  ( $l_0$  and  $t_0$  being microscopic length and time scales, respectively) and only for  $L(t) > \xi$  activated dynamics obeying (15) sets in. Thus a crossover from critical to activated dynamics happens at a time of order  $\tau_0(T)/t_0 \sim (\xi(T)/l_0)^z$ , when the typical domain size reaches  $\xi(T)$ :

$$L(t)/\xi(T) \propto g(t/\tau_0(T)) \quad \text{with} \quad g(x) \sim \begin{cases} x^{1/z} & \text{for } x \ll 1 \\ (\ln x)^{1/\psi} & \text{for } x \gg 1 \end{cases} \quad (20)$$

Thus, if one plots  $L(t) \cdot (T_c - T)^\nu$  versus  $t \cdot (T_c - T)^{\nu z}$  one expects a data collapse for the time dependent typical domain size at different temperatures. Indeed such a data collapse has been observed in numerical studies of the 4d EA model.<sup>124</sup>

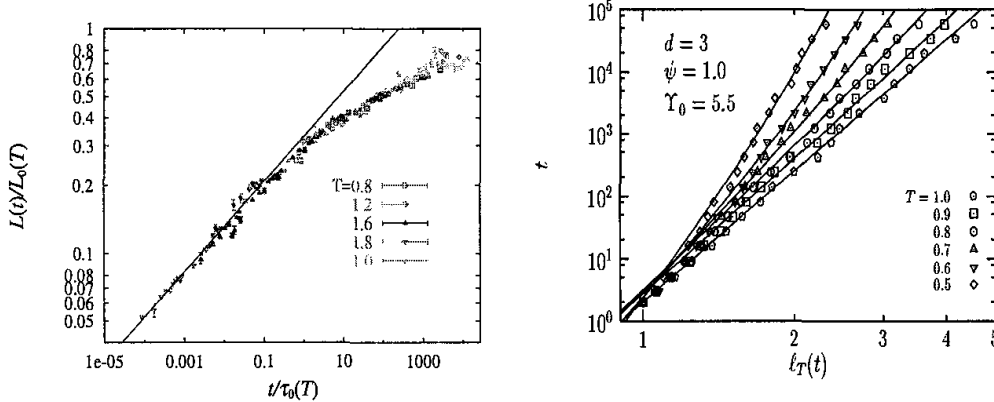


Fig. 9.6. **Left:** Scaling plot of  $L(t)$  of the 4d EA model according to (20), where the SG transition temperature  $T_c = 2.0$  and the critical exponent  $\nu = 0.93$  are fixed, but the dynamical exponent  $z$  is obtained to be 4.98(5) from the best scaling. (From [125].) **Right:** Growth laws of the coherence length in the 3d EA model with fitting curves according to (21). (From [126].)

One can go one step further<sup>132,126</sup> and write down a more explicit form for the relation between length and time scales, similar to (15) but now taking into account critical fluctuations:

$$t(L) \approx \tau_0 L^z \exp\left(\frac{\Delta(T)L^\psi}{k_B T}\right) \quad \text{with} \quad \Delta(T) \approx \Delta_0 / \xi(T)^\psi \quad (21)$$

where  $\Delta_0$  is an energy scale of order  $T_c$ . Here, following [115], the temperature dependent free energy scale  $\Delta(T)$  is assumed to vanish at  $T_c$  since one might expect that, in analogy to random bond ferromagnets, the surface

tension of the domain walls vanishes at  $T_c$ . The pre-factor  $\tau_0 L^z$  reflects the critical dynamics on short length scales (when the exponential term is still small) and might be interpreted as a renormalized microscopic time scale  $\tilde{\tau}_0$  due to critical fluctuations. In this way, we obtain  $t(L)/\tilde{\tau}_0 \approx f(L/\xi(T))$ , with  $f(x) = \exp(cx^\psi)$  (and  $c = \Delta_0/k_B T$ ) in reminiscence of (20). Note, however, that now the short time critical dynamics is absorbed into  $\tilde{\tau}_0$ .

In [126] numerical data for the typical domain size  $L(t)$  for the 3d and 4d EA model, obtained via Monte-Carlo simulations, were successfully fitted to the form (21). For the barrier exponent,  $\psi = 1.0$  was obtained in three dimensions using  $\nu = 1.65$  and  $z = 7.0$ , while in four dimensions  $\psi = 2.3$  was obtained using  $\nu = 0.8$  and  $z = 5.9$ .

As we mentioned above, experimentally it appears to be impossible to have a direct access to spatial correlations in spin glass models. However an indirect way to estimate a typical size of correlated volumes has recently been suggested in [127]. When measuring the waiting-time ( $t_w$ ) dependent thermo-remnant magnetization  $M_{\text{TRM}}(t, t_w)$ , which is a two-time quantity discussed further below, its logarithmic derivative  $S(t) = -d M_{\text{TRM}}(t, t_w)/d(\ln t)$  at the time  $t$  after the field has been switched off has a characteristic peak at an *effective* waiting time  $t_w^{\text{eff}}$ . One observes that the peak position depends on the strength of the field that is applied. Since this time scale is related, via the thermal activation  $\tau_{\text{relax}} \sim \tau_0 \exp(\Delta/k_B T)$ , to the typical value of the free energy barriers that can be explored over experimental time scales:  $\Delta(t_w) \sim k_B T \ln(t_w/\tau_0)$ , the shift in the peak position of  $S(t)$  contains information on the field dependence of the free energy barriers:  $\Delta(t_w) - E_z \sim k_B T \ln(t_w^{\text{eff}}/\tau_0)$ , where in [127] it is assumed that  $E_z$  is the magnetic (or Zeeman) energy associated with the change in the magnetic field. The latter is connected to the number  $N_s$  of spins that are involved in the barrier shift induced by the field change via  $E_z \approx N_s \chi_{\text{fc}} H^2$ , where  $\chi_{\text{fc}}$  is the field cooled susceptibility per spin and  $H$  the magnetic field strength. If one assumes that the  $N_s$  spins to be effectively locked together one gets an estimate for a correlated volume  $N_s \propto \xi^3$ , i.e. an estimate for the coherence length  $\xi$  as a function of the waiting time  $t_w$ .

By analyzing their data for the peak position of  $S(t)$  to obtain  $\xi(t_w)$  in the way just described the authors of [127] find that it fits to (18) with  $\alpha(T) \approx 0.169 T/T_g$ , in agreement with the numerical results reported in [120,121]. A fit to the logarithmic form (15) works equally well, but best-fit value of  $\psi$  turns out to be rather large ( $\approx 5$ ), which does not agree with the numerical estimates cited above. These experiments probe a time window that is different from the one accessible to numerical simulations; each is

roughly 6 decade wide but centered around times roughly 10 decades apart. Thus only the algebraic growth law (18), or the form (21) that interpolates between critical and activated dynamics, would consistently match the data of both time windows.

### 9.5.2. Two Time Quantities: Isothermal Aging

The out-of-equilibrium properties of glassy materials, quenched rapidly below the glass transition temperature  $T_g$  and then aged *isothermally* (i.e. at constant temperature  $T < T_g$ ), manifest themselves most prominently in two-time quantities, typically response functions, susceptibilities or correlation functions. The magnetic response function is defined as

$$R(t + t_w, t_w) = N^{-1} \sum_i \frac{\delta \langle S_i(t + t_w) \rangle}{\delta h_i(t_w)} \Big|_{h_i=0} \quad (22)$$

In experiments as well as numerical simulations one usually does not apply field pulses after a waiting time but one switches a constant magnetic field on or off after a waiting time  $t_w$  — the corresponding susceptibility is then related to the response function via a time integral

$$\chi(t + t_w, t_w) = \int_{t_w}^{t+t_w} dt' R(t + t_w, t') \quad (23)$$

If one switches the field on at time  $t_w$  after the quench and measure the susceptibility, one calls it *zero-field-cooled* (ZFC), whereas if it is switched off it is called *field-cooled* (FC). In the former case the magnetization, which is within the *linear response regime* simply related to the susceptibility via  $M(t, t_w) = h \cdot \chi(t, t_w)$ , increases with the time  $t$  spent in the field, whereas in the latter case it decreases with the time  $t$  after the field has been switched off — it is then also called the *thermo-remnant magnetization* (TRM).

Very useful for the development of theoretical concepts is the two-time spin autocorrelation function

$$C(t + t_w, t_w) = N^{-1} \sum_i \langle S_i(t + t_w) S_i(t_w) \rangle . \quad (24)$$

In *equilibrium* it is related to the response function, the susceptibility and the ZFC/FC magnetization via a *fluctuation-dissipation theorem* (FDT). (We discuss the violation of the FDT in the subsection 9.5.4.) However, since we are out of equilibrium, we have first to regard  $C$  as being an independent quantity.

The huge amount of experimental data that have been collected are nicely over-viewed in [111,112]. Let us here simply state the main results.

For the field cooled magnetization one observes that the remnant magnetization can be decomposed into a stationary part  $M_{\text{eq}}(t)$  that depends on  $t$  only and an aging part  $M_{\text{aging}}(t + t_w, t_w)$ . Sometimes this decomposition is assumed to be multiplicative,  $M(t + t_w, t_w) = M_{\text{eq}}(t) \cdot M_{\text{aging}}(t + t_w, t_w)$ , as in the universal short time dynamics for coarsening at the critical point,<sup>133,134</sup> and sometimes additive,  $M(t + t_w, t_w) = M_{\text{eq}}(t) + M_{\text{aging}}(t + t_w, t_w)$ , as in coarsening dynamics of pure systems<sup>114</sup> and in the out-of-equilibrium theory of mean-field spin glasses.<sup>110</sup> Since  $M_{\text{aging}}(t + t_w, t_w)$  is approximately constant for  $t \ll t_w$  both forms usually fit the data well, although they are fundamentally different. For instance the multiplicative decomposition is incompatible with the existence of a plateau in  $C(t + t_w, t_w)$  that occurs in mean-field theories of spin glasses at low temperatures for long waiting times.<sup>110</sup> Analogously it is also hardly compatible with a non-vanishing long time limit of  $\lim_{t_w \rightarrow \infty} C(t + t_w, t_w)$ , which is, within the droplet theory, identical to the order-parameter  $q_{EA}$ .

The most remarkable feature of the aging part is that it scales to a good approximation with  $t/t_w$

$$M_{\text{aging}}(t + t_w, t_w) \approx \tilde{M}_{\text{aging}}(t/t_w) \quad (25)$$

In ZFC experiments, instead of applying a constant field after a waiting time  $t_w$ , one usually applies a small oscillating field with frequency  $\omega$ , which essentially means that one measures the  $t$ -Fourier transform  $\chi(\omega, t_w)$  of  $\chi(t + t_w, t_w)$ . The frequency  $\omega$  plays the role of an inverse observation time  $1/t$ , with  $t \ll t_w$ . The waiting time  $t_w$  is usually in the range of hours or more, while  $\omega$  is in the range of 0.1Hz to 100Hz, i.e.,  $t$  is less than ten seconds. Again  $\chi(t + t_w, t_w)$  can be decomposed into a stationary part  $\chi_{\text{eq}}(\omega)$  and an aging part  $\chi_{\text{aging}}(\omega, t_w)$  that now scales to a good approximation with  $\omega t_w$ :

$$\chi_{\text{aging}}(\omega, t_w) \approx \tilde{\chi}_{\text{aging}}(\omega t_w) \quad (26)$$

corresponding to the aforementioned  $t/t_w$  scaling for  $M_{\text{FC}}$ . Numerically one also has access to the spin autocorrelation function (24), which can also be decomposed into two parts. In [120] it has been shown that (i) the equilibrium part  $C_{\text{eq}}(t)$  decays algebraically with a very small temperature-dependent exponent  $x(T)$  and (ii) that  $C_{\text{age}}(t + t_w, t_w)$  again obeys to a good approximation the  $t/t_w$  scaling:

$$C_{\text{eq}}(t) \approx A t^{-x(T)} \quad \text{and} \quad C_{\text{age}}(t + t_w, t_w) \approx \tilde{c}(t/t_w), \quad (27)$$

where the scaling function  $\tilde{c}$  behaves as  $\tilde{c}(x) \propto x^{-\lambda(T)}$  with  $\lambda(T)$  being a temperature-dependent exponent much larger than  $x(T)$ . This behavior was

also found for the 4d EA model.<sup>105</sup> Later studies<sup>126</sup> focused on small but systematic deviations in the aging part from a simple  $t/t_w$  scaling behavior; the values of  $C_{\text{age}}(t + t_w, t_w)$  for fixed ratio  $t/t_w$  show a slight tendency to decrease with increasing  $t_w$ , which is called *sub-aging* and is interpreted in terms of an *effective relaxation time*  $t_{\text{eff}}$  that is smaller than the actual waiting time  $t_w$ . We shall return to this point later.

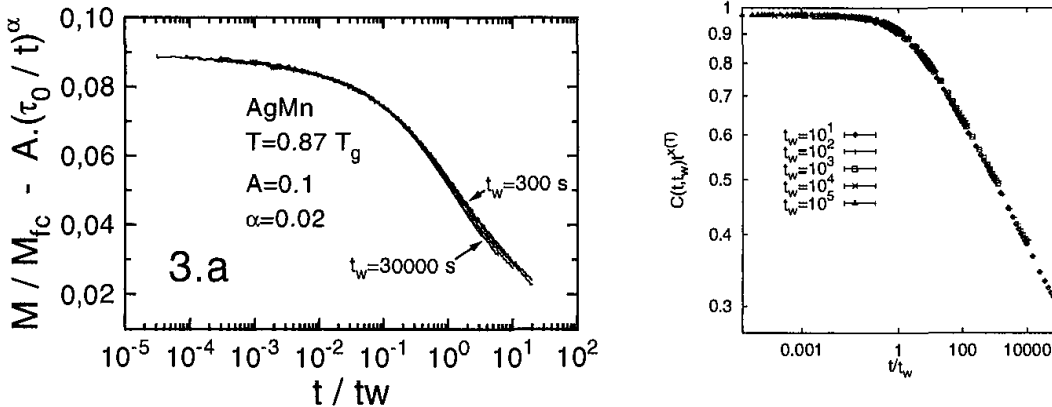


Fig. 9.7. **Left:** Aging part of the FC magnetization  $M_{\text{FC}}(t + t_w, t_w)$  measured in an AgMn spin glass: the estimated stationary contribution  $M_{\text{eq}}(t)$  has been subtracted from the full measured value. The data is plotted versus  $t/t_w$ . The deviations from perfect  $t/t_w$  scaling occur for  $t \sim t_w$  (sub-aging) and can be accounted for by choosing  $h(t + t_w)/h(t_w)$  with  $h(t)$  given in (30) as a scaling variable. (From [111].) **Right:** Autocorrelation function  $C(t + t_w, t_w)$ , divided by  $t^{-x(T)} \propto C_{\text{eq}}(t)$ , versus  $t/t_w$  for  $T = 0.4$  in the 3d EA model. (From [120].)

Within a domain growth (or droplet) picture of the out-of-equilibrium dynamics of spin glasses,<sup>115</sup> only *one* characteristic length scale  $L(t)$  for a given time  $t$  after the quench is assumed to exist. One would then expect that two-time quantities depend only on the ratio of the two length scales that are equilibrated within the two times  $t_w$  and  $t + t_w$ :

$$O_{\text{aging}}(t + t_w, t_w) \sim \tilde{o}(L(t + t_w)/L(t_w)), \quad (28)$$

where  $O(t + t_w, t_w)$  is any two-time observable (such as  $R$ ,  $\chi$ ,  $M$  or  $C$ ) and  $\tilde{o}$  the corresponding scaling function. The first observation is that an algebraic growth law, (18) for instance, would then be completely compatible with the  $t/t_w$  scaling of the aging part of various observable reported so far. Note also that as long as  $L(t)$  depends algebraically on  $t$  the use of the scaling variable  $L(t_w)/L(t)$  is equivalent to using  $L(t + t_w)/L(t_w)$ , both end up to be some function of  $t/t_w$ .

In the case of logarithmic domain growth (15), on the other hand, the scaling with  $L(t_w)/L(t)$  is different from the scaling with  $L(t + t_w)/L(t_w)$ , and one should note that droplet scaling,<sup>115</sup> as it is usually applied to the experimental and numerical data, is assumed to work with  $L(t_w)/L(t)$ ,<sup>135,124,131</sup> where  $L(t_w)$  is the typical size of the domains after waiting time  $t_w$  and  $L(t)$  is the typical size of the droplets being activated in the time  $t$  or being polarized by an ac field of frequency  $\omega = 1/t$ . The basic physical idea behind this scaling form is that the presence of a domain wall effectively reduces the excitation gap of droplets that it touches.

However, assuming the simple logarithmic growth law (15),  $L(t) \approx ((k_B T / \Delta) \ln(t/\tau_0))^{1/\psi}$ , the numerical as well as the experimental data turn out not to scale with  $L(t_w)/L(t)$  as suggested by the droplet theory<sup>115,135</sup> (it does not scale with  $L(t + t_w)/L(t_w)$ , either, which is incompatible with the experimental observation of sub-aging). For some time this observation was taken as an indication that the droplet theory might be inappropriate to describe the out-of-equilibrium properties of spin glasses, at least for the time scales accessible to experiments and to numerical studies. However, recently it was pointed out<sup>131</sup> that, taking into account the crossover from critical to activated dynamics already discussed in the last subsection, the apparent inconsistency of the data with the droplet theory disappears. There experimental data for the (imaginary part of the) susceptibility  $\chi(\omega, t_w)$ , measured for the 3d Ising spin glass  $\text{Fe}_{0.5}\text{Mn}_{0.5}\text{TiO}_3$  and the 3d Heisenberg spin glass Ag(11% at Mn), were presented. The aging part  $\chi''_{\text{aging}}(\omega, t_w)$  (obtained after subtracting a fitted equilibrium part  $\chi''_{\text{eq}}$ ) was shown to scale as  $L(t_w)/L(1/\omega)$  with  $L(t)$  following the logarithmic growth law (15), where the microscopic time and energy scale  $\tau_0$  and  $\Delta$  replaced by a temperature dependent characteristic time and energy scale,  $\tau_c(T)$  and  $\Delta(T)$ . This replacement captures the features of the critical, short-time dynamics close to the critical point:  $\tau_c(T) \sim \tau_m \xi^z$  and  $\Delta(T) \sim \xi^{-\psi}$  ( $\xi = |1 - T/T_c|^{-\nu}$  being the correlation length), which is in the same spirit as (20) and (21).

The authors of [131] found a very good data collapse when plotting their data for  $(\chi''(\omega, t_w) - \chi_{\text{eq}})/\chi''(\omega, t_w)$  versus the scaling variable  $\ln(t/\tau_c(T))/\ln(\omega^{-1}\tau_c(T))$  (which is  $L(t)/L(1/\omega)$ , since  $\Delta(T)$  and  $k_B T$  cancel in this ratio). Given the critical exponents  $\nu$  and  $z$  from earlier studies, the fitting parameters are  $\psi$ , the whole equilibrium part  $\chi_{\text{eq}}$  (for which an explicit functional form predicted by the droplet theory was used) and a microscopic time scale  $\tau_m$ . They found  $\psi \approx 1.9$  for the Ising spin glass, which was much larger than what had been reported before in experiments<sup>136</sup> (see also [130,132]) and in the numerical simulations discussed in the previous

subsection, and  $\psi \approx 1.3$  for the Heisenberg spin glass. The authors of [131] showed that their experimental data are also compatible to the  $\omega t_w$  scaling.

So far, we have discussed the compatibility of numerical and experimental data with a simple (or simplified) domain growth picture. Mean field models, however, show a more complicated behavior.<sup>110,137</sup> The mean field theory for the out-of-equilibrium dynamics predicts “ultra-metric behavior” in the time domains<sup>138,139,140</sup>:

$$O_{\text{aging}}(t + t_w, t_w) = \sum_i \mathcal{O}_i(h_i(t + t_w)/h_i(t_w)) , \quad (29)$$

where the infinite sum over the index  $i$  refers to various large time sectors<sup>138,110</sup> defined by the ratio of  $h_i(t + t_w)/h_i(t_w)$  being of order 1, where the different (unknown) functions  $h_i(t)$  represent different physical mechanisms at work during aging and need not necessarily to be related to domain sizes. They are monotonously increasing and grow differently such that when  $0 < h_i(t + t_w)/h_i(t_w) < 1$  holds for an index  $i$  then  $h_j(t + t_w)/h_j(t_w) = 1$  for all larger indices  $j > i$  — implying that if two times  $t_1$  and  $t_2$  belong to the time sector defined by  $h_i$  and  $t_2$  and  $t_3$  to the one defined by  $h_j$  with  $j > i$ , then  $t_1$  and  $t_3$  also belong to the sector defined by  $h_i$ . One simple example for  $h_i(t)$  is

$$h_i(t) = \exp\{(t/t_0)^{1-\mu_i}/(1-\mu_i)\} , \quad (30)$$

with  $0 < \mu_i < 1$  ( $\mu = 1$  yields a  $t/t_w$ -scaling,  $\mu = 0$  time-translational invariance).

A consequence of such an Ansatz is for instance a hierarchy in these large-time sectors, called *dynamic ultrametricity*, which for the correlation function  $C$  means that in the limit of large times  $t_1 < t_2 < t_3$

$$C(t_3, t_1) = \min\{C(t_2, t_1), C(t_3, t_2)\} \quad (31)$$

holds. A number of consequences can be drawn from this Ansatz.<sup>110,137</sup> Among them is a particular form of the violation of the fluctuation-dissipation relation, which we discuss later. Let us here just state that mean-field theory predicts a richer scenario for glassy out-of-equilibrium dynamics than the domain growth picture with only one waiting-time-dependent length-scale. However, as rich as this scenario is, all experimental data for real spin glasses and all numerical data for spin glasses with short-range interactions obtained for isothermal aging up to now can, to our knowledge, be scaled nicely with one single large-time domain, i.e. with only one term appearing in the infinite sum (29).

For instance, the aforementioned sub-aging property of two-time quantities that has been observed in experimental data<sup>111,141</sup> (and also in analytically tractable coarsening, non-spin glass, models<sup>142,143</sup>) can easily be accounted for by taking only a single term in the sum (29) with  $h(t)$  being the function defined in (30) and with the exponent  $\mu$  now being a fitting parameter. This form was actually used in the earliest experiments on aging in polymer glasses,<sup>144</sup> and later also in spin glass experiments.<sup>111</sup> The exponent  $\mu$  commonly turns out to be not very different from 1, accounting for the fact that the deviations from simple  $t/t_w$  scaling are usually very small. In numerical simulations of  $3d$  models the scaling with  $t/t_w$ , i.e.  $\mu = 1$ , is almost perfect. In four dimensions the numerical data for  $C(t + t_w, t_w)$  tend to show *super-aging*,<sup>126</sup> i.e. the values of  $C_{\text{age}}(t + t_w, t_w)$  for fixed ratio  $t/t_w$  show a slight tendency to increase with increasing  $t_w$ . This can be interpreted by an effective relaxation time that grows faster than  $t_w$ , and it can be shown that the aging part  $C_{\text{age}}(t + t_w, t_w)$  scales nicely with  $h(t + t_w)/h(t_w)$ , when  $\mu > 1$  for  $h(t)$  in from (30) is chosen (which bears unfortunately mathematical inconsistencies<sup>145</sup>). However, the data can also be scaled with a domain growth scaling form (21) and a non-vanishing long time limit for the equilibrium part.<sup>126</sup>

### 9.5.3. More Complicated Temperature Protocols

From what we learned from isothermal-aging experiments described in the last subsection, it follows that the dynamics of a spin glass depends crucially on the age of the system, i.e. the time  $t_w$  that it spent in the glass phase, i.e. at  $T < T_g$ . Moreover, as experiments have impressively demonstrated,<sup>111,112</sup> it depends sensitively on changes of temperature (and also field) *during* this waiting time  $t_w$ . A major goal of their systematic study described in this subsection is to understand the different phenomena that are measurable by applying different protocols (i.e. temperature variations during aging) and relating them to a theoretical picture, if not a theory, of the out-of-equilibrium dynamics of spin glasses.

The simplest experiments in this direction are small-temperature-shift experiments.<sup>146</sup> The protocol is as follows. First the system is rapidly quenched below  $T_c$  to a temperature  $T_1$  where it is aged for a waiting time  $t_w$ . Then the temperature is shifted to a new temperature  $T_2 = T_1 \pm \Delta T$  and the measurement is started. The first systematic numerical study of such a protocol was performed for the  $3d$  EA model in [147] and a little later in [126]. It was observed that the decay of the correlation function is slower

for negative shifts ( $T_2 < T_1$ ) when compared with the same function aged isothermally at  $T_1$ . For small shifts  $\Delta T$  the functional form of  $C(t + t_w, t_w)$  is the same as that for isothermal aging, and it can be matched with it using an effective waiting time  $t_w^{\text{eff}} < t_w$  for  $T_2 < T_1$ . If one assumes that the barriers that the system can surmount during a time  $t_w$  at temperature  $T_1$  are of the same size as those that it can surmount during a time  $t_w^{\text{eff}}$  at temperature  $T_2$ , one obtains a good agreement with the numerical data, only if one replaces the microscopic time  $\tau_0$  by the typical time scale for critical dynamics as in (21).<sup>126</sup>

Obviously such an interpretation of the numerical results implies that successive aging at two different temperatures will add to each other in a full accumulative way. The effective age  $t_w^{\text{eff}}$  is a monotonically increasing function of  $t_w$  and also depends on the pair  $(T_1, T_2)$ :  $t_w^{\text{eff}} = f_{T_1, T_2}(t_w)$ , and  $t_w$  can be related to  $t_w^{\text{eff}}$  by the inverse:  $t_w = f_{T_1, T_2}^{-1}(t_w^{\text{eff}})$ . In [148] twin-experiments — negative shift from  $T_1$  to  $T_2$  and positive shift from  $T_2$  to  $T_1$  — were considered. A criterion for purely accumulative aging would be  $f_{T_1, T_2}^{-1}(t) = f_{T_2, T_1}(t)$  and in contrast to the aforementioned numerical results deviations from it were observed in these experiments for  $\Delta T/T_c \geq 0.01$ , i.e. still very small shifts. The authors then concluded that positive and negative temperature shifts both cause a restart of aging and these findings were then interpreted as a symmetrical *temperature-chaos* effect.<sup>148,149,150</sup>

The temperature chaos in spin glasses is one of the basic ingredients of the droplet theory<sup>115</sup> and implies that the equilibrium configurations at two different temperatures  $T_1$  and  $T_2 = T_1 \pm \Delta T$  below  $T_g$  are uncorrelated beyond a length scale called the *overlap-length*,  $l_{\Delta T} \sim (\Delta T)^{-1/\zeta}$ , where  $\zeta$  is the chaos exponent. A number of experimental results, in particular obtained from temperature-shift or temperature-cycling experiments,<sup>112</sup> have been interpreted within this scenario. Numerical estimates of the value of  $\zeta$  are based on small variations of the *couplings*  $J_{ij}$  (via  $J_{ij} \rightarrow J_{ij} + \delta_{ij}$  with  $\delta_{ij}$  small and random) at  $T = 0$ <sup>151,152</sup> rather than variations of the temperature, simply because ground states of spin glasses, in particular in  $d = 2$  can be obtained more easily than equilibrated configurations at small  $T$ . The reported estimates are  $\zeta \approx 1$  both in two and three dimensions. While the same exponent was reported for temperature chaos (via Monte-Carlo simulations) in the two dimensional case, recent large scale numerical studies of the 3d EA model did not show any evidence for temperature chaos in spin glasses on the length and time scales that could be probed.<sup>153</sup> Even if temperature-chaos exists in three dimensional spin glasses, the overlap length might be much larger than the length-scales that

have been equilibrated during a particular waiting time, which then makes the chaotic rearrangements due to the temperature shift invisible. However, there still might be some effect due to dangerously irrelevant droplets whose free energy gaps are quite small, as discussed in [125,150,154].

The next temperature protocols that we discuss here are larger shifts and cycles  $T_1 \rightarrow T_2 \rightarrow T_1$ .<sup>111</sup> The first shift experiments was reported in [155] whereas the cycle experiments can be found in [156]. The first qualitative numerical study of this kind was reported in [157]. In the theory of the asymptotic out-of-equilibrium dynamics of mean-field spin glass models one can understand these effects on the basis of infinitely many time scales organized in a hierarchical — ultra-metric — way (which we will discuss in section 9.5.4).

A systematic numerical study of large-shift and cycle experiments was recently performed for the 3d and 4d EA model in [126]. The basic message of large temperature shift experiments is that, independent of the sign of  $T_1 - T_2$ , aging is “restarted” at the new temperature. This *rejuvenation effect* can nicely be observed in experiments as well as in simulations through the measurement of the susceptibility  $\chi(\omega, t_w)$ . Rejuvenation after a negative temperature shift comes from fast modes<sup>158,159,126</sup> which were equilibrated at  $T_1$ , but fall out of equilibrium and are slow at  $T_2$ . Therefore, one should expect to see this phenomenon if the spin configurations in the equilibrated regions (on length scales  $\leq L_{T_1}(t_w)$ ) are sufficiently different at the two temperatures. This mechanism is obviously qualitatively different from the interpretation involving the notion of temperature chaos (see above), which implies that length scale smaller than the overlap length are essentially unaffected by the temperature shift, while larger length scales are completely reshuffled by the shift. In this picture, rejuvenation is thus attributed to *large* length scales and strong rejuvenation effects therefore require a very small overlap length.

No clear rejuvenation effects have ever been observed in simulations of the 3d EA model.<sup>157,160,161,162</sup> This was first attributed to the fact that the overlap length was perhaps numerically large, so that no large scale reorganization could be observed on the time scale of the simulation. However, in the fast-mode mechanism mentioned above, the crucial ingredient is the small-scale reorganization due to a temperature shift. When comparing the spatial correlation function  $G_T(r, t_w)$  at two different temperatures and waiting times such that the length scales  $L_{T_1}(t_{w_1}) = L_{T_2}(t_{w_2})$ , there is nearly no difference even for quite large  $\Delta T = T_1 - T_2$  in three dimensions but significant differences in four dimensions,<sup>126</sup> which is compatible with

the observation that the exponent  $\beta(T)$  in (17) remains roughly constant for a large temperature interval in three dimensions whereas it varies significantly in four dimensions. This observation suggests that the 4d EA model should be more favorable in studying temperature shift/cycle protocols. The numerical simulations of the 4d EA model show indeed a clear rejuvenation effect in  $\chi(\omega, t_w)$ , increasing smoothly with  $\Delta T$ , which one would not expect within the temperature chaos picture. (See Fig.9.8 (Right).)

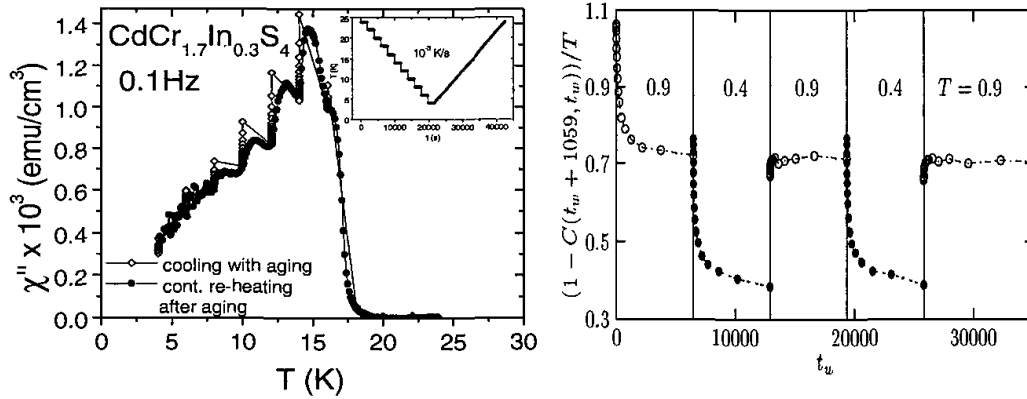


Fig. 9.8. **Left:** Series of ‘dip’ imprinted on the a.c. susceptibility by successive stops at different temperatures while the system is cooled. Further cooling ‘rejuvenates’ the system (i.e. the susceptibility goes up). However, the dips are one by one remembered by the system when heated back. For more details, see [163]. (The figure is adopted from [132]). **Right:** Evolution of the ‘a.c.’ correlation function taken from Monte-Carlo simulations of the 4d EA model in the procedure  $T = \infty \rightarrow T_1 = 0.9 \rightarrow T_2 = 0.4 \rightarrow T_1 \rightarrow T_2$ , showing, as in experiments the coexistence of rejuvenation and memory effects (from [126]).

The experimental procedure for cycles is  $T = \infty \rightarrow T_1 \rightarrow T_2 < T_1 \rightarrow T_1$ . The time spent at  $T_1$  is  $t_s$  and the time spent at  $T_2$  is  $t'_s$ . The spectacular *memory effect* arises when the temperature is shifted back to  $T_1$ . It is observed that although aging was fully restarted at  $T_2$ , the system has a strong memory of the previous aging at  $T_1$ . The dynamics at  $T_1$  proceeds almost as if no cycle to  $T_2$  has been performed.<sup>155</sup> The coexistence of rejuvenation and memory was made even more impressive in a multiple step, or *dip* experiment,<sup>163</sup> in which the temperature was decreased to  $T_1$ , then maintained for some time, then further decreased to  $T_2 < T_1$ , again maintained, then further decreased to  $T_3 < T_2$  etc. At some lowest temperature the sample was then re-heated with the same rate as it was cooled before, but now without the interrupts at  $T_1, T_2, T_3, \dots$ . As shown in Fig.9.8

(Left), on the way down to the final temperature the susceptibility  $\chi(\omega)$  as a function of the temperature showed clear dips at  $T_1, T_2, T_3, \dots$ , which is the rejuvenation effect. Most remarkably the same dips reappear in  $\chi(\omega)$  on the way up, which is the memory effect. The spin glass has memorized the individual temperatures at which the constant cooling was interrupted for some time.

According to [132] the memory effect is a simple consequence of the separation of time and length scales, also observable in simpler slowly coarsening systems with activated dynamics.<sup>159</sup> When the system is at  $T_2 < T_1$ , rejuvenation involves very small length scales as compared to the length scales involved in the aging at  $T_1$ . Thus when the temperature is shifted back to  $T_1$ , the correlation of length scale  $L_{T_2}(t'_s)$  nearly instantaneously re-equilibrate at  $T_1$ . The memory is just stored in the intermediate length scales, between  $L_{T_2}(t'_s)$  and  $L_{T_1}(t_s)$ . How such a storage mechanism actually works in a microscopic model for a finite-dimensional spin glass, like the EA model, is a challenging question. Progress has been made for simpler microscopic models, such as the 2d Mattis model, a simple coarsening model,<sup>164</sup> or the directed polymer in a random medium.<sup>165</sup> Also experiments on random *ferromagnetic* systems,<sup>166,167,168,169,170</sup> on random *ferroelectric* systems<sup>171,172</sup> and on frustrated systems without a spin glass transition at finite temperatures<sup>173</sup> show strong rejuvenation effects and a weak memory effect. This indicates that the existence of “many pure states” as predicted by Parisi’s equilibrium solution of the Sherrington-Kirkpatrick model and the interpretation of these non-equilibrium effects based on it (in terms of a diffusion in a hierarchical space<sup>174,111</sup>) are not necessary prerequisites to observe rejuvenation and memory in the out-of-equilibrium dynamics.

Nevertheless the hierarchical picture might be relevant in more complex situations and a concrete implementation was proposed in [175] in terms of a thermally activated random energy model (for an overview see [110]). Here to each level of a hierarchical tree a transition temperature is associated, such that for each level the dynamics is stationary for higher temperatures and aging for lower temperatures. A small decrease of temperature induces some rejuvenation by driving out of equilibrium a new level of the tree, while freezing out the dynamics at the upper levels, thereby allowing the memory to be conserved. This model was recently studied further,<sup>176</sup> where it was shown numerically that the rejuvenation/memory effect is indeed already reproduced with two levels. A real space interpretation of this hierarchical tree was proposed in [175,177], and further developed in [159] in terms of

a multi-scale dynamics. Low levels of the tree correspond to short wavelength modes, which are only frozen at low temperature, while large wavelength modes are frozen at a higher temperature and constitute a *backbone*, where memory is imprinted. In the context of domain walls this picture is particularly clear<sup>159</sup> and should apply directly to disordered ferromagnets where the slow dynamics comes from the motion of these pinned domain walls.<sup>166,167,168,169,170</sup>

#### 9.5.4. Violation of the Fluctuation-Dissipation Theorem

In a system in equilibrium the response  $R$  to an external magnetic field (Eq.(22)) and the autocorrelation function  $C$  (Eq.(24)) depend only on the time difference  $t$ , i.e.,  $R(t + t_w, t_w) = R_{\text{eq}}(t)$  and  $C(t + t_w, t_w) = C_{\text{eq}}(t)$ , and are related to each other through the fluctuation-dissipation theorem (FDT)

$$R_{\text{eq}}(t) = -\frac{1}{T} \frac{\partial C_{\text{eq}}(t)}{\partial t}. \quad (32)$$

In a system that is out-of-equilibrium this relation is generally not valid and the violation of FDT can be parameterized through a violation factor  $X(t + t_w, t_w)$ :

$$R(t + t_w, t_w) = -\frac{X(t + t_w, t_w)}{T} \frac{\partial C(t + t_w, t_w)}{\partial t_w}, \quad (33)$$

where the differentiation is done with respect to  $t_w$ , not the time difference  $t$  as in (32). In analytic studies of mean-field systems it can be shown<sup>138</sup> that for large times ( $t_w \rightarrow \infty$ )  $X$  depends on  $t$  and  $t_w$  only through the value of the correlation function. Hence  $X(t + t_w, t_w) = X[C(t + t_w, t_w)]$ . In particular, when  $C > q_{EA}$  it is  $X = 1$  and the FDT is recovered. In essence, the asymptotic dependence of  $X$  on the values of  $C$  alone underlies the decomposition into asymptotic time domains discussed in subsection 9.5.2 under (29). It turns out<sup>178</sup> that the *effective temperature*  $T_{\text{eff}}(t + t_w, t_w) = T/X(t + t_w, t_w)$  is precisely the temperature which would be read on a thermometer with response time  $t$  (or frequency  $\omega \sim 1/t$ ) when connected to the magnetization at time  $t_w$ . A “fast” thermometer of response time  $t \ll t_w$  will then probe the stationary regime for which  $X = 1$  and thus measure the heat-bath temperature.

Different scenarios of the FDT violation can occur. **(A)**  $X(C) = 1$  for all  $C$  implies the system is in equilibrium, e.g. in the paramagnetic phase of a spin glass. **(B)** Coarsening systems with  $q_{EA} = m^2$  have  $X(C) = 1$

for  $C > q_{EA}$  and  $X(C) = 0$  for  $C < q_{EA}$ . **(C)** So called *discontinuous* spin glasses, such as the spherical mean field spin glass model with  $p$ -spin interactions ( $p \geq 3$ ),<sup>138</sup> have  $X(C) = 1$  for  $C > q_{EA}$  and  $X(C) = x_1 < 1$  for  $C < q_{EA}$ , where  $x_1$  is a constant. This corresponds to the existence of only *one* asymptotic time domain (see (29)), and the two-time quantities are expected to scale with only one (possibly unknown) function  $h(t)$ <sup>179</sup> **(D)** So called *continuous* spin glasses, like the SK model, have  $X(C) = 1$  for  $C > q_{EA}$  and  $X(C)$  continuously varying, non-constant function of  $C$  for  $C < q_{EA}$ .<sup>138</sup>

A convenient way to extract the function  $X(C)$  is to measure the auto-correlation function  $C(t + t_w, t_w)$  and the susceptibility  $\chi(t + t_w, t_w)$ , (23), for a situation in which a (infinitesimal) small homogeneous external field  $h$  is switched on after a time  $t_w$  (in which case the induced magnetization is zero-field-cooled and  $\chi(t + t_w, t_w) = \lim_{h \rightarrow 0} M_{ZFC}(t + t_w, t_w)/h$ ). In this case we have

$$\begin{aligned}\chi(t + t_w, t_w) &= \int_{t_w}^{t+t_w} dt' R(t + t_w, t') \\ &= \frac{1}{T} \int_{t_w}^{t+t_w} dt' X[C(t + t_w, t')] \frac{\partial C(t + t_w, t')}{\partial t'}.\end{aligned}\quad (34)$$

As long as the function  $C(t + t_w, t')$  is monotonously increasing with  $t'$  for fixed time  $t + t_w$ , the substitution of  $X(t + t_w, t')$  by  $X[C(t + t_w, t')]$  is legitimate. One should keep in mind that then  $X[C]$  still has a  $t_w$ -dependence (that we could indicate by  $X_{t_w}[C]$ ), which however vanishes in the limit  $t_w \rightarrow \infty$ . Hence one gets (with  $C(t + t_w, t + t_w) = 1$ ):

$$\chi(t + t_w, t_w) = \int_{C(t + t_w, t_w)}^1 dC X[C] \quad \text{or for fixed } t_w : \quad \frac{d\chi}{dC} = -\frac{X[C]}{T} \quad (35)$$

which implies that for fixed waiting time the slope of a parametric plot of  $\chi(t + t_w, t_w)$  versus  $C(t + t_w, t_w)$  yields  $X_{t_w}[C]$ . In the limit  $t_w \rightarrow \infty$  one should obtain the desired FDT-violation  $X[C] = \lim_{t_w \rightarrow \infty} X_{t_w}[C]$ .

The first study of the FDT violation function  $X(C)$  in the 3d EA model was performed in [180] (the first report of an FDT violation was actually already presented earlier in [181]). The non-constant part of  $X(C)$  still showed a small but systematic  $t_w$ -dependence for the small- $C$  branch of the curve  $X(C)$ . Since no tendency to approach a straight line (scenario B or C) could be observed the data were interpreted as an indication for scenario D, which implies that the 3d EA model has an out-of-equilibrium dynamics that is similar to the SK model. Later studies confirmed this

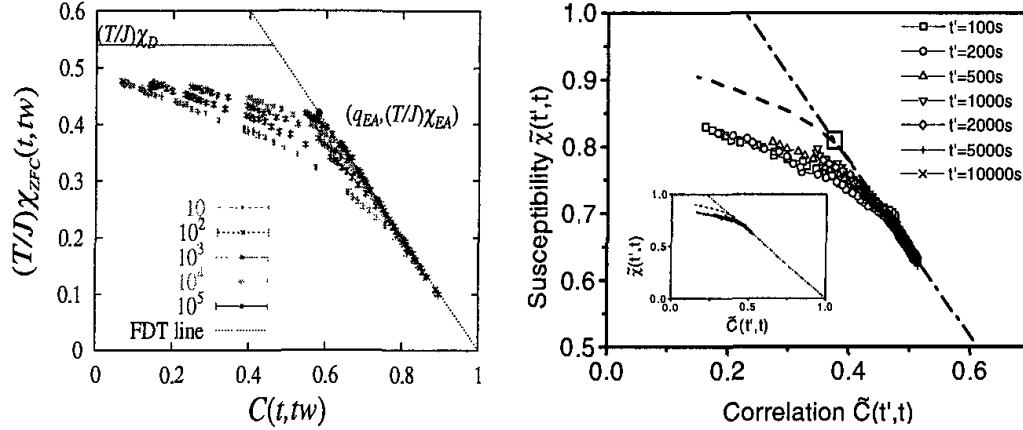


Fig. 9.9. **Left:** Parametric plot  $(T/J)\chi_{ZFC}(t + t_w, t_w)$  vs  $C(t + t_w, t_w)$  at  $T/J = 1.2$  for the 4d EA model. The straight tangent lines represents the FDT. The convergence points of the break points of time translational invariance ( $q_{EA}$ ,  $(T/J)\chi_{EA}$ ) and the break points of FDT ( $q_D$ ,  $(T/J)\chi_D$ ). (from [125]) **Right:** FDT-plot obtained from the experiments performed in [185]. Relaxation measurements are plotted versus correlation functions for each  $t'$ . The dot-dashed line (FDT line) is calculated for  $T = 0.8Tg = 13.3K$ , from a calibration obtained with a copper sample. The dashed line represents the scaling extrapolation for  $t' \rightarrow \infty$ . The branching point with the FDT line, corresponds to  $\tilde{C} = q_{EA}$  (square symbol, with size giving the error range). In Inset, the same data in the whole range. (from [185]).

result, in three dimensions<sup>123</sup> as well as in four dimensions.<sup>182</sup> However, in [125] it was proposed that the numerical data for the FDT-violation in the 3d EA-model (as well as those for the spatial correlations and the two-time quantities) can be interpreted in view of an extended droplet theory and that for the 3d EA model scenario *B* (essentially slow coarsening in the spirit of the droplet model) is appropriate. (See Fig.9.9 (Left).) Since numerical simulations can cover only a few decades of the waiting time  $t_w$  and there is, as mentioned above, still a significant  $t_w$  dependence in  $X(C, t_w)$  in the numerical data,<sup>183,184</sup> a definite statement is hard to make.

For a clear experimental demonstration of the FDT violation one has to measure both; response and autocorrelation function (in [186] possible indications of the FDT violation based only on the response have been discussed). Such an experimental evidence of the violation of the FDT in spin glasses has been presented for the first time in [185] (for a structural glass, glycerol, it has been measured in [187], for a colloidal glass, laponite, in [188]), where autocorrelation function  $C(t + t_w, t_w)$  has been measured via the magnetization fluctuations in a spin glass sample and the susceptibility  $\chi(t + t_w, t_w)$  in the usual way by applying a magnetic field. (See Fig.9.9

(Right).) The  $\chi$  versus  $C$  plots show still a strong waiting time dependence and give some room for extrapolations to the long time limit — one that is suggested by the authors has similarities to the one for the SK-model. On the other hand, the aging part of their data for  $C$  and  $\chi$  scale perfectly with  $h(t_w)/h(t)$  where  $h(u) = \exp(u^{1-\mu}/(1-\mu))$  with  $\mu = 0.85$ , which would not correspond to what one expects for the SK model.

The action for the long-time asymptotic behavior of the generating functional for the correlation and response functions is invariant under a time re-parameterization  $t \rightarrow h(t)$ , simply because in the long-time regime a re-parameterization of time with a monotonous function does not change the ultra-metric relation in the time ordering. The global invariance under the re-parameterization group (RpG) for mean-field models was recently extended<sup>189,190</sup> to its local variant for short range models to treat fluctuations. In analogy to Heisenberg magnets, where the global spin rotation invariance lead to the existence of spin waves in finite dimensional models via the Goldstone modes, the authors proposed that local time re-parameterizations play a similar role for the asymptotic dynamics of short-range spin glasses. One consequence of this observation is that one expects fluctuations in local correlation functions and local susceptibilities

$$C_r(t+t_w, t_w) = \bar{S}_r(t+t_w)\bar{S}_r(t_w), \quad \chi_r(t+t_w, t_w) = \bar{S}_r(t+t_w)|_{h_r(t)=h\theta(t)}/h, \quad (36)$$

where  $\bar{S}_r(t)$  means a slightly coarse-grained spin value at position  $r$  and time  $t$ , i.e. it involves a spatial average of the spin values over a small volume centered around  $r$  and a time average over a small time window centered around  $t$ . If the volume is extended to the system size, the usual global quantities discussed above are recovered. These spatially fluctuating quantities then have a joint probability distribution  $\rho(C_r, \chi_r)$  that stretches along the FDT-relation  $\chi(C)$  for the global quantities  $\chi$  and  $C$ , as has been shown numerically in [190].

### 9.5.5. Hysteresis in Spin Glasses

Due to the complex energy landscape of spin glasses one expects strong hysteresis effects, which were studied recently via Monte-Carlo simulations<sup>191,192,193,194</sup> also using new techniques such as the recently introduced First Order Reversal Curve (FORC) method.<sup>195</sup>

In [193], the zero temperature dynamics of the 2d EA spin glass model was simulated with a varying external field  $H$ . The procedure used there was as follows. The magnetic field is changed in small steps, first downward

from positive saturation and then upward from a reversal field  $H_R$ . After each field step, the effective local field  $h_i$  of each spin  $S_i$  is calculated:  $h_i = \sum_j J_{ij}S_j - H$ . A spin is unstable if  $h_iS_i < 0$ . A randomly chosen unstable spin is flipped and then the local fields at neighboring sites are updated. This procedure is repeated until all spins become stable.

The first important observation was of a memory effect in the hysteresis of the 2d EA spin glass model that emerged when the magnetic field was first decreased from its saturation value and then increased again from some reversal field  $H_R$ . It was found that the EA spin glass exhibited a singularity at the negative of the reversal field,  $-H_R$ , in the form of a kink in the magnetization of the reversal curve (See Fig.9.10).

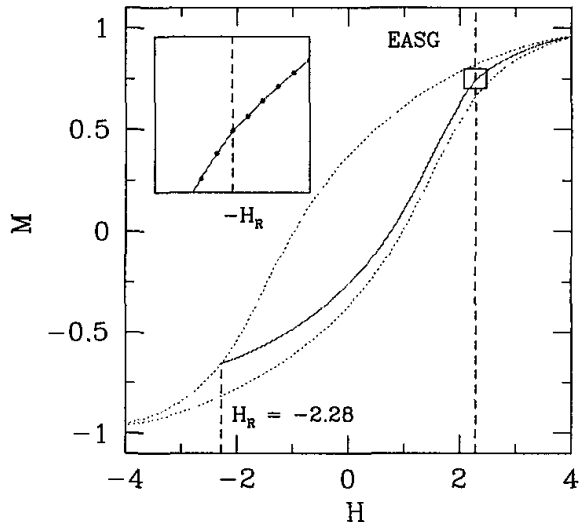


Fig. 9.10. Reversal curve (solid line) and major hysteresis loop (dotted line) for a two-dimensional (2D) EA spin glass with  $10^4$  spins and  $H_R = -2.28$ . In the inset a kink is seen around  $-H_R$ . (From [193]).

One can describe this effect within a phenomenological approach to hysteretic systems, the Preisach model.<sup>196</sup> In the Preisach model a magnetic system is described as a collection of independent two-state ( $\pm 1$ ) switching units, or “hysterons”. Unlike Ising spins, which always align with their local field, the hysteron’s state changes from  $-1$  to  $+1$  at a field  $H_b + H_c$ , different from the field  $H_b - H_c$ , required to switch the hysteron from  $+1$  to  $-1$ . Different systems are distinguished by their different distributions

$\rho(H_b, H_c)$  of hysterons of a given bias  $H_b$  and coercivity  $H_c$ . Here  $\rho(H_b, H_c)$  is the so-called “Preisach function”.

This function was extracted by a tool developed for analyzing experimental data of hysteretic systems.<sup>195</sup> A family of First Order Reversal Curves (FORCs) with different  $H_R$  was generated, with  $M(H, H_R)$  denoting the resulting magnetization as a function of the applied and reversal fields. Computing the mixed second order derivative  $\rho(H, H_R) = -(1/2)[\partial^2 M / \partial H \partial H_R]$  and changing variables to  $H_c = (H - H_R)/2$  and  $H_b = (H + H_R)/2$ , the local coercivity and bias, respectively, yielded the “FORC distribution”  $\rho(H_b, H_c)$ . For phenomenological Preisach models, the FORC distribution is equal to the Preisach function. However, the definition of the FORC distributions is more general, because it is extracted from numerical or experimental data, and thus is model-independent.

Fig. 9.11 shows the FORC diagram of the EA spin glass. The ridge along the  $H_c$  axis in the range  $1.5 < H_c < 4.0$  corresponds to the kinks of Fig. 9.10. Thus FORC diagrams capture the reversal-field memory effect in the form of a ridge along the  $H_c$  axis. In Fig. 9.11 also the experimentally determined FORC diagram of thin films of well-dispersed single-domain magnetic Co- $\gamma$ -Fe<sub>2</sub>O<sub>3</sub> particles provided by Kodak Inc is shown. It clearly exhibits the horizontal ridge associated with the reversal-field memory effect. This striking similarity between the experimentally determined FORC diagram of the Co- $\gamma$ -Fe<sub>2</sub>O<sub>3</sub> films and the numerically determined FORC diagram of the EASG indicates not only that Co- $\gamma$ -Fe<sub>2</sub>O<sub>3</sub> films exhibit reversal-field memory but also that frustration may be a component of the physics of the Co- $\gamma$ -Fe<sub>2</sub>O<sub>3</sub> films. Note that for instance the 2d random field Ising model does NOT exhibit a reversal-field memory and that its FORC diagram has a vertical ridge rather than a horizontal one.<sup>193</sup>

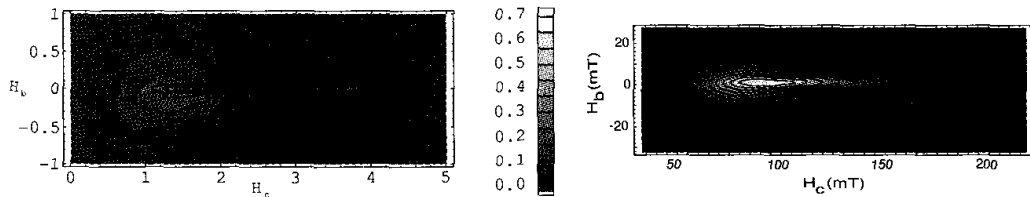


Fig. 9.11. **Left:** FORC Diagram of the EASG. Note the ridge along the  $H_c$  axis. **Right:** Experimental FORC diagram of a Kodak sample. Note the similarity to the FORC diagram of the EASG shown in the left diagram. (From [193]).

## 9.6. Equilibrium Properties of Classical XY and Heisenberg Spin Glasses

### 9.6.1. Continuous Spin Models in Three Dimensions

Compared to Ising spin glass models, less effort has been devoted to the models with continuous spins. One of the reasons might be that the minimal model of spin glasses, the Ising spin glass model, already shows a highly non-trivial behavior and poses serious difficulties to reach a final conclusion. Nonetheless, the continuous spin models are worth studying for several reasons. An obvious reason is that, in many real spin glass materials such as AuFe and CuMn, the magnetic anisotropy is much smaller than the (isotropic) exchange interaction. For these materials, therefore, the Heisenberg spin glass models would be more realistic than the Ising spin glass models.

However, the continuous spin models in three dimensions had long been thought of as models without a spin glass transition, which is another reason why the continuous spin models have not been studied so extensively until recently. The scenario that seemed to explain this apparent disagreement between the models and the materials was that the anisotropy is a relevant perturbation and, no matter how small it may be, it changes the system to an Ising-like spin glass, giving rise to a finite temperature phase transition. This is quite analogous to what happens when a small amount of Ising anisotropy was introduced to the isotropic Heisenberg model (with no disorder) in two dimensions. If this scenario is valid, the critical behavior of any spin glass material should be the same and fall into the Ising-spin-glass universality class. However, there are some qualitative differences between experimental results for materials with a small anisotropy and numerical results for the Ising spin glasses. In particular in a series of recent torque experiments [197,198] of Heisenberg spin glass samples with varying degree of anisotropies indications for a freezing transition even within an external field were found (implying the applicability of a mean field or RSB scenario rather than a droplet scenario to these Heisenberg spin glass systems). More surprisingly, the transition in spin glass materials with lower anisotropy (more Heisenberg-like) appeared to be more robust against the application of an external field than those with higher anisotropy (more Ising like), which is in contrast with the traditional view that higher anisotropy implies a stronger tendency to order. These observations call for further theoretical investigations, and here we report on recent theoretical efforts to scrutinize the existence of a transition in pure Heisenberg spin glasses without

anisotropy. Below we present two sets of evidences that seem to contradict each other. (The conflict has not been solved yet.) While the first set of evidences supports a novel phase transition via the chirality scenario (see below), the other suggests an apparently more familiar spin glass transition.

The first one was proposed by Kawamura and coworkers. (For a review, see [199].) It was suggested that a phase transition may exist in three dimensional Heisenberg model even if there is no anisotropy, and belong to a new universality class different from that of the Ising spin glass model. In a series of numerical works (e.g., [71]), the origin of the disagreement between the experimental and numerical results was scrutinized by reconsidering the role of the magnetic anisotropy in the mechanism of the spin glass transition. The resulting hypothesis was that there is a phase transition already in the isotropic system but the spins do not show long-range correlations even below this critical point. It is therefore difficult, if not impossible, to detect an anomalous behavior in spin-spin correlations which had been focused on in most preceding numerical simulations. Only the anisotropy gives rise to the long range correlations in spins, not the transition itself, by coupling them to other degrees of freedom that have been already ordered. It was proposed that these degrees of freedom relevant for the transition are the chiralities defined as

$$\chi_i = \mathbf{S}_i \cdot (\mathbf{S}_{i+\delta} \times \mathbf{S}_{i+\delta'})$$

where  $\delta$  and  $\delta'$  are two distinct unit lattice-vectors.

The dynamical behavior of the three-dimensional Heisenberg model with and without a uni-axial spin anisotropy was studied<sup>71</sup> and a clear aging phenomena, for both the isotropic and the anisotropic cases, was found in the autocorrelation function of the chirality at sufficiently low temperatures. For the isotropic Heisenberg spin glass model in three dimensions with the Gaussian bond distribution, the critical temperature and the exponent were estimated as

$$T_{\text{ch}} = 0.157(1), \quad \beta_{\text{ch}} = 1.1(1).$$

Such a clear aging phenomena, however, was observed in the bare spin degrees of freedom only when the anisotropy exists. It was therefore suggested<sup>72</sup> that this phase transition is not accompanied by a freezing of spins in the isotropic case. As can be seen in Fig.9.12, the estimate of the Binder parameter for the bare spins decreases as the system size increases at any temperature and does not show any crossing. In contrast, the Binder parameter of the chirality crosses.

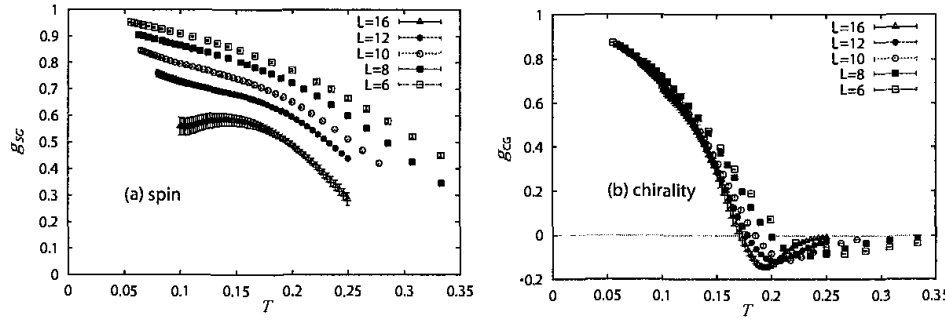


Fig. 9.12. The binder parameter for the  $\pm J$  Heisenberg spin glass model in three dimensions. The left panel is for the spin overlap distribution and the right panel is for the chirality overlap distribution. (From [72].)

An evidence of a finite temperature phase transition was also found for the plane-rotator model (i.e., the  $XY$  model with two-component spins) in three dimensions. In [76] an equilibrium Monte Carlo simulation was performed and a crossing in the Binder parameter defined in terms of the chirality was observed while, again, no such crossing was observed for the Binder parameter defined with the bare spins. For the 3d plane-rotator model with  $\pm J$  bond-distribution their estimates are

$$T_{ch} = 0.39(3), \quad \nu = 1.2(2), \quad \eta_{ch} = 0.15(20), \quad z_{ch} = 7.4(10).$$

It was further argued that, if a small but finite anisotropy exists, the spins and the chiralities are coupled, and therefore the spin sector, being dragged by anomalies in the chirality sector, also shows anomalies at the transition point. It follows that, as a function of the anisotropy, the transition temperature continuously approaches its isotropic limit. Moreover, the singular part of dragged quantities, i.e., those which diverge when the system is anisotropic and do not diverge when it is isotropic, are proportional to the quantity that drags them, namely, the chirality. The spin glass susceptibility, for instance, is given by

$$\chi_{SG}(T, D) \sim D^4(T - T_c)^{-\gamma_{SG}^{chiral}}$$

The exponent  $\gamma_{SG}$  characterizing the spin glass susceptibility is the same as the one characterizing the chiral spin glass susceptibility. Their estimates of critical indices were compared with those of real materials, and many experimental estimates are closer to those of chirality transition than the Ising spin glass transition (See, Table 9.1).

The second set of evidences contradicts to these findings. In a few recent reports on the  $XY$  and the Heisenberg spin glasses in three dimensions, it

was suggested that spins are ordered at the same finite temperature as the chiral degrees of freedom even in the isotropic case. The first such evidence was obtained<sup>200</sup> through the computation of the domain-wall energy of the  $XY$  model in two and three-dimensions. The authors of [200] computed the spin and the chiral domain-wall energies and estimated the corresponding stiffness exponents. In the three-dimensional case, they obtained a positive value for the spin stiffness exponent,

$$\theta_S^{\text{spin}} = 0.056(11),$$

while they obtained a much larger stiffness exponent for the chiral domain-wall energy. The positivity of the stiffness exponent was reconfirmed by another computation based on the Coulomb gas representation.<sup>201</sup> However, since the estimated value is close to zero and the actual increase observed in the domain-wall energy was only about 10 percent for the whole range of system size explored, these results on the stiffness exponent alone could not be taken as a conclusive evidence.

Additional evidences came from Monte Carlo simulations at finite temperature,<sup>202,203,73</sup> in which the Binder parameters for the magnetization and the chirality of the three-dimensional  $\pm J$  Heisenberg model were computed. A common crossing of the curves for different system sizes was found in both Binder parameters. The two crossing temperatures, one for the spin and the other for the chirality, were close to each other. Based on this result, the presence of a finite temperature phase transition at which both the spin and the chiral degrees of freedom are ordered was suggested.

This result was confirmed in [74] where again the  $\pm J$  Heisenberg spin glass in three dimensions was studied. There the relaxation of several quantities at temperatures close to the critical one were measured, starting from a completely random initial configuration. In the time regime where the time-dependent length scale discussed in subsection 9.5.1 is smaller than the system size, the size dependence was absent in the auto-correlation function and the observed time-dependence could be regarded as the one in the thermodynamic limit. Right at the critical temperature, this time dependence was well described by an algebraic function for diverging quantities. For example, for the spin glass susceptibility, we have

$$\chi_{\text{SG}} \propto t^\lambda \tag{37}$$

with  $\lambda = \gamma_{\text{SG}}/z\nu$ .<sup>204</sup> Using this asymptotic form, the critical temperature as well as the critical exponents (divided by  $z\nu$ ) can be determined through the observation of the time dependence of some quantity. The exponent  $z\nu$

can be obtained from the temperature dependence of the characteristic time

$$\tau(\Delta T) \propto (\Delta T)^{-z\nu},$$

where  $\Delta T \equiv T - T_{\text{sg}}$ . In addition,  $z$  was estimated from the results of relatively small system sizes for which the correlation length was larger than the system size. In such a setting, the size dependence of the correlation time near the critical point should be described by

$$\tau(\Delta T = 0) \propto L^z.$$

The estimated critical temperature and exponents for the Heisenberg spin glass model with  $\pm J$  bond-distribution in three dimensions were

$$T_{\text{sg}}/J = 0.21^{+0.01}_{-0.03}, \quad \gamma_{\text{sg}} = 1.9(4), \quad \nu = 1.1(2), \quad \beta = 0.72(6).$$

It should be noted that this estimate of  $\nu$  agrees with some of the experiments on spin glass materials that appear not to be in the Ising universality class.

A clearer demonstration of the existence of the spin ordering was presented in [75], in which an equilibrium Monte Carlo simulation was performed covering not only the critical point but also a fairly large region in the low temperature phase. Instead of the Binder parameter, which is an indirect probe of the presence of the long range order, they used the correlation length itself as in the estimation of the transition temperature of the Ising spin glass model<sup>51</sup> (See Fig.9.3). For both the XY and the Heisenberg spin glass with the Gaussian bond distribution in three dimensions, a clear crossing in the correlation length divided by the system size as a function of the temperature was observed (Fig.9.13). The critical indices were estimated as

$$T_{\text{sg}} = 0.34(2), \quad \nu = 1.2(2) \quad (\text{XY})$$

and

$$T_{\text{sg}} = 0.16(2), \quad \nu = 1.1(2) \quad (\text{Heisenberg}).$$

It is rather puzzling to have two conflicting sets of numerical evidences, represented, e.g., by Fig.9.12 and Fig.9.13, each would pass as a convincing evidence if the other did not exist. This puzzling situation has not been resolved yet. It is at least clear that there is an unexpectedly large correction to scaling and that we need to answer why one of the seemingly legitimate methods for detecting the long-range order failed in the present case.

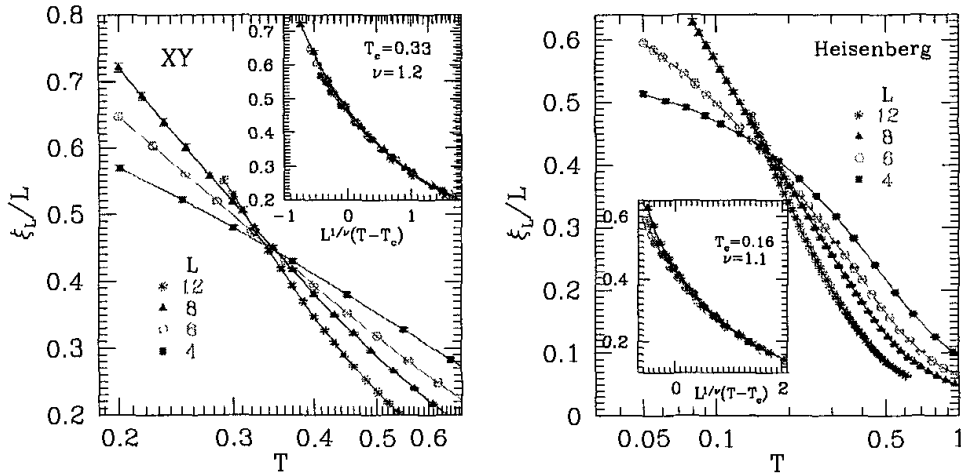


Fig. 9.13. Correlation lengths of bare spins of the XY model (left) and of the Heisenberg model (right) divided by the system size. (From [75].)

### 9.6.2. Continuous Spin Models in Higher Dimensions

The Heisenberg spin glass model with Gaussian couplings was studied in four and in five dimensions via equilibrium Monte Carlo simulations in [205]. As in the study of the three-dimensional case<sup>72</sup> the Binder parameter for spins and chiralities was calculated. In the four dimensional case, it was found that the spin Binder parameters for various system sizes do not intersect while the chirality Binder parameters do. In contrast, in the five dimensional case, both kinds of the Binder parameters intersect. Based on these results it was suggested that the spin chirality separation occurs only in four or lower dimensions while in five or higher dimensions an ordinary phase transition, at which both degrees of freedom freeze, takes place. In five dimensions, the transition temperature was estimated as  $T_c = 0.60(2)$  and the critical indices as

$$\alpha = -1.0(3), \beta_{SG} = 0.7(3), \gamma_{SG} = 1.7(2), \nu_{SG} = 0.6(2).$$

Indications were found that the chiral order phase is characterized by one-step replica symmetry breaking unlike the mean-field model. The findings for the four dimensional model were not as clear as those for the five dimensional model. In four dimensions, the chiral transition temperature was estimated to be  $T_c = 0.38(2)$  but no reliable estimates for the critical indices for the four dimensional model could be obtained. This may be because four dimensions is marginal or nearly marginal and the critical region is rather narrow.

For these numerical evidences based on the Binder parameters, however,

one has to be aware that the same ambiguities might be present in four and five dimensions as in the three-dimensional case discussed in the previous subsection. Therefore, while the existence of a phase transition has been established in four and five dimensions as well as in three, we still cannot make a conclusive statement concerning the nature of the phase transition in continuous spin models for the same reason as in the three-dimensional case.

### 9.6.3. Potts Spin Glasses

Potts spin variables are discrete variables that can take on  $q$  different states  $S_i \in \{1, 2, \dots, q\}$  and that interact with one another in such a way that only two cases are discriminated: either both interacting spins are in the same state or they are in different states. The Hamiltonian of the  $q$ -state Potts glass is given by

$$H = - \sum_{(i,j)} J_{ij} (q\delta_{S_i, S_j} - 1), \quad (38)$$

where the coupling constants  $J_{ij}$  are quenched random variables and the sum runs over all interacting spin pairs (i.e., all possible spin pairs in a mean-field model).

The  $q$ -state infinite range Potts glass with  $q > 4$ <sup>206,207</sup> displays a dynamical phase transition at a temperature  $T_d$ , where the dynamics freezes and, for instance, the spin auto-correlations do not decay any more (i.e. they reach asymptotically a non-vanishing plateau value). The second, static, transition takes place at a lower temperature  $T_c$ , below which the EA spin glass order parameter has a non-vanishing value and the replica symmetry is broken. On the mean-field level there is a close connection between Potts glasses for  $q \geq 4$ , and Ising spin glass models with  $p$ -spin interactions for  $p \geq 3$ , which again display similar self-consistency equations as the mode-coupling equations describing structural glasses above the glass transition temperature.<sup>208,209</sup> Therefore Potts spin glasses can also be regarded as simple prototypical models for structural glasses.

The question unanswered to date is, whether this analytically well-established mean-field scenario with the two separate transitions is also valid in finite-dimensional models with short range interactions. Recently, the  $q$ -state Potts glass was thoroughly investigated via Monte Carlo simulations in three dimensions,<sup>210,211</sup> on the simple cubic lattice, with  $q = 10$  for a discrete, bimodal bond-distribution as well as a Gaussian distribution. In both cases, the first two moments of the distribution were chosen

such that no ferromagnetic ordering of the Potts spins could occur. It was found that for all temperatures investigated the spin glass susceptibility remained finite, the spin-glass order-parameter remained zero, and that the specific heat had only a smooth Schottky-like peak. These results could be understood quantitatively by considering small but independent clusters of spins. These observations imply that there is no static phase transition at any nonzero temperature. Consistent with these findings, only very minor size effects were observed, which implied that all correlation lengths of the models remained very short.

Moreover, the auto-correlation function  $C(t)$  of the Potts spins was computed. While in the Gaussian model  $C(t)$  shows a smooth uniform decay, the correlation for the  $\pm J$  model has several distinct steps. These steps correspond to the breaking of bonds in small clusters of ferromagnetically coupled spins (dimers, trimers, etc.). The relaxation times follow simple Arrhenius laws, with activation energies that are readily interpreted within the cluster picture, giving an evidence that the system does not have a dynamic transition at a finite temperature. Hence one can conclude that all the transitions known for the mean-field version of the model are completely wiped out in three dimensions.

It should also be mentioned that the mean-field model of the Potts spin glass was studied numerically via Monte-Carlo simulations.<sup>212,213,214</sup> It turned out the it is extremely difficult to control the finite size effects in the mean-field model and that the fourth order cumulant  $g_4(N, T)$  and the Guerra parameter  $G(N, T)$  could not be used to locate the static transition temperature for the system sizes investigated. Also the spin-autocorrelation function  $C(t)$  showed strong finite size effects and did not display a plateau even for temperatures around the dynamical critical temperature  $T_d$ .

## 9.7. Weak Disorder

While there are only very few exactly known facts about spin glass models, they serve as helpful guides to numerical studies. This is particularly the case in the study of random spin system with weak disorder. An example is the findings based on the gauge invariance (a brief review can be found in [215]). A line in the phase space, commonly referred to as the Nishimori line (simply N-line, hereafter), was found on which the free energy can be computed exactly. The line is associated with the crossover from the high-temperature ferromagnetic region to the low-temperature disorder-dominated region. The results derived from the gauge invariance seem to

have a close connection to a number of renormalization group studies. In the following, we present a gross survey of these findings and related works.

### 9.7.1. Phase Diagram of the Discrete Spin Models

It was pointed out<sup>216</sup> that the gauge invariance of the partition function under the transformation  $S_i \rightarrow \sigma_i S_i$  (with an arbitrary choice of  $\sigma_i \in \{-1, +1\}$  for every site) can be used to derive a number of exact relations among various quantities in spin glass models. This gauge transformation relates thermal fluctuations to the geometrical properties of the bond configurations. Consequently, a *geometric temperature*,  $T_p$ , can be defined that depends only on the bond distribution. This temperature appears in various exact relationships derived from this gauge invariance. An example is the identity for correlation functions in  $\pm J$  models:

$$[\langle S_i S_j \rangle_T] = [\langle S_i S_j \rangle_T \langle S_i S_j \rangle_{T_p}] \quad (39)$$

where  $\langle \dots \rangle_T$  is the thermal average at temperature  $T$ . In particular,  $\langle \dots \rangle_{T_p}$  means the thermal average with the real temperature and the geometrical temperature being equal to each other. The symbol  $[\dots]$  denotes, as usual, the bond-configuration average. The geometric temperature  $T_p$  is defined as

$$p = (1 + \tanh(J/T_p)) / 2, \quad \text{or} \quad T_p = \frac{2J}{\log \frac{p}{1-p}}$$

where  $p$  is the concentration of the ferromagnetic bonds. The higher the randomness ( $p \rightarrow 1/2$ ), the higher the geometric temperature ( $T_p \rightarrow \infty$ ). The line in the  $p - T$  phase diagram defined by  $T_p = T$  is the N-line. Along this line, (39) infers  $m = q$ , i.e., the spin-glass order is always accompanied by the ferromagnetic order. Therefore, no part of the line lies inside the pure spin-glass phase. (Here, we define the spin-glass phase by the conditions  $m = 0$  and  $q > 0$ .) Another consequence of (39) is that the ferromagnetic long-range order is absent at any temperature if the concentration  $p$  is such that the point  $(p, T_p)$  falls in the paramagnetic region in the  $p - T$  plane. This can be understood by an inequality directly derived from (39):

$$|[\langle S_i S_j \rangle_T]| \leq |[\langle S_i S_j \rangle_{T_p}]|. \quad (40)$$

If the point  $(p, T_p)$  belongs to the paramagnetic region, the right hand side of the inequality is zero in the limit of  $R_{ij} \rightarrow \infty$ , which makes the left hand side also zero, meaning the absence of ferromagnetic order at  $(p, T)$ . Assuming that the topology of the  $T - p$  phase diagram is as depicted in Fig.9.14(a),

this fact implies that any phase in the region  $p < p_N$  (or  $T_p > T_N$ ) cannot have a ferromagnetic long-range order where  $p_N$  is the ferromagnetic bond concentration at the N-point. Here the N-point  $(p_N, T_N)$  is defined as the point at which the paramagnetic phase boundary intersect with the N-line. It follows that the phase boundary separating the ferromagnetic phase from the other low-temperature phase (paramagnetic or spin-glass) must be strictly vertical or bend toward the ferromagnetic side. (See Fig.9.14.)

The inequality (40) also means that the ferromagnetic order is maximal on the N-line when  $p$  is fixed. When  $T_p < T_N$ , as we decrease the temperature departing from the N-line, the magnetization decreases and the spin glass order parameter becomes larger than the square of the magnetization squared. This hints a cross-over from the purely ferromagnetic region to the randomness-dominating region at the temperature  $T = T_p$ .

It was further argued<sup>217</sup> that the phase boundary below the N-line is strictly vertical. The argument is based on the fact that the free energy on the N-line is the same as the geometric entropy, i.e., the entropy of the frustration distribution at  $p$ :

$$S(p) \equiv - \sum_F P(F) \log P(F)$$

where  $F$  is a configuration of frustrated plaquettes and  $P(F)$  is the probability of  $F$  being realized. Since the free energy (or its derivative with respect to some external field) must have some singularity at the N-point when one moves along the N-line, so does the geometric entropy. The latter singularity is, however, solely due to the geometric properties of the bond configuration, in which the temperature does not play any role. Therefore, it is reasonable to suspect that the same singularity with the geometric origin may affect the spin system defined on it at  $p = p_N$  regardless of the temperature. This leads to a temperature-independent transition point, i.e., the strictly vertical phase boundary (See Fig.9.14). Note that the argument applies also to models with continuous degrees of freedom, such as the  $XY$  model and the Heisenberg model, if the ferromagnetic phase exists in the pure model. It was claimed<sup>217</sup> that the vertical phase boundary between the ferromagnetic phase and the other is universal.

In order to substantiate this argument, the authors of [218] considered the random  $Z_q$  model with gauge symmetry,  $\mathcal{H} = - \sum_{(ij)} V(S_i - S_j + J_{ij})$  with  $S_i, S_j, J_{ij}$  takes on a value  $0, 1, 2, \dots$  or  $q-1$ , and  $V(\dots)$  is a periodic function of the period  $q$ . This model includes the  $\pm J$  Ising spin glass model as a special case. The sample-to-sample fluctuations of the energy along

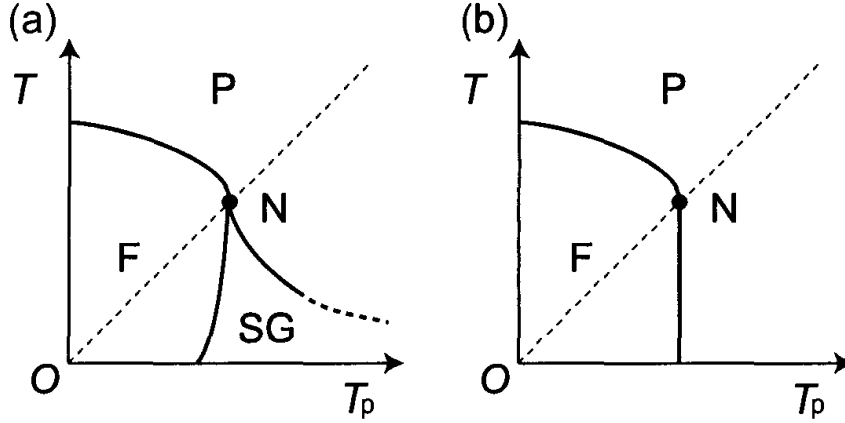


Fig. 9.14. The schematic  $p - T$  phase diagram the  $\pm J$  Ising model for (a) the generic case and (b) the two-dimensional case. The thin dashed lines represent the N-line.

the N-line was computed via the exact relationship between the sample-to-sample fluctuations and the thermal fluctuations:

$$[(\Delta E)^2] \equiv [E^2] - [E]^2 = N_B(\{V^2\} - \{V\}^2) - [\langle H^2 \rangle - \langle H \rangle^2].$$

Here,  $E \equiv \langle \mathcal{H} \rangle$ ,  $N_B$  the number of nearest-neighbor pairs, and  $\{\dots\}$  denotes a single-bond average defined by  $\{Q(l)\} \equiv \sum_{l=0}^{q-1} \exp(-\beta V(l)) Q(l) / \sum_{l=0}^{q-1} \exp(-\beta V(l))$ . The sample-to-sample fluctuations are proportional to the ‘geometric specific heat’, i.e., the energy differentiated by  $K_p \equiv 1/T_p$ . The results showed that  $[(\Delta E)^2]$  takes its maximum at the N-point. The authors of [218] argued that this indicates the existence of a singularity in the geometric nature of the system at the N-point, though the nature of the singularity is not known possibly because of the size limitation in their calculation.

It is interesting to note that the correlation length exponent  $\nu$  at the zero-temperature phase transition from the paramagnetic phase to the ferromagnetic phase in two dimension was found<sup>219,31</sup> to be very close to (or perhaps exactly equal to) the one for two-dimensional percolation. This fact, together with the geometric mechanism of the transition, makes it very attractive to speculate that the transition is due to a percolation of something that is defined geometrically. However, this “something” has not yet been identified.

### 9.7.2. Dynamical Properties

Based on the gauge invariance of the model, several interesting exact relations were derived<sup>220</sup> for the dynamics. Particularly important is the one

that relates the auto-correlation function with the totally aligned initial state and that with the initialization at  $T = T_p$ . Specifically,

$$[\langle S_i(t + t_w)S_i(t_w) \rangle_T^{(F)}] = [\langle S_i(t + t_w)S_i(T_w) \rangle_T^{T_p}]. \quad (41)$$

The superscripts specify the initial spin configurations: “(F)” indicates that the initial state is the totally aligned ferromagnetic state, and “ $T_p$ ” an equilibrium spin configuration at  $T_p$ . The left hand side is the autocorrelation function of a spin  $S_i$  at the  $t_w$ -th Monte Carlo step (MCS) after the initialization (at  $t = 0$ ) and itself at the  $(t + t_w)$ -th step. At  $t > 0$  the system evolves with the dynamics of a finite temperature  $T$ . The right hand side is the autocorrelation function after a quenching from the temperature  $T_p$  to  $T$  (or a sudden heating up, depending upon whether  $T > T_p$  or  $T < T_p$ ). Of particular interest is the relation obtained by setting  $t_w = 0$  and  $T = T_p$  in the above

$$[\langle S_i(t) \rangle_{T_p}^{(F)}] = [\langle S_i(t)S_i(0) \rangle_{T_p}^{T_p}].$$

This indicates the equivalence of the equilibrium auto-correlation function on the N-line to the non-equilibrium relaxation of the single-spin expectation value starting from the all-aligned condition. By using this relation, we can simply measure the value of a spin without equilibrating at all to obtain the equilibrium autocorrelation function. This is a considerable advantage from the computational point of view.

### 9.7.3. The Renormalization Group Approach for the Discrete Models

The Harris criterion<sup>221</sup> is well-known as the criterion by which one can decide whether introduction of a weak disorder to a pure system is relevant or irrelevant: If the specific heat diverges at the critical point of the pure system, i.e., the specific heat exponent  $\alpha$  is positive, the universality class of the transition in the disordered system will be different from the one of the pure system. In particular, it was argued that if the disorder is relevant the specific heat divergence is smeared out by the effect of the quenched disorder.

The argument was elaborated further with the help of the renormalization group theory.<sup>222</sup> The analysis of the randomly diluted  $m$ -vector model showed that the quenched disorder is relevant around the “pure” fixed point (denoted as “P” hereafter), if the specific exponent  $\alpha$  is positive at P. As a result, the existence of another fixed point, called the random fixed point

(denoted as “R”), was suggested, and the renormalization group flow leads the system to R when starting in the vicinity of P. However, because of the small cross-over exponent, i.e.,  $\alpha$  in this case, the critical region where the true critical behavior of R can be observed may be very narrow in many cases, such as the random Ising model in three dimensions ( $\alpha \sim 0.11$ ). For instance results of Monte Carlo simulations of the site-disordered Ising system<sup>223</sup> were interpreted in terms of a non-universal behavior, i.e., continuously varying critical exponent depending on the strength of the disorder. It was argued that this apparent non-universal behavior can be interpreted as a cross-over from P to R.

As for the critical indices at R, the following values for three dimensional systems were reported<sup>224</sup> based on the four-loop order field-theoretic renormalization group calculation:

$$\beta = 0.348, \gamma = 1.321, \nu = 0.671, \eta = 0.032. \quad (42)$$

In [225] the role of the gauge invariance in the renormalization group method was scrutinized. It was found that the defining condition of the N-line,  $T_p = T$  is invariant under a certain renormalization group transformation. More specifically, in an extended phase space an invariant manifold exists that intersects with the  $p - T$  plane with the intersection being the N-line. A fixed point is located on this manifold and can be identified with the one corresponding to the multi-critical point that is shared by three phases: paramagnetic, ferromagnetic and spin-glass. One of the directions of the two scaling axes is also found to be parallel to the temperature axis while the other is tangent to the N-line. The fixed point is unstable in both directions.

The authors of [226] studied the site-diluted Ising model with Monte Carlo simulation. Their estimates for the critical indices were

$$\beta = 0.3546(18), \gamma = 1.342(5), \nu = 0.6837(24), \eta = 0.0374(36).$$

These are very close to the corresponding estimates of the indices for the pure model such as:<sup>227</sup>

$$\beta = 0.3250(15), \gamma = 1.241(2), \nu = 0.6300(15).$$

Therefore it is technically rather difficult to discriminate a critical point corresponding to the random fixed point from the pure fixed point.

The numerical renormalization group approach based on Monte Carlo simulation<sup>228</sup> suggested the simplest flow diagram consistent with all of these predictions. The variance and the mean of the domain wall free energy were computed and analyzed with the method of the domain-wall

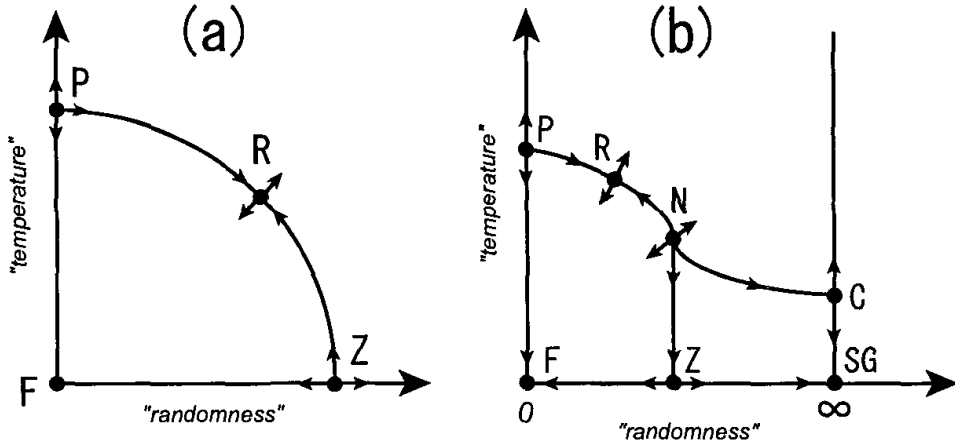


Fig. 9.15. A schematic RG flow diagram for (a) non-frustrated models (e.g., the randomly diluted ferromagnet) and (b) frustrated models (e.g., the  $\pm J$  model) in three dimensions.

renormalization group.<sup>28</sup> For the randomly diluted spin systems in three dimensions the flow diagram turned out to be the simplest one consistent with preceding theoretical predictions (see Fig. 9.15). The RG flow diagram for the bond-diluted model consists of two finite temperature fixed points (the pure fixed point (P) and the random fixed point (R)) together with two zero-temperature fixed points (the ferromagnetic fixed point (F) and the zero-temperature percolation fixed point (Z)). The two eigen values of the linearized RG transformation were evaluated at R. The positive one turned out to be

$$y_1 = 1.47(4)$$

which is consistent with the previous estimates of  $\nu = 1/y \sim 0.68$  mentioned above. The other negative one was

$$y_2 = -1.3(4).$$

A similar calculation for the site-diluted system yielded the result consistent with these.

When in addition the system is randomly frustrated, the simplest flow diagram must contain at least three more fixed points: the multi-critical or Nishimori fixed point (N), the spin-glass critical fixed point (C), and the spin-glass zero-temperature fixed point (SG). The findings in [228] were indeed consistent with this simplest flow diagram (Fig. 9.15). In this case the exponent at R was estimated as

$$y_1 = 1.52(2), \quad \text{and} \quad y_2 = -0.42(13).$$

While the positive one agrees with the estimate for the non-frustrated system, the other does not agree. The reason for this has not been clarified yet.

#### 9.7.4. The Location of the Multi-Critical Point

For the location of the multi-critical point, or the N-point, of the  $\pm J$  model, there are a number of numerical estimates. In particular, the non-equilibrium simulation was employed effectively to deduce the equilibrium properties. The basic idea of the method can be traced back to the dynamical scaling hypothesis.<sup>229,230</sup> Various scaling relations, such as (37), can be derived from it. It is assumed that a generating function, which is an extension of the equilibrium free energy, exists and that the time-dependence of various quantities can be obtained as its derivatives. The hypothetical generating function has the form

$$f(\Delta T, h, L, t) = L^{-d} \tilde{f}(\Delta T L^y, h L^{y_h}, t L^{-z}) \quad (43)$$

analogous to the ordinary form of the finite size scaling. While this form is presumably valid in the near-equilibrium time regime, it was suggested<sup>133</sup> that there exists an initial time regime where the dynamics is governed by another critical exponent independent of those which appear in (43).

Using the scaling relations derived from (43), the non-equilibrium relaxation of the system was studied. The authors of [231] measured the magnetization  $m(t) \equiv [\langle S_i(t) \rangle_T^{(F)}]$  on the N-line, which is proved to be the same as the equilibrium autocorrelation function  $q(t)$  as mentioned above (see subsection 9.7.2). Then they used the following scaling form

$$m(t) = L^{-\beta y} \tilde{q}((T - T_N)L^y, t L^{-z})$$

that can be derived from (43). In particular, the long-time asymptotic form at  $T = T_N$

$$m(t) \sim t^{-\beta y/z}$$

was used to obtain the effective exponent at a finite time,

$$\lambda(t) \equiv -\frac{d \log m(t)}{d \log t},$$

which should converge to  $\lambda \equiv \beta y/z$  as  $t \rightarrow \infty$  at the critical point. A good convergence to a finite value was observed around the N-point for the two and three dimensional models, although the convergence in the latter case seemed more unstable. They quoted the values

$$p_N = 0.8872(8), \quad \lambda = 0.021(1) \quad (44)$$

for the two dimensional model and

$$p_N = 0.7673(3), \quad \lambda = 0.090(3) \quad (45)$$

for the three dimensional model.

In two dimensions, the exact location of the N-point was predicted by [232]. The authors studied the duality transformation formulated in [233], applying it to a random model with  $Z_q$  symmetry. The model is defined in terms of variables,  $\xi_i$ , each taking one of  $q$  values ( $\xi = 0, 1, 2, \dots, q - 1$ ). The partition function is defined as

$$Z = \sum_{\{\xi_i\}} e^{\sum_{(ij)} V(\xi_i - \xi_j + J_{ij})}$$

where  $V(l)$  is a periodic function defined on integers with the period  $q$  and  $J_{ij}$  is a quenched random variable that takes on  $0, 1, 2, \dots, q - 1$ . They obtained an equation that yields a (possibly exact) value of the critical concentration  $p_c$ . The resulting values of  $p_c$  agreed with numerical estimates for various models such as the  $\pm J$  Ising model and the three state Potts gauge glass. In addition, a similar equation derived for the random Ising model with Gaussian bond distribution yielded a value very close to the numerically obtained critical value of  $J/\Delta J$  where  $J$  and  $\Delta J$  are the mean and the standard deviation of the bond distribution, respectively.

The replica method was employed in the derivation of the key equation; the duality relation of the  $n$  replica system was considered. As reported in [234], a quantity, which we denote as  $\alpha$ , defined with the physical parameters, such as  $p$  and  $T$  for the Ising model, has a very simple transformation rule under the duality transformation:

$$\alpha \rightarrow q^n / \alpha,$$

Therefore,  $\alpha = q^{n/2}$  defines a manifold that is invariant under the duality transformation. The virtue of this equation is that we can explicitly take its  $n \rightarrow 0$  limit, resulting in

$$\sum_{l=0}^{q-1} p_l \log \left( \sum_{\eta=0}^{q-1} e^{V(\eta+l) - V(l)} \right) = \frac{1}{2} \log q, \quad (46)$$

where  $p_l$  is the probability of  $J_{ij}$  being  $l$ . If a well-defined duality equation in the  $n \rightarrow 0$  limit exists and if a self-dual point lies on our real  $p-T$  plane, the condition (46) must be satisfied on it. The problem is that we do not know what the  $n \rightarrow 0$  self-dual equation is nor whether a self-dual point lies on our  $p-T$  phase diagram.

However, with the assumption that a self-dual point coincides with the N-point, it becomes possible to obtain a number, which may be an exact value of  $p_c$ . Specifically, the intersection of the N-line and the line defined by (46) for the  $\pm J$  Ising model is located at

$$p_c = 0.889972 \dots$$

which agrees with preceding numerical estimates of the N-point such as

$$p_c = 0.8905(5)$$

in [235]. This remarkable agreement, together with similar agreements for a few other models, seems a little too much to regard as a mere coincidence; the exact transition points of these models may have been derived from the duality.

#### 9.7.5. Phase Diagram of the Random XY Model in Two Dimensions

The effect of weak randomness in the  $XY$  model in two dimensions is of special relevance due to its relationship to various other models, such as the Coulomb gas and Josephson junction arrays. The model discussed most frequently is the random phase  $XY$  model

$$\mathcal{H} = - \sum_{(ij)} J_{ij} \cos(\theta_i - \theta_j - \phi_{ij})$$

with  $J_{ij}$  being a uniform constant  $J > 0$  and  $\phi_{ij}$  a quenched random variable. However, other models, such as the one with random  $J_{ij}$  and uniform  $\phi_{ij}$ , most likely have essentially the same property.

In an early study<sup>236</sup> the random phase model was studied and it was suggested that a sufficiently strong disorder destroys the quasi-long-range order of the pure  $XY$  model. More strikingly, the amount of the disorder sufficient to destroy the quasi-order is vanishing as we approach the zero temperature. Consequently, the system undergoes a re-entrant phase transition as the temperature is lowered with the magnitude of the disorder being fixed at a sufficiently small value.

The latter prediction concerning the re-entrance phase transition was corrected later by a number of groups.<sup>237,238,239,240,241</sup> Here we follow the heuristic argument given by the authors of [238]. They argued that there is a disorder induced phase transition at zero temperature in the two-dimensional  $XY$  model. Generalizing the Kosterlitz argument for the KT transition, they considered the balance between the energy-cost for creating

a topological excitation (vortex) and the energy-gain due to the interaction of the vertex with the disordered potential. They estimated the probability  $p_{\text{defect}}$  of creating a vortex on a given site being energetically favored. It depends algebraically on the area of the system  $A$  with an exponent  $\alpha$ :

$$p_{\text{defect}} \sim A^{-\alpha}$$

where  $\alpha$  depends on the magnitude of the disorder and the temperature. The ordered phase is stable against the introduction of disorder when the total number of sites on which the creation of the vortex is favored is zero in the thermodynamic limit. That is,  $A p_{\text{defect}} \rightarrow 0$ . Therefore,  $\alpha = 1$  defines the phase boundary. This result contradicts preceding studies such as the one mentioned above<sup>236,242</sup> that suggest that the ground state of the pure system is unstable at any finite disorder.

They argued that the preceding renormalization group theories failed to capture the correct physics because they neglected the fluctuation in the local energy gain due to disorder potential, which can be very large with a small but finite probability. In particular, we cannot neglect such a fluctuation when it exceeds the thermal fluctuation. This means that the previous argument may fail near and below the N-line because the N-line can be regarded as the cross-over line below which the geometrical fluctuation dominates (see subsection 9.7.1).

They also discussed a finite temperature phase diagram introducing the thermal fluctuations in their argument. This yields another interesting feature of their results; the straight phase boundary between the ordered phase and the disordered phase in the  $T - T_p$  phase diagram, in agreement with the Nishimori's claim (see subsection 9.7.1). Generalizing the simple argument based on the energy-balance, they computed the exponent  $\alpha$  for finite temperature:

$$\alpha = \begin{cases} \frac{T^*}{T_p} & (T_p > \lambda T) \\ \frac{T^*}{T_p} \left( \frac{T_p}{\lambda T} \left( 2 - \frac{T_p}{\lambda T} \right) \right) & (T_p < \lambda T) \end{cases} \quad (47)$$

where  $T^*$  and  $\lambda$  are model-dependent parameters. The phase boundary is again given by  $\alpha = 1$ . Therefore, for the region where the disorder fluctuation dominates, ( $T_p > \lambda T$ ), the phase boundary is  $T_p = T^*$ , independent of the temperature, whereas it depends on the temperature in the region where the thermal fluctuation dominates ( $T_p < \lambda T$ ). If one identifies, quite naturally, the line  $T_p = \lambda T$  with the N-line, the result is perfectly in parallel with Nishimori's picture based on the gauge invariance.

In fact, the gauge invariance can be used for deriving exact results for continuous spin models, such as the  $XY$  models and the Heisenberg models. In [215], the author derived a number of exact equations for the Villain model on the N-line. For example, the exact solution for the energy along the N-line was obtained. As we have seen in subsection 9.7.1 for the discrete models, one can argue, based on the exact results, that the N-line ( $T = T_p$ ) is the cross-over line separating the purely ferromagnetic region and the disorder dominant region. Interestingly, the renormalization group theory on the  $XY$  model<sup>237</sup> indicates that there is a freezing transition or a cross-over at  $T = 2T_p$  with the difference of a factor 2 from the N-line. It is plausible that this difference is only due to the approximation involved in the renormalization group theory, and they both reflect the same physics.

## 9.8. Quantum Spin Glasses

A quantum spin glass is a magnetic system that can be described by a quantum mechanical Hamiltonian with spin-glass like features (randomness and frustration). In such a system, a spin glass phase may exist while at the same time quantum fluctuations play an important role, possibly a dominant role, in particular, in the absence of thermal fluctuations at zero temperature. Such a Hamiltonian is, for instance, the spin-1/2 Heisenberg spin glass

$$H = \sum_{(ij)} J_{ij} (\sigma_i^x \sigma_j^x + \sigma_i^y \sigma_j^y + \sigma_i^z \sigma_j^z), \quad (48)$$

where  $\sigma^{x,y,z}$  are Pauli spin-1/2 operators,  $J_{ij}$  random exchange interactions (e.g., Gaussian), and the sum runs over all nearest neighbors on some  $d$ -dimensional lattice. Another example is the Ising spin glass in a transverse field

$$H = - \sum_{(ij)} J_{ij} \sigma_i^z \sigma_j^z + \Gamma \sum_i \sigma_i^x, \quad (49)$$

where  $\Gamma$  denotes the transverse field strength. This Hamiltonian becomes diagonal if  $\Gamma$  is zero, in which case it reduces simply to the classical Ising spin glass that we have discussed in the previous sections. Thus the role of the parameter  $\Gamma$  is to tune the strength of quantum fluctuations, they do not play a role in the equilibrium statistical physics of a diagonal Hamiltonian. An important experimental realization of this model Hamiltonian is the system  $\text{LiHo}_x\text{Y}_{1-x}\text{F}_4$ ,<sup>243</sup> an insulating magnetic material in which the magnetic ions (Ho) are in a doublet state due to crystal field splitting.

The interactions between Ho ions can be described by an Ising model with dipolar couplings. For  $x = 1$  the system is a ferromagnet with a critical temperature of  $T_c = 1.53$  K at  $\Gamma = 0$  and as  $x$  is reduced the critical temperature decreases. For concentrations below 25% Ho and above 10% Ho a thermal phase transition to a spin glass phase occurs indicated by a diverging nonlinear susceptibility (for instance at  $x = 0.167$  the spin glass transition temperature is  $T_g = 0.13$  K at  $\Gamma = 0$ ). If a transverse field is applied ( $\Gamma > 0$ ) the spin glass transition temperature decreases monotonically to zero (see Fig. 9.16). This particular point, at zero temperature and at a critical field strength is what we denote as a quantum-phase-transition point.<sup>244</sup>

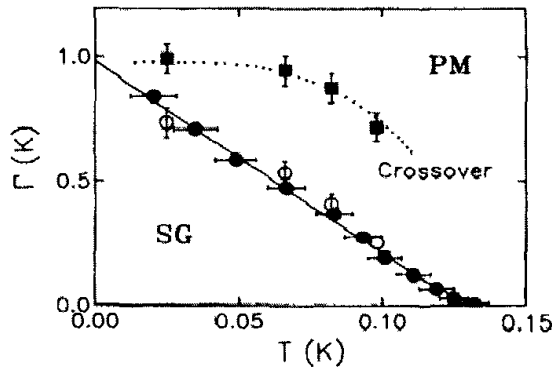


Fig. 9.16. Phase diagram of  $\text{LiHo}_{0.167}\text{Y}_{0.833}\text{F}_4$  according to the measurement of the nonlinear susceptibility. From [243].

Earlier reviews on quantum spin glasses and in particular the Ising spin glass in a transverse field can be found in [245, 246, 247]. Here we try to focus on a number of new developments that have been made since then.

### 9.8.1. Random Transverse Ising Models

The generic phase diagram for the EA Ising spin glass model in a transverse field  $\Gamma$  is shown in Fig. 9.17 for two dimensions and for three dimensions. In the three-dimensional case, starting from the classical spin glass transition temperature  $T_c$  for  $\Gamma = 0$  the critical temperature decreases monotonically with increasing transverse field strength  $\Gamma$  until it reaches  $T = 0$ . One expects that the universality class of the transition at any non-vanishing temperature is the same as the one of the classical Ising spin glass transition at  $T_c$ . The zero-temperature quantum phase transition, however, establishes

a new universality class. This transition exists in any dimension, including one and two dimensions. A critical value  $\Gamma_c$  for the transverse field strength separates a disordered or paramagnetic phase for  $\Gamma > \Gamma_c$  from an ordered phase for  $\Gamma < \Gamma_c$ . This transition is characterized by a diverging length scale  $\xi \sim |\Gamma - \Gamma_c|^{-\nu}$  and a vanishing characteristic frequency  $\omega \sim \Delta E \sim \xi^{-z}$ . The latter is the quantum analog of “critical slowing-down” in the critical dynamics of classical, thermally driven transitions. The new and most important property occurring at zero temperature in the random transverse Ising model is the *infinite randomness fixed point* (IRFP) that governs the quantum critical behavior at the critical value  $\Gamma_c$  of the transverse field.<sup>248</sup> One feature of the IRFP is that the dynamical exponent  $z$  is formally infinite, the relation between length and energy scales is not algebraic but exponential:  $\Delta E \sim \exp(-A\xi^\psi)$ .

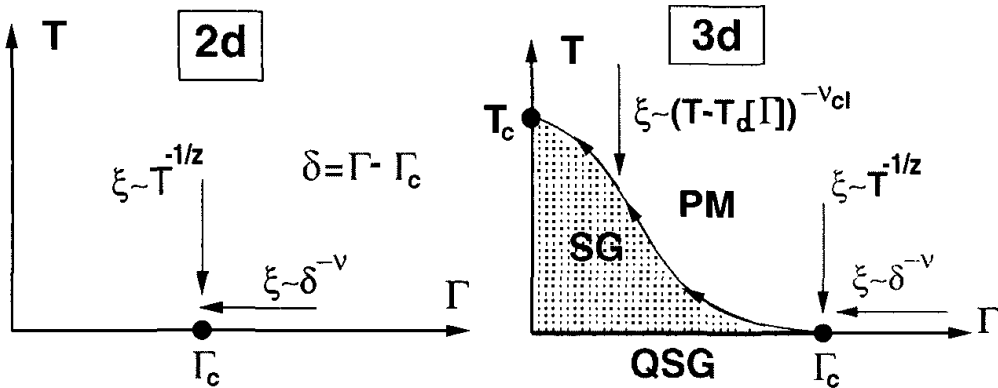


Fig. 9.17. **Left:** Generic phase diagram for the two-dimensional Ising spin glass in a transverse field  $\Gamma$ . Since no spin glass phase is present in  $d = 2$  for  $T > 0$ , only a quantum spin glass phase and a quantum phase transition at  $T = 0$  exists. Approaching the quantum critical point at  $\Gamma_c$  by decreasing the temperature  $T$ , the correlation length diverges like  $T^{-1/z}$ , where  $z$  is the dynamical critical exponent (if  $z$  is formally infinite, it increases logarithmically). **Right:** Generic phase diagram of a three-dimensional Ising spin glass in a transverse field. The classical transition temperature (at  $\Gamma = 0$ ) is  $T_c$  and the corresponding classical correlation length exponent is  $\nu_{cl}$ .

To describe this scenario we generalize the discussion of the transverse Ising spin glass by including also random *ferromagnetic* interactions  $J_{ij} > 0$ , because many more analytical and numerical results are available for the ferromagnetic rather than the spin glass case and the same main features are expected to hold in both cases.

Let us start with a review of the one-dimensional case, in which the sign (if it can be negative) of the nearest neighbor couplings can be gauged

away so that all interactions are ferromagnetic and the resulting model is the random Ising chain in a transverse field or a random transverse-field Ising model (RTIM) in one dimension:

$$\mathcal{H} = - \sum_i J_i \sigma_i^z \sigma_{i+1}^z + \sum_i h_i \sigma_i^x . \quad (J_i > 0) \quad (50)$$

A uniform transverse field is represented by  $h_i = \Gamma$  for all sites. Since this case and the case of random transverse fields turn out to belong to the same universality class, we also consider random transverse field here. The couplings  $J_i$  and the transverse fields  $h_i$  are random variables with distributions  $\pi(J)$  and  $\rho(h)$ , respectively. The Hamiltonian in (50) is closely related to the transfer matrix of a classical two-dimensional layered Ising model, which was first introduced and studied by McCoy and Wu.<sup>249</sup> Extensive researches on this model were initiated by D. Fisher<sup>250</sup> with an application of the Ma-Dasgupta-Hu renormalization group scheme,<sup>251</sup> followed by numerical and analytical work.<sup>252,253,254,255,256,257,258,259</sup> We briefly summarize the results. The quantum control-parameter of the model is given by

$$\delta = \frac{[\ln h]_{av} - [\ln J]_{av}}{\text{var}[\ln h] + \text{var}[\ln J]} . \quad (51)$$

For  $\delta < 0$  the system is in the ordered phase with a non-vanishing average magnetization, whereas the region  $\delta > 0$  corresponds to the disordered phase. There is a phase transition in the system at  $\delta = 0$  with rather special properties, which differs in several respects from the usual second-order phase transitions of pure systems. One of the most striking phenomena is that some physical quantities are not self-averaging, which is due to very broad, logarithmic probability distributions. As a consequence the *typical value* (which is the value in a frequent event) and the *average value* of such quantities can be drastically different. Thus the critical behavior of the system is primarily determined by rare events that give dominating contributions to the averaged values of various observables.

The average bulk magnetization is characterized by an exponent  $\beta$ , which is  $\beta = 2 - \tau$  where  $\tau = (1 + \sqrt{5})/2$  is the golden-mean. The average spin-spin correlation function  $C(r) = [\langle \sigma_i^z \sigma_{i+r}^z \rangle]_{av}$  involves the average correlation length  $\xi$ , which diverges at the critical point as  $\xi \sim |\delta|^{-\nu_{av}}$ , and  $\nu_{av} = 2$ . On the other hand, the typical correlations have a faster decay, since  $\xi_{typ} \sim |\delta|^{-\nu_{typ}}$  with  $\nu_{typ} = 1$ .

Close to the critical point the relaxation time  $t_r$  is related to the correlation length as  $t_r \sim \xi^z$ , where  $z$  is the dynamical exponent. The random

transverse-field Ising spin chain is strongly anisotropic at the critical point, since according to the RG-picture<sup>250</sup> and to numerical results<sup>260</sup>

$$\ln t_r \sim \xi^{1/2}, \quad (52)$$

which corresponds to  $z = \infty$ . On the other hand the relaxation time is related to the inverse of the energy-level spacing at the bottom of the spectrum  $t_r \sim (\Delta E)^{-1}$ . Then, as a consequence of (52), some quantities (such as specific heat, bulk and surface susceptibilities, etc.) have an essential singularity at the critical point, and the correlation function of the critical energy-density has a stretched exponential decay, in contrast to the usual power law behavior.

Away from the critical point in the disordered phase the rare events with strong correlations still play an important role, up to the point ,  $\delta = \delta_G$ . Above this point, all transverse-fields are bigger than the interactions. In the region  $0 < \delta < \delta_G$ , which is called the Griffiths-McCoy phase, the magnetization is a singular function of the uniform longitudinal field  $H_z$  as  $m_{\text{sing}} \sim |H_z|^{1/z}$ , where the dynamical exponent  $z$  varies with  $\delta$ . At the two borders of the Griffiths-McCoy phase it behaves as  $z \approx 1/2\delta \times (1 + \mathcal{O}(\delta))$ <sup>250</sup> as  $\delta \searrow 0$  and  $z = 1$  as  $\delta \nearrow \delta_G$ , respectively.

All these results could be obtained and understood by the application of a Ma-Dasgupta-Hu renormalization group scheme,<sup>250</sup> in which strong bonds or fields are successively decimated either by elimination of spins (in case of large transverse fields) or formation of strongly coupled clusters (in case of large ferromagnetic bonds). With decreasing energy scale  $\Delta$  of the bonds and fields to be decimated the typical size  $L$  of these strongly coupled clusters increases as

$$L \sim |\ln \Delta|^{1/\psi} \quad (53)$$

defining an exponent  $\psi$  that is  $1/2$  in the random transverse-field Ising chain. Such a cluster typically contains

$$\mu \sim L^{\phi\psi} (= |\ln \Delta|^\phi) \quad (54)$$

spins that essentially behave collectively (for instance in response to the application of a longitudinal magnetic field  $H$  — and thus generating a huge contribution to the spin susceptibility). This defines another exponent  $\phi$ , which is  $(1 + \sqrt{5})/2$  in the RTIM. Finally there is the correlation length exponent  $\nu$  that defines the characteristic length scale of spin-spin correlations away from the critical point.

The RG runs into a fixed point that is fully determined by the geometrical features of the clusters that are generated asymptotically — very much

in reminiscence of the percolation fixed point in conventional percolation. This picture is expected to hold also for higher-dimensional RTIMs, and even for the spin glass case. Therefore we summarize its essence here. The distribution of the random bonds and fields not yet decimated during the RG procedure becomes broader and broader. Hence the name, *infinite randomness fixed point* (IRFP). It is characterized by the three exponents  $\psi$ ,  $\phi$  and  $\nu$  and the critical behavior of the physical observables is determined by them. For instance the correlation function (at criticality) for two spins at site  $i$  and  $j$  with a distance  $r$  from each other is simply given by their probability to belong to the same cluster of size  $r$ :  $[C_{ij}]_{\text{av}} \sim |\mathbf{r}_i - \mathbf{r}_j|^{-2(d-\phi\psi)}$ . Other relations follow straightforwardly from this scheme<sup>248</sup>:

lowest energy scale:	$-\ln \Delta$	$\sim L^\psi$
magnetic moment:	$\mu$	$\sim (-\ln \Delta)^\phi$
average correlations:	$[C_{ij}]_{\text{av}}$	$\sim  \mathbf{r}_i - \mathbf{r}_j ^{-2(d-\phi\psi)}$
typical correlations:	$-\ln [C_{ij}]_{\text{av}}$	$\sim \kappa_{ij}  \mathbf{r}_i - \mathbf{r}_j ^\psi$
finite $T$ -susceptibility:	$\chi$	$\sim T^{-1} (-\ln T)^{2\phi-d/\psi}$
finite $H$ -magnetization:	$M$	$\sim (-\ln H)^{-\phi+d/\psi}$

Away from the critical point ( $\delta \neq 0$ ) the correlation length is finite and its average and typical value scale differently:

average correlation length:	$\xi_{\text{av}}$	$\sim \delta^{-\nu}$
typical correlation length:	$\xi_{\text{typ}}$	$\sim \xi_{\text{av}}^{1-\psi}$
spontaneous magnetization:	$M_0$	$\sim (-\delta)^{\nu(d-\phi\psi)}$

In spite of the finiteness of the average correlation length away from the critical point still arbitrarily large strongly-coupled clusters exist — though with an exponentially small probability — leading to algebraically decaying correlations in imaginary time. Phenomenologically, one can see that as follows.<sup>261,262</sup> Let  $L$  be the size of a region of *strongly coupled* spins. In a random system in the paramagnetic phase they occur with an exponentially small probability  $P(L) \propto \exp(-\lambda L^d)$ . For instance in the diluted ferromagnet strongly coupled regions are connected clusters and their probability is  $p^V$ , where  $V$  is the region's volume and  $p$  is the site occupation probability ( $0 < p < 1$ ). Then,  $\lambda$  is given by  $\lambda = |\ln p| > 0$ . The special feature of transverse-field Ising systems is that in first order perturbation theory the gap of a finite system containing  $L^d$  spins is exponentially small:  $\Delta_0 \sim \exp(-sL^d)$ . An exponentially small gap means an exponentially large tunneling time, and combining the two observations on cluster probability and relaxation time one obtains an algebraical decay for the

spin-spin correlation function:  $C(\tau) = [\langle \sigma_i(\tau)\sigma_i(0) \rangle]_{\text{av}} \sim \tau^{-\lambda/s} = \tau^{-d/z(\delta)}$ . The parameter  $z(\delta) = s/d\lambda$  is called the *dynamical exponent* in the Griffiths phase and it varies continuously with the distance from the critical point. The consequences, e.g., for the susceptibility are dramatic:  $\chi(\omega = 0) = \int_0^{1/T} d\tau C(\tau) \propto T^{-1+d/z(\delta)}$  which implies that for  $z > d$  the susceptibility diverges for  $T \rightarrow 0$  even away from the critical point. Since in random transverse-field Ising system  $z(\delta)$  grows without bounds for  $\delta \rightarrow 0$  (and thus merging with the critical dynamical exponent at  $\delta = 0$ , which is infinite), there is always a region around the critical point, where the susceptibility diverges.

In general the dynamical exponent  $z(\delta)$  introduced above is expected to determine all singularities occurring in the Griffiths-McCoy phase close to an IRFP<sup>248</sup>:

dynamical exponent:	$z(\delta)$	$\propto$	$\delta^{-\psi\nu}$
lowest energy scale:	$\Delta$	$\sim$	$L^{-z(\delta)}$
finite $H$ -magnetization:	$M$	$\sim$	$H^{1/z(\delta)}$
susceptibility:	$\chi(\omega = 0)$	$\sim$	$T^{-1+d/z(\delta)}$
nonlinear susceptibility:	$\chi_{nl}(\omega = 0)$	$\sim$	$T^{-1+d/3z(\delta)}$
specific heat:	$c$	$\sim$	$T^{d/z(\delta)}$

The last three tables summarize the scaling predictions at and close to a IRFP and in  $1d$  they have been confirmed many times, analytically and numerically.<sup>252,253,254,255,256,257,258,259</sup> In higher dimensions  $d \geq 2$  the randomly diluted Ising-ferromagnet in a transverse field is a show-case for a quantum phase transition governed by an IRFP. The site diluted model is defined by the Hamiltonian

$$H = -J \sum_{(ij)} \varepsilon_i \varepsilon_j \sigma_i^z \sigma_j^z - \Gamma \sum_i \varepsilon_i \sigma_i^x \quad (55)$$

and the bond diluted model by

$$H = -J \sum_{(ij)} \varepsilon_{ij} \sigma_i^z \sigma_j^z - \Gamma \sum_i \sigma_i^x \quad (56)$$

where  $\varepsilon_i$  and  $\varepsilon_{ij}$  are random variables that take on the values 1 with probability  $p$  and 0 with probability  $1 - p$ . Its phase diagram is depicted in Fig. 9.18

Along the vertical line starting from the point  $(p, \Gamma) = (p_c, 0)$  up to the multi-critical point the transition from the paramagnetic to the ferromagnetic phase is a *classical percolation transition*.<sup>263,264</sup> Denoting the distance from the critical point with  $\delta = p_c - p$  the connectivity correlation length

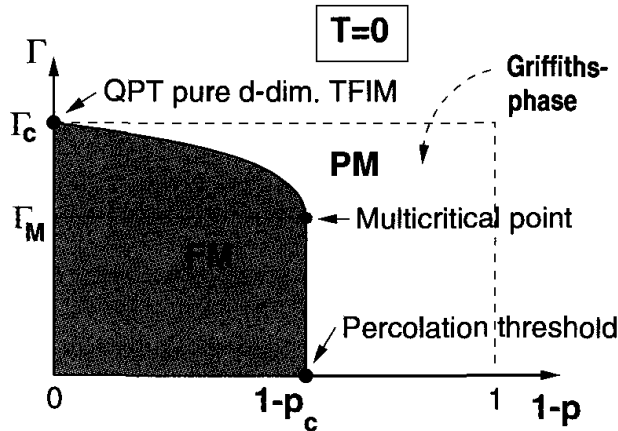


Fig. 9.18. Phase diagram of the diluted Ising ferromagnet in an transverse field  $\Gamma$  at zero temperature  $T = 0$ .

diverges upon approaching the percolation point  $1 - p_c$  as  $\xi \sim |\delta|^{-\nu_{\text{perc}}}$ . The number of spins  $M$  in the percolating cluster at  $p = p_c$  scales with the linear system-size  $L$  as  $M \sim L^{D_{\text{perc}}}$ , where  $D_{\text{perc}}$  is the fractal dimension of the percolating clusters. For small values of the transverse field  $\Gamma$  one expects the percolating cluster to be fully magnetized, which implies that the gap scales as  $\Delta \sim \exp(-L^{D_{\text{perc}}})$ . This means that  $\psi = D_{\text{perc}}$  in the IRFP scenario described above. Moreover, the connectivity correlation function at the percolation threshold  $p_c$  decays as  $C(r) \sim r^{-(d-2+\eta_{\text{perc}})}$ , which means that the exponent  $\phi$  is given by the relation  $2(d - \psi\phi) = (d - 2 + \eta_{\text{perc}})$ . To summarize the exponents characterizing the IRFP in the randomly diluted ferromagnet in a transverse field are related to the classical percolation exponents (which are exactly known in dimensions  $d = 2$  and in  $d > 6$ ) via:

$$\nu = \nu_{\text{perc}}, \quad \psi = D_{\text{perc}}, \quad \phi = (d + 2 - \eta_{\text{perc}})/D_{\text{perc}}. \quad (57)$$

For the random bond ferromagnet in a transverse field in dimensions  $d \geq 2$  one has to rely only on numerical calculations: In the  $2d$  ferromagnetic case quantum Monte-Carlo simulations<sup>265,266</sup> provided an evidence for an infinite randomness fixed point with  $\psi \approx 0.42$  and  $\phi \approx 2.1$ . Later a numerical implementation of the Ma-Dasgupta-Hu RG scheme indeed provided another evidence for an infinite randomness fixed point<sup>267</sup> with  $\psi = 0.42 \pm 0.06$ ,  $\phi = 2.5 \pm 0.4$ , which agrees with the QMC estimate within the error bars, and  $\nu = 1.07 \pm 0.15$ . For random Ising ferromagnets in a transverse field the existence of the IRFP dominating the quantum critical behavior thus appears to be confirmed for finite dimensions. Strictly speak-

ing detailed numerical studies have only been performed for  $d = 1$  and  $d = 2$  up to now, but there seems to be no strong argument against the existence of the IRFP also in higher, finite, dimensions although one expects the numerical and experimental visibility of the IRFP to diminish for increasing dimension  $d$ . In the mean field limit ( $d \rightarrow \infty$ ) the quantum phase transition is *not* described by an IRFP and obeys conventional scaling laws. In particular  $z$  is finite and Griffiths-McCoy singularities are absent.

What about the spin glass case? Quantum Monte Carlo simulations on the Ising spin glass with a transverse-field have been performed for the cases  $d = 2^{268,262}$  and  $d = 3^{269,270}$  they are reviewed in [246,247]. The main result is that the numerical data appeared to be compatible with a finite value for the dynamical exponent in  $d = 2$  and  $3$  and that the critical behavior can be described by conventional scaling laws. However, the existence of a Griffiths-McCoy phase away from the critical point has been uncovered, with a continuously varying dynamical exponent describing the singularities of the susceptibility and non-linear susceptibility. In contrast to the quantum Monte-Carlo simulations of the random bond ferromagnets no cluster-algorithm could be used in the quantum spin glass case, which restricted the system sizes and in particular the temperatures to rather small values (note that anisotropic finite size scaling demands that the temperature has to decrease exponentially with the system size at a quantum critical point described by an IRFP). In addition a homogeneous rather than a random transverse field has been used, which causes strong cross-over effects and the true asymptotic scaling behavior might be more difficult to extract. Therefore it might very well be that the indications found for the absence of a IRFP in the  $2d$  and  $3d$  quantum spin glass are still pre-asymptotic and that studies using larger system sizes and more sophisticated simulation methods could detect evidence for the IRFP also here.

Finally a word about the consequences of the aforementioned theoretical developments for the experiments. There it was observed that upon approaching the quantum critical point the divergence of the non-linear susceptibility was drastically suppressed indicating even the absence of a divergence at zero temperature. The numerical results, on the other hand, hint at a strong divergence of the non-linear susceptibility at the quantum critical point — even more than the IRFP scenario. Up to now no clear reason for the discrepancy has been pinned down. The possibility of a second-order transition turning a first-order one at low temperatures has been raised,<sup>271</sup> but this possibility can definitely be ruled out for a sys-

tem that can be described by the Hamiltonian (50) that we discussed here. We do not think that dipolar interactions of a magnetically diluted system cause substantial modifications of the picture that emerged for short range interactions. At this point one cannot rule out the possibility that the transverse field Ising Hamiltonian with quenched disorder is simply not a sufficiently detailed description of LiHo<sub>0.167</sub>Y<sub>0.833</sub>F<sub>4</sub>.

### 9.8.2. Mean-Field Theory

As a mean-field model of quantum Ising spin glass, we consider the Sherrington-Kirkpatrick model in a transverse field

$$H = - \sum_{(i,j)} J_{ij} \sigma_i^z \sigma_j^z - \Gamma \sum_i \sigma_i^x. \quad (58)$$

The first sum is over all pairs of spins and the couplings  $J_{ij}$  are quenched random variables that obey the Gaussian distribution with zero mean and variance  $J^2/N$ , where  $N$  is the number of spins.  $\Gamma$  is the strength of the transverse field. Although no exact solution has been found for finite  $\Gamma$ , the phase diagram of this model has been well delineated. At zero transverse field the transition is the well-known classical transition of the SK model at  $T_c(\Gamma = 0) = J$ . For sufficiently high temperature and/or sufficiently large  $\Gamma$ , thermal and/or quantum fluctuations destroy the spin glass order, yielding a paramagnet.<sup>272</sup> For low  $T$  and small  $\Gamma$  one finds a SG ordered phase, apparently with broken replica symmetry.<sup>273</sup> Monte Carlo calculation, numerical spin summation<sup>274</sup> and perturbation expansion<sup>275</sup> in  $1/\Gamma$  have determined the phase boundary to some precision. As in the classical model, the infinite range interactions apparently wipe out the Griffiths singularities discussed in the last subsection. The critical behavior along the line  $T_c(\Gamma)$  is expected to be the same as the classical critical behavior, i.e., the non-linear susceptibility diverges as  $\chi_{nl} \sim (T - T_c(\Gamma))^{-\gamma}$  with  $\gamma = 1$ , the specific heat exponent is  $\alpha = 0$ , etc.

The zero temperature quantum critical point  $\Gamma_c(T = 0)$  is in a different universality class and has been studied in [276,277,278]. The static approximation — the approximation usually applied to small field values in which the imaginary time correlation function  $C(\tau) = \langle \sigma_i(\tau) \sigma_i(0) \rangle$  is assumed to be time independent — is not valid at  $T = 0$  (large fields) and the full functional form of  $C(\tau)$  has to be explored. The dynamical self-consistency equations obtained via standard manipulations<sup>272,279</sup> was analyzed at  $T = 0$  at the quantum critical point in [276,277,278], and it turned out that the quantum critical point is located at  $\Gamma_c \approx 0.7J$ . At  $\Gamma > \Gamma_c$  (and

zero temperature)  $C(\tau)$  decays exponentially with  $\tau$  as  $\tau \rightarrow \infty$ , indicating a gap  $\Delta$  in the corresponding spectral density; at  $\Gamma = \Gamma_c$ ,  $C(\tau)$  decays as  $1/\tau^2$ , and in the ordered phase,  $C(\tau) \rightarrow q_{\text{EA}}$ . The Fourier transform of  $C(\tau)$  has the form  $C(\omega) \sim \text{const.} - \sqrt{\omega^2 - \Delta^2}$  for  $\Gamma \geq \Gamma_c$ , which is responsible for the  $1/\tau^2$  behavior at  $\Gamma_c$  and it turned out that the correlation time diverges as  $\xi_\tau \sim 1/\Delta \sim [(\Gamma - \Gamma_c)^{-1} \ln(\Gamma - \Gamma_c)]^{1/2}$ . Thus we can define an exponent  $z\nu$ , anticipating anisotropic scaling in space and time in the short range model, which takes the value  $z\nu = 1/2$  in the infinite-range model. Since  $C(\tau \rightarrow \infty) = q_{\text{EA}}$  is the Edwards-Anderson order parameter, we may also define  $q_{\text{EA}} = (\Gamma_c - \Gamma)^\beta$  and it was found that  $\beta = 1$ . At  $\Gamma = \Gamma_c$  one expects  $C(\tau) \sim \tau^{-\beta/z\nu}$ , which is satisfied with the values obtained. The non-linear susceptibility diverges as  $1/\Delta$ , which implies with  $\chi_{nl} \sim (\Gamma - \Gamma_c)^{-\gamma}$  that  $\gamma = 1/2$ . Studying Gaussian fluctuations around the saddle-point solution valid for infinite range one finds<sup>278</sup> for the correlation length exponent above the upper critical dimension (i.e.  $d \geq 8$ ) that  $\nu = 1/4$  and therefore  $z = 2$ . Moreover  $\eta = 0$  in mean field theory. The complete collection of critical exponents obtained so far in comparison with the classical model ( $T > 0$ , where we assume to cross the phase boundary under a non-vanishing angle) are as follows:

	$\beta$	$\gamma$	$\nu$	$z$
quantum ( $T = 0$ )	1/2	1/2	1/4	2
classical ( $T = 0$ )	1	1	1/2	—

(59)

Note that as a consequence of the absence of Griffiths-singularities in mean-field models the dynamical exponent  $z$  is finite in contrast to the IRFP scenario that is supposedly valid for the finite-dimensional models. In a longitudinal field one obtains, in analogy to the classical case, an AT manifold in the  $T, \Gamma, h$  phase diagram below which replica symmetry is broken and the system is in the SG phase.

The dynamics of the model (58) in the paramagnetic phase has been studied in [280], where the dynamical single-site self-consistency equations have been iteratively solved using a quantum Monte Carlo scheme developed in [281]. They mapped the spin-glass transition line in the  $\Gamma-T$  plane using the stability criterion  $1 = J\chi_{\text{loc}}$ , where  $\chi_{\text{loc}} = \int_0^\beta d\tau C(\tau)$  is the local susceptibility. They found a second-order transition line ending at a quantum critical point at  $T = 0$  in agreement with the argument presented above. Going down in temperature to  $T \sim 0.01J$  and extrapolating the results to  $T = 0$  they determined a precise value for the critical field  $\Gamma_c = 0.76 \pm 0.01$ , which lies between previous estimates.<sup>273,276</sup> The asymp-

totic form of  $C(\tau) \sim \tau^{-2}$  found in [276] was also confirmed. A comparison of the results for the low-frequency susceptibility with the experimental curves obtained for LiHo<sub>0.167</sub>Y<sub>0.833</sub>F<sub>4</sub> in [243] yields a good agreement.

A different class of mean-field spin-glass models has been studied in [271] — simplified in so far as spherical spins rather than Ising spins were considered and more general in so far as  $p$ -spin interactions were considered. The quantum fluctuations are introduced via a kinetic energy rather than the transverse field. The corresponding quantum spherical  $p$ -spin-glass Hamiltonian is defined by

$$H = \frac{1}{2M} \sum_{i=1}^N \hat{p}_i^2 - \sum_{i_1, \dots, i_p} J_{i_1, \dots, i_p} s_{i_1} \cdots s_{i_p} \quad (60)$$

where  $s_i$  are “soft-spins” fulfilling the spherical constraint  $\sum_{i=1}^N s_i(t)^2 = N$  for all times  $t$ . Quantum mechanics is introduced into the classical  $p$ -spin glass via the canonical momenta  $\hat{p}_i$  that fulfill the commutation relation  $[\hat{p}_i, s_j] = -i\hbar\delta_{ij}$ . The multi-spin coupling constants are taken from a Gaussian distribution with zero mean and variance  $\tilde{J}p!/(2N^{p-1})$  with  $\tilde{J}$  being a constant of  $\mathcal{O}(1)$ .

Before we discuss this model we want to clarify the connection to the SK model in a transverse field discussed above. The replacement of Ising spins  $S_i = \pm 1$  by continuous spins  $s_i \in [-\infty, +\infty]$  is often performed in the theory of critical phenomena — the discrete symmetry is then enforced by a quartic term  $\sum_i s_i^4$  in the Hamiltonian (this is just the usual  $\Phi^4$  Ginzburg-Landau theory for critical phenomena with a discrete symmetry), which also restricts automatically the spin length. Analytically the quartic term causes extra complications in all computations, saddle point evaluations, RG calculations, dynamical formalism etc. — for which reason one often skips it and replaces it by a spherical constraint (either strictly or via a Lagrangian parameter having the same effect as a chemical potential). Unfortunately the classical spherical mean-field spin-glass model with the usual 2-spin interactions does not have a non-trivial spin glass phase. Therefore, generalizations to  $p$ -spin interactions are sometimes considered.<sup>138</sup> At this point a clear connection to the original magnetic system of interest is already lost. Nevertheless, one might expect that one can learn something about possible scenarios.

Finally spherical spins cannot be quantized in the same way as Ising spins via the application of a transverse field. Therefore they are usually quantized via the introduction of a kinetic energy term as in (60). In addi-

tion, various analytical techniques available for interacting soft spins with kinetic energy, such as the Schwinger-Keldysh formalism,<sup>282</sup> are not available for spin operators. The microscopic details of the quantum dynamics described by either a transverse field or a kinetic energy term might be very different, on large timescales, however, one expects a similar behavior for the following reason. To see this, let us consider a model that consists of two terms; an arbitrary classical Hamiltonian,  $H_{\text{cl}}$ , that is diagonal in the  $z$ -representation of the spins, and the transverse-field term. Performing a Trotter decomposition of the partition function of this model, one obtains

$$\begin{aligned} \text{Tr} e^{-\beta(\Gamma\sigma^x + H_{\text{cl}}(\sigma^z))} &= \lim_{\Delta\tau \rightarrow 0} \prod_{\tau=1}^{L_\tau} \left\langle S_\tau \left| e^{-\Delta\tau[\Gamma\sigma^x + H_{\text{cl}}(\sigma^z)]} \right| S_{\tau+1} \right\rangle \\ &\propto \lim_{\Delta\tau \rightarrow 0} \sum_{S_1, \dots, S_{L_\tau}} \exp \left( -\Delta\tau \left[ \sum_{\tau=1}^{L_\tau} K(S_\tau - S_{\tau+1})^2 + H_{\text{cl}}(S_\tau) \right] \right) \quad (61) \end{aligned}$$

where  $L_\tau$  is the number of Trotter slices in the imaginary time direction,  $\Delta\tau = \beta/L_\tau$  and  $K$  given by  $e^{-2K} = \tanh(\Delta\Gamma)$ . For  $\Delta\tau \ll 1$  it is  $K = |\ln(\Delta\tau\Gamma)|/2$ . In the last step we neglected a constant factor  $\cosh(\Delta\tau\Gamma)^{L_\tau}$ . If we choose  $\Delta\tau$  as a small time cut-off (representing the typical spin flip time) we can approximate the last Trotter sum as the imaginary time path integral

$$Z \approx \int \mathcal{D}S(\tau) \exp \left( \int_0^\beta d\tau \left[ \frac{M}{2} \left( \frac{\partial S}{\partial \tau} \right)^2 + H_{\text{cl}}(S(\tau)) \right] \right) \quad (62)$$

where  $M = 2K\Delta\tau = \Delta\tau|\ln(\Gamma\Delta\tau)|$ . The first term in the integral of the action is identical to what one would obtain for the kinetic energy if one writes down the imaginary time path integral for the partition sum of the Hamiltonian (60). In this way, the transverse-field term and the kinetic-energy term are related.

In [271] the equilibrium properties of the model were obtained using a replicated imaginary-time path integral formalism<sup>279</sup> and analyzing the dynamical self-consistency equations for the spin auto-correlation function  $C(\tau)$  arising in the limit  $N \rightarrow \infty$  from a saddle point integration. The result for the phase diagram, EA order-parameter and linear susceptibility in the case  $p = 3$  are depicted in Fig. 9.19, where the parameter  $\Gamma = \hbar^2/(JM)$  has been used — resembling the transverse field strength (since for  $\Gamma \rightarrow 0$  one recovers the classical case). Above a temperature  $T^*$  one has a continuous transition at a critical point  $\Gamma = \Gamma_c(T)$  from a paramagnetic phase with

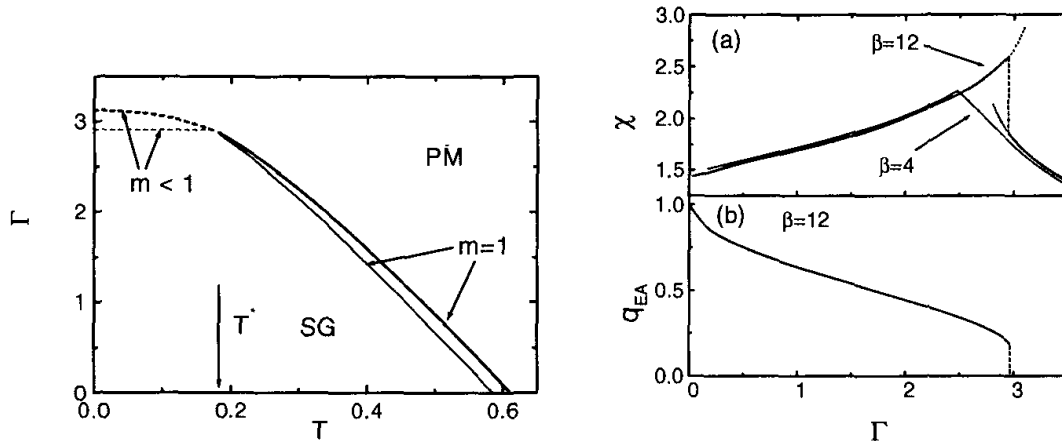


Fig. 9.19. **Left:** Static (thin lines) and dynamic (thick lines) phase diagrams of the  $p$ -spin model for  $p = 3$ . Solid and dashed lines represent second and first order transitions, respectively. **Right:** Magnetic susceptibility (a) and Edwards-Anderson order parameter (b) of the  $p=3$  model. (From [271]).

vanishing EA order parameter to a spin glass phase with  $q_{EA} \neq 0$  and one-step replica-symmetry-breaking (1RSB). Although the EA order-parameter jumps discontinuously the transition is second order: there is no latent heat (as in the classical case  $\Gamma = 0$ ) and the susceptibility has only a cusp. This is due to the fact that the parameter  $m$  characterizing the Parisi order parameter function  $q(x)$  (which is a step function with a single step at  $x = m$ ) is unity at the transition. However, for temperatures below  $T^*$  this parameter jumps at the transition, too, and the transition becomes discontinuous; for  $T < T^*$  the transition is of the first order with latent heat and a discontinuous susceptibility (see Fig. 9.19).

### 9.8.3. Mean-Field Theory — Dissipative Effects

An important question that arises for interacting quantum spins at low temperatures are the effects of a dissipative environment.<sup>283,284</sup> This is usually described in terms of its collective excitations, lattice vibrations, spin or charge fluctuations, etc., which may be thought of as an ensemble of independent quantum harmonic oscillators.<sup>285,286,287,288,289</sup> A concrete example of a single quantum degree of freedom, a spin-1/2 or a so-called two-level-system (TLS), coupled to a bath of bosons is the well-known spin-boson-model:<sup>283,284</sup>

$$H = H_S + H_B + H_{SB} \quad (63)$$

where  $H_S$ ,  $H_B$  and  $H_{SB}$  denote the Hamiltonian of the system, the bath and their coupling, respectively. These are given by

$$\begin{aligned} H_S &= -\Gamma\sigma^x \\ H_B &= \frac{1}{2}\sum_n(p_n^2/m_n + m_n\omega_n^2x_n^2) \\ H_{SB} &= -\sum_nc_nx_n\sigma^z \end{aligned} \quad (64)$$

where  $\Gamma$  is the transverse field (or tunneling matrix element in the context of TLSs),  $n$  the index enumerating an infinite number of harmonic oscillators with coordinates and momenta,  $x_n$  and  $p_n$ , and mass and frequency,  $m_n$  and  $\omega_n$ , respectively. The constant  $c_n$  is the coupling between oscillator  $n$  and the spin. The spectral density of the environment,  $I(\omega) = \pi\sum_n(|c_n|^2/(m_n\omega_n)\delta(\omega - \omega_n))$ , is commonly assumed to take the standard form<sup>284</sup>

$$I(\omega) = 2\alpha\hbar(\omega/\omega_{ph})^{s-1}\omega e^{-\omega/\omega_c}, \quad (65)$$

where  $\alpha$  is a dimensionless coupling constant,  $\omega_c$  a high frequency cut-off (which can be set to  $\omega_c = \infty$  if  $0 < s < 2$ ), and  $\omega_{ph}$  a phonon frequency necessary in the non-ohmic ( $s \neq 1$ ) case to keeps  $\alpha$  dimensionless.

With standard techniques<sup>290,283</sup> one can integrate out the oscillator degrees of freedom to express the partition function of the system solely in terms of the spin variables

$$Z = \text{Tr } e^{-\beta H} = \int \mathcal{D}\sigma(\tau) \mathcal{T} \exp(-S/\hbar), \quad (66)$$

where  $\int \mathcal{D}\sigma(\tau)$  denotes a path integral over all spin configurations (in time),  $\mathcal{T}$  is the imaginary time ordering operator and the action is

$$S = -\int_0^{\beta\hbar} d\tau \Gamma\sigma^x(\tau) - \frac{1}{2}\int_0^{\beta\hbar} d\tau \int_0^{\beta\hbar} d\tau' K(\tau - \tau')\sigma^z(\tau)\sigma^z(\tau'). \quad (67)$$

The kernel  $K(\tau)$  is related to the spectral density  $I(\omega)$  and is for the ohmic case ( $s = 1$ ) essentially an inverse square  $K(\tau - \tau') \propto \alpha/(\tau - \tau')^2$ . The effect of the dissipative environment is therefore a long range interaction of the quantum spin in imaginary time. In analogy to the Ising model with inverse square interactions<sup>291</sup> depending on the strength of the coupling constant  $\alpha$ , the system is ferromagnetically ordered or paramagnetic in the imaginary time direction; for large  $\alpha$  the spin is frozen and for small  $\alpha$  the spin will tunnel.

Indeed, for the ohmic case, at zero temperature, there is a phase transition at  $\alpha = 1$ .<sup>286,287</sup> For  $\alpha < 1$  there is tunneling and two distinct regimes

develop. If  $\alpha < 1/2$ , the system relaxes with damped coherent oscillations; in the intermediate region  $1/2 < \alpha < 1$  the system relaxes incoherently. For  $\alpha > 1$  quantum tunneling is suppressed and  $\langle \sigma^z \rangle \neq 0$ , signaling that the system remains localized in the state in which it was prepared. These results also hold for sub-Ohmic baths while weakly damped oscillations persist for super-Ohmic baths.<sup>283</sup> At finite temperatures (but low enough such that thermal activation can be neglected) there is no localization but the probability of finding the system in the state it was prepared decreases slowly with time for  $\alpha > \alpha_c$ .

These conclusions hold for a single spin interacting with a bath. The question then arises as to which are the effects of the interplay between the spin-spin interactions and the spin-noise coupling in the physics of the interacting system. In [282] the effect of a dissipative bath on a mean-field spin glass model with  $p$ -spin interactions has been investigated. They studied the dissipative spin-boson system (64) for  $N$  interacting spins  $H = H_S + H_B + H_{SB}$ , where the bath Hamiltonian is the same, the coupling Hamiltonian gets an additional sum over the spin index  $i$  and  $H_S$  is now the  $p$ -spin Hamiltonian with transverse field

$$H_S = -\Gamma \sum_{i=1}^N \sigma_i^x - \sum_{i_1, \dots, i_p} J_{i_1, \dots, i_p} \sigma_{i_1}^z \cdots \sigma_{i_p}^z. \quad (68)$$

The second term, namely, the multi-spin interaction term is the same as the one in (60). For the reason explained in the last section it is analytically easier to study spherical spins instead of quantum spin-1/2 degrees of freedom and the quantization of the spherical spins is done via the introduction of a kinetic energy term. The partition function then reads

$$Z = \int \mathcal{D}\sigma(\tau) \exp(-S/\hbar), \quad (69)$$

with the action

$$\begin{aligned} S = & \int_0^{\hbar\beta} d\tau \left[ \frac{M}{2} \sum_i \left( \frac{\partial s_i(\tau)}{\partial \tau} \right)^2 - \sum_{i_1 < \dots < i_p} J_{i_1, \dots, i_p} s_{i_1}(\tau) \cdots s_{i_p}(\tau) \right. \\ & \left. + z \sum_i [s_i^2(\tau) - 1] \right] - \int_0^{\hbar\beta} d\tau \int_0^{\hbar\beta} d\tau' K(\tau - \tau') s_i(\tau) s_i(\tau'), \end{aligned} \quad (70)$$

where the first term is the kinetic-energy term already motivated in (61-62) replacing the transverse-field term, the second is the  $p$ -spin interaction term, the third a term with the Lagrangian multiplier  $z$  enforcing the spherical

constraint and the last term is the long range interaction imaginary time (67) that is generated by the integration over the bath variables.

Starting from (70) the saddle point equations for the self-consistent single-spin dynamics were derived<sup>282</sup> and the phase diagram computed. Analogous to the non-dissipative case discussed in the previous subsection a critical line with a second-order section (close to the classical critical point ( $T_d, \Gamma = 0$ )) and a first-order section (close to the quantum critical point ( $T = 0, \Gamma_d$ )) was obtained in the presence of a dissipative environment. The second order critical line is determined by the condition  $m = 1$ , the first order critical line is defined as the locus of the points where a marginally stable solution first appears with decreasing  $\Gamma$  for  $T$  fixed. For each  $\Gamma$  and  $\alpha$  this defines a *dynamic* transition temperature  $T_d(\Gamma, \alpha)$ . The qualitative features of the phase diagram, similar to those found for the isolated system, see the discussion in the previous section. Notice that the line  $T_d(\Gamma, \alpha)$  lies always *above*  $T_s(\Gamma, \alpha)$ , the static critical line that we shall discuss below.

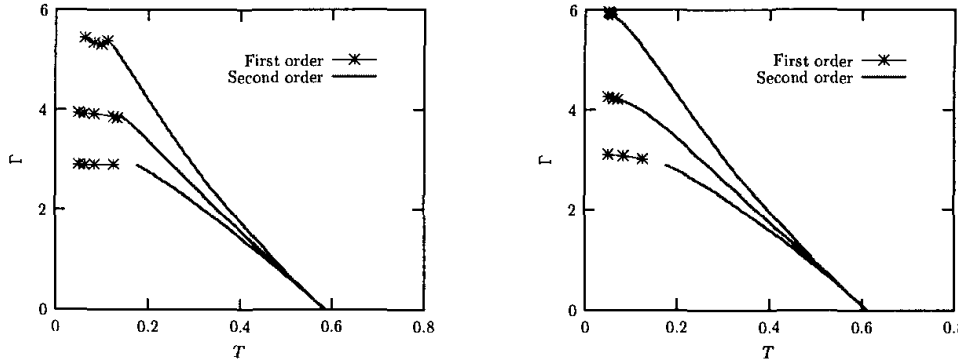


Fig. 9.20. Static (left) and dynamic (right) phase diagrams for the  $p = 3$  spin model coupled to an Ohmic bath ( $s = 1$ ). The couplings to the bath are  $\alpha = 0, 0.25$ , and  $0.5$  from bottom to top. The solid line and line-points represent second and first order transitions, respectively. (From [282]).

On the right side of Fig. 9.20 the dynamic phase diagrams obtained for  $p = 3$  and three values of the coupling to an Ohmic bath,  $\alpha = 0, 0.25, 0.5$  is shown. The full line and the line-points represent second and first order transition, respectively.

The first observation that can be made is that in the limit  $\Gamma \rightarrow 0$  the transition temperature is independent of the strength of the coupling to the bath. This is a consequence of the fact that in the limit  $\Gamma \rightarrow 0$  the partition

function is essentially determined by the zero-frequency components of the pseudo-spin which are decoupled from the bath. This result is however non-trivial from a dynamical point of view, since it implies that the dynamic transition of a classical system coupled to a colored classical bath is not modified by the latter.

The second observation is that the size of the region in the phase space where the system is in the ordered state increases with  $\alpha$ . Coupling to the dissipative environment thus stabilizes this state. This follows from simple physical considerations. The interaction term in the action favors spin-glass order. Coupling to the bath favors localization and its effect is to reduce the effective tunneling frequency. Therefore, in the presence of the bath, the value of the bare tunneling frequency needed to destroy the ordered state must increase with  $\alpha$ . Even if the localized state and the glassy state may seem superficially similar, they are indeed very different. In the former, the correlation function  $C(t + t_w, t_w)$  approaches a plateau as a function of  $t$  and never decays toward zero while in the latter the relaxation first approaches a plateau but it eventually leaves it to reach zero for  $t \gg t_w$ . The fact that the coupling to the environment favors the ordered state also reflects itself in the value taken by the order parameters  $C(\tau)$  and  $q_{EA}$ . As  $\alpha$  increases,  $q_d(\tau)$  reaches a higher plateau level at long imaginary times.

#### 9.8.4. Mean-Field Theory — Dynamics

The out-of-equilibrium dynamics in real time of the quantum spherical  $p$ -spin glass model coupled to a dissipative environment, which was discussed in the last subsection, was actually studied earlier<sup>292</sup> than the equilibrium properties. The response and correlation function are defined in analogy to the classical case;  $C(t + t_w, t_w) = N^{-1} \sum_i (s_i(t + t_w)s_i(t_w) + s_i(t_w)s_i(t + t_w))$  (note that the time evolution is now governed by the quantum dynamics and  $C$  has to be symmetrized in the operators  $s_i(t + t_w)$  and  $s_i(t_w)$ ) and  $R(t + t_w, t_w) = N^{-1} \sum_i \delta s_i(t + t_w)/\delta h_i(t_w)$ .

In equilibrium the quantum FDT relates  $R(t)$  and  $C(t)$ :

$$R(t) = \frac{2i}{\hbar} \theta(t) \int \frac{d\omega}{2\pi} e^{-i\omega t} \tanh(\beta\hbar\omega/2) C(\omega) \quad (71)$$

Away from the critical line,  $C$  and  $R$  decay to zero very fast with oscillations. Approaching the critical line  $T_d(\alpha)$ , the decay slows down and if  $T_d > 0$  a plateau develops in  $C$ . At the critical line the length of the plateau tends to infinity.

In the glassy phase (below the transition) the system does not reach equilibrium. For small time differences the dynamics is stationary and time translational invariance as well as the QFDT holds:  $\lim_{t_w \rightarrow \infty} C(t+t_w, t_w) = q + C_{\text{eq}}(t)$ . For large times the dynamics is non-stationary, time translational invariance nor the QFDT does not hold, and the correlations decay from  $q$  to 0. The decay of  $C$  becomes monotonic in the aging regime, which implies  $C_{\text{aging}}(t+t_w, t_w) = c(h(t_w)/h(t+t_w))$  (see subsection 9.5.2). One can generalize the QFDT in the same spirit as the classical FDT was generalized (see subsection 9.5.4):

$$R(t+t_w, t_w) = \frac{2i}{\hbar} \theta(t) \int \frac{d\omega}{2\pi} e^{-i\omega t} \tanh(X(t+t_w, t_w) \beta \hbar \omega / 2) C(t+t_w, \omega) \quad (72)$$

with  $C(t, \omega) = 2\text{Re} \int_0^t ds \exp[i\omega(t-s)]C(t, s)$ . Again, as in the classical case (see subsection 9.5.4),  $T_{\text{eff}} \equiv T/X(t+t_w, t_w)$  acts as an effective temperature in the system. For a model with two time-sectors it is proposed

$$X(t+t_w, t_w) = \begin{cases} X_{\text{st}} = 1 & \text{if } t \leq T(t_w) \\ X_{\text{age}}(\hbar, T) & \text{if } t > T(t_w) \end{cases} .$$

with  $X_{\text{age}}$  a non-trivial function of  $\hbar$  and  $T$  and  $T(t_w)$  is a certain time-scale that separates the stationary and aging time-regimes. When  $t$  and  $t_w$  are widely separated, the integration over  $\omega$  in (72) is dominated by  $\omega \sim 0$ . Therefore, the factor  $\tanh(X_{\text{age}}(t+t_w, t_w) \beta \hbar \omega / 2)$  can be substituted by  $X_{\text{age}} \beta \hbar \omega / 2$  (even at  $T = 0$  if  $X_{\text{age}}(\hbar, T) = x(\hbar)T$  when  $T \sim 0$ ). Hence,

$$R_{\text{age}}(t+t_w, t_w) \sim \theta(t) X_{\text{age}} \beta \partial_{t_w} C_{\text{age}}(t+t_w, t_w) \quad (73)$$

and one recovers, in the aging regime, the *classical* modified FDT.<sup>138,293</sup>

The self-consistency equations for  $C(t+t_w, t_w)$  and  $R(t+t_w, t_w)$  were evaluated numerically in [292]. An example of the solution is shown in Fig. 9.21 for  $p = 3$ . In all figures the following parameters have been chosen: zero temperature  $T = 0$ , the width of the coupling distribution  $J = 1$ , the frequency cut-off for the oscillator bath set to  $\omega_c = 5$ , the mass in the kinetic energy term  $M = 1$ , and the strength of the quantum fluctuations  $\tilde{\hbar} = \alpha \hbar$  (where  $\alpha$  is the spin-bath coupling strength) is  $\tilde{\hbar} = 0.1$ .

These plots demonstrate the existence of the stationary and aging regimes. For  $t < T(t_w)$  (e.g.  $T(40) \sim 5$ ) time translational invariance and fluctuation dissipation theorem are established while beyond  $T(t_w)$  they break down. For  $\tilde{\hbar} = 0.1$  the plateau in  $C$  is at  $q \sim 0.97$ .  $C$  oscillates around  $q$  but is monotonous when it goes below it. In the inset the dependence of  $q_{EA}$  on  $\tilde{\hbar}$  for  $T = 0$  is presented. Quantum fluctuations generate

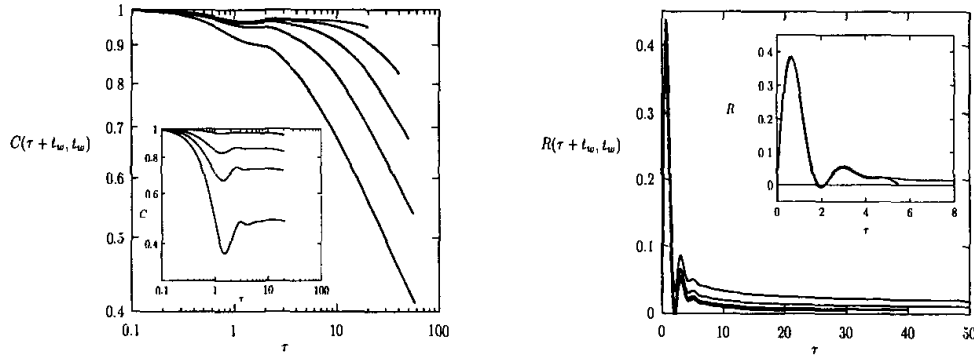


Fig. 9.21. **Left:** The correlation function  $C(\tau + t_w, t_w)$  vs  $\tau$  for the  $p = 3$  quantum spherical  $p$ -spin SG model. The waiting times are, from bottom to top,  $t_w = 2.5, 5, 10, 20, 40$ .  $q_{EA} \sim 0.97$ . In the inset, the same curves for  $t_w = 40$  and, from top to bottom,  $\tilde{h} = 0.1, 0.5, 1, 2$ . **Right:** The response function for the same model as in the left part. The waiting-times increase from top to bottom. In the inset, check of FDT in the stationary regime. The full line is  $R(t + t_w, t_w)$  for  $t + t_w = 40$  fixed and  $t_w \in [0, 40]$ . The dots are obtained from Eq.(72) with  $X_{st} = 1$ , using the numerical data for  $C_{\text{stat}}(t) = C(t + t_w, t_w) - q$  ( $q_{EA} \sim 0.97$ , see left part). In both cases the response is plotted against  $t$ . (From [292]).

a  $q_{EA} < 1$  such that the larger  $\tilde{h}$  the smaller  $q_{EA}$ . The addition of thermal fluctuations has a similar effect, the larger  $T$ , the smaller  $q_{EA}$ . In order to check the FDT in the stationary regime, in the inset of the right part of Fig. 9.21 a comparison is shown of  $R(t + t_w, t_w)$  from the numerical algorithm for  $t + t_w = 40$  fixed and  $t_w \in [0, 40]$  (full line) with  $R(t + t_w, t_w)$  from Eq.(72) with  $X = 1$  using  $C_{\text{stat}}(t) = C(t + t_w, t_w) - q$ ,  $q \sim 0.97$  obtained from the algorithm (dots). The accord is very good if  $t \leq T(t_w) \sim 5$ . Finally, when one plots parametrically the integrated response  $\chi$  vs.  $C$  one finds that for  $C < q \sim 0.97$  the  $\chi$  vs  $C$  curve approaches a straight line of *finite* slope  $1/T_{\text{eff}} = X_{\text{age}}/T \sim 0.60$ .

### 9.8.5. Heisenberg Quantum Spin Glasses

The spin-1/2 Heisenberg quantum spin glass is defined by the Hamiltonian (48) where the random exchange interactions  $J_{ij}$  can be ferromagnetic and anti-ferromagnetic. The system cannot be studied efficiently with quantum Monte-Carlo methods, due to the sign problem arising from the frustration. Therefore, not much is known about these models in finite dimensions, and also the mean field theory becomes tractable only in certain limits and approximations.

### 9.8.5.1. Finite Dimensions

In [294] and later in [295] small clusters of the two-dimensional Heisenberg quantum spin glass were studied using exact diagonalization. The average total spin in the ground state turned out to scale as  $S \propto \sqrt{N}$ , where  $N$  is the number of sites. The spin glass order parameter in the ground state extrapolates to a small but non-vanishing value in the thermodynamic limit and the spin stiffness does not scale to zero either in the thermodynamic limit. Ma-Dasgupta-Hu renormalization group studies<sup>251,296</sup> were performed for randomly frustrated spin-ladders<sup>297</sup> and in  $d = 2$  and  $3$ <sup>298</sup> for various lattices and spin-values. The general idea of this RG procedure was already described in subsection 9.8.1; large energies (in the form of exchange interactions) are successively decimated, ferromagnetic bonds lead to large spin formation and anti-ferromagnetic bonds to a spin reduction or even elimination in case of equal effective spins connected by the bond to be decimated. In two and three dimensions, it was also observed that the final magnetic moment to be eliminated increased with system size as  $\sqrt{N}$ , which corresponds to the aforementioned observation for the ground state spin in small clusters. In addition the Ma-Dasgupta-Hu RG calculations in [298] showed that the probability distribution of the low energy excitations scales as  $P(\Delta) \sim \Delta^\omega$  with  $\omega = 0$  for  $2d$  and  $3d$  and that the dynamical critical exponent is  $z = 2$  in  $d = 2$  and  $z = 3/2$  in  $d = 3$ .

### 9.8.5.2. Mean-Field Model

The first analytical treatment of the mean-field model of the Heisenberg quantum spin glass was performed in [279] applying the replica theory. Although the solution was confined to the paramagnetic state, the arguments for the existence of a low-temperature spin-glass phase were given and the critical temperature was estimated.

Later a Landau theory for quantum rotors on a regular  $d$ -dimensional lattice was studied in [278], which is defined by the Hamiltonian

$$H = \frac{g}{2} \sum_i \hat{\mathbf{L}}_i^2 - \sum_{\langle ij \rangle} J_{ij} \hat{\mathbf{n}}_i \cdot \hat{\mathbf{n}}_j , \quad (74)$$

where  $\hat{\mathbf{n}}_i$  are  $M$ -component vectors of unit length ( $\hat{\mathbf{n}}_i^2 = 1$ ) and represent the orientation of the rotors on the surface of a sphere in  $M$ -dimensional rotor space. The operators  $\hat{\mathbf{L}}_{i\mu\nu}$  ( $\mu < \nu$ ,  $\mu, \nu = 1, \dots, M$ ) are the  $M(M - 1)/2$  components of the angular momentum  $\hat{\mathbf{L}}_i$  of the rotor: the first term in  $H$  is the kinetic energy of the rotor with  $1/g$  the moment of inertia.

The different components of  $\hat{\mathbf{n}}_i$  constitute a complete set of commuting observables and the state of the system can be described by a wave function  $\Psi(n_i)$ . The action of  $\hat{\mathbf{L}}_i$  on  $\Psi$  is given by the usual differential form of the angular momentum  $\hat{\mathbf{L}}_{i\mu\nu} = -i(n_{i\mu}\partial/\partial_{i\nu} - n_{i\nu}\partial/\partial_{i\mu})$ . The difference between rotors and Heisenberg-Dirac quantum spins is that the components of the latter at the same site do not commute, whereas the components of the  $\hat{\mathbf{n}}_i$  do.

In [278] a Landau theory for this model is derived and it is shown that for a suitable distribution of exchange constants  $J_{ij}$  this model displays spin-glass and quantum paramagnetic phases and a zero-temperature quantum phase transition between them. The mean-field phase diagram near the  $T = 0$  critical point is mapped out as a function of  $T$ , the strength of the quantum coupling  $g$  and applied fields. The spin glass phase has replica symmetry breaking. Moreover, the consequences of fluctuations in finite dimensions are considered and above  $d = 8$  the transition turned out to be controlled by a Gaussian fixed point with mean-field exponents. Below  $d = 8$  a runaway RG flow to strong coupling was found.

Recently the mean-field Heisenberg quantum spin glass model was generalized from the  $SU(2)$  spin algebra to an  $SU(N)$  symmetry and solved in the limit  $N \rightarrow \infty$ .<sup>299</sup> Certain universal critical properties are shown to hold to all orders in  $1/N$ . A spin-glass transition was found for all values of the spin  $S$  and the phase diagram as a function of the spin  $S$  and temperature  $T$  was described. The quantum critical regime associated with the quantum transition at spin value  $S = 0$  and the various regimes in the spin-glass phase at high spin are analyzed. The specific heat is shown to vanish linearly with temperature.

The out-of-equilibrium dynamics of the the same model in the same limit  $N \rightarrow \infty$ , but coupled to a thermal bath, was studied in [300]. It was found that the model displays a dynamical phase transition between a paramagnetic and a glassy phase. In the latter, the system remains out-of-equilibrium and displays an aging phenomenon, which we characterize using both analytical and numerical methods. In the aging regime, the quantum fluctuation-dissipation relation is violated and replaced over a very long time-range by its classical generalization, as in models involving simple spin algebras studied previously.

In the context of Heisenberg spin glasses also the work on metallic spin glasses should be mentioned, which were first considered in [301] and later more extensively in [302], [303] and [304]. The main ingredient of a metallic spin glass is an itinerant electron systems with random (and frustrated)

exchange interactions between the electron spins. Thus in contrast to the spin glass systems discussed so far the spins are not fixed to particular sites but can diffuse (quantum mechanically) from site to site. These systems are motivated by experiments on heavy-fermion compounds such as  $Y_{1-x}U_xPd_3$ ,<sup>305</sup> which appear to show a paramagnetic to spin-glass transition with increasing doping,  $x$ , in a metallic regime. To be concrete the Hamiltonian studied in [303] is

$$H = - \sum_{i < j, \alpha} t_{ij} c_{i\alpha} c_{j\alpha} - \sum_{i < j, \mu} J_{ij} S_{i\mu} S_{j\mu} + H_{\text{int}}, \quad (75)$$

where  $c_{i\alpha}$  annihilates an electron on site  $i$  with spin  $\alpha = \uparrow, \downarrow$ , and the spin operator is given by  $S_{i\mu} = \sum_{\alpha\beta} c_{i\alpha}^+ \sigma_{\alpha\beta}^\mu c_{i\beta}/2$ , with  $\sigma^\mu$  the Pauli spin matrices. The sites  $i, j$  lie on a  $d$ -dimensional lattice, the hopping matrix elements  $t_{ij}$  are short-ranged and possibly random, and the  $J_{ij}^\mu$  are Gaussian random exchange interactions, possibly with spin-anisotropies. The remainder  $H_{\text{int}}$  includes other possible short-range interactions between the electrons, and the resulting total Hamiltonian  $H$  has a metallic ground state.

Starting from this Hamiltonian, in [303], an effective field theory for the vicinity of a zero temperature quantum transition between a metallic spin glass (“spin density glass”) and a metallic quantum paramagnet was introduced. Following a mean-field analysis, a perturbative renormalization-group study was performed and it was found that critical properties are dominated by static disorder-induced fluctuations, and that dynamic quantum-mechanical effects are dangerously irrelevant. A Gaussian fixed point was found to be stable for a finite range of couplings for spatial dimensionality  $d > 8$ , but disorder effects always lead to runaway flows to strong coupling for  $d \leq 8$ . Moreover, scaling hypotheses for a *static* strong-coupling critical field theory were proposed. The non-linear susceptibility has an anomalously weak singularity at such a critical point.

In [304] the competition between the Kondo effect and RKKY interactions near the zero-temperature quantum critical point of an Ising-like metallic spin-glass was studied. In the ‘quantum- critical regime,’ non-analytic corrections to the Fermi liquid behavior were found for the specific heat and uniform static susceptibility, while the resistivity and NMR relaxation rate have a non-Fermi liquid dependence on temperature.

## 9.9. Summary and Remaining Problems

In this review we have tried to provide an overview on the recent developments in spin glasses. We concentrated on the topics to which substantial

efforts have been devoted in recent years and for which, in our view, the most significant progress has been achieved: 1) The numerical investigation of the equilibrium thermodynamics of finite-dimensional spin glass models with short range interactions using new and powerful methods, such as combinatorial optimization for ground state calculations (through which excited states can also be studied) and extended-ensemble Monte Carlo methods (e.g., the replica exchange method) for the location and characterization of the phase transition. The most challenging task remaining here is still the unification of the two paradigmatic pictures: the droplet picture and the mean-field scenario. Although being unsolved for several decades now, we see promising steps toward the unification of these two approaches. 2) The experimental and theoretical investigation of non-equilibrium dynamics and aging phenomena in spin glasses, especially the study of fluctuation-dissipation-theorem violations in the glassy phase and the concept of an effective (non-equilibrium) temperature. Still a lot of work has to be done, experimentally in particular, in order to put the fascinating theoretical ideas on a firm and consistent experimental ground. 3) The theoretical exploration of quantum effects in spin glasses, statically and dynamically, for mean-field models as well as finite dimensional models. Here the most demanding challenge appears to be handling the *real* time quantum dynamics at low temperatures for realistic (i.e. finite dimensional short-range interacting) models.

Unfortunately, we could not cover in this review many “glassy” topics related to and inspired by the spin-glass world. First and most actively pursued in recent years is the theory of the structural glass transition and the glass “phase”. A lot of progress has been made to make contact between spin glasses and structural glasses, the main difference being that the disorder is self-induced in the latter during the freezing process, whereas spin glasses live with frozen, time-independent disorder. Recently, it was discussed extensively that this might not be a major obstacle in relating the two systems. From a theoretical point of view, a more substantial difference between them with concrete experimental consequences is that spin glasses have a well-defined order parameter. A diverging correlation length and a divergent susceptibility defined in terms of this order parameter signify the transition. In the theory of structural glasses, apparently one cannot depend on these helpful vehicles.

Other related issues are vortex, gauge and Bragg glasses. All three appear in the context of disordered superconductors. The gauge glass model is essentially an  $XY$  spin-glass model with a random (quenched) vector poten-

tial, originally devoted for describing amorphous granular superconductors but later also taken as a paradigmatic model for amorphous high- $T_c$  superconductors. It can be analyzed in the same way as  $XY$  spin glasses and also has the same order parameter. The major questions concern the existence of a finite-temperature phase transition with or without screening effects. The vortex-glass model is a model of interacting, elastic magnetic flux lines in a random potential, which freezes at low temperatures into a glassy phase (which however escapes a clean theoretical description, since an order parameter is hard to define). If the disorder is weak, topological defects can be neglected and an elastic description is possible, starting from the Abrikosov flux line lattice and taking into account its small elastic deformation via thermal fluctuations and disorder. For such weakly disordered elastic systems a Bragg glass phase is predicted in which the true long-range order of the Abrikosov flux line lattice is transformed into a quasi long-range order. This glassy phase manifests itself also via an extremely sluggish dynamics. Upon increasing the strength of the disorder or the density of the lines (via an increased magnetic field), topological defects will proliferate, the quasi long-range order of the Bragg glass phase vanishes and the system becomes a vortex glass.

Finally one should mention Bose, Fermi and Coulomb glass models, which occur in the context of the low-temperature physics of quantum-mechanical, disordered, electronic or bosonic systems. The origin of the interesting physics is the competition between the quenched random potential and the interactions between particles, usually long ranged as in the Coulomb case. The major issues concern the phase transition between conducting (metallic or superconducting) and insulating phases, in which the particles are localized. Again the name “glass” for the low-temperature phases is justified by the anomalously slow dynamics present here.

To conclude this tour through the glass zoo we hope to have demonstrated that a review on spin glasses should not only be useful for people working in the field of frustrated magnets, but also for those encountering strong disorder and strong interactions at low temperatures in other fields of condensed matter physics.

## Acknowledgments

N.K.’s work was supported by the grant-in-aid (Program No.14540361) from Monka-sho, Japan. H.R. acknowledges financial support from the Deutsche Forschungsgemeinschaft (DFG) and from the European Commu-

nity's Human Potential Programme under contract HPRN-CT-2002-00307, DYGLAGEMEM, and thanks the KITP at UC Santa Barbara for its hospitality, where he composed large parts of this review. The authors are indebted to H. E. Castillo, C. Chamon, L. Cugliandolo, K. Hukushima, H. Kawamura, J. Kurchan, C. M. Newman, D. L. Stein, and A. P. Young for useful comments.

## References

1. J. L. van Hemmen and I. Morgenstern, Lecture Notes in Physics 192: *Heidelberg Colloquium on Spin Glasses* (Springer, 1983).
2. J. L. van Hemmen and I. Morgenstern, Lecture Notes in Physics 275: *Heidelberg Colloquium on Spin Glasses* (Springer, 1986).
3. K. H. Fischer and J. A. Hertz, *Spin Glasses* (Cambridge, 1991).
4. J. A. Mydosh, *Spin Glasses: An Experimental Introduction*, Taylor and Francis (London · Washington, DC, 1993).
5. A. P. Young (editor), *Spin Glasses and Random Fields* (World Scientific, 1998).
6. P. E. Jönsson, H. Yoshino and P. Nordblad, Phys. Rev. Lett. **89** (2002) 097201.
7. K. Binder and A. P. Young, Rev. Mod. Phys. **58** (1986) 801.
8. M. Mézard, G. Parisi and M. A. Virasoro, *Spin Glass Theory and Beyond* (World Scientific, Singapore, 1987).
9. E. Marinari *et al.*, J. Stat. Phys. **98** (2000) 973.
10. C. M. Newman and D. L. Stein, J. Phys.: Condens. Matter **15** (2003) R1319.
11. G. Parisi, Phys. Rev. Lett. **43** (1979) 1754.
12. G. Parisi, J. Phys. A: Math. Gen. **13** (1980) 1101.
13. G. Parisi, J. Phys. A: Math. Gen. **13** (1980) 1887.
14. G. Parisi, Phys. Rev. Lett. **50** (1983) 1946.
15. D. Sherrington and S. Kirkpatrick, Phys. Rev. Lett. **35** (1975) 1792.
16. M. Mezard, G. Parisi, N. Sourlas, G. Toulouse and M. Virasoro, Phys. Rev. Lett. **52** (1984) 1156.
17. M. Mezard, G. Parisi, N. Sourlas, G. Toulouse and M. Virasoro, J. Phys. (Paris) **45** (1984) 843.
18. D. J. Thouless, P. W. Anderson and R. G. Palmer, Phil. Mag. **35** (1977) 593.
19. J. R. L. de Almeida and D. J. Thouless, J. Phys. A: Math. Gen. **11** (1978) 983.
20. F. Guerra and F. L. Toninelli, J. Math. Phys. **43** (2002) 3704; J. Math. Phys. **43** (2002) 6224; Commun. Math. Phys. **230** (2002) 71; cond-mat/0205123, cond-mat/0208579.
21. C. M. Newman and D. L. Stein, Phys. Rev. Lett. **76** (1996) 515.
22. M. A. Moore and A. J. Bray, J. Phys. C **17** (1984) L613.
23. A. J. Bray and M. A. Moore, in *Heidelberg Colloquium on Spin Glasses* eds. J. L. van Hemmen and I. Morgenstern, Springer (1986) p.121.

24. D. S. Fisher and D. A. Huse, Phys. Rev. Lett. **56** (1986) 1601.
25. D. S. Fisher and D. A. Huse, Phys. Rev. B **38** (1988) 373.
26. D. S. Fisher and D. A. Huse, Phys. Rev. B **38** (1988) 386.
27. B. Drossel, H. Bokil, M. A. Moore, and A. J. Bray, Eur. Phys. J. B **13** (2000) 369.
28. W. L. McMillan, Phys. Rev. B **29** (1984) 4026.
29. W. L. McMillan, Phys. Rev. B **30** (1984) 476.
30. A. K. Hartmann and A. P. Young, Phys. Rev. B **64** (2001) 180404.
31. N. Kawashima and H. Rieger, Europhys. Lett. **39** (1997) 85.
32. C. Amoruso, E. Marinari, O. C. Martin, A. Pagnani, Phys. Rev. Lett. **91** (2003) 087201.
33. T. Shirakura and F. Matsubara, J. Phys. Soc. Jpn. **65** (1996) 3138.
34. N. Kawashima and M. Suzuki, J. Phys. A **25** (1992) 4985.
35. N. Kawashima, H. Hatano and M. Suzuki, J. Phys. A: Math. Gen. **25** (1992) 4985.
36. S. Liang, Phys. Rev. Lett. **69** (1992) 2145.
37. Y.-C. Lin, N. Kawashima, F. Iglói and H. Rieger, Prog. Theor. Phys. Suppl. **138** (2000) 479.
38. H. Rieger et al, J. Phys. A **30** (1997) 3939.
39. M. Ney-Nifle, A. P. Young, J. Phys. A **30** (1997) 5311.
40. N. Kawashima and T. Aoki, Int. J. Mod. Phys. C **10** (1999) 1453.
41. N. Kawashima, J. Phys. Soc. Jpn. **69** (2000) 987.
42. A. K. Hartmann and M. A. Moore, Phys. Rev. Lett. **90** (2003) 127201.
43. A. A. Middleton, Phys. Rev. Lett. **83**, (1999) 1672.
44. M. Palassini and A. P. Young, Phys. Rev. B **60** (1999) R9919.
45. T. Shirakura and F. Matsubara, Phys. Rev. Lett. **79** (1997) 2887.
46. R. N. Bhatt and A. P. Young, Phys. Rev. Lett. **54** (1985) 924.
47. A. T. Ogielski, Phys. Rev. B **32** (1985) 7384.
48. E. Marinari, G. Parisi and F. Ritort, J. Phys. A: Math. Gen. **27** (1994) 2687.
49. N. Kawashima and A. P. Young, Phys. Rev. B **53** (1996) R484.
50. M. Palassini and X. Caracciolo, Phys. Rev. Lett. **82** (1999) 5128.
51. H. G. Ballesteros *et al*, Phys. Rev. B **62** (2000) 14237.
52. M. Tesi, E. J. van Resburg, E. Orlandini and S. G. Whillington, J. Stat. Phys. **82** (1996) 155.
53. K. Hukushima and K. Nemoto, J. Phys. Soc. Jpn. **65** (1996) 1604.
54. F. Cooper, B. Freedman and D. Preston, Nucl. Phys. B **210** (1989) 210.
55. E. Marinari *et al.*, Phys. Rev. Lett. **81** (1998) 1698.
56. K. Gunnarsson, P. Svedlindh, P. Nordblad, L. Lundgren, H. Aruga and A. Ito, Phys. Rev. B **43** (1991) 8199.
57. R. R. P. Singh and S. Chakravarty, Phys. Rev. B **36** (1987) 559.
58. R. N. Bhatt and A. P. Young, Phys. Rev. B **37** (1988) 5606.
59. D. Iñigues, G. Parisi and J. J. Ruiz-Lorenzo, J. Phys. A **29** (1996) 4337.
60. E. Marinari and G. Parisi and J. J. Ruiz-Lorenzo, Phys. Rev. B **58** (1998) 14852.
61. B. A. Berg and W. Janke, Phys. Rev. Lett. **80** (1998) 4771.

62. P. O. Mari and I. A. Campbell, Phys. Rev. E **59** (1999) 2653.
63. P. O. Mari and I. A. Campbell, Phys. Rev. B **65** (2002) 184409.
64. T. Nakamura, S. Endoh and T. Yamamoto, J. Phys. A: Math. Gen. **36** (2003) 10895.
65. N. de Courtenay, H. Bouchiat, H. Hurdequin and A. Fert, J. Phys. (Paris) **47** (1986) 71.
66. H. Bouchiat, J. Physique **47** (1986) 71.
67. L. P. Levy and A. T. Ogielsky, Phys. Rev. Lett. **57** (1986) 3288.
68. M. Simpson, J. Phys. F **9** (1979) 1377.
69. B. R. Coles and G. Williams, J. Phys. F **18** (1988) 1279.
70. E. Vincent and J. Hammann, J. Phys. C: Solid State Phys. **20** (1987) 2659.
71. H. Kawamura, Phys. Rev. Lett. **24** (1998) 5421.
72. K. Hukushima and H. Kawamura, Phys. Rev. E **61** (2000) 1008(R).
73. F. Matsubara, T. Shirakura and S. Endoh, Phys. Rev. B **64** (2001) 092412.
74. T. Nakamura and S. Endoh, J. Phys. Soc. Jpn. **71** (2002) 2113.
75. L. W. Lee and A. P. Young, Phys. Rev. Lett. **90** (2003) 227203.
76. H. Kawamura and M. S. Li, Phys. Rev. Lett. **29** (2001) 187204.
77. M. Palassini and A. P. Young, Phys. Rev. B **63** (2001) 140408(R).
78. F. Krzakala and O. C. Martin, Europhys. Lett. **53** (2001) 749.
79. A. K. Hartmann, Europhys. Lett. **45** (1999) 619.
80. B. A. Berg, U. E. Hansmann, and T. Celik, Phys. Rev. B **50** (1994) 16444.
81. A. K. Hartmann, Europhys. Lett. **40** (1997) 429.
82. A. K. Hartmann, Europhys. Lett. **44** (1998) 249.
83. A. K. Hartmann and H. Rieger, *Optimization Algorithms in Physics*, (Wiley, Berlin 2002).
84. A. K. Hartmann, Euro. Phys. B **13** (2000) 539.
85. A. Sandvik, Europhys. Lett. **45** (1999) 745.
86. M. Palassini and A. P. Young, Phys. Rev. Lett. **83** (1999) 5126.
87. M. Palassini and A. P. Young, Phys. Rev. Lett. **85** (2000) 3017.
88. A. A. Middleton, Phys. Rev. B **63** (2001) 060202(R).
89. M. A. Moore, cond-mat/0203469.
90. J. Lamarcq, J.-P. Bouchaud, O. C. Martin and M. Mézard, Europhys. Lett. **58** (2002) 321.
91. M. Palassini, F. Liers, M. Jünger and A. P. Young, Phys. Rev. B **68** (2003) 064413.
92. M. Jünger, G. Reinelt and S. Thienel, in *DIMACS Series in Discrete Mathematics and Theoretical Computer Science*, Volume 20, W. Cook, L. Lovasz and P. Seymour eds. (American Mathematical Society, 1995)
93. E. Marinari and G. Parisi, Phys. Rev. Lett. **85** (2000) 3332.
94. E. Marinari and G. Parisi, Phys. Rev. B **62** (2000) 11677.
95. E. Marinari and G. Parisi, Phys. Rev. Lett. **86** (2001) 3887.
96. M. Palassini and A. P. Young, Phys. Rev. Lett. **85** (2000) 3333.
97. F. Krzakala, J. Houdayer, E. Marinari, O. C. Martin, and G. Parisi, Phys. Rev. Lett. **87** (2001) 197204.
98. J. Houdayer and O. C. Martin, Europhys. Lett. **49** (2000) 794.
99. F. Krzakala and O. C. Martin, Phys. Rev. Lett. **85** (2000) 03013.

100. J. Houdayer, F. Krzakala, and O. C. Martin, Eur. Phys. J. B **18** (2000) 467.
101. H. G. Katzgraber, M. Palassini, and A. P. Young, Phys. Rev. B **63** (2001) 184422.
102. D. Huse and D. Fisher, J. Phys. A **20** (1987) L997.
103. E. Marinari and G. Parisi and J. J. Ruiz-Lorenzo, in *Spin Glasses and Random Fields* (ed. A. P. Young, World Scientific, 1998).
104. R. R. P. Singh and S. Chakravarty, Phys. Rev. Lett. **57** (1986) 245.
105. G. Parisi, F. Ricci-Tersenghi, and J. J. Ruiz-Lorenzo, J. Phys. A **29** (1996) 7943.
106. J. D. Reger, R. N. Bhatt and A. P. Young, Phys. Rev. Lett. **64** (1990) 1859.
107. A. K. Hartmann, Phys. Rev. E **60** (1999) 05135.
108. H. G. Katzgraber and A. P. Young, Phys. Rev. B **67** (2003) 134410.
109. H. G. Katzgraber and A. P. Young, Phys. Rev. B **68** (2003) 224408.
110. J.-P. Bouchaud, L. F. Cugliandolo, J. Kurchan, and M. Mézard, in *Spin glasses and Random Fields*, ed. A. P. Young (World Scientific Singapore, 1998), pp. 161-224.
111. E. Vincent, J. Hamman, M. Ocio, J.-P. Bouchaud, and L. F. Cugliandolo, in *Complex Behaviour of Glassy Systems*, Lecture Notes in Physics **492**, ed. M. Rubi (Springer-Verlag, Berlin, 1997), pp. 184-219.
112. P. Nordblad and P. Svedlindh, in *Spin glasses and Random Fields*, ed. A. P. Young (world Scientific Singapore, 1998), pp. 1-28.
113. C. A. Angell, Science **267** (1995) 1924.
114. A. J. Bray, Adv. Phys. **43** (1994) 357.
115. D. S. Fisher and D. A. Huse, Phys. Rev. B **38** (1988) 373; **38** (1988) 386.
116. For a review see T. Natterman, in *Spin glasses and Random Fields*, ed. A. P. Young (world Scientific Singapore, 1998).
117. D. S. Fisher and D. A. Huse, **43** (1991) 10728.
118. H. Rieger, B. Steckemetz and M. Schreckenberg, Europhys. Lett. **27** (1994) 485.
119. H. Rieger, Annual Review of Computers and Physics II, edited by D. Stauffer (World Scientific, Singapore, 1995).
120. J. Kisker, L. Santen, M. Schreckenberg and H. Rieger, Phys. Rev. B **53** (1996) 6418.
121. E. Marinari, G. Parisi, F. Ritort, and J. J. Ruiz-Lorenzo, Phys. Rev. Lett. **76** (1996) 843.
122. T. Komori, H. Yoshino , and H. Takayama, J. Phys. Soc. Jpn. **68** (1999) 3387.
123. E. Marinari, G. Parisi, F. Ricci-Tersenghi, and J. J. Ruiz-Lorenzo, J. Phys. A **33** (2000) 2373.
124. K. Hukushima, H. Yoshino, and H. Takayama, Prog. Theor. Phys. Suppl. **138** (2000) 568.
125. H. Yoshino, K. Hukushima, H. Takayama, Phys. Rev. B **66**, (2002) 064431.
126. L. Berthier and J.-P. Bouchaud, Phys. Rev. B **66** (2002) 054404.
127. Y. G. Joh, R. Orbach, G. G. Wood, J. Hamman, E. Vincent, Phys. Rev. Lett. **82** (1999) 438.
128. G. J. Koper and H. J. Hilhorst, J. Phys. (France) **49** (1988) 429.

129. H. Rieger, J. Phys. A **26** (1993) L615.
130. V. Dupis, E. Vincent, J.-P. Bouchaud, J. Hammann, A. Ito, and H.A. Katori, Phys. Rev. B **64** (2001) 174204.
131. P.E. Jönsson, H. Yoshino, P. Nordblad, H. Aruga Katori, and A. Ito, Phys. Rev. Lett. **88** (2002) 257204.
132. J.-P. Bouchaud, V. Dupuis, J. Hamman, and E. Vincent, Phys. Rev. B **65** (2001) 024439.
133. H. K. Janssen, B. Schaub, and B. Schmittmann, Z. Phys. B. **73** (1989) 539.
134. D. Huse, Phys. Rev. B **40** (1989) 304.
135. A. G. Schins, A. F. M. Arts, and H. W. de Wijn, Phys. Rev. Lett. **70** (1993) 2340.
136. J. Mattson, T. Jönsson, P. Nordblad, H. Aruga Katori, Phys. Rev. Lett. **74** (1995) 4305.
137. For a comprehensive review over the various analytical predictions of mean field theory for glassy dynamics see: L. F. Cugliandolo, eprint cond-mat/0210312.
138. L. F. Cugliandolo and J. Kurchan, J. Phys. A **27** (1994) 5749.
139. L. Berthier, J.-L. Barrat, and J. Kurchan, Phys. Rev. E **63** (2001) 016105.
140. E. Bertin and J. P. Bouchaud, J. Phys. A **35** (2002) 3039.
141. M. Picco, F. Ricci-Tersenghi, and F. Ritort, Eur. Phys. J. B **21** (2001) 211.
142. L. Berthier, Eur. Phys. J. B **17** (2000) 689.
143. D. S. Fisher, P. Le Doussal, and C. Monthus, Phys. Rev. E **64** (2001) 066107.
144. L. C. E. Struik, *Physical Aging in Amorphous Polymers and Other Materials* (Elsevier, Amsterdam, 1978).
145. J. Kurchan, Phys. Rev. E **66** (2002) 017101.
146. J. Hamman, M. Lederman, M. Ocio, R. Orbach, and E. Vincent, Physica A **185** (1992) 278.
147. T. Komori, H. Yoshino, and H. Takayama, J. Phys. Soc. Jpn. **69** Suppl. A (2000) 228.
148. P. E. Jönsson, H. Yoshino, and P. Nordblad, Phys. Rev. Lett. **89** (2002) 097201.
149. Ludovic Berthier et al., Phys. Rev. Lett. **90** (2003) 059701.
150. P. E. Jönsson, H. Yoshino and P. Nordblad, Phys. Rev. Lett. **90** (2003) 059702.
151. A. J. Bray and M. A. Moore, Phys. Rev. Lett. **58** (1987) 57.
152. H. Rieger, L. Santen, U. Blasum, M. Diehl, and M. Jünger, J. Phys. A **29** (1996) 3939.
153. A. Billoire and E. Marinari, J. Phys. A **33** (2000) L265.
154. H. Yoshino, K. Hukushima, and H. Takayama, cond-mat/0202110.
155. P. Réfrégier, E. Vincent, J. Hamman, and M. Ocio, J. Phys. (France) **48** (1987) 1533 .
156. L. Lundgren, P. Svedlindh, and O. Beckman, J. Magn. Magn. Mat. **31-34** (1983) 1349.
157. H. Rieger, J. Physique I **4** (1994) 883.
158. L. F. Cugliandolo and J. Kurchan, Phys. Rev. B **60** (1999) 922 .
159. J. P. Bouchaud, in *Soft and Fragile Matter*, ed. M. E. Cates and M. R. Evans

- (Institute of Physics, Bristol, 2000), e-print cond-mat/9910387.
160. H. Takayama, H. Yoshino, and T. Komori, cond-mat/9909228.
  161. M. Picco, F. Ricci-Tersenghi, and F. Ritort, Phys. Rev. B **63**, (2000) 174412.
  162. L. W. Bernardi, H. Yoshino, K. Hukushima, H. Takayama, A. Tobe, and A. Ito, Phys. Rev. Lett. **86** (2001) 720.
  163. K. Jonason, E. Vincent, J. Hamman, J.-P. Bouchaud, and P. Nordblad, Phys. Rev. Lett. **81** (1998) 3243.
  164. H. Yoshino, A. Lemaitre, and J. P. Bouchaud, Eur. Phys. J. B **20** (2001) 367.
  165. M. Sales and H. Yoshino, Phys. Rev. E **65** (2002) 066131.
  166. K. Jonason, J. Mattsson, and P. Nordblad, Phys. Rev. Lett. **77** (1996) 2562.
  167. K. Jonason and P. Nordblad, Europ. Phys. J. B **10** (1999) 23.
  168. E. Vincent, V. Dupuis, M. Alba, J. Hammann, and J.-P. Bouchaud, Europhys. Lett. **50** (2000) 674.
  169. J. Hamman, E. Vincent, V. Dupuis, M. Alba, M. Ocio, and J.-P. Bouchaud, J. Phys. Soc. Jap. **69** Suppl. A (2000) 296.
  170. E. Vincent, F. Alet, J. Hamman, M. Ocio, and J. P. Bouchaud, Europhys. Lett. **50** (2000) 674.
  171. P. Doussineau, T. de Lacerda-Aroso, A. Levelut, Europhys. Lett. **46** (1999) 401.
  172. J.-P. Bouchaud, P. Doussineau, T. de Lacerda-Aroso, and A. Levelut, Eur. Phys. J B **21** (2001) 335.
  173. A.V. Kityk, M.C. Rheinstädter, K. Knorr, and H. Rieger, Phys. Rev. B **65** (2002) 144415.
  174. E. Vincent, J. Hamman, M. Ocio, in *Recent Progress in Random Magnets* (World Scientific, Singapore, 1992).
  175. J.-P. Bouchaud and D. S. Dean, J. Phys. I (France) **5** (1995) 265.
  176. M. Sasaki and K. Nemoto, J. Phys. Soc. Jpn. **69** (2000) 2283; **69** (2000) 2642.
  177. L. Balents, J.-P. Bouchaud, and M. Mézard, J. Phys. I (France) **6** (1996) 1007.
  178. L. F. Cugliandolo, J. Kurchan, and L. Peliti Phys. Rev. E **55** (1997) 3898.
  179. L. F. Cugliandolo and J. Kurchan, Phys. Rev. Lett. **71** (1993) 173.
  180. S. Franz and H. Rieger, J. Stat. Phys. **79** (1995) 749.
  181. J. O. Andersson, J. Mattsson, and P. Svedlindh, Phys. Rev. B **46** (1992) 8297.
  182. E. Marinari, G. Parisi, F. Ricci-Tersenghi, and Juan J. Ruiz-Lorenzo, J. Phys. A **31** (1998) 2611 .
  183. L. Berthier, J.-L. Barrat and J. Kurchan, Eur. Phys. J. B **11** (1999) 635.
  184. A. Barrat and L. Berthier, Phys. Rev. Lett. **87** (2001) 087204.
  185. D. Herisson and M. Ocio, Phys. Rev. Lett. **88** (2002) 257202.
  186. L. F. Cugliandolo, D. R. Grempel, J. Kurchan, and E. Vincent, Europhys. Lett. **48** (1997) 699 .
  187. T. S. Grigera and N. E. Israeloff , Phys. Rev. Lett. **83** (1999) 5038 .
  188. L. Bellon and S. Ciliberto, preprint cond-mat/0201224.
  189. C. Chamon, M. P. Kennett, H. E. Castillo, and L. F. Cugliandolo, Phys.

- Rev. Lett. **89** (2002) 217201.
- 190. H. E. Castillo, C. Chamon, L. F. Cugliandolo, M. P. Kennett, Phys. Rev. Lett. **88** (2002) 237201 .
  - 191. F. Pazmandi, G. Zarand, G. T. Zimanyi, Phys. Rev. Lett. **83** (1999) 1034.
  - 192. G. Zaránd, F. Pázmándi, K. F. Pál, and G. T. Zimányi, Phys. Rev. Lett. **89** (2002) 150201.
  - 193. H. G. Katzgraber, F. Pazmandi, C. R. Pike, Kai Liu, R. T. Scalettar, K. L. VeroSub, and G. T. Zimanyi, Phys. Rev. Lett. **89** (2002) 257202.
  - 194. H. G. Katzgraber, Gary Friedman, and G. T. Zimanyi, Physica B **343**, (2004) 10; cond-mat/0307178.
  - 195. C. R. Pike, A. P. Roberts, and K. VeroSub, J. Appl. Phys. **85** (1999) 6660.
  - 196. F. Preisach, Z. Phys. **94** (1935) 277.
  - 197. D. Petit, L. Fruchter, and I. A. Campbell, Phys. Rev. Lett. **83**, (1999) 5130.
  - 198. D. Petit, L. Fruchter, and I. A. Campbell, Phys. Rev. Lett. **88**, (2002) 207206.
  - 199. H. Kawamura, Can. J. Phys. **79** (2001) 1447.
  - 200. J. Maucourt and D. R. Grempel, Phys. Rev. Lett. **80** (1998) 770.
  - 201. N. Akino and J. M. Kosterlitz, Phys. Rev. B **66** (2002) 054536.
  - 202. F. Matsubara, S. Endoh and T. Shirakura, J. Phys. Soc. Jpn. **69** (2000) 1927.
  - 203. S. Endoh, F. Matsubara and T. Shirakura, J. Phys. Soc. Jpn. **70** (2001) 1543.
  - 204. A. Sadic and K. Binder, J. Stat. Phys. **35** (1984) 517.
  - 205. D. Imagawa and H. Kawamura, Phys. Rev. B **67** (2003) 224412.
  - 206. T. R. Kirkpatrick and D. Thirumalai, Phys. Rev. B **36** (1987) 8552.
  - 207. T. R. Kirkpatrick and D. Thirumalai, Phys. Rev. B **37** (1988) 5342.
  - 208. U. Bengtzelius, W. Götze, and A. Sjölander, J. Phys. C **17** (1984) 5915.
  - 209. W. Götze, *Liquids, freezing and the glass transition*, ed. J. P. Hansen, D. Levesque, and J. Zinn-Justin (Amsterdam, North Holland, 1990), p.287.
  - 210. C. Brangian, W. Kob, and K. Binder, Europhys. Lett. **59**, 546 (2002); J. Phys. A in press; cond-mat/0211195.
  - 211. C. Brangian, W. Kob, and K. Binder, J. Phys. A: Math. Gen. **36** (2003) 10847.
  - 212. C. Brangian, W. Kob, and K. Binder, J. Phys. A : Math. Gen. **35** (2002) 191.
  - 213. C. Brangian, W. Kob, and K. Binder, Phil. Mag. B **82** (2002) 663.
  - 214. C. Brangian, W. Kob, and K. Binder, Europhys. Lett. **53** (2001) 756.
  - 215. H. Nishimori, Physica A **306** (2002) 68.
  - 216. H. Nishimori, Prog. Theor. Phys. **66** (1981) 1169.
  - 217. H. Nishimori, J. Phys. Soc. Jpn. **55** (1986) 3305.
  - 218. H. Nishimori, C. Falvo and Y. Ozeki, J. Phys. A: Math. Gen. **39** (2002) 8171.
  - 219. R. R. P. Singh and J. Adler, Phys. Rev. B **54** (1996) 364.
  - 220. Y. Ozeki, J. Phys.: Condens. Matter **9** (1997) 11171.
  - 221. A. B. Harris, J. Phys. C **7** (1974) 1671.
  - 222. G. Grinstein and A. Luther, Phys. Rev. B **13** (1976) 1329.

223. H.-O. Heuer, J. Phys. A: Math. Gen. **26** (1993) L333.
224. I. O. Mayer, J. Phys. A: Math. Gen. **22** (1989) 2815.
225. P. Le Doussal and A. B. Harris, Phys. Rev. Lett. **61** (1988) 625.
226. H. G. Ballesteros *et al*, Phys. Rev. B **58** (1998) 2740.
227. J. C. LeGuillou and J. Zinn-Justin, Phys. Rev. B **21** (1980) 3976.
228. K. Hukushima, J. Phys. Soc. Jpn. **69** (2000) 631.
229. M. Suzuki, Prog. Theor. Phys. **58** (1977) 1142.
230. M. Suzuki, Phys. Lett. A **58** (1978) 435.
231. Y. Ozeki and N. Ito, J. Phys. A: Math. Gen. **31** (1998) 5451.
232. H. Nishimori and K. Nemoto, Physica A **321** (2003) 108.
233. F. Y. Wu and Y. K. Wang, J. Math. Phys. **17** (1976) 439.
234. H. Nishimori, J. Phys. C **12** (1979) L905.
235. F. D. A. Arao Reis, S. L. A. de Queiroz and R. R. dos Santos, Phys. Rev. B **60** (1999) 6740.
236. M. Rubinstein, B. Shraiman and D. R. Nelson, Phys. Rev. B **27** (1983) 1800.
237. T. Nattermann, S. Scheidl, S. E. Korshunov and M. S. Li, J. Phys. (France) I **5** (1995) 565.
238. M.-C. Cha and H. A. Fertig, Phys. Rev. Lett. **74** (1995) 4867.
239. L.-H. Tang, Phys. Rev. B **54** (1996) 3350.
240. S. Scheidl, Phys. Rev. B **55** (1997) 457.
241. D. Carpentier and P. Le Doussal, Nucl. Phys. B **588** (2000) 565.
242. D. R. Nelson, Phys. Rev. B **27** (1983) 2902.
243. W. Wu, B. Ellmann, T. F. Rosenbaum, G. Aeppli, and D. H. Reich, Phys. Rev. Lett. **67** (1991) 2076; W. Wu, D. Bitko, T. F. Rosenbaum, and G. Aeppli, Phys. Rev. Lett. **71** (1993) 1919.
244. S. Sachdev: *Quantum Phase Transitions* (Cambridge University Press, 1999).
245. B. K. Chakrabarti, A. Dutta, and P. Sen, *Quantum Ising Phases and Transitions in Transverse Ising Models*, (Springer, Heidelberg, 1996).
246. H. Rieger and A. P. Young: *Quantum Spin Glasses*, Lecture Notes in Physics **492** "Complex Behaviour of Glassy Systems", p. 254, ed. J.M. Rubi and C. Perez-Vicente (Springer Verlag, Berlin-Heidelberg-New York, 1997).
247. R. N. Bhatt in *Spin glasses and Random Fields*, ed. A. P. Young (World Scientific, Singapore, 1998).
248. D. S. Fisher, Physica A **263** (1999) 222.
249. B.M. McCoy and T.T. Wu, Phys. Rev. **176** (1968) 631; **188** (1969) 982; B.M. McCoy, Phys. Rev. **188** (1969) 1014.
250. D.S. Fisher, Phys. Rev. Lett. **69** (1992) 534; Phys. Rev. B **51** (1995) 6411.
251. S. K. Ma, C. Dasgupta, and C.-K. Hu, Phys. Rev. Lett. **43** (1979) 1434; C. Dasgupta and S. K. Ma, Phys. Rev. B **22** (1980) 1305.
252. F. Iglói and H. Rieger, Phys. Rev. Lett. **78** (1997) 2473.
253. F. Iglói and H. Rieger, Phys. Rev. B **57** (1998) 11404.
254. H. Rieger and F. Iglói, Europhys. Lett. **39** (1997) 135.
255. F. Iglói, D. Karevski and H. Rieger, Europ. Phys. J. B **1** (1998) 513; **5** (1998) 613.
256. F. Iglói and H. Rieger, Phys. Rev. E **58** (1998) 4238.

257. F. Iglói, R. Juhász and H. Rieger, Phys. Rev. B **59** (1999) 11308.
258. H. Rieger and F. Iglói, Phys. Rev. Lett. **83** (1999) 3741.
259. F. Iglói, R. Juhász und H. Rieger, Phys. Rev. B **61** (2000) 11552.
260. A. P. Young and H. Rieger, Phys. Rev. B **53** (1996) 8486.
261. M. J. Thill and D. A. Huse, Physica A **214**, (1995) 321.
262. H. Rieger and A. P. Young, Phys. Rev. B **54** (1996) 3328.
263. T. Senthil and S. Sachdev, Phys. Rev. Lett. **77**, (1996) 5292.
264. T. Ikegami, S. Miyashita and H. Rieger, J. Phys. Soc. Jap. **67** (1998) 2761.
265. C. Pich, A. P. Young, H. Rieger and N. Kawashima, Phys. Rev. Lett. **81** (1998) 5916.
266. H. Rieger and N. Kawashima, Europ. Phys. J. B **9** (1999) 233.
267. O. Motrunich, S.-C. Mau, D. A. Huse, D. S. Fisher, Phys. Rev. B **61** (2000) 1160.
268. H. Rieger and A. P. Young, Phys. Rev. Lett. **72** (1994) 4141.
269. M. Guo, R. N. Bhatt, and D. A. Huse, Phys. Rev. Lett. **72** (1994) 4137.
270. M. Guo, R. N. Bhatt, and D. A. Huse, Phys. Rev. B **54** (1996) 3336.
271. L. F. Cugliandolo, D. R. Gremel, and C. A. da Silva Santos, Phys. Rev. Lett. **85** (2000) 2589; Phys. Rev. B **64** (2001) 014403.
272. Y. V. Fedorov and E. F. Shender, Zh. Eksp. Teor. Fiz. **43** (1986) 526 [JETP Lett. **43** (1986) 681].
273. Y. Y. Goldschmidt and P. Y. Lai, Phys. Rev. Lett. **64** (1990) 2467.
274. K. D. Usadel and B. Schmidt, Solid State Comm. **64** (1987) 975.
275. T. Yamamoto and H. Ishii, J. Phys. C. **20** (1987) 6053.
276. J. Miller and D. A. Huse, Phys. Rev. Lett. **70** (1993) 3147.
277. J. Ye, S. Sachdev, and N. Read, Phys. Rev. Lett. **70** (1993) 4011.
278. N. Read, S. Sachdev, and J. Ye, Phys. Rev. B **52** (1995) 384.
279. A. J. Bray and M. A. Moore, J. Phys. C **13** (1980) L655.
280. M. J. Rozenberg and D. R. Gremel, Phys. Rev. Lett. **81** (1998) 2550.
281. D. R. Gremel and M. J. Rozenberg, Phys. Rev. Lett. **80** (1998) 389.
282. L. F. Cugliandolo, D. R. Gremel, G. Lozano, H. Lozza, and C. A. da Silva Santos, Phys. Rev. B **66** (2002) 014444.
283. A. J. Leggett et al., Rev. Mod. Phys. **59** (1987) 1; **67** (1995) 725.
284. U. Weiss, in Series Modern Condensed Matter Physics Vol. 2. (World Scientific, Singapore, 1993).
285. A. O. Caldeira and A. J. Leggett, Phys. Rev. Lett. **46** (1981) 211; Ann. Phys. N.Y. **149** (1983) 374.
286. A. J. Bray and M. A. Moore, Phys. Rev. Lett. **49** (1982) 1545.
287. S. Chakravarty, Phys. Rev. Lett. **49** (1982) 681; S. Chakravarty and A. J. Leggett, ibid. **52** (1984) 5.
288. R. P. Feynman and F. L. Vernon, Jr., Ann. Phys. N.Y. **24** (1963) 118.
289. N. V. Prokof'ev and P. C. E. Stamp, Phys. Rev. Lett. **80** (1998) 5794.
290. H. Grabert, P. Schramm, and G-L. Ingold, Phys. Rep. **168** (1988) 115.
291. P. W. Anderson and G. Yuval, Phys. Rev. Lett. **32**,(1969) 89; J. Phys. C **4** (1971) 607; P. W. Anderson, G. Yuval, and D. R. Hammann, Phys. Rev. B **1** (1970) 4464.
292. L. F. Cugliandolo and G. Lozano, Phys. Rev. Lett. **80** (1998) 4979.

293. T. Giamarchi and P. Le Doussal, Phys. Rev. **B53** (1996) 15206.
294. Y. Nonomura and Y. Ozeki, J. Phys. Soc. Jpn., **64** (1995) 2710.
295. J. Oitmaa and O. P. Sushkov, Phys. Rev. Lett. **87** (2001) 167206.
296. D. S. Fisher, Phys. Rev. B **50** (1994) 3799.
297. R. Mélin, Y.-C. Lin, P. Lajkó, H. Rieger and F. Iglói, Phys. Rev. B **65** (2002) 104415.
298. Y.-C. Lin, R. Mélin, H. Rieger and F. Iglói, Phys. Rev. B **68** (2003) 024424.
299. A. Georges, O. Parcollet, and S. Sachdev, Phys. Rev. Lett. **85** (2000) 840; Phys. Rev. B **63** (2001) 134406.
300. G. Biroli and O. Parcollet, Phys. Rev. B **65** (2002) 094414.
301. J. A. Hertz, Phys. Rev. B **19** (1979) 4796.
302. R. Oppermann and M. Binderberger, Ann. Phys. (N.Y.) **3** (1994) 494.
303. S. Sachdev, N. Read, and R. Oppermann, Phys. Rev. B **52** (1995) 10286.
304. A. Sengupta and A. Georges, Phys. Rev. B **52** (1995) 10295.
305. W. D. Wu et al., Phys. Rev. Lett. **72** (1994) 3722.

## INDEX

- 120° structure, 5  
16-vertex model, 10  
32-vertex model, 12
- AC-susceptibility measurements, 436  
AFT, 65, 76  
aging, 492, 523, 532, 533, 545, 580, 585  
AKLT point, 315, 318, 337, 340  
Anderson's model antiferromagnet, 375  
antiferromagnetic triangular lattice, 6  
antiferromagnetic triangular lattice, AFT, 62
- bct, 184, 193, 198, 199  
breakdown of symmetry, 178, 179, 193  
breakdown of symmetry, ferromagnets, 179  
breakdown of symmetry, frustrated systems, 181
- chiral order parameter, 7  
continuous spin models, 544  
critical exponents, 108, 117, 120, 122, 123, 127, 128, 130, 139, 144, 160, 163, 166, 170, 180, 193, 198–200, 213  
critical exponents, spin glass, 500, 508, 522, 526, 531, 547, 556, 564, 572, 582  
critical indices, spin glass, 500, 503, 522, 546, 556
- critical point, spin glass, 504, 505, 517, 522, 529, 545, 555, 556, 564, 568, 570, 572, 574, 583, 584  
critical slowing-down, 564  
crystal field interactions, 380  
cubic lattice, 185, 193  
cubic term, 191, 193
- deconfined phases, 255  
deconfined spinons, 256, 282  
degeneracy, 60, 62, 65, 69, 76, 78, 82, 102  
dihedral lattice, 189, 191, 193, 195, 197–199  
dimerization, 328–330, 336, 339, 343, 347  
dipolar interactions, 393  
dipolar spin ice model, 393  
disorder lines, 9, 30, 33, 35, 51, 55  
disorder solutions, 9, 23, 28, 31, 34, 40, 55  
droplet picture, 492, 496, 500, 502, 509, 511, 515, 517, 519, 520, 530, 585
- edge states, 319–321, 326, 331, 354  
Ewald summation method, 397  
exact diagonalizations, 236, 243, 245, 263, 275, 280
- fcc, 187, 193  
ferromagnets, 193  
fixed point, 120, 126, 128, 131, 134, 137, 138, 141, 143, 156, 170, 193,

- 196, 220  
 free-fermion condition, 13  
 frustration, 181  
 frustration, definition, 2, 177  
 fully frustrated lattice, 193, 210  
 fully frustrated simple cubic lattice, 186  
 Ginzburg-Landau-Wilson model, 136  
 Goldstone modes, 113, 132, 148, 152, 262  
 Haldane gap, 241, 313, 315, 317, 318, 320  
 Haldane's conjecture, 293, 294  
 hcp, 187, 193  
 Heisenberg quantum spin glasses, 581  
 Heisenberg spin, 193, 197, 199, 201, 214  
 Heisenberg spin glasses, 549, 562  
 helicity, 213  
 helimagnets, 184, 193  
 hidden order, 316, 317  
 incommensurability, 310, 340–342, 344, 345, 354  
 Ising antiferromagnetic triangular lattice, 65  
 Ising paramagnet, 96  
 Ising spin glasses, 498, 503, 508, 531  
 Ising stacked antiferromagnetic triangular lattice, 87  
 J1-J2 model, 212, 231  
 J1-J2 square lattice model, 185  
 Kagomé lattice, 101, 102, 241, 253, 266, 274, 284  
 Kagomé lattice, 31  
 kinks, 312, 313, 327, 336, 338  
 Kosterlitz-Thouless transition, 211, 212, 219  
 Landau–Ginzburg, 191, 220  
 large- $N$  approach, 245, 247, 295  
 liquid-gas type transition, 415  
 loop Monte Carlo methods, 404  
 lower critical dimension, 493, 499, 503  
 magnetization measurements, 419, 443  
 Majorana fermions, 315, 323, 328, 343, 347, 351  
 Majumdar-Ghosh model, 336, 337  
 Monte Carlo simulation, 216  
 multi-critical point, spin glass, 558  
 multiple-spin exchange, MSE, 230, 274  
 neutron scattering, 391  
 neutron scattering measurements, 433, 436  
 neutron scattering methods, 413  
 non perturbative approaches, 107, 128, 129, 131, 170  
 non perturbative method, 143  
 non universal scaling, 130  
 non-collinear spin configuration, 5  
 Nonlinear Sigma model, 131  
 nonperturbative renormalization group, 128  
 order by disorder, 9, 231, 232, 247  
 partial disorder, 38, 50, 52–54, 56, 68  
 partially ordered phase, 31  
 Pauling's Model, 371  
 perturbative approaches, 108, 129, 152, 169, 170  
 perturbative series, 130  
 Potts model, 50, 179, 180, 205  
 pyrochlores, 188, 193  
 QDM, 256, 262, 264, 267, 273, 280, 289  
 quantum dimer models, QDM, 230, 256  
 quantum hexagonal lattice, 262  
 quantum Monte Carlo, 236, 255  
 quantum spin glasses, 562, 570, 581  
 rare earth titanates, 380, 447

- reentrance, 26, 50  
renormalization group, 107, 194, 220  
replica-symmetry-breaking, 493  
resonating valence-bond, RVB, 230  
RSB, 493, 495, 502, 507, 512, 516,  
  520, 544  
RVB, 246, 256, 262, 264, 276, 278,  
  292, 306
- Schwinger bosons, 245  
self-averaging, 495, 498, 507, 521, 565  
series expansions, 234, 244  
Sherrington-Kirkpatrick model, 493,  
  537, 571  
specific heat measurements, 385, 419  
spin dynamics, 433  
spin glass, 491  
spin glass, mean-field picture, 493  
spin ice, 368  
spin ice model - definition of, 378  
spin ice materials, 368, 380  
spin-ice, 101  
spinons, 255, 271, 310–313, 322, 330,  
  333, 334, 343, 346  
square lattice, 212  
STA, 109, 120, 181, 188, 193, 195,  
  198–200  
stacked triangular antiferromagnets,  
  109, 188, 195  
stacked triangular antiferromagnets,  
  STA, 181  
STAR, 188, 193, 198, 199  
Stiefel model, 207, 215  
string order, 317, 319–321, 325, 326
- topological defect, 210, 214, 216  
topological distinction, 321, 325, 326,  
  330, 354  
triangular antiferromagnetic lattice,  
  193  
triangular lattice, 210, 212, 213, 263  
trihedral lattice, 189, 193, 197  
two-leg ladders, 276  
two-leg spin ladder, 321, 323–329,  
  331, 336, 339, 343, 354
- underconstraining arguments, 383  
universality class, 179, 193  
universality class, spin glass, 505
- valence bond solids, VBS, 240  
valence-bond crystals, VBC, 238  
VBC, 243, 246, 290  
VBS, 247, 289  
VBS state, 316–318, 320  
vertex models, 10, 376  
Villain lattice, 6, 50, 60, 62, 65, 97,  
  186, 193, 207, 210
- Wigner crystal, 276
- XY spin, 193, 195, 198–200, 210
- zero point entropy, 371, 385, 428  
zig-zag model, 188, 193